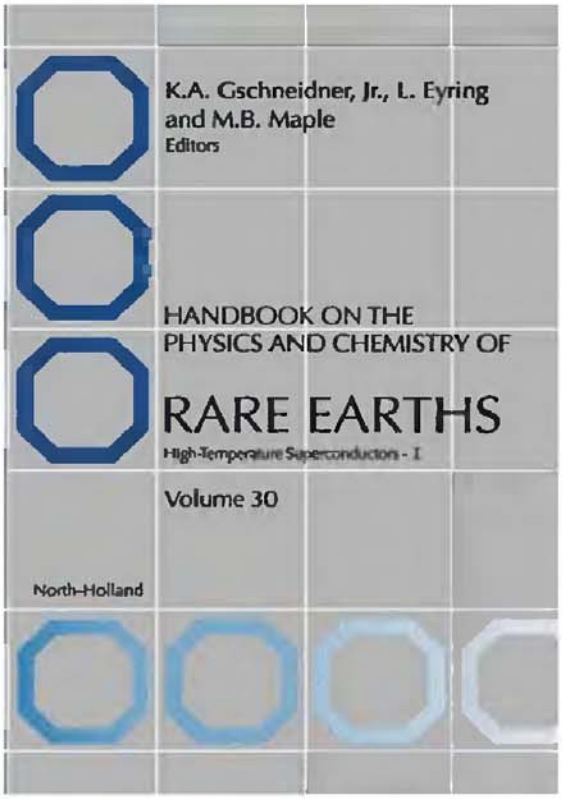

Handbook on the Physics and Chemistry of Rare Earths, **volume 30**

High-Temperature Superconductors - I

Elsevier, 2000

Edited by: Karl A. Gschneidner, Jr., LeRoy Eyring and M. Brian Maple
ISBN: 978-0-444-50528-6

Handbook on the Physics and Chemistry of Rare Earths
Vol. 30
edited by K.A. Gschneidner, Jr., L. Eyring and M.B. Maple

PREFACE

Karl A. GSCHNEIDNER, Jr., LeRoy EYRING, and M. Brian MAPLE

These elements perplex us in our rearches [sic], *baffle us in our speculations, and haunt us in our very dreams. They stretch like an unknown sea before us – mocking, mystifying, and murmuring strange revelations and possibilities.*

Sir William Crookes (February 16, 1887)

This volume of the Handbook is the first of a two-volume set of reviews devoted to the rare-earth-based high-temperature oxide superconductors (commonly known as hiT_C superconductors). The history of hiT_C superconductors is a few months short of being 14 years old as of the date of composing this Preface. The initial breakthrough came late in 1986 when Bednorz and Müller published their results which showed that $(La,Ba)_2CuO_4$ had a superconducting transition of ~30 K, which was about 7 K higher than any other known superconducting material. Within a year the upper temperature limit was raised to nearly 100 K with the discovery of an ~90 K superconducting transition in $YBa_2Cu_3O_{7-\delta}$. The announcement of a superconductor with a transition temperature higher than the boiling point of liquid nitrogen set-off a frenzy of research on trying to find other oxide hiT_C superconductors. Within a few months the maximum superconducting transition reached 110 K ($Bi_2Sr_2Ca_2Cu_3O_{10}$), and then 122 K ($TlBa_2Ca_3Cu_4O_{11}$). It took several years to push T_C up another 11 K to 133 K with the discovery of superconductivity in $HgBa_2Ca_2Cu_3O_8$, which is still the record holder today.

Because of the rapid development of our knowledge of these materials, a review on this topic several years ago would have been hopelessly out of date even before the paper would be sent to the publisher. About five years ago the field began to mature and we felt it would be a good time to look into the possibility of publishing a series of review papers on rare-earth-containing hiT_C superconductors.

Because of the size of this project and the limited knowledge of the senior editors on this topic we recruited Prof. Brian Maple to assist us in undertaking this task. Our efforts have paid off in the form of volumes 30 and 31 of the Handbook series.

There are eight chapters in this volume, and ten more will follow in volume 31. The lead-off chapter (187), an overview, by M.B. Maple, sets the tone for this series of eighteen chapters. He notes that significant progress has been made in both our basic understanding of these oxide superconductors and the development of technological applications. One of

the major hurdles was the quality of these hiT_C compounds – it was not a simple matter of "shake and bake". Once high-quality polycrystalline samples, single crystals and thin film materials were available, reliable and reproducible measurements of the electrical, magnetic and other physical properties provided important information on the anomalous normal-state properties, the symmetry of the superconducting order parameter, and the vortex phases and dynamics in the cuprate materials.

The crystal chemistry of the rare-earth cuprates is discussed in chapter 188 by B. Raveau, C. Michel and H. Hervieu. These authors noted that all of the hiT_C superconductors are derived from the perovskite structure. This is done by disconnecting the CuO_6 octahedra of the perovskite structure along one direction so then an infinite number of CuO_2 layers are formed. These layers are responsible for the superconductivity. Raveau *et al.* note that the rare-earth cations are not directly responsible for the appearance of superconductivity, but by virtue of their large size and trivalent character they help stabilize these layered structures.

This topic is followed by an extensive review (chapter 189) on preparing single crystals of these hiT_C oxides by Y. Shiohara and E. Goodilin. These authors describe (1) the fundamentals of crystal growth, including supersaturation effects, and rate limiting factors, such as interfacial kinetics; (2) the mechanism of the crystal growth of the $RBa_2Cu_3O_{7-\delta}$ phases from the melt; (3) the common techniques utilized in growing these phases; (4) the characterization of the single crystals; and (5) practical ways of improving their quality and perfection, yield and size.

The road maps needed to obtain these high-quality single crystals and, for that matter, polycrystalline materials, are presented in chapter 190 by P. Karen and A. Kjekshus in their extensive review of the phase diagrams and thermodynamic properties of the $RBa_2Cu_3O_{7-\delta}$ and related materials, and the other phases which are in equilibrium with the hiT_C compounds.

The last four chapters in this volume, as well as the ten chapters in the second of this special two-volume set (Volume 31), are concerned with the electronic structure and various chemical, physical and optical properties of the hiT_C oxides. This sequence of 14 chapters is started by B. Elschner and A. Loidl, who reviewed electron paramagnetic resonance (EPR) studies of cuprate superconductors and their parent compounds (chapter 191). As noted by the authors, EPR is a valuable tool for studying the local electronic and magnetic properties of the hiT_C materials, as well as their magnetically ordered and insulating parent phases. EPR has yielded important information about the charge carriers doped into the CuO_2 planes; the paramagnetic chain fragments in the Cu–O chains; the magnetic behavior of Fe and Mn doped into the superconducting planes; and the slowing down of spin fluctuations.

The annihilation of positrons has been reviewed by A.A. Manuel, chapter 192. Studies of the annihilation of a positron by interaction with an electron have established the existence of Fermi surfaces in $YBa_2Cu_3O_{7-\delta}$ and related oxide phases; and provided a large body of information on the structural and compositional defects in these cuprate materials.

Our knowledge of the electronic structure of the hiT_C compounds is summarized by W.E. Pickett and I.I. Mazin in their overview, chapter 193. They have addressed three topics: the link between full first-principles band structure theory and the description in

terms of a minimal basis set; the question of what uniaxial strains may reveal about the microscopic cause of hiT_C *per se*; and a theoretical picture of the unusual properties of $PrBa_2Cu_3O_7$.

The final chapter, 194, by U. Staub and L. Soderholm, reviews the crystal field splitting of the 4f states in the $RBa_2Cu_3O_{7-\delta}$ phases. The authors discuss the formalism of the crystal field potential, and the lanthanide energy levels and wave functions in the $RBa_2CuO_{7-\delta}$ and related phases, such as Ce-doped R_2CuO_4.

CONTENTS

Preface v

Contents ix

Contents of Volume 31 (preliminary) x

Contents of Volumes 1–29 xi

187. M. Brian Maple
High-temperature superconductivity in layered cuprates: overview 1

188. B. Raveau, C. Michel and M. Hervieu
Crystal chemistry of superconducting rare-earth cuprates 31

189. Yuh Shiohara and Eugene A. Goodilin
Single-crystal growth for science and technology 67

190. Pavel Karen and Arne Kjekshus
Phase diagrams and thermodynamic properties 229

191. B. Elschner and A. Loidl
Electron paramagnetic resonance in cuprate superconductors and in parent compounds 375

192. Alfred A. Manuel
Positron annihilation in high-temperature superconductors 417

193. W.E. Pickett and I.I. Mazin
$RBa_2Cu_3O_7$ compounds: electronic theory and physical properties 453

194. U. Staub and L. Soderholm
Electronic 4f state splittings in cuprates 491

Author index 547

Subject index 621

CONTENTS OF VOLUMES 1–29

VOLUME 1: Metals

1978, 1st repr. 1982, 2nd repr. 1991; ISBN 0-444-85020-1

1. Z.B. Goldschmidt, *Atomic properties (free atom)* 1
2. B.J. Beaudry and K.A. Gschneidner Jr, *Preparation and basic properties of the rare earth metals* 173
3. S.H. Liu, *Electronic structure of rare earth metals* 233
4. D.C. Koskenmaki and K.A. Gschneidner Jr, *Cerium* 337
5. L.J. Sundström, *Low temperature heat capacity of the rare earth metals* 379
6. K.A. McEwen, *Magnetic and transport properties of the rare earths* 411
7. S.K. Sinha, *Magnetic structures and inelastic neutron scattering: metals, alloys and compounds* 489
8. T.E. Scott, *Elastic and mechanical properties* 591
9. A. Jayaraman, *High pressure studies: metals, alloys and compounds* 707
10. C. Probst and J. Wittig, *Superconductivity: metals, alloys and compounds* 749
11. M.B. Maple, L.E. DeLong and B.C. Sales, *Kondo effect: alloys and compounds* 797
12. M.P. Dariel, *Diffusion in rare earth metals* 847

Subject index 877

VOLUME 2: Alloys and intermetallics

1979, 1st repr. 1982, 2nd repr. 1991; ISBN 0-444-85021-X

13. A. Iandelli and A. Palenzona, *Crystal chemistry of intermetallic compounds* 1
14. H.R. Kirchmayr and C.A. Poldy, *Magnetic properties of intermetallic compounds of rare earth metals* 55
15. A.E. Clark, *Magnetostrictive RFe_2 intermetallic compounds* 231
16. J.J. Rhyne, *Amorphous magnetic rare earth alloys* 259
17. P. Fulde, *Crystal fields* 295
18. R.G. Barnes, *NMR, EPR and Mössbauer effect: metals, alloys and compounds* 387
19. P. Wachter, *Europium chalcogenides: EuO, EuS, EuSe and EuTe* 507
20. A. Jayaraman, *Valence changes in compounds* 575

Subject index 613

VOLUME 3: Non-metallic compounds – I

1979, 1st repr. 1984; ISBN 0-444-85215-8

21. L.A. Haskin and T.P. Paster, *Geochemistry and mineralogy of the rare earths* 1
22. J.E. Powell, *Separation chemistry* 81
23. C.K. Jørgensen, *Theoretical chemistry of rare earths* 111
24. W.T. Carnall, *The absorption and fluorescence spectra of rare earth ions in solution* 171
25. L.C. Thompson, *Complexes* 209
26. G.G. Libowitz and A.J. Maeland, *Hydrides* 299
27. L. Eyring, *The binary rare earth oxides* 337
28. D.J.M. Bevan and E. Summerville, *Mixed rare earth oxides* 401
29. C.P. Khattak and F.F.Y. Wang, *Perovskites and garnets* 525
30. L.H. Brixner, J.R. Barkley and W. Jeitschko, *Rare earth molybdates (VI)* 609

Subject index 655

VOLUME 4: Non-metallic compounds – II

1979, 1st repr. 1984; ISBN 0-444-85216-6

31. J. Flahaut, *Sulfides, selenides and tellurides* 1
32. J.M. Haschke, *Halides* 89
33. F. Hulliger, *Rare earth pnictides* 153
34. G. Blasse, *Chemistry and physics of R-activated phosphors* 237
35. M.J. Weber, *Rare earth lasers* 275
36. F.K. Fong, *Nonradiative processes of rare-earth ions in crystals* 317
37A. J.W. O'Laughlin, *Chemical spectrophotometric and polarographic methods* 341
37B. S.R. Taylor, *Trace element analysis of rare earth elements by spark source mass spectroscopy* 359
37C. R.J. Conzemius, *Analysis of rare earth matrices by spark source mass spectrometry* 377
37D. E.L. DeKalb and V.A. Fassel, *Optical atomic emission and absorption methods* 405
37E. A.P. D'Silva and V.A. Fassel, *X-ray excited optical luminescence of the rare earths* 441
37F. F.W.V. Boynton, *Neutron activation analysis* 457
37G. S. Schuhmann and J.A. Philpotts, *Mass-spectrometric stable-isotope dilution analysis for lanthanides in geochemical materials* 471
38. J. Reuben and G.A. Elgavish, *Shift reagents and NMR of paramagnetic lanthanide complexes* 483
39. J. Reuben, *Bioinorganic chemistry: lanthanides as probes in systems of biological interest* 515
40. T.J. Haley, *Toxicity* 553
Subject index 587

VOLUME 5

1982, 1st repr. 1984; ISBN 0-444-86375-3

41. M. Gasgnier, *Rare earth alloys and compounds as thin films* 1
42. E. Gratz and M.J. Zuckermann, *Transport properties (electrical resitivity, thermoelectric power and thermal conductivity) of rare earth intermetallic compounds* 117
43. F.P. Netzer and E. Bertel, *Adsorption and catalysis on rare earth surfaces* 217
44. C. Boulesteix, *Defects and phase transformation near room temperature in rare earth sesquioxides* 321
45. O. Greis and J.M. Haschke, *Rare earth fluorides* 387
46. C.A. Morrison and R.P. Leavitt, *Spectroscopic properties of triply ionized lanthanides in transparent host crystals* 461
Subject index 693

VOLUME 6

1984; ISBN 0-444-86592-6

47. K.H.J. Buschow, *Hydrogen absorption in intermetallic compounds* 1
48. E. Parthé and B. Chabot, *Crystal structures and crystal chemistry of ternary rare earth–transition metal borides, silicides and homologues* 113
49. P. Rogl, *Phase equilibria in ternary and higher order systems with rare earth elements and boron* 335
50. H.B. Kagan and J.L. Namy, *Preparation of divalent ytterbium and samarium derivatives and their use in organic chemistry* 525
Subject index 567

VOLUME 7

1984; ISBN 0-444-86851-8

51. P. Rogl, *Phase equilibria in ternary and higher order systems with rare earth elements and silicon* 1
52. K.H.J. Buschow, *Amorphous alloys* 265
53. H. Schumann and W. Genthe, *Organometallic compounds of the rare earths* 446
Subject index 573

VOLUME 8

1986; ISBN 0-444-86971-9

54. K.A. Gschneidner Jr and F.W. Calderwood, *Intra rare earth binary alloys: phase relationships, lattice parameters and systematics* 1
55. X. Gao, *Polarographic analysis of the rare earths* 163
56. M. Leskelä and L. Niinistö, *Inorganic complex compounds I* 203
57. J.R. Long, *Implications in organic synthesis* 335
Errata 375
Subject index 379

VOLUME 9

1987; ISBN 0-444-87045-8

58. R. Reisfeld and C.K. Jørgensen, *Excited state phenomena in vitreous materials* 1
59. L. Niinistö and M. Leskelä, *Inorganic complex compounds II* 91
60. J.-C.G. Bünzli, *Complexes with synthetic ionophores* 321
61. Zhiquan Shen and Jun Ouyang, *Rare earth coordination catalysis in stereospecific polymerization* 395
Errata 429
Subject index 431

VOLUME 10: High energy spectroscopy

1988; ISBN 0-444-87063-6

62. Y. Baer and W.-D. Schneider, *High-energy spectroscopy of lanthanide materials – An overview* 1
63. M. Campagna and F.U. Hillebrecht, *f-electron hybridization and dynamical screening of core holes in intermetallic compounds* 75
64. O. Gunnarsson and K. Schönhammer, *Many-body formulation of spectra of mixed valence systems* 103
65. A.J. Freeman, B.I. Min and M.R. Norman, *Local density supercell theory of photoemission and inverse photoemission spectra* 165
66. D.W. Lynch and J.H. Weaver, *Photoemission of Ce and its compounds* 231
67. S. Hüfner, *Photoemission in chalcogenides* 301
68. J.F. Herbst and J.W. Wilkins, *Calculation of 4f excitation energies in the metals and relevance to mixed valence systems* 321
69. B. Johansson and N. Mårtensson, *Thermodynamic aspects of 4f levels in metals and compounds* 361
70. F.U. Hillebrecht and M. Campagna, *Bremsstrahlung isochromat spectroscopy of alloys and mixed valent compounds* 425
71. J. Röhler, *X-ray absorption and emission spectra* 453
72. F.P. Netzer and J.A.D. Matthew, *Inelastic electron scattering measurements* 547
Subject index 601

VOLUME 11: Two-hundred-year impact of rare earths on science

1988; ISBN 0-444-87080-6

H.J. Svec, *Prologue* 1
73. F. Szabadváry, *The history of the discovery and separation of the rare earths* 33
74. B.R. Judd, *Atomic theory and optical spectroscopy* 81
75. C.K. Jørgensen, *Influence of rare earths on chemical understanding and classification* 197
76. J.J. Rhyne, *Highlights from the exotic phenomena of lanthanide magnetism* 293
77. B. Bleaney, *Magnetic resonance spectroscopy and hyperfine interactions* 323
78. K.A. Gschneidner Jr and A.H. Daane, *Physical metallurgy* 409
79. S.R. Taylor and S.M. McLennan, *The significance of the rare earths in geochemistry and cosmochemistry* 485
Errata 579
Subject index 581

VOLUME 12

1989; ISBN 0-444-87105-5

80. J.S. Abell, *Preparation and crystal growth of rare earth elements and intermetallic compounds* 1
81. Z. Fisk and J.P. Remeika, *Growth of single crystals from molten metal fluxes* 53
82. E. Burzo and H.R. Kirchmayr, *Physical properties of $R_2Fe_{14}B$-based alloys* 71
83. A. Szytuła and J. Leciejewicz, *Magnetic properties of ternary intermetallic compounds of the RT_2X_2 type* 133
84. H. Maletta and W. Zinn, *Spin glasses* 213
85. J. van Zytveld, *Liquid metals and alloys* 357
86. M.S. Chandrasekharaiah and K.A. Gingerich, *Thermodynamic properties of gaseous species* 409
87. W.M. Yen, *Laser spectroscopy* 433
Subject index 479

VOLUME 13

1990; ISBN 0-444-88547-1

88. E.I. Gladyshevsky, O.I. Bodak and V.K. Pecharsky, *Phase equilibria and crystal chemistry in ternary rare earth systems with metallic elements* 1
89. A.A. Eliseev and G.M. Kuzmichyeva, *Phase equilibrium and crystal chemistry in ternary rare earth systems with chalcogenide elements* 191
90. N. Kimizuka, E. Takayama-Muromachi and K. Siratori, *The systems R_2O_3–M_2O_3–$M'O$* 283
91. R.S. Houk, *Elemental analysis by atomic emission and mass spectrometry with inductively coupled plasmas* 385
92. P.H. Brown, A.H. Rathjen, R.D. Graham and D.E. Tribe, *Rare earth elements in biological systems* 423
Errata 453
Subject index 455

VOLUME 14

1991; ISBN 0-444-88743-1

93. R. Osborn, S.W. Lovesey, A.D. Taylor and E. Balcar, *Intermultiplet transitions using neutron spectroscopy* 1
94. E. Dormann, *NMR in intermetallic compounds* 63
95. E. Zirngiebl and G. Güntherodt, *Light scattering in intermetallic compounds* 163
96. P. Thalmeier and B. Lüthi, *The electron–phonon interaction in intermetallic compounds* 225
97. N. Grewe and F. Steglich, *Heavy fermions* 343
Subject index 475

VOLUME 15

1991; ISBN 0-444-88966-3

98. J.G. Sereni, *Low-temperature behaviour of cerium compounds* 1
99. G.-y. Adachi, N. Imanaka and Zhang Fuzhong, *Rare earth carbides* 61
100. A. Simon, Hj. Mattausch, G.J. Miller, W. Bauhofer and R.K. Kremer, *Metal-rich halides* 191
101. R.M. Almeida, *Fluoride glasses* 287
102. K.L. Nash and J.C. Sullivan, *Kinetics of complexation and redox reactions of the lanthanides in aqueous solutions* 347
103. E.N. Rizkalla and G.R. Choppin, *Hydration and hydrolysis of lanthanides* 393
104. L.M. Vallarino, *Macrocycle complexes of the lanthanide(III) yttrium(III) and dioxouranium(VI) ions from metal-templated syntheses* 443
Errata 513
Subject index 515

MASTER INDEX, Vols. 1–15
1993; ISBN 0-444-89965-0

VOLUME 16
1993; ISBN 0-444-89782-8

105. M. Loewenhaupt and K.H. Fischer, *Valence-fluctuation and heavy-fermion 4f systems* 1
106. I.A. Smirnov and V.S. Oskotski, *Thermal conductivity of rare earth compounds* 107
107. M.A. Subramanian and A.W. Sleight, *Rare earths pyrochlores* 225
108. R. Miyawaki and I. Nakai, *Crystal structures of rare earth minerals* 249
109. D.R. Chopra, *Appearance potential spectroscopy of lanthanides and their intermetallics* 519
Author index 547
Subject index 579

VOLUME 17: Lanthanides/Actinides: Physics – I
1993; ISBN 0-444-81502-3

110. M.R. Norman and D.D. Koelling, *Electronic structure, Fermi surfaces, and superconductivity in f electron metals* 1
111. S.H. Liu, *Phenomenological approach to heavy-fermion systems* 87
112. B. Johansson and M.S.S. Brooks, *Theory of cohesion in rare earths and actinides* 149
113. U. Benedict and W.B. Holzapfel, *High-pressure studies – Structural aspects* 245
114. O. Vogt and K. Mattenberger, *Magnetic measurements on rare earth and actinide monopnictides and monochalcogenides* 301
115. J.M. Fournier and E. Gratz, *Transport properties of rare earth and actinide intermetallics* 409
116. W. Potzel, G.M. Kalvius and J. Gal, *Mössbauer studies on electronic structure of intermetallic compounds* 539
117. G.H. Lander, *Neutron elastic scattering from actinides and anomalous lanthanides* 635
Author index 711
Subject index 753

VOLUME 18: Lanthanides/Actinides: Chemistry
1994; ISBN 0-444-81724-7

118. G.T. Seaborg, *Origin of the actinide concept* 1
119. K. Balasubramanian, *Relativistic effects and electronic structure of lanthanide and actinide molecules* 29
120. J.V. Beitz, *Similarities and differences in trivalent lanthanide- and actinide-ion solution absorption spectra and luminescence studies* 159
121. K.L. Nash, *Separation chemistry for lanthanides and trivalent actinides* 197
122. L.R. Morss, *Comparative thermochemical and oxidation–reduction properties of lanthanides and actinides* 239
123. J.W. Ward and J.M. Haschke, *Comparison of 4f and 5f element hydride properties* 293
124. H.A. Eick, *Lanthanide and actinide halides* 365
125. R.G. Haire and L. Eyring, *Comparisons of the binary oxides* 413
126. S.A. Kinkead, K.D. Abney and T.A. O'Donnell, *f-element speciation in strongly acidic media: lanthanide and mid-actinide metals, oxides, fluorides and oxide fluorides in superacids* 507
127. E.N. Rizkalla and G.R. Choppin, *Lanthanides and actinides hydration and hydrolysis* 529
128. G.R. Choppin and E.N. Rizkalla, *Solution chemistry of actinides and lanthanides* 559
129. J.R. Duffield, D.M. Taylor and D.R. Williams, *The biochemistry of the f-elements* 591
Author index 623
Subject index 659

VOLUME 19: Lanthanides/Actinides: Physics – II

1994; ISBN 0-444-82015-9

130. E. Holland-Moritz and G.H. Lander, *Neutron inelastic scattering from actinides and anomalous lanthanides* 1
131. G. Aeppli and C. Broholm, *Magnetic correlations in heavy-fermion systems: neutron scattering from single crystals* 123
132. P. Wachter, *Intermediate valence and heavy fermions* 177
133. J.D. Thompson and J.M. Lawrence, *High pressure studies – Physical properties of anomalous Ce, Yb and U compounds* 383
134. C. Colinet and A. Pasturel, *Thermodynamic properties of metallic systems* 479
Author index 649
Subject index 693

VOLUME 20

1995; ISBN 0-444-82014-0

135. Y. Ōnuki and A. Hasegawa, *Fermi surfaces of intermetallic compounds* 1
136. M. Gasgnier, *The intricate world of rare earth thin films: metals, alloys, intermetallics, chemical compounds, ...* 105
137. P. Vajda, *Hydrogen in rare-earth metals, including RH_{2+x} phases* 207
138. D. Gignoux and D. Schmitt, *Magnetic properties of intermetallic compounds* 293
Author index 425
Subject index 457

VOLUME 21

1995; ISBN 0-444-82178-3

139. R.G. Bautista, *Separation chemistry* 1
140. B.W. Hinton, *Corrosion prevention and control* 29
141. N.E. Ryan, *High-temperature corrosion protection* 93
142. T. Sakai, M. Matsuoka and C. Iwakura, *Rare earth intermetallics for metal–hydrogen batteries* 133
143. G.-y. Adachi and N. Imanaka, *Chemical sensors* 179
144. D. Garcia and M. Faucher, *Crystal field in non-metallic (rare earth) compounds* 263
145. J.-C.G. Bünzli and A. Milicic-Tang, *Solvation and anion interaction in organic solvents* 305
146. V. Bhagavathy, T. Prasada Rao and A.D. Damodaran, *Trace determination of lanthanides in high-purity rare-earth oxides* 367
Author index 385
Subject index 411

VOLUME 22

1996; ISBN 0-444-82288-7

147. C.P. Flynn and M.B. Salamon, *Synthesis and properties of single-crystal nanostructures* 1
148. Z.S. Shan and D.J. Sellmyer, *Nanoscale rare earth–transition metal multilayers: magnetic structure and properties* 81
149. W. Suski, *The $ThMn_{12}$-type compounds of rare earths and actinides: structure, magnetic and related properties* 143
150. L.K. Aminov, B.Z. Malkin and M.A. Teplov, *Magnetic properties of nonmetallic lanthanide compounds* 295
151. F. Auzel, *Coherent emission in rare-earth materials* 507
152. M. Dolg and H. Stoll, *Electronic structure calculations for molecules containing lanthanide atoms* 607
Author index 731
Subject index 777

VOLUME 23

1996; ISBN 0-444-82507-X

153. J.H. Forsberg, *NMR studies of paramagnetic lanthanide complexes and shift reagents* 1
154. N. Sabbatini, M. Guardigli and I. Manet, *Antenna effect in encapsulation complexes of lanthanide ions* 69
155. C. Görller-Walrand and K. Binnemans, *Rationalization of crystal-field parametrization* 121
156. Yu. Kuz'ma and S. Chykhrij, *Phosphides* 285
157. S. Boghosian and G.N. Papatheodorou, *Halide vapors and vapor complexes* 435
158. R.H. Byrne and E.R. Sholkovitz, *Marine chemistry and geochemistry of the lanthanides* 497
Author index 595
Subject index 631

VOLUME 24

1997; ISBN 0-444-82607-6

159. P.A. Dowben, D.N. McIlroy and Dongqi Li, *Surface magnetism of the lanthanides* 1
160. P.G. McCormick, *Mechanical alloying and mechanically induced chemical reactions* 47
161. A. Inoue, *Amorphous, quasicrystalline and nanocrystalline alloys in Al- and Mg-based systems* 83
162. B. Elschner and A. Loidl, *Electron-spin resonance on localized magnetic moments in metals* 221
163. N.H. Duc, *Intersublattice exchange coupling in the lanthanide–transition metal intermetallics* 339
164. R.V. Skolozdra, *Stannides of rare-earth and transition metals* 399
Author index 519
Subject index 559

VOLUME 25

1998; ISBN 0-444-82871-0

165. H. Nagai, *Rare earths in steels* 1
166. R. Marchand, *Ternary and higher order nitride materials* 51
167. C. Görller-Walrand and K. Binnemans, *Spectral intensities of f–f transitions* 101
168. G. Bombieri and G. Paolucci, *Organometallic π complexes of the f-elements* 265
Author Index 415
Subject Index 459

VOLUME 26

1999; ISBN 0-444-50815-1

169. D.F. McMorrow, D. Gibbs and J. Bohr, *X-ray scattering studies of lanthanide magnetism* 1
170. A.M. Tishin, Yu.I. Spichkin and J. Bohr, *Static and dynamic stresses* 87
171. N.H. Duc and T. Goto, *Itinerant electron metamagnetism of Co sublattice in the lanthanide–cobalt internetallics* 177
172. A.J. Arko, P.S. Riseborough, A.B. Andrews, J.J. Joyce, A.N. Tahvildar-Zadeh and M. Jarrell, *Photoelectron spectroscopy in heavy fermion systems: Emphasis on single crystals* 265
Author index 383
Subject index 405

VOLUME 27

1999; ISBN 0-444-50342-0

173. P.S. Salamakha, O.L. Sologub and O.I. Bodak, *Ternary rare-earth–germanium systems* 1
174. P.S. Salamakha, *Crystal structures and crystal chemistry of ternary rare-earth germanides* 225
175. B.Ya. Kotur and E. Gratz, *Scandium alloy systems and intermetallics* 339
Author index 535
Subject index 553

VOLUME 28

2000; ISBN 0-444-50346-3

176. J.-P. Connerade and R.C. Karnatak, *Electronic excitation in atomic species* 1
177. G. Meyer and M.S. Wickleder, *Simple and complex halides* 53
178. R.V. Kumar and H. Iwahara, *Solid electrolytes* 131
179. A. Halperin, *Activated thermoluminescence (TL) dosimeters and related radiation detectors* 187
180. K.L. Nash and M.P. Jensen, *Analytical separations of the lanthanides: basic chemistry and methods* 311
Author index 373
Subject index 401

VOLUME 29: The role of rare earths in catalysis

2000; ISBN 0-444-50472-9

P. Maestro, *Foreword* 1
181. V. Paul-Boncour, L. Hilaire and A. Percheron-Guégan, *The metals and alloys in catalysis* 5
182. H. Imamura, *The metals and alloys (prepared utilizing liquid ammonia solutions) in catalysis II* 45
183. M.A. Ulla and E.A. Lombardo, *The mixed oxides* 75
184. J. Kašpar, M. Graziani and P. Fornasiero, *Ceria-containing three-way catalysts* 159
185. A. Corma and J.M. López Nieto, *The use of rare-earth-containing zeolite catalysts* 269
186. S. Kobayashi, *Triflates* 315
Author index 377
Subject index 409

Handbook on the Physics and Chemistry of Rare Earths
Vol. 30
edited by K.A. Gschneidner, Jr., L. Eyring and M.B. Maple

Chapter 187

HIGH-TEMPERATURE SUPERCONDUCTIVITY IN LAYERED CUPRATES: OVERVIEW

M. Brian MAPLE
Department of Physics and Institute for Pure and Applied Physical Sciences, University of California, San Diego, La Jolla, CA 92093, USA

Contents

List of symbols and acronyms 1
1. Introduction 2
2. High-T_c superconducting cuprates 3
   2.1. The materials 3
   2.2. Rare-earth- and actinide-based cuprates 4
   2.3. Structure and charge carrier doping 6
3. Some other noteworthy superconducting materials 9
   3.1. Cubic high-T_c superconductors 9
   3.2. Sr_2RuO_4 9
   3.3. Quantum spin ladder materials 9
4. Superconducting properties 9
   4.1. Critical fields and current densities 9
   4.2. Superconducting pairing mechanism 11
5. Symmetry of the superconducting order parameter 12
   5.1. Probing the magnitude of the superconducting order parameter 13
   5.2. Probing the phase of the superconducting order parameter 14
6. Normal state properties 15
   6.1. Normal ground state 18
   6.2. Pseudogap 20
7. Generic phase diagram 23
8. Spin and charge stripe phases 24
9. Technological applications of superconductivity 24
10. Concluding remarks 26
   Acknowledgments 26
   References 27

List of symbols and acronyms

AFM	antiferromagnetic
ARPES	angle resolved photoemission spectroscopy
α_s	ultrasonic attenuation coefficient
BSCCO	$Bi_2Sr_2Ca_{n-1}Cu_nO_{2n+4}$
C	specific heat
2D (3D)	two- (three-) dimensional
DOS	density of states
e	charge of electron
$\mathcal{E}$	Energy
E	electric field
H_{c2}	upper critical field
IBAD	ion beam assisted deposition
J_c	critical current density
k	wavevector
LSCO	$La_{1-x}Sr_xCuO_4$
LTO phase	low-temperature orthorhombic phase
LTT phase	low-temperature tetragonal phase
MRI	magnetic resonance imaging
$N(E)$	electronic density of states
NCCO	$Nd_{2-x}Ce_xCuO_{4-y}$
NMR	nuclear magnetic resonance
PLD	pulsed laser deposition
R	chemical symbol for rare earth

$\mathcal{R}$	reflectance	YBCO-124, Y-124	$YBa_2Cu_4O_8$
R_H	Hall coefficient	χ	magnetic susceptibility
RABiTS	rolling assisted biaxially-textured substrates	λ	superconducting penetration depth
RVB	resonating valence bond	θ_c	Curie temperature (ferromagnetic ordering temperature)
S	thermoelectric power	θ_H	Hall angle
SQUID	superconducting quantum interference device	λ_{so}	spin–orbit scattering
T_c	superconducting critical temperature	κ	thermal conductivity parameter
T_M	magnetic ordering temperature	ρ	electrical resistivity
T_N	Néel temperature (antiferromagnetic ordering temperature)	ρ_s	superfluid density
T^*	pseudogap crossover temperature	τ_l^{-1}	longitudinal scattering rate
T_ϕ	phase coherence temperature	τ_t^{-1}	transverse scattering rate
T_1^{-1}	NMR spin lattice relaxation rate	ω	frequency
TBCCO	$TlBa_2Ca_{n-1}Cu_nO_{2n+3}$ or $Tl_2Ba_2Ca_{n-1}Cu_nO_{2n+4}$	ξ	superconducting coherence length
Tl2201	$Tl_2Ba_2CuO_{6+x}$	σ	electrical conductivity
YBCO, YBCO-123, Y-123	$YBa_2Cu_3O_{7-\delta}$	Δ	superconducting energy gap

1. Introduction

The discovery of superconductivity at ~30 K in the La–Ba–Cu–O system by Bednorz and Müller (1986) set off an explosion of research on high-temperature superconductivity on a worldwide scale that still persists after more than a decade. This extraordinary episode in the history of science has been driven by two challenging objectives: the development of a fundamental understanding of high-temperature superconductivity and the widespread use of high-temperature superconductors in technological applications. Although an enormous amount of progress has been made since 1986, many obstacles remain to be overcome before these two objectives can be achieved. However, in our view, prospects are good for attaining an understanding of high-temperature superconductivity on a fundamental level and realizing technological applications of high-temperature superconductors on a broad scale during the next decade. The articles in these volumes review the progress that has been made on this subject and identify outstanding problems that remain to be solved.

Although several other types of exotic superconductors (e.g., organic superconductors, heavy-fermion f-electron superconductors, magnetically ordered superconductors, multinary rare-earth, actinide, and transition-metal superconductors) have been investigated intensely since 1986, the cuprate superconductors have received by far the most attention because the highest values of the superconducting critical temperature T_c are found in this class of materials. Rare-earth and actinide elements are key constituents of many of the high-temperature cuprate superconductors and have played a prominent role in the development of the first and some of the more important cuprate superconductors.

In view of the importance of high-temperature superconductivity in the layered cuprates and the role played by the rare earths, it seemed appropriate to prepare these volumes of the *Handbook on the Physics and Chemistry of Rare Earths* on "High-Temperature Superconductivity in Layered Cuprates". We believe that researchers already working in this field, as well as those intending to enter this field, will find valuable information in the review articles contained in these volumes. Since many of the cuprate superconductors do not contain rare-earth or actinide elements, yet have characteristics and properties similar to those that do, the range of materials considered in these volumes has been broadened to a limited extent to include all high-temperature cuprate superconductors, irrespective of whether they contain rare-earth or actinide elements.

2. High-T_c superconducting cuprates

2.1. *The materials*

Since 1986, dramatic increases in the superconducting critical temperature T_c have been achieved in the layered perovskite-like cuprate superconductors, as illustrated in the plot of the maximum value of T_c vs. date in fig. 1. Prior to 1986, the record

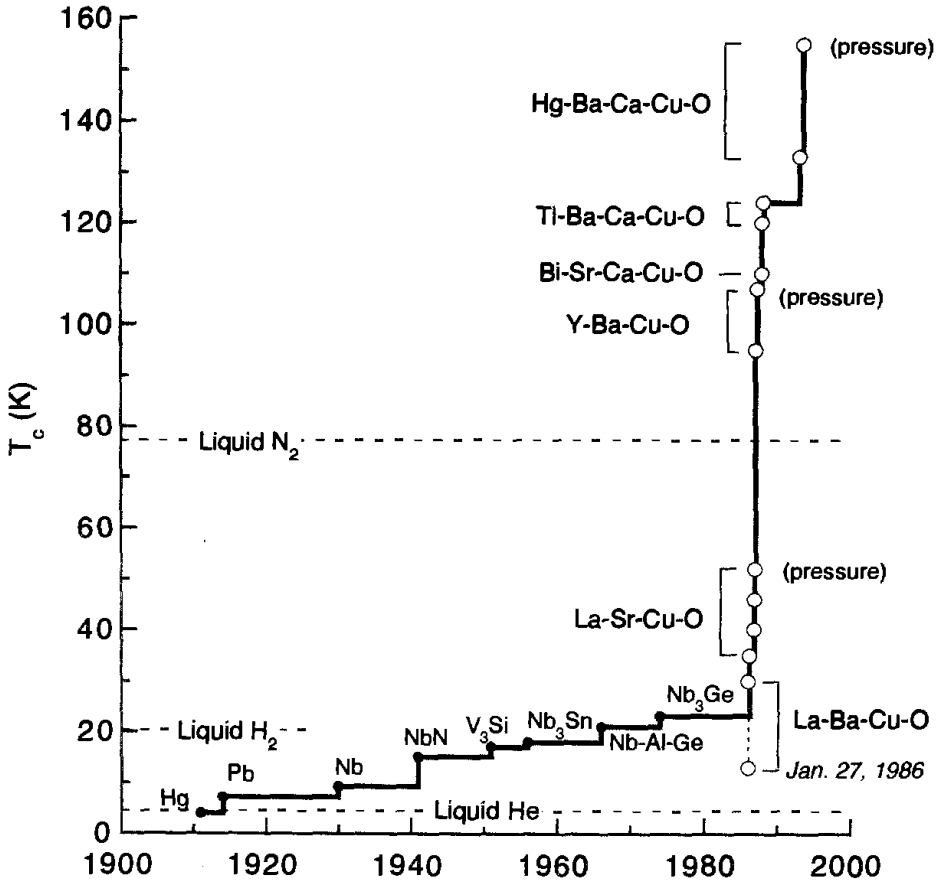

Fig. 1. Maximum superconducting critical temperature T_c vs date.

Table 1
Some important classes of cuprate superconductors and the maximum value of T_c observed in each class.

Material		Maximum T_c (K)
$La_{2-x}M_xCuO_4$	M = Ba, Sr, Ca, Na	~40
$Ln_{2-x}M_xCuO_{4-y}$	Ln = Pr, Nd, Sm, Eu; M = Ce, Th	~25
$YBa_2Cu_3O_{7-\delta}$		92
$LnBa_2Cu_3O_{7-\delta}$	Ce, Tb do not form phase; Pr forms phase; neither metallic nor superconducting	~95
$RBa_2Cu_4O_8$		80
$Bi_2Sr_2Ca_{n-1}Cu_nO_{2n+4}$	$n = 1, 2, 3, 4$	($n = 3$) 110
$TlBa_2Ca_{n-1}Cu_nO_{2n+3}$	$n = 1, 2, 3, 4$	($n = 4$) 122
$Tl_2Ba_2Ca_{n-1}Cu_nO_{2n+4}$	$n = 1, 2, 3, 4$	($n = 3$) 122
$HgBa_2Ca_{n-1}Cu_nO_{2n+2}$	$n = 1, 2, 3, 4$	($n = 3$) 133

for the highest value of T_c (~23 K) was held by the A15 compound Nb_3Ge (Gavaler 1973). Currently, the maximum value of T_c at atmospheric pressure is ~133 K for the compound $HgBa_2Ca_2Cu_3O_8$ (Putilin et al. 1993, Schilling et al. 1993). When this compound is subjected to a high pressure ~30 GPa, the T_c onset increases to ~164 K (more than half way to room temperature!) (Chu et al. 1993, Nuñez-Regueiro et al. 1993). While $HgBa_2Ca_2Cu_3O_8$ cannot be used in applications of superconductivity at such high pressures, this striking result suggests that values of T_c in the neighborhood of 160 K, or even higher, are attainable in cuprates at atmospheric pressure. Furthermore, there do not appear to be any compelling reasons that preclude the possibility of observing superconductivity at temperatures near, or even above, room temperature! Approximately 100 different cuprate materials, many of which are superconducting, have been discovered since 1986. Several of the more important high-T_c cuprate superconductors are listed in table 1, along with the maximum values of T_c observed in each class of materials. For brevity, "shorthand" designations ("nicknames") for specific cuprate materials (e.g., $YBa_2Cu_3O_{7-\delta}$ = YBCO, YBCO-123, Y-123), rather than complete chemical formulas, will often be used throughout these volumes (see List of symbols and acronyms).

2.2. *Rare-earth- and actinide-based cuprates*

The first high-T_c cuprate superconductors discovered, which are also some of the more important materials with respect to both scientific interest and technological potential, are based on rare-earth and actinide elements; see, e.g., Markert et al. (1989a). The first superconducting oxide system found with T_c values exceeding the 23 K record value held by Nb_3Ge was $La_{2-x}Ba_xCuO_4$ which has a maximum value of T_c of ~30 K for $x \approx 0.15$ (Bednorz and Müller 1986, Takagi et al. 1987). Shortly thereafter, $La_{2-x}M_xCuO_4$ systems with M = Sr, Ca, and Na were synthesized which exhibited superconductivity with

maximum T_c values of ~40 K for M = Sr (Cava et al. 1987), ~20 K for M = Ca (Kishio et al. 1987), and ~20 K for M = Na (Markert et al. 1988, Subramanian et al. 1988).

The first superconductors with values of T_c exceeding the boiling point of liquid nitrogen (77 K) belong to the $RBa_2Cu_3O_{7-\delta}$ family. Superconductivity was reported to occur for R = Y (Wu et al. 1987) and all of the lanthanides except Ce and Tb (which do not form the phase) and Pr (which forms the phase, but is insulating and thereby not superconducting) with T_c values that range from ~92 K for R = Y to ~95 K for R = Nd (see, for example, Maple et al. 1987). (Superconductivity at ~90 K in the lanthanide analogues of $YBa_2Cu_3O_{7-\delta}$ was discovered independently in laboratories at several institutions throughout the world. See, for example, Maple et al. 1987 and references cited therein.) Surprisingly, superconductivity with $T_c \approx 85$ K has recently been reported in $PrBa_2Cu_3O_x$ samples prepared by the traveling-solvent floating-zone method (Zou et al. 1998). These materials show large inhomogeneity in both lattice parameters and transport and magnetic properties. In the parts of the sample that exhibit bulk superconductivity, the c-axis lattice constant is reported to be larger than that of the nonsuperconducting ceramic polycrystalline or single crystal samples prepared by standard methods. The pressure dependence of T_c of the $PrBa_2Cu_3O_x$ samples is quite large and comparable to values observed in underdoped cuprates. These results illustrate the complexity of these materials and how sensitive their properties are to the conditions of their growth. Further research on this fascinating material is clearly warranted.

The $La_{2-x}M_xCuO_4$ and $RBa_2Cu_3O_{7-\delta}$ compounds are hole-doped superconductors, as are most of the high-T_c cuprates. The first system of electron-doped cuprate superconductors discovered was $Ln_{2-x}M_xCuO_{4-y}$ (Ln = Pr, Nd, Sm, Eu; M = Ce, Th; $x \approx 0.1$–0.18; $y \approx 0.02$) (Tokura et al. 1989, Markert and Maple 1989, Markert et al. 1989b, Early et al. 1989). The highest values of T_c found among the electron-doped superconductors are ~25 K.

There has been considerable interest in systems of the type $R_{1-x}Pr_xBa_2Cu_3O_{7-\delta}$, especially for R = Y (see, for example, Maple et al. 1994). This was initially inspired by the puzzling observation that $PrBa_2Cu_3O_{7-\delta}$, when prepared by standard methods, is insulating and nonsuperconducting, whereas the other $RBa_2Cu_3O_{7-\delta}$ compounds that can be formed are metallic and superconducting with T_c's ≈ 92–95 K, as noted above. The $Y_{1-x}Pr_xBa_2Cu_3O_{7-\delta}$ system is replete with extraordinary physical phenomena including a metal–insulator transition at $x_{cr} \approx 0.55$, a monotonic depression of T_c with x that vanishes near x_{cr} in the metallic phase, a striking crossover in the pressure dependence of T_c from positive to negative with increasing x, a large γT contribution to the low-temperature specific heat that is reminiscent of heavy fermion behavior, and Cu^{2+} and Pr^{n+} antiferromagnetic (AFM) ordering in the insulating phase with $T_N(Cu^{2+}) > T_N(Pr^{n+})$, where T_N is the Néel temperature. It has been suggested that these and other peculiar properties of this system are related to hybridization between the Pr localized 4f states and the valence band states associated with the conducting CuO_2 planes (Maple et al. 1994). A theoretical model that involves the hybridization between the 4f states of Pr and the 2p states of neighboring oxygen atoms in the $Y_{1-x}Pr_xBa_2Cu_3O_{7-\delta}$ system has, in fact, been developed by Fahrenbacher and Rice (1993). Similar phenomena are found

in the related $Y_{1-x}Pr_xBa_2Cu_4O_8$ system which has also been extensively investigated (Herrmann et al. 1994).

Recently, several compounds containing CuO_2 and RuO_2 planes have been fabricated in which superconductivity and ferromagnetism are apparently confined to the CuO_2 and RuO_2 planes, respectively, and coexist with one another microscopically. Examples of these materials include $R_{1.4}Ce_{0.6}RuSr_2Cu_2O_{10-\delta}$ [$T_c \approx 42$ K, 32 K and Curie temperature $T_M \approx 180$ K, 122 K for R = Gd and Eu, respectively (Felner et al. 1997)], and $GdRuSr_2Cu_2O_8$ [$T_c \approx 46$ K, $T_M \approx 132$ K (Bauernfeind et al. 1996, Bernard et al. 1999)]. In compounds previously observed to exhibit superconductivity and ferromagnetism, such as $ErRh_4B_4$ (Fertig et al. 1977) and $HoMo_6S_8$ (Ishikawa and Fischer 1977), the superconductivity that occurs below a critical temperature T_{c1} is destroyed by the onset of ferromagnetic order at a second lower critical temperature T_{c2} that is the order of the Curie temperature. Small angle neutron scattering studies on $ErRh_4B_4$ (Moncton et al. 1980, Sinha et al. 1982) and $HoMo_6S_8$ (Lynn et al. 1981) have revealed the existence of a sinusoidally modulated magnetic state with a wavelength of ~10^2 Å that coexists with superconductivity in a narrow temperature interval above T_{c2}. In $ErRh_4B_4$, the regions in which superconductivity and the sinusoidally modulated magnetic state coexist appear to be interspersed with normal ferromagnetic domains to form a spatially inhomogenous state.

In addition to these rare-earth- and actinide-based cuprates, many other high-T_c cuprates have been discovered, a number of which also contain rare-earth elements.

2.3. *Structure and charge carrier doping*

The high-T_c cuprate superconductors have layered perovskite-like crystal structures which consist of conducting CuO_2 planes separated by layers comprised of other elements A and oxygen, A_mO_n, and, in some cases, layers of Ln ions (Sleight 1991, Jorgensen 1991). The mobile charge carriers, which can be electrons but are usually holes, are generally believed to reside primarily within the CuO_2 planes. The A_mO_n layers apparently function as charge reservoirs that control the doping of the CuO_2 planes with charge carriers and as spacers that govern the anisotropy of the physical properties of the materials. In several of the compounds containing Ln layers, the Ln ions with partially-filled 4f electron shells and magnetic moments have been found to order antiferromagnetically at low temperature (see, for example, Maple et al. 1987 and Markert et al. 1989a). Specific heat data for $RBa_2Cu_3O_{7-\delta}$ with R = Nd, Sm, Gd, Er and Dy that exhibit AFM ordering of the R ions at low temperatures reveal pronounced peaks near the Néel temperature T_N as shown in fig. 2 (Markert et al. 1989a).

Many of the cuprates can be doped with charge carriers and rendered superconducting by substituting appropriate elements into an AFM insulating parent compound. For example, substitution of divalent Sr for trivalent La in the AFM insulator La_2CuO_4 dopes the CuO_2 planes with mobile holes and produces superconductivity in $La_{2-x}Sr_xCuO_4$ with a maximum T_c of ~40 K at $x \approx 0.17$ (Cava et al. 1987). Similarly, substitution of tetravalent Ce for trivalent Nd in the AFM insulating compound Nd_2CuO_4 apparently

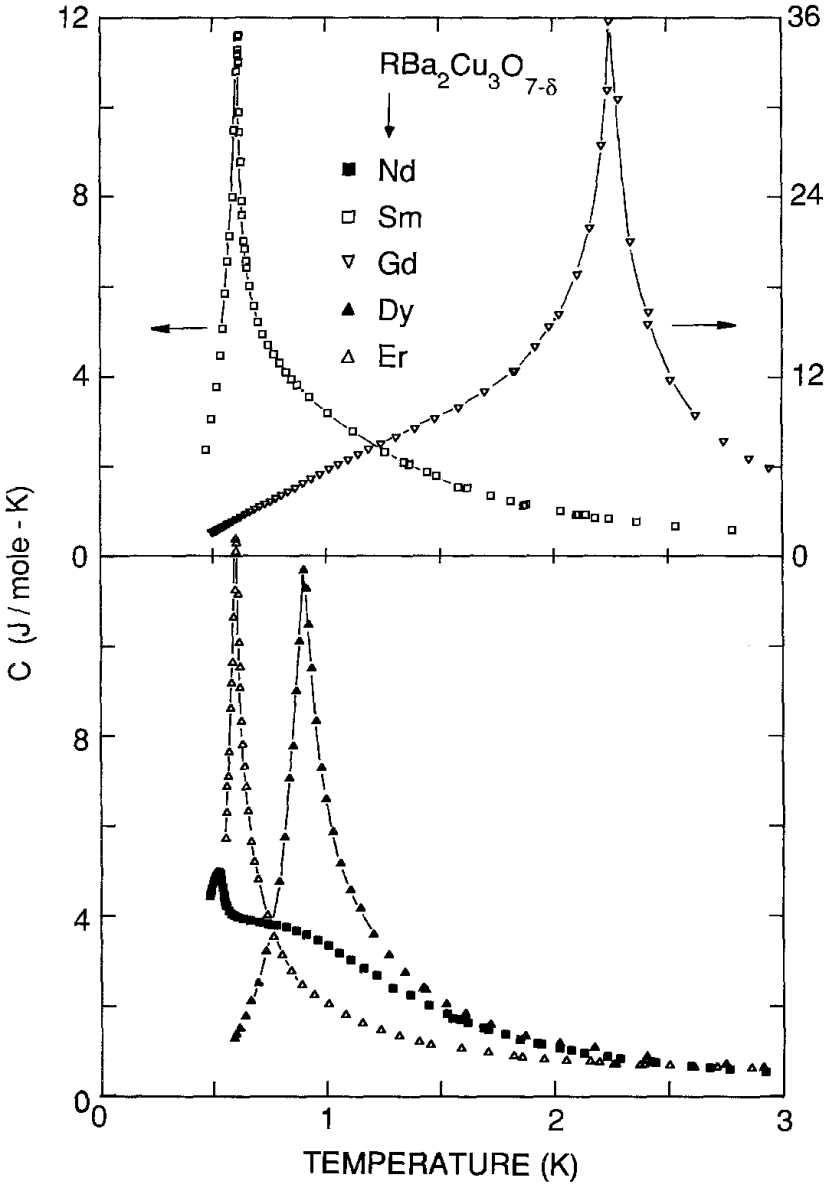

Fig. 2. Specific heat C vs temperature between 0.5 K and 3 K for $RBa_2Cu_3O_{7-\delta}$ compounds with R = Nd, Sm, Gd, Dy, and Er. From Markert et al. (1989a).

dopes the CuO_2 planes with electrons, resulting in superconductivity in $Nd_{2-x}Ce_xCuO_{4-y}$ with a maximum T_c of ~25 K at $x \approx 0.15$ for $y \approx 0.02$ (Tokura et al. 1989, Maple 1990). The temperature T vs. x phase diagrams for the $La_{2-x}Sr_xCuO_4$ and $Nd_{2-x}Ce_xCuO_{4-y}$ systems are shown in fig. 3 (Maple 1990). The $Ln_{2-x}M_xCuO_{4-y}$ electron-doped materials have a tetragonal crystal structure that is similar to that of the $La_{2-x}M_xCuO_4$ hole-doped materials, but without the apical oxygen atoms. The crystal structures of the La_2CuO_4 and Nd_2CuO_4 parent compounds are displayed in fig. 4. The $La_{2-x}Sr_xCuO_4$ and $Nd_{2-x}Ce_xCuO_{4-y}$ systems have one CuO_2 plane per unit cell and are referred to

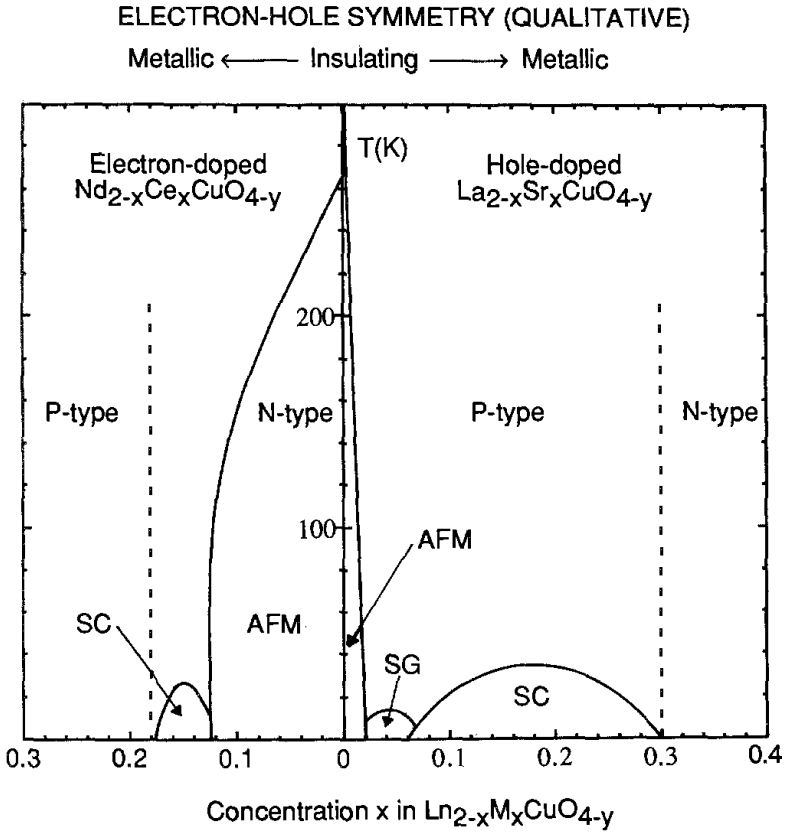

Fig. 3. Temperature–dopant concentration (T–x) phase diagram delineating the regions of superconductivity and antiferromagnetic ordering of the Cu^{2+} ions for the hole-doped $La_{2-x}Sr_xCuO_4$ and electron-doped $Nd_{2-x}Ce_xCuO_{4-y}$ systems. AFM, antiferromagnetic phase; SG, spin-glass phase; SC, superconducting phase. From Maple (1990).

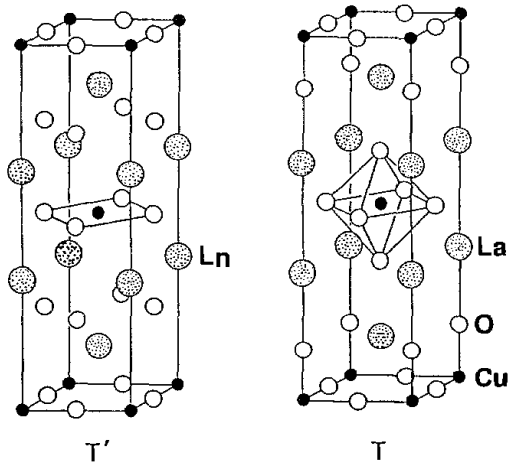

Fig. 4. Crystal structures of La_2CuO_4 (T-phase) and Ln_2CuO_4 (Ln = Pr, Nd, Sm, Eu, Gd; T′-phase) parent compounds. From Maple (1990).

as single CuO_2 layer compounds. Other superconducting cuprate systems have more than one CuO_2 plane per unit cell: $LnBa_2Cu_3O_{7-\delta}$ has two CuO_2 planes per unit cell

(double CuO_2 layer compound), while $Bi_2Sr_2Ca_{n-1}Cu_nO_x$ has n CuO_2 layers per unit cell (n CuO_2 layer compound) and can be synthesized by conventional methods for $n = 1, 2, 3$.

3. Some other noteworthy superconducting materials

3.1. *Cubic high-T_c superconductors*

Superconductivity with values of T_c in the neighborhood of 30 K have been found in two noncuprate cubic materials: the cubic perovskite $Ba_{1-x}K_xBiO_3$ ($T_c \approx 30$ K; Mattheis et al. 1988, Cava et al. 1988) and the fcc "buckyball" compound Rb_3C_{60} ($T_c \approx 29$ K; Rosseinsky et al. 1991, Holczer et al. 1991).

3.2. *Sr_2RuO_4*

The superconducting compound Sr_2RuO_4 has the same structure as the $La_{2-x}M_xCuO_4$ (M = Ba, Sr, Ca; Na) high-T_c cuprate superconductors (Maeno et al. 1994). While the T_c of Sr_2RuO_4 is only ~1 K, this compound is of considerable interest because it is the only layered perovskite superconductor without Cu. The anisotropy of the superconducting properties of Sr_2RuO_4 is very large ($\gamma = \xi_{ab}/\xi_c \approx 26$). Although this anisotropy is larger than that of $La_{2-x}M_xCuO_4$, the in-plane and c-axis resistivities of Sr_2RuO_4 vary as T^2 at low temperature, indicative of Fermi liquid behavior. It has been suggested that Sr_2RuO_4 may exhibit p-wave superconductivity (Rice and Sigrist 1995), a view that has been supported by a growing amount of experimental evidence (Julian et al. 1999).

3.3. *Quantum spin ladder materials*

Quantum spin ladder materials have attracted much recent interest (Takano 1996, Maekawa 1996). These materials consist of ladders made of AFM chains of $S = 1/2$ spins coupled by inter-chain AFM bonds. Examples of 2-leg ladder materials are $SrCu_2O_3$ and $LaCuO_{2.5}$; an example of a 3-leg ladder material is $Sr_2Cu_2O_5$. Superconductivity has apparently been discovered in the ladder material $Sr_{0.4}Ca_{13.6}Cu_{24}O_{41.84}$ under pressure with $T_c \approx 12$ K at 3 GPa (Uehara et al. 1996). Interest in quantum spin ladder materials is partly due to the fact that they are simple model systems for theories of superconductivity based on magnetic pairing mechanisms.

4. Superconducting properties

4.1. *Critical fields and current densities*

With values of T_c in excess of the boiling temperature of liquid nitrogen (77 K), the high-T_c cuprates were immediately recognized as promising candidates for technological

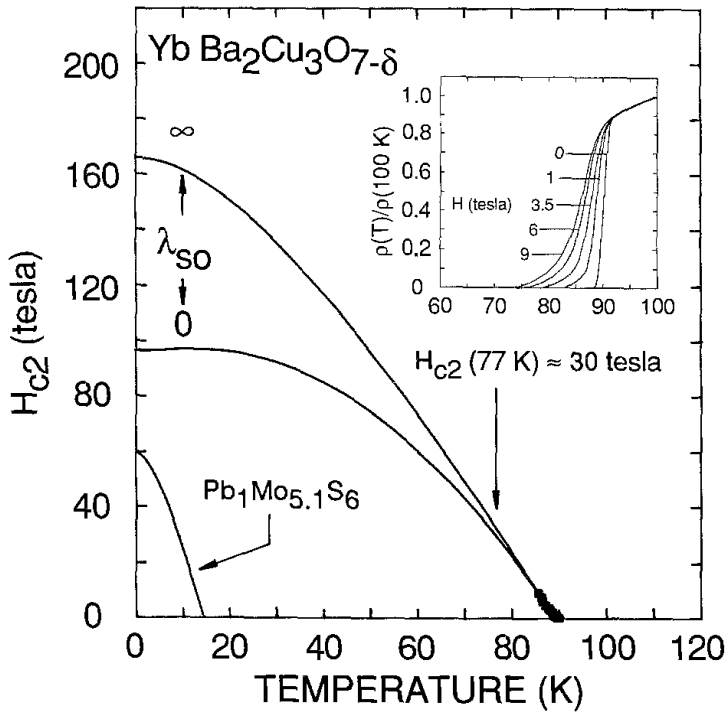

Fig. 5. Upper critical field H_{c2} vs temperature for the compound $YbBa_2Cu_3O_{7-\delta}$. The solid lines are based on standard WHH (Werthamer et al. 1966) theory for a conventional type II superconductor in the limits of maximum (spin–orbit scattering parameter $\lambda_{so}=0$) and minimum ($\lambda_{so}=\infty$) paramagnetic limitation and have been fitted to the data near T_c. Inset: Normalized electrical resistivity vs temperature in several magnetic fields between 0 and 9 tesla. From Markert et al. (1989a).

applications of superconductivity. Whereas liquid helium is currently employed to cool conventional superconducting materials such as Nb, NbTi, and Nb_3Sn into the superconducting state (Nb is employed in SQUIDs and NbTi and Nb_3Sn are used to make superconducting wires), the cuprate materials have the advantage that they can be cooled into the superconducting state using liquid nitrogen, closed cycle refrigerators, and other refrigeration techniques. Cuprates such as the $LnBa_2Cu_3O_{7-\delta}$ (Ln = lanthanide) compounds (T_c in the range 92–95 K) have enormous critical fields ~10^2 tesla (Maple et al. 1987, Orlando et al. 1987) that are more than adequate for technological applications. Shown in fig. 5 is the resistively determined upper critical field $H_{c2}(T)$ curve for the compound $YbBa_2Cu_3O_{7-\delta}$. Extrapolation of the $H_{c2}(T)$ curves measured between 0 and ~10 T to $T=0$ K, using the theory developed by Werthamer, Helfand and Hohenberg (WHH) in 1966 without paramagnetic limiting, yields values of $H_{c2}(0) \approx 160$ T (Maple et al. 1987).

Epitaxially grown thin films of $YBa_2Cu_3O_{7-\delta}$ on single crystal $SrTiO_3$ substrates have critical current densities $J_c \approx 10^6$ A/cm^2 in zero field which decrease relatively slowly with magnetic field, making them suitable for technological applications (Chaudhari et al. 1987). Unfortunately, polycrystalline bulk materials have J_c's that are disappointingly low, ~10^3–10^4 A/cm^2, and are strongly depressed by a magnetic field (see, for example,

Markert et al. 1989a). The situation can be improved substantially by subjecting $YBa_2Cu_3O_{7-\delta}$ to a melt textured growth process which yields values of J_c of ~10^5 A/cm^2 at 77 K that are not too strongly depressed by an applied magnetic field (Jin et al. 1988). Fortunately, techniques have recently been devised which yield values of J_c in high fields for in-plane grain oriented thin films of $YBa_2Cu_3O_{7-\delta}$ on flexible substrates at 64 K (pumped liquid nitrogen temperatures) that exceed those of NbTi and Nb_3Sn at liquid helium temperatures, as described in sect. 9.0. Presently, two of the leading candidates for technological applications of superconductivity are the $LnBa_2Cu_3O_{7-\delta}$ and $Bi_2Sr_2Ca_{n-1}Cu_nO_{2n+4}$ ($n=2,3$) materials. The first generation superconducting tapes and wires are based on both substituted and unsubstituted $Bi_2Sr_2Ca_{n-1}Cu_nO_{2n+4}$ ($n=2,3$) superconductors prepared by the powder-in-tube technique (Marezio 1998).

4.2. *Superconducting pairing mechanism*

Two features in the T–x phase diagrams for $La_{2-x}Sr_xCuO_4$ and $Nd_{2-x}Ce_xCuO_{4-y}$ in fig. 3 would appear to be relevant to cuprate superconductivity: (i) the apparent electron–hole symmetry may provide a constraint on viable theories of high-T_c superconductivity in cuprates, and (ii) the proximity of antiferromagnetism suggests that superconducting electron pairing in the cuprates may be mediated by AFM spin fluctuations. An AFM pairing mechanism is consistent with the occurrence of d-wave pairing with $d_{x^2-y^2}$ symmetry that is suggested by experiments on several hole-doped cuprates (discussed later in this article). Several theoretical models (for example, Scalapino 1995, Pines 1994), based on AFM spin fluctuations have predicted d-wave superconductivity with $d_{x^2-y^2}$ symmetry for the cuprates.

Other features are consistent with non-phonon-mediated pairing in the hole-doped cuprates. The curve of T_c vs. carrier concentration can be approximated by an inverted parabola with the maximum value of T_c occurring at an optimal dopant concentration x_o (Uchida 1993). (Note that the terminology "under-doped" refers to values of x smaller than the "optimally-doped" value x_o, whereas "over-doped" refers values of x larger than x_o.) The isotope effect on T_c for optimally-doped material is essentially zero (i.e., $T_c \; \alpha \; M^{-\alpha}$ with $\alpha \approx 0$; M = ion mass) (Franck 1994).

On the other hand, microwave penetration depth (Anlage et al. 1994) and Raman spectroscopy measurements (Stadloper et al. 1995) on the electron-doped superconductor $Nd_{1.85}Ce_{0.15}CuO_{4-y}$ indicate that the superconducting order parameter of this material has s-wave symmetry.

It is interesting that superconductivity with values of T_c exceeding ~40 K has only been observed in layered cuprates which have strongly anisotropic, nearly two-dimensional electronic properties. An important issue for these materials is the nature of interlayer transport and the role it plays in the superconductivity. Reflectance $\mathcal{R}(\omega)$ measurements with polarized light reveal that $\mathcal{R}(\omega)$ for the electric field $\mathcal{E}$ parallel to the CuO_2 planes, $\mathcal{E} \parallel CuO_2$, exhibits a metallic response, while $\mathcal{R}(\omega)$ for $\mathcal{E} \perp CuO_2$ resembles that of ionic insulators with characteristic phonon peaks in the far infrared. This is illustrated in fig. 6 where R vs. ω data for $Tl_2Ba_2CuO_{6+x}$ (Tl2201) from Basov et al. (1999) are displayed.

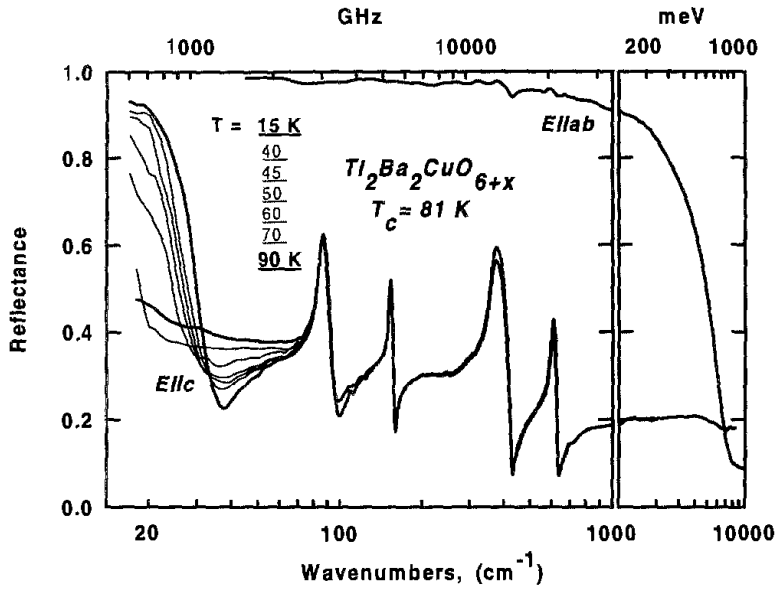

Fig. 6. Reflectance of $Tl_2Ba_2CuO_{6+x}$ measured with $\mathcal{E} \| c$ and $\mathcal{E} \| ab$ polarizations of incident radiation. The c-axis reflectance is nearly insulating in the normal state but at $T < T_c \approx 80$ K is dominated by the Josephson-like plasma edge. From Basov et al. (1999).

For temperatures below T_c, a sharp plasma edge at $\omega = 37\,\mathrm{cm}^{-1}$ evolves out of a nearly "insulating" normal state spectrum since the supercurrents flow in all crystallographic directions. In an effort to explore the relationship between changes in the incoherent c-axis conductivity below T_c and the c-axis superfluid density, Basov et al. (1999) have analyzed the interlayer conductivity of the cuprate high-T_c superconductors $Tl_2Ba_2CuO_{6+x}$, $La_{2-x}Sr_xCuO_4$, and $YBa_2Cu_3O_{6.6}$, all of which all show incoherent interlayer response in the normal state. The analysis reveals that the magnitude of the superfluid density ρ_s significantly exceeds the weight missing from the real part of the conductivity in the frequency region comparable to the superconducting energy gap 2Δ. This indicates that a significant fraction of ρ_s is derived from mid infrared frequencies. Basov et al. (1999) suggest that the discrepancy between the magnitude of ρ_s and the spectral weight that is missing from the far infrared part of the conductivity can be interpreted in terms of an interlayer kinetic energy change associated with the superconductivity.

Because of their high T_c's, short coherence lengths, long penetration depths, and large anisotropy, the cuprate superconductors exhibit a wealth of striking vortex phases and phenomena that are currently being vigorously investigated. (For reviews see, for example, Huse et al. 1992, Blatter et al. 1994, Farrell 1994, Brandt 1995, and Crabtree and Nelson 1997.)

5. Symmetry of the superconducting order parameter

During the last several years, a great deal of effort has been expended to determine the symmetry of the superconducting order parameter of the high-T_c cuprate superconductors

(Cox and Maple 1995, Levi 1993, 1996). The pairing symmetry provides clues to the identity of the superconducting pairing mechanism which is essential for the development of the theory of high-temperature superconductivity in the cuprates.

Shortly after the discovery of high-T_c superconductivity in the cuprates, it was established from flux quantization, Andreev reflection, Josephson effect, and nuclear magnetic resonance (NMR) Knight-shift measurements, that the superconductivity involves electrons that are paired in singlet spin states (Batlogg 1990). Possible orbital pairing states include s-wave, extended s-wave, and d-wave states. In the s-wave state, the energy gap $\Delta(\boldsymbol{k})$ is *isotropic*; i.e., $\Delta(\boldsymbol{k})$ is constant over the Fermi surface. This leads to "activated" behavior of the physical properties in the superconducting state for $T << \Delta$; e.g., the specific heat $C_e(T)$, ultrasonic attenuation coefficient $\alpha_s(T)$, and NMR spin lattice relaxation rate $1/T_1(T)$ vary as $\exp(-\Delta/T)$. For the extended s-wave state, the energy gap $\Delta(T)$ is *anisotropic*; i.e., $\Delta(\boldsymbol{k})$ exhibits a variation over the Fermi surface which has the same symmetry as the rotational symmetry of the crystal. Similarly, for the d-wave case, the energy gap $\Delta(\boldsymbol{k})$ is *anisotropic*, but with a symmetry that is *lower* than the symmetry of the crystal. The d-wave state that is consistent with most of the experiments discussed below has $d_{x^2-y^2}$ symmetry, which can be expressed as $\Delta(\boldsymbol{k}) = \Delta_0[\cos(k_x a) - \cos(k_y a)]$. For both the extended s-wave and d-wave cases, $\Delta(\boldsymbol{k})$ vanishes at lines on the Fermi surface, resulting in a density of states $N(E)$ that is linear in energy E at low values of E. This leads to "power law" T^n (n = integer) behavior of the physical properties for $T << \Delta$; e.g., $C_e(T) \sim T^2$, the superconducting penetration depth $\lambda(T) \sim T$, and $1/T_1(T) \sim T^3$. The establishment of the symmetry of the superconducting order parameter requires the determination of both the *magnitude* and the *phase* of $\Delta(\boldsymbol{k})$. Shown in fig. 7 (overleaf) is a schematic diagram of the variation of the energy gap over the Fermi surface and the density of states $N(E)$ vs. E for the "s", extended "s", and "d"$_{x^2-y^2}$ states (Cox and Maple 1995).

5.1. *Probing the magnitude of the superconducting order parameter*

A number of different types of measurements have been performed on the high-T_c cuprate superconductors which are sensitive to $|\Delta(\boldsymbol{k})|$. These include microwave penetration depth $\lambda(T)$ (Hardy et al. 1993), microwave surface conductivity (Bonn et al. 1993), nuclear magnetic resonance (NMR) relaxation rate $1/T_1(T)$ (Martindale et al. 1993), magnetic field dependence of the electronic specific heat $C_e(T)$ (Moler et al. 1994), thermal conductivity (Aubin et al. 1997), angle resolved photoemission spectroscopy (ARPES) (Shen et al. 1993), quasiparticle tunneling (Mandrus et al. 1990, Coffey and Coffey 1993) and Raman scattering (Deveraux et al. 1994). The results of these studies are generally consistent with a superconducting state with $d_{x^2-y^2}$ or extended s-wave symmetry for the hole-doped cuprates such as YBCO-123, 124, LSCO, and BSCCO, and s-wave symmetry for the electron-doped superconductor NCCO (Wu et al. 1993, Anlage et al. 1994, Stadloper et al. 1995). The experiments discussed below indicate a dominant component of $d_{x^2-y^2}$ symmetry in the superconducting order parameter of hole-doped cuprates. Superconductivity with d-wave symmetry for hole-doped cuprates

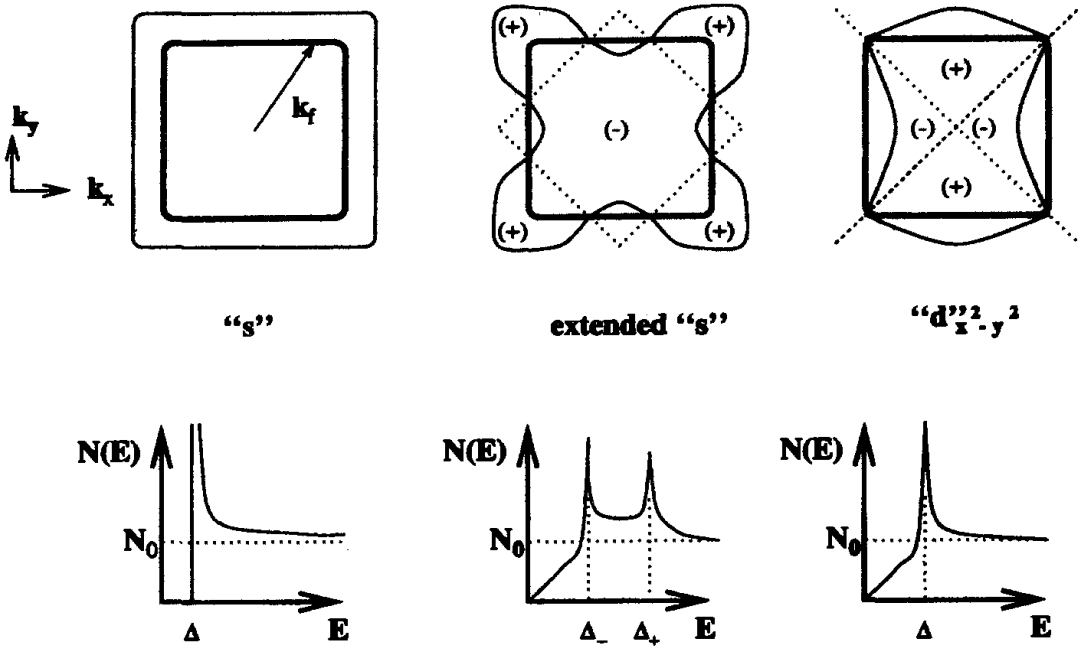

Fig. 7. Fermi surface gap functions and densities of states of a superconductor with tetragonal symmetry for various pairing symmetries. The gap functions in the $k_z = 0$ plane (top) are represented by the light solid lines; distance from the Fermi surface (dark solid lines) gives the amplitude, a positive value being outside the Fermi surface, a negative value inside. The corresponding density of states for one-quasiparticle excitations $N(E)$ is shown below each gap function, with N_0 the normal state value. Gap node surfaces are represented by the dashed lines. Left: The classic s-wave case, where the gap function is constant, with value Δ. This gives rise to a square-root singularity in $N(E)$ at energy $E = \Delta$. Middle: The extended s-wave case derives from pairs situated on nearest-neighbor square lattice sites in real space, with an approximate k-space form of $\cos(k_x a) + \cos(k_y a)$. For the Fermi surface shown here, the gap function has lines of nodes running out of the page. Right: A d-wave function of $x^2 - y^2$ symmetry. The extended s-wave and d-wave functions shown here each have a linear density of states up to order Δ, which measures the maximum gap amplitude about the Fermi surface. From Cox and Maple (1995).

and s-wave symmetry for electron-doped cuprates is a rather surprising result, considering the similarities in the structures of the hole-doped and electron-doped superconductors and the fact that they are both derived from chemical substitution of antiferromagnetic insulating parent compounds.

5.2. *Probing the phase of the superconducting order parameter*

Several different types of measurements which are sensitive to the phase of $\Delta(\boldsymbol{k})$ have been performed. These measurements, all of which involve the Josephson effect, include superconducting quantum interference device (SQUID) interferometry (Wollman et al. 1993, Brauner and Ott 1994, Mathai et al. 1995), single junction modulation (Wollman et al. 1995, Miller et al. 1995), tricrystal ring magnetometry (Tsuei et al. 1994, 1996, Kirtley et al. 1995), c-axis Josephson tunneling (Sun et al. 1994, 1995, 1996, Lesueur et al. 1997, Kleiner et al. 1996), and grain boundary tunneling (Chaudhari and Lin 1994). The SQUID interferometry, single junction modulation, and tricrystal ring

magnetometry measurements were performed on YBCO, while tricrystal magnetometry experiments have also been carried out on TBCCO. These experiments indicate that the superconducting order parameter in the YBCO and TBCCO hole-doped materials has $d_{x^2-y^2}$ symmetry. However, *c*-axis Josephson tunneling studies on junctions consisting of a conventional superconductor (Pb) and twinned or untwinned single crystals of YBCO indicate that the superconducting order parameter of YBCO has a significant s-wave component (Sun et al. 1994, 1995).

Recently, a new class of *c*-axis Josephson tunneling experiments in which a conventional superconductor (Pb) was deposited across a single twin boundary of a YBCO single crystal were performed by Kouznetsov et al. (1997). The Josephson critical current I_c was then measured as a function of magnitude and angle ϕ of magnetic field applied in the plane of the sample. For B aligned perpendicular to the twin boundary, a maximum in I_c as a function of B was observed at $B=0$, whereas for B parallel to the twin boundary, a minimum in I_c was observed at $B=0$. In all samples investigated, a clear experimental signature of an order parameter phase shift across the twin boundary was observed. The results provide strong evidence for mixed d- and s-wave pairing in YBCO and are consistent with predominant d-wave pairing with $d_{x^2-y^2}$ symmetry and a sign reversal of the s-wave component across the twin boundary.

An anomaly in the thermal conductivity κ at low temperature of the high-T_c superconductor $Bi_2Sr_2Ca(Cu_{1-x}Ni_x)_2O_8$ was recently reported by Movshovich et al. (1998). The anomaly takes the form of a sharp reduction of κ at a temperature $T_c^* \approx 200\,\text{mK}$, which separates a higher temperature region where κ varies as T^α with α between 1.6 and 1.75 and a lower temperature region where κ is linear in T. The low-temperature anomaly was found to be suppressed by the application of a small magnetic field. Movshovich et al. proposed that the observed behavior is consistent with a phase transition into a second bulk low-temperature superconducting state at T_c^*. They note that the presence of a second superconducting state would constitute direct evidence for unconventional superconductivity in $Bi_2Sr_2CaCu_2O_8$.

Various mixed s- and d-wave pairing models that have been developed to account for the superconducting properties of the orthorhombic YBCO-123 system are reviewed by Béal-Monod (1998).

6. Normal state properties

It was realized at the outset that the normal state properties of the high-T_c cuprate superconductors are unusual and appear to violate the Landau Fermi liquid paradigm (Anderson 1987, Levi 1990, Levin et al. 1991, Laughlin 1988, Varma et al. 1989). Some researchers share the view that in so far as the normal state properties reflect the electronic structure that underlies high-T_c superconductivity, it will be necessary to develop an understanding of the normal state before the superconducting state can be understood.

The anomalous normal state properties first identified in the high-T_c cuprate superconductors include the electrical resistivity and Hall effect. The electrical resistivity $\rho_{ab}(T)$

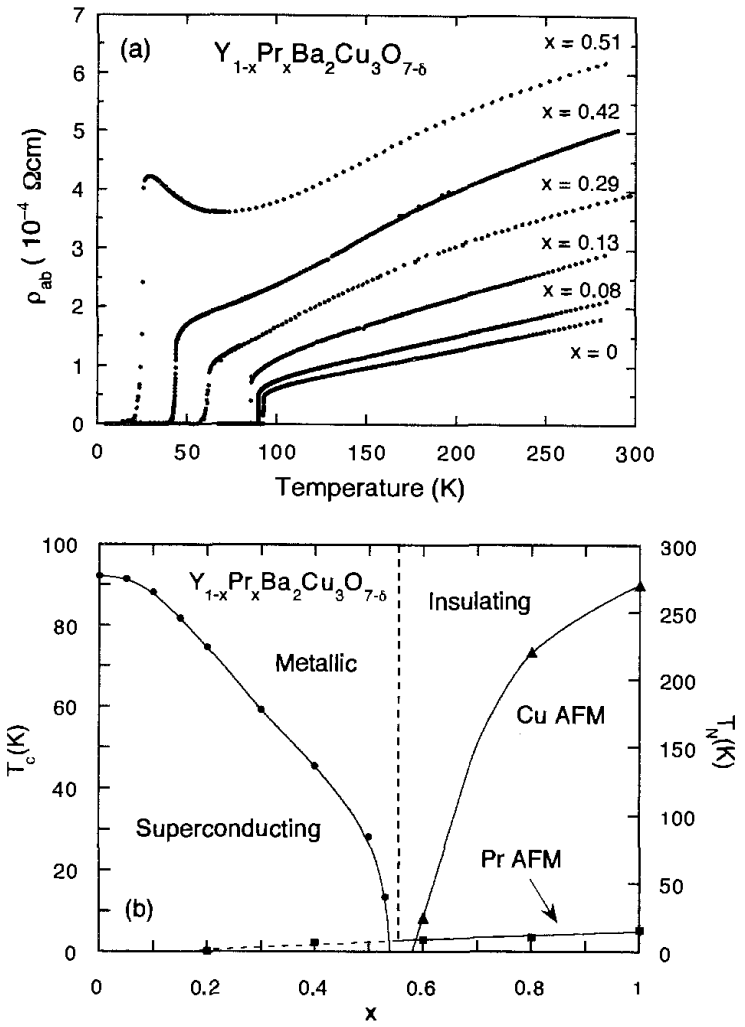

Fig. 8. (a) In-plane electrical resistivity ρ_{ab} vs temperature T curves for $Y_{1-x}Pr_xBa_2Cu_3O_{7-\delta}$ $(0 \leqslant x \leqslant 0.51)$ single crystals. From Maple et al. (1994). (b) Temperature T vs Pr concentration x phase diagram for the $Y_{1-x}Pr_xBa_2Cu_3O_{7-\delta}$ system, delineating metallic, superconducting, insulating, and antiferromagnetically ordered regions. After Maple et al. (1994) and Neumeier and Maple (1992).

in the *ab*-plane of many of the hole-doped cuprate superconductors near optimal doping has a linear temperature dependence between T_c and high temperatures ~1000 K, with an extrapolated residual resistivity $\rho_{ab}(0)$ that is very small; i.e., $\rho_{ab}(T) \approx \rho_{ab}(0) + cT$, with $\rho_{ab}(0) \approx 0$ and the value of c similar within different classes of cuprate materials (Iye 1992). The Hall coefficient R_H is inversely proportional to T and the cotangent of the Hall angle $\theta_H = R_H/\rho$ varies as T^2; i.e., $\cot(\theta_H) \equiv \sigma_{xx}/\sigma_{xy} = AT^2 + B$ (Chien et al. 1991). The linear T-dependence of $\rho(T)$ and the quadratic T-dependence of $\cot(\theta_H)$ have been attributed to longitudinal and transverse scattering rates τ_l^{-1} and τ_t^{-1} that vary as T and T^2, respectively Anderson (1991). In the RVB model, the constant and T^2 terms in τ_t^{-1} and, in turn, $\cot(\theta_H)$, are ascribed to scattering of spinons by magnetic impurities and other spinons, respectively.

An example of the linear T-dependence of $\rho_{ab}(T)$ is displayed in fig. 8a for the $Y_{1-x}Pr_xBa_2Cu_3O_{7-\delta}$ system (Maple et al. 1994). According to experiments in which Ca^{2+} ions are counter-doped with Pr for Y in $YBa_2Cu_3O_{7-\delta}$, the Pr ions localize holes at a rate of ~one hole per substituted Pr ion (Neumeier et al. 1989) (see below). Thus, as x is increased, the $Y_{1-x}Pr_xBa_2Cu_3O_{7-\delta}$ system becomes more and more under-doped and T_c decreases, vanishing near the metal–insulator transition that occurs at $x_{mi} \approx 0.55$. Displayed in fig. 8b is the T–x phase diagram for the $Y_{1-x}Pr_xBa_2Cu_3O_{7-\delta}$ system which reveals the behavior of $T_c(x)$ as well as the Néel temperatures $T_N(x)$ for AFM ordering of Cu and Pr magnetic moments (Maple et al. 1994, Neumeier and Maple 1992). It has been argued that the depression of T_c with x is primarily due to the decrease in the number of mobile holes with increasing Pr concentration, although magnetic pair breaking by Pr may also be involved (Neumeier et al. 1989, Neumeier and Maple 1992) (see below). In contrast, both $\rho_{ab}(T)$ and $\rho_c(T)$ of the optimally-doped electron-doped cuprate $Sm_{1.83}Ce_{0.17}CuO_{4-y}$ vary as T^2, indicative of three-dimensional Fermi liquid behavior (Dalichaouch et al. 1991).

Shown in fig. 9a are plots of T_c vs. Ca concentration y for four Pr concentrations x in the $Y_{1-x-y}Ca_yPr_xBa_2Cu_3O_{7-\delta}$ system (Neumeier et al. 1989). Curves formed by solid and dashed lines represent the equation $T_c(x,y) = (97\,\mathrm{K}) - (425\,\mathrm{K})(0.1 - 0.95x + y)^2 - (96.5\,\mathrm{K})x$. The first term is the maximum attainable value of T_c (97 K), the second term represents the effect of hole generation by Ca (y) ions and localization of holes by Pr (x) ions (0.1 is

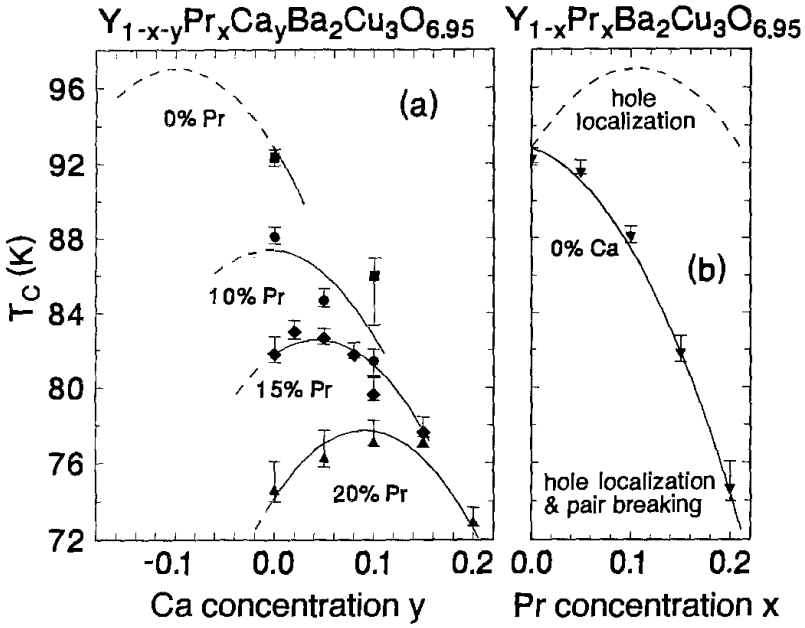

Fig. 9. (a) Superconducting critical temperature T_c vs Ca concentration y for four Pr concentrations x in the $Y_{1-x-y}Ca_yPr_xBa_2Cu_3O_{7-\delta}$ system (Neumeier et al. 1989). Curves formed by solid and dashed lines represent the equation $T_c(x,y) = (97\,\mathrm{K}) - (425\,\mathrm{K})(0.1 - 0.95x + y)^2 - (96.5\,\mathrm{K})x$ whose meaning is explained in the text. (b) T_c vs Pr concentration x. The dashed line represents the function $T_c(x, y=0) + (96.5\,\mathrm{K})x$ which describes pure hole localization; the solid line represents the function $T_c(x, y=0)$ which includes hole localization and pair breaking. After Maple et al. (1994) and Neumeier et al. (1989).

an optimal hole concentration), while the last term describes the overall depression of T_c with x due to pair breaking interactions in the linear low concentration regime. These data illustrate the inverted parabolic dependence of T_c on charge carrier concentration observed in many superconducting cuprate systems. Displayed in fig. 9b is a plot of T_c vs. Pr concentration x. The dashed line represents the function $T_c(x,y=0)+(96.5\,\mathrm{K})x$ which corresponds to pure hole localization, while the solid line represents the function $T_c(x,y=0)$ which includes hole localization and pair breaking.

6.1. *Normal ground state*

The evolution of the normal ground state of the cuprates as a function of dopant concentration is particularly interesting. This is reflected in the temperature dependences of the *ab*-plane and *c*-axis electrical resistivities $\rho_{ab}(T)$ and $\rho_c(T)$ (Cooper and Gray 1994). Both $\rho_{ab}(T)$ and $\rho_c(T)$ exhibit insulating behavior (i.e., $d\rho/dT<0$) in the under-doped region, $\rho_{ab}(T)$ is metallic (i.e., $d\rho/dT>0$) and $\rho_c(T)$ is insulating or metallic in the optimally-doped region, depending on the system, and $\rho_{ab}(T)$ and $\rho_c(T)$ are both metallic in the over-doped region. The linear T-dependence of $\rho_{ab}(T)$ and the insulating behavior of $\rho_c(T)$ suggest two-dimensional non-Fermi liquid behavior near the optimally-doped region, whereas the metallic $\rho(T)\,\alpha\,T^n$ with $n>1$ reflects a tendency towards three-dimensional Fermi liquid behavior in the over-doped region. Recent measurements in 61-tesla pulsed magnetic fields to quench the superconductivity have been particularly useful in elucidating the evolution of $\rho_{ab}(T)$ and $\rho_c(T)$ with dopant concentration in the $La_{2-x}Sr_xCuO_4$ system (Boebinger et al. 1996). Both $\rho_{ab}(T)$ and $\rho_c(T)$ were found to exhibit a $-\ln T$ divergence in the under-doped region, indicative of a three-dimensional non-Fermi liquid (Ando et al. 1995). Shown in fig. 10 is the temperature–Sr concentration (T–x) phase diagram of the $La_{2-x}Sr_xCuO_4$ system, after the superconductivity has been suppressed by an intense pulsed magnetic field (Boebinger et al. 1996). The insulator–

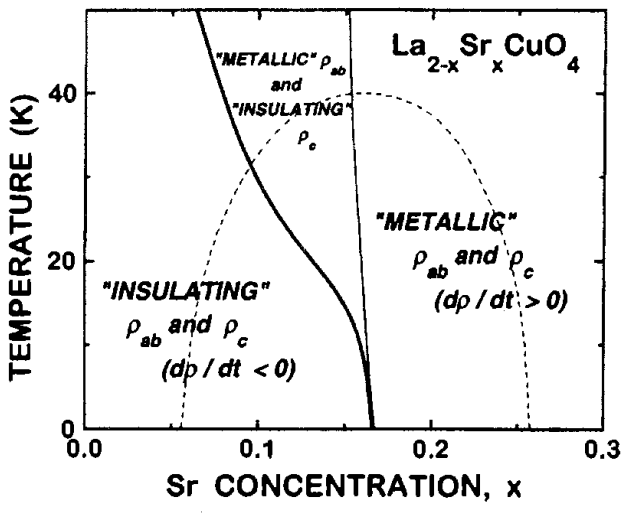

Fig. 10. Temperature–Sr concentration (T–x) phase diagram of the $La_{2-x}Sr_xCuO_4$ system, after superconductivity has been suppressed by an intense pulsed magnetic field. The insulator–metal crossover occurs near optimum doping, and a new insulating regime is revealed, in which the electrical resistivity diverges as the logarithm of the temperature. The dashed line represents the T_c vs x curve in zero field; the two solid lines delineate the insulating ρ_{ab} and ρ_c, metallic ρ_{ab} and insulating ρ_c, and metallic ρ_{ab} and ρ_c regions in the normal state accessed by high magnetic fields. From Boebinger et al. (1996).

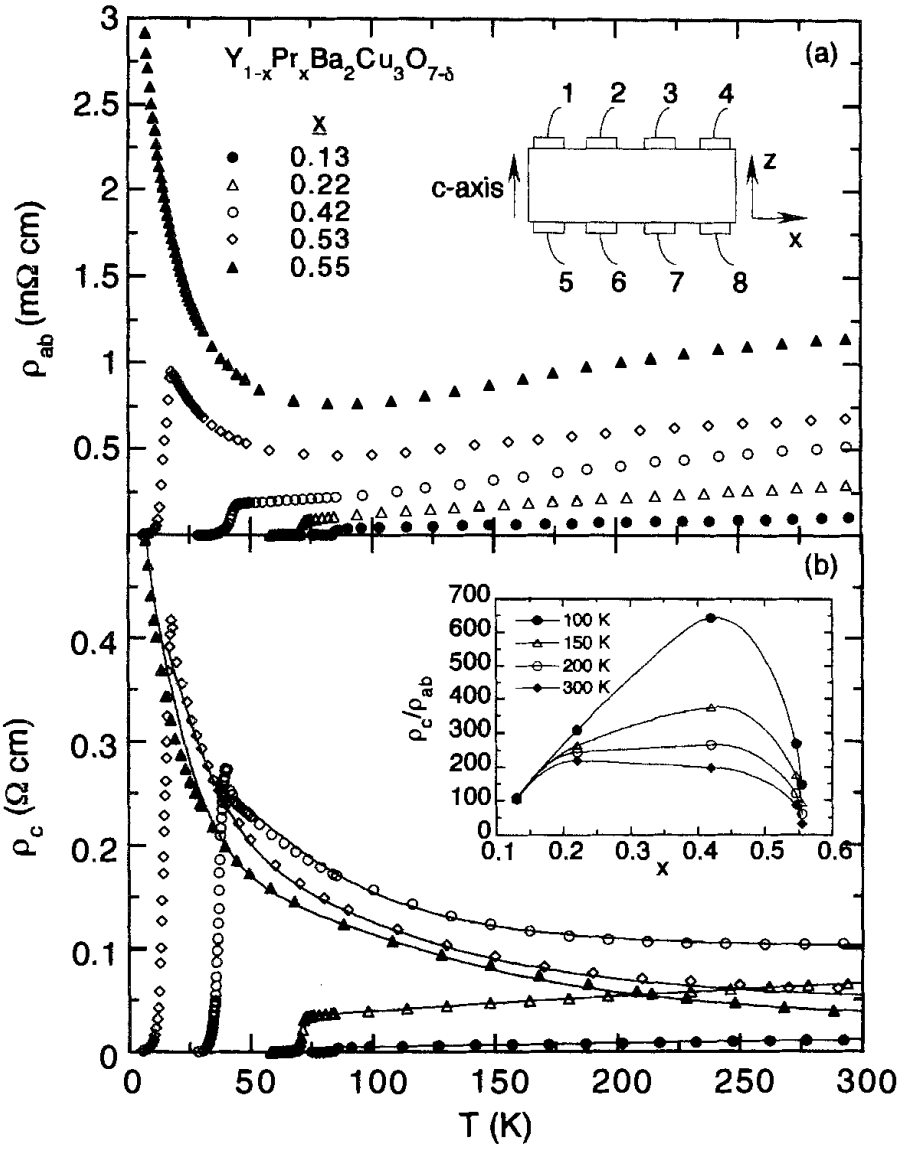

Fig. 11. (a) In-plane resistivity $\rho_{ab}(T)$ and (b) out-of-plane resistivity $\rho_c(T)$ for $Y_{1-x}Pr_xBa_2Cu_3O_{7-\delta}$ single crystals. The solid lines in (b) are fits to the data using a model described by Jiang et al. (1997). Inset to fig. 11a: the configuration of leads used in the measurements. Inset to fig. 11b: Anisotropy ρ_c/ρ_{ab} vs Pr concentration x at different temperatures. The solid lines are guides to the eye. From Jiang et al. (1997).

metal crossover occurs near optimum doping and a new insulating regime is revealed, in which the electrical resistivity diverges as the logarithm of the temperature.

As an example of the evolution of $\rho_{ab}(T)$ and $\rho_c(T)$ with doping, we again refer to the $Y_{1-x}Pr_xBa_2Cu_3O_{7-\delta}$ system. Shown in fig. 11 are $\rho_{ab}(T)$ and $\rho_c(T)$ data for $Y_{1-x}Pr_xBa_2Cu_3O_{7-\delta}$ single crystals in the range of Pr concentrations $0 \leqslant x \leqslant 0.55$ (Jiang et al. 1997). The following features in the $\rho_{ab}(T)$ and $\rho_c(T)$ data in fig. 11 are evident: a nonmonotonic evolution of $\rho_c(T)$ with x, the transformation of both $\rho_{ab}(T)$ and $\rho_c(T)$ from metallic to semiconducting with x, and the coexistence of metallic $\rho_{ab}(T)$ and

semiconducting $\rho_c(T)$ for a certain range of doping. The nonmonotonic variation of $\rho_c(T)$ with x in fig. 11b can be described with a phenomenological model (Jiang et al. 1997) which assumes that the c-axis conductivity takes place via incoherent elastic tunneling between CuO_2 bilayers and CuO chain layers with a gap in the energy spectrum of the CuO chains (solid lines in fig. 11b).

6.2. *Pseudogap*

Perhaps the most remarkable aspect of the normal state is the pseudogap in the charge and spin excitation spectra of under-doped cuprates (Levi 1996). The pseudogap has been inferred from features in various transport, magnetic, and thermal measurements including $\rho_{ab}(T)$ (Bucher et al. 1993, Batlogg et al. 1994, Ito et al. 1993), $R_H(T)$ (Hwang et al. 1994), thermoelectric power $S(T)$ (Tallon et al. 1995), NMR Knight shift K(T) (Warren et al. 1989), NMR spin-lattice relaxation rate $1/T_1(T)$ (Takigawa et al. 1991, Alloul et al. 1993, Imai et al. 1988), magnetic susceptibility $\chi(T)$ (Hwang et al. 1994), neutron scattering (Rossat-Mignod et al. 1991), and specific heat $C(T)$ (Loram et al. 1993), as well as spectroscopic measurements such as infrared absorption (Homes et al. 1993, Basov et al. 1994, Puchkov et al. 1996) and ARPES (Ding et al. 1996, Loeser et al. 1996).

An example of the features in $\rho_{ab}(T)$ that are associated with the pseudogap can be seen in the $\rho_{ab}(T)$ data displayed in figs. 8a and 11a for the $Y_{1-x}Pr_xBa_2Cu_3O_{7-\delta}$ system. As the system becomes more under-doped with increasing x, $\rho_{ab}(T)$ deviates from linear behavior at higher temperature at a characteristic temperature T^* which represents a crossover into the pseudogap state at $T < T^*$.

The transport, thermal, magnetic, and infrared studies of the pseudogap have been carried out on several cuprate materials, including LSCO, YBCO-123, YBCO-124, and BSCCO-2212, while the ARPES investigations of the pseudogap have mainly focused on BSCCO, although ARPES measurements have also been made on oxygen-deficient YBCO.

The ARPES measurements reveal several striking aspects of the pseudogap. The magnitude of the pseudogap has the same k-dependence in the ab-plane as the magnitude of the superconducting energy gap, with maxima in the directions of k_x and k_y and minima at 45° to these directions. In fact, the symmetry is consistent with $d_{x^2-y^2}$ symmetry inferred from Josephson tunneling measurements on hole-doped cuprates discussed previously. Furthermore, measurements of the temperature dependence of the pseudogap at the angles where it is a maximum show that the superconducting gap grows continuously out of the pseudogap and that the value of the sum of both gaps at low temperatures is constant, independent of the temperature T^* at which the pseudogap opens, or T_c. This is in marked contrast to the situation in conventional superconductors where the energy gap is proportional to T_c.

These features of the pseudogap are illustrated in figs. 12a,b which show the k-dependence of the energy gap and the dependence of the maximum gap on temperature from the ARPES measurements of Ding et al. (1996) on BSCCO-2212 samples with T_c's of 87 K, 83 K, and 10 K. The pseudogap and superconducting regions for BSCCO-2212

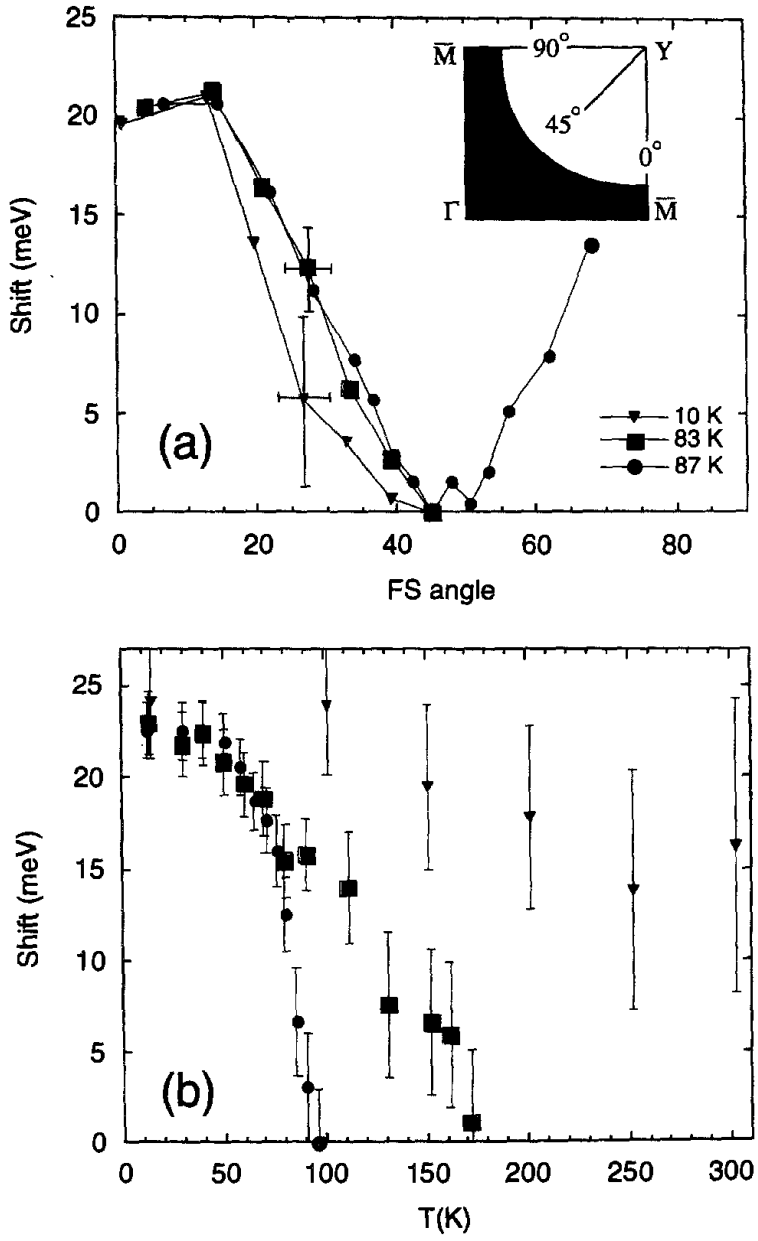

Fig. 12. Momentum and temperature dependence of the energy gap estimated from leading edge shifts of ARPES spectra for BSCCO-2212. (a) k-dependence of the gap in the $T_c = 87$ K, 83 K, and 10 K samples, measured at 14 K. The inset shows the Brillouin zone with a large Fermi surface (FS) closing the (π, π) point, with the occupied region shaded. (b) Temperature dependence of the maximum gap in a near-optimal $T_c = 87$ K sample (circles), and two underdoped samples with $T_c = 83$ K (squares) and $T_c = 10$ K (triangles). From Ding et al. (1996).

derived from the ARPES measurements of Ding et al. (1996) are summarized in the temperature T vs. charge carrier doping plot in fig. 13.

Recently, direct measurements of the quasiparticle density of states (DOS) by scanning tunneling spectroscopy on $Bi_2Sr_2CaCu_2O_{8+\delta}$ (BSCCO-2212) single crystals as a function

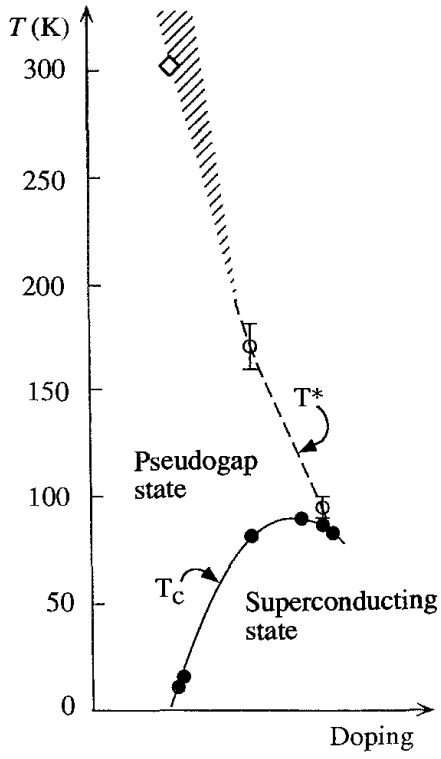

Fig. 13. Schematic phase diagram of BSCCO-2212 as a function of doping. The solid symbols represent the T_c's determined from magnetic susceptibility measurements. The open symbols are the T^*'s at which the pseudogap closes, derived from the data shown in fig. 12. From Ding et al. (1996).

of oxygen doping and temperature were made by Renner et al. (1998). It was found that the shape of the DOS in the superconducting state is essentially doping independent, the pseudogap above T_c scales with the superconducting gap, and the pseudogap is also present in overdoped samples. Both gaps were found to be essentially temperature independent.

The behavior of the pseudogap in the normal state excitation spectrum of optimally and underdoped high-T_c cuprate superconductors was investigated in high magnetic fields by Gorny et al. (1999). High-accuracy measurements of the magnetic field dependence of the ^{63}Cu spin lattice relaxation rate T_1^{-1} in near optimally doped $YBa_2Cu_3O_{7-\delta}$ revealed that there is no magnetic field dependence of the copper relaxation rate in this material. While the magnetic fields employed in the experiments shift T_c down by 8 K, they do not affect the temperature of the onset of the pseudogap, indicating that the pseudogap is unrelated to conventional fluctuations into the superconducting state. From the absence of any magnetic field effect, it was concluded that a relatively large energy scale is associated with the gap mechanism, and, if dynamical pairing correlations or preformed pairs are involved, the length scale must be very short.

The pseudogap and the superconducting energy gap appear to be intimately related to one another, with the former the precursor of the latter. The results described above support the view that a unified theory of both the normal and superconducting states of the cuprates is imperative.

7. Generic phase diagram

Based upon investigations on LSCO, YBCO-123, YBCO-124, BSCCO, and other systems, one can construct a generic T–x phase diagram which is shown schematically in fig. 14. The phase diagram is very rich and contains insulating, antiferromagnetic, superconducting, pseudogap, two-dimensional (2D) non-Fermi liquid like, and three-dimensional (3D) Fermi liquid like regions.

A number of models and notions have been proposed to explain the part of the phase diagram delineated by the curves of T^* and T_c vs. x (for example, Suzumura et al. 1988, Fukuyama 1992, Nagaosa and Lee 1992, Randeria et al. 1992, Emery and Kivelson 1995, Uemura 1996, Zhang 1997, Castellani et al. 1997). Generally, these models involve the local pairing of electrons (or holes) at the temperature T^* leading to a suppression of the low-lying charge and spin excitations and the formation of the normal state pseudogap, followed by the onset of phase coherence at T_c that results in superconductivity. Since the phenomenon of superconductivity involves coherent pairing, a bell shaped curve of T_c vs. x results as shown schematically in fig. 15. For example, in resonating valence bond (RVB) models (Anderson 1987, Suzumura et al. 1988, Fukuyama 1992, Nagaosa and Lee 1992, Randeria et al. 1992, Zhang 1997) which incorporate spin–charge separation into "spinons" with spin $s=1/2$ and charge $q=0$ and "holons" with $s=0$ and $q=+e$, where e is the charge of the electron, the spinons become paired (spin pseudogap) at T^* and coherent pairing of holons (Bose–Einstein condensation) occurs at T_ϕ, resulting in superconductivity.

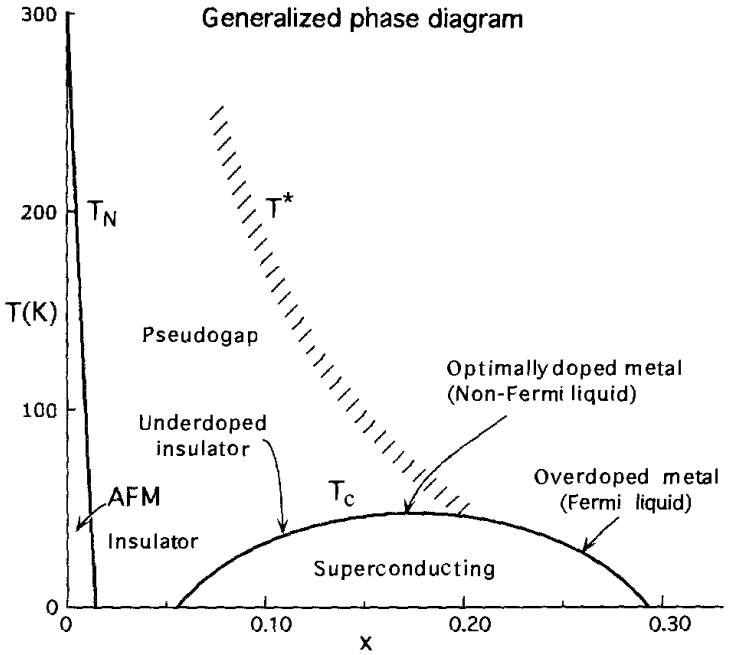

Fig. 14. Generic temperature–dopant concentration, T–x, phase diagram for cuprates (schematic). The solid lines labeled T_N and T_c delineate the antiferromagnetic (AFM) and superconducting regions, respectively. The "hatched" line denoted T^* represents the crossover into the pseudogap state.

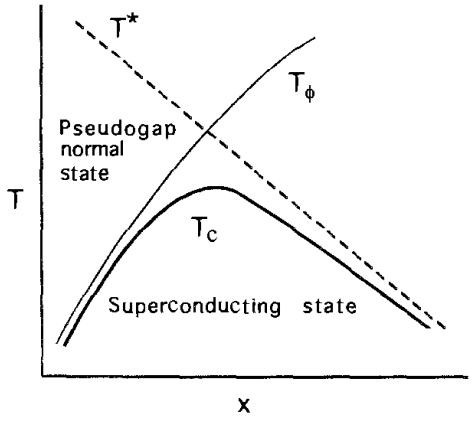

Fig. 15. Schematic temperature–dopant concentration, T–x, phase diagram for the cuprates. The dashed line labeled T^* represents the temperature below which some type of local pairing occurs leading to a suppression of low-energy excitations and the formation of the pseudogap. The solid line labeled T_ϕ denotes the temperature below which phase coherence develops, resulting in superconductivity. The thick solid line labeled T_c delineates the superconducting region.

8. Spin and charge stripe phases

Extraordinary "stripe phases" that consist of spin or charge modulations with a periodicity different from that of the lattice (incommensurate) have recently been observed in certain cuprates (Levi 1998). In the $La_{2-x}Sr_xCuO_4$ system, inelastic neutron scattering experiments have yielded evidence for dynamical two-dimensional spin correlations characterized by an incommensurate wave vector (Cheong et al. 1991, Mason et al. 1992, Thurston et al. 1992). An intriguing question is what roles do these dynamical spin and charge stripe correlations play in the anomalous normal state properties and the superconducting pairing mechanism in the cuprates. It is interesting that the stripe order in $La_{1.6-x}Nd_{0.4}Sr_xCuO_4$ is static, and there is evidence for both spin and charge stripes (Tranquada et al. 1995). In this material, the partial substitution of Nd for La results in a change in crystal structure from the usual low-temperature orthorhombic (LTO) phase to the low-temperature tetragonal (LTT) phase, and a depression of T_c near $x=0.125$. The LTO–LTT structural transition occurs at ~70 K in $La_{1.6-x}Nd_{0.4}Sr_xCuO_4$ for $x=0.12$, and evidence for static spin and charge stripes comes from neutron scattering as well as x-ray scattering experiments (Tranquada et al. 1995, v. Zimmermann et al. 1998). The characteristic wave vectors associated with magnetic scattering in $La_{1.85}Sr_{0.15}CuO_4$ and $La_{1.48}Nd_{0.4}Sr_{0.12}CuO_4$, are essentially identical. Thus, the major difference between the two systems appears to be the static vs. dynamic character of the correlations. This similarity suggests that dynamical stripe correlations of both spin and charge exist in superconducting $La_{1.85}Sr_{0.15}CuO_4$. Static charge stripes have been observed in the insulating phase of the cuprate relatives, nickel and manganese oxides.

9. Technological applications of superconductivity

Technological applications of superconductivity can be divided into two major areas: superconducting electronics and superconducting wires and tapes. While the widespread use of high-T_c cuprate superconductors in technology has not yet been realized, steady and

significant progress has been made towards this objective during the past decade. Recent developments suggest that high-T_c cuprate superconductors will begin to have a significant impact on technology during the next decade. The applications in superconducting electronics that are likely to be realized on this time scale have been summarized in an article by Rowell (1997). In the order in which they are anticipated, these applications include: SQUIDs, NMR coils, wireless communications subsystems, magnetic resonance imaging (MRI) coils and NMR microscopes, and digital instruments. In the area of superconducting wires and tapes, applications that appear to be feasible within this same time period include: power transmission lines, motors and generators, transformers, current limiters, magnetic energy storage, magnetic separation, research magnet systems, and current leads.

An example of recent progress in the area of superconducting wires and tapes is the development of flexible superconducting ribbons consisting of deposits of YBCO on textured substrates which have critical current densities $J_c \approx 10^6$ A/cm^2 in fields up to 8 T at 64 K, a temperature that can be achieved by pumping on liquid nitrogen (Hawsey and Peterson 1996). The performance of these prototype conductors in strong magnetic fields already surpasses that of NbTi and Nb_3Sn, which are currently used in commercial superconducting wires at liquid helium temperatures, in a comparable field range. The YBCO tapes are based on processes developed at two U.S. Department of Energy (DOE) National Laboratories, Los Alamos (LANL) and Oak Ridge (ORNL), under the DOE's National Superconductivity Program for Electric Power Applications. The essential step in both the LANL and ORNL processes is the preparation of a textured substrate, or "template," onto which a thick film of YBCO is deposited with well-aligned YBCO grains, that match the alignment of the underlying substrate. The alignment of the YBCO grains results in the high critical current density. The substrate technology in the LANL process relies on a technique called "ion-beam assisted deposition" (IBAD) (Wu et al. 1994), while in the ORNL process it involves "rolling assisted biaxially-textured substrates" (RABiTS) (Goyal et al. 1997). In both the LANL and the ORNL processes, pulsed laser deposition (PLD) is used to deposit the superconducting YBCO layer and some of the buffer layers.

Shown in fig. 16 is the magnetic field dependence of the critical current density for the IBAD and RABiTS based YBCO coated samples recently produced at LANL and ORNL, respectively. These coated samples operated in the liquid nitrogen temperature range clearly outperform the metallic superconductors (NbTi, Nb_3Sn) at 4.2 K. Furthermore, even in the worst field direction ($H \parallel c$), and for temperatures below 65 K, the short sample YBCO coated conductors operated in a 8-tesla background field have at least an order of magnitude higher J_c than pre-commercial BSCCO-2223 wire with no applied field.

The high-T_c YBCO coated tapes have been shown to be extremely flexible and to retain the high current carrying capacity, so that they appear to be suitable for wound magnet and coil applications. A significant challenge that remains is the development of efficient, continuous commercially viable processes for fabricating long lengths of these high current carrying in-plane aligned YBCO coated conductors with uniform properties.

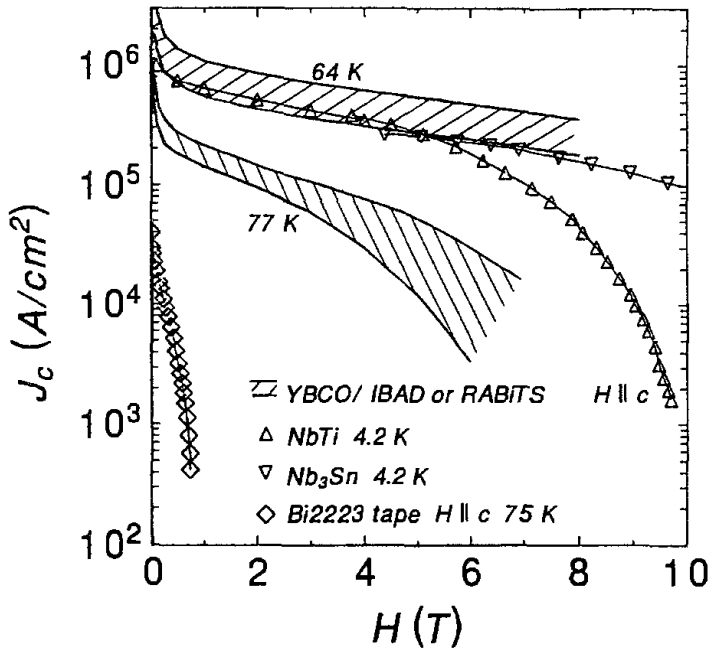

Fig. 16. Magnetic field dependence of the critical current density for a range of short sample YBCO conductors produced using either IBAD or RABiT substrates. These data are compared with typical values obtained for NbTi and Nb_3Sn wires at 4.2 K and for BSCCO, oxide-powder-in-tube wires at 77 K. From Hawsey and Peterson (1996).

10. Concluding remarks

During the past decade, remarkable progress in the areas of basic research and technological applications has been made on the high-T_c cuprate superconductors. The availability of high-quality polycrystalline and single-crystal bulk and thin film materials has made it possible to make reliable measurements of the physical properties of these materials and to optimize superconducting properties (e.g., J_c) that are important for technological applications. These investigations have provided important information regarding the anomalous normal state properties, the symmetry of the superconducting order parameter, and vortex phases and dynamics in the cuprates. The next decade of research on the high-T_c cuprate superconductors as well as other novel superconducting materials promises to yield significant advances toward the development of a theory of high-temperature superconductivity and the realization of technological applications of these materials on a broad scale. It is possible that significantly higher values of T_c will be found in new cuprate compounds or other classes of materials.

Acknowledgments

Research at UCSD upon which this article is based was supported by the U.S. Department of Energy under Grant No. DE-FG03-86ER-45320.

References

Alloul, H., A. Mahajan, H. Casalta and O. Klein, 1993, Phys. Rev. Lett. **70**, 1171.

Anderson, P.W., 1987, Science **235**, 1196.

Anderson, P.W., 1991, Phys. Rev. Lett. **67**, 2092.

Ando, Y., G.S. Boebinger, A. Passner, T. Kimura and K. Kishio, 1995, Phys. Rev. Lett. **75**, 4662.

Anlage, S.M., D.-H. Wu, J. Mao, S.N. Mao, X.X. Xi, T. Venkatesan, J.L. Peng and R.L. Greene, 1994, Phys. Rev. B **50**, 523.

Aubin, H., K. Behnia, M. Ribault, R. Gagnon and L. Taillefer, 1997, Phys. Rev. Lett. **78**, 2624.

Basov, D.N., T. Timusk, B. Dabrowski and J.D. Jorgensen, 1994, Phys. Rev. B **50**, 3511.

Basov, D.N., S.I. Woods, A.S. Katz, E.J. Singley, R.C. Dynes, M. Xu, D. Hinks, C.C. Homes and M. Strongin, 1999, Science **283**, 49.

Batlogg, B., 1990, in: High Temperature Superconductivity, Proc. Los Alamos Symp. 1989, eds K.S. Bedell, D. Coffey, D.E. Meltzer, D. Pines and J.R. Schrieffer (Addison-Wesley, Redwood City) p. 37.

Batlogg, B., H.Y. Hwang, H. Takagi, R.J. Cava, H.L. Rao and J. Kwo, 1994, Physica C **235–240**, 130 and references therein.

Bauernfeind, L., W. Widder and H.F. Braun, 1996, J. Low Temp. Phys. **105**, 1605.

Béal-Monod, M.T., 1998, Physica C **298**, 59.

Bednorz, J.G., and K.A. Müller, 1986, Z. Phys. B 64, 189.

Bernard, C., J.L. Tallon, Ch. Niedermayer, Th. Blasius, A. Golnik, E. Brücher, R.K. Kremer, D.R. Noakes, C.E. Stronach and E.J. Ansaldo, 1999, Phys. Rev. B **59**, 14099.

Blatter, G., M.V. Feigel'man, V.B. Geshkenbein, A.I. Larkin and V.M. Vinokur, 1994, Rev. Mod. Phys. **66**, 1125.

Boebinger, G.S., Y. Ando, A. Passner, T. Kimura, M. Okuya, J. Shimoyama, K. Kishio, K. Tamasaku, N. Ichikawa and S. Uchida, 1996, Phys. Rev. Lett. **77**, 5417.

Bonn, D.A., R. Liang, T.M. Riseman, D.J. Baar, D.C. Morgan, K. Zhang, P. Dosanjh, T.L. Duty, A. MacFarlane, G.D. Morris, J.H. Brewer, W.N. Hardy, C. Kallin and A.J. Berlinsky, 1993, Phys. Rev. B **47**, 11314.

Brandt, E.H., 1995, Rep. Prog. Phys. **58**, 1465.

Brauner, D.A., and H.R. Ott, 1994, Phys. Rev. B **50**, 6530.

Bucher, B., P. Steiner, J. Karpinski, E. Kaldis and P. Wachter, 1993, Phys. Rev. Lett. **70**, 2012.

Castellani, C., C. Di Castro and M. Grilli, 1997, Z. Phys. B **103**, 137.

Cava, R.J., R.B. van Dover, B. Batlogg and E.A. Rietman, 1987, Phys. Rev. Lett. **58**, 408.

Cava, R.J., B. Batlogg, J.J. Krajewski, R. Farrow, L.W. Rupp Jr, A.E. White, K. Short, W.F. Peck and T. Kometani, 1988, Nature **332**, 814.

Chaudhari, P., and S.-Y. Lin, 1994, Phys. Rev. Lett. **72**, 1084.

Chaudhari, P., R.H. Koch, R.B. Laibowitz, T.R. McGuire and R.J. Gambino, 1987, Phys. Rev. Lett. **58**, 2684.

Cheong, S.-W., G. Aeppli, T.E. Mason, H. Mook, S.M. Hayden, P.C. Canfield, Z. Fisk, K.N. Clausen and J.L. Martinez, 1991, Phys. Rev. Lett. **67**, 1791.

Chien, T.R., Z.Z. Wang and N.P. Ong, 1991, Phys. Rev. Lett. **67**, 2088.

Chu, C.W., L. Gao, F. Chen, Z.J. Huang, R.L. Meng and Y.Y. Xue, 1993, Nature **365**, 323.

Coffey, D., and L. Coffey, 1993, Phys. Rev. Lett. **70**, 1529.

Cooper, S.L., and K.E. Gray, 1994, in: Physical Properties of High Temperature Superconductors IV, ed. D.M. Ginsberg (World Scientific, Singapore) ch. 3.

Cox, D.L., and M.B. Maple, 1995, Phys. Today (February), 32.

Crabtree, G.W., and D.R. Nelson, 1997, Phys. Today (April), 38.

Dalichaouch, Y., C.L. Seaman, C.C. Almasan, M.C. de Andrade, H. Iwasaki, P.K. Tsai and M.B. Maple, 1991, Physica B **171**, 308.

Deveraux, T.P., D. Einzel, B. Stadlober, R. Hackl, D.H. Leach and J.J. Neumeier, 1994, Phys. Rev. Lett. **72**, 396.

Ding, H., T. Yokoya, J.C. Campuzano, T. Takahashi, M. Randeria, M.R. Norman, T. Mochiku, K. Kadowaki and J. Giapintzakis, 1996, Nature **382**, 51.

Early, E.A., N.Y. Ayoub, J. Beille, J.T. Markert and M.B. Maple, 1989, Physica C **160**, 320.

Emery, V.J., and S.A. Kivelson, 1995, Nature **374**, 434.

Fahrenbacher, R., and T.M. Rice, 1993, Phys. Rev. Lett. **70**, 3471.

Farrell, D.E., 1994, in: Physical Properties of High Temperature Superconductors IV, ed. D.M. Ginsberg (World Scientific, Singapore) ch. 2.

Felner, I., U. Asaf, Y. Levi and O. Millo, 1997, Phys. Rev. B **55**, R3374.

Fertig, W.A., D.C. Johnston, L.E. Delong, R.W. McCallum, M.B. Maple and B.T. Matthias, 1977, Phys. Rev. Lett. **38**, 387.

Franck, J.P., 1994, in: Physical Properties of High Temperature Superconductors IV, ed. D.M. Ginsberg (World Scientific, Singapore) p. 189.

Fukuyama, H., 1992, Prog. Theor. Phys. Suppl. **108**, 287.

Gavaler, J.R., 1973, Appl. Phys. Lett. **23**, 480.

Gorny, K., O.M. Vyaselev, J.A. Martindale, V.A. Nandor, C.H. Pennington, P.C. Hammel, W.L. Hults, J.L. Smith, P.L. Kuhns, A.P. Reyes and W.G. Moulton, 1999, Phys. Rev. Lett. **82**, 77.

Goyal, A., D.P. Norton, D.M. Kroeger, D.K. Christen, M. Paranthaman, E.D. Specht, J.D. Budai, Q. He, B. Saffian, F.A. List, D.F. Lee, E. Hatfield, P.M. Martin, C.E. Klabunde, J. Mathis and C. Park, 1997, J. Mater. Res. **12**, 2924.

Hardy, W.N., D.A. Bonn, D.C. Morgan, R. Liang and K. Zhang, 1993, Phys. Rev. Lett. **70**, 3999.

Hawsey, R., and D. Peterson, 1996, Superconductor Industry (Fall), and references cited therein.

Herrmann, J., U.-C. Boehnke, M. Krötzsch, B. Lippold and F. Schlenkrich, 1994, Physica C **221**, 76.

Holczer, K., O. Klein, S.-M. Huang, R.B. Kaner, K.-J. Fu, R.L. Whetten and F. Diederich, 1991, Science **252**, 1154.

Homes, C.C., T. Timusk, R. Liang, D.A. Bonn and W.N. Hardy, 1993, Phys. Rev. Lett. **71**, 1645.

Huse, D.A., M.P.A. Fisher and D.S. Fisher, 1992, Nature **358**, 553.

Hwang, H.Y., B. Batlogg, H. Takagi, H.L. Kao, J. Kwo, R.J. Cava, J.J. Krajewski and W.F. Peck Jr, 1994, Phys. Rev. Lett. **72**, 2636.

Imai, T., T. Shimizu, H. Yasuoka, Y. Ueda and K. Kosuge, 1988, J. Phys. Soc. Japan **57**, 2280.

Ishikawa, M., and Ø. Fischer, 1977, Solid State Commun. **23**, 37.

Ito, T., K. Takenaka and S. Uchida, 1993, Phys. Rev. Lett. **70**, 3995.

Iye, Y., 1992, in: Physical Properties of High Temperature Superconductors III, ed. D.M. Ginsberg (World Scientific, Singapore) ch. 4.

Jiang, C.N., A.R. Baldwin, G.A. Levin, T. Stein, C.C. Almasan, D.A. Gajewski, S.H. Han and M.B. Maple, 1997, Phys. Rev. B **55**, R3390.

Jin, S., T.H. Tiefel, R.C. Sherwood, M.E. Davis, R.B. van Dover, G.W. Kammlott, R.A. Fastnacht and H.D. Keith, 1988, Appl. Phys. Lett. **52**, 2074.

Jorgensen, J.D., 1991, Phys. Today (June), 34.

Julian, S.R., A.P. Mackenzie, G.G. Lonzarich, C. Bergemann, R.K.W. Haselwimmer, Y. Maeno, S. Nishizaki, A.W. Tyler, S. Ikeda and T. Fujita, 1999, Physica B **259–261**, 928.

Kirtley, J.R., C.C. Tsuei, J.Z. Sun, C.C. Chi, L.S. Yu-Jahnes, A. Gupta, M. Rupp and M.B. Ketchen, 1995, Nature **373**, 225.

Kishio, K., K. Kitazawa, S. Kanbe, T. Yasuda, N. Sugii, H. Takagi, S. Uchida, K. Fueki and S. Tanaka, 1987, Chem. Lett., p. 429.

Kleiner, R., A.S. Katz, A.G. Sun, R. Summer, D.A. Gajewski, S.H. Han, S.I. Woods, E. Dantsker, B. Chen, K. Char, M.B. Maple, R.C. Dynes and J. Clarke, 1996, Phys. Rev. Lett. **76**, 2161.

Kouznetsov, K.A., A.G. Sun, B. Chen, A.S. Katz, S.R. Bahcall, J. Clarke, R.C. Dynes, D.A. Gajewski, S.H. Han, M.B. Maple, J. Giapintzakis, J.-T. Kim and D.M. Ginsberg, 1997, Phys. Rev. Lett. **79**, 3050.

Laughlin, R.B., 1988, Science **244**, 525.

Lesueur, J., M. Aprili, A. Goulan, T.J. Horton and L. Dumoulin, 1997, Phys. Rev. B **55**, 3308.

Levi, B.G., 1990, Phys. Today (March), 20 and references therein.

Levi, B.G., 1993, Phys. Today (May), 17 and references therein.

Levi, B.G., 1996, Phys. Today (January), 19 and references therein.

Levi, B.G., 1998, Phys. Today (June), 19.

Levin, K., J.H. Kim, J.P. Lu and Q. Si, 1991, Physica C **175**, 449.

Loeser, A.G., Z.-X. Shen, D.S. Dessau, D.S. Marshall, C.H. Park, P. Fournier and A. Kapitulnik, 1996, Science **273**, 325.

Loram, J.W., K.A. Mirza, J.R. Cooper and W.Y. Liang, 1993, Phys. Rev. Lett. **71**, 1740.

Lynn, J.W., G. Shirane, W. Thombinson, R.N. Shelton and D.E. Moncton, 1981, Phys. Rev. B **24**, 3817.

Maekawa, S., 1996, Science **273**, 1515.

Maeno, Y., H. Hashimoto, K. Yoshida, S. Nishizaki, T. Fujita, J.G. Bednorz and P. Lichtenberg, 1994, Nature **372**, 532.

Mandrus, D., J. Hartge, C. Kendziora, L. Mihaly and L. Forro, 1990, Europhys. Lett. **22**, 460.

Maple, M.B., 1990, MRS Bull. **XV**(6), 60.

Maple, M.B., Y. Dalichaouch, J.M. Ferreira, R.R. Hake, B.W. Lee, J.J. Neumeier, M.S. Torikachvili, K.N. Yang, H. Zhou, R.P. Guertin and M.V. Kuric, 1987, Physica B **148**, 155.

Maple, M.B., C.C. Almasan, C.L. Seaman, S.H. Han, K. Yoshiara, M. Buchgeister, L.M. Paulius,

B.W. Lee, D.A. Gajewski, R.F. Jardim, C.R. Fincher Jr, G.B. Blanchet and R.P. Guertin, 1994, J. Superconductivity **7**, 97.

Marezio, M., 1998, ISTEC J. **11**(3), 20.

Markert, J.T., and M.B. Maple, 1989, Solid State Commun. **70**, 145.

Markert, J.T., C.L. Seaman, H. Zhou and M.B. Maple, 1988, Solid State Commun. **66**, 387.

Markert, J.T., Y. Dalichaouch and M.B. Maple, 1989a, in: Physical Properties of High Temperature Superconductors I, ed. D.M. Ginsberg (World Scientific, Singapore) ch. 6.

Markert, J.T., E.A. Early, T. Bjørnholm, S. Ghamaty, B.W. Lee, J.J. Neumeier, R.D. Price, C.L. Seaman and M.B. Maple, 1989b, Physica C **158**,178.

Martindale, J.A., S.E. Barrett, K.E. O'Hara, C.P. Schlichter, W.C. Lee and D.M. Ginsberg, 1993, Phys. Rev. B **47**, 9155.

Mason, T.E., G. Aeppli and H.A. Mook, 1992, Phys. Rev. Lett. **68**, 1414.

Mathai, A., Y. Gin, R.C. Black, A. Amar and F.C. Wellstood, 1995, Phys. Rev. Lett. **74**, 4523.

Mattheis, L.F., E.M. Gyorgy and D.W. Johnson Jr, 1988, Phys. Rev. B **37**, 3745.

Miller, J.H., Q.Y. Ying, Z.G. Zou, N.Q. Fan, J.H. Xu, M.F. Davis and J.C. Wolfe, 1995, Phys. Rev. Lett. **74**, 2347.

Moler, K.A., D.J. Baar, J.S. Urbach, R. Liang, W.N. Hardy and A. Kapitulnik, 1994, Phys. Rev. Lett. **73**, 2744.

Moncton, D.E., D.B. McWhan, P.H. Schmidt, G. Shirane, W. Thomlinson, M.B. Maple, H.B. MacKay, L.D. Woolf, Z. Fisk and D.C. Johnston, 1980, Phy. Rev. Lett. **45**, 2060.

Movshovich, R., M.A. Hubbard, M.B. Salamon, A.V. Balatsky, R. Yoshizaki, J.L. Sarrao and M. Jaime, 1998, Phys. Rev. Lett. **80**, 1968.

Nagaosa, N., and P.A. Lee, 1992, Phys. Rev. B **45**, 966.

Neumeier, J.J., and M.B. Maple, 1992, Physica C **191**, 158.

Neumeier, J.J., T. Bjørnholm, M.B. Maple and I.K. Schuller, 1989, Phys. Rev. Lett. **63**, 2516.

Nuñez-Regueiro, M., J.-L. Tholence, E.V. Antipov, J.-J. Capponi and M. Marezio, 1993, Science **262**, 97.

Orlando, T.P., K.A. Delin, S. Foner, E.J. McNiff Jr, J.M. Tarascon, L.H. Greene, W.R. McKinnon and G.W. Hull, 1987, Phys. Rev. B **36**, 2394.

Pines, D., 1994, Physica B **199&200**, 300 and references therein.

Puchkov, A.V., P. Fournier, D.N. Basov, T. Timusk, A. Kapitulnik and N.N. Kolesnikov, 1996, Phys. Rev. Lett. **77**, 3212.

Putilin, S.N., E.V. Antipov, O. Chmaissem and M. Marezio, 1993, Nature **362**, 226.

Randeria, M., N. Trivedi, A. Moreo and R.T. Scalettar, 1992, Phys. Rev. Lett. **69**, 2001.

Renner, C.H., B. Revaz, J.-Y. Genoud, K. Kadowaki and Ø. Fischer, 1998, Phys. Rev. Lett. **80**, 149.

Rice, T.M., and M. Sigrist, 1995, J. Phys.: Condens. Matter **7**, 643.

Rossat-Mignod, J., L.P. Regnault, C. Vettier, P. Bourges, P. Burlet, J. Bossy, J.Y. Henry and G. Lapertot, 1991, Physica **185-189 C**, 86.

Rosseinsky, M.J., A.P. Ramirez, S.H. Glarum, D.W. Murphy, R.C. Haddon, A.F. Hebard, T.T.M. Palstra, A.R. Kortan, S.M. Zahurak and A.V. Makhija, 1991, Phys. Rev. Lett. **66**, 2830.

Rowell, J.M., 1997, Solid State Commun. **102**, 269.

Scalapino, D.J., 1995, Phys. Rep. **250**, 329 and references therein.

Schilling, A., M. Cantoni, J.D. Guo and H.R. Ott, 1993, Nature **363**, 56.

Shen, Z.-X., D.S. Dessau, B.O. Wells, D.M. King, W.E. Spicer, A.J. Arko, D. Marshall, L.W. Lombardi, A. Kapitulnik, P. Dickenson, S. Doniach, J. DiCarlo, T. Loeser and C.H. Park, 1993, Phys. Rev. Lett. **70**, 1553.

Sinha, S.K., G.W. Crabtree, D.G. Hinks and H.A. Mook, 1982, Phys. Rev. Lett. **48**, 950.

Sleight, A.W., 1991, Phys. Today **44**(June), 24.

Stadloper, B., G. Krug, R. Nemetschek, R. Hackl, J.L. Cobb and J.T. Markert, 1995, Phys. Rev. Lett. **74**, 4911.

Subramanian, M.A., J. Gopalakrishnan, C.C. Torardi, T.R. Askew, R.B. Flippen, A.W. Sleight, J.J. Lin and S.J. Poon, 1988, Science **240**, 495.

Sun, A.G., D.A. Gajewski, M.B. Maple and R.C. Dynes, 1994, Phys. Rev. Lett. **72**, 2267.

Sun, A.G., S.H. Han, A.S. Katz, D.A. Gajewski, M.B. Maple and R.C. Dynes, 1995, Phys. Rev. B **52**, R15731.

Sun, A.G., A. Truscott, A.S. Katz, R.C. Dynes, B.W. Veal and C. Gu, 1996, Phys. Rev. B **54**, 6734.

Suzumura, Y., Y. Hasegawa and H. Fukuyama, 1988, J. Phys. Soc. Japan **57**, 2768.

Takagi, H., S. Uchida, K. Kitazawa and S. Tanaka, 1987, Jpn. J. Appl. Phys. **26** L123.

Takano, M., 1996, Physica C **263**, 468.

Takigawa, M.A., P. Reyes, P.C. Hammel, J.D. Thompson, R.H. Heffner, Z. Fisk and K.C. Ott, 1991, Phys. Rev. B **43**, 247.

Tallon, J.L., J.R. Cooper, P. deSilva, G.V.M. Williams and J.W. Loram, 1995, Phys. Rev. Lett. **75**, 4114.

Thurston, T.R., P.M. Gehring, G. Shirane, R.J. Birgeneau, M.A. Kastner, Y. Endoh, M. Matsuda, K. Yamada, H. Kojima and I. Tanaka, 1992, Phys. Rev. B **46**, 9128.

Tokura, Y., H. Takagi and S. Uchida, 1989, Nature **337**, 345.

Tranquada, J.M., B.J. Sternlieb, J.D. Axe, Y. Nakamura and S. Uchida, 1995, Nature **375**, 561.

Tsuei, C.C., J.R. Kirtley, C.C. Chi, L.-S. Yu-Jahnes, A. Gupta, T. Shaw, J.Z. Sun and M.B. Ketchen, 1994, Phys. Rev. Lett. **72**, 593.

Tsuei, C.C., J.R. Kirtley, M. Rupp, J.Z. Sun, A. Gupta, M.B. Ketchen, C.A. Wang, Z.F. Ren, J.H. Wang and M. Bhushan, 1996, Science **271**, 329.

Uchida, S., 1993, Jpn. J. Appl. Phys. **32**, 3784.

Uehara, M., T. Nagata, J. Akimitsu, H. Takahashi, N. Môri and K. Kinoshita, 1996, J. Phys. Soc. Japan **65**, 2764.

Uemura, Y.J., 1996, in: Proc. 10th Anniversary HTS Workshop on Physics, Materials, and Applications, eds B. Batlogg, C.W. Chu, W.K. Chu, D.U. Gubser and K.A. Müller (World Scientific, Singapore) p. 68.

v. Zimmermann, M., A. Vigliante, T. Niemoeller, N. Ichikawa, T. Frello, J. Madsen, P. Wochner, S. Uchida, N.H. Andersen, J.M. Tranquada, D. Gibbs and J.R. Schneider, 1998, Europhys. Lett. **41**, 629.

Varma, C.M., P.B. Littlewood, S. Schmitt-Rink, E. Abrahams and A.E. Ruckenstein, 1989, Phys. Rev. Lett. **63**, 1996.

Warren Jr, W.W., R.E. Walstedt, G.F. Brennert, R.J. Cava, R. Tycko, R.F. Bell and G. Dabbagh, 1989, Phys. Rev. Lett. **62**, 1193.

Werthamer, N.R., E. Helfand and P.C. Hohenberg, 1966, Phys. Rev. **147**, 295.

Wollman, D.A., D.J. Van Harlingen, W.C. Lee, D.M. Ginsberg and A.J. Leggett, 1993, Phys. Rev. Lett. **71**, 2134.

Wollman, D.A., D.J. Van Harlingen, J. Giapintzakis and D.M. Ginsberg, 1995, Phys. Rev. Lett. **74**, 797.

Wu, D.-H., J. Mao, S.N. Mao, J.L. Peng, X.X. Xi, R.L. Greene and S.M. Anlage, 1993, Phys. Rev. Lett. **70**, 85.

Wu, M.K., J.R. Ashburn, C.J. Torng, P.H. Hor, R.L. Meng, L. Gao, Z.J. Huang, Y.Q. Wang and C.W. Chu, 1987, Phys. Rev. Lett. **58**, 908.

Wu, X.D., S.R. Foltyn, P. Arendt, J. Townsend, C. Adams, I.H. Campbell, P. Tiwari, Y. Coulter and D.E. Peterson, 1994, Appl. Phys. Lett. **65**, 1961.

Zhang, S.-C., 1997, Science **275**, 1089.

Zou, Z., J. Ye, K. Oka and Y. Nishihara, 1998, Phys. Rev. Lett. **80**, 1074.

Handbook on the Physics and Chemistry of Rare Earths
Vol. 30
edited by K.A. Gschneidner, Jr., L. Eyring and M.B. Maple

Chapter 188

CRYSTAL CHEMISTRY OF SUPERCONDUCTING RARE-EARTH CUPRATES

B. RAVEAU, C. MICHEL and M. HERVIEU
Laboratoire CRISMAT, UMR 6508-CNRS, ISMRA,
6 Boulevard du Maréchal Juin, 14050 Caen Cedex, France

Contents

Introduction 31
1. La_2CuO_4- and Nd_2CuO_4-type superconductors 32
2. $La_{2-x}A_{1+x}Cu_2O_{6-\delta}$ superconductors 34
3. The "123" superconductors 35
   3.1. The orthorhombic 92 K superconductor $YBa_2Cu_3O_7$ 35
   3.2. Oxygen non-stoichiometry in the "123" phase $YBa_2Cu_3O_{7-\delta}$ 37
   3.3. Microtwinning in $YBa_2Cu_3O_7$ 42
   3.4. Extended defects in $YBa_2Cu_3O_7$ 46
   3.5. Other rare-earth "123" cuprates 47
4. The "124" superconductor $YBa_2Cu_4O_8$ and its intergrowth with $YBa_2Cu_3O_7$ 48
5. Introduction of rare earth in Bi, Tl, Pb and Hg layered cuprates 49
6. Layered cuprates involving double fluorite layers 59
7. Copper oxycarbonates containing a rare earth 62
References 63

Introduction

The discovery of superconductivity at 35 K by Bednorz and Müller (1986) in the "BaLaCuO" system has induced the exploration of cuprates by a considerable number of researchers. In fact the study of these oxides, started as early as 1980, shows that the crystal chemistry is very complex. This is especially the case for the so-discovered 35 K superconductor which was rapidly revealed not to be $La_4BaCu_5O_{13}$ (Michel et al. 1985) but in fact $La_{2-x}Ba_xCuO_4$ (Michel and Raveau 1984) prepared several years before. All these high-T_c superconductors derive from the perovskite structure by disconnecting the CuO_6 octahedra along one direction so that $[CuO_2]_\infty$ layers are formed, which are responsible for superconductivity at high temperature. In these materials, rare-earth cations do not play a direct role for the appearance of superconductivity, but due to their relatively large size and to their trivalent character, they allow in many cases such layered structures to be stabilized. In the present chapter we give an overview of the relationships between crystal structure extended defects and superconducting properties of rare-earth-based cuprates.

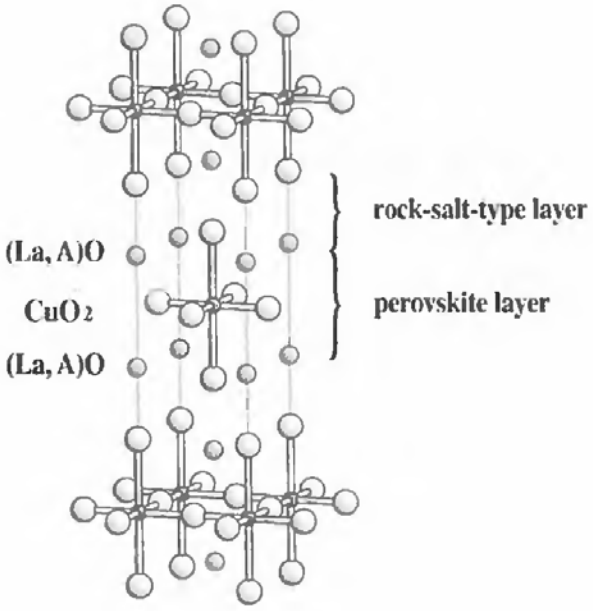

Fig. 1. Structure of the oxides $La_{2-x}A_xCuO_4$ (A = Ca, Sr, Ba), an intergrowth of single rock-salt-type layers and single perovskite layers.

1. La_2CuO_4- and Nd_2CuO_4-type superconductors

The oxides $La_{2-x}A_xCuO_4$ with A = Ca, Sr, Ba are superconductors with T_c ranging from 20 to 38 K. These oxides exhibit the K_2NiF_4-type structure, i.e. they can be described as an intergrowth of single perovskite layers with single rock-salt-type layers (fig. 1). In such a structure the $[La_{1-x}A_xO]_\infty$ planes are at the interface of the perovskite layers $[La_{1-x}A_xCuO_3]_\infty$ and of the rock-salt layers $[La_{1-x}A_xO]_\infty$. In other words, such a structure can also be described as a stacking of $[CuO_2]_\infty$ and $[La_{1-x}A_xO]_\infty$ planes alternating according to the sequence: "Cu–La–La–Cu". In these compounds, the rare-earth and alkaline-earth cations are distributed at random in the rock-salt-type layers. The substitution rate x depends on the nature of the alkaline earth element: $0 \leqslant x \leqslant 0.20$ for A = Ca, Ba, and $0 \leqslant x \leqslant 1.3$ for A = Sr. However, superconductivity is only observed for a narrow homogeneity range, $x \approx 0.10$–0.20. Moreover, the oxygen content varies according to x, and to the oxygen pressure used for the synthesis, so that the actual formula of these oxides is better described as $La_{1-x}A_xCuO_{4-\delta}$. The symmetry of the cell depends on x and on δ. For instance, the Ba and Ca oxides prepared in air at 1100°C and quenched to room temperature exhibit an orthorhombic symmetry, with $a \approx b \approx \sqrt{2}a_p$ and $c \approx 13$ Å, for x ranging from 0 to 0.2, whereas by annealing these samples, a tetragonal cell with $a \approx a_p$ and $c \approx 13$ Å is obtained for $x > 0.05$ (Fujiita et al. 1987), as shown for A = Ba in table 1 (see Raveau et al. 1991 for the detailed complex crystal chemistry of these phases).

The oxide La_2CuO_4, which corresponds to $x = 0$, deserves particular attention, in spite of the fact that it also belongs to the K_2NiF_4 series. The air-synthesized phase can be considered as nearly stoichiometric, and is semi-metallic without any signature of superconductivity. In contrast, the phase annealed under oxygen pressure becomes a superconductor with a T_c of 38 K (Beille et al. 1987). The neutron diffraction study

Table 1
Lattice parameters (Å) for the oxides $La_{2-x}Ba_xCuO_{4-\delta}$[a]

x	Quenched samples			Annealed samples		
	a	b	c	a	b	c
0	3.794	3.820	13.15	3.79	3.83	13.15
0.05	3.791	3.804	13.20	3.79	–	13.25
0.10	3.789	3.793	13.24	3.797	–	13.25
0.20	3.787		13.32	3.797	–	13.25

[a] a and b values should be multiplied by $\sqrt{2}$ for orthorhombic samples.

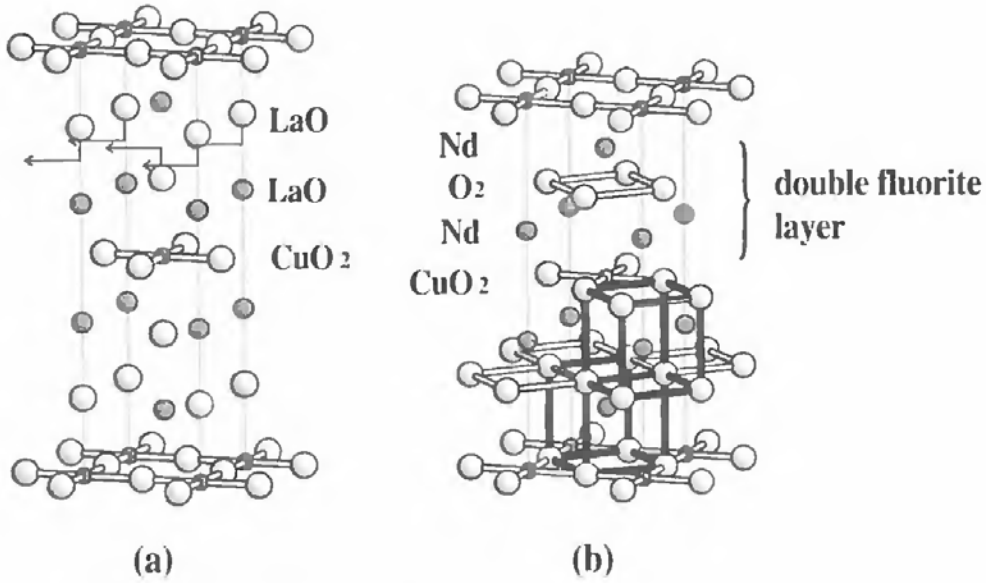

Fig. 2. Relationships between (a) La_2CuO_4 and (b) Nd_2CuO_4. The two structures are drawn showing the identical $[CuO_2]_\infty$ layers. The migration of oxygens belonging to the $[LaO]_\infty$ layers leading to the formation of fluorite cages is outlined.

of the latter (Jorgensen et al. 1988) shows that, although it is also orthorhombic, its parameters are different from the former, and it contains excess oxygen according to the formula $La_2CuO_{4+\delta}$. The electrochemical intercalation of oxygen in La_2CuO_4 (Grenier et al. 1992) allowed T_c to be increased up to 44 K.

When the size of the lanthanide decreases, the K_2NiF_4 structure is no longer stable. The other Ln_2CuO_4 oxides (Müller-Buschbaum and Wollschlager 1975, 1977), although characterized by a very similar tetragonal cell ($a \approx a_p$, $c \approx 12$ Å), exhibit a different structure, which is denoted as the Nd_2CuO_4 type. The latter structure (fig. 2) exhibits identical $[CuO_2]_\infty$ layers compared to La_2CuO_4, i.e., the Cu^{2+}, Ln^{3+}, and oxygen atoms forming the CuO_4 square planar groups are the same in both structures. The two structures differ by the position of the remaining two oxygen atoms: the oxygen atoms of the $[LaO]_\infty$ layers in La_2CuO_4 (fig. 2a) have migrated between two Nd layers in Nd_2CuO_4

(fig. 2b) in such a way that they form a fluorite-type lattice with the oxygen atoms of the $[CuO_2]_\infty$ layers (fig. 2b). Consequently, the Nd_2CuO_4 structure consists of double $[Nd_2O_4]_\infty$ fluorite-type layers parallel to (001). Along the $[Nd_2O_4]_\infty$ fluorite layers share the faces of their NdO_8 distorted cubes. Thus, the $[Nd_2O_4]_\infty$ lattice is derived from the fluorite structure by a shearing phenomenon in the (001) plane. Most of these oxides are poor semiconductors. The Nd_2CuO_4 oxide doped either with cerium or with thorium is the exception. The oxides $Nd_{2-x}Th_xCuO_4$ and $Nd_{2-x}Ce_xCuO_4$ are indeed superconductors with T_c 24 K or less. Although the critical temperature of these oxides is rather low, they are of the highest interest since they are the only *n*-type superconducting cuprates known so far.

2. $La_{2-x}A_{1+x}Cu_2O_{6-\delta}$ superconductors

The oxides $Ln_{2-x}A_{1+x}Cu_2O_{6-\delta}$ have been synthesized in air for Ln = La with $0 \leqslant x \leqslant 0.14$ for A = Sr and $x = 0.10$ for A = Ca (Nguyen et al. 1980). For Ln ≠ La, only oxides involving strontium could be obtained, with $x = 0.14$ for Ln = Pr, $0 < x \leqslant 0.2$ for Ln = Nd, $0.7 \leqslant x \leqslant 0.9$ for Ln = Sm, Gd, and $0.6 \leqslant x \leqslant 0.9$ for Ln = Eu. Under normal oxygen pressure conditions, none of these compounds can be obtained as a superconductor. In contrast, superconductivity up to 60 K could be obtained for the cuprate $La_{2-x}Sr_xCaCu_2O_6$ synthesized under 20 atm. oxygen pressure (Cava et al. 1990).

The ideal structure of these oxides is directly derived from that of $Sr_3Ti_2O_7$ by eliminating rows of oxygen atoms between two copper layers, as shown in fig. 3 for the cuprate $La_2CaCu_2O_6$. Their crystallographic cell is tetragonal with $a \approx a_p$ and $c \approx 20$ Å (see table 2). It consists of double oxygen-deficient perovskite layers $[LaCaCu_2O_5]_\infty$

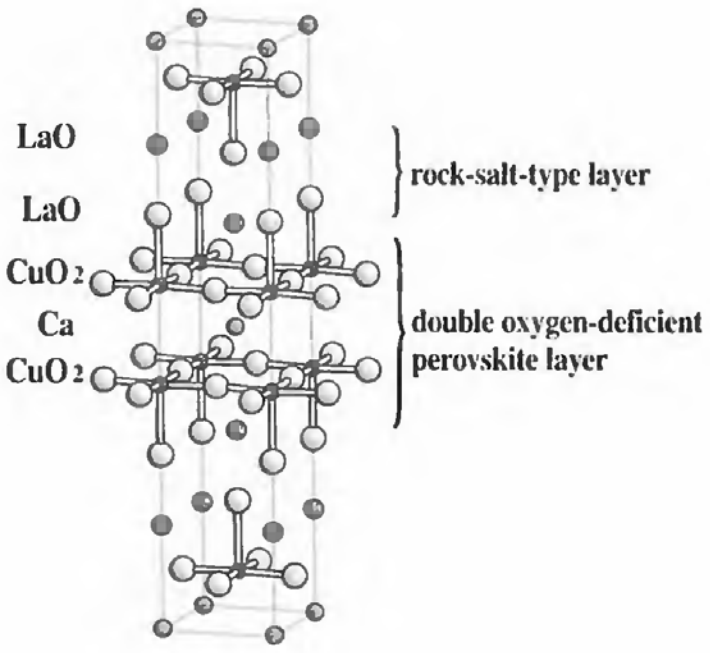

Fig. 3. Structure of $La_2CaCu_2O_6$, intergrowth of single rock salt layer with double oxygen-deficient perovskite layers.

Table 2
Crystallographic parameters of $Ln_{2-x}Sr_{1+x}Cu_2O_{6-x/2+\delta}$

Ln	Compound	x	a (Å)	b (Å)	c (Å)	V (Å^3)
Nd	$NdSr_2Cu_2O_{5.66}$ (or $Sr_6Nd_3Cu_6O_{17}$)	1	3.755	11.488	20.098	866.9
	$NdSr_2Cu_2O_{5.76}$	1	3.770	11.438	20.094	866.5
Sm	$Sm_{1.30}Sr_{1.70}Cu_2O_{5.65}$	0.70	3.746	11.416	20.068	858.2
	$Sm_{1.10}Sr_{1.90}Cu_2O_{5.55}$	0.90	3.747	11.439	20.058	859.7
Eu	$Eu_{1.40}Sr_{1.60}Cu_2O_{5.70}$	0.60	3.742	11.325	20.052	849.8
	$Eu_{1.30}Sr_{1.70}Cu_2O_{5.65}$	0.70	3.744	11.337	20.047	850.9
	$Eu_{1.10}Sr_{1.90}Cu_2O_{5.55}$	0.90	3.742	11.380	20.020	852.5
Gd	$Gd_{1.30}Sr_{1.70}Cu_2O_{5.65}$	0.70	3.738	11.350	20.045	850.4
	$Gd_{1.10}Sr_{1.90}Cu_2O_{5.55}$	0.90	3.738	11.385	20.015	851.8
La	$La_{1+x}Sr_{2-x}Cu_2O_{5.5+\delta}$	0.05–0.15	3.80	11.48	20.23	882.5

intergrown with single rock-salt layers $[LaO]_\infty$. The ordered distribution of oxygen vacancies at the level of the calcium cations leads to a pyramidal coordination of copper. In this structure the calcium sites exhibit a pseudocubic coordination; in fact, calcium and the surrounding oxygens of the basal planes of the CuO_5 pyramids form a single fluorite-type layer. Note that a partial cationic disorder may appear (exchange between Ca^{2+} and La^{3+}), especially when calcium is replaced by strontium, as for instance, in $La_2Sr_{1-x}Ca_xCu_2O_6$, due to the similar sizes of Sr^{2+} and La^{3+} cations.

In all these compounds oxygen can be intercalated and de-intercalated by varying the oxygen pressure and temperature during annealing. This results in strong variations of the conductivity, going from semiconducting to semimetallic behavior. But in any case superconductivity can only be obtained by using higher oxygen pressure close to 20 bar.

3. The "123" superconductors

3.1. *The orthorhombic 92 K superconductor $YBa_2Cu_3O_7$*

The $YBa_2Cu_3O_7$ superconductor was isolated after the discovery of superconductivity at 92 K in the system Y–Ba–Cu–O by Wu et al. (1987).

This oxide is synthesized (Cava et al. 1987, Michel et al. 1987, Lepage et al. 1987) from a mixture of Y_2O_3, $BaCO_3$ or BaO_2 and CuO in air at 900°C, followed by sintering at 1000°C in an oxygen flow, and finally cooling slowly or annealing under oxygen at low temperature (400–500°C). The latter operation is of capital importance to tune the oxygen stoichiometry to "O_7". The structure of this phase (fig. 4a), determined from neutron diffraction data (Beno et al. 1987, Capponi et al. 1987), is characterized by an orthorhombic symmetry with $a = 3.81\,\text{Å} \approx a_p$, $b = 3.88\,\text{Å} \approx a_p$, $c = 11.63\,\text{Å} \approx 3a_p$. It can be described as an ordered oxygen-deficient perovskite. It derives indeed from the

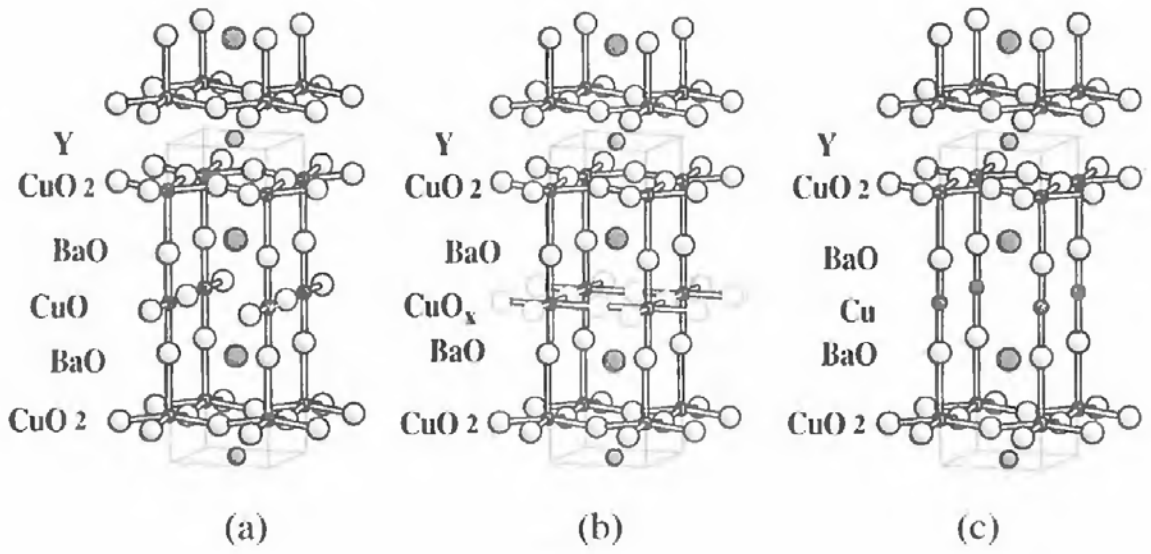

Fig. 4. Structure of the cuprates $YBa_2Cu_3O_{7-\delta}$: (a) the 92 K superconductor $YBa_2Cu_3O_7$, (b) the non-superconductor $YBa_2Cu_3O_{6.3}$ (T1) and (c) the insulating $YBa_2Cu_3O_6$.

stoichiometric perovskite by elimination of rows of oxygen atoms parallel to [010] at the level of yttrium ($z=0$) and copper ($z=\frac{1}{2}$ in the orthorhombic cell) and by an ordered distribution of the Ba^{2+} and Y^{3+} ions in the A sites of the ABO_3 perovskite, in such a way that two barium planes alternate with one yttrium plane along c. This structure is built up from triple $[Cu_3O_7]_\infty$ layers of copper polyhedra, interleaved with yttrium layers. Each $[Cu_3O_7]_\infty$ layer itself consists of two pyramidal copper layers $[CuO_{2.5}]_\infty$ interconnected through $[CuO_2]_\infty$ chains of corner-sharing CuO_4 square planar groups running along $\vec{b}$. Thus two copper sites have to be distinguished in this structure: Cu1 located in the chains of square planar groups, and Cu2 located in the CuO_5 pyramids.

This phase has two features in common with the superconductors $La_{2-x}A_xCuO_4$ and $La_{2-x}A_{1+x}Cu_2O_{6+\delta}$ discussed above:

(i) the structure exhibits a two-dimensional character with respect to the copper polyhedra. In the three structures the latter are indeed not 3D-interconnected by forming $[CuO_2]_\infty$ layers of corner-sharing CuO_4 square planar groups. These $[CuO_2]_\infty$ layers are interconnected through $[LaO]_\infty$ and/or $[Ca]_\infty$ or $[Y]_\infty$ layers or through $[CuO]_\infty$ chains in these various structures.

(ii) The oxygen stoichiometry implies a mixed valence of copper, Cu(II)–Cu(III), which corresponds in fact to the presence of delocalized holes in the material. The latter are distributed in a conduction band built from the overlapping of the 3d orbitals of copper and 2p orbitals of oxygen. Nevertheless it is worth pointing out that the hole-carrier density deduced from the mean oxidation state of copper is much higher for $YBa_2Cu_3O_7$ ($Cu^{+2.33}$) than for the other cuprates ($Cu^{+2.20}$).

These two factors, two-dimensionality of the structure and mixed valency of copper appear to be absolutely necessary for the appearance of superconductivity. The fact that, to date, no tridimensional cuprate has been found to be a superconductor strongly supports

this viewpoint. Note that the important role of the two-dimensional character of the structures (and of the band diagram) for the appearance of superconductivity at high temperature had been pointed out very early by several theorists as early as 1987 (Friedel 1988, Mattheiss 1987, Labbé and Bok 1988).

3.2. *Oxygen non-stoichiometry in the "123" phase* $YBa_2Cu_3O_{7-\delta}$

$YBa_2Cu_3O_7$ begins to lose oxygen at about 450°C, even if it is heated in a pure oxygen flow, leading to the non-stoichiometric oxides $YBa_2Cu_3O_{7-\delta}$. Although not all results coincide, it is well established that T_c decreases drastically from 92 K for $\delta = 0$ to 28 K for $\delta = 0.7$. Beyond the latter δ value, the samples become semiconductors. At the same time as superconductivity disappears, the symmetry of the cell becomes tetragonal. In fact, the tetragonal non-superconducting phase $YBa_2Cu_3O_{6.3}$ can be synthesized by heating a mixture of CuO, Y_2O_3 and $BaCO_3$ in air at 900–1000°C and then quenching to room temperature. The structure of this tetragonal form (fig. 4b), labelled T1 ($a = 3.838$ Å, $c = 11.792$ Å), differs from the orthorhombic one only in the positions of some oxygen atoms, and by its oxygen content ($0.6 \leqslant \delta \leqslant 0.8$) (Izumi et al. 1987a,b, Jorgensen et al. 1987, Domengès et al. 1988). One observes again triple copper layers of corner-sharing CuO_n polyhedra interleaved by one yttrium layer. The ordering of the yttrium and barium planes of "1–2" type along $\vec{c}$ remains unchanged. In each triple layer of Cu polyhedra one also recognizes the $[CuO_{2.5}]_\infty$ layers of corner-sharing CuO_5 pyramids corresponding to the Cu2 atoms. The main difference with the orthorhombic form deals with the distribution of oxygen and vacancies at the level of Cu1. At the latter level, oxygen and vacancies are statistically distributed at the apices of a square lattice in the (001) plane, so that one does not observe any more only a square planar coordination for Cu1. In other words, oxygen vacancies are statistically distributed at the apices of the basal plane of the Cu1 octahedra (see fig. 4).

The decrease of oxygen content in the crystals can be carried further without destroying the structure, leading to the tetragonal oxide $YBa_2Cu_3O_6$ (Santoro et al. 1987, Roth et al. 1987), denoted T2. This oxide, with parameters $a = 3.86$ Å, $c = 11.85$ Å, can be synthesized by heating the orthorhombic superconducting phase $YBa_2Cu_3O_7$ up to 600°C in vacuum. The structure of the T2 phase (fig. 4c) is simply derived from the orthorhombic or T1 structures by removing the oxygen atoms of the $[CuO]_\infty$ rows located at the Cu1 level. From the analysis of this framework, it appears that Cu2 keeps its pyramidal coordination, i.e. the corresponding $[CuO_{2.5}]_\infty$ pyramidal copper layers remain unchanged, whereas Cu1 exhibits a two-fold linear coordination. Thus the pyramidal copper layers are interconnected with CuO_2 sticks. From the interatomic Cu–O distances it can be assumed that the pyramidal copper sites are occupied by divalent copper, whereas univalent copper sits in the Cu1 site, leading to the formulation $YBa_2Cu_2^{II}Cu^{I}O_6$. Such an electronic localisation explains the insulating properties of this material, and is confirmed by XANES studies, which allow Cu(I) and Cu(II) to be identified.

It must be noted that the (non)appearance of superconductivity for $0 < \delta \leqslant 0.7$ depends on the experimental method of synthesis. For instance, a tetragonal phase T3, with

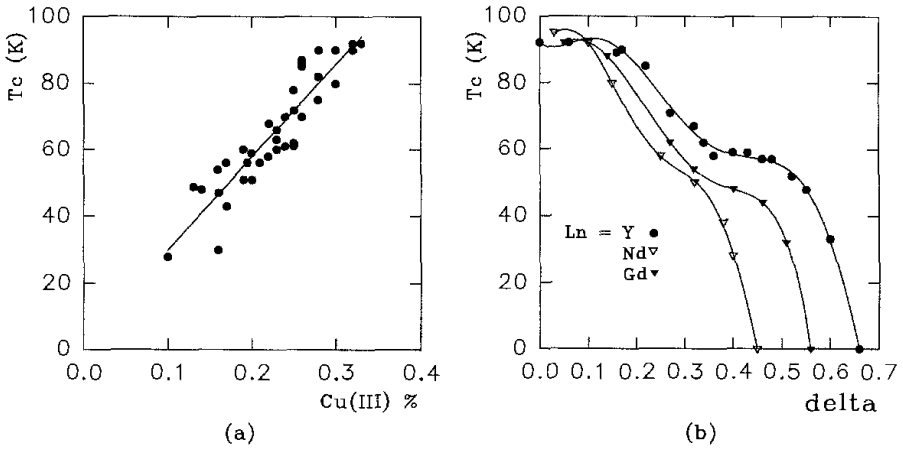

Fig. 5. (a) T_c vs Cu(III)% for various $YBa_2Cu_3O_{7-\delta}$ samples obtained after short annealings. (b) T_c vs δ for long annealed $LnBa_2Cu_3O_{7-\delta}$ samples.

insulating properties, $YBa_2Cu_3O_{6.8}$ ($\delta = 0.2$) also exists (Caignaert et al. 1990). It is metastable and can only be synthesized by ceramic techniques using a wet medium for grinding and heating in an oxygen flow at temperatures ranging from 850°C to 930°C. The structure of this phase is similar to that of the T1 form (fig. 4b), i.e., oxygen and vacancies are distributed statistically in the basal planes of the Cu1 octahedra. But the structure of T3 is more isotropic than T1, $c/a = 3$ ($a = 3.866$ Å, $c = 11.599$ Å), so that the perovskite subcell is cubic. Consequently one observes numerous 90°-oriented small domains by electron microscopy in agreement with the absence of mismatch between a and $c/3$ parameters.

The existence of superconductivity for $\delta \geqslant 0.50$ raises the issue of hole delocalization in connection with the valence state of copper. For instance, $YBaCu_3^{II}O_{6.5}$ should contain only divalent copper according to electroneutrality, and like other divalent copper oxides should not be superconducting. For $\delta \geqslant 0.50$, electroneutrality would impose the mixed valence Cu(I)–Cu(II), which is in contradiction with the above statement that superconductivity originates from the mixed valence Cu(II)–Cu(III) (equivalent to hole delocalization). The model of copper disproportionation (Raveau et al. 1988) allows the superconducting properties of these oxygen-deficient YBCO oxides to be explained. This model is based on a disordered intergrowth between two limiting structures "O_7" and "O_6", so that for a given δ value a partial disproportionation of Cu(II) into Cu(I) and Cu(III) is obtained according to the general formula

$$[YBa_2Cu_2^{II}Cu^{III}O_7]_{1-\delta}[YBa_2Cu_2^{II}Cu^{I}O_6]_{\delta}.$$

XANES studies (Oyanagi et al. 1987, Baudelet et al. 1988, Lengeler et al. 1988, Maurer et al. 1988) which reveal systematically univalent copper for all δ values ($0 \leqslant \delta \leqslant 1$) strongly supports this model. In this way, the presence of trivalent copper, for $\delta \geqslant 0.50$ can be explained, allowing superconductivity to be preserved. From this formulation, T_c vs "formal Cu(III) content" can be plotted (fig. 5a) showing that roughly T_c increases with Cu(III) content. Nevertheless it must be emphasized that the experimental value of T_c for a fixed δ value varies according to the method of synthesis. For example, when

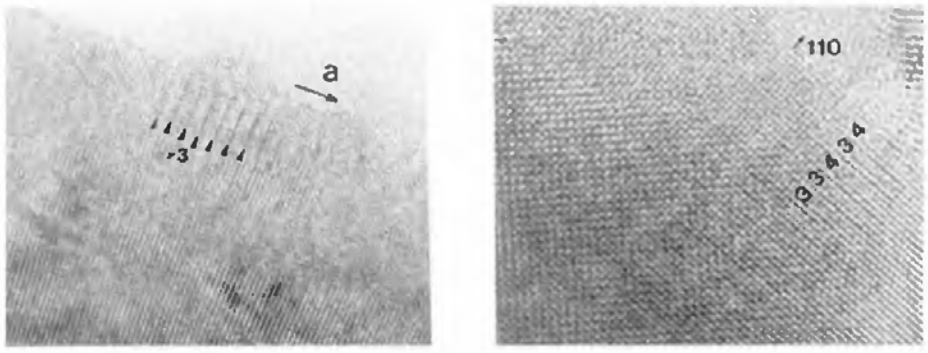

Fig. 6. $YBa_2Cu_3O_{7-\delta}$: [001] HREM images of crystallites exhibiting local superstructures corresponding to a new periodicity (a) $a' = 3a$ and (b) 3 and 4 d_{110}.

samples are obtained from short annealings at high temperature and low oxygen pressure, a monotonic decrease of T_c is observed (Tarascon et al. 1987, Monod et al. 1987), whereas plateaus are observed for samples annealed for a long time (Veal et al. 1989) (see fig. 5b). Such plateaus result from an ordering of oxygen.

Electron-microscopy study of the 60 K superconductor $YBa_2Cu_3O_{7-\delta}$ (Hervieu et al. 1989), with $\delta \approx 0.37$–0.45, reveals clearly the order-disorder phenomenon that appears in this phase, in connection with the formation of $YBa_2Cu_2^{II}Cu^{I}O_6$ insulating domains intergrown with $YBa_2Cu_2^{II}Cu^{III}O_7$ superconducting domains. The examination of numerous crystals shows that besides the highly disordered aspect of these microcrystals, there exist numerous microstructures and modulations. Such microstructures are directly interpretable in terms of the projected structure. They show that Y and Ba cations and oxygen vacancies are ordered, but concomitantly numerous contrast modulations attest to the complexity of the structural features. The most striking results concern the oxygen ordering observed in many crystals. The mean directions of the oxygen ordering leading to the microstructures are $[100]_p$, $[110]_p$, $[210]_p$ and $[310]_p$. An example of ordering along the a-axis is depicted in fig. 6a; the resulting parameter is $3a_0$ (a_0 is the parameter of the orthorhombic "123" superconductor). Another example is shown in fig. 6b; in an area of an orthorhombic crystal, superstructures are set up along the $[110]_p$ with local three- and four-fold periodicities. In fact, the superstructures are not well established, strictly speaking, over large domains, but, in very tiny areas, there are new periodicities.

Structural models of oxygen orderings can be proposed to explain such phenomena. They are based on the copper disproportionation $2Cu(II) \rightleftarrows Cu(III) + Cu(I)$, assuming that three-fold coordination for Cu is unlikely, and considering thus a two-fold coordination for Cu(I) and the coordinations 4, 5 and 6 for Cu(II) and Cu(III). Some idealized models, in fig. 7, illustrate the way the oxygen ordering can settle along favored directions, but these illustrations are far from unique. For instance, the doubling of "a" may correspond to the composition "$O_{6.5}$" (fig. 7a) in which $[Cu_2]_\infty$ rows of CuO_4 groups alternate with $[Cu^{I}O]_\infty$ rows [Cu(I) in two-fold coordination]. Tripling of "a" is explained either by the composition "$O_{6.66}$" (fig. 7c), in which double $[CuO_2]_\infty$ rows

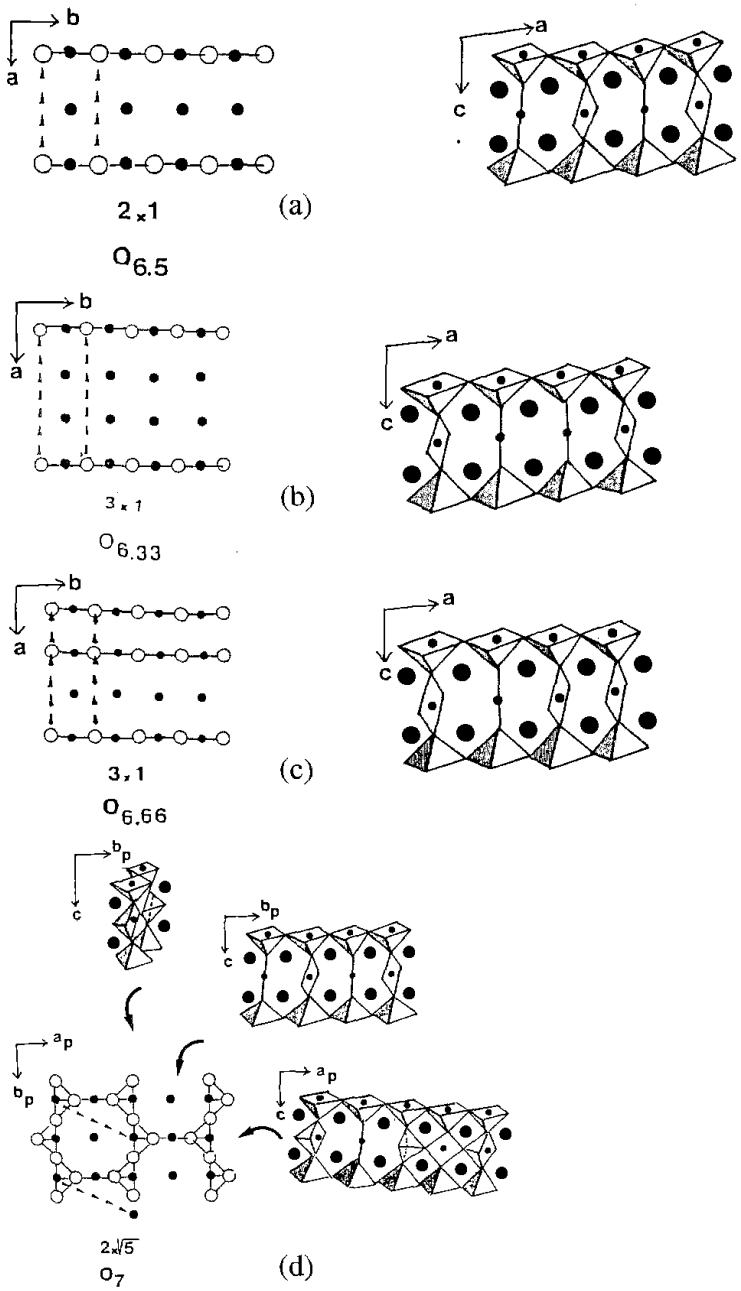

Fig. 7. Some idealized models of oxygen and vacancy ordering in the median copper plane. The new periodicities and oxygen contents are specified. The projected and perspective view along the different chains are drawn.

of CuO_4 groups alternate with $[Cu^{I}O]_\infty$ rows, or by the composition $O_{6.33}$, in which double $[Cu^{I}O]_\infty$ rows of CuO_2 sticks alternate with single $[CuO_2]_\infty$ rows (fig. 7b). Frameworks of interconnected CuO_5 pyramids and CuO_4 square planar groups can be proposed for the superstructures "$2a_p \times \sqrt{5}a_p$" (fig. 7d), "$2a_p \times \sqrt{10}a_p$" (fig. 7e), and "$2\sqrt{a_p} \times 2\sqrt{2a_p}$" (fig. 7f) corresponding to "O_7", "$O_{6.83}$" and "$O_{6.75}$", respectively. Modulations suggest that these local variations of oxygen stoichiometry and ordering

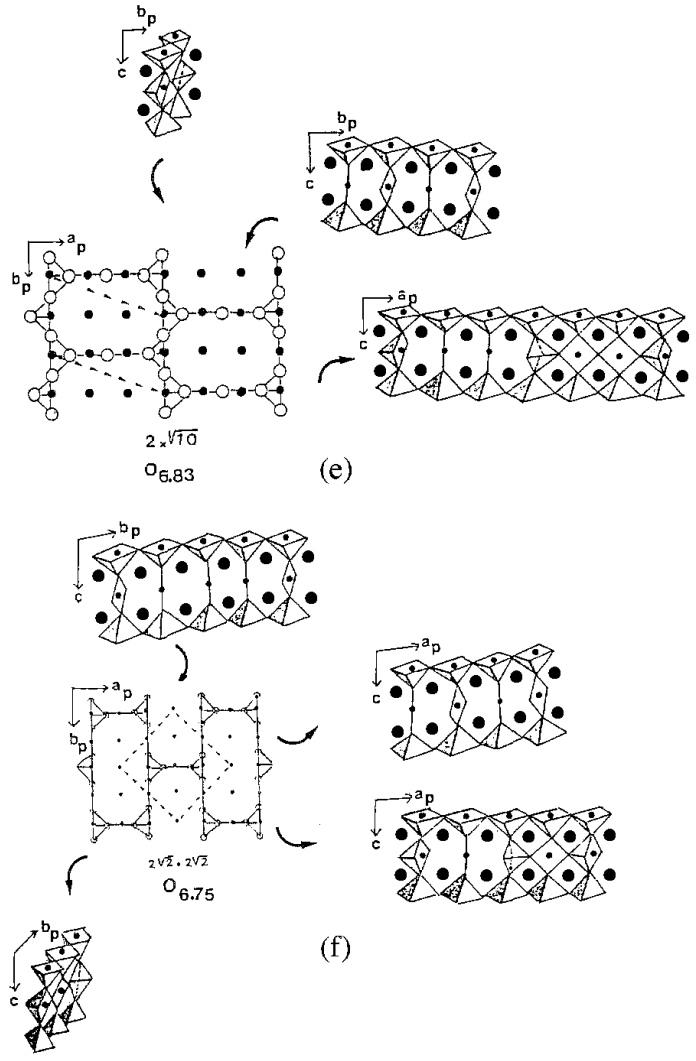

Fig. 7 (continued).

appear more or less simultaneously in the same crystal. It should be noted that the existence of a "$2\sqrt{2a_p}\times 2\sqrt{2a_p}$" supercell was reported for two ranges of oxygen content: close to O_7 and close to O_6 (Hervieu et al. 1989, Alario Franco et al. 1988, Reyes-Casga et al. 1989). For the latter composition, a model was proposed by Krekels et al. (1990) based on a Jahn–Teller-type deformation of the CuO_5 pyramid deduced from electron-microscopy observations.

These complex orderings of oxygen vacancies are more clearly visible along the [001] direction, owing to the orientation of the crystal. For $[100]_p$ oriented crystals, only the superstructure along $\vec{a}_0$ (or $\vec{b}_0$) can actually be observed. Figure 8a shows a $2a_p$ superstructure and fig. 8b displays a more complex one, existing along the c-axis of the "123" cell. On the micrograph, two planes of atoms are involved: Y and Cu1. The superstructure corresponds to a double alternation of $[CuO_2]_\infty$ chains of corner-sharing CuO_4 square planar groups with $[Cu^IO]_\infty$ rows in which Cu(I) is in two-fold

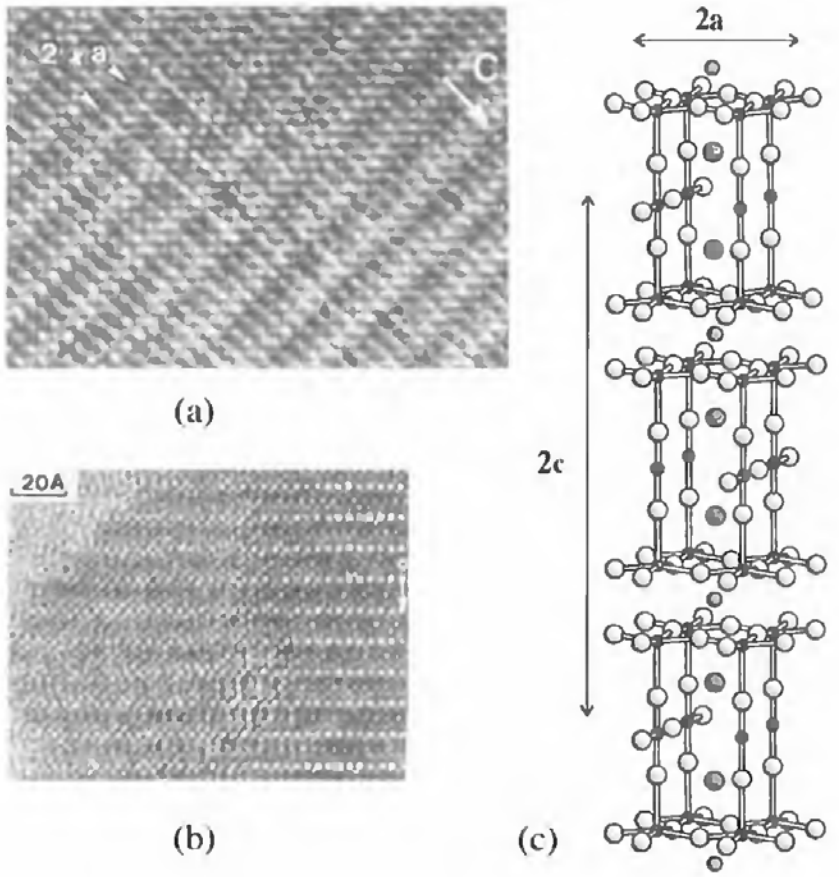

Fig. 8. [010] images of local superstructures corresponding to: (a) $2a_0 \times c$; (b) $2a_0 \times 2c$ and (c) idealized model of the superstructure $2a_0 \times 2c$. The corresponding stoichiometry is $YBa_2Cu_3O_{6.5}$.

coordination (fig. 8c). The variation of the contrast in the "yttrium" layer may be correlated to cation displacements induced by oxygen disorder.

Thus the electron microscopy study of these phases clearly establishes that various microphases are responsible for the appearance of superconductivity with different critical temperatures, compared to the stoichiometric oxide $YBa_2Cu_3O_7$. Moreover the oxygen content (i.e., the hole-carrier density) is not the only factor which governs T_c. The degree of ordering of the oxygen is also susceptible to affect T_c dramatically.

3.3. *Microtwinning in $YBa_2Cu_3O_7$*

The existence of twinning domains in $YBa_2Cu_3O_7$ was revealed very early when $YBa_2Cu_3O_7$ was synthesized (Raveau et al. 1991). This phenomena originates from the transition between the tetragonal high-temperature form and the orthorhombic low-temperature form. Twins are characteristic of the orthorhombic distortion resulting from the oxygen-vacancy ordering. Twinned crystals exhibit electron diffraction patterns with split reflections as shown in fig. 9a; in those patterns the $hk0$ are unsplit due to the fact that they are common to both components. The selection of a 220 reflection with the

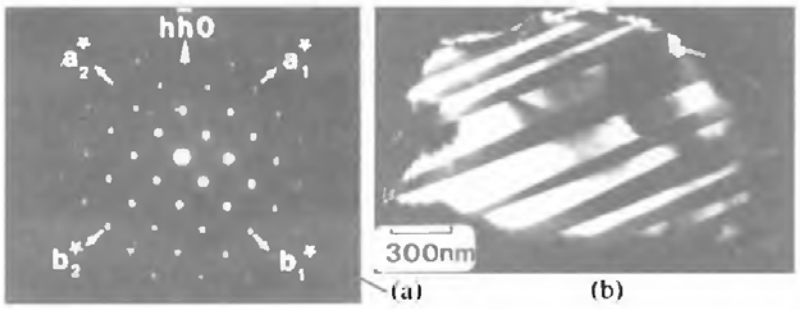

Fig. 9. (a) Typical electron pattern and (b) dark-field [001] image of an orthorhombic crystal $YBa_2Cu_3O_{7-\delta}$.

objective aperture allows the corresponding twinned domains to be revealed in the dark-field image (fig. 9b). The width of the domains usually ranges from 500 to 1000 Å, and the orthorhombic to tetragonal transformation is easily evidenced by the disappearance of the twinned domains by heating with the electron beam; this transformation is shown to be reversible by cooling in the electron microscope.

The twinning domains result from the variation in the ordering of oxygen vacancies along [010] at the level of Cu1 chains. Consequently the CuO_4 groups of one domain are oriented at 90° with respect to those of the adjacent one (fig. 10). In order to explain this change of orientation several models have been proposed (Raveau et al. 1991), which are projected along c in fig. 11. In order to simplify the drawing, only three types of atoms are presented in the projection of the structure along [001], all the others being omitted. The oxygen and copper atoms ($z=0$) of the median plane are presented (fig. 11a) so that the CuO_4 groups appear as straight lines of circles (oxygen atoms) and small black dots (copper atoms). The large black dots represent the barium positions at the upper level ($z=0.18$), in order to show that the cationic lattice is unchanged from one

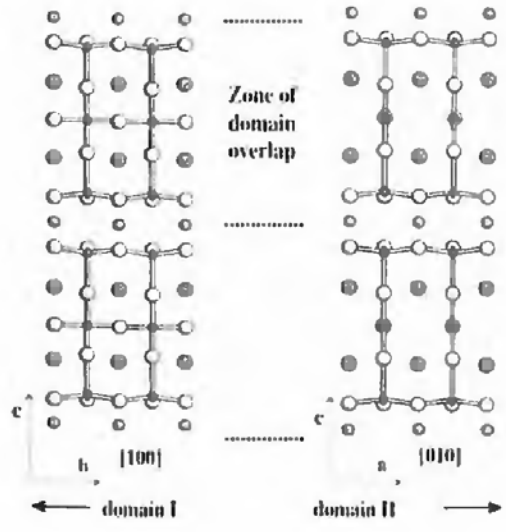

Fig. 10. Projection of twinning domains in a crystal. The change in the orientation of the CuO_4 groups is observed in one perovskite triple layer.

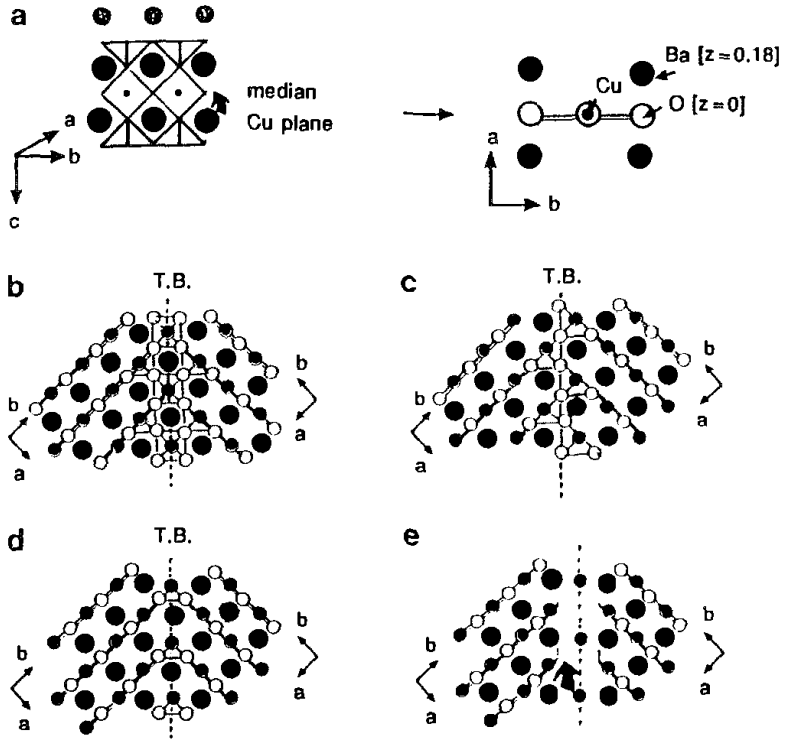

Fig. 11. $YBa_2Cu_3O_7$: (a) Principle of schematization of the drawing of the twin boundaries (T.B.'s). (b–e) Four idealized models of junctions between the twinning domains in the $[CuO_2]_\infty$ layers: (b) junction in a mirror plane through CuO_6 octahedra and CuO_5 pyramids; (c) junction through CuO_5 pyramids; (d) junction in a mirror plane through CuO_4 tetrahedra; (e) junction through twofold coordinated copper, according to Bordet et al. (1988a), implying a threefold coordination for the adjacent copper atoms (*arrow*). Note that, unlike the third and fourth models, the first two imply additional oxygen at the boundary; such arrangements between octahedra and pyramids are frequently observed in oxygen-deficient perovskites.

domain to the next. Two models for the junction (figs. 11b,c) imply the presence of additional oxygen at the boundary, through the existence of CuO_6 octahedra and CuO_5 pyramids, but no drastic displacements occur in the cation framework. A third model (fig. 11d), the simplest because the junctions are achieved solely through tetrahedra, can be proposed: it does not lead to a variation of the oxygen content, but the existence of such CuO_4 tetrahedra would involve a displacement of the copper atoms, and thus this appears to be less favorable. The last model (fig. 11e) implies a substoichiometry with a two-fold coordination of copper [Cu(I)] and a three-fold coordination of the adjacent coppers, and so seems unrealistic. The equivalence of the [110] and [1$\bar{1}$0] directions is illustrated in fig. 12a by the simultaneous existence of quasi-perpendicular twinning domains in the thicker crystals. The idealized model (fig. 12b) shows the arrangement of the $[CuO_2]_\infty$ rows at the quasi-perpendicular boundaries (the junction through octahedra of the model in fig. 11b was chosen for the drawing, but the other models are valid, too). Such a phenomenon can easily occur because the domains result from a single change in vacancy ordering in the core of the matrix without any large displacement of the cationic host lattice.

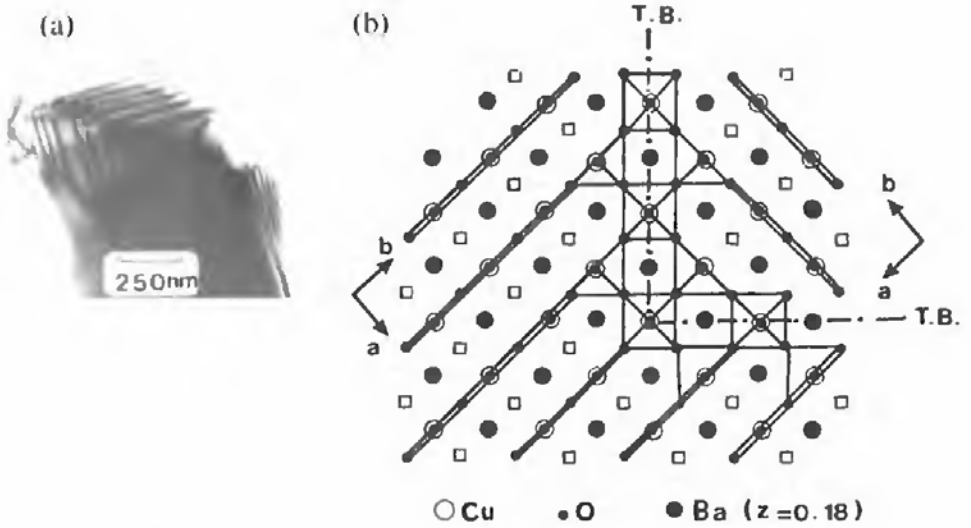

Fig. 12. $YBa_2Cu_3O_7$: (a) [001] image of quasi-perpendicular twinning domains; (b) idealized model of the boundaries.

Several crystal orientations can be chosen to observe the twin boundaries by high-resolution electron microscopy. [010] and [100] are, theoretically, favorable for the observation of these changes in the orientation of the CuO_4 groups, since they can be distinguished through characteristic variations of the contrast for some particular values of the focus. However, the orthorhombic distortion of the cell implies a slight misorientation of a domain with respect to the adjacent one and, additionally, the 45° orientation of the domain boundary with respect to the *a* and *b* axes implies an overlapping of the two adjacent domains whose apparent width is a function of the crystal thickness. Such an overlapping obviously affects the contrast and hinders the detection of local defects in the intermediate neighborhood of the boundary.

The best orientation for observing the twin boundaries is [001]. HREM micrographs of well-oriented crystals show a similar contrast from one domain to another, making them hardly distinguishable (fig. 13). It is necessary to use a smaller objective aperture to make the twin boundaries appear in the thicker part of the bulk. Enlargements of the thin part of the crystal close to the twin boundaries (T.B.) allow two points to be noted:

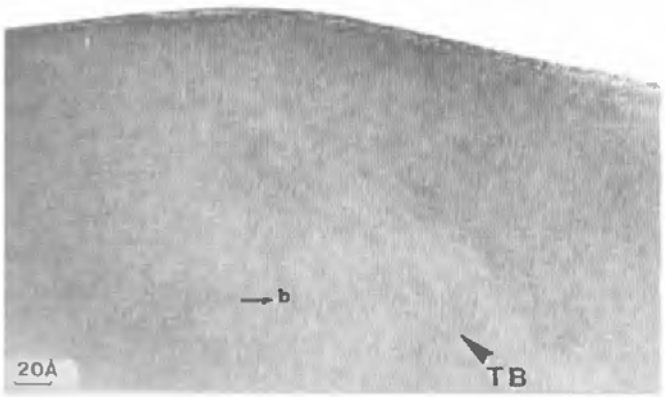

Fig. 13. [001] HREM of twinning domains. The twin boundary (TB) is indicated by a black arrowhead.

(i) Confirmation of the observations along [110]. The crystals often exhibit many defects but they are not specifically localized at the level of the boundary areas and are formed throughout the whole matrix.

(ii) The nature of the junction. It is not possible to draw any conclusions either about any particular model of the junction or about the existence of a single model for such a junction. Note that viewing the crystals along c shows that the quality of the boundaries (planar or not, apparent width) is strongly dependent of the thermal process.

The influence of the twins upon the superconducting properties is not understood to date. There is no doubt that they are not necessary for the appearance of this phenomenon, and that they do not influence T_c. In contrast it appears most probable that they play a key role in enhancing the critical current in YBCO since they seem to be very efficient pinning defects.

3.4. *Extended defects in $YBa_2Cu_3O_7$*

Besides the twinning boundaries, "YBCO" exhibits several kinds of defects due to local variations of composition (Raveau et al. 1991). Strong variations of the contrast with respect to the normal contrast are currently observed for domains with size ranging from 30 to 100 Å^2 as shown in the [001] image in fig. 14a. Such variations can be interpreted as the result of the presence of additional oxygen (Hervieu et al. 1987). Enlargement of such areas (fig. 14b) shows indeed that the expected contrast which consists of large and small dots, correlated to the positions of "2 oxygens + 1 vacancy" and "3 oxygens", respectively, has disappeared and is replaced by dots of equivalent intensity. The theoretical images calculated for an oxygen rich material (O_8) are consistent with the experimental images. Thus, these defects correspond to the replacement of the CuO_4 groups between the

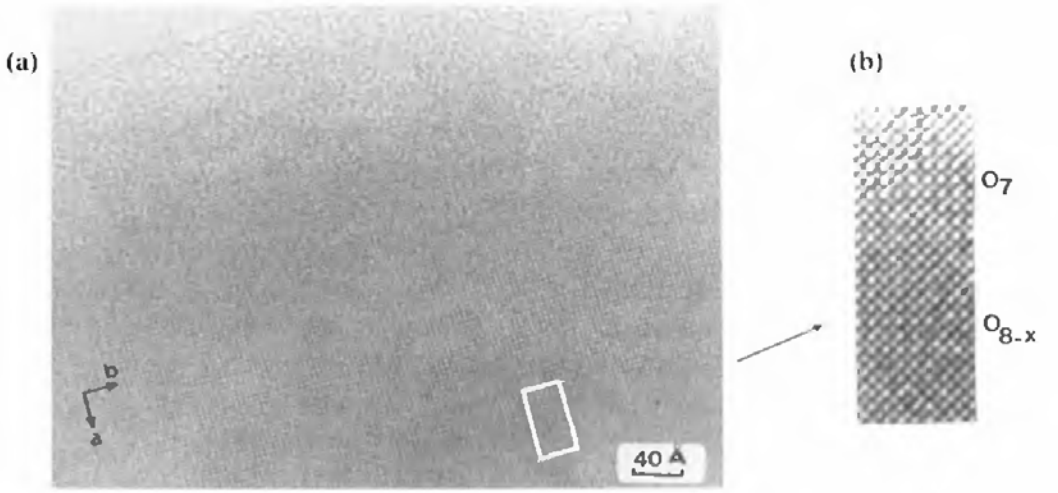

Fig. 14. (a) [001] HREM of a crystallite where contrast variations are observed in the form of small domains, a few nanometers wide. (b) The crystal area in the white rectangle is enlarged. Image calculations, carried out with different oxygen contents, show that such a contrast variation can be correlated with the presence of additional oxygen.

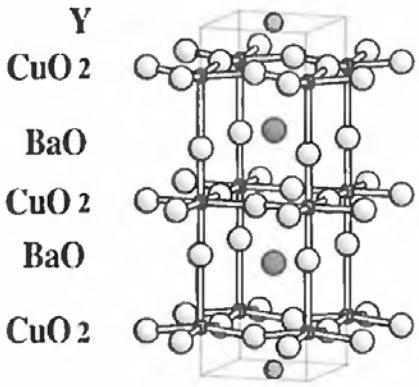

Fig. 15. Idealized drawing of the $YBa_2Cu_3O_{8-x}$ structure.

pyramidal layers by CuO_5 pyramids or by CuO_6 octahedra (fig. 15). The observations of the crystals along [100] or [110] confirm the existence of these domains whose contrast has also been simulated (Hervieu et al. 1987). Extended defects corresponding to a decrease of the molar ratio (Y + Ba)/Cu, and consequently to an oxygen deficiency, are also observed. Such defects (fig. 16a) were shown very early (Domengès et al. 1987) to be the result of a shearing phenomenon, i.e. due to the replacement of a single row of corner-sharing CuO_4 square planar groups by a double row of edge-sharing CuO_4 square planar groups (fig. 16b). Locally, the $YBa_2Cu_4O_8$ structure synthesized by Bordet et al. (1988b) is formed. All these defects modify the oxygen stoichiometry and consequently are susceptible to affect T_c.

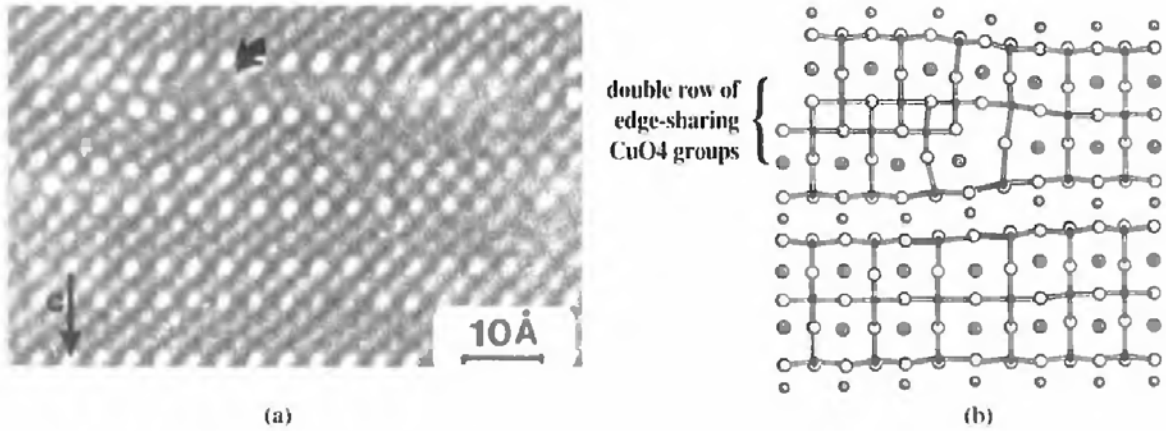

Fig. 16. (a) HREM image of a defect interpreted by the existence of a double row of edge-sharing CuO_4 square planar groups replacing a single row of CuO_4 square planar groups; (b) idealized model of the defect.

3.5. *Other rare-earth "123" cuprates*

Yttrium can be replaced by a rare earth (Ln = Yb to La except Ce, Tb) without dramatically changing the critical temperature, except for lanthanum and for praseodymium (Raveau et al. 1991). Most of the "stoichiometric" "123" cuprates ($LnBa_2Cu_3O_7$) are indeed superconductors with T_c ranging from 88 to 92 K. The fact that T_c is not

significantly affected by the presence of magnetic rare-earth cations is remarkable, compared to classical superconductors such as A15's for which traces of magnetic impurities kill the superconductivity. This demonstrates that the interactions between the superconducting copper layers and the magnetic Ln^{3+} layers are very weak. In contrast, $PrBa_2Cu_3O_7$ is not superconducting, while the critical temperature of $LaBa_2Cu_3O_7$ depends on the method of synthesis: T_c ranges from 75 K to 90 K, according to the thermal treatment. It seems that the T_c variation for the latter is linked to order–disorder phenomena between La^{3+} and Ba^{2+} cations which also induce an oxygen non-stoichiometry so that the oxides $LaBa_2Cu_3O_{7-\delta}$ with T_c smaller than 90 K correspond to $\delta > 0$.

In other-non stoichiometric "123" rare-earth cuprates $LnBa_2Cu_3O_{7-\delta}$, T_c is dramatically affected by the oxygen stoichiometry (fig. 5b, above), as for $YBa_2Cu_3O_{7-\delta}$. However, it must be noted that T_c varies differently with δ from one rare earth to the other. This is illustrated in fig. 5b by comparing $NdBa_2Cu_3O_{7-\delta}$ and $GdBa_2Cu_3O_{7-\delta}$ obtained after long annealings. One observes that the δ regions where the samples are superconductors and the width of the plateaus become narrower as the size of the rare-earth cation increases.

Finally, it is worth pointing out that barium can be partly replaced by a rare earth in the "123" phases $LnBa_2Cu_3O_7$. In this way oxides with the formulation $LnBa_{2-x}Ln_xCu_3O_{7+\delta}$ can be synthesized for Ln = Nd, Sm, Eu, Gd, Dy. These cuprates are also superconductors, but their critical temperature decreases sharply as x increases, in agreement with the decrease of their charge carrier concentration.

4. The "124" superconductor $YBa_2Cu_4O_8$ and its intergrowth with $YBa_2Cu_3O_7$

The 80 K superconductor $YBa_2Cu_4O_8$ has been observed for the first time as a defect in the $YBa_2Cu_3O_7$ matrix, by high-resolution electron microscopy (Domengès et al. 1987). In fact it was synthesized as a pure phase one year later by Bordet et al. (1988b). This orthorhombic structure (fig. 17a) consists of quadruple copper layers, built up themselves of pyramidal copper layers interconnected though double chains of edge-sharing CuO_4 square planar groups. In other words, it derives from the $YBa_2Cu_3O_7$ structure by simply replacing the single Cu1 chains of corner-sharing square planar groups by double chains of edge-sharing square planar groups.

The two-dimensional accord between the $YBa_2Cu_4O_8$ and $YBa_2Cu_3O_7$ structures is made from sharing one yttrium layer. This is the case for the 95 K superconductor $Y_2Ba_4Cu_7O_{15}$ (Chaillout et al. 1989), whose structure (fig. 17b) can be described as an intergrowth of the two structures along $\vec{c}$. These results suggest that a series of phases with the generic formulation $(YBa_2Cu_3O_7)_n(YBa_2Cu_4O_8)_m$ should exist. The latter would correspond to the stacking of "123" blocks with m "124" blocks alternately; $Y_2Ba_4Cu_7O_{15}$ represents the first member of this series ($n = m = 1$).

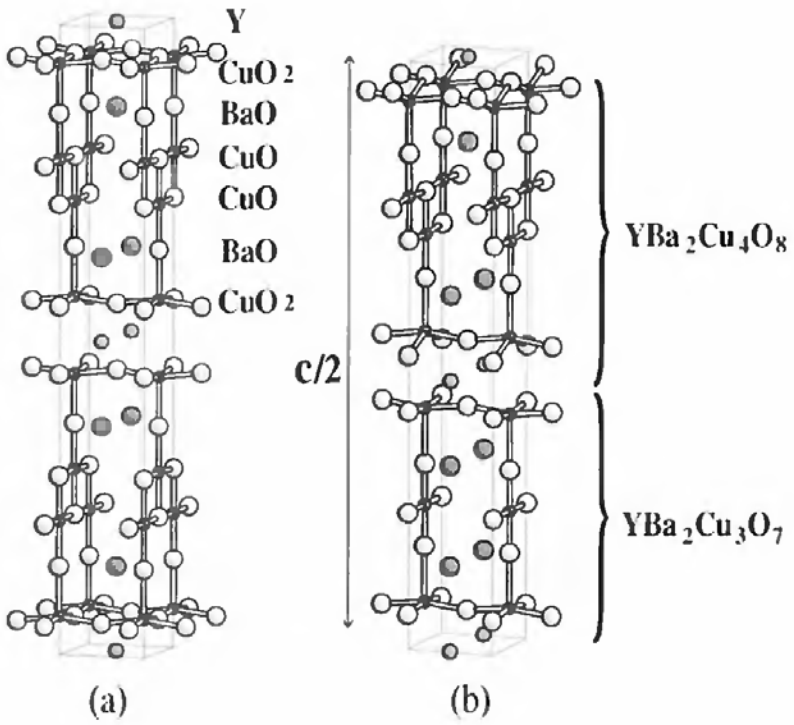

Fig. 17. Structures of (a) $YBa_2Cu_4O_8$ and (b) $Y_2Ba_4Cu_7O_{15}$.

5. Introduction of rare earth in Bi, Tl, Pb and Hg layered cuprates

Rare-earth elements stabilize different layered structures involving thallium, lead, and mercury, owing to their large size and also to their trivalent character allowing more oxygen to be incorporated.

In the case of lead cuprates, several structures have been generated thanks to the introduction of rare-earth elements. The first of these oxides is the 68 K superconductor $Pb_2Sr_2Ln_{1-x}Ca_xCu_3O_8$ (Cava et al. 1988) with $x \approx 0.50$, whose structure (fig. 18a) consists of double pyramidal copper layers $[Cu_2O_5]_\infty$ interleaved with calcium and yttrium ions, as already observed in $YBa_2Cu_3O_7$, associated with single rock-salt-type layers $[(Sr,Pb)_1O]_\infty$ similar to those observed in La_2CuO_4-type oxides. The rock-salt layers are themselves connected through layers of monovalent copper, with Cu(I) in two-fold coordination, showing a great similarity with $YBa_2Cu_3O_6$. Let us consider the hypothetical oxide "$Pb_2Sr_2YCu_3O_{10}$", whose structure (fig. 18b) consists of double oxygen-deficient perovskite layers and single perovskite layers intergrown with single rock-salt-type layers $[(Pb,Sr)_1O]_\infty$. Such an oxide corresponds to a double intergrowth, i.e., an intergrowth of the La_2CuO_4-type structure (single perovskite layers) with the $La_2CaCu_2O_6$-type structure (double perovskite layers). The elimination of the oxygen atoms of the basal planes of the CuO_6 octahedra, belonging to the single perovskite layers of "$Pb_2Sr_2YCu_3O_{10}$", leads to the 68 K superconductor. It results that oxygen can be intercalated in the structure of $Pb_2Sr_2Y_{1-x}Ca_xCu_3O_8$. It is worth pointing out that such an oxide can be obtained as a superconductor only by reaction in a reducing atmosphere.

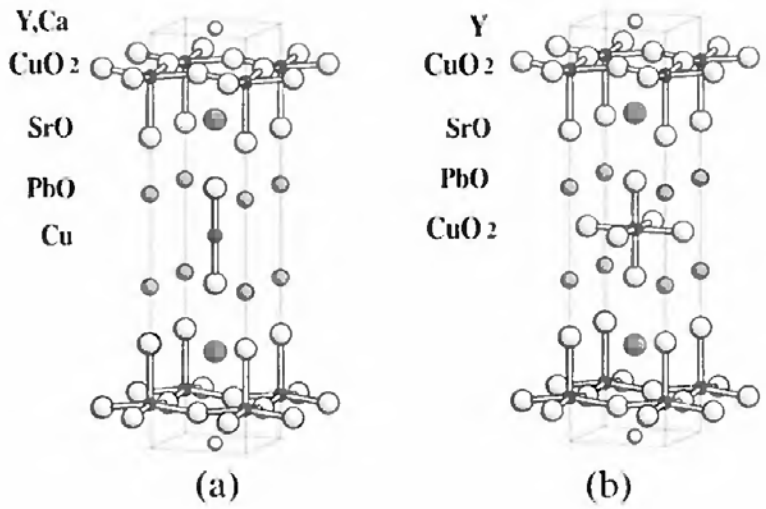

Fig. 18. (a) Structure of $Pb_2Sr_2Y_{1-x}Ca_xCu_3O_8$, derived from (b) the hypothetical "double intergrowth" $Pb_2Sr_2YCu_3O_{10}$.

This leads one to consider a disproportionation of Cu(II) into Cu(III) and Cu(I) for the final formula. The substitution of bismuth for lead allows T_c to be increased up to 80 K for $Pb_{2-x}Bi_xY_{1-y}Ca_yCu_3O_8$ (Retoux et al. 1989) with $0 \leqslant x \leqslant 0.50$ and $0 \leqslant y \leqslant 1$.

The oxide $Pb_2Sr_{2-x}La_xCu_2O_{6+\delta}$ (Zandbergen et al. 1989) exhibits a great similarity with $Pb_2Sr_2Ca_{0.5}Y_{0.5}Cu_3O_8$. It is indeed also characterized by a mean oxidation state of copper smaller than 2 in spite of its superconducting properties ($T_c \approx 30$ K). Its structure (fig. 19a) can be described as the intergrowth of single rock-salt layers $[(Sr, La, Pb)O]_\infty$ with single oxygen-deficient perovskite layers. Two sorts of copper layers must

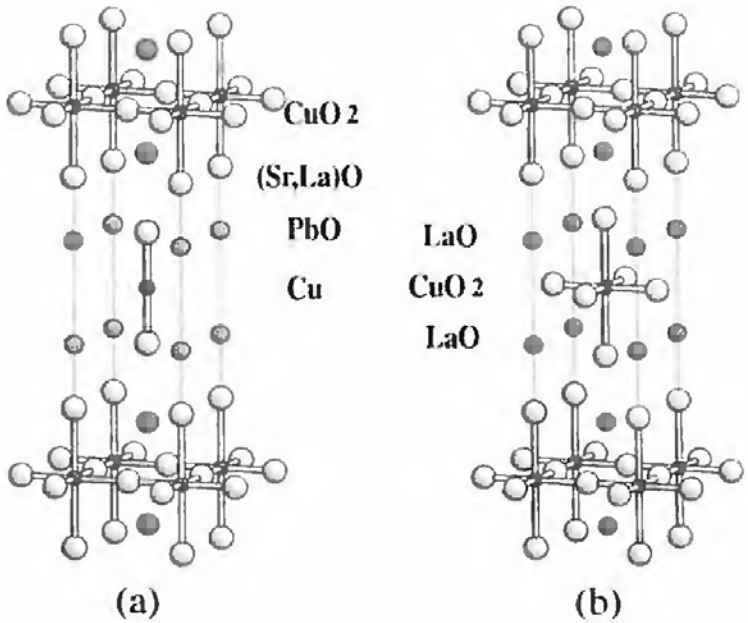

Fig. 19. (a) Structure of $Pb_2Sr_{2-x}La_xCu_2O_{6+\delta}$, compared to (b) that of La_2CuO_4-type oxides (b).

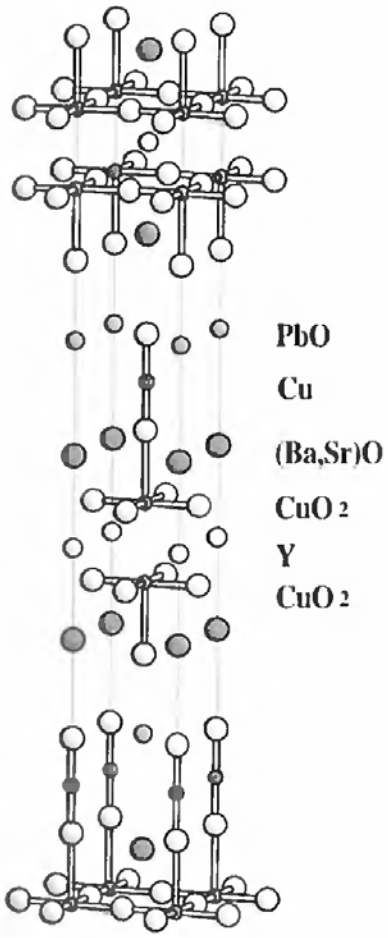

Fig. 20. Structural model for $PbBaYSrCu_3O_7$.

be distinguished: octahedral layers, i.e. non-deficient perovskite layers as in La_2CuO_4, and layers of CuO_2 sticks as in $Pb_2Sr_2Ca_{0.5}Y_{0.5}Cu_3O_8$. Thus, this structure is derived from that of La_2CuO_4 (fig. 19b) by removing rows of oxygen atoms; it implies a copper disproportionation with monovalent copper in the CuO_2 sticks and mixed-valence copper, Cu(II)–Cu(III), in the superconductive octahedral layers.

$PbBaYSrCu_3O_{8-\delta}$ (Rouillon et al. 1989) represents a new member of the intergrowth family. The structure of this phase has not been completely elucidated. Although its structure consists of triple copper layers, the geometry of the layer seems to be different from that of the other members. A structural model deduced from HREM and neutron-diffraction studies is proposed in fig. 20. The limit oxide $PbBaYSrCu_3O_7$ consists of triple copper layers built up from two pyramidal copper layers, between which yttrium ions are interleaved and one layer of $Cu^{I}O_2$ sticks. These triple oxygen-deficient copper layers are intergrown with single rock-salt layers involving $[(Ba,Sr)O]_\infty$ and $[PbO]_\infty$ planes. This phase is not superconducting but the partial replacement of yttrium by calcium, leading to the phase $PbBaSrY_{1-x}Ca_xCu_3O_{8-\delta}$, allows 1–2% diamagnetism to be detected below 50 K. Bulk superconductivity was confirmed for $x=0.3$ with $T_c=37$ K (Tokiwa et al. 1990).

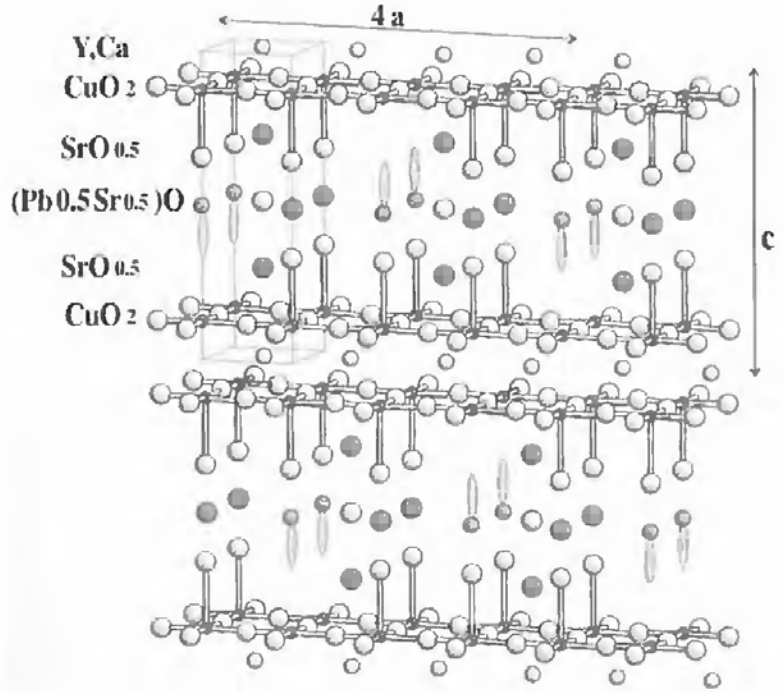

Fig. 21. $Pb_{0.5}Sr_{2.5}Y_{1-x}Ca_xCu_2O_{7-\delta}$: model of a perfect ordering of the Pb(II) and Sr in the intermediate rock salt layers. This idealized drawing shows that $4a\times c$ superstructure can be built up. Other models can be obtained by translation of the adjacent layers. On the left of the figure, the tetragonal subcell $a\times a\times c$ is drawn. The orientation of the Pb(II) lone pair is also drawn.

The oxide $Pb_{0.5}Sr_{2.5}Y_{1-x}Ca_xCu_2O_{7-\delta}$ (Rouillon et al. 1990), is the only pure lead cuprate which exhibits double copper layers. Its structure (fig. 21) belongs to "1212", i.e. intergrowth of double rock-salt and perovskite slabs. Mixed lead–strontium monolayers $[Pb_{0.5}Sr_{0.5}O]_\infty$ replace the $[TlO]_\infty$ monolayers in the double rock-salt slabs. However, an important difference with the thallium cuprates concerns the existence of oxygen vacancies at the boundary between the perovskite and rock-salt-type layers. It results in the existence of several superstructures which can be interpreted in terms of ordering of lead, strontium and anionic vacancies. An isostructural solid solution has been isolated by completely replacing strontium by calcium in the mixed monolayers, leading to the formulation $Pb_{0.50}Ca_{0.50}Sr_2Y_{1-x}Ca_xCu_2O_{7-\delta}$. Both oxides exhibit a wide homogeneity range, $0 \leqslant x \leqslant 0.60$, but curiously superconductivity is only observed for $0.50 \leqslant x \leqslant 0.60$. All the oxides of this series are superconductors with T_c ranging from 60 to 70 K, but they all exhibit broad resistive transitions.

In contrast to the lead cuprates, most of the thallium cuprates do not require the presence of a rare-earth element for their stabilisation. The 40 K superconductor $Tl_{1-x}Pr_xSr_{2-y}Pr_yCuO_{5-\delta}$ (Bourgault et al. 1989) seems to be the only one whose structure is stabilised by the presence of praseodymium. The isostructural phase $TlSr_2CuO_{5-\delta}$ could indeed not be isolated, but was only observed as a mixture with an unknown phase. In this "1201" structure (fig. 22), single perovskite layers $[(Sr,Pr)CuO_3]_\infty$ are intergrown with double rock-salt layers $[(Tl,Pb,Sr)_2O_2]_\infty$. On the other hand it is

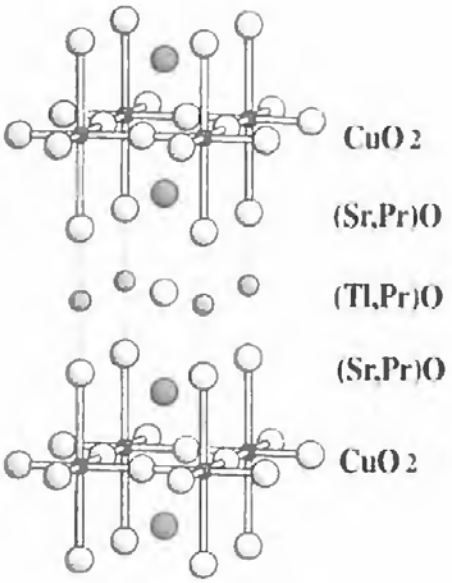

Fig. 22. Structure of 1201-type $Tl_{1-x}Pr_xSr_{2-y}Pr_yCuO_5$.

worth pointing out that the substitution of rare earth for calcium in the 1212 structure of $TlBa_2CaCu_2O_7$ is possible without destroying the structure. A partial substitution of Ln for Ca enhances T_c, as shown for instance for $TlBa_2Ca_{1-x}Y_xCu_2O_7$ (Nakajima et al. 1989), for which T_c increases from 73 K to 103 K as x increases from 0 to 0.2. Even the complete substitution of calcium is possible, leading to the oxides $TlBa_2LnCu_2O_7$, but it kills superconductivity (Ganguli et al. 1989, Martin et al. 1989). A similar behaviour is observed for the 1212 cuprates $TlSr_2Ca_{1-x}Ln_xCu_2O_7$, which exhibit superconductivity in the region 60–90 K. In contrast, the introduction of rare earths in Tl cuprates involving a number of copper layers larger than two has not been observed to date.

It is not necessary to introduce a rare-earth element to stabilize the structure of bismuth cuprates. Nevertheless, it is worth pointing out that in such phases calcium can be partly replaced by a rare earth. This is the case for the "2212"-type superconductor $Bi_{2-x}Pb_xSr_2Ca_{1-x}Y_xCu_2O_8$ (Koyama et al. 1988) for which T_c remains constant, i.e. close to 85 K, for $0 \leqslant x \leqslant 0.5$, and then drops abruptly above $x = 0.50$.

The mercury cuprates are difficult to synthesize as pure phases, due to their low stability which originates form the dumbbell coordination of mercury. The difficulty in isolating pure phases increases with the number of copper layers. Moreover, only the barium layered cuprates $HgBa_2Ca_{m-1}Cu_mO_{2m+2}$ are obtained, whereas the strontium homologous series could not be synthesized. The introduction of a rare earth into the Hg sites allows the anionic sites at the level of the Hg sites to be partially filled, and consequently the structure can be stabilized (for a review see Raveau et al. 1995a).

The exploration of the Hg–Ba–Ca–Cu–Ln–O systems has indeed allowed isolation of two "1212" superconducting cuprate series: the oxide $Y_{0.6}Ca_{0.4}Ba_2Cu_2(Hg_{1-x}M_x)O_{6+\delta}$ for M = Ca + Cu, with $0.40 \leqslant x \leqslant 0.60$, and the phase $Nd_{1-x}Ca_xBa_2Hg_{1-x'}Cu_{2+x'}O_{6+\delta}$, with $0.40 \leqslant x \leqslant 0.60$ and $0.0 \leqslant x' \leqslant 0.20$. The superconducting properties of these materials have so far not been optimized as they show very broad transitions that might be

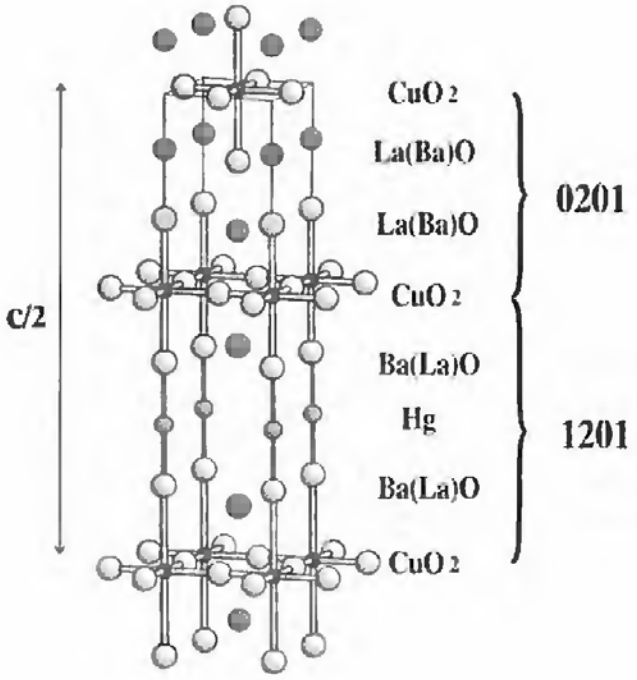

Fig. 23. Structure of the superconductor $HgBa_2La_2Cu_2O_{8+\delta}$: intergrowth of the "0201" and "1201" structures.

due to disordering of cations and oxygen or anionic vacancies. Nevertheless, the critical temperatures that can be reached, up to 110 K for the neodymium compound, are very promising.

Besides these two phases, a cuprate $HgBa_2La_2CuO_{8+\delta}$ (Huvé et al. 1994), with a novel structure can be synthesized. The juxtaposition of $HgBa_2CuO_4$ layers with La_2CuO_4 type layers allows indeed an intergrowth of the "0201" (La_2CuO_4) and "1201" ($HgBa_2CuO_4$) to be generated (fig. 23). Thus this structure consists of octahedral copper layers interconnected through layers of HgO_2 sticks and through single rock-salt layers alternately. This intergrowth is a superconductor, characterized by a rather sharp transition with a critical temperature of 53 K (table 3).

Concerning the Hg–Sr–Cu–O system, no mercury strontium cuprate has been synthesized to date, even at high pressure. A remarkable result deals with the synthesis of two "Hg–Sr" cuprates with the "1201" and "1212" structures by introducing praseodymium into the mercury sites. A second spectacular feature is that one of these compounds is a very good superconductor in spite of the presence of large amounts of praseodymium in the structure. Two series of Pr-substituted Sr cuprate phases have indeed been synthesized (Goutenoire et al. 1993, Hervieu et al. 1993a) (table 3): the cuprates $Hg_{0.4}Pr_{0.6}Sr_{2-x}Pr_xCuO_{4+\delta}$, with $0 \leqslant x \leqslant 0.1$, and the oxides $Hg_{0.4}Pr_{0.6}Sr_2A_{1-x}Pr_xCu_2O_{6+\delta}$, for A = Ca, Sr and with $0.20 \leqslant x \leqslant 0.70$. The first series belongs to the "1201" structural type; however, it differs from the classical "1201" classical mercury cuprates by its orthorhombic symmetry, characterized by a doubling of one parameter of the tetragonal subcell ($a \approx 2a_p$, $b \approx a_p$, $c \approx c_{1201}$). The [010] HREM image of this phase (fig. 24a) shows that this situation is due to an ordering of the Hg and Pr atoms in the mercury layers in such a way that mercury and praseodymium

Table 3
Characteristics of mercury compounds substituted by rare earths, Bi, Pb and Tl

Composition	x	unit-cell parameters			T_c (K)
		a (Å)	b (Å)	c (Å)	
'1201' structure					
$Hg_{0.5}Bi_{0.5}Sr_{2-x}La_xCuO_{4+\delta}$	0–0.75	3.765–3.778		8.94–8.84	27
$Hg_{0.3}Pb_{0.7}Sr_{2-x}La_xCuO_{4+\delta}$	0–0.65	3.749–3.768		8.87–8.99	40
$Hg_{0.4}Pr_{0.6}Sr_{2-x}Pr_xCuO_{4+\delta}$	0–0.1	7.606	3.683	8.88	NS
$Hg_{0.4}Ce_{0.5}Cu_{0.1}Sr_{2-x}La_xCuO_{4+\delta}$	0.4–0.8	3.733–3.738	7.575–7.750	17.946–17.96	NS
'1212' structure					
$Hg_{0.3}Pb_{0.7}Sr_2Ca_{0.7}Nd_{0.3}Cu_2O_7$		3.81		12.13	100
$Hg_{0.5}Bi_{0.5}Sr_2Ca_{1-x}Nd_xCu_2O_{6+\delta}$	0.35–1	3.809–3.854		11.99–12.06	94
$Hg_{0.5}Bi_{0.5}Sr_2Ca_{0.65}Y_{0.35}Cu_2O_{6+\delta}$		3.795		12.036	92
$Hg_{0.5}Bi_{0.5}Sr_2Ca_{0.65}Pr_{0.35}Cu_2O_{6+\delta}$		3.805	3.819–3.838	12.054	95
$Hg_{0.4}Pr_{0.6}Sr_2Sr_{1-x}Pr_xCu_2O_{6+\delta}$	0.2–0.7	3.838–3.864	3.795–3.802	12.22–12.26	85
$Hg_{0.4}Pr_{0.6}Sr_2Ca_{1-x}Pr_xCu_2O_{6+\delta}$	0.2–0.7	3.833–3.846		12.15	85
$Hg_{1-x}M_xBa_2Y_{0.6}Ca_{0.4}Cu_2O_{6+\delta}$	0.4	3.870		12.537	90
$HgBa_2Nd_{1-x}Ca_xCu_2O_{6+\delta}$	0.4–0.6	3.877		12.607	110
$Hg_{0.4}Ce_{0.5}Sr_{2.5}Ca_{0.5}Cu_{2.1}O_7$		7.626	3.813	12.19	51
'1201–0201' intergrowth					
$HgBa_2La_2Cu_2O_{8+\delta}$		3.824		32.067	53
Double mercury layers					
$Hg_{1.5}(Cu,Pr)_{0.5}Ba_2PrCu_2O_{8-\delta}$		3.924		28.993	NS

rows alternate along $\vec{a}$ (fig. 24b). Contrary to the bismuth or lead mercury-based superconductors, this phase does not exhibit bulk superconductivity. Nevertheless traces of superconductivity, i.e. <1%, are detected, which might also be due to a secondary phase.

The structural behaviour of the second series of cuprates is very similar to that of the "1201" series. The "1212"-type oxides $(Hg_{0.4}Pr_{0.6})Sr_2Sr_{1-x}Pr_xCu_2O_{6+\delta}$ also exhibit orthorhombic symmetry. However, two kinds of crystals are observed for the same composition as shown from their electron diffraction (ED) patterns (fig. 25); the first one is characterized by a doubling of the a parameter only ($a \approx 2a_p$, $b \approx a_p$, $c \approx c_{1212}$), whereas the second one exhibits a doubling of the a and c parameters with respect to the tetragonal subcell ($a \approx 2a_p$, $b \approx a_p$, $c \approx 2c_{1212}$). The corresponding HREM images (figs. 26a,b) show clearly that this phenomenon corresponds to an ordering of the praseodymium and mercury ions within the mercury layers, similar to that observed for the "1201" "Pr–Hg" cuprate. In both kinds of crystals one mercury row alternates with one praseodymium row along $\vec{a}$, leading to a doubling of this parameter; in the first kind of crystals (labelled O_I) two successive mercury rows are above each other along $\vec{c}$ (fig. 26a),

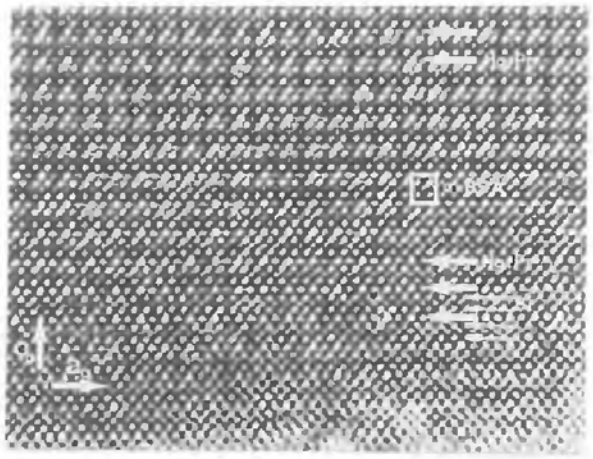

(a)

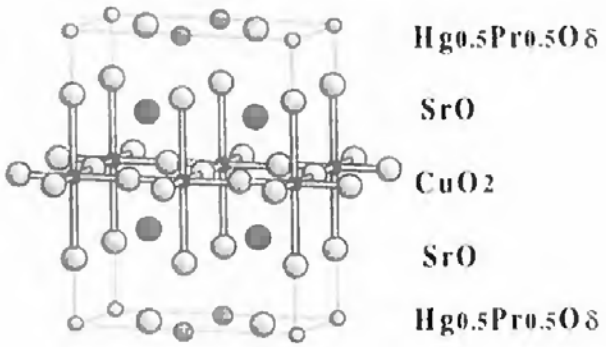

(b)

Fig. 24. (a) [010] image of $Hg_{0.4}Pr_{0.6}Sr_2CuO_{4+\delta}$. The mixed $[Hg_{0.4}Pr_{0.6}O_\delta]$ layers are indicated by large white arrows and the [Sr–O] layers by small ones. (b) Structure of the ideal cuprate $Hg_{0.5}Pr_{0.5}Sr_2CuO_{4+\delta}$ with an orthorhombic double cell.

so that $c \approx c_{1212}$, whereas such successive rows are shifted by $a/2$ in the second kind of crystal (fig. 26b), leading to a doubling of the c parameter. However, the most spectacular feature deals with the superconducting properties of these phases, which exhibit a critical temperature up to 85 K, as shown, for instance, for the phase $Hg_{0.4}Pr_{0.6}Sr_{2.7}Pr_{0.3}Cu_2O_{6+\delta}$ (fig. 27a) for which a very high diamagnetic volume fraction (90%) and a sharp transition are observed. This effect of praseodymium which dramatically enhances the superconducting properties of the "1212" phase, and especially increases the T_c values, is fundamentally opposite to what is observed for other cuprates, such as the "123" phase in which the introduction of praseodymium kills the superconductivity. A systematic study of this phase will be of crucial importance in understanding the role of praseodymium in the appearance or disappearance of superconductivity in the layered cuprates, taking special account of the oxidation state of praseodymium (III or IV or mixed) and its location (within the rock-salt layers or in the fluorite-type layers between the CuO_5 pyramids).

The cuprates $Hg_{1.5}(Cu,Pr)_{0.5}Ba_2PrCu_1O_{8-\delta}$ and $Hg_{2-x}M_xBa_2Pr_2Cu_2O_{10-\delta}$ were the first mercury cuprates with mercury bilayers that were synthesized (Martin et al. 1995, Huvé et al. 1995). The first one has 2212 structure (fig. 28a), whereas the second one has the 2222 structure (fig. 28b). These oxides are not superconductors, but superconducting

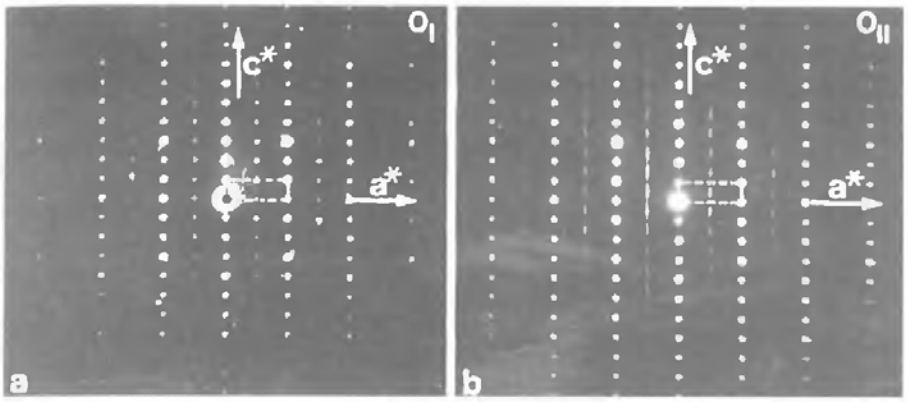

Fig. 25. $Hg_{0.4}Pr_{0.6}Sr_{2.7}Pr_{0.3}Cu_2O_{6+\delta}$ [010] ED patterns of (a) the orthorhombic I and (b) the orthorhombic II structures. The supercells are drawn.

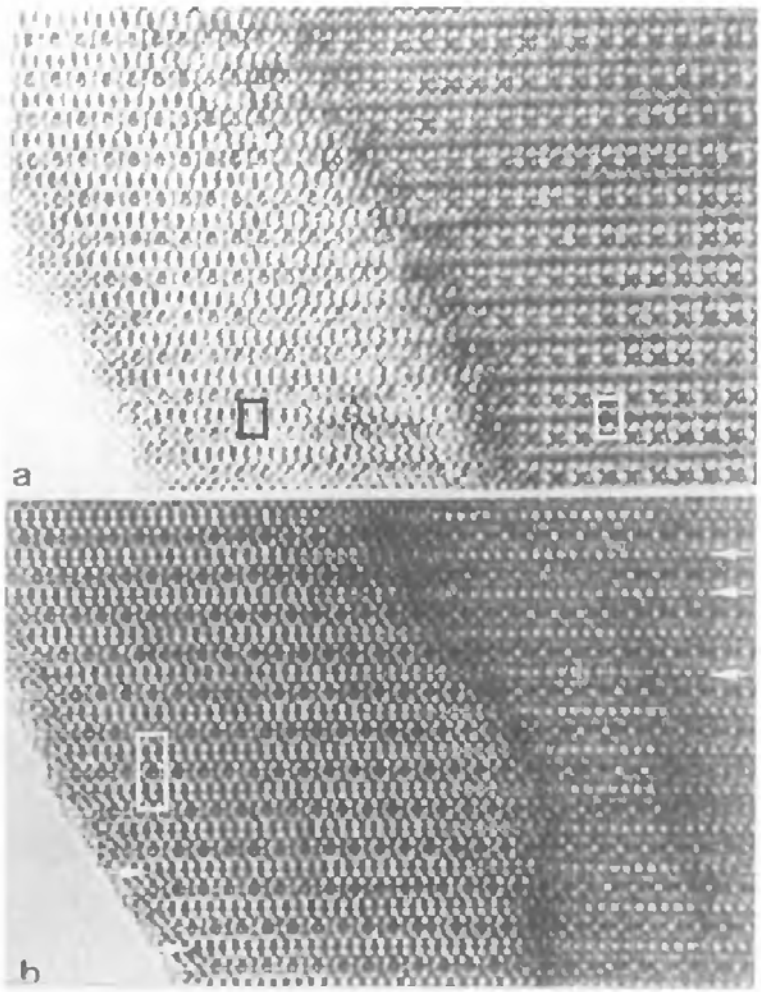

Fig. 26. $Hg_{0.4}Pr_{0.6}Sr_{2.7}Pr_{0.3}Cu_2O_{6+\delta}$: [010] HREM image of the ordered crystals. One Hg row alternates with one Pr row along $\vec{a}$. (a) orthorhombic I and (b) orthorhombic II supercells.

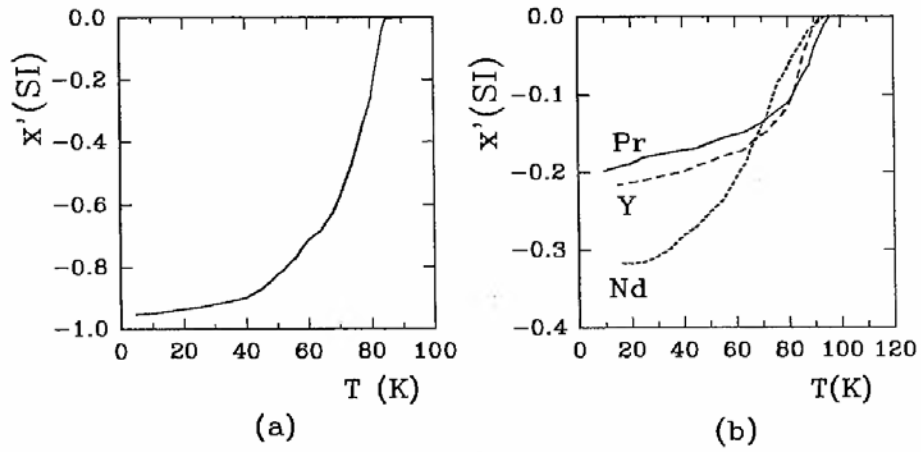

Fig. 27. (a) $\chi'(T)$ curve for $Hg_{0.4}Pr_{0.6}Sr_{2.7}Pr_{0.3}Cu_2O_{6+\delta}$; (b) $\chi'(T)$ curve for $Hg_{0.5}Bi_{0.5}Sr_2Ca_{0.65}Ln_{0.35}Cu_2O_{6+\delta}$ (Ln = Y, Nd, Pr).

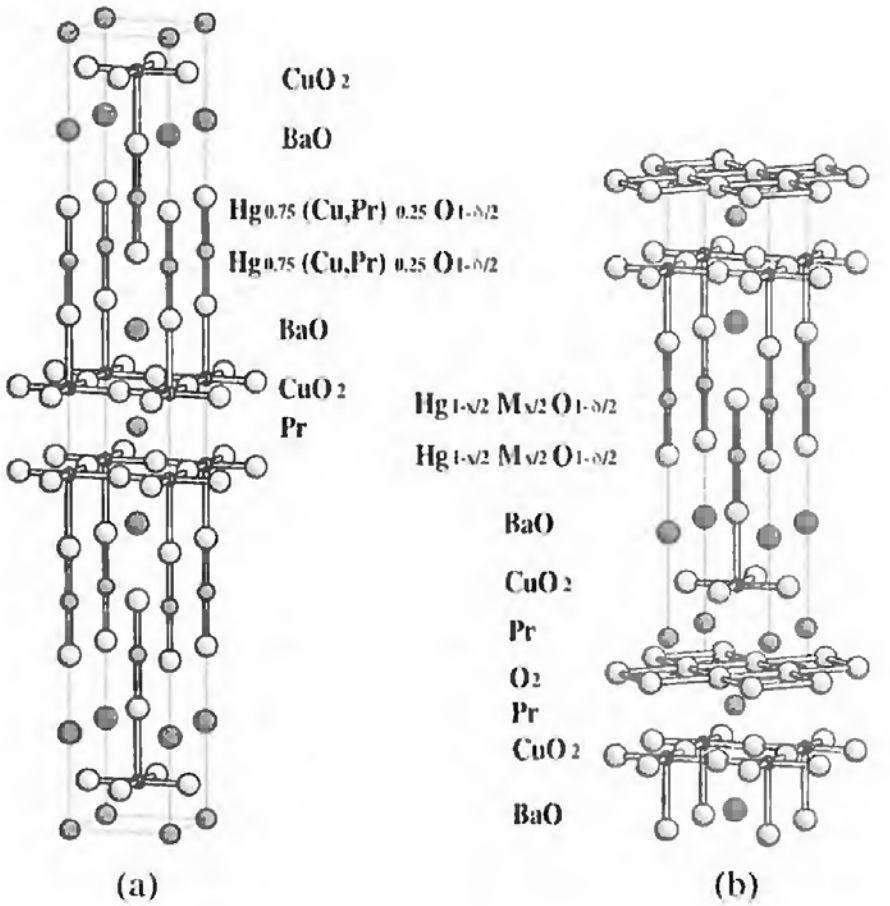

Fig. 28. Structures of (a) $Hg_{1.5}(Cu,Pr)_{0.5}Ba_2PrCu_2O_{8-\delta}$ and (b) $Hg_{2-x}M_xBa_2Pr_2Cu_2O_{10-\delta}$ non-superconducting cuprates.

2212-type mercury cuprates have been isolated later under high pressure (Radaelli et al. 1994).

Rare-earth cations can be introduced either into the Sr sites or into the Ca sites of the Bi- and Pb-stabilized mercury cuprates (for a review, see Raveau et al. 1995a). This is the case for the 1201 superconductors $Hg_{0.5}Bi_{0.5}Sr_{2-x}La_xCuO_{4+\delta}$, with $0 \leqslant x \leqslant 0.75$, and $Hg_{0.3}Pb_{0.7}Sr_{2-x}La_xCuO_{4+\delta}$, with $0 \leqslant x \leqslant 0.65$, which exhibit rather broad transitions with T_c ranging from 27 K to 40 K. Three other series of oxides, $Hg_{0.5}Bi_{0.5}Sr_2Ca_{1-x}Ln_xCu_2O_{6+\delta}$ with Ln = Nd, Y, Pr, are of high interest. These oxides, synthesized for $0.35 \leqslant x \leqslant 1$, exhibit the 1212-type structure already described. The important feature concerning these materials deals with their rather sharp transition with T_c close to 90 K (fig. 27b). But most remarkable is the fact that the Pr phase is superconducting and moreover exhibits the highest T_c; such a result is in contrast with the "123" phase for which the substitution of Pr for Y between the pyramidal copper layers kills superconductivity.

6. Layered cuprates involving double fluorite layers

The structures of layered cuprates involving double fluorite layers are derived from those of the 1212, 2212 and "123" cuprates by replacing the single fluorite layer located between the pyramidal copper layers by a double fluorite layer. In other words, a $[Ca]_\infty$ or $[Y]_\infty$ layer is replaced by a $[Ln_2O_2]_\infty$ layer. Consequently, the presence of the rare earth is absolutely necessary to stabilize such structures. Although a great number of these oxides are not superconductors or exhibit low T_c, they are of great interest for the study of superconductivity since they fulfil the two conditions – two-dimensional character and copper mixed valence – for the appearance of superconductivity. The absence or weakness of superconductivity in these oxides may result from the higher distance between the pyramidal copper layers. All these oxides will not be described in detail here (for a review see Raveau et al. 1991).

The oxides $Tl_{1+x}A_{2-y}Ln_2Cu_2O_9$ with Ln = Pr, Nd, Ce and A = Sr, Ba represent the first series that were isolated. They crystallize in the tetragonal system. As can be seen from the structure of two of them, $Tl_{1.30}Sr_{1.6}Pr_2Cu_2O_9$ and $Tl_{1.3}Ba_{1.7}Pr_2Cu_2O_9$ (fig. 29a) one observes a triple intergrowth of double pyramidal copper layers (oxygen deficient perovskite layers) with double fluorite-type layers and double rock-salt-type layers. The latter are built up from one thallium monolayer sandwiched between two "BaO" or "SrO" layers. In these structures some of the barium (or strontium) sites are occupied by the excess thallium. In fact, this structure is directly derived from the 1212-type oxides $TlBa_2CaCu_2O_7$ by just replacing the $[CaO_2]_\infty$ single fluorite layer by a $[Pr_2O_4]_\infty$ double fluorite layer, leading to the idealized formula "$TlBa_2Pr_2Cu_2O_9$". Contrary to the 1212 thallium cuprates, this oxide is not superconducting.

The oxide $Nd_{2.64}Sr_{0.82}Ce_{0.54}Cu_2O_{8-y}$ (Akimitsu et al. 1988, Sawa et al. 1989), called T*, is also tetragonal ($a \approx 3.9$ Å, $c \approx 12.5$ Å). Its structure (fig. 29b) is also built

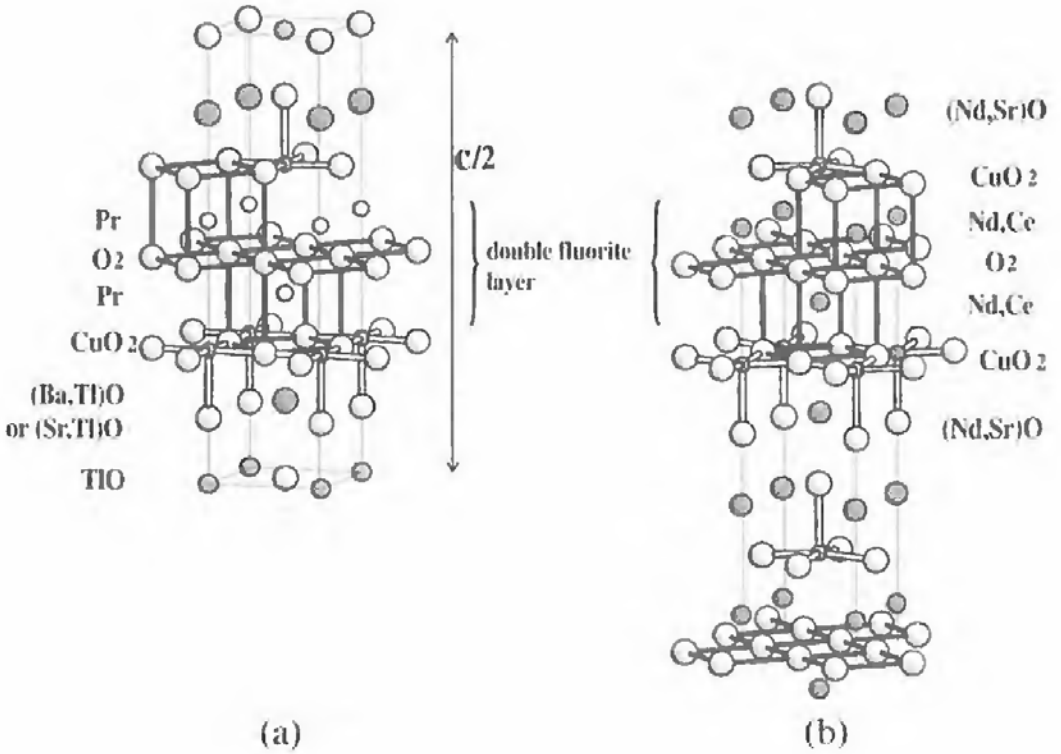

Fig. 29. (a) Crystal structure of the oxides $Tl_{1-x}A_{2-y}Ln_2Cu_2O_9$ (A = Sr, Ba ; Ln = Pr, Nd, Ce). (b) Crystal structure of the T phase $Nd_{2.64}Sr_{0.82}Ce_{0.54}Cu_2O_{8-y}$. In the double fluorite layers some LnO_8 cages are drawn.

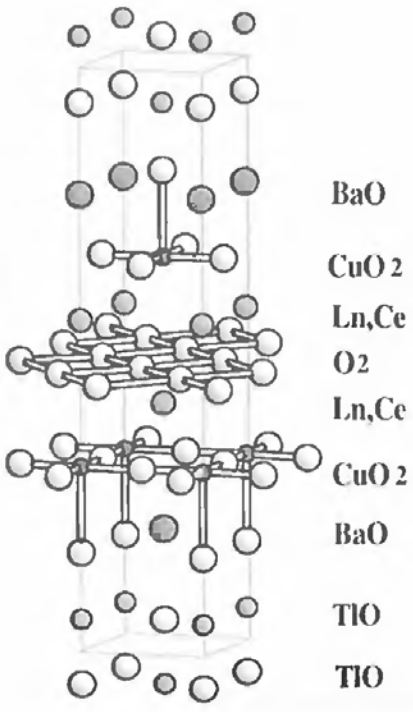

Fig. 30. Crystal structure of the oxides $Tl_2Ba_2Ln_{2-x}Ce_xCu_2O_{10}$.

up from double pyramidal copper layers, double $[(Nd,Ce)_2O_4]_\infty$ layers and single rock-salt layers $[(Nd,Sr)O]_\infty$. In fact, this structure can be derived from the $La_2CaCu_2O_6$-type structure by replacing the $[CaO_2]_\infty$ single layer by a double fluorite-type layer $([Nd,Ce)_2O_4]_\infty$.

The oxides $Bi_2Sr_2Ln_{2-x}Ce_xCu_2O_{10}$ and $Tl_2Ba_2Ln_{2-x}Ce_xCu_2O_{10}$, which were synthesized for Ln = Sm, Eu or Gd, correspond to the replacement of thallium monolayers by thallium or bismuth bilayers in the idealized $TlA_2Ln_2Cu_2O_9$ "structure". They crystallize in the tetragonal system ($a \approx 3.88$, $c \approx 17.28$ Å) for thallium. In contrast to the Tl derivatives, the Bi compounds are slightly orthorhombic. Their structure (fig. 30) can be described as a triple intergrowth of double copper layers, with double fluorite-type layers and triple rock-salt-type layers. Thus this structure can be derived from the 2212 oxides $Bi_2Sr_2CaCu_2O_8$ and $Tl_2BaCaCu_2O_8$ by just replacing $[CaO_2]_\infty$ single fluorite layers by $[Ln_2O_4]_\infty$ double fluorite layers. Thermal treatment at 823–873 K of Bi oxides under an oxygen pressure of 80 bars allowed superconducting properties to be obtained with T_c (onset) around 25 K.

The oxides $Pb_2Sr_2LnCeCu_3O_{10+\delta}$ with Ln = Pr, Nd, Sm, La are orthorhombic ($a \approx b \approx a_p\sqrt{2} \approx 5.4$ Å, $c \approx 36.9$ Å). They represent the most complex intergrowth in this family. Their structure (fig. 31a) consists of double pyramidal copper layers, $[LnCeO_4]_\infty$

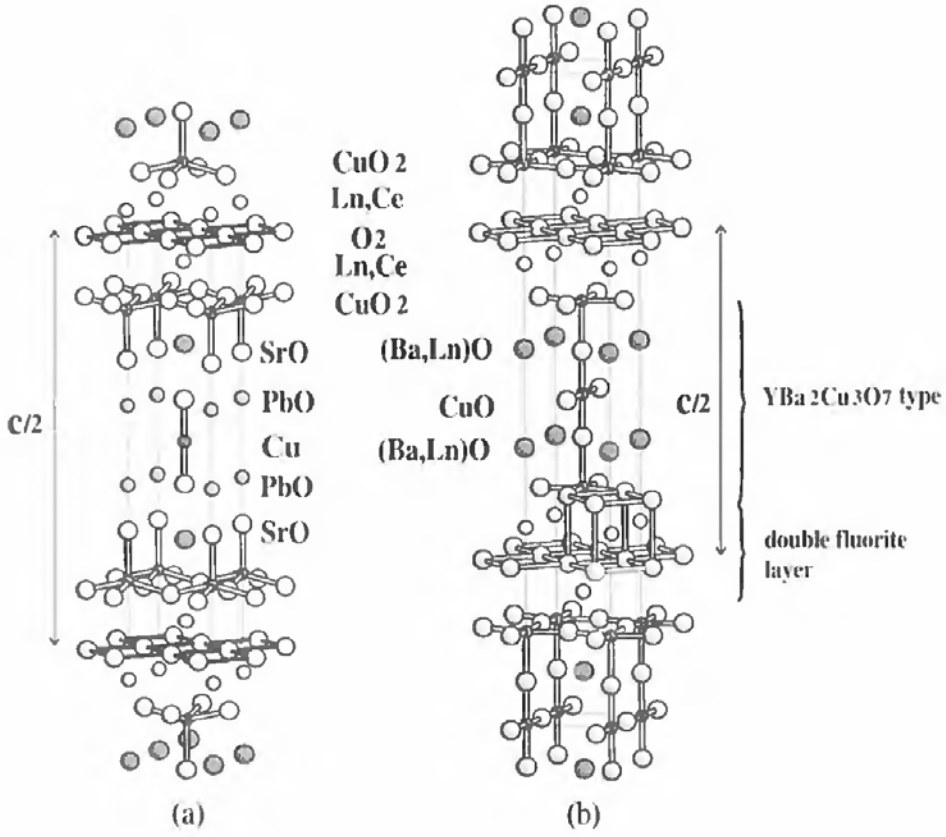

Fig. 31. (a) Crystal structure of the oxides $Pb_2A_2LnCeCu_3O_{10+\delta}$ (A = Sr, Ba; Ln = Pr, Nd, Sm, La); (b) Crystal structure of the oxides $(Ln_{1-x}Ce_x)_2(Ba_{1-y}Ln_y)_2Cu_3O_{10-\delta}$.

double fluorite-type layers, single layers of CuO_2 sticks, and single rock-salt-type layers $[(Pb,Sr)O]_\infty$. In fact these oxides are derived from the $Pb_2Sr_2Ca_{0.5}Y_{0.5}Cu_3O_8$ structure with the single $[Ca_{0.5}Y_{0.5}O_2]_\infty$ fluorite layers replaced by double fluorite-type layers $[LnCaO_4]_\infty$. Thus, they can also be described as an intergrowth of the $(Nd,Sr)_2(Nd,Ce)_2Cu_2O_8$-type structure (fig. 29b) with the oxygen-deficient K_2NiF_4-type structure $A_2CuO_2\square_2$. The disproportionation of copper, leading to the mixed valency Cu(II)–Cu(III) in the pyramidal layers while monovalent copper forms the CuO_2 sticks, appears as most likely. In spite of that, no superconductivity has been detected in this oxide until now.

The oxides $(Ln_{1-x}Ce_x)_2(Ba_{1-y}Ln_y)_2Cu_3O_{10-\delta}$ do not exhibit any rock-salt layers. These tetragonal oxides ($a \approx 3.9$ Å, $c \approx 28.6$ Å) can be described as an intergrowth of oxygen-deficient triple perovskite copper layers with double fluorite-type layers. In fact the idealized structure $(Ln_{1-x}Ce_x)_2(Ba_{1-y}Ln_y)_2Cu_3O_9$ (fig. 31b) corresponds to the replacement of the $[YO_2]_\infty$ single fluorite by $[Ln_{2-2x}Ce_{2x}O_4]_\infty$ double fluorite-type layers in the "123"-type $Ba_2YCu_3O_7$ structure. The synthesis of these oxides under high oxygen pressures of several hundred bars allows critical temperatures ranging from 36 to 43 K to be reached.

7. Copper oxycarbonates containing a rare earth

Very few copper oxycarbonates with a layer structure containing a rare earth are actually known. Only the $(Y,Ca)_n(Ba,Sr)_{2n}Cu_{3n-1}O_{7n-3}$ compounds have been synthesized to date (Miyazaki et al. 1992, Akimitsu et al. 1992, Domengès et al. 1993, Hervieu et al. 1993b). The structures of these oxides (fig. 32) derive from that of the "123" cuprate by replacing the rows of CuO_4 square planar groups by CO_3 groups in an ordered way. The superconducting oxycarbonates $(Y_{1-x}Ca_x)_{0.95}Sr_{2.05}Cu_{2.4}(CO_3)_{0.6}O_y$ (Akimitsu et al. 1992) and $YCaBa_4Cu_5(NO_3)_{0.3}(CO_3)_{0.7}O_{11}$ (Hervieu et al. 1993b) represent the members $n=2$ of this series (fig. 32a): in this structure one row of carbonate groups alternates with one row of CuO_5 pyramids. The $n=4$ member is obtained for $Y_4Sr_8Cu_{11}CO_3O_{25}$ (Domengès et al. 1993) whose structure (fig. 32b) derives from the "123" one by replacing one row of CuO_4 groups out of four by one row of carbonate groups.

Such oxycarbonates do not seem to be good candidates for superconductivity, contrary to thallium or mercury oxycarbonates (Raveau et al. 1995b). For instance, the $n>2$ members are still superconductors with T_c ranging from 66 to 82 K, but their resistive transition is broad, and the $n=4$ member is not superconducting.

It is finally important to emphasize that electron microscopy studies have shown that $YBa_2Cu_3O_7$ can be partially carbonated during the synthesis, depending on the experimental conditions and on the nature of the precursors. As a result, the existence of oxycarbonate domains coherently intergrown in the "123" matrix has been revealed for incorrectly synthesized "123" samples. The decrease of T_c (smaller than 92 K) obtained for the latter is easily explained by the presence of such oxycarbonate domains.

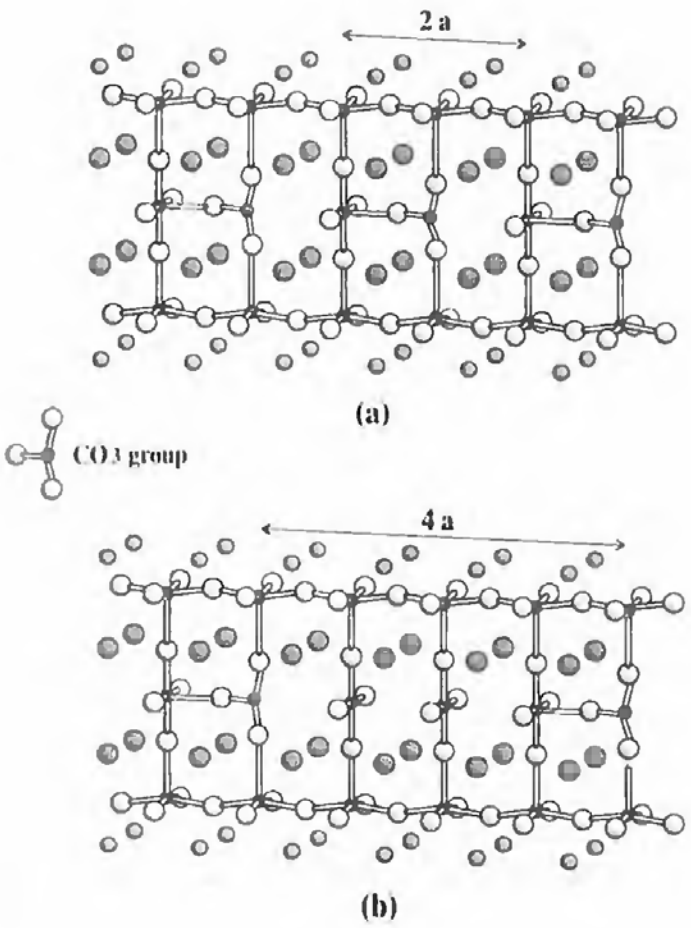

Fig. 32. Structural model for the members (a) $n=2$ and (b) $n=4$ of the series $(Y,Ca)_n(Ba,Sr)_{2n}Cu_{3n-1}O_{7n-3}$.

References

Akimitsu, J., S. Suzuki, M. Watanabe and H. Sawa, 1988, Jpn. J. Appl. Phys. **27**, L1859.

Akimitsu, J., M. Uehara, M. Ogawa, H. Nakata, K. Tomimoto, Y. Miyazaki, H. Yamane, T. Hirai, K. Kinoshita and Y. Matsui, 1992, Physica C **201**, 320.

Alario Franco, M., C. Chaillout, J.J. Capponi and J. Chenavas, 1988, Mater. Res. Bull. **22**, 1685.

Baudelet, F., G. Collin, E. Dartyge, A. Fontaine, J.P. Kappler, G. Krill, J.P. Itie, J. Legoudez, M. Maurer, Ph. Monod, A. Revcolevski, H. Tolentino, G. Tourillon and M. Verdaguer, 1988, Z. Phys. B **69**, 141.

Bednorz, J.G., and K.A. Müller, 1986, Z. Phys. B **64**, 189.

Beille, J., R. Cabanel, B. Chevalier, C. Chaillout, G. Demazeau, F. Deslandes, J. Etourneau, P. Lejay, C. Michel, J. Provost, A. Sulpice, J.L. Tholence and R. Tournier, 1987, C.R. Acad. Sci. **304**(II), 10967.

Beno, M.A., L. Soderholm, D.W. Capone, D. Hinks, J.D. Jorgensen, I.K. Schuller, C.U. Segre, K. Zhang and J.D. Grace, 1987, Appl. Phys. Lett. **51**, 57.

Bordet, P., J.J. Capponi, C. Chaillout, J.L. Hodeau and M. Marezio, 1988a, in: Progress in High Temperature Superconductivity, Vol. 7, ed. C.N.R. Rao (World Scientific, Singapore) p. 76.

Bordet, P., C. Chaillout, J. Chenevas, J.L. Hodeau, . Marezio M, J. Karpinski and E. Kaldis, 1988b, Nature **334**, 596.

Bourgault, B., C. Martin, C. Michel, M. Hervieu, J. Provost and B. Raveau, 1989, J. Solid State Chem. **78**, 326.

Caignaert, V., M. Hervieu, J. Wang, G. Desgardin, B. Raveau, F. Boterel and J.M. Haussonne, 1990, Physica C **170**, 139.

Capponi, J.J., C. Chaillout, A.W. Hewat, P. Lejay, M. Marezio, N. Nguyen, B. Raveau, J.L. Soubeyroux, J.L. Tholence and R. Tournier, 1987, Europhys. Lett. **12**, 1301.

Cava, R.J., B. Battlog, R.B. Vandover, D.N. Murphy, S. Sunshine, T. Siegrist, J.P. Remeika, E.A. Rietman, S. Zahurak and G.P. Espinosa, 1987, Phys. Rev. Lett. **58**, 1676.

Cava, R.J., B. Battlog, J.J. Krajewski, L.W. Rupp, L.F. Schneemeyer, T. Siegrist, R.B. Vandover, P. Marsh and P. Trevor, 1988, Nature **336**, 211.

Cava, R.J., B. Battlog, R.B. Vandover, J.J. Krajewski, J.W. Waszczak, R.M. Fleming, W.F. Peck, L.W. Rupp, P. Marsh, A.C. James and L.F. Schneemeyer, 1990, Nature **345**, 602.

Chaillout, C., P. Bordet, J. Chenevas, J.L. Hodeau and M. Marezio, 1989, Solid State Commun. **70**, 275.

Domengès, B., M. Hervieu, C. Michel and B. Raveau, 1987, Europhys. Lett. **4**, 211.

Domengès, B., M. Hervieu, V. Caignaert, B. Raveau, J.L. Tholence and R. Tournier, 1988, J. Microsc. Spectrosc. Electron. **13**, 75.

Domengès, B., M. Hervieu and B. Raveau, 1993, Physica C **207**, 65.

Friedel, J., 1988, J. Phys. France **48**, 1787.

Fujiita, T., Y. Aoki, Y. Maeno, J. Sakurai, H. Fukuba and H. Fujii, 1987, Jpn. J. Appl. Phys. **26**, L368.

Ganguli, A.K., R. Nagarajan, K.S. Nanjun and C.N.R. Rao, 1989, Mater. Res. Bull. **24**, 103.

Goutenoire, F., P. Daniel, M. Hervieu, G. Van Tendeloo, C. Michel, A. Maignan and B. Raveau, 1993, Physica C **216**, 243.

Grenier, J.C., A. Wattiaux, J.P. Doumerc, L. Fournès, J.P. Chaminade, P. Dordor and M. Pouchard, 1992, J. Solid State Chem. **96**, 20.

Hervieu, M., D. Domengès, C. Michel and B. Raveau, 1987, Europhys. Lett. **4**, 205.

Hervieu, M., B. Domengès, B. Raveau, M. Post, M.W. McKinnon and J.M. Tarascon, 1989, Mater. Lett. **8**, 73.

Hervieu, M., G. Van Tendeloo, A. Maignan, C. Michel, F. Goutenoire and B. Raveau, 1993a, Physica C **216**, 264.

Hervieu, M., C. Michel and B. Raveau, 1993b, Chem. Mater. **5**, 1126.

Huvé, M., C. Martin, G. Van Tendeloo, A. Maignan, C. Michel, M. Hervieu and B. Raveau, 1994, Solid State Commun. **90**, 37.

Huvé, M., C. Martin, A. Maignan, C. Michel, G. Van Tendeloo, M. Hervieu and B. Raveau, 1995, J. Solid State Chem. **114**, 230.

Izumi, F., H. Azano, T. Ishigaki, E. Takayama, Y. Uchida, N. Watanabe and T. Nishikawa, 1987a, Jpn. J. Appl. Phys. **26**, 649.

Izumi, F., H. Azano, T. Ishigaki, E. Takayama, Y. Uchida and N. Watanabe, 1987b, Jpn. J. Appl. Phys. **26**, 1214.

Jorgensen, J.D., M. Beno, D.G. Hinks, L. Soderholm, K.J. Volkin, R.L. Hitterman, J.D. Grace, I.K. Schuller, C.U. Segre, K. Zhang and M.S. Kleefisch, 1987, Phys. Rev. B **36**, 3608.

Jorgensen, J.D., B. Dabrowski, S. Pei, D.G. Hinks, L. Soderholm, B. Morosin, J.E. Schirber, E.L. Venturini and D.S. Ginley, 1988, Phys. Rev. **38**, 11337.

Koyama, S., U. Endo and T. Kawai, 1988, Jpn J. Appl. Phys. **27**, L1861.

Krekels, T., T.S. Shi, J. Reyes-Casga, G. Van Tendeloo, J. Van Landuyt and S. Amelinckx, 1990, Physica C **167**, 677.

Labbé, J., and J. Bok, 1988, Europhys. Lett. **3**, 1225.

Lengeler, M., M. Wilhelm, B. Jobst, W. Schwaen, B. Seebacher and U. Hillebrecht, 1988, Physica C **153–155**, 143.

Lepage, Y., W.R. McKinnon, J.M. Tarascon, L.H. Greene, G.N. Hull and D.M. Hwang, 1987, Phys. Rev. B **35**, 7245.

Martin, C., D. Bourgault, C. Michel, M. Hervieu and B. Raveau, 1989, Mod. Phys. Lett. **3**, 93.

Martin, C., M. Hervieu, G. Van Tendeloo, F. Goutenoire, C. Michel, A. Maignan and B. Raveau, 1995, Solid State Commun. **93**, 53; J. Solid State Chem. **114**, 230.

Mattheiss, L.F., 1987, Phys. Rev. Lett. **58**, 1028.

Maurer, M., M.F. Ravet, J.C. Ousset, T. Gourieux, A. Fontaine, H. Tolentino, E. Dartyge, G. Tourillon, G. Kril and P.H. Kess, 1988, Physica C **153–155**, 145.

Michel, C., and B. Raveau, 1984, Rev. Chim. Miner. **21**, 407.

Michel, C., L. Er-rakho and B. Raveau, 1985, Mater. Res. Bull. **20**, 667.

Michel, C., F. Deslandes, J. Provost, P. Lejay, R. Tournier, M. Hervieu and B. Raveau, 1987, C.R. Acad. Sci. **304**(II), 1050.

Miyazaki, Y., H. Yamane, N. Ohnishi, T. Kajitani, K. Hiraga, Y. Morii, S. Funahashi and T. Hirai, 1992, Physica C **198**, 7.

Monod, Ph., M. Ribaud, F. d'Yvoire, J. Jegoudez, G. Collin and A. Revcolevscki, 1987, J. Phys. France **48**, 1369.

Müller-Buschbaum, H.K., and W. Wollschlager, 1975, Z. Anorg. Allg. Chem. **414**, 76.

Müller-Buschbaum, H.K., and W. Wollschlager, 1977, Z. Anorg. Allg. Chem. **428**, 120.

Nakajima, S., M. Kikuchi, N. Kobayashi, H. Iwasaki, D. Shindo, Y. Syono and Y. Muto, 1989, in: Advances in Superconductivity II, eds T. Ishiguro and K. Kajimura (Springer, Berlin) p. 219.

Nguyen, N., L. Er-rakho, C. Michel, J. Choisnet and B. Raveau, 1980, Mater. Res. Bull. **15**, 891.

Oyanagi, H., H. Ihara, T. Matsubara, M. Tokumoto, T. Matsushita, M. Hirabayashi, K. Murato, N. Terada, T. Yao, H. Iwasaki and Y. Kimura, 1987, Jpn. J. Appl. Phys. **26**, L1561.

Radaelli, P.G., M. Perroux, M. Marezio, S. de Brion and J.L. Tholence, 1994, Science **265**, 380.

Raveau, B., C. Michel, M. Hervieu and J. Provost, 1988, Physica C **153–155**, 5.

Raveau, B., C. Michel, M. Hervieu and D. Groult, 1991, Crystal Chemistry of High T_c Superconducting Oxides (Springer, New York) 301 pp.

Raveau, B., C. Michel, M. Hervieu and A. Maignan, 1995a, J. Mater. Chem. **5**, 803.

Raveau, B., C. Michel, B. Mercey and J.F. Hamet, 1995b, J. Alloys & Compounds **229**, 134.

Retoux, R., C. Michel, M. Hervieu and B. Raveau, 1989, Mod. Phys. Lett. B **3**, 591.

Reyes-Casga, J., T. Krekels, G. Van Tendeloo, J. Van Landuyt, W.H. Bruggink, H. Vermeij and S. Amelinckx, 1989, Solid State Commun. **70**, 269.

Roth, G., B. Renker, G. Heger, M. Hervieu, B. Domengès and B. Raveau, 1987, Z. Phys. B **69**, 53.

Rouillon, T., J. Provost, M. Hervieu, C. Michel and B. Raveau, 1989, Physica C **159**, 201.

Rouillon, T., J. Provost, M. Hervieu, C. Michel and B. Raveau, 1990, J. Solid State Chem. **84**, 375; Physica C **171**, 7.

Santoro, A., S. Miraglia, F. Beech, S.A. Sunshine, D.W. Murphy, L.F. Schneemayer and J.Y. Waszczak, 1987, Mater. Res. Bull. **22**, 1007.

Sawa, H., S. Suzuki, M. Watanabe, J. Akimitsu, H. Matsubara, H. Watabe, S. Uchida, K. Koshuho, H. Asano, I. Izumi and E. Takayama-Muromachi, 1989, Nature **337**, 347.

Tarascon, J.M., L.H. Greene, B.G. Bagley, W.R. McKinnon, P. Barboux and G.W. Hull, 1987, in: Novel Superconductivity, eds A. Wolf and V. Kresin (Plenum Press, New York) p. 705.

Tokiwa, A., M. Nagoshi, T. Oku, N. Kobayashi, M. Kikuchi, K. Hiraga and H. Syono, 1990, Physica C **168**, 285.

Veal, B.W., A.P. Paulikas, J.W. Downey, H. Claus, K. Van der Woort, G. Toulins, H. Shi, M. Jenen and L. Morss, 1989, Physica C **162–164**, 97.

Wu, M.K., J.R. Ashburn, C.J. Torng, P.H. Hor, R.L. Meng, L. Gao, Z.J. Huang, Y.Z. Wang and C.W. Chu, 1987, Phys. Rev. Lett. **58**, 908.

Zandbergen, H.W., W.T. Fu, J.M. Van Ruitebeek, L.J. de Jongh, G. Van Tendeloo and S. Amelinckx, 1989, Physica C **159**, 81.

Handbook on the Physics and Chemistry of Rare Earths
Vol. 30
edited by K.A. Gschneidner, Jr., L. Eyring and M.B. Maple

Chapter 189

SINGLE-CRYSTAL GROWTH FOR SCIENCE AND TECHNOLOGY

Yuh SHIOHARA and Eugene A. GOODILIN*
Div. IV, Superconductivity Research Laboratory (SRL),
International Superconductivity Technology Center (ISTEC),
1-10-13 Shinonome, Koto-Ku, Tokyo, 135, Japan Fax: 81-3-3536-5714;
Phone: 81-3-3536-5711; E-mail: shiohara@istec.or.jp

Contents

1. Introduction 69
1.1. Common problems of single-crystal growth of high-temperature superconductors 69
1.2. Motivations of single-crystal production at present 71
2. Fundamental principles of crystal growth 72
2.1. Crystal growth phenomenon 72
2.2. Supersaturation as driving force 73
2.2.1. Metastable states and common theories of nucleation 73
2.2.2. Constitutional supercooling and the stability of a planar crystallization front 76
2.3. Rate-limiting factors and interface kinetics 77
2.3.1. Formation of a facetted shape 77
2.3.2. Two-dimensional nucleation and spiral growth 83
2.3.3. Terrace–ledge–kink (TLK) model 85
2.3.4. Real crystal morphology 85
2.3.5. Striations 88
3. Mechanism of R123 crystal growth from the melt 89
3.1. Phase diagrams related to crystal growth 89
3.1.1. Y–Ba–Cu–O system 89
3.1.2. Phase diagrams with light rare-earth elements ($NdO_{1.5}$–BaO–CuO_x) 92
3.1.2.1. Solubility of rare-earth elements in barium–copper oxide fluxes 94
3.1.2.2. "$Nd_4Ba_2Cu_2O_{10}$–($3BaCuO_2 + 2CuO$)" section 100
3.1.2.3. "$BaCuO_2$–($Nd_2CuO_4 + CuO$)" section and $Nd_{1+x}Ba_{2-x}Cu_3O_z$ solid-solution field 101
3.1.2.4. Three-dimensional model of Nd–Ba–Cu–O phase diagram (copper-rich corner) 105
3.1.2.5. Oxygen nonstoichiometry and stability of $Nd_{1+x}Ba_{2-x}Cu_3O_z$ at different p_{O_2} 108
3.1.3. Phase diagrams of other rare-earth elements (Pr, Yb) 112

* Permanent address: Inorganic Chemistry Division, Faculty of Chemistry, Moscow State University, Vorobyovi Gori, 119899, Moscow, Russia; goodilin@inorg.chem.msu.ru.

3.2. Crystallization from melt 114
3.2.1. Primary crystallization field and influence of additives 114
3.2.2. Quantitative compositional relationships between equilibrium solid and liquid 116
3.2.3. XANES examination of molten state 119
3.3. Mass transport phenomena 121
3.3.1. Basic model of solute diffusion in Y123 crystal pulling experiments 121
3.3.2. $R_{1+x}Ba_{2-x}Cu_3O_z$ solid-solution growth: diffusion of ions in liquid and tie-line selection 124
3.3.3. Hydrodynamics and computer simulation of crystal growth 125
3.4. Growth mechanism and interfacial phenomena 131
3.4.1. Spiral growth pattern and influence of growth conditions 131
3.4.2. Growth rate anisotropy and shape controllability 133
3.4.2.1. Experimental estimation of growth rate anisotropy 133
3.4.2.2. Experimental controllability of crystal shapes in the pulling method 136
3.4.3. Alternative growth mechanisms (twin-plane-re-entrant-edge growth) 138
4. Common crystal-growth techniques for high-temperature superconductors 139
4.1. Classification 139
4.2. Techniques in practice 139
4.2.1. Semisolid melt solidification 139
4.2.2. Flux and self-flux growth 143
4.2.3. TSFZ method 144
4.2.4. Liquid phase epitaxy 144
4.2.5. Solute-rich liquid crystal pulling (SRL–CP) method 145
4.2.6. TSSG method 146
5. Progress in R123 single-crystal growth 146
5.1. Flux-grown crystals, morphology and growth problems 146
5.2. Whisker-like crystals 153
5.3. TSFZ crystals 153
5.4. Liquid phase epitaxy 156
5.4.1. Practical importance of LPE 156
5.4.2. Demands and restrictions for substrate materials. R123 single crystals as substrates 157
5.4.3. Initial steps of bulk single-crystal growth and preparation of LPE crystal layers 161
5.5. Crystal pulling method 164
5.5.1. Y123 crystals grown by automatic crystal pulling in high p_{O_2} atmosphere 164
5.5.2. $Nd_{1-x}Ba_{2-x}Cu_3O_z$ crystals grown by modified TSSG method with liquid composition control 165
5.5.3. Other R123 crystals 166
5.6. Single-crystal growth of other superconductors 168
6. Characterization of R123 single crystals 170
6.1. Classification of defects 170
6.2. Variety of shapes, sizes and morphology. Optical microscopy and etch figures 171
6.3. Twins and tweed pattern due to strains in the orthorhombic phase. Hot-stage microscopy 174
6.4. Low-angle misoriented grains. Laue XRD, rocking curves, pole figures, XRD topography 177
6.5. Microcracks and dislocations. XRD line-broadening analysis 181
6.6. Spirals and growth steps. AFM 182
6.7. Chemical macro-uniformity, flux and foreign particle inclusions. EPMA and ICP AES 183
6.8. Nanoscale composition fluctuations. TEM and micro-EDX 187
6.9. Stacking faults and intergrowth. TEM, STM 190
6.10. Crystal structure. Four-circle diffractometer, neutron diffraction, Raman spectroscopy 190
6.11. Superstructure. HREM, SAED 192
6.12. Anisotropic physical properties. Resistivity, magnetization, T_c, J_c, vortex lattice visualization 193
7. Practical ways of crystal perfection, yield and size improvement 196
7.1. Crucible wetting and melt contamination control 196
7.2. Crystallinity enhancement 196

7.2.1. Floating particles and seed crystal rotation control 196
7.2.2. Application of seeds with high crystallinity 197
7.2.3. Cooling process 197
7.3. Crystal size enlargement 198
7.3.1. Expanding the pulling period 198
7.3.2. Increased growth rate 198
7.4. Improvement of superconducting characteristics 199
7.4.1. Crystallization in low-p_{O_2} atmosphere 199
7.4.2. Liquid composition control 200
7.4.3. Oxygenation procedure 200
7.4.3.1. Anisotropic oxygen diffusion in single crystals 201
7.4.3.2. Optimal oxygen content for higher T_c 203
7.4.3.3. High-oxygen-pressure treatment 204
7.4.3.4. Oxygen and cation nonstoichiometry with respect to pinning properties 204
7.4.3.5. Detwinning by mechanical stress 208
8. Advantages, problems and prospects: motivations of single-crystal production in the future 209
9. Notes added in Proof 212
Acknowledgments 214
References 215

1. Introduction

1.1. *Common problems of single-crystal growth of high-temperature superconductors*

High-temperature superconductive cuprate materials have played an extraordinary role since their discovery by Bednorz and Müller in 1986. This discovery initiated throughout the world an extremely fast progress and intensive investigations of this class of complex oxide materials (Larbalestier 1991, Agarwal and Narlikar 1994, Batlogg et al. 1997, Shiohara and Endo 1997). The process of searching for new HTSCs led to an exciting improvement of the superconducting transition temperature (T_c) from 35 K for the Bednorz–Müller $La_{2-x}Sr_xCuO_4$ composition to temperatures above the 77 K boiling point of liquid nitrogen: 92–96 K for $RBa_2Cu_3O_{7-\delta}$ systems, 110 K for $Bi_2Sr_2Ca_2Cu_3O_y$, 125 K for the Tl–Ba–Ca–Cu–O family and, recently, 135–165 K for the mercury-based superconductors (Chen 1998, Cava 2000; see also ch. 188 of this Handbook). The HTSC materials not only stimulated thousands of researchers worldwide, but also opened up the possibility of commercial applications of HTSC in numerous fields (Batlogg et al. 1997), since liquid (and solid) nitrogen can be used as a coolant, which is much less expensive, easier to handle, and has a higher heat capacity than liquid helium.

The initial quick and easy synthesis of superconducting substances by the ceramic "beat-and-heat" technology, first visually perfect small crystals etc., have mistakenly led many researchers to believe that most of the problems with HTSCs materials preparation are over (Tretyakov and Goodilin 2000). In reality, at present it is understood that the unprecedented difficulties in the growth of high-quality single crystals to be described in sect. 2, as well as in other material production technologies, stem from the chemical and structural complexity and the resulting thermal and chemical instability of modern classes of HTSCs (Scheel 1993). From a phase-diagram point of view almost all HTSCs

are multicomponent and incongruently melting phases, creating numerous difficulties for crystal growth. As an example, the mercury-based superconductors combine the highest known T_c (achieved recently in the worldwide competition for superconducting transition temperatures) with extraordinarily low thermal stability and tremendous toxicity. A crystal of this compound can be produced under special conditions only (sect. 5.6).

The $RBa_2Cu_3O_{7-\delta}$ (R123) phases are the most widely studied and the most famous class of high-temperature superconductors among the many HTSC materials. Their basic investigation as well as present and future applications demand further improvement of single-crystal quality and size enlargement accompanied by optimization of growth techniques. Being complex cuprates, as are most other HTSCs, the R123 phases combine such chemically different components as oxygen-stoichiometric and difficult-to-melt rare-earth and alkaline-earth basic oxides together with a low-melting, "acid", transition-metal oxide, CuO, which may form Cu_2O or "Cu_2O_3" with significantly different oxygen contents and copper valences. As a consequence, it has been difficult to grow large single crystals of R123 continuously because of the unique properties of these systems (sect. 3).

$YBa_2Cu_3O_{7-\delta}$-type materials have a distorted and oxygen-deficient perovskite structure, where $\delta = 0$–1 (Agarwal and Narlikar 1994, F. Izumi and Takayama-Muromachi 1995, Skakle 1998, Cava 2000). As a result, the problem of oxygen nonstoichiometry naturally occurs, as mentioned above. It immediately introduces an additional "fluent" component (oxygen) to be taken into consideration upon crystal growth, and the commonly used quasiternary isothermal phase diagrams $RO_{1.5}$–BaO–CuO become actually four-component and p_{O_2}-dependent ($RO_{1.5}$–BaO–CuO_x–O_2) with intricate "p_{O_2}-T-composition" relations (sect. 3.1, see also ch. 190 of this Handbook). Additionally, in the R123 superconductors T_c is thought to be significantly dependent on carrier concentration; it changes drastically and nonmonotonically with δ (Shiohara and Endo 1997). Therefore, crystal growth itself (sects. 4, 5) cannot guarantee the highest T_c, and low-temperature treatment is needed, which adds additional post-annealing effects (sects. 6, 7). Large single crystals require a longer time for oxygenation although thin films, powders and porous ceramic samples are considered to be readily equilibrated with oxygen.

In principle, Y can be substituted with R without any destructive effects on the superconducting characteristics of Y123 except for Ce, Pr and Pm (Tarascon et al. 1987, Radousky 1992) which may have the specific f-electronic layer configuration. However, a set of problems, partially coupled with the difficulties mentioned already, and an additional degree of freedom are introduced since the rare-earth elements have entered into the structure. The larger size of light rare-earth elements (La, Pr, Nd, Sm, Eu, Gd) permits the trivalent R ions to be placed into the divalent Ba site simultaneously with occupation of the Y position (ch. 188 of this Handbook). It means that these elements form the $R_{1+x}Ba_{2-x}Cu_3O_z$ solid solution which is supposed to be in equilibrium with a liquid of a certain composition at a given temperature and p_{O_2} (sect. 3.2.2). This complicates the overall picture of phase relations and the optimization of chemically and structurally uniform high-T_c single-crystal production (sect. 7) as in the Bi–Sr–Ca–Cu–O system, where no stoichiometric compounds are found among the superconductors

(reviewed by F. Izumi and Takayama-Muromachi 1995). Thus, in general, the main optimistic goal of growth techniques for R123 compounds consists in the preparation of large, structurally perfect bulk single crystals of the oxygen- and cation-nonstoichiometric solid solution with a certain distribution of constituents on both macro- and micro-scale levels.

1.2. *Motivations of single-crystal production at present*

The best way to determine correctly any kind of physical, chemical and structural properties of a crystalline phase is using a single crystal. Without single crystals no basic understanding of the fundamental physical properties and the high-temperature superconductivity phenomenon itself could be achieved. Most of the advantages of a single crystal originate from its perfection, homogeneity and the possibility to study anisotropic characteristics by simple manipulations with a crystal of a reasonable size. This was, is and will be an essential and sufficient reason for producing single crystals of HTSCs, in spite of the numerous scientific and technological problems to be solved.

In principle, there are three categories of HTSC applications: (1) high-J_c wire and tape materials for transportation of large electric currents without power loss and for the generation of high magnetic fields, (2) bulk materials with strong magnetic flux pinning for levitation and shielding, and (3) thin films for superconducting devices with quantum phenomena (i.e. Josephson tunneling effect).

For the first and second categories (Batlogg et al. 1997, Shiohara and Endo 1997), large critical current densities (10^4 to 10^6 A/cm^2) as well as high superconducting transition temperatures T_c are required in the operating magnetic field. High-J_c applications require a perfect matrix of bulk superconductors (Goyal et al. 1997, MacManus-Driscoll 1998) with homogeneously dispersed defects or inclusions acting as magnetic flux pinning sites. This is similar to the preparation of large silicon crystals of very high perfection with a controlled amount of uniformly distributed dopants.

The third type of applications (Scheel 1994, MacManus-Driscoll 1998, Saba et al. 2000) demands thin films with an atomically flat surface and sharp interface for electronic devices. However, improvement of HTSC film quality seems to be rather difficult because the films may interact with substrates or, at best, grow heteroepitaxially on a substrate with a large misfit and a different thermal expansion coefficient (sect. 5.4). Therefore, large HTSC single crystals with high perfection are expected to be employed (sect. 5.4). At present, such a bulk crystal can be produced by melt growth only. To control the as-grown surfaces, it is important to understand the mechanism that forms the surface because its shape is an overall result of the growth process and contains much information to assist comprehension of the growth phenomena (sects. 2, 3.3, 3.4). The necessity to extend the solidification theory (sects. 2, 3) for multicomponent oxide systems may attract researchers into the field of HTSC materials. At the same time, clarifying the growth mechanism of R123 could also assist in understanding crystal growth of other oxide materials.

The $RBa_2Cu_3O_{7-\delta}$ phases seem to attract physicists because in the case of R-elements with large magnetic moments, superconductivity of R123 might be in conflict with conventional BCS theory (Batlogg et al. 1997, Radousky 1992, Hilscher et al. 1994, Mesot and Furrer 1997). Moreover, some R123 (see, e.g., Skakle 1998, Shiohara and Endo 1997) demonstrated unexpectedly high T_c like 96 K for Nd123, which is combined with better chemical and thermal stability in comparison with Y123. Excellent J_c properties in high magnetic fields (5–10 T) are observed in Sm123 and Nd123 systems (Murakami et al. 1996, Pradhan et al. 1998a, Koblischka et al. 1998). On the other hand the crystal pulling process brought great success in the production of centimeter-sized single crystals of the Nd123 phase (Shiohara and Endo 1997, Yao and Shiohara 1997, 1998). Hence, Nd123 single crystals are quite promising for the investigation of fundamental superconducting properties as well as for future applications of oxide superconductors. One may even predict progress that would be achieved by the replacement of Y123 by Nd123 as happened to Ge single crystals in the Si epoch. These results accelerate investigations on the R123 family such as the pinning mechanism due to R/Ba substitution, substitution itself, and the solidification mechanism following ternary phase diagrams (sect. 3.3.2) etc.

Growth of small crystals, mostly by the self-flux method or zone melting, is extensively reviewed in the literature (see, e.g., Demyanets 1991, Assmus and Schmidbauer 1993, Scheel 1994, Wolf 1996, Gornert 1997, MacManus-Driscoll 1997, Revcolevschi and Jegoudez 1997, Chen 1998, Karpinski et al. 1999). At the same time, practical aspects of large crystal growth by the advanced pulling method have not yet been discussed widely (Shiohara and Endo 1997, Yao and Shiohara 1997). Thus, crystal-production-related high-temperature phase diagrams, progress in growth, investigation of properties, quality improvement and practical applications of bulk single crystals of high-temperature superconductors will be overviewed in this chapter. As the most important examples, advances in processing, understanding growth mechanisms, and promising new developments are discussed for $RBa_2Cu_3O_{7-\delta}$ superconductors.

2. Fundamental principles of crystal growth

2.1. *Crystal growth phenomenon*

From common knowledge, the "ideal single crystal" is a homogeneous portion of crystalline matter, whether bounded by faces or not, and this crystalline matter possesses a triperiodic structure on the atomic scale (Weast et al. 1987). It is characterized by discontinuous vectorial properties that create "crystal planes" ("faces" in crystal growth, cleavage planes in cohesion, twin planes in twinning, "reflecting" planes in X-ray and neutron diffraction etc.). Thus, a single crystal is a three-dimensional macroscopical manifestation of a crystalline phase, and the best presentation of its bulk properties because imperfections such as surface introduce only a negligible contribution.

In principle, single crystals as a highly ordered condensed state of matter can be grown by the assemblage of their constituents from any other surrounding phase containing the constituents in a "disordered" form: solution, melt, vapor, or even another solid phase, although the latter is not an effective way to obtain a crystal (see, however, Wan et al. 1988). All these types of growth have been examined for HTSC materials. At the same time, in this chapter we will emphasize growth from the melt and from high-temperature solution. Thin film deposition from vapor is discussed elsewhere (Becht 1996, Goyal et al. 1996, 1997, MacManus-Driscoll 1998, Tretyakov and Goodilin 2000).

Classical thermodynamics is concerned with equilibrium states of systems while in crystal growth non-equilibrium conditions have to be assumed. At the same time, thermodynamic descriptions of steady-state and transient processes can be accurate enough as long as these processes are slow in comparison with the kinetics of the atoms and concentration gradients are not too steep. Consequently, crystallization as a first-order phase transformation must be characterized generally in terms of the free-energy difference between solid and liquid phases as a driving force for the process. In fig. 1 (overleaf), (C_i, T_i) corresponds to points on the liquid free-energy curve G_L near the interface of solid and liquid phases. In this case C_1 and C_2 represent equilibrium liquidus and solidus concentrations for the interface temperature T_i. When a departure from the equilibrium state exists, C_i will deviate from C_1, and the solid concentration C_S will leave the C_2 point. Using the well-known parallel tangent construction, it is possible to see that C_S yields an interface driving force ΔG_i.

In a real case, the situation is much more complicated (Tiller 1991a,b). Macroscopically, there are two different uniform phases separated by a thin interface region. Processes at this moving interface transform chemical constituents from one (mother or nutrient) phase into the other (crystalline) phase. Additionally, the growth of a crystal from this surrounding melt can be classified into two distinguishable cases connected with directions of heat transfer: the case in which the crystal temperature is lower than that of the melt from which it is growing is called constrained growth, while the case of the crystal having the higher temperature is known as unconstrained free growth. Thus, crystal growth deals with serious studies of phase equilibria and thermodynamics (sects. 3.1, 3.2), nucleation phenomena (sects. 2.2, 2.3), solute partitioning (sect. 3.2.2), hydrodynamics and fluid motion, heat and mass transfer (sect. 3.3), interface attachment kinetics (sect. 3.4), and interface morphology and defect generation (sect. 6). Such a highly complex task has to adhere to different areas of human knowledge, and sometimes its practical solutions can be perceived as an art.

2.2. *Supersaturation as driving force*

2.2.1. *Metastable states and common theories of nucleation*

Without the existence of a driving force (i.e. a supersaturated or undercooled or, in general, metastable, nutrient phase) it is hard to hypothesize crystal growth. One concept of metastability, intuitively acceptable to most people, is based on the consideration of the kinetics when a system in its equilibrium state is brought out of equilibrium by a sudden

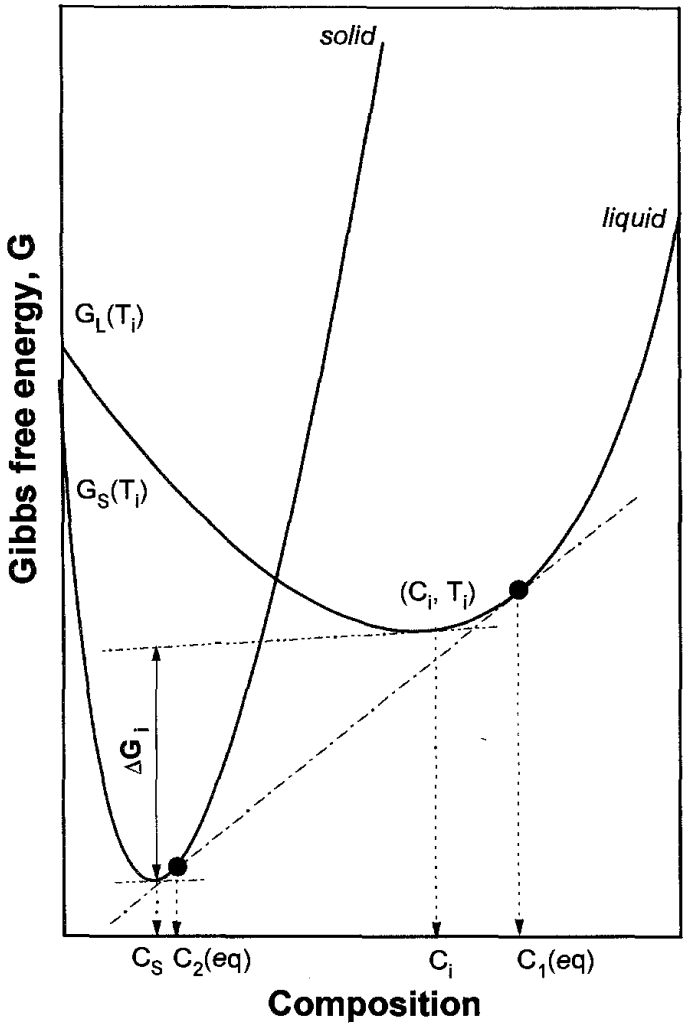

Fig. 1. Gibbs free energy curves with respect to composition near a solid–liquid interface (schematically). C_1 and C_2 points correspond to an equilibrium state at the interface, and chemical potentials of components in the phases (tangents to the curves at these points) are equal. Deviation of the actual liquid composition (C_i) at the interface temperature T_i from the equilibrium concentration C_1 generates a tendency to restore the equilibrium ($C_i \rightarrow C_1$, $C_s \rightarrow C_2$) or a driving force (ΔG_i) for nucleation.

change of the external parameters followed by prolonged relaxation (Roy 1992). Another concept (Wagner and Kampmann 1991) estimates the intrinsic limit of the metastability by the condition that the free-energy barrier against nucleation decreases to the order of the thermal energy fluctuations ($\sim kT$). A barrier against formation of a new phase is not only a function of the driving force but it is sensitive to the nucleus/matrix interface energy and many other factors.

In the case of solution growth, the driving force for crystallization is frequently represented by supersaturation. Several different forms of this definition can be found; however, all of them require knowledge about actual solution concentration C together with the equilibrium concentration C_e. Supersaturation can be defined as

$$\Delta C = C - C_e, \qquad s = \frac{C}{C_e} \quad \text{or} \quad \sigma = \frac{C - C_e}{C_e}. \tag{1}$$

The relative supersaturation σ is independent of the units in which the concentration values are expressed. At the same time these definitions of supersaturation assume an

ideal solution, while in strongly nonideal solutions as well as in precise studies activity coefficients might be needed.

A region of supersaturated solution is often divided into a metastable (Ostwald–Miers region) and a labile zone, and the boundary between them indicates the maximum supersaturation at which the excess solute does not crystallize under given operating conditions (Roy 1992). From a pragmatic point of view, knowledge about the width of the metastable zone provides recommendations about the supersaturation which is available in practice to grow a crystal, while on theoretical grounds such a boundary is not real since crystallization will occur even with little supersaturation despite the slow rate. In general, the definition of the width of the metastable zone should be based on a certain nucleation rate which is usually unknown in the experiment. Therefore, in the definition of the metastable zone width, a time scale should be introduced which can be related to the surviving time of the supersaturated solution under the selected experimental conditions. This time should not exceed the incubation or induction period t_i between the moment when a given supersaturation has been reached and the moment when the metastability is evidently broken by the formation of a detectable macroscopic volume, V_{macro}, of the new phase with a fraction $\alpha = V_{\text{macro}}/V$. In this case,

$$t_i = \left(\frac{\alpha}{aJG^3}\right)^{1/4}, \tag{2}$$

where a is a shape factor for the crystal formed, and J and G are the primary nucleation and growth rates respectively (van der Heijden and Van Rosmalen 1994). A more complicated theoretical model to predict the metastable zone width has been described recently by Mersmann and Bartosch (1998); this is based on the birth of nuclei on the surface of crystals present in the solution and their outgrowth.

It is evident from the preceding discussion that the analysis of the structure of a metastable solution and its evolution with time is closely related to nucleation theories. The separation of a metastable phase into a new stable, solute-rich phase, and a solute-poor old phase occurs as a result of fluctuations forming small clusters (embryos or nuclei) of the new phase. The small embryos are unstable and eventually dissolve. They must be large enough to compensate the unfavorable energy change at the interface. The embryos with a size greater than the critical one are supposed to survive and become centers of the macroscopic formation of the new phase.

The Gibbs thermodynamic approach, based on the consideration of the balance between volume and surface energies, gives an equation for the change in the free energy ΔG associated with formation of a spherical nucleus with radius ρ (Elwell and Scheel 1975):

$$\Delta G = 4\pi r^2\gamma - \tfrac{4}{3}\pi\rho^3\Delta G_V + \Delta G_E + \Delta G_c, \tag{3}$$

where γ is the interfacial surface energy of the solid phase, ΔG_V is the difference in the free energy per unit volume between the solid and liquid phases, and ΔG_E and ΔG_c are the free-energy changes due to changes in strain energy and configuration entropy which, in principle, can be neglected for the melt–crystal transformation. The critical

radius ρ_c of the nucleus can be estimated from this expression as $\rho_c = 2\gamma V_M/RT\sigma$, where V_M is the molar volume of the solution. It is evident that a higher supersaturation σ decreases the critical radius and it will tend to nucleate. The real situation, however, can be more complicated, as demonstrated, for example, by modeling of peritectic $YBa_2Cu_3O_{7-\delta}$ growth using transparent organic analogues (Yasuda et al. 1996, Terborg and Schmitz 1997).

A number of other theories (cluster theory of Volmer–Doring, Frenkel, Zeldovich, Lifshitz–Slyozov theories etc.) are widely described in the literature (Wagner and Kampmann 1991). All of the classical models approximate the solid–liquid interface as sharp and with no thickness i.e., it is assumed that the microscopic structure of the interface, involving description on the atomic scale, is much smaller than the characteristic length scale of the diffusion field. However, the discovery of spinodal decomposition led to a new theoretical model developed by Cahn and Hilliard (Wagner and Kampmann 1991) which considers the interface between two regions of different compositions as diffuse, i.e. possessing a finite thickness. According to this approach, the non-equilibrium (solid) solution can be unstable with respect to the formation of non-localized, spatially extended thermal composition fluctuations with small amplitudes. In the spinodal theories a "composition wave" mechanism rather than the classical "discrete droplet" formalism describes the early stages of decomposition in terms of amplitude and wavelength evolution of a certain stable "homophase" fluctuation. Hence, the unmixing reaction of such a solution can be initiated via spontaneous formation and growth of coherent "homophase" fluctuations of composition. This theory makes a step forward because the actual reaction path of a supersaturated solution can be highly complex, involving formation of intermediate non-equilibrium phases (Ostwald's step rule) prior to reaching the equilibrium of a "heterophase" mixture of products. The most recent diffuse-interface approach has been developed for the crystallization of R123 compounds from the melt, by Steinbach et al. (1996). This is the so-called phase-field model of a solid/liquid phase transition, which is, in general, an extension of Cahn and Hilliard's idea discussed above. In this model an additional continuous function is included, called the phase field, which acts as an order parameter to identify regions of solid and liquid. For a simulation of R123 solidification processing by this method, Seeßelberg et al. (1997a) have applied at a microscopic level a set of nonlinear parabolic differential equations coupled with a diffusion equation determining the local concentration of R^{3+} in melt at any position and time, and at a macroscopic level temperature fields in the specimen of arbitrary geometry were calculated and visualized during solidification. Such an approach is of considerable interest to deepen the understanding of crystal growth kinetics.

2.2.2. *Constitutional supercooling and the stability of a planar crystallization front*

An important feature of the interface between a growing crystal and liquid is its stability against a certain morphological perturbation. If the perturbation disappears under the given growth conditions the interface is called stable. However, if the perturbation is amplified during growth, the interface is called unstable. This happens because several

competing forces exist to make the interface stable or unstable. Solute or heat diffusion often acts to cause instability as has been analyzed by many authors (for example, Cheronov and Nishinaga 1987).

The average crystal front velocity is determined in time by the macroscopic transport of mass and heat. At the same time, the microscopic shape of the interface may select one of several possible morphologies, and these can be considered as metastable dynamic interface states. Under given growth conditions, one morphology can be the most kinetically stable and this morphology is usually observed experimentally. It is possible also to treat the problem when focusing on an increment of the interface and the volume surrounding the increment, since atomic-scale motions always produce microfluctuations of the thermodynamic state variables.

A thermodynamic criterion for interface stability is commonly connected with the concept of constitutional supercooling (Rutter and Chalmers 1953, Flemings 1974, Cheronov and Nishinaga 1987, Cima et al. 1992). The criterion consists in comparison of the local temperature T_L in the melt ahead of the interface with the corresponding equilibrium liquidus temperature $T_E = T_M + mc_L$. The equilibrium concentrations of the coexisting melt and the crystal are fixed by the phase diagram relationship. The melt is constitutionally supersaturated (metastable liquid) if its phase point moves away from the liquidus into the liquid-crystal coexistence region. The temperature of this region of the melt close to the moving interface is below the equilibrium temperature of the liquidus for the same composition, therefore this supercooling is generally called constitutional supercooling. In the case of a temperature gradient at the growth interface, constitutional supercooling exists if the actual concentration gradient in the nutrient phase at the growth interface is larger than the corresponding equilibrium liquidus slope of the phase diagram. In this case T_L is smaller than T_E, and supersaturation increases with distance into the nutrient phase. This is usually a necessary condition for pattern formation in a crystallizing system: due to the point effect of solute diffusion around a bump on the surface, the bump will grow faster, giving birth to a nonplanar pattern (fig. 2a, see also sect. 5.3).

2.3. *Rate-limiting factors and interface kinetics*

2.3.1. *Formation of a facetted shape*

The growth morphology of a crystal depends on the crystal structure as well as on growth parameters (e.g. growth temperature, supersaturation, impurities etc.). The growth might be limited by (1) kinetics of growth-unit attachment to the interface, (2) diffusion of solute from the environmental phase and (3) diffusion of the latent heat of crystallization. A complete description of solution growth requires the consideration of the heat transport (3). However, this can be neglected, because the growth rate of R123 phases is sufficiently small compared to the heat transfer, suggesting that heat dissipation is relatively rapid. Therefore the assumption of an isothermal solution or a steady-state, constant temperature gradient seems to be reasonable (Shiohara and Endo 1997). Figure 2b schematically illustrates the spatial distribution of the concentration of

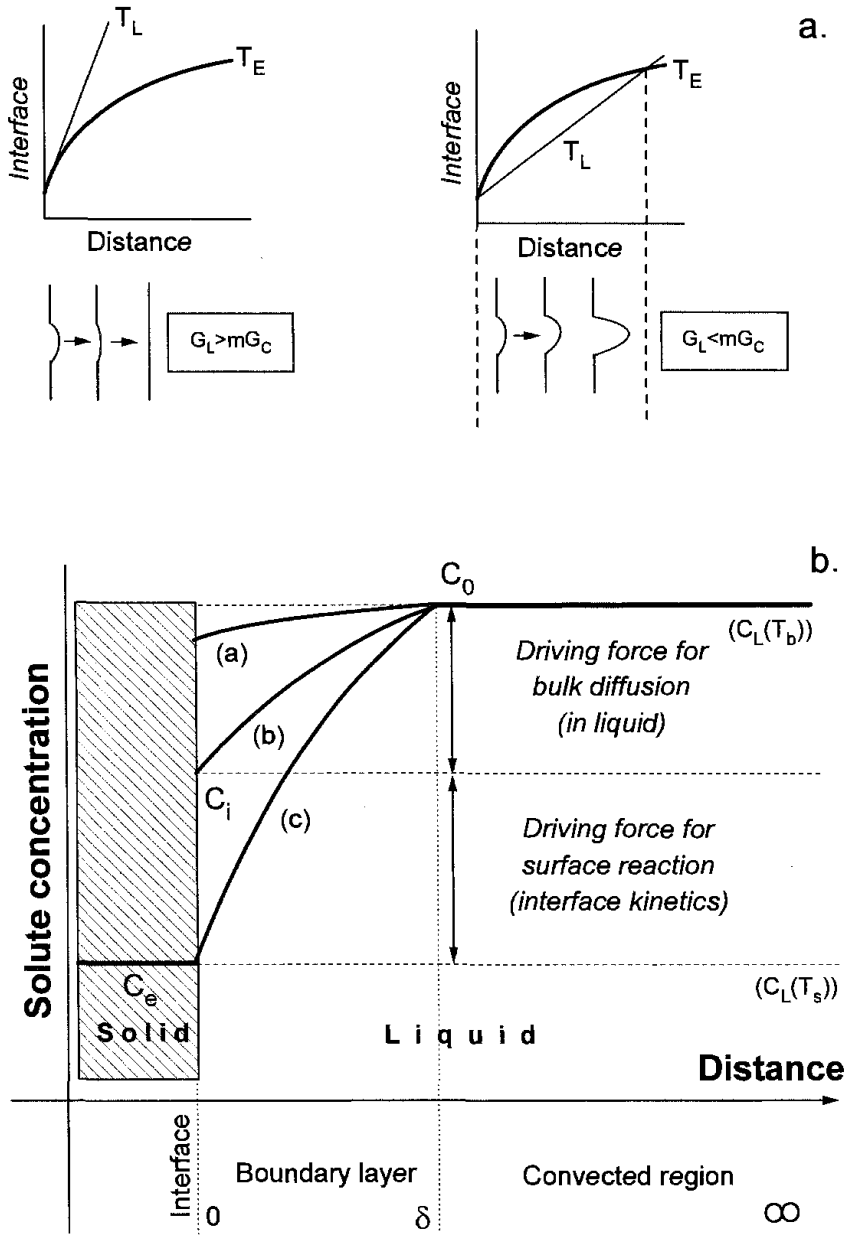

Fig. 2. Solute distribution and transport phenomena at the interface of a growing crystal: (a) Instability of the crystal–liquid interface and formation of a nonplanar pattern (schematically). (b) Faceted growth. It is assumed that the solute concentration in the liquid far from the interface (C_0) is constant due to forced and natural convection (stirring) whereas a thin solute diffusion layer (δ) is quiet and possesses a solute distribution profile depending on the crystallization process type: (a) interfacial control or a surface reaction (interfacial kinetics), $C_e < C_i \approx C_0$; a difference between C_e and C_i is responsible for the driving force to build up the crystal surface; (c) diffusion control $C_e \approx C_i < C_0$, providing a driving force for bulk diffusion in the liquid; (b) mixed control.

solute during crystal growth for the two general cases (1) and (2). Assuming an ideal solution, the concentration differences $C_o - C_i$ and $C_i - C_e$ will represent the differences in chemical potentials and hence, the driving forces for diffusion and interface kinetics,

respectively. If the interfacial liquid concentration C_i corresponds under given growth conditions to the equilibrium concentration C_e which is smaller than the bulk solute concentration C_0 in the supersaturated solution, the growth rate is totally controlled by diffusion. When the attached growth units at the crystal surface require some time to find their preferential sites, then $C_e \neq C_i$ and macroscopic (overall) growth becomes a two-step process where the rate of incorporation of growth units is balanced by the diffusion in solution. In the case of $C_i = C_o$, it is controlled by the interface reaction process (Pamplin 1980). The latter is very important when dealing with the construction and morphology of the growing crystal surface.

R123 crystals grown by a solidification process show faceted crystal habits. This indicates that the growth is considered to be controlled by the interface kinetics. A faceted interface is smooth at the atomic scale. On the other hand, a non-faceted interface is rough even though it can be visually flat. A kinetically or thermodynamically rough interface appears at a high supersaturation or upon the growth of a crystal above the temperature of the thermodynamic roughening transition. At high supersaturation many 2D and 3D nuclei cover the whole growing surface giving a kinetic roughening. The thermodynamic roughening occurs as a 2D phase transition above a certain ratio of temperature to the excess bond energy per one atomic interface site (Cheronov and Nishinaga 1987). At low temperatures this excess bond energy associated with the interface exceeds the configurational entropy of the surface atoms. On the contrary, at higher temperatures the entropy term in the interface free energy might overcome the binding-energy term and the flat interface will not resist thermal fluctuations above the thermodynamic roughening transition temperature. Jackson, in the frame of the Ising lattice gas approach (Jackson et al. 1967), has proposed a model for explaining the roughness of the interface at its equilibrium state in a simple case of a two-dimensional crystal consisting of 'square atoms' of one type which interact only with their nearest neighbors and form a single-layer interface. In the model, the melting entropy is used as a convenient criterion for predicting the crystallization behavior. According to this model, the roughness of an interface is determined by the Jackson parameter

$$\alpha = \xi\left(\frac{L}{kT}\right), \tag{4}$$

where ξ is the orientation factor (<1) depending on the crystallographic anisotropy, L is the latent heat of melting or dissolution, k is Boltzmann's constant, and T is the equilibrium (melting) temperature. Values of α less than 2 can be taken to imply a tendency to non-faceted crystal growth, while higher α-values correspond to faceted growth. A number of authors have suggested similar expressions (reviewed by Cheronov and Nishinaga 1987): $\alpha = -2\varphi_{ss}/(kT_G)$; $\alpha = 4[\varphi_{sf} - \frac{1}{2}(\varphi_{ss} - \varphi_{ff})]/(kT_G)$; $\alpha = \xi(1-\chi_s^2)(-\ln\chi_s + C)$. In these equations φ_{ss} is the potential energy of the nearest neighbors in the solid and it corresponds to the average binding energy for a pair; φ_{sf} is the average potential energy of solid–liquid; φ_{ff} is the interaction energy of the two nearest neighbors in the liquid phase; T_G is the growth temperature; χ_s is the density of

the solute part of the solution over the density of the solid; and C is a constant dependent on the force energy of solute particles. Temkin has extended the Jackson model to a multilayer model (Temkin 1966). The value of α for the Y123 crystals has been estimated as about 10–20 (sect. 3.4.1). Consequently, the interface of the Y123 crystals is considered to be facetted.

A development of this idea results in molecular attachment models. Being a reasonable simplification, the models help to understand the crystal growth phenomena. As suggested by Bravais in 1866, by Niggli in 1919, by Donnay and Harker in 1937 and by Hartman and Perdok in 1955 (Scheel 1993), the equilibrium form of a crystal can be derived from the packing density, or the density of strong bonds in the Periodic Bond Chain (PBC) concept which can give a theoretical growth morphology of a crystal derived exclusively from the crystal structure. According to this theory, the attachment energy (E_{att}) on a facet surface is approximately proportional to the growth rate of the surface; consequently, the crystal habit is determined by the relative E_{att} for each surface. Here, E_{att} is defined as the energy released per molecule when one slice of thickness d_{hkl} crystallizes onto a crystal face (hkl). Recently, this concept and its historical development has been reviewed by Bennema and Liu (Bennema 1996, Liu and Bennema 1996) in an attempt to integrate in a logical way the Hartman–Perdok theory, the theory of roughening transition, the spiral growth theory and extensive molecular dynamical simulations of the fluid part of the interface between a crystal and the mother phase.

Crystal faces with the highest PBC density parallel to the surfaces are called flat (F) faces, faces with unidirectional PBC are called stepped (S) faces, and surfaces without PBC are named kinked (K). It can be assumed for many crystals that there is a step in the interface and a kink in the step. Considering the growth of an atomically flat (i.e. faceted) close-packed interface as shown in fig. 3, a transition from liquid to solid is envisioned to take place across a single atomic or molecular layer. If an atom (building unit or add-atom) from the nutrient phase deposits on the growing crystal at the point A, it is joined to the close-packed plane by one face releasing a small amount of fusion/crystallization heat. However, if the atom deposits at the kink site (K), it will have nearest neighbors both in the close-packed plane below and in its own plane, i.e. more "free bonds" will be saturated and more links will be established. As a result, much more heat of fusion/crystallization will be liberated depending on the lattice symmetry and the exact number of neighbors. Thus, the driving force for deposition of an atom at the kink site is essentially higher than that for position A, and any atom that deposits at point A can lower its energy further by diffusing on the surface and depositing finally at K. In other words, the kinks are preferred sites for growth. During crystal growth in the case of faceted materials, the following processes are repeated on the surface; (a) an atom or molecule adsorbs on the surface by bulk diffusion, (b) the atom migrates to a kink site by surface diffusion, resulting in a kink advance, and the step sweeps laterally across the interface until it completely covers the surface, (c) a new step forms and then process (a) restarts. This growth mechanism has been introduced by Kossel (1927) and is called lateral growth because the crystal grows layer by layer. A quite similar approach is used sometimes in the so-called cellular automata technique for simple computer simulation of crystal growth

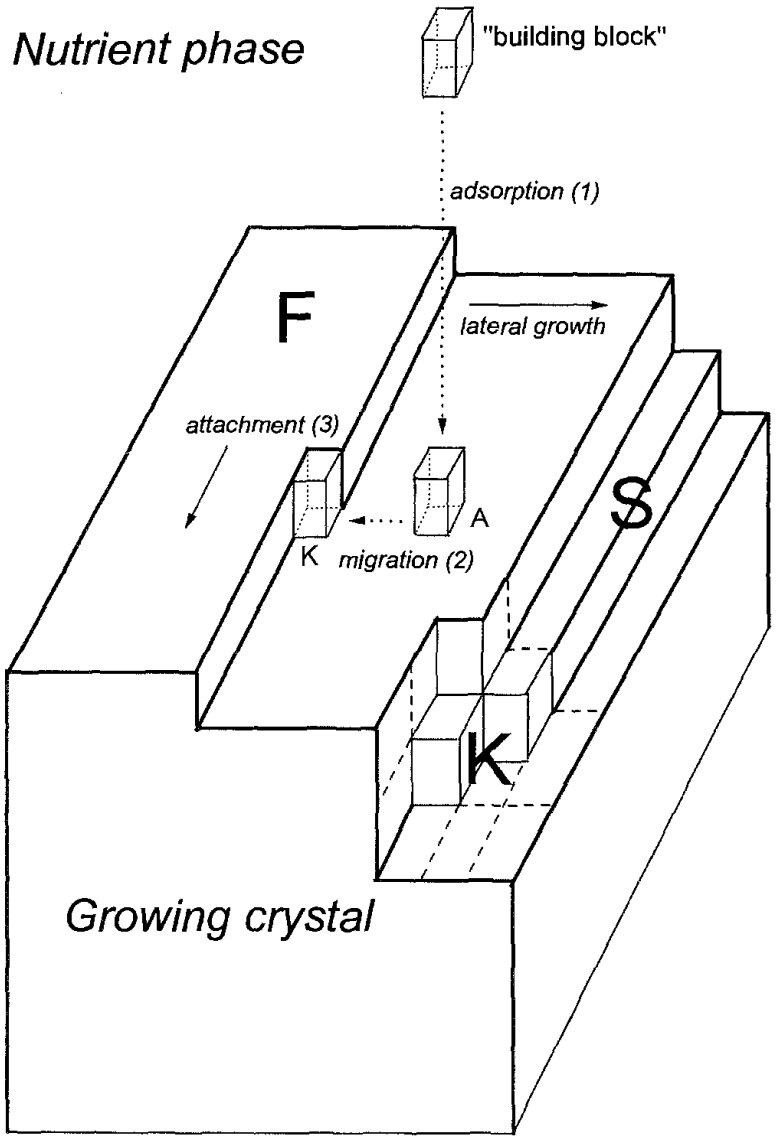

Fig. 3. Kossel's model of molecular attachment kinetics (layer-by-layer growth). Building blocks from a liquid nutrient phase are attached (adsorbed) by a growing crystal surface at a site (A) and migrate on it to join the most beneficial attachment places with the largest number of "free bonds" to be saturated by such a linking (kink sites K). (S) and (F) correspond to the stepped and closely packed (flat) faces, respectively.

(Dreysse and Riedinger 1987, Hesselbarth and Gobel 1991, Gudilin et al. 1995). The slowest process among steps (a)–(c) limits the growth rate of a material and determines the relation between the growth rate and supersaturation (σ) or kinetic undercooling (ΔT_k). Depending on the slowest process (rate-limiting process), the growth mechanisms are classified into three modes: (1) roughening or continuous growth, (2) growth by two-dimensional nucleation, and (3) growth by screw dislocations. Figure 4 shows the growth rate versus the kinetic undercooling according to the three classical laws (Tiller 1991a).

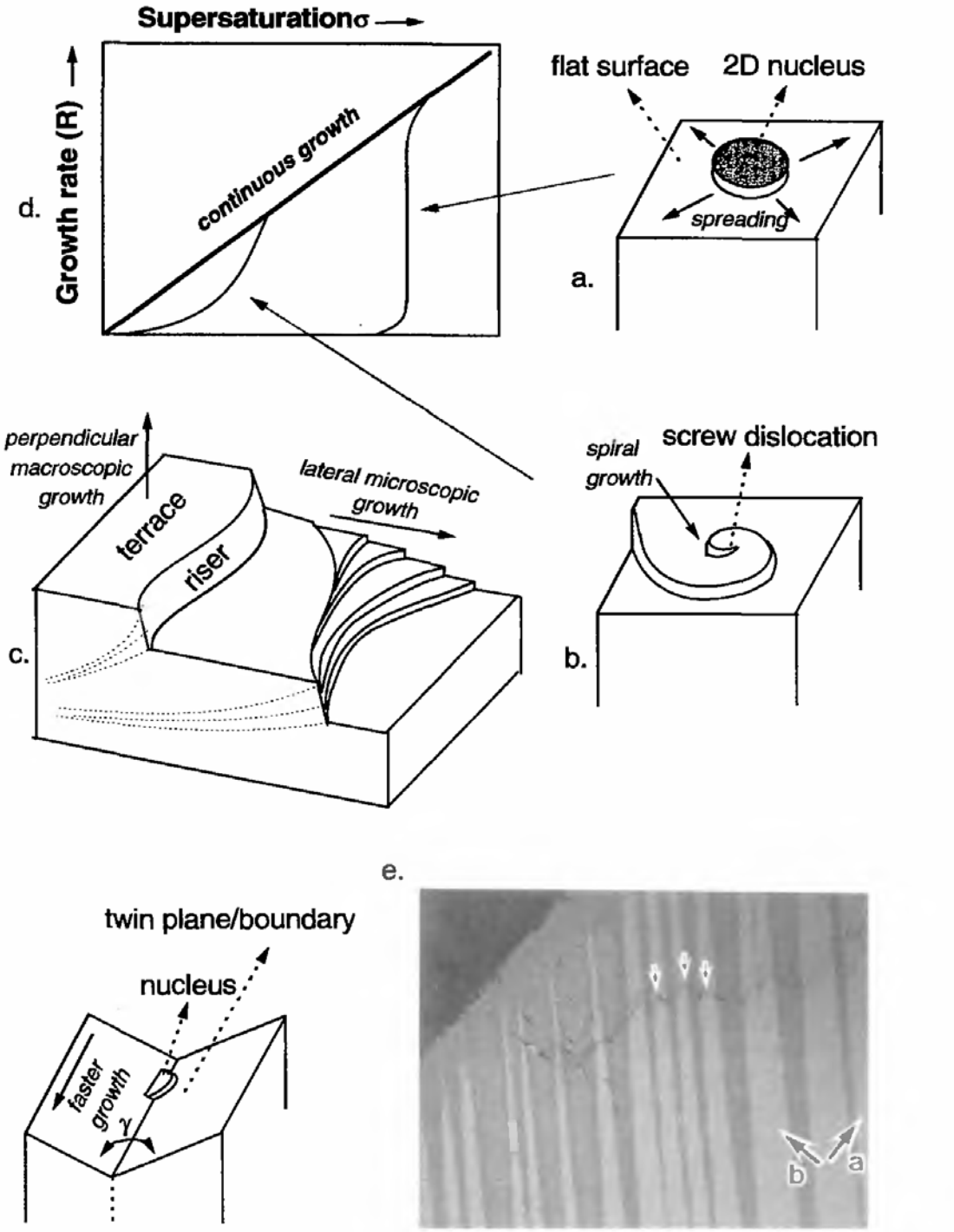

Fig. 4. (a–c) Common mechanisms of crystal growth versus (d) their dependence on supersaturation σ. 2D nucleation on a flat surface (a) demands a high supersaturation to overcome a high activation barrier. Spiral growth (b) or terrace–ledge–kink growth (TLK, c) are much more likely to occur. An alternative mechanism (Twin-Plane-Re-entrant-Edge growth) is based on the lowering of the nucleation energy along 2D angles formed by twins, as found for an orthorhombic $Nd_{1.85}Ba_{1.15}Cu_3O_z$ phase in the Nd–Ba–Cu–O system (Goodilin et al. 1998b).

2.3.2. *Two-dimensional nucleation and spiral growth*

For the layer growth of a smooth crystal surface, two mechanisms are widely discussed: spiral growth and two-dimensional growth (figs. 4a,b). The latter includes formation of two-dimensional islands on the surface which are assumed to spread laterally. The island can either grow and cover the whole surface before a new island is formed on the top of the growing island or islands are allowed to nucleate all over the surface (birth and spread model). Two-dimensional growth takes place when either no structural defect like a dislocation or reentrancy corner is present or supersaturation is high enough to overcome the nucleation barrier for the formation of such a nucleus. Fast growth can be achieved even at low supersaturation due to existing dislocations with a screw component which are terminated in the growth face and act as a permanent step source. The steps originating from dislocations arrange themselves in spirals or closed loops. If epitaxial layers grow by the motion of monomolecular straight and equidistant steps at the solid–liquid interface, a crystalline material of unique quality can be obtained. Thus, although dislocations are considered as extended defects they play an exceptional role in perfect crystal growth because they look like the most precise generators of elementary steps (Bauser 1994).

Burton, Cabrera and Frank (1951) investigated quantitatively the flux of adsorbed molecules from surface to steps caused by surface diffusion, starting from the Ising model of a two-dimensional lattice gas (BCF theory). According to BCF theory, the velocity of movement of the straight step is estimated as

$$\upsilon = 2\sigma x_s \nu \exp\left(\frac{-W}{kT}\right), \tag{5}$$

where x_s is the average diffusive distance of an adsorbed atom, ν is the vibration frequency of a molecule, and W is the dissolution energy of the attached molecule from the surface of the crystal. When a number of steps separated by a constant length (λ) exist on a crystal surface, the velocity of movement of the step, υ_λ, could be modified, considering the diffuse length and the step width, i.e.

$$\upsilon_\lambda = \nu \tanh\left(\frac{\lambda}{2x_s}\right). \tag{6}$$

Thus, the steps on the crystal surface move past a given point with velocity (υ) and then the point moves ahead with one step height (a) as each plane passes. Therefore, the growth rate perpendicular to the step-advance direction is

$$R = \nu_\lambda \frac{a}{\lambda}, \tag{7}$$

where ν_λ/λ is the frequency of passage of steps past a given point. Equation (7) is a general equation representing the rate of solidification as a function of the step movement.

In the particular case of 2D nucleation to form steps on a flat surface (Becker and Doring 1935, Volmer 1939), the rate of formation of new nuclei is proportional to

$\exp(-\Delta G^*_{2D}/kT)$, where ΔG^*_{2D} is the free-energy barrier required to form a critical two-dimensional nucleus of step height a. Assuming that the growth rate of each nucleus is sufficiently rapid in comparison with the nucleation rate of a new critical nucleus (single nucleation growth), υ/λ becomes exactly the rate of nucleation times the surface area of the growing face. Thus, eq. (7) becomes

$$R = C_1 \exp\left(-\frac{\Delta G^*_{2D}}{kT}\right), \tag{8}$$

where C_1 is a constant.

Frank (1949) suggested that screw dislocations having a displacement vector parallel to the surface would provide a source of steps which would persist and not grow out. In this case, the lateral growth can take place continuously without formation of new steps. If a step is not flat but has a curvature ρ, the velocity of movement of a straight step (eq. 5) can be replaced by

$$\upsilon_\rho = \nu \frac{\rho - \rho_c}{\rho}, \tag{9}$$

where ρ_c is the critical radius of a two-dimensional nucleus evaluated from the classical Gibbs–Thomson expression (sect. 2.2.1), $\rho_c = \gamma a/(kT\sigma)$, γ is the step energy per unit length, and a is the distance between growth units. According to Cabrera and Levine (1956), a better approximation of the step width of a spiral dislocation is given by

$$\lambda = 19\rho_c = 19\gamma \frac{a}{kT\sigma}. \tag{10}$$

Upon substituting eqs. (5), (6), (9) and (10) into eq. (7), the growth rate by a screw dislocation can be written as

$$R = a\nu \exp\left(\frac{-W}{kT}\right) \frac{\sigma^2}{\sigma_1} \tanh\left(\frac{\sigma_1}{\sigma},\right), \quad \frac{\sigma}{\sigma_1} = \frac{2x_s}{\lambda} = \frac{x_s}{9.5\rho_c} = \sigma \frac{x_s kT}{9.5\gamma a}. \tag{11}$$

In general, the predicted supersaturation required for 2D growth is much larger than has ever been observed. At lower (real) supersaturations the screw dislocation mechanism is much more feasible and two situations can be distinguished. If the supersaturation σ is sufficiently smaller than σ_1, $\tanh(\sigma_1/\sigma)$ becomes equal to ~1 (eq. 11). On the other hand, for $\sigma > \sigma_1$ one has $\tanh(\sigma_1/\sigma) \approx \sigma_1/\sigma$. The relationships between the growth rate and supersaturation for each case can be written respectively as:

$$R \propto \sigma^2 \text{ for } \sigma < \sigma_1, \qquad R \propto \sigma \text{ for } \sigma > \sigma_1. \tag{12}$$

The predicted growth rate as a function of supersaturation is shown in fig. 4. At high supersaturations, the rate of two-dimensional nucleation becomes so high that many nuclei form on each growing plane. If the distance between steps approaches the order of the

interatomic spacing, the actual growth rate deviates from that given by eq. (8). As an upper limit it approaches the continuous growth law, which is called the Hertz–Knudsen formula for vapor growth or the Wilson–Frenkel formula for melt growth and solution growth (fig. 4d). The continuous growth is derived on the basis of non-faceted growth, i.e. if the concentration of kink sites is high, building blocks striking the interface can join the kinks instantaneously. The continuous growth model gives the maximum growth rate (R_{max}) at some supersaturation value, and the relation between R_{max} and supersaturation (σ) is described as

$$R_{max} \propto \sigma. \tag{13}$$

At high supersaturations, the growth rate with screw dislocations approaches the continuous growth law, which is similar to the two-dimensional nucleation growth (however, strictly speaking it is not exactly the case of the Wilson–Frenkel formula, eq. 13). Thus, the relationships between supersaturation (or kinetic undercooling) and growth rate can actually give important information about the interface kinetics (see sects. 3.3.1, 3.4.1).

2.3.3. *Terrace–ledge–kink (TLK) model*

Terrace growth (fig. 4c) is not only the most frequently used idea, but also is a commonly observed crystal growth morphology (Tiller 1991a, Bauser 1994). A growth terrace is generally described in terms of a shape-preserving "steep riser" and "a flat tread" with a large linear size as compared with that of the riser. The real riser is not necessarily plane but is often composed of curved surfaces. Since terraces are present at the growth interface, two different processes can be distinguished which make a contribution to the macroscopic growth of the crystal. One of them is attachment of growth units at the riser portion of the growth terrace and lateral motion of the single terrace; the second, simultaneous process consists in a lateral motion of small steps on the terrace tread (lateral microscopic growth). These small steps emerge from the base of the terrace risers and advance on the tread with a high velocity which is usually higher than the overall development velocity of the riser portion. The small and fast steps run on a riser tread until they reach the upper edge of the next riser where they stop but do not wrap over. Depending on the balance between the small steps having reached the upper edge of the riser and the steps pulled out from the base of the riser, the riser can be unchanged or can decrease or increase its height (perpendicular macroscopic growth). The terrace decay increases the terrace lateral velocity and flatness. The traces of the small terraces are arranged almost parallel to the growth interface and are "S"-shaped. The riser of terraces with a constant height is usually a straight stripe with a fixed inclination to the growth face.

2.3.4. *Real crystal morphology*

The real morphology deviates from the ideal models (or modes) of crystal growth discussed above, and several typical examples can be given. They are connected with distortion or interaction of the growth front whenever it is spiral or TLK growth.

In terms of the TLK model, the kinetics of crystallization depend strongly on the density of kink sites as well as on the interface driving force. At small driving forces, the phase change can occur at the kink sites only on the ledges, so the interface moves forward by movement of kinks on the ledges and the lateral passage of the ledges over the surface. At intermediate driving forces the ledge becomes more diffuse (higher kink density) because kinks can form spontaneously on the ledge. At very large driving forces, kinks form spontaneously on the terrace as well, therefore the phase change can occur anywhere on the interface and attachment becomes uniform. In the case of an easy supply of ledges, the crystallization velocity is proportional to both density ρ_L and height h_L of the ledges on the interface and the rate v_L of their movement: $v = h_L \rho_L v_L$ (Tiller 1991a).

For spiral growth, when a spiral is not perturbed, i.e. the growth temperature or supersaturation over the surface are constant and interaction between different spiral sources is negligibly small, the spiral can possess an Archimedean shape with equidistant step separation λ except for a few turns at the center. According to BCF theory (sect. 2.3.2), it is reasonable to expect (Sunagawa 1987) that (1) the higher the spiral step height is, the larger λ; (2) the stronger φ_{sf} is, the smaller λ is, since an increase of φ_{sf} reduces γ; (3) spirals on morphologically more important faces will have wider step separation λ. If a spiral step is rough enough with a high kink density, the step development is isotropic with equal advancing rates in all directions because these rates are not controlled by the directions of strong bonds; as a result a circular spiral is produced. For a smooth step with a lower kink density, the advancing rates are controlled by the strong bond directions (periodic bond chains, sect. 2.3.1) within crystal face because steps along the stronger bonds contain a lower kink density. Accordingly, the spiral accepts a polygonal morphology and follows the symmetry and crystallographic anisotropy of the face. It predicts that the structural characteristics of the surface will be reflected in the morphological characteristics of growth spirals. The spirals will be more polygonal in the following cases: (1) on morphologically more important faces (under given conditions), because ξ decreases with decreasing morphological importance; (2) on the same face, if T_G decreases since α is inversely proportional to T; (3) under the same growth temperature, if φ_{sf} becomes weaker; (4) if the solubility is smaller; (5) for structures with stronger φ_{ss}; (6) for steps with higher height.

The most common situation, however, is cooperation or interference between neighboring spiral steps, i.e. a non-Archimedean spiral pattern. A wide variety of step patterns may occur depending on the mutual separation of the spirals, Burgers vectors of initiating screw dislocations, signs of the neighboring screw dislocations, presence of other spatial defects, as well as nonuniform supersaturation or temperature field over the growing surface (Elwell and Scheel 1975, Sunagawa 1987). Certain special considerations are contemplated:

- When the mutual separation of screw dislocations is larger than $19\rho_c/2$ (with ρ_c the radius of critical 2D nuclei), independent spirals appear at first and after some turns, and the spirals demonstrate a parallel nonintersecting step system.
- When the separation is smaller than $19\rho_c/2$, the above-mentioned nonintersecting spiral system arises at the beginning, resulting in the so-called composite spiral. At every turn

an exchange of spiral centers is necessary. Depending on the center separation and the time delay in spiral appearance, the composite spiral may show many turns or none with an equal step separation, but in any case only a step parallel to the spiral steps will be dominant.

- When the step separation is narrower than a certain critical value, diffusion fields from the neighboring steps can overlap, and in general, the probability of occurrence of bunched steps increases as the step separation becomes smaller.
- When spiral steps from two dislocations are separated by a distance larger than $19\rho_c/2$, two-dimensional re-entrant corners may appear and preferential growth will start after that, i.e. the steps will advance faster at the re-entry corners in comparison with other directions. When the step separation is much wider than a critical value, it becomes possible that the supersaturation between neighboring steps can achieve a level sufficient to overcome the barrier of 2D nucleation and to permit nucleation on the surface of spiral layers.
- When a supersaturation (or temperature) gradient exists over a spiral, most probably, the spiral will grow eccentrically with different advancing rates of the spiral layers in accordance with the gradient. Starting from a fixed dislocation point, a wider step separation occurs at the higher supersaturation side, and a narrower one at the lower supersaturation side. A supersaturation gradient is also assumed to exist between the central portion and that near the edge of a growing crystal (Berg effect); i.e., a higher supersaturation is expected near the edge, hence step separation can be wider near the edge in comparison with the central part of the growing crystal face.
- When "wobbling" of the center of a spiral occurs (for example, at a helicoidal screw dislocation), a rhythmic bunching pattern can be observed. The same is possible for the center of a group of cooperating spirals originating from screw dislocations at various distances, or for the decomposition of a regular system of spiral steps of large height consisting of many layers stacked in a zig-zag way, or because of differences in the advancing rates of steps of different heights.
- When two screw dislocations have opposite signs, the two spiral steps coalesce, giving a closed loop which may appear from the beginning or after several turns of the spirals.
- When the Burgers vectors of neighboring screw dislocations are different, a fault line appears along the boundary between the territory of the interacting spirals.
- When a stress field is concentrated around a dislocation, the step velocity can be changed as well as the driving forces for growth or dissolution. As a result, a depressed area or change of the spiral curvature or formation of a hollow core in the center for crew dislocations with large Burger vectors might appear depending on the state of the stress field and its contribution as a strain term in the advancing step velocity of a spiral. The hollow core may be stable or unstable depending on supersaturation. It is closed above a critical supersaturation.

A difference between the periphery and the growing face center, sudden fluctuations in the supersaturation and/or temperature during growth, incorporation of impurities, and all other factors discussed above may drastically modify the step pattern. Thus step separation of the real spirals is not equidistant but fluctuating and, as a result, probabilities of

bunching of advancing elementary spiral steps increase, i.e. the formation of large steps by bunching is governed more likely by kinetics rather than thermodynamics. Therefore, thick bunched steps are commonly formed and are often observed visually. They are generally attributed to the "spiral growth of real crystals".

The bunching of atomic steps at the growth interface and macrostep formation can often be observed in the TLK model as well (Cheronov and Nishinaga 1987, Danilewsky et al. 1995). The step bunching increases the average height and distance of steps at the growth interface and the step may attain macroscopic (visual) dimensions; it is then usually referred to as "growth terrace". For occurrence and disappearance of macrosteps, the local growth rates and the temperature gradients are considered to be significant factors. On a macroscopic scale, the variation of the surface supersaturation results in a variation of riser slope and width. A decreasing growth rate decreases the slope of a macrostep riser, i.e. to keep the height unchanged, the width of the macrostep has to be increased. On a microscopic level, the starting high supersaturation at the upper terrace allows a higher number of fast small steps to join the upper riser edge while at lower supersaturation at the lower edge only a small number of elementary steps can disappear, in other words, the macrostep gains height. The temperature gradient can flatten the concentration field and the concentration difference between upper and lower edges is reduced. Therefore a larger number of steps are to be left at the lower edge and the slope of the riser has to decrease. The same macroscopic effect can be connected with decreasing growth rate, and finally it might lead to disappearance of the macrostep. A generalized kinetics of the step bunching with estimation of a kinetic coefficient, which is a nonlinear function of the supersaturation and crystallographic orientation, has been discussed recently by Coriell et al. (1998). The TLK requirement of ledge creation, interaction and annihilation results in the formation of flats, ridges and corners on real crystals as well as in the wide variety of crystallization anisotropies observed in nature and technology.

2.3.5. *Striations*

For the growth of a solid phase with variable composition, or to control macroscopic dopant or impurity distribution, the classical works on crystal growth apply a distribution coefficient term. The difference between a solid solution and a doped crystal is that the term "solid solution" is restricted to members of an isostructural series whereas dopants may differ a great deal in structure from the host. If polythermal methods are used, the resulting crystals will normally be inhomogeneous, and exceptions to this rule require rather unusual conditions.

There are two general types of concentration variations: relatively long-range variations due to a change in the solution composition, growth temperature or growth rate as the crystal grows, and short-range variations attributed to transitions within the solution. The oscillatory fluctuations of temperature or solution concentration normally lead to periodic variations of the solid solution composition called striations of type I. In highly doped crystals the traces of macrosteps produce dopant inhomogeneities, so-called type II striations. In both cases the incorporation of impurities or the change in composition of

the solid solution are characterized by a distribution coefficient defined as the ratio of the concentrations of the dopant in the solid (crystal) and in the liquid (nutrient phase). The equilibrium solute partition coefficient k_0 can be, in principle, determined as the ratio of solubilities on the solidus and the liquidus curves of an equilibrium phase diagram at the interface temperature. In general, however, the effective value k_{eff} will differ from k_0 (for example, for growth of crystals from stirred melts) and the following expression for this phenomenon (famous mostly because of its simplicity rather than deep physical meaning) was suggested by Burton, Prim and Slichter (Elwell and Scheel 1975):

$$k_{\text{eff}} = \frac{k_0}{k_0 + (1 - k_0)\exp(-\upsilon\delta/D)}, \tag{14}$$

where k_{eff} is defined as the ratio of the solute content in the crystal at the interface and that in the bulk liquid; δ is the thickness of the boundary layer (see sect. 3.3), υ is the growth rate, and D is the diffusion coefficient in the liquid; k_{eff} will tend to k_0 at low values of υ and δ or if the diffusion in liquid (D) is very fast.

3. Mechanism of R123 crystal growth from the melt

In order to control the crystal growth for HTSC materials, we should clarify various phenomena taking place at each stage of this process (liquid, liquid/solid phase transition, solid) and the present section deals with this subject.

3.1. *Phase diagrams related to crystal growth*

3.1.1. *Y–Ba–Cu–O system*

Phase diagrams are visual representations of the state of a material as a function of temperature, pressure, and concentrations of the constituent components (Kattner 1997), therefore the phase diagrams are useful tools for optimizing the parameters used in the fabrication processes of materials and for understanding the crystal growth mechanisms. The first outlook to the growth phenomena should be started from this very important point. In the field of HTSC materials, much effort has been made to determine the thermodynamics of stable and metastable (Degterov and Voronin 1991, Brosha et al. 1995, Williams et al. 1991) phases as a function of temperature and oxygen partial pressure. Different phase diagrams of the Y–Ba–Cu–O system, when a liquid phase is present, have been investigated by many authors; data have been presented, for example, by Fraze and Clarke (1987), Roth et al. (1987), Aselage and Keefer (1988), Bykov et al. (1988), Fischer et al. (1988), Karpinski et al. (1988a, 1989), K. Oka et al. (1988), Osamura et al. (1988), Licci et al. (1989), Lindemer et al. (1989), Maeda et al. (1989), McCallum (1989), Ullman et al. (1989), Dembinski et al. (1990), Lay and Renlund (1990), Kawabata et al. (1990), Voronin and Degterov (1991), Sestak (1992), Zhou and Navrotsky (1992), Erb et al. (1993), Shitova et al. (1993), J.-S. Kim and Gaskell (1994), Krabbes et al. (1994,

1995), Brosha et al. (1995), Chandrachood et al. (1995), Boudene et al. (1996), Makarova et al. (1996), Lamberti et al. (1997), Wong-Ng and Cook (1998), and have been reviewed by Karen et al. (1992), Assmus and Schmidbauer (1993), Scheel (1994), Sestak et al. (1994), MacManus-Driscoll (1997), and Chen (1998). The reader can partially find these data in the corresponding chapters of this Handbook (chs. 190, McCallum et al.). Such a rich history from the discovery of HTSC until the present, is explained, on one hand, by the great importance of these investigations for crystal growth and, on the other hand, by the difficulties in the construction of a high-temperature phase diagram.

According to Aselage and Keefer, who performed one of the first investigations, about 11 melt-involved interactions can be identified in air, such as $YBa_2Cu_3O_{7-\delta} + BaCuO_2 + CuO \rightarrow L_1$ (ternary eutectics at about 890°C, liquid composition $Y:Ba:Cu \approx 1.0:32.5:66.5$), $BaCuO_2 + CuO \rightarrow L_2$ (binary eutectics at about 910–920°C, about 69–71 mol% CuO), $YBa_2Cu_3O_{7-\delta} + CuO \rightarrow Y_2BaCuO_5 + L_3$ (at about 940°C, liquid composition $Y:Ba:Cu \approx 2.0:23.0:75.0$), $BaCuO_2 \rightarrow L_4$ (at about 1015°C) and the so-called melting or decomposition reaction at about 1000–1015°C as reported by different authors:

$$YBa_2Cu_3O_{7-\delta} \rightarrow Y_2BaCuO_5 + L_5. \tag{15}$$

This set of reactions probably originates from the expansion of the copper-rich liquid phase region around the $Ba:Cu = 1:2$ composition (confirmed by Kambara et al. (1998) for the Nd–Ba–Cu–O system), initially directed toward both barium- and copper-rich regions and further to the barium-rich region at elevated temperatures as suggested by Wong-Ng and Cook (1998). Another point of discussion is the existence of a second liquid enriched by barium, which can also supply a "Y123–melt" compatibility section and the Y123 primary crystallization field (Wong-Ng and Cook 1998). In addition, Osamura and Zhang (1991) have clarified seven univariant reactions for the Y–Ba–Cu–O system, where four condensed phases coexist in equilibrium. Based on these experimental data, a reaction scheme has been proposed for the whole system, where eight additional hypothetical univariant reactions are suggested to take place; in particular, a suggestion has been made that the peritectic decomposition of the Y123 phase might involve the Y143 phase formation besides the commonly accepted "211 + L" reaction (see also Aleshina et al. 1996).

On the basis of reported experimental results [which are usually in quantitative disagreement even in this basic case because of errors in dynamic measurement techniques including TGA/DTA (Wiesner et al. 1997), carbon or alumina impurities, and so on] B.J. Lee and Lee (1989, 1991) calculated the phase diagram, as it should be done in the final stage of investigations of this kind, since the calculation reduces the effort required to determine equilibrium conditions in a multicomponent system. The vertical section containing Y_2BaCuO_5 (Y211), $YBa_2Cu_3O_{7-\delta}$ (Y123) and a mixture of $3BaCuO_2$ and 2CuO in fig. 5 demonstrates that the liquidus line of liquid/Y123 is very steep and the Y123 phase is formed by the peritectic reaction between Y211 and liquid.

Phase relations for the HTSC systems, applied for melt preparation and crystal growth, are often called tentatively "working" or "schematic" diagrams (as discussed, for example,

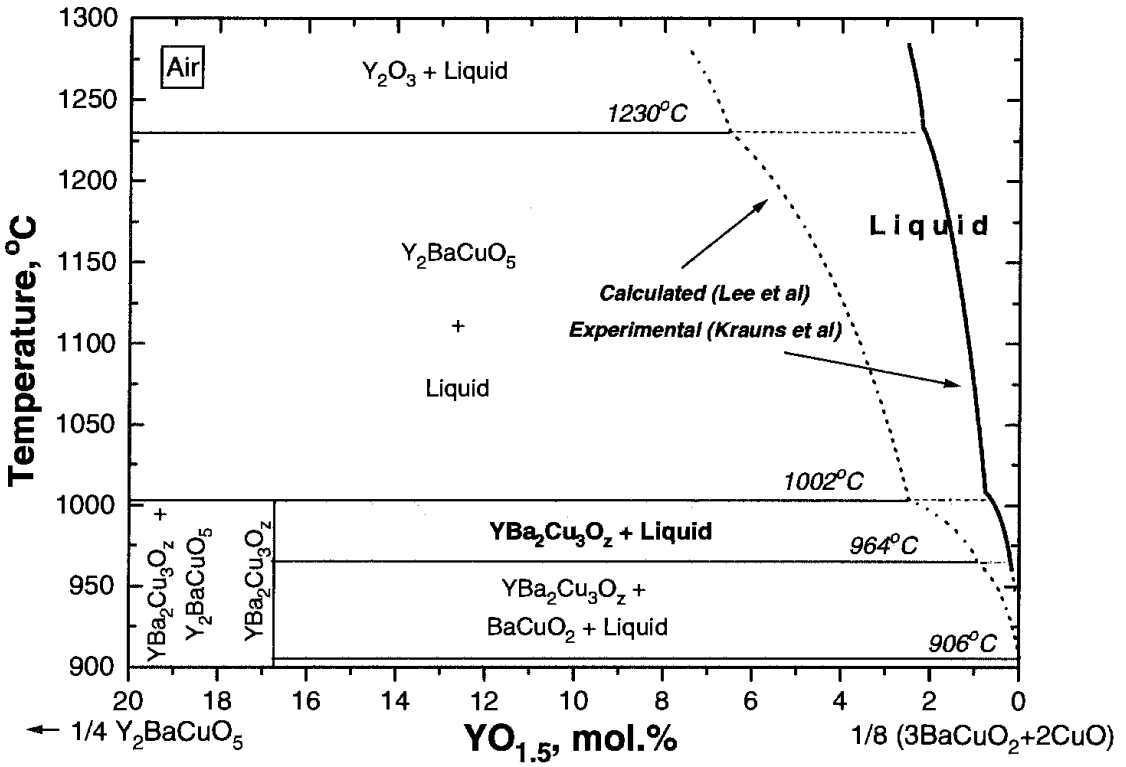

Fig. 5. The calculated quasibinary Y_2BaCuO_5–("$Ba_3Cu_5O_8$") section of the Y–Ba–Cu–O phase diagram in air. The Y123 phase liquidus is characterized by a small solubility of Y^{3+} and a large slope. Note that the direct measurement of the liquidus composition leads to even smaller solubility parameters (B.J. Lee and Lee 1991, Krauns et al. 1994a).

by Voronin and Degterov 1991, MacManus-Driscoll 1997, and Chen 1998). In fact, in accordance with the Gibbs phase rule, for eq. (15) the system is quasi-three-component ($C=3$) and three phases ($P=3$) are assumed to be in equilibrium, therefore, the number of degrees of freedom (F) is equal to 2 and, strictly speaking, the reaction is not formally invariant ($F \neq 0$) as would be expected.

In order to find an explanation, it should be noted that the decomposition temperature of the oxygen-nonstoichiometric Y123 phase increases at high p_{O_2} as shown, for example, by Karpinski et al. (1989) (for 1–3000 bar of oxygen), Idemoto and Fueki (1990), Hu et al. (1992), Kimura et al. (1992), Arnott et al. (1993), and Chandrachood et al. (1995). At the same time it is strongly lowered at low p_{O_2} as found by Ahn et al. (1990), Beyers and Ahn (1991), Fischer et al. (1993), MacManus-Driscoll (1997), etc. Accordingly, the composition of the lowest-Y123-melting liquid is close to pure $BaCu_2O_2$ at low p_{O_2} because the solubility of the rare-earth element in the melt decreases both with temperature and with oxygen partial pressure (sect. 3.1.2.1). It seems that an oxygen-deficient liquid, based on the monovalent barium cuprate $BaCu_2O_2$, should not readily accept the Y^{3+} cation. At p_{O_2} as low as 4.0×10^{-4} atm, a liquid-free decomposition of Y123 is suggested (Ahn et al. 1990):

$$YBa_2Cu_3O_6 \rightarrow Y_2BaCuO_5 + \text{"}YBa_3Cu_2O_y\text{"} + BaCu_2O_2 + O_2. \quad (16)$$

The Ba–rich Y132 phase is the most questionable point of this reaction and it was postulated that it might have the Y163 and Y184 compositions as well. This phase dissolves in liquid as soon as p_{O_2} increases sufficiently, and disappears under most crystallization conditions, particularly in air or oxygen. Y123 becomes unstable under high-p_{O_2} conditions as well (Karpinski et al. 1989, Degterov and Voronin 1991, Williams et al. 1991).

As soon as oxygen is considered, the system becomes four-component, with four phases involved in the reaction. The oxygen partial pressure must be fixed, i.e. a number of additional conditions $\alpha = 1$, therefore $F = 1$. However, it is thought that simply under unchanging p_{O_2} the temperature of the peritectic reaction (schematically) $YBa_2Cu_3O_{7-\delta} \rightarrow Y_2BaCuO_5 + L + O_2$ is a constant. The situation becomes clear when discussing the solid-phase composition restrictions. For example, the experimental decomposition temperatures of the $Nd_{1+x}Ba_{2-x}Cu_3O_z$ solid solution (see sect. 3.1.2.3) depend not only on p_{O_2}; in addition the substitution parameter x is important ($\alpha = 2$, $F = 0$, $z = f(x)$). Therefore, for a complete description of the phase relations of quaternary systems, the phase diagram should be displayed three-dimensionally by a regular tetrahedron for a constant temperature. In practice, however, no confusion occurs within fixed oxygen partial pressure for a set of isothermal quasiternary (triangular) diagrams (see sect. 3.1.2.4).

From the Y–Ba–Cu–O phase diagram and its dependence on oxygen pressure, one can find its complexity which is usually ignored because of the practical needs. However, three characteristic features should certainly be pointed out:

(1) The Y123 tetragonal phase is formed by a peritectic reaction from Y211 solid and Y-deficient BaO–CuO liquid. Therefore, it is impossible to grow Y123 crystals by a congruent melt crystal growth procedure, for example, by the simple conventional Czochralski method.
(2) The liquidus slope near the Y123 peritectic reaction is very large, which suggests that it is difficult to obtain a larger growth rate even if large undercooling is applied.
(3) The Y concentration in the BaO–CuO liquid is very low. Therefore, the self-flux method, which is commonly used to obtain single crystals in incongruent melting systems, might not be helpful in production of large crystals.

3.1.2. *Phase diagrams with light rare-earth elements ($NdO_{1.5}$–BaO–CuO_x)*

At present, many research works have been performed to elaborate phase diagrams in the R–Ba–Cu–O systems (R: Nd, Sm, Pr, La, Yb, ...), most of them, however, were focused on the solid state, probably due to difficulties in investigating the complex oxide melts at elevated temperatures. Phase relations between solid phases in the R–Ba–Cu–O systems (see ch. 190 of this Handbook), for example, were investigated by Klibanow et al. (1988), Hodorowicz et al. (1990), Czerwonka and Eick (1991), Wong-Ng et al. (1990, 1994), Osamura and Zhang (1993), Yoo and McCallum (1993), Kramer et al. (1994b), Lindemer et al. (1993, 1994, 1995), Lindemer and Specht (1996), Chodorowiczbak et al. (1995), Przybylo et al. (1996). An important feature of systems with a light rare-earth element

(LR = La, Nd, Sm, Eu, Gd) in comparison with Y–Ba–Cu–O is the partial LR substitution for barium and, as a consequence, the presence of solid solutions $LR_{1+x}Ba_{2-x}Cu_3O_z$ (LR123ss). The substitution range increases from 0 to 0.2, 0.4, 0.55 and >0.7 for Y, Gd, Sm, Nd and La, respectively, as briefly reviewed by Murakami et al. (1996). Other investigations, however, demonstrate $x \approx 0.75$ (Sm) (Grigorashev et al. 1997), $x \approx 0.9$ (Pr) (Osamura and Zhang 1993, Bertrand et al. 1999, Luo et al. 2000), $x \approx 0.9$–1 (Nd) (Abbattista et al. 1991, Osamura and Zhang 1993, Goodilin et al. 1996, 1998b, 1999, Petrykin et al. 1999a,b), $x \approx 0.95$ (La) (Petrykin et al. 1997, 1999a). Besides that, the high-temperature stable phase $LR_{4-2x}Ba_{2+2x}Cu_{2-x}O_{10-2x}$ (or "brown" phase, $0.15 \leqslant x \leqslant 0.25$ for La, $0 \leqslant x \leqslant 0.1$ for Nd; Klibanow et al. 1988, W. Wong-Ng et al. 1994) seems to be a non-stoichiometric compound of another structural type as compared to the "green phase" Y211, and the abbreviation "422" instead of "211" notes this fact.

From the phase diagram viewpoint, the LR123 phase is only a particular case of the LR123ss solid solution with $x = 0$. It is remarkable that recent results allow one to assume that the outstanding characteristics of melt-processed Nd-based high-temperature bulk superconductors actually might be connected with the formation of the Nd123ss solid solution and the consequent complicated transformations (sect. 7.4.3.4). Thus the understanding the most interesting and applicable features of the Nd-based materials cannot be complete without an analysis of the structure of the LR123ss solid solution and its behavior at different levels of substitution. Ignoring the possibility of formation of the solid solution can also lead to serious mistakes in the correct interpretation of phase relations in this system especially when using classical methods of materials characterization like XRD and DTA without an estimation of the actual chemical compositions of the equilibrium phases.

Incongruent melting points of R123 (T_p) are different (see, for example, Iwata et al. 1989, Osamura and Zhang 1993, Lindemer et al. 1993, 1994, 1995, Lindemer and Specht 1996, Krauns et al. 1994a, Goodilin et al. 1994, Chen 1998). For most of the R elements a simple correlation exists between their ionic radii and T_p (sect. 3.1.2.1), and only a few exceptions can be found (sect. 3.1.3). La also has its own features of the high-temperature phase relations (N. Sakai et al. 1997, see also fig. 7) because the largest ionic radius of this element among other R allows a number of ternary solid solutions and "cation stoichiometric" phases to exist in addition to La123ss and La422, such as La415, $(La_{1-x/2}Ba_{x/2})_2BaCu_2O_z$, $(Ba_{1-y}La_y)_2CuO_{3+w}$ (Klibanow et al. 1988, Wada et al. 1989, Wong-Ng et al. 1990, Karen et al. 1992, Osamura and Zhang 1993, Lindemer et al. 1994, N. Sakai et al. 1997, 1998). Unfortunately, high-temperature phase diagrams of LR123, and especially the "LR123 + Liquid" regions, have not yet been studied well. In the "simplest" Y–Ba–Cu–O case, equilibrium tie-lines are connected with the cation stoichiometric Y123 phase; consequently, liquid coexists with the 123 phase ($x = 0$) only. However, in the LR–Ba–Cu–O systems, two solutions of variable compositions are equilibrated, namely the liquid solution or melt and the solid solution or $LR_{1+x}Ba_{2-x}Cu_3O_z$. In other words, for different initial composition or/and growth conditions, the composition of LR123ss is different as well, as determined by tie-lines (Kambara et al. 1998, Kakimoto and Shiohara 1996). Therefore, quantitative

phase diagrams including equilibrium tie-lines in the LR123ss + L region are necessary in order to control the LR123ss composition in homogeneous single-crystal growth. Construction of these quasi-ternary phase diagrams (T = const, p_{O_2} = constant) could consist of three steps. The first stage is the evaluation of the liquidus curves, the second is the determination of the solidus, and finally the true equilibrium tie-lines and tie-triangles have to be found. As an important example with most of the usual difficulties included, we will discuss crystal-growth-related phase relations in the Nd–Ba–Cu–O system which seems to be the most promising for the modern techniques of R123 single crystal production. A number of different representations of HTSC phase diagrams was reviewed by Chen (1998), Tretyakov and Goodilin (2000), and others.

3.1.2.1. *Solubility of rare-earth elements in barium–copper oxide fluxes.* The necessary information for crystal growth can be supplied from a knowledge of the solubility curve of the phase to be crystallized. The solubility is usually determined by one of several methods, including the dissolution-extraction method, quenching experiments, hot-stage microscopy, liquid-phase-epitaxy or crystal-growth experiments, differential thermal analysis, etc., (Roy 1992, Chen 1998). To determine the liquidus surface, a number of quasibinary sections "$NdBa_2Cu_3O_{7-\delta}$–$Ba_3Cu_nO_y$ (n = 5–7)" were evaluated by means of thermal analysis by Kuroda et al. (1996, 1997a), and such an approach is quite common. Unfortunately, the complexity of the ternary phase relations, copper valence change and the slow equilibration with the external gaseous atmosphere, the sluggish reactions typical for peritectic systems, a possible liquid supercooling, contamination due to crucible corrosion (Al_2O_3), and other problems, make this method uncertain in a number of cases. Klemenz and Scheel (1993, 1999a) applied another method based on crystal growth and liquid-phase epitaxy experiments. Aswal et al. (1998, 1999a,b, 2000) and Nishimura et al. (1999) used high-temperature optical microscopy and different oxygen atmospheres to observe in situ phase transformations including melting and crystallization events as well as the liquidus position. Emelchenko et al. (1991) and Maljuk et al. (1995, 1996) employed a complex of methods (visual-polythermal, "last droplet", XRD, DTA) to investigate the solubility of Nd_2O_3 (Nd_2CuO_4) in copper oxide melts. A successful technique of melt composition analysis has been applied by Krauns et al. (1994a), M. Nakamura et al. (1996a,b), Kambara et al. (1998), Yao and Shiohara (1997), Sumida et al. (1995), Tagami et al. (1997), Goodilin et al. (1997a), Yoshizumi et al. (2000) and Qi and MacManus-Driscoll (2000). In this method, single crystals of MgO connected with an alumina rod were used to take a small portion of the solution by dipping into the melt. The stuck melt was analyzed by inductively coupled plasma atomic emission spectroscopy (sect. 6.7). Single-crystalline MgO is the most suitable material for such a procedure because it only slightly reacts with the high-temperature cuprate melt and it provides only a small Mg contamination (~0.5 at%) to interfere with the measurement of rare-earth element solubility (M. Nakamura et al. 1996b, Tellez et al. 1999). Another feature of the method is using a large number of experimental points (small temperature step) compiled both from heating and cooling ramps in order to improve the statistical representation and to guarantee the reproducibility of the data.

Obviously, the application of contamination-free crucibles of Y_2O_3, Nd_2O_3 etc., long-term (3–10 h) holding period at every temperature as well as the direct sampling of the melt are other objective advantages, which compensate for the time spent in equilibrium data collection. From these experiments it has been discovered that, in general, the solubility is higher at higher temperatures, higher p_{O_2}, for rare-earth elements with larger ionic radii, and for fluxes with larger copper content.

As a first example, the liquidus lines of yttrium for the $3BaCuO_2 + 2CuO$ melt at 1, 0.21 and 0.02 atm oxygen pressures were investigated by Krauns et al. (1994a) and M. Nakamura et al. (1996b) to establish the effect of oxygen partial pressure on the phase equilibria (fig. 6a). When comparing the results with literature data, it should be noted that the solubility of Y calculated by B.J. Lee and Lee (1991) is about twice as high, and the solubility of Y reported by Maeda et al. (1989) on the basis of DTA measurements is approximately four times higher, than the solubility in air given in fig. 6a. A similar discrepancy was reported by Chen (1998). The reasons for this difference are illustrative since Maeda et al. used a Pt crucible which reacts with the melt, while the calculations of Lee et al. are judged by the initial set of literature data accepted (sect. 3.1.1). The bends in slopes in fig. 6a correspond to the Y123 phase peritectic temperatures at each p_{O_2}. These results indicate that higher oxygen partial pressure raises the peritectic temperature and decreases the steepness of the liquidus. As a result, the solubility of Y at the peritectic temperature is higher at higher p_{O_2} (~0.4 at% Y at 0.02 atm of oxygen and 985°C, 0.6 at% Y at 1005°C and 0.21 atm, 0.7 at% Y at 1030°C and 1 atm). For comparison, the neodymium solubility data are presented in table 1. No drastic variation in the liquidus steepness is observed in this case.

Secondly, fig. 6b shows the liquidus of R = Y, Yb, Dy, Gd, Sm and Nd in the $(3BaCuO_2 + 2CuO)$ melt under an air atmosphere (Shiohara and Endo 1997). The peritectic temperature (T_p) increases with decreasing atomic number of R element (i.e., with increasing ionic radius). This trend is reported by several groups (fig. 7). Simultaneously, the liquidus slope in the "R123-liquid" field decreases and solubility increases for rare-earth elements with smaller atomic numbers (larger radii) near their T_p. Among them, Sm and Nd feature the highest solubility at T_p (about 1.7 and 3.2 at%, respectively, i.e. several times higher than that for Y). The changes of liquidus slope and solubility, which are the most important factors for crystal growth, are similar with an increase of both the atomic number of R and the oxygen partial pressure.

The third example is given in fig. 6c for different Ba:Cu ratios in the Nd–Ba–Cu–O system (Kambara et al. 1998, Goodilin et al. 1997a). As one can see, higher temperature results in a higher solubility of Nd in a solvent with a fixed composition. A higher copper content in the Ba–Cu–O solvent also increases the solubility. Accordingly, the actual liquid composition should always be taken into consideration together with the influence of temperature. Both of the factors discussed lead to a range of Nd content in fig. 6c from 0.5–4.9 at% at 1000°C to 2.3–7 at% at 1065°C (note that the figure includes only a part of the liquidus). Moreover, it is easy to see that the liquidus have different slopes with respect to the Cu:Ba ratio. This occurs because of an exchange of the equilibrium solid phase from Nd123ss to Nd201 (sect. 3.1.2.3). The boundary

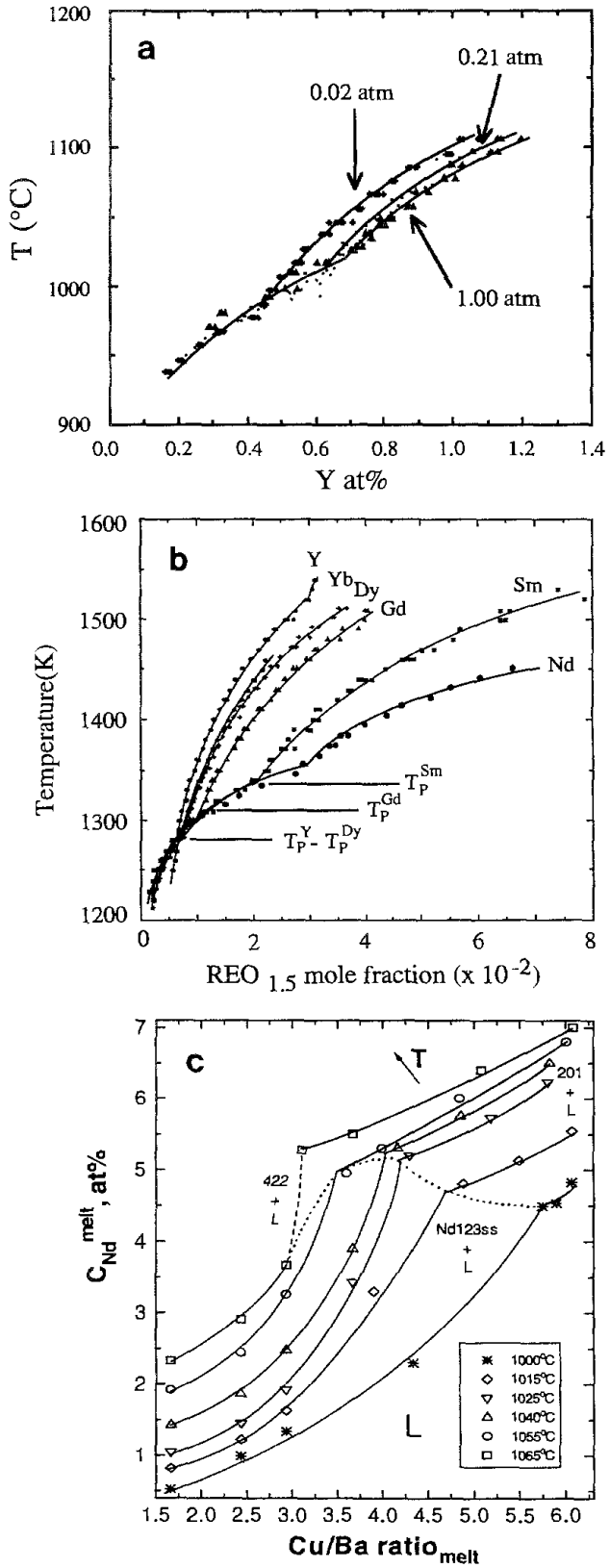

Fig. 6. The influence of different parameters on the R-element solubility in barium–copper oxide melts (M. Nakamura et al. 1996b, Yao and Shiohara 1997, Goodilin et al. 1997a): (a) Y^{3+} solubility increase with an increase of temperature and p_{O_2}; note that bending in the slope occurs at the temperatures of Y123 peritectic decomposition. (b) R^{3+} solubility increase with an increase of the ionic radius of R; the maximum of solubility has been observed for rare-earth elements such as Nd and Sm. (c) Nd^{3+} solubility increase with an increase of the copper content in the melt; the dotted line corresponds to points of triple equilibria ($Nd_{1+x}Ba_{2-x}Cu_3O_z + Nd_2CuO_4 + L$) or ($Nd_{1+x}Ba_{2-x}Cu_3O_z + Nd_4Ba_2Cu_2O_{10} + L$).

Table 1
Liquidus lines in different quasibinary $RBa_2Cu_3O_{7-\delta}$–$Ba_nCu_mO_z$ ($0nm$) systems

System	123 phase			T_p, K [±5 K]	C_{REE} at T_p, at% [±0.3 at%]	Liquidus slope below/above T_p, K/at%	Stable phase	"211-like" phase		
	A, B in $C_{REE}(at\%) = A\exp(-B/T)$ [±0.3 at%]		ΔH_{diss}, kJ/mol R^{3+} [±10%]					A, B in $C_{REE}(at\%) = A\exp(-B/T)$ [±0.3 at%]		ΔH_{diss}, kJ/mol R^{3+} [±10%]
	A ($\times 10^{10}$)	B ($\times 10^4$)						A ($\times 10^4$)	B ($\times 10^4$)	
Yb-035	–	–	–	<1253	<0.5	–/~227	211	0.958	1.22	101
Y123-035, O_2	0.014	2.47	205	1295	0.73	93/220	211	0.258	1.06	88
air	0.444	2.90	241	1278	0.62	91/230	211	1.08	1.26	105
air[a]	0.37	2.89	240	1278	0.61	101/254	211	0.24	1.06	88
1% O_2	48.9	3.49	290	1255	0.41	110/283	211	0.942	1.25	100
Dy-035, air	0.569	2.91	242	1278	0.73	76/187	211	2.02	1.32	110
Gd-035, air	0.484	2.93	244	1318	1.07	55/120	211	3.46	1.37	114
Sm-035, air	4.13	3.19	265	1333	1.67	33/67	211	9.03	1.44	120
Nd123-035, O_2	11.6	3.33	277	1384	3.51	14/36	422	20.0	1.52	126
air	125	3.62	301	1359	3.10	15/37	422	47.5	1.62	135
1% O_2	3910	3.99	332	1316	2.02	17/49	422	138.0	1.77	147
Pr-013, air	0.125	2.55	212	1244	1.50	40/100	110	0.554	1.02	85

[a] Independent measurement.

between "201 + Liquid" and "Nd123ss + Liquid" fields ("Nd123ss–201–Liquid" three-phase equilibrium points) is shown schematically in fig. 6c by a dotted curve as explained in sect. 3.1.2.4. A broken line exhibits a concentration jump due to the appearance of a new (422 + Nd123ss + Liquid) equilibrium near 1065°C (sect. 3.1.2.4). Thus, the liquidus is very sensitive to any transformation of the equilibrium solids.

At the same time, a number of important thermodynamic parameters can be estimated quantitatively from equilibrium solubility curves:

(1) the dissolution enthalpy ΔH_{diss} of a solid phase in the melt can be established by linearisation in the coordinates $\ln(c)$–$1/T$, since $-(\Delta H_{diss}/R)\times(1/T) + \text{const.} = \ln(c^{melt})$, where c^{melt} is the experimentally measured concentration of R^{3+} in the melt of a fixed Ba:Cu ratio (quasibinary system assumption, Krauns et al. 1994a). Klemenz and Scheel (1996) suggested a similar formula $L_{sol} = RT_1T_2(\ln c_{sat}(1) - \ln c_{sat}(2))/(T_1 - T_2)$ in order to determine the partial heat of a saturated solution L_{sol} over the temperature range T_1 to T_2 and the concentration range $c_{sat}(1)$ to $c_{sat}(2)$.

(2) The peritectic temperature T_p is established by bends in the slope of the solubility curve since an equilibrium solid phase and its dissolution enthalpy are different below and above T_p.

(3) The hypothetical congruent melting temperatures, are included in the "const." term in item (1).

(4) The standard free energy of the peritectic reaction "a_1 211 + L + a_2 O_2 = a_3 123" is established by an analysis under different p_{O_2} atmospheres with the relationship $\Delta G^0 = a_2 RT_p \ln(p_{O_2})$ (Kambara et al. 1997c, Lindemer and Specht 1996).

(5) the Jackson α-factor (sect. 2.3.1) for the R123 phases, assuming $\alpha = (1 - E_{att}/E_{cr}) \times \Delta H_{diss}/(RT)$, where E_{att} and E_{cr} are the attachment and crystallization energies (M. Nakamura et al. 1996b).

The calculated data are summarized in table 1 (see also Notes added in Proof, point 1). Most of these equations are restricted to a regular solution (at least, diluted) and some additional conditions are necessary in each case as well. However, several important interrelations become clear after such calculations and they are indeed quite reasonable, as shown in fig. 7. In this picture several parameters rise simultaneously when the ionic radius of R becomes larger: (1) the thermal stability as characterized by the peritectic decomposition temperature, (2) the thermodynamic stability or dissolution enthalpy of the R123 phases, (3) the supersaturation capability because the liquidus slope near the peritectic temperature decreases with an increase of the ionic radii. All these changes are explained by the higher geometrical stability of the R123 perovskite lattice for larger R (the tolerance factor or bond length mismatch for a stable lattice is between 0.8 and 1.0, Manthiram et al. 1990). A similar universal relationship is suggested using the Madelung expression for the lattice (cohesive) energy by Osamura and Zhang (1993): $T_p \times R_0^2 = A(R_0 - \rho^*)$, where R_0 is the nearest-neighbour ionic distance, A is a constant which only depends on the crystal structure, and ρ^* is the screening distance (~0.16 nm for R123, 0.13 nm for R211).

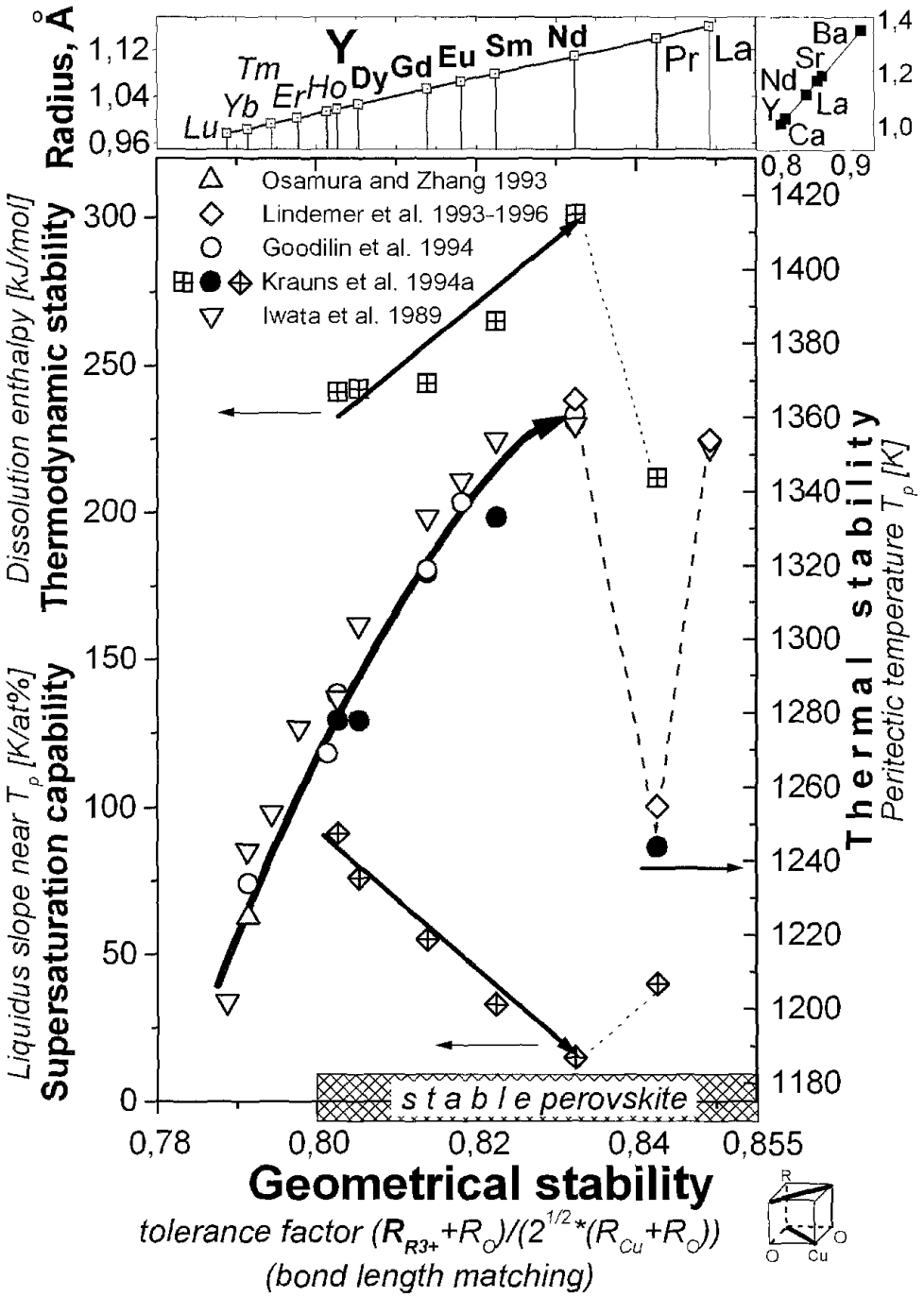

Fig. 7. Dependencies of thermal (peritectic decomposition temperature) and thermodynamic (dissolution enthalpy) stability of R123 lattices upon their geometrical stability, calculated using ionic radii of R^{3+} (top of the picture). For a stable perovskite lattice, bond length mismatch or the tolerance factor $\frac{R_{R^{3+}} + R_{O^{2-}}}{\sqrt{2}(R_{Cu^{2+}} + R_{O^{2-}})}$ should be within the 0.8–1.0 range. Note that for R^{3+} with larger radii all the parameters (geometrical, thermal, thermodynamic stability) are coupled and become obviously larger, supersaturation capability is higher as well (slope near T_p is smaller). At the same time La and especially Pr demonstrate anomalous behavior connected with peculiarities of their phase diagram.

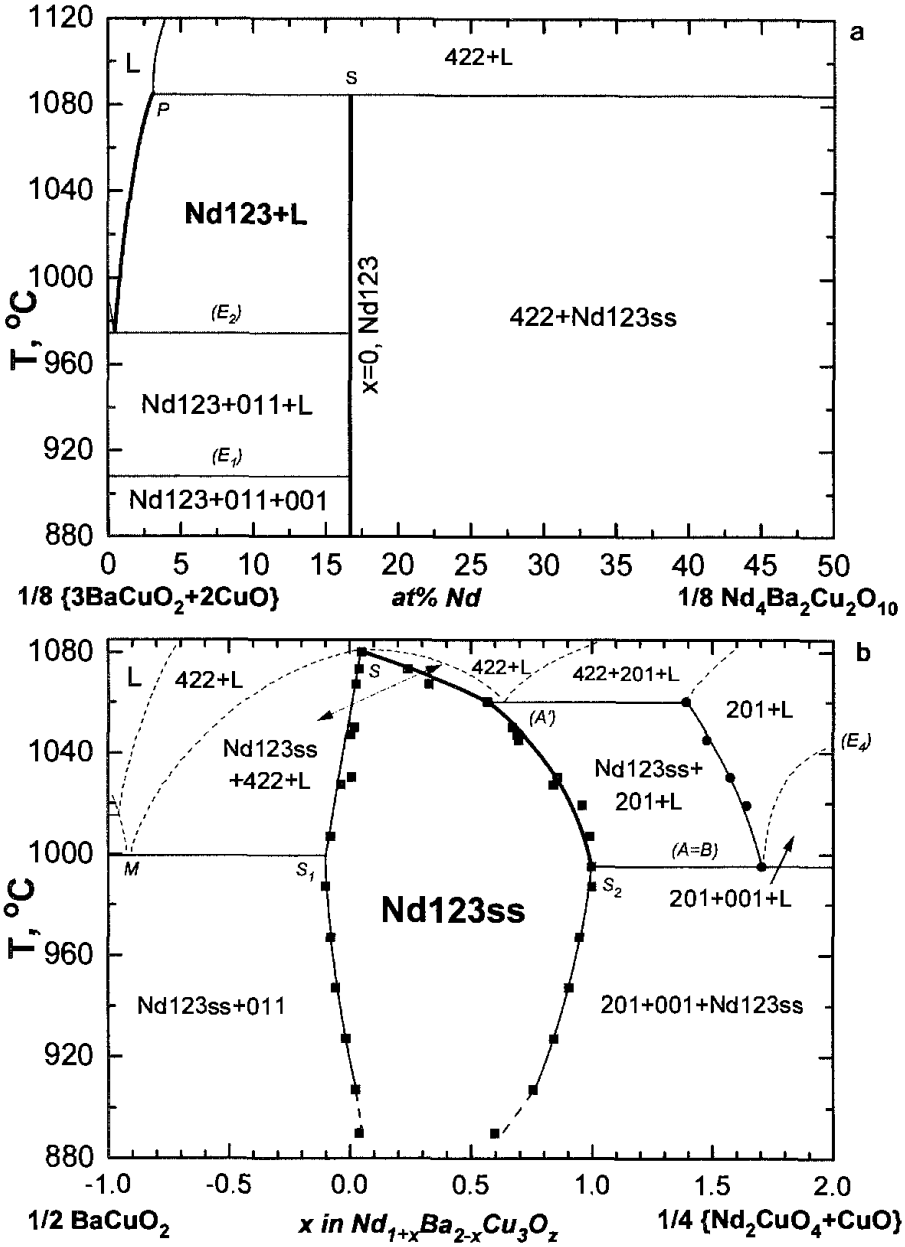

Fig. 8. Selected quasibinary sections through the $Nd_{1+x}Ba_{2-x}Cu_3O_z$ solid solution field (solid symbols and lines represent experimental data taken from different works; dotted lines give schematically boundaries of possible phase fields): (a) $\frac{1}{8}(3BaCuO_2+2CuO)-\frac{1}{8}\ Nd_4Ba_2Cu_2O_{10}$ section containing the $x=0.0$ phase; (b) $\frac{1}{2}BaCuO_2-\frac{1}{4}(Nd_2CuO_4+CuO)$ section and the actual shape of the Nd123ss field. Note that solid solution is extended between S_1 and S_2 ($S_2 \approx 1.0 = x_{lim}$) and the S point does not necessarily correspond to the $x=0.0$ substitution.

3.1.2.2. *"$Nd_4Ba_2Cu_2O_{10}$–$(3BaCuO_2+2CuO)$" section.* This quasibinary section (fig. 8a) is important for a number of techniques of Nd123 single-crystal production since the Nd123 phase (assuming $x=0$) belongs to the "422–035" section and the Nd123 phase

formation takes place via the interaction of 422 with the melt of the $3BaCuO_2 + 2CuO$ composition (Ba : Cu is 3 : 5). Phase relationships in the vicinity of the Nd123 phase in air change with temperature, as studied, for example, by K. Oka and Unoki (1990), Kuroda et al. (1996, 1997a) and Kambara et al. (1997c). The last work combines DTA data, the results of quenching experiments and direct solubility measurements (sect. 3.1.2.1); it was confirmed also by crystal growth and EPMA measurements. At the same time, Kuroda et al. employed mainly DTA data. Nevertheless, all of these works consider the Nd123 phase peritectic melting temperature (points S and P for the solid phase and an equilibrium liquid respectively, data in table 1) as high as 1090°C: 1090±10°C (K. Oka et al.), 1080°C (Kuroda et al.), 1086°C (Kambara et al.; see, however, discussion in sect. 3.1.2.3). The first liquid due to the $BaCuO_2 - CuO$ binary eutectic (E_1, sect. 3.1.1) appears at 900±10°C (K. Oka et al.), 890°C (Kuroda et al., W. Zhang et al. 1990), 906°C (Kambara et al.), and finally the $BaCuO_2$ disappears (E_2) at about 970±10°C (K. Oka et al.) or 976°C (Kambara et al.). Thus, the data are in reasonable agreement and the "Nd123 + L" two-phase coexistence region, allowing one to form the Nd123 from the melt, is expanded between 970–975°C and 1080–1090°C.

3.1.2.3. *"$BaCuO_2$–(Nd_2CuO_4 + CuO)" section and $Nd_{1+x}Ba_{2-x}Cu_3O_z$ solid-solution field.* This section (fig. 8b) is directed exactly along the Nd123ss solid-solution field. For LR with large ionic radii the $Y_2Cu_2O_5$-type phases become structurally unstable (Wong-Ng et al. 1994), therefore no real quasibinary section "LR123ss–LR202" exists or, in other words, to form the solid solution, two phases (LR201 and CuO) must be "dissolved" simultaneously in the LR123 ($x = 0.0$) phase. The quasibinary system under question demonstrates other essential differences in the phase diagram from the Y case and it is very instructive to understand how the presence of a solid-solution field affects the phase relations and how it changes conditions available for crystal growth.

It should be noted first of all that the substitution of Ba with Nd initiates structural transformations of the Nd123ss in the solid state as well as changing its physical properties (Segre et al. 1987, Zhang et al. 1987, F. Izumi et al. 1987, Li et al. 1988, Takita et al. 1987, 1988, 1992, Kramer et al. 1994b, Fomichev et al. 1994, Goodilin et al. 1996, Skakle 1998, Tretyakov and Goodilin 2000), and that is the most important motivation to select appropriate conditions for single-crystal growth. At high p_{O_2} (air or oxygen), the solubility limit in the Nd123ss solid phase up to $x = 1.0$ is attainable (Osamura and Zhang 1993, Goodilin et al. 1996, 1997b). This region can be subdivided into three parts. In the first ($0 \leqslant x \leqslant 0.3$–$0.4$), the as-prepared samples are tetragonal ($a = b < c/3$) and both a and $c/3$ decrease with increasing x. The Nd123ss solid solution of this range undergoes a tetragonal-to-orthorhombic transition upon atmospheric oxygenation. The higher Nd content destroys the orthorhombicity of such a solution and at $x = 0.3$–0.6 both as-prepared and fully oxygenated Nd123ss are quasicubic with $a = b \approx c/3$. For more extensive substitution, at $x = 0.7$–0.9, an orthorhombic distortion of the tetragonal structure occurs both for as-prepared and oxygenated samples.

The structure of less-substituted Nd123ss is based on the parent structure of $NdBa_2Cu_3O_{7-\delta}$ with a partial substitution of Nd^{3+} for Ba^{2+} and oxygen ion rearrange-

ment (F. Izumi et al. 1987, Kramer et al. 1994b, Skakle 1998). The main feature of the Nd213 phase is the increase of the basic primitive subcell because of the superstructure $a' = 2a_{sub}$, $b' = b_{sub}$, $c' = 2c_{sub}$ (Goodilin et al. 1996, Petrykin et al. 1999b, see also sect. 6.11). The orthorhombic $Nd_{1+x}Ba_{2-x}Cu_3O_z$ solid solution at $x = 0.9$ has the $a \neq b \neq c/3$ relationship between its sublattice constants as evident from its in-situ measured, high-temperature XRD pattern (1000°C, air, fig. 9). Moreover, both at high and at room temperature the 107 and 117 peaks near $2\Theta \approx 28$ and 37.5°, respectively, are supposed to be the brightest superstructure peaks of this new orthorhombic phase, indicating that ordering phenomena occur at a high level of substitution in the Nd123ss. An orthorhombic-to-tetragonal phase transition has not been observed for the $Nd_{1.9}Ba_{1.1}Cu_3O_z$ composition (Goodilin et al. 1998b). All these structural differences might have interrelations with the Nd123ss thermodynamic properties, at least the large wideness of the solid solution field prohibits several possible tie-triangles such as "Nd213–422–L", and the overall picture becomes more complicated.

From fig. 8b it is evident that in the left part of the "011–(201 + 001)" section the Nd123 and $BaCuO_2$ solids are present below about 1000°C, however above this temperature (S_1) the Nd123ss solid solution with minimum substitution of Ba with Nd can be in equilibrium only with the 422 phase and liquid as discussed in sect. 3.1.2.2. Consequently, this important equilibrium relation should be considered quantitatively rather than qualitatively (sect. 3.2.2). At the same time the Nd123ss solid solution with higher neodymium content in the right-hand part decomposes at lower temperatures than the Nd123 phase ($x \rightarrow 0$, S) and it can be in equilibrium with Cu-rich melt and different solid phases: $Nd_4Ba_2Cu_2O_{10}$ (1060–1085°C) or Nd_2CuO_4 (995–1060°C). At high temperatures less-substituted Nd123ss solid solution ($x < 0.6$) and the 422 phase are allowed to be in equilibrium with liquid only (Bieger et al. 1996, Kambara et al. 1998). The temperature decrease causes broadening the Nd123ss field and below 1060°C (A′, $x \approx 0.57$ in air, Goodilin et al. 1997b) the $Nd_{1+x}Ba_{2-x}Cu_3O_z$ with maximum x values coexists with the Ba-less high-temperature stable Nd_2CuO_4 phase (201) and the Cu-rich liquid. One can observe slightly different slopes of the solidus above and below 1060°C (table 2) because of the equilibrium solid-phase exchange from 422 to the 201. At lower temperatures, the stability region of Nd123ss is extended enough (from S_1 to S_2) and its maximum range was found in air at ~990°C ($0.0 \leqslant x \leqslant 1$) as mentioned. Below this temperature a mixture of solid phases (Nd123ss + CuO + Nd_2CuO_4) is present.

Thus, in the "$\frac{1}{2}BaCuO_2$–$\frac{1}{4}$(Nd_2CuO_4+CuO)" quasibinary system, two melting reactions associated with the Nd123 and Nd213 terminal solid solutions take place in air at about 1000°C in the barium-rich region (S_1 in fig. 8b, Osamura and Zhang 1993), and at about 990°C in the copper-rich region (S_2 in fig. 8b, Osamura and Zhang 1993, Goodilin et al. 1997b). The first reaction occurs due to expansion of the liquid field originated from the $BaCuO_2$–CuO binary eutectic through the line connecting $BaCuO_2$ and $NdBa_2Cu_3O_{7-\delta}$ points. This temperature (M) is obviously higher than that in the 422–(3$BaCuO_2$ + 2CuO) quasibinary system (E_2 in fig. 8a, 970°C), however, it is perhaps lower than the decomposition temperature of $BaCuO_2$ (1015°C, Aselage and Keefer 1988; 1016°C, Zhang et al. 1990). Goodilin et al. (1997b) found traces of $BaCuO_2$ in quenching

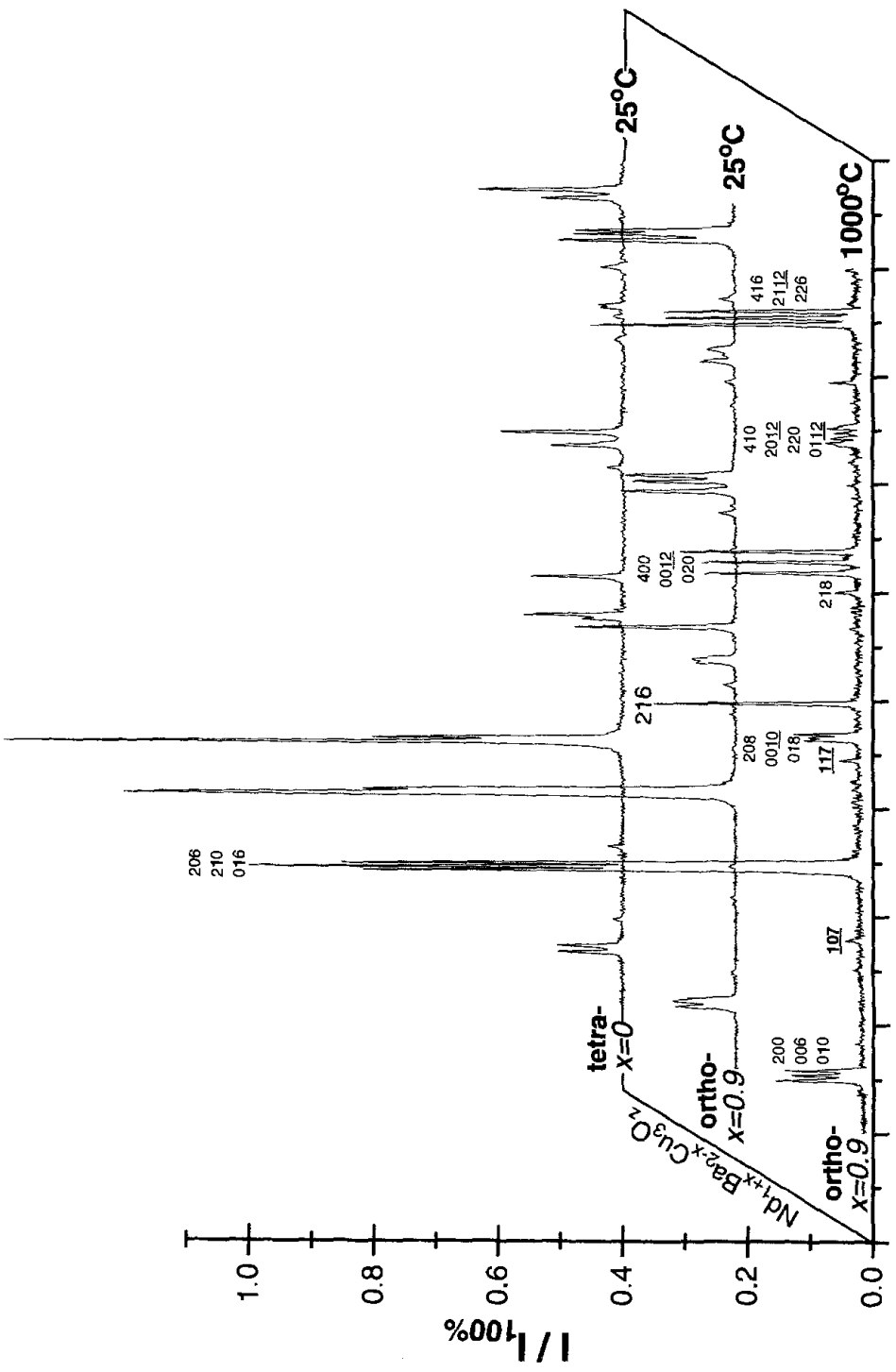

Fig. 9. High-temperature X-ray diffraction pattern of the $Nd_{1.9}Ba_{1.1}Cu_3O_z$ phase taken at 1000°C in air, which demonstrates orthorhombicity of this phase (multiple triplets) as well as the presence of superstructure peaks (107 and 117 as the brightest ones). The same is observed at room temperature and no orthorhombic-to-tetragonal transition exists for this Nd-rich phase. On the contrary, the oxygen- and "Nd-poor" $NdBa_2Cu_3O_{7-\delta}$ phase, annealed at 1000°C, possesses a tetragonal symmetry of the lattice.

Table 2
The $Nd_{1+x}Ba_{2-x}Cu_3O_z$ solidus in Arrhenius coordinates $-\ln((1+x)/6) = A/T + B$

T (°C)	x range	equilibrium secondary phase	A	B	R	SD
1020–1060	0.95–0.6	201	−8.8(6)	8.0(5)	0.9906	0.0114
1060–1084	0.6–0.02	422	−34(3)	27(2)	0.9851	0.0296

experiments and the EPMA study at 995°C for compositions close to $BaCuO_2$ in the "Nd123–L–$BaCuO_2$" region. Kambara et al. (1998) observed that at 1030°C no $BaCuO_2$ is present and, on the other hand, the "123–L" boundary of the "422–123–L" tie-triangle still does not pass through the $BaCuO_2$–123 line within the experimental accuracy. However, it certainly takes place above 1045°C because the "422–L" field penetrates deeply in the quasibinary section under question.

The second, 990°C, reaction in the copper-rich corner is connected with the Nd213-phase peritectic decomposition, and it is suitable to discuss it later using a 3D model of the phase relations. However, since the melting reactions are present, it perhaps means that the terminal solid solutions with minimum and maximum substitutions (x) exist only at about 1000°C and 990°C, respectively. In other words, if the temperature rises, both left and right boundaries of the solid solution field (S_1S and S_2S) might asymmetrically incline toward a point between them (S), i.e. the width of the Nd123ss field becomes smaller. Most probably, this is the solid solution with $x = 0.02$–0.05 substitution which is often considered as a "single-phase Nd123" and has the maximum melting/decomposition temperature around 1090°C as discussed in sect. 3.1.2.2. At the same time, the $x = 0.0$ phase may have a lower decomposition temperature (Iwata et al. 1989, Osamura and Zhang 1993, Kambara et al. 1998, Goodilin et al. 2000). Wu et al. (1997, 1998) noted that the maximum melting temperatures do not occur at the stoichiometric $x = 0.0$ compound both in air and pure oxygen. At $p_{O_2} = 1$ atm the maximum corresponds to about $x = 0.1$ substitution while at lower p_{O_2} it shifts to $x \approx 0.05$ ($p_{O_2} = 0.01$–0.2 atm) and then close to $x \approx 0.0$ at $p_{O_2} = 0.001$ atm.

In the literature, many authors have reported difficulties in the formation of the stoichiometric $x = 0.0$ Nd123 phase, especially with high T_c values (see, for example, Lindemer et al. 1995 and Murakami et al. 1996). On the other hand, at about 500–600°C a number of authors reported formation of $BaCuO_2$ and a solid solution with a small x value due to decomposition of the polycrystalline $x = 0.0$ phase (Okai et al. 1988, Goodilin et al. 1996). This is consistent with a suggestion that at temperatures below the S_1 point the Nd-enriched solid solution is more stable again, as well as that in the right part the barium-enriched solid solution forms below the S_2 point. Wu et al. (1997, 1998) confirmed that the solid-solution field becomes narrower at lower temperatures, at least from the Ba-rich side. A specific finding of Osamura and Zhang (1993), Goodilin et al. (1996), C.T. Lin et al. (1996), Murakami et al. (1996), Yoshizumi et al. (2000), N. Watanabe et al. (1998) and Osabe et al. (2000) is a possible "negative" substitution in Nd123ss (solubility

of $BaCuO_2$ at S_1) ranging from −0.03 to −0.1. On the other hand, Wu et al. (1997, 1998) found that the solid solution is limited to a very narrow range of $-0.05 < x < 0.05$ at 990°C in $p_{O_2} = 0.001$ atm and does not expand beyond the $x \approx -0.05$–0.0 composition at higher p_{O_2} to form the solid solution with larger "negative" x. These important data about the Ba substitution for the Nd site have not yet been finally confirmed. In summary, the possible substitution range in Nd123ss might be assumed as $-0.1 \cdots 1.0$ with a maximum melting temperature at about $x = 0.02$–0.05. Most probably, this is connected with the possibility of a complex ordering of Ba and Nd in the Nd123ss lattice. The influence of p_{O_2} on the shape of the solid solution field will be discussed briefly below [fig. 11b, Osamura and Zhang 1993, Goodilin et al. 1996, 1998b, Kambara et al. 1998, Yoshizumi et al. 2000, Yoo and McCallum 1993, Lindemer et al. 1995, Wu et al. 1997, 1998, Kramer et al. 1994a, Bieger et al. 1996; some data from the above-mentioned papers have been excluded because of uncertainty of the dynamic DTA experiments at high heating rates (10°C/min), especially under low p_{O_2} atmosphere].

3.1.2.4. *Three-dimensional model of Nd–Ba–Cu–O phase diagram (copper-rich corner).* In fig. 10a, a number of experimental isothermal quasiternary sections of the copper-rich corner of the Nd–Ba–Cu–O phase diagram in air are presented (Goodilin et al. 1997b) together with a projection of liquidus onto the $BaCuO_2$–CuO–Nd_2CuO_4 plane (Goodilin et al. 1998b). The 3D model in fig. 10b is compiled from these sections as suggested in sect. 3.1.2. It summarizes the results of several phase diagrams which were found to be in satisfactory agreement. To construct a solid-solution field (thick black lines), data of Osamura and Zhang (1993), Yoo and McCallum (1993), Kambara et al. (1998) and Goodilin et al. (1997b) were used (as in the sect. 3.1.2.3). Liquid surfaces (thick light-gray lines), quantitative solid–liquid relations and equilibrium tie-lines (thin gray lines) were taken from results of M. Nakamura et al. (1996a), Kambara et al. (1998) and Goodilin et al. (1997a). Solidus points S, S_1, S_2, peritectic decomposition temperature P, eutectic E_1, E_2, A′ and M points correspond to those discussed in sects. 3.1.2.2 and 3.1.2.3. The eutectic point E_4 in the Nd–Cu–O system was accepted as 1045°C and 90 mol% of CuO in accordance with K. Oka and Unoki (1989) and Osamura and Zhang (1993).

As soon as liquid appears in the copper-rich corner (E_1), the terminal Nd123ss solid solution turns out to be in equilibrium with CuO and liquid. In this case a tangent to the liquid composition curve cuts the "Nd123ss–CuO" side of the "Nd123ss–CuO–L" tie-triangle and a mixture of both CuO and Nd123ss can form the liquid L with increasing temperature, $Nd123ss + CuO_x \rightarrow L$. This is a reaction ($E_3$) of the eutectic type (West 1982). The same reasoning leads to the conclusion that "Nd201–CuO_x–L" tie-triangles at higher temperatures describe the eutectic liquid formation and the "B" triple equilibrium points represent the path of the liquid compositions participating in the $Nd201 + CuO_x \rightarrow$ L eutectic reaction (fig. 10). The maximal expansion of the "Nd201 + Liquid" field occurs when the Nd_2CuO_4–CuO eutectic temperature is exceeded in the "Nd_2O_3–CuO" quasibinary system (E_4).

At 995–1060°C the Nd123ss phase equilibria are different. A tangent drawn to the liquidus L at the liquid composition corner (A) of the "Nd123ss–Liquid–Nd201" tie-

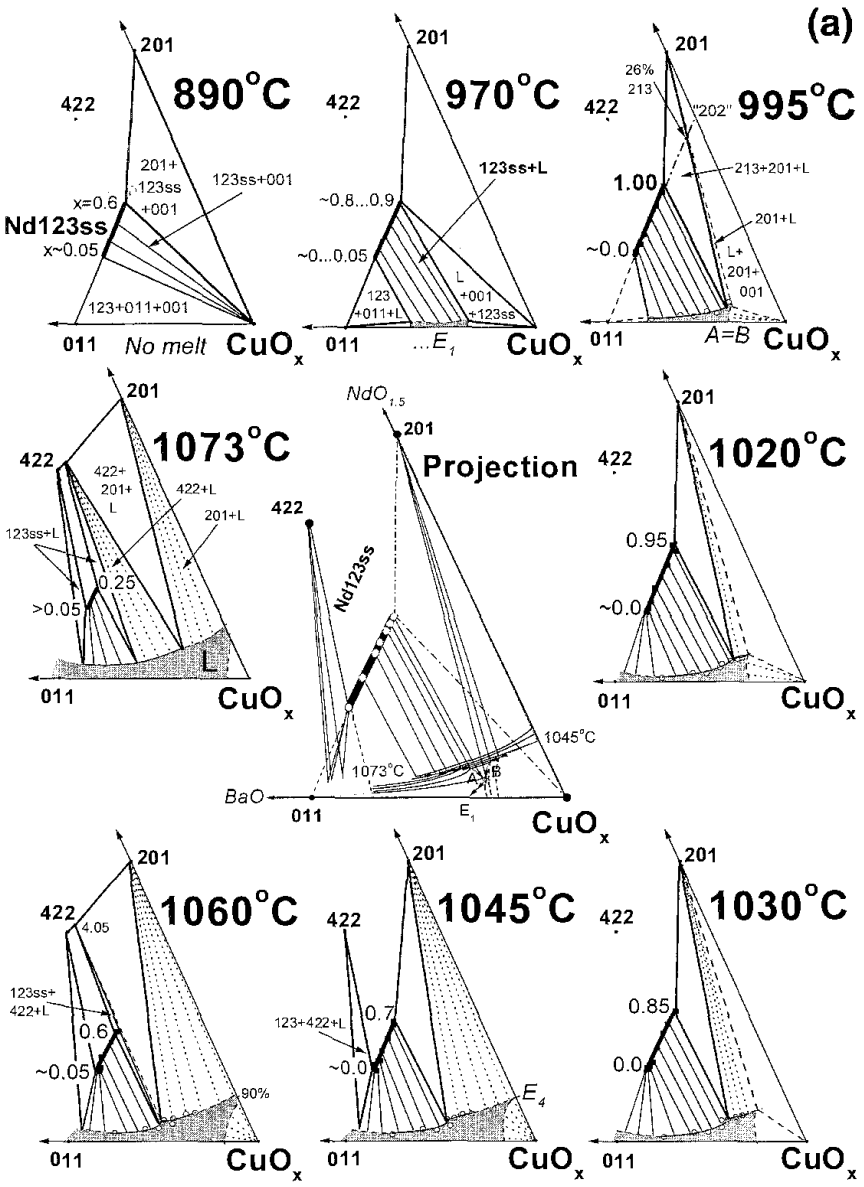

Fig. 10. Three-dimensional model of the phase relations in the copper-rich corner of the Nd–Ba–Cu–O system in air at 890–1090°C: a. partial set of quasi-ternary isothermal sections used for construction of the 3D diagram (Goodilin et al. 1997b); b. three-dimensional view of the phase relations (Osamura and Zhang 1993, Yoo and McCallum 1993, Kambara et al. 1998, Goodilin et al. 1997a,b, K. Oka and Unoki 1989). Thick dark lines represent the $Nd_{1+x}Ba_{2-x}Cu_3O_z$ solid solution field and thick light-gray curves give experimentally determined liquidus position at different temperatures. Tie-triangles and tie-lines (partially) are given by thin lines. 422 phase is marked tentatively as a solid solution compound. S_1SS_2 contour is a part of the Nd123ss solid solution field coexisting with liquid (high-temperature stability boundary). The $E_1E_2MPA'AE_3E_1$ loop is a range of liquid composition in the equilibrium with the Nd123ss solid phase (at different temperatures). E_1 and E_4 are eutectic points in the $BaCuO_2$–CuO and Nd_2CuO_4–CuO quasibinary system, respectively. P and S points correspond to the liquid and solid phase compositions at the peritectic decomposition temperature of Nd123 ($x \approx 0$). The A′ point reflects bending at the liquidus and solidus curves due to a secondary phase exchange in the equilibria (Nd123ss+201+L)/(Nd123ss+422+L). Arrows (PA′A and E_4B) indicate a path of liquid composition down to the point of the peritectic–eutectic reaction Nd213+CuO → 201+L.

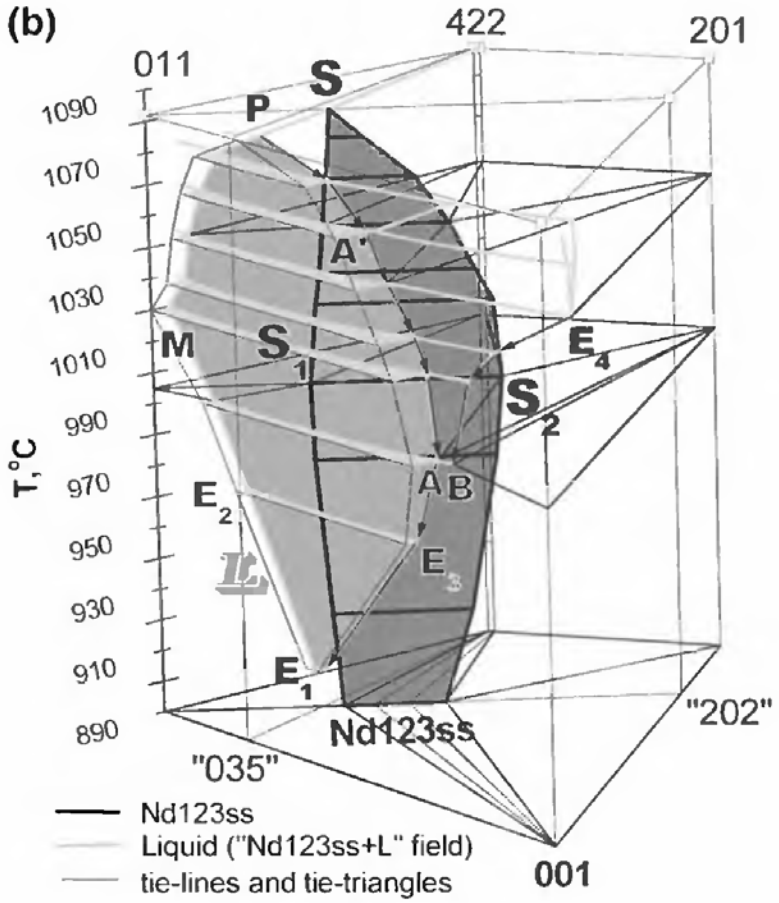

Fig. 10 (continued).

triangle is placed outside the triangle and cannot intersect the "Nd123ss–Nd201" side. Consequently, the reaction Nd123ss → Nd201 + L has to be considered as peritectic and the points "A" (Nd123ss–Nd201–L) represent the liquid composition curve for this reaction. Above 1060°C the "A′" points represent the same for the reaction Nd123ss → Nd422 + L. The "Nd123ss–L" two-phase field above 1060°C becomes jammed from both the barium-rich and copper-rich ends by the "Nd123ss($x \to 0$) + Nd422 + L" and "Nd123ss($x > 0$) + Nd422 + L" three-phase fields which collide into the one two-phase field "Nd422–L" after Nd123 phase decomposition (P point for the liquid).

With lower temperatures, the "A" and "B" points move toward the intersection A = B in the Cu-rich region (P–A′–A and E_4–B). At 990–995°C the above-mentioned curves intersect each other and this temperature has to be accepted as the point of the invariant peritectic–eutectic reaction

$$\text{Nd123ss} + \text{CuO} \rightarrow \text{Nd201} + \text{L}. \tag{17}$$

From this point the eutectic valley trajectory for the reaction L → Nd123ss + CuO runs to lower temperatures (A–E_3–E_1) and the projected points shift away from the

A=B intersection. Therefore, the $x=1.0$ composition actually represents the upper possible level of substitution in Nd123ss, at least at $p_{total}=1$ atm and $p_{O_2}=0.21$ atm (sect. 3.1.1). The corresponding invariant reactions are given in table 3.

Thus, in principle, a wide temperature range and a wide range of liquid compositions inside the E_1–E_3–A–A′–P–M–E_2–E_1 loop are available for the Nd123ss single-crystal growth. However higher viscosity and low Nd solubility in liquid make "eutectic" temperatures below 990–1000°C unattractive for bulk crystal growth (without additives such as BaF_2, sect. 3.2.1; see, however, Emelchenko et al. 1994). Actually the crystal growth has to be associated with a peritectic reaction. On the other hand the upper temperature limit for neodymium-rich Nd123ss solid-solution growth is determined by the solidus behavior (sect. 3.1.2.3). Accordingly, temperatures ~1070–1080°C and Ba-rich liquid are suitable for growth of $x \rightarrow 0$ Nd123 crystals (although temperatures ~1030°C seem to be better, sect. 3.2.2) while the 995–1060°C range and copper-rich melts are available for growth of neodymium-rich crystals with x values from about 0.6 to 1.0. In practice, to obtain the Nd213 phase, tightly controlled conditions might be demanded because of the small steepness of the solidus near this phase; in other words, it is expected that only a crystal with a slightly smaller substitution can be grown. The steepness of the solidus in the barium-rich region is much greater and the Nd123 phase can be grown easily (sect. 3.1.2.2 and 3.2.1). However, the superconducting critical temperature T_c of this phase is drastically suppressed even by a minor substitution; again, therefore, high-T_c crystals can be grown under some certain conditions only, as will be discussed later.

3.1.2.5. *Oxygen nonstoichiometry and stability of $Nd_{1+x}Ba_{2-x}Cu_3O_z$ at different p_{O_2}.* The phase relations described above and, hence, conditions for crystal growth, can be strongly affected by p_{O_2}, since p_{O_2} has a strong effect on oxygen content in the $R_{1+x}Ba_{2-x}Cu_3O_z$ solid solution. Therefore, it is important to know the relationship between the cation and oxygen nonstoichiometry of the solid solution as well as its stability at different p_{O_2}. The oxygen nonstoichiometry of $YBa_2Cu_3O_{7-\delta}$ and a number of $R_{1+x}Ba_{2-x}Cu_3O_z$ solid solutions (R = La, Pr, Nd) has been systematically studied by Lindemer et al. (1989, 1993, 1994, 1995), Lindemer and Specht (1996) up to $x=0.6$ in the case of $Nd_{1+x}Ba_{2-x}Cu_3O_z$. In fig. 11, the oxygen content (z) in air at $x=0$–0.9 is presented (fig. 11a, Goodilin et al. 1998a,c, Limonov et al. 1998) together with the possible substitution range (x_{lim}) at different oxygen partial pressures (fig. 11b, 0.1–100% oxygen).

As a general feature, at elevated temperatures (1000°C) the formal copper valence and overall oxygen content become higher in the solid solution when x extends from 0 to 0.9 (18% $Cu^{1+} \rightarrow$ 5% Cu^{3+}, $O_{6.26} \rightarrow O_{7.01}$). This phenomenon can be explained by the necessity of additional oxygen uptake to neutralize the charge which appeared because of the heterovalent substitution of Ba^{2+} with Nd^{3+} (F. Izumi et al. 1987, Kramer et al. 1994b, Petrykin et al. 1999a). The temperature lowering demands additional oxygen to be absorbed by the solid solution, i.e. it is directed similarly to the increase of oxygen content at higher substitution x. Consequently, two oxygen-rich regions can be found near the ortho-123 and ortho-213 phases (fig. 11a). In the solid solution a charge transfer takes place between "superconducting" CuO_2 layers and "reservoir" CuO_{1+x} chains

Table 3
Melting reactions in the Nd–Ba–Cu–(O) quasiternary system in air (p_{O_2} = 0.21 atm) and regions available for single-crystal growth of the $Nd_{1+x}Ba_{2-x}Cu_3O_z$ solid solution[a]

Quasibinary system	Reaction[b] (schematically)	Temperature (°C), and liquid composition (at.% Nd, Ba/Cu ratio)	Estimated availability for crystal growth	Remarks
$BaCuO_2$–CuO	011 + 001 → L(e1)	906–911, (0%, 3/7, E_1)	for $x \approx 0$: ltd	low Nd solubility, high viscosity
(3$BaCuO_2$–2CuO)–Nd123[c]	123 + 011 → L(e2)	970–976 (~0.5%, 3/5, E_2)	for $x \approx 0$: ltd	possible with addition of BaF_2, Ag etc.
$BaCuO_2$–Nd123[c]		~1000 (~1%, 3/3, M)	for $x = 0$: ltd	viscosity increasing
(3$BaCuO_2$–2CuO)–$Nd_4Ba_2Cu_2O_{10}$	123 → 422 + L(p1)	1086–1090 at $x \approx 0$ (3.2%, 3/5 or >3/5, P, S)	for $x \approx 0$: av	(see corresponding sections)
Nd123ss[d]–CuO	123ss + 001 → L(e3)	906(e1) → 990(pe2) = $f(x)$	for $0.6 < x < 1.0$: none	low Nd solubility, CuO precipitation
$Nd_2Ba_1Cu_3O_y$–"$Ba_3Cu_{16.5}O_z$"	213 + 001 → 201 + L(pe2)	990 at $x = 1.0$ (4.2–4.5%, 1/5.5–1/5.9, A = B)	for $x \approx 1$: none	solidus slope is small
Nd123ss[d]–(Nd_2CuO_4 + CuO)	123ss → 201 + L(p1')	990(pe2) → 1060(p3) = $f(x)$ (1/5.5–1/2.8, A), see sect. 3.2.2.	for $0.6 < x < 1.0$: av	(see corresponding sections)
Nd123ss[d]–(Nd_2CuO_4 + CuO)	201 + L(p3) → 422	1060 (A')	–	change of a solid phase equilibrated with Nd123ss
Nd123ss[d]–(Nd_2CuO_4 + CuO)	123ss → 422 + L(p1'')	1060(p3) → 1086(p1) = $f(x)$ (1/2.8 up to <3/5), see sect. 3.2.2.	for $0 < x < 0.6$: av for $x = 0$: none	at least small substitution in Nd123ss
Nd_2CuO_4–CuO	201 + 001 → L(e4)	~1045 (~90 mol% CuO, E_4)	–	–

[a] Abbreviations: e, eutectic melting, p, peritectic decomposition, pe, peritectic–eutectic reaction, av, available for crystal growth, ltd, limited possibility for crystal growth, none, not recommended for crystal growth.

[b] e1, e2 and e3 correspond to expansion of the $BaCuO_2$–CuO binary eutectic around the Ba-rich and Nd-rich ends of the Nd123ss solid solution field, respectively; this liquid approaches the Nd_2CuO_4–CuO side and assimilates the e4 binary eutectic at about 1045°C; p1, p1'', p1', pe2 describe the Nd123ss high-temperature stability boundary at $0 < x < 1$ (peritectic decomposition).

[c] Assuming no Nd → Ba and Ba → Nd substitutions.

[d] Terminal compositions at a given temperature.

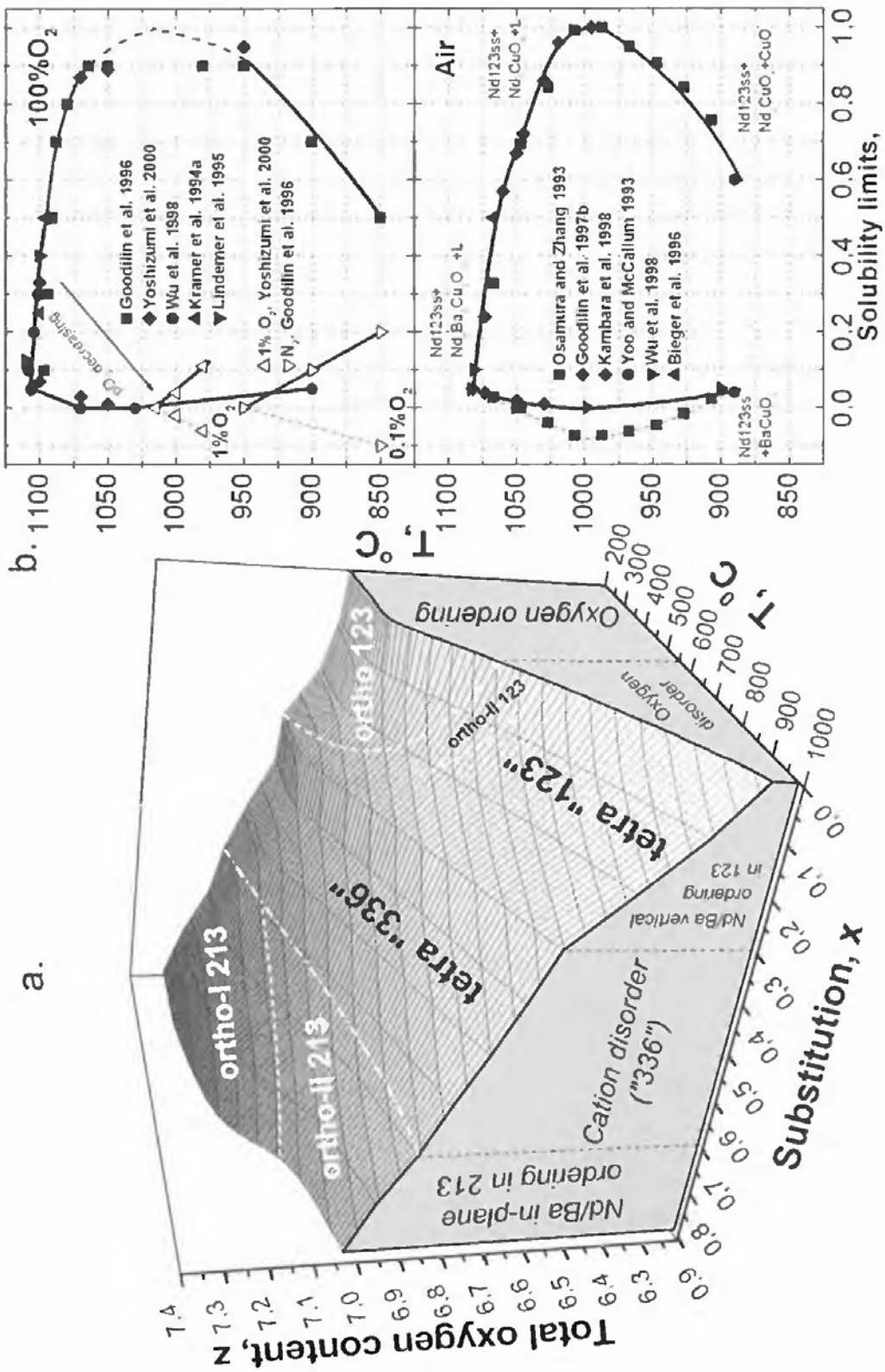

Fig. 11. Relationships between neodymium and oxygen contents (a) in the $Nd_{1+x}Ba_{2-x}Cu_3O_z$ solid solution at $p_{O_2} = 0.21$ atm at different temperatures and (b) the Nd123ss field width at different p_{O_2}. The corresponding positions of possible structural phase transitions are marked tentatively by dotted lines in (a).

(Takita et al. 1988, Akinaga et al. 1988, Kramer et al. 1994b, Petrykin et al. 1999a). As a result, the oxygenated form of the solid solution loses superconductivity above approximately $x \approx 0.3$, but no sign of superconductivity has ever been found for the oxygen-poor solid solution. In other words, only a small range of cation and oxygen contents is available here for high-temperature superconductivity.

From a more specified viewpoint, the $Nd_{1+x}Ba_{2-x}Cu_3O_z$ solid solution, belonging to three different compositional ranges of $0.0 < x < 0.3$, $0.3 < x < 0.6$ and $0.6 < x < 1.0$, exhibits different behavior with respect to the oxygen content (Goodilin et al. 1998a), which is distinguishable by (1) symmetry changes of the crystal lattice (XRD, sect. 3.1.2.3), (2) nonlinear x-dependence of the frequency and linewidth of the apical oxygen mode (Raman spectra), (3) different average copper oxidation state in the quenched or oxygenated samples (iodometric titration and XANES spectra), (4) different oxygen nonstoichiometry (TGA), and (5) different temperature slopes of TGA curves (DTG). The cation and oxygen ordering have a close relationship because of the structural changes in the $Nd_{1+x}Ba_{2-x}Cu_3O_z$ solid solution initiated by the increase of x.

The well-known "123" structure is characterized by a "vertical" ordering of Nd and Ba. Barium-free (CuO_2–Nd–CuO_2) and neodymium-free (CuO_2–BaO–CuO_y) perovskite-like blocks are present in the structure. Therefore, it is the oxygen ordering itself in the basal plane that causes the tetragonal-to-orthorhombic transition of the $x = 0$ phase with a sufficient amount of oxygen. The oxygen nonstoichiometry of the solid solution of this type ($\Delta z_{max} \approx 0.7$ between 300 and 1000°C in air) is the highest. The oxygen ordering is destroyed in the case of extra Nd entering into the Ba sites. It is impossible to keep highly ordered Cu–O chains and unoccupied vacancy chains if Nd at Ba sites requires oxygen atoms to enter occasionally into the vacancy chains. The solid solution of this cation composition (oxygen and cation disordered "336" type, $0.3 < x < 0.6$) is always tetragonal and has a smaller oxygen nonstoichiometry ($\Delta z_{max} \approx 0.4$).

The $Nd_{1.9}Ba_{1.1}Cu_3O_z$ solution demonstrates both the highest total oxygen content and the smallest oxygen nostoichiometry ($\Delta z \approx 0.3$–0.33, fig. 11a), because a new type of heavy-atom ordering (Nd/Ba) becomes stable at large substitution x, and leads to the "336(tetra)" → "213(ortho)" structural phase transition. In the crystal structure model of the Nd213 phase refined from neutron diffraction data (Goodilin et al. 1998a, 1999, Petrykin et al. 1999b), the doubling of parameters of a primitive "123"-like unit cell along the a- and c-axis directions is caused by the "in-plane" ordering of Ba and Nd atoms. The sequential chain-like arrangement of these heavy atoms predetermines the oxygen distribution in the (CuO_y) plane. In the high-temperature modification of the Nd213 phase ($z \approx 7.0$), one of the oxygen positions along the shortest axis (i.e. the b-axis) of the lattice is partially occupied (O*), whereas Cu and O atoms form strongly distorted chains. The complete occupancy of O* positions can result in a total oxygen content $z = 7.5$. Probably, ordered rows of CuO_5 pyramids would be formed in the CuO plane in that case. However, $z \approx 7.3$–7.33 can be obtained only at $p_{O_2} = 0.21$ and 1 atm, and that may produce a variety of oxygen-ordered structures (superstructures) in the "fully oxygenated" low-temperature orthorhombic modification of the Nd213 phase (Petrykin et al. 1999b, ortho I 213 – ortho II 213 transition, fig. 11a).

Despite its complexity, fig. 11a actually is only a 3D section of a four-dimensional p_{O_2}–T–x–z diagram at $p_{O_2} = 0.21$ atm. However, it predicts that at low p_{O_2} the oxygen chemical potential in the gaseous phase equilibrated with the $Nd_{1+x}Ba_{2-x}Cu_3O_z$ cuprate becomes unfavorable to stabilize the higher copper valence and extra oxygen content which are vital for the Nd-rich solution. Therefore a solid solution with large x can exist in oxygen or air atmosphere only, the solidus slopes become steeper, and the x value is markedly reduced when decreasing the oxygen partial pressure (fig. 11b). Additionally, peritectic temperatures of the R123 phases become lower at low p_{O_2} as discussed in sect. 3.1.1. for Y123. Thus, the oxygen partial pressure seems to be an effective way to obtain, on one hand, higher T_c values as a result of substitution suppression in $R_{1+x}Ba_{2-x}Cu_3O_z$ and, on the other hand, crystal growth can be performed at lower temperatures when p_{O_2} is lowered. Unfortunately, only a few studies related to phase-diagrams at low p_{O_2} have been reported (Ullman et al. 1989, Ahn et al. 1990, Fisher et al. 1993, Kakimoto and Shiohara 1996, MacManus-Driscoll 1997, Yoshizumi et al. 2000, Aswal et al. 1999b, Nishimura et al. 1999). This makes it difficult to optimize the growth conditions (sect. 7.4.1), although the higher/lower solubility of rare-earth elements both in the liquid and solid phases observed for higher/lower p_{O_2} and larger/smaller ionic sizes of R, respectively, can be accepted as an empirical rule.

Phase relations at $p_{O_2} > 1$ atm have not yet been studied. However, it is noted that a high-p_{O_2}–low-temperature treatment (sect. 7.4.3.3) may essentially increase T_c even for a solid solution with high substitution ($x = 0.5$), while to achieve superconductivity at $p_{O_2} \leqslant 1$ atm it is plausible to apply the above-mentioned low-p_{O_2}–high-temperature treatment in order to reduce the substitution or to rebuild the Nd/Ba heavy-ion ordering in the structure at a given substitution (sect. 7.4.1).

3.1.3. *Phase diagrams of other rare-earth elements (Pr, Yb)*

Most of the rare-earth elements can completely substitute for yttrium in the 123 structure, except Ce which does not form the 123 phase. The stability of the substituted phase is governed by the second-periodicity phenomenon in the lanthanide group and, particularly, the decreasing size of the R^{3+} ion with atomic number and the possibility to be in a four-valent state for a number of rare-earth elements (Ce, Pr etc.). Since an internal strain exists in the Y123 structure because of the small Y^{3+} ion sandwiched between two CuO_2 layers (Manthiram et al. 1990), larger LR (Nd, Sm etc.) stabilize this structure while smaller R^{3+} (Yb, Lu etc.) strongly decrease the peritectic decomposition temperature (fig. 7). Two specific examples will be given here.

The first example is the Pr–Ba–Cu–O system, which is important in the frame of possible practical applications. The high-temperature stable phase in this case is $PrBaO_4$ (Pr110) and the R211 compound has never been found (Osamura and Zhang 1993, Chen et al. 1993, Sumida et al. 1995, Park et al. 1996, Reddy and Rajasekharan 1998). The substitution range x for Pr123ss was reported to be $0 \leqslant x \leqslant 0.8$ at 950°C in air (Osamura and Zhang 1993) and the $x = 0$ phase is a widely used barrier and substrate material in thin film device technology. Since the Pr123 phase can be stoichiometrically

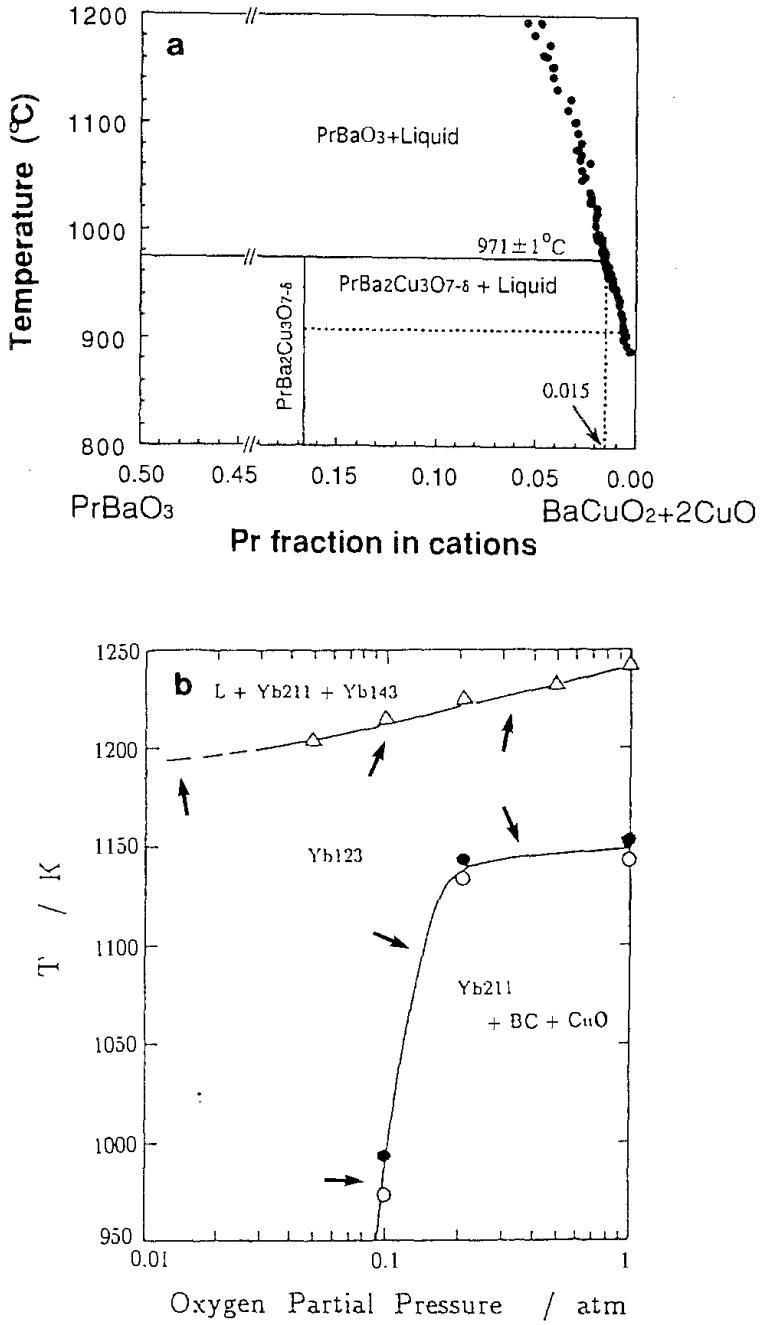

Fig. 12. Phase diagrams of "anomalous" R123: (a) Pr110–($BaCuO_2$ + 2CuO) quasibinary section (Sumida et al. 1995); 211 phase type does not exist in this system; (b) presence of both high- and low-temperature stability boundaries for Yb123 (Osamura and Zhang 1993).

formed via the reaction of the Pr110 phase with melt of the $BaCu_3O_4$ overall composition, the quasibinary "Pr110–($BaCuO_2$ + 2CuO)" system was investigated by Sumida et al. (1995) using DTA, quenching experiments and direct solubility measurements (fig. 12a). The peritectic temperature of the Pr123 phase was determined as 971°C ($x \approx 0$, Sumida et

al. 1995) and 975°C ($x \approx 0.1$, Park et al. 1996). This value as well as the Pr123 dissolution enthalpy (241 kJ/mol) is lower than those for Y (1005°C and 241 kJ/mol, respectively) although the ionic radius of Pr is larger (0.101 nm) than that of Y (0.090 nm), fig. 7.

Another "anomalous" example is connected with the Yb–Ba–Cu–O system (fig. 12b) since the ionic radius of Yb is small (0.087 nm) and results in low stability of the Yb123 phase. The Yb123 peritectic temperature was determined in air as about 970°C (Iwata et al. 1989), 975°C (Osamura and Zhang 1993), 960°C (Goodilin et al. 1994), and 964°C (Oniyama et al. 1997). However, Osamura and Zhang (1993) suggested that, additionally, a low-temperature stability boundary exists for this phase. Below about 875°C Yb123 is unstable in air and can decompose into the Yb211 phase, $BaCuO_2$ and CuO. Probably, this is the most remarkable reported example of such a kind for all R–Ba–Cu–O systems.

3.2. *Crystallization from melt*

3.2.1. *Primary crystallization field and influence of additives*

Within the so-called primary crystallization field (PCF), which is related to equilibrium phase diagrams, R123 phases can be primarily crystallized from melt, without simultaneous solidification of additional phases such as $BaCuO_2$, CuO etc. Even in the Y123 case PCF is disputed (reviewed by Nevriva et al. 1991, Scheel 1994, MacManus-Driscoll 1997 and Chen 1998), although it is clear that it is not possible to crystallize a single phase (Y123) from a liquid of the same composition due to the formation of Y-rich phases (see, however, Nagashio et al. 1999). The PCF boundaries were estimated by different authors as 3.0–5.0, 1.0–2.0, 2.0–4.0 and 0.5–3.5 at% Y and Ba:Cu ratios of 17:83–44:56, 24:76–46:54, 18:82–46:54 and 24:76–42:58. For the Nd–Ba–Cu–O system the PCF has been established in a much smaller number of studies, for example, K. Oka and Unoki (1990) have drawn a possible PCF between Ba:Cu = 3:5–3:6 and 2.0–4.0 at% Nd. C.T. Lin et al. (1996) found that the coexistence area of liquid and the $NdBa_2Cu_3O_{7-\delta}$ phase is placed near Nd:Ba:Cu = 1.25:36.25:62.50 and between 970°C and 1090°C. Goodilin et al. (1997a) observed that copper-enriched fluxes (Ba:Cu = 3:12) might crystallize the Nd123ss solution ($x > 0.7$) instead of the $x = 0.0$ Nd123 phase after lowering the temperature, corresponding to the Nd-saturated liquid, down to the "Nd123ss–L" two-phase field. This occurs if the initial content of Nd exceeds 4 at%, otherwise the CuO phase may precipitate first. The former is evident from fig. 13 (4–6 at% Nd), where additional exothermic peaks of Nd123ss crystallization are present on cooling at about 1020–1025°C while only CuO crystallization from this melt occurs below 970°C (0–2 at% Nd). The figure also demonstrates the inconsistency of cooling and heating ramps typically observed in the thermal analysis due to the supercooling of the melt (see also Hunt et al. 1998). The sudden onset of a strong exothermic peak near 800°C suggests with evidence that this reaction takes place far away from equilibrium. Since this low-temperature peak can be assigned to an intermediate ternary eutectic BaO–CuO–Cu_2O (Fischer et al. 1993), it becomes obvious that the cooling process does not allow the entire oxygen uptake. Therefore such sluggish processes are to

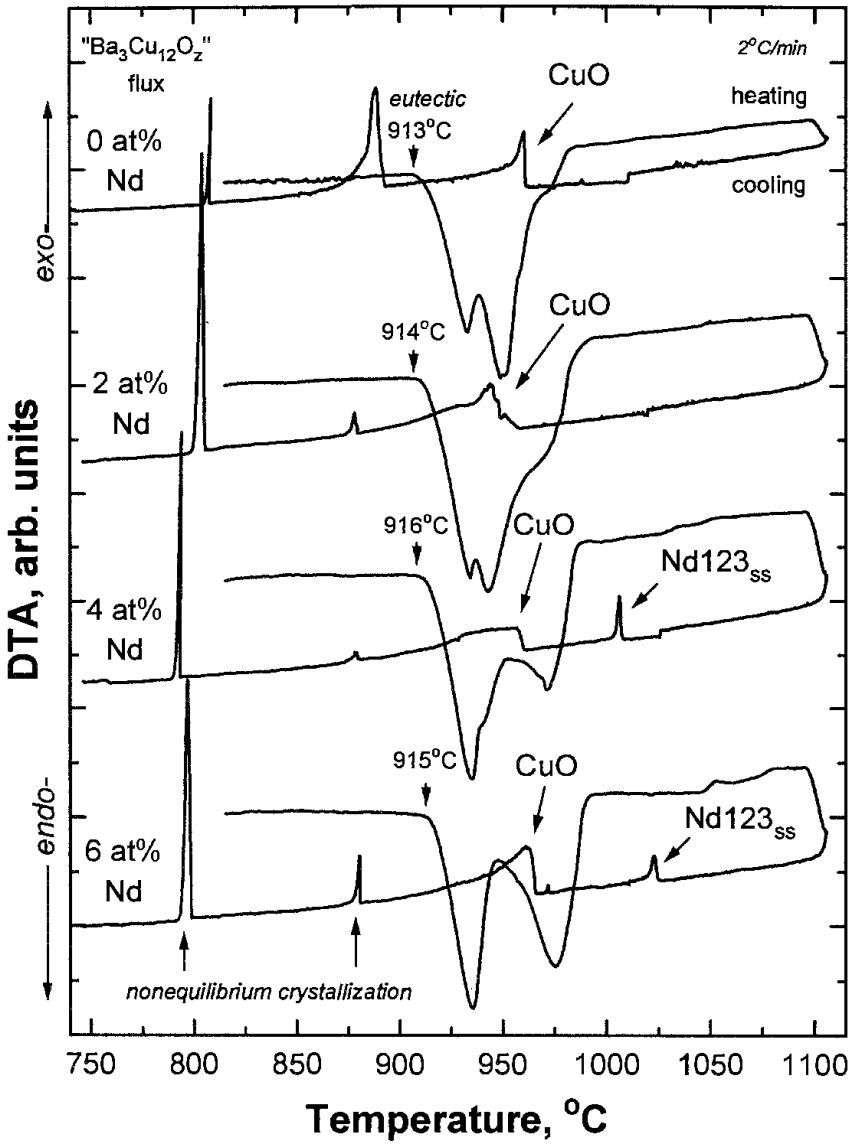

Fig. 13. Typical heating and cooling DTA curves of a Ba–Cu–O flux (Ba:Cu = 3:12) with different initial R^{3+} content (Goodilin et al. 1997a). Heating and cooling curves are essentially inconsistent due to sluggish kinetics of peritectic reactions. Note additional exothermic peaks of Nd123ss crystallization from a supersaturated melt (at a certain initial content of $NdO_{1.5}$).

be recognized in the determination of the "true" PCF. Moreover, it was observed in this particular experiment that being in surrounding melt, the initially crystallized Nd123ss solid solution changes its composition over time (Goodilin et al. 1997a). This makes the meaning of PCF of the "superconducting" ($x \rightarrow 0$) Nd123 phase to be even more intricate and less useful for practical applications. Perhaps, the solubility curves (sect. 3.1.2.1) and the 3D phase diagram presented should be a powerful and universal guideline in this subject (table 1, fig. 6). (See also Notes added in Proof, point 2.)

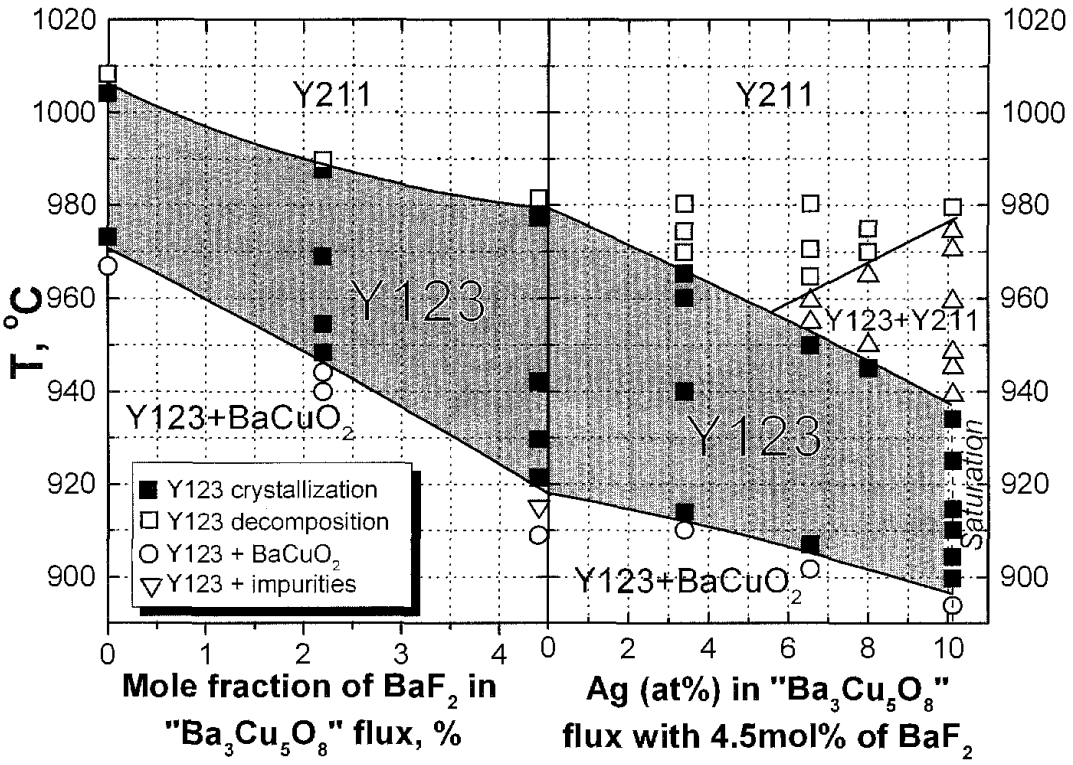

Fig. 14. Expanding of the Y123 primary crystallization field and decreasing the lowest temperature of the Y123 primary crystallization by additives (BaF_2 and Ag) (Yamada et al. 1997b).

A special question to be discussed with respect to the PCF is the influence of a small amount of additives allowing the easier growth of larger single crystals. BaF_2, B_2O_3, Bi_2O_3, Ag, $BaCl_2$, etc., are usually used for this purpose. BaF_2 was found to be the most effective for a significant improvement of the crystal size, yield and superconducting properties of the Y123 superconductor owing to changes in the growth mode and reducing Al contamination (Chen 1998). It was reported that the BaF_2 additive expands the PCF of R123. R123 crystalline film formation in LPE (sect. 5.4) is usually limited between 970°C and 1005°C for the yttrium system and between 970°C and 1070°C for Nd123, with $BaCuO_2$ formation below 970°C. The BaF_2 addition, nevertheless, decreases the lowest crystallization temperature of the 123 phase down to 920°C (Ba:Cu = 3:5 flux) for both Y and Nd (fig. 14, Yamada et al. 1997b). From a practical point of view, the BaF_2 additive is still the best substance for expanding PCF, although no distinct mechanism has yet been proposed (see, however, Chen 1998).

3.2.2. *Quantitative compositional relationships between equilibrium solid and liquid*

It is evident from the discussion above that a key issue of any melt-preparation technique is the compositional relationship between solid and liquid phases. The compositional

Table 4
Polynomial regression analysis of the Nd concentration in the melt (y, at%) vs the Nd content in the equilibrium Nd123ss (x, at%): $y = a_0 + a_1 \times x + a_2 \times x^2$

T (°C)	x range	a_0	a_1	a_2	R	SD
995	0.04–1.00	0.0144	–0.102	0.499	0.998	0.00074
1020	0.05–0.96	0.0269	–0.243	0.986	0.999	0.00045
1030	0.07–0.86	0.0249	–0.229	1.031	0.999	0.0003
1045	0.14–0.70	0.0451	–0.371	1.302	0.999	0.00028
1060	0.06–0.57	0.0413	–0.309	1.165	0.9998	0.00086

experimental data for the A-type triple points (fig. 10) can be fitted by the following polynomials above the peritectic–eutectic reaction at 995°C (Goodilin et al. 1998b):

$$1 + x = -134.54 + 0.27324T - 1.3670 \times 10^{-4} T^2 \quad (x \approx 0\text{–}1 \text{ in solid phase}, T \text{ in °C}), \tag{18a}$$

$$C_{\mathrm{Nd}}^{\mathrm{melt}} \text{ (at\%)} = 845413.83 - 3271.3187T + 4.7446T^2 - 3.057 \times 10^{-3} T^3 + 7.3817 \times 10^{-7} T^4, \tag{18b}$$

$$\frac{C_{\mathrm{Cu}}^{\mathrm{melt}}}{C_{\mathrm{Ba}}^{\mathrm{melt}}} = -194818.80 + 746.1754T - 1.0713T^2 + 6.8341 \times 10^{-4} T^3 - 1.6345 \times 10^{-7} T^4. \tag{18c}$$

It should be noted that the Nd partition ratio between liquid and solid is the most variable parameter of the equilibrium couples "Nd123ss–melt" (table 4). On the contrary, the Ba partition ratio between the liquid and solid phases is almost fixed and equal to ~1, while the Cu partition ratio increases gradually with increasing Nd content in the solid phase (Goodilin et al. 1997b). Therefore the tie-lines "Nd123ss–L" are almost parallel graphically to the $NdO_{1.5}$–CuO side except in the region close to the $x = 0$ Nd123 phase. The maximum of the neodymium "solubility" in liquid at 1030°C (fig. 15) originates from two opposite factors – increasing Nd content in the liquid with temperature and simultaneous shifting of the ternary equilibrium point toward the Ba-rich liquid with smaller Nd content equilibrated with less-substituted Nd123ss. The coordinates of the three-phase equilibrium point of the terminal Nd123ss solid solution, liquid and the 201 (422) phase predict temperatures and initial compositions allowing one to form the Nd123ss with maximal substitution. The equilibrium liquid composition is changed much for the Nd123ss phase with different neodymium contents, subsequently the Nd-rich ($x = 1.0$) and Nd-poor ($x \to 0$) Nd123ss can be in equilibrium with melt of higher (up to 16:3) and lower (7:6~5:3) Cu:Ba ratios respectively. In this case the initial flux composition can allow one to control effectively the substitution x in the solid phase at appropriate growth temperatures (sect. 5.5.2).

The most important features of the equilibrium liquidus position around $x = 0.0$ were described by Kambara et al. (1998). The liquidus curve is shifted to the side of

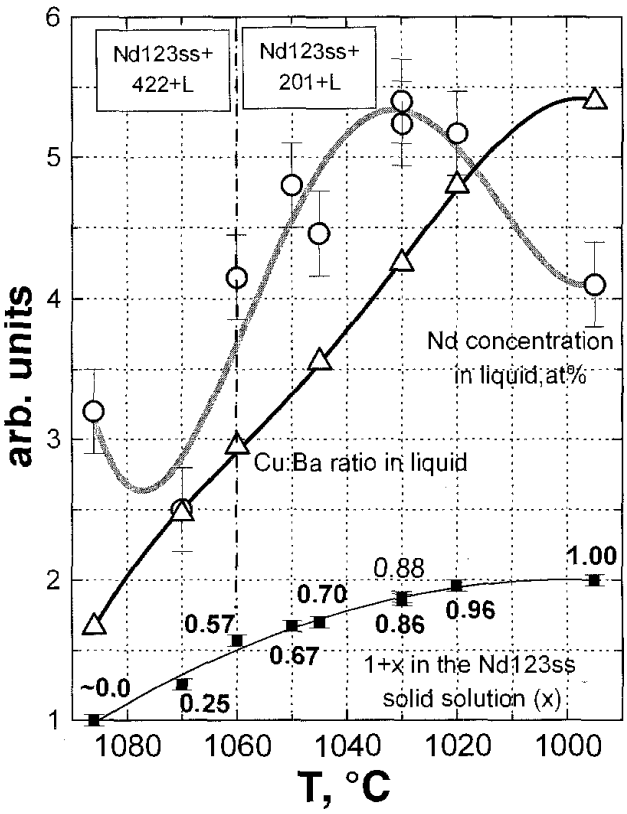

Fig. 15. Temperature dependence of composition of the Nd123 solid phase (x; $1+x$ values are used to draw the ordinate) and liquid (Nd concentration and Cu:Ba ratio in liquid) corresponding to triple equilibrium points (Nd123ss–201–L)/(Nd123ss–422–L). The Nd content in such an equilibrium liquid depends not only on the temperature (Nd solubility limit in a flux of a given composition) but also on the Cu:Ba ratio in the flux (Goodilin et al. 1997b).

higher Nd concentration with rising temperature (see eqs. 19a–f and fig. 16). At every temperature, the point of minimum Nd concentration in the liquid is centered around Ba:Cu=1:2 (as in the Y–Ba–Cu–O system, sect. 3.1.1), and the Nd content in the liquid increases from this point with both increase or decrease of the Ba:Cu ratio. The relationship between the Nd composition of Nd123ss (C_S^{Nd}) and that of the equilibrium liquid (C_L^{Nd}, C_L^{Cu}) is expressed as

$$C_L^{Nd}(1030°C) = \frac{1}{C_S^{Nd} - 16.5} + \frac{C_S^{Nd} - 10.9}{2.65} - 2.20, \tag{19a}$$

$$C_L^{Nd}(1050°C) = \frac{1}{C_S^{Nd} - 16.7} + \frac{C_S^{Nd} - 10.5}{2.65} - 1.80, \tag{19b}$$

$$C_L^{Nd}(1073°C) = \frac{1}{C_S^{Nd} - 17.0} + \frac{C_S^{Nd} - 10.5}{3.02} - 1.15. \tag{19c}$$

$$C_L^{Nd}(1030°C) = 0.0163\left(C_L^{Cu}\right)^2 - 2.11C_L^{Cu} + 69.6, \tag{19d}$$

$$C_L^{Nd}(1050°C) = 0.0186\left(C_L^{Cu}\right)^2 - 2.45C_L^{Cu} + 81.9, \tag{19e}$$

$$C_L^{Nd}(1073°C) = 0.0213\left(C_L^{Cu}\right)^2 - 2.83C_L^{Cu} + 96.1. \tag{19f}$$

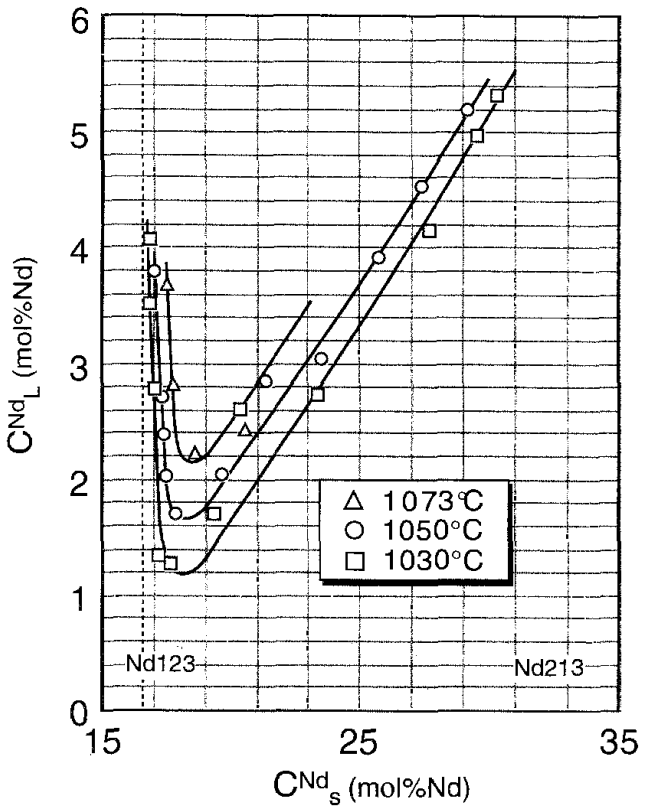

Fig. 16. Relationship between the Nd contents in the equilibrium solid and liquid phases at different temperatures near the Nd123 ($x \approx 0$) phase (Kambara et al. 1998).

Quite similar polynomial approximations of liquidus surfaces were suggested by Yoshizumi et al. (2000) for both low- (0.01 atm) and high-p_{O_2} (1 atm.) atmospheres (see Notes added in Proof, point 3).

It is evident (fig. 16) that due to the upward curvature of the liquidus (see also eqs. 19d–19f) with the minimum Nd content in liquid at Ba:Cu $\approx$ 1:2, the Nd content in the Nd123ss solid solution gradually approaches the ideal stoichiometry $x = 0.0$ with the Nd concentration increasing in the Ba-rich melts. In the former region, an asymptotic line almost corresponds to the ideal $x = 0.0$ Nd123 phase, which is shifted to lower Nd concentrations as temperature decreases. As a result, it is considered by the authors that the $x \approx 0$ substitution could be obtained by using a flux with a larger Ba/Cu ratio and by decreasing the growth temperature (see also Kakimoto and Shiohara 1996 and Goodilin et al. 2000). This is consistent with the phase-diagram considerations in fig. 10.

3.2.3. *XANES examination of molten state*

The structure of the nutrient phase, namely molten barium–copper oxides doped with a rare-earth element, obviously is an important factor in the single-crystal growth. In this section, the term "structure" simply has the meaning of a local coordination/arrangement and valence of transition metal ions (copper) in the melt. It is well-known that some "structural" changes might be associated with a metastable state (supersaturated or supercooled melt), which produces a single crystal. Although it is difficult to determine

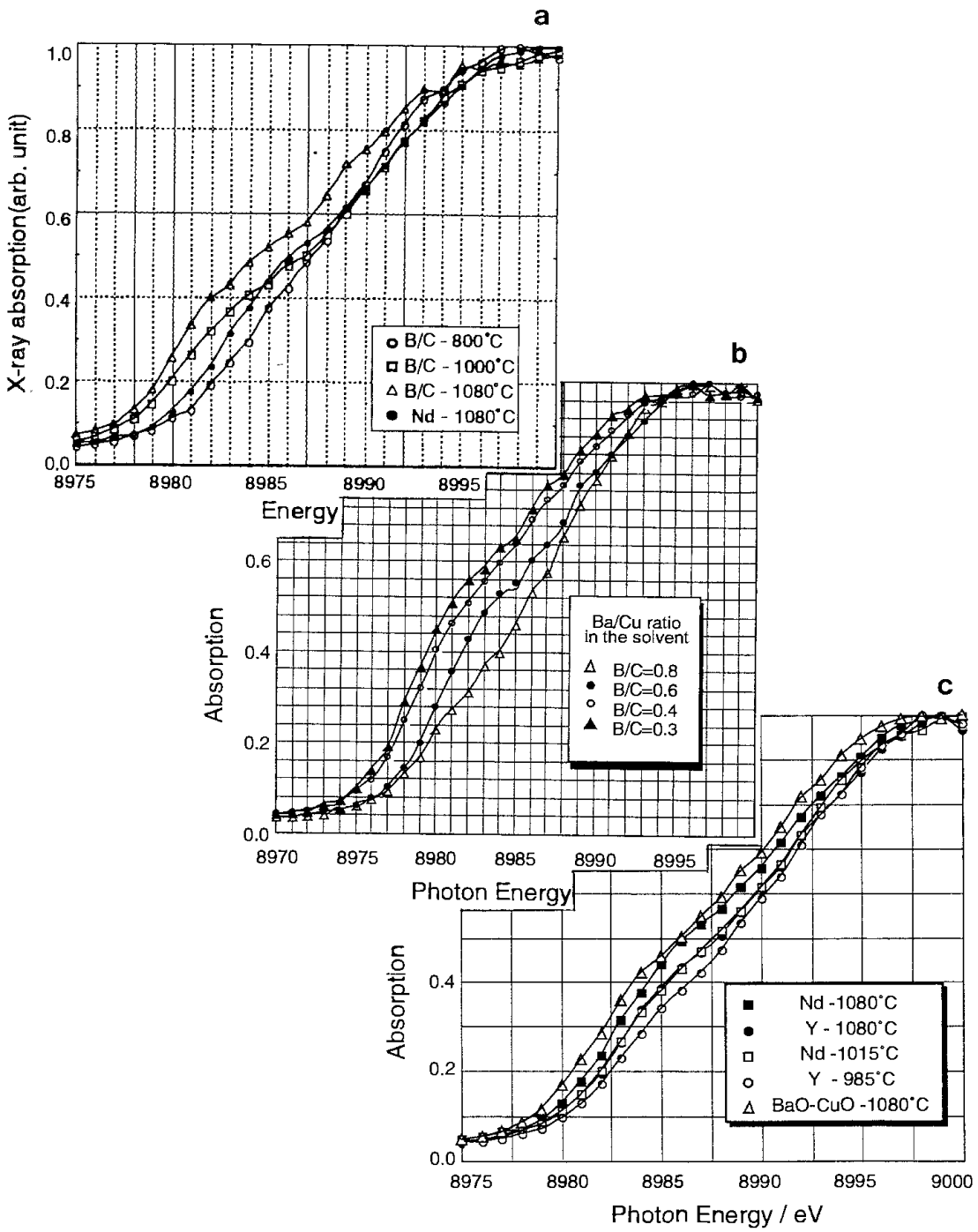

Fig. 17. In situ XANES of Ba–Cu–O fluxes at different temperatures (Chauhan et al. 1997, Kambara et al. 1997a): (a) temperature dependence of the Cu K-edge position for molten ($3BaCuO_2 + 2CuO$) flux. Note that due to copper valence reduction with temperature the copper edge is shifted in the lower-energy direction compared to the solid state (800°C); (b) Cu K-edge shift in the higher-energy direction with increasing BaO content in molten fluxes; (c) larger shift of the Cu K-edge in the higher-energy direction upon doping the flux by Y^{3+} in comparison with Nd^{3+}.

such kind of changes, X-ray-adsorption spectroscopy (XANES and EXAFS) can be applied to probe the molten state since it is sensitive both to the arrangement of atoms around the absorbing atom and its state (Guo et al. 1990). Chauhan et al. (1997) and Kambara et al. (1997a) have investigated in situ high-temperature copper oxide melts by measuring Cu K-edge XANES spectra (fig. 17). It was found that

(1) For the commonly used "$Ba_3Cu_5O_8$" flux the Cu K-edge is shifted to the lower energy region (fig. 17a) by a temperature rise (800–1080°C). At the same time the characteristic peak of Cu(I) appears at 1080°C since, being molten, this flux contains only a small amount of divalent copper and a large amount of monovalent copper (see also Hunt et al. 1998). Note that the $BaCu_2O_2$ phase (see sect. 3.1.1) is usually observed by XRD diffraction of the rapidly quenched high-temperature barium–copper oxide melts.
(2) "Dilution" of the copper oxide by the barium oxide and melting the fluxes with a higher Ba:Cu ratio (0.3, 0.4, 0.6, 0.8) results (fig. 17b) in a pronounced shift of the copper absorption edge to the higher energy direction (1050°C). This probably means that the alkaline-earth element stabilizes the higher copper valence.
(3) Doping of the molten $Ba_3Cu_5O_8$ flux with yttrium or neodymium even in amounts as low as 0.5 at% shifts the copper absorption edge to the higher energy field. Therefore, the melt characteristics are very sensitive to the presence of a rare-earth element as well (fig. 17c).
(4) The shift of the copper absorption edge to the higher energy field for doped fluxes is higher for the smaller Y^{3+} rather than for the larger Nd^{3+}; therefore, yttrium causes more serious changes of the local structure, copper valence or effective charge in the melt compared to neodymium (fig. 17c).

Thus, the characteristics of the melt can be strongly affected by its composition and temperature. As a result, the composition and properties of the crystallized solid phase might be different.

3.3. *Mass transport phenomena*

A boundary layer is a simplified description of a system fluctuating with time. The concept of an "unstirred" layer was introduced by Noyes and Whitney (Elwell and Scheel 1975). There are three terms with a simple relationship between them – the "solute diffusion boundary layer", the thermal diffusion boundary layer and the "hydrodynamic" momentum boundary layer, which is a layer of a solution considered as stagnant because of adhesion to the crystal surface while the remainder of the solution is flowing past this surface. The solute diffusion boundary layer has an important physical meaning in the subsequent considerations. It is common to use this concept with reference to a flat crystal surface growing uniformly in a supersaturated solution. In the following sections transport phenomena at the interface as well as in the surrounding liquid will be discussed.

3.3.1. *Basic model of solute diffusion in Y123 crystal pulling experiments*

Two basic ideas can be considered for discussion of the crystal growth mechanism from the liquid. The first is that the crystal grows in a steady state, and the mass balance

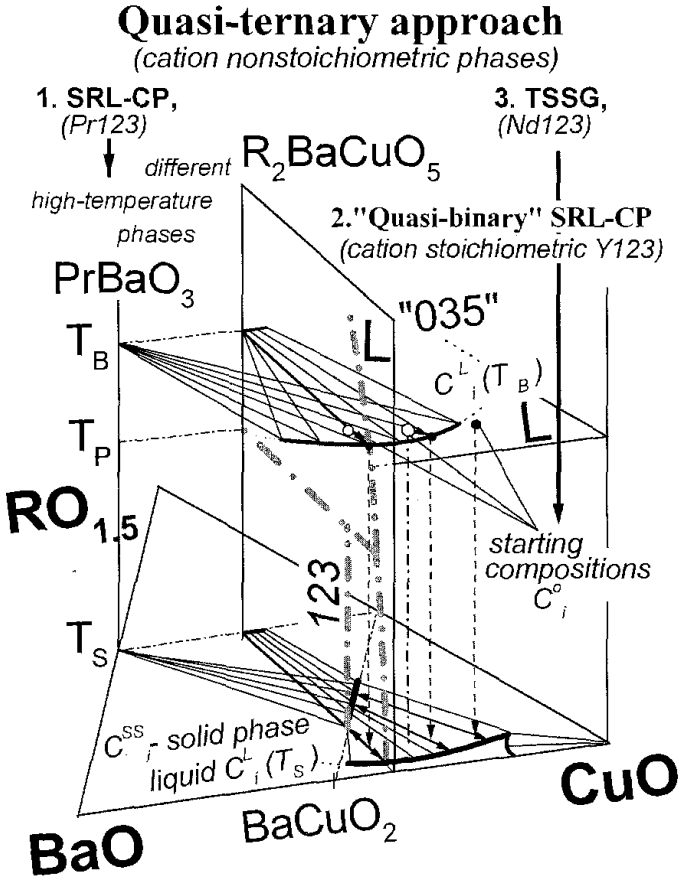

Fig. 18. Selection of a tie-line and the crystallizing solid phase composition in three different cases: (1) cation stoichiometric Y123 phase in the SRL–CP method, (211–035) section (quasibinary approach is valid); (2) cation nonstoichiometric Pr123 phase in the SRL–CP method (quasibinary approach is not valid due to the possibility of formation of the Pr123ss solid solution; note that the high-temperature stable phase in this case is Pr110 rather than 211); (3) cation nonstoichiometric Nd123 phase in the TSSG method (quasibinary approach is also not valid due to the possibility of formation of the Nd123ss solid solution; note that the high-temperature stable phase in this case is the Nd422 solid solution). Starting compositions are given by C_i^0, liquidus composition at the temperature T_B, $C_i^L(T_B)$, is presented by a solid line in the quasiternary section of the copper-rich corner at T_B. The same at the temperature $T_S < T_B$ below the R123 phase peritectic decomposition (T_P) is given by $C_i^L(T_S)$. Equilibrium solid phase compositions at T_S are given by C_i^{ss}. Light-gray thick lines show a quasi-binary phase diagram in the (211–035) vertical section for the case of Y123. Two-sided arrows link equilibrium solid and liquid phase compositional points in a given quasi-ternary isothermal section.

between the amount of R^{3+} from the solution and the amount of R^{3+} necessary for R123 growth is kept at a solid/liquid interface (sect. 2.3.1). The second is that the crystallization process should require a relatively large interface kinetic supersaturation for its faceted growth. Therefore, the composition of the liquid at the interface C_i is not necessarily equal to the equilibrium composition C_e (fig. 2).

A vertical plane in fig. 18 schematically illustrates single-crystal growth in the frame of a quasibinary system approach which is valid in a particular case of the cation-stoichiometric Y123 phase, belonging to the 211–035 section. If T_B and T_i are the

temperatures at the bottom of the crucible and at the interface, the corresponding equilibrium compositions will be $C^L(T_B)$ and C_i. We assume that the R^{3+} concentration is uniform in the bulk liquid maintained by the natural and forced convections, except in the solute boundary layer with the thickness δ (fig. 2).

Using Fick's first law, the solute flux towards the crystal growth interface (J_c) is approximately expressed as $J_c = D_L \times (C^L(T_B) - C_i)/\delta$ (Yamada et al. 1995a) because the solvent ("035" or $3BaCuO_2 + 2CuO$) saturated by solute (Y) near the 211 phase at the hot crucible bottom is transported to the melt surface and, hence, to the growing crystal. Under equilibrium conditions, $C^L(T_B)$ can be determined from the liquidus in the (211–L) two-phase region. On the other hand, the solute flux (J_s), which is required for growth, could be calculated by multiplying the growth rate (R) and the composition difference at the interface between the crystallizing phase and the surrounding liquid layer, i.e. $J_s = R(C^{ss} - C_i)$, where C^{ss}(fig. 18) $= C_e$(fig. 2) is the concentration of solute in the solid phase (Y123). In order to achieve steady-state growth, these solute fluxes must be equal, i.e. $J_c = J_s$ and therefore

$$R = \frac{D_L}{\delta} \frac{C^L(T_B) - C_i}{C^{ss} - C_i}. \tag{20}$$

Under the Cochran (1934) assumptions for a fluid flow near a rotating disk, Burton et al. (1953) introduced the solute boundary layer thickness as

$$\delta = 1.6 D_L^{1/3} \nu^{1/6} \omega^{-1/2}, \tag{21}$$

where D_L, ν and ω are the diffusion coefficient of the solute, the kinematic viscosity and the angular velocity of the rotating crystal, respectively. Assuming a linear relationship between the temperature and the concentration near the peritectic temperature T_p, eq. (20) becomes

$$R = \frac{D_L^{2/3} \omega^{1/2} \left[(T_b - T_p)/m_L^{211} + (T_p - T_i)/m_L^{123} \right]}{1.6 \nu^{1/6} (C_s^{123} - C_i)}, \tag{22}$$

where m_L^{211} and m_L^{123} represent the tangents to the liquidus above and below T_p, respectively. Moreover, assuming that the interface kinetics for crystal growth is infinitely rapid, i.e. $T_i = T_s$ or C_i is equal to the equilibrium value $C^L(T_s)$ at a given T_s (fig. 18), the growth rate becomes maximum (R_{max}). R_{max} can be estimated as 0.36 mm/h by substituting the physical parameters and the experimental conditions listed elsewhere (Yamada et al. 1995a, Tagami and Shiohara 1997, Namikawa et al. 1995b). Consequently, C_i should be about 0.64 at%. After converting C_i to the kinetic undercooling (ΔT_k) with the Y123 phase liquidus, ΔT_k seems to be about 7 K. The value of R_{max} is larger than the experimental growth rate ($R \approx 0.1$ mm/h). These results indicate that the crystal growth of Y123 might be controlled by interface kinetics and by the solute diffusion.

3.3.2. *$R_{1+x}Ba_{2-x}Cu_3O_z$ solid-solution growth: diffusion of ions in liquid and tie-line selection*

As mentioned above, the substitution phenomena affect J_c properties as well as T_c values in the R123 systems. It is sufficient to discuss the growth mechanism of Y123 crystals in the SRL–CP method on the basis of the pseudo-binary phase diagram (sect. 3.3.1). On the other hand, in the case of a solid solution such as $Nd_{1+x}Ba_{2-x}Cu_3O_z$, $Pr_{1+x}Ba_{2-x}Cu_3O_z$, etc., it should be considered using a quasiternary phase diagram, since the number of degrees of freedom becomes larger (Kakimoto and Shiohara 1996). A simple model has been suggested by Tagami et al. (1997) to predict the composition of the solid solution in the Pr–Ba–Cu–O system under the conditions of the SRL–CP growth (sect. 4.2.5).

From a phase-diagram point of view, the compositions of the equilibrium solid solution and coexisting liquid are uniquely determined by the tie-line on the isothermal section of the PrO_y–BaO–CuO ternary phase diagram at the growth temperature. However, growth of a crystal in the SRL–CP method occurs in a steady state, therefore the temperature dependence of the tie-line as well as diffusivity and interdiffusivity of cations, and probably oxygen, should be taken into account. Figure 18 shows the corresponding schematic 3D phase diagram if the temperature at the bottom of the crucible is higher than the peritectic temperature. T_b, T_p and T_s are the temperature at the bottom of the crucible, the peritectic temperature and the temperature at the surface of the liquid, respectively. C_i^0, C_i^{110}, C_i^{ss}, $C_i^L(T_b)$ and $C_i^L(T_s)$ are the mole fractions of each cation in the initial starting composition, in the $PrBaO_3$ phase, in the solid solution and in the liquid at T_b and T_s, respectively (i = Pr, Ba and Cu). At first, it is considered that the liquid composition in the crucible except for the solute boundary layer is uniform due to the natural and forced convections. Then, C_i^0 is located on the tie-line connected with C_i^{110} and $C_i^L(T_b)$. The liquid of the $C_i^L(T_b)$ composition is transported to the solute boundary layer by natural and forced convections. Accordingly, the liquid near the solute boundary layer is supersaturated because the temperature around the growing crystal is lower than the peritectic temperature T_p. This supersaturation is the driving force for crystal growth. However, it is still uncertain which tie-line is selected at the growing interface.

The following can be assumed to simplify this problem: (1) local equilibrium exists at the interface between the crystal and the liquid, i.e. diffusion-controlled growth takes place; (2) the solidification occurs in a steady state; (3) dilute-solution approximation is permitted for diffusion of Pr; (4) Ba and Cu ions are Raoultians; (5) the difference between unit volume of crystal and that of the Ba–Cu–O solvent is negligible, therefore the supersaturation estimated for the mole fraction causes crystallization of the same volume fraction and the growth rate of the crystal can be calculated from the supersaturation in the solution given by the mole fraction; (6) the interface of the solidifying crystal is planar; (7) the peritectic reaction takes place isothermally; (8) thermo-physical properties are constant.

Taking into consideration that the nutrient solution is diluted with respect to Pr (sect. 3.1.2.1), but the interdiffusivity of Cu and Ba due to their high concentrations cannot be neglected, two expressions for the diffusion boundary layer thickness are needed:

$\delta_c = 1.61 D_{Pr}^{1/3} \nu^{1/6} \omega^{-1/2}$ (for Pr) and $\delta_c^* = 1.61 \tilde{D}^{1/3} \nu^{1/6} \omega^{-1/2}$ (for Ba and Cu), where D_{Pr} is the diffusion coefficient of Pr in liquid and $\tilde{D}$ is the interdiffusion coefficient between barium and copper in the liquid.

Defining for simplicity the difference in liquid concentrations between the bottom and the top of the crucible by the term $\Delta C_i^L = C_i^L(T_B) - C_i^L(T_S)$, the difference in the element concentrations between solid and liquid phases at the interface as $\Delta C_i^{SL} = C_i^{SS} - C_i^L(T_S)$, (i = Pr, Ba, Cu), the ratio between the diffusion coefficient and the boundary layer thickness as $t = D_{Pr}/\delta_c$ (Pr), $t^* = \tilde{D}/\delta_c^*$ (Ba, Cu) and the relative content of the element (i) at the interface as $\chi_i = C_i^L(T_S)/(1 - C_{Pr}^L(T_S))$ (Ba, Cu), the following mass-balance equations for each element are derived at a given crystal growth rate R:

$$\Delta C_{Pr}^{SL} = \frac{\Delta C_{Pr}^L t}{R}, \tag{23a}$$

$$\Delta C_{Ba}^{SL} = \frac{\Delta C_{Ba}^L t^* - \chi_{Ba} \Delta C_{Pr}^L (t - t^*)}{R}, \tag{23b}$$

$$\Delta C_{Cu}^{SL} = \frac{\Delta C_{Cu}^L t^* - \chi_{Cu} \Delta C_{Pr}^L (t - t^*)}{R}. \tag{23c}$$

Tagami et al. (1997) determined the relationship between equilibrium concentrations of liquid and the Pr123ss solid solution as

$$C_{Cu}^L = (5.273T - 5212)(C_{Pr}^L)^2 + (-0.1831T + 185.7) C_{Pr}^L + 2.462 \times 10^{-4} T + 0.3994, \tag{24a}$$

$$C_{Pr}^{SS} = (-8.427 \times 10^{-2} T + 86.28) C_{Pr}^L + 1.182 \times 10^{-3} T - 1.007, \tag{24b}$$

(obviously, other "missing" concentrations are given by the relations $C_{Cu}^L + C_{Ba}^L + C_{Pr}^L = 1$, $C_{Ba}^{SS} = 0.5 - C_{Pr}^{SS}$ and $C_{Cu}^{SS} = 0.5$.)

When C_i^{ss} and $C_i^L(T_s)$ satisfy eqs. (23) and (24) simultaneously it gives a tie-line at the growing interface. The selected tie-line depends on $\tilde{D}$ and D_{Pr} since the boundary layer thickness can be calculated using these diffusion coefficients under given hydrodynamic conditions in the crucible. In the case of $D_{Pr} = \tilde{D}$, $C_i^L(T_b)$ points are located on the equilibrium tie-line at the growth interface, while in the case of $D_{Pr} \neq \tilde{D}$ the tie-line is shifted as determined by the relationship between D_{Pr} and $\tilde{D}$ particularly, at $\tilde{D} : D_{Pr} < 1$ the selected tie-line shifts to the Pr-rich region, and in the case $\tilde{D} : D_{Pr} > 1$ it is shifted to the opposite side. Assuming the simplest case that unknown diffusion coefficients $\tilde{D}$ and D_{Pr} are equal, the composition of the grown single crystal could be estimated and the values are in good agreement with experimental results for various starting compositions.

3.3.3. *Hydrodynamics and computer simulation of crystal growth*

In the crystal pulling growth technique, two types of convection have to be taken into consideration, namely natural and forced convections (Dupret and Van Den Bogaert 1994). The behavior of the meniscus is also important for the control of the diameter and

overall morphology of a growing crystal. The shape of the growing crystal is determined by the angle at which the meniscus contacts the crystal at the three-phase boundary and subsequent solute redistributing in this zone. Macroscopically, the rotating crystal produces a fan effect which moves the melt upwards along the central axis and radially outwards in a spiral-like mode along the upper region of the melt. This forced flow meets the natural convection flow originated from the hot crucible wall or thermal gradient that causes liquid to move upward along the crucible wall and inward along the upper region of the melt. These collisions produce coupled rotating cells or other complicated patterns, or under a certain condition one type of flow completely dominates over the other. In any case the convective liquid results in thermal fluctuations (and vice versa) and both of them have a significant influence on crystal growth. It is extremely important to control the forced convection because it could help to homogenize the liquid, to develop a thermal and solutal symmetry in the growing crystal, to control the interface shape, and to change the crystallization velocity due to controlling the heat balance at the crystallization front. One important example of the forced convection arises also in the accelerated crucible rotation technique (ACRT) in which the crucible rotation is periodically accelerated and decelerated to achieve an excellent efficiency of mixing. A number of examples are described by Tiller (1991b).

The heat transfers partially by conduction, convection and radiation directly from the crucible to the melt and also radiated from the crucible to the crystal. The heat in the melt is transferred to the interface and the melt surface by both conduction and convection. Heat is dissipated from the melt-free surface to the atmosphere by both gaseous convection and radiation. In addition, for a growing crystal the latent heat is generated at the solid/liquid interface. The factors which must vary during the crystal growth are the crystal size, the height of the melt and the meniscus shape, which are also determined by the time-dependent heat transfer. The melt height markedly influences the heat transfer through the crucible wall so far the crucible may play the role of an afterheater. This means that a number of parameters (rotation rate, crucible size, crucible shape, growth rate etc.) will play an exceptional role in the formation of a less concave or more concave crystal–melt interface. Additionally, in the SRL–CP method, the nucleation probability at the crucible wall (i.e. heterogeneous nucleation) cannot be neglected. However, high-speed rotation may prevent the floating particles from attaching to the growing crystal (sect. 7.2.1). Accordingly, a deeper understanding of melt convection phenomena is extremely important for single-crystal growth by pulling, for example, by the SRL–CP method.

It was found experimentally (Makarova et al. 1996) that the densities of Ba–Cu–O melts vary from 4.8 to 5.4 g/cm^3 depending on temperatures and compositions with a minimum at the eutectic ratio BaO : CuO = 28 : 72. After Makarova et al. (1996), the densities of barium-cuprate melts (ρ, g/cm^3) can be typically expressed as $\rho(23:77) = 5.34 - 0.00191(t - 937°C)$, $\rho(28:72) = 5.32 - 0.00598(t - 906°C)$, and $\rho(30:70) = 5.13 - 0.00120(t - 925°C)$ for a given temperature (t, °C) above the melting point, and for a fixed ratio of BaO : CuO (23 : 77, 28 : 72 and 30 : 70, respectively). It was also observed that the surface tension and viscosity of the melts have a similar temperature behavior

and they are larger at a higher BaO concentration. The melt viscosity (960–980°C) is estimated to be close to 0.05–0.15 N s/m^2 while the surface tension coefficient is in the range 0.3–0.6 N/m. It should also be noted that the melts possessed a mixed (mostly electronic) conductivity, and the whole set of the data allowed the authors to assume a weakly-ionic nature of the melts and a small extent of their clustering.

Thus, similar to other oxide melts, the BaO–CuO flux has a rather high viscosity, hence it has high Schmidt (*Sc*) and Prandtl (*Pr*) numbers; the former is defined as a ratio of the kinematic viscosity of melt ν and its thermal diffusivity α_L, $Pr = \nu/\alpha_L$. Therefore the Y-solute is transferred to the growing Y123 crystal from the Y211 phase placed at the bottom of the crucible mainly by melt convection. In order to calculate the melt convection, several governing equations have to be considered (Namikawa et al. 1996a):

- mass conservation $\nabla V = 0$, where V is the velocity of flow;
- the Navier–Stokes equations, i.e.
  momentum conservation: $\partial V/\partial t + (V \times \nabla) \times V = -(1/\rho)\nabla p' + (\mu/\rho)\Delta V - \beta T'_j g$, where ρ, μ and β are the density, the viscosity and the volumetric thermal expansion coefficient of the melt, g is the gravitational constant; $p' = p - p_0$, $T'_j = T_j - T_0$, where p and p_0 are the pressure and the average melt reference pressure, and T_j and T_0 are the temperature and the average reference temperature, and
  energy conservation: $\partial T'_j/\partial t + V \times \nabla T'_j = \alpha_j \Delta T'_j$, where α is the thermal diffusivity, and the subscript j indicates crucible, melt or crystal.

Figures 19a–c show the results of a numerical simulation by a finite difference method for a 2-dimensional axially symmetric viscous fluid system. The left-hand and right-hand part of each picture show the stream lines of the melt and isotherms, respectively, within the right-hand halves of the vertical section of the crucible (see also Seeßelberg et al. 1997b). Convection below the crystal is induced by the crystal rotation and the natural convection near the crucible wall. As the crystal rotation rate and/or the crystal diameter increases, the forced convection becomes stronger and the meeting point of the forced and the natural convections near the melt surface moves from the crystal to the crucible wall. The isotherms are coupled strongly to the convection, and the temperature at the crystal growth interface increases with the acceleration of forced convection (increasing the crystal rotation rate) as well as with increasing the size of the crystal.

This tendency has been confirmed by experimental results using MgO dummy crystals. Namikawa et al. (1995a) estimated by observation of the melt flow pattern the forced and natural convections near the melt surface. The tiny floating particles put on the melt surface were accumulated in the experiment in a steady circular position on the melt. This circular position seems to indicate the meeting point of the forced and natural convections near the melt surface. For each tested crystal size at low crystal rotation rate, the particles were almost attached to the central seed crystal connected with the rotating pulling mechanism. Then, with increasing rotation rate, the particles spread toward the crucible wall and finally settled near the wall. In the region of lower rotation rates the forced convection is weak and exists only below the crystal. Consequently, natural convection should be dominant and the particles were condensed near the crystal by this type of convection. As the crystal rotation rate increases, the forced convection becomes stronger

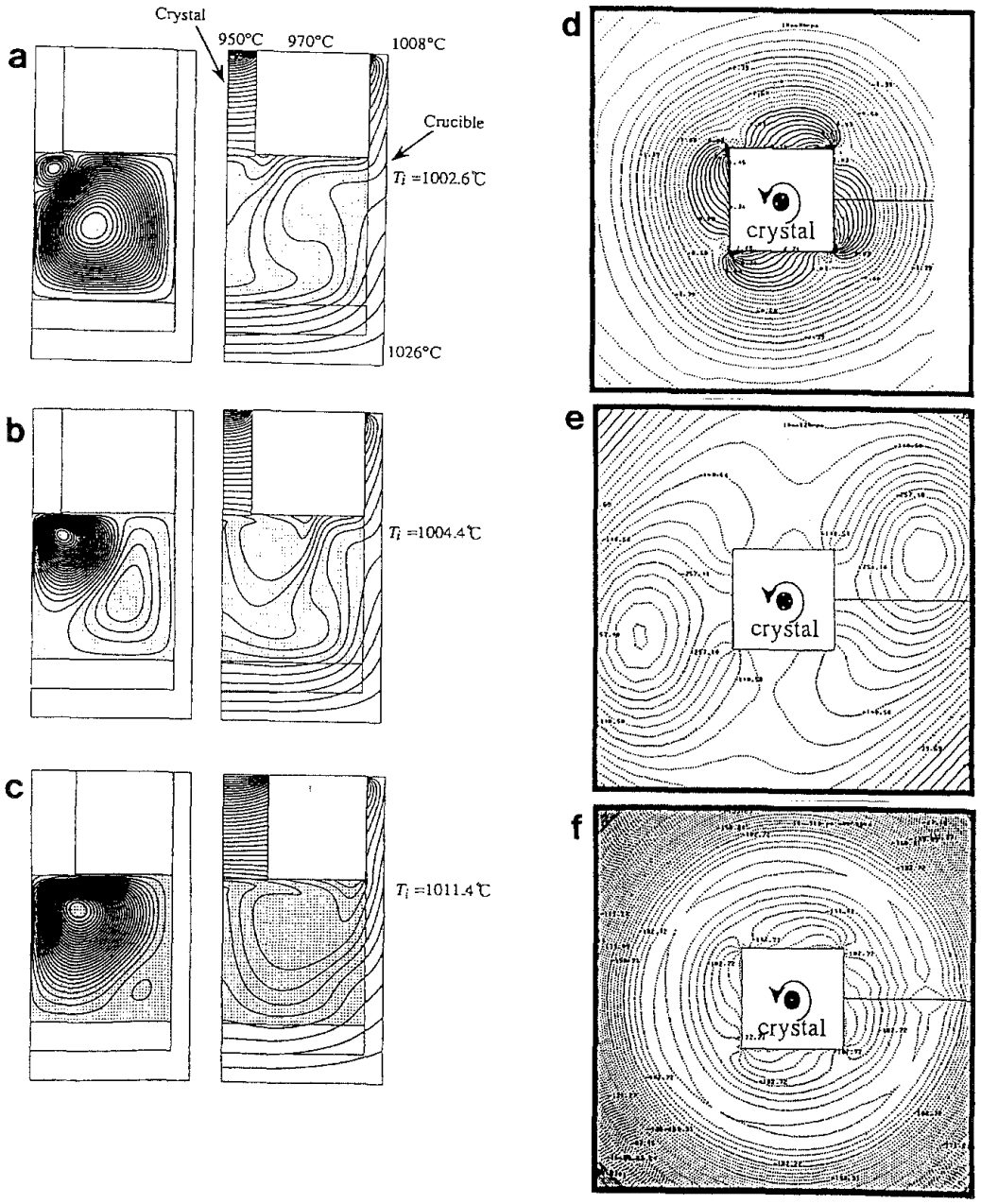

Fig. 19. Computer simulation of hydrodynamic conditions in crystal pulling experiments (Namikawa et al. 1996a, Egami et al. 1997: (a–c) numerical calculation results for a 10 mm diameter rotating crystal at rotation rates of (a) 50 rpm and (b) 150 rpm as well as the situation (c) with a larger, 16 mm diameter crystal rotating at 50 rpm (rev. min^{-1}); the left part of each figure shows the stream lines of melt convection and the right side demonstrates the corresponding temperature distribution (isotherms); only half the longitudinal section is given because of the picture symmetry; (d–f) the solute pressure distribution near rotating 10 mm square crystal (cross-section perpendicular to the rotation direction): pressure contour lines at 30 rpm (d); the same for 120 rpm (e) and average pressure contour lines at 120 rpm (f). (g) Dimensionless analysis of the meeting point of natural and forced convection and the (h) dimensionless temperature, which demonstrates the primary importance of hydrodynamic conditions in single-crystal pulling experiments (Namikawa et al. 1996b).

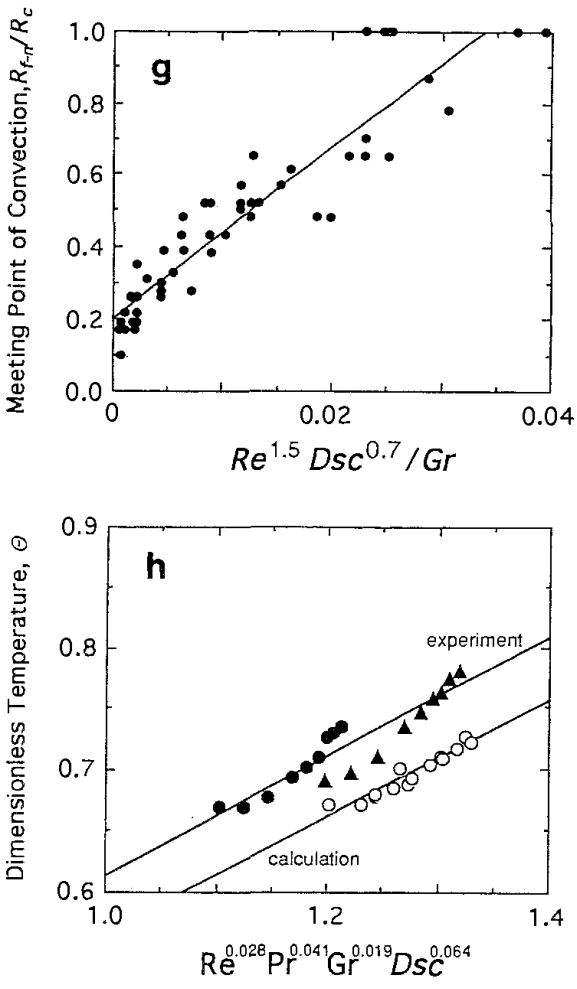

Fig. 19 (continued).

and the meeting point of the forced and the natural convection, namely, the steady position of the floating particles, shifts toward the crucible wall. The crystal rotation rate at which the floating particles move apart from the crystal decreases with increasing crystal size because it accelerates the forced convection.

The above-mentioned behavior of both flux convection and temperature redistribution can be generalized using dimensionless analysis (Namikawa et al. 1995b). During real Y123 crystal growth, the crystal diameter increases with increasing growth time and this continuously changes the crystal growth conditions. In general, the relative contributions of forced and natural convection to the mixed convection is evaluated by the ratio Re/Gr, where Gr is the Grashof number and Re is the Reynolds number, defined as $Gr = g\beta\Delta T L_m^3/\nu$ and $\mathrm{Re} = \omega D_s^2/2\nu$, respectively. In these expressions ΔT is the temperature difference between the surface and the bottom of the melt, L_m is the characteristic length of the melt, ν is the kinematic viscosity of the melt, ω is the angular velocity of the crystal, and D_s is the crystal diameter. It was estimated from the above-mentioned experimental data that the meeting point of convection is linearly correlated with the dimensionless numbers (fig. 19g), namely, with the ratio $Re^{1.5}/Gr$, multiplied

by the diameter ratio factor $D_{sc}^{0.7}=(D_s/D_c)^{0.7}$ which includes crucible geometrical characteristics (inner diameter D_c) with respect to those of the growing crystal (D_s). Moreover, the dimensionless temperature $\Theta=(T_i-T_{Top})/(T_B-T_{Top})$, i.e. the difference in temperature between the crystal–melt interface (T_i) and the crucible top (T_{Top}) normalized using the total temperature gradient between the crucible bottom and top (T_B-T_{Top}), is expressed as $\Theta=0.47\times Re^{0.028}\,Pr^{0.041}\,Gr^{0.019}\,D_{sc}^{0.064}+0.10$ (fig. 19h). Accordingly, in order to keep the crystal growth conditions constant, the rotation rate could be precisely adjusted with increasing crystal diameter. Another, more practically important way is to use a large crucible to make the system insensitive to the change of the crystal diameter. This means that the effect of crystal rotation on the temperature distribution in the melt would be smaller if the crystal diameter with respect to the crucible size is small enough as shown in fig. 19 (see also sect. 7.3.1).

It is evident also that the effect of a rotating crystal on the environmental solution flow in the surface layer could be very important in terms of feed-back influence on the growing crystal morphology (figs. 19d–f). It was shown (Egami et al. 1997) that a drastic change in the velocity boundary layer thickness around the squared edge may occur under certain conditions. Particularly, at small rotation rates (about 30 rpm for a 10 mm square crystal) a steady distribution of solution pressure exists around each crystal corner accompanied by different solute boundary layer thickness. This fluid-flow nonuniformity is believed to cause the corresponding step instability for the crystal and its rough morphology. On the contrary, much more uniform pressure and solute boundary layer thickness is confirmed by calculations at a faster rotation (120 rpm). In this case the whole crystal is exposed to negative pressure and each side of the crystal corner feels almost zero difference in the pressure distribution, which results in a better morphology.

In other crystal-growth techniques, other convection types may play an important role (Bohm et al. 1994). The surface tension of a hot melt is generally lower than that of a cold one, and a difference in the solute concentration may cause the same. Therefore, if there are differences in the temperature of the free melt surface, the melt tends to minimize its surface energy by extending the area of lower surface tension. In other words, the free surface is pulled from the hot regions to the colder ones and the spatial gradient of the surface tension results in a tangential action force, which drives the so-called Marangoni convection. To describe the Marangoni convection, the dimensionless Marangoni number is used: $Ma=(\partial\gamma/\partial T)\Delta T L_m/\eta k$, where $\partial\gamma/\partial T$ is the temperature coefficient of the surface tension, ΔT is temperature difference, L_m is the characteristic length (half zone length), η is the dynamic viscosity, and k is the thermal diffusivity. The Marangoni number gives a measure of the relation between the heat transfer by Marangoni convection and the heat conduction. The role of the Marangoni number is analogous to that of the (thermal) Rayleigh number for the natural convection. If the Marangoni number exceeds a critical value (say, 10^5), the laminar flow becomes unstable, leading to turbulence of the flow, temperature fluctuations and concomitant fluctuations in melt composition. Generally, the Marangoni convection might be important in the TSFZ method (sect. 4.2.3) for a relatively small zone up to 10 mm diameter. Under

practical conditions, however, both the thermal (buoyancy) and rotation effects dominate the Marangoni effect by orders of magnitude.

3.4. *Growth mechanism and interfacial phenomena*

3.4.1. *Spiral growth pattern and influence of growth conditions*

A detailed examination of the {001} surfaces of Y123 crystals grown by the self-flux method was performed by Komatsu et al. (1988) and Sun et al. (1991). They observed a change of morphology from circular to polygonal spirals with falling growth temperature and explained it by the roughness of spiral steps, which can be described by the Jackson factor (sect. 2.3.1 and 2.3.4). In the case of the {001} face of Y123, the spiral will be a square bounded by the ⟨010⟩ and ⟨100⟩ directions, which is predicted by PBC theory. From sect. 2.3.1, the lower the temperature, the higher the α-factor is, and hence the growth spiral on the {001} face of Y123 will be more polygonalized, i.e. with the growth temperature falling the evolution of growth spiral morphology is circular → octagonal → squared spiral. This prediction is in a good agreement with the observations.

An extensive spiral pattern study of Y123 crystals grown by the SRL–CP method under different growth conditions allowed Kanamori and Shiohara (1996) and Kusao et al. (1997) to investigate the relationship between the composition at the interface, C_i, corresponding to the supersaturation for interface kinetics, and the growth rate R. The relation between the terrace width and the supersaturation σ is given by the approximation of Cabrera and Levine in sect. 2.3.2; supersaturation is defined as $\sigma=(C_i-C_L(T_i))/C_L(T_i)$, where $C_L(T_i)$ is the Y concentration at temperature T_i at the crystal–melt interface. C_i can be obtained from eq. (20) using the experimental results, namely, R and $C_L(T_b)$. $C_L(T_i)$ is assumed to be equal to the Y concentration at the temperature T_S at the surface of the melt since T_i could not be measured precisely. Consequently, the supersaturation σ can be calculated. The observed terrace width in the spiral growth is plotted against the supersaturation in fig. 20. This experimental curve is fitted well by the theoretical relationship (10) when using an appropriate value of $\gamma a/kT=0.13$ nm. It is evident that the terrace width on the as-grown *ab* surfaces of Y123 single crystals satisfies the BCF theory.

Considering the interface kinetics, the growth rate is given in accordance with BCF theory by $R=k_i\sigma^2$ when the supersaturation is sufficiently small; k_i is the interface kinetic coefficient. The height of the single step is approximately equal to the c lattice constant of the Y123 crystal. When the advance speed of the step growing with the spiral growth mode is expressed via v_λ (sect. 2.3.2), the growth rate of the Y123 single crystal along the c-axis is given by $R=v_\lambda d/\lambda$, and $v_\lambda=\lambda\nu\exp(-W/kT)\,\sigma^2 x_s kT/(19\gamma a)$. Here, d is the lattice constant, λ is the step width, ν is the frequency of a molecule, W is the dissolution energy of an attached molecule from the surface of the crystal and x_s is the mean diffusive distance, as in sect. 2.3.2.

$$k_i = d\nu\exp\left(-\frac{W}{kT}\right)x_s\frac{kT}{19\gamma a}. \tag{25}$$

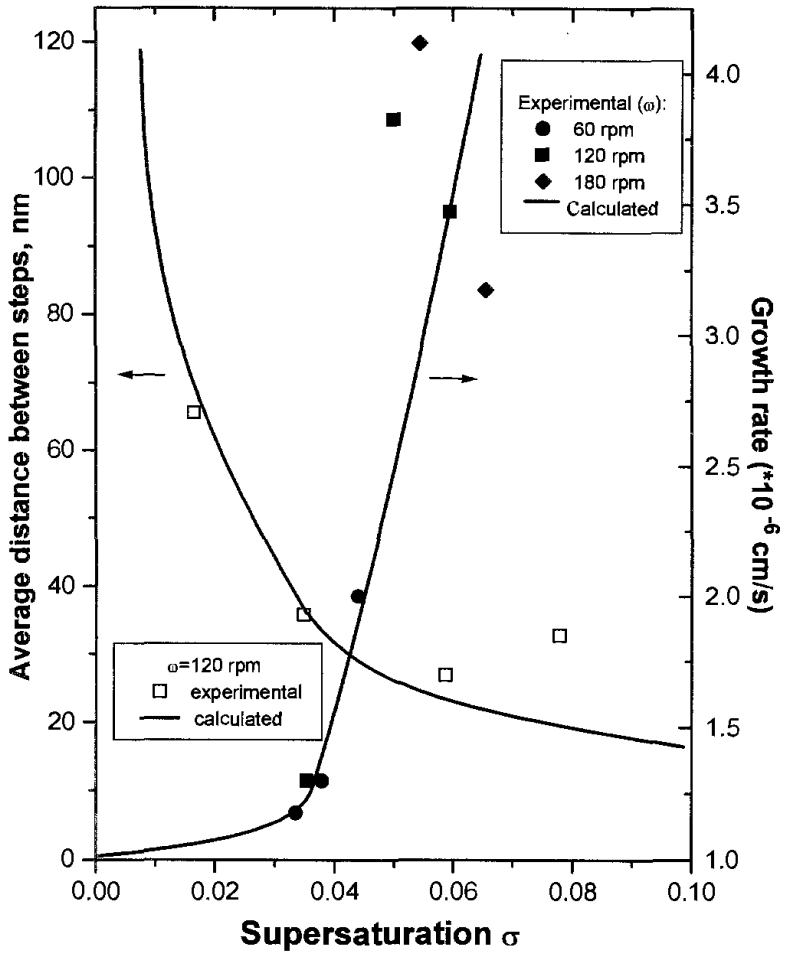

Fig. 20. Influence of supersaturation on the average distance between steps and on the single-crystal growth rate (summarized for different rotation speeds) in the case of Y123 grown by the SRL–CP method (Kanamori and Shiohara 1996).

After substituting into eq. (25) $d \cong 10^{-7}$ (cm) (c-axis length of the Y123 lattice), $W \cong 50$ (kcal/mol) (this value was estimated several times larger than the value for the vapor growth), $x_s \cong 100a \cong 4 \times 10^{-6}$ (cm) (a is the a-axis length), $\nu \cong \frac{1}{3} k_B T/h \cong 10^{13}$ (1/s) (h is the Planck constant and the coefficient $\frac{1}{3}$ indicates that the solute molecule oscillates only in the direction perpendicular to the surface of the crystal), the interface kinetic coefficient is calculated as $k_i = 10^{-3}$ (cm/s). Figure 20 depicts the relation between the growth rate and the supersaturation for the experimental and calculated results. The data are in a good agreement. Consequently, the crystal growth by the SRL–CP method of Y123 crystals pulled along the c-axis can be explained by bulk diffusion combined with interface kinetics.

Evidence for growth spirals was observed on the {001} face and probably on the {100} face of a crystal grown by the SRL–CP method by Yamada et al. (1995b). The shape of the steps on the {001} face was found to be square and that on the {100} face was elliptical under the same supersaturation. This morphological difference was partially

attributed to the difference of the α-factor, and the value $\alpha_{\{100\}}/\alpha_{\{001\}}$ was calculated to be about 0.75–0.9. The variation of the surface morphologies on the {100} face was explained by a modification of Temkin's roughening diagram and it was concluded that the morphology of the {100} face is more sensitive to an increase of supersaturation in comparison with the {001} face. The step width of the spirals on the {001} face was 500 nm. The major and minor radii of the growth steps on the {100} face were observed to be in the ⟨010⟩ and ⟨001⟩ directions. Due to the difference in the step advancing velocities, the ratio of the shape anisotropy was about 1.3 on the elliptical and 1.8 on the more polygonal growth steps.

The morphology difference between the *ab*-plane and the *ac*-plane was discussed on the basis of PBC theory by Sun and Schmid (1990). Klemenz and Scheel (1996) analyzed the spiral pattern in liquid-phase epitaxial growth of the Y123. Using the geometrical factor calculated by Yamada et al. (1995b) the authors estimated $\alpha_{\{001\}} \approx 13.25$ and $\alpha_{\{100\}} \approx 9.96$. M. Nakamura et al. (1996b) reported $\alpha_{\{001\}} = 22$ and $\alpha_{\{100\}} = 20.5$ at $p_{O_2} = 0.21$ and 1000°C. In fact, the growth of Y123 single crystals is faceted, therefore the α-factor is actually large. In this growth the {001} face is smoother than the {100} face. Further study, however, is needed to clarify the interface kinetics for the *ac*-plane, including the mechanism of macrostep formation.

3.4.2. *Growth rate anisotropy and shape controllability*

3.4.2.1. *Experimental estimation of growth rate anisotropy.* Crystal growth anisotropy is a complex phenomenon which depends on many experimental conditions. However, from a practical point of view it is very important to employ this factor in crystal production techniques since it may help to control the crystal morphology and to explain better the crystal growth phenomena.

The growth rate anisotropy has been investigated in several groups as briefly reviewed, for example, by Namikawa and Shiohara (1996) and Shiohara and Endo (1997). Flux-grown crystals are usually plate-like with a small thickness along the ⟨001⟩ direction, and in many cases the growth rate of {100} faces (R_a) was reported to be about 5 times larger than that of {001} faces (R_c) at relatively high cooling rates ("kinetic control"). An aspect ratio of up to 1000 has even been obtained at cooling rates >50°C/h (Wolf 1996). Van de Leemput et al. (1989), Sun et al. (1990) and Sun and Schmid (1990) investigated the morphology of the Y123 crystals using PBC theory (sect. 2.3.1). It was demonstrated that the $YBa_2Cu_3O_6$ crystal is bounded by the {001} and {100} planes and the aspect ratio [100]/[001] ≈ 5–10. Accordingly, the growth rate of the ⟨100⟩ direction (i.e. *a*-axis) is predicted to be about 5–10 times faster than that of the ⟨001⟩ direction (i.e. *c*-axis). These calculation results are consistent with the morphology of the crystals grown by the flux method with respect to index of planes terminating the crystals and the aspect ratio (except for crystals grown at a very slow cooling rate).

Reducing the cooling rate (0.5–1°C/h) in the flux method may give block-like crystals of several millimeters thickness in the ⟨001⟩ direction. Below 0.5°C/h, thick isometric crystals with aspect ratios between 1 and 10 can be grown (Wolf et al. 1989). Under those

conditions, besides {100}, {010} and {001} faces, {101} and {011} faces also appear, indicating that growth occurs near equilibrium ("thermodynamic control"). A further decrease of supersaturation results in crystals with an aspect ratio <1 and, rarely, in formation of a {111} face. Wolf (1996) suggested that in the case of Y123 grown by the self-flux method the {001} faces grow layer-by-layer, whereas the {100}, {010}, {101}, {011} and {111} faces grow by the leading-edge mechanism. The growth velocities of these faces are varied between 0.002 and 2 mm/h by changing the supersaturation. On the other hand, the growth velocity of the {001} face was proposed to be almost constant, 0.004 mm/h. Accordingly, for crystal growth in unstirred melts, the aspect ratio is a measure of the supersaturation during growth (fig. 21a).

Y. Nakamura et al. (1994) have investigated the three-dimensional interface morphology of Y123 crystals in directional solidification. Cabre et al. (1998) have proposed an interpretation of the mechanism of the natural single-domain selection and have also reconstructed the real three-dimensional morphology of the recrystallization front. Observations of several sections of the samples demonstrated that the faceted interface has a trigonal pyramidal shape and is formed by the {100}, {010} and {001} faces, which are perpendicular to each other (Y. Nakamura et al. 1994). From geometrical considerations, the crystal face toward the growth direction was found to be close to the {112} face, which is selected as a result of the preferential growth. The growth rate (R_a) of the {100} faces was evaluated to be about 1.5 times faster than that (R_c) of the {001} faces. Further, $R_a/R_c \approx 2$ was reported by D. Muller and Freyhardt (1995) from observations of microstructures around Y211 particles in melt-textured Y123 samples, when the growth interface is located in the liquid. At the same time, as soon as the growth interface touched the Y211 solid phase, R_a/R_c was reported to be about 12. This multistage character of growth was also observed by Aswal et al. (1999a) using high-temperature optical microscopy. Imagawa and Shiohara (1996) estimated the ratio R_a/R_c in directional solidification using a similar method as Y. Nakamura et al. (1994). Figure 21b shows that $R_a/R_c > 1$ for all nominal compositions analyzed, and that it increases with pulling rate. Since faster pulling throughout the hot zone tends to increase the undercooling (ΔT) at the crystal growth interface, these results indicate that the R_a/R_c ratio depends on ΔT. Marinel et al. (1998) found that the crystal growth anisotropy R_a/R_c becomes smaller with increasing melt temperature although the anisotropy seems to be lower for samples textured in a microwave cavity, as compared to samples obtained in a classical furnace.

In order to obtain information on the interface kinetics of Y123 crystal growth, Endo et al. (1996) and Shi et al. (1997, 1998) applied a top-seeding melt-texture method combined with constant-undercooling solidification, which has the advantages of proper estimation of the interface temperature and control over the crystal orientation. The growth rates along the a-axis and the c-axis as functions of ΔT (difference between peritectic and growth temperatures) were evaluated from the relationship between growth time and the crystal growth distances (fig. 21c). It is clear that $R_c > R_a$ at least in the range $\Delta T < 20$ K, and the dependence of R_a on ΔT is different from that for R_c, as follows:

$$R_a = 4.5 \times 10^{-7} \Delta T^{1.9} \text{ (mm/s)}, \qquad R_c = 2.8 \times 10^{-6} \Delta T^{1.3} \text{ (mm/s)}. \tag{26a,b}$$

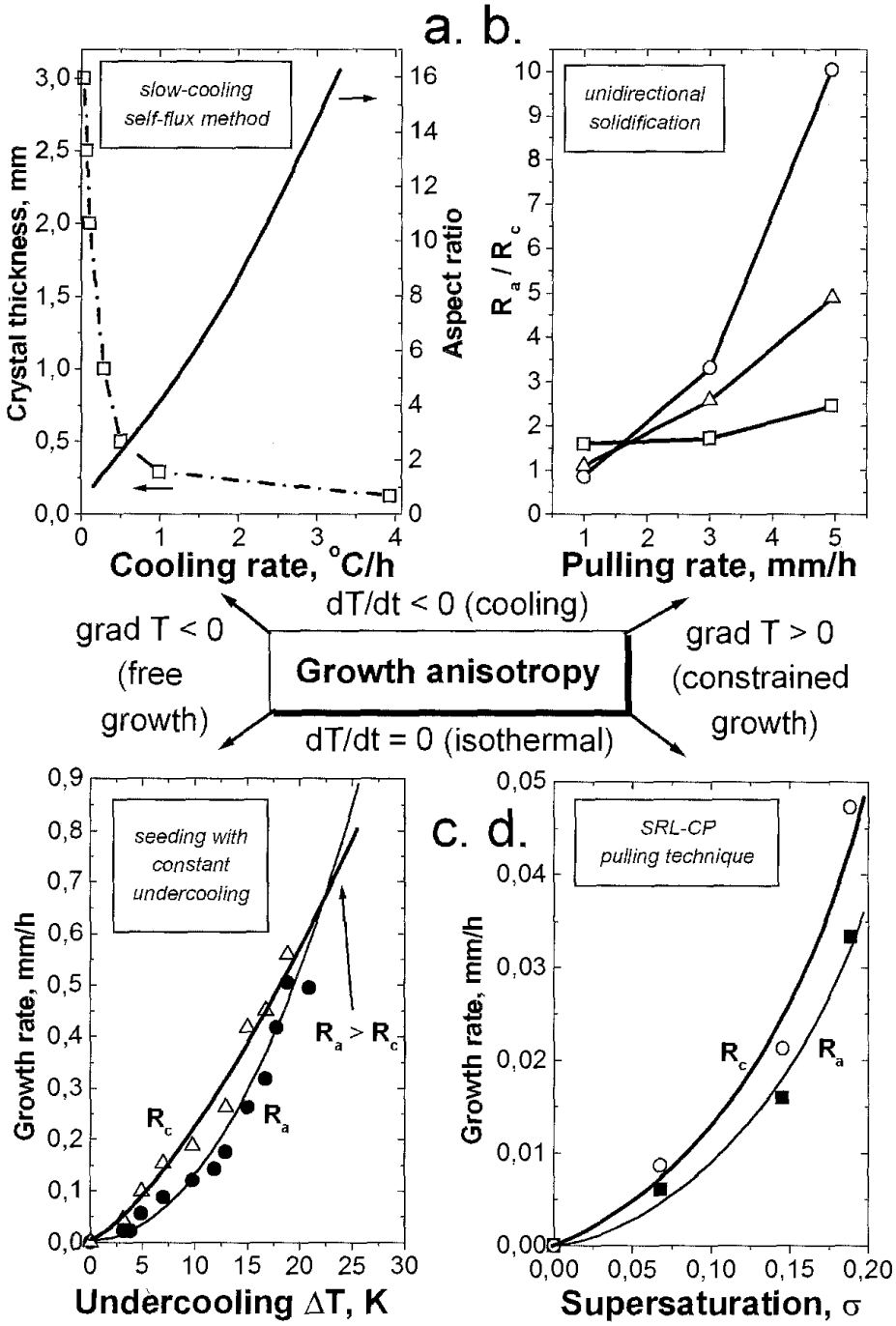

Fig. 21. Experimental growth anisotropy of Y123 along the principal crystallographic directions [a-axis (R_a) and c-axis (R_c)] as observed in different crystal growth techniques: (a) crystal thickness and aspect ratio dependencies on cooling rate in the slow-cooling self-flux method (Wolf 1996); (b) R_a/R_c ratio in unidirectional solidification experiments with different scanning (pulling) rates and nominal compositions (Imagawa and Shiohara 1996); (c) relationship between growth rates and undercooling in top-seeded (Sm123) melt-texturing experiments with constant undercooling (Endo et al. 1996); (d) macroscopic growth rates of side faces ({100} and {001}) of a crystal grown along the ⟨100⟩ direction at different supersaturations in the SRL–CP method (Namikawa and Shiohara 1996).

Equations (26) indicate that at a high undercooling of above 27 K, R_a becomes larger than R_c. Therefore, the results of the constant-undercooling method are not in conflict with those of unidirectional solidification when considering the difference in undercooling. These results can qualitatively explain also the trend of the R_a/R_c ratio as a function of the pulling rate (fig. 21b).

Thus, the crystal-growth anisotropy depends strongly on the supersaturation, i.e. at low supersaturation $R_a < R_c$, however, $R_a > R_c$ for high supersaturation. The difference between experimental results and theoretical predictions may be ascribed to the interaction between the Y123 crystal and the Ba–Cu–O liquid phase. A crystal with faceted interfaces needs a driving force for its growth, such as the interface kinetic undercooling (ΔT_k). In this case, the growth rate shows different dependences on ΔT_k according to the growth mode. For example, quadratic and proportional dependences on undercooling indicate spiral growth and roughening, respectively (sect. 2.3.2). Therefore, the different powers of ΔT in eq. (26) suggest a difference in growth mechanisms between the *ab*-plane and the *ac*-plane, although it should be noted that the undercooling affects not only the interface kinetics but also the solute diffusion (see also Nagashio et al. 1999).

Kambara et al. (1997b, 2000) investigated, in a similar way, the growth-rate anisotropy of Nd123ss for the Nd–Ba–Cu–O system, varying the flux composition and the seeding temperature. It was found that the growth rates in both *a*- and *c*-directions decreased with increasing Ba/Cu ratio in the flux, probably because of the liquidus curvature effect. However, in this case ΔT (undercooling value) as a surrogate for ΔG (see sects. 2.1, 2.2) does not reflect exclusively the driving force for solid phase crystallization because of the cation nonstoichiometry of Nd123ss. The Nd/Ba ratio was observed to decrease down to its equilibrium value in the Nd123 matrix from the seed crystal to the edge of solidified Nd123 due to non-steady state solidification of Nd123 even under isothermal undercooling processing (Kambara et al. 2000). The method described in sect. 3.3.2 should probably be applied. More detailed investigations are needed to clarify the growth mechanism and its anisotropy.

3.4.2.2. *Experimental controllability of crystal shapes in the pulling method.* In the pulling method (sect. 4.2.5), which allows one to produce the largest known R123 crystals in a steady state, lower supersaturation is expected in comparison with other crystal growth methods (Namikawa and Shiohara 1996, Namikawa et al. 1996b). Thus, the $R_a < R_c$ growth-rate anisotropy should be expected there. Typical macroscopic growth rates were estimated in this method along the pulling direction as 0.108 mm/h (Y123, air, SRL–CP method, Yamada and Shiohara 1993), 0.075 mm/h (Y123, air, SRL–CP method, Yao and Shiohara 1997), 0.1 mm/h (Pr123, air, SRL–CP method, Tagami et al. 1995), 0.16 mm/h (Y123, oxygen, SRL–CP method, Yao et al. 1996a), 0.24 mm/h (Nd123, air, TSSG method, Yao et al. 1997).

Crystals grown by the SRL–CP method usually possess a pyramid-like overall shape. Namikawa and Shiohara (1996) investigated the crystal growth-rate anisotropy of the Y123 phase in the modified pulling method. The growth rate of {001} faces appearing on the side of the crystal grown along the ⟨100⟩ direction was found to be 1.3 times higher

than that of {100} faces. At the same time the growth rate of {001} faces appearing on the bottom of the crystal grown along the ⟨001⟩ direction was found to be about 1.6–2.0 times higher than that of {100} faces appearing on the bottom of the crystal grown along the ⟨100⟩ direction. The latter is more sensitive to the change of supersaturation than the crystal growth rate of crystallographically the same {100} type of faces appearing on the *side* of the crystals grown along the ⟨100⟩ direction, at least for the selected experimental conditions (low pulling rate and low supersaturation regime). These differences were attributed to the increase in the temperature at the crystal bottom face during the crystal growth. Manipulations with the growth anisotropy as well as hydrodynamic conditions in the crystal pulling experiment (sect. 3.3.3) allowed to achieve shape controllability in the modified pulling method:

(1) Crystal growth in the ⟨001⟩ direction, when making the supersaturation higher than 0.19 and maintaining the balance between the pulling rate and the crystal growth rate of the bottom face, demonstrates a possibility of producing a crystal which has a long ($1.4\times1.4\times1.4\,\mathrm{cm}^3$) and nearly straight body with expanding angle as small as about 25°. This is in good agreement with the single crystal shapes which have been obtained by the pulling technique (Namikawa et al. 1996b, sect. 6.2).

(2) Crystal pulling under certain conditions for the forced convection exhibits a potentiality of both flat or concave crystal production (Namikawa et al. 1996a, sect. 6.2). To attain suitable growth conditions for a flat crystal, the crystal rotation rate should satisfy simultaneously at least the following three requirements:
   - keeping the temperature constant at the crystal growth interface to avoid striations, poor morphology and "partial melting" of the growing face due to rising interface temperature when the enlarged crystal increases the forced convection;
   - ensuring outward flow at the periphery of the growing crystal to avoid attachment of floating particles and polycrystallization;
   - making the boundary layer thickness of the solute small by appropriately increasing the rotation speed.

   The experimental observations of the crystal morphology (Namikawa et al. 1995a) are in a good agreement with Nikolov's empirical correlation between the crystal size and the critical rotation rate ω_{cr} at which a flat crystal/liquid interface can be obtained:

$$\omega_{cr} = \frac{3.16(g\beta\Delta T)^{0.43} D_{cruc}^{0.24} h^{0.15} \nu^{0.14}}{D_s^{1.08}}, \tag{27}$$

   where ΔT is the temperature difference between the crucible wall and the crystal, D_{cruc} is the crucible diameter, and h is the melt depth. Under strong forced convection, a concave interface shape of the growing crystal can be obtained (sect. 6.2). This shape reflects the isotherm and it indicates that the temperature at the center of the crystal growth interface is raised (as high as about 6 K) above the peritectic melting temperature of the Y123 phase by the heat transported with the forced convection from the hot crucible bottom. Therefore, the crystal growth interface

becomes concave and rough with a high crystal rotation rate, smaller crucible and with a large crystal size due to an increase of the interface temperature.

(3) Round-shaped crystals for future steady industrial production have been obtained in the automatic pulling method by adjusting the anisotropy of growth as reported by Egami and Shiohara (1997) (sect. 6.2). The automatic pulling system includes a crystal–solution interface temperature estimator, a weight signal analyzer, a compensator for oxygen concentration, a crystal growth rate estimator that considers the effect of supersaturation, solute boundary layer thickness and the oxygen concentration. Under these conditions, a round-cornered 4 mm diameter Y123 crystal has been obtained when keeping the solution surface temperature at only 2°C lower than the Y123 peritectic temperature and making the crystal–solution interface position to be close to the crystal detachment. The region between {100} and {110} faces of the crystal has shown large macroscopic steps. The {110} face consisted of small {100} and {010} facet faces and macroscopically rough surfaces. The {100} face was found to be macroscopically flat, however, microscopically it contained rough areas. Along the solution meniscus the seed crystal was remelted and that resulted in the whisker-like edges at the corners. However, the round corner did not appear due to the meniscus shape effect only. Keeping the crystal closer to the roughening temperature (see sect. 2.3.1), when the higher growth temperature has been selected, might be important. When the growth temperature is raised, the difference in the crystallization energy released for the {100} and {110} faces becomes small since the corner is disadvantageous for the crystallization from a thermodynamic point of view. Additionally, upstream flow of the solution under the selected conditions and average supersaturation were both reduced when the crystal and solution were set to the position near their detachment. Then, the supersaturation is expected to be small at the corner and large at the center of the {001} bottom face. Therefore the driving force should be lower in the case of the {110} face because this face has a larger distance from the center to the edge in comparison with the {100} face. As a result, a round-cornered crystal can be grown.

3.4.3. *Alternative growth mechanisms (twin-plane-re-entrant-edge growth)*

As shown in sect. 3.1.2.3, when barium is substituted by Nd up to x values of about 1.0 in the $Nd_{1+x}Ba_{2-x}Cu_3O_z$ solid solution, it becomes orthorhombic even at temperatures as high as 1000°C. Consequently, a necessary condition for twinning of the neodymium-rich Nd123ss solid solution in the *ab*-plane is provided.

Two common mechanisms are available for the formation of twins – mechanical or thermal stress and, on the other hand, the probability events that lead to enhanced interface attachment kinetics (Tiller 1991a). The first corresponds to the "usual" $x \approx 0$ case of R123 phases due to oxygen diffusion and the P4/mmm → Pmmm tetragonal-to-orthorhombic phase transition around 450–700°C. For the heavily substituted Nd123ss solid solution a particularly powerful nucleation site is formed (Goodilin et al. 1998b) during crystal growth when the faces of twins meet along the twin plane (fig. 4e).

The growth layers are then produced by nucleation at even higher frequency because the re-entrance lowers the formation energy of new-born growing sites at the re-entrant corners. The crystals grow by the faster propagation of layers in the twin boundary direction, giving a typical zigzag pattern of the growing front as shown in fig. 4e. Thus, a new crystal-growth mechanism can be suggested in the case of a heavily substituted solid solution: twin-plane-re-entrant-edge growth (TPRE) (Elwell and Scheel 1975). Many "oxygen-stoichiometric" crystals grow in this alternative way when the molecular attachment aspects begin to become significant. This mechanism was found, for example, in the case of $NdAlO_3$, Al_2O_3, BeO, $BaTiO_3$ and $Ba_2TiP_2O_9$. Obviously, however, it would never be found in the case of superconducting R123 phases with the $x = 0.0$ substitution.

4. Common crystal-growth techniques for high-temperature superconductors

4.1. *Classification*

In this section, we will describe practical methods commonly used to obtain R123 single crystals and crystal layers. These methods can be classified using different schemes depending on the aim of the classification, and it is difficult and even nonessential to have a universal classification. A number of methods (flux growth) is beneficial due to their simplicity, other methods (SRL–CP, TSFZ) can be easily automated; some of the methods use a strict control of nucleation and are performed in a steady state (SRL–CP, modified TSSG), others employ non-steady-state conditions (slow-cooling flux method); a thermal gradient is essential for one group of methods (TSFZ, SRL–CP) and useless for others (modified TSSG); most of the methods have a crucible contamination problem (flux method), but several methods are containerless (TSFZ); sometimes the problem of separation of the as-grown crystal from the melt appears (flux method), in other cases it is not important at all owing to the construction of the crystallizer (SRL–CP, TSFZ); the crystal size, shape and defect concentrations are also dependent on the method applied (sect. 6). Small crystals have been obtained by nearly-solid-phase re-crystallization (Wan et al. 1988), by the laser-assisted Verneuil method (Nakada et al. 1988), and by crystallization from immiscible systems or electrocrystallization (Chen 1998). Most other crystals have been produced by the flux method, but their size is limited. Therefore, continuous growth processes, i.e. TSFZ and TSSG methods, have been applied widely to the R–Ba–Cu–O system, permitting the production of large crystals. Figure 22 summarizes several widely spread growth methods for HTSC crystals and different interfacial phenomena taking place in these processes (fig. 22a). An example of a classification using hydrodynamic considerations has been given by G. Muller and Osrogorsky 1994. The characteristic features of each process will be briefly introduced in this section.

4.2. *Techniques in practice*

4.2.1. *Semisolid melt solidification*

The melt-textured Y123 materials show a highly aligned structure, which is formed by a peritectic reaction between Y211 and the liquid phase (see, for example, Shiohara

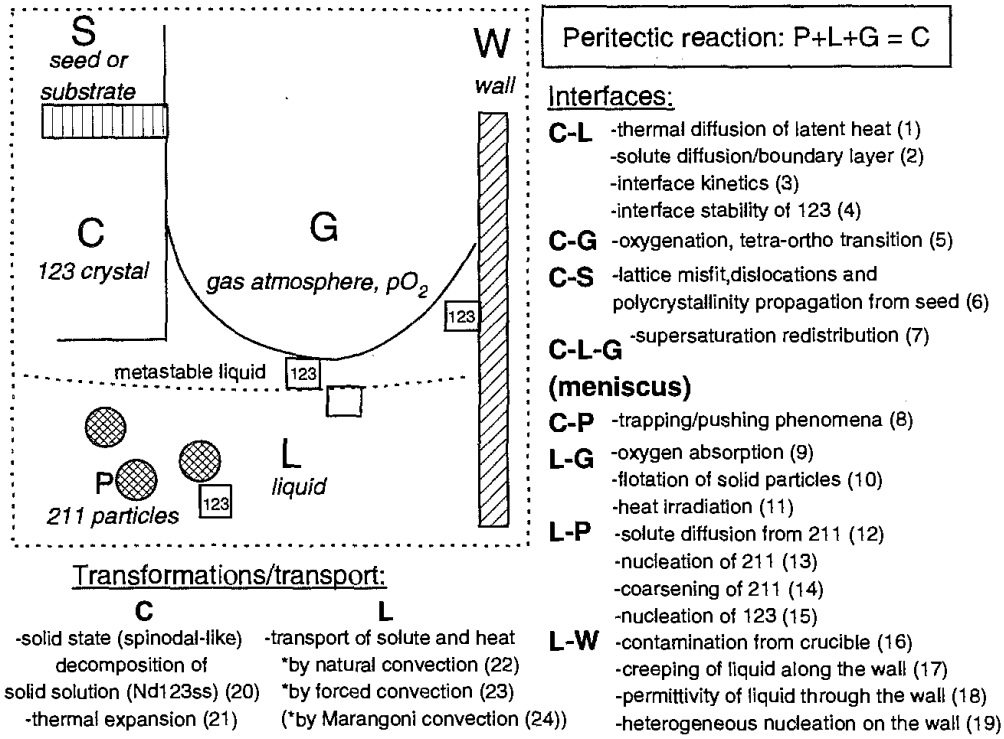

a.

Fig. 22. A brief classification of R123 crystal growth techniques on a basis of different phenomena taking place at various interfaces between solid, liquid and gaseous phases participating in the solidification process: (a) possible interface boundaries and phenomena connected with the presence of such interfaces; (b) different interfaces present in the self-flux method; note that numbers in brackets correspond to the general scheme of classification (a); (c) a number of interfaces and phenomena of some importance for the unidirectional solidification method; note that (crystal–high-temperature phase and melt–high-temperature phase) interfaces are close to each other; (d) different interfaces and phenomena to be considered in the SRL–CP pulling technique of bulk crystal production; note that solute transport and nucleation can be controlled in order to achieve a desired morphology of the crystal.

and Endo 1997, Lo et al. 1998, C.-J. Kim and Hong 1999). The variety of semisolid melt solidification techniques (Desgardin et al. 1999, Tretyakov and Goodilin 2000) falls mainly into three categories according to the method used to create supersaturation: (1) Slow cooling with or without a thermal gradient and with no transport of a sample or a furnace, (2) slow cooling through a temperature gradient by sample or furnace transport, and (3) isothermal growth below the peritectic temperature without sample transport. An obvious feature of such methods is a high sensitivity to the original chemical composition and microstructural organization of precursors or charge materials since all of these processes involve a reaction between the liquid and the surrounding solid particles resulting mainly in the formation of polycrystalline material with large "quasi-single-crystalline" domains misoriented by high-angle boundaries and containing, as a rule, low-angle grain boundaries and nonsuperconducting inclusions (211 and CuO phases, solidified melt).

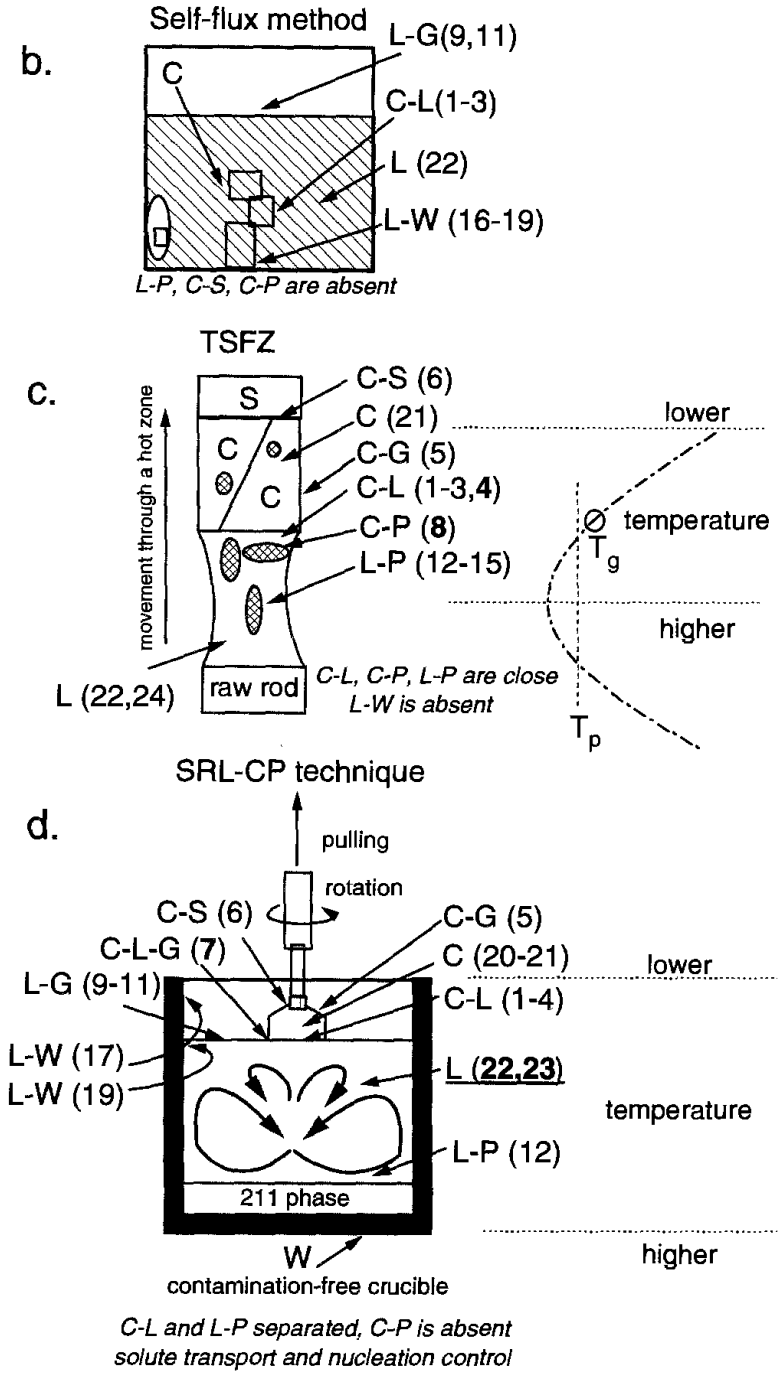

Fig. 22 (continued).

Multiplication of the above-mentioned methods (1)–(3) by the number of possibilities to employ additional fields or treatments in order to control the solidification reaction gives approximately 25 known schemes for semisolid melt solidification with commonly used abbreviations (Tretyakov and Goodilin 2000). Method (1) includes the largest

number of modifications, such as heat-treatment optimization (liquid-aided process, melt-texture growth, liquid-phase processing), doping (platinum-doped melt growth), melt soaking (liquid-phase-removal process), application of a magnetic field (magnetically induced alighnment), various ways of multiphase precursor preparation (powder–melt process, solid–liquid melt growth, two-powder process, quenched-melt growth, melt–powder–melt-growth, quenched directional recrystallization, oxygen-controlled melt growth, melt casting), seeding (top-seeded melt growth, constant-undercooling solidification processing, graphically-aligned-seeds melt growth, composite-reaction texturing). For method (2), Joule-heat-zone melting, floating-zone melting, laser-zone melting, seeded directional solidification and vertical-gradient freezing have been reported. Oxygen partial pressure changes (isothermal melt crystallization, gas-pressure method) or rare-earth ion constitutional gradients (constitutional-gradient melt growth) can be used to conduct isothermal crystallization (method 3) besides the method of constant-undercooling solidification processing. Since these methods, strictly speaking, lead only to polycrystalline materials with enormously enlarged grains, and, on the other hand, semisolid melt solidification has been widely discussed by a number of authors (Jin et al. 1991, Murakami 1992, Salama and Lee 1994, Shiohara and Endo 1997, Cardwell 1998, and others), we will not discuss it in depth here. (See Notes added in Proof, point 4, for brief descriptions.)

Only a few groups have reported surface morphologies of melt-textured Y123 phases. Jin et al. (1991) observed a spiral-like growth on the {001} surface of Y123 ribbons by SEM although the actual spirals are not clearly defined and the step height is much coarser (10–100 nm) than a unit-cell-height step. Marella et al. (1994) found macrospirals on the {001} surface of melt-processed Y123 domains. The macrospirals showed circular–octagonal–square shapes, depending on the supersaturation and temperature fluctuations during the melt-texture growth. Goyal et al. (1993) reported platelet/ledge growth, growth hillocks and stepped hopper-like growth morphology of semisolid melt solidified Y123. Vandewalle et al. (1995) observed pyramid-like growth patterns of a melt-textured Dy123 grain (see also Vandewalle 1998) and calculated the growth anisotropy {100}/{001} as ~50 using a simple kinetic model (the Eden model, Herrmann 1986). In order to achieve controlled growth of large Y123 pseudocrystals for electromagnetic applications, Lo et al. (1997) investigated the morphology of semisolid-melt-crystallized, top-seeded Y123 with addition of platinum. Although the surface morphology of the pseudocrystals was smooth and faceted in the vicinity of the seed, growth in this region produced cell-like inhomogeneities. Shi et al. (1997), however, demonstrated the possibility of achieving a planar crystallization front and the growth of large pseudocrystalline domains by such a seeded melt growth. Note that these morphologies deal with free surfaces, which are considered to reflect the solid/liquid interface during growth indirectly. It is difficult experimentally to pick up only growing Y123 crystals from a semi-solid melt contrary to thin films or pulling crystals. Moreover, Y211 particles dispersed in the Ba–Cu–O liquid may increase the effective viscosity of the liquid, and usually clean surfaces cannot be easily obtained.

4.2.2. *Flux and self-flux growth*

Flux growth is the most commonly used technique for crystal growth from high-temperature solutions (Elwell and Scheel 1975). The main advantage of this method is its relative simplicity and the fact that the crystals are grown below the melting or decomposition temperature. Thermal strains are minimized in this technique owing to relatively low temperature, small thermal gradient applied and the free growth into a liquid (fig. 22b).

The flux method requires an appropriate solvent. The best solvent should satisfy some ideal conditions. The main requirement is that the solvent should dissolve the solute to an appreciable amount: a practical minimum is usually considered to be about 1%. The solvent must not react with the solute to form new solid compounds because the crystal phase required should be the only stable phase in the crystallization temperature range. Furthermore the range of solid solutions between solute and solvent should be as small as possible to avoid elements which are incorporated into the growing crystal. At the same time, the solubility change with temperature should have an appreciable level to increase yield of crystals by any regular technique used to obtain supersaturation, mostly by slow cooling. A low viscosity of the solution is desirable to achieve better homogenization and fast stable growth. An ideal solvent should supply both a low melting point and low growth temperatures to prevent destructive phase transitions and a high concentration of equilibrium defects; this is the most important point in the case of growth of incongruently melting compounds. The lower temperature is also more beneficial with respect to furnace and crucible materials. The last problem with the crucible materials is also primarily important, because high reactivity with the container materials as well as high tendency of the solvent to creep out of the crucible can change the solution composition and melting point during the growth process, introduce impurities and damage the equipment used. Obviously, for an ideal solvent easy separation from the grown crystals, low cost and low toxicity are required. Unfortunately, no real universal solvent exists which successfully fulfills all these ideal properties, and experimental compromises are always necessary. One of them is using an eutectic mixture composed of compounds present in the crystallizing system and compatible with the required crystallizing phase (so-called self-flux growth).

The main disadvantage of the flux method is the low growth rate, which is much smaller than in the melt growth. Hence, flux-grown crystals usually have small size because of difficulties with the nucleation control. Moreover, since the crystals normally develop facets and the linear growth rate of each grain might be different, it leads to inhomogeneities in the crystals. The next disadvantage is the unavoidable presence of ions of the flux as impurities in the crystals except for the case of self-flux. Frequently, the flux inclusions can be found in the crystals.

In general, however, crystal growth from fluxes is commonly preferable whenever possible because small crystals are often needed for basic investigations and measurements of physical properties although this method cannot supply the large single crystals of HTSCs desired for industrial and many other practical applications.

4.2.3. *TSFZ method*

The traveling solvent floating zone method is a valuable growth technique for producing high-quality and large single crystals which melt incongruently (Tiller 1991b, Bohm et al. 1994). In the great variety of modifications of this very famous method, a zone of solution is made to travel through a solid in a temperature gradient so that a feed rod supplies the melt at the high-temperature side, and a crystal grows at the low-temperature side (TSFZ, fig. 22c). The important parameters of this process should include the number of passes, zone length, interzone spacing, travelling rate, diffusion boundary layer thickness, heater power per zone, and stirring power per zone. The solution zone can be moved by relative motion of the heater (or sample), which may be a resistance heater strip, radio-frequency coil, or the focus of an infrared light source or laser when growing fibers. In principle, this is a method for growing crystals of reactive materials which keeps the molten substance completely out of contact with solid crucibles. The other advantages of this method are that uniform material characteristics can be obtained, automation can be applied, and the required apparatus is more or less simple in construction and maintenance. For applications of large critical currents, uniform grain alignment of HTSCs over long length is desired. Directional solidification has a potential of producing highly textured superconductors. Since the location of the solidification zone is controlled in directional solidification, multiple nucleation can be avoided. It should be noted that directional solidification can reach a steady-state growth contrary to continual cooling methods, although in this technique large single-domain bulk crystals probably cannot be obtained (Cabre et al. 1998).

4.2.4. *Liquid phase epitaxy*

Liquid phase epitaxy (LPE) is an epitaxial growth technique by which crystal growth originates from solution (Tiller 1991a, Bauser 1994). The basic principle of this method is to place a suitable substrate in a slider which is moved across the surface of molten material held at the temperature at which the melt is supersaturated (undercooled). Being a combination of solution growth and epitaxy, LPE combines advantages of both methods. The solution growth occurs in closely thermodynamic equilibrium and the driving force needed to achieve the growth is small, although a high driving force can be applied to produce a broader range of results. Supersaturation is generated by means of step cooling, ramp cooling, or by a constant temperature gradient. At the same time epitaxy gives any desired orientation or misorientation through orientation of the substrate crystallographic plane, i.e. the initial substrate orientation and morphology constitute one of the important controlling parameters for LPE, and a particular growth mechanism can be chosen by selecting the appropriate substrate and its orientation. In principle, it is desirable that the lattice parameters and the linear thermal expansion coefficient of the substrate and the depositing material be similar otherwise the mismatch can introduce strains into the film, resulting in cracks and dislocations. If the epitaxial film has the same composition as the substrate, the method is called homoepitaxy, while for significantly different compositions it is called heteroepitaxy.

4.2.5. *Solute-rich liquid crystal pulling (SRL–CP) method*

The crystal pulling methods originate from the pioneering work of Czochralski (Roy 1992, Scheel 1993, Hurle and Cockayne 1994). Actually, modern crystal pulling was first developed as a technique for the production of semiconductor single crystals with large size and high perfection, and now it is, in fact, the dominant technique for the commercial manufacture of most of these materials. Crystal pulling has an evident advantage in growing large single crystals of silicon, more than 12 inches in diameter and 1 m in length. The primary advantage of this method is that undesirable nucleation and polycrystallization can be suppressed by selecting appropriate processing conditions. Another advantage is its flexibility, since growth conditions can be changed easily during pulling. In addition, the melt–crystal interface and the growing crystal can be observed in situ, and any dopants can be added at any stage of growth because of the easy access to the melt surface.

In its simplest form, the pulling apparatus consists of a crucible which contains the charge material to be crystallized surrounded by a heater and a hermetic chamber to obtain the necessary gas environment. A pull rod with a chuck attached to its lower part is mounted co-axially above the crucible together with a precise rotating driver and a sensitive *in situ* balance. A seed crystal is attached to the chuck and the pull rod is slowly lowered to minimize thermal shock until the seed is dipped into the melt, which is being held at a temperature providing the necessary undercooling. The temperature and seed position are critical and have to be adjusted until the seed stably supports a liquid meniscus. Too high temperatures cause the seed to be dissolved in the liquid, however too low temperatures result in a rapid freezing over the seed. Once an appropriate thermal steady state has been achieved, the pull rod is slowly lifted and rotated, allowing the seed to grow.

Yamada and Shiohara (1993) have succeeded in the continuous growth of Y123 single crystals by a pulling method using a BaO–CuO solution with the solid Y211 as a solute in yttria crucibles. This modified method has been renamed as the SRL–CP (solute-rich liquid crystal pulling) method since the solution is steadily enriched by the solute from the Y211 solid. The innovation of a suitable crucible for the Y–Ba–Cu–O system is a significant contribution to the success of large single-crystal growth of Y123. Yamada and Shiohara (1993) found yttria crucibles with an addition of 0.5 mol% TiO_2 to be one of the best vessels for solution growth with a BaO–CuO solvent (sect. 7.1). This crucible, which is highly sintered by the TiO_2 addition, demonstrates a smaller permeated depth and reaction layers than a highly pure yttria crucible, and it holds the solution for a relatively long time although the experimental period is still limited due to creeping of the solution along the crucible wall. Erb et al. (1995, 1997) have found that crucibles made of $BaZrO_3$ are not reactive with melts of RBCO (at least, R = Y and Pr) systems (sect. 7.1). This novel inert crucible may be used for crystal pulling.

Figure 22d shows a schematic drawing of the configuration of the SRL–CP method; the growth mechanism of the SRL–CP method was described in sect. 3.3.1. Briefly, Y211 powder is placed at the bottom of the crucible and BaO–CuO composite

(Ba:Cu cation ratio 3:5) is placed on the layer of Y211 powder. In terms of mass balance, the solute Y211 and the solvent BaO–CuO can react completely and form the Y123 phase without any residual products, Y_2BaCuO_5(solid) + "$Ba_3Cu_5O_8$"(liquid) → $2YBa_2Cu_3O_{6.5}$(solid). Therefore, the composition of the solvent does not change with time as the crystal grows. A temperature gradient is provided in the melt to satisfy the conditions that the temperature at the melt surface (about 1000°C) be lower than the Y123 peritectic temperature ($T_p = 1005$°C) and that the temperature at the bottom be higher than T_p (about 1015°C). Accordingly, the Y211 solid can exist at the bottom of the crucible as a source of the solute. The surface of the melt is supersaturated by yttrium and a Y123 single crystal grows there. In this method, the transport of the solute from the bottom of the crucible to the growing crystal is a key factor for achieving a high constant growth rate. The solute is mainly transported by the melt convection. A Y123 single crystal prepared separately or an in-plane aligned Y123 thin film deposited on a MgO single crystal are used as seeds. The Y123 crystal is grown with a rotation rate of about 120 rpm (sect. 3.3.3) and a typical pulling rate is about 0.1–0.5 mm/h.

4.2.6. *TSSG method*

The top-seeded solution-growth technique may be used also to grow crystals at the surface of an open crucible when the surface temperature is lower than the bottom temperature (Roy 1992). However, in this case, contrary to the situation in melt growth, the temperature gradient should be small and the growth temperature has to be continuously lowered by slow cooling of the melt. A seeding crystal can be introduced from above at the saturation temperature and sometimes a cold finger can be used for that purpose. All these conditions were essentially changed in the modified TSSG applied for Nd123ss growth from MgO or Nd_2O_3 crucibles (sect. 5.5.2), because relatively large solubility of the solute is essentially required for this method otherwise a sufficient size of single crystals can not be easily obtained.

5. Progress in R123 single-crystal growth

5.1. *Flux-grown crystals, morphology and growth problems*

As mentioned in sect. 4.2.2, the flux method is one of the most commonly used processes to produce single crystals in the case of incongruent melting systems. Accordingly, since the discovery of HTSC materials great efforts to grow high-quality, large single crystals using various flux methods have been carried out mainly for fundamental studies (as reviewed, for example, by Hidaka and Suzuki 1991, Demyanets 1991, Chen 1992, Assmus and Schmidbauer 1993, Shiohara and Endo 1997, and Chen 1998). A large number of works under the self-flux growth can be summarized by mentioning a few semi-empirical rules and practical findings aimed to solve problems with the appropriate flux choice, crucible corrosion and contamination, crystal removal, and size and morphology

control. It should be noted, however, that this method has probably lost the professional competition with other modern and obviously more advantageous techniques.

A large number of high-temperature solvents have been tried as low-melting fluxes, particularly In_2O_3 (Ono et al. 1988), B_2O_3 (Wanklyn et al.1988), PbO, PbF_2, KOH–NaOH (Sandford et al. 1995, Sunshine et al. 1997), KCl–NaCl (Murugaraj et al. 1990, Gencer and Abell 1991, Aswal et al. 1995). The crystals grown from the KCl–NaCl flux were found to be relatively large in size, $8\times7\times2\,mm^3$, although they seemed to have a poor morphology and a large number of defects as well using most of the listed solvents.

In addition to the restriction of the suitable solvents, the progress in growth is also hampered by the pronounced reactivity of the melt with most crucible materials, which tends to contaminate the growing crystals. Thus, the choice of crucible materials is very limited. Many kinds of crucible materials have been used for the flux method, such as Pt, Au, Al_2O_3, ThO_2, ZrO_2, SnO_2, MgO and so on. However, gold is too soft to be used for a long time and allows a strong creeping of the self-flux, platinum reacts with the Ba–Cu–O flux seriously, producing phases such as $Y_2Ba_2CuPtO_8$ and $Ba_4CuPt_2O_9$ (C.-J. Kim et al. 1997), SnO_2 crucibles give Nd_2SnO_4 (C.T. Lin et al. 1996), and yellow-greenish $YBa_3Al_2O_{7.5}$ is formed due to the melt reaction with an alumina crucible (Wolf et al. 1989). In the case of Al_2O_3, MgO, and ThO_2 crucibles, Al^{3+} and Mg^{2+} substitute for copper sites (up to 0.25 at% in the case of Al, Nevriva et al. 1991, Christensen et al. 1996, Chen 1998, Zhokhov et al. 1999) and the thorium ion substitutes for the yttrium site whereas zirconium does not substitute. These substitutions lead to deterioration of the superconducting properties while corrosion drastically reduces the lifetime of the crucibles and the duration of crystallization experiments. In addition, ThO_2 is radioactive and toxic (Assmus and Schmidbauer 1993). Sun et al. (1989) have tried a self-made CuO crucible on a zirconia support. Frieling et al. (1993) suggested a "self-crucible" made of dense isostatically pressed $YBa_2Cu_3O_{7-\delta}$. During crystal growth such a crucible could not only prevent pollution of the flux, but also supply solute due to partial dissolution of the crucible. Liang et al. (1992) have systematically investigated the crucible materials and concluded that yttria-stabilized zirconia (YSZ) is one of the best choices for Y123 crystal growth ($5\times5\times1\,mm^3$ crystals with $T_c\approx93.2\,K$ and $\Delta T_c<0.25\,K$), although YSZ may form a thick reaction layer and reacts with the melt above 930°C (Yamada et al. 1997b). A Y_2O_3 crucible has been tried and found to be useful for preventing the contamination from crucible materials during growth (Dembinski et al. 1990, Asaoka et al. 1993) (see sect. 7.1). Os'kina et al. (1995) have suggested a compromise decision to cover alumina crucibles by a protective layer consisting of 96 mol% Y_2O_3 and 4 mol% Y_2BaCuO_5 followed by sintering at about 1100°C for 10 hrs. A new class of contamination-free inert $BaZrO_3$ crucibles was suggested by Erb et al. (1995, 1996a,b, 1997), although this idea has been known since 1987 (Roth et al. 1987; thermodynamic properties of zirconates reviewed by Dash et al. 1996). It is noted that the 98.5% dense $BaZrO_3$ crucibles neither formed a reaction layer (as YSZ did) nor were strongly wetted by the flux, they are not so expensive, have a high melting point (about 2600°C), and a smaller thermal expansion coefficient than that of ZrO_2 (this helps to resist thermal shocks). An isomorphic $SrZrO_3$ compound exists to prepare crucibles for melt growth of Bi–Ca–Sr–

Cu–O and many other HTSCs. The impurity level of the crystals obtained in such crucibles is primarily controlled by purity of the starting material (Erb et al. 1996b, Krauns et al. 1997, Liang et al. 1998). Several $3\times2\times0.5\,mm^3$ $RBa_2Cu_3O_{7-\delta}$ crystals (R = Y, Er, Dy, Pr) were grown from the crucibles by the slow cooling (0.7°C/h) method, and their physical properties were observed to confirm the improved quality (Erb et al. 1996b).

The problem of the separation of the grown crystals can be solved in different ways (reviewed by Assmus and Schmidbauer 1993 and Chen 1998). (1) The simplest and most successful way is to remove the flux by decantation. It is easier to do so for the uncontaminated melt (for example, when using $BaZrO_3$ crucibles, Erb et al. 1996b) since its viscosity is lower. The flux removal can be performed if the residual solution is drained through holes bored in the bottom of the crucible (Asaoka et al. 1993), or by tipping the crucible over while remaining in the hot furnace to avoid a thermal shock of the grown crystals (C.T. Lin et al. 1992), or by turning over a crucible standing on a ceramic cylinder by a quartz rod (Liang et al. 1992), etc. A re-melting process can be applied at 910–920°C for an isolated body of the solidified eutectic flux with grown crystals (Folkerts et al. 1988, Hayashi et al. 1988b). A porous ceramic rod can be dipped into the melt to suck up the residual flux at the end of crystal growth. The porous ceramic can also cause a constant material flow at the cooled tip where crystal growth may take place. A lateral temperature gradient across the crucible or application of a well-wetting container material can result in creeping and self-decanting of the flux ("slurry method", for example, a gold crucible or foil, Kaiser et al. 1987). Jayavel et al. (1994) demonstrated that, in addition to the melt creep, the thermal gradient may play a significant role in growing twin-free crystals. (2) Another method is the cavity formation where the free-standing crystals can be found after the termination of the experiment. This can be done by careful adjustment of the thermal pattern as well as the raw density and volume of the charged material in the crucible. Pieces of a broken crucible can be inserted into the powdered charge material or the double crucible method can be applied. An easy method includes usage of alternate layers of flux powder and 123 powder because cavities are formed at high temperatures during the growth process due to oxygen loss inside the flux.

A commonly used solvent at present is an excess of CuO and $BaCuO_2$ (Schneemeyer et al. 1987, Hermann and Sheng 1987, Takekawa and Iyi 1987, Damento et al. 1987, Fischer et al. 1988, Darlington et al. 1988, Holtzberg et al. 1988, Balestrino et al. 1988, Sadowski et al. 1989, Tatarchenko et al. 1989); this is called the self-flux method because the $BaCuO_2$ and CuO phases have a eutectic at about 920°C in air (sect. 3.1.1), and therefore they can be used as a "contamination-free" nutrient phase (table 5). Schneemeyer et al. (1987) grew $4\times4\times0.5\,mm^3$ single crystals using a melt of "$YBa_4Cu_{10}O_x$" overall composition and a cooling rate of 4–15°C/h. Darlington et al. (1988) reported $8\times8\times0.1\,mm^3$ single crystals. Hunter et al. (1991) obtained $20\times20\times0.7\,mm^3$ Y123 crystals. Such crystals form with a layered-type morphology, similar to mica, but generally with square corners. The *c*-axis is normal to the platelets. In the flux method, thinner crystals with aspect ratios (*a*-axis/*c*-axis) of 2–20 are often obtained as will be shown in sect. 6.2. These crystals were not suitable for investigating

the anisotropic superconducting properties, particularly, for measuring physical properties along the *c*-axis.

Shamoto (1988), Kowalewski et al. (1988) and Wolf et al. (1989) optimized the melt composition and the cooling rate to obtain thick crystals. As a result, isometric and free-standing 88 K Y123 crystals ($5\times5\times2\,mm^3$) were grown in alumina crucibles using initial compositions centered around 4 at% Y, 30 at% Ba and 66 at% Cu, and cooling rates below 0.5°C/h (Wolf et al. 1989, see also sect. 3.2.1). Outside of this range thin platelets up to $8\times8\,mm^2$ with aspect ratio $\gg10$ could be mostly obtained. At cooling rates over 30°C/h, a non-equilibrium dendritic morphology with a zig-zag habit of the edge of the {001} face was observed.

Similar thick crystals along the *c*-axis have been observed by several groups. Chen et al. (1988) obtained isometric ($7\times3\,mm^2$) crystals. To control nucleation, C.T. Lin et al. (1992) applied crucibles with a smooth inner wall as well as an oscillatory thermal regime with a low cooling rate of 0.1–0.4°C/h. Takei et al. (1991) and Asaoka et al. (1993) have grown $4.3\times4.3\times3.6\,mm^3$ Y123 crystals with $T_c=91$ K after oxygenation at a slow cooling rate of 0.5°C/h in an Y_2O_3 crucible with a cooled wall to create a horizontal gradient about 7–10°C. The longitudinal direction was observed along the *c*-axis and the crystal had an aspect ratio much smaller than 1. Voronkova et al. (1995), Leonyuk et al. 1995 and Thomas et al. (1999) obtained $8\times8\times1.5\,mm^3$ Tm123 crystals with $T_c=91$ K by the self-flux method at 0.5°C/h. The changes of the aspect ratios with cooling rates may be explained qualitatively, considering the anisotropic dependence of the growth rate on the undercooling in Y123 crystal growth (sect. 3.4.2). These results confirm that the growth morphology of a crystal depends not only on the crystal structure but also on growth parameters such as undercooling or supersaturation.

Changkang et al. (1994) and Chen (1998) confirmed that the BaF_2 additive (see sect. 3.2.1) at an optimum concentration of as low as 0.5–1 wt% allows one to increase the crystal size of the Y123 phase by 3–5 times ($20\times10\times0.5\,mm^3$, $12\times10\times1\,mm^3$) and to reduce the contamination of the crystals by Al from the crucible; $T_c=93$ K with $\Delta T_c<1$ K was obtained. An optimum initial composition of $0.13\times\frac{1}{6}YBa_2Cu_3O_{7-\delta}$–$0.87(0.28BaO+0.72CuO)+1$ wt% BaF_2 and growth temperature range of 940–900°C were suggested. Addition of about 5–10 wt% of silver (as Ag_2O or $AgNO_3$) is found to be beneficial enough in a number of papers for the crystal size enhancement and reduction of the post-growth oxygenation time (Aswal et al. 1995, MacManus-Driscoll 1997, T.G. Chen et al. 1998, Y. Nakamura et al. 1998, Kohayashi et al. 1998, Ikuta et al. 1998), since depending on silver content, an enhanced oxygen concentration can be detected in the melt (Wiesner et al. 1998). A crystal of $8\times6\times2\,mm^3$ size with a 90 K ($R=0$) superconducting transition temperature in the as-grown state (Aswal et al. 1995) was obtained using the silver admixture. However, a monotectic reaction might take place in the silver-added Y123 system (Furuya et al. 1994, Wiesner et al. 1998), i.e. the melt separates into two liquids – the BaCuO phase with a small amount of silver ($Ba_{35.6}Cu_{58.6}Ag_{5.9}O_y$) and metallic droplets of liquid silver, which disperses in the solidified Y123 crystal because of the less than 0.1 wt% solubility of silver in the solid.

Table 5
Progress in production of bulk superconducting single crystals

R123 phase	Preparation			Size (mm^3)	T_c (K)	Remarks
	Method	Flux	Thermal treatment			
Y123	self-flux growth	$YBa_4Cu_{10}O_x$	air, cooling 4–15°C/h	4×4×0.5 (volume 8 mm^3)		Schneemeyer et al. (1987)
Y123	self-flux growth	near 4 at% Y, 30 at% Ba, 66 at% Cu	air, cooling 1010–960°C, 0.5°C/h	5×5×2	88	Wolf et al. (1989), Al_2O_3 crucible
Y123	self-flux growth	1:6:18	air, cooling 1000–970°C, 0.1–0.4°C/h	5×4×1.5	90	C.T. Lin et al. (1992), smooth Al_2O_3 crucible, temperature oscillations
Y123	self-flux growth	1:18:45	air, cooling 990–950°C, 0.3–0.8°C/h	5×3×0.7	93.2	Liang et al. (1992), YSZ crucible
Y123	self-flux growth	$0.64YBa_2Cu_3O_y$–$0.36(7BaCuO_2+11CuO)$	air, cooling 1050–970°C, 0.5°C/h	4.3×4.3×3.6	91	Asaoka et al. (1993), Y_2O_3 crucible, grad T
Y123	self-flux growth	$0.13\times\frac{1}{6}YBa_2Cu_3O_y$–$0.87(0.28BaO+0.72CuO)$+1 wt%$BaF_2$	air, cooling 1000–900°C, 2°C/h	20×10×0.5, 12×10×1	93	Changkang et al. (1994), Al_2O_3 crucible
Y123	flux growth	$YBa_2Cu_3O_{7-\delta}$ mixed with KCl:NaCl=1:1 and 5 wt% $AgNO_3$	air, cooling 1030–850°C, 1°C/h	8×6×2	90	Aswal et al. (1995), Al_2O_3 crucible
Y123, Pr123	self-flux growth	10 mol% R123 in flux of eutectic composition	air, cooling 1005–950°C, 0.7°C/h	2×2×0.5	91	Erb et al. (1995), 98.5% dense, $BaZrO_3$ inert crucible
Y123	self-flux growth	1.5 mol% $YBa_2Cu_3O_{7-\delta}$ in $2CuO\times BaCuO_2$ flux	constant $T=910$°C, p_{O_2} increasing (5×10^2 Pa → 0.2×10^5 Pa for 50 h)	5×5×0.1	92	Fischer et al. (1993), YSZ crucible
Nd123	self-flux growth	flux of eutectic composition	5% O_2, slow cooling 1030–950°C	4×4×4	94.8	Wolf et al. (1997), YSZ crucible
Y123	TSSG	$0.15\times\frac{1}{6}YBa_2Cu_3O_y$–$0.85(0.3BaCuO_2-0.7CuO)$	air, 930°C, pulling, 2–8 rpm (crucible)	8×6×5	90	Emelchenko et al. (1994), 17 days, Al_2O_3 crucible

continued on next page

Table 5, *continued*

R123 phase	Preparation			Size (mm^3)	T_c (K)	Remarks
	Method	Flux	Thermal treatment			
La123, Nd123, Sm123	TSFZ	123 rods, 1:4:6–1:29:66 flux	$p_{O_2} = 10^{-2}$–10^{-4} atm, 0.4–1 mm/h	Ø 6×27 (boles), 3×1.5×1.5 (single grains)	90 91 94	Oka and Ito (1994), two-scanning method
Nd123	TSFZ	123 rods (CIP), 1:7.6:21.5 flux	0.1% O_2, 0.46–0.50 mm/h	Ø 3 × 32	94	Kuroda et al. (1996), 93.4% dense rods
Y123[a]	SRL–CP	211+0:3:5, 5:36:59	air, pulling, 1000°C, 0.2 mm/h, 120 rpm	8×8, 5[b]	89	Y. Yamada and Shiohara (1993), Y_2O_3 crucible
Y123	SRL–CP	211+0:3:5	air, pulling, 1002–997°C, 0–0.14 mm/h, 120 rpm	14×14×14 (expanding angle <25°)	92	Namikawa et al. (1996b), 100 mm diameter Y_2O_3 crucible
Y123	SRL–CP	211+0:3:5, 5:36:59	pulling at p_{O_2} = 1 atm, 1015°C, 0.05 mm/h, 70–120 rpm, cooling in N_2	19.8×19.5, 16.5[b]	92.7	Yao et al. (1996a), Y_2O_3 crucible
Nd,Ga-123	TSSG	~0.84–1.98 at% Nd, 28.49–28.16 at% Ba, 70.67–69.86 at% Cu	air, cooling 1030–960°C, 0.5°C/h, 15 rpm (crucible)	22×15×3	92	C.T. Lin et al. (1996), cold finger, SnO_2 crucible
Nd123	modified TSSG	0:0.78:1	air, pulling, 1058–1070°C, 0.1–0.25 mm/h, 70–120 rpm	24×24, 21[b] (volume ≈ 1000×8 mm^3)	95	Yao et al. (1997), Nd_2O_3 crucible, 67 h

[a] Also Sm, Nd, Pr etc.

[b] Pyramidal crystal height is given after commas.

Crystallization of Nd123ss (Katsui 1987, Iwata 1988, Magnone et al. 1994, Tanaka 1996, Auguste et al. 1998; see also Kambara et al. 2000) as a cation-nonstoichiometric, solid solution compound might be more complicated in comparison with a stoichiometric phase such as Y123 (sect. 3.2.1). Consequently, growth of high-quality single crystals of the Nd123ss solid solution in a high-p_{O_2} atmosphere by the self-flux method probably cannot be widely recommended because it creates the possibility of segregation of the solid-solution composition. This is clearly demonstrated by the first works in this field. K. Oka and Unoki (1990) have tried to obtain a single-crystalline Nd123 phase by the slow-cooling self-flux and TSSG methods based on the starting composition 25% $NdBa_2Cu_3O_{7-\delta}$ and 75% $Ba_3Cu_5O_8$. A cooling ramp from 1100°C to 900°C with 10°C/h was applied in air, and that yielded $3\times3\times0.5\,mm^3$ crystals. From TSSG growth (50 mm height and 50 mm diameter platinum crucibles, melt cooling of about 5–10°C/h, 0.5 mm/h rate of pulling and 20–30 rpm rotation speed, Pt wire as a seed), an assembly of small square pillar-like, $5\times6\times1\,mm^3$ crystals was obtained. After oxygenation at 600°C in oxygen for 40 h, only a $T_c \approx 70$ K was achieved. Recently, Gong et al. (1997) have demonstrated the same inaccurate approach to the growth of the Nd123ss crystals in air. The authors used slow cooling from 1080 to 1000°C at the rate of 1°C/h for the molten charge material in a zirconia crucible followed by quenching on a copper plate at room temperature. Crystals about 2–3 mm in size were obtained with T_c as low as 77 K. In other experiments (Wolf et al. 1997, Auguste et al. 1998) a T_c value above 90 K was achieved owing to p_{O_2} and/or liquid composition control.

At the same time, various twin-free Ca- or Sr-substituted R1113 crystals ($RBaSrCu_3O_z$, $RBaCaCu_3O_z$) have been obtained for light rare-earth elements (sect. 7.4.3.5; reviewed by Chen 1998). Several $3\times3\,mm^2$ plate-like crystals were grown from the 28 mol% BaO–72 mol% CuO flux with an addition of the Ca-R1113 phases in the mol ratio 3 : 1 (Rao et al. 1993). A maximum temperature of 1030°C, Pt or Al_2O_3 crucibles and a 2°C/h cooling rate down to 800°C were applied followed by oxygenation at 500°C for one week. Striation stripes 50–100 μm apart, and growth spirals were found for the crystals, however, twinning was not observed. An orthorhombic splitting of reflexes was not detected by XRD of powders obtained by crushing the crystals ($a = 3.87$ Å, $c = 11.64$ Å for $CaLaBaCu_3O_{7-\delta}$, $a = 3.86$ Å, $c = 11.62$ Å for $CaPrBaCu_3O_{7-\delta}$, $a = 3.84$ Å, $c = 11.60$ Å for $CaNdBaCu_3O_{7-\delta}$); the Laue diffraction gave well-defined spots. Except for the Pr1113 semiconducting crystal, other crystals demonstrated superconducting properties: 72 K and 69 K for La1113 and Nd1113, respectively. The Sr-doped ($Nd_{1.18}Ba_{1.53}Sr_{0.29}Cu_3O_z$) crystals grown by the TSFZ method in a 0.1% oxygen atmosphere (Tanaka et al. 1997) did not demonstrate twin domains after oxygen annealing at 400°C for 48 hrs, and the observed T_c (84 K) was only 8 K lower than that for $Nd_{1.10}Ba_{1.90}Cu_3O_z$ crystals (92 K). Both the reported values exceeded the T_c values for ceramic samples of similar compositions. $PrBa_{2-x}Sr_xCu_3O_z$ crystals of $5\times4\times0.3\,mm^3$ up to $11\times9\times0.4\,mm^3$ size and up to $x = 1.3$ Sr content were grown in alumina crucibles from the BaO : SrO : CuO = 14 : 14 : 72 + 10 mol% $\frac{1}{6}PrBa_2Cu_3O_{7-\delta}$ flux by cooling from 1000°C to 950°C (1°C/h, 1060°C as a maximum temperature, Cao et al. 1998). No twins were detected unlike the case of undoped $PrBa_2Cu_3O_{7-\delta}$. The c-axis was unusually small in these tetragonal

nonsuperconducting crystals: $a = 3.9078(3)$ Å, $c = 11.4008(8)$ Å. The crystals contained Al in accordance with the EDX analysis $(Pr(Sr_{0.65}Ba_{0.31}Pr_{0.04})_2(Cu_{0.94}Al_{0.06})_3O_y)$, and the authors claimed that this helped to stabilize the Sr-rich phase.

(Y,Pr)123 mixed crystals, for example, were grown by Nevriva et al. (1991) and Merz et al. (1996). Growth of (Y,Nd)123 crystals was studied by Aswal et al. (2000). Copper-substituted crystals were reported as well (e.g., Fe, Andrianov et al. 1990; Co, Christensen et al. 1996; Zn, Shvanskaya et al. 1999).

5.2. *Whisker-like crystals*

Whiskers, as quasi-one-dimensional single crystals, attract much attention to clarify the growth mechanisms, some intrinsic physical and admirable mechanical properties of superconducting materials close to the limit of their unit cell. As an example, $LuBa_2Cu_3O_{7-\delta}$ submicrometer single crystals exhibited a tensile strength as high as 4.8 GPa at 78 K (Talantsev 1994), and the equation of state for $PrBa_2Cu_3O_{7-\delta}$ was suggested by Weishaupt et al. (1998). In the Bi–Sr–Ca–Cu–O system such crystals were repeatedly obtained and they may find practical applications owing to the high J_c values achieved (10^5 A/cm^2). H. Zhang et al. (1995) reported synthesis in air of whisker-like (needle) crystals of $SmBa_2Cu_3O_{7-\delta}$ up to 3 mm in length on the surface of melt-textured samples. This was confirmed by Goodilin et al. (1996), Klemenz and Scheel (1999b), Goodilin et al. (2000) and Tretyakov and Goodilin (2000) for the Nd–Ba–Cu–O system, and then a simple Nd123ss-whisker production technique in a hollow pellet has been suggested, based on the understanding of the Nd–Ba–Cu–O phase diagram (Goodilin et al. 2000). The Sm123 needle-like crystals were found to be either an assembly of whiskers stacked with the same orientation or one-dimensional polycrystals composed of lamellar grains misoriented with respect to each other. Lattice constants of the whisker-like crystals ($a = 3.90$ Å, $b = 3.85$ Å, $c = 11.75$ Å) and semi-quantitative EDX analysis demonstrated that the needles have a perovskite structure which is close to that of Sm123. Terraces, growth steps and spirals were observed for several crystals. Since such crystals have never been obtained in other systems such as Y–Ba–Cu–O (Y123 whiskers were observed only once, see Pathak et al. 1996), it is uncertain what kind of growth mechanism results in the complicated morphology of Sm123 whiskers (see also Tretyakov and Goodilin 2000).

5.3. *TSFZ crystals*

Directional solidification is an appropriate method in the production of high-performance current leads, therefore much research is directed towards this method (McGinn et al. 1990, Chunlin et al. 1991, Y. Nakamura et al. 1994, Figueredo et al. 1995, Egi et al. 1995, 1996, Salama and Sathyamurthy 1996, Obradors et al. 1997, Imagawa et al. 1997, Sumida et al. 1997, 1998, Cabre et al. 1998, Sandiumenge et al. 1997, 1998a; see also the review by Revcolevschi and Jegoudez 1997). Actually, the temperature gradient (G) and growth rate (R) are the most important process parameters in directional solidification, and the morphological changes occurring in directional solidification can be explained,

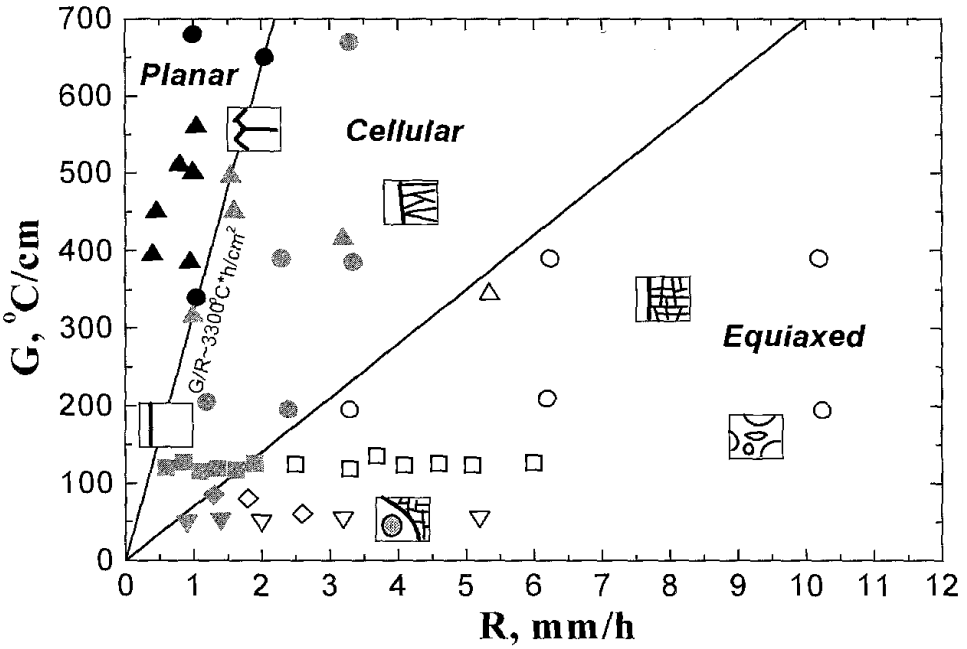

Fig. 23. Influence of temperature gradient (G) and growth rate (R) on growth morphology and stability of the planar Y123/Liquid interface in directional solidification experiments (Shiohara and Endo 1997). Note that only high G/R ratios (>3300 K h/cm^2) permit the interface to be planar during solidification resulting in large single-crystal grains.

in principle, on the basis of constitutional supercooling theory (sect. 2.2.2). When growth conditions are changed, for example the ratio G_L/R or the solubility of the solute in the liquid, the planar front morphology can be drastically modified. Figure 23 summarizes the effect of G and R on the morphology of the solidification front (Shiohara and Endo 1997), including the results of zone-melting and Bridgman methods investigated by several groups (Cima et al. 1992, Mori et al. 1992, T. Izumi and Shiohara 1992, T. Izumi et al. 1993).

Several kinds of R123 crystals have been produced with the TSFZ method by Oka and colleagues (K. Oka and Ito 1994, 1996, K. Oka et al. 1997) at low p_{O_2} (10^{-2}–10^{-4} atm). A solvent and R123 (R = Y, La, Pr, Nd and Sm) rods were used. The feed rod and the solvent zone were composed of the a rare-earth–barium–copper-oxide mixture in ratios of 1:2:3 and 1:4:6–1:29:66, respectively. Then the R123 crystals were grown continuously with different pulling rates in the range of 0.4–1.0 mm/h in an infrared radiation furnace. One substantial advantage of TSFZ is the containerless crystal growth. At the same time, however, we come across the problem of keeping the molten zone stable during the crystal growth. Since the viscosity of the solvent composed of BaO–CuO is low, the solvent easily falls down onto and penetrates deeply into the feed rod. This makes it difficult to hold the rod continuously and to avoid changing the solvent composition with time. K. Oka and Ito (1994) have overcome this problem by using high-density, crystallized feed rods pre-scanned at a relatively high pulling rate of 2–15 mm/h. As a result, they have succeeded in the growth of $RBa_2Cu_3O_{7-\delta}$ crystals. The maximum

dimension of the grown boules was 6 mm diameter and 27 mm length. However, the maximum size of the single-grain cross sections was only a few mm^2. Oxygen-annealed crystals (500°C, 25hrs, 400°C, 60hrs) demonstrated high T_c (90 K for La, 91 K for Nd, 94 K for Sm, table 5).

To produce Nd123 crystals (sect. 6.2), Egi et al. (1995, 1996) and Kuroda et al. (1997a,b) used 93.4%-dense precursor rods produced by cold isostatic pressing (CIP), a Nd:Ba:Cu = 1:7.6:21.5 solvent, second scanning rate 0.46–0.50 mm/h, rotation rate 28 rpm, and 0.1% oxygen atmosphere. The largest single-crystalline grain obtained was found to be 3 mm in diameter and 32 mm in length. T_c values as high as 94 K and $J_c \approx 71\,000$ A/cm^2 at 77 K and 10^4 Oe were reported for the Nd123 crystals as well as a pronounced field-induced peak effect (sect. 7.4.3.4). Crystal lattice parameters $a = 3.826$ Å, $b = 3.893$ Å, $c = 11.741$ Å have been determined after 14 days of oxygen annealing at 320°C, however, the Ba/Nd ratios at initial and final regions in the rods were found larger than those of the intermediate region (2.0±0.1). Nd123 crystals were also produced by Yao et al. (1995) and Sandiumenge et al. (1998a) using TSFZ, and by Shibata et al. (1997, 1999) using the horizontal Bridgman method. Sm123 was obtained by Sumida et al. (1997, 1998).

Yao et al. (1996c) demonstrated that in the Y–Ba–Cu–O system a decrease of the oxygen partial pressure (1 atm → 0.02 atm) or an increase of the pulling rate (1 → 5 mm/h) caused the morphology of the solidified interface to change from planar to cellular, equiaxed and further – mushy or blocky. The low oxygen partial pressure makes it difficult to keep the crystallizing front planar. Additional casuses for instability of the crystallization front at lower p_{O_2} are higher viscosity of the melt as reported by Egi et al. (1996) and low solubility of the rare-earth element in the liquid (sect. 3.1.2.1). The liquid migration produced by capillary absorption during the thermal texturing also hinders the stable and continuous solidification process (Cabre et al. 1998).

The above causes of the instability of the crystallization front at low p_{O_2} might explain why the important result of preparation of a superconducting Pr123 phase by the TSFZ method in 0.1% oxygen atmosphere reported by K. Oka et al. (1997) has not been reproduced yet. The authors used starting feed and solvent materials obtained from Pr:Ba:Cu initial mixtures of 1:2:3 and 1:3:5–1:7:14 ratios, respectively. After presintering and a first scan at 10 mm/h, the second scan at 0.4–0.5 mm/h resulted in $2 \times 2 \times 1$ mm^3 single crystals within 4–5 $mm^2 \times 120$ mm boules. The crystals were subjected to a unique oxygenation procedure which included heating up to 850°C in 3 h and holding at this temperature for 12 h. After that the samples were slowly cooled down to 350°C and maintained for 12 h. The resistivity of two measured samples demonstrated metallic behavior and superconductivity below 80 K. The field-cooled magnetization displayed a Meissner effect of about 15% of the total volume; consequently, the superconductivity was assumed to be bulk-type. In most of previous works such superconductivity has not been found (Lowe-Ma and Vanderah 1992, Sadowski et al. 1994, Lamberti et al. 1996, Moolenaar et al. 1996, Tagami and Shiohara 1997, Narozhnyi et al. 1999, etc.) because of possible magnetic pair breaking, localization of holes, hole depletion, local 4f(Pr)–$2p_\pi$(O) hybridization etc., as reviewed,

for example, by Maple et al. (1992) and Radousky (1992). Therefore, superconductivity in the TSFZ-Pr123 crystals might be explained by some lattice defects or Pr and Ba cation ordering/disordering. Indeed, lattice constants $a = 3.9125$ Å, $c = 11.8939$ Å and $a = 3.881$ Å, $b = 3.937$ Å, $c = 11.844$ Å were obtained for the as-grown and oxygen annealed samples, respectively. The c-axis was found to be larger than that of the reference samples prepared by the self-flux method (see also Chen et al. 1993, Sadowski et al. 1994, Zhokhov et al. 1999) and than that reported in literature (e.g., Lowe-Ma and Vanderah 1992, Radousky 1992). Recently, the superconductivity transition temperature in the TSSG-grown Pr123 crystals has been demonstrated to exceed 100 K under a pressure over 8 GPa (Zou et al. 1998) as usual for other "typical" R123 crystals (C.C. Kim et al. 1993, J.G. Lin et al. 1995, etc.). The phenomenon of superconductivity in Pr123 crystals has been reproduced by Shukla et al. (1999), Luszczek et al. (1999) and Grevin et al. (2000). Moreover several explanations have been given based on specific Pr/Ba ordering scenarios (Shukla et al. 1999, Muroi and Street 1999) or defect network development in crystals (Sandiumenge et al. 1998b).

R123 phases with the smallest rare-earth elements (Yb, Lu) have not been obtained by the TSFZ method, probably due to peculiarities in their phase diagrams (sect. 3.1.3).

5.4. *Liquid phase epitaxy*

5.4.1. *Practical importance of LPE*

The LPE technique is important for the study of the initial stage of crystal growth and for the preparation of high-quality seeds. This process is flexible and allows growth of a crystal layer under a selected p_{O_2} and near equilibrium conditions, therefore it demands, as in the case of bulk crystals, sufficient knowledge of phase relations, solubility and effects of interaction with a substrate. The process development is more complex than physical deposition methods, however in terms of practical applicability, LPE crystal layers might play a significunt role. Partially it is similar to that of sliced and carefully polished output materials obtained from large commercial single crystals of HTSCs. The potential importance of LPE growth consists also in the possibility of fabrication of base electrodes and interconnects in microelectronics with quasi-atomically flat surfaces and extremely thin pinhole-free barrier layers for tunnel devices (Scheel et al. 1994). The LPE method combined with other deposition techniques could result in the preparation of SQUIDs, microwave detectors and mixers, integrated tunnel devices at high yields with minimal scattering of parameters. LPE at present could be the basic technology for high-performance optoelectronic devices for digital applications (Scheel et al. 1991). LPE layers or single crystals with a sharp resistive transition may find their ways as precise and sensitive bolometers in space physics etc.

Due to the short coherent length of HTSCs, only smooth surfaces on structurally perfect layers allow these planar technologies. A number of modern deposition techniques (physical vapor deposition including sputtering, laser ablation, molecular beam epitaxy as well as metallorganic chemical vapor deposition etc.; see, e.g., Becht 1996) result in high values of critical temperature and critical current. However compact single-crystalline

epitaxial layers with the required surface flatness can be achieved only by exception. PVD-grown surfaces are relatively rough for many applications (Scheel 1994). This demonstrates that very high supersaturation exists normally in PVD techniques, while the layer-by-layer formation mechanism of a flat surface requires low supersaturation. The supersaturation has to be small enough to prevent spontaneous 3D nucleation and step bunching. In LPE the supersaturation can be gently adjusted to the desirable level, in particular to the level required for layer-by-layer growth (about 1000 times lower than in PVD methods). The lateral distances between steps reflect this fact since they are usually 20–50 nm in vapor growth and up to 10 μm in LPE (Scheel 1994). The thickness of the YBCO layers varies between 1 and 100 μm and the growth rate is in the order of 1 μm/min (Gornert 1997).

5.4.2. *Demands and restrictions for substrate materials. R123 single crystals as substrates*

Substrates and buffer layers play a significant role in the development of R123 epitaxy (Scheel et al. 1991). The substrates (1) should be chemically, mechanically and thermally stable, especially in the environment of the reactive Ba–Cu–O fluxes, (2) should have no structural phase transitions (such as twinning) affecting the microstructure of the grown film due to surface corrugations, (3) should have a sufficiently small dielectric constant [$\varepsilon < 20$, like Si (12), MgO (12), YSZ (27), Y_2O_3 (9), Al_2O_3 (9), $LaAlO_3$ (15), $LaGaO_3$ (26), $NdGaO_3$ (25), $SrLaAlO_4$ (16.7), $YAlO_3$ (16); but $\varepsilon \approx 310$ for $SrTiO_3$], (4) should have appropriate microwave properties [low microwave losses, $\tan\delta < 10^{-3}$, such as 0.0091 (MgO), 0.0054 (YSZ), 0.002 ($SrTiO_3$), 0.0006 ($LaAlO_3$), 0.0003 ($NdGaO_3$), 0.001 (Si)], and (5) should exhibit misfit less than 0.2%, at least at the epitaxial growth, and application ($<T_c$) temperatures. The misfit can not only induce cracks and dislocations in the deposited films, but can also lead to quenching the step-flow regime in layer-by-layer growth which is beneficial for a flat surface formation. The difference in thermal expansion coefficient between the HTSC layer and the substrate should be smaller than 20%. On cooling, cracking can easily occur if the Y123 film is influenced by tensile forces rather than compression due to the smaller thermal expansion coefficient of a substrate material. (6) All of these demands and restrictions for a substrate material should be accompanied by low cost and an easy production technology (for example, the Czochralski method for congruently melting compounds).

These strict demands are not fulfilled by any known substrate material as shown in fig. 24. Except for $KTaO_3$ all simple perovskites have one or more structural phase transitions (for example, at temperatures as low as 150°C for $LaGaO_3$, 780°C for $SmAlO_3$, ~790°C for $PrGaO_3$, O'Bryan et al. 1990). Fortunately, site substitution and cation mixing in perovskites permits the design of substrate materials by adjustment of both the lattice misfit and thermal expansion coefficients as well as by shifting the point of a possible phase transition to avoid twinning in the working range of temperatures (Scheel et al. 1991). In view of the probability of phase transitions in perovskites, other structural classes of substrate materials could be examined

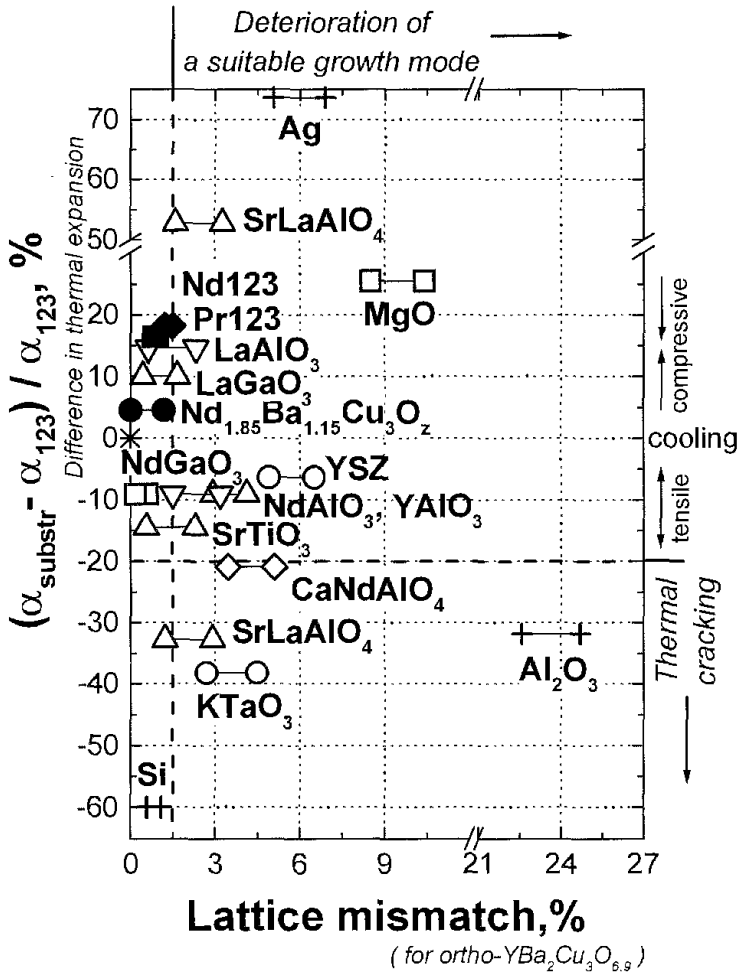

Fig. 24. Classification of substrate materials for preparation of crystalline layers by LPE. Two essential parameters are involved in the classification: the thermal expansion coefficient and the lattice misfit between the substrate and a Y123 film. The Y123 thermal expansion coefficient was accepted to be $11\times10^{-6}\,K^{-1}$, $a_{Y123}=3.883$ Å, $b_{Y123}=3.817$ Å, $c_{Y123}=11.637$ Å. In the misfit calculation the left point for each line represents the mismatch between a_{Y123} and the largest lattice constant of the substrate, while the right end corresponds to the relative difference between b_{Y123} and the smallest lattice constant of the substrate. A vertical dotted line gives approximately the usually accepted limit for the layer-by-layer growth mode below about 1% of lattice misfit. A horizontal line at about –20% of difference in thermal expansion coefficients sets a thinkable limit for the deposited films without thermal cracking. Plus and minus for the difference in thermal expansion correspond to compressive and tensile forces between the substrate and the deposited film (on cooling). Lattice mismatch was calculated using absolute values of the lattice parameter difference.

[cubic structures (CeO_2, Y_2O_3), K_2NiF_4 ($SrLaAlO_4$), diamond (Si), fluorite (YSZ), corundum (α–Al_2O_3), gehlenite, etc.]. In these cases (and in a number of others) epitaxy is possible only under a certain reciprocal orientation of the film and the substrate (for example, $a/\sqrt{2}$ for YSZ, $a/\sqrt{2}, c/3$ for $LaAlO_3$, $a(b)/\sqrt{2}, c/2$ for $NdGaO_3$, $a/2, b$ for $Nd_{1.85}Ba_{1.15}Cu_3O_z$, and so on).

In practice, MgO, YSZ, $SrTiO_3$, $SrLaAlO_4$, $LaAlO_3$ and $LaGaO_3$ substrates are applied more or less successfully (see, e.g., Qi and MacManus-Driscoll 2000). Jose

et al. (1997) and Yadava et al. (1998) suggested to use $RBa_2ZrO_{5.5}$ (R = La, Ce, Eu, Yb) materials as inert substrates. Babu and Koshi (1997) found that $Ba_{2-x}Sr_xDyTaO_6$ perovskite is suitable for 90 K-thick film production of $YBa_2Cu_3O_z$ by dip-coating and partial melting. $NdGaO_3$ seems to be a good compromise due to the small misfit, a thermal expansion coefficient similar to R123, and other reasons. Twins in such a substrate can be avoided by selecting an appropriate growth mode (sect. 6.3), by detwinning and polishing, or by substitutions in the cation sublattice ($La_{0.95}Gd_{0.05}GaO_3$). MgO substrate could also be used succesfully in a number of cases because of the larger thermal expansion coefficient (13.6×10^{-6} K) compared to Y123, and the so-called pseudoepitaxy phenomenon (Wen et al. 1997). In all cases the preparation of the substrate requires special care. For example, in the case of MgO, in the sequence of chemical polishing → mechanical polishing → annealing at high temperature (>12 h at >1100°C in air or oxygen), FWHM values of 1.02°, 0.72° and 0.30°, respectively, were measured (Moeckly et al. 1990), which become close to typical values obtained using $SrTiO_3$ (0.23°), $NdGaO_3$ (0.12°) and Y123 (~0.14°) single-crystalline substrates. The values reported often include instrumental broadening of the XRD lines, therefore it is hard to compare them directly when using different XRD sources [for example, values of 0.04° ($SrTiO_3$), 0.1° (MgO) and 0.0002° (Si) were summarized by Shiohara and Endo (1997) and 0.016° FWHM on the Y123 substrate was measured by H. Zama (SRL, private communication)].

Recently, a method for thermomechanical processing of base flexible materials such as metallic Cu or Ni has been developed (reviewed by Goyal et al. 1996, 1997 and MacManus-Driscoll 1998) to obtain a very sharp, well-developed cube structure, which is followed by deposition of chemically and structurally appropriate buffer layers (YSZ etc.), for example, by ion-beam-assisted deposition (IBAD, Iijima et al. 1996, Freyhardt et al. 1996) and inclined-substrate deposition (ISD, Hasegawa et al. 1996). Such a substrate with biaxially textured, chemically and structurally compatible surfaces for epitaxial growth of superconducting films and multilayers for large-scale applications is called a rolling-assisted biaxially textured substrate (RABiTS). Photo-assisted MOCVD (Becht 1996, Ignatiev et al. 1996) and melt-processing [LPE; isothermal melt-processing, MacManus-Driscoll (1997), Qi and MacManus-Driscoll (2000); texturing by geometrical arrangement of reactive precursors, Schmitz et al. (1998b); infiltration processing, Reddy et al. (2000)] have been tried to deposit superconducting (thick) films on such a flexible substrate (tape).

At present, R123-based single-crystal materials are considered as possible substrates (Shiohara and Endo 1997, Saba et al. 2000). They can be hypothetically classified as (1) superconductive substrates with essential oxygen nonstoichiometry and the tetra–ortho transition (Y123, Nd123 etc.); (2) nonsuperconductive substrates with essential oxygen nonstoichiometry and the tetra–ortho transition (Pr123); (3) superconductive tetragonal substrates with essential oxygen nonstoichiometry and with no tetra–ortho transition (so-called R1113 phases, X.Z. Wang et al. 1992, Ca and Sr substitution for Ba, sect. 5.1); (4) nonsuperconductive tetragonal substrates with reduced oxygen nonstoichiometry and with no tetra–ortho transition (such as $Nd_{1.5}Ba_{1.5}Cu_3O_z$, R^{3+} substitution for Ba^{2+});

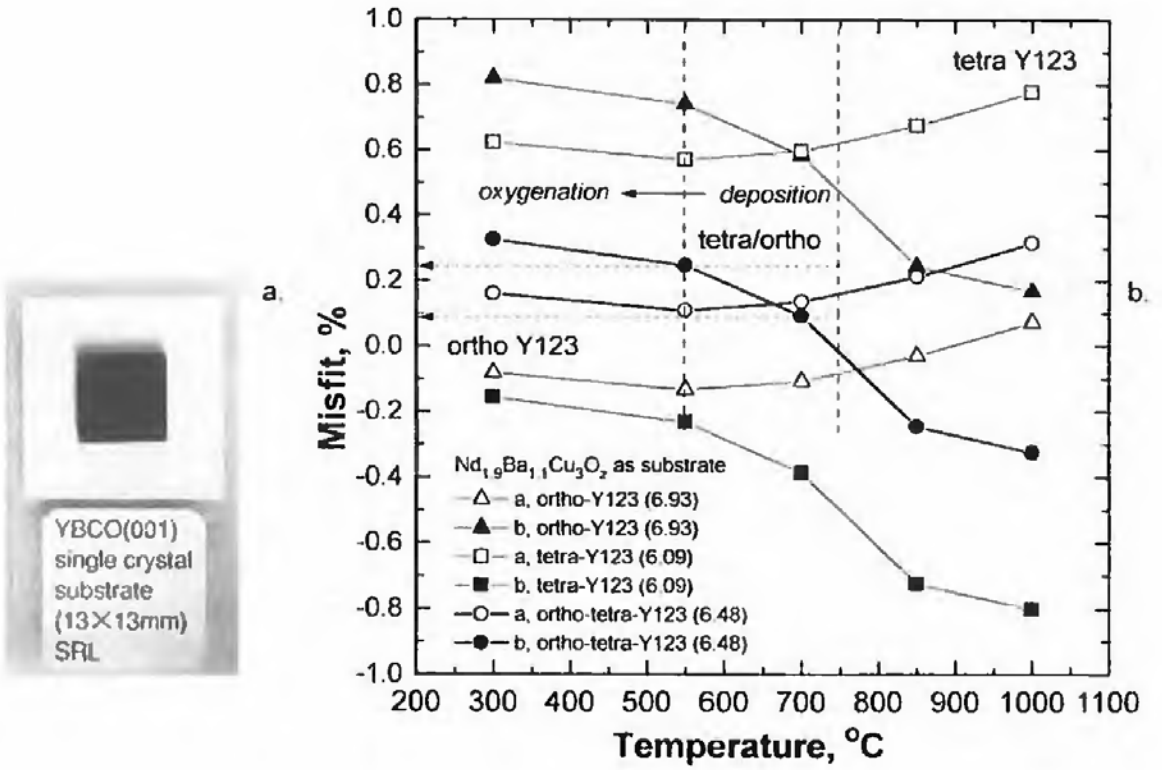

Fig. 25. Prospective materials for R123 film epitaxy growth: (a) mechanically polished Y123 substrate for homoepitaxy with surface roughness less than 1 nm obtained using a bulk crystal produced by the SRL–CP method (Sakai et al. 1995); (b) comparison of lattice mismatch between insulating orthorhombic, less-oxygen nonstoichiometric $Nd_{1.9}Ba_{1.1}Cu_3O_z$ phase (Nd213) and the Y123 phase with different oxygen content. The Nd213 lattice constants were obtained after quenching from different temperatures and the thermal expansion coefficients were estimated to be similar to those of the Y123 phase (Goodilin et al. 1998b). Note that deposition of $YBa_2Cu_3O_{7-\delta}$ with oxygen content $\delta = 0.52$ ($O_{6.48}$) in the usual deposition temperature range 550–750°C would give the best results.

(5) insulating orthorhombic substrates with small oxygen nonstoichiometry and with no tetra–ortho transition (such as $Nd_2Ba_1Cu_3O_z$, sects. 3.1.2.3, 6.3).

As a pilot project, large single crystals have been applied already for preparation of homoepitaxial thin films of the Y123 superconductor. An attempt to deposit Y123 thin film homoepitaxially on a self-flux-grown Y123 single crystal was performed by molecular beam epitaxy (Shimizu et al. 1994) after cleaning the crystal surface with ozone. 2D nucleation growth was observed in the experiment where the nucleation occurs on the terrace of the single crystal and 2D islands grow at ledges. Further, Y123 {100} and {001} substrates with roughness less than 1 nm were prepared for homoepitaxy by mechanical polishing of bulk single crystals by H. Sakai et al. (1995), Zama et al. (1996) and Usagawa et al. (1997a) (fig. 25a). Chemical etching enhances the quality of such R123 single-crystal substrates (Tanaka et al. 1999). It was confirmed that the surface roughness of the substrate is formed by the step height of one unit cell. The homoepitaxy was attempted by the MOCVD method. As a result, a thin film with a perfect in-plane alignment and a zero-resistance superconducting transition at $T_c(0) \approx 89$ K was

obtained even without additional post-annealing. Konishi et al. (1997) succeeded in the deposition of *a*-axis oriented films on {100} Y123 single-crystal substrates at 760°C by off-axis RF magnetron sputtering. Tagami et al. (1994, 1998) obtained a sharp interface for the Pr123 crystal growth on a Y123 seed (sect. 6.7), Usagawa et al. (1997b) achieved superconductivity in {110} $PrBa_2Cu_3O_{7-\delta}$ thin films pseudomorphically grown on {110} $YBa_2Cu_3O_{7-\delta}$ single-crystal substrates. A successful attempt to fabricate a Josephson junction using a single crystal was made by Konishi and Enomoto (1995).

These results support the idea that R123 single crystals can be used as a substrate material in a certain range of conditions. Moreover, the surface of a Nd123 single crystal was found to be stable in air (Ting et al. 1996, 1998, Zhou et al. 1997) and clean. For Nd123 single crystals Ting et al. (1996) observed by STM investigations that the natural termination layer of the as-prepared surfaces consists of CuO chains. The authors estimated the effective tunneling barrier height to be about 0.4 eV. This value is in a good agreement with those reported on vacuum-cleaved samples and on a clean Y123 film, indicating the formation of a good tunneling junction. Wang et al. (1997) investigated the {001} and {100} surfaces of Y123 single crystals as a function of temperature and oxygen partial pressure. The Y123 surfaces were found stable at temperatures up to 780°C in the oxygen partial pressure range of 1 mTorr–1 Torr, while beyond this range the surfaces deteriorated at higher temperatures.

As mentioned however, cracking of these kinds of substrates is possible, due to the tetra–ortho transition, and this was actually observed by Konishi et al. (1997). At 580°C, the cracks were formed in the Y123 single-crystal substrate along the *ab*-plane at about 25 μm intervals due to the cleavage characteristics and the stress associated with the tetragonal–orthorhombic transition. The 1113-type of single crystals (sects. 5.1, 7.4.3.5) seems to be free of this problem since the solid solution composing the crystals possesses a tetragonal unit cell, and no structural phase transition occurs during oxygenation. This is similar to the behavior of always-tetragonal $Nd_{1.5}Ba_{1.5}Cu_3O_z$ crystals (Goodilin et al. 1998b). Applications of the always-orthorhombic insulating Nd213 phase [sects. 3.1.2.3 and 5.5.2 and table 6 (overleaf)] can not be affected by the ortho–tetra transition either. In particular, fig. 25b shows that only a small misfit could occur between the Nd213 substrate and the Y123 phase at 550–750°C, and this small misfit is preserved upon the cooling and oxygenation procedures, preventing the deposited film from crack formation. It would be possible to adjust the lattice constants of the LR213 phases by varying the size of the light rare-earth element (LR) in order to have the smallest misfit in couples of "R123 film–LR213 substrate" (Y123–Nd213; Nd123–Pr213, etc.).

5.4.3. *Initial steps of bulk single-crystal growth and preparation of LPE crystal layers*

LPE has been tried for Y123, Nd123, Yb123, Bi2212 and Tl-1223 phases (reviewed by Scheel 1994 and Gornert 1997). Dubs et al. (1996) obtained the Y123 *a*- or *b*-oriented films on a $NdGaO_3$ substrate using both standard horizontal and vertical dipping techniques. AFM investigation revealed growth monosteps of 3.7–6.8 Å in height

Table 6
Comparison of $Nd_1Ba_2Cu_3O_z$ and "$Nd_2Ba_1Cu_3O_z$" single crystals

Phase → / Parameter ↓	Nd123 ($NdBa_2Cu_3O_7$) (Yao and Shiohara 1997)	Nd213 ($Nd_{1.85}Ba_{1.15}Cu_3O_z$) (Goodilin et al. 1998b)
Growth method	Modified TSSG, Nd_2O_3 crucible, Ba/Cu in flux = 0.78–0.6, 1058–1070°C, 0.1–0.25 mm/h pulling, 70–120 rpm rotation	Modified TSSG, MgO crucible, Ba/Cu in flux = 0.21, 1014–1017°C, 0–0.1 mm/h pulling, 120–150 rpm rotation
Crystal growth mechanism	Spiral growth	Spiral growth and twin-plane-re-entrant-edge growth
Unit cell	primitive tetragonal P4/mmm (as-prepared, at high temperatures) or orthorhombic Pmmm (oxygenated, at low temperatures) 1 formula unit per cell	face-centered (Bmmm) always orthorhombic (1000–20°C), superstructure $a'=2a$, $b=b$, $c'=2c$ due to ordering of Nd, Ba atoms, 4 formula units per cell
Oxygen nonstoichiometry	high	low
Twin formation	due to tetra–ortho transition at low temperatures because of oxygen diffusion	depends on growth regime, no ortho–tetra transition caused by temperature or oxygen
Expansion coefficients	$13–19\times10^{-6}\,K^{-1}$ (Marti et al. 1993)	$\sim11–16\times10^{-6}\,K^{-1}$
Lattice constants (after oxygenation)	$a=3.914$ $b=3.855$ $c=11.736$	$(2\times)3.884$ 3.864 $(2\times)11.585$
Lattice mismatch for *a*/*b*/*c* (%)		
MgO, 4.20 Å	7.3/8.9/–	8.1/8.7/–
$SrTiO_3$, 3.905 Å	0.23/1.30/–	0.54/1.06/–
$NdGaO_3$, 5.493 Å, 5.428 Å, 7.729 Å, $\frac{1}{2}(a^2+b^2)^{1/2}=3.86$ Å	1.38/0.13/–	0.62/0.10/–
Pr123, 3.930 Å, 3.874 Å, 11.717 Å	0.41/0.49/0.16	1.18/0.26/1.14
Y123, 3.888 Å, 3.817 Å, 11.678 Å	0.66/0.99/0.49	0.10/1.2/0.80
Sm123, 3.899 Å, 3.854 Å, 11.721 Å	0.38/0.02/0.13	0.39/0.26/1.17
Nd123, 3.914 Å, 3.855 Å, 11.736 Å	0/0/0	0.77/0.23/1.3
Properties after oxygen annealing	96 K superconductor with natural effective pinning centers (anomalous peak effect)	dielectric, resistivity 350 kΩ cm at 77 K, ε_r(80 K, 0 kHz) = 60, ε_r(80 K, 100 kHz) = 20
Applications	superconductor	substrate/buffer/barrier

and macrosteps up to 200 Å. HREM proved the perfection of the crystal lattice near the substrate layer. $T_c \approx 91$ K with ΔT_c about 2 K was achieved. Kitamura et al. (1996) and Aichele et al. (1997) have grown Y123 films on {110} $NdGaO_3$ substrate by a modified TSSG method. They confirmed that the crystal orientation of the epitaxially grown films depends on growth temperature and melt composition. With a copper-poor melt (Ba:Cu=3.0:5.0–6.0), only *c*-axis-oriented growth was observed. The *c*-axis orientation dominated at lower temperatures while the *a*(*b*) orientation dominated at higher temperatures in copper-enriched melts (Ba:Cu=3.0:6.5–7.0). It was noted that the *a*(*b*) orientation requires higher surface kinetics in comparison with the *c*-oriented growth as explained by the difference in the growth mechanisms at different preferable orientations. The growth of *c*-axis-oriented films occurs by step flow. The width of the flat terraces of the step was found to be about 5000 Å at a step height of about 20–30 Å. No macrosteps were observed in the case of *a*(*b*)-orientation growth. The surface roughness of the film was lower with a typical step height about 1.6 Å, i.e. a half the *a* side of the Y123 unit cell, which causes a difficulty for new layer formation and hence demands higher surface kinetics. Klemenz and Scheel (1993) succeeded in the preparation of Y123 and 0.5 mm Nd123 LPE layers with quite flat surfaces and steps less than 100 Å (a thick film of Nd123 was obtained by Takagi et al. 1997). With improved experimental conditions, the desired layer-by-layer growth has been achieved on a $LaGaO_3$ {001} substrate with 0.3° misorientation. A growth rate as low as 30 Å/s was estimated along the ⟨001⟩ direction, and 50 Å/s along ⟨100⟩ at the selected conditions. Macrosteps were also observed between 100 and 1000 Å in height and up to 17 μm apart for both Nd123 and Y123 crystal layers. This would theoretically correspond to a size of the critical surface nucleus of about 0.9–1.3 μm (sect. 2.3.2).

Ishida et al. (1997) and Kakimoto et al. (2000) investigated the initial stages of the Y123 LPE growth on the MgO substrate with a deposited thin film as a seed. At the beginning, island crystallite formation was observed. The size of a typical square island crystallite was found to be about $1.5 \times 1.5\ \mu m^2$ with a height of about 1300 Å. The steps grew from the edge on the island surface. Terraces were observed to be flat, with a step height between them of about 6 unit cells along the *c* direction (69 Å). It was suggested on the basis of experimental data that the island crystallites grow by 2D nucleation in the *c*-plane. Since the morphology of the *a*-oriented plane was rough, it has been suggested also that the growth rate in this direction is higher than that along the *c*-axis, therefore, at the initial step the substrate surface could be covered by a Y123 layer in seconds. However, the grains in the seed film oriented differently from $[100]_{Y123} \parallel [100]_{MgO}$ had a size smaller than the critical one and they readily dissolved in the solution. The larger $[100]_{Y123} \parallel [100]_{MgO}$-oriented grains survived to be nuclei of the island crystallites. Finally, the island crystallites extended laterally and coalesced, spiral growth took place, and an almost single-crystalline, well in-plane oriented film was grown despite the large misfit with the MgO substrate.

In order to lower the deposition temperature and to minimize the interaction with the substrate materials, Yamada et al. (1996a, 1997a) prepared Y123 single-crystalline oxide coated fibers for power applications on the YSZ ⟨100⟩ and $SrTiO_3$ ⟨100⟩ substrate

fibers below 930°C using the BaF_2-containing $BaF_2:BaO:CuO = 5:32.5:62.5$ flux and the SRL–CP method ideology ($BaZrO_3$ is formed easily from YSZ and the flux at temperatures higher than 930°C). Yet lower growth temperature can be achieved by the addition of silver (Yamada et al. 1996a, see also sects. 3.2.1, 5.1). The fibers demonstrated a 90 K superconducting transition and $J_c \approx 10^5$ A/cm^2 at 77 K (self-field) with gradual dependence of the critical current density on the applied magnetic field. Films grown for 5 min had a thickness of 50 Å. The Y123 layer grew by the {001} face parallel to the {100} face of the fiber and showed good in-plane orientation.

An alternative decision was suggested by T. Kimura et al. (1997). An Yb123 crystalline layer with 90 K transition temperature after oxygenation has been grown on $SrTiO_3$ and MgO substrates at 900°C in low-p_{O_2} atmosphere using a vertical dipping technique in Yb_2O_3 crucibles. This becomes possible due to the common tendency of the peritectic temperature falling when decreasing either p_{O_2} or the ionic radius of the rare-earth element (sect. 3.1.3). In principle, the lower formation temperature of the Yb123 phase could allow one to "cure" cracks and other similar defects in the Y123 layers of a complicated configuration by dipping in the Y–Yb saturated melt. Recently, a similar idea has been applied by Schmitz et al. (1998a) to join superconductive components using $YbBa_2Cu_3O_z$/$BaCuO_2$/CuO solder.

The critical current densities are expected to be small in LPE films on lattice-matched substrates (in the order of 10^2–10^4 A/cm^2 which is similar to perfect single crystals) compare with 10^6 A/cm^2 at 77 K for vapor-deposited films containing a larger number of defects acting as pinning centers. An additional irradiation of LPE films by protons etc. can produce new effective pinning centers (Gornert 1997). The actual critical transport current densities of *c*-oriented Y123 films on {100} MgO substrate show values of about 2.6×10^6 A/cm^2 at 77 K due to misfit dislocations between the film and the substrate (Kitamura et al. 1997).

5.5. *Crystal pulling method*

The variety of shapes and morphologies achieved by the pulling method (sect. 3.4.2.2) is connected with the easy control of most of the growth-determining factors in such a process (solute transport, nucleation, growth rate and growth anisotropy control, etc.). Actually, the largest bulk crystals of R123 were obtained by crystal pulling after development of appropriate technological schemes for their production (Yamada and Shiohara 1993, Shiohara 1996, Shiohara and Endo 1997, Yao and Shiohara 1997).

5.5.1. *Y123 crystals grown by automatic crystal pulling in high p_{O_2} atmosphere*

SRL–CP is the only method that allows to grow continuously large Y123 single crystals using transport of solute-rich liquid from a Y source (the 211 phase) at the bottom of a crucible to the rotating seed at the solution surface. By optimizing the various growth conditions, large and high-quality bulk single crystals of Y123 have been produced in an atmosphere with high oxygen partial pressure (1 atm of oxygen) where the solubility of Y is higher (sect. 3.1.2.1). The shape of the Y123 single crystal pulled along the

c-axis will be discussed in sect. 6.2. The 20 g-crystal is bulky with a typical size about $19.8 \times 19.5\,mm^2$ in the ab-plane and 16.5 mm in height (Yao et al. 1996a). The authors claimed that to the best of their knowledge this is the largest bulk Y123 single crystal yet obtained. X-ray Laue diffraction images of the bottom end of the crystal demonstrated a clear 4-fold symmetry. This indicated that the bottom surface was a {001} plane and the Y123 crystals grew epitaxially from the seed crystal. The 1.5–2.5 times faster growth rate under these conditions, as compared to air, does not conflict with the high $T_c \approx 92.7$ K of the crystal. Consequently, the results are highly promising for future industrial production of large high-quality Y123 crystals although they could be predicted in advance from the peculiarities of the phase relations discussed earlier.

5.5.2. *$Nd_{1+x}Ba_{2-x}Cu_3O_z$ crystals grown by modified TSSG method with liquid composition control*

The TSSG method in a rotated Al_2O_3 crucible was applied to grow YBCO crystals by Zhokhlov and Emelchenko (1993), Emelchenko et al. (1994). The authors found that the width of the metastable zone of YBCO is about 0.8 K only under the growth conditions from $BaCuO_2$–CuO eutectic at about 930°C. Under a supercooling of less than 0.8 K a bulk crystal of the polyhedral type grows on a seed. At supercooling larger than 0.8 K, a spontaneous crystallization takes place and crystals mostly in the form of thin plates can be produced. The maximum size of a polyhedral bulk crystal obtained for 17 days was reported to be $8 \times 6 \times 5\,mm^3$ and the mean growth rates were estimated as 0.18 mm/day and 0.12 mm/day. The crystal contained small Al impurity and after two weeks oxygenation at 485°C in oxygen displayed an orthorhombic phase [$a = 3.8325(3)$ Å, $b = 3.8840(3)$ Å, $c = 11.703(1)$ Å] with $T_c = 90$ K and $\Delta T_c = 2$ K.

Such extremely low growth rates in the case of the Y123 crystal (about 20–40 times smaller than those mentioned in sect. 3.4.2.2) are the direct result of the small solubility of Y in melt, especially under the selected low-temperature eutectic crystallization from the melt containing impurities (Al). As mentioned, this problem has been successfully solved in the SRL–CP method. On the other hand, this problem does not exist for the rare earths with higher solubility, and the TSSG method can be applied, e.g., for R = Nd. The modified TSSG method actually has been employed to grow the largest Nd123 bulk single crystals in the world (Yao et al. 1997). This becomes possible because the solubility of Nd is several times higher than that of Y, and its low slope of liquidus allows one to produce and keep a sufficiently high level of supersaturation at almost isothermal conditions for the crystal growth in the undercooled melt. Another advantage of this method is the utilization of contamination-free Nd_2O_3 crucibles containing no TiO_2 or other inorganic impurities. In this case, the high-temperature stable phase is not placed at the bottom of a crucible as in the SRL–CP method, and the Nd solute required for crystal growth is sufficiently supplied only from the crucible owing to the high solubility of Nd in the Ba–Cu–O liquid phase. As a result, under optimized technological conditions (Ba/Cu ratio in the flux about 0.78, constant temperature 1058–1070°C, pulling at 0.1–0.25 mm/h, rotation rate 70–120 rpm) a $NdBa_2Cu_3O_{7-\delta}$ crystal as large as $24 \times 24\,mm^2$ in the ab-plane and

21 mm in the c-axis direction was produced after only 67 h in air (fig. 26a). The most remarkable result, however, was that the crystal, after oxygen-annealing at 340°C for 200 h ($p_{O_2} = 1$ atm.) demonstrated a T_c value about 95 K with a transition width of only 0.5 K, while commonly used melt-processed NdBaCuO bulk polycrystalline materials, prepared in air, possess $T_c \approx 50$–70 K and special care about the preparation conditions should be taken (Bieger et al. 1996, Dimesso et al. 1997, Fujihara et al. 1997, Y. Watanabe et al. 1997, Kambara et al. 1997d, Krabbes et al. 1998, Goodilin et al. 2000, Schatzle et al. 2000).

An additional merit of the method under discussion is the possibility to easily control the composition of the solid phase (substitution value x in the $Nd_{1+x}Ba_{2-x}Cu_3O_z$ solid solution) by selecting an appropriate flux composition (Kambara et al. 1997e). On the basis of the experimental phase relations discussed in sect. 3.1.2 several neodymium-rich crystals of Nd123ss were grown by the TSSG method from copper-rich fluxes (Goodilin et al. 1997a). As an example, a bulk crystal with $x = 0.85$ grown from the Ba : Cu = 3 : 14.5 flux is shown in fig. 26b.

These crystals ($x \approx 0$ and $x \approx 0.85$) are composed from the solid solution of two drastically different compositions which belong to the opposite edges of the Nd123ss stability field (sect. 3.1.2.3). As a result, the physical properties are contrasting (table 6). The as–grown $x \approx 0$ crystal is tetragonal (P4/mmm) and it has excellent superconductivity after oxygenation (95 K). The as–grown as well as fully oxygenated $x \approx 0.85$ crystals ("Nd213") are orthorhombic, and an estimation of the lattice constants in the frame of a primitive subcell gives $a = 3.884(1)$ Å, $b = 3.864(1)$ Å, $c = 11.585(2)$ Å. These constants were found smaller than those of the $NdBa_2Cu_3O_{7-\delta}$ single crystals due to the substitution of Ba with Nd. The crystal was confirmed to be orthorhombic by TEM investigation, with a B-type superstructural lattice possessing doubled a and c parameters of the primitive subcell (sect. 6.11). Formation of the solid solution can be confirmed by the absence of superconducting properties. The resistivity of the fully oxygenated $x = 0.85$ crystal was about 350 kΩ cm at 77 K, therefore it is an insulator. From an engineering point of view, the Nd123–Nd213 couple demonstrates two phases (a superconductor and a substrate) which can be jointly applied in the superconducting device technology (table 6). On the other hand, the Nd123 and Nd213 crystals would represent macroscopically separated parts of a spinodally decomposed system if the spinodal decomposition of a solid solution actually takes place (sect. 7.4.3.4).

5.5.3. *Other R123 crystals*

SRL–CP has also been applied to other $RBa_2Cu_3O_{7-\delta}$ materials, (R = Pr, Sm etc.). It was found that bulk single crystals several mm in size (usually 7–10×7–10×5–7 mm^3) are repeatedly produced by this method (see Shiohara and Endo 1997, Yao and Shiohara 1997, Krauns et al. 1997). In the case of Sm123, the growth rate was about a factor of five faster than that of Y123 (sect. 7.3.2). Contrary to the superconducting Pr123 crystal produced by TSFZ, as described in sect. 5.3, the typical ("normal") Pr123 crystals obtained by SRL–CP exhibit semiconducting behavior (Tagami et al. 1995, Tagami and

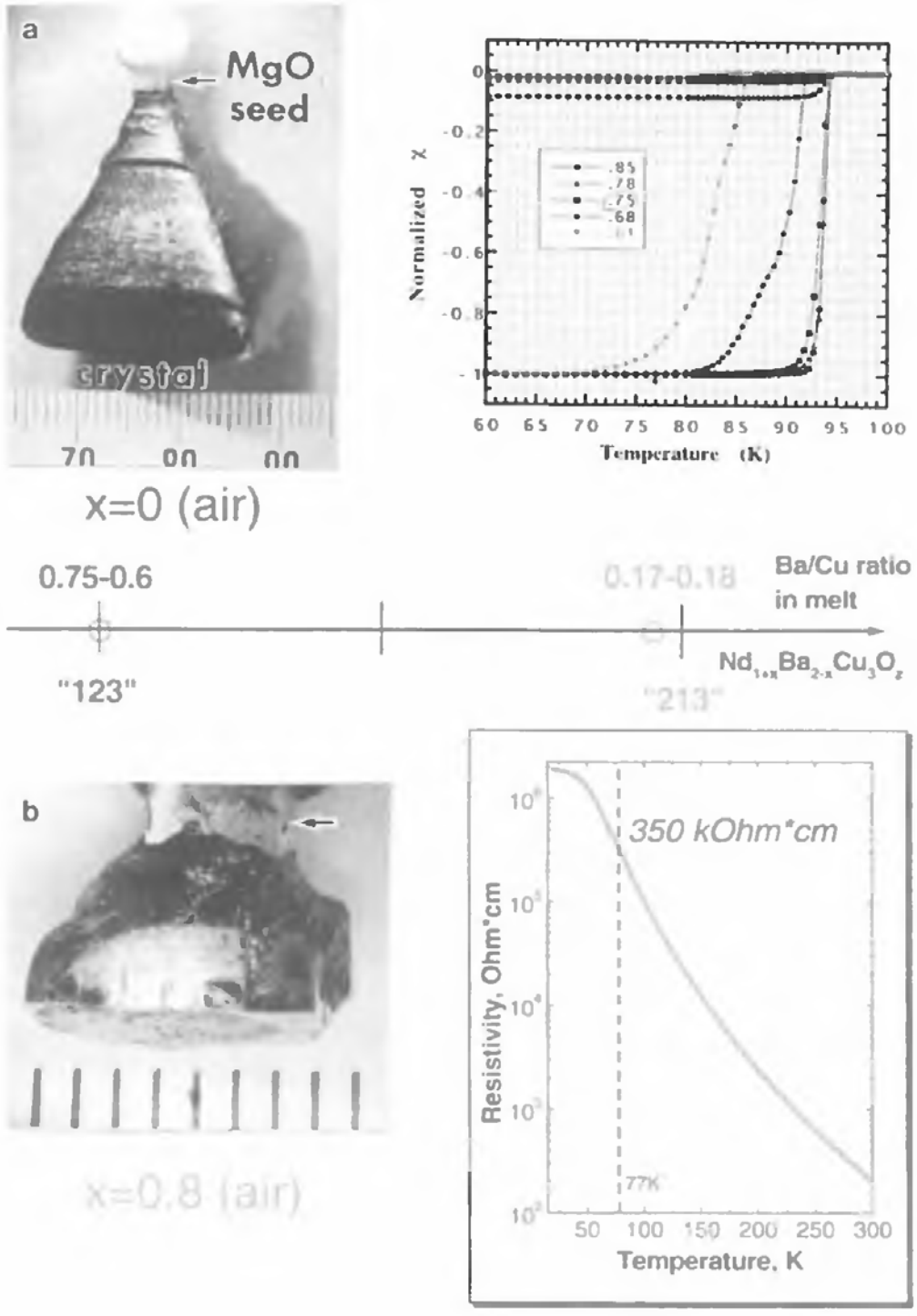

Fig. 26. General view of two $Nd_{1+x}Ba_{2-x}Cu_3O_z$ crystals with essentially different compositions (substitution x) grown in air by the modified TSSG method with liquid composition control: $x \rightarrow 0$, 95 K after oxygenation (a, Yao et al. 1997, Yao and Shiohara 1997) and $Nd_{1.85}Ba_{1.15}Cu_3O_z$, resistivity 350 kΩ cm after oxygenation (b, Goodilin et al. 1997a). The first crystal is probably the largest R123 bulk crystal obtained up until the present moment.

Shiohara 1997). Therefore, large single crystals of Pr123ss are expected to be applicable as substrates (see also sect. 5.1).

Yao et al. (1996b) investigated $9\times9\times4\,mm^3$ Zn-doped $YBa_2(Cu_{1-x}Zn_x)_3O_z$ crystals with $x=0.004$–0.03 grown by the SRL–CP method. The effective distribution coefficient of Zn was found to be about 0.35 at growth temperatures 986–1005°C. T_c decreased almost linearly and rapidly with a slope 12 K per 1 at% of Zn (see also sect. 5.1).

Substitution of copper in the 123 type structure for Ga was successfully performed by C.T. Lin et al. (1996) using the TSSG method. This is important for the investigation of the effects of local magnetic moments, disorder and carrier concentration on superconductivity. Large $Nd_{1+x}Ba_{2-x}Cu_{3-y}Ga_yO_z$ single crystals of about $22\times15\times3\,mm^3$ in size were obtained from an oxide flux in a rotated (15 rpm) SnO_2 crucible using a cold finger (thermal gradient of about 5°C/cm between cold finger and surface of molten solution). Stepwise cooling from 1030°C to 960°C in air was applied at a cooling rate of 0.5°C/h between the steps, followed by decantation of the flux into porous materials at 960°C. To study electrical properties the samples were annealed at 535°C for 3 weeks in flowing oxygen. In the crystals the upper solubility limit of Ga was found to be as high as $y=0.58$ and the Ga fraction in the crystals $C_{Ga}/(C_{Ga}+C_{Cu})$ was almost linearly correlated with that in the liquid due to a constant distribution coefficient of 4.69. The resistivity measurements indicated that Nd substitution for Ba or Ga for Cu causes a significant change in electrical and superconducting properties. T_c was found to be about 90 K for $x=0.02$ and lower than 35 K for $x=0.26$ ($y=0$). T_c decreased gradually with increasing total content $(x+y)$ of Nd and Ga. Generally the crystals were superconducting at a Ga content less than about 0.08. Superconductivity vanished and the crystals became metallic at $x=0.23$, $y=0.09$ as well as at $x=0$, $y=0.1$. Semiconductivity was observed at $y>0.15$. A further study of substituted systems can give essential information about the mechanism of superconductivity.

5.6. *Single-crystal growth of other superconductors*

After Karpinski et al. (1988b), 124 and 247 homologues of the 123 phase have been prepared in single-crystal form by a number of authors (see, for example, the reviews by Karpinski et al. 1997b, 1999). Stacy and coworkers succeeded in the preparation of $EuBa_2Cu_4O_8$ small crystals and $LnCu_2O_4$ (Ln = La, Nd, Sm, Eu, Gd, Dy, Ho, Y, Er) phases by means of a solution technique involving reactive precipitation from molten hydroxide melt (Sandford et al. 1995, Luce and Stacy 1997). The melt consisted of a mixture of NaOH, KOH and $Ba(OH)_2$ and was heated at 475°C for about 2 h prior to the addition of reactants. The Eu124 crystals were then obtained in several hours. The as-grown product was a single phase [$a=3.868(2)$ Å, $b=3.878(2)$ Å, $c=27.30(1)$ Å] with the onset critical temperature as high as that typical for 124 phases (78 K). Using a similar technique, Sunshine et al. (1997) obtained several nonsuperconducting Y–Ba–Cu–O compounds with the $Sr_3Ti_2O_7$-type structure and Y123 crystals with the 91 K transition.

Yamaguchi et al. (1990a) obtained a Ca-stabilized Y124 phase at $p_{O_2} = 3$atm. Genoud et al. (1997) reported growth of high-purity (up to 99.995%) $320 \times 160 \times 20\ \mu m^3$ Y124 single crystals in a $BaZrO_3$ contamination-free crucible using an autoclave under 1400 bar of oxygen and 0.05°C/min cooling rate. The eutectic temperature was determined to be 1113°C. The 81.5 K sharp superconducting transition and no "fishtail" anomaly, but a monotonous decrease of the magnetic hysteresis were observed in fields up to 5.5 T and 10 K. The crucible material (ZrO_2, BeO, Al_2O_3, MgO) and substitution (Zn, Ni) effects were studied for $YBa_2Cu_4O_8$ single crystals (Dabrowski 1998) grown by the self-flux method under $p_{O_2} = 600$ atm at about 1100°C (2–5°C/h cooling rate).

Large tetragonal $R_{2-x}M_xCuO_4$ single crystals up to $4\ cm^3$ (R = La, Nd, Sm, Gd; M = Sr, Ce, Nd) were grown from solutions containing excess CuO by C.T. Lin et al. (1997). The surfaces of the crystals were identified to be primary crystallographic faces of {100}, {001} and {011} types. At a cooling rate of 0.5°C/h a pyramidal morphology of crystals with faces {011} was observed. The growth rates were estimated to be $v_{\{100\}} \approx 128\ \mu m/h$, $v_{\{001\}} \approx 108\ \mu m/h$ and $v_{\{011\}} \approx 68\ \mu m/h$ and they were found to be anisotropically dependent on the cooling rate.

Large and perfect Bi2212 crystals with sizes of about $20 \times 5.5 \times 1.5\ mm^3$ and 91 K transition temperature were succesfully grown by Gu et al. (1993, 1996); a 85 K single crystal of the Bi2212 phase was grown in air by K. Oka and Ito (1996) by the TSSG method with a $Bi_{2.4}Sr_{1.5}Ca_{1.0}Cu_{1.8}O_x$ solvent (pulling at 0.3–0.5 mm/h, rotation 30–40 rpm, cooling rates 0.5–1.0°C/h). Crystal growth of this phase by a flux technique involving a large temperature gradient was reported by Yang et al. (1996). Bi2212 and Bi2223 crystals were grown by Balestrino et al. (1994) using KCl flux.

Tl-2223 crystals with a T_c of 115 K have been reported by Matsushita et al. (1995).

Synthesis and characterization of single crystals of $Hg_{0.8}Bi_{0.2}Ba_2Ca_{n-1}Cu_nO_{2n+2+y}$ ($n = 2, 3$) superconductors have been performed, for example, by Pelloquin et al. (1996). S. Lee et al. (1998b) have grown small single crystals of the $HgBa_2Ca_2Cu_3O_{8+y}$ phase by the ampoule method and have found that flux pinning properties in high magnetic fields are essentially improved by substitutions of Hg by Pb and Ba by Sr (S. Lee et al. 1998a). The Hg-12$(n-1)n$ ($n < 4$) crystals with a T_c onset up to 130 K as well as thin films on $BaZrO_3$ substrates have been grown from a melt by Karpinski et al. (1997a, 1999) in 10–15 kbar of Ar gas pressure in PbO and $BaCuO_2$–CuO fluxes. Yttria crucibles and crystallization temperatures of $930 < T < 1070$°C were applied. The crystals obtained demonstrated double-spiral growth steps. A similar high-gas-pressure technique for mercury-based high-temperature superconductors was applied by Morawski et al. (1998). Again, single crystals of $Hg_{0.75}Re_{0.22}Ba_2Ca_5Cu_6O_{15}$ ($T_c = 100$K) and of $Hg_{1-x}Re_x$ $Ba_2Ca_6Cu_7O_{16+4x+y}$ ($T_c = 84$ K) representing the $n = 6, 7$ members of the mercury-based cuprate superconductors have been grown with the same gas-phase high-pressure technique at 10 kbar (Schwer et al. 1999).

Centimeter-sized single crystals of the chain cuprates $SrCuO_2$, Sr_2CuO_3 and spin-ladder $Sr_{14}Cu_{24}O_{41}$ (14:24 AEC) were grown by the floating-zone technique by Revcolevschi et al. (1997). The 14:24 AEC has an interesting structure comprising isolated copper chains and layers made of chains assembled into "ladders". The

superconductivity transition at about 12 K was observed at a pressure of several GPa in this compound after substitution of Sr by Ca.

Growth of rare-earth- and copper-free $BaPb_{1-x}Bi_xO_3$ crystals was discussed by Chen (1998).

Tachibana et al. (1996) reported that large ($4.5\times3.0\times1.5\,mm^3$) C_{60} (fullerene) single crystals have been grown from vapor by a continuous-pulling technique, consequently even this (still exotic) class of superconductor-related compounds has been obtained in single-crystal form.

Thus, common principles presented in this chapter allow one to perform single-crystal growth of a wide variety of incongruently melting, chemically and structurally complex multicomponent phases. Crystal growth of several types of HTSCs has been overviewed by Assmus and Schmidbauer (1993) and by Chen (1998).

6. Characterization of R123 single crystals

6.1. *Classification of defects*

An ideal single crystal has no defects. However, since the Gibbs energy of crystal formation ($\Delta G = \Delta H - T\Delta S$) is a balance between the energetic "ΔH" term (or the tendency to have the most perfect and well-packed structure) and the entropic "$T\Delta S$" term (or the tendency for disorder), the minimum ΔG for a real crystal in the equilibrium state at $T \neq 0$ K could be attained only if a certain non-zero concentration of "equilibrium" defects is present. Thus, defects are a natural and thermodynamically permitted feature of any existing crystal.

Overall and internal morphology of single crystals, such as size, facetting, growth spiral pattern, macrostep height, distribution of dislocations and compositional fluctuations, twinning and cracks, point defects and other lattice defects represent a record of the crystal growth and post-growth histories. Since the growth of a crystal takes place exclusively at the solid–liquid interface, the surface morphology and microtopography represents the final stage of growth, i.e. if a crystal face seems to be perfectly flat over a wide area, it could be assumed that the technique used for this observation is not sensitive enough. Although actual surface morphology is usually complicated, it is formed by elementary processes and hence reflects the structural features of the face and the growth process. The general characteristics of the surface and internal morphology are essentially similar for crystals grown under the same governing factors, and they could be markedly different in their dependence on the selected conditions giving a powerful criterion to be used in crystal diagnostics as well as in the prediction and optimization of their growth. That is the reason for the desire to understand how all these features are related to the growth and the structure of the solid phase produced.

On the other hand, for structure-sensitive properties a knowledge of the ideal structure also is not sufficient because the structural defects play an important role in determining the properties. In the case of HTSCs, defects of an appropriate size can act as pinning

centers in single- or polycrystalline materials (Weber, Vol. 31, ch. 196 of this Handbook) resulting in high J_c, while a perfect crystal with minimum defects is supposed to have low J_c values at the same fundamental T_c parameter (see, e.g., Erb et al. 1997, Liang et al. 1998). Different defects can make different contributions at different temperatures, applied magnetic fields and angular orientations of a crystal in the magnetic field, therefore it is important to describe the defect hierarchy and origin at different scales ("magnifications") of the crystalline matter.

Defects can be classified using their size and dimension (as well as typical energy of formation, physical nature and so on). It is convenient to consider point defects (0-dimensional), line defects (1-dimensional), surface defects (2-dimensional) and 3-dimensional defects and their interacting groups (see, for example, Wilke 1973). In practice, it also is important to demarcate different kinds of defects belonging to different structural levels of a single crystal, which are arbitrary, macroscale, mesoscale and microscale levels (see also Gudilin et al. 1994, Tretyakov and Goodilin 2000). This is necessary because defects of different structural levels predetermine different aspects in the physical behavior of the single crystal. When we increase "magnification" from unaided eye vision (overall shape of the crystal) to the scale of atoms it is necessary to substantially increase the resolution of our instrumental characterization technique or even change the physical principles of the probing method. Therefore only a combination of several complimentary methods can allow us to establish properly what kind of crystals we hold in our hands.

Many literature sources can be recommended for a comprehensive study of defects in single crystals, polycrystalline materials and films, as well as instrumental methods for their characterization (e.g., Flewitt and Wild 1994, Elwell and Scheel 1975). In this section only typical and practically important considerations will be introduced with respect to R123 single crystals.

6.2. *Variety of shapes, sizes and morphology. Optical microscopy and etch figures*

In fig. 27, several frequently achievable morphologies of single crystals are summarized, excluding types observed in semisolid melt solidification such as the lamellar growth of pseudo-single-crystalline domains consisting of stacked parallel R123 plates, dendrite and spherulitic growth, etc. (see sect. 4.2.1).

The variety of these forms originates from the peculiarities of the crystal growth technique applied. A description of the causes of and growth mechanisms resulting in such different morphologies has been presented in the preceding sections of this chapter:

- rectangular thin plate-shape ("leaf") of self-flux-grown Nd123 crystal, sect. 5.1;
- needle-like crystals of the Nd123 phase, sect. 5.2;
- directionally solidified rods consisting of several single grains enlarged in the growth direction, sect. 5.3;
- bulk single crystals grown by pulling methods (modified TSSG and SRL–CP):
  - usual large pyramidal-like crystals, sect. 5.5;
  - straight-body crystals grown under special conditions, sect. 3.4.2.2;

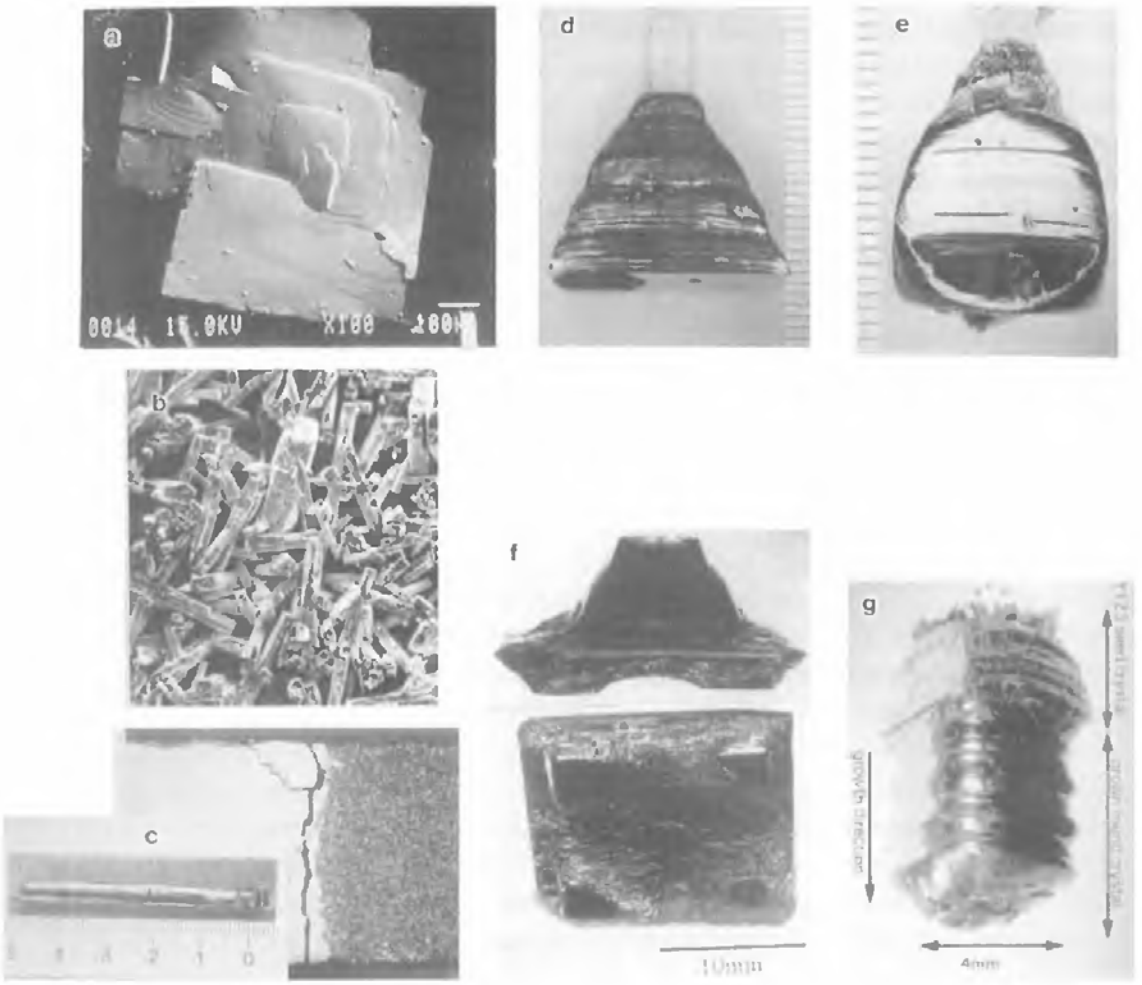

Fig. 27. Variety of shapes of R123 single crystals: (a) self-flux grown Nd123 crystal demonstrating a grown macrospiral; (b) needle-like Nd123 crystals (Goodilin et al. 1996); (c) TSFZ-produced Nd123 rod with several large-crystalline grains inside (Kuroda et al. 1997b), background picture shows an example of a plane front development; (d) the largest Y123 single crystal with the usual pyramidal-like shape obtained by the automatic SRL–CP method in pure oxygen (Yao et al. 1996a); (e) straight-body Y123 single crystal obtained under carefully controlled growth conditions by the SRL–CP method (Namikawa et al. 1996c); (f) concave Y123 crystal produced at a high rotation rate in the SRL–CP method (Namikawa et al. 1996b); (g) round-cornered Y123 single crystal obtained under special conditions using the automatic crystal pulling setup (Egami and Shiohara 1997).

– pyramidal crystals with concave growth interface, sect. 3.4.2.2;
– round-cornered crystals, sect. 3.4.2.2.

The essential progress in crystal preparation techniques as well as improvements in flexibility and automation are evident from fig. 27. Depending on the desire of a crystal grower, it is now possible to achieve almost any required morphology.

Historically, a simple method of this "macroscopic" structural level characterization is connected with optical microscopy and etch figure analysis. The first and easiest step of single-crystal characterization is to observe the overall growth shape and macrodefects

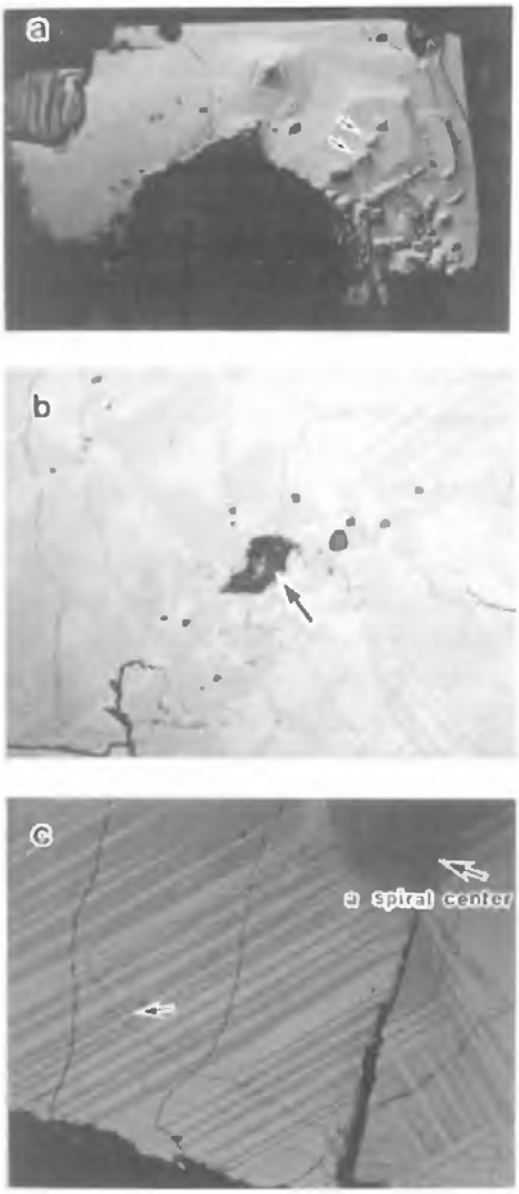

Fig. 28. Visual defects in single crystals: (a) hillocks; (b) a macrospiral with a hollow core in its center; (c) cooling cracks.

such as growth macrospirals, macrosteps and macrocracks due to thermal shock etc. This is mostly based on optical microscopy of at least low resolution (10–100× magnification, centimeter–millimeter scale). It helps to say briefly how the crystal has been grown. In fig. 28a, a group of hillocks is shown along a crystal imperfection at the crystal growth interface. Figure 28b demonstrates a macrospiral formation with a hollow core in its center as discussed in sect. 2.3.4. In fig. 28c cooling cracks are evidently formed because of strain relaxation (thermal shock due to fast removal of the crystal from a furnace). The cracks intersect "as-grown" twins which exist due to the TPRE growth mechanism found in the case of the $Nd_{1.85}Ba_{1.15}Cu_3O_z$ solid solution (sect. 3.4.3). An alternative technique of crack determination in HTSC materials is acoustic microscopy (very common in metallurgy), as demonstrated by Egi et al. (1996).

At present the chemical etching technique is being replaced by nondestructive instrumental analysis, however it is useful to recall this method because it easily allows one to clarify some fine details of crystal structure using optical microscopy only. The etching method is based on preferential, faster dissolution of the HTSC material at the defect sites compared with the defect-free area. For example, the lattice strain associated with screw dislocations greatly enhances the rate of etching (C.T. Lin 1994, C.T. Lin and Liang 1994). Many solutions can be suggested for etching, but only a few are actually useful because the etching must proceed slowly and controllably and the etching products must be easily removed from the partially dissolved surface. "Ice" (99%) acetic acid, dilute solutions of HNO_3, HCl or $HClO_4$ in water or organic solvents, and Br_2 solution in methanol are commonly used for the etching. Water solutions of salts (for example 3–5 wt% $(NH_4)_2C_4H_4O_6$ + 3–5 wt% NH_4NO_3 + 1–3 wt% $NaNO_2$ + 1–2 wt% NaCl with pH ≈ 3–5 at 50–60°C, 20–150 s of etching time, Emelchenko et al. 1994) are also available for selective etching.

The size and shape of etching pits strongly depend on the etching behavior. The etching rate is usually of the order of several micrometers per hour. C.T. Lin and Liang (1994) found clear evidence by this method for growth hillocks and steps in self-flux-grown Y123 crystals. Three types of etching pits were observed: a square pyramid with growth steps along the ⟨100⟩ and ⟨010⟩ directions; an octagonal pattern truncated along the ⟨110⟩ direction; and a shallow ellipse with long and short axes in the ⟨100⟩/⟨010⟩ and ⟨001⟩ directions, respectively. The first two types of pit pattern have been designated screw dislocation etch pits, and the third type was found to be of Hopper-like morphology. Clustering and tangling of dislocation etch pits have also been observed. The etching rate V has been found to be anisotropic with different speeds in the four principal directions: $V_{\langle 110\rangle} > V_{\langle 100\rangle/\langle 010\rangle} > V_{\langle 001\rangle} > V_{\langle 111\rangle}$. The octagonal shape of the growth hillocks indicated the anisotropy in the step advancing velocity along the ⟨100⟩/⟨010⟩ and ⟨110⟩ directions (sect. 3.4.2.1). The hillocks also give evidence for existence of screw dislocations. The densities of the dislocation etch pits have been estimated at $10^6\,cm^{-2}$ in the {001} and $10^5\,cm^{-2}$ in the {100}/{010} surfaces. The difference in the distribution was assumed to be related to the fact that thermal stress can be more readily released near the edges than at the center of the crystal. Emelchenko et al. (1994) found that the characteristics of the etch-figure distribution on the {100} face is indicative of the occurrence of microcracks parallel to the *ab*-plane. Thus, this aged classical method, in principle, is informative and effective.

6.3. *Twins and tweed pattern due to strains in the orthorhombic phase. Hot-stage microscopy*

All the crystals of the R123 superconductors grow at high temperatures where the tetragonal, oxygen-poor modification is stable only (a rare exception was demonstrated by Stacy and coworkers, see sect. 5.6). The transition of the tetragonal to the orthorhombic R123 phase due to oxygen in-diffusion on cooling is normally accompanied by the spontaneous formation of twin domains because the internal strains are relieved. It has

been suggested (Shaw et al. 1989) that the spacing of the twins, $\Delta\lambda$, varies as the square root of the size G of the transforming region: $\Delta\lambda = \sqrt{(128\pi\gamma G/(ES^2)}$, where γ is the twin boundary energy per unit area, S is the orthorhombicity ratio, and E is the elastic modulus of the material. Similar expressions can be found elsewhere (Sarikaya et al. 1988). It is obvious that the twins can be negligibly small and undetectable in tiny particles, however, in large single crystals these twin domains are visible and give contrasted images in polarized optical microscopy. The presence of twins poses a problem in obtaining a clear resolution of the *a–b* anisotropy of physical properties. The importance of twin and micro-twin structures in superconducting transport and pinning properties is also well-recognized. The twin boundary and microcracking due to oxygenation and to change in lattice volume is a problem when large single crystals are applied as homoepitaxial substrates for electronic devices.

Salje and coworkers (C.T. Lin et al. 1995) suggested that annealing the orthorhombic phase above the transition temperature at high oxygen partial pressure for a short period of time followed by quenching could result in a tetragonal oxygen-rich phase. Since the oxygen-rich tetragonal phase is a nonequilibrium state, the intrinsic strains can manifest themselves as orthogonally modulated structure distortions with a length of several tens to hundreds of angstroms (tweed structure). C.T. Lin et al. (1995) demonstrated the existence of the tweed tetragonal phase in oxygen-rich pure $YBa_2Cu_3O_{7-\delta}$ ($\delta < 0.6$) prepared by a similar method. The samples were superconducting with a sharp transition. In $Nd_{1+x}Ba_{2-x}Cu_{3-y}Ga_yO_z$ crystals (C.T. Lin et al. 1996), X-ray single-crystal diffraction demonstrated that the tetragonal symmetry occurs in three cases: $x \geqslant 0.18$, $y = 0$; $x = 0$, $y > 0.10$, and $x + y \geqslant 0.16$. Optical microscopy revealed the twin structure in pure $Nd_{1+x}Ba_{2-x}Cu_3O_z$ with $x = 0.15$, while TEM provided evidence of the tweed tetragonal phase in the highly Ga-doped compound. At the same time, no twins can be observed for the more substituted Nd123ss solid solution ($x = 0.4$–0.6, $y = 0$) because the crystals are always tetragonal (sect. 3.1.2.3).

The most interesting feature (Goodilin et al. 1998b) of the as-grown $Nd_{1.85}Ba_{1.15}Cu_3O_z$ single crystals is, again, the twin-like structure parallel to the {110} planes observed by optical microscopy in polarized light for the as-grown bottom facet (figs. 4d and 26). However, in this case it is not connected with the tetra–ortho phase transition as in the $x = 0.0$ case, but actually the solid solution of this kind is orthorhombic even at high temperatures (sect. 3.1.2.3), and the TPRE growth mechanism is considered to be the cause of the twinning phenomenon (sect. 3.4.3). In accordance with AFM profile analysis in this specific case, the twin ensembles consist of small periodic lamellae of about 5–10 nm in height with 2–4 μm spacing, while the same parameters for the primary lamellae are several times larger (Goodilin et al. 1998b). The twin formation is quite reproducible for this "always-orthorhombic", heavily Nd-doped solid solution. Usually it can be easily found by optical microscopy under polarized light after rotation on a certain angle. Further rotation leads to inverted contrast of the twin image. The backscattering Laue XRD pattern demonstrates the doubling of reflections and simultaneous shifting them up and down as typical for the presence of twin domains in the usual $x = 0.0$ case. However, future applications may likely demand to avoid this twinning phenomenon by

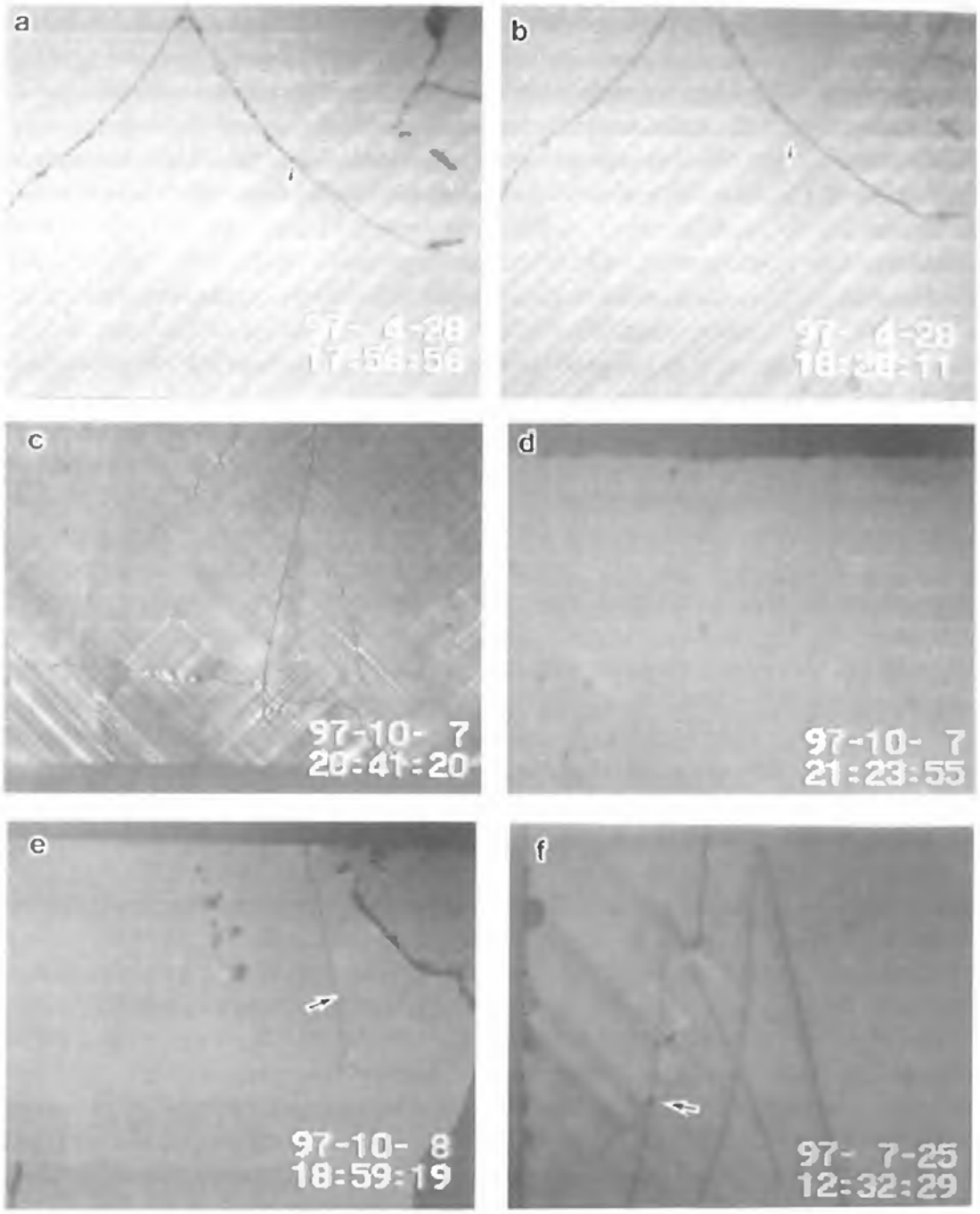

Fig. 29. *In situ* observation of twinning under different conditions using hot-stage optical microscopy (A. Oka et al. 1998): (a,b) stability of as-grown twins of an orthorhombic $Nd_{1.85}Ba_{1.15}Cu_3O_z$ crystal under 900°C and 1% oxygen + 99% Ar atmosphere, at (a) beginning of the heat treatment and (b) after 30 min. holding, no changes are observed; (c,d) detwinning of an Y123 crystal in pure oxygen with twins formed at 500°C (a/c), and after holding at 800°C for 10 min. (b/d); (e,f) temperature difference in the onset of twin formation for originally twin-free R123 with different R sizes (e, oxygen, Y123, 780°C; f, Nd123, 680°C).

varying the growth regime. In principle, the same problem exists in the Czochralski growth of another "always orthorhombic" $NdGaO_3$ perovskite material which is promising as a substrate with a very small misfit for the Y123 phase deposition (see table 6, sect. 5.4) while having a favourable combination of mechanical and dielectric properties. Twinning was suppressed when the formation of a rapidly grown region below the seed was avoided (Uecker et al. 1994) by precisely adjusting the shape of the (re)melting isotherm to that of the "solid–liquid" interface at the starting period of the crystal growth.

Thus, two types of twin structure can be observed in the whole range of the $Nd_{1+x}Ba_{2-x}Cu_3O_z$ solid solution: due to the tetragonal-to-orthorhombic phase transition in the region $x < 0.3$, and due to peculiarities of the crystal growth mechanism at $x > 0.6$. Additionally, the tweed structure can be observed near $x = 0.3$ and $x = 0.6$. A strong confirmation of the as-grown nature of the twins in $Nd_{1.85}Ba_{1.15}Cu_3O_z$ (together with the data of high-temperature XRD, sect. 3.1.2.3) can be found by high-temperature (hot-stage) in situ optical microscopy (fig. 29, A. Oka et al. 1998). This is a powerful method for visualizing the twin behavior and for a kinetic study of processes in any desired environment and conditions (at certain T, p_{O_2} and applied uniaxial pressure). In figs. 29a,b this method demonstrates the stability of twin structure in $Nd_{1.85}Ba_{1.15}Cu_3O_z$ crystals even at 900°C in low-p_{O_2} atmosphere. The twins do not disappear after this high-temperature–low-p_{O_2} anneal, contrary to the usual behavior of twins in the $x = 0$ case (figs. 29c,d). To eliminate the twin structure in $Nd_{1.85}Ba_{1.15}Cu_3O_z$ it is necessary to destroy the crystals or to obtain them without twins under some other growth conditions. At the same time, detwinning in the $x = 0.0$ single crystals occurs for several minutes depending on the temperature and p_{O_2}. Thus an essential difference in the behavior and formation mechanisms of these two different kinds of twins is revealed.

It should be noted that hot-stage microscopy can directly confirm the tetragonal-to-orthorhombic second-order phase transition similarly to other in-situ measuring techniques (Kogachi et al. 1990, Marti et al. 1993), while quenching experiments are not necessarily authentic. In figs. 29e,f, one can easily see an essential difference in the onset temperature of twin formation as observed using Y123 and Nd123 bulk single crystals. In the latter case the transition temperature is about 50–100°C lower, as mentioned in other literature sources (Jorgensen et al. 1988, Shaked et al. 1990; sect. 7.4.3).

6.4. *Low-angle misoriented grains. Laue XRD, rocking curves, pole figures, XRD topography*

Low-angle misoriented grains are a common problem in the production of small (Hayashi et al. 1988a) and, especially, large crystals (Namikawa et al. 1996c). One type of misoriented domains are twins as described above. They can be observed by Laue back-scattering X-ray diffraction (LBXRD), a simple basic method for determining crystal orientation (Yamada and Shiohara 1993, M. Nakamura et al. 1994, Tagami et al. 1995, Namikawa et al. 1996c, Aswal et al. 2000). In this technique X-rays reflected (diffracted) from the crystal surface are detected by a photographic film of some kind placed before the fixed sample. The symmetry of the picture obtained is determined by the crystal

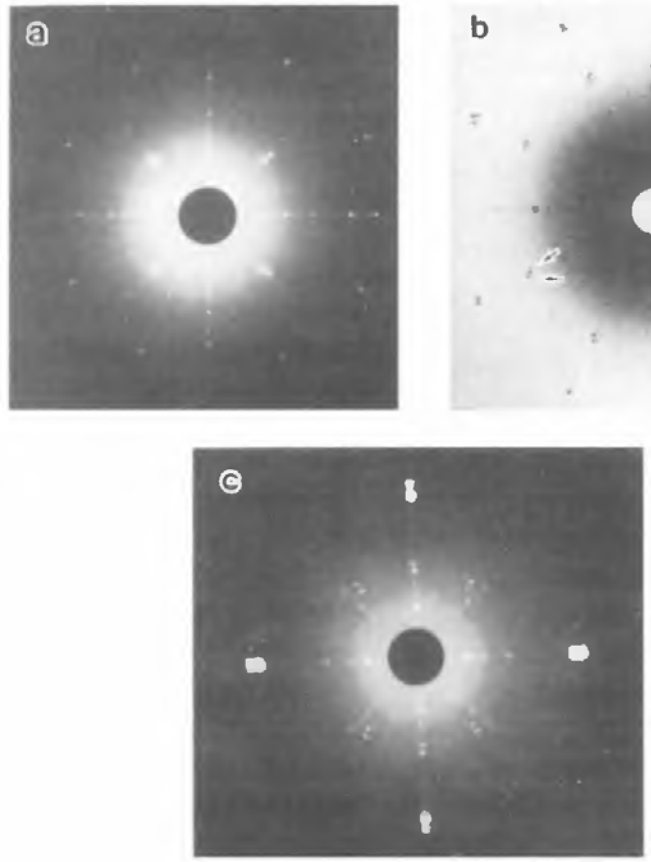

Fig. 30. Laue backscattered patterns of large Y123 crystals produced by the SRL–CP method after pulling along the *c*-axis direction: (a) bottom face (*ab* orientation) with almost four-fold symmetry; (b) bottom face in the *ab* orientation, note that reflexes are doubled due to the presence of twins; (c) side face (*ac* orientation) with two-fold symmetry.

symmetry group, orientation (the angle between the X-ray beam, the crystallographic plane and the distance between the crystal and the film) as well as by the surface morphology (twins, crack, etc.). On the LBXRD picture spots from one reflecting plane zone belong to a hyperbola. In a particular case the hyperbola transforms into a straight line going through the center of the picture. Therefore, visually the *ab*-oriented {001} surface gives a typical "four-fold" symmetric picture (strictly speaking this is not completely true for an orthorhombic crystal with $a \neq b$) while the *ac* {010} and *bc*{100} surfaces demonstrate 'two-fold" pictures. If twins are present, characteristic doubling of the reflections occurs as shown in fig. 30.

Namikawa et al. (1996c) investigated the crystallinity of single crystals grown by the SRL–CP method from MgO single crystals with in-plane aligned Y123 thin films deposited by RF thermal plasma evaporation. This type of film is considered to be one of the best seeds and is commonly used. Figure 31 shows X-ray rocking curves for the 005 line of the as-grown bottom face of the crystals. The size of the crystal was $13.0 \times 15.5\,mm^2$ in the *ab*-plane, and 10 mm in the *c*-direction. There are several peaks,

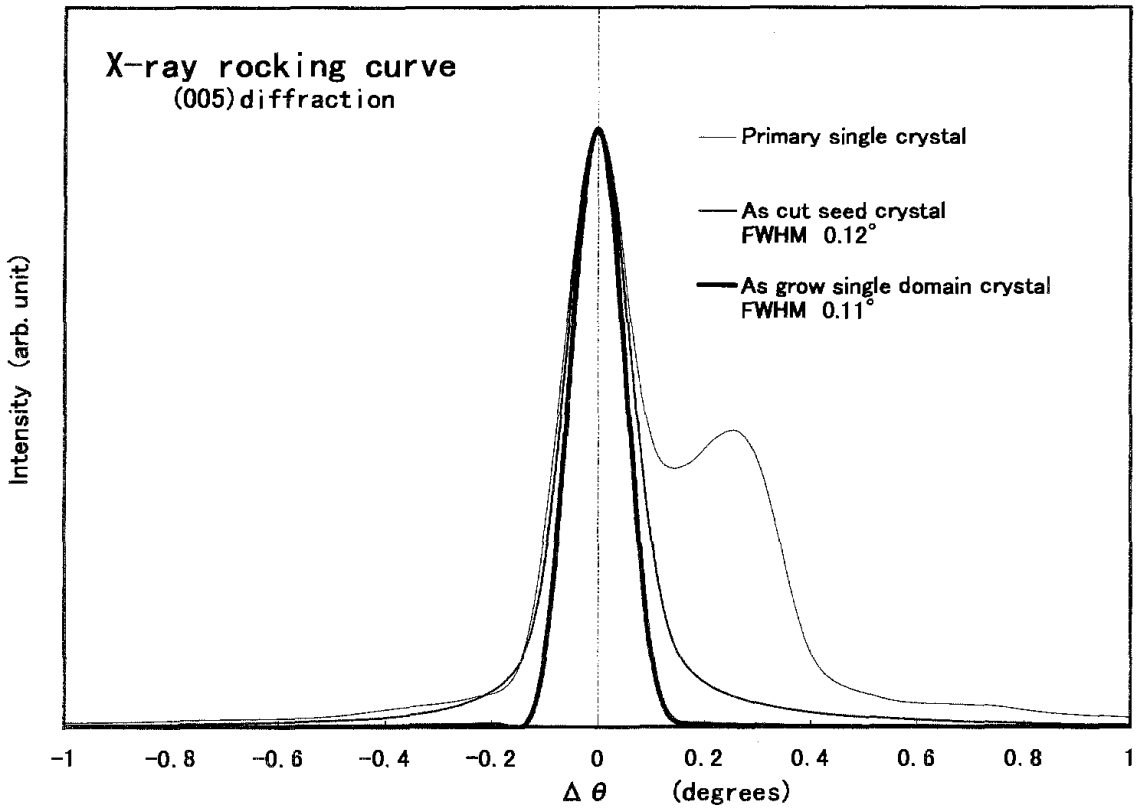

Fig. 31. X-ray rocking curves (005 reflection) of a Y123 crystal, produced by the SRL–CP method, demonstrating improvement of crystallinity in the necking process; the thin line profile corresponds to a bottom facet of an initially grown seed crystal; the profile with an intermediate line thickness is given for the as-cut (necked) single crystal used to grow the final crystal; the thickest profile characterizes the final crystal with the smallest FWHM (Namikawa et al. 1996c, Kusao et al. 1997).

separated by a few tenths of degrees. This indicates some low-angle subgrain boundaries inclined by 0.1–0.8 degrees relative to each other in the area irradiated by the incident X-ray beam. At the same time in the as-grown surface no grain boundary could be observed by optical microscopy among the macrosteps, small hillocks and wavy patterns due to the rotation of the crystal during growth. The X-ray topograph shown in fig. 32 is a superimposed image of the lattice distortion of the crystal, the surface morphology and two macrocracks in the crystal induced by the thermal shock during the cooling after crystal growth. Most of the inhomogeneities of the X-ray topograph are caused by the low-angle subgrain boundaries. The MgO single crystal seed has been indicated as the origin of these subgrains which are extended along the growth direction. It is common for the seed film to consist of small grains with a size of about 0.1–1.0 μm.

Then, in order to obtain a Y123 single crystal with high crystallinity, Y123 seed crystals have been prepared by cutting the seed from the best possible crystalline part of the Y123 single crystal. Figure 31 shows an X-ray rocking curve of a crystal grown from the new, Y123, seed after slicing and polishing. It is a fine single peak. The FWHM of the peak was about 0.11 degrees, slightly wider than that of the single subgrain. This

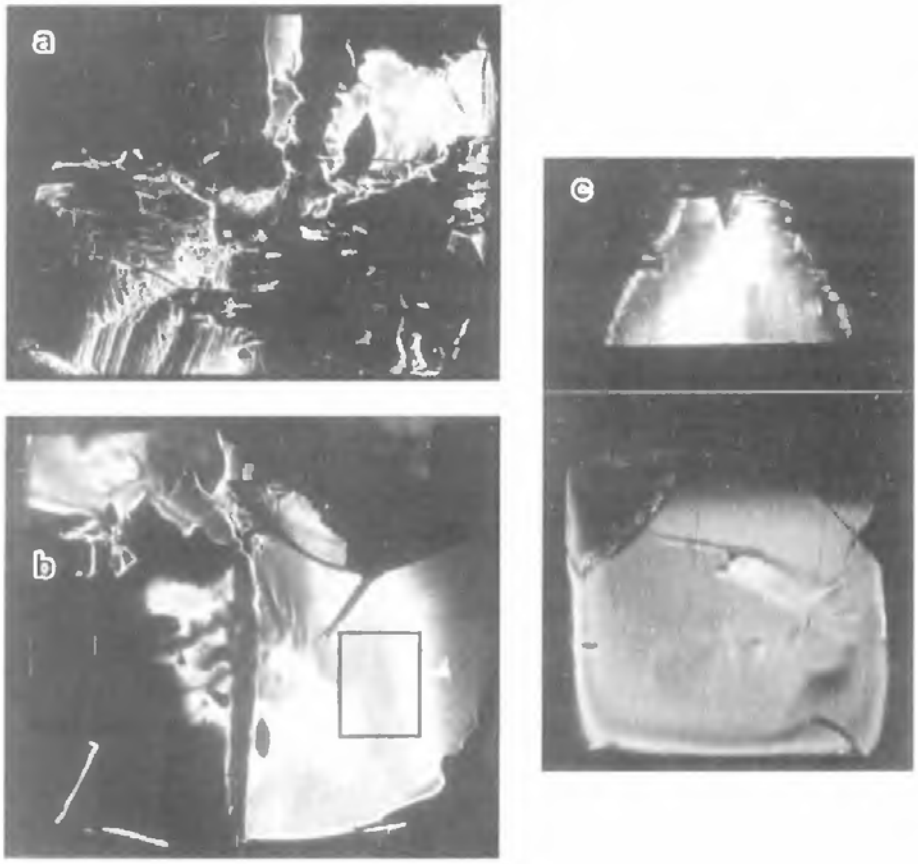

Fig. 32. X-ray topographs for the necking process (Namikawa et al. 1996c): (a) initial crystal; (b) as-grown Y123 crystal used as a seed (the part marked by a rectangle); (c) vertical and horizontal sections of the final crystal with much better crystallinity achieved.

result indicated that the crystal might consist of a single domain. In fact, no marked subgrain boundaries were found by X-ray topography in the entire area of the horizontal section of this crystal. These results demonstrate that perfect Y123 single crystals could be obtained by using Y123 single-crystal seeds consisting of a pure single domain. For a bulk Y-Pr123 crystal grown by the SRL–CP method (Yamada et al. 1996b, Kuroda et al. 2000) a misorientation angle within the crystal body less than 0.2° was confirmed by neutron diffraction.

Another technique for crystallinity analysis is the measurement of pole figures. It is widely applied for thin films, LPE films, melt-processed polycrystalline samples with a noticeable texture (Goyal et al. 1993). In fig. 33, a good crystallinity of the Y123 LPE film is evidently obtained due to a specific growth mechanism, mentioned above (sect. 5.4), despite the large misfit between the film and the MgO substrate. Differential interference contrast (DIM or Nomarski) microscopy can be successfully applied to observe misorientation on flat ("mirror-like") surfaces (Klemenz and Scheel 1993).

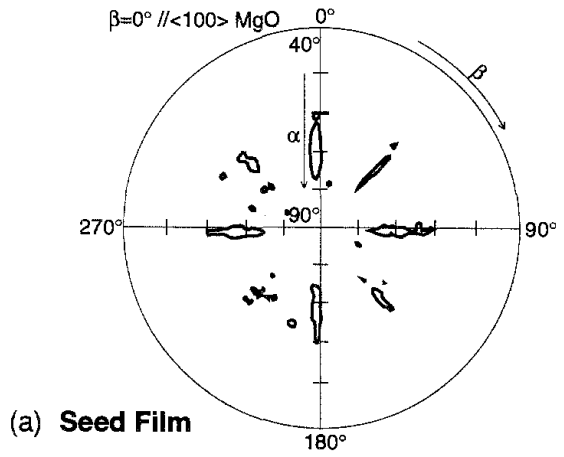

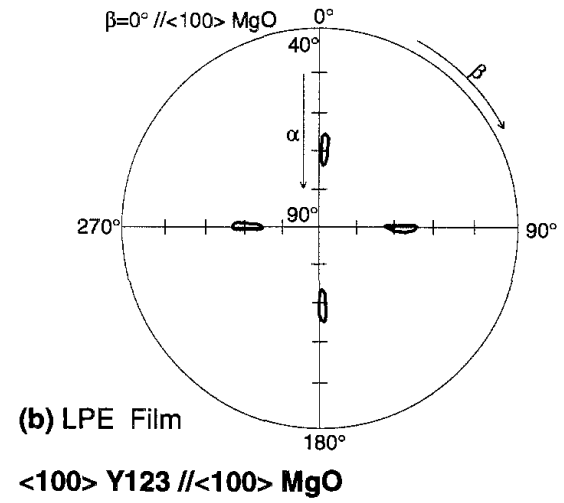

Fig. 33. X-ray pole figures of the (108) peak of (a) a seed film prepared by RF plasma evaporation on a MgO single-crystal substrate and (b) a Y123 LPE-grown film. Note that several types of grain orientation exist for the seed film, however the obtained LPE film demonstrates a good crystallinity because formation of in-plane aligned island crystallites on the {100} MgO surface is followed by their coalescence and a spiral growth development over the whole surface (Ishida et al. 1997).

6.5. *Microcracks and dislocations. XRD line-broadening analysis*

If a stress field exists in a crystal, it converts a part of the total strain, ε, to plastic strain, depending on the yield stress of the material, σ_y. The amount of plastic strain which results in dislocation appearing in the material can be represented by the expression $\varepsilon_p = (\sigma - \sigma_y)/E$, where E is the Young modulus, and the number n_D of dislocations per square unit can be estimated as $n_D \approx \varepsilon_p/b = 2(\sigma - \sigma_y)/(E \times b)$, where b is the Burgers vector of the dislocation. A number of different mechanisms can be suggested for the introduction of dislocations into crystals, for example, thermal, mechanical stresses, vacancy and interstitial supersaturation and constitutional stresses (Tiller 1991b, see also Ullrich et al. 1998). Changes in dislocation density, their multiplication, annihilation and interaction can lead to formation of a dislocation network and boundaries in the crystal, affect the crystal growth mechanism, and can lead to a track of antisites (Nd/Ba in Nd123, Sandiumenge et al. 1998b) or copper concentration oscillations (Vargas et al. 1997).

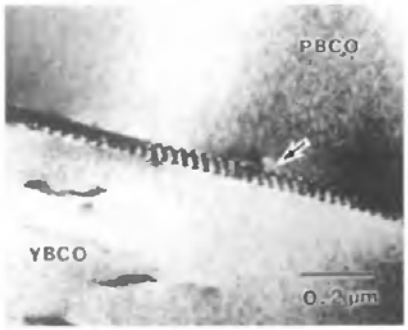

Fig. 34. Misfit dislocations near the Y123–Pr123 interface of two single crystals (the Y123 crystal was used as a seed for the Pr123 crystal growth by the SRL–CP method).

Dislocations in the seed crystal may intersect the growth interface and extend into the growing bulk crystal. The presence of inclusions (Yamaguchi et al. 1990b), overgrowth of floating particles, or other intruders from different parts of the growing interface, may lead to complex dislocations with a large screw component. Due to different effective sizes of dopants in comparison with host atoms, all sources of microsegregation may give rise to constitutional strains associated with an abrupt concentration fluctuation, and then a new dislocation may appear. Dislocation loops also can be formed in the cooling process (Diko 1998b) or due to thermal gradients.

In all these cases, it is important to analyze the dislocation densities, which can be performed by several methods. The most common is X-ray line-broadening analysis, allowing one to estimate the strain level and dislocation densities when precisely inspecting the shape, width and asymmetry of selected reflections or their families from the XRD pattern. Unfortunately, this analysis is strongly dependent on the assumed models and the software used for this purpose. However, physically the line-broadening analysis is based on the clear fact that any distortion in the ideal lattice results in local (or collective) changes in the "XRD-reflecting" plane distances, therefore it is directly reflected in broadening the corresponding XRD lines. It is very safe to combine this integral method with the local TEM observation of the actual microstructure to distinguish the real defects that distort the lattice. In fig. 34 a dislocation network near a boundary between Pr123 and Y123 single crystals is shown which appeared due to the lattice misfit on the interface of two solids and, probably, slightly different thermal expansion coefficients (Tagami et al. 1998).

6.6. *Spirals and growth steps. AFM*

The fact that this chapter so often mentions growth steps and spiral formations on the solid–liquid interface is naturally explained by their primary importance in the understanding of HTSC crystal growth phenomena. Subsequently, in this section a few typical examples of growth spirals observed in R123 single crystals are presented. The reader may recall the growth spiral variety and interacting spiral pattern formation in sect. 2.3.4, the terrace–ledge–kink crystal growth model in sect. 2.3.3, the experimental achievements in the preparation of quasi-atomic flat surfaces in LPE treated in sect. 5.4, etc.

In figs 35a,b (overleaf) single growth spirals with a small height are revealed by atomic force microscopy (AFM). This unique method allows one to visualize the surface up to the resolution of atomic arrays (Lozanne 1999). It is evident that the spiral in the *ab*-plane of the Y123 crystal is approximately square-shaped (fig. 35a) or rounded at higher supersaturation (fig. 35b). The step height corresponds to the unit cell length along the *c*-direction. This result indicates that continuous spiral growth could be achieved in the SRL–CP process. Bunching of spirals is demonstrated in figs. 35c,d. The spiral in fig. 35c is composed of 3 steps while in fig. 35d a macrospiral is presented. The large step height (about 200 nm) makes it possible to observe the spiral even by optical microscopy. Another interesting example is shown in figs. 35e,f. An island crystallite (sect. 5.4) is presented which means the beginning of a crystalline layer formation on a substrate in the LPE experiment.

6.7. *Chemical macro-uniformity, flux and foreign particle inclusions. EPMA and ICP AES*

Chemical composition analysis as well as the confirmation of chemical uniformity and the search for striation inhomogeneities (sect. 2.3.5) are very important tasks of any single crystal characterization. Macroscopically this provides evidence that a desired chemical compound has been obtained, in other words, it gives a set of chemical elements from the Periodic Table which build up the lattice of the crystal.

Inductively coupled plasma atomic emission spectrometry (ICP AES) is a suitable method for determining crystal composition. It has replaced a routine of chemical titration methods (except maybe iodometric titration which is still widely used in the determination of the oxygen content in HTSC). This method is precise enough and it demands only a small amount of substance to be analyzed. Standard solutions as well as an automated measuring procedure are also available. Applications of this method to the analysis of HTSC crystal composition can easily be found in the literature (Yao and Shiohara 1997, Kuroda et al. 1997a,b, Tagami and Shiohara 1997), although some restrictions are evident: the ICP technique is destructive and non-local, and it is very sensitive to the selection of the sample to be analyzed since even small flux inclusions in the crystal can affect the results drastically.

Compared to ICP, scanning electron microscopy (SEM) can easily establish whether flux or foreign particle inclusions are present in the crystal. Kanamori et al. (1994) demonstrated that Y123 single crystals fabricated using MgO crucibles contain fine precipitates of MgO with a rectangular shape (fig. 36a) because the solubility of MgO in the solid phase is smaller than that in the melt. The existence of MgO impurities can affect T_c characteristics due to the Mg substitution for the R123 structure. Moreover, MgO inclusions can result in worse crystallinity of the R123 crystals, although it cannot be excluded that fine particles could cause better pinning properties indirectly. Figure 36b shows flux inclusions in the matrix of Nd123ss crystals grown by the pulling method. It is evident that in this secondary-electron image (SEI) the copper-rich dendrite droplets

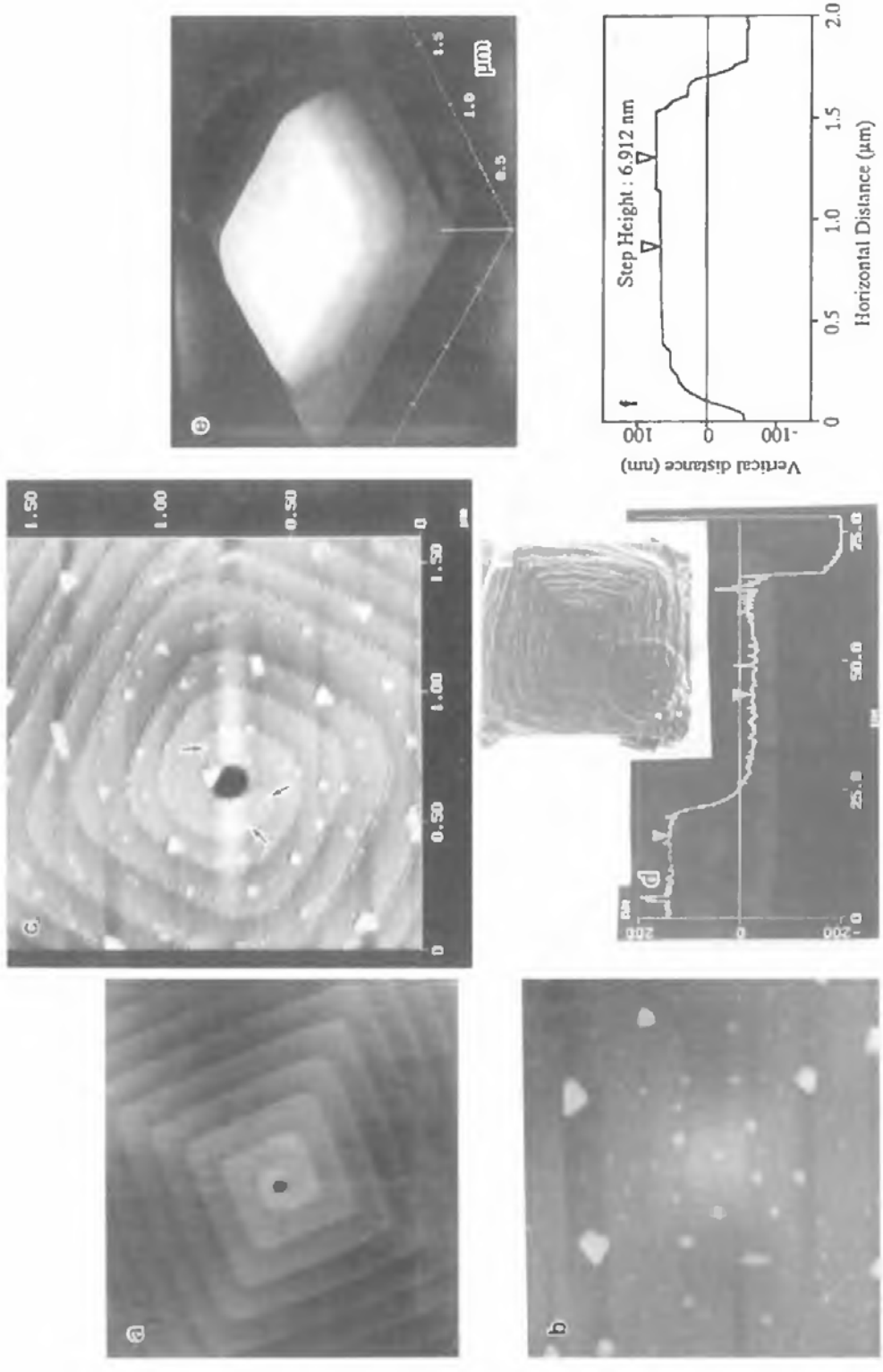

Fig. 35. Microscopic observation of crystal growth morphology by AFM: (a) polygonized spiral on the bottom facet of a crystal grown by the SRL–CP method; (b) rounded spiral development with many equidistant turns; (c) a spiral composed of three steps; (d) a macrospiral with about 200 nm macrostep height; (e) island crystallite formation during initial steps of a single-crystalline layer growth on a MgO substrate by LPE; (f) height profile of the crystallite (e).

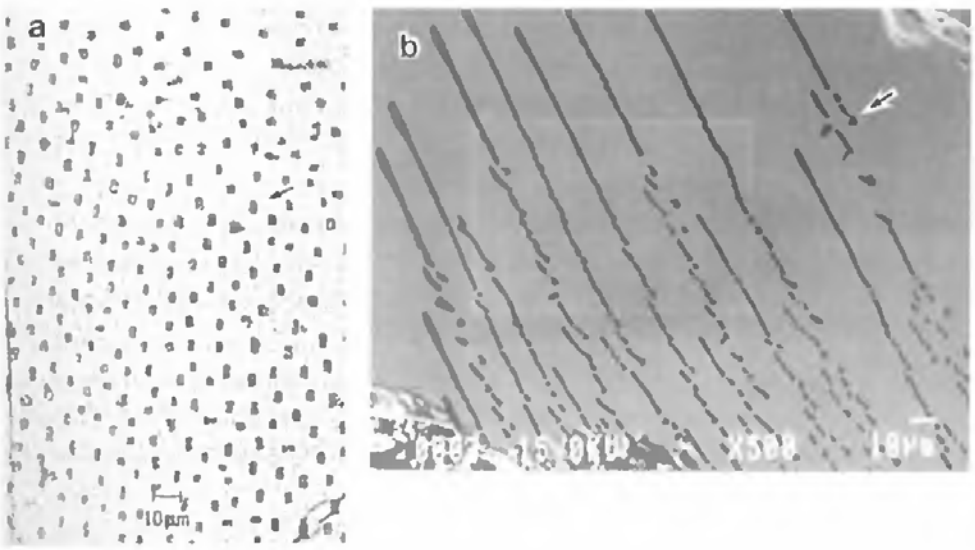

Fig. 36. Growth inclusions observed occasionally in crystals produced by the pulling technique: (a) square-shaped microcrystals of MgO in a Y123 crystal obtained using MgO crucibles; (b) flux inclusions (dark stripes) in a $Nd_{1+x}Ba_{2-x}Cu_3O_z$ crystal along the *c*-axis pulling direction.

("fingers") of the flux appear in a different shade than the Nd and Ba-rich matrix because of the composition difference.

The most popular and powerful method of local and almost nondestructive "chemical" analysis is electron probe microanalysis (EPMA), based on the excitation of characteristic X-rays by a finely focused electron beam. Actually this method combines several techniques [energy dispersive X-ray (EDX), wave dispersive X-ray (WDX) analysis etc.]. In any case the best results can be achieved by using carefully prepared preanalyzed standard samples (for example, single crystals with a defined composition).

Figure 37 demonstrates the interface between Y123 and Pr123 single crystals obtained by the pulling technique (Tagami et al. 1994, 1998). In the first case Pr123 (fig. 37a,b) was a seed for Y123 crystal growth. It is evident that the interface has a mushy structure and a thick diffusion layer within 0.75 mm (fig. 37b). The white grains in fig. 37a are $Y_{1-x}Pr_xBa_2Cu_3O_z$ phase and the black regions are the solidified melt. The Pr concentration increases inversely with the Y content in the layer. In the second case (fig. 37c), growth of Pr123 has been performed on a Y123 single-crystal seed. In this case good crystallinity and a sharp interface within the resolution of EPMA is observed. The difference between these two examples is that the decomposition temperature of Pr123 is lower than that of Y123 (sect. 3.1.3), therefore in the first case the mushy interface might be caused by beginning Pr123 decomposition during contact with the Y-supersaturated nutrient liquid, while fabrication of such a heterostructure with a sharp interface is possible in the second, particularly interesting case.

Figure 38 shows EPMA data for highly uniform $Nd_{1+x}Ba_{2-x}Cu_3O_z$ solid-solution crystals grown at a constant temperature by the pulling technique, without striations. The composition profile is not matched with the as-grown twin structure found in this crystal (sect. 6.3) i.e. one can ascribe the twins to the structure peculiarities rather than to the

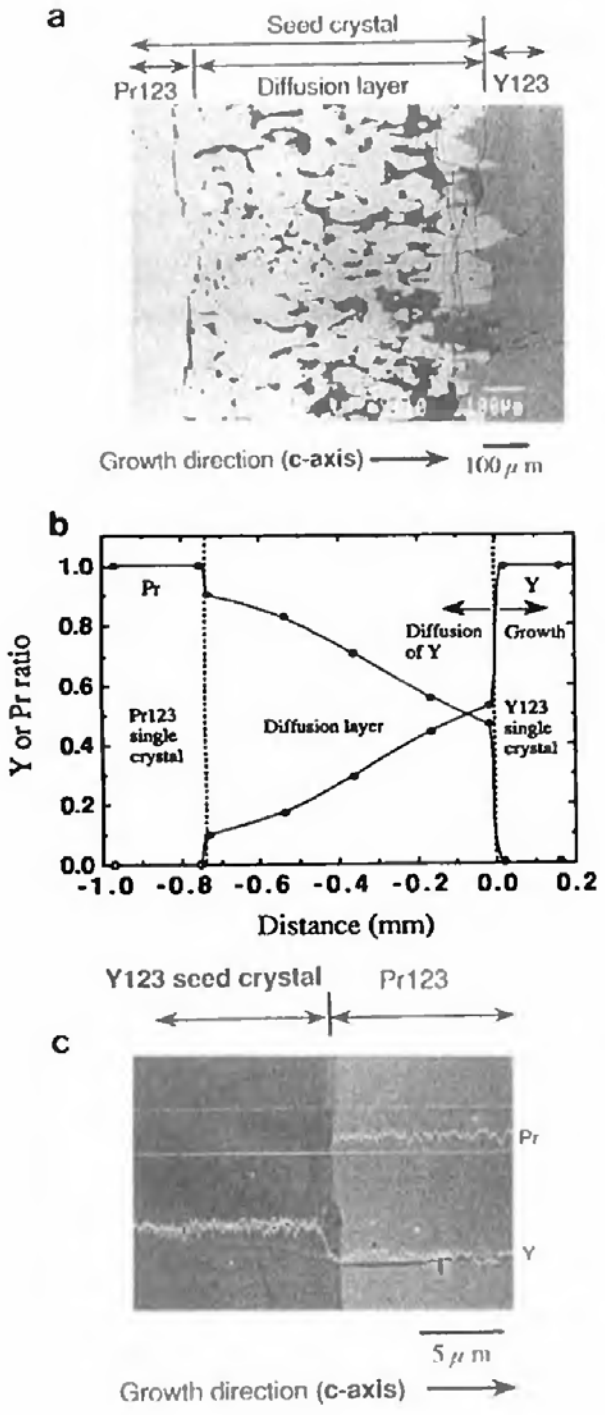

Fig. 37. Y123–Pr123 interfaces under different growth conditions along the *c*-axis pulling direction (Tagami et al. 1994): (a) Pr123 crystal as a seed for growing a Y123 crystal; mushy interface is formed due to the lower melting temperature of Pr123 compared to the growth temperature of Y123 phase. (b) Compositional profile along the Pr123–Y123 interface in the case that a Pr123 single crystal is used as a seed. (c) Application of Y123 as a seed to grow Pr123 crystal: a sharp interface is formed.

influence of impurities. A quantitative line-analysis technique has been applied in this case with a small successive step of 4 μm which is close to the maximum spatial resolution typical for regular EPMA (see next sect. 6.8).

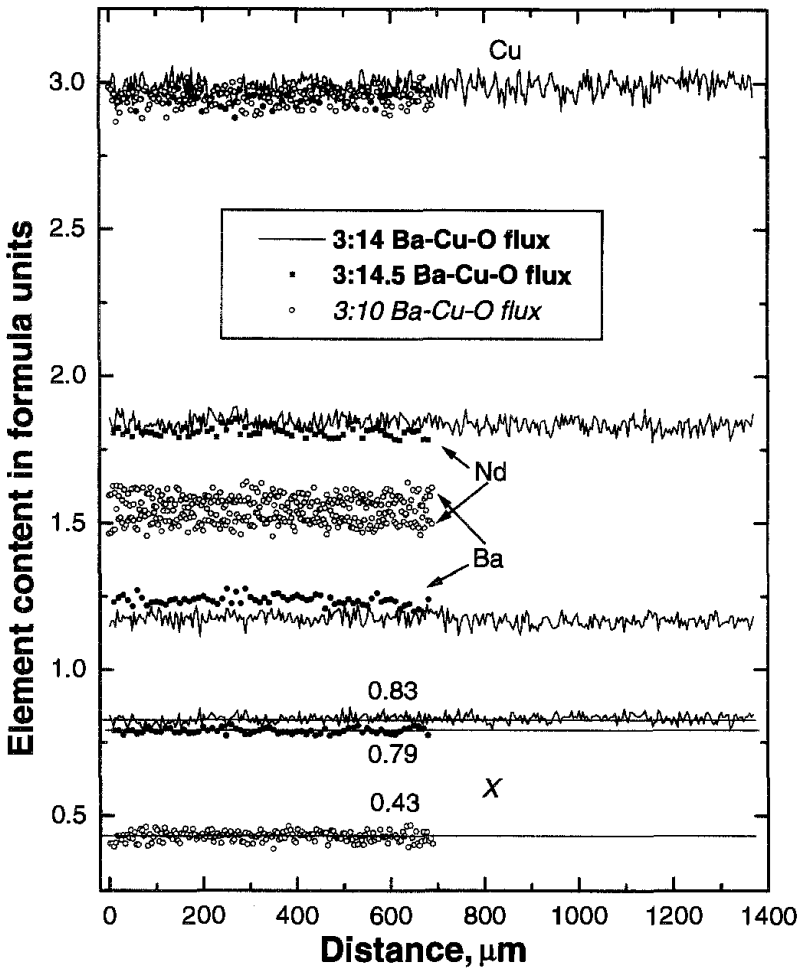

Fig. 38. Absence of striations and remarkable compositional fluctuations in $Nd_{1+x}Ba_{2-x}Cu_3O_z$ crystals ($x = 0.43$, 0.79, 0.83) grown by the TSSG method from copper-rich Ba–Cu–O fluxes (3:10, 3:14.5 and 3:14 Ba:Cu ratios respectively). EPMA quantitative analysis is applied with a small successive 4 μm step (Goodilin et al. 1998b).

6.8. *Nanoscale composition fluctuations. TEM and micro-EDX*

As discussed earlier, it is necessary to know not only the types of chemical elements composing a crystal and how uniform on the micrometer level the crystal is after its growth. For HTSC it is significant to find out whether spatial nano-scale composition fluctuations are present or not. M. Nakamura et al. (1996c) have succeeded in preparing two types of Nd123 single crystals with low and high J_c values, respectively, by simply varying the post-annealing treatment at fixed conditions of the oxygenation procedure itself (see the discussion in sect. 7.4.3.4). The TEM image of the Nd123 crystal with high J_c ($\langle 001 \rangle$ direction) exhibits a modulated structure (tweed-like image, fig. 39a). The electron diffraction patterns show that this Nd123 crystal has an orthorhombic structure, and high-order reflection spots are extended along the $\langle 110 \rangle$ direction (M. Nakamura et al. 1996d). On the contrary, the low-J_c Nd123 crystal was found to be much more

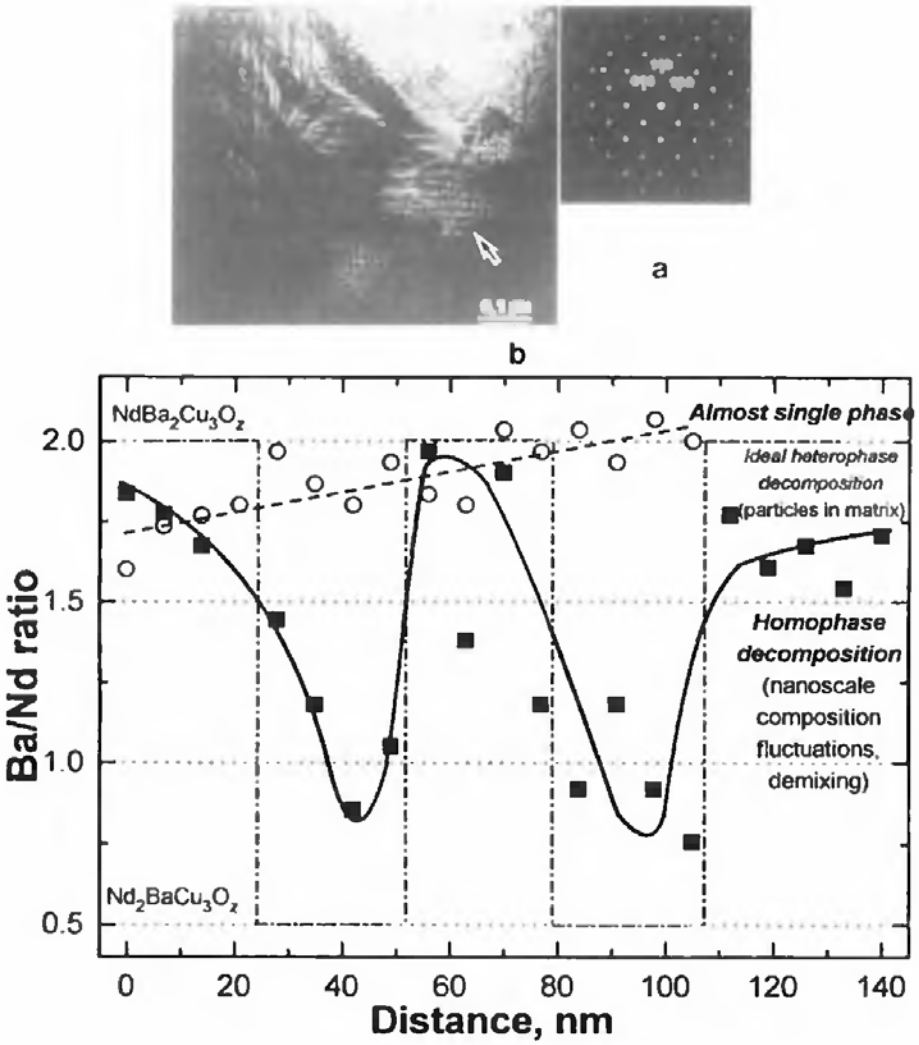

Fig. 39. Micro-EDX analysis of Nd123 crystals grown by the modified TSSG method in low-p_{O_2} atmosphere from contamination-free Nd_2O_3 crucibles with different post-growth heat treatments. In all the cases final oxygenation at 340°C in oxygen was applied. The picture demonstrates (a) tweed structure formation and (b) nanoscale composition fluctuations in crystals with the anomalous peak effect on a magnetization curve. Note that the composition profile for heavy atoms (Ba/Nd ratio) is similar to wave-like fluctuations typical for demixing behavior or a spinodal homophase decomposition rather than for a heterophase decomposition with the formation of a boundary between the crystal matrix and the precipitated phase (M. Nakamura et al. 1996c).

perfect with no modulated structure. Since the tweed-like structure is quite possibly due to inhomogeneous oxygen redistribution, especially around the tetra–orthorhombic transitions (sect. 6.3), EDX analysis with electron beam size of about 1 nm was performed by the authors to clarify the phenomenon. The analysis revealed (fig. 39b) that in the first, high-J_c, crystal the Ba/Nd ratio fluctuated between 2.0 and 0.7 with a wavelength of a few tens of nanometers while the second, low-J_c, crystal was found to be almost homogenous in composition with a Ba/Nd ratio of about 2.0. This result indicates that in the first case

the superconducting $NdBa_2Cu_3O_{7-\delta}$ and nonsuperconducting $Nd_{1.8}Ba_{1.2}Cu_3O_z$ phases might mingle with each other (Hirayama et al. 1997).

Using the TEM dark-field diffraction contrast Egi et al. (1996) have shown that white and black, finely dispersed spots can be observed for another high-J_c Nd123 single crystal, however, the same has not been observed for a Y123 crystal which was selected as a reference state. The size of the regions ("spots") with different contrasts was found to be about several tens of nanometers as in the previous investigation. The scattering factors of Nd^{3+} and Ba^{2+} are similar, therefore it is not plausible to consider this as the direct reason for such a contrast. However, in this system heterovalent substitution and oxygen redistribution are very much coupled phenomena (sect. 3.1.2.5). Accordingly, the phenomenon might be ascribed to a slight lattice distortion due to the substitution of Nd^{3+} for Ba^{2+} since the different valence of the cations results in different oxygen content in a local area. The Ba/Nd ratio in the large area of the sample was evaluated to have a value 1.88 by nano-scale EDX analysis, although this ratio in smaller regions ("spots") fluctuated from 1.2 to 1.8. Dimesso et al. (1997), using the dark-field TEM image, also observed strain features related to the coexistence of different $Nd_{1+x}Ba_{2-x}Cu_3O_z$ domains in melt-solified samples. Thus, on the nanoscale level the possibility is believed to exist of reproducible compositional fluctuations in Nd123 single crystals.

Chikumoto et al. (1997b,c) observed that the above-mentioned contrast and the spatial variation of the Ba/Nd atomic ratio become almost negligible after annealing at high temperatures (1050°C). M. Nakamura et al. (1996d) demonstrated that even 900°C is enough to rule out the inhomogeneity for longer annealing times. In principle, these TEM observations prove that a solid-state reaction such as spinodal decomposition might be responsible for the phase separation leading to the nano-scale microstructure, however there are some discrepancies in the explanation of this phenomenon (see the discussion in sect. 7.4.3.4). It should be noted also that the same idea has been employed to explain oxygen-content microfluctuations observable often even in the cation-stoichiometric Y123 superconductor. It was found by a systematic TEM study that microscopic values of $\Delta a/a$ varied for the Y123 superconductor from zero to more than twice the macroscopic value over typical spatial dimensions 1000 Å (Sarikaya and Stern 1988). Both single crystals and epitaxial films with high-superconducting properties may frequently contain structural/oxygen inhomogeneities as found by a sophisticated XRD technique (Claus et al. 1992, Qadri et al. 1997). Vargas et al. (1997) observed a regular pattern of oscillatory-increased copper concentration along ⟨001⟩ tilt boundaries in flux-grown Y123 bicrystals, with the wavelength of the observed composition variation being about 75–100 nm. The spacing of the maxima corresponded to the wavelength of a periodic strain field and dislocation arrays on the boundary. However, in the case under question the Nd/Ba heavy atoms demonstrate the demixing behavior followed by oxygen-atom redistribution. Hence, the oxygen sublattice itself or the boundary strain are not the primary reasons for the peak effect, as in the Y123 case. It should also be noted that demixing and related microstructures have been observed for the Bi–Pr–Sr–Ca–Cu–O 2212 superconductor (Hiroi et al. 1998, Crossley et al. 1999) therefore this behavior seems to be common for different classes of HTSCs.

6.9. *Stacking faults and intergrowth. TEM, STM*

It is common enough to observe different growth defects like inserted extra-planes of Cu–O (Domengès et al. 1987), Y and Cu–O (Ourmasd et al. 1987), antiphase boundaries (Van Tendeloo and Amelinckx 1987), etc.; probably, these defects could be the cause of the "copper deficiency" detected in single crystals (Klester 1988, Leonyuk et al. 1994, Odier et al. 1998). Dubs et al. (1996) found by HREM that the crystal lattice of the Y123 superconductor is perfect near the interface between the LPE crystalline layer and the substrate, except for a few stacking faults. However, upon comparing micrographs of different film regions it was concluded that the number of stacking defects increases with increasing distance from the interface. Moreover, several regions of stacking defects exhibited a value of the c-parameter as high as 13.6 Å ($2c = 27.2$ Å, see sect. 5.6). This value most probably corresponded to the c-parameter of the Y124 phase due to incorporation of an additional CuO-plane. Therefore, this structure has to be attributed to the intergrowth defects of the Y123 and Y124 phases.

Ting et al. (1996) reported that elliptical regions with sizes ranging from several to several tens of nanometers were found in the surface of Nd123 crystals by scanning tunnel microscopy (STM). These regions and the matrix were observed to have different conductivities at room temperature. It was suggested that the regions act as field-induced pinning centers.

6.10. *Crystal structure. Four-circle diffractometer, neutron diffraction, Raman spectroscopy*

The elementary cell or lattice is the lowest structural level of a crystal. The lattice is characterized by a space symmetry group, atom positions and thermal displacement parameters of the atoms as well as by the position occupancies. In principle, the lattice is the smallest building block for creating an ideal crystal of any size by simple translations, and it is the lattice that is responsible for the fundamental T_c parameter. Therefore, it is extremely important to perform the structure refinement of a crystal obtained, especially if the crystal represents a solid solution compound or demonstrates unusual properties or has unknown oxygen content or is assumed to form a new structure modification.

Several methods allow one to clarify the crystal structure (F. Izumi and Takayama-Muromachi 1995; see also ch. 188 of this Handbook). For single crystals, the XRD four-circle diffractometer method is important. Since usage of a R123-single crystal or a fragment (usually about 0.05–0.1 mm^3) makes it possible to collect intensities of more than 1000 unique reflections in comparison with only 50–70 visible reflections for powder XRD, the structure refinement becomes reliable and precise although it remains sensitive mostly to the heavy atoms (cations). This method is strongly affected by structural imperfections in the crystals such as twins, therefore the detwinning procedure (sect. 7.4.3.5) should precede the measurement, or special calculation methods have to be applied (for example, see Casalta et al. 1996). Several examples of such experiments are listed in table 7 (Kutami et al. 1996, M. Nakamura et al. 1996c, Jang et al. 1996,

Table 7
Examples of structure refinement by using four-circle single-crystal diffractometer for bulk single crystals grown by crystal pulling[a]

Chemical composition	Atom	Fractional coordinates			B_{eq}
		x/a	y/b	z/c	
Oxygenated, detwinned,	Y	0.5000	0.5000	0.5000	0.33(1)
orthorhombic $YBa_2Cu_3O_{6.84}$	Ba	0.5000	0.5000	0.18407(4)	0.448(5)
Pmmm	Cu(1)	0.0000	0.0000	0.0000	0.39(2)
$a=3.8877(6)$ Å	Cu(2)	0.0000	0.0000	0.35517(8)	0.34(1)
$b=3.8185(6)$ Å	O(1)	0.0000	0.0000	0.1600(6)	0.62(7)
$c=11.6938(8)$ Å	O(2)	0.0000	0.5000	0.0000	0.6(1)
6.349 g/cm^3	O(3)	0.5000	0.0000	0.3790(5)	0.51(6)
$R=4.9\%$, $R_W=5.8\%$	O(4)	0.0000	0.5000	0.3788(5)	0.44(6)
As-grown ($p_{O_2}=0.01$ atm),	Nd	0.5000	0.5000	0.5000	0.309(8)
tetragonal $Nd_{1.01}Ba_{1.97}Cu_3O_y$	Ba	0.5000	0.5000	0.1904(1)	0.713(9)
P4/mmm	Cu(1)	0.0000	0.0000	0.0000	0.82(2)
$a=3.9065(7)$ Å; $b=a$	Cu(2)	0.0000	0.0000	0.3537(2)	0.39(1)
$c=11.823(2)$ Å	O(1)	0.0000	0.0000	0.152(2)	1.1(2)
6.494 g/cm^3	O(2)	0.0000	0.5000	0.0000	1.7(2)
$R=5.1\%$, $R_W=6.1\%$	O(3)	0.0000	0.5000	0.3724(7)	0.46(9)
					Occupancy
Air-grown, tetragonal	Pr(1)	0.5000	0.5000	0.5000	0.971(50)
$Pr_{1.14}Ba_{1.86}Cu_{2.95}Mg_{0.05}O_y$	Pr(2)	0.5000	0.5000	0.18803	0.086
P4/mmm	Ba(1)	0.5000	0.5000	0.18803(2)	0.914(45)
$a=3.907(1)$ Å	Ba(2)	0.5000	0.5000	0.5000	0.029
$b=a$	Cu(1)	0.0000	0.0000	0.0000	0.950(8)
$c=11.768(2)$ Å	Cu(2)	0.0000	0.0000	0.35158(4)	0.994(3)
$R=1.6\%$, $R_W=1.9\%$	Mg(1)	0.0000	0.0000	0.0000	0.050
	Mg(2)	0.0000	0.0000	0.35158(4)	0.006
	O(1)	0.0000	0.0000	0.1540(3)	0.960(24)
	O(2)	0.0000	0.5000	0.0000	0.912(32)
	O(3)	0.0000	0.5000	0.3696(2)	1.00

[a] Classical cation stoichiometric, superconducting $YBa_2Cu_3O_{7-\delta}$ phase in its orthorhombic modification, tetragonal $x\approx 0$ solid solution $Nd_{1+x}Ba_{2-x}Cu_3O_z$ grown under low p_{O_2}, MgO-contaminated insulating $Pr_{1+x}Ba_{2-x}Cu_3O_z$ solid solution.

Tagami and Shiohara 1997). The neutron diffraction permits to refine both cations and the oxygen atoms because of the higher oxygen scattering factor in this method (Cava et al. 1990, Jorgensen et al. 1990, Shaked et al. 1990, Hunter et al. 1991, Christensen et al. 1996). Large and perfect bulk single crystals are preferable, and they can be applied for in situ studies at different temperatures, including analysis of superconductivity properties at low temperatures (Brandstatter et al. 1997). At the same time, Casalta et al. (1996) have

used relatively small 10 mm^3 crystals to investigate the dependence on oxygen content of $YBa_2Cu_3O_{7-\delta}$ structural parameters (see also Krüger et al. 1997). Poulsen et al. (1996) have analyzed precisely, by synchrotron X-ray diffraction, the structural behavior of mm^3-sized single crystals of $YBa_2Cu_3O_{7-\delta}$ with oxygen concentrations close to the metal–insulator transition.

The oxygen content, distribution and related changes of structure and properties are believed to be a specific problem in the case of HTSC as mentioned above and comprehensively discussed by Kaldis (Vol. 31, ch. 195 of this Handbook). An admirable method for the study of the oxygen behavior in R123 as well as other HTSCs is Raman spectroscopy (Limonov et al. 1998, N. Watanabe et al. 1998, Panfilov et al. 1998, Martin et al. 1998, Cooper et al., Vol. 31, ch. 203 of this Handbook). This method is greatly enhanced by employing single crystals because in this case polarization dependencies of line intensities and frequency (or energy of vibrations, Raman shift) in the spectra allow one to assign them a certain symmetry, i.e. to predict coordinations of different atoms (Thomsen 1991). For a known system, the line intensities in Raman spectra as well as the diffraction methods can allow one to estimate the oxygen content in a single crystal. Electron energy loss spectroscopy (EELS) and X-ray adsorption near-edge spectroscopy (XANES) of the oxygen K–edge are also very useful for studying the oxygen concentration in $RBa_2Cu_3O_{7-\delta}$ (Zhu 1995, Merz et al. 1996). Cu K-edge EXAFS refinement was applied to the study of oxygen configurations and their relationship with a peak effect for $YBa_2Cu_3O_z$ single crystals (Oka et al. 1999a). Inelastic neutron scattering on crystals is helpful (Lister et al. 2000) for measurements of magnetic excitations. Emission Mössbauer spectroscopy on crystals allows to probe their local structure (Andrianov et al. 1990).

6.11. *Superstructure. HREM, SAED*

The term "superstructure" originates from the existence of additional order parameters resulting in enlargement of the basic unit cell. Usually introduction of the superstructure is necessary to describe more precisely the lattice of some phases exhibiting additional weak reflections in the XRD patterns or electron diffraction patterns etc. It is well known that the so-called ortho-II Y123 phase (oxygen content about $O_{6.5}$) is considered to be "superstructural" due to ordering of oxygen and vacancies in a different way from both the tetragonal and the orthorhombic type I (O_7) phases (Cava et al. 1990, Jorgensen et al. 1990, Shaked et al. 1990, de Fontaine et al. 1990, Casalta et al. 1996). Recently, it has been demonstrated that the Nd213 phase displays a superstructure (sect. 3.1.2.3). This can be shown by the selected area electron diffraction (SAED) pattern of the $Nd_{1.85}Ba_{1.15}Cu_3O_z$ crystal where the presence of additional reflexes along the [100]* zone is obvious. This is evidence for the face-centered type of the supercell (B mmm) consisting of four primitive Nd123-like cells due to the doubling of the a- and the c-parameters for this as-grown crystal: $a = 2 \times 3.884$ Å, $b = 3.864$ Å, $c = 2 \times 11.585$ Å. The high-resolution electron micrograph of this structure is also depicted in fig. 40. The brightest atomic rows in the TEM picture correspond to the primitive cell edges along the c-axis, while the intensity of almost each $h + l \neq 2n$ ($n = 1, 2\ldots$) spot decreases (an extinction rule for

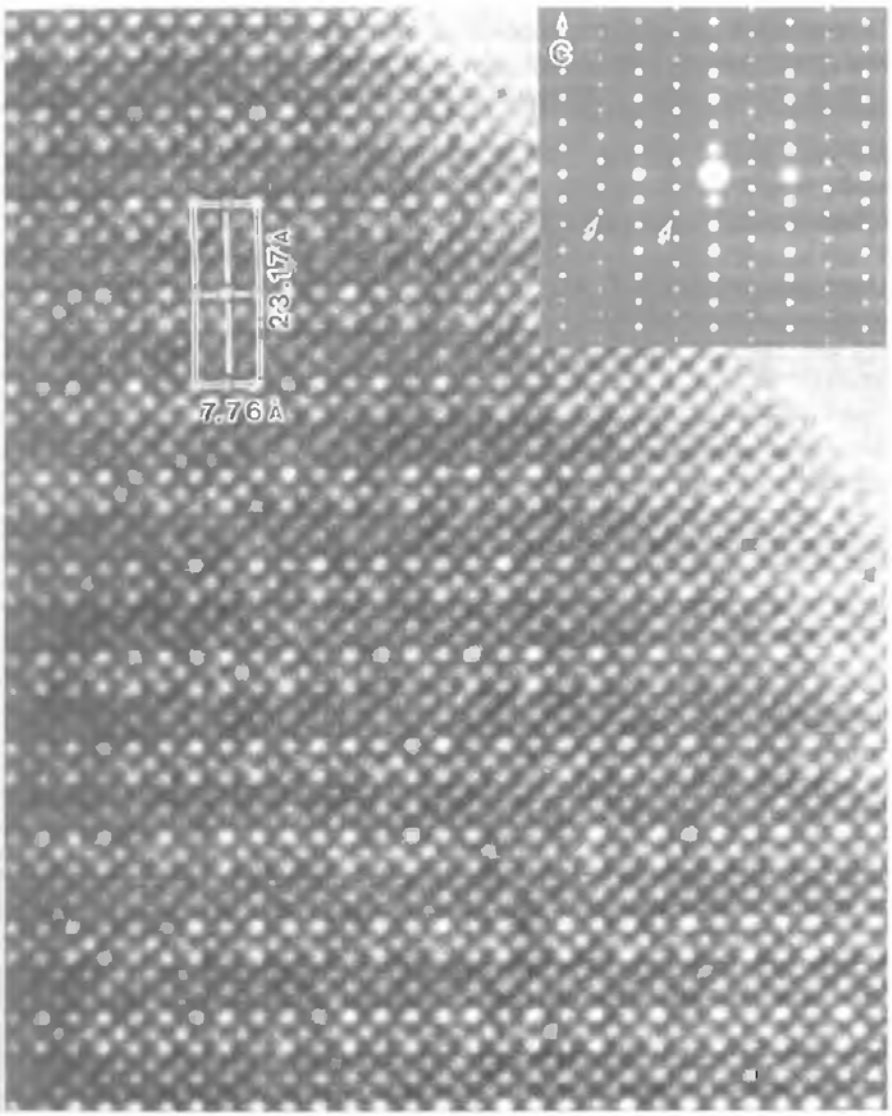

Fig. 40. HREM of the [100]* zone of the as-grown $Nd_{1.85}Ba_{1.15}Cu_3O_z$ crystal exhibiting a superstructure and the basic primitive subcell enlargement (*a*- and *c*-axis doubling) as schematically indicated. ED pattern on the inset reveals additional reflexes corresponding clearly to the superstructure and the Bmmm type of superlattice. The lattice was found to be orthorhombic (Goodilin et al. 1998b).

this type of centering). The HREM and ED methods are significantly important for an extended analysis of the R123 and R123ss structures. For example, in $Nd_{1.85}Ba_{1.15}Cu_3O_z$ it reveals ordering of oxygen or/and heavy atoms in the structure, which explains why Nd213 is orthorhombic even at high temperatures, as already described.

6.12. *Anisotropic physical properties. Resistivity, magnetization, T_c, J_c, vortex lattice visualization*

The superconducting transition temperature and other superconducting characteristics of a crystal can be determined in different ways, mainly by measuring resistivity

and magnetization curves (Weber, Vol. 31, ch. 196 of this Handbook). Both of these methods prove the anisotropic nature of the R123 superconductors. As an example, fig. 41a presents resistivity curves for a Y123 crystal grown by the SRL–CP technique. The sample cut from the as-grown crystal was post-annealed at 400°C in an oxygen atmosphere for two months. Since the sample had a sufficient length along the *c*-axis, it permitted resistivity measurements along the *c*-axis by the four-probe method. The temperature dependence is linear from room temperature down to $T_c \approx 92$ K for both in-plane (ρ_{ab}) and out-of-plane (ρ_c) resistivities. From this experiment, ρ_c is larger than ρ_{ab} by a factor of about 20 (Shiohara and Endo 1997, see also Kovacik et al. 1991, Nevriva et al. 1991). Anisotropy within the *ab*-plane was measured by Kim et al. (1996).

After V.K. Vlasko-Vlasov and co-workers (Indenbom et al. 1990), the magneto-optical technique or visualization of magnetic flux penetration, for example, by iron-garnet films with in-plane magnetization, has become a powerful method to determine the physical picture of this phenomenon in single crystals. Using a high-resolution magneto-optical technique, it was found that up to temperatures close to T_c twin boundaries in Y123 single crystals are effective barriers for flux motion transverse to the boundaries. For flux motion parallel to the boundary the characteristic "flame"-shaped flux patterns indicative of weak link behavior of the boundary were observed. The magnetic flux dynamics of an Nd123 superconductor (Zamboni et al. 1997) demonstrated that while the flux motion is isotropic for an applied magnetic film parallel to the *c*-axis of the sample, anisotropic penetration and expulsion of the flux lines can be directly observed for the perpendicular orientation. In the configuration mentioned before, the flux lines were found to move in and out of the sample predominantly parallel to the *ab*-plane. The microcracks along the basal plane were found to provide a channel for easy flux motion. At the same time, the data obtained are well-consistent with those estimated when interpreting the magnetization measurements within the frame of the extended Bean model (Porcar et al. 1998).

The method of resistivity measurement remains applicable in the determination of electric characteristics even if the crystal has no superconducting properties (tetragonal oxygen-poor Y123 phase, Pr123 phase, Nd213 phase). As an example, fig. 41b presents the resistivity behavior of single crystals of the $Pr_{1+x}Ba_{2-x}Cu_3O_z$ solid solution with different x values obtained by the modified TSSG method (Tagami and Shiohara 1997). It is evident that this material becomes a better insulator with increasing x value. The same tendency (fig. 41c) is observed for the $Nd_{1+x}Ba_{2-x}Cu_3O_z$ solid solution (Goodilin et al. 1997a). The relative permittivity of the $Nd_{1.85}Ba_{1.15}Cu_3O_z$ crystal varied from $\varepsilon_r \approx 1700$ (287 K, 0 kHz) to $\varepsilon_r \approx 60$ (80 K, 0 kHz) and $\varepsilon_r \approx 20$ (80 K, 100 kHz).

Even using an ordinary electric balance, Chan et al. (1994) found an essential anisotropy of magnetic levitation force acting on a superconductive Y123 single crystal. It will be noted also in sect. 7.4.3.4 that anisotropic pinning properties might exist in Nd123 single crystals. Pronounced anisotropy in oxygen diffusion will be discussed in sect. 7.4.3. Thermal conductivity anisotropy was investigated, for example, by Matsukawa et al. (1996). These are only a few examples of the anisotropic properties of single crystals.

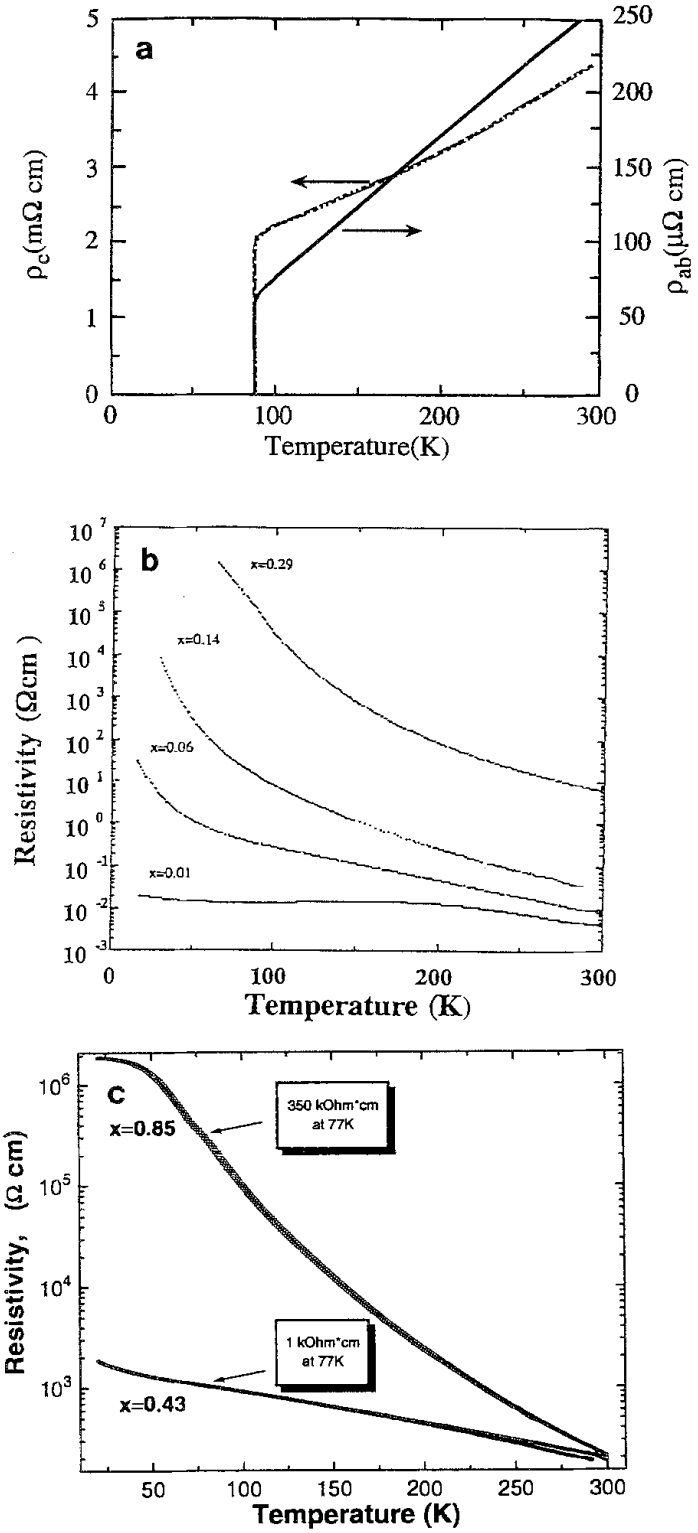

Fig. 41. Resistivity curves of R123 crystals: (a) essential anisotropy of the in-plane and out-of-plane resistivity for completely oxygenated bulk Y123 crystals (Shiohara and Endo 1997); (b, c) non-metallic behavior of the $R_{1+x}Ba_{2-x}Cu_3O_z$ solid solution crystals (b, R = Pr; c, R = Nd).

7. Practical ways of crystal perfection, yield and size improvement

7.1. *Crucible wetting and melt contamination control*

Perhaps, the crucible is the first important part to be considered for the growth of large and perfect HTSC single crystals, which is the only way to initiate wide commercial application. The crucible material should not react with the melt and the crystal, it should have high melting point, thermal stability and hardness, and small wall creep of the molten charge material. Partially the problem of the appropriate choice of a crucible has been discussed in sect. 5.1 with respect to the flux-growth method. Krauns et al. (1994b) investigated the wetting between prospective crucible materials and the Ba–Cu–O melt. It was confirmed that YSZ, $LaAlO_3$, $SrTiO_3$ materials react with the melt and can be wetted well by the melt, leading to melt creep on the crucible walls. In the case of MgO crystals no wetting or reactive layer has been observed, although over time an increasing amount of MgO can be dissolved, up to its saturation concentration of about 0.4–0.5 at%. However, the melt completely permeates samples with an apparent density of up to 85%. The permeated depth becomes very thin starting from 95% density. It was found also that Y_2O_3 is a better barrier to the melt at lower densities but the surface wetting occurs at a slightly faster rate compared to MgO. To date, the R_2O_3 contamination-free crucibles have demonstrated good applicability for crystal growth, at least for a limited time of contact with the melt. The content of inorganic binding substances (TiO_2 etc.) used for sintering is small in these crucibles or completely absent (Nd_2O_3). Recently, the $BaZrO_3$ phase has been successfully tested as a pure material for the crystal growth of cuprate materials (sect. 5.1). It is noted that the high chemical purity of crystals thus produced may have a relationship with their better crystallinity (Liang et al. 1998, Chen 1998). A tentative comparison of the crucibles is given in table 8 (see also Chen 1998). Containerless processing has also been attempted (Todt and Schmitz 1993, Nagashio et al. 1999, Olive et al. 1999).

7.2. *Crystallinity enhancement*

7.2.1. *Floating particles and seed crystal rotation control*

The pulling mechanism has to provide controlled rates of both pulling and rotation with minimal vibration and great accuracy to maintain a precise seed orientation with respect to the melt surface. Another problem in the case of R123 HTSCs is particles floating on the melt surface which are formed due to crystallization of the supersaturated melt at the "melt–air" boundary or on the crucible wall. The floating particles generated on the melt surface may cause polycrystalline growth and unnecessary consumption of the solute in the melt and hence reduction of the growth rate of the crystal growing on the seed. If the melt surface is finally covered with floating particles, crystal growth may become impossible. Adjustment of the crucible size and the rotation rate as described in sect. 3.3.3 can be quite helpful to avoid formation of floating particles. For a 10 mm dummy crystal the steady circle position of the floating particles (in 100 mm diameter

Table 8
Contamination of melt and grown crystals by widely used crucible materials

Crucible	Impurity level in crystals	Remarks
$YBa_2Cu_3O_{7-\delta}$	–	not available commercially, low-melting, toxic
Al_2O_3	up to 5 at% Al (<95%)	reacts with melt, suppresses T_c
SnO_2	2–4 at% Si (<98%)	up to 8 wt% of Sn in melt and Si traces
Pt	Pt impurities	reacts with melt
Au	1.5% Au (<98.5%)	too soft, strong flux creep
MgO	1 at% Mg (<99%)	suppresses T_c
ZrO_2 (YSZ)	Mg, Al, Fe, Mn, Ti (99.5)	forms a thick interaction layer with flux
Y_2O_3,	possible impurities: (sintering with 0.5% TiO_2)	may act as R^{3+} supply for continuous growth by SRL–CP and modified TSSG methods
Nd_2O_3	no TiO_2	
$BaZrO_3$	La, Sr, Zr about 0.0014 at% (99.995%)	high melting point (~2600°C), small thermal expansion coefficient, not expensive, neither reaction layer nor remain flux on crucible after growth

crucible) reached 20 mm at 100 rpm rotation, and this rate (or one slightly higher) could be accepted as a practical recommendation for R123 growth by the pulling method. On the other hand Hattori et al. (1997) have applied a low-p_{O_2} atmosphere at the beginning of crystal growth to avoid floating particles at the melt surface. After dissolving the particles supersaturation can be created by increasing p_{O_2} at constant temperature rather than by lowering the temperature at constant p_{O_2}.

7.2.2. *Application of seeds with high crystallinity*

Imperfections, such as polycrystallinity, dislocations etc., once initiated, often propagate through the whole crystal. Therefore, it is important to supply a seed with the highest possible purity and perfection. One classical solution of this problem has been discussed already in sect. 6.4. It is evident that the so-called necking process, described in sect. 6.4, greatly improves the quality of the target large crystal grown after preparation and necking the first, smaller, crystal, acting as a highly crystalline seed for the final crystal. Note that large and high-T_c $x = 0.0$ Nd123 single crystals, described in sect. 5.5.2, were grown using this scheme.

7.2.3. *Cooling process*

The cooling process is another important part of single-crystal production. First of all, the cooling rate should be optimized to avoid thermal shock after termination of the crystal growth and removal of the crystals from the nutrient liquid phase. During cooling from high growth temperatures to room temperature even small self-flux-grown crystals have a tendency to delaminate parallel to the {001} planes as a consequence of their considerable anisotropic thermal expansion coefficients. For the Y123 phase, these are estimated to

be $\alpha_a \approx 7.2$–$13 \times 10^{-6}\,K^{-1}$, $\alpha_b \approx 7.9$–$10 \times 10^{-6}\,K^{-1}$, $\alpha_c \approx 14.8$–$20 \times 10^{-6}\,K^{-1}$ (Wolf et al. 1989). Therefore, the cooling should be gentle enough although this depends, of course, on crystal size and composition (Diko 1998a).

On the other hand, it has been reported that Y123 single crystals grown under an air atmosphere possess twins and a nonuniform distribution of oxygen concentration near the crystal surface, degrading its crystallinity. The twin structure is caused by the tetragonal-to-orthorhombic transition during cooling (especially slow cooling) in a high-p_{O_2} environment. To solve these problems, M. Nakamura et al. (1994) attempted to grow Y123 crystals by the SRL–CP method under low oxygen partial pressure ($p_{O_2} = 0.02$ atm) and cooling under a pure nitrogen atmosphere (6N) after the crystal pulling. As a result, twin-free Y123 crystals were obtained. Low-p_{O_2} crystal pulling is not favorable, however, for Y123 crystal growth for opposite reasons to those in favor of the high-p_{O_2} growth, which gives larger growth rates, as mentioned above. At the same time the possibility remains to obtain tetragonal crystals if the growth is maintained under high-p_{O_2} atmosphere and this atmosphere is substituted by an inert one after termination of the pulling experiment, cooling down the crystals in the new environment.

7.3. *Crystal size enlargement*

We can easily find two criteria for pulling a larger single crystal from the solution: (1) increasing the time for crystal pulling and (2) enhancement of the growth rate, although usually it is better to keep an optimal growth rate to preserve the crystallinity and flatness of the crystal growth interface.

7.3.1. *Expanding the pulling period*

A larger crucible is effective in reducing nucleation at the crucible wall since the wall temperature can be set higher in the case of a larger crucible for the same growth conditions. Additionally, this larger size creates favorable convection conditions for the crystal growth (sect. 3.3.3) and provides a larger overall volume of supersaturated melt for growth, for example, in the case of the modified TSSG method. Namikawa et al. (1996c) used a large crucible with 100 mm inner diameter to grow a large Y123 single crystal of typical size $14.5 \times 14.5 \times 13\,mm^3$ (sect. 6.2). In the large crucible the melt surface could be kept clear and without floating particles for a longer period of time; consequently, it was possible to sustain crystal growth for longer than 200 hours as opposed to less than 100 hours for a 50 mm-inner diameter crucible. Another illustrative result of the application of a large crucible (Nd_2O_3) was given in sect. 5.5.2.

7.3.2. *Increased growth rate*

A larger single crystal can be obtained in a shorter period of time if the growth rate is significantly enhanced. From equations in sect. 3.3.1 it is easy to see that for enlarging the single crystal, several growth-rate determining parameters can be considered as suggested by X. Yao and Shiohara (1997). Firstly, the R concentration at the interface temperature is

higher if the solubility of R is higher. This leads to reduction of the difference $C_s^{123} - C_i$ and, consequently, the growth rate becomes larger. Secondly, a lower liquidus slope may cause a higher supersaturation under a given temperature gradient. A higher temperature gradient can be simply applied in the crucible by (1) lowering the surface temperature (a deeper supercooling) or (2) by raising the bottom temperature to dissolve a larger amount of the 211 phase. In this case, however, the problem of floating particles can appear. Thirdly, using a higher rotation speed, it is possible to decrease the thickness of the solute boundary layer. Moreover a higher growth temperature, additives or p_{O_2} can result in a higher solute diffusion coefficient and a lower kinematic viscosity.

Yao et al. (1996a) produced Y123 crystals by the SRL–CP method under a pure oxygen atmosphere (sect. 5.5.1). In this case the growth rate is about twice as large as that in air, because at $p_{O_2} = 1.0$ atm yttrium solubility is higher (sect. 3.1.2.1), the liquidus slope is lower and the crystallization temperature is higher than at $p_{O_2} = 0.21$ atm, resulting in higher mass and heat transport for the growth and easiness in achieving higher supersaturation for interface kinetics. Another approach is growth of mixed Y–R123 (R = Nd, Sm) crystals (Yao and Shiohara 1997). The higher growth rate in this case is achieved owing to the higher solubility of Nd and Sm in the melt and their favorable liquidus slopes with temperature compared to Y, as discussed in sect. 3.1.2.1. The application of some additives can also be expected in the future. As an example, Yamada et al. (1997b) have tested BaF_2 in bulk crystal growth, and the results are promising.

7.4. *Improvement of superconducting characteristics*

7.4.1. *Crystallization in low-p_{O_2} atmosphere*

One advantage of low-p_{O_2} crystal growth in the case of Y123 was claimed to lower the growth temperature (Idemoto and Fueki 1990, Arnott et al. 1993, Loh 1998). Self-flux crystal growth under the reduced p_{O_2} has been successfully demonstrated by Fischer et al. (1993) and Nishimura et al. (1999). High-quality crystals (92 K) were obtained by an isothermal growth at 910°C. Crystallization was controlled by an incremental increase of p_{O_2} from 2.5×10^{-3} to 2.0×10^{-1} atm (table 5). The increase of Cu(II) concentration in this process could be tentatively attributed to creating supersaturation as in the slow cooling procedure. The potential advantages of this low-temperature, p_{O_2}-controlled process is that incorporation of impurities in the YBCO lattice is minimized and the crystal size can be controlled under carefully monitored oxygen partial pressure.

In the case of LR123 materials a broad range of the fundamental T_c^{onset} parameter can be observed depending on the preparation conditions (Lindemer et al. 1994, 1995). Usually this temperature is rather low, and most papers reported the impossibility to obtain a high-T_c Nd123 phase in air or oxygen by sintering or even by melt-processing. In pioneering papers solving this problem for ceramic samples, an additional post-annealing in low-p_{O_2} atmosphere has been developed (Kramer et al. 1994a; see also Iwata et al. 1989, Wada et al. 1989, Lindemer et al. 1994). It was clearly shown that not only for stoichiometric Nd123 but also for less substituted Nd123ss, T_c characteristics can be drastically improved by calcination at 950°C in 1 at% of oxygen without any visible

changes in the microstructure (Kramer et al. 1994a). This phenomenon can be explained in terms of relocating Nd ions in Ba sites since it was suggested that low-p_{O_2} treatment favors Nd ions pairing to conserve oxygen, resulting in fewer disrupted fourfold-coordinated coppers and the consequent increase of charge transfer from the planes to the chains. The next step in this direction has been made with the development of oxygen-controlled-melt-growth method (sect. 7.4.3.4), and by employing low-p_{O_2} post-annealing to improve superconductivity in air–melt-processed samples (Hu et al. 1997, Chikumoto et al. 1997b, Sandiumenge et al. 1998a). It seems that p_{O_2} is a suitable parameter for the successful melt processing of LR123-type superconductors because the reduced oxygen atmosphere allows one to obtain smaller substitution (sect. 3.1.2.5) and high T_c with a sharp transition.

Using a low-p_{O_2} (≈ 0.01 atm) atmosphere M. Nakamura et al. (1995) have successfully grown an Sm123 single crystal of about $7\times7\times7\,mm^3$ in size and with a sharp superconducting transition (0.3 K) at 93 K by the pulling method. Krauns et al. (1997) succeeded in growth of Sm123 crystals from a $BaZrO_3$ crucible. No Ba substitution has been detected in the crystals. Similarly, an Nd123 single crystal was produced with superconducting transition at about 96 K (M. Nakamura et al. 1996c). Under the applied growth conditions, increasing the p_{O_2} in this experiment from 1% oxygen resulted in increasing Ba substitution from $Nd_{1.01}Ba_{1.97}Cu_3O_z$ towards $Nd_{1.07}Ba_{1.95}Cu_3O_z$ in air, or even $Nd_{1.10}Ba_{1.90}Cu_3O_z$ in pure oxygen. Consequently, the T_c value dropped to 92 K for $p_{O_2}=0.21$ atm and even 88 K for $p_{O_2}=1$ atm with a concomitant broadening of the transition. Recently, Nd123 single crystals up to $4\times4\times4\,mm^3$ with high T_c (about 95 K), J_c (4×10^4–1.2×10^5 A/cm^2) and irreversibility field (13.4 T parallel to the c-axis) have been grown by Wolf et al. (1997) using the slow-cooling method in 50 mbar air/950 mbar Ar atmosphere starting from the Nd-poor side of the phase diagram.

7.4.2. *Liquid composition control*

In the case of Y123, variation of the initial flux composition is advantageous in the preparation of thick crystals by the self-flux method (sect. 5.1) or in the control of crystalline film orientation in the LPE method (sect. 5.4). However, for LR123 crystals the control of liquid composition is crucial even for their superconductivity enhancement.

As discussed in sect. 5.5.2, lowering the partial oxygen pressure is not the only method to enhance the T_c parameter in the case of the LR123 single-crystal growth. It also becomes possible due to understanding the mechanism of this process and by precise control of the growth conditions, especially when using Ba-richer fluxes. According to phase diagram considerations, (sect. 3.2.2) substitution in a growing crystal can be reduced in this case, and it actually happens since T_c as high as 95 K has been successfully achieved by the liquid composition control (sect. 5.5.2).

7.4.3. *Oxygenation procedure*

Oxygenation is necessary to enhance superconductivity, and this is a very delicate procedure in the case of single crystals. Oxygen diffusion and oxygen nonstoichiometry

of $RBa_2Cu_3O_{7-\delta}$ in polycrystalline and thin films are discussed in many publications overviewed by Kaldis (Vol. 31, ch. 195 of this Handbook). Reviews of p_{O_2}–T–x pseudobinary phase diagrams for the $YBa_2Cu_3O_x$ superconductor have been given by Hauck et al. (1998), Rudnyi et al. (1998) and others. However, some remarks should certainly be made here with respect to single crystals. This process has to be performed more carefully compared to polycrystalline materials because of the slow bulk diffusion kinetics, its great anisotropy, the possibility of twin and microcrack formation due to the tetra–ortho-transition, (sect. 6.3) as well as the danger of nanoscale composition fluctuations (sect. 6.8) and the necessity of providing an optimal oxygen content because of the easiness to achieve overdoped or underdoped states with lower T_c.

7.4.3.1. *Anisotropic oxygen diffusion in single crystals.* Diffusion of oxygen in $RBa_2Cu_3O_{7-\delta}$ is anisotropic due to crystallographic anisotropy of their orthorhombic unit cells. Therefore, diffusion in such crystals should be described by (at least) three independent diffusion coefficients along the principal crystallographic directions (Rothman et al. 1991). The anisotropy is expected to be rather large since the oxygen ion vacancies are concentrated exclusively in CuO basal planes, i.e. diffusion in the perpendicular direction (c-axis) could be much slower than that in the ab-plane. The diffusion is affected by many factors, including p_{O_2}–T–δ phase-diagram considerations (Rudnyi et al. 1998), chemical substitutions in $RBa_2Cu_3O_{7-\delta}$ (R-ion effect etc.), grain size, surface quality (Kemnitz et al. 1997, Claus et al. 1998, Tretyakov and Goodilin 2000), internal stress, availability of oxygen vacancies for diffusion jumps in the almost oxygenated state ($\delta_{lim} \approx 0.003$–$0.08$ according to data of different authors, Rothman et al. 1991, Kruger et al. 1997) etc. Therefore, the overall mechanism of diffusion and, consequently, fitting parameters [pre-exponential factor D_0, activation energy ΔE etc., $D = D_0 \exp(-\Delta E/(kT))$] are usually different depending on experimental conditions (Bokshtein et al. 1973). In addition, application of different evaluation techniques (electrochemical potentiometry, O^{18} isotope tracer and SIMS, in situ electrical resistivity measurements, differential scanning calorimetry, determination of XRD peak intensity, dynamic and isothermal thermogravimetry, observation of twin propagation front etc.) explains the discrepancy of numerical values in literature. However, from a practical point of view it is important to note that the chemical (D_{chem}) and self-diffusion coefficients (D_{self}) may differ by several orders of magnitude, $D_{chem} = D_{self}\,\Phi$, where Φ is a thermodynamic factor, which is nearly constant between $1 \leqslant \delta \leqslant 0.8$ and grows rapidly approaching $\delta \approx 0$ (Erb et al. 1996a). Usually the observable rate of in-diffusion is faster than the rate of out-diffusion because a surface-controlled process of some kind may take place especially for polycrystalline samples (Tu et al. 1988, Erb et al. 1996a). The intrinsic mechanism of oxygen diffusion was studied, for example, by Xie et al. (1989), Rothman et al. (1991) and Bredikhin et al. (1991).

(1a) For the polycrystalline Y123 material, chemical diffusion coefficients are reported to be in a wide range (Claus et al. 1998), 10^{-5}–10^{-11} cm^2/s with $\Delta E \approx 1.0$–1.5 eV, for example, ~10^{-10} cm^2/s (Tang and Lo 1991, TGA, 500°C), 10^{-11}–10^{-9} cm^2/s (Tu et al. 1988, in-diffusion, 400–600°C), 5×10^{-8} cm^2/s (O'Sullivan and Chang 1988, 94% dense

Y123, solid-state electrochemical cell, 500°C), 5×10^{-8}–5×10^{-7} cm^2/s (LaGraff and Payne 1993, out-diffusion, 350–600°C), ~5×10^{-5} cm^2/s (Elschner et al. 1992, 450–850°C), 7.5×10^{-7}, 1.9×10^{-6}, 3.4×10^{-6}, 6.2×10^{-6}, 1.3×10^{-5}, 1.8×10^{-5}, 2.8×10^{-5} cm^2/s (Shi et al. 1989, both in- and out-diffusion in air, direct observation of the oxygen diffusion front, 300, 400, ..., 900°C, respectively). The reasons for such a variety of diffusion coefficients, about 5 orders in magnitude, were discussed, for example, by Erb et al. (1996a). Three-dimensional experimental models of "p_{O_2}–temperature"-dependencies of diffusion coefficients based on e.m.f. measurements were determined both in polycrystalline Y123 and Nd123 materials by Mozhaev and Chernyaev (1994) and Mozhaev et al. (1996).

(1b) The self-diffusion coefficients are reported to be ~10^{-9}–10^{-13} cm^2/s, namely $D_{self} = 1.4\times10^{-4}\exp(-0.97\,\text{eV}/kT)$ cm^2/s (Rothman et al. 1991, both for ortho- and tetra-Y123, O^{18} tracer, 300–850°C), 1.7×10^{-13}, 6.7×10^{-13}, 2.9×10^{-12}, 1.3×10^{-11}, 5.3×10^{-11}, 1.7×10^{-10} cm^2/s (Xie et al. 1989, internal friction, 400, 450, ..., 650°C respectively), ~3×10^{-12} and 3.8–10×10^{-11} cm^2/s (Routbort 1993, $NdBa_2Cu_3O_{7-\delta}$, O^{18} tracer, 400 and 500°C), 8×10^{-13} –~10^{-9} cm^2/s (Y123, 350–645°C), 2×10^{-11}–2×10^{-9} cm^2/s (Gd123, 350–610°C), 3×10^{-11}–2×10^{-9} cm^2/s (Nd123, 350–564°C) (Tallon and Mellander 1992, internal friction, the highest temperatures in parentheses correspond to tetra–ortho-transitions). Since the repulsion energy between oxygen ions on the O(1) and O(5) sites is lower for R with larger ionic radii (0.124 eV for Nd123 in comparison with 0.200 eV for Y123, Routbort 1993), one might expect that the activation energy for oxygen self-diffusion would be lower and the diffusion faster in R123 rather than in Y123, as in the former mentioned work.

(2a) For Y123 single crystals (Claus et al. 1998), the oxygen self-diffusion coefficient in the c direction was found to be ~10^6 times lower ($D_c \approx 10^{-16}$–10^{-17} cm^2/s) than the diffusion coefficient in polycrystals (D_{poly}) at 400°C, and diffusion in the b direction at 300°C in untwinned crystals ($D_b \approx 2\times10^{-12}$ cm^2/s) was observed to be at least 100 times faster than that in the a direction ($D_a \approx 5\times10^{-14}$–$5\times10^{-15}$ cm^2/s) (Rothman et al. 1991). Thus, the diffusion is highly anisotropic for a single crystal, as expected, $D_{ab} \approx (10^4$–$10^6)D_c$, $D_b \approx 100\,D_a$, $D_{ab} \approx D_{poly}$, $D_b \approx 10\,D_{ab}$.

Tsukui et al. (1991) estimated in a similar manner $D_{ab} \approx 10^{-10}$ and $D_c \approx 2\times10^{-16}$ cm^2/s at 450°C, $D_{ab} \approx 7\times10^{-10}$ and $D_c \approx 2\times10^{-15}$ cm^2/s at 530°C. Bredikhin et al. (1991) demonstrated that $D_{ab} \approx 3\times10^{-12}$ and $D_c \approx 4\times10^{-17}$ cm^2/s at 400°C, $D_{ab} \approx 7.8\times10^{-9}$ and $D_c \approx 6.2\times10^{-11}$ cm^2/s at 800°C. These data, and the values of the surface exchange constants, (8×10^{-9} cm/s at 400°C; 5.2×10^{-6} cm/s at 800°C) suggest that diffusion in Y123 crystals at 400°C is a real two-dimensional diffusion in the ab-plane in which only oxygen O(1) in chains is exchangeable. At 800°C diffusion occurs also along the c-axis, i.e. jumps into O(2) and O(3) sites might be permissible while, according to authors, O(4) still remains fixed.

(2b) The most practically important values of the chemical diffusion coefficient were also calculated in a number of works. For example, Yamada and Shiohara (1993), analyzing the thickness of the surface twinned area in bulk Y123 crystals cooled down from the growth to room temperature, roughly estimated an average $D_{chem} \approx 10^{-7}$ cm^2/s.

The chemical diffusion coefficients in single crystals were reported also to be ~10^{-5} cm^2/s (in-diffusion) and 10^{-6} cm^2/s (out-diffusion) at 725°C (LaGraff and Payne 1993; this is re-analyzed by Gupta et al. 1998), and 5×10^{-9} cm^2/s at 680°C (Fiory et al. 1988). Using in situ resistivity measurements, Erb et al. (1996a) reported $D_{chem} \approx 3\times10^{-8}$ cm^2/s at 550°C and 8×10^{-9} cm^2/s at 420°C with $D_0 = 4.94\times10^{-5}$ cm^2/s and $\Delta E = 0.52$ eV for $Gd_{0.8}Y_{0.2}Ba_2Cu_3O_z$ crystals. In- and out-diffusion coefficients were found almost identical (see also Gupta et al. 1998), and ΔE for the pure Y123 single crystal was estimated as 0.8 eV. Using direct observation of the movement of the oxygenation front in the hot-stage optical microscope, A. Oka et al. (1998) found that oxygen chemical diffusion coefficients of Nd123 single crystals grown by the modified TSSG technique seem to be 2–4 times larger in the temperature range 300–600°C than those of Y123 crystals. The absolute values were estimated at 300, 400, 500 and 600°C as 4.5×10^{-8}, 5×10^{-7}, 7×10^{-7}, 10^{-6} cm^2/s for Nd123 and 3×10^{-8}, 2×10^{-7}, 4×10^{-7}, 4.5×10^{-7} cm^2/s for Y123, respectively.

It is obvious that cation diffusion can also play a significunt role in the processes discussed. Unfortunately, numerical data have not yet been measured for many systems and therefore they are not widely available. The diffusion of cations in HTSC crystals occurs by means of regular mechanisms using vacancies, dislocations, point defects etc. and, in addition, a faster surface diffusion can be observed for polycrystalline materials (Dzhafarov 1996). As an example, self-diffusion of Cu^{2+} is studed using tracer distribution analysis (Dzhafarov 1996, Rebane et al. 1994, 1996, 1997). It is observed that the Cu^{2+} diffusion coefficient does not exceed ~5×10^{-12}–10^{-13} cm^2/s at 780–900°C and 6–9×10^{-14} cm^2/s at 600°C (extrapolated); the process is found to be essentially anisotropic with an activation energy of about 165–255 kJ/mol. Similarly, the self-diffusion coefficient of the larger Ba^{2+} cation falls in the ~10^{-14}–5×10^{-15} cm^2/s range under the same conditions, while it is 10^{-14}–10^{-16} cm^2/s for Y^{3+} at 780–980°C (activation energy about 280 kJ/mol). Thus, it is believable that the oxygen self-diffusion is 10–1000 times faster, and this finding is especially true at commonly used oxygenation temperatures (nevertheless a solid-phase decomposition process might take place in the case of light RE elements as discussed above).

7.4.3.2. *Optimal oxygen content for higher* T_c. It is well known that there is an optimal oxygen content in single crystals such as R123, Bi2212, (Bi,Pb)2223, Hg1223, (Nd,Ce)201, etc., which results in maximum T_c values (Tallon and Flower 1993, Batlogg et al. 1997), while both "underdoped" and "overdoped" crystals demonstrate a lower T_c (this is often called optimal doping by carriers). For example, T_c can be as low as 87 K for "underdoped" $YBa_2Cu_3O_{6.85}$, it reaches a maximum at 91.5 K for "optimally doped" $YBa_2Cu_3O_{7-\delta}$ with $\delta = 0.06$, and then falls again to 87.5 K near "overdoped" $YBa_2Cu_3O_7$ (Hauff et al. 1994). Graf et al. (1990), Loram et al. (1991) and Tallon and Flower (1993), reported, however, maximum values of 93.4 K ($\delta \approx 0.06$), 93.5 K ($\delta \approx 0.1$) and about 94 K ($\delta \approx 0.05$), respectively. $T_c \approx 93$ K at $\delta \approx 0.07$ was suggested by Wolf et al. (1997). Obviously, the achievable maximum in T_c depends strongly on the quality of the single crystals since this parameter is sensitive even to minor impurities. Moreover, the

optimal oxygen content is different for different rare earths. Rare-earth elements with smaller radii exhibit a tendency to have maximum $T_c < 90$ K [T_c(Yb123) ≈ 87 K] at lower oxygen content near $O_{6.90}$ whereas T_c for Nd123 (95–96 K) might have a maximum at $O_{7.0}$ and La123 is predicted to display the highest $T_c \approx 98$–100 K above $O_{7.0}$ (Tallon and Flower 1993), although a special heat treatment and sample preparation might be needed (Wada et al. 1989, Lindemer et al. 1994). This explains why high-oxygen-pressure, long-term (about 100–300 h in 1 atm of oxygen) and low-temperature (about 300–350°C) annealing procedures are more favorable for the Nd123 phase to be optimally oxygenated (Murakami et al. 1996). The effect of rare-earth ion size on T_c probably originates from the strain-induced charge redistribution between the charge reservoir and the CuO_2 plane (J.G. Lin et al. 1995, Samoylenkov et al. 1997) or from different in-plane arrangement of oxygen (Lutgemeier et al. 1996).

7.4.3.3. *High-oxygen-pressure treatment.* For a deeper understanding of fundamental mechanisms of superconductivity and because of practical needs, the application of low-temperature–high-p_{O_2} treatment should be systematically studied in the future, especially with respect to the behavior of $R_{1+x}Ba_{2-x}Cu_3O_z$ solid solutions grown in the form of a single crystal. Indeed, the best way to improve the superconducting properties of $R_{1+x}Ba_{2-x}Cu_3O_z$ is to suppress the substitution (x) in the solid solution by high-temperature–low-p_{O_2} treatment (sect. 3.1.2.5), or by crystal growth at lower p_{O_2} (sect. 7.4.1), or by controlling the liquid composition (sect. 7.4.2). However, an increase of p_{O_2} is able to change the situation as well, at least for the less-substituted solid solution. Tsurumi et al. (1988) were able to make $Nd_{1.5}Ba_{1.5}Cu_3O_z$ superconducting by annealing under high oxygen pressure (about 49 atm). In this sample the oxygen content at the chain sites increased according to structure refinement analysis. At the same time, slight changes in the crystal structure parameters were also observed; the distance between the Nd layer, CuO_2 layer and the (Ba, Nd)O layer became shorter and the apical oxygen shifted away from the CuO chain and toward the CuO_2 layer. Takita et al. (1992) also observed an increase in T_c of the solid-solution samples after high-oxygen partial pressure annealing (600–1000 atm, 350°C). $T_c \approx 20$ K was reported for the $x = 0.5$ substitution while the sample was not superconducting under normal conditions. Singh et al. (1994) reported that it is possible to achieve $T_c \approx 38$ K (!) after high-oxygen pressure annealing (200 atm) for this usually nonsuperconductive tetragonal compound. Dyakonov et al. (1997) induced 30 K-superconductivity in $NdBa_2Cu_3O_{6.67}$ by a pressure of 1 GPa at room temperature. After releasing the pressure, the superconductivity was observed to disappear within 1.3 h, and the process was found to be reversible. All of the facts mentioned are attributed to charge redistribution between CuO_2 planes and CuO chains as a result of oxygen ordering under high pressure.

7.4.3.4. *Oxygen and cation nonstoichiometry with respect to pinning properties.* The unique electric and magnetic characteristics of HTSC materials as type-II superconductors are determined by their layered structure connected with a space modulation of the superconducting charge carrier density located mainly in the CuO_2 layers and separated

by dielectric block fragments. The most essential from an engineering point of view is not only the fundamental T_c parameter but also the absolute value and the field stability of the critical current density J_c, which is related to the presence of pinning centers and the Abrikosov flux lattice creep in an external magnetic field. Recently, it has been reported that $R_{1+x}Ba_{2-x}Cu_3O_z$ (R: Nd, Sm, Eu, Gd) superconductors, prepared by oxygen-controlled melt growth (OCMG; 0.1–0.06% oxygen in gaseous atmosphere seems to be optimal: Shibata et al. 1999), exhibit higher T_c and higher critical current density in the high magnetic-field region than melt-processed Y123 (Murakami et al. 1996). The most impressive advantage of the OCMG method is connected with this anomalous peak effect. The M–H loop is kept open up to 7 T and the irreversibility field exceeds 8 T at 77 K. The former is the highest known value for all the R123 superconductors. It is believable that stronger flux pinning in the OCMG samples in the high-field region probably originates from both enhanced T_c and the presence of a new type of "chemical" pinning centers never observed for the Y123 system and as strong as irradiation ("physical") pinning centers (Trappeniers et al. 1999).

A relatively simple explanation of a similar peak effect in Y123 crystals has been given by a number of authors (D'Anna et al. 1994, Gordeev et al. 1994, Klein et al. 1994, Asaoka et al. 1996, Kupfer et al. 1996, Erb et al. 1997, Wolf et al. 1997, Saito et al. 1998, Oka et al. 1999a,b). In these models the increasing branch in the J_c–B curve is attributed to local oxygen-deficient regions with suppressed T_c in a superconducting matrix with higher T_c (see, however, Angadi et al. 1991). When the magnetic field increased, these regions turn into a normal phase and become pinning centers. Obviously, the same can be observed in the case of LRE123. Wolf et al. (1997) supported the idea that a pronounced peak effect for the Nd123 superconducting material results from small clusters of oxygen vacancies whereas a second peak observed by them is related to the twin structure. Erb et al. (1997) declared that the so-called "fishtail" effect in most R123 crystals is explained by the presence of residual metallic impurities (from crucible and/or from everywhere) which suppress the oxygen mobility and create oxygen redistribution inhomogeneities. Sarikaya and Stern (1988) suggested, however, that the oxygen inhomogeneities may occur in Y123 crystals due to the spinodal decomposition of a solution formed from $YBa_2Cu_3O_7$ and $YBa_2Cu_3O_6$ (sect. 6.8).

The idea that the defects responsible for the anomalous peak effect in LR123 systems have another nature, is not less constructive as supported by another extended group of publications (Yoo et al. 1994, 1998, Egi et al. 1995, Murakami et al. 1996, Hyun et al. 1996, Shiohara and Endo 1997, Higuchi et al. 1998, 1999, Pradhan et al. 1998b,c, Nagashima et al. 1998, Kawano et al. 1998, Oka et al. 1999b). The first model of the anomalous peak effect was based on the simple assumption of the existence of areas with Nd-enriched composition (Murakami et al. 1996). These substituted regions are still superconducting in low fields and may not contribute to flux pinning. Upon increasing the magnetic field these finely dispersed Nd-rich areas probably have a stronger field dependence of superconductivity in comparison with the surrounding matrix and can manifest themselves as very small coherent nonsuperconducting inclusions, i.e. effective

pinning centers. A further increase of the magnetic field suppresses superconductivity both in these regions and the main matrix.

Egi et al. (1995) have investigated the superconducting properties of Nd123 single crystals grown by the TSFZ method under 0.1% O_2 in Ar atmosphere. These crystals were annealed at 320°C for 14 days in an O_2 atmosphere. They also have observed an anomalous peak effect in the M–B loop, similar to the OCMG results, and finely dispersed white regions in the dark-field image due to the Nd substitution for Ba in the Nd123 matrix (sect. 6.8). The size of the white spots varied from several nanometers to several tens of nanometers, which is consistent with the size of pinning centers observed by STM (sect. 6.9). Pradhan et al. (1996) studied magnetoresistance and magnetization of the Nd123 phase to elaborate a magnetic phase diagram. It was demonstrated that the magnetic relaxation rate and the pinning energy have a plateau, and this suggests a specific distribution of pinning potentials produced by the Nd-enriched areas. These results seem to support the pinning mechanism proposed by Murakami et al. (1996).

A further attempt to explain the formation mechanism of these pinning centers has been performed by Shiohara and co-workers (M. Nakamura et al. 1996c,d, Shiohara and Endo 1997, see sect. 6.8). In order to investigate whether the anomalous peak effect in the M–B loop is an intrinsic property or not, different series of heat treatments have been performed, using bulk Nd123 single crystals. The Nd123 single crystals were grown by the TSSG method in contamination-free Nd_2O_3 crucibles under a 1% oxygen partial pressure atmosphere. The as-grown crystals were removed from the furnace immediately after termination of their growth. The typical removing time was approximately 10 min which corresponds to a cooling rate of about 100°C/min. The Nd : Ba : Cu = 1.01 : 1.97 : 3.00 composition of the crystals was determined by ICP AES. Single-crystal X-ray structure analysis confirmed that the as-grown single crystals were tetragonal (P4/mmm) with no significant neodymium substitution into the barium site.

Heat treatment at 340°C for 200 h in oxygen resulted in a steep superconductive transition of the crystals at around 96.5 K with no peak effect. This result indicates that these crystals were sufficiently perfect with no strong pinning centers or crystal defects. On the other hand, continuous cooling from 600°C to 350°C for 200 h followed by oxygenation at 340°C for 200 h led to the anomalous peak effect at around 4 T in the J_c–B curve with the $B \parallel c$-axis orientation, although in the $B \parallel a$-axis orientation the anomalous peak effect was not detectable (fig. 42). To clarify these results, a two-stage heat treatment was conducted in which the first stage was a heat treatment to investigate the solid-state transformation temperature and the second stage was aimed at a simple oxygenation. In this experiment, the first stage temperature was changed as a variable parameter (600, 500 and 400°C for 100 h) and immediately after the isothermal holding, the samples were quenched in air. The second stage was carried out at 340°C for 200 h in oxygen. As a result, after annealing at 500°C and oxygenation, the anomalous peak effect in the $B \parallel c$-axis orientation was reproducibly observed, however temperatures below 400°C were found to be too low for any sluggish phase separation connected with heavy atom movements; subsequently, oxygenation occurred only. In addition, the sample with the peak effect was heated up to 900°C, and held for 100 h. After subsequent

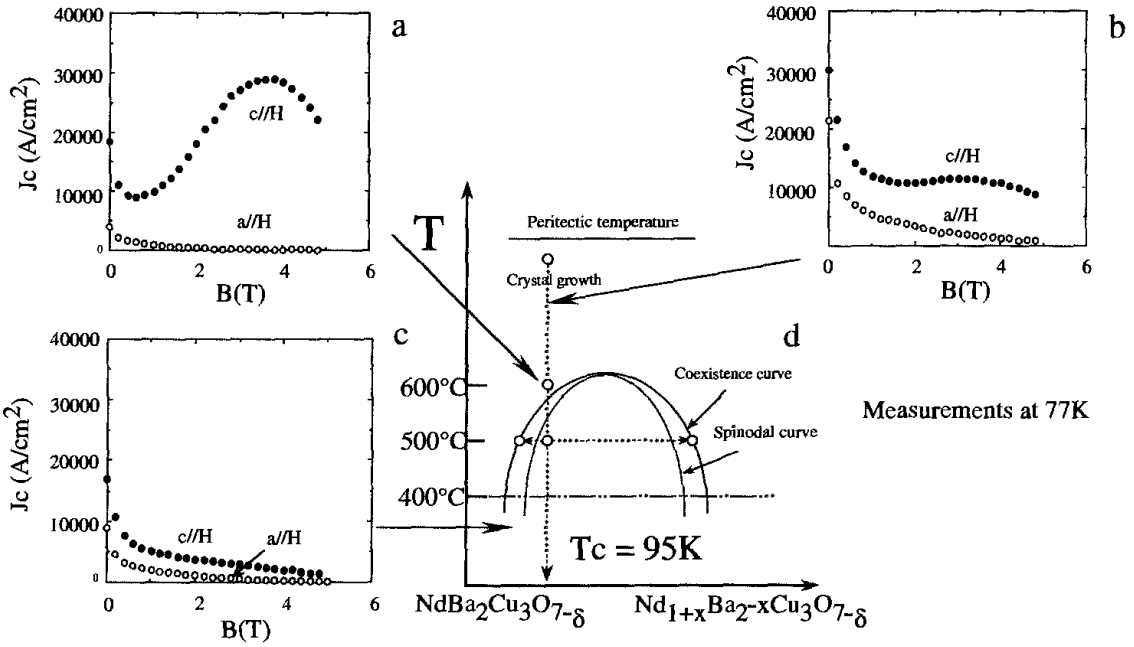

Fig. 42. (a–c) The anomalous peak effect on the magnetization curves of Nd123 single crystals subjected to different post-growth heat-treatment, and (d) its possible relationship with a spinodal decomposition phenomenon (M. Nakamura et al. 1996d). T_c values in all cases were measured to be high (about 95 K).

oxygenation, the initial anomalous peak effect almost disappeared, i.e. the solid reaction seems to be reversible. In all cases the T_c values were constantly high (>95 K). The results were confirmed by measuring the in-plane resistivity transition in static fields up to 8 T (Mimura et al. 1998). It was proved that the crystals with the peak effect consist of at least two phases – superconducting (95 K) and an insulating phase (like a solid solution $Nd_{1+x}Ba_{2-x}Cu_3O_z$ with $x > 0.3$–0.4). Since the fraction of nonsuperconducting phase was small enough to affect the total Meissner effect of the crystals, it might exist within the crystals as a thin wall perpendicular to the CuO_2 plane that dams up the external current. In the magnetization experiments described above, this phase (or, one should say, composition fluctuations) may act as pinning centers with anisotropic behavior.

These results indicate that the anomalous peak effect perhaps is not an intrinsic property but is process-dependent. The anisotropy of the peak effect is thought to be caused by the anisotropic microstructure in the Nd123 crystals. Actually, the TEM image of a crystal with the anomalous peak effect exhibits a modulated structure. On the contrary, an Nd123 crystal with no peak effect demonstrates no modulated structure (sect. 6.8). Therefore the authors assumed that a nano-scale microstructure (the modulated structure) causes the peak effect and the anisotropy in the J_c–B curve. The authors also have proposed tentatively that such a phase separation might be derived from a spinodal decomposition of the Nd123 unstable solid solution even though no significant amount of Nd–Ba substitution was detected in X-ray analysis. Accepting the idea (sect. 3.1.2.3) that polycrystalline $x = 0.0$ Nd123 samples decompose macroscopically into the $Nd_{1+x}Ba_{2-x}Cu_3O_z$ and $BaCuO_2$ exactly in the temperature

range under discussion (500–600°C in oxygen), it is not impossible that for the more perfect and uniform Nd123 single crystals such a process is replaced by the formation of modulated microstructure to reach a local minimum of the free energy. Wu et al. (1997, 1998) and Wu and Wang (1999) suggested that due to differences in the solidus slope and the solubility limit at different p_{O_2} in the Ba-rich region, the stoichiometric $x = 0.0$ solid solution might be metastable upon oxygenation treatment. Therefore, precipitation of metastable transition phases could occur in the crystal matrix of "supersaturated" solid solution before the macroscopic phase separation into equilibrium products (sect. 2.2.1). The transition phases, with structures intermediate between those of the matrix and the equilibrium phase (according to Ostwald's step rule in general, and particularly in accordance with experiments on supersaturated alloys), may form coherent and semicoherent interfaces, which decreases the interfacial energy and hence lowers the activation barrier for nucleation. A typical phase diagram of a spinodally decomposing system is represented in fig. 42. Under some idealized assumptions Goodilin et al. (1997b) suggested that the mixing energy interaction parameter in the regular solution model might be positive for the Nd123ss solid solution (about 25–40 kJ/mol), which supports the possibility of spinodal decomposition. If the spinodal decomposition scenario actually takes place in Nd123 crystals, we can reversibly control their microstructures and J_c, depending on purpose, by a simple heat treatment.

Probably, this model is not inconsistent with others, especially with those which put forward the data on the peak effect disappearing after "appropriate oxygenation" as an argument against spinodal decomposition. In sect. 7.4.3.3 it was demonstrated that high-p_{O_2}–low-temperature treatment can make the $Nd_{1+x}Ba_{2-x}Cu_3O_z$ solid solution superconducting even at a substitution x as high as 0.5. In accordance with that, Chikumoto et al. (1997a) found that the peak effect is present in OCMG-processed samples oxygenated under 900 atm of oxygen, but it is shifted toward higher field with a depression in the peak height (see also Puig et al. 1998). The authors explained this phenomenon in terms of enhanced superconductivity of the Nd-rich inclusions. Thus, both phenomena (spinodal decomposition and nonuniformity in oxygen distribution) would exist simultaneously, at least hypothetically, because they should be strongly coupled due to the different oxygen nonstoichiometry of the Nd123ss with different substitution (sect. 3.1.2.5).

7.4.3.5. *Detwinning by mechanical stress.* In the annealing process, to attain superconductivity, the a-axis of a tetragonal phase separates into the a- and b-axis of the orthorhombic phase, and this separation occurs randomly, leading to the twin structure (sect. 6.3). Small crystals (~1 mm^2) can be obtained in a twin-free form (Rice and Ginsberg 1991) while larger crystals demand a special detwinning procedure. Since the stiffness of the materials becomes minimal in the middle of the structural transformation, this phenomenon allows one to obtain a twin-free orthorhombic phase starting with the tetragonal one. This process originates from the idea of ferroelasticity (Aizu 1970) and has been widely investigated (Schmid et al. 1989, Voronkova and Wolf 1993, Asaoka et al. 1996, Rykov et al. 1997, Kutami et al. 1997, Oka et al. 1999b), therefore only a few practical examples will be given here.

In thin (about 100 μm) flux-grown crystals the twin structure changes under uniaxial pressure of a few MPa, starting from a temperature 200–300°C. The single-domain crystals obtained in this way show a "memory effect" (Voronkova and Wolf 1993, Rykov et al. 1997), i.e. they retain internal stresses and become retwinned under subsequent annealing without uniaxial pressure. The configuration of the twin-domain walls returns to its initial state as predetermined by microstructural defects. Thick (for example, SRL–CP-produced) crystals can not be detwinned at such low temperature. In contrast, when raising the temperature to 500–700°C, complete detwinning occurs without returning to the initial twin structure. The Ar preheating favors "memory cleaning" because it anneals the defects and cures microcracks of the as-grown crystals as well as homogenizes the oxygen content and removes it from rare twins if present. Therefore a typical procedure of detwinning is as follows (Rykov et al. 1997, Kutami et al. 1997): A rectangular piece is cut off from a large single crystal. Uniaxial stress of about 6 MPa is applied. Then the sample is heated under this uniaxial pressure in argon gas flow up to 600°C. Then the gas is changed to oxygen and the sample is cooled at a rate of about 6°C/h. The resulting microstructure according to polarized optical microscopy observation consists of about 99.9% surface fraction of the twin-free orthorhombic $YBa_2Cu_3O_7$ phase (Rykov et al. 1997).

Kutami et al. (1997) pressed a single crystal ($1\times1\times0.3$ mm^3) with a tetragonal structure at 1000 kgf/cm^2 for 120 h under an oxygen atmosphere. As a result, the crystal annealed with the uniaxial compression was an orthorhombic phase without twins as confirmed by Laue X-ray backscattering, TEM observation and T_c measurements. Onset of T_c of the twin-free crystal was about 92 K and the J_c value at 1 T was one fifth that of the twinned crystal, which indicates a high crystallinity.

In a number of works (sects. 5.1, 5.4.2.) it was suggested to use doping with Sr to avoid the tetra–ortho transition and twinning. For the light rare-earth elements (Nd, La, Sm etc.) this might be connected with partial exchange between R and Ba sites (Sr substitutes for R and R substitutes for Ba, Hellebrand et al. 1996), followed by the so-called 1113-type ($SrBaRCu_3O_z$) tetragonal phase formation (Wang and Bauerle 1991, Wang et al. 1992, Zelenay et al. 1994). However, such doping deteriorates the superconducting properties of the crystals (Fueki et al. 1990, Karen et al. 1991, Psycharis et al. 1996). Most probably, thermomechanical detwinning will remain the favorite method of twin-free crystal production (see, however, sect. 7.2.3.).

8. Advantages, problems and prospects: motivations of single-crystal production in the future

At present, large-grain materials and single crystals of HTSCs are expected to be applied mainly in two different directions, namely scientific and commercial (fig. 43). The first direction is more or less supplied by the existing stream of the single crystal production, however, the second one is far from saturation (Batlogg et al. 1997). The repulsive and attractive forces between a permanent magnet and a superconductor obviously can be applied to magnetic bearing, fly-wheels, magnetically levitated transport systems and so on. Melt-processed HTSC can do this. Tapes and wires can also partially quench requests

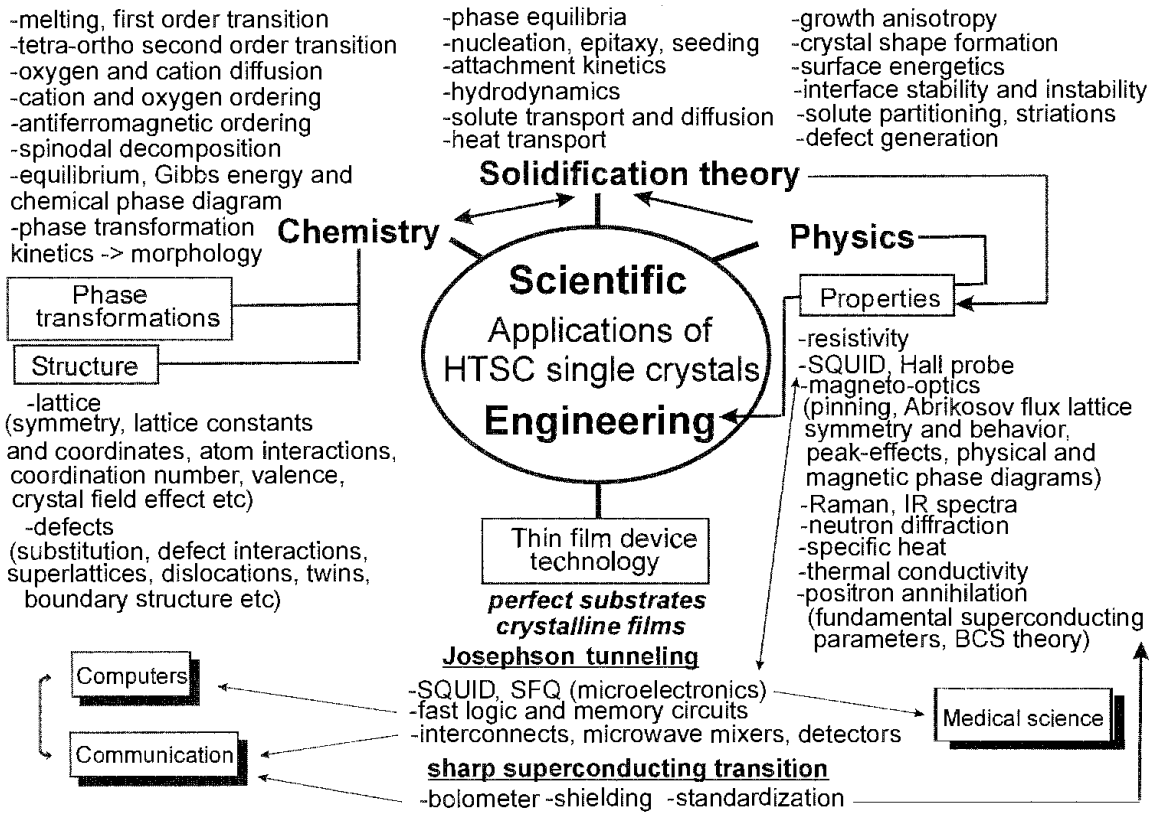

Fig. 43. Possible applications of single crystals and their relationship with different fields of human knowledge.

to the materials makers (Batlogg et al. 1997). On the other hand, the very short coherence length of HTSC poses specific requirements of atomically flat surfaces, sharp interfaces and patterning on the sub-nanometer scale to design a new class of substrate/barrier materials, contacts, logical circuits, SQUID detectors, and other multilayer structures in microelectronics (Batlogg et al. 1997). A number of substrate materials have been used for the epitaxial deposition of HTSC, however, no substrate material has been found which fulfills all the ideal requirements (sect. 5.4). R123 single-crystal substrates are considered to be the best for the homoepitaxial growth (sect. 5.4). It is also interesting to note that the lattice constants of Nd213 insulating crystals are very close to those of the superconducting R123 phases and the estimated lattice mismatch is even smaller than in the generally used Pr123 and $SrTiO_3$ materials. On the other hand the composition variation of Nd123ss allows one to flexibly adjust lattice parameters of Nd123ss to the level demanded for epitaxial growth of depositing materials. In principle, this makes Nd123ss a promising material for high-temperature superconductor thin-film device technology. Unfortunately, crystallinity and size of R123 single crystals are still not sufficient, prices and efforts in production are still high, although bulk single crystals can be applied in this field even by such exotic ways as high-density uniform targets for physical deposition. Li et al. (1998) reported that smooth Nd123 thin films with $T_{c0} \approx 91$ K can be successfully deposited on $SrTiO_3$ {100}, $LaAlO_3$ {100} and $NdGaO_3$ {110} substrates by the laser ablation

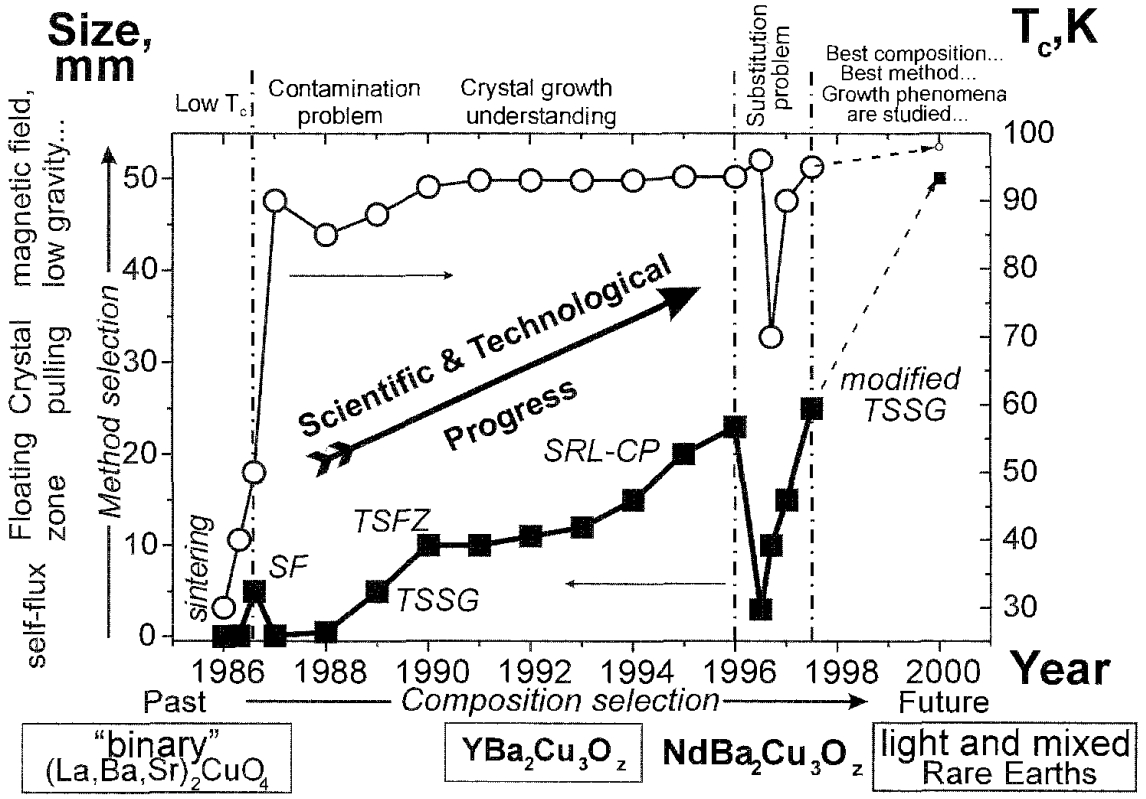

Fig. 44. Progress in production of high-quality bulk single crystals connected with understanding crystal growth phenomena and subsequent technological improvements of crystal growth methods.

technique using a bulk Nd123 single-crystalline target. In this experiment the density of droplets on the surface has been reduced by a factor 10^4 in comparison with 10^6 cm^{-2} for sintered targets, and a surface roughness of less than 40 Å has been achieved. However, for an application of this kind the crystals at least should not be expensive.

In order to satisfy the increasing demands of novel technologies with respect to quality, size, purity, chemical and structural complexity and stoichiometry, flatness of surface and interfaces, sophisticated multilayers and other structures, further significant progress in investigations of crystal growth and the crystal production technologies is most vital. A magnetic field markedly reduces fluctuations in the melt temperature, and this has led to a high interest in applications of a magnetic field in different configurations for the pulling technique (Hurle and Series 1994). Other advantages can be achieved in microgravity experiments in space (Gatos 1982). Hydrodynamic conditions in the crystallizer should also be further improved (ACRT technique etc.). The effect of substitution and additives, other chemical modifications, have not yet been investigated sufficiently. New chemical systems or compound innovations in single-crystal growth are also expected to make the situation better.

As a pleasant result of fundamental research on crystal growth and owing to obvious technological improvements (some of them have been described in this chapter), progress in crystal size and perfection takes place as shown chronologically in fig. 44. It is evident

that since the first small crystals an essential jump in the crystal size (about 1000 times for their volume, table 5), quality and growth techniques has been achieved and new advancements can be predicted in the near future. However, the problem of HTSC single-crystal growth should overcome the status of an art and become both a science and a commercial technology. This problem is multidisciplinary, and economical and temporal factors are present for its solution. Finally, the crystal growth enhancements are believed to increase the economic/commercial yield of high-quality single crystals and make them inexpensive – exactly as has been done with semiconducting materials after the elaboration of appropriate technological schemes for their industrial growth.

9. Notes added in Proof

(1) Other nucleation thermodynamic parameters such as the interfacial energy between Nd123 or Y123 and melt, metastable zone width, Gibbs free energy, critical nucleation radii etc. were estimated by Paul et al. (1999, 2000) using classical nucleation theory.

(2) It is also important that the "PCF" can be drastically different when considering strongly non-equilibrium conditions for crystallization. For example, $NdBa_2Cu_3O_z$ melt was undercooled to ~935°C using aero-acoustic levitation and solidified congruently afterward (Nagashio et al. 1999). The direct crystallization of the $YBa_2Cu_3O_7$ orthorhombic superconductor was achieved by a rapid solidification using laser-zone melting (Nagaya et al. 1991). Similar results were found in drop-tube experiments (Todt and Schmitz 1993, Olive et al. 1999).

(3) Polynomial approximations of the liquidus surface $C_L^{Nd}(T,p_{O_2}) = a_2(C_L^{Cu})^2 - a_1 C_L^{Cu} + a_0$ within the "$Nd_{1+x}Ba_{2-x}Cu_3O_z + L$" two-phase region (Kambara et al. 1998, Yoshizumi et al. 2000) are given in table 9.

(4) The following common abbreviations of semisolid melt-solidification techniques (given in alphabetical order) are often used in the literature (for details, see, e.g., Shiohara and Endo 1997, Desgardin et al. 1999, Tretyakov and Goodilin 2000):

CUSP Constant-Undercooling Solidification Processing; often reported method of isothermal crystallization of undercooled top-seeded ceramic samples

CRT Composite Reaction Texturing; trial application of numerous MgO whiskers as seeds for a crystallizing system

CGMG Constitutional-Gradient Melt Growth; emerging method of crystallization along a constitutional gradient of rare earths with different ionic radii (for example, $R = Nd^{3+}$, $R' = Yb^{3+}$) providing different melting temperatures of mixed (R,R')123 solid solutions

IMC Isothermal Melt Crystallization; rare but effective method of isothermal crystallization under gradually increasing p_{O_2}; this method is similar to the so-called gas-pressure method in the case of Bi-based superconductors

Table 9
Polynomial approximations for liquidus surface in "$Nd_{1+x}Ba_{2-x}Cu_3O_z + L$" two-phase region

Conditions		a_2	a_1	a_0
T (°C)	p_{O_2} (atm)			
980	0.01	0.0155	1.96	62.6
1000	0.01	0.00957	1.15	35.1
1020	0.01	0.00653	0.765	23.9
1030	0.21	0.0163	2.11	69.6
1050	0.21	0.0186	2.45	81.9
1073	0.21	0.0213	2.83	96.1
1050	1	0.00831	0.98	30.1
1070	1	0.0101	1.18	36.5
1090	1	0.0114	1.27	37.9
1100	1	0.0116	1.31	40.2

GAS-MG Graphically-Aligned-Seeds Melt Growth; trial method of crystallization along a constitutional gradient provided by overlapping rare-earth-element diffusion profiles around arranged multiple seeds

LAP Liquid-Aided Process; sintering near peritectic decomposition

LPP Liquid-Phase Processing; famous modification of the MTG technique allowing for reduced duration of preparation of large-grain ceramics, by slower cooling within a certain temperature window only to provide most effective grain growth in semisolid melts

LPRP Liquid-Phase Removal Process; rather rare modification of the MTG method employing soaking of excess liquid from crystallite boundaries by a porous substrate made of the Y_2BaCuO_5 phase

MTG Melt-Textured Growth; first and simplest method of constant cooling from above peritectic temperature down to room temperature

MPMG Melt Powder Melt Growth; effective famous method of achieving smaller Y_2BaCuO_5 inclusions in a slowly cooled crystallizing HTSC matrix when using finely crushed and pelletized powders of high-temperature melt rapidly quenched down from the temperatures of the "$Y_2O_3 + L$" region, ~1400°C

MIA Magnetically Induced Alignment; trial crystallization method in magnetic fields above 1 Tesla assisted by the addition of those rare-earth elements that have the largest magnetic moments, like Nd, Gd, Ho, Dy, ...

OCMG Oxygen-Controlled Melt Growth; well-known effective method for the preparation of "peak effect" large grain ceramics of light-rare-earth barium cuprates (LR = La, Nd, Sm, Eu or a mixture of these elements) based on crystallization in a low-p_{O_2} atmosphere that prevents LR/Ba substitution and T_c suppression

PDMG Platinum-Doped Melt Growth; wide-spread method of achieving smaller Y_2BaCuO_5 inclusions in a HTSC matrix owing to the introduction of small amounts of Pt or PtO_2 in the LPP method; Pt additives are often combined with CeO_2 additions

PMP Powder-Melt Process; known method that uses finely milled and then pressed mixture of powders of $BaCuO_2$, CuO and Y_2BaCuO_5 phases involved later in a crystallization process; this method is similar to the so-called two-powder-process in the case of Bi-based superconductors

QMG Quenched-Melt Growth; original method of achieving smaller Y_2BaCuO_5 inclusions in a slowly cooled crystallizing HTSC matrix when using chunk of melt rapidly quenched down from the "$Y_2O_3 + L$" region; this method is similar to melt-casting in the case of Bi-based superconductors

QDR Quench-and-Directional Recrystallization; original low-temperature fast method of thermal-gradient re-crystallization of chunk of melt rapidly quenched down from the "$Y_2O_3 + L$" region; the reduced process temperature (below peritectic melting) is achieved because of the high content of monovalent copper in the dense precursor thus prepared

SDS Seeded Directional Solidification; trial modification of the Bridgman-type crystallization of a bar with one seeded edge

SLMG Solid–Liquid Melt Growth; known method that imitates MPMG methodology, i.e., uses finely milled and then pressed mixture of powders of $BaCuO_2$, CuO and Y_2O_3 phases involved later in a crystallization process to achieve submicron sizes of Y_2BaCuO_5 inclusions

TSMG Top-Seeded Melt Growth; common method of constant-cooling crystallization of top-seeded ceramic samples

VGF Vertical-Gradient Freezing; rather rare method of constant-cooling solidification in a vertical temperature gradient

ZM (Joule Heat) Zone Melting; first simple method of directional solidification owing to the movement of a hot thermal zone along a sample

Acknowledgments

The authors express their sincere gratitude to Dr. S. Tanaka of SRL–ISTEC for his kind encouragement. The authors gratefully thank Dr. A. Endo for collecting and summarizing material for some parts of this chapter and Dr. X. Yao for critically reading the manuscript. The authors cordially appreciate assistance of Mrs. A. Nakayama and Mrs. A. Ueda. We would like to thank Dr. M. Kambara, O. Kusao, A. Oka, M. Egami and all other researchers of Div. IV of SRL–ISTEC for providing their results and helpful discussions, and Dr. J.G. Wen for TEM micrographs. Parts of the studies presented in this chapter were supported by New Energy and Industrial Technology Development Organization for the R&D Industrial Science and Technology Frontier Program.

References

Abbattista, F., D. Mazza and M. Vallino, 1991, Eur. J. Solid State Inorg. Chem. **28**, 649.

Agarwal, S.K., and A.V. Narlikar, 1994, Progr. Cryst. Growth Charact. Mater. **28**, 219.

Ahn, B.T., V.Y. Lee and R. Beyers, 1990, Physica C **167**, 529.

Aichele, T., S. Bornmann, C. Dubs and P. Gornert, 1997, Cryst. Res. Technol. **32**, 1145.

Aizu, K., 1970, Phys. Rev. B **2**, 754.

Akinaga, H., H. Katon and K. Takita, 1988, Jpn. J. Appl. Phys. **27**, L610.

Aleshina, N.N., L.M. Fisher and V.N. Lisitskii, 1996, J. Supercond. **9**, 535.

Andrianov, V.A., O.L. Anisimova and M.G. Kozin, 1990, Physica C **166**, 248.

Angadi, M.A., Z.X. Shen and A.D. Caplin, 1991, Physica C **185**, 2159.

Arnott, M., B.A. Glowasky and B. Soylu, 1993, IEEE Trans. Appl. Supercond. **3**, 1037.

Asaoka, H., H. Takei, Y. Iye, M. Tamura and M. Kinoshita, 1993, Jpn. J. Appl. Phys. **32**, 1091.

Asaoka, H., Y. Kazumata, H. Takei and K. Noda, 1996, Physica C **268**, 14.

Aselage, T., and K. Keefer, 1988, J. Mater. Res. **3**, 1279.

Assmus, W., and W. Schmidbauer, 1993, Supercond. Sci. Technol. **6**, 555.

Aswal, D.K., S.K. Gupta and S.C. Gadkari, 1995, Supercond. Sci. Technol. **8**, 710.

Aswal, D.K., M. Shinmura and Y. Hayakawa, 1998, J. Cryst. Growth **193**, 61.

Aswal, D.K., M. Shinmura and Y. Hayakawa, 1999a, J. Cryst. Growth **197**, 379.

Aswal, D.K., M. Shinmura and Y. Hayakawa, 1999b, J. Cryst. Growth **200**, 427.

Aswal, D.K., T. Mori and Y. Hayakawa, 2000, J. Cryst. Growth **208**, 350.

Auguste, F., N. Vandewalle, M. Ausloos and J. Macmanus-Driscoll, 1998, Appl. Supercond. **6**, 77.

Babu, T.G.N., and J. Koshi, 1997, J. Solid State Chem. **133**, 522.

Balestrino, G., S. Barbanera and G. Castellano, 1988, Mater. Res. Bull. **23**, 1119.

Balestrino, G., E. Milani, A. Paoletti and A. Tebano, 1994, Appl. Phys. Lett. **64**, 1735.

Batlogg, B.J., R. Buhrman, J.R. Clem, D. Gubser and D. Larbalestier, 1997, J. Supercond. **10**, 583.

Bauser, E., 1994, Atomic mechanisms in semiconductor liquid phase epitaxy, in: Handbook of Crystal Growth, Vol. 2b, ed. D.T.J. Hurle (North-Holland, Amsterdam) ch. 20, pp. 880–939.

Becht, M., 1996, Appl. Supercond. **4**, 465.

Becker, R., and W. Doring, 1935, Ann. Phys. **24**, 719.

Bednorz, J.G., and K.A. Müller, 1986, Z. Phys. B 64, 189.

Bennema, P., 1996, J. Cryst. Growth **166**, 17.

Bertrand, C., P. Galez, R.E. Gladyshevskii and J.L. Jorda, 1999, Physica C **321**, 151.

Beyers, R., and B.T. Ahn, 1991, Annu. Rev. Mater. Sci. **21**, 335.

Bieger, W., G. Krabbes and P. Schatzle, 1996, Physica C **257**, 46.

Bohm, J., A. Ludge and W. Schroder, 1994, Crystal growth by floating zone melting, in: Handbook of Crystal Growth, Vol. 2b, ed. D.T.J. Hurle (North-Holland, Amsterdam) ch. 4, pp. 215–250.

Bokshtein, B.S., S.Z. Bokshtein and A.A. Zhukhovitskii, 1973, Thermodynamics and kinetics of diffusion in solids (Metallurgiya Publishers, Moscow). Translated from Russian: 1985 (Amerind Publishing) 310 pp.

Boudene, A., K. Hack and A. Mohammad, 1996, High Temp. Mater. Sci. **35**, 159.

Brandstatter, G., A. Vostner and H.W. Weber, 1997, Physica C **282–287**, 2089.

Bredikhin, S.I., G.A. Emelchenko, V.Sh. Shechtman and A.A. Zhokhlov, 1991, Physica C **179**, 286.

Brosha, E.L., F.N. Garzon and I.D. Raistrick, 1995, J. Am. Ceram. Soc. **78**, 1745.

Burton, J.A., R.C. Prim and W.P. Slichter, 1953, J. Chem. Phys. **21**, 1987.

Burton, W.K., N. Cabrera and F.C. Frank, 1951, Philos. Trans. R. Soc. **A243**, 299.

Bykov, A.B., L.N. Demiannets and J.P. Zibrov, 1988, J. Cryst. Growth **91**, 302.

Cabre, R., J. Gavalda, J. Massons, R. Sole and X. Ruiz, 1998, Supercond. Sci. Technol. **11**, 30.

Cabrera, N., and M.M. Levine, 1956, Philos. Mag. **1**, 450.

Cao, G., X. Zhang, H. Song, Y. Zeng, Z. Jiao and Q. Zhang, 1998, J. Cryst. Growth **183**, 159.

Cardwell, D.A., 1998, Mater. Sci. Eng. B **53**, 1.

Casalta, H., P. Schleger, P. Harris and B. Lebech, 1996, Physica C **258**, 321.

Cava, R.J., 2000, J. Am. Ceram. Soc. **83**, 5.

Cava, R.J., A.W. Hewat, E.A. Hewat and B. Batlogg, 1990, Physica C **165**, 419.

Chan, W.C., D.S. Jwo, Y.F. Lin and Y. Huang, 1994, Physica C **230**, 349.

Chandrachood, M.R., K.K. Singh and D.E. Morris, 1995, Physica C **241**, 319.

Changkang, Ch., A.J.S. Chowdhury and H. Yongle, 1994, Supercond. Sci. Technol. **7**, 795.

Chauhan, H.S., A. Endo, M. Kambara, T. Umeda and Y. Shiohara, 1997, X-Ray absorption study of rare-earth doped Ba–Cu–O melt systems under elevated temperatures, in: Proc. ISS'96, Sapporo, Japan, eds S. Nakajima and M. Murakami, Vol. IX of Advances in Superconductivity (Springer, Tokyo) pp. 161–164.

Chen, C.K., 1992, Progr. Cryst. Growth Charact. Mater. **24**, 213.

Chen, C.K., 1998, Progr. Cryst. Growth Charact. Mater. **36**, 1.

Chen, C.K., A.T. Boothroyd and Y.L. Hu, 1993, Physica C **214**, 231.

Chen, L., Y.T. Qian and D.M. Sun, 1988, Physica C **153–155**, 409.

Chen, T.G., S. Li, W. Gao and Z. Xianyu, 1998, Supercond Sci. Technol. **11**, 1193.

Cheronov, A.A., and T. Nishinaga, 1987, Growth shapes and their stability at anisotropic interface kinetics: theoretical aspects for solution growth, in: Morphology of Crystals, ed. I. Sunagawa (Terrapub, Tokyo) ch. 3, pp. 207–267.

Chikumoto, N., N. Hayashi, H. Kojo, T. Egi, T. Machi, N. Koshizuka and M. Murakami, 1997a, High-pressure oxygenation studies in melt-textured Sm123 and Nd123 superconductors, in: Proc. ISS'96, Sapporo, Japan, eds S. Nakajima and M. Murakami, Vol. IX of Advances in Superconductivity (Springer, Tokyo) pp. 531–534.

Chikumoto, N., J. Yoshioka and M. Murakami, 1997b, Physica C **291**, 79.

Chikumoto, N., J. Yoshioka, M. Otsuka, N. Hayashi and M. Murakami, 1997c, Physica C **281**, 253.

Chodorowiczbak, A., E. Hodorowicz and A. Hodorowicz, 1995, Cryst. Res. Technol. **30**, 63.

Christensen, A.N., A.A. Zhokhov and S. Grundvig, 1996, Acta Chem. Scand. **50**, 979.

Chunlin, J., F. Zhanguo, Z. Guofan and Z. Guiyi, 1991, Supercond. Sci. Technol. **4**, 49.

Cima, M.J., M.C. Flemings and A.M. Figueredo, 1992, J. Appl. Phys. **72**, 179.

Claus, H., U. Gebhard, G. Linker and K. Rohberg, 1992, Physica C **200**, 271.

Claus, J., G. Borchardt, S. Weber and S. Scherrer, 1998, Z. Phys. Chem. **206**, 49.

Cochran, W.G., 1934, Proc. Cambridge Philos. Soc. **30**, 365.

Coriell, S.R., A.A. Chernov, B.T. Murray and G.B. McFadden, 1998, J. Cryst. Growth **183**, 669.

Crossley, A.L., Y.H. Li, A.D. Caplin and J.L. MacMannus-Driscoll, 1999, Physica C **314**, 12.

Czerwonka, J., and H.A. Eick, 1991, J. Solid State Chem. **90**, 69.

Dabrowski, B., 1998, Supercond. Sci Technol. **11**, 54.

Damento, M.A., K.A. Gschneidner Jr and R.W. McCallum, 1987, Appl. Phys. Lett. **51**, 690.

Danilewsky, A.N., Y. Okamoto, T. Nishinaga and K.W. Benz, 1995, J. Cryst. Growth **146**, 171.

D'Anna, G., M.V. Indenbom, M.O. Andre and W. Benoit, 1994, Europhys. Lett. **25**, 225.

Darlington, C.N.W., D.A.O. Connor and C.A. Hollin, 1988, J. Cryst. Growth **91**, 308.

Dash, S., D.D. Sood and R. Prasad, 1996, J. Nucl. Mater. **228**, 83.

de Fontaine, D., G. Ceder and M. Asta, 1990, Nature **343**, 544.

Degterov, S.A., and G.F. Voronin, 1991, Physica C **178**, 213.

Dembinski, D., M. Gervais, P. Odier and J.P. Coutures, 1990, J. Less-Common Met. **164–165**, 177.

Demyanets, L.N., 1991, Usp. Fiz. Nauk **161**, 71.

Desgardin, G., I. Monot and B. Raveau, 1999, Supercond. Sci. Technol. **12**, R115.

Diko, P., 1998a, Supercond. Sci. Technol. **11**, 68.

Diko, P., 1998b, Mater. Sci. Eng. B **53**, 149.

Dimesso, L., M. Marchetta, G. Calestani and A. Migliori, 1997, Supercond. Sci. Technol. **10**, 347.

Domengès, B., M. Hervieu and C. Michel, 1987, Europhys. Lett. **4**, 211.

Dreysse, H., and R. Riedinger, 1987, J. Phys. France **48**, 915.

Dubs, C., S. Bornmann, M. Schmelz, T. Schuler and F. Sandiumenge, 1996, J. Cryst. Growth **166**, 836.

Dupret, F., and N. Van Den Bogaert, 1994, Modelling Bridgman and Czochralski growth, in: Handbook of Crystal Growth, Vol. 2b, ed. D.T.J. Hurle (North-Holland, Amsterdam) ch. 15, pp. 877–1010.

Dyakonov, V., I. Fita and N. Doroshenko, 1997, Physica C **276**, 245.

Dzhafarov, T.D., 1996, Phys. Status Solidi (a) **158**, 335.

Egami, M., and Y. Shiohara, 1997, Physica C **282**, 463.

Egami, M., K. Kuwahara and Y. Shiohara, 1997, Appl. Supercond. **5**, 61.

Egi, T., J.G. Wen, K. Kuroda, H. Unoki and K. Koshizuka, 1995, Appl. Phys. Lett. **16**, 2406.

Egi, T., J.G. Wen, K. Kuroda, H. Mori, H. Unoki and N. Koshizuka, 1996, Physica C **270**, 223.

Elschner, S., W. Becker, H. Bestgen and M. Brand, 1992, Physica C **202**, 401.

Elwell, D., and H.J. Scheel, 1975, Crystal Growth from High-Temperature Solutions (Academic Press, New York).

Emelchenko, G.A., N.V. Abrosimov and A.V. Bazhenov, 1991, IEEE Trans. Magn. **27**, 1146.

Emelchenko, G.A., A.A. Zhokhov and I.G. Naumenko, 1994, Supercond. Sci. Technol. **7**, 541.

Endo, A., H.S. Chauhan, Y. Nakamura and Y. Shiohara, 1996, J. Mater. Res. **11**, 1114.

Erb, A., T. Biernath and G. Müller-Vogt, 1993, J. Cryst. Growth **132**, 389.

Erb, A., E. Walker and R. Flukiger, 1995, Physica C **245**, 245.

Erb, A., B. Greb and G. Muller-Vogt, 1996a, Physica C **259**, 83.

Erb, A., E. Walker and R. Flukiger, 1996b, Physica C **258**, 9.

Erb, A., E. Walker, J.-Y. Genoud and R. Flukiger, 1997, Physica C **282–287**, 89.

Figueredo, A.M., M.J. Cima, M.C. Flemings and J.S. Haggerty, 1995, Physica C **241**, 92.

Fiory, A.T., S. Martin, F. Schneemeyer, R.M. Fleming and A.E. White, 1988, Phys. Rev. B **38**, 7129.

Fischer, K., R. Hergt and D. Linzen, 1988, Cryst. Res. Technol. **23**, 1169.

Fischer, K., N.M. Chebotarev and S. Naumov, 1993, J. Cryst. Growth **132**, 444.

Flemings, M.C., 1974, Solidification Processing (McGraw-Hill, New York) p. 290.

Flewitt, D.E.J., and R.K. Wild, 1994, Physical Methods for Materials Characterisation (Institute of Physics, Bristol) 517 pp.

Folkerts, T.Y., P. Klavins and R.N. Shelton, 1988, Physica C **153–155**, 417.

Fomichev, D.V., O.G. Dyachenko, A.V. Mironov and E.V. Antipov, 1994, Physica C **225**, 25.

Frank, F.C., 1949, Disc. Faraday Soc. **5**, 48.

Fraze, K.G., and D.R. Clarke, 1987, Adv. Ceram. Mater. **2**, 295.

Freyhardt, H.C., J. Hoffmann, J. Wiesmann and J. Dzick, 1996, Appl. Supercond. **4**, 435.

Frieling, T., J. Kowalewski and W. Assmus, 1993, J. Alloys & Compounds **195**, 7.

Fueki, K., Y. Idemoto and H. Ishizuka, 1990, Physica C **166**, 261.

Fujihara, S., N. Yoshida and T. Kimura, 1997, Physica C **276**, 69.

Furuya, K., Y. Nakamura, T. Izumi and Y. Shiohara, 1994, Effect of Ag addition on unidirectional solidification processing of YBCO superconducting oxides, in: Proc. ISS'93, Hiroshima, Japan, eds T. Fujita and Y. Shiohara, Vol. VI of Advances in Superconductivity (Springer, Tokyo) pp. 795–798.

Gatos, H.C., 1982, Semiconductor crystal growth and segregation problems on Earth and in Space, in: Materials Processing in the Reduced Gravity Environment of Space, Proc. MRS Annual Meeting, November 1981, Boston, USA, Vol. 9, ed. G.E. Rindone (North-Holland, New York) pp. 355–371.

Gencer, F., and J.S. Abell, 1991, J. Cryst. Growth **112**, 337.

Genoud, J.-Y., A. Erb, B. Revaz and A. Junod, 1997, Physica C **282–287**, 457.

Gong, S., D. Shi, G. Zhou, C. Cai, Y. Fu and H. Zhang, 1997, Physica C **282–287**, 469.

Goodilin, E.A., D.B. Kvartalov, N.N. Oleynikov and Y.D. Tretyakov, 1994, Physica C **235–240**, 449.

Goodilin, E.A., N.N. Oleynikov, G.Yu. Popov and V.A. Shpanchenko, 1996, Physica C **272**, 65.

Goodilin, E.A., M. Kambara, T. Umeda and Y. Shiohara, 1997a, Physica C, **289**, 37.

Goodilin, E.A., M. Kambara, T. Umeda and Y. Shiohara, 1997b, Physica C, **289**, 251.

Goodilin, E.A., M. Limonov, A. Panfilov, N. Khasanova and A. Oka, 1998a, Physica C **300**, 250.

Goodilin, E.A., A. Oka, J.G. Wen, M. Kambara, T. Umeda and Y. Shiohara, 1998b, Physica C **299**, 279.

Goodilin, E.A., F. Saba, Y. Enomoto and Y. Shiohara, 1998c, Characterisation and possible applications of the $Nd_2Ba_1Cu_3O_z$ phase, in: Proc. ISS'97, Gifu, Japan, eds K. Osamura and I. Hirabayashi, Vol. X of Advances in Superconductivity (Springer, Tokyo) pp. 717–720.

Goodilin, E.A., N. Khasanova, X.J. Wu, T. Kamiyama, F. Izumi, S. Tajima and Y. Shiohara, 1999, Phase diagram and structure-related studies of the Nd-rich $Nd_{1+x}Ba_{2-x}Cu_3O_z$ solid solution, in: High-Temperature Superconductors and Novel Inorganic Materials, eds G. Van Tendeloo, E.V. Antipov and S.N. Putilin (Kluwer Academic Publishers, Dordrecht) pp. 145–150.

Goodilin, E.A., A.P. Soloshenko, V.V. Lennikov and A.V. Knot'ko, 2000, Zh. Neorg. Khim. [Russ. J. Inorg. Chem.] **45**, 917.

Gordeev, S.N., W. Jahn, A.A. Zhukov, H. Kupfer and T. Wolf, 1994, Phys. Rev. B **49**, 15420.

Gornert, P., 1997, Cryst. Res. Technol. **32**, 7.

Goyal, A., K.B. Alexander, D.M. Kroeger and P.D. Funkenbusch, 1993, Physica C **210**, 197.

Goyal, A., D.P. Norton, D.K. Christen and E.D. Specht, 1996, Appl. Supercond. 4, 403.

Goyal, A., D.P. Norton, D.M. Kroeger and D.K. Christen, 1997, J. Mater. Res. **12**, 2924.

Graf, T., G. Triscone and J. Muller, 1990, J. Less-Common Met. **159**, 349.

Grevin, B., Y. Berthier, P. Mendels and G. Collin, 2000, Phys. Rev. B **61**, 4334.

Grigorashev, D.I., E.A. Trofimenko and N.N. Oleynikov, 1997, Inst. Phys. Conf. Ser. **158**, 929.

Gu, G.D., K. Takamuku, N. Koshizuka and S. Tanaka, 1993, J. Cryst. Growth **130**, 325.

Gu, G.D., T. Egi and N. Koshizuka, 1996, Physica C **263**, 180.

Gudilin, E.A., N.N. Oleynikov and S.R. Lee, 1994, Zh. Neorg. Khim. **39**, 1043.

Gudilin, E.A., N.N. Oleynikov, G.Y. Popov and Y.D. Tretyakov, 1995, Inorg. Mater. **31**, 1255.

Guo, J., D.E. Ellis, E.E. Alp and G.L. Goodman, 1990, Phys. Rev. B **42**, 251.

Gupta, S.K., D.K. Aswal, J.C. Vyas and V.C. Sahni, 1998, Physica C **303**, 151.

Hasegawa, K., K. Fujino, H. Mukai and M. Konishi, 1996, Appl. Supercond. **4**, 487.

Hattori, O., T. Koyama and Y. Shiohara, 1997, Fabrication of $NdBa_2Cu_3O_{7-\delta}$ single crystals by the SRL-CP method, in: Proc. ISS'97, Gifu, Japan, eds K. Osamura and I. Hirabayashi, Vol. X of Advances in Superconductivity (Springer, Tokyo) pp. 713–716.

Hauck, J., K. Bickmann and K. Mika, 1998, Supercond. Sci. Technol. **11**, 63.

Hauff, R., V. Breit, H. Claus and D. Herrmann, 1994, Physica C **235–240**, 1953.

Hayashi, K., M. Tokumoto and K. Takanashi, 1988a, Jpn. J. Appl. Phys. **27**, L1646.

Hayashi, S., T. Ohno and T. Inoue, 1988b, J. Cryst. Growth **91**, 331.

Hellebrand, B., X.Z. Wang, D. Bauerle and M. Guillaume, 1996, Physica C **261**, 97.

Hermann, A.M., and Z.Z. Sheng, 1987, Appl. Phys. Lett. **51**, 1854.

Herrmann, H.J., 1986, Phys. Rep. **136**, 153.

Hesselbarth, H.W., and I.R. Gobel, 1991, Acta Metall. Mater. **39**, 2135.

Hidaka, Y., and M. Suzuki, 1991, Progr. Cryst. Growth Charact. Mater. **23**, 179.

Higuchi, T., S.I. Yoo and M. Murakami, 1998, Supercond. Sci. Technol. **11**, 138.

Higuchi, T., S.I. Yoo and M. Murakami, 1999, Phys. Rev. B **59**, 1514.

Hilscher, G., T. Holubar, G. Schaudy and J. Dumschat, 1994, Physica C **224**, 330.

Hirayama, T., Y. Ikuhara, M. Nakamura, Y. Yamada and Y. Shiohara, 1997, J. Mater. Res. **12**, 293.

Hiroi, Z., I. Chong and M. Takano, 1998, J. Solid State Chem. **138**, 98.

Hodorowicz, S.A., J. Czerwonka and H.A. Eick, 1990, J. Solid State Chem. **88**, 391.

Holtzberg, F., P. Strobel and T.K. Worthington, 1988, J. Magn. Magn. Mater. **76&77**, 626.

Hu, A.M., Z.X. Zhao, W. Gawalek, M. Wu and T. Strasser, 1997, Physica C **282–287**, 431.

Hu, S., H. Hojaji and A. Barkatt, 1992, J. Mater. Res. **7**, 808.

Hunt, R.D., E.C. Beahm and G.F. Voronin, 1998, Physica C **302**, 130.

Hunter, B.A., S.L. Town and D.N. Matthews, 1991, Austr. J. Physics **44**, 421.

Hurle, D.T.J., and B. Cockayne, 1994, Czochralski growth, in: Handbook of Crystal Growth, Vol. 2b, ed. D.T.J. Hurle (North-Holland, Amsterdam) ch. 3, pp. 101–211.

Hurle, D.T.J., and R.W. Series, 1994, Use of a magnetic field in melt growth, in: Handbook of Crystal Growth, Vol. 2b, ed. D.T.J. Hurle (North-Holland, Amsterdam) ch. 5, pp. 261–285.

Hyun, O.B., M. Yoshida, T. Kitamura and I. Hirabayashi, 1996, Physica C **258**, 365.

Idemoto, Y., and K. Fueki, 1990, Jpn. J. Appl. Phys. **29**, 2729.

Ignatiev, A., P.C. Chou, Q. Zhong, X. Zhang and Y.M. Chen, 1996, Appl. Supercond. **4**, 455.

Iijima, Y., M. Hosaka, N. Tanabe and N. Sadakata, 1996, Appl. Supercond. **4**, 475.

Ikuta, H., S. Ikeda, A. Mase and M. Yoshikawa, 1998, Appl. Supercond. **6**, 109.

Imagawa, Y., and Y. Shiohara, 1996, Physica C **262**, 243.

Imagawa, Y., K. Kakimoto and Y. Shiohara, 1997, Physica C **280**, 245.

Indenbom, M.V., N.N. Kolesnikov, M.P. Kulakov and I.G. Naumenko, 1990, Physica C **166**, 486.

Ishida, Y., T. Kimura, K. Kakimoto and Y. Yamada, 1997, Physica C **292**, 264.

Iwata, T., 1988, J. Cryst. Growth **91**, 274.

Iwata, T., M. Hikita and S. Tsurumi, 1989, New experimental results concerning the difference between various T_cs of $LnBa_2Cu_3O_{7-\delta}$ (Ln = Lanthanide), in: Advances in Superconductivity, Proc. ISS'88, Nagoya, Japan, eds K. Kitazawa and T. Ishiguro (Springer, Tokyo) p. 197.

Izumi, F., and E. Takayama-Muromachi, 1995, Crystal structures and phase equilibria, in: High-Temperature Superconducting Materials Science and Engineering. New Concepts and Technology, ed. D. Shi (Pergamon Press, Oxford) pp. 81–130.

Izumi, F., S. Takekawa and Y. Matsui, 1987, Jpn. J. Appl. Phys. **26**, L1616.

Izumi, T., and Y. Shiohara, 1992, J. Mater. Res. **7**, 16.

Izumi, T., Y. Nakamura and Y. Shiohara, 1993, J. Cryst. Growth **128**, 757.

Jackson, K.A., D.R. Uhlmann and J.D. Hunt, 1967, J. Cryst. Growth **1**, 1.

Jang, W.J., H. Mori, M. Watahiki and S. Tajima, 1996, J. Solid State Chem. **122,** 371.

Jayavel, R., A. Thamizhavel, P. Murugakoothan and C.R.V. Rao, 1994, J. Cryst. Growth **137**, 273.

Jin, S., G.W. Kammlott, S. Nakahara, T.H. Tiefel and J.E. Graebner, 1991, Science **253**, 427.

Jorgensen, J.D., H. Shaked, D.G. Hinks and B. Dabrowski, 1988, Physica C **155**, 578.

Jorgensen, J.D., B.W. Veal, A.P. Paulikas and L.J. Nowicki, 1990, Phys. Rev. B **41**, 1863.

Jose, R., A.M. John, J. Kurian, P.K. Sajith and J. Koshy, 1997, J. Mater. Res. **12**, 2976.

Kaiser, D.L., F. Holtzberg, M.F. Chisholm and T.K. Worthington, 1987, J. Cryst. Growth **85**, 593.

Kakimoto, K., and Y. Shiohara, 1996, Appl. Supercond. **4**, 519.

Kakimoto, K., Y. Sugawara, T. Izumi and Y. Shiohara, 2000, Physica C **334**, 249.

Kambara, M., H.S. Chauhan, A. Endo, Y. Shiohara and T. Umeda, 1997a, Physica C **282–287**, 447.

Kambara, M., K. Miyake, K. Murata, Y. Shiohara and T. Umeda, 1997b, Microstructural control of Nd123 bulk superconductors by initial compositions, Proc. of ISS'97, Gifu, Japan, eds K. Osamura and I. Hirabayashi, Vol. X of Advances in Superconductivity (Springer, Tokyo) pp. 729–732.

Kambara, M., M. Nakamura, Y. Shiohara and T. Umeda, 1997c, Physica C **275**, 127.

Kambara, M., Y. Watanabe, K. Miyake, A. Endo and K. Murata, 1997d, J. Mater. Res. **12**, 2873.

Kambara, M., X. Yao, M. Nakamura, Y. Shiohara and T. Umeda, 1997e, J. Mater. Res. **12**, 2866.

Kambara, M., M. Tagami, X. Yao, E.A. Goodilin and Y. Shiohara, 1998, J. Am. Ceram. Soc. **81**, 2116.

Kambara, M., K. Miyake, K. Murata and T. Izumi, 2000, Physica C **330**, 191.

Kanamori, Y., and Y. Shiohara, 1996, J. Mater. Res. **11**, 2693.

Kanamori, Y., K. Ohtsu, S. Koyama, Y. Yamada and Y. Shiohara, 1994, Fabrication of large $YBa_2Cu_3O_{7-\delta}$ single crystals by crystal pulling method, in: Proc. ISS'93, Hiroshima, Japan, eds T. Fujita and Y. Shiohara, Vol. VI of Advances in Superconductivity (Springer, Tokyo) pp. 783–786.

Karen, P., H. Fjellvåg and A. Kjekshus, 1991, J. Solid State Chem. **92**, 57.

Karen, P., O. Braaten and A. Kjekshus, 1992, Acta Chem. Scand. **52**, 805.

Karpinski, J., C. Beeli and E. Kaldis, 1988a, Physica C **153–155**, 830.

Karpinski, J., E. Kaldis, E. Jilek, S. Rusiecki and B. Bucher, 1988b, Nature **336**, 660.

Karpinski, J., E. Kaldis and S. Rusiecki, 1989, J. Less-Common Met. **150**, 207.

Karpinski, J., H. Schwer, E. Kopnin, R. Molinski and G.I. Meijer, 1997a, Physica C **282–287**, 77.

Karpinski, J., H. Schwer, K. Conder and G.I. Meijer, 1997b, Solid State Ionics **101**, 985.

Karpinski, J., G.I. Meijer and H. Schwer, 1999, Supercond. Sci. Technol. **12**, R153.

Katsui, A., 1987, Jpn. J. Appl. Phys. **26**, L1521.

Kattner, U.R., 1997, J. Met. **12**, 14.

Kawabata, S., H. Hoshizaki, N. Kawahara and H. Enami, 1990, Jpn. J. Appl. Phys. **29**, L1490.

Kawano, M., K. Fujinami and H. Suematsu, 1998, Mater. Sci. Eng. B **54**, 123.

Kemnitz, E., A.A. Galkin, T. Olesch and S. Scheurell, 1997, J. Therm. Anal. **48**, 997.

Kim, C.-J., and G.W. Hong, 1999, Supercond Sci. Technol. **12**, R27.

Kim, C.-J., K.-B. Kim, I.-H. Kuk and C.-W. Hong, 1997, Physica C **281**, 244.

Kim, C.C., E.F. Skelton and M.S. Osofsky, 1993, Phys. Rev. B **48**, 6431.

Kim, J.-S., and D.R. Gaskell, 1994, J. Am. Ceram. Soc. **77**, 753.

Kim, J.T., J. Giapintzakis and D.M. Ginsberg, 1996, J. Supercond. **9**, 481.

Kimura, S., R. Shimpo and Y. Nakamura, 1992, J. Jpn. Inst. Met. **56**, 1145.

Kimura, T., Y. Ishida and Y. Shiohara, 1997, Fabrication of $YbBa_2Cu_3O_{7-\delta}$ films by LPE, in: Ext. Abstr. Book of IWS'97, Hawaii, USA, p. 309–310.

Kitamura, T., Y. Yamada, Y. Shiohara, I. Hirabayashi and S. Tanaka, 1996, J. Cryst. Growth **166**, 854.

Kitamura, T., S. Taniguchi, Y. Sugawara, Y. Ikuhara and I. Hirabayashi, 1997, Pinning effect of misfit dislocations in $YBa_2Cu_3O_{7-\delta}$ superconducting film by liquid phase epitaxy, in: Proc. ISS'96, Sapporo, Japan, eds S. Nakajima and M. Murakami, Vol. IX of Advances in Superconductivity (Springer, Tokyo) pp. 737–740.

Klein, L., E.R. Yacoby, Y. Yeshurun and A. Erb, 1994, Phys. Rev. B **49**, 4403.

Klemenz, C., and H.J. Scheel, 1993, J. Cryst. Growth **129**, 421.

Klemenz, C., and H.J. Scheel, 1996, Physica C **265**, 126.

Klemenz, C., and H.J. Scheel, 1999a, J. Cryst. Growth **200**, 435.

Klemenz, C., and H.J. Scheel, 1999b, J. Cryst. Growth **203**, 534.

Klester, K.L., 1988, J. Cryst. Growth **91**, 295.

Klibanow, D., K. Sujata and T.O. Mason, 1988, J. Am. Ceram. Soc. **71**, C-267.

Koblischka, M.R., A.J.J. Dalen, T. Higuchi, S.I. Yoo and M. Murakami, 1998, Phys. Rev. B **58**, 2863.

Kogachi, M., K. Nakahigashi, S. Minamigawa and S. Nakanishi, 1990, Jpn. J. Appl. Phys. **29**, L911.

Kohayashi, S., S. Yoshizawa and H. Miyairi, 1998, Mater. Sci. Eng. B **53**, 70.

Komatsu, H., S. Hayashi and T. Inoue, 1988, Power & Power Met. **35**, 313.

Konishi, M., and Y. Enomoto, 1995, Jpn. J. Appl. Phys. **34**, L1271.

Konishi, M., J.G. Wen, Y. Matsunaga and Y. Enomoto, 1997, J. Cryst. Growth **179**, 451.

Kossel, W., 1927, Naturwissenschaften **18**, 901.

Kovacik, V., V.V. Moschalkov and V.N. Nikiforov, 1991, Physica C **185**, 1263.

Kowalewski, J., D. Nikl and W. Assmus, 1988, Physica C **153–155**, 429.

Krabbes, G., W. Bieger and U. Wiesner, 1994, J. Electron. Mater. **23**, 1135.

Krabbes, G., P. Schatzle and W. Bieger, 1995, Physica C **244**, 145.

Krabbes, G., W. Bieger, P. Schatzle and U. Wiesner, 1998, Supercond. Sci. Technol. **11**, 144.

Kramer, M., S.I. Yoo, R.W. McCallum, W.B. Yelon and H. Xie, 1994b, Physica C **219**, 145.

Kramer, M.J., A. Karion and K.W. Dennis, 1994a, J. Electronic Mater. **23**, 1117.

Krauns, C., B. Bringmann, C. Brandt and M. Ullrich, 1997, Appl. Supercond. **1–2**, 833.

Krauns, Ch., M. Sumida, M. Tagami, Y. Yamada and Y. Shiohara, 1994a, Z. Phys. B **96**, 207.

Krauns, Ch., M. Tagami, Y. Yamada, M. Nakamura and Y. Shiohara, 1994b, J. Mater. Res. **9**, 1513.

Kruger, Ch., K. Conder, H. Schwer and E. Kaldis, 1997, J. Solid State Chem. **134**, 356.

Kupfer, H., A.A. Zhukov, A. Will and W. Jahn, 1996, Phys. Rev. B **54**, 644.

Kuroda, K., I.H. Choi, T. Egi, H. Unoki and N. Koshizuka, 1996, $NdBa_2Cu_3O_{7-\delta}$ single crystals grown by the Travelling Solvent Floating Zone Method, in: Proc. ISS'95, Hamamatsu, Japan, eds H. Hayakawa and Y. Enomoto, Vol. VIII of Advances in Superconductivity (Springer, Tokyo) pp. 329–332.

Kuroda, K., K. Itoi, J. Okano, S. Segawa, K. Abe and I. Choi, 1997a, Jpn. J. Appl. Phys. **36**, 6730.

Kuroda, K., K. Abe, S. Segawa, J.G. Wen, H. Unoki and N. Koshizuka, 1997b, Physica C **275**, 311.

Kuroda, K., T. Kamiyama, K. Oikawa and Y. Yamada, 2000, Jpn. J. Appl. Phys. **39**, 41.

Kusao, T., M. Egami, S. Koyama and Y. Shiohara, 1997, Appl. Supercond. **5**, 71.

Kutami, H., Y. Yamada, H. Mori, W.J. Jang and M. Nakamura, 1996, Physica C **262**, 173.

Kutami, H., Y. Yamada, S. Koyama, Z. Nakagawa and Y. Shiohara, 1997, Preparation of twin-free $YBa_2Cu_3O_{7-\delta}$ crystal without twin formation, in: Proc. ISS'96, Sapporo, Japan, eds S. Nakajima and M. Murakami, Vol. IX of Advances in Superconductivity (Springer, Tokyo) pp. 689–692.

LaGraff, J.R., and D.A. Payne, 1993, Physica C **212**, 470.

Lamberti, V.E., M.A. Rodrigues, J.D. Trybulski and A. Navrotskiy, 1996, J. Mater. Res. **11**, 1061.

Lamberti, V.E., M.A. Rodriguez, J.D. Trybulski and A. Navrotsky, 1997, Chem. Mater. **9**, 932.

Larbalestier, D., 1991, Phys. Today **6**, 74.

Lay, K.W., and G.M. Renlund, 1990, J. Am. Ceram. Soc. **73**, 1208.

Lee, B.J., and D.N. Lee, 1989, J. Am. Ceram. Soc. **72**, 314.

Lee, B.J., and D.N. Lee, 1991, J. Am. Ceram. Soc. **72**, 78.

Lee, S., T. Akao, H. Suematsu, H. Yamauchi and N.P. Kiryakov, 1998a, Appl. Phys. Lett. **73**, 3586.

Lee, S., N.P. Kiryakov, D.A. Emelyanov and M.S. Kuznetsov, 1998b, Physica C **305**, 57.

Leonyuk, L., G.J. Babonas and A. Vetkin, 1994, Supercond. Sci. Technol. 7, 573.

Leonyuk, L., A. Arakcheeva and G.J. Babonas, 1995, Supercond. Sci. Technol. **8**, 540.

Li, S., A. Hayri, K.V. Ramanujachary and M. Greenblatt, 1988, Phys. Rev. B **38**, 2450.

Li, Y., X. Yao and K. Tanabe, 1998, Physica C **304**, 239.

Liang, R., P. Dosanjh, D.A. Bonn, D.J. Baar and J.F. Carolan, 1992, Physica C **195**, 51.

Liang, R.X., D.A. Bonn and W.N. Hardy, 1998, Physica C **304**, 105.

Licci, F., P. Tissot and H.J. Scheel, 1989, J. Less-Common Met. **150**, 21.

Limonov, M., E.A. Goodilin, X. Yao, S. Tajima and Y. Shiohara, 1998, Phys. Rev. B **58**, 12368.

Lin, C.T., 1994, J. Cryst. Growth **143**, 110.

Lin, C.T., and W.Y. Liang, 1994, Physica C **225**, 275.

Lin, C.T., W. Zhou and W.Y. Liang, 1992, Physica C **195**, 291.

Lin, C.T., J. Chrosch, Y. Yan, W.Y. Liang and E.K.H. Salje, 1995, Physica C **242**, 105.

Lin, C.T., A.M. Niraimathi, Y. Yan, K. Peters and H. Bender, 1996, Physica C **272**, 285.

Lin, C.T., E. Schonherr and K. Peters, 1997, Physica C **282–287**, 491.

Lin, J.G., C. Huang, Y.Y. Xue, C.W. Chu, X.W. Cao and J.C. Ho, 1995, Phys. Rev. B **51**, 12900.

Lindemer, T.B., and E.D. Specht, 1996, Physica C **268**, 271.

Lindemer, T.B., J.F. Hunley and J.E. Gates, 1989, J. Am. Ceram. Soc. **72**, 1775.

Lindemer, T.B., E.D. Specht, C.S. MacDougal and G.M. Taylor, 1993, Physica C **216**, 99.

Lindemer, T.B., B.C. Chakoumakos, E.D. Specht and R.K. Williams, 1994, Physica C **231**, 80.

Lindemer, T.B., E.D. Specht, P.M. Martin and M.L. Flitcroft, 1995, Physica C **255**, 65.

Lister, S.J.S., A.T. Boothroyd and N.H. Andersen, 2000, Physica B **276**, 799.

Liu, X.Y., and P. Bennema, 1996, J. Cryst. Growth **166**, 117.

Lo, W., D.A. Cardwell, C.D. Dewhurst and H.-T. Leung, 1997, J. Mater. Res. **12**, 2888.

Lo, W., D.A. Cardwell and J.C.L. Chow, 1998, J. Mater. Res. **13**, 2035.

Loh, R., 1998, Ceram. Intl. **24**, 559.

Loram, J.W., J.R. Cooper and K.A. Mirza, 1991, Supercond. Sci. Technol. **4**, S391.

Lowe-Ma, C.K., and T.A. Vanderah, 1992, Physica C **201**, 233.

Lozanne, A., 1999, Supercond. Sci. Technol. **12**, R43.

Luce, J.L., and A.M. Stacy, 1997, Chem. Mater. **9**, 1508.

Luo, H.M., B.N. Lin, Y.H. Lin and H.C. Chiang, 2000, Phys. Rev. B **61**, 14825.

Luszczek, M., W. Sadowski, T. Klimczuk and J. Olchowik, 1999, Physica C **322**, 57.

Lutgemeier, H., S. Schmenn, P. Meuffels and O. Storz, 1996, Physica C **267**, 191.

MacManus-Driscoll, J.L., 1997, Adv. Mater. **9**, 457.

MacManus-Driscoll, J.L., 1998, Annu. Rev. Mater. Sci. **28**, 421.

Maeda, M., M. Kadoi and T. Ikeda, 1989, Jpn. J. Appl. Phys. **28**, 1417.

Magnone, E., M. Ferretti and G.L. Olcese, 1994, Nuovo Cim. D **16**, 1679.

Makarova, N.G., A.N. Nikolaevskij, A.V. Beluj, T.M. Dmitruk and O.P. Kniga, 1996, Physical-chemical aspects of the $YBa_2Cu_3O_z$ single crystal solution-melt growth, preprint DonGU-96-1 (Donetsk State University, Donetsk, Ukraine) 42 pp.

Maljuk, A.N., A.B. Kulakov and G.A. Emel'chenko, 1995, J. Cryst. Growth **151**, 102.

Maljuk, A.N., G.A. Emel'chenko and A.V. Kosenko, 1996, J. Alloys & Compounds **234**, 52.

Manthiram, A., X.X. Tang and J.B. Goodenough, 1990, Phys. Rev. B **42**, 138.

Maple, M.B., B.W. Lee, J.J. Neumeier and G. Nieva, 1992, J. Alloys & Compounds **181**, 135.

Marella, M., B. Molinas and B.B. Fabris, 1994, J. Mater. Sci. **29**, 3497.

Marinel, S., J. Provost and G. Desgardin, 1998, Physica C **294**, 129.

Marti, W., F. Altorfer, P. Fisher and H.J. Scheel, 1993, Physica C **206**, 158.

Martin, A.A., T. Ruf, T. Strach, M. Cardona and T. Wolf, 1998, Phys. Rev. B **58**, 14349.

Matsukawa, M., T. Mizukoshi, K. Noto and Y. Shiohara, 1996, Phys. Rev. B **53**, R6034.

Matsushita, Y., M. Hasegawa and F. Sakai, 1995, Jpn. J. Appl. Phys. **34**, L1263.

McCallum, R.W., 1989, J. Met. **41**, 50.

McGinn, P.J., W. Chen, N. Zhu and U. Balachadran, 1990, Physica C **165**, 480.

Mersmann, A., and K. Bartosch, 1998, J. Cryst. Growth **183**, 240.

Merz, M., N. Nucker and E. Pellegrin, 1996, J. Low Temp. Phys. **105**, 347.

Mesot, J., and A. Furrer, 1997, J. Supercond. **10**, 623.

Mimura, T., I. Terasaki, K. Tomimoto and S. Tajima, 1998, Physica C **300**, 212.

Moeckly, B.H., S.E. Russek, D.K. Lathrop and R.A. Buhrman, 1990, Appl. Phys. Lett. **57**, 1687.

Moolenaar, A.A., P.C.M. Gubbens and J.J. van Loef, 1996, Physica C **267**, 279.

Morawski, A., T. Lada, A. Paszewin and K. Przybylski, 1998, Supercond. Sci. Technol. **11**, 193.

Mori, N., H. Hata and K. Ogi, 1992, J. Jpn. Inst. Met. **6**, 648.

Mozhaev, A.P., and S.V. Chernyaev, 1994, J. Mater. Chem. **4**, 1107.

Mozhaev, A.P., G.N. Mazo, A.A. Galkin and N.V. Khramova, 1996, Zh. Neorg. Khim. **41**, 916.

Muller, D., and H.C. Freyhardt, 1995, Physica C **242**,283.

Muller, G., and A. Osrogorsky, 1994, Convection in melt growth, in: Handbook of Crystal Growth, Vol. 2b, ed. D.T.J. Hurle (North-Holland, Amsterdam) ch. 13, pp. 711–819.

Murakami, M., 1992, Melt Processed High-Temperature Superconductors (World Scientific, Singapore) 650 pp.

Murakami, M., N. Sakai, T. Higuchi and S.I. Yoo, 1996, Supercond. Sci. Technol. **9**, 1015.

Muroi, M., and R. Street, 1999, Physica C **314**, 172.

Murugaraj, P., A. Rabenau and J. Maier, 1990, Solid State Ionics **43**, 113.

Nagashima, K., N. Hayashi and S.I. Yoo, 1998, Mater. Sci. Eng. B **53**, 164.

Nagashio, K., Y. Takamura, K. Kuribayashi and Y. Shiohara, 1999, J. Cryst. Growth **200**, 118.

Nagaya, S., M. Miyajima, I. Hirabayashi, Y. Shiohara and S. Tanaka, 1991, IEEE Trans. Magn. **27**, 1487.

Nakada, I., M. Itoh, I. Ogura and K. Koga, 1988, Mon. J. Inst. Industr. Sci. **40**, 19.

Nakamura, M., Y. Yamada and Y. Shiohara, 1994, J. Mater. Res. **9**, 1946.

Nakamura, M., Ch. Krauns and Y. Shiohara, 1995, Jpn. J. Appl. Phys. **34**, 6031.

Nakamura, M., M. Kambara, T. Umeda and Y. Shiohara, 1996a, Physica C **266**, 178.

Nakamura, M., Ch. Krauns and Y. Shiohara, 1996b, J. Mater. Res. **11**, 1076.

Nakamura, M., H. Kutami and Y. Shiohara, 1996c, Physica C, **260**, 297.

Nakamura, M., Y. Yamada, T. Hirayama, Y. Ikuhara and Y. Shiohara, 1996d, Physica C **259**, 295.

Nakamura, Y., K. Furuya, T. Izumi and Y. Shiohara, 1994, J. Mater. Res. **9**, 1350.

Nakamura, Y., K. Tachibana and H. Fujimoto, 1998, Physica C **306**, 259.

Namikawa, Y., and Y. Shiohara, 1996, Physica C **268**, 1.

Namikawa, Y., M. Egami, Y. Yamada and Y. Shiohara, 1995a, J. Mater. Res. **10**, 1593.

Namikawa, Y., M. Egami and Y. Shiohara, 1995b, J. Jpn. Inst. Met. **10**, 1047.

Namikawa, Y., M. Egami and Y. Shiohara, 1996a, J. Mater. Res. **11**, 288.

Namikawa, Y., M. Egami and Y. Shiohara, 1996b, Jpn. J. Appl. Phys. **35**, 6029.

Namikawa, Y., M. Egami, S. Koyama and Y. Shiohara, 1996c, J. Mater. Res. **11**, 804.

Narozhnyi, V.N., D. Eckert, K.A. Nenkov and G. Fuchs, 1999, Physica C **312**, 233.

Nevriva, M., E. Pollert, J. Hejtmanek and S. Durcok, 1991, Physica C **179**, 253.

Nishimura, Y., S. Miyashita and S.D. Durbin, 1999, J. Cryst. Growth **205**, 503.

Obradors, X., R.Y.F. Sandiumenge and B. Martinez, 1997, Supercond. Sci. Technol. **10**, 884.

O'Bryan, H.M., P.K. Gallagher, G.W. Berkstresser and C.D. Brandle, 1990, J. Mater. Res. **5**, 183.

Odier, P., F.J. Gotor, N. Pellerin, R.P.S.M. Lobo, K. Dembinski and J. Ayache, 1998, Mater. Sci. Eng. **B52**, 117.

Oka, A., S. Koyama and Y. Shiohara, 1998, Physica C **305**, 213.

Oka, A., S. Koyama, T. Izumi and Y. Shiohara, 1999a, Physica C **319**, 249.

Oka, A., S. Koyama, T. Izumi and Y. Shiohara, 1999b, Physica C **314**, 269.

Oka, K., and T. Ito, 1994, Physica C **227**, 77.

Oka, K., and T. Ito, 1996, Growth of large $LaBa_2Cu_3O_{7-y}$ and $Bi_2Sr_2CaCu_2O_{8-y}$ crystals, in: Proc. ISS'95, Hamamatsu, Japan, eds H. Hayakawa and Y. Enomoto, Vol. VIII of Advances in Superconductivity (Springer, Tokyo) pp. 333–336.

Oka, K., and H. Unoki, 1989, Jpn. J. Appl. Phys. **28**, L937.

Oka, K., and H. Unoki, 1990, J. Cryst. Growth **99**, 922.

Oka, K., K. Nakane, M. Ito, M. Saito and H. Unoki, 1988, Jpn. J. Appl. Phys. **27**, L1065.

Oka, K., Z. Zou and T. Ito, 1997, Physica C **282–287**, 479.

Okai, B., M. Kosuge, H. Nozaki, K. Takahashi and M. Ohta, 1988, Jpn. J. Appl. Phys. **27**, L41.

Olive, J.R., W.H. Hofmeister and R.J. Bayuzick, 1999, J. Mater. Res. **14**, 3843.

Oniyama, E., P. Wahlbeck, D.E. Peterson, J.Y. Coulter and E.J. Peterson, 1997, Physica C **288**, 151.

Ono, A., H. Nozaki and Y. Ishizawa, 1988, Jpn. J. Appl. Phys. **27**, L340.

Osabe, G., S.I. Yoo, N. Sakai and T. Higuchi, 2000, Supercond. Sci. Technol. **13**, 637.

Osamura, K., and W. Zhang, 1991, Z. Metallkd **82**, 408.

Osamura, K., and W. Zhang, 1993, Z. Metallkd **84**, 522.

Osamura, K., W. Zhang, T. Yamashita, S. Ochiai and B. Predel, 1988, Z. Metallkd. **79**, 693.

Os'kina, T.E., D. Wehler, H. Piel, R. Roth and Yu.D. Tretyakov, 1995, Physica C **242**, 85.

O'Sullivan, E.J.M., and B.P. Chang, 1988, Appl. Phys. Lett. **52**, 1441.

Ourmasd, A., J.A. Rentschlev and J.C.H. Spence, 1987, Nature **327**, 308.

Pamplin, B., 1980, in: Crystal Growth, Science of the Solid State, ed. B. Pamplin (Pergamon Press, Oxford) p. 16.

Panfilov, A.G., A.I. Rykov, S. Tajima and A. Yamanaka, 1998, Phys. Rev. B **58**, 12459.

Park, M., M.J. Kramer, K.W. Dennis and R.W. McCallum, 1996, Physica C **259**, 43.

Pathak, L.C., S.K. Mishra and D. Bhattacharya, 1996, Mater. Res. Bull. **31**, 1.

Paul, D.P., A. Thamizhavel and C. Subramanian, 1999, Cryst. Res. Technol. **34**, 503.

Paul, D.P., R. Jayavel and C. Subramanian, 2000, Bull. Mater. Sci. **23**, 79.

Pelloquin, D., V. Hardy and A. Maignan, 1996, Phys. Rev. B **54**, 16246.

Petrykin, V., A. Karpov, V. Poltavec, S. Lee and M. Kakihana, 1997, Appl. Supercond. **5**, 47.

Petrykin, V., M. Kakihana and Y. Tretyakov, 1999a, Study of holes distribution in the $Ln_{1+x}Ba_{2-x}Cu_3O_z$ solid solutions (Ln = La and Nd) by Raman spectroscopy, in: High-Temperature Superconductors and Novel Inorganic Materials, eds G. Van Tendeloo, E.V. Antipov and S.N. Putilin (Kluwer Academic Publishers, Dordrecht) pp. 173–176.

Petrykin, V.V., P. Berastegui and M. Kakihana, 1999b, Chem. Mater. **11**, 3445.

Porcar, L., D. Bourgault and X. Chaud, 1998, Mater. Sci. Eng. B **53**, 189.

Poulsen, H.F., M. von Zimmermann and J.R. Schneider, 1996, Phys. Rev. B **53**, 15335.

Pradhan, A.K., K. Kuroda, K. Nakao and N. Koshizuka, 1996, Physica C **272**, 161.

Pradhan, A.K., K. Kuroda, B. Chen and N. Koshizuka, 1998a, Jpn. J. Appl. Phys. **37**, 4764.

Pradhan, A.K., K. Kuroda and T. Takagi, 1998b, Physica C **300**, 77.

Pradhan, A.K., B. Chen and W. Ting, 1998c, Supercond. Sci. Technol. **11**, 408.

Przybylo, W., B. Onderka and K. Fitzner, 1996, J. Solid State Chem. **126**, 38.

Psycharis, V., C. Mitros and A. Koufoudakis, 1996, Physica C **267**, 211.

Puig, T., X. Obradors, B. Martinez and J.A. Alonso, 1998, Physica C **308**, 115.

Qadri, S.B., E.F. Skelton and M.S. Osofsky, 1997, Physica C **282–287**, 93.

Qi, X., and J.L. MacManus-Driscoll, 2000, J. Cryst. Growth **213**, 312.

Radousky, H.B., 1992, J. Mater. Res. **7**, 1917.

Rao, C.R.V., P. Murugakoothan and R. Jayavel, 1993, Supercond. Sci. Technol. **6**, 443.

Rebane, J.A., A.R. Kaul and Yu.D. Tretyakov, 1996, Fresenius J. Anal. Chem. **356**, 484.

Rebane, J.A., N.V. Yakovlev and D.S. Chicherin, 1997, J. Mater. Chem. **7**, 2085.

Rebane, Y.A., I.E. Korsakov and A.V. Kandidov, 1994, Physica C **235–240**, 605.

Reddy, E.S., and T. Rajasekharan, 1998, J. Mater. Res. **13**, 3389.

Reddy, E.S., J.G. Noudem and M. Tarka, 2000, Supercond. Sci. Technol. **13**, 716.

Revcolevschi, A., and J. Jegoudez, 1997, Progr. Mater. Sci. **42**, 321.

Revcolevschi, A., A. Vietkine and H. Moudden, 1997, Physica C **282–287**, 493.

Rice, J.P., and D.M. Ginsberg, 1991, J. Cryst. Growth **109**, 432.

Roth, R.S., K.L. Davis and J.R. Dennis, 1987, Adv. Ceram. Mater. **2**(3b), 303.

Rothman, S.J., J.L. Routbort and U. Welp, 1991, Phys. Rev. B **44**, 2326.

Routbort, J.L., 1993, Physica C **214**, 408.

Roy, B.N., 1992, Crystal Growth from Melts (Wiley, New York) 322 pp.

Rudnyi, E.B., V.V. Kuzmenko and G.F. Voronin, 1998, J. Phys. Chem. Ref. Data **27**, 855.

Rutter, J.W., and B. Chalmers, 1953, Can. J. Phys. **31**, 15.

Rykov, A., W.J. Jang, H. Unoki and S. Tajima, 1997, Detwinning and retwinning of $YBa_2Cu_3O_{7-\delta}$ single crystals with variable oxygen stoichiometry, in:

Proc. ISS'96, Sapporo, Japan, eds S. Nakajima and M. Murakami, Vol. IX of Advances in Superconductivity (Springer, Tokyo) pp. 341–344.

Saba, F., M. Tagami, E.A. Goodilin, Y. Shiohara and Y. Enomoto, 2000, Superconducting device, Japanese Patent n. 2980570 (filed June 12, 1997). Accepted for publication in IEEE Trans. Appl. Supercond.

Sadowski, W., E. Walker and G. Triscone, 1989, Physica C **162–164**, 897.

Sadowski, W., M. Gazda, B. Kusz and T. Klimczuk, 1994, Physica C **235–240**, 363.

Saito, K., H.U. Nissen, C. Beeli and T. Wolf, 1998, Phys. Status Solidi A **166**, 861.

Sakai, H., R. Itti, Y. Yamada, Y. Shiohara and S. Tanaka, 1995, Physica C **241**, 292.

Sakai, N., S.I. Yoo, S. Goshima and M. Murakami, 1997, Effect of processing conditions on the melt processed La123 superconductor, in: Proc. ISS'96, Sapporo, Japan, eds S. Nakajima and M. Murakami, Vol. IX of Advances in Superconductivity (Springer, Tokyo) pp. 709–712.

Sakai, N., S. Goshima, M. Kawaguchi and S.I. Yoo, 1998, Mater. Sci. Eng. B **53**, 109.

Salama, K., and D.F. Lee, 1994, Supercond. Sci. Technol. **7**, 177.

Salama, K., and S. Sathyamurthy, 1996, Appl. Supercond. **4**, 547.

Samoylenkov, S.V., O.Yu. Gorbenko and A.R. Kaul, 1997, Physica C **278**, 49.

Sandford, D., L. Marquez and A.M. Stacy, 1995, Appl. Phys. Lett. **67**, 422.

Sandiumenge, F., B. Martinez and X. Obradors, 1997, Supercond. Sci. Technol. **10**, a93.

Sandiumenge, F., B. Martinez, N. Vilalta and R. Yu, 1998a, Supercond. Sci. Technol. **11**, 165.

Sandiumenge, F., N. Vilalta, J. Rabier and X. Obradors, 1998b, Appl. Phys. Lett. **73**, 2660.

Sarikaya, M., and E.A. Stern, 1988, Phys. Rev. B **37**, 9373.

Sarikaya, M., R. Kikuchi and A. Aksay, 1988, Physica C **152**, 161.

Schatzle, P., G. Ebbing, W. Bieger and G. Krabbes, 2000, Physica C **330**, 19.

Scheel, H.J., 1993, Historical introduction, in: Handbook of Crystal growth, Vol. 1a, ed. D.T.J. Hurle (North-Holland, Amsterdam) pp. 18–39.

Scheel, H.J., 1994, MRS Bulletin (September), p. 26.

Scheel, H.J., M. Berkowski and B. Chabot, 1991, J. Cryst. Growth **115**, 19.

Scheel, H.J., C. Klemenz, F.-K. Reinhart and H.P. Lang, 1994, Appl. Phys. Lett. **65**, 901.

Schmid, H., E. Burkhardt, B.N. Sun and J.P. Rivera, 1989, Physica C **157**, 555.

Schmitz, G.J., A. Tigges and J.C. Schmidt, 1998a, Supercond. Sci. Technol. **11**, 73.

Schmitz, G.J., J.C. Schmidt, M. Tarka and A. Tigges, 1998b, Supercond. Sci. Technol. **11**, 950.

Schneemeyer, L.F., J.V. Waszczak and T. Sigrist, 1987, J. Cryst. Growth **328**, 601.

Schwer, H., R. Molinski, E.M. Kopnin, G.I. Meijer and J. Karpinski, 1999, J. Solid State Chem. **143**, 277.

Seeßelberg, M., G.J. Schmitz and B. Nestler, 1997a, IEEE Trans. Appl. Supercond. **7**, 1739.

Seeßelberg, M., G.J. Schmitz and T. Wilke, 1997b, Inst. Phys. Conf. Ser. **158**, 841.

Segre, C.U., B. Dabrowski, D.G. Hinks, K. Zhang and J.D. Jorgensen, 1987, Nature **329**, 227.

Sestak, J., 1992, Pure Appl. Chem. **64**, 125.

Sestak, J., G.K. Moiseev and D.S. Tzagareishvili, 1994, Jpn. J. Appl. Phys. **33**, 97.

Shaked, H., B.W. Veal, J. Faber Jr and R.L. Hitterman, 1990, Phys. Rev. B **41**, 4173.

Shamoto, S., 1988, Solid State Commun. **66**, 1151.

Shaw, T.M., S.L. Shinde and D. Dimos, 1989, J. Mater. Res. **4**, 248.

Shi, D., J. Krucpzak, M. Tang, N. Chen and R. Bhadra, 1989, J. Appl. Phys. **66**, 4325.

Shi, D., K. Lahiri, D. Qu and S. Sagar, 1997, J. Mater. Res. **12**, 3036.

Shi, D., D. Qu and B. Tent, 1998, Mater. Sci. Eng. B **53**, 18.

Shibata, S., H. Unoki, K. Kuroda and N. Koshizuka, 1997, A new slow cooling method of synthesizing $NdBa_2Cu_3O_{7-\delta}$ single crystals, in: Proc. ISS'96, Sapporo, Japan, eds S. Nakajima and M. Murakami, Vol. IX of Advances in Superconductivity (Springer, Tokyo) pp. 453–456.

Shibata, S., A.K. Pradhan and N. Koshizuka, 1999, Jpn. J. Appl. Phys. **38**, L1169.

Shimizu, T., F. Hirayama, K. Oka, H. Nonaka and M. Matsuda, 1994, Appl. Phys. Lett. **64**, 1289.

Shiohara, Y., 1996, Mater. Sci. Forum **215–216**, 347.

Shiohara, Y., and A. Endo, 1997, Mater. Sci. Eng. R **19**, 1.

Shitova, V.I., G.A. Mikirticheva and A.I. Sechnoi, 1993, Russ. J. Appl. Chem. **66**, 1509.

Shukla, A., B. Barbiellini and A. Erb, 1999, Phys. Rev. B **59**, 12127.

Shvanskaya, L., L. Leonyuk and G.J. Babonas, 1999, J. Cryst. Growth **199**, 600.

Singh, K.K., D.E. Morris and A.P.B. Sinha, 1994, Physica C **224**, 231.
Skakle, J.M.S., 1998, Mater. Sci. Eng. R **23**, 1.
Steinbach, I., F. Pezzolla, B. Nestler, M. Seebelberg and G.J. Schmitz, 1996, Physica D **94**, 135.
Sumida, M., M. Tagami, Ch. Krauns, Y. Shiohara and T. Umeda, 1995, Physica C **249**, 47.
Sumida, M., Y. Nakamura, T. Umeda and Y. Shiohara, 1997, J. Mater. Res. **12**, 1979.
Sumida, M., S. Matsuoka, Y. Shiohara and T. Umeda, 1998, J. Mater. Res. **13**, 2807.
Sun, B.N., and H. Schmid, 1990, J. Cryst. Growth **100**, 297.
Sun, B.N., R. Boutellier and H. Schmid, 1989, Physica C **157**, 189.
Sun, B.N., P. Hartman, C.F. Woensdregt and H. Schmid, 1990, J. Cryst. Growth **100**,605.
Sun, B.N., K.N.R. Taylor, B. Hunter and D.N. Matthews, 1991, J. Cryst. Growth **108**, 473.
Sunagawa, I., 1987, Surface microtopography of crystal faces, in: Morphology of Crystals, ed. I. Sunagawa (Terrapub, Tokyo) ch. 5, pp. 321–365.
Sunshine, S.A., T. Siegrist and L.F. Schneemeyer, 1997, J. Mater. Res. **12**, 1210.
Tachibana, M., M. Michiyama and H. Sakuma, 1996, J. Cryst. Growth **166**, 883.
Tagami, M., and Y. Shiohara, 1997, J. Cryst. Growth **171**, 409.
Tagami, M., M. Sumida, Ch. Krauns, Y. Yamada and Y. Shiohara, 1994, Interface structure of heteroepitaxially grown Y123/Pr123 crystals by the SRL–CP method, in: Proc. ISS'93, Hiroshima, Japan, eds T. Fujita and Y. Shiohara, Vol. VI of Advances in Superconductivity (Springer, Tokyo) pp. 633–636.
Tagami, M., M. Sumida, Ch. Krauns, Y. Yamada and T. Umeda, 1995, Physica C **250**, 240.
Tagami, M., T. Umeda and Y. Shiohara, 1997, J. Mater. Res. **12**, 2880.
Tagami, M., M. Nakamura and Y. Sugawara, 1998, Physica C **298**, 185.
Takagi, A., U. Mizutani and T. Kitamura, 1997, IEEE Trans. Appl. Supercond. **7**, 1388.
Takei, H., H. Asaoka, Y. Iye and H. Takeya, 1991, Jpn. J. Appl. Phys. **30**, L1102.
Takekawa, S., and N. Iyi, 1987, Jpn. J. Appl. Phys. **26**, L851.
Takita, K., H. Akinaga, H. Kato, T. Ipposhi and K. Masuda, 1987, Jpn. J. Appl. Phys. **26**, L854.
Takita, K., H. Katoh and H. Akinaga, 1988, Jpn. J. Appl. Phys. **27**, L57.
Takita, K., H. Akinaga, T. Oshima, Y. Takeda and M. Takano, 1992, Physica C **191**, 509.
Talantsev, E.F., 1994, Supercond. Sci. Technol. **7**, 491.
Tallon, J.L., and N.E. Flower, 1993, Physica C **204**, 237.
Tallon, J.L., and B.-E. Mellander, 1992, Science **258**, 781.
Tanaka, I., K. Hioki and H. Kojima, 1997, in: Extended Abstract Book, Int. Workshop on Superconductivity, IWS'97, June 15–18, 1997, Big Island, Hawaii, USA (co-sponsored by ISTEC and MRS) S1-1-6.
Tanaka, N., H. Zama and T. Morishita, 1999, Jpn. J. Appl. Phys. **38**, L731.
Tanaka, S., 1996, Mater. Sci. Eng. B **41**, 1.
Tang, T.B., and W. Lo, 1991, Physica C **174**, 463.
Tarascon, J.M., W.R. McKinnon and L.H. Greene, 1987, Phys. Rev. B **36**, 326.
Tatarchenko, V.A., G.A. Emel'chenko and N.V. Abrosimov, 1989, Int. J. Mod. Phys. B **3**, 289.
Tellez, D.A.L., Y.P. Yadava and J.M. Ferreira, 1999, Supercond. Sci. Technol. **12**, 18.
Temkin, D.E., 1966, Crystallization Process (Consultants Bureau, New York) p. 15.
Terborg, R., and G.J. Schmitz, 1997, J. Mater. Res. **12**, 2002.
Thomas, J.V., G.K. Perkins and D.E. Lacey, 1999, Supercond. Sci. Technol. **12**, 135.
Thomsen, C., 1991, in: Light Scattering in Solids, Vol. VI, eds M. Cardona and G. Güntherodt (Springer, Berlin) p. 285.
Tiller, W.A., 1991a, The Science of Crystallization. Microscopic Interfacial Phenomena (Cambridge University Press, Cambridge) 392 pp.
Tiller, W.A., 1991b, The Science of Crystallization. Macroscopic Phenomena and Defect Generation (Cambridge University Press, Cambridge) 484 pp.
Ting, W., T. Egi, R. Itti, K. Kuroda, N. Koshizuka and S. Tanaka, 1996, Jpn. J. Appl. Phys. **35**, 4034.
Ting, W., N. Koshizuka and S. Tanaka, 1998, Appl. Phys. Lett. **72**, 2035.
Todt, V.R., and G.J. Schmitz, 1993, J. Mater. Res. **8**, 411.
Trappeniers, L., J. Vanacken, L. Weckhuysen and K. Rosseel, 1999, Physica C **313**, 1.
Tretyakov, Y.D., and E.A. Goodilin, 2000, Russ. Chem. Rev. **69**, 3.
Tsukui, S., T. Yamamoto, M. Adachi, Y. Shono and K. Kawabata, 1991, Physica C **185–189**, 929.
Tsurumi, S., T. Iwata, Y. Tajima and M. Hikita, 1988, Jpn. J. Appl. Phys. **27**, L80.

Tu, K.N., C.C. Tsuei, S.I. Park and A. Levi, 1988, Phys. Rev. B. **38**, 772.

Uecker, R., P. Reiche and V. Alex, 1994, J. Cryst. Growth **137**, 278.

Ullman, J.E., R.W. McCallum and J.D. Verhoeven, 1989, J. Mater. Res. **4**, 752.

Ullrich, M., A. Leenders and J. Krelaus, 1998, Mater. Sci. Eng. B **53**, 143.

Usagawa, T., Y. Ishimaru, J. Wen, S. Koyama and Y. Enomoto, 1997a, Jpn. J. Appl. Phys. **36**, L100.

Usagawa, T., Y. Ishimaru, J. Wen, T. Utagawa and S. Koyama, 1997b, Jpn. J. Appl. Phys. **36**, L1583.

van de Leemput, L.E.C., P.J.M. Van Bentum and F.A.J.M. Driessen, 1989, J. Cryst. Growth **98**, 551.

van der Heijden, A.E.D.M., and G.M. Van Rosmalen, 1994, Industrial mass crystallisation, in: Handbook of Crystal Growth, Vol. 2b, ed. D.T.J. Hurle (North-Holland, Amsterdam) ch. 7, p. 334.

Van Tendeloo, G., and S. Amelinckx, 1987, Phys. Status Solidi (a) **103**, K1.

Vandewalle, N., 1998, Supercond. Sci. Technol. **11**, 35.

Vandewalle, N., R. Cloots and M. Ausloos, 1995, J. Mater. Res. **10**, 268.

Vargas, J.L., N. Zhang, D.L. Kaiser and S.E. Babcock, 1997, Physica C **292**, 1.

Volmer, M., 1939, Kinetik der Phasenbildung (Theodor Steinkopff, Dresden/Leipzig) p. 205.

Voronin, G.F., and S.A. Degterov, 1991, Physica C **176**, 387.

Voronkova, V.I., and Th. Wolf, 1993, Physica C **218**, 175.

Voronkova, V.I., V.K. Yanovskii, Th. Wolf and E.W. Seibt, 1995, J. Cryst. Growth **149**, 74.

Wada, T., N. Suzuki, A. Maeda, T. Yabe and K. Uchinokura, 1989, Phys. Rev. B. **39**, 9126.

Wagner, R., and R. Kampmann, 1991, Homogeneous second phase precipitation, in: Materials Science and Technology, A comprehensive treatment, Vol. 5, ed. P. Haasen (VCH, Weinheim) ch. 4, pp. 213–303.

Wan, R.X., G.M. Zhao and X.M. Tang, 1988, J. Appl. Phys. **64**, 3754.

Wang, F., H. Zama, H. Ohtsuka, M. Sato and T. Morishita, 1997, Physica C **282–287**, 555.

Wang, X.Z., and D. Bauerle, 1991, Physica C **176**, 507.

Wang, X.Z., B. Hellenbrand and D. Bauerle, 1992, Physica C **200**, 12.

Wanklyn, B.M., C. Chen, B.E. Watts, P. Haycock and F. Platt, 1988, Solid State Commun. **66**, 441.

Watanabe, N., K. Kuroda, K. Abe and N. Koshizuka, 1998, Physica C **300**, 301.

Watanabe, Y., K. Miyake, A. Endo, K. Murata, Y. Shiohara and T. Umeda, 1997, Physica C **280**, 215.

Weast, R.C., M.J. Astle and W.H. Beyer, eds, 1987, CRC Handbook of Chemistry and Physics, 68 edition (CRC Press, Boca Raton, FL) F-76.

Weishaupt, K., J.Th. Held, H.D. Hochheimer and S.B. Qadri, 1998, J. Phys. Chem. Solids **59**, 211.

Wen, J.G., S. Miura, A. Takagi and K. Hashimoto, 1997, Microstructures of 123 thick films grown on various substrates by Liquid Phase Epitaxy, in: Proc. ISS'97, Gifu, Japan, eds K. Osamura and I. Hirabayashi, Vol. X of Advances in Superconductivity (Springer, Tokyo) pp. 1023–1028.

West, D.R.F., 1982, Ternary Equilibrium Diagrams (Chapman and Hall, London) 81 pp.

Wiesner, U., W. Bieger and G. Krabbes, 1997, Thermochim. Acta **290**, 115.

Wiesner, U., G. Krabbes, M. Ueltzen, C. Magerkurth and J. Plewa, 1998, Physica C **294**, 17.

Wilke, K.-Th., 1973, Kristallzuchtung (VEB Deutscher Verlag der Wissenschaften, Berlin) p. 471.

Williams, R.K., K.B. Alexander and J. Brynestad, 1991, J. Appl. Phys. **70**, 906.

Wolf, Th., 1996, J. Cryst. Growth **166**, 810.

Wolf, Th., W. Goldacker and B. Obst, 1989, J. Cryst. Growth **96**, 1010.

Wolf, Th., A.-C. Bornarel, H. Kupfer and R. Meier-Hirmer, 1997, Phys. Rev. B. **56**, 6308.

Wong-Ng, W., and L.P. Cook, 1998, J. Res. Natl. Inst. Stand. **103**, 379.

Wong-Ng, W., B. Paretzkin and E.R. Fuler, 1990, J. Solid State Chem. **85**, 117.

Wong-Ng, W., L.P. Cook and B. Paretzkin, 1994, J. Am. Ceram. Soc. **77**, 2354.

Wu, H., and S.S. Wang, 1999, IEEE Trans. Appl. Supercond. **9**, 2211.

Wu, H., M.J. Kramer, K.W. Dennis and R.W. McCallum, 1997, Physica C **290**, 252.

Wu, H., K.W. Dennis, M.J. Kramer and R.W. McCallum, 1998, Appl. Supercond. **6**, 87.

Xie, X.M., T.G. Chen and Z.L. Wu, 1989, Phys. Rev. B **40**, 4549.

Yadava, Y.P., D.A.L. Telez, M.T. Melo and J.M. Ferreira, 1998, Appl. Phys. A **66**, 455.

Yamada, Y., and Y. Shiohara, 1993, Physica C **217**, 182.

Yamada, Y., Ch. Krauns, M. Nakamura, M. Tagami and Y. Shiohara, 1995a, J. Mater. Res. **10**, 1601.

Yamada, Y., M. Nakamura, Y. Shiohara and S. Tanaka, 1995b, J. Cryst. Growth **148**, 241.

Yamada, Y., J. Kawashima, Y. Niiori and I. Hirabayashi, 1996a, Appl. Supercond. **4**, 497.

Yamada, Y., M. Nakamura, Ch. Krauns, M. Tagami and Y. Shiohara, 1996b, J. Cryst. Growth **166**, 804.

Yamada, Y., J. Kawashima, Y. Niiori, T. Masegi and I. Hirabayashi, 1997a, Liquid phase epitaxy of YBCO on single crystalline oxide fibers for power applications, in: Proc. ISS'96, Sapporo, Japan, eds S. Nakajima and M. Murakami, Vol. IX of Advances in Superconductivity (Springer, Tokyo) pp. 653–655.

Yamada, Y., Y. Niiori, I. Hirabayashi and S. Tanaka, 1997b, Physica C **278**, 180.

Yamaguchi, K., T. Miyatake, T. Wada, N. Suzuki and T. Takata, 1990a, Physica C **169**, 289.

Yamaguchi, K., M. Murakami, H. Fujimoto and S. Gotoh, 1990b, Jpn. J. Appl. Phys. **29**, L1428.

Yang, G., J.S. Abell, P. Shang, I.P. Jones and C.E. Gough, 1996, J. Cryst. Growth **166**, 820.

Yao, X., and Y. Shiohara, 1997, Supercond. Sci. Technol. **10**, 249.

Yao, X., and Y. Shiohara, 1998, Mater. Sci. Eng. B **53**, 11.

Yao, X., K. Furuya, Y. Nakamura, J. Wen and A. Endo, 1995, J. Mater. Res. **10**, 3003.

Yao, X., N. Egami, Y. Namikawa, T. Mizukoshi and Y. Shiohara, 1996a, J. Cryst. Growth **165**, 198.

Yao, X., K. Ohtsu, S. Tajima, H. Zama, F. Wang and Y. Shiohara, 1996b, J. Mater. Res. **11**, 1120.

Yao, X., M. Sumida and Y. Shiohara, 1996c, J. Mater. Res. **11**, 2711.

Yao, X., N. Kambara, T. Umeda and Y. Shiohara, 1997, Jpn. J. Appl. Phys. **36**, L400.

Yasuda, H., I. Ohnaka, Y. Matsunaga and Y. Shiohara, 1996, J. Cryst. Growth **158**, 128.

Yoo, S.I., and R.W. McCallum, 1993, Physica C **210**, 147.

Yoo, S.I., M. Murakami, N. Sakai, T. Higuchi and S. Tanaka, 1994, Jpn. J. Appl. Phys. **33**, L1000.

Yoo, S.I., T. Higuchi and N. Sakai, 1998, Mater. Sci. Eng. B **53**, 203.

Yoshizumi, M., M. Kambara, Y. Shiohara and T. Umeda, 2000, Physica C **334**, 77.

Zama, H., F. Wang, S. Koyama, Y. Shiohara and T. Morishita, 1996, Jpn. J. Appl. Phys. **35**, L421.

Zamboni, M., S. Yoo, T. Higuchi and K. Waki, 1997, Physica C **281**, 218.

Zelenay, I., A. Nafidi, C. Greaves and R. Suryanarayanan, 1994, Physica C **231**, 207.

Zhang, H., G. Wang and H. Wu, 1995, J. Cryst. Growth **154**, 293.

Zhang, K., B. Daborwski, C.U. Segre and D.G. Hinks, 1987, J. Phys. C **20**, L935.

Zhang, W., K. Osamura and S. Ochiai, 1990, J. Am. Ceram. Soc. **73**, 1958.

Zhokhlov, A.A., and G.A. Emelchenko, 1993, J. Cryst. Growth **129**, 786.

Zhokhov, A.A., A.N. Christensen and S. Grundvig, 1999, Acta Chem. Scand. **53**, 74.

Zhou, J., R.K. Lo and J.T. McDevitt, 1997, J. Mater. Res. **12**, 2958.

Zhou, Z., and A. Navrotsky, 1992, J. Mater. Res. 7, 2920.

Zhu, Y., 1995, Structural defects in $YBa_2Cu_3O_{7-\delta}$ superconductors, in: High-Temperature Superconducting Materials Science and Engineering. New concepts and Technology, ed. D. Shi (Pergamon Press, Oxford) pp. 199–258.

Zou, Z., J. Ye, K. Oka and Y. Nishihara, 1998, Phys. Rev. Lett. **80**, 1074.

Handbook on the Physics and Chemistry of Rare Earths
Vol. 30
edited by K.A. Gschneidner, Jr., L. Eyring and M.B. Maple

Chapter 190

PHASE DIAGRAMS AND THERMODYNAMIC PROPERTIES

Pavel KAREN and Arne KJEKSHUS
Department of Chemistry, University of Oslo, Blindern, N-0315 Oslo, Norway

Contents

1. Introduction 230
1.1. Symbols and units 231
2. Elements 233
3. Rare-earth (R) oxides 235
3.1. R,R′ oxides 241
3.2. Oxide carbonates 242
4. Alkaline-earth (A) oxides 243
4.1. Oxides and peroxides 243
4.1.1. Simple A oxides 243
4.1.2. A,A′ oxides 245
4.1.3. Peroxides 245
4.1.4. Thermodynamics 246
4.2. Carbonates and CO_2 enviroument 247
4.2.1. Thermodynamics 247
5. Copper oxides 248
6. Systems A(O)–R(O) 250
6.1. Trivalent R 250
6.1.1. Ca(O)–R(O) 250
6.1.2. Sr(O)–R(O) 250
6.1.3. Ba(O)–R(O) 251
6.2. Tetravalent R 252
6.2.1. Ca(O)–R(O) 252
6.2.2. Sr(O)–R(O) 252
6.2.3. Ba(O)–R(O) 253
6.3. Oxide carbonate variants 253
7. Systems A(O)–Cu(O) 253
7.1. Calcium cuprates 254
7.1.1. High-pressure phases 256
7.1.2. Thermodynamics 256
7.1.3. Oxide carbonates 256
7.2. Strontium cuprates 257
7.2.1. Ambient p_{O_2} or moderate oxidizing conditions 257
7.2.2. Low p_{O_2} or reducing conditions 258
7.2.3. High p_{O_2} or oxidizing conditions 259
7.2.4. High-pressure phases 260
7.2.5. Thermodynamics 260
7.2.6. Oxide carbonates 260
7.3. Barium cuprates 261
7.3.1. Ambient p_{O_2} or moderate oxidation conditions 261
7.3.2. Low p_{O_2} or reducing conditions 263
7.3.3. High p_{O_2} or oxidizing conditions 264
7.3.4. High-pressure phases 266
7.3.5. Thermodynamics 266
7.3.6. Oxide carbonates 267
7.4. Calcium strontium cuprates 267
7.4.1. Ambient p_{O_2} or moderate oxidation conditions 267
7.4.2. High p_{O_2} or oxidizing conditions 269
7.4.3. High pressures 270
7.5. Calcium barium cuprates 270
7.5.1. Oxide carbonates 271
7.6. Strontium barium cuprates 272
7.6.1. Oxide carbonates 272
8. Systems R(O)–Cu(O) 273
8.1. Ambient p_{O_2} or moderate oxidizing conditions 274
8.2. Low p_{O_2} or reducing conditions 278
8.3. High p_{O_2} or oxidizing conditions 280
8.4. High pressures 281
8.5. Thermodynamics 281

9. Systems R,R′(O)–Cu(O) 282
10. Systems R(O)–Ca(O)–Cu(O) 285
11. Systems R(O)–Sr(O)–Cu(O) 288
11.1. Ambient p_{O_2} or moderate oxidizing conditions 288
11.2. High p_{O_2} or oxidizing conditions 292
11.3. High-pressure phases 293
11.4. Thermodynamics 293
12. Systems R,R′(O)–Sr(O)–Cu(O) 295
13. Subsolidus systems R(O)–Ba(O)–Cu(O) 295
13.1. Ambient p_{O_2} or moderate oxidizing conditions 295
13.1.1. The Lu(O)–Ba(O)–Cu(O) phase system 295
13.1.2. Phases emerging for R = Yb, Tm, Er, Ho, Dy and Y 297
13.1.3. Phases emerging for R = Eu and Gd 301
13.1.4. Phases emerging for R = Sm 303
13.1.5. Phases emerging for R = Nd 303
13.1.6. Phases emerging for R = Pr 305
13.1.7. Phases emerging for R = La 305
13.2. High p_{O_2} or oxidizing conditions 306
13.3. Low p_{O_2} or reducing conditions 311
13.3.1. Reduction by low p_{O_2} 311
13.3.2. Reduction by high temperatures 315
13.4. High-pressure phases 316
13.5. Oxide carbonates 316
13.6. Thermodynamics 319
14. Solidus–liquidus systems R(O)–Ba(O)–Cu(O) 324
15. R,R′(O)–Ba(O)–Cu(O) 326
15.1. Trivalent R 326
15.2. Tetravalent R 329
16. Systems R(O)–A,A′(O)–Cu(O) 329
16.1. R(O)–Ca,Sr(O)–Cu(O) 329
16.2. R(O)–Ca,Ba(O)–Cu(O) 330
16.3. R(O)–Sr,Ba(O)–Cu(O) 333
17. $RBa_2Cu_3O_7$, chemical behaviour 334
17.1. Chemical properties 334
17.1.1. Properties relevant to Cu 334
17.1.2. Properties relevant to Ba 335
17.2. Oxygen-exchange equilibrium 337
17.2.1. Experimental data 337
17.2.2. The defect chemistry approach 338
17.2.3. The lattice-gas approach 343
18. Structural and chemical variants of $YBa_2Cu_3O_7$ 345
18.1. Substitution by hydrogen, proton and hydroxyl 345
18.2. Substitution by halogen 348
18.3. Substitution by metal except A and R 348
18.3.1. Solid solubility at the R site 349
18.3.2. Solid solubility at the Ba site 349
18.3.3. Solid solubilities at the Cu sites 349
18.4. Isostructural triple perovskites 352
18.4.1. R(O)–Ba(O)–M(O) 352
18.4.2. R(O)–Ba(O)–M,M′(O) 354
18.4.3. R(O)–Sr(O)–M,M′(O) 355
References 355

1. Introduction

Phase diagrams and thermodynamic data for selected cuprates of alkaline-earth (A) and rare-earth (R) elements except Sc are presented in this chapter, covering binary to quintenary oxides, and including relevant solid-solution series with other elements. Attempts have been made to list all known occurring solid phases up to date. A short information on crystal structure is listed for each phase giving it its identity, as well as the concise chemical information which defines its character. The chemistry of phases is illustrated in mostly subsolidus isothermal phase diagrams, drawn after original sources, and referring to diverse chemical conditions defined by partial pressures of oxygen in particular. Reactivity towards CO_2 and formation of oxide carbonates are treated systematically as well, having been one of the major experimental obstacles in pursuit

of data relevant to pure oxides. Nevertheless, in some cases, the Ba-rich regions are still unclear as to the identity of the occurring phases.

For phase diagrams of the individual elements, the reader is directed to the monograph by Young (1991) as well as the books edited by Massalski (1990) and by Villars et al. (1995) for selected and evaluated binary and ternary systems of the elements, respectively. Although not cited in the following text because only original works have been consulted for this matter, an excellent monograph edited by Whitler and Roth (1991) on phase diagrams related to high-T_c superconductors should be mentioned.

When available, chemical information on the thermodynamics of solid phases is represented also in a numerical form. Treatment of liquid phases as well as most of the solid miscibilities is beyond the scope of this review, but references are given to those original communications where complete phase diagrams are assessed and such data provided. In this chapter, essential thermodynamic data for evaluations of phase equilibria appear in the form of entropies and enthalpies at standard and phase-transition temperatures together with heat-capacity functions. Other possibilities are temperature polynomials for standard Gibbs energies of formation, or for partial pressures of gaseous components. Efforts have been made to compile such suitable data for chemical phases relevant to superconducting oxides containing rare earths. When possible, for elements and simple oxides in particular, data selected in monographs by JANAF (1971), Hultgren et al. (1973), Pankratz (1982), Gschneidner et al. (1973), Dinsdale (1991) and Barin et al. (1993) have been chosen. However, the majority of data for the more complex oxide phases in this rapidly expanding field stems from original sources.

1.1. *Symbols and units*

(1) The identity of the chemical phases in the text is established by presenting the crystal-structure information in a condensed form comprising *some or all* of the following information in a square bracket: [formula; space group, or a lattice-symmetry identifier; unit-cell parameters in the order: a, b, c, α, β, γ (always in units of pm or °, but not specified)]. The data appear as given by the authors, *i.e.*, no conversion to standard crystallographic settings is attempted even if applicable. References to overall structure data appear with the words *structure* or *crystallize*, or at the crystal system, whereas data in square brackets refer to the unit cell. When more than one data source is available, attempts have been made to select the best.

(2) The lattice-symmetry identifier is the crystal-family symbol (c cubic, h hexagonal and trigonal, t tetragonal, o orthorhombic, m monoclinic, a anorthic or triclinic) appended optionally with the Bravais-centering symbol (P, F, I, R, A, B, C,), e.g. cP, cI, cF, hR, hP, ..., according to International Tables for Crystallography (Hahn 1995), and may appear either preceding chemical formulae when necessary for distinction, or in square brackets as described in the previous paragraph. (The appended symbol is identical with the Pearson symbol truncated of its numerals.)

(3) Attempt has been made to use chemical inorganic nomenclature in accordance with the IUPAC recommendations (1990). However, consistency for formulae of cuprates

concerning the sequence of rare-earth (R) and alkaline-earth (A) elements has been reached by following the said order which conforms with the traditional way for the formula $YBa_2Cu_3O_7$, and the consequent $Y \rightarrow Ba \rightarrow Cu$ anticlockwise orientation of the apices in ternary diagrams.

(4) Short-hand symbols of the type 123 (as for $YBa_2Cu_3O_7$) will be used when the relative cationic proportions of a phase rather than its complete formula is of importance. In phase diagrams, only the principal oxygen content is often provided even if a full formula is used. A formula in quotation marks refers to an approximate and/or uncertain composition with respect to the metal atoms. Square brackets placed around a chemical formula indicate a specific composition, not the chemical phase.

(5) When general compositional variables are used in chemical formulae, x relates to the R host site in the structure, y to A, z to Cu, w to oxygen, and u to all other anions.

(6) Symbols for physical variables are printed in italics, partial and relative values in lower case, absolute values in capitals.

(7) Physical units follow the SI system. However, the absolute temperature unit (K) will be used only when the information is based or expressed in a thermodynamic connection. Centigrades are used for melting points, reaction temperatures, etc.

(8) Standard deviations appear in parentheses ( ), referring to the last decimal.

(9) *Phase identifiers* in phase diagrams are L for liquid, AF antiferromagnetic, SC superconducting. *Frame lines* are drawn as solid lines. In areas where the enclosed information is not available, the frame lines are thin. In tetrahedral diagrams, the hidden frame line may appear dashed for better contrast. Mol fractions are used as composition units throughout, and the appropriate mol-unit formulae are printed in larger type at the corners of the diagrams even when identical with the phase actually present (in smaller type). Composition scales on the frame lines are omitted for all isothermal sections. *Phase boundary lines* are drawn as solid lines. Dashed lines are used for uncertain and/or speculative boundaries. *Single-phase fields* are black and solid solutions in (pseudo)binary systems are hence drawn by thick lines. Uncertain boundaries of these single-phase fields are serrated.

Tie lines are drawn thin. Chain lines are used for *auxiliary lines or planes* (the latter being drawn as non-transparent in order to improve the visual perception). Dotted lines then appear at intersections of these auxiliary planes with phase boundaries and tie lines.

(10) Abbreviations:

A	alkaline-earth element symbol
DTA	differential thermal analysis
EDAX	energy dispersive analysis by X-rays
EMF	electromotive force (measurement)
EXAFS	extended X-ray absorption fine structure

HREM	high-resolution (transmission) electron microscopy
NMR	nuclear magnetic resonance
NQR	nuclear quadrupole resonance
PND	powder neutron diffraction
PXD	powder X-ray diffraction
R	rare-earth element symbol
SEM	scanning electron microscopy
TEM	transmission electron microscopy
TGA	thermogravimetric analysis

(11) Thermodynamic variables:

Variable :	T	P,p	C_p	$S°$	$H°$	$G°$
Unit :	K	Pa	J/mol K	J/mol K	kJ/mol	kJ/mol

Absolute entropy may also be given in a dimensionless form $S°/R$, where R is the universal gas constant.

Heat capacities are expressed using virial coefficients of an up to six-term polynomial:

$$C_p = A + BT + CT^{-2} + DT^2 + ET^{-3} + FT^3, \tag{1}$$

in some cases fitted by the present authors to the selected, original, high-temperature heat-capacity data. In some cases, up to six-term polynomials are given directly for the Gibbs energy:

$$G = A + BT + CT \ln T + T^2 + ET^3 + \frac{F}{T}, \tag{2}$$

where G refers to any of the Gibbs energy values, e.g., standard Gibbs energy of a reaction ($\Delta_r G°$), or standard Gibbs energy of formation from elements ($G° - H^{SER}$; given relative to the enthalpy of the selected reference state, SER, for the elements at 298.15 K and 101 325 Pa). Used mostly in empirical equations, "log" denotes decadic logarithms whereas "ln" refers to natural logarithms. In table entries, e introduces a decimal exponent.

(12) The systematic arrangement of the references in this contribution has been changed editorially from progressive numbering (used in the manuscript of the authors) to the author(s)–year classification (used in the Handbook). The replacement may mean that the order of references at the text items is not chronological.

2. Elements

With the notable exception of dioxygen, individual elements do not occur often in the common chemistry of the rare-earth superconducting oxides. However, thermodynamic

Table 1
Selected standard thermodynamic values for R metals and their phase transitions[a]

R	Phase	T	$S°$	$H°$
Y	hP	298.15	44.434[b]	0
	hP → cI	1752	Δ2.849[b]	Δ4.992[b]
	cI → (*l*)	1799	Δ6.335[b]	Δ11.397[b]
La	hP	298.15	56.904[b]	0
	hP → cF	550	Δ0.67[b]	Δ0.36[b]
	cF → cI	1134	Δ2.76[b]	Δ3.12[b]
	cI → (*l*)	1193	Δ5.19[b]	Δ6.197[b]
Ce	cF	298.15	69.45[b]	0
	cF → cI	999	Δ2.99[b]	Δ3.00[b]
	cI → (*l*)	1071	Δ5.46[b]	Δ5.10[b]
Pr	hP	298.15	73.93[b]	0
	hP → cI	1068	Δ2.97[b]	Δ3.17[b]
	cI → (*l*)	1204	Δ5.69[b]	Δ6.89[b]
Nd	hP	298.15	71.09[b]	0
	hP → cI	1128	Δ2.68[b]	Δ3.03[b]
	cI → (*l*)	1289	Δ5.52[b]	Δ7.14[b]
Sm	hR	298.15	69.5[b]	0
	hR/hP → cI	1190	Δ2.64[b]	Δ3.11[b]
	cI → (*l*)	1345	Δ6.40[b]	Δ8.62[b]
Eu	cI	298.15	77.82[c]	0
	cI → (*l*)	1090	Δ8.45[c]	Δ9.21[c]
Gd	hP	298.15	67.95[b]	0
	hP → cI	1533	Δ2.55[b]	Δ3.91[b]
	cI → (*l*)	1585	Δ6.36[b]	Δ10.05[b]
Tb	hP	298.15	73.3[b]	0
	hP → cI	1560	Δ3.22[b]	Δ5.02[b]
	cI → (*l*)	1630	Δ6.65[b]	ΔI0.79[b]
Dy	hP	298.15	75.55[d]	0
	hP → cI	1657	Δ2.51[b]	Δ4.16[b]
	cI → (*l*)	1682	Δ6.57[b]	Δ11.06[b]
Ho	hP	298.15	75.02[b]	0
	hP → cI	1701	Δ2.76[b]	Δ4.69[b]
	cI → (*l*)	1743	Δ6.99[b]	Δ12.18[b]
Er	hP	298.15	73.18[b]	0
	hP → (*l*)	1795	Δ11.09[b]	Δ19.90[b]
Tm	hP	298.15	74.01[b]	0
	hP → (*l*)	1818	Δ9.29[b]	Δ16.84[b]

continued on next page

Table 1, *continued*

R	Phase	T	$S°$	$H°$
Yb	hP	298.15	59.83[b]	0
	hP ↔ cF	550	Δ0	Δ0
	cF → cI	1033	Δ1.67[b]	Δ1.75[b]
	cI → (*l*)	1097	Δ6.99[b]	Δ7.66[b]
Lu	hP	298.15	50.96[b]	0
	hP → (*l*)	1936	Δ9.62[b]	Δ18.65[b]

[a] Δ is shorthand for $\Delta S°$ = or $\Delta H°$ =; for units see the Introduction.
[b] Hultgren et al. (1973). [c] Gschneidner Jr (1997). [d] Amitin et al. (1983).

data of all component elements are useful for estimates and calculations relevant to compounds. In this section, selected thermodynamic data from Hultgren et al. (1973), Gschneidner Jr (1997) and Amitin et al. (1983) are presented for the group of the rare-earth metals (tables 1 and 2) and for alkaline-earth metals, copper and oxygen (tables 3 and 4). The accompanied structural and chemical description of the occurring phases is limited to a minimum, in contrast with the following subchapters devoted to oxides. For the special Y–Ba–Cu ternary system of metals, details on thermodynamics and phase diagrams are found in publications by Mey et al. (1990), Konetzki et al. (1994), Rudnyi (1996) and Rudnyi and Voronin (1996).

3. Rare-earth (R) oxides

A review by Eyring (1979) on binary R oxides has appeared in this Handbook previously, and the following text is only a concise summary and update.

Divalence. The only significant relatively stable oxides with divalent R are formed by europium: EuO [$Fm\bar{3}m$; 514.39; Eick et al. (1967)] and Eu_3O_4 [*Pnam*; 1009.4, 1206.8, 350.0; Bärninghausen and Brauer (1962)].

Trivalence. Several polymorphic modifications occur, depending on temperature, pressure and atom size (Foëx and Traverse 1966). At ambient pressure the sesquioxides of La, Ce, Pr and Nd are hexagonal (Müller-Buschbaum and von Schnering 1965) (hP or hR) when subject to free cooling from any temperature up to nearly the melting point. The sesquioxides of Sm and smaller R atoms adopt (Roth and Schneider 1960) the bixbyite-type structure [Y_2O_3; $Ia\bar{3}$; 1060.3; O'Connor and Valentine (1969)]. The bixbyite-type oxides transform slowly into a monoclinic (mC) modification at temperatures increasing from some 900 to some 2000°C across the Sm, Eu, Gd, Dy and Ho series. However, the temperatures of these transformations are nearly impossible to establish precisely due to the sluggishness of the change which, moreover, is very much dependent on the thermal history as well as trace impurities in the samples and exhibits strong hysteresis. Oxides of Sm, Eu and Gd, where the transformation temperature is apparently

Table 2
Virial heat-capacity coefficients (eq. 1) for R metals; units have been omitted

R	Phase	T interval	A	B	C	D	E	F	Ref.[a]
Y	hP	298–1752	24.5	0.006548		4.552e-7			[1]
	cI	1752–1799	35.0						[1]
	(*l*)	1799	43.1						[1]
La	hP	298–550	26.03	0.003871		–2.8e-9			[1]
	cF	550–1134	21.06	0.009339	67657	2.5864e-6			[1]
	cI	1134–1193	39.54						[1]
	(*l*)	1193	34.31						[1]
Ce	cF	298–999	22.37	0.01342	36251	1.9415e-6			[1]
	cI	999–1071	37.61						[1]
	(*l*)	1071	37.70						[1]
Pr	hP	298–1068	21.17	0.012725	173556	6.183e-6			[1]
	cI	1068–1204	38.45						[1]
	(*l*)	1204	42.97						[1]
Nd	hP	298–1128	25.87	0.001995	–26578	1.409e-5			[1]
	cI	1128–1289	44.56						[1]
	(*l*)	1289	48.79						[1]
Sm	hR/hP	298–1190	–25.6	0.2174	–89492	–2.319e-4	256780000	8.5203e-8	[1]
	cI	1190–1345	46.9						[1]
	(*l*)	1345	50.2						[1]
Eu	cI	298–1090	31.48	–0.015	–118256	2.169e-5			[2]
	(*l*)	1090	38.12						[1]
Gd	hP	400–1533	25.5	0.003943	76690	3.0e-6			[1]
	cI	1533–1585	28.28						[1]
	(*l*)	1585	37.15						[1]

continued on next page

Table 2, *continued*

R	Phase	T interval	A	B	C	D	E	F	Ref.[a]
Tb	hP	298–1560	−8.72	0.07611	3555000	−4.8615e-5	−558750000	1.419e-8	[1]
	cI	1560–1630	27.61						[1]
	(*l*)	1630	46.48						[1]
Dy	hP	298–1657	35.34	−0.0219	−214800	1.85e-5			[1]
	cI	1657–1682	28.0						[1]
	(*l*)	1682	50.0						[1]
Ho	hP	298–1701	45.45	−0.0449	−1175000	3.72e-5	135550000	−4.917e-9	[1]
	cI	1701–1743	28.0						[1]
	(*l*)	1743	44.0						[1]
Er	hP	298–1795	28.385	−0.002	−19160	5.715e-6			[1]
	(*l*)	1795	38.7						[1]
Tm	hP	298–1818	−1.214	0.051217	3426900	−2.707e-5	−618200000	5.688e-9	[1]
	(*l*)	1818	41.4						[1]
Yb	hP	298–550	39.1	−0.07875		1.25e-4			[1]
	cF	550–1033	26.7	0.005236					[1]
	cI	1033–1097	36.11						[1]
	(*l*)	1097	36.78						[1]
Lu	hP	298–1936	25.3	0.003145		1.348e-5			[1]
	(*l*)	1936	48.0						[1]

[a] Reference from which C_p data were selected for fits.

References

[1] Hultgren et al. (1973).

[2] Gschneidner Jr (1997).

Table 3
Selected standard thermodynamic values for relevant non-rare-earth elements and their phase transitions[a]

Element	Phase	T	$S°$	$H°$
O_2	(g)	298.15	205.147[b]	0
Cu	cF	298.15	33.164[b]	0
	cF → (l)	1358	Δ9.675[b]	Δ13.138[b]
Ca	cF	298.15	41.42[c]	0
	cF → cI	720	Δ1.278[c]	Δ0.920[c]
	cI → (l)	1112	Δ7.675[c]	Δ8.535[c]
Sr	cF	298.15	55.690[b]	0
	cF → cI	820	Δ1.021[b]	Δ0.837[b]
	cI → (l)	1050	Δ7.077[b]	Δ7.431[b]
Ba	cI	298.15	62.417[c]	0
	↔	582	Δ0	Δ0[c]
	cI → (l)	1002	Δ7.734[c]	Δ7.749[c]

[a] Δ is shorthand for $\Delta S°$ = or $\Delta H°$ =; for units see the Introduction.
[b] JANAF (1971). [c] Hultgren et al. (1973).

below 1200°C, the atom mobility is so slow that the monoclinic modifications are readily synthesized [Sm_2O_3; $C2/m$; 1418, 363.3, 884.7, 99.96; Cromer (1957)] although technically metastable. Several other polymorphic modifications are seen at very high temperatures close to melting.

Tetravalence. Ce, Pr, and Tb can take both trivalent and tetravalent states in their oxides. In line with the close structural relationship between the bixbyite (for the sesquioxides) and the fluorite (for the dioxides) structure types (Sawyer et al. 1965), a sequence of related intermediate phases occurs. The underlying structural features of these phases have recently been generalized using a modular approach. This gave a general formula R_nO_{2n-2m} for the RO_w composition, where $m = n - (nw)/2$ (Kang and Eyring 1997). An overview of the occurrence, empirical and modular compositions and the established phase designations is given in table 5, based mainly on Kang and Eyring (1997); they also give the most recent update on the (still incomplete) phase diagrams in the $RO_{1.5}$–RO_2 phase systems for R = Ce, Pr and Tb. Isobars of p_{O_2} are shown in figs. 1 and 2 for R = Ce and Pr, according to Hauck et al. (1998). The p_{O_2} data for the still rather incomplete phase system for R = Tb are similar to those of R = Pr (Kordis and Eyring 1968).

The most oxygen-rich CeO_2 [$Fm\bar{3}m$; 541.1; Brauer and Gingerich (1960)] remains practically stoichiometric in ambient O_2 up to some 1300°C (Bevan and Kordis 1964). At room temperature, CeO_2 has a rather narrow range of homogeneity, whereas above some 600°C, an appreciable amount of oxygen vacancies can be formed in reducing atmospheres. The most oxygen-rich PrO_2 [$Fm\bar{3}m$; 539.3(1)] forms only under enhanced oxygen pressure (Sieglaff and Eyring 1957). However, TbO_2 [$Fm\bar{3}m$; 521.9(1)] is formed

Table 4
Virial heat-capacity coefficients (eq. 1) for selected non-rare-earth elements; units have been omitted

	Phase	T interval	A	B	C	D	E	F	Ref.[a]
O_2	(*g*)	298–2000	25.887	0.016065	−473710	−8.459e-6	125700000	1.7144e-9	[1]
Cu	cF	298–1358	−6.994	0.0837	2710000	−7.798e-5	−472100000	2.767e-8	[1]
	(*l*)	1358	32.844						[1]
Ca	cF	298–720	24.115	−0.0033295	33399	2.03947e-5			[2]
	cI	720–1112	−0.3785	0.04128	692				[2]
	(*l*)	1112	29.29						[2]
Sr	cF	298–820	27.73	−0.0037897	−140087	1.92723e-5			[1]
	cI	820–1050	37.656						[1]
	(*l*)	1050	35.146						[1]
Ba	cI	298–582	25.12	−0.0054		1.654e-7			[2]
		582–1002	20816	−38.502	−3926310000	0.028205	1017070000000	−7.56892e-6	[2]
	(*l*)	1002–1300	74.1	−0.0378		7.105e-9			[2]

[a] Reference from which data were selected for fits.

References

[1] JANAF (1971)

[2] Hultgren et al. (1973)

Table 5
Occurrence and compositions of the higher Ce, Pr and Tb oxides R_nO_{2n-2m}; x of the older $2R_2O_3 \cdot xRO_2$ formulae and w of the empirical RO_w formulae.

Designation	Examples	Unit cell	n	m	x	w
ι	Ce Pr Tb	R_7O_{12}	7	1	3	1.714
ζ	Ce? Pr	R_9O_{16}	9	1	5	1.778
δ(1)	Ce Tb	$R_{11}O_{20}$	11	1	7	1.818
β(0)	Pr	$R_{12}O_{22}$	12	1	8	1.833
π	Ce? Pr Tb	$R_{16}O_{30}$	16	1	12	1.875
M19	Ce	$R_{19}O_{34}$	19	2		1.789
β(1)	Pr Tb	$R_{24}O_{44}$	24	2	8	1.833
M29	Ce	$R_{29}O_{52}$	29	3		1.793
M39	Ce	$R_{39}O_{70}$	39	4		1.795
ε	Ce? Pr	$R_{40}O_{72}$	40	4	6	1.800
β(3)	Tb	$R_{48}O_{88}$	48	4	8	1.833
δ′	Ce Pr Tb	$R_{62}O_{112}$	62	6		1.806
δ(2)	Pr	$R_{88}O_{160}$	88	8	7	1.818

only on disproportionation in acidic solutions (Brauer and Pfeiffer 1963) (similarly to PbO_2) and decomposes above 340°C in 100 kPa O_2 into $Tb_{11}O_{20}$ (Sastry et al. 1966). The latter phase is the most oxygen-rich terbium oxide which can be obtained by oxidation with O_2 (TbO_2 forms in atomic oxygen, Gruen et al. 1951) and decomposes into Tb_7O_{12} at ~450°C (p_{O_2} = 1.3 kPa) and subsequently into Tb_2O_{3+w} at ~800°C at the same pressure (Burnham et al. 1968). However, the most common preparation route for R oxides, which involves thermal decomposition of oxalate in air at 600 to 1000°C, gives reproducibly Tb_4O_7. This composition is, moreover, invariably obtained during various synthesis reactions in O_2 at ambient and reduced pressures (Gruen et al. 1951, Ivanov-Emin and Medvedev 1990, Prandtl and Rieder 1938). Correspondingly, distinct plateaus at the Tb_4O_7 composition are observed (Ramdas et al. 1970, Rudenko and Boganov 1971) by TGA. However, diffraction methods failed to reveal any specific superstructure for the Tb_4O_7 composition which accordingly is suggested to occur only as a consequence of a sluggish kinetics (Burnham et al. 1968, Baenziger et al. 1961).

Thermodynamics. Owing to the occurring polymorphism for the trivalent R oxides and the redox instability for the mixed trivalent–tetravalent R oxides, even precisely obtained thermodynamic data may refer to uncertain compositions. In particular, this is the case for the cI to mC transformation, where the transformation temperatures are not well defined and the high-temperature heat capacities are therefore uncertain. On the other hand, the standard enthalpies and entropies themselves of these transformations are known, yet rather small (around +1.0 and +0.6 per R_2O_3, respectively). Owing to these problems, data involving these transitions as well as data for oxides subject to extensive redox interactions are not included in the essential thermodynamic data listed in tables 6 and 7.

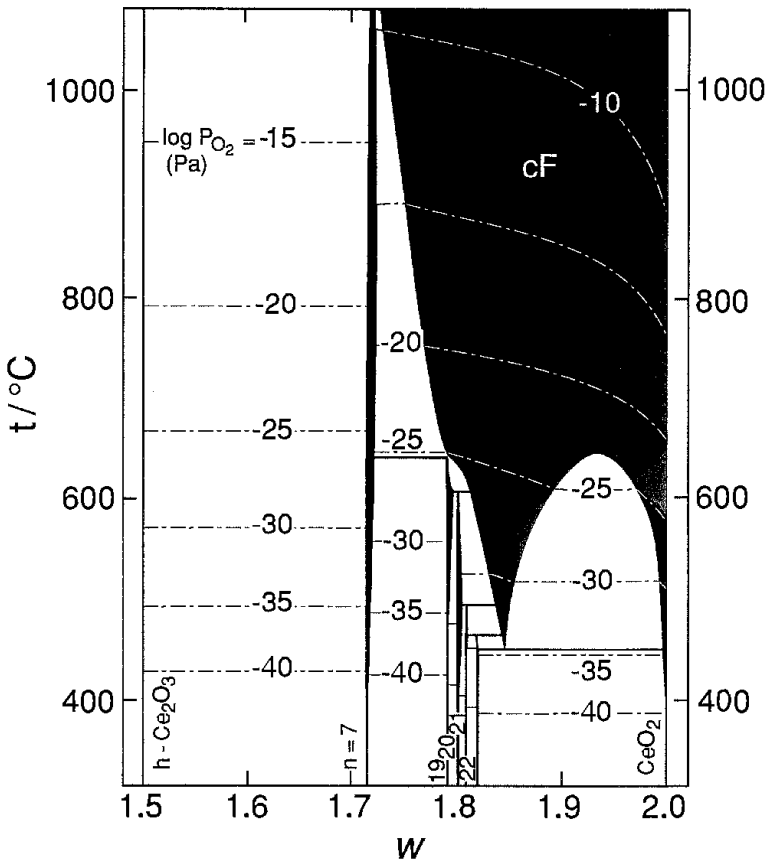

Fig. 1. A w–t diagram of CeO_w. (After Hauck et al. 1998.)

3.1. *R,R′ oxides*

With the exception of the most different pairs of Rs by size, which form a 1 : 1 ternary oxide, no further ternary compounds are found, but wide ranges of solid solubility occur for the R sesquioxides. The structure of these solid solutions follows the behaviour of the binary oxides as a function of temperature and ionic size (Foëx and Traverse 1966). Owing to the very high melting temperatures, the solid-state diffusion rate in these oxides is low and formation of the 1 : 1 ternary oxides requires temperatures above 1600°C, long sintering times and the use of pressure (Schneider and Roth 1960). It has therefore been suggested (Jørgensen et al. 1965) that they in fact are metastable under ambient conditions. Structurally, these oxides are perovskite-related [$LaYO_3$; *Pnam*; 587.7, 849.3, 608.7; Müller-Buschbaum and Teske (1969), Müller-Buschbaum and Graebner (1971), Moreau (1968)]. When based on La, they occur for Ho (or Y) and smaller Rs (Schneider and Roth 1960, Moreau 1968), but only for Lu when based on Pr (Moreau 1968). The fluorite-type CeO_2 phase forms (at say 1600°C) an almost continuous series of solid solutions with trivalent Rs, maximum extent being found between Sm and Ho (or Y) (Brauer and Gradinger 1954, Barker and Wilson 1968, Bevan et al. 1964). These elements of similar size are able (or nearly able) to form the cubic sesquioxide, the structure

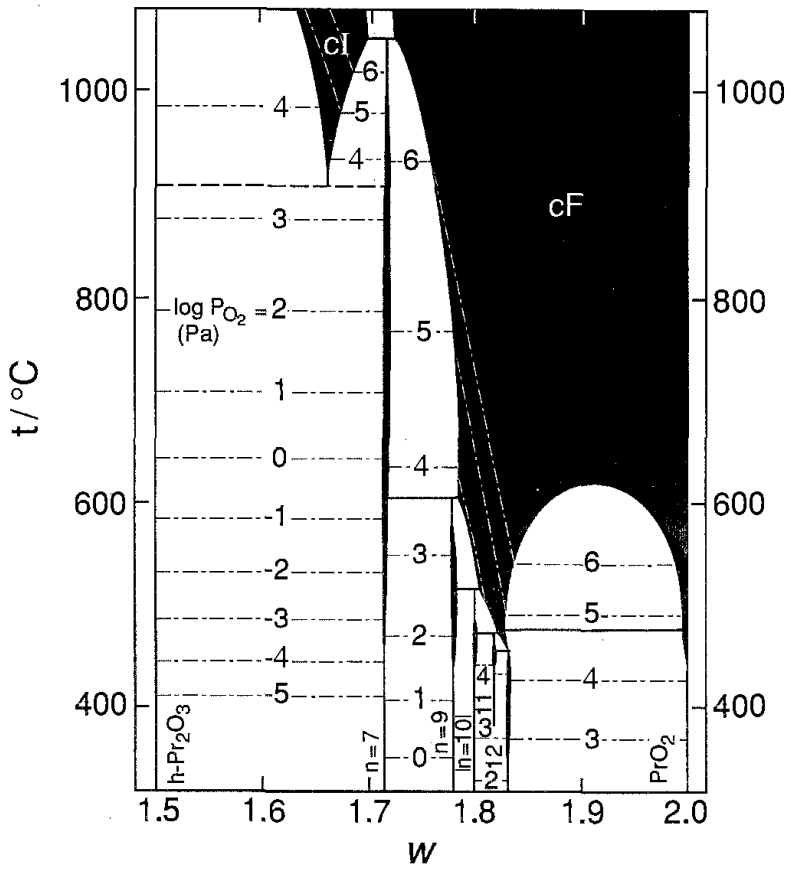

Fig. 2. A w–t diagram of PrO_w. (After Hauck et al. 1998.)

of which is closely related to fluorite. A nearly continuous conversion occurs from the fluorite-type CeO_2 phase through a (related vacant) cI solid-solution oxide, followed by a narrow ($\Delta x \approx 0.1$) miscibility gap into the regime of either a cF or monoclinic sesquioxide (Bevan et al. 1964). These trends are subject to alterations when equilibrium is established at lower temperature than 1600°C (Foëx and Traverse 1966) or low O_2 pressures are used. The latter specification is particularly important for the otherwise analogous systems with R^{IV} = Pr (McGullough and Britton 1952, McGullough 1950) and Tb (Wolf and Schwab 1964).

3.2. *Oxide carbonates*

As intermediate products of thermal decomposition of hydrated R carbonates or oxalates, oxide carbonates $R_2O_2CO_3$ are obtained for practically all Rs (Petrů et al. 1966, Sawyer et al. 1972). Several metastable phases with defined crystal structures are formed as a function of temperature, before hexagonal (type-II) $R_2O_2CO_3$ appears, with crystal structure (Christensen 1970, Attfield and Férey 1989) [$La_2O_2CO_3$; $P6_3/mmc$; 407.55(6), 1595.7(1)] related to that of the hexagonal oxides of the early lanthanides. For R = La, Pr, Nd, Sm, and Gd, these oxide carbonates are relatively stable and can be isolated as single

Table 6
Selected standard thermodynamic values for R oxides[a]

Oxide	Phase	T	$S°$	$H°$
Y_2O_3	cI	298.15	99.12[b]	−1905.6[c]
La_2O_3	hP	298.15	127.32[b]	−1794.18[c]
Ce_2O_3	hP	298.15	148.11[b]	−1796.23[c]
CeO_2	cF	298.15	62.3[b]	−1088.68[c]
Pr_2O_3	hP	298.15	155.64[b]	−1823.39[c]
Nd_2O_3	hP	298.15	158.57[b]	−1807.95[c]
Sm_2O_3	mC	298.15	151.04[b]	−1823.64[c]
Sm_2O_3	cI	298.15	144.77[b]	−1827.40[c]
EuO	cF	298.15	83.64[b]	−597.89[c]
Eu_3O_4	oP	298.15	232.21[c]	−2254.76[c]
Eu_2O_3	mC	298.15	146.44[b]	−1651.42[c]
Eu_2O_3	cI	298.15	140.16[b]	−1662.72[c]
Gd_2O_3	mC	298.15	156.90[b]	−1815.60[c]
Gd_2O_3	cI	298.15	150.62[b]	−1826.90[c]
Tb_2O_3	cI	298.15	156.90[b]	−1865.23[c]
Dy_2O_3	cI	298.15	157.32[c]	−1863.22[c]
Ho_2O_3	cI	298.15	158.16[b]	−1880.92[c]
Er_2O_3	cI	298.15	155.64[b]	−1897.82[c]
Tm_2O_3	cI	298.15	148.41[c]	−1888.66[c]
Yb_2O_3	cI	298.15	133.05[b]	−1814.52[c]
Lu_2O_3	cI	298.15	109.96[b]	−1878.20[c]

[a] See the text for a discussion on the phase transition concerned; for units see the Introduction.
[b] Data from Pankratz (1982). [c] Data from Gschneidner Jr et al. (1973).

phases (Sawyer et al. 1972). For thermodynamics of their decomposition into R_2O_3 and CO_2 see Olafsen and Fjellvåg (1999).

4. Alkaline-earth (A) oxides

4.1. *Oxides and peroxides*

4.1.1. *Simple A oxides*

The melting points decrease from CaO, 2576°C through SrO, 2430°C to BaO, 1923°C (Schumacher 1926). An analogous trend is observed for vapor pressures (Lamoreaux et al. 1987). As an example, a partial pressure of 1 Pa of the oxides (CaO, SrO and BaO) in synthetic air is reached at ~2350, ~2100 and 1450°C, respectively. The crystal structures

Table 7
Virial heat-capacity coefficients (eq. 1) for R oxides; units have been omitted

Oxide	Phase	T interval	A	B	C	D	E	F	Ref.[a]
Y_2O_3	cI	298–1330	95.23	0.08353	−784427	−7.1324e-5	−79840800	2.0703e-8	[1]
La_2O_3	hP	298–2000	76.516	0.03727	893400	−1.591e-5	−359700000	2.927e-9	[1]
Ce_2O_3	hP	298–1000	137.06	0.003456	−1918000	1.145e-5			[1]
CeO_2	cF	298–2000	76.7	0.0084675	−3211000	−6.773e-6	505353000	2.966e-9	[1]
Pr_2O_3	hP	298–1800	121.3	0.026594	−998470	−5.9024e-7			[1]
Nd_2O_3	hP	298–2000	109.6	0.04255	−914640	−6.469e-6			[1]
Sm_2O_3	cI	298–1150	110.8	0.06547	−1060000	−2.833e-5			[1]
Sm_2O_3	mC[b]	298–1195	107.94	0.06795	−988190	−2.8616e-5			[1]
EuO	cF	298–1700	50.734	−0.002745	125470	7.888e-6	−83550000	−2.027e-9	[2]
Eu_3O_4	oP	298–2000	140.6	0.07484	6766000	−2.837e-5	−1994000000	5.363e-9	[2]
Eu_2O_3	cI	298–1350	130.4	0.0251	−1144600	−3.619e-6			[1]
Eu_2O_3	mC[b]	298–895	126.8	0.021235	−1035800	3.0284e-6			[1]
Gd_2O_3	cI	298–1550	112.04	0.02824	−1258000	−8.0027e-6			[1]
Gd_2O_3	mC[b]	298–2000	140.0	−0.03449	−4464700	3.398e-5	645770000	−8.0044e-9	[1]
Tb_2O_3	cI	298–1800	139.9	−0.0241	−1707000	3.51e-5	−36200000	−8.087e-9	[1]
Dy_2O_3	cI	298–1590	180.3	−0.09725	−7810000	7.4535e-5	1237000000	−1.661e-8	[1]
Ho_2O_3	cI	298–2000	127.23	0.0054035	−1233850				[1]
Er_2O_3	cI	298–2000	117.27	0.01769	−1225000	−3.232e-6			[1]
Tm_2O_3	cI	298–1680	133.9	−0.01344	−1350000	1.763e-5	15364000	−5.5415e-9	[1]
Yb_2O_3	cI	298–1365	123.5	0.03417	−1786000	−3.5823e-5	123360000	1.169e-8	[1]
Lu_2O_3	cI	298–2000	91.3	0.054	2840000	−2.286e-5	−945400000	3.268e-9	[1]

[a] Reference from which C_p data were selected for fits.
[b] Metastable below some 1200 to 1500 K.

References

[1] Pankratz (1982)

[2] Gschneidner Jr (1997)

are of the NaCl-type; CaO [481; Guillatt and Brett (1970)], SrO [514; Burgers (1933)] and BaO [552; Burgers (1933)].

4.1.2. *A,A′ oxides*

SrO and BaO have unlimited solid solubility above 1083(4)°C (Jacob and Varghese 1995). At lower temperatures, segregation of the solid solutions occurs (Jacob and Varghese 1995, Abalduev and Bolchakov 1972). However, the precipitation of the two components is hindered kinetically, and solid solutions in the complete region are readily obtained upon cooling (Grebenyuk et al. 1967). A similar situation occurs in the Ca(O)–Sr(O) system (Ostapchenko 1956, Jacob et al. 1995).

4.1.3. *Peroxides*

At relatively low temperatures, peroxides of A metals become stable. The equilibrium oxygen pressure for CaO_2 is estimated (Satterfield and Stein 1954) to reach 100 kPa at around ambient temperature, at ~350°C for SrO_2 (Holtermann and Laffitte 1939), and at ~820°C for BaO_2 (Kedrovskii et al. 1967). A significant solid-state miscibility occurs between oxides and peroxides of the A metals (Kedrovskii et al. 1967). This should be taken into consideration in the evaluation of the oxygen dissociation pressure, which will vary not only with temperature but also with the content of peroxide in the solid-solution phase (Kedrovskii et al. 1967). To illustrate rough trends, equilibrium oxygen pressures for $SrO_{1.97}$ (Holtermann and Laffitte 1939) and for the oxide-saturated barium peroxide are expressed (p in Pa, T in K) as (Holtermann and Laffitte 1939, Kedrovskii et al. 1967)

$$SrO_{1.97(s)} \rightleftharpoons SrO_{(s)} + \frac{0.97}{2}O_{2(g)}, \quad \log p_{O_2} = 11.4 - \frac{4050}{T}; \tag{3}$$

$$BaO_{1-w}(O_2)_{w(s)} \rightleftharpoons BaO_{(s)} + \frac{w}{2}O_{2(g)}, \quad \log p_{O_2} = 11.83 - \frac{7500}{T}, \quad \log(1-w) = 0.975 - \frac{1552}{T}. \tag{4}$$

The peroxides crystallize (Abrahams and Kalnajs 1954, Wong-Ng and Roth 1994) with the CaC_2-type structures: CaO_2 [*P4/mmm*; 356, 596; Brosset and Vannerberg (1956)], SrO_2 [355, 655; Bernal et al. (1935)] and BaO_2 [381.14(6), 682.15(11); Wong-Ng and Roth (1994)].

A portion of the BaO–BaO_2 y–t phase diagram (Kedrovskii et al. 1967) which represents the experimental data in the solid-state system (liquidus equilibria omitted) is shown in fig. 3. The reason for this caution is that the recently computationally assessed Ba–O phase diagram (Zimmermann et al. 1995, Okamoto 1997) gives strongly differing temperature stability for the barium peroxide phase (exceeding the experimental data by nearly 300°C) as well as the shape of the liquidus, while showing similar essential features. The uncertainty in the heat-capacity and other data for BaO_2 could be at the root of the problem.

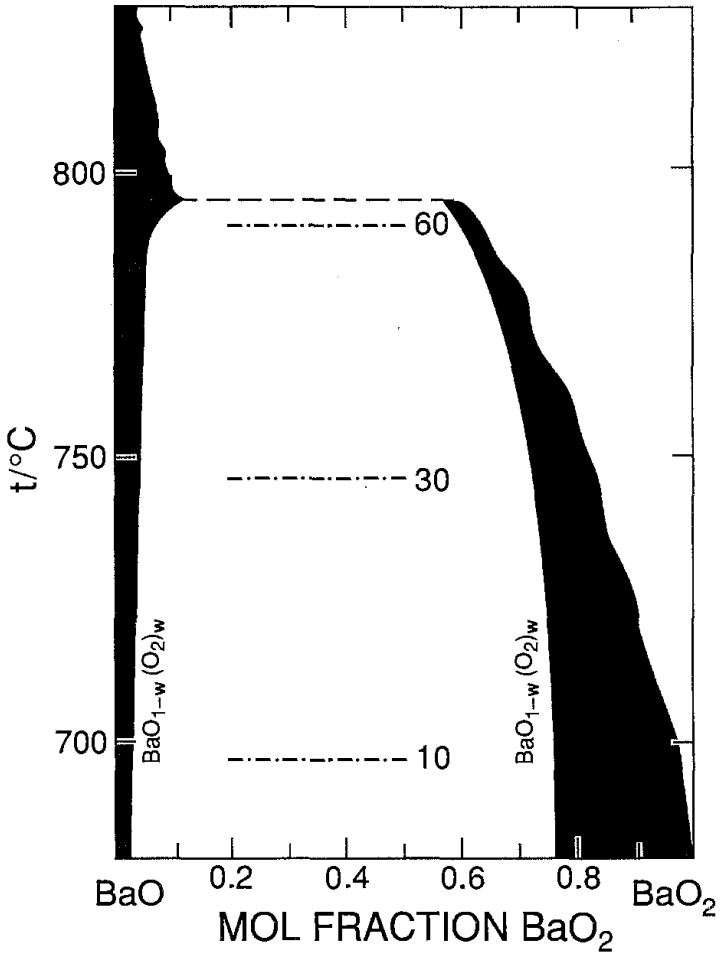

Fig. 3. A w–t diagram for the BaO–BaO_2 system with some equilibrium O_2 pressures (in kPa) indicated. (After Kedrovskii et al. 1967.)

Table 8
Selected standard thermodynamic values for alkaline-earth oxides; for units see the Introduction

Oxide	Phase	T	$S°$	$H°$
CaO	cF	298.15	38.07[a]	−635.09[a]
SrO	cF	298.15	54.39[a]	−590.53[a]
BaO	cF	298.15	72.069[b]	−548.04[b]

[a] Pankratz (1982). [b] Parker (1995).

4.1.4. *Thermodynamics*

Essential thermodynamic data (Pankratz 1982, Parker 1995) for the simple A oxides are listed in tables 8 and 9.

Table 9
Virial heat-capacity coefficients (eq. 1) for alkaline-earth oxides[a]; units have been omitted

	Phase	T interval	A	B	C	D	E	F
CaO	cF	298–2000	50.565	0.003837	−856760			
SrO	cF	298–1800	41.446	0.0271	−201742	−1.594e-5	−24310000	3.712e-9
BaO	cF	298–1300	42.62	0.02527	−65095	−1.402e-5	−21770000	3.34e-9

[a] Data from Pankratz (1982).

4.2. *Carbonates and CO_2 environment*

Carbonates are the usual immediate precursors of the A oxides in in many synthesis routes to multicomponent oxides. Their decomposition reaction proceeds essentially under evolution of CO_2, but a subsequent formation of CO and a possibility for its further reactions elsewhere in the reaction system under different conditions must be considered when high temperatures and/or low partial pressures of oxygen are applied to assist the course of the reaction. The temperature when the CO_2 pressure of the carbonate dissociation reaches 100 kPa increases from 897(1)°C for $CaCO_3$ (Gleixner and Chang 1985) to 1250°C for $SrCO_3$ (Tamaru and Siomi 1932). The corresponding temperature for $BaCO_3$ (expectedly, some 1600°C) is not directly measured, since strong sintering hampers the kinetics. At ambient temperature, the stable modification of calcium carbonate is calcite (Chessin and Hamilton 1965, Effenberger et al. 1981) [$CaCO_3$; $R\bar{3}c$; 499.00(2), 1700.2(1)], whereas the structures (De Villiers 1971) of strontium and barium carbonate are of the aragonite-type: $SrCO_3$ [(7% Ca, 4% Ba); *Pmcn*; 509.0(2), 835.8(2), 599.7(4)], $BaCO_3$ [531.26(5), 889.58(5), 642.84(5)].

4.2.1. *Thermodynamics*

Essential data relevant to A carbonates are listed in tables 10 and 11.

Table 10
Selected standard thermodynamic values for alkaline-earth carbonates and CO_2[a]

	Phase	T	$S°$	$H°$
CO_2	(*g*)	298.15	213.677[b]	−393.509[b]
$CaCO_3$	hR	298.15	92.902[b]	−1206.921[b]
$CaCO_3$	oP	298.15	88.701[b]	−1207.126[b]
$SrCO_3$	oP	298.15	97.069[b]	−1219.845[b]
	oP → hR	1197	Δ16.429[b]	Δ19.665[b]
$BaCO_3$	oP	298.15	112.10[c]	−1213.03[c]
	oP → hR	1079	Δ16.274[b]	Δ17.56[b]
	hR → c	1241	Δ2.522[b]	Δ3.13[b]

[a] Δ is shorthand for $\Delta S°$ = or $\Delta H°$ =; for units see the Introduction.
[b] Barin et al. (1993). [c] Parker (1995).

Table 11
Virial heat-capacity coefficients (eq. 1) for alkaline-earth carbonates and CO_2 [a]; units have been omitted

	Phase	T interval	A	B	C	D	E	F
CO_2	(g)	298–1600	31.522	0.04014	−813900	−2.063e-5	120000000	3.9686e-9
$CaCO_3$	hR	298–1200	99.82	0.02663	−2161000	1.8147e-7		
	oP	298–700	81.335	0.04649	−1140000	−7.81e-7		
$SrCO_3$	oP	298–1197	89.62	0.035814	−1421000			
	hR	1197–1400	142.256					
$BaCO_3$	oP	298–1079	92.51	0.037356	−1694400	8.942e-6		
	hR	1079–1241	154.808					
	c	1241–1400	158.992					

[a] Data from Barin et al. (1993).

5. Copper oxides

CuO is monoclinic (Åsbrink and Norrby 1970) [*C2/c*; 468.37(5), 342.26(5), 512.88(6), 99.54(1)] and Cu_2O is cubic (Wrigge and Meisel 1932) [$Pn\bar{3}m$; 425.7; Niggli (1922)]. Both have very narrow homogeneity ranges (Roberts and Smyth 1921, Collins et al. 1989, Gundermann and Wagner 1937). Recently, a metastable oxidized "extension" of the latter structure is reported (Lenglet et al. 1995) [Cu_3O_2; $Pn\bar{3}m$; 431(1)]. A true intermediate Cu^{I},Cu^{II}-oxide has been known for a long time as the mineral paramelaconite, Cu_4O_3. This phase is tetragonal (O'Keeffe and Bovin 1978) [$I4_1/amd$; 582, 988] and has been considered metastable before the recent successful synthesis by a long-term air-oxidation of metallic copper in boiling concentrated aqueous ammonia (Morgan et al. 1996). Of near precursors to the copper oxides, the metallic $Cu_7O_{8-w}NO_3$ [$Fm\bar{3}m$; 948] is worth mentioning as the last intermediate product of the thermal decomposition of copper nitrate (Yazawa et al. 1990).

Copper oxides have a limited thermal stability which depends strongly on the partial pressure of oxygen in the surrounding atmosphere. The Cu–O phase diagram (Hallstedt et al. 1994) in ambient O_2 is shown in fig. 4. At p_{O_2} = 100 kPa, Cu_2O melts at some 1230°C, whereas CuO melts around 1100°C (Roberts and Smyth 1921, Schmid 1983). In air, however, dissociation of CuO into Cu_2O and O_2 at 1030°C precedes the melting of the monoxide. The temperature dependence of the dissociation pressure for CuO has been obtained by mass spectrometry (Ait-Hou et al. 1995) ($679 < T < 1033$ K) as well as by direct measurements (Roberts and Smyth 1921) at higher temperatures ($1173 < T < 1373$ K).

Thermodynamics. The copper–oxygen phase diagram has been assessed in detail including liquidus equilibria and solid solubilities (Hallstedt et al. 1994). Obtained standard Gibbs energies for the formation of copper oxides are given in table 12. Essential thermodynamic values for CuO and Cu_2O are listed in tables 13 and 14.

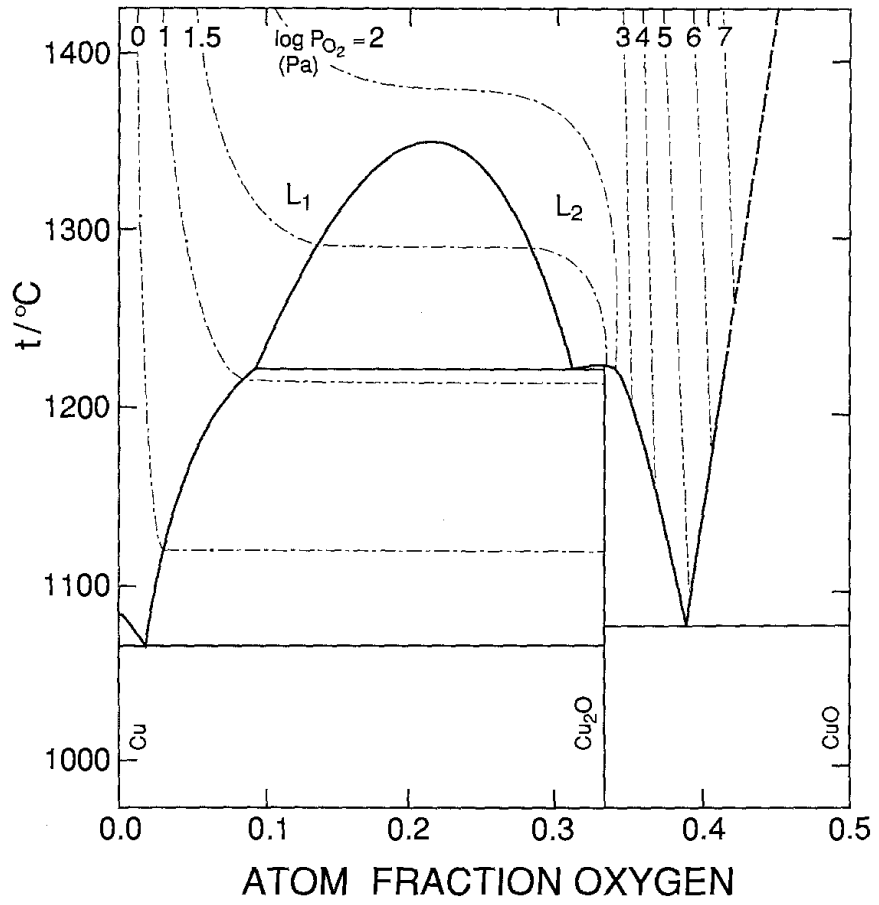

Fig. 4. A *w–t* diagram for the Cu–O system. (After Hallstedt et al. 1994.)

Table 12
Standard Gibbs-energy functions ($\Delta_r G^\circ$; eq. 2) of formation of copper oxides at $700 < T < 1304$ K according to Hallstedt et al. (1994); units have been omitted

Reaction	*A*	*B*	*C*
$2Cu_{(s)} + 1/2O_{2(g)} \rightleftharpoons Cu_2O_{(s)}$	−174.01	0.12548	−0.00679
$Cu_2O_{(s)} + 1/2O_{2(g)} \rightleftharpoons 2CuO_{(s)}$	−143.380	0.18532	−0.01137

Table 13
Selected standard thermodynamic values for copper oxides[a]

Oxide	Phase	*T*	S°	H°
Cu_2O	cP	298.15	92.68[b]	−170.26[b]
	cP→ (*l*)	1501		Δ60.7[b]
CuO	mC	298.15	43.06[b]	−155.19[b]

[a] Δ is shorthand for ΔH° =; for units see the Introduction.
[b] Hallstedt et al. (1994).

Table 14
Virial heat-capacity coefficients (eq. 1) for copper oxides; units have been omitted

	Phase	T interval	A	B	C	D	E	F	Ref.
Cu_2O	cP	298–1501	17.675	0.163	1995100	−1.6383e-4	−349830000	6.192e-8	[1]
	(*l*)	1501	60.7						[2]
CuO	mC	298–1400	−52.19	0.2674	7726500	−2.5037e-4	−1381560000	8.3279e-8	[1]

References

[1] Pankratz (1982)
[2] Hallstedt et al. (1994)

6. Systems A(O)–R(O)

The refractory character of the components suggests low rates of diffusion and problems with the establishment of equilibrium. The A(O)–R(O) systems are also very sensitive to moisture (Kwestroo et al. 1974). Owing to the presence of the very electropositive A elements, these ternary oxides will tend to react with CO_2 (and other Lewis acids as well for that matter). At high temperatures, the first step of such a reaction leads to a formation of oxide carbonates (De Leeuw et al. 1988a, Karen and Kjekshus 1991, Gotor et al. 1995).

6.1. *Trivalent R*

6.1.1. *Ca(O)–R(O)*

No stable ternary compounds are reported (Lopato 1976) at ambient temperature for the largest Rs, but some solid solubility in (hexagonal) R_2O_3 is found (Lopato 1976, Foëx 1961), *e.g.*, $x = 0.08$ for R = La (Foëx 1961). Starting from Sm, the smaller Rs are able to form a high-temperature stable phase CaR_4O_7. For R = Dy and smaller, a CaR_2O_4 phase occurs.

6.1.2. *Sr(O)–R(O)*

The large ionic size of Sr causes the CaR_2O_4-type structure to tolerate somewhat larger trivalent Rs. Only La is too large (Lopato 1976). Except for R = Nd where decomposition occurs before melting, all these phases [SrY_2O_4; *Pnam*; 1008, 1191, 340; Müller-Buschbaum (1968)] melt congruently at temperatures around 2100°C (Lopato 1976). Another intermediate compound of the formula $R_3R_4O_9$ is formed for La, Pr and Nd, but is assumed metastable at ambient temperatures (Lopato 1976, Lopato et al. 1973). The crystal structure (Schulze and Müller-Buschbaum 1980a,b, Müller-Buschbaum and Boehlke 1987) is monoclinic [$Sr_3La_4O_9$; *Cc*; 1165.7, 734.8, 1347.1, 115.6; Schulze and Müller-Buschbaum (1980a)].

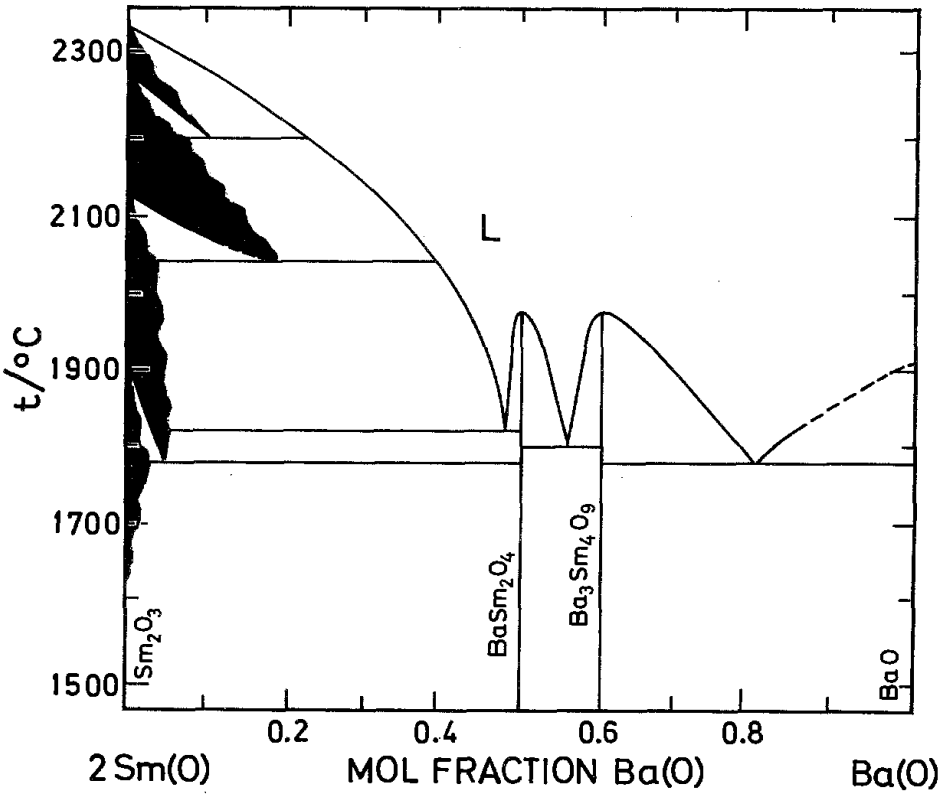

Fig. 5. An x–t diagram for the Sm(O)–Ba(O) system in air. (After Lopato 1976.)

6.1.3. *Ba(O)–R(O)*

The ionic size of Ba makes the CaR_2O_4-type structure available for the largest trivalent Rs. BaR_2O_4 occurs for La to Er and Y (Lopato 1976) [$BaLa_2O_4$; *Pnam*; 1066.8(2), 1264.2(2), 370.4(1); Wong-Ng and Paretzkin (1991); BaY_2O_4; *Pnam*; 1039.85(8), 1211.94(9), 345.06(2); Karen and Kjekshus (2000)]. For R = Nd and Sm, this phase melts congruently, whereas for the larger and smaller Rs decomposition occurs before melting; between 1850°C for R = La (Lopato 1976) and 1400°C for R = Y (Lopato 1976, W. Zhang and Osamura 1991) (a markedly different value of ~1030°C was reported by Costa et al. 1988). The phase diagram for R = Sm (Lopato 1976) is illustrated in fig. 5 and for R = Y (W. Zhang and Osamura 1991, Kale and Jacob 1989a) in fig. 6; for further diagrams, see Lopato (1976) and Lopato et al. (1970, 1972), for thermodynamics by EMF, see Subasri and Sreedharan (1998).

For Sm and smaller Rs, a $Ba_3R_4O_9$ phase occurs, which is not isostructural with the Sr phase of the same composition. When its synthesis is attempted from R oxides and $BaCO_3$, rather high temperatures are required, increasing with the electropositive character of the involved R; from 1000°C for R = Lu to 1550°C for R = Sm (Lopato 1976). The crystal structures (Müller-Buschbaum and Scheikowski 1990) of the $Ba_3R_4O_9$ phases are rhombohedral [$Ba_3Tm_4O_9$; *R3*; 605.56(4), 2495.7(2)].

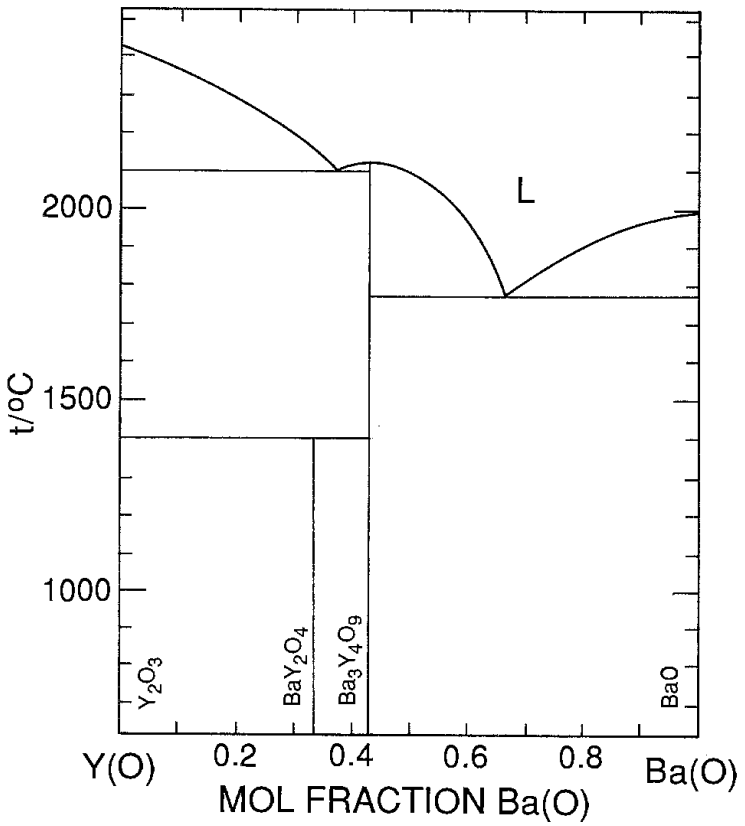

Fig. 6. An x–t diagram for the Y(O)–Ba(O) system in dry Ar/O_2 mixture with $p_{O_2} = 21$ kPa. (After Kale and Jacob 1989a and W. Zhang and Osamura 1991.)

6.2. *Tetravalent R*

6.2.1. *Ca(O)–R(O)*

No ternary oxide has been found for $R = Ce^{IV}$ (Longo et al. 1981).

6.2.2. *Sr(O)–R(O)*

Ce, Pr and Tb form two ternary oxides in the Sr(O)–R(O) systems, $SrRO_3$ and Sr_2RO_4, the latter being known only for Ce (stable up to ~1400°C, where it decomposes into $SrCeO_3$ and SrO, Longo et al. 1981). The crystal structure (Smith and Welch 1960) of the former is derived from perovskite [$SrCeO_3$; $P2_12_12_1$; 601.1, 858.8, 615.6]. Sr_2CeO_4 is reported (Mastromonaco et al. 1969) to be triclinic [607.0, 897.6, 1059.8, 94.7, 90.4, 95.8], but the present authors have indexed 32 of the first 36 PXD reflections orthorhombically [1034.(5), 612.4(2), 360.0(2)]. Under reducing conditions, phases typical for trivalent Rs are formed, like $SrTb_2O_4$, which adopts the calcium ferrite-type structure (Paletta and Müller-Buschbaum 1968).

6.2.3. *Ba(O)–R(O)*

In O_2 atmosphere, only one intermediate compound occurs for R = Ce, Pr and Tb, *viz.*, $BaRO_3$, which adopts a slightly distorted perovskite-type structure (orthorhombic for R = Ce and Pr, rhombohedral for R = Tb (Jacobson et al. 1972, Banks et al. 1972). Naturally, under reducing conditions, BaR_2O_4 is obtained also for R = Ce, Pr, Tb (Lopato 1976, Hodorowicz et al. 1990). The phase diagram for the BaO–CeO_2 system has been constructed experimentally by Guha and Kolar (1971). $BaCeO_3$ melts incongruently (close to eutecticum) at 1480°C under formation of CeO_2 and a liquid. Thermochemical data of formation for $BaCeO_3$ (as well as $SrCeO_3$) have been determined by Cordfunke et al. (1998).

6.3. *Oxide carbonate variants*

In the $Ba(O/CO_3)$–$Y(O/CO_3)$ system, at least two oxide carbonates occur. One has a triple-perovskite structure (Karen and Kjekshus 2000) with a (disordered) carbonate group at one of the three small metal-atom sites occurring per unit cell [$Ba_3Y_2(CO_3)O_5$; *P4/mmm*; 438.63(4), 1185.9(2); Karen and Kjekshus (1991)]. This phase has proved (Karen and Kjekshus 1991, Karen et al. 1990a) to be identical with $Y_2Ba_2O_5$ claimed by Kwestroo et al. (1974), Kovba et al. (1983) and Antipov et al. (1984). Another oxide carbonate of composition $Ba_4Y_2O_7{\cdot}CO_2$ is suggested (De Leeuw et al. 1988a), corresponding to what was originally (with some caution due to unindexable PXD data) proposed as an oxide phase (Kwestroo et al. 1974). Like carbonates, also oxide carbonates release CO_2 at high enough temperatures, depending on the partial pressure of CO_2 in the reaction atmosphere. As an example, $Ba_3Y_2(CO_3)O_5$ decomposes (Karen and Kjekshus 1991) at 960°C in oxygen atmosphere with ~5 ppm CO_2 into the $Ba_3Y_4O_9$ phase and what can be identified (by PXD) as the uncertain $Ba_4Y_2O_7{\cdot}CO_2$. The formation and decomposition temperatures of oxide carbonates in the $Ba(O/CO_3)$–$Y(O/CO_3)$ system for an air atmosphere have been studied by W. Zhang and Osamura (1991). A phenomenological chemical phase diagram (W. Zhang and Osamura 1991) showing, *inter alia*, the observed lower temperature limits for formation from a $BaCO_3$-containing starting mixtures, is given in fig. 7.

7. Systems A(O)–Cu(O)

The alkaline earth cuprates belong among "difficult" systems. The variability of the Cu valence, combined with basicity of the A oxides, results in a tendency to form more oxidized cuprates when the A content increases and on going from Ca to Ba. In parallel, reactivity towards CO_2 increases, demanding higher and higher temperatures for syntheses of pure oxides. The eventually formed oxide carbonate phases are difficult to identify. Occurrences of both oxide carbonates and highly oxidized cuprates intermingle in the picture of the redox equilibria, since the entropy of the liberated gas is the main factor governing their thermodynamics. In addition, structural characterizations of these phases

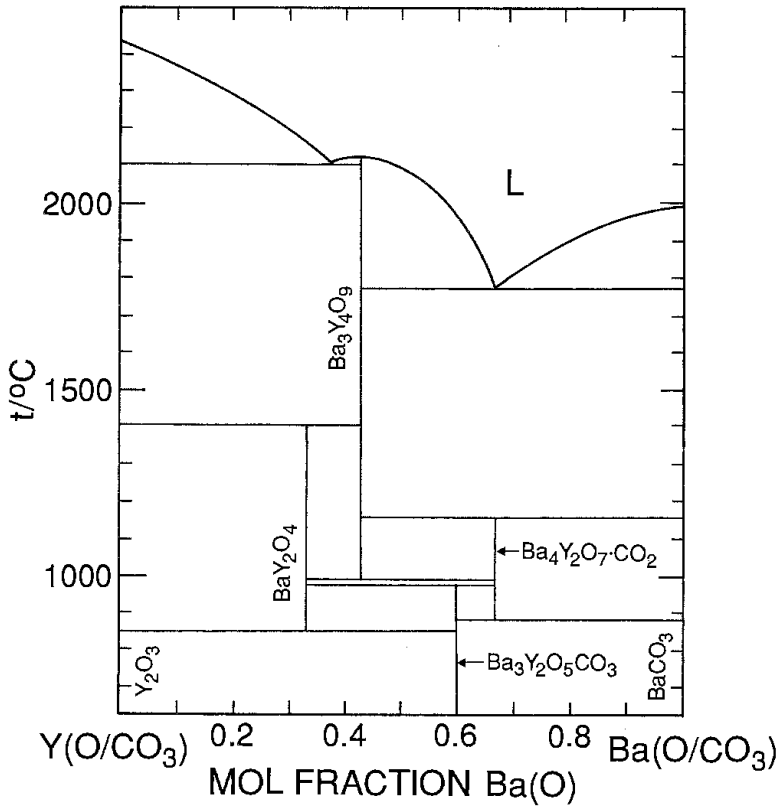

Fig. 7. Phenomenological x–t diagram for $BaCO_3$-based syntheses in the $Y(O/CO_3)$–$Ba(O/CO_3)$ system in air. (After W. Zhang and Osamura 1991.)

are often complicated by vacancies encountered in both the oxygen and the A sublattices, and this leads to a variety of order–disorder phenomena.

7.1. *Calcium cuprates*

Mapping of the Ca(O)–Cu(O) phase system, including redox equilibria, has been attempted by Suzuki et al. (1994) in the form of a three-dimensional y–p–t phase diagram covering the interval of $10^{-9} < p_{O_2} < 10^5$ Pa. An example for the y–t phase diagram is shown in fig. 8, based on consensus data referring to an air atmosphere (Gadalla and White 1966, Roth et al. 1989a, 1991), and similar to what is seen for pure oxygen atmosphere (Gadalla and White 1966, Tsang et al. 1995). Three ternary oxides are encountered:

Ca_2CuO_3, with orthorhombic crystal structure (Teske and Müller-Buschbaum 1970a, Hjorth and Hyldtoft 1990) [*Immm*; 1220.8(6), 376.8(2), 324.9(2); Weller and Lines (1989)]. This phase has the highest thermal stability of these four intermediate phases, and melts incongruently at 1085(3)°C in oxygen (Tsang et al. 1995). In the same atmosphere at temperatures below some 700°C, this phase is not formed and CaO and $Ca_{1-y}CuO_2$ are seen instead (Roth et al. 1991, Mathews et al. 1993). The oxygen content of this phase (Krüger et al. 1992) does not vary significantly from what corresponds to $\upsilon_{Cu} = 2$ and this is apparently the reason for its instability against the more oxidized phase at low temperatures.

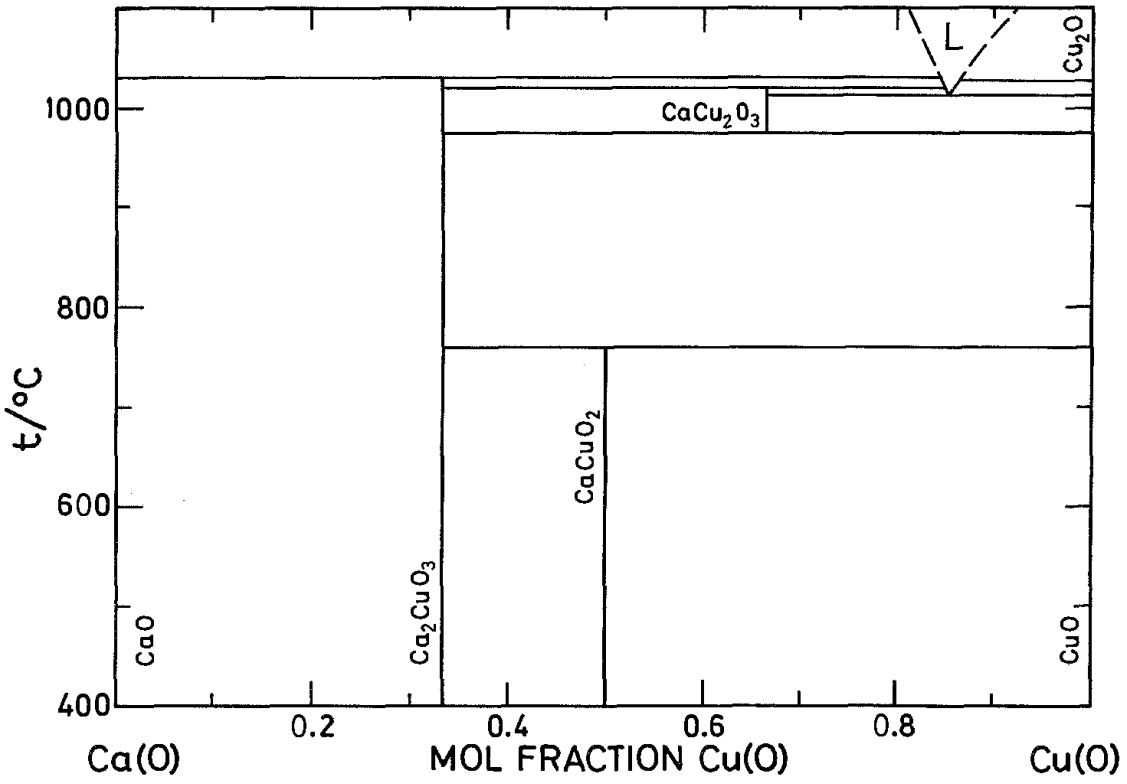

Fig. 8. A y–t diagram for the Ca(O)–Cu(O) system in air; after Roth et al. (1989a, 1991.)

$Ca_{1-y}CuO_2$, actually a structural series with superstructures or incommensurate orderings based on a $CaCuO_2$ subcell [*Fmmm*; 280.7(1), 635.1(2), 1059.7(3); Siegrist et al. (1990)]. The crystal structure (Siegrist et al. 1990) contains linear edge-sharing chains of cuprate squares. Such an arrangement does not usually allow for any significant occurrence of oxygen vacancies, yet an oxygen content of 1.93(1) for $y = 0.167$ has been measured, practically independent of temperature (Mathews et al. 1993). Since the Cu valence is high, the phase decomposes at the relatively low temperature of 835°C in oxygen, whereas in air already at 755°C (Roth et al. 1991). The Ca deficiency is associated with various possibilities for superstructure ordering, such as in $Ca_4Cu_5O_{10}$ [*Pnca*; $a' = 5a$; Siegrist et al. (1990)] or $Ca_5Cu_6O_{12}$. The latter was indexed on a monoclinic supercell [1680, 632, 1095, 75; Milat et al. (1992)]. The "homogeneity" range for A depends somewhat on temperature and oxygen pressure, since, despite the fixed oxygen content, the Cu valence may still tend to vary through the change in the A content.

$CaCu_2O_3$ [*Pmmm*; 985, 411, 347] has tetrahedrally distorted square copper–oxygen coordination, with each square (a flat tetrahedron) sharing three of its four corners to form double chains (Teske and Müller-Buschbaum 1969a). Probably as a result of the tetrahedral deformation, the oxygen content is fixed (Cu^{II}), and this contributes to the narrow range of thermal stability for this phase which occurs between 977(3) and 1045(5)°C in oxygen (Tsang et al. 1995), or at somewhat lower temperatures in air.

Recently, based on EDAX analysis, a composition $Ca_3Cu_7O_{10}$ is suggested [o; 994.2, 407.9, 345.9; Tsang et al. (1995)], but a crystal structural confirmation of this claim is yet lacking.

7.1.1. *High-pressure phases*

During the 1990s, experimentalists became generally aware of the contamination problems occurring when syntheses are conducted in the closed systems at high pressures in belt- or anvil-cell-type instruments (Wang et al. 1997). Studies can be identified which conducted experiments with appropriate precautions. Several new calcium cuprate structures have been reported in such studies at high pressures:

t-$CaCuO_2$ appears when the anvil-cell synthesis at 3 GPa from oxides is conducted above 1025°C [*P4/mmm*; 385.26(3), 317.66(3); Kobayashi et al. (1997)]. Under higher pressures or at higher temperatures, a polymorphic transformation is seen:

m-$CaCuO_2$ is formed [$P2_1$; 541.50(4), 1070.79(1), 315.01(2), 90.886(7)], which can be quenched to ambient conditions with only a minor appearance of the above phase (Kobayashi et al. 1997). Details on the phase diagram boundaries at the synthesis conditions are given by Kobayashi et al. (1997).

7.1.2. *Thermodynamics*

Thermodynamic assessment of this phase system including redox and liquidus equilibria has been attempted by Risold et al. (1995). The optimized Gibbs-energy functions for selected compositions of the three intermediate phases are listed in table 15 according to Risold et al. (1995) which lists also an extensive bibliography of the experimental data. More recently, some equilibrium partial pressures of oxygen have been measured (Yankin et al. 1996) for the thermal decomposition of Ca_2CuO_3.

Table 15
Standard Gibbs-energy functions ($\Delta_r G^\circ$; eq. 2) of formation of calcium cuprates from oxides according to Risold et al. (1995); units have been omitted

Reaction	*A*	*B*	*C*
$2CaO + CuO \rightleftharpoons Ca_2CuO_3$	−7.565	0.011255	−0.00089
$0.833CaO + CuO + 0.0485O_2 \rightleftharpoons Ca_{0.833}CuO_{1.93}$	−12.558	0.01061	
$CaO + 2CuO \rightleftharpoons CaCu_2O_3$	−3.1933	0.001983	

7.1.3. *Oxide carbonates*

In line with Ca being the least electropositive of the A elements, calcium cuprate carbonates are the least stable in this array.

$Ca_3Cu_2CO_3O_4$ phase has been obtained (Matveev et al. 1997) by a high-pressure synthesis, with crystal structure apparently of the triple-perovskite type [*P4/mmm*; 384.2, 1033.6]. $T_c = 47$ K has been measured.

7.2. *Strontium cuprates*

Mapping of the Sr(O)–Cu(O) phase system across widely varied conditions has been attempted (Suzuki et al. 1992, Alcock and Li 1990) by means of EMF measurements and the phase relationships were displayed in a three-dimensional x–p–t phase diagram covering the interval of $10^{-9} < p_{O_2} < 10^{11}$ Pa (Suzuki et al. 1992).

7.2.1. *Ambient p_{O_2} or moderate oxidizing conditions*

As an example for ambient conditions, the y–t diagram (Roth et al. 1990) referring to air atmosphere is shown in fig. 9. Three ternary phases are encountered:

Sr_2CuO_3 [*Immm*; 1269, 391, 348]. The crystal structure (Teske and Müller-Buschbaum 1969b), seen already for Ca_2CuO_3, contains chains of copper–oxygen coordination squares, and does not hence exhibit any profound variations in the oxygen content as a function of temperature (Alcock and Li 1990). However, at high pressures, the oxygen content may increase substantially.

o-$SrCuO_{2+w}$ [*Cmcm*; 357.7(1), 1634.2(1), 391.82(7); Matsushita et al. (1994)]. The crystal structure (Teske and Müller-Buschbaum 1970a, Matsushita et al. 1994) contains edge sharing, slightly deformed, double-square cuprate anions, connected into zig-zag chains. Only minor variations in the oxygen content are allowed in this arrangement, $1.975 < w < 2.035$, as observed for $0.01 < p_{O_2} < 100$ kPa at 900°C (Alcock and Li 1990).

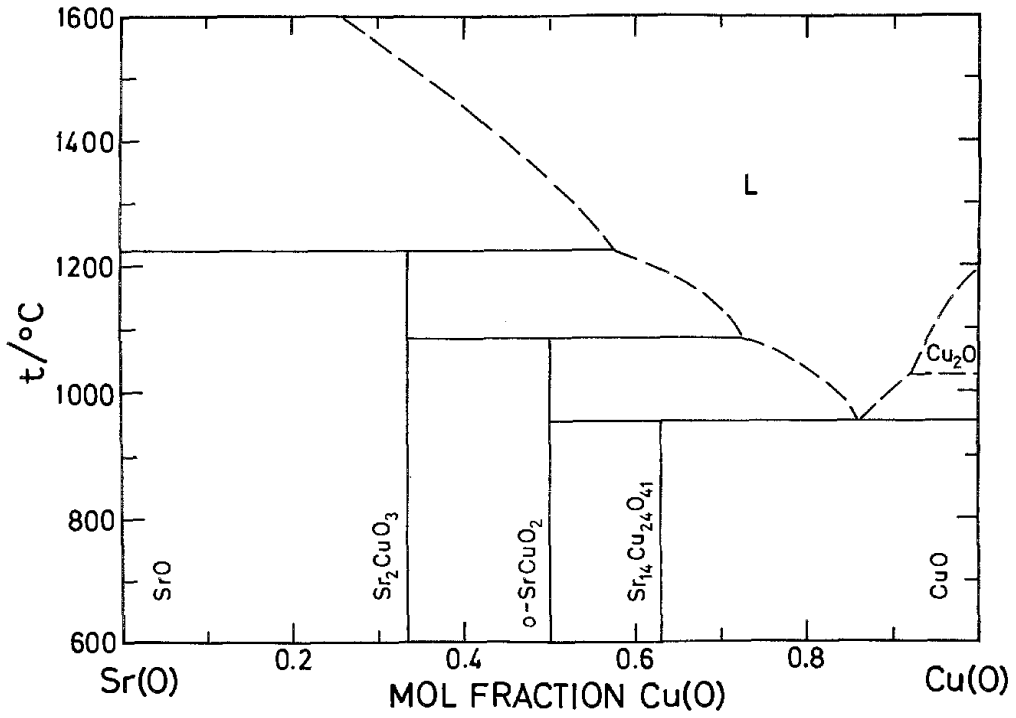

Fig. 9. A y–t diagram for the Sr(O)–Cu(O) system in air. (After Roth et al. 1990.)

$Sr_{14}Cu_{24}O_{41}$, with crystal structure (McCarron et al. 1988, Ukei et al. 1994) described as being incommensurate [$Sr_2Cu_2O_3$; *Fmmm*, 1145.7(5), 1340.9(9), 393.5(3); + $\frac{10}{7}CuO_2$; *Amma*; 1145.7(5), 1340.9(9), 274.0(2); Ukei et al. (1994)] and it is nearly compatible with a $7c = 10c'$ superstructure (Roth et al. 1990, McCarron et al. 1988). The oxygen content is almost independent of temperature ($\Delta w < 0.002$ per Cu between 670 and 970°C), and the relatively high Cu valence $v_{Cu} \approx 2.24$ is preserved until decomposition.

7.2.2. *Low p_{O_2} or reducing conditions*

The y–t diagram (Suzuki et al. 1992) at $p_{O_2} = 10$ Pa, based on both phase formation and EMF data is shown in fig. 10 and is nearly identical with the diagram of Alcock and Li (1990), based on EMF measurements. One new ternary phase is seen, compared with the ambient-pressure situation:

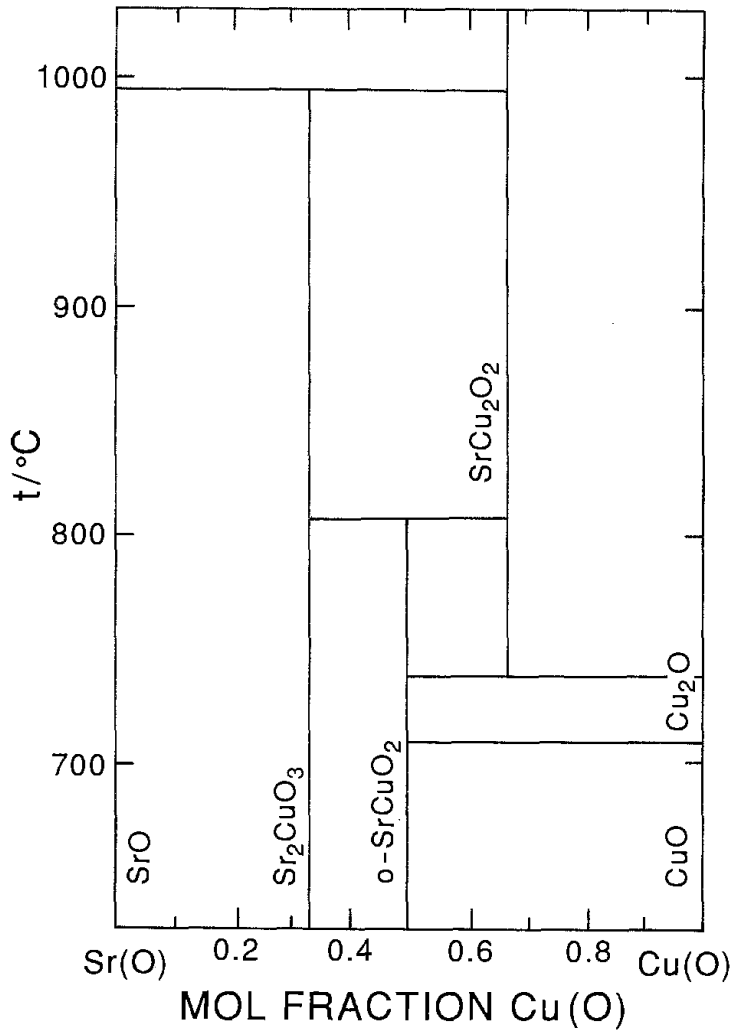

Fig. 10. A y–t diagram for the Sr(O)–Cu(O) system at $p_{O_2} = 10$ Pa calculated from thermodynamic data. (After Suzuki et al. 1992.)

$SrCu_2O_2$ [$I4_1amd$; 548, 982], has crystal structure (Teske and Müller-Buschbaum 1970b) with a typical linear coordination at each monovalent Cu, which is in turn located tetrahedrally around each oxygen atom. This phase is the last ternary oxide appearing upon reduction of the more oxidized phases. As an example of the redox reactions, $Sr_{14}Cu_{24}O_{41}$ decomposes (Alcock and Li 1990) at 920°C and p_{O_2} = 6 kPa into $SrCuO_2$ and CuO. The $SrCuO_2$ phase gives in turn $SrCu_2O_2$ at 820°C when p_{O_2} = 10 Pa (Alcock and Li 1990). Under the same conditions, the Sr_2CuO_3 phase is still stable.

7.2.3. *High p_{O_2} or oxidizing conditions*

The y–p isothermal phase diagram (Sastry et al. 1995) for 775°C, up to p_{O_2} = 60 MPa, is shown in fig. 11. Highly oxidized phases are stabilized under such pressures of oxygen:

Sr_2CuO_{4-w} [*I4/mmm*; 376.31(1), 1256.01(9); Shimakawa et al. (1994)] and related $Sr_{n+1}Cu_nO_{2n+2-w}$ series (Hiroi et al. 1993) The crystal structure (Shimakawa et al. 1994) of Sr_2CuO_{4-w} is basically of the K_2NiF_4 type (also designated as the T type). It differs from the ambient-pressure Sr_2CuO_3 in that the Cu–O coordination squares are appended to approach octahedral coordination, while some oxygen vacancies are created. The symmetry of the oxygen ordering is complex and the superstructure is considered to be incommensurate (Wang et al. 1995, H. Zhang et al. 1995). An oxygen vacancy content as low as $w = 0.1$ is reported (Lobo et al. 1990) after treatment under 16 MPa of oxygen at 400°C, whereas $w \approx 0.5$ is obtained after a high-pressure synthesis at 6 GPa and 850°C, with $KClO_4$ as a source of oxygen. The significance of this high-pressure phase is in its superconductivity, reaching a maximum T_c of some 90 K at intermediate levels of oxygen content (Han et al. 1994).

The high oxygen pressure samples are not usually phase pure. One such minor phase has recently been identified as monoclinic $SrCuO_{7/3+w}$, $0 < w < 1$ [*Pm*; 843, 1110, 364, 83.2], based on HREM (Wu et al. 1994). Another minority phase designated as $Sr_6Cu_8O_w$

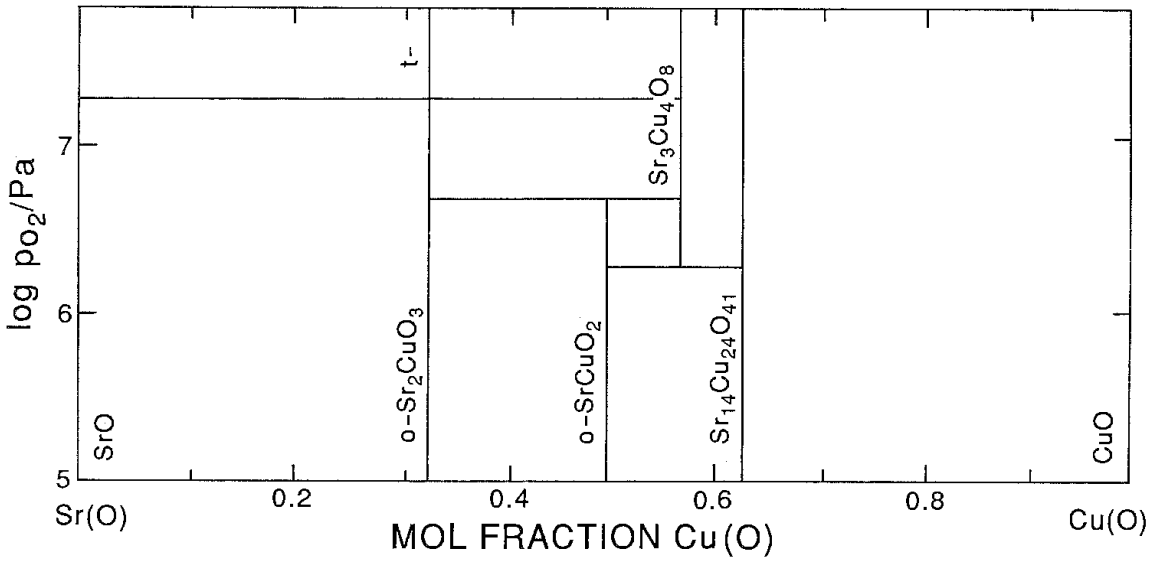

Fig. 11. A y–p diagram for the Sr(O)–Cu(O) system at 775°C in oxygen. (After Sastry et al. 1995.)

[o; 378.9, 802.7,1250] has been reported under $KClO_3$-assisted experiments (Ono 1992). However, the same technique led to the synthesis of a bulk phase:

$Sr_2Cu_2O_5$ with orthorhombic crystal structure (Chen et al. 1996) [*Pbam*; 542.4(2), 1083.7(4), 373.1(1)], having exclusively square-pyramidal copper coordinations, connected at their apices. This non-superconducting (Chen et al. 1996) phase is of the $Ca_2Mn_2O_5$ type and has also analogues where Sr is completely replaced by La (Bringley et al. 1990a) or Nd (Chen et al. 1995b).

7.2.4. *High-pressure phases*

Three additional oxides emerge:

t-$SrCuO_2$ [*P4/mmm*; 392.6, 343.2; Takano et al. (1989)]. The crystal structure (Takano et al. 1989) of the phase obtained at 6 GPa and 1050°C contains sheets of corner sharing, copper–oxygen coordination squares in an extremely simple, perovskite-like arrangement.

$Sr_{1-y}CuO_2$, $y \approx 1/4$, has an incommensurate structure (Sastry et al. 1995) [oI; 681.82(12), 371.13(7), 1102.03(17); + oF; 681.82(12), 272.90(3), 1102.03(17)], $25b \approx 34b'$, and is related or analogous to the series occurring (Siegrist et al. 1990, Milat et al. 1992) for A = Ca. This phase has later also been obtained (Karpinski et al. 1997) in high oxygen-pressure synthesis (p_{O_2} = 200 MPa), illustrating the overlap of the high-pressure and high oxygen pressure techniques.

$Sr_{n-1}Cu_{n+1}O_{2n}$ is a structure (Kazakov et al. 1997, Kobayashi et al. 1997) series (Hiroi et al. 1991) related to o-$SrCuO_{2+w}$ having n = 3 [$SrCuO_2$; *Cmmm*; 392.99(5), 1156.15(4), 349.26(1); Kobayashi et al. (1997)] and n = 5 [$Sr_2Cu_3O_5$; *Cmmm*; 393.01(1), 1940.16(5), 346.05(1); Kobayashi et al. (1997)]. Both phases are metastable under ambient conditions and decompose when the activation energy is supplied at elevated temperatures (Kobayashi et al. 1997). No superconductivity has been observed (Kazakov et al. 1997).

7.2.5. *Thermodynamics*

Thermodynamic assessment of this phase system at ambient oxygen pressure (p_{O_2} = 101 kPa), including redox and liquidus equilibria, was presented by Risold et al. (1997a). Fitting of the literature (experimental) values against the phase diagram gives optimized Gibbs-energy functions for the four phases stable under ambient conditions (table 16), however, neglecting variations in oxygen content.

7.2.6. *Oxide carbonates*

For compositions most rich in Sr, oxide carbonates occur:

$Sr_2CuO_2(CO_3)$ has been identified (Babu et al. 1991) as an intermediate in the synthesis of Sr_2CuO_3 from $SrCO_3$ and CuO. The crystal structure (Babu et al. 1991), solved from PND data [*P4/mmm*; 390.33(2), 749.25(4)], consists of CuO_2 planes interconnected at octahedral apices by CO_3 groups. In a further investigation of the crystal structure (Miyazaki et al. 1992a), a determination was attempted for the orientation of

Table 16
Standard Gibbs-energy functions ($\Delta_r G°$; eq. 2) of formation of strontium cuprates from oxides according to Risold et al. (1997a); units have been omitted

Reaction	*A*	*B*
$SrO + Cu_2O \rightleftharpoons SrCu_2O_2$	−15.5	0.0018
$2SrO + CuO \rightleftharpoons Sr_2CuO_3$	−27.82	0.00008
$SrO + CuO \rightleftharpoons SrCuO_2$	−22.74	0.0023
$14SrO + 24CuO + 1.5O_2 \rightleftharpoons Sr_{14}Cu_{24}O_{41}$	−625.5	0.254

the carbonate groups in a single-phase material [$I\bar{4}$; 780.5, 1499.3]. The same structure (Uehara et al. 1993) is obtained by replacing, say, 20% of the carbonate groups by borate [$I\bar{4}$; 778.81(15), 1496.8(3)]. Above some 220°C, a structural transition is observed [$P42_12$; 554.36(1), 753.82(1); Nakata et al. (1995)].

$Sr_3Cu_2(CO_3)O_4$ was obtained (Yamaura et al. 1994) almost single-phase in an anvil-cell synthesis [$Sr_3Cu_2(CO_3)O_4$; t; 391.47, 1088.75; Wang et al. (1997)] having obviously the crystal structure of the triple-perovskite type.

7.3. *Barium cuprates*

These phases exhibit the highest Cu oxidation states and have the highest reactivity towards CO_2 and H_2O of all alkaline earth cuprates. This makes the Ba(O)–Cu(O) system highly dependent on partial pressures of oxygen and impurity gases in the chemical atmosphere. Redox equilibria in the Ba(O)–Cu(O) system have been examined (Voronin and Degterov 1994) by means of a thermodynamic assessment considering a selected set of reasonably well defined phases. An experimental verification (Lindemer and Specht 1995) of these data together with their extension into the Ba-rich and liquidus regions, accompanied by detailed characterizations of the investigated phases (including residual-carbon analyses) confirmed the features reported. As an example for the occurring subsolidus redox relationships, the situation (Voronin and Degterov 1994) at 727°C is shown in fig. 12 (overleaf).

7.3.1. *Ambient p_{O_2} or moderate oxidation conditions*

Experimental investigations (Wong-Ng et al. 1988, W. Zhang et al. 1990, Lindemer and Specht 1995) by PXD, microscopy, DTA and TGA of this phase system in an air atmosphere (both synthetic and natural) revealed two intermediate phases present at the usual ceramic firing conditions above 800°C:

Ba_2CuO_{4-w} takes a K_2NiF_4-type, orthorhombically deformed structure (Wong-Ng et al. 1988). At 810°C and p_{O_2} = 21 kPa, an orthorhombic-to-tetragonal transition is observed (W. Zhang et al. 1990). According to the *p–t–w* diagram (Lindemer and Specht 1995) this transition occurs around $4 - w = 3.2$ and is accompanied by a small discontinuity (a jump) in the oxygen content of the phase, yielding the high-temperature phase with an oxygen content of $\leqslant 3.1$ per formula. The oxygen content at the onset of

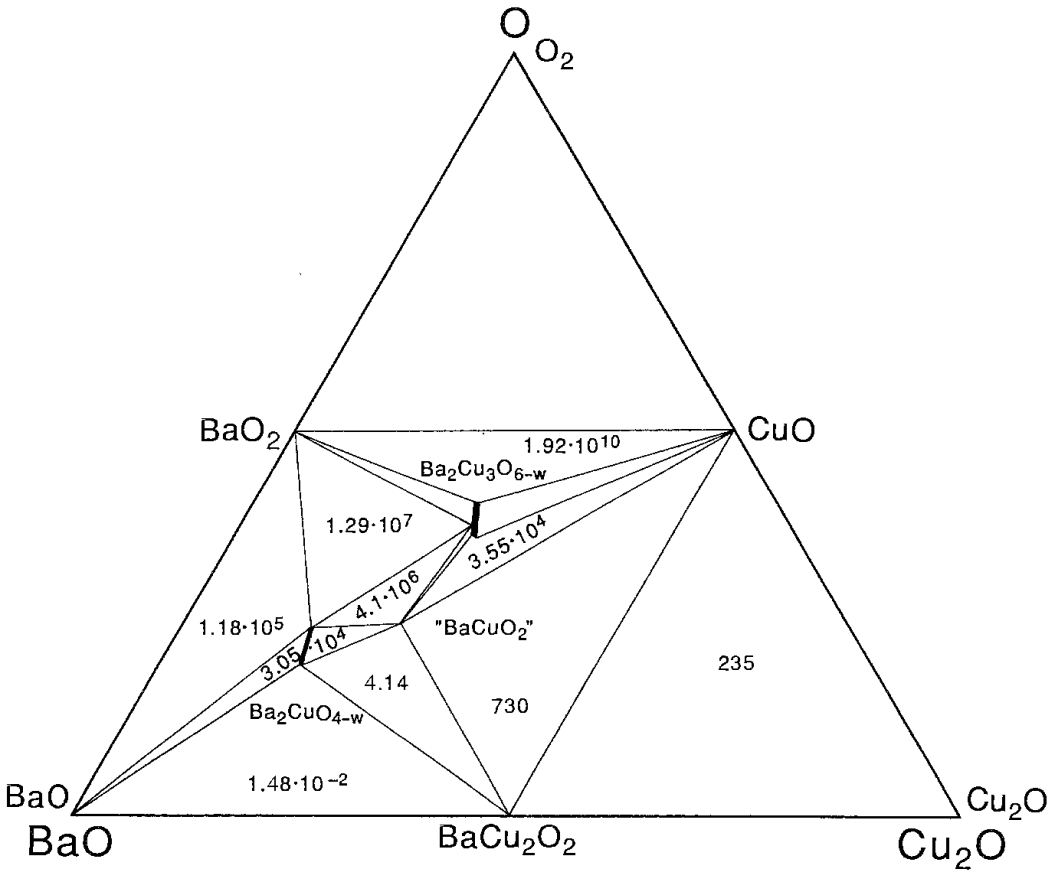

Fig. 12. Isothermal BaO–Cu_2O–O diagram at 727°C calculated from thermodynamic data (after Voronin and Degterov 1994); p_{O_2} in Pa is given in 3-phase fields.

the transition (when varied by p_{O_2}) increases slightly with increasing temperature. The phases can be quenched to room temperature, *e.g.*, tetragonal $Ba_2CuO_{3.10}$ [*I4/mmm*; 399.2, 1298.5; Mazza et al. (1990)] from 850°C when $p_{O_2} = 10^3$ Pa, or orthorhombic $Ba_2CuO_{3.30}$ [*Immm*; 1296.6, 410.1, 390.7; Wong-Ng et al. (1988)] from 700°C in oxygen (Lindemer and Specht 1995). The relatively high oxidation state of Cu occurs in accordance with the high BaO content in the oxide. The Ba_2CuO_{4-w} phase is not formed on firing of carbonaceous starting materials or in air at temperatures below the melting point in the carbonate system (which is lower (Rian 1992) than the melting point of 890°C (Lindemer and Specht 1995) for Ba_2CuO_{4-w}), but it is readily obtained (W. Zhang et al. 1990) from the oxides or BaO_2.

$BaCuO_{2+w}$ is apparently a somewhat approximate formula for this cubic phase with an unusually large unit cell. A slight cation nonstoichiometry is suggested, based on experiments with samples accurately positioned in the phase system (Wong-Ng and Cook 1996) and on some crystal-structure studies. Also the copper valence can change over a modest range, between $v_{Cu} = 1.96(2)$ [c; 1830.3(6)] and $v_{Cu} = 2.18(2)$ [c; 1828.8(4); Karen et al. (1990a)]. An experimental mapping of the stability is attempted by an equilibration and quenching technique and plotted into a p–t diagram (Genoud et al. 1995). Although the

oxygen contents are not directly analyzed by Genoud et al. (1995), it is seen that the phase indeed decomposes at both the oxidized and reduced end of the stability range at temperatures predicted by Voronin and Degterov (1994). The crystal structure (Kipka and Müller-Buschbaum 1977) has several complex and crystallographically somewhat disturbing features and has therefore been a subject of many studies by a variety of structural techniques (Weller and Lines 1989, Gutau and Müller-Buschbaum 1989, Paulus et al. 1991, 1994). Two explanations for the encountered structural problems have been suggested: (i) partial occupancies at several Cu- and O-sites, and/or (ii) stabilization by the presence of carbonate ions. As an example concerning the vacancy problem, two different formula units (Z = 96 assumed for both) are obtained for a fully oxidized sample by a single-crystal method (Paulus et al. 1994) and Rietveld refinements from PXD data (Guskos et al. 1995), *viz.*, $Ba_{0.92}Cu_{1.06}O_{2.14}$ and $Ba_{0.92}Cu_{1.01}O_{2.17}$, respectively. However, PND data (Weller and Lines 1989) give yet another answer, $Ba_{0.92}Cu_{0.94}O_{1.94}$. The idea that this phase actually is an oxide carbonate has been supported by a structural (Aranda and Attfield 1993) evaluation based on PND and PXD data. Rietveld refinements were able to localize carbon where previously a Cu, or, alternatively, an O atom was considered to have a "strange" environment, and enabled even the location of the eight O sites appearing owing to the statistical disorder of the carbonate-group orientations [$Ba_{44}Cu_{48}(CO_3)_6O_{81+w}$; $Im\bar{3}m$; 1830.69(2)]. Structure refinements by Peitola et al. (1999) give $w = 12$ and $w = 5$ (in terms of the latter formula) for the most and least oxidized compositions, respectively. The possibility that $BaCuO_2$ is an oxide carbonate cannot easily be dismissed based on the synthesis conditions, because the temperatures are generally under 1000°C and traces of CO_2 are omnipresent in the chemical environment, starting materials, *etc.* Further support may be obtained from the fact that the only structural analogue to $BaCuO_{2+w}$ is a nickel oxide carbonate (Torkar et al. 1969, Gottschall and Schöllhorn 1993). There are also observations of some CO_2 evolution during the acid hydrolysis of the sample, and of abnormally high contents of residual CO_2 as compared with other Ba cuprates (Ba_2CuO_{4-w} as an example) (Lindemer and Specht 1995).

It has been suggested that additional, Cu-rich phases exist in this system, appearing as satellite phases during the crystallization of the $YBa_2Cu_3O_7$ superconductor. One such example (Bertinotti et al. 1989, Yakhou et al. 1996) is given here, identified from an electron diffraction pattern of the satellite reflections (Bertinotti et al. 1989) as well as from such reflections (Yakhou et al. 1996) obtained by single-crystal synchrotron X-ray diffraction: $BaCu_3O_4$ [*Cmmm*; 1098, 550, 392; Bertinotti et al. (1989)]. The formation of this phase is believed to be dependent on the epitaxy growth on the main phase and hence a synthesized bulk $BaCu_3O_4$ is not available.

7.3.2. *Low p_{O_2} or reducing conditions*

Two new phases appear at low partial pressures of oxygen and high temperatures:

$BaCu_2O_2$, with the crystal structure (Teske and Müller-Buschbaum 1972) already encountered in the Sr version [$I4_1amd$; 572.2, 1006.4] having monovalent Cu. This is the last ternary oxide appearing upon reduction in the Ba(O)–Cu(O) system.

Ba_3CuO_4 [h; 788.3, 1555; Abbattista et al. (1988a)], perhaps somewhat surprisingly belongs also in this category of reduced phases. The reason is that it decomposes into Ba_2CuO_{4-w} when exposed to an ambient oxygen atmosphere at elevated temperatures. This means that Ba_3CuO_4 has a structurally fixed oxygen content and divalent copper, which, owing to the large content of Ba, can only be maintained at relatively reducing conditions (950°C and $p_{O_2} = 0.1$ Pa).

7.3.3. *High p_{O_2} or oxidizing conditions*

Investigations of chemical phase relations in the Ba(O)–Cu(O) system at temperatures below 800°C or at high pressures of oxygen has proved extremely demanding on experimental and analytical techniques. In particular, this is due to the sluggish kinetics during the syntheses at low temperatures, strong affinity of both the starting materials and products towards the carbon dioxide and the possibility for reaching relatively very high oxidation states of Cu. The phases then can decompose upon liberation of CO_2 and/or O_2 as a function of pressure and temperature, and this complicates their identification. In this situation it was not unreasonable to approach the problem by thermodynamic modelling (Voronin and Degterov 1994). The *y–t* phase diagram at ambient oxygen pressure, which includes also the region of the highly oxidizing conditions at low temperatures (based on Voronin and Degterov 1994), has been constructed by Lindemer and Specht (1995) and is shown in fig. 13. Figure 14 shows the situation as calculated (Voronin and Degterov 1994) for a relatively low temperature of 827°C under a varied pressure of oxygen.

One highly oxidized phase appears:

$Ba_2Cu_3O_{6-w}$, the elusive low-temperature phase, has only recently been synthesized phase pure (Brosha et al. 1996). The crystal structure is suggested (Brosha et al. 1996) to be related to those of $NaCuO_2$ and $KCuO_2$ (Brese et al. 1989), and therefore analogous to the $A_{1-y}CuO_2$ phases where A = Ca or Sr. The structure contains edge-sharing chains of square coordinated copper interleaved by Ba layers having mutually incommensurate (sub)structures (Migliori et al. 1999) of orthorhombic symmetry [0.67 to 0.70 Ba; *Ammm*, 570(5), 730(3), 391(3); + CuO_2; *F222*, 1140(5), 730(3), 273(3)]. Previously reported more elementary structural arrangements (Thompson et al. 1989, 1990, Chmaissem et al. 1993) are based on the Ba sublattice.In line with the suggested structural prototypes, it is also proposed (Brosha et al. 1996) that there exists a homogeneity region with respect to Ba, $0.33 < y < 0.25$, referring to the formula $Ba_{1-y}CuO_2$. The PXD pattern of $Ba_2Cu_3O_{6-w}$ can be identified as the main component in most of the previously published reports on the high-oxygen $BaCuO_{2.5}$ phase, either as synthesized at high pressures (Arjomand and Machin 1975, Laffez et al. 1994), or low temperatures (Machida et al. 1991, Petriček et al. 1992, Mingmei et al. 1994). Very often, one of the minor components is then barium carbonate. The saturated oxygen content of this phase (Thompson et al. 1990, Maiorova et al. 1993) at 21 kPa O_2 and 300°C corresponds to $v_{Cu} = 2.51$. It can be reduced (Maiorova et al. 1993) to some $v_{Cu} = 2.37$ before thermal decomposition above some 700°C (Brosha et al. 1995) into the less oxidized Ba_2CuO_{4-w} and CuO (Voronin and Degterov 1994), or into, also less oxidized, "$BaCuO_{2+w}$"-oxide carbonate and CuO

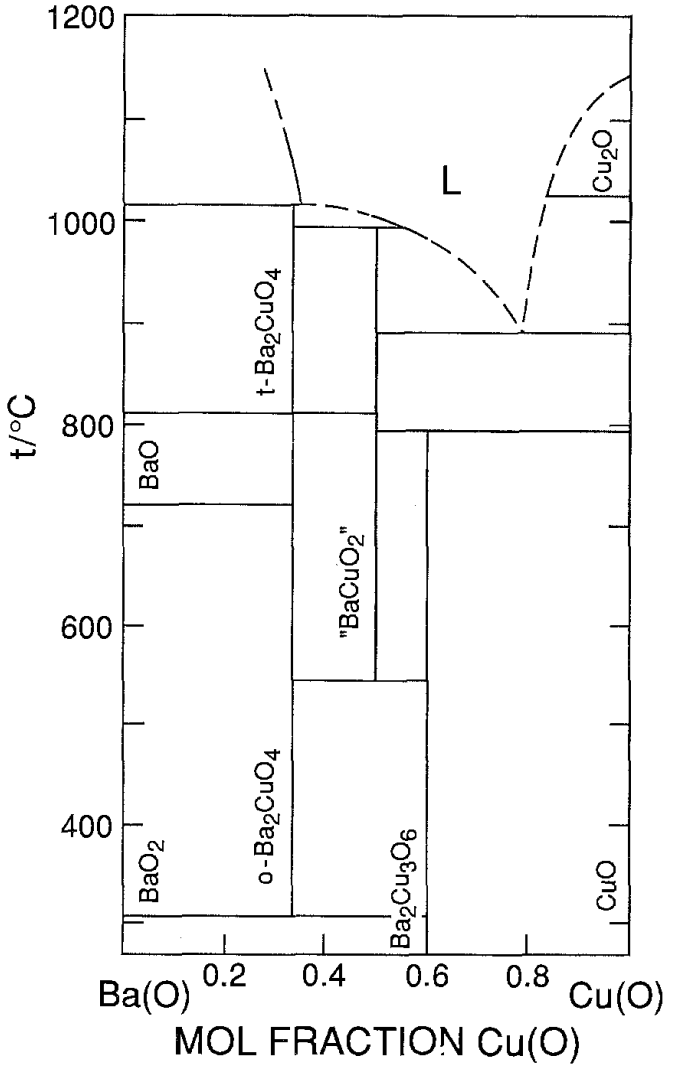

Fig. 13. A y–t diagram for the Ba(O)–Cu(O) system at p_{O_2} = 21 kPa, calculated from thermodynamic data. (After Lindemer and Specht 1995.)

(Brosha et al. 1996, Laffez et al. 1994, Maiorova et al. 1993, Chang et al. 1994). Barium carbonate would be necessary for the latter reaction, but it can be identified in the PXD diagrams in small amounts in all these cases. The onset of the $Ba_2Cu_3O_{6-w}$ decomposition is reported (Chang et al. 1994) to be as low as 600°C, and the completion to take a considerable amout of time. The reverse of this reaction, *viz.*, the decomposition of the "$BaCuO_{2+w}$" oxide carbonate into $Ba_2Cu_3O_{6-w}$ (and $BaCO_3$) is observed at low temperatures (Bazuev and Krasilnikov 1991) or at high pressures (Graf et al. 1991), indicating that the redox component and not the eventual carbonatization is the dominant driving force for the decomposition of $Ba_2Cu_3O_{6-w}$. The low thermal stability of the highly oxidized $Ba_2Cu_3O_{6-w}$ severely limits its synthesis conditions to carbonate-free and reactive, usually nitrate-based starting materials (Petriček et al. 1992, Graf et al. 1991, George et al. 1995, Klinkova et al. 1992).

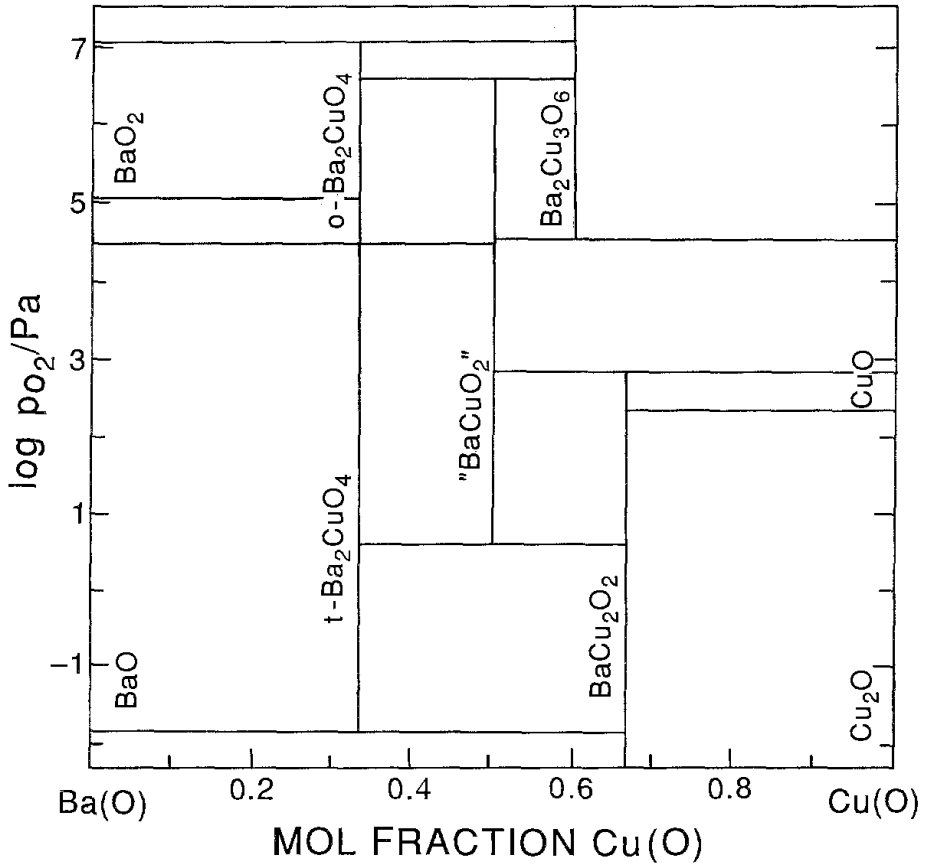

Fig. 14. A y–p diagram for the Ba(O)–Cu(O) system at 827°C calculated from thermodynamic data. (After Voronin and Degterov 1994.)

7.3.4. *High-pressure phases*

One phase occurs in addition to those included in fig. 14:

$BaCuO_{3-w}$, with crystal structure (Laffez et al. 1994) [$P222_1$; 982.7(1), 567.83(7), 952.52(4)] resembling that of $BaMnO_3$, but containing an extensive amount of oxygen vacancies.

7.3.5. *Thermodynamics*

Gibbs energy functions for nominal compositions of the important intermediate phases have been calculated from critically assessed data by Voronin and Degterov (1994), and were experimentally reevaluated (Lindemer and Specht 1995) from a TGA equilibrium study of reactions involving carbonates. The data based on Voronin and Degterov (1994) are listed in table 17. For the $Ba_2Cu_3O_{5+w}$ phase which has a wide range of oxygen contents, an approximation is adopted by Voronin and Degterov (1994), based on fitting of (four) oxygen-content vs. temperature points and the equilibrium dependence of the $Ba_2Cu_3O_{5+w}$ thermal decomposition in air from Thompson et al. (1989). Terms $\ln p_{O_2} \propto \ln[w/(1-w)]$ and $RT \ln p_{O_2} = 2[\partial \Delta_r G/\partial w]_T$ are used to relate the variable

Table 17
Standard Gibbs-energy functions ($\Delta_r G°$; eq. 2) of formation of barium cuprates from oxides according to Voronin and Degterov (1994); units have been omitted

Reaction	A	B	C	Note
$BaO + Cu_2O \rightleftharpoons BaCu_2O_2$	−46.08	0.003517	0.0004	
$BaO + CuO + (w/2)O_2 \rightleftharpoons BaCuO_{2+w}$	−38.82	−0.00327	0.0011	w as at 1100 K
$2BaO + CuO + 0.05O_2 \rightleftharpoons$ t-$Ba_2CuO_{3.1}$	−76.24	0.02486		
$2BaO + CuO + 0.15O_2 \rightleftharpoons$ o-$Ba_2CuO_{3.3}$	−76.24	0.02486		

Table 18
Third-law standard thermodynamic values for $BaCuO_{2+w}$ according to Minenkov et al. (1996); for units see the Introduction

	Phase	T	$S°$	$H°_T - H°_0$
$BaCuO_{2.00}$	c	298.15	117.6(6)	−17.375(30)
$BaCuO_{2.09}$	c	298.15	121.0(5)	−17.89(3)

oxygen content to the thermodynamic variables. The original reference is suggested for the actual data.

Heat capacities for two compositions of the "$BaCuO_{2+w}$" phase have been measured (Minenkov et al. 1996) in the range of 8 to 305 K. The third-law data obtained are listed in table 18.

7.3.6. *Oxide carbonates*

Except for the "$BaCuO_2$" phase which, as discussed above, actually may be a carbonate-stabilized phase, a true oxide carbonate occurs in the Ba-rich region:

$Ba_2CuO_2(CO_3)$, is analogous [t, 400.2(1), 797.4(3); Armstrong et al. (1993)] to the previously described $Sr_2CuO_2(CO_3)$. Both the oxygen and carbonate contents appear to be variable, the former upon depletion of the square planar cuprate coordinations, the latter, as suggested by Matacotta et al. (1997), in a solid-solution range of these with the carbonate ions, according to the formula $Ba(CuO_w)_{1-u}(CO_3)_u$. When the carbonate content u is low, the structural features are very close to that of the oP-$BaCO_3$ (aragonite). The syntheses of single-phase products is burdened with sluggish kinetics in closed-system syntheses, and this is preventing characterizations by conventional methods.

7.4. *Calcium strontium cuprates*

7.4.1. *Ambient p_{O_2} or moderate oxidation conditions*

Wide ranges of solid solubility exist between pairs of corresponding cuprates, as can be seen from the phase diagrams for the Ca(O)–Sr(O)–Cu(O) subsolidus system (Risold et al. 1997b, Jacob et al. 1995, Roth et al. 1989a, George et al. 1995, Schulze et al.

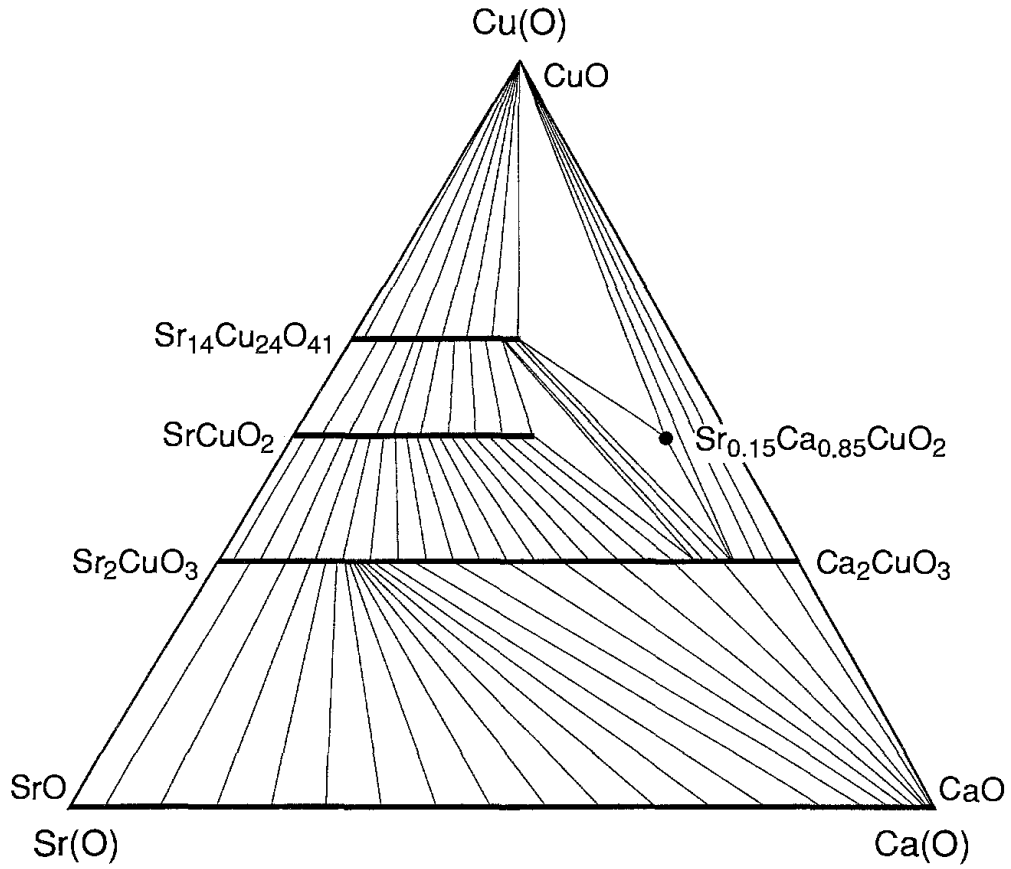

Fig. 15. Subsolidus Sr(O)–Ca(O)–Cu(O) phase diagram at 1000°C and 101 kPa O_2. (After Risold et al. 1997b.)

1990). The situation at 1000°C in 101 kPa oxygen according to Risold et al. (1997b) is shown in fig. 15, where the system is assessed thermodynamically over a wide range of temperatures and partial pressures of oxygen, including the solidus equilibria. The diagram in fig. 15 is very similar to that observed for syntheses from oxides at 850°C in air by Roth et al. (1989a) and Schulze et al. (1990). Below some 900°C, a miscibility gap in the (Ca,Sr)O solid solution appears, correctly drawn in by Jacob et al. (1995) and Risold et al. (1997b).

A complete solid solubility occurs between Sr_2CuO_3 and Ca_2CuO_3 (Jacob et al. 1995, Roth et al. 1989a, George et al. 1995, Schulze et al. 1990, Krüger et al. 1992). Roughly half of the strontium may be replaced by Ca in $Sr_{14}Cu_{24}O_{41}$, and in the ambient-pressure phase o-$SrCuO_{2+w}$ at 850°C (Schulze et al. 1990). Higher solid solubilities are observed at higher temperatures (Jacob et al. 1995, Roth et al. 1989a, George et al. 1995). Structural details for these solid solutions have been given by McCarron et al. (1988) and Heinau et al. (1994). In addition, a very specific partial Sr/Ca replacement may stabilize the high-pressure structure of the t-$SrCuO_2$ type also under ambient conditions:

$Ca_{1-y}Sr_yCuO_2$ is obtained single phase for $0.10 < y < 0.16$ (Zhao et al. 1996), as examples, for $y = 0.14$ [*P4/mmm*; 386.11(2), 319.95(2); Siegrist et al. (1988)] and for $y = 0.16$ [*P4/mmm*; 386.7(2), 321.95(2); Roth et al. (1989a)]. Detailed variation

of the unit-cell parameters as a function of composition was shown by Kikkawa et al. (1995). The discovery of this phase was given considerable attention, since its crystal structure contains only the infinite sheets of corner-shared squares as the copper oxygen coordinations, and was quickly dubbed "the parent structure of the high-T_c superconductors". [Eventually, the phase has been made superconducting by using high-pressure syntheses for doped versions: A p-type superconductor with T_c = 110 K is obtained by introducing A-vacancies (Azuma et al. 1992), and an n-type superconductor by Nd doping (Smith et al. 1991).]

7.4.2. *High p_{O_2} or oxidizing conditions*

Both the high pressure and the highly oxidative environment of these experiments affect the stability of the solid-solution phases. The phase diagram (Robertson et al. 1996) at a high pressure of oxygen (p_{O_2} = 35 MPa) and a relatively low temperature (775°C) in fig. 16 is a good example of the situation under oxidizing conditions. The most remarkable change noted here is the restricted solid solubility of Sr_2CuO_{3+w} and Ca_2CuO_3, which otherwise are completely miscible (George et al. 1995) both at ambient conditions and at high pressure (1 GPa; not of oxygen). The obvious reason is that the Sr phase oxidizes into the K_2NiF_4-type structure under the oxygen pressure, whereas the Ca counterpart does not, and retains its structural coordination squares around Cu. The other

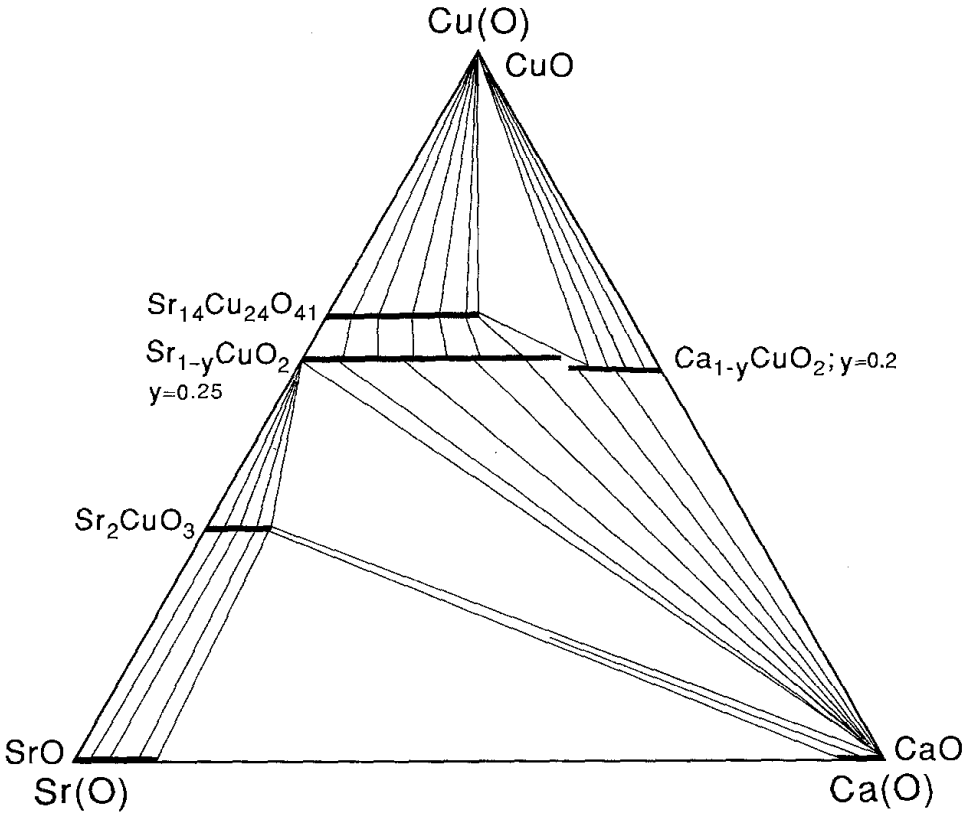

Fig. 16. Subsolidus Sr(O)–Ca(O)–Cu(O) phase diagram at 775°C under high-pressure oxygen, p_{O_2} = 35 MPa. (After Robertson et al. 1996.)

changes introduced by the high oxygen pressure are that the highly oxidized phases (or structural series) $Ca_{1-y}CuO_2$ and $Sr_{1-y}CuO_2$ emerge, with what appears as complete solid solubility. The $SrCuO_2$-based solid solution is unstable, and so is the $Ca_{1-y}Sr_yCuO_2$ ($0.13 < y < 0.17$) phase (Robertson et al. 1996).

7.4.3. *High pressures*

In contrast with the situations at both ambient (fig. 15) and high p_{O_2} (fig. 16), the phase diagram at 1020°C in fig. 17 shows that the highly oxidized phases are not stabilized under the 4 GPa anvil-cell synthesis (Kobayashi et al. 1997). This illustrates the differences in the chemical environment and state conditions among these techniques. Complete Ca/Sr solid solubilities are seen for A_2CuO_3 and t-$ACuO_2$ with essentially divalent copper (Kobayashi et al. 1997). A possible ordering of the latter structure is reported (Ramírez-Castellanos et al. 1996) by HREM for the 1 : 1 composition of the latter phase.

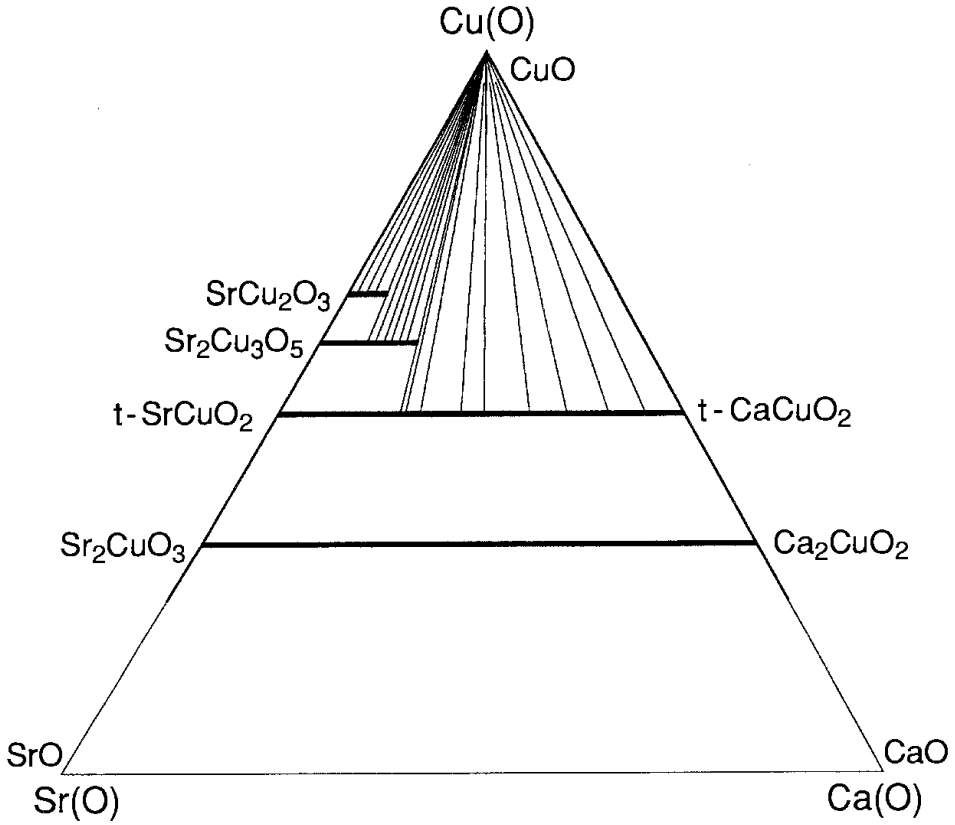

Fig. 17. Subsolidus Sr(O)–Ca(O)–Cu(O) phase diagram at 1020°C under anvil-cell synthesis at 4 GPa (a portion indicated by the thick frame). (After Kobayashi et al. 1997.)

7.5. *Calcium barium cuprates*

As the size difference between Ba and Ca is appreciable, true quaternary oxides emerge in the Ca(O)–Ba(O)–Cu(O) subsolidus phase diagram (Greaves and Slater 1990, Kubat-Martin et al. 1990) shown in fig. 18:

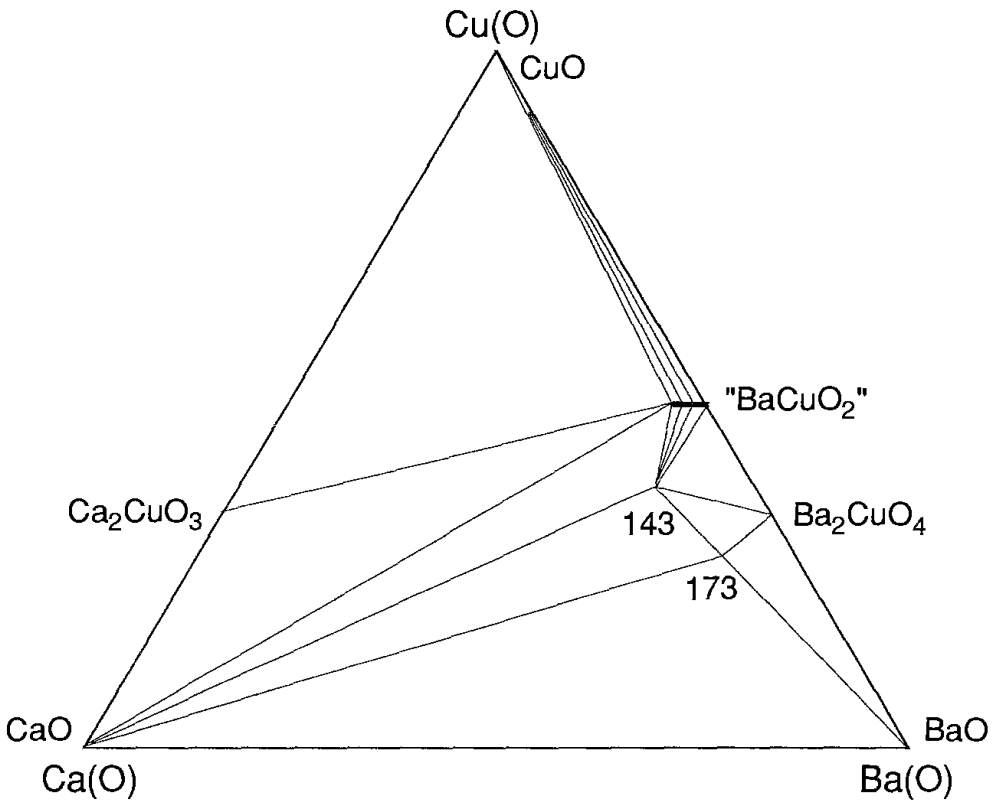

Fig. 18. The subsolidus Ca(O)–Ba(O)–Cu(O) phase diagram as observed for syntheses from BaO_2, $BaCuO_2$ and Ca_2CuO_3 precursors in oxygen at 900°C. (After Kubat-Martin et al. 1990 and Lin and Wu 1996.)

$CaBa_4Cu_3O_w$, with a cubic, perovskite-related structure (Kubat-Martin et al. 1992) which contains Cu-coordination octahedra and (disordered) squares [$CaBa_4Cu_3O_w$; $Im\bar{3}m$; 813.98(1)].

According to experiments (Lin and Wu 1996) conducted in pure oxygen at 900°C, a more Ba-rich phase, assigned $CaBa_7Cu_3O_w$, occurs between $CaBa_4Cu_3O_w$ and BaO. The occurrence of these two quaternary phases makes this part of the phase diagram very similar to what is found when Ca is replaced by Y (see sect. 13).

7.5.1. *Oxide carbonates*

In line with the just mentioned analogy with the system containing Y, a variety of oxide carbonates occur. The phase-diagram mapping by Lin and Wu (1996) appears to indicate the existence of a solid-solution region with several oxide-carbonate phases located around the composition 184. This could possibly be a oxide-carbonate solid-solution region analogous to that found (Karen and Kjekshus 1991) in the Y-analogue system, where the Cu- and Y-coordination polyhedra and carbonate anions replace each other to a limited extent in the crystal structure of the perovskite-related solid solution.

One specific ordering has been structurally identified in detail:

$CaBa_4Cu_2CO_3O_6$ with tetragonal structure (Kikuchi et al. 1995) contains isolated copper–oxygen coordination squares, bridged at their octahedral apices by carbonate anions, and linear copper–oxygen dumbbels, also occurring in the vicinity of the carbonate groups [*P4/mmm*; 578.79(2), 814.09(3)]. Despite the different coordinations, copper is divalent on the average. A similar or identical phase has been also obtained previously, showing that the details in the oxygen and carbonate content can be variable (Greaves and Slater 1991a, Kikuchi et al. 1994). The compound is so stable that it can be obtained by direct synthesis in air from carbonaceous components at some 960°C (Kikuchi et al. 1995).

Several other related structure types are suggested by Lin and Wu (1996). Other less stable phases, or perhaps structural patterns, occur in thin layers formed by laser ablation, adopting the general formula $(CaCuO_3)_m(Ba_2CuO_2CO_3)_n$ (Hervieu et al. 1996).

7.6. *Strontium barium cuprates*

Owing to the similarity of Sr and Ba, no true quaternary oxide occurs, but there are ranges of solid solubility between the corresponding cuprates (fig. 19; Roth et al. 1989b). Of these mixed systems, the mutual solid solubility of Ba_2CuO_{3+w} and Sr_2CuO_3 is investigated in particular (Mazza et al. 1990). Since the oxygen content of the former phase is variable, whereas rather constant in the latter at ambient conditions, the homogeneity range is very much dependent on the partial pressure of oxygen, and subsequently on the quenching procedure. For samples quenched from 1000°C (*viz.*, relatively reducing conditions) there is an extended range of solid solubility between Ba_2CuO_{4-w} ($w \approx 1$) and Sr_2CuO_3, with continuous variation in the unit-cell parameters and oxygen content across the composition range. At 975°C in O_2 and a cooling rate of 40°C/h (*viz.*, ample opportunity for oxidation) the Sr-rich region $(Sr_{1-y})_2Ba_yCuO_3$ is found (Slater et al. 1995) to extend to $y = 0.3$. In the Ba-rich region, a composition $(Ba_{0.6}Sr_{0.4})_2CuO_{3.26}$ has been prepared with crystal structure of the K_2NiF_4 type [*I4/mmm*; 389.88(3), 1281.5(3)] that exhibits a high-T_c superconductivity ($T_c \approx 50$ K) (Hodges et al. 1996).

7.6.1. *Oxide carbonates*

No new structural arrangements appear as a result of the simultaneous presence of Sr and Ba as compared to the systems with one A. However, a complete solid solubility is seen in the $(Sr_{1-y}Ba_y)_2CuO_{3-w}(CO_3)$ system (Armstrong et al. 1993, Lappas et al. 1993). The unit cell of these solid solutions has been described for both the low- and high-temperature types of $Sr_2Cu(CO_3)O_6$. Although a $y = 0.5$ sample is of the low-temperature type [*P4/mmm*; 392.81(1), 760.45(2)] according to a PND study (Armstrong and Edwards 1992), single-crystal investigation (Shibata et al. 1994) seems to indicate that a further Sr,Ba mixing stabilizes the ordering of the carbonate groups [$y \approx 0.5$; $P42_12$; 556.1, 782.3]. This solid-solution phase is remarkable by its superconductivity ($T_c \approx 30$ K), occurring after oxygen doping at 5 MPa (Kinoshita and Yamada 1992).

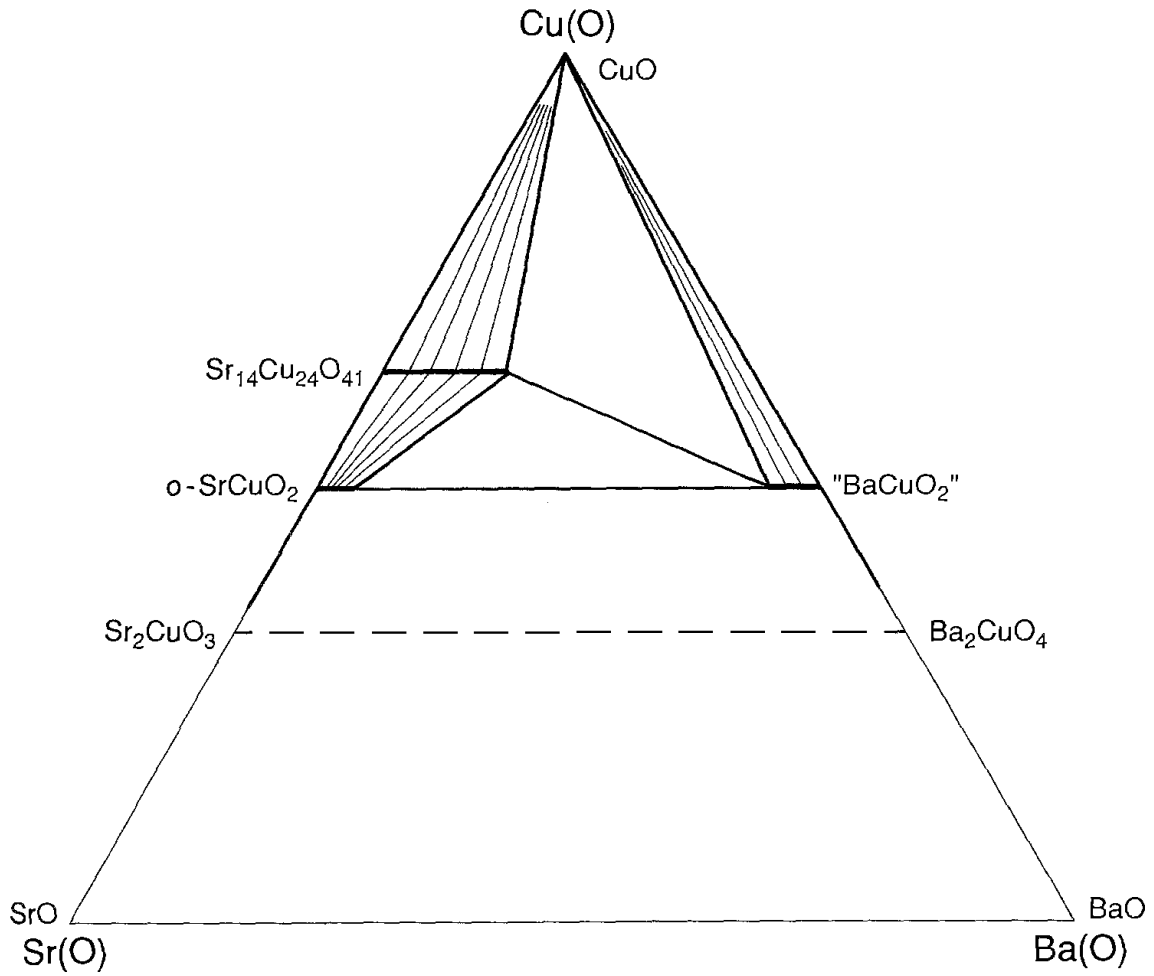

Fig. 19. A portion (indicated by the thick frame) of the subsolidus Sr(O)–Ba(O)–Cu(O) phase diagram as observed in oxygen at 950°C. (After Roth et al. 1989b.)

8. Systems R(O)–Cu(O)

Various intermediate phases are formed with trivalent R elements depending on the ionic size of R and the partial pressure of oxygen. No ternary oxides of tetravalent Ce, Pr and Tb with CuO are hitherto reported (Jorda and Cohen-Adad 1991, Cheong et al. 1989). The attainable oxidation state of Cu is somewhat lower than it was the case with the A elements, in conformity with the difference in the electropositive character between R and A. In general, the Cu^{II} compounds are formed at ambient oxygen pressures, below 1000–1100°C. Formation of ternary oxides with trivalent copper is observed only for the most electropositive Rs at high pressures of oxygen. Compounds of Cu^{I} are obtained under reducing conditions or at rather high-temperatures. The redox equilibria in relation to phase diagrams have been studied in detail by electrochemical measurements for R=Gd (Jacob et al. 1993, Kale and Fray 1995a), Ho (Kale and Fray 1995b), Y (Kale and Jacob 1989b, Suzuki et al. 1990, Konetzki and Schmid-Fetzer 1992), Yb (Kale and Fray 1995b) and Lu (Przybyło and Fitzner 1996).

8.1. *Ambient p_{O_2} or moderate oxidizing conditions*

The x–t phase diagrams for R cuprates gradually change features when going across the R series, but can be divided into three typical groups. A diagram typical for the smaller trivalent R ions is shown in fig. 20 for the Y(O)–Cu(O) system in air, as obtained (Kale and Jacob 1989b, Gadalla and Kongkachuichay 1991) by DTA and PXD. The diagram for the Nd(O)–Cu(O) system in air, as obtained (Jorda and Cohen-Adad 1991, Wong-Ng et al. 1994) by DTA, TGA, SEM and PXD, is shown in fig. 21. A similar diagram is valid (Fotiev et al. 1990) for R = Eu. The phase diagram for the La(O)–Cu(O) system in air (Skakle and West 1994a) is shown in fig. 22.

Two intermediate compositions are observed, $R_2Cu_2O_5$ and R_2CuO_4, both appearing in two structure types, their stability (Takayama-Muromachi and Navrotsky 1993) being dependent on the R size. Starting with the smallest R:

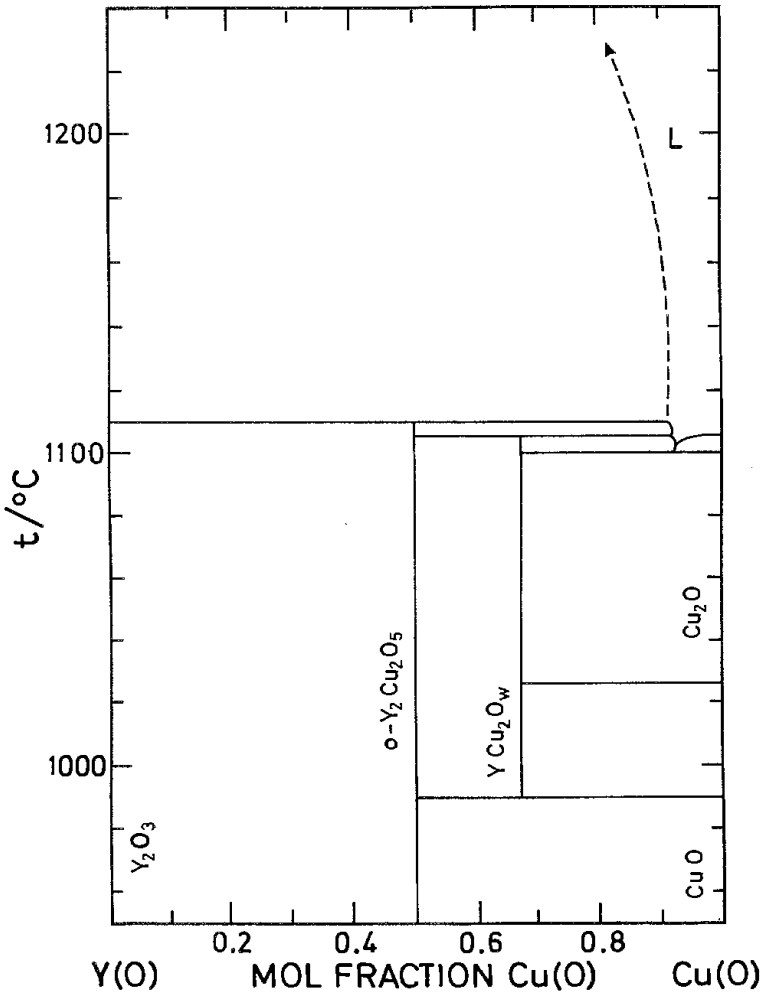

Fig. 20. An x–t diagram for the Y(O)–Cu(O) system in air. (After Kale and Jacob 1989b and Gadalla and Kongkachuichay 1991.)

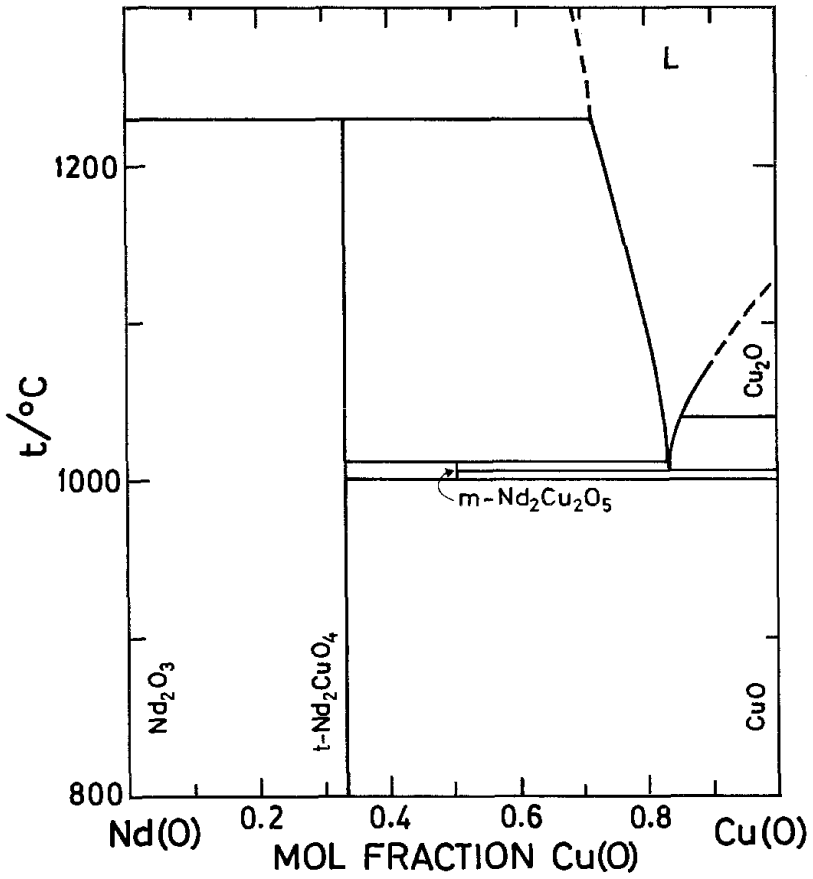

Fig. 21. An x–t diagram for the Nd(O)–Cu(O) system in air. (After Jorda and Cohen-Adad 1991 and Skakle and West 1995a.)

o-$R_2Cu_2O_5$, is formed for R = Dy–Lu, Y and Sc, (Wong-Ng et al. 1990a) as an example, $Y_2Cu_2O_5$ [*Pna*2_1; 1080.03(8), 349.53(2), 1245.88(8); Fjellvåg et al. (1988a)]. The crystal structure (Fjellvåg et al. 1988a, Freund and Müller-Buschbaum 1977a,b, Aride et al. 1989, García-Muñoz and Rodríguez-Carvajal 1990) contains slightly deformed Cu–O coordination tetrahedra, and the oxygen content is therefore structurally fixed. The phase is entropy stabilized and, as an example, $Y_2Cu_2O_5$ is accordingly not formed under a minimum temperature of around 700°C (Kale and Jacob 1989b, Brosha et al. 1994).

m-$R_2Cu_2O_5$, has been observed (Norrestam et al. 1991, Cava et al. 1991, Skakle and West 1994a, 1995a) for large trivalent R = Nd and La in an extremely narrow region of temperatures just above 1000°C. The crystal structure (Cava et al. 1991, Skakle and West 1994a, 1995a) [$Nd_2Cu_2O_5$; *C2/c*; 1372.8(2), 365.66(2), 27.549(3), 105.19(1); Skakle and West (1995a)], contains Cu-coordination octahedra connected by coordination squares, and has divalent copper. This phase is considered (Cava et al. 1991) to be a member of a structural series $R_{4+4n}Cu_{8+2n}O_{14+8n}$, seen so far only for $n = 2$ and $n = 3$.

t-R_2CuO_4, also referred to as the T′ phase, forms for large Rs except La (R = Gd, Eu, Sm, Nd and Pr) (Wong-Ng et al. 1990a). As examples: Gd_2CuO_4 [*I4/mmm*; 380, 1180;

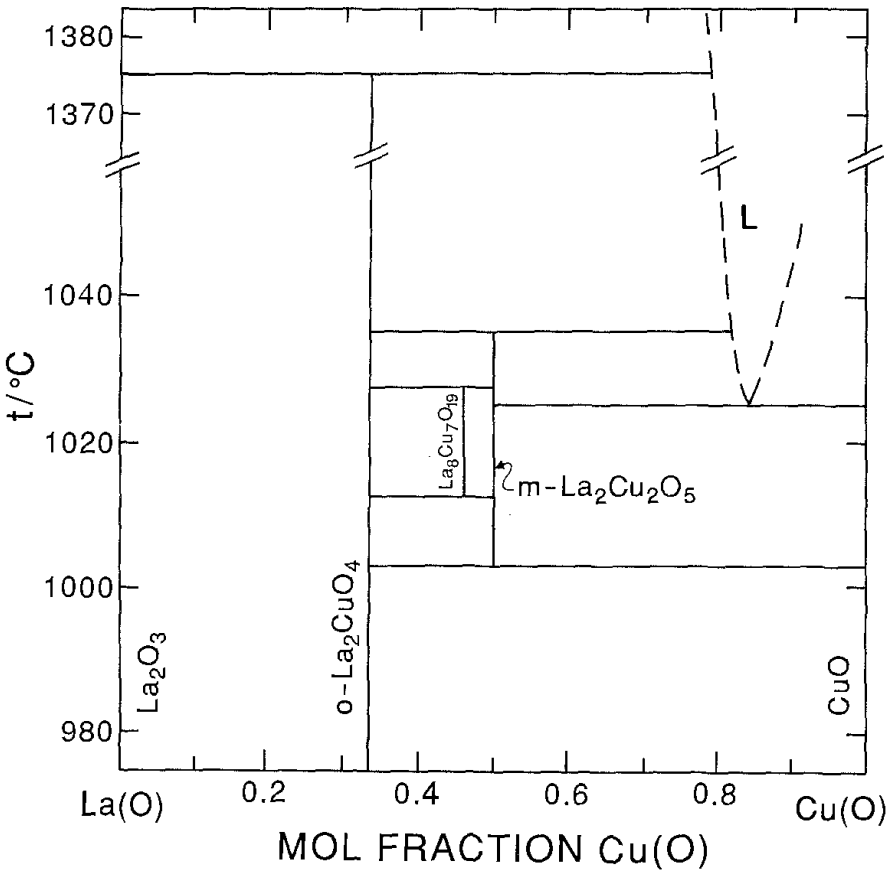

Fig. 22. An x–t diagram for the La(O)–Cu(O) system in air. (After Skakle and West 1994a.)

Grande et al. (1977)], Nd_2CuO_4 [394.5, 1217.1; Müller-Buschbaum and Wollschläger (1975)], and Pr_2CuO_4 [396.01(3), 1223.0(1); Cox et al. (1989)]. The latter is high-temperature stable in air, maintaining trivalent Pr (Hodorowicz et al. 1990). The crystal structure (Grande et al. 1977, Müller-Buschbaum and Wollschläger 1975, Cox et al. 1989, Martin et al. 1988) contains sheets of square-planar, corner-sharing cuprate anions, alternating with layers of isolated oxide anions, both layers interleaved by R. Therefore t-R_2CuO_4 is really a cuprate oxide, and the formula could as well be written $R_2(CuO_2)O_2$. Also this phase appears to be entropy stabilized (Kale and Fray 1995a). This series of phases is remarkable in the sense that its members become superconducting upon electron doping, which may be achieved either by partial F for O (James et al. 1989) or Ce for Nd (= R) (Tokura et al. 1989) substitution, but not by deoxidation, since the oxygen content is structurally fixed.

o-R_2CuO_4, also referred to as a T phase, forms only for R=La and has an orthorhombically distorted structure (Grande et al. 1977, Longo and Raccah 1973) of the K_2NiF_4 type [La_2CuO_4; *Bmab*; 536.3(5), 540.9(5), 1317(1); Longo and Raccah (1973)]. This structure contains layers of octahedral, corner-sharing cuprate anions. The layers are slightly buckled, due to a tilt of the octahedral building units. At ~200°C, the tilt disappears and a transformation into the tetragonal K_2NiF_4-type structure is observed

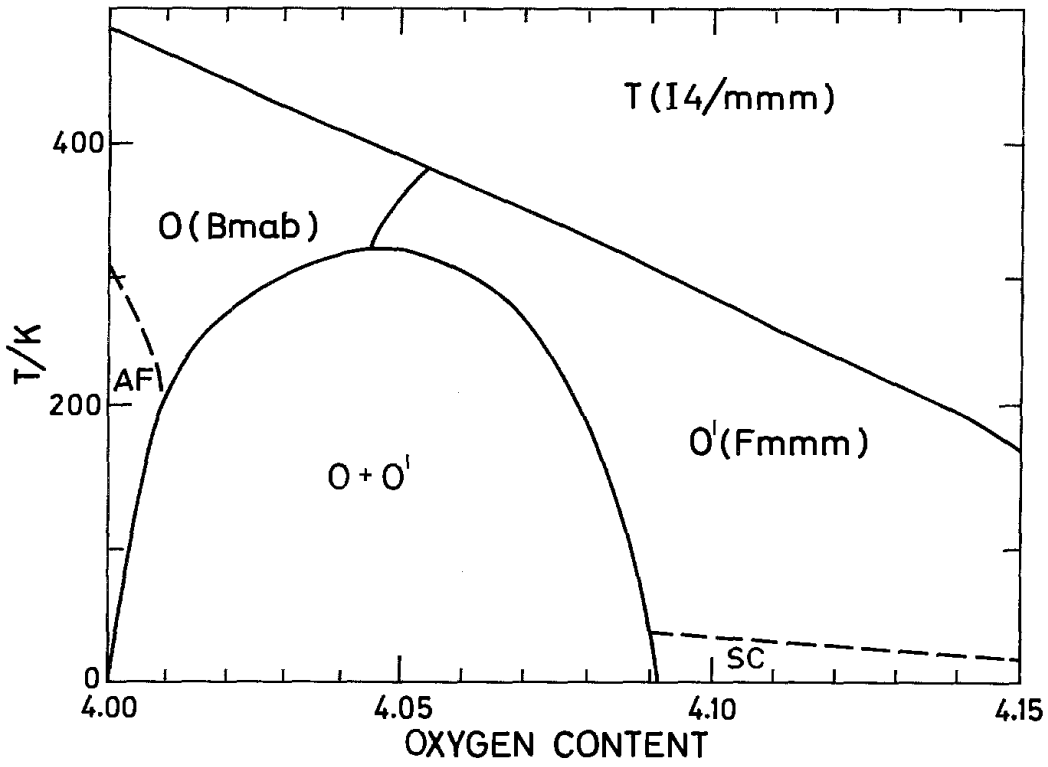

Fig. 23. Low-temperature w–T diagram for La_2CuO_{4+w}. (After Dąbrowski et al. 1989b.)

(Dąbrowski et al. 1989a). Weak indications of superconductivity were rather surprisingly recorded for this virtually insulating oxide, when synthesized in oxidative environments at low temperatures (*e.g.*, by an electrochemical oxidation). Later it is realized that additional oxygens can be inserted into the structure and that, below a certain temperature, this results in a separation into two phases: an insulating La_2CuO_4 and a conducting La_2CuO_{4+w}, the latter being responsible for the superconductivity (Dąbrowski et al. 1989b, Hundley et al. 1990, Chaillout et al. 1990, Zolliker et al. 1990, McCarty et al. 1991). The distinction in oxygen content, which may amount up to 0.09 per formula, depends on temperature (Dąbrowski et al. 1989b) and can be structurally (Chaillout et al. 1989, 1990, Xiong et al. 1996) located. The phase diagram of La_2CuO_{4+w} has been assessed many times (Dąbrowski et al. 1989b, Goodenough et al. 1993, Hor et al. 1996, Chou and Johnston 1996) and the various versions differ in details. An example according to Dąbrowski et al. (1989b) is given in fig. 23.

One additional phase with suggested composition $YCu_2O_{2.5}$ is seen (Gadalla and Kongkachuichay 1991) at some 1000–1100°C by high-temperature PXD. This phase could not be quenched to room temperature. No structural interpretation is given, but the relatively simple PXD diagram could correspond to a spinel phase. From fig. 20, however, it seems not likely that it contains Cu^{I} as suggested by the formula.

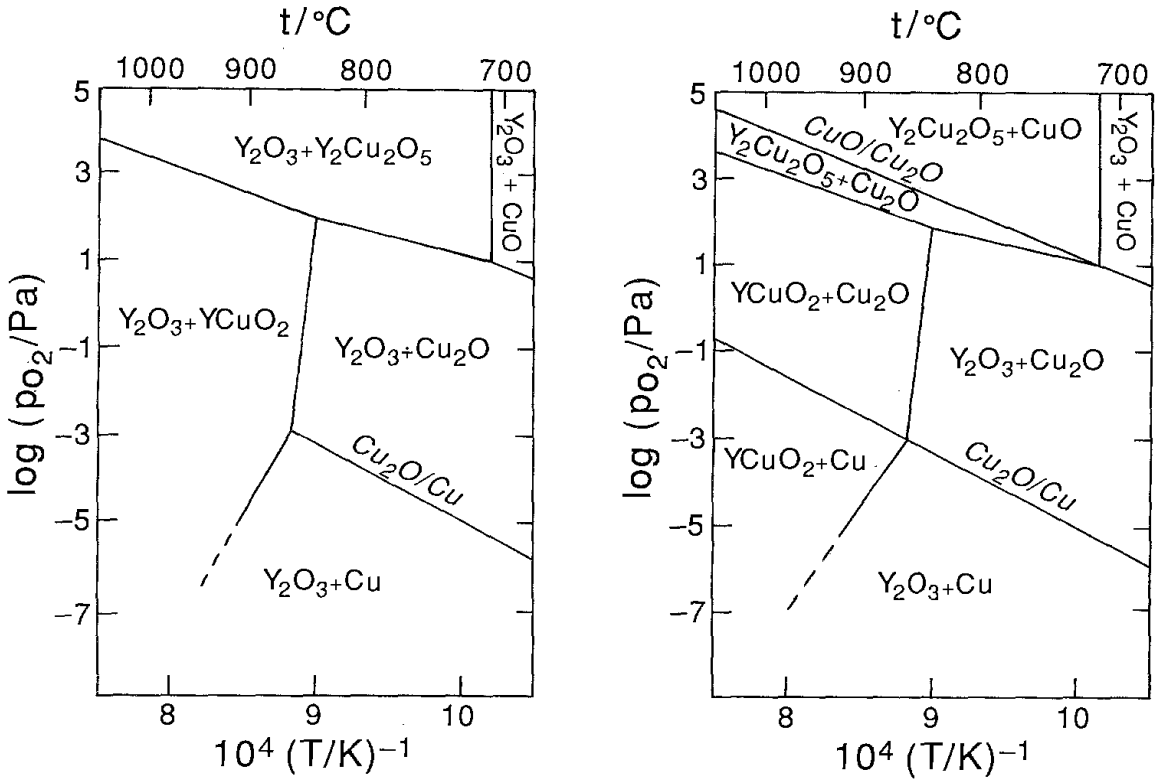

Fig. 24. An isoplethal, Y- and Cu-rich (left and right, respectively) p–t diagram of chemical stability for the Y(O)–Cu(O) system, as calculated from thermodynamic data. (After Konetzki and Schmid-Fetzer 1992.)

8.2. *Low p_{O_2} or reducing conditions*

The redox equilibria typical for the system containing the smallest R atoms can be illustratred for the Y–Cu–O system. Investigations of the phase relationships proved rather difficult, particularly owing to problems with metastability. However, a series of five isothermal Y–Cu–O phase diagrams can be composed from Kale and Jacob (1989b) and Konetzki and Schmid-Fetzer (1992) with an excellent mutual agreement. Since only 1 : 1 intermediate phases occur, two isoplethal p–t diagrams, one Y-rich and one Cu-rich, are sufficient (Konetzki and Schmid-Fetzer 1992) to cover the entire field, as shown in fig. 24. The redox equilibria for the systems with the largest Rs are illustrated in fig. 25 on an isothermal phase diagram (Kale and Fray 1995a) and in fig. 26 on an x–p diagram of the Gd–Cu–O system. At low (partial) pressures of oxygen, only the R_2CuO_4 phases become extensively oxygen deficient. For R = La, the composition $La_2CuO_{3.89}$ is obtained at 1000°C and p_{O_2} = 20 Pa close to the decomposition limit (Opila and Tuller 1994). Detailed p_{O_2}, t-dependences of the oxygen content were measured and evaluated by Opila and Tuller (1994). Also the Nd_2CuO_4- and $Y_2Cu_2O_5$-type phases decompose (Kale and Jacob 1989b, Jorda and Cohen-Adad 1991) at high temperatures and low oxygen pressures (*e.g.*, at 1120°C when p_{O_2} = 400 Pa for Nd_2CuO_4).

Compared with the ambient pressures, one new phase appears:

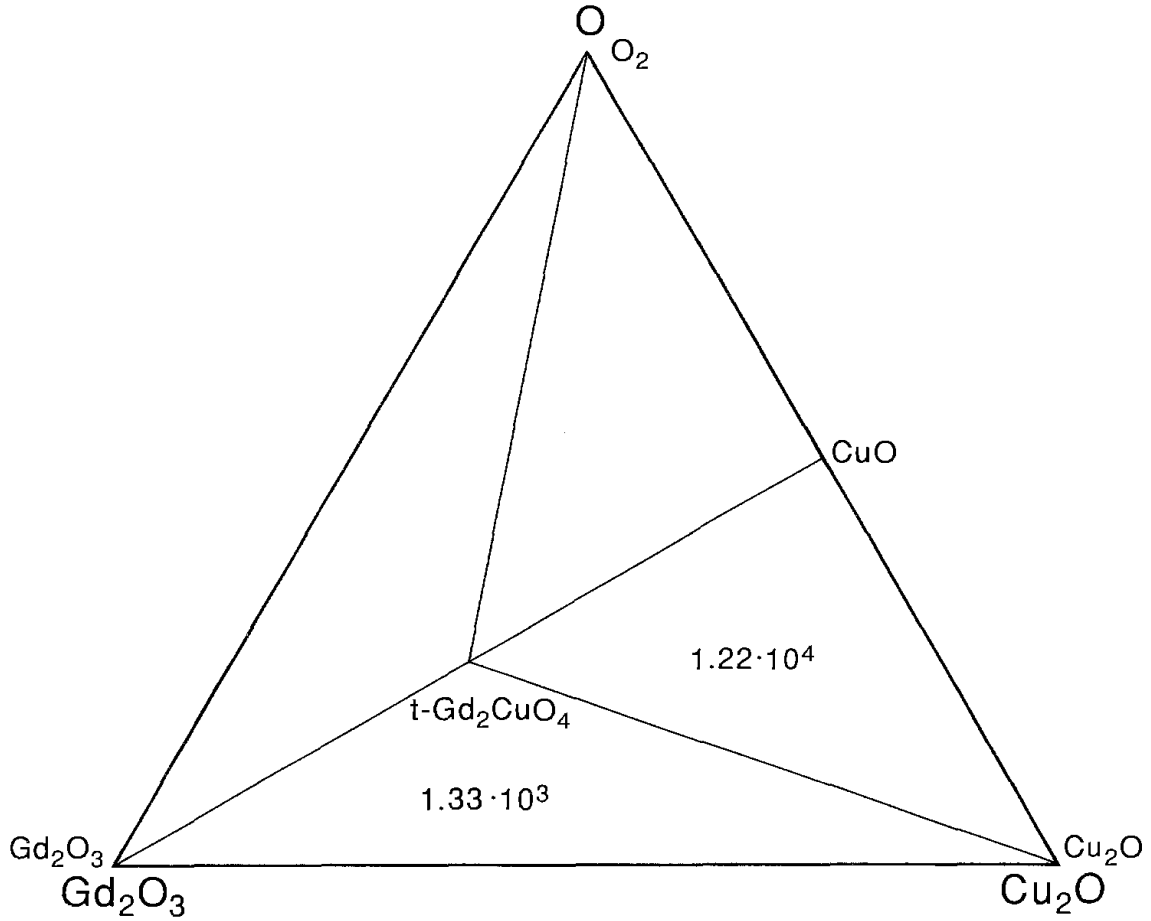

Fig. 25. Isothermal Gd_2O_3–Cu_2O–O diagram at 1000°C as obtained from solid-state galvanic-cell measurements (after Kale and Fray 1995a); p_{O_2} in Pa is given in 3-phase fields.

$RCuO_2$, containing monovalent copper in a rhombohedral structure (Haas and Kordes 1969, Köhler and Jansen 1986) of the delafossite type. This structure type is adopted by many $MCuO_2$ compounds with monovalent Cu, over a wide range of sizes of the trivalent metal M. From the R series, the La, Pr, Nd, Eu, Y and Sc variants have been obtained, however, somewhat different synthesis conditions may be required in order to obtain the products (Isawa et al. 1997). [$LaCuO_2$; $R\bar{3}m$; 383.3(2), 1711.0(9); Ramirez et al. (1986). $EuCuO_2$; 363.3(1), 1709.1(4); Ramirez et al. (1986). $YCuO_2$; 353.3(2), 1713.6(2); Köhler and Jansen (1986).] The CuO_2 linear coordinations typical of monovalent copper connect layers of the R–O octahedra and can be subjected to a partial oxidation under low-temperature "soft-chemistry" conditions (Trari et al. 1994).

When, in contrast, a reduction of Nd_2CuO_4 is conducted under soft-chemistry conditions, a different Cu^I phase appears:

$Nd_4Cu_2O_7$, with a monoclinic structure (Pederzolli and Attfield 1998) [*A2/m*, 844.93(2), 375.91(1), 1260.06(5), 109.576(4)].

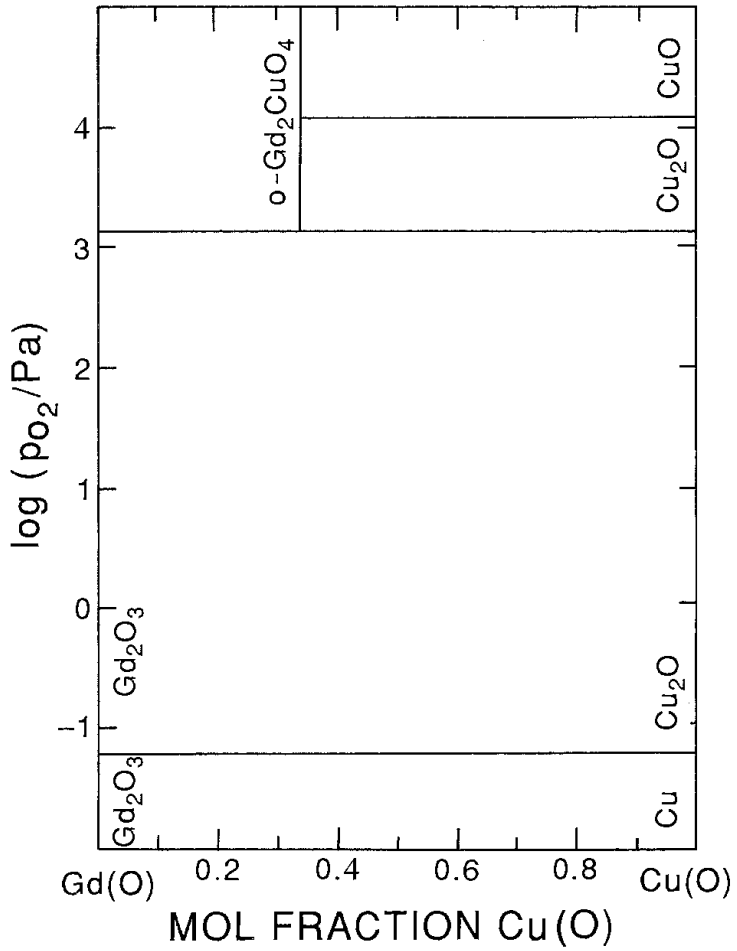

Fig. 26. An x–p diagram (low-pressure) for the Gd(O)–Cu(O) system at 1000°C in oxygen. (After Kale and Fray 1995a.)

8.3. *High p_{O_2} or oxidizing conditions*

$R_2Cu_2O_5$ is reported to be stable at p_{O_2} = 20 MPa (Chandrachood et al. 1990). At even higher pressures, a phase based on Cu^{III} is expected to take over, but this prediction has so far only been confirmed (Bringley et al. 1990a, Webb et al. 1989, Webb et al. 1993) for R = La:

$LaCuO_{3-w}$, with a rhombohedrally distorted perovskite structure of the $LaNiO_3$ type [$LaCuO_{3.00}$; r; 550.19(3), 1321.21(5); Webb et al. (1993)] is synthesized at pressures of around 6 GPa of oxygen (generated from $KClO_4$) and high temperatures of up to 1500°C. The rhombohedral structure undergoes a transformation into a low-temperature modification (but still probably metastable, La Placa et al. 1995) of tetragonal (Bringley et al. 1990a) symmetry [$LaCuO_{3.00}$; *P4/m*; 381.88(1), 397.27(1)], which represents a Jahn–Teller elongated, single-perovskite cell. This phase is obtained in the range of $0 < w < 0.17$ when the high-pressure rhombohedral $LaCuO_3$ is heated at temperatures of some 500°C, necessary to enable some diffusion, but not high enough to cause

any reduction in the oxygen content. When the variation in the oxygen content is attempted either by controlling the partial pressure of oxygen at low temperature (La Placa et al. 1993) or by a careful heating at ambient pressures (Karppinen et al. 1997), the compositions seem to vary over a very broad region of $0 < w < 0.5$. This is associated with the formation of (at least) two structurally ordered variants:

$La_5Cu_5O_{15-w'}$ with a range of homogenenity of $1.00 < w' < 1.90$ and a monoclinic structure (La Placa et al. 1995) [*P2/m*; 862.88(1), 383.08(1), 865.15(1), 90.217(1)].

$La_2Cu_2O_{5+w''}$ with an orthorhombic structure (Bringley et al. 1990a, La Placa et al. 1993, Khasanova et al. 1996) and a homogeneity range (La Placa et al. 1993) of $0.00 < w'' < 0.14$ [*Pbam*; 554.90(1), 1047.74(2), 387.96(1)]. The phase has corner-sharing square-pyramidal coordinations, and has neodymium (Chen et al. 1995b) and strontium (Chen et al. 1996) analogues.

High-pressure oxidation of the o-La_2CuO_4 (T-type) phase leads to a insertion of extra oxygen atoms into the K_2NiF_4-type structure. A limit of 0.10 to 0.13 per formula (800°C; $p_{O_2} = 2.5$ GPa) is observed (Rapp et al. 1994) under appearance of $LaCuO_{3-w}$. Oxidation at 1500°C and $p_{O_2} = 4$ GPa applied to the t-Nd_2CuO_4 phase (T′-type) causes a more extensive ordering:

$Nd_{12}Cu_6O_{25}$ with a monoclinic structure (Steiner et al. 1996) synthesized with the help of BaO_2 in the Belt-type instrument [*C2/m*; 1712.8(6), 372.88(6), 1836.4(6), 111.22(1)].

8.4. *High pressures*

Under the conditions of the anvil-cell apparatus (in absence of oxidants), the existence ranges of the ambient structures are shifted along the R array. Thus the T′ phase (t-Nd_2CuO_4) transforms (Wilhelm et al. 1996) under 25 GPa into the T phase (o-La_2CuO_4 type), whereas it is now being formed also for smaller R = Y, Dy, Ho, Er and Tm (Okada et al. 1990). Under high pressures, m–$La_2Cu_2O_5$ becomes more stable and forms at lower temperatures than under ambient pressure, as an example, at 950°C for 3 GPa (Geny et al. 1996a). One new phase has been reported:

RCu_2O_4, a spinel-type oxide which is formed across the R series. The crystal structure (Chen et al. 1995a) is monoclinic owing to a distortion and contains, somewhat surprisingly for a spinel, square-planar copper coordination polyhedra [$NdCu_2O_4$; *I2/a*, 582.2(2), 969.5(3), 574.8(2), 92.34].

8.5. *Thermodynamics*

As was the case for the A cuprates, problems are encountered with consistency of the measured data. One of the reasons for this is the occurring nonstoichiometry. Whereas data obtained from solution calorimetry refer to the chosen composition, enthalpies and entropies of formation from redox EMF measurements relate in general to one of the two limiting compositions depending on whether the R cuprate in question appears as the oxidized or reduced product in the actual redox system investigated. As a consequence of this, redox EMF data may give widely different temperature dependences of standard

Table 19
Some EMF-determined standard Gibbs-energy functions ($\Delta_r G°$; eq. 2) of formation of $RCuO_2$ from oxides; units have been omitted

Reaction	A	B	T interval	Redox definition	Ref.
$\frac{1}{2}Y_2O_3 + \frac{1}{2}Cu_2O \rightleftharpoons YCuO_2$	−2.32	0.00131	1130–1250	Y_2O_3–Cu–$YCuO_2$	[1]
	−5.17	0.00364	780–1130	Y_2O_3–CuO–$YCuO_2$	[1]
	−5.79	0.0039	873–1323	Y_2O_3–Cu–$YCuO_2$	[2]
$\frac{1}{2}Sm_2O_3 + \frac{1}{2}Cu_2O \rightleftharpoons SmCuO_2$	−32.47	0.0266	1017–1088	Sm_2O_3–Cu–$SmCuO_2$	[3]
	−20.27	0.0067	968–1203	Sm_2O_3–Sm_2CuO_4–$SmCuO_2$	[3]

References
[1] Pankajavalli and Sreedharan (1996)
[2] Kale and Jacob (1989b)
[3] Subasri et al. (1997)

Gibbs energies of formation (Subasri et al. 1997). An example on such differing results is given in table 19 for the $RCuO_2$ phases. In particular for the latter compounds, the EMF results appear also in conflict with data (Konetzki and Schmid-Fetzer 1995) obtained by coulometric titration. The only remedy to this problem is to measure the point-defect equilibria in both branches of the redox system with a single-phase nonstoichiometric oxide and include the evaluated partial molar values for oxygen into the thermodynamic description. A somewhat better situation occurs with cells having CaF_2 or BaF_2 as an electrolyte and where a constant p_{O_2} is maintained. However, in such cases, p_{O_2} should be chosen so that it maintains the phase very near the stoichiometric composition under the expected temperature change needed to conduct the EMF measurement.

Even for phases with a low extent of nonstoichiometry, like $R_2Cu_2O_5$, there is a considerable scatter in the reported Gibbs-energy functions. Temperature dependences of the standard Gibbs energy of formation from oxides obtained by EMF measurements (Kale and Fray 1995b, Zhanguo et al. 1990, Przybyło and Fitzner 1996, Pankajavalli and Sreedharan 1996, Shimpo and Nakamura 1990, Pankajavalli and Sreedharan 1988, Kale and Jacob 1989b, Skolis and Kitsenko 1989, Azad et al. 1991, Kopyto and Fitzner 1996, Kale 1996) are listed in table 20. It follows from the data that all $R_2Cu_2O_5$ phases are entropy stabilized. Similar statement can be made about the data (Kopyto and Fitzner 1996, Raghavan 1996, Idemoto et al. 1992) for the T'-type phases, as follows from table 21 for the R_2CuO_4 phases.

9. Systems R,R′(O)–Cu(O)

The similarity of the Rs is reflected in the formation of solid solutions with wide ranges of homogeneity in the R(O)–R′(O)–Cu(O) phase diagrams. Individual quaternary oxides are formed exceptionally and are then closely structurally related to the ternary phases. These systems have attracted considerable attention owing to the fact that they comprise the t-R_2CuO_4 (T′-type) structure with square-planar cuprate anions in sheets, which becomes superconducting upon *electron* doping; and the La_2CuO_4 (T-type) structure with octahedral cuprate anions in layers, which becomes superconducting upon *hole* doping.

Table 20
Some EMF-determined standard Gibbs-energy functions ($\Delta_r G°$; eq. 2) of formation of $R_2Cu_2O_5$ from oxides; units have been omitted

Reaction	A	B	T interval	Redox definition	Ref.
$Y_2O_3 + 2CuO \rightleftharpoons Y_2Cu_2O_5$	10.91	−0.01341	1097–1292	Y_2O_3–Cu_2O–$Y_2Cu_2O_5$	[1]
	12.75	−0.01714	1025–1220	Y_2O_3–Cu_2O–$Y_2Cu_2O_5$	[2]
	11.21	−0.01507	873–1323	Y_2O_3–$YCuO_2$–$Y_2Cu_2O_5$	[3]
	14.30	−0.017	950–1200	CaF_2 ellyte, 101 kPa O_2	[4]
	12.2	−0.0178	1052–1313	CaF_2 ellyte, 101 kPa O_2	[5]
	18.47	−0.0219	860–980	CaF_2 ellyte, 101 kPa O_2	[6]
$Dy_2O_3 + 2CuO \rightleftharpoons Dy_2Cu_2O_5$	16.65	−0.01229	950–1350	Dy_2O_3–Cu_2O–$Dy_2Cu_2O_5$	[7]
$Ho_2O_3 + 2CuO \rightleftharpoons Ho_2Cu_2O_5$	18.165	−0.01949	950–1350	Ho_2O_3–Cu_2O–$Ho_2Cu_2O_5$	[7]
	22.87	−0.02316	1000–1325	Ho_2O_3–Cu_2O–$Ho_2Cu_2O_5$	[8]
$Er_2O_3 + 2CuO \rightleftharpoons Er_2Cu_2O_5$	17.427	−0.01961	950–1350	Er_2O_3–Cu_2O–$Er_2Cu_2O_5$	[7]
	21.261	−0.02200	1000–1325	Er_2O_3–Cu_2O–$Er_2Cu_2O_5$	[8]
$Yb_2O_3 + 2CuO \rightleftharpoons Yb_2Cu_2O_5$	19.43	−0.02202	950–1350	Yb_2O_3–Cu_2O–$Yb_2Cu_2O_5$	[7]
	13.8	−0.019	1050–1234	CaF_2 ellyte, 101 kPa O_2	[5]
	17.13	−0.02007	1000–1325	Yb_2O_3–Cu_2O–$Yb_2Cu_2O_5$	[9]
$Lu_2O_3 + 2CuO \rightleftharpoons Lu_2Cu_2O_5$	39.39	−0.03812	920–1380	Lu_2O_3–Cu_2O–$Lu_2Cu_2O_5$	[10]
	15.8	−0.01933		estimated from the R trend	[9]

References

[1] Pankajavalli and Sreedharan (1988)
[2] Shimpo and Nakamura (1990)
[3] Kale and Jacob (1989b)
[4] Zhanguo et al. (1990)
[5] Skolis and Kitsenko (1989)
[6] Azad et al. (1991)
[7] Kopyto and Fitzner (1996)
[8] Kale and Fray (1995b)
[9] Kale (1996)
[10] Przybyło and Fitzner (1996)

Table 21
Some EMF-determined standard Gibbs-energy functions ($\Delta_r G°$; eq. 2) of formation of R_2CuO_4 from oxides; units have been omitted

Reaction	A	B	T interval	Redox definition	Ref.
$La_2O_3 + CuO \rightleftharpoons La_2CuO_4$	−12.7	−0.0088	1147–1273	CaF_2 ellyte, 101 kPa O_2	[1]
$Nd_2O_3 + CuO \rightleftharpoons Nd_2CuO_4$	−13.2	−0.0027	1000–1223	Nd_2O_3–Cu_2O–Nd_2CuO_4	[2]
$Sm_2O_3 + CuO \rightleftharpoons Sm_2CuO_4$	−3.2	−0.0061	990–1210	Sm_2O_3–Cu_2O–Sm_2CuO_4	[2]
$Eu_2O_3 + CuO \rightleftharpoons Eu_2CuO_4$	0.7	−0.0062	990–1210	Eu_2O_3–Cu_2O–Eu_2CuO_4	[2]
$Gd_2O_3 + CuO \rightleftharpoons Gd_2CuO_4$	9.562	−0.0123	950–1350	Gd_2O_3–Cu_2O–Gd_2CuO_4	[3]
	8.230	−0.0112	900–1350	Gd_2O_3–Cu_2O–Gd_2CuO_4	[4]

References

[1] Raghavan (1996)
[2] Idemoto et al. (1992)
[3] Kopyto and Fitzner (1996)
[4] Jacob et al. (1993)

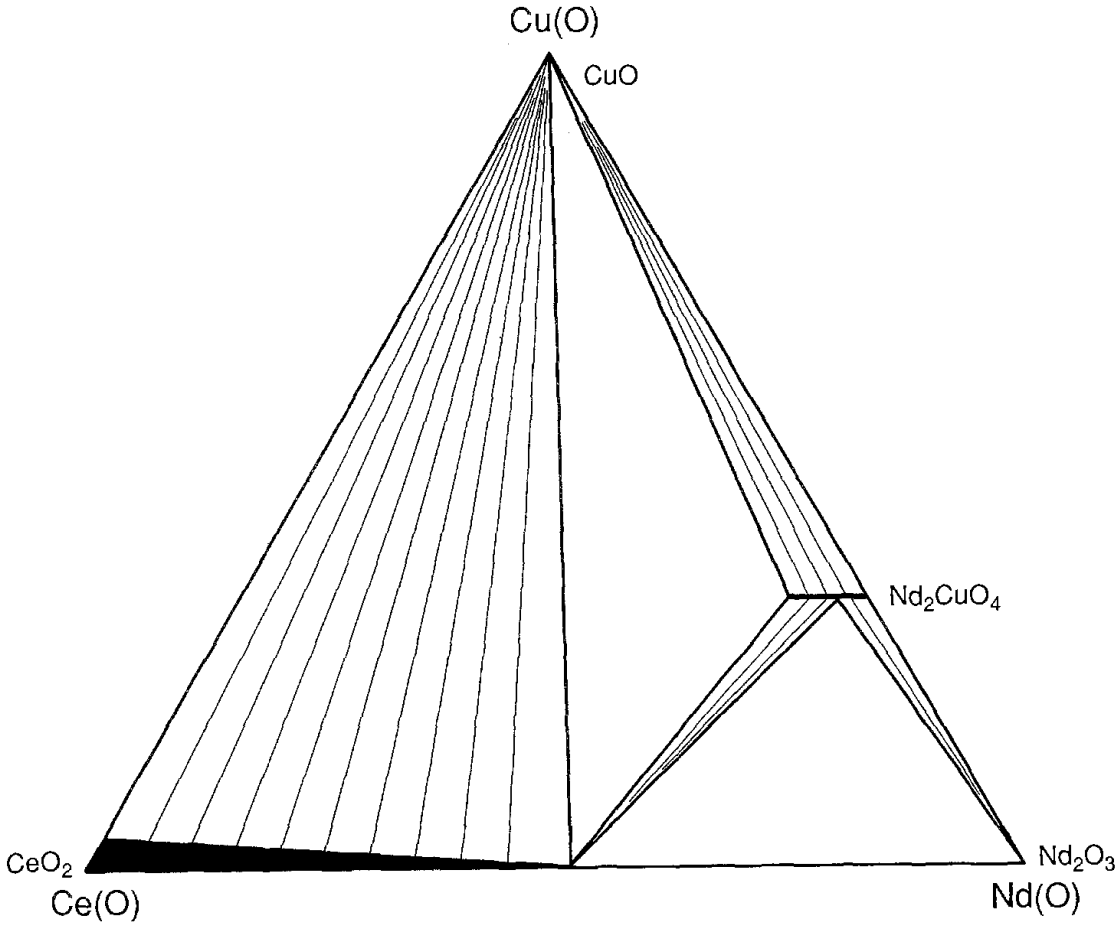

Fig. 27. Subsolidus Ce(O)–Nd(O)–Cu(O) phase diagram at 500°C. (After Jorda and Cohen-Adad 1991.)

When mixed crystals are formed involving two Rs, each pertinent to one of the two structure types, the choice between the T or T′ type depends on the average size of the atom at the R site (Bringley et al. 1990b, Bringley et al. 1990c). However, when a smaller R′ atom is introduced into the $(La_{1-x}R'_x)_2CuO_{4+w}$ solid solution (which does not normally support formation of either the T or T′ phase) a hybrid structure (Lightfoot et al. 1990a) emerges, designated as the T* type:

$(La_{1-x}R'_x)_2CuO_4$ is obtained for R′ = Dy and Tb (in a limited extent also for R′ = Gd) within the interval $0.4 < x < 0.5$ (Bringley et al. 1990b). The crystal structure (Lightfoot et al. 1990a) contains isolated oxide atoms and square-pyramidal copper–oxygen coordinations sharing the corners of their basal plane to form sheets [$(La_{0.625}Dy_{0.375})_2CuO_3O$; *P4/nmm*; 386.61(1), 1244.75(2); Lightfoot et al. (1990a)]. The phase is apparently stabilized by the presence of La in the T-like part of the structure (located between the apices of the cuprate pyramids), whereas the smaller R′ prevails in the T′-like part (separating the square-planar bases of the pyramids). When syntheses of the T* phase are attempted for Y, Ho and smaller Rs, three-phase mixtures are obtained, consisting of La_2CuO_4 and $R_2Cu_2O_5$-type phases and CuO (Bringley et al.

1990b). The T*-type phase is encountered also for other combinations of larger and smaller Rs, however, only upon the condition that the site of the larger R is shared with another relatively large atom, Sr as an example. Otherwise, the T′-type structure emerges. Considering the square-pyramidal cuprate layers, it is not surprising that the hybrid T*-type phases become superconducting on *hole* doping, either by oxidation under high pressure of oxygen (Hundley et al. 1989) or by a Sr substitution for the larger Rs (Sawa et al. 1989a). Electron doping is not successfull in this respect (Lightfoot et al. 1990a, Fisk et al. 1991).

On the other hand, the T′-type phases with square-planar cuprate anions in sheets become superconducting upon *electron* doping, *e.g.*, $(R_{1-x}Ce_x)_2CuO_{4+w}$ (Tokura et al. 1989). Hole doping does not lead to superconductivity (Hiratani et al. 1989). Superconductivity is observed when the phase is slightly oxygen-deficient (Takayama-Muromachi et al. 1989a), $(Nd_{1-x}Ce_x)_2CuO_{4+w}$ ($w = -0.01$), in a modest interval of the dopant concentrations ($0.075 < x < 0.085$) (Kajitani et al. 1990). The same effect may also be achieved by other means of electron doping, *e.g.*, by a partial substitution of Cu by In (Ayoub et al. 1990).

The Ce(O)–Nd(O)–Cu(O) system has been investigated in detail by Jorda and Cohen-Adad (1991) and is shown in fig. 27. A small section describing the incongruent melting of $(Nd_{1-x}Ce_x)_2CuO_4$ analogous to that of the unsubstituted phase (Jorda and Cohen-Adad 1991) has been given by Oka and Unoki (1990), Maljuk et al. (1996) and Serquis et al. (1996). The thermodynamics of the peritectic and eutectic reactions has been studied by Daturi et al. (1996) as a function of temperature and partial pressure of oxygen.

10. Systems R(O)–Ca(O)–Cu(O)

The Y(O)–Ca(O)–Cu(O) phase diagram (Davies et al. 1991), representative of the smaller Rs, is shown in fig. 28. The diagram as seen at 1000°C in air indicates none or very narrow regions of the solid solubility for the Ca- and Y-containing ternary oxides, in line with their rather different structures. However, a quaternary phase appears:

$(R_{1-x}Ca_x)_{1-y}CuO_2$, where R = Y, $y = 0.2$ and $0.5 < x < 0.7$, which is nothing else than the low-temperature, high Cu-valence $Ca_{1-y}CuO_2$-type phase now stabilized also at higher temperatures by lowering the valence owing to the substitution by Y. The main subcell is completely analogous to the prototype [$x = 0.5$; *Fmmm*; 281.7, 618.5, 1059.4; Davies et al. (1991)] but large changes occur in the relatively strong (incommensurate) superstructure reflections when x is varied.

The Nd(O)–Ca(O)–Cu(O) phase diagram (Davies et al. 1991) at 1000°C in air shown in fig. 29 contains an identical quaternary phase as the Y(O) variant above, except that the Nd version occurs in a narrower region ($0.50 < x < 0.57$) of this solid-solution phase $(Nd_{1-x}Ca_x)_{1-y}CuO_2$; still having $y = 0.2$. In addition, however, another solid-solution region is adjacent to this for higher Nd contents ($x < 0.5$), but not as a simple continuation. A single phase is observed between $Nd_2Ca_2Cu_5O_{10}$ and $Nd_2CaCu_4O_8$, *viz.*,

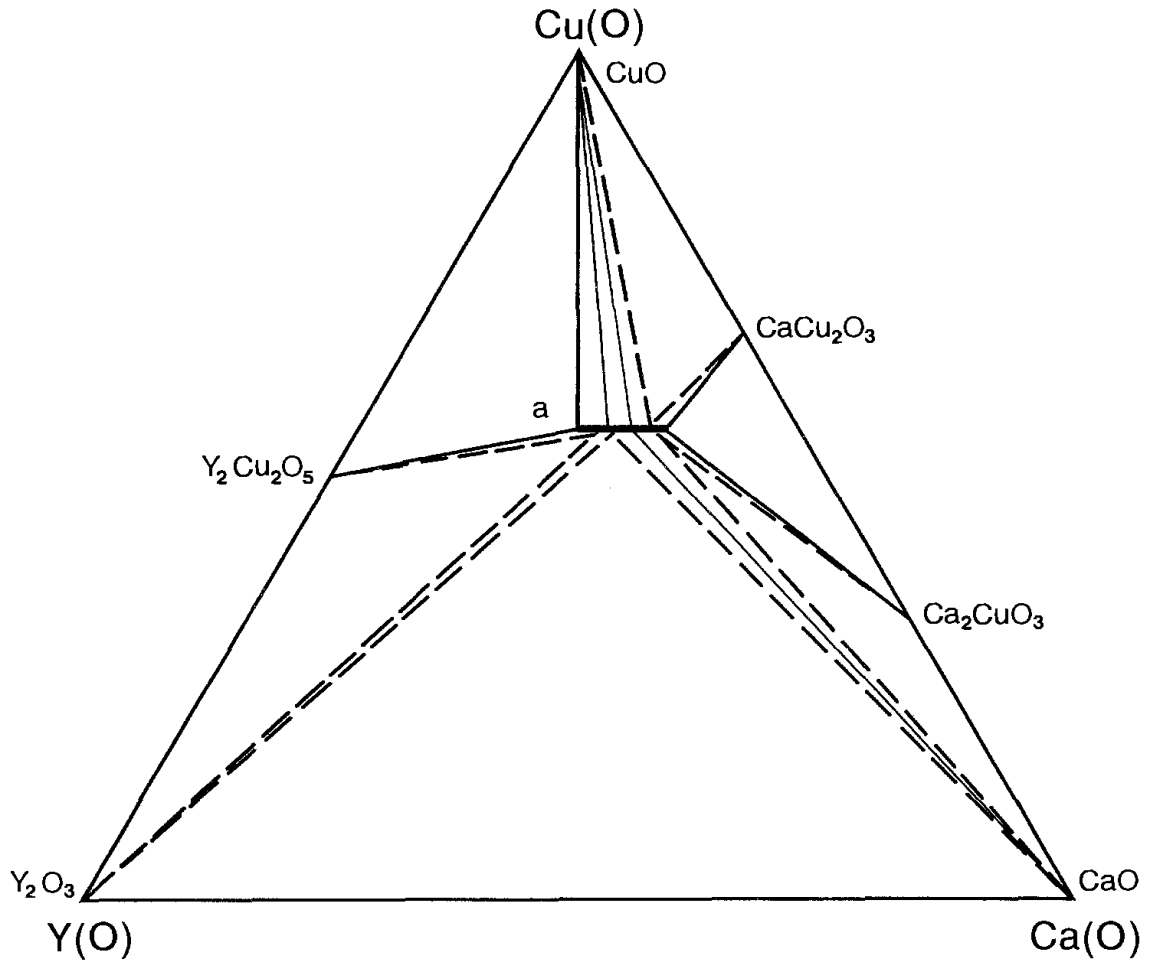

Fig. 28. Subsolidus Y(O)–Ca(O)–Cu(O) phase diagram at 1000°C in air (after Davies et al. 1991). Phase designation: a, $(Y_{1-x}Ca_x)_4Cu_5O_{10}$ $(0.5 < x < 0.7)$.

in the direction towards 203. At the Nd-rich limit, the (incommensurate) superstructure peaks merge into a simple PXD pattern corresponding to $a' = 4a$.

The La(O)–Ca(O)–Cu(O) phase diagram as seen under the same conditions (Skakle and West 1994a, Zhong et al. 1994) does not contain the $Ca_{1-y}CuO_2$-type phase. Two genuine quaternary oxides are seen instead (fig. 30):

$R_2CaCu_2O_6$, actually a solid-solution phase $(La_{1-x}Ca_x)_2CaCu_2O_{6+w}$, $0.0 < x < 0.1$ (Nguyen et al. 1980, Fuertes et al. 1990, Doverspike et al. 1989). The range of homogeneity is somewhat tentative for the lower end. For example, the $x = 0$ variant is reported (Fuertes et al. 1990) only when La_2CuO_4 is used as a starting material. Oxygen contents of no more than some 6.0 per formula are obtained upon treatment in oxygen (Doverspike et al. 1989). The tetragonal crystal structure (Fuertes et al. 1990, Lightfoot et al. 1990b, Caignaert et al. 1990a) [$La_2CaCu_2O_{6.04}$; *I4/mmm*; 383.35(1), 1951.7(1)] is derived from the Ruddlesden–Popper-type ($Sr_3Ti_2O_7$) on distributing oxygen vacancies over the corner-sharing Cu-coordination octahedra upon formation of sheets of square pyramids. The La

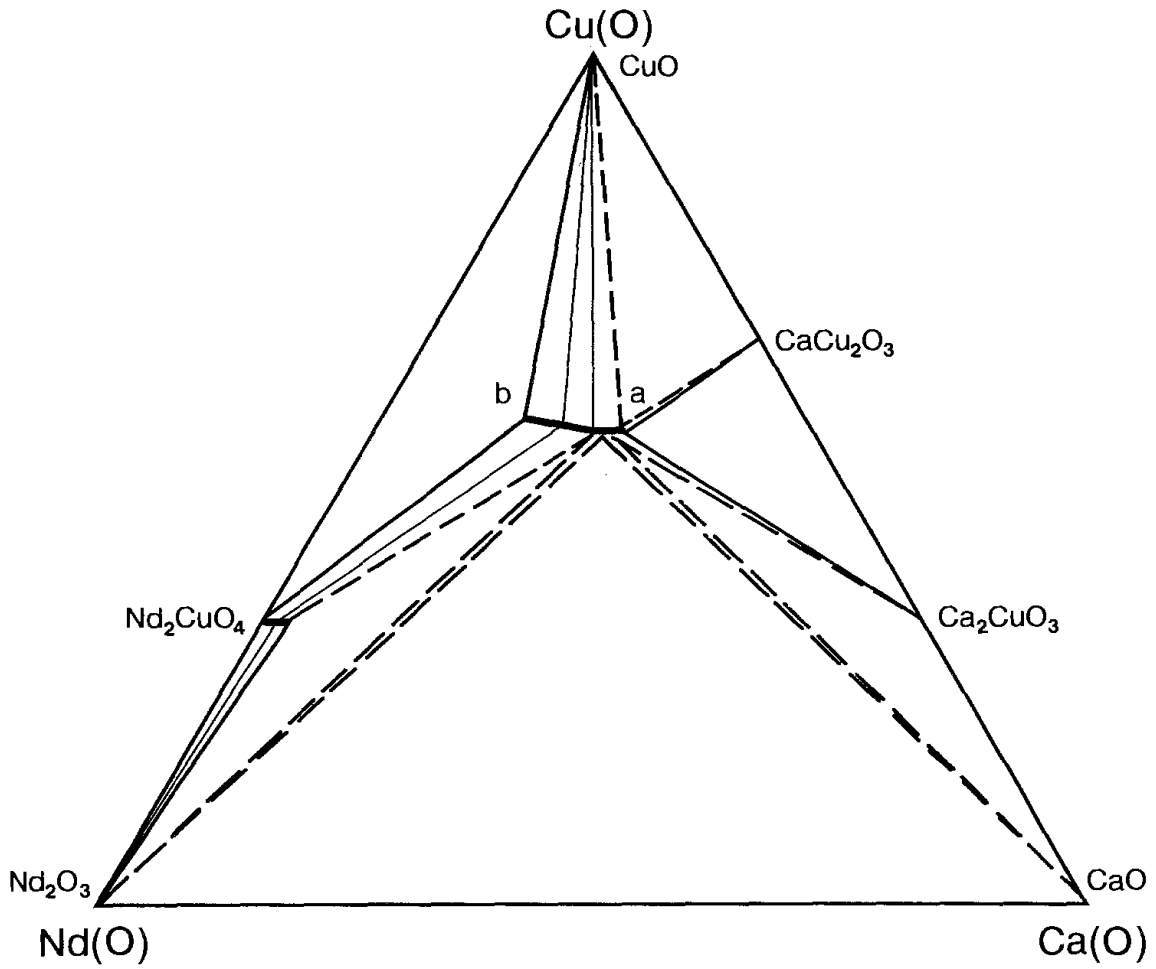

Fig. 29. Subsolidus Nd(O)–Ca(O)–Cu(O) phase diagram at 1000°C in air (after Davies et al. 1991). Phase designations: a, $(Nd_{1-x}Ca_x)_4Cu_5O_{10}$ $(0.50 < x < 0.57)$; b, $Nd_2Ca_{2-y}Cu_{5-y}O_{10-2y}$ $(0 < y < 1)$.

atoms are then located predominantly on the sheet side of the pyramids and Ca atoms predominantly on the apex side. The fact that this structure contains only the square-pyramidal cuprate sheets has drawn considerable attention, since this represents another parent structure for the high-T_c superconductors (Cava et al. 1990a). In $La_2CaCu_2O_6$, the copper–oxygen square-chains are missing, which are considered to act as the "charge reservoirs" in the $YBa_2Cu_3O_7$ superconductor. In line with this (and in parallel to La_2CuO_{4+w}), only weak indications of superconductivity were observed, even when the oxygen content exceeds the stoichiometric composition. However, bulk superconductivity was achieved by alternative ways of hole-doping, *e.g.*, by a substitution of (20% of) La by Sr (Cava et al. 1990a), or by a heat treatment under high oxygen pressure (40 MPa) (Kinoshita et al. 1992). A minute amount of pressure-intercalated oxygen atoms, 0.014(7) per formula, located (Kinoshita et al. 1992) between the square-pyramidal cuprate sheets is able to generate superconductivity. It is interesting to note that Ba did not have the desired effect as hole dopant (Hiratani et al. 1990), and neither could the Sr variant (Ca

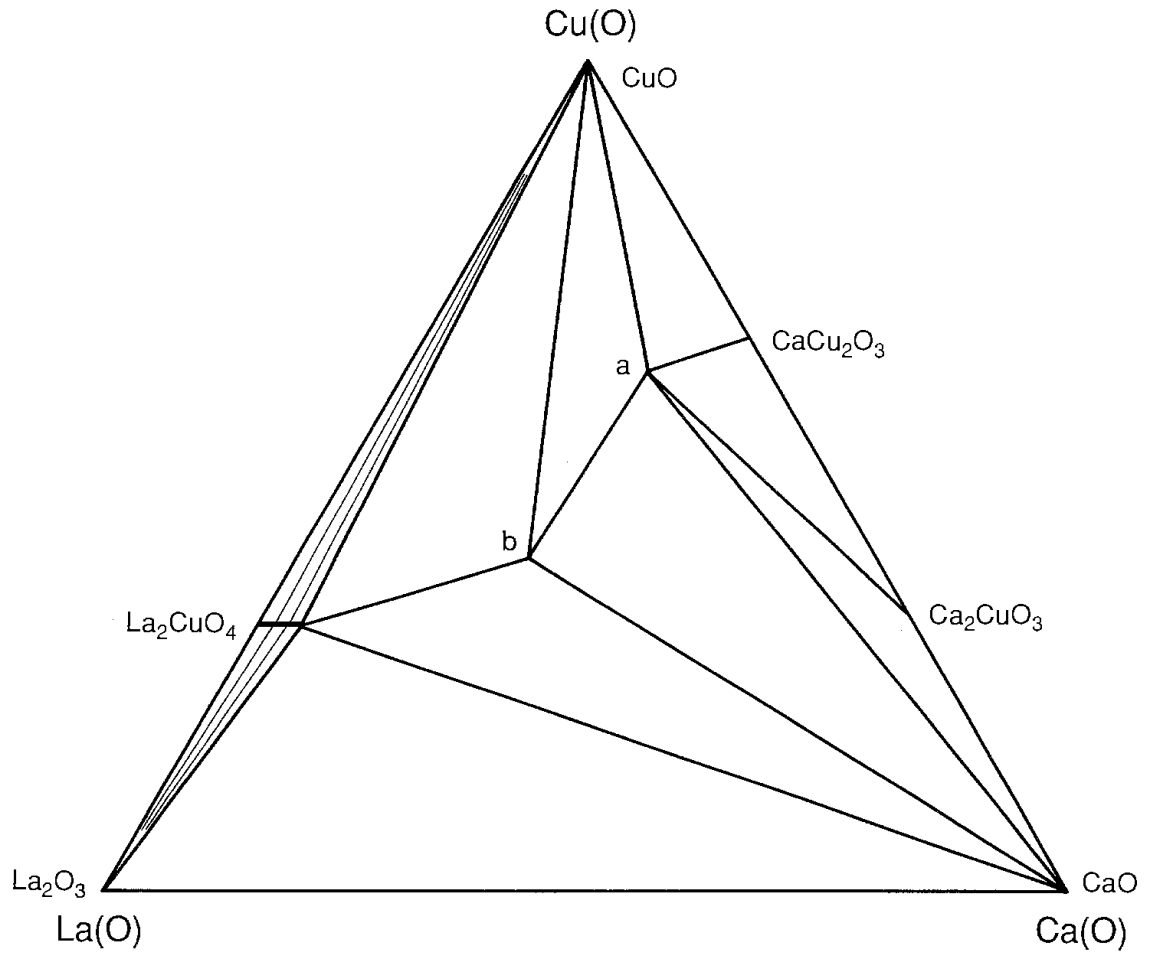

Fig. 30. Subsolidus La(O)–Ca(O)–Cu(O) phase diagram at 1000°C in air (after Skakle and West 1994a and Zhong et al. 1994). Phase designations: a, $LaCa_2Cu_5O_{8.6}$; b, $(La_{0.95}Ca_{0.05})_2CaCu_2O_6$.

replaced by Sr) be made superconducting by substitution. These facts have been discussed in terms of a fine tuning of the Cu–O bond distances (Cava et al. 1990a).

$RCa_2Cu_5O_{8+w}$, which is seen only for R = La, is "isostructural" (Skakle and West 1994a, Zhong et al. 1994) with the $Sr_{14}Cu_{24}O_{41}$ prototype [$LaCa_2Cu_5O_{8.57}$; *Cccm*; 1130.5, 1261.0, 2760.8; Zhong et al. (1994)]. In contrast with the prototype, this phase contains almost exactly divalent copper and is stable up to 1030°C where it melts incongruently (Zhong et al. 1994).

11. Systems R(O)–Sr(O)–Cu(O)

11.1. *Ambient p_{O_2} or moderate oxidizing conditions*

The Y(O)–Sr(O)–Cu(O) phase diagram (De Leeuw et al. 1988b, Jacob and Waseda 1994) at 900°C in ambient oxygen is shown in fig. 31. No genuine quaternary intermediate phase occurs, and no Y,Sr solid solubility is seen in the fixed-valence compounds $Y_2Cu_2O_5$ and

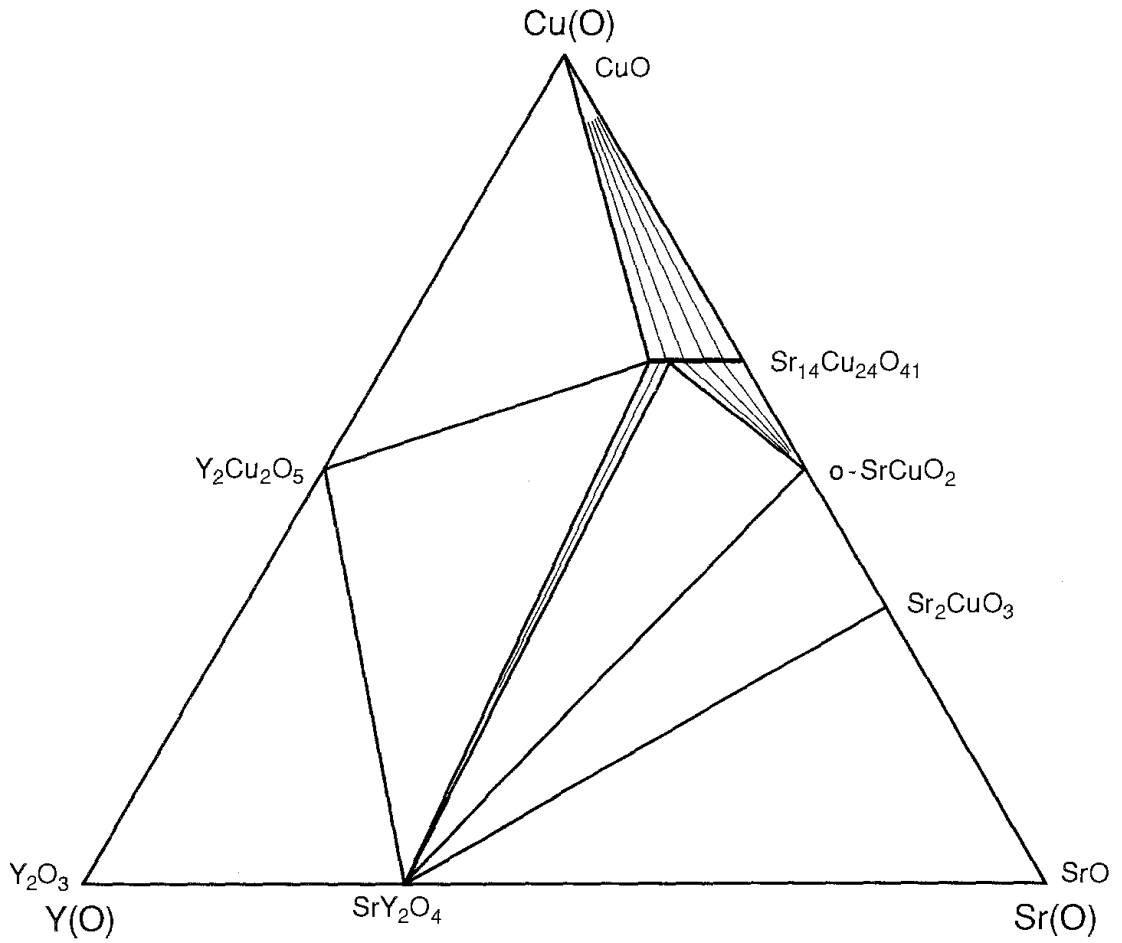

Fig. 31. Subsolidus Y(O)–Sr(O)–Cu(O) phase diagram at 900°C in oxygen at ambient pressure. (After De Leeuw et al. 1988b and Jacob and Waseda 1994.)

o-$SrCuO_{2+w}$, whereas a significant portion of Sr in $Sr_{14}Cu_{24}O_{41-w}$ can be replaced by yttrium.

The Ho(O)–Sr(O)–Cu(O) phase diagram by Wong-Ng et al. (2000) is essentially identical to that in fig. 31, with one notable exception:

Ho_2SrCuO_5, a green coloured phase of the Y_2BaCuO_5 type [*Pbnm*; 709.71(13), 1202.62(23); Wong-Ng et al. (2000)]. Interestingly, Y_2SrCuO_5 is not formed under comparable conditions.

The La(O)–Sr(O)–Cu(O) phase diagram is compiled from the literature data (Roth et al. 1989b, Nguyen et al. 1980, De Leeuw et al. 1988b, 1989a, De Leeuw 1989, Er-Rakho et al. 1988), as it is expected to look at 950°C in oxygen (fig. 32). Some ternary phases show a significant solid miscibility:

$(Sr_{1-y}La_y)_{14}Cu_{24}O_{41}$ appears up to $y = 0.36$ (De Leeuw et al. 1989a), and $Sr_{14}Cu_{24}O_{41}$ is the only strontium cuprate which shows a significant La for Sr solid solubility.

$(La_{1-x}Sr_x)_2CuO_4$ has a broad homogeneity range with respect to Sr; up to $x = 0.75$ (De Leeuw et al. 1989a). Upon increasing substitution of La by Sr, the origi-

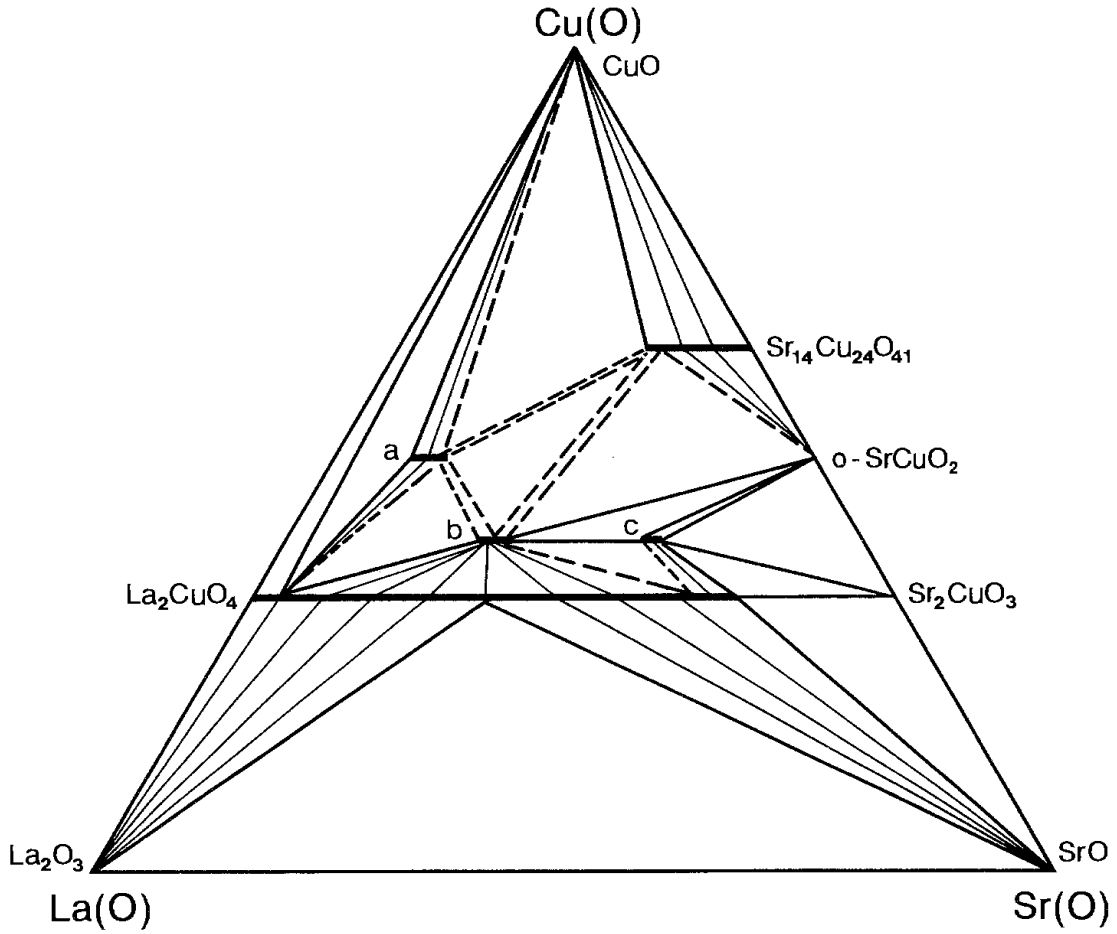

Fig. 32. Subsolidus La(O)–Sr(O)–Cu(O) phase diagram at 950°C in oxygen at ambient pressure; compiled from Roth et al. (1989b), Nguyen et al. (1980), De Leeuw et al. (1988b, 1989a), De Leeuw (1989) and Er-Rakho et al. (1988). Phase designations: a, $(Sr_{1-y}La_y)CuO_{3-w}$ ($0.16 < y < 0.24$, Er-Rakho et al. 1988); b, $(La_{1-x}Sr_x)_2SrCu_2O_{6+w}$ ($0.00 < x < 0.07$, Nguyen et al. 1980); c, $La(Sr_{1-y}La_y)_2Cu_2O_{5+w}$ ($0.025 < y < 0.075$, De Leeuw et al. 1989a).

nally orthorhombic lanthanum cuprate structure changes into tetragonal symmetry [$(La_{0.925}Sr_{0.075})_2CuO_4$; *I4/mmm*; 377.17(8), 1322.6(3); Gai and McCarron III (1990)], with a critical concentration of $x = 0.04$ as seen (Huang et al. 1989, Nguyen et al. 1983, Moret et al. 1987) by PXD at room temperature. An EXAFS study (Haskel et al. 1996) shows that this composition-induced transition has both displacive and disorder components, maintaining the local tilt of the copper oxygen octahedra. Detailed unit-cell parameter data as a function of x and the analyzed oxygen content were given by Huang et al. (1989). The oxygen content as obtained in oxygen at 600°C is very slightly above-stoichiometric and remains practically constant up to some $x = 0.15$ at ambient pressure. Beyond this substitution level (in O_2 at 600°C), as well as under low partial pressures of oxygen, divalent Sr is compensated by the creation of oxygen vacancies; $w \leqslant x/2$ in $(La_{1-x}Sr_x)_2CuO_{4-w}$. Detailed p_{O_2}–t–x–w dependences have been measured by Opila and Tuller (1994) and intepretations in terms of point-defect modelling are

suggested. A similar modelling based on literature data has been attempted by Shen et al. (1994). The $(La_{1-x}Sr_x)_2CuO_4$ phase melts incongruently, which means that single crystals cannot be grown directly from melts, and a CuO solvent technique must be used instead (Scheel and Licci 1991). The interest in the $(La_{1-x}Sr_x)_2CuO_4$ solid solution originates from superconductivity which this phase exhibits in the region $0.06 < x < 0.26$ (with a maximum T_c at some 40 K), being a semiconductor below and a "metallic" (having a resistivity decrease upon increasing temperature) conductor above these limits (Boebinger et al. 1996).

Except for the solid solutions based on the ternary oxides, several new *quaternary phases* are encountered:

$R_6Sr_2Cu_8O_{20}$, actually a solid-solution phase with range expressed for R=La, as an example, by the $(La_{1-x}Sr_x)_8Cu_8O_{20-w}$ formula with $0.16 < x < 0.24$ (Er-Rakho et al. 1988). A slightly different value of $x = 0.20$ is found for the lower limit in De Leeuw et al. (1989a). The phase is formed in an oxygen atmosphere at 950°C, and represents an oxygen-deficient perovskite with structural (Er-Rakho et al. 1988) ordering over 8 single-perovskite units ($a = a_p 2\sqrt{2}$) [$(La_{0.8}Sr_{0.2})_8Cu_8O_{19.8}$; *P4/mbm*; 1084.0(4), 386.1(2)], forming corner-sharing Cu-coordination octahedra, pyramids and squares (Er-Rakho et al. 1988, Lee et al. 1990, Tokura et al. 1987). The oxygen content is not easily varied, although some formation of Cu vacancies in the copper–oxygen octahedra is indicated (Lee et al. 1990). Different orderings may occur instead: $(La_{1-x}Sr_x)_5Cu_5O_{13}$ with $x = 0.167$ formed upon further oxidation (Otzschi et al. 1993) or $(La_{1-x}Sr_x)_8Cu_8O_{20-w}$ with $0.135 < x < 0.15$ (Otzschi and Ueda 1993), formed under low-temperature conditions. Despite the rather fixed oxygen content, a mixed Cu valence occurs in these compounds and is manifested in a metallic nature of the phases. Yet, no superconductivity is observed (Tokura et al. 1987).

$R_2Sr_6Cu_8O_{16}$, or the solid solution (R=La); $(La_{1-x}Sr_x)_8Cu_8O_{16}$ with $x \approx 0.75$ (Otzschi et al. 1995), is not observed at the conditions relevant to fig. 32, but is obtained (Fu et al. 1990) under slightly reducing conditions. This phase has a crystal structure (Otzschi et al. 1995) similar to the previous one, but the La/Sr ratio is inverted and the oxygen content somewhat different [$(La_{0.25}Sr_{0.75})_8Cu_8O_{16.07}$; *P4/mbm*; 1104.64(2), 363.90(1)]. Assuming that the oxygen content in this and the other similar phases in question is structurally fixed, stable structures would be formed only under narrowly specified conditions, where both the La/Sr ratio and the structurally desired oxygen content are precisely adjusted to the attainable Cu valence defined by the average electronegativity of the La/Sr atom. This indeed seems to be the case, as yet another ordered and somewhat more oxidized variant appears, having 18 oxygens per formula [$(La_{0.25}Sr_{0.75})_8Cu_8O_{18.14}$; *P4/mbm*; 1084.20(1), 376.27(1); Otzschi et al. (1995).

$R_2SrCu_2O_6$, is actually a solid solution expressed, *e.g.*, for R=La by the formula: $(La_{1-x}Sr_x)_2SrCu_2O_{6+w}$ with $0.00 < x < 0.07$ (Nguyen et al. 1980). A slightly different value of $x = 0.025$ is given for the lower limit by De Leeuw et al. (1989a). The phase has an "air-quenched" oxygen content corresponding to $w \approx 0.0$, which can be increased to some $w = 0.25$ upon heating in pure oxygen at ambient pressure and temperatures between 200 and 400°C (Lightfoot et al. 1990b). The latter treatment converts the original

semiconductor into a metal (Michel and Raveau 1984). The tetragonal crystal structure (Lightfoot et al. 1990b, Caignaert et al. 1990a) is derived from that of the Ruddlesden–Popper type in the same manner as seen for the Ca variant in sect. 10. Contrary to the Ca variant, however, the more electropositive and larger Sr atoms allow accommodation of more oxygens, and the homogeneity range for oxygen extends from $La_2SrCu_2O_{6.08}$ [*I4/mmm*; 386.7(2), 1991(1); Doverspike et al. (1989)] to $(La_{0.925}Sr_{0.075})_2SrCu_2O_{6.25}$ [385.30(1), 2008.33(3); Lightfoot et al. (1990b)], for R = La as an example. Formation of analogous structures is observed also for R = Pr, Nd, Sm, Eu and Gd (Hayri and Larese 1990, Grasmeder and Weller 1990). However, except for R = Pr, a specific ordering of oxygen vacancies with a tripling of *b* is observed by PXD (Grasmeder and Weller 1990, Nguyen et al. 1982), HREM (Hervieu et al. 1990) and PND (Dann and Weller 1995) (the latter on a Co-version). The presence of, *inter alia*, the infinite square-pyramidal cuprate sheets in this structure suggested that this phase should become superconducting upon hole doping. Quite surprisingly, despite the "correct" *overall* Cu-valence, superconductivity was not observed (see also sect. 10).

$RSr_2Cu_2O_6$ has a crystal structure (Caignaert et al. 1991) related to the Ruddlesden–Popper-type phases by tripling the unit-cell parameter *b* and ordering of both cations and oxygen vacancies. As an example, $NdSr_2Cu_2O_{5.66}$ [*Immm*; 375.47(1), 1148.82(4), 2009.76(7)]. The ordering involves chopping the Ruddlesden–Popper double octahedra layers into segments or "ribbons" of square-pyramidal coordinations connected by distorted squares, *i.e.*, tripled (along *b*), much like in the $YBa_2Cu_3O_7$ superconductor, but much more distorted. This is apparently the reason why this structure shows only minor variation in the oxygen content (between 5.66 and 5.76 per formula) (Caignaert et al. 1991, Caignaert et al. 1990b). Despite the mixed-valence state of copper, superconductivity is not observed (Caignaert et al. 1990b). This phase actually represents an end member of a solid solution where the R atom can replace a portion of Sr. For R = La, a non-zero lower limit of this solid solution is seen ($0.025 < x < 0.075$) in $La(Sr_{1-y}La_y)_2Cu_2O_{5+w}$ (De Leeuw et al. 1989a).

11.2. *High p_{O_2} or oxidizing conditions*

The Y(O)–Sr(O)–Cu(O) system has been investigated under conditions of very high oxygen pressures created at high temperatures from $KClO_3$ in gold capsules (Ono 1992), in particular for formation of phases analogous to $YBa_2Cu_3O_7$. As an example, several PXD-indexable phases emerge after treatment at an oxygen pressure of $p_{O_2} = 7$ GPa and 1380°C:

$YSr_2Cu_3O_w$, as an example, is obviously a structural analogue (Ono 1992, Okai 1990) of the known superconductor [*P4/mmm*; 379.5, 1141; Okai (1990)]. At somewhat lower oxygen pressures, an orthorhombic version appears (Ono 1992). The compound could not, however, be obtained completely phase pure. Owing to the nature of the synthesis procedure, the stabilization of the phase by Cl or K and/or by CO_2 from the chemical environment cannot be excluded. In a similar theme, a controlled replacement of a portion of Cu by a variety of other metals stabilizes Sr in the structure, and not so high oxygen

pressures are needed for the synthesis (see also sect. 18.4). Whereas $YSr_2Cu_3O_w$ is a superconductor (Okai 1990) with $T_c \approx 60$ K, the latter substitutions, in general, decrease the transition temperature which depends strongly on the oxidation state of Cu (Shi et al. 1996).

The La(O)–Sr(O)–Cu(O) system, when subject to high oxygen pressure at high temperatures does not seem to form new phases, but the oxygen content of several of the quaternary phases is increased (Otzschi et al. 1995). Another effect is to extend the range of solid solutions formed by acceptor substitutions, which would otherwise tend to create oxygen vacancies and destabilize the structure. Several solid-solution phases can be listed as examples for the latter effect:

$La_{1-x}Sr_xCuO_3$, is obtained single-phase up to $x \approx 0.20$ in a two-step solid-state synthesis, where $KClO_3$ was added in the second step to obtain full oxygen occupancy under treatment in the belt-type apparatus at 7 GPa and 1000°C. The composition corresponds to a valence of copper well above III (Darracq et al. 1995). The crystal structure (Hiroi 1996) of this solid-solution series is of the $CaMnO_{2.5}$ type [$La_{0.80}Sr_{0.20}CuO_{2.5}$; *Pbam*; 5.5221(1), 10.5295(2), 3.8650(1)].

$(R_{1-x}Sr_x)_8Cu_8O_{20-w}$, (R = Nd, Pr) where the solid-solution range is increased up to some $x = 0.40$ when the synthesis is conducted under $p_{O_2} = 20$ MPa (Ammamoto et al. 1996).

11.3. *High-pressure phases*

Syntheses at high pressures have been essential for obtaining superconductivity in the t-$SrCuO_2$ perovskite which contains infinite sheets of copper oxygen squares. Electron doping by a R substitution leads to n-type superconductivity.

$(Sr_{1-y}Nd_y)CuO_2$ with $0.00 < y < 0.16$ can be given as an example of such doping, where bulk superconductivity with maximum $T_c \approx 40$ K is achieved in the composition interval of $0.14 < y < 0.16$ (Smith et al. 1991). Other variants of the same solid-solution phase with R = La to Er have been obtained in anvil-type cells under pressures up to 7 GPa at temperatures around 1000°C (Ikeda et al. 1993, Kuzmicheva et al. 1996).

The La(O)–Sr(O)–Cu(O) phase diagram (Geny et al. 1996b) at 950°C and 1 GPa shows little difference from that in fig. 32 at ambient pressure, except that the solid-solution ranges of $(La_{1-x}Sr_x)_8Cu_8O_{20-w}$ and $(La_{1-x}Sr_x)_{14}Cu_{24}O_{41}$ are somewhat widened. When the pressure is further increased to 3 GPa (fig. 33), a different solid-solution phase emerges:

$(La_{1-x}Sr_x)_2Cu_2O_5$ ($0.00 < x < 0.54$) (Geny et al. 1997) which is apparently based on the m-$La_2Cu_2O_5$ phase and replaces $(La_{1-x}Sr_x)_8Cu_8O_{20-w}$. Another difference seen at 3 GPa is that the solid solution $La(Sr_{1-y}La_y)_2Cu_2O_{5+w}$ is no longer stable.

11.4. *Thermodynamics*

The $(La_{1-x}Sr_x)_2CuO_{4-w}$ superconductor is the only phase significant enough so that it has justified thermodynamic characterizations. Gibbs-energy functions for selected

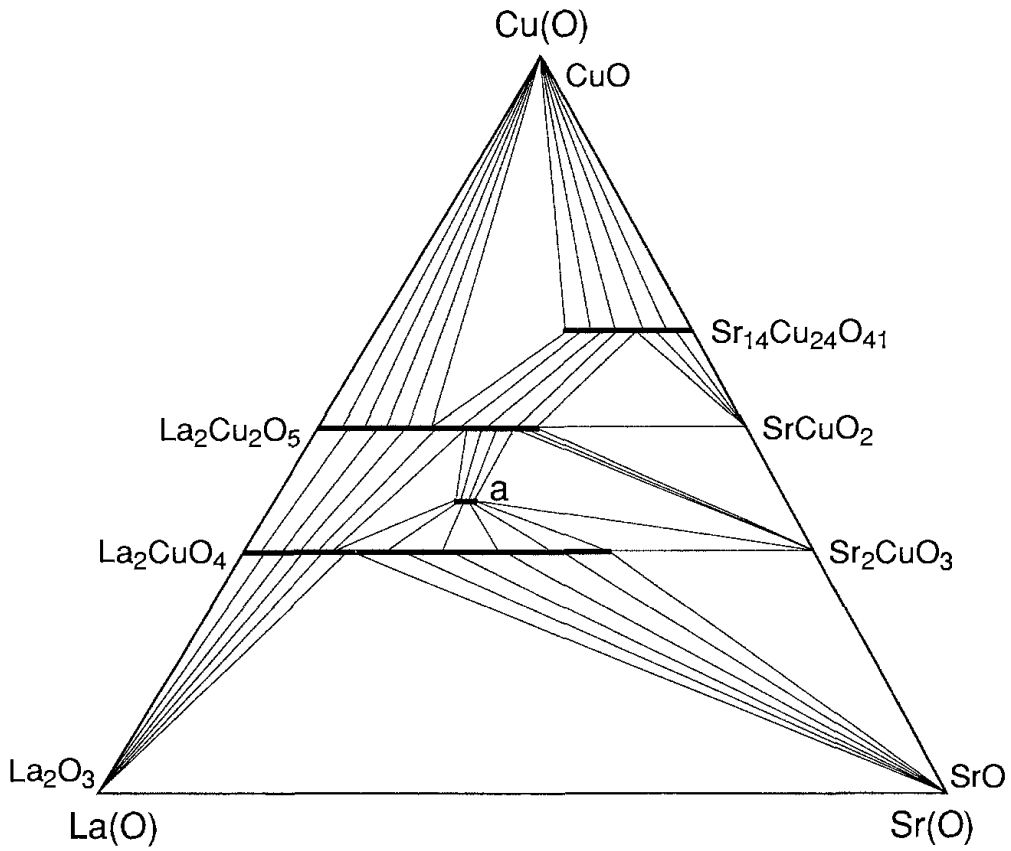

Fig. 33. Subsolidus La(O)–Sr(O)–Cu(O) phase diagram at 950°C under 3 GPa pressure (after Geny et al. 1997). Phase designation: a, $(La_{1-x}Sr_x)_2SrCu_2O_{6+w}$ $(0.01 < x < 0.20)$

Table 22
EMF-determined standard Gibbs-energy functions ($\Delta_r G^\circ$; eq. 2) of formation of $(La_{1-x}Sr_x)_2CuO_4$ from $(1-x)La_2O_3 + 2xSrO + CuO + \frac{x+w}{2}O_2$, according to Idemoto et al. (1993); units have been omitted

Composition	A	B	T interval	Redox definition
$x = 0.00$	−15.6	−0.00357	966–1204	La_2O_3–SrO–$LaCuO_2$–$(La_{1-x}Sr_x)_2CuO_4$
$x = 0.02$	−17.5	−0.00437	1073–1226	La_2O_3–SrO–$LaCuO_2$–$(La_{1-x}Sr_x)_2CuO_4$
$x = 0.04$	−22.1	−0.00107	1011–1210	La_2O_3–SrO–$LaCuO_2$–$(La_{1-x}Sr_x)_2CuO_4$
$x = 0.06$	−22.7	−0.00167	1110–1216	La_2O_3–SrO–$LaCuO_2$–$(La_{1-x}Sr_x)_2CuO_4$
$x = 0.08$	−26.5	0.00113	1057–1261	La_2O_3–SrO–$LaCuO_2$–$(La_{1-x}Sr_x)_2CuO_4$
$x = 0.10$	−28.8	0.00183	1110–1216	La_2O_3–SrO–$LaCuO_2$–$(La_{1-x}Sr_x)_2CuO_4$
$x = 0.12$	−31.0	0.00263	976–1219	La_2O_3–SrO–$LaCuO_2$–$(La_{1-x}Sr_x)_2CuO_4$
$x = 0.12$	−32.9	0.00373	1084–1228	La_2O_3–SrO–$LaCuO_2$–$(La_{1-x}Sr_x)_2CuO_4$

compositions are listed in table 22 as determined by EMF measurements referring to the reduced end of the phase stability (Idemoto et al. 1993). Thermodynamics of the oxygen nonstoichiometry has been studied by Opila and Tuller (1994) based on

TGA measurements, showing that the evaluated standard partial molar enthalpy of oxygen h_O° [the enthalpy of dissolution of 1/2 mole of O_2 in an infinite amount of $(La_{1-x}Sr_x)_2CuO_{4-w}$] for constant x depends on w. The range in h_O° as a function of the oxygen vacancy content w moreover varies with the substitution level x having largest span and most negative values when w is low.

12. Systems R,R′(O)–Sr(O)–Cu(O)

Solid solutions of Sr in the T* phases are widely studied as means of hole doping and for fine tuning and stabilizing the T* phases [the $(La_{1-x}R_x)_2CuO_{4+w}$ type, see sect. 8]. The Sr-substituted T* phases accommodate a wide variety of R combinations, R = Sm, Eu, Gd, Tb, Dy, and Y as compared to only Tb and Dy stable in the structure without the Sr substitution (Takayama-Muromachi et al. 1989b). Other Rs than La are also stabilized by the Sr substitution at the R site. $(Nd,Sr,Ce)_2CuO_4$ was actually the first T* phase observed and found superconducting (Akimitsu et al. 1988). There is no oxygen excess detected in the Sr-substituted samples (3.99 per formula, Takayama-Muromachi et al. 1989b), and the attainable oxygen deficiency is also very low, corresponding to some 0.03 per formula unit between 1000°C and ambient temperature (Takayama-Muromachi et al. 1989b). An ordered distribution of the metal atoms between the non-equivalent sites is observed (Izumi et al. 1989, Tan et al. 1990), with the larger Rs and Sr preferring the site between the pyramid apices (resembling the T phase) and the smaller Rs preferring the site between the pyramid squares (resembling the T′ phase).

Owing to the similarity of the Rs, new phases appear rarely as a consequence of addition of R′ into the system. A notable exception is when tetravalent Ce is introduced. Phases with structures combining the layered cuprate features with the fluorite arrangement pertinent to CeO_2 are then formed for combinations of R and R′ = Ce, which conform with the cuprate network:

$RSr_2Cu_3O_7(CeO_2)_2$, containing double fluorite units (see sect. 3) which are interleaved with the cuprate triple-perovskite layers (see sect. 13) (Wada et al. 1990a). As an example: $(Ho_{0.33}Ce_{0.67})_3Sr_2Cu_3O_{11}$ [*P4/mmm*; 382.4(1), 1722(1)].

13. Subsolidus systems R(O)–Ba(O)–Cu(O)

The extent of the data for these systems makes it necessary to focus on subsolidus phase relationships (this section) while only selected composition–temperature diagrams follow separately in sect. 14. Since the subsolidus phase descriptions vary significantly across the series of the R elements, the description begins at the smallest R atom and continues with the increasing size of the trivalent ions.

13.1. *Ambient p_{O_2} or moderate oxidizing conditions*

13.1.1. *The Lu(O)–Ba(O)–Cu(O) phase system*

The Lu(O)–Ba(O)–Cu(O) phase diagram is shown in fig. 34. The diagram is constructed from the phase diagram of Hodorowicz et al. (1992a) and data from Vallino et al. (1991),

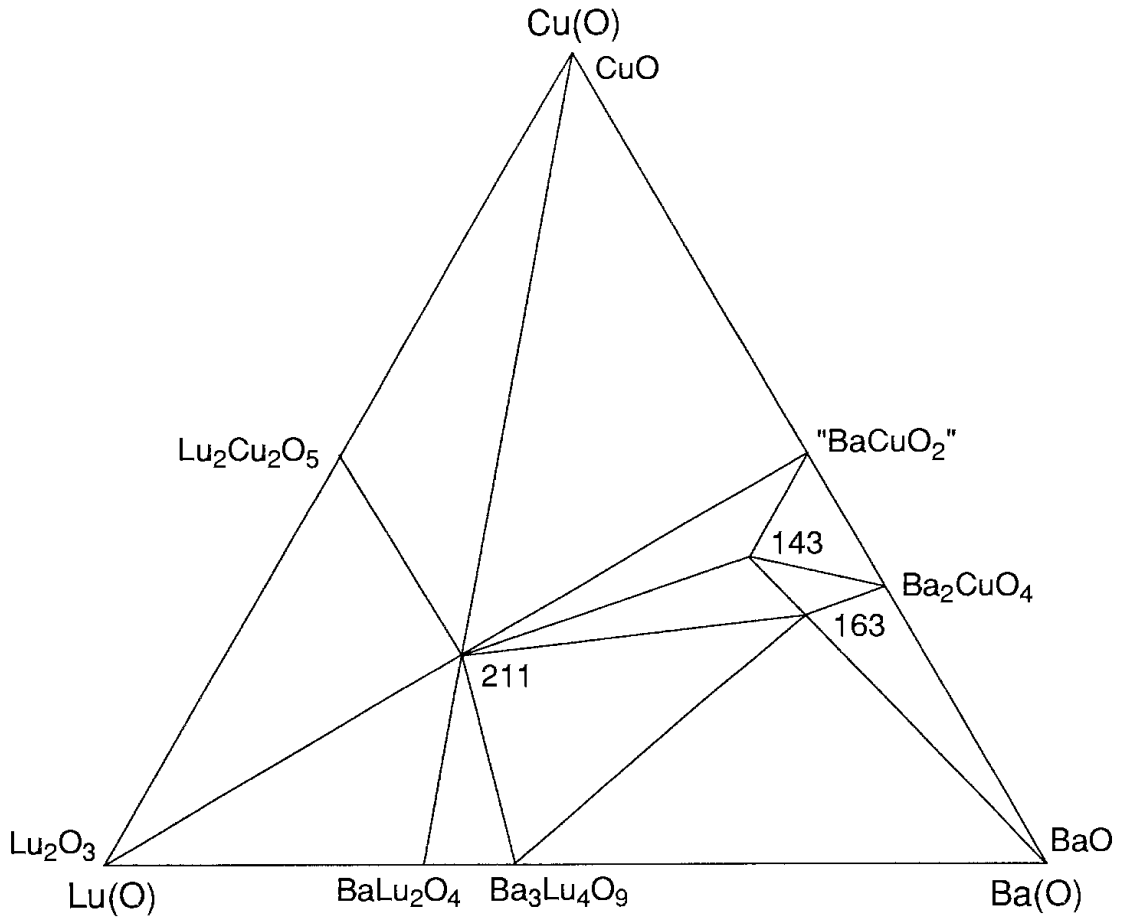

Fig. 34. Subsolidus Lu(O)–Ba(O)–Cu(O) phase diagram at 950°C in oxygen at ambient pressure; compiled from Hodorowicz et al. (1992a) and Vallino et al. (1991).

combining the synthesis information based on carbonates [Hodorowicz et al. (1992a); 950°C in air] with the information relevant to the Ba-rich region (Vallino et al. 1991). Three (quaternary) oxides occur inside the plane of the diagram:

o-R_2BaCuO_5 (R = Lu, Yb, Tm, Er, Ho, Dy, Gd, Eu, Sm and Y) (Michel and Raveau 1982) represents a typical stoichiometric compound with very low electrical conductivity. The bright green colour of the oxide conforms with the isolated square-pyramidal cuprate anions present in the crystal structure (Fjellvåg et al. 1987, Norrestam et al. 1988, Sato and Nakada 1989, Pei et al. 1990). For a Cu^{II} compound, R_2BaCuO_5 is extremely stable and the R = Y variant [Y_2BaCuO_5; *Pbnm*; 713.35(6), 1217.63(6), 565.90(4); Fjellvåg et al. (1987)] melts (incongruently) at 1270°C (Aselage and Keefer 1988). Considering the structurally fixed Cu valence of this compound, practically no homogeneity range for aliovalent substitutions should occur. The suggested (Izakovich et al. 1989) substitution of Cu for Y in Y_2BaCuO_5 is unlikely, and, since the expected three-phase mixture is reported to indeed appear at higher temperatures, it could rather indicate a formation of an intermediate oxide carbonate from the carbonate starting materials used, which subsequently decomposes.

$RBa_4Cu_3O_{8.5+w}$ (R = Lu, Yb, Tm, Er, Ho, Dy, Gd, Eu and Sm) (Vallino et al. 1991, Zhu et al. 1998a,b, 1999) is a mixed-valence compound with crystal structure (De Leeuw et al. 1989b) already considered in sect. 7 for the version where Ca occurs instead of R [$YBa_4Cu_3O_{9.2}$; $Pm\bar{3}$; 810.2; Karen et al. (1990a); $EuBa_4Cu_3O_{9.33}$; $Pm\bar{3}$; 816.68; Zhu et al. (1998a)]. The oxygen content is variable depending on the temperature and partial pressure of oxygen. After oxidation in ambient oxygen at 320°C, $w = 0.7$ is reached (Karen et al. 1990a), whereas quenching from 1000°C results in $w = 0$ (De Leeuw et al. 1989b). The $YBa_4Cu_3O_{8.5+w}$ phase is formed readily from nitrate precursors, while an unsuccessful synthesis is reported (De Leeuw et al. 1989b) from carbonates. However, above 960°C in pure O_2, the carbonate route is possible, but the system is close to melting (Karen and Kjekshus 2000). These facts give confidence in that this phase is not an oxide carbonate.

$RBa_6Cu_3O_{10+w}$ (R = Lu, Yb, Tm, Er, Ho, Dy, Gd, Eu and Sm) (Vallino et al. 1991) has not yet been appropriately characterized. This series of compounds appears close to the composition where an oxide carbonate solid-solution region occurs (see sect. 13.5). The conditions for syntheses are generally very demanding in this Ba-rich area owing to the high basicity of BaO, and strict precautions must be adopted to maintain CO_2-free conditions (Abbattista et al. 1988b). The crystal structure is proposed (Abbattista et al. 1988b) to be of an orthorhombically distorted Ruddlesden–Popper type, *i.e.*, corresponding to the formula $Ba_3(Cu_{0.75}Y_{0.25})_2O_{7-w}$. The shared crystallographic site between Cu and Y represents a somewhat disturbing feature of this model, since this is normally not attained above a 2% level even for the smallest R = Sc in $YBa_2Cu_3O_7$ (Karen et al. 1990b) and not found for the related R cuprates of the single K_2NiF_4 type. In a positive sense, however, this could be explained in terms of a structural ordering. This phase is reported by Vallino et al. (1991) to have a considerable variation in oxygen content; *e.g.*, from $YBa_6Cu_3O_{10.2}$ [*I4/mmm*; 398.1(8), 406.5(8), 2211(1)] to $YBa_6Cu_3O_{11.0}$ [400.4(4), 411.1(4), 2158.5(8)] fo R = Y as an example.

13.1.2. *Phases emerging for R = Yb, Tm, Er, Ho, Dy and Y*

The subsolidus phase diagram of the Y(O)–Ba(O)–Cu(O) phase system is shown in fig. 35. The diagram refers to $p_{O_2} = 100$ kPa and 900°C and is based on data (Karen et al. 1990a, Fjellvåg et al. 1987, Abbattista et al. 1989a) selected with particular attention on phase-identification problems occurring when oxide carbonates may appear in the picture. A consensus appears in the copper- and yttrium-rich portion among the numerous diagrams published for Y (De Leeuw et al. 1988a, Roth et al. 1987, 1988, Steinfink et al. 1987, Frase et al. 1987, Wang et al. 1987, Frase and Clarke 1987, Yang et al. 1988, Graf et al. 1989, Saltykova et al. 1990, Koscheeva et al. 1990). Large discrepancies occur, however, in the Ba-rich region.

Fig. 35 is also representative for the phase diagrams for the other R elements of this group: R = Yb (Hodorowicz et al. 1992a, Oniyama et al. 1997), Tm (Hodorowicz et al. 1989), Er (Wong-Ng et al. 1990a), Ho (no reference) and Dy (Koscheeva et al. 1990, Shamrai et al. 1992).

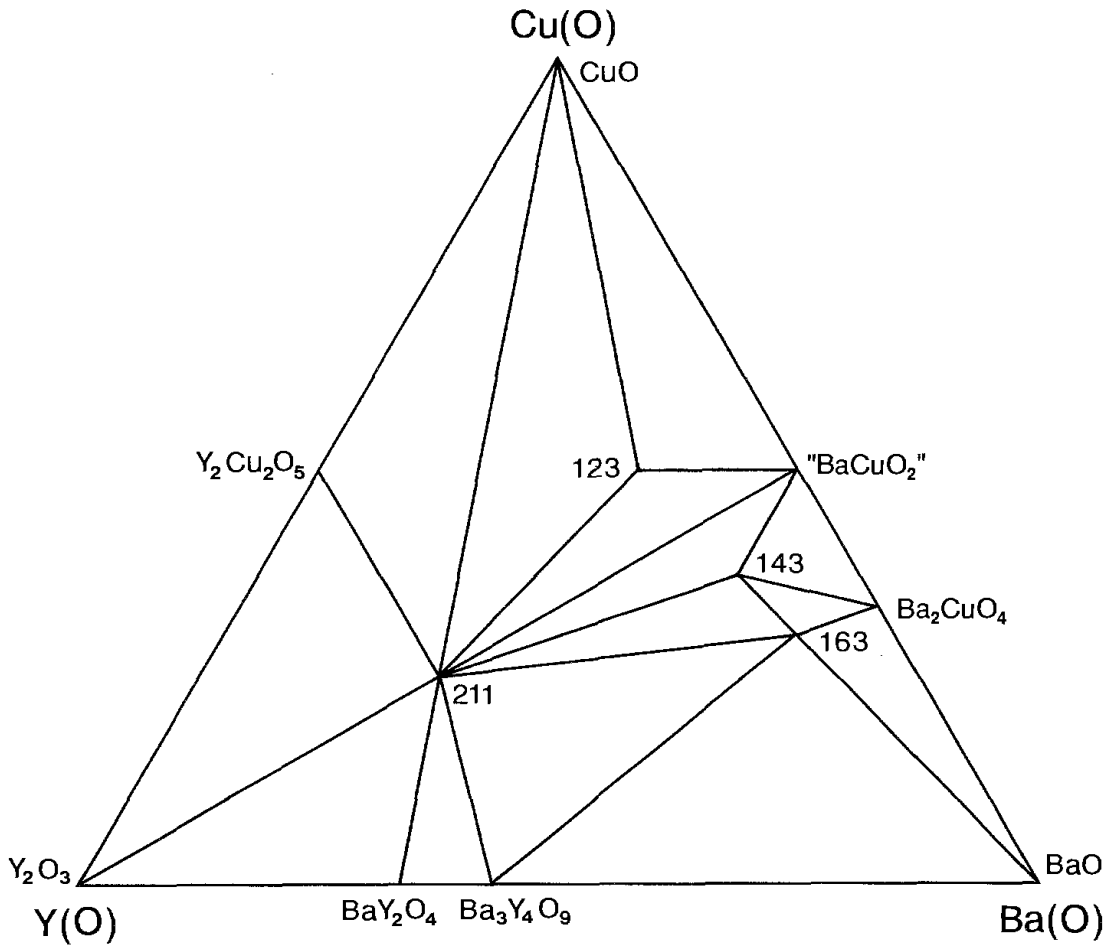

Fig. 35. Subsolidus Y(O)–Ba(O)–Cu(O) phase diagram at 900°C in oxygen at ambient pressure; compiled from Karen et al. (1990a), Fjellvåg et al. (1987) and Abbattista et al. (1989a), with special attention to avoidance of oxide carbonates.

In addition to the quaternary oxides with structure types seen already for R = Lu in the preceeding section, one new oxide appears in fig. 35:

$RBa_2Cu_3O_{6+w}$ is formed for all Rs except Lu and the typically tetravalent elements Ce and Tb (Hodorowicz et al. 1992a, Karen et al. 1990b, Hor et al. 1987). Also the end members of this series require specific precautions for the synthesis: For R = Yb, the temperature must be lowered in order to prevent decomposition (Karen and Kjekshus 2000). The variants with R = Nd, Pr and La can only be obtained upon ceramic syntheses at low partial pressures of oxygen at temperatures between 850 and 875°C (Skakle and West 1994b). The fully oxygen saturated version can then be obtained by a standard oxygen treatment at lower temperatures. Normal firing procedure would otherwise lead to a replacement of a portion of Ba by these large R atoms (Karen et al. 1990b), see sect. 13.1.3.

As a representative example, the crystal structure of $YBa_2Cu_3O_{6+w}$ contains cuprate triple-perovskite layers formed by linear (w = 0) or square-planar (w = 1) coordinations

connecting two layers of corner-sharing square pyramids, much like in a sandwich. Upon variation in the oxygen content, the crystal symmetry switches from tetragonal (Hewat et al. 1987, Garbauskas et al. 1988, Jorgensen et al. 1990a, Casalta et al. 1996) for the reduced version [$YBa_2Cu_3O_{6.00(5)}$; *P4/mmm*; 385.83(1), 1182.53(8); Karen et al. (1990a)] to orthorhombic (Casalta et al. 1996, Cava et al. 1990b, Beno et al. 1987) for the oxidized version [$YBa_2Cu_3O_{6.95(2)}$; *Pmmm*, 381.87(3), 388.59(3), 1167.95(11); Karen et al. (1990a)]. For details on the structural parameters as functions of oxygen content w, see the PND studies by Jorgensen et al. (1990a), Casalta et al. (1996) (single crystals) and Cava et al. (1990b). Structural details have been studied as functions of temperature by Hewat et al. (1987) and François et al. (1988), and as functions of pressure by Jorgensen et al. (1990b) (hydrostatic) and Ludwig et al. (1992) (calculated, both hydrostatic and uniaxial). Detailed unit-cell parameter data are also provided, as a function of w, *e.g.* by Andersen et al. (1990a) and Graf et al. (1990); and as a function of temperature (thermal expansion) by Andersen et al. (1990a) and Mizusaki et al. (1995). Small deviations from the ideal symmetry have been discussed by François et al. (1988), Wong-Ng et al. (1990b, 1999) and Kaldis et al. (1997). For systematic treatment of the structure data for $RBa_2Cu_3O_{6+w}$ over the entire series, see the PND studies by Guillaume et al. (1993) (oxygen saturated; the occurring partial substitution of R = Nd, Pr and La-for-Ba has not been considered).

The maximum oxygen content of $YBa_2Cu_3O_{6+w}$ corresponds to $w = 0.96(2)$ and is reached in ambient oxygen at a relatively low temperature of some 310°C (Fjellvåg et al. 1988b). For details on models for the oxygen equilibria and diffusion, see sect. 17.2. Since the deoxidation of this phase can be induced thermally, an orthorhombic to tetragonal transition is observed upon heating of the fully oxidized version (Fjellvåg et al. 1987, Hewat et al. 1987), depending also on the O_2 pressure (Andersen et al. 1990a, Meuffels et al. 1989). This transformation into the tetragonal structure is a combined result of the thermally induced deoxidation and a thermally induced disorder of the remaining fraction w of the oxygen atoms at the originally square-planar-coordinated copper site (Shaked et al. 1989). The transition temperature $T_{o,t}$ therefore decreases with decreasing oxygen content $w_{o,t}$ and hence decreasing p_{O_2} in the equilibrium atmosphere. For the interval of $823 < T_{o,t} < 973$ K, a linear approximation is valid (Meuffels et al. 1989):

$$w_{o,t} = 0.152 + 0.483 \cdot 10^{-3}\ T_{o,t} \tag{5}$$

or, in terms of the equilibrium oxygen pressure (in Pa, for $714 < T_{o,t} < 1000$ K, calculated from data of Mizusaki et al. 1995):

$$\log p_{O_2} = 14.87(70) - \frac{9734(609)}{T_{o,t}}. \tag{6}$$

This is the main reason why orthorhombic or tetragonal samples can be obtained for the same w in the interval (approximately) $0.25 < w < 0.4$, depending on the synthesis conditions (Jorgensen et al. 1990a, Cava et al. 1990b, Cava et al. 1987a). At temperatures below some 300°C, further, gradual orderings of the oxygen atoms and vacancies into

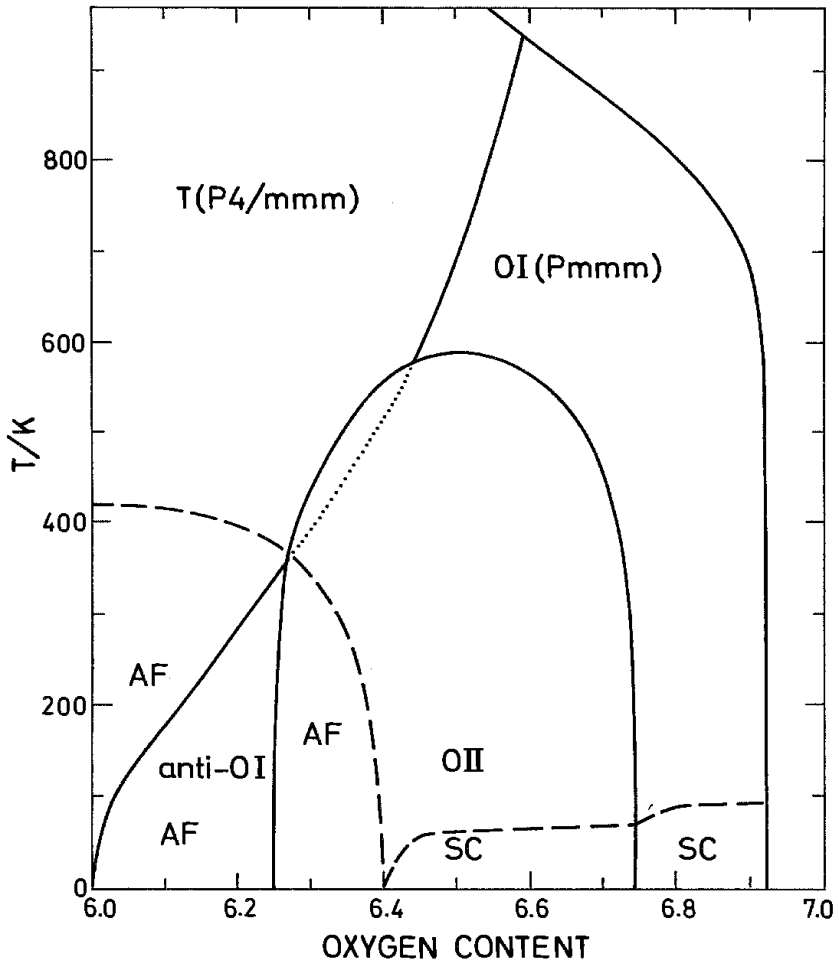

Fig. 36. Low-temperature w–T diagram for $YBa_2Cu_3O_{6+w}$, constructed from data for OII/OI (Ceder et al. 1990), AF (Vettier et al. 1989), SC (Cava et al. 1987a) and o/t (Andersen et al. 1990a) transitions.

several superstructures occur, depending on w, as observed by TEM techniques (Ourmazd and Spence 1987, Ichihashi et al. 1988, Lin et al. 1990, Hou et al. 1990, Alario-Franco et al. 1989) and X-ray (Simon et al. 1993, Poulsen et al. 1996, Straube et al. 1998) or neutron diffraction (Sonntag et al. 1991, Schleger et al. 1995) on single crystals. The kinetics of these processes is rather slow, but it has been established (Jorgensen et al. 1990c) that rapidly quenched oxygen-deficient powder samples undergo subtle changes even at room temperature.

Formation of one such orthorhombic phase at $w = 0.5$, with the simplest additional ordering of the oxygens, denoted OII, has first been proposed from physical properties and theoretical calculations (Cava et al. 1987b, Nakazawa et al. 1987, Verweij 1988). The superstructure model for the OII phase involves alternation of the square-planar "chains" and rows of the linear coordinations at Cu (Simon et al. 1993). The corresponding phase diagram is usually created by computational modelling (Ceder et al. 1990, Lapinskas et al. 1995), and the combined phase properties are illustrated in fig. 36, based on data

from Cava et al. (1990b), Andersen et al. (1990a,b), Ceder et al. (1990) and Vettier et al. (1989).

13.1.3. *Phases emerging for R = Eu and Gd*

The Eu(O)–Ba(O)–Cu(O) subsolidus phase diagram is shown in fig. 37 compiled from phase diagrams of Hodorowicz et al. (1988) and Pieczulewski et al. (1990) and other data from Lopato (1976), Vallino et al. (1991) and Abbattista et al. (1988b) for 950°C and oxygen atmosphere. For all larger trivalent Rs than Gd, the o-$Y_2Cu_2O_5$-type cuprate is no longer stable. However, for R = Gd and Eu, the pseudoternary R(O)–Ba(O)–Cu(O) field (at say, 950°C in ambient oxygen) remains similar to that for smaller Rs in that there still occurs a tie line between 211 and CuO (Wong-Ng et al. 1990a). Another very important distinction occurs for Gd and all larger trivalent Rs in the possibility of their partial replacing Ba in the occurring oxides, *i.e.*, creating a certain occupancy distribution of R over the R and Ba sites:

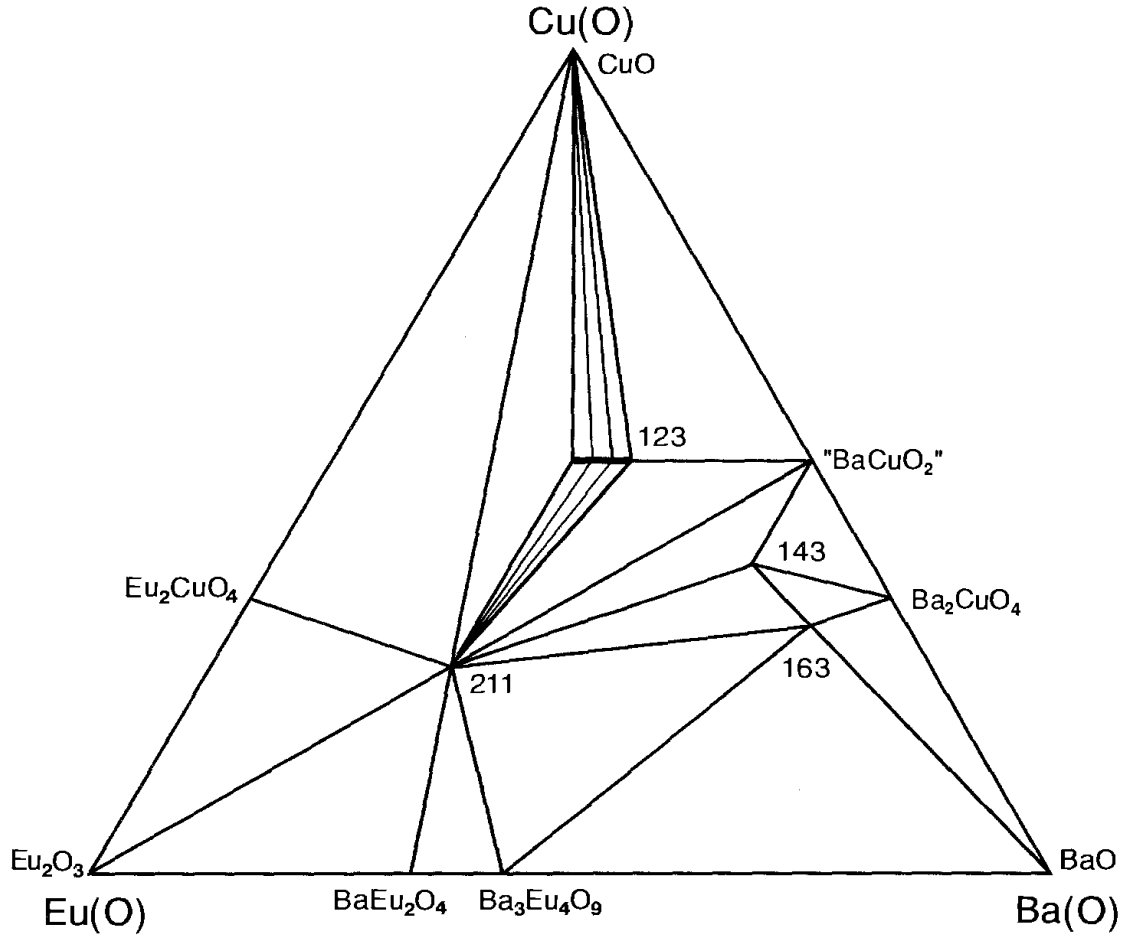

Fig. 37. Subsolidus Eu(O)–Ba(O)–Cu(O) phase diagram at some 950°C in oxygen at ambient pressure. Compiled from Lopato (1976), Vallino et al. (1991), Abbattista et al. (1988b), Hodorowicz et al. (1988) and Pieczulewski et al. (1990), with special attention to avoidance of oxide carbonates.

$\mathbf{R(Ba_{1-y}R_y)_2Cu_3O_{6+w+y}}$ becomes a solid-solution range appended or close to the 123 composition (K. Zhang et al. 1987). It is derived by a simple replacement of some Ba in the 123 structure by the R atom. The extent of the solid solubility of R at the Ba site increases towards the group of the four largest trivalent R atoms, $y \leqslant 0.10, 0.25, 0.30, 0.33, 0.35$ and 0.36 for R = Gd, Eu, Sm, Nd, Pr and La, respectively, referring to 950°C and air atmosphere (Wong-Ng et al. 1990a, Pieczulewski et al. 1990, Skakle and West 1994c, Plackowski et al. 1995). These data are not easy to establish precisely, since, upon the possible formation of a related oxide carbonate phase (see sect. 13.5), the solid-solubility limits are substantially increased (Karen and Kjekshus 1991). Also the lower limit of solid solubility varies as a function of increasing R size. For Nd, Pr and La, the R site (located between the cuprate layers) will not accommodate the atom concerned unless some R is simultaneously present at the Ba site inside the cuprate network. This is manifested by the appearance of a non-zero lower limit of homogeneity (y) (Karen et al. 1990b, K. Zhang et al. 1987). When the synthesis of the $y = 0$ compositions is attempted for these Rs (O_2 atmosphere, 910°C) $R(Ba_{1-y}R_y)_2Cu_3O_{6.96+y}$ is formed instead, with $y = 0.030(5)$, 0.05(1), and 0.09(2) for R = Nd, Pr and La, respectively (Karen et al. 1990b). In contrast to these oxidized samples, moderate reducing conditions achieved either by low p_{O_2} or high enough temperature (Wu et al. 1997) decrease the lower solubility limit to zero, and Ba and large R are hence accommodated separately at their sites. This determines the appropriate synthesis conditions for these compositions (Skakle and West 1994b). The replacements of the trivalent R for divalent Ba result in an almost proportional increase in the attainable oxygen content (ambient oxygen pressure), which may then exceed seven per formula unit (Karen et al. 1990b). The formal Cu valence decreases only slightly, being defined by the degree of electropositive character for the "cations" as counterparts to the poly-cuprate "anions". The symmetry of the crystal structure as a function of the degree of the substitution y and the oxygen content w is governed by the order/disorder situation in the square-planar coordinations around Cu(1). Both the accommodation of the relatively small R atoms at the Ba site and either increase or decrease of the oxygen content from 7 per formula act in the direction of disorder at Cu(1), *i.e.*, a tetragonal symmetry for the phase. The combined effects of the variations in y and w on the unit-cell parameters (*e.g.*, for Sm, Plackowski et al. 1995) result hence in an orthorhombic envelope, centered at $y = 0$ and $w = 1$, similar to that determined by Karen et al. (1992a) for the La-for-Ba substitution in 123. Several specific examples illustrating these relationships may be mentioned. At the lower limit of solid solubility, the crystal structure of the oxygen saturated $R(Ba_{1-y}R_y)_2Cu_3O_{6+w+y}$ phases is orthorhombic [$Nd(Ba_{0.97}Nd_{0.03})_2Cu_3O_{6.99(1)}$; *Pmmm*; 386.14(5), 391.60(8), 1175.1(2)], except for the La version, where this limit is so high that the phase already is tetragonal (Karen et al. 1990b). An increase in y modifies also the oxygen saturated variants of R = Eu, Sm, Nd, and Pr to tetragonal symmetry (Hodorowicz et al. 1990, K. Zhang et al. 1987, Plackowski et al. 1995, Li et al. 1988, Malik et al. 1996) [$Nd(Ba_{0.8}Nd_{0.2})_2Cu_3O_{7.19(1)}$ *P4/mmm*; 387.4(3), 1165.9(4); Li et al. (1988)]. The p–t–y–w equilibria governing the formation of the $R(Ba_{1-y}R_y)_2Cu_3O_{6+w+y}$ solid solutions were studied for R = La (Lindemer et al. 1993) and Nd (Lindemer et al. 1995, Goodilin et al.

1997a) and evaluated also in terms of thermodynamic models. For the solid solubility of Nd at the Ba site at high temperatures it is typical that the maximum y decreases rapidly to zero when the temperature increases above the liquidus level (Goodilin et al. 1997a). This has significance for compositions of single crystals grown from melts.

13.1.4. *Phases emerging for R = Sm*

Upon the increasing size of Rs, Sm is the last to form the 143 phase and probably also the 163 phase (Vallino et al. 1991). However, to obtain any conclusive data for these Ba-rich phases requires strong precautions against oxide carbonate formation and that involves also exclusion of $BaCO_3$ as the starting material for the solid-state synthesis.

13.1.5. *Phases emerging for R = Nd*

A tentative phase diagram for the Nd(O)–Ba(O)–Cu(O) system is selected here from the diagrams of Hodorowicz et al. (1990), Wong-Ng et al. (1994), Abbattista et al. (1991) and Yoo and McCallum (1993), and other data from Karen and Kjekshus (2000), Karen et al. (1990a) and Vallino et al. (1991), and is shown in fig. 38. Several important solid solutions appear adjacent to the ternary oxides at the boundaries of the diagram:

$\mathbf{(R_{1-x}Ba_x)_2CuO_4}$ appears with a moderate solid-solution range and is interesting in that the La variant is the phase which can be identified (Jorgensen et al. 1987) as behind the discovery of high-T_c superconductivity (Bednorz and Müller 1986). A detailed study of the relationship between T_c, oxygen content and the structural features of the La variant is, *e.g.*, given by Rial et al. (1996).

$\mathbf{(Ba_{1-y}R_y)_2CuO_{4-w}}$ appears to have a rather large solid-solution range for R = Nd replacing partially Ba in the Ba_2CuO_{4-w}-type structure (Abbattista et al. 1991). When quenched from 950°C, the series with increasing y exhibits a crystal symmetry change at around $y = 0.05$, from the original high-temperature tetragonal symmetry (pertinent to the parent phase) to the orthorhombic symmetry, which is normally adopted by the more oxidized low-temperature version of Ba_2CuO_{4-w} (Abbattista et al. 1991). The reason for this behaviour is that the oxygen atoms necessary for this transition are supplied by the R substitution for Ba. A similar situation is seen also for R = La (Abbattista et al. 1989b), except for a higher solid-solubility limit (up to $x = 0.33$) and a possible miscibility gap between $x = 0.025$ and 0.125 (950°C), which separates the just mentioned tetragonal and orthorhombic solid solutions.

$\mathbf{(Ba_{1-y}R_y)CuO_2}$. A possibility for a minute substitution of Ba by the larger Rs (Nd, Pr, La) in the "$BaCuO_{2+w}$" phase follows from observations of unit-cell volume changes for this phase in samples in equilibrium with the neighbouring quaternary oxides (Karen and Kjekshus 2000).

One principal difference occurs in the Nd(O)–Ba(O)–Cu(O) phase field as compared with Eu (and smaller Rs), in that the o-R_2BaCuO_5 structure no longer is stable, and another phase with similar composition is formed instead:

t-$(R_{1-x}Ba_x)_2BaCuO_5$, where R = Nd, Pr or La, a brown oxide (cf. the green Y_2BaCuO_5) with a homogeneity range (Karen and Kjekshus 2000) of $0.00 < x < 0.15$

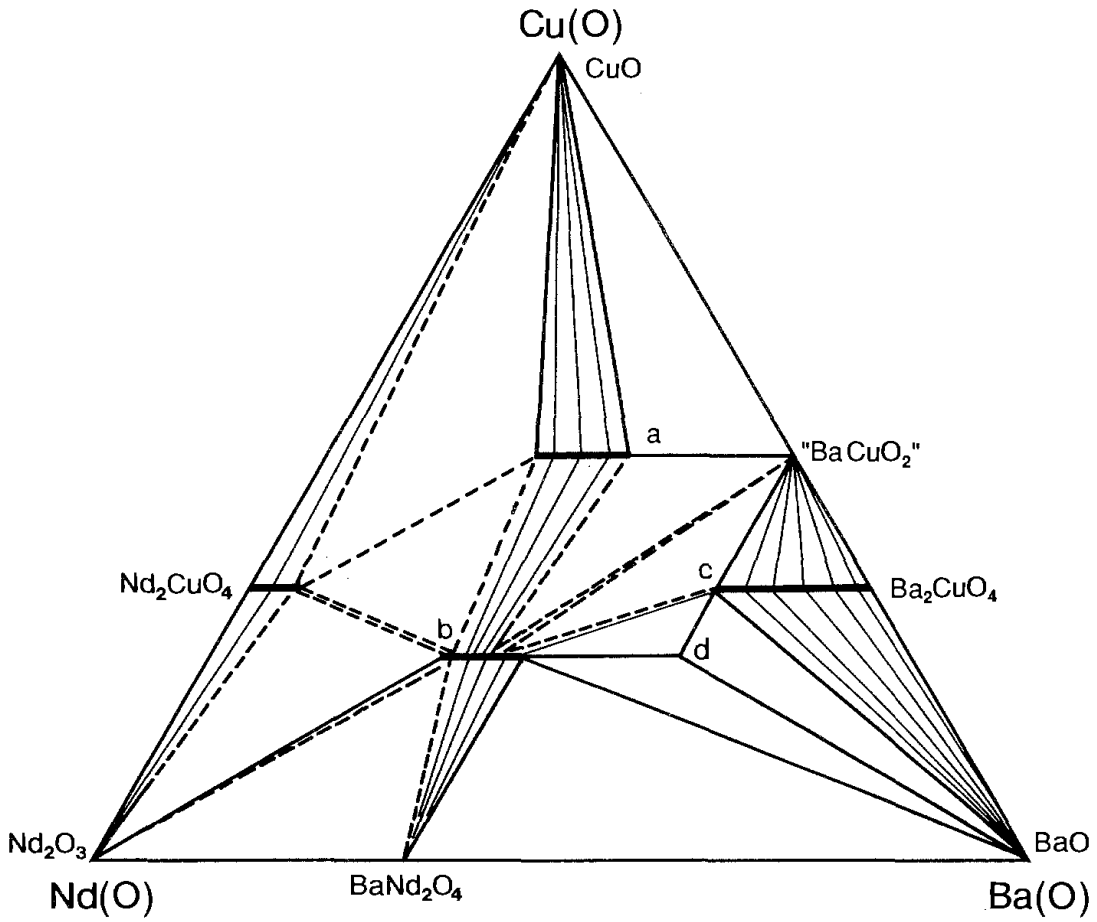

Fig. 38. Subsolidus Nd(O)–Ba(O)–Cu(O) phase diagram at some 950°C in oxygen at ambient pressure. Compiled from Karen and Kjekshus (2000), Hodorowicz et al. (1990), Karen et al. (1990a), Wong-Ng et al. (1994), Vallino et al. (1991), Abbattista et al. (1991) and Yoo and McCallum (1993) with special attention to avoidance of oxide carbonates. Phase designations: a, $Nd(Ba_{1-y}Nd_y)_2Cu_3O_{6+w+y}$ ($0.03 < y < 0.33$, Hodorowicz et al. 1990, Karen et al. 1990b, Skakle and West 1996); b, $(Nd_{1-x}Ba_x)_2BaCuO_5$ ($0.00 < x < 0.15$, Karen and Kjekshus 2000, Abbattista et al. 1990); c, $(Ba_{1-y}Nd_y)_2CuO_{3+w+y}$ ($0.06 < y < 0.25$, Vallino et al. 1991); d, $Nd_2Ba_4Cu_2O_9$ (Domenges et al. 1993).

and crystal structure (Michel et al. 1981, Mizuno et al. 1990, Stalick and Wong-Ng 1990) having isolated square-planar cuprate anions. As an example for R = Nd at the homogeneity limits: Nd_2BaCuO_5 [*P4/mbm*; 669.80(2), 582.10(2)], and $(Nd_{0.85}Ba_{0.15})_2BaCuO_5$ [670.36(5), 582.19(4); Karen and Kjekshus (2000)]. This phase is formed for Nd and the larger Rs (Karen et al. 1990a). For R = La, one observes an analogous (converse) size effect to the Ba–R occupation discussed above, in that the phase exists with a full occupation at the Ba site only when Ba is partially present at the La site. The range of homogeneity does not include $x = 0$, and extends from $x = 0.04$ [$(La_{0.96}Ba_{0.04})_2BaCuO_5$; *P4/mbm*; 685.64(5), 587.37(6); Karen and Kjekshus (2000)] to $x = 0.4$ (Abbattista et al. 1990). The instability of the "stoichiometric" composition has apparently confused the structural description by Michel et al. (1981) and led to the rather complicated formula

$La_{4-2x}Ba_{2+2x}Cu_{2-x}O_{10-2x}$ for this phase. Also the incorrect 311 formula, proposed (Hodorowicz et al. 1990) for this 211 phase, must be originating from a misjudgement of these solid-solution features.

$Nd_2Ba_4Cu_2O_9$, is an quaternary oxide which appears when the R size is increased to that of Nd (Abbattista et al. 1991). Owing to its location in the Ba-rich region, synthesis conditions which strictly exclude any CO_2 or carbonates from the reaction environment are neccessary. The oxide is tetragonal (Domenges et al. 1993) [$P\bar{4}n2$; 1207.2, 387.4], and contains corner sharing cuprate square-pyramids connected into chains. In the R = La system, this phase apparently disappears, and, instead, there occurs a broad region of homogeneity for the $(R_{1-x}Ba_x)_2BaCuO_5$ type.

13.1.6. *Phases emerging for R = Pr*

The Pr(O)–Ba(O)–Cu(O) system (Hodorowicz et al. 1990, Park et al. 1996) has features very similar to the R = Nd analogue, and Pr behaves approximately as a trivalent R in the phase system under ambient (Karen et al. 1990b) and low (Park et al. 1996) oxygen pressures. Of the quaternary phases, only the 211 phase is not formed, and the $BaPrO_3$ perovskite dominates the region instead, still stable at p_{O_2} = 10 Pa (Park et al. 1996).

13.1.7. *Phases emerging for R = La*

The La(O)–Ba(O)–Cu(O) phase diagram at 950°C in oxygen is shown in fig. 39, compiled from phase diagrams of De Leeuw (1989), Abbattista et al. (1990) and Klibanow et al. (1988) and other data from Karen and Kjekshus (2000), Vallino et al. (1991), Karen et al. (1990b), Abbattista et al. (1989b) and Michel et al. (1987). In addition to the already discussed features, two additional phases emerge for La which is the largest and most electropositive R:

$BaLa_4Cu_5O_{13+w}$, is an ordered, oxygen-deficient perovskite with $a = a_p\sqrt{5}$, containing a network of octahedral and square-pyramidal cuprate coordinations (Michel et al. 1987). The oxide is a metallic conductor but no superconductivity is reported. The oxygen saturated phase of tetragonal symmetry (Michel et al. 1987) has a rather high copper valence [$BaLa_4Cu_5O_{13.16}$; *P4/m*; 864.75(1), 385.94(1)] and the oxygen content decreases only slightly ($-0.2 < w < 0.16$) with increasing temperature up to 1015°C at ambient oxygen pressure (Davies and Katzan 1990). At low oxygen partial pressures and high temperatures, the oxygen content can be varied between $-0.5 < w < 0.16$ without bulk decomposition into Cu and La,Ba oxides (Davies and Katzan 1990). However, when the oxygen content is varied in contact with a hydrogen-containing atmosphere at temperatures lower than 400°C, the oxygen content can be further reduced (to $w = -2.0$) upon formation of structural variants with, *inter alia*, linear Cu^I coordinations in the still intact matrix of metal atoms (Davies and Katzan 1990, Rangavittal et al. 1995), *e.g.*, $BaLa_4Cu_5O_{12}$ [*P2/m*; 890.1(2), 377.1(2), 869.1(2), 88.60(2)]. All these reduced compounds can be reoxidized into the oxygen saturated structure (Davies and Katzan 1990). The thermodynamics of the oxygen-exchange reaction was investigated by Thiele and Davies (1991).

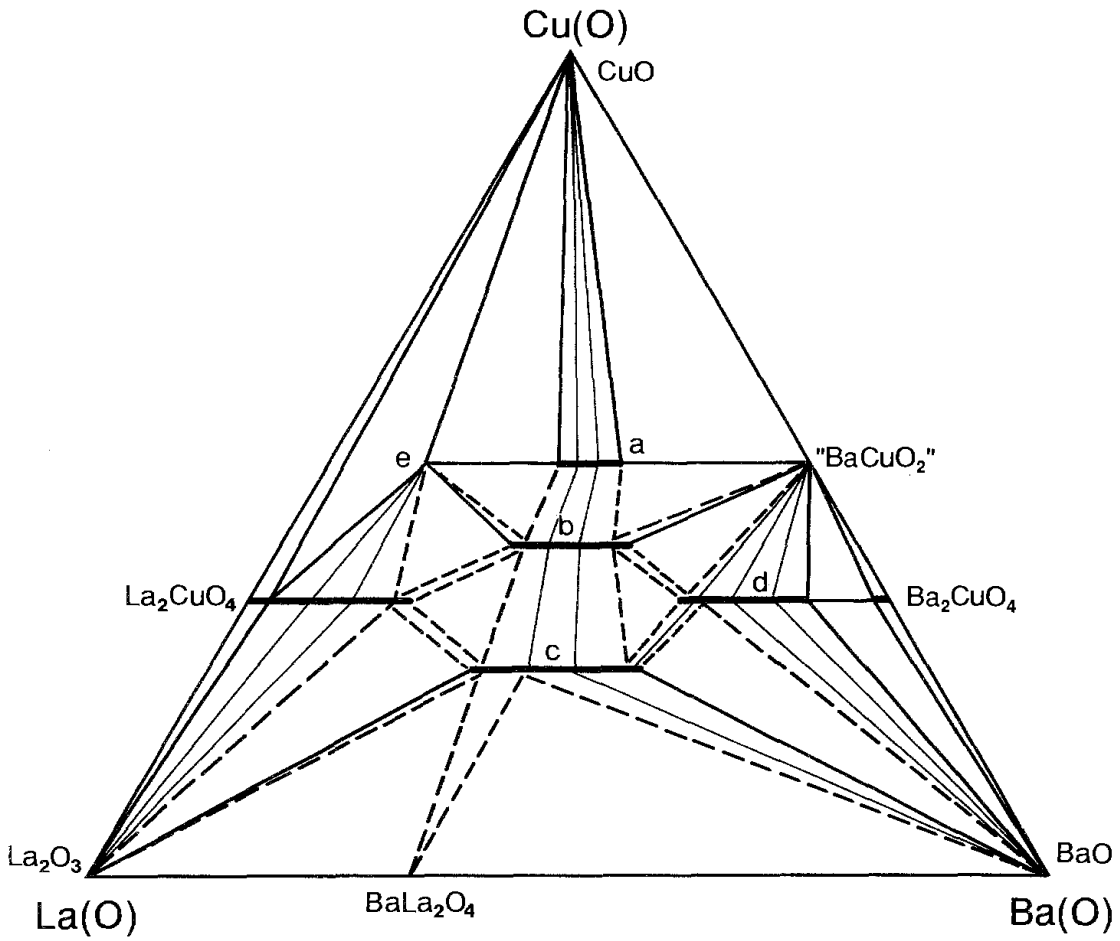

Fig. 39. Subsolidus La(O)–Ba(O)–Cu(O) phase diagram at some 950°C in oxygen at ambient pressure. Compiled from Karen and Kjekshus (2000), De Leeuw (1989), Vallino et al. (1991), Karen et al. (1990b), Abbattista et al. (1989b, 1990), Klibanow et al. (1988) and Michel et al. (1987), with special attention to avoidance of oxide carbonates. Phase designations: a, $La(Ba_{1-y}La_y)_2Cu_3O_{6+w+y}$ ($0.09 < y < 0.26$, Karen and Kjekshus 2000, Karen et al. 1990b); b, $(La_{1-x}Ba_x)_2BaCu_2O_{6+w}$ ($0.10 < x < 0.40$, De Leeuw 1989); c, $(La_{1-x}Ba_x)_2BaCuO_5$ ($0.04 < x < 0.40$, Karen and Kjekshus 2000, Abbattista et al. 1990); d, $(Ba_{1-y}La_y)_2CuO_{3+w+y}$ ($0.12 < y < 0.33$, Vallino et al. 1991); e, $BaLa_4Cu_5O_{13}$ (Davies and Katzan 1990).

$\mathbf{(La_{1-x}Ba_x)_2BaCu_2O_{6+w}}$, with $0.1 < x < 0.4$ (De Leeuw 1989), is of the Ruddlesden–Popper-type structure, analogous to the Sr variants described in sect. 11.

13.2. *High p_{O_2} or oxidizing conditions*

As seen in previous sections, highly oxidized cuprates of A or R are formed under ambient or elevated pressures of oxygen at moderate temperatures, and similar situation may be expected in the pseudoternary field in question. The phase diagram as seen in pure oxygen around 800°C, compiled from experimental (synthesis) data based on reactive (Karen et al. 1990a) and/or carbon free (Brosha et al. 1995, Abbattista et al. 1989a, W. Zhang and Osamura 1992) precursors, is shown in fig. 40. One additional quaternary oxide is seen:

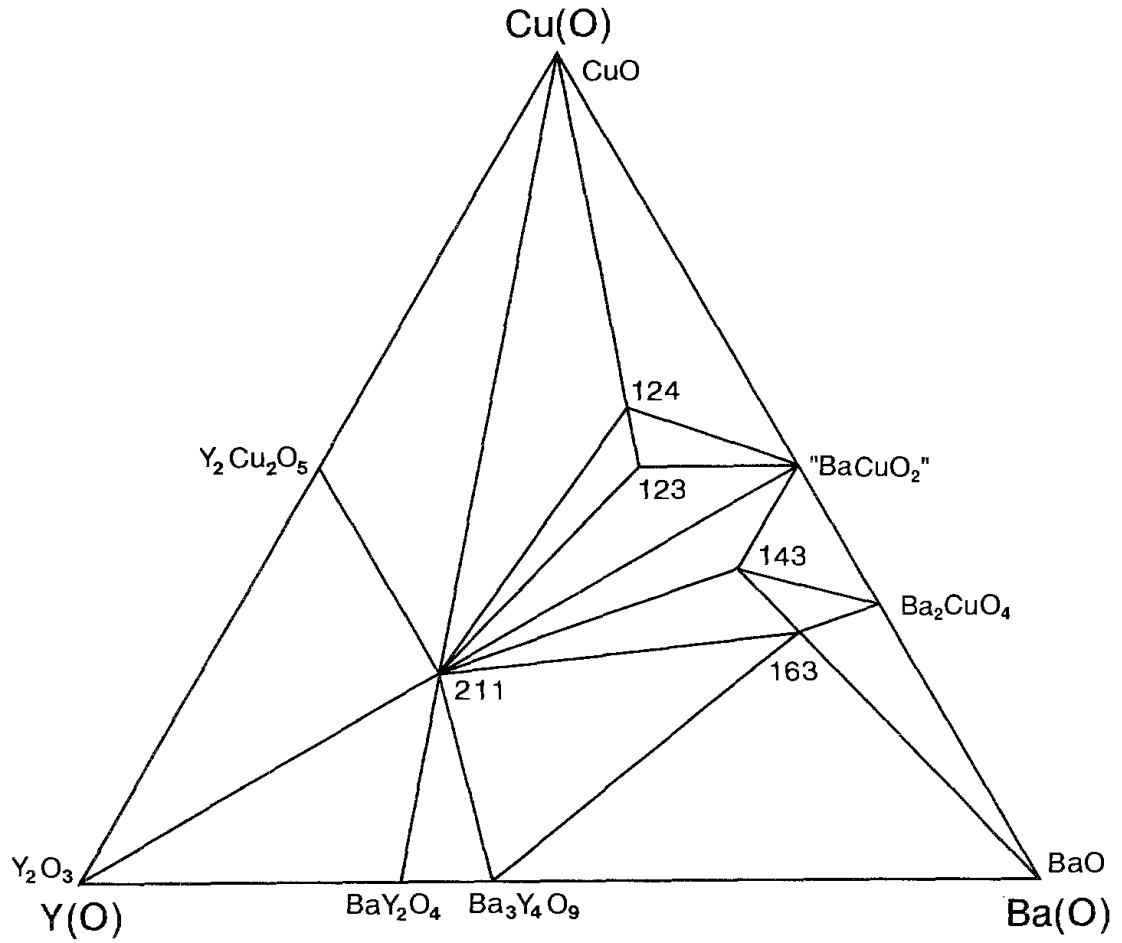

Fig. 40. Subsolidus Y(O)–Ba(O)–Cu(O) phase diagram at 800°C in oxygen at ambient pressure. (After Karen et al. 1990a, Brosha et al. 1995, Abbattista et al. 1989a and W. Zhang and Osamura 1992.)

$RBa_2Cu_4O_8$ has a crystal structure (Bordet et al. 1989, Kaldis et al. 1989) which contains double Cu–O squares appended into chains through a zig-zag edge sharing. These chains appear instead of the simple corner-sharing chains in the related $YBa_2Cu_3O_7$-type structure [$YBa_2Cu_4O_{7.995}$ *Ammm*; 384.3(1), 387.0(1), 2725.0(5); Karen et al. (1990a)]. The edge-sharing of the coordination squares makes the oxygen content structurally fixed and this highly oxidized phase is hence less thermally stable (Karpinski et al. 1989a). Although it was obtained originally at high pressures (Karpinski et al. 1988), $YBa_2Cu_4O_8$ can be prepared at some 820°C from atomic-mixed carbonate starting-materials in purified oxygen (Karen et al. 1992b, Karen and Kjekshus 1994a), and also nitrate (Cava et al. 1989) and (123 + CuO) (Jin et al. 1990) routes are described. In an oxygen atmosphere at ambient pressure, $YBa_2Cu_4O_8$ decomposes above 840°C into CuO and $YBa_2Cu_3O_{6.44}$ (Zhou and Navrotsky 1993). Note the low oxygen content for the latter phase, which is of significance for the pressure–stability relationships. The structural building principle of this phase can be generalized into a structural series the members of which have an increasing content of Cu and a rapidly decreasing stability (Señaris-Rodriguez et al. 1991).

As an example, thermodynamic prediction of existence conditions for $YBa_2Cu_5O_9$ gives a stability limit of 470°C in ambient oxygen (Voronin 1994a). Also a structural combination between the 124 and 123 phases is possible:

$R_2Ba_4Cu_7O_{14+w}$, whose crystal structure (Bordet et al. 1988a) is a combination of the $RBa_2Cu_3O_7$ and $RBa_2Cu_4O_8$ arrangements [$Y_2Ba_4Cu_7O_{15}$; *Ammm*; 385, 387, 5030]. In accordance with this, there occurs a homogeneity range of some $0.0 < w < 1.0$ (for the R = Y variant) with respect to the oxygen content (Tallon et al. 1990a, Karpinski et al. 1989b, Karpinski et al. 1989c). This phase can be formed by deoxidation of $YBa_2Cu_4O_8$ at elevated oxygen pressures in a narrow temperature range above 900°C (Karpinski et al. 1989c), and also appears briefly around 885°C in ambient oxygen (Morris et al. 1989a). An equilibrium p–t diagram is experimentally determined (Karpinski et al. 1989c, Karpinski et al. 1990) for the nominal 124 composition and oxygen pressures up to 300 MPa, showing regions of stability for the solid phases involved (fig. 41). Similar stability fields have also been obtained by calculation from thermodynamic data derived from calorimetry, EMF measurements and equilibration procedures (Zhou and Navrotsky 1993, 1999, Voronin and Degterov 1991).

The 247 and 124 phases have been synthesized and studied also for R = Er (Tallon et al. 1990a, Cava et al. 1989), Ho (Cava et al. 1989), Dy (Morris et al. 1989b,c), Gd (Morris et al. 1989b,c), Eu (Valo et al. 1995, Morris et al. 1989b,c), Sm (Morris et al. 1989b), Nd (Morris et al. 1989b) and Pr (Seiji et al. 1994) systems, and the stability regions become narrower with the increasing ionic size of R (Morris et al. 1989c). The Pr variant can only be obtained under rather specific high-pressure conditions, but retains all the structural (Seiji et al. 1994) features of the prototype, including the oxygen content [$PrBa_2Cu_4O_8$; *Ammm*; 388.59(1), 390.31(1), 2732.06(7)].

The R(O)–Ba(O)–Cu(O) system changes profoundly when exposed to highly oxidative environments at very high oxygen pressures (fig. 42; Graf et al. 1991). Under an oxygen pressure of 9 MPa at 1000°C, $YBa_2Cu_3O_{6+w}$ becomes unstable against decomposition into the more oxidized and now stable phase $Ba_2Cu_3O_{6+w}$ (plus 124 and 211). The $YBa_2Cu_4O_8$ phase, which has a structurally fixed high oxygen content, is promoted in stability by a high oxygen pressure.

Even more than the diagrams for ambient-conditions, the published results for the high oxygen pressures (Graf et al. 1991, Chandrachood et al. 1990) show considerable disagreement about the Ba-rich corner, which is therefore excluded in fig. 42. Several phases have been suggested seen, but the claims do not withstand the scrutiny of excluding the possibility that they are in fact oxide carbonates, formed in the closed systems from traces of carbonate in the starting materials and/or CO_2 in the (compressed) atmosphere. As another example, a failed attempt to prepare $YBa_4Cu_3O_{8.5+w}$ at high O_2 pressures is contrasted by the finding that it persists (100 hrs) under the same conditions, when first synthesized at ambient pressure (Graf et al. 1991). This illustrates another problem of the studies at high oxygen pressures. The experimental points in the recorded phase diagrams are often obtained starting from mixtures of binary oxides and actually performing the syntheses under high oxygen pressure conditions instead of cross-checking both the formation and stability of the products based on carbon-free amorphous precursors.

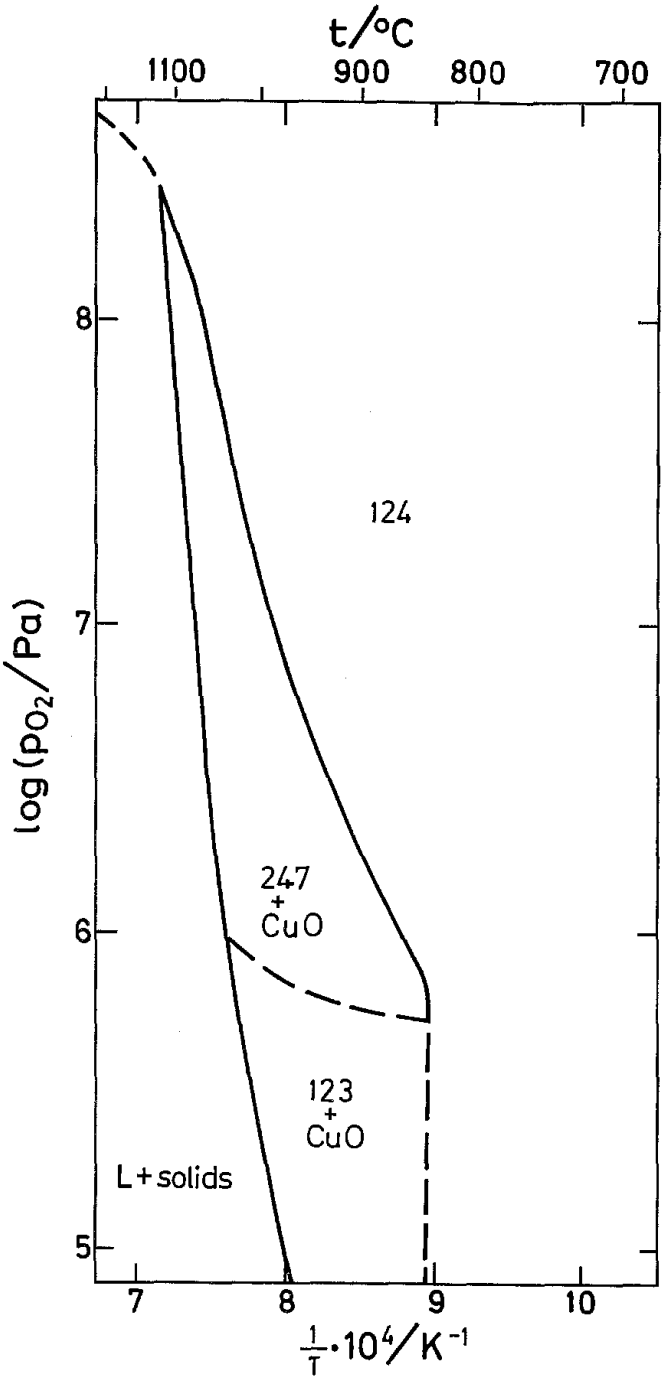

Fig. 41. A p–t diagram for the 124 ($YBa_2Cu_4O_8$) composition. (After Karpinski et al. 1989c, 1990.)

Similar problems are encountered when isothermal phase systems are investigated in ambient atmospheres at temperatures lower than the thermodynamic firing temperatures from carbonaceous precursors. Below some 700 to 800°C the difficulties are so severe that the phase diagrams are rather constructed by calculation from measured thermodynamic data. Unfortunately, unavailable structural and compositional definitions for some of

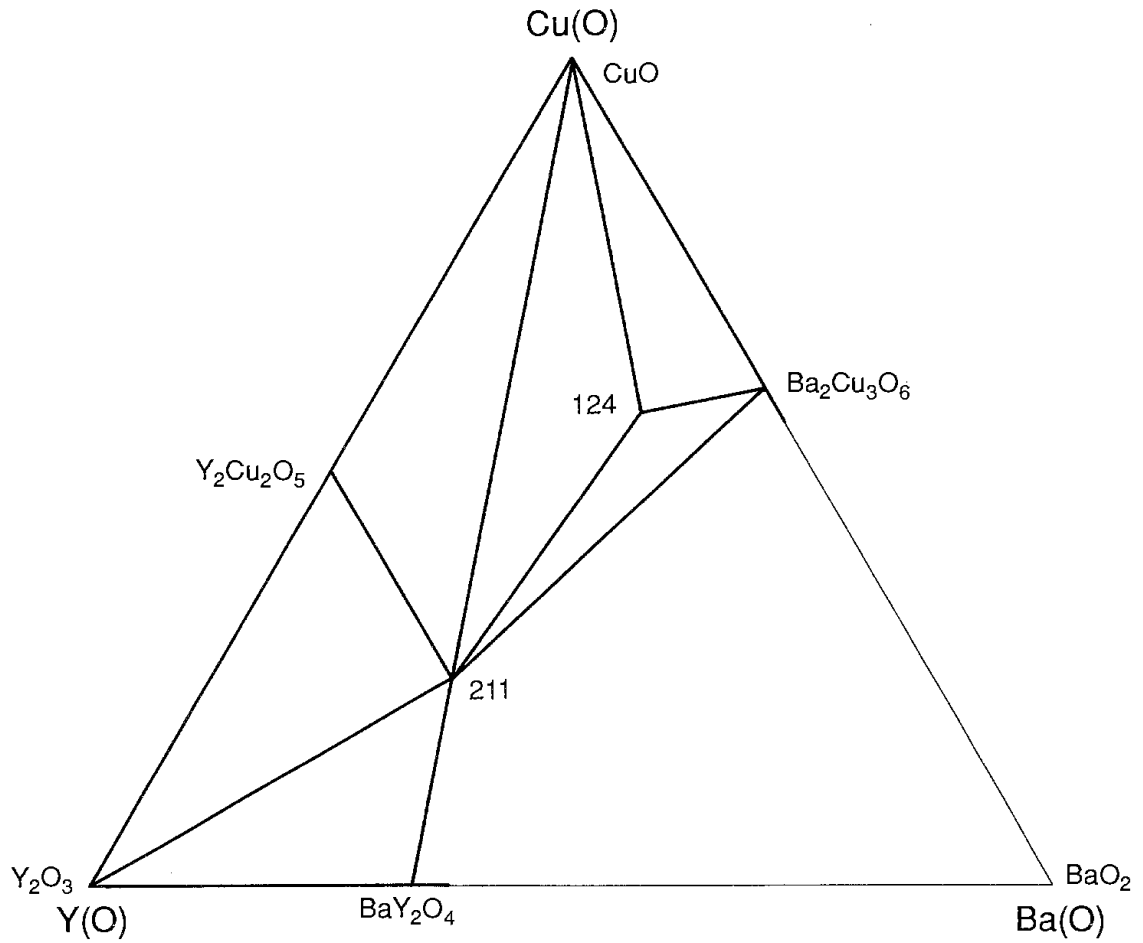

Fig. 42. Subsolidus Y(O)–Ba(O)–Cu(O) phase diagram at 1000°C in oxygen under p_{O_2} = 9 MPa (after Graf et al. 1991). The Ba-rich region has been omitted.

the variable-valence phases, rather than the error margins, seem to be at the root of the problem. This concerns in particular $Ba_2Cu_3O_{6-w}$, as discussed, *e.g.*, by Williams et al. (1994). Nevertheless, the calculations (referring to oxygen at ambient pressure) are quite consistent in showing that the highly oxidized phases indeed become more stable upon lowering the temperature (corresponding to the increased oxidation effect), and that they occur at the expense of the phases which have lower Cu valence under the given conditions. According to Garzon et al. (1991) and Brosha et al. (1995), $YBa_2Cu_3O_{6+w}$ and Y_2BaCuO_5 become unstable under some 650 to 750°C against formation of $Ba_2Cu_3O_{6-w}$ and Y_2O_3 and Ba_2YO_4. Ultimately, the most oxidized phase, $Ba_2Cu_3O_{6-w}$, becomes stable next to binary oxides and BaO_2, as calculated for 25°C. However, none of these reactions can actually be observed owing to kinetic hindering. As an example, the calculated isothermal phase diagram at 700°C is shown in fig. 43.

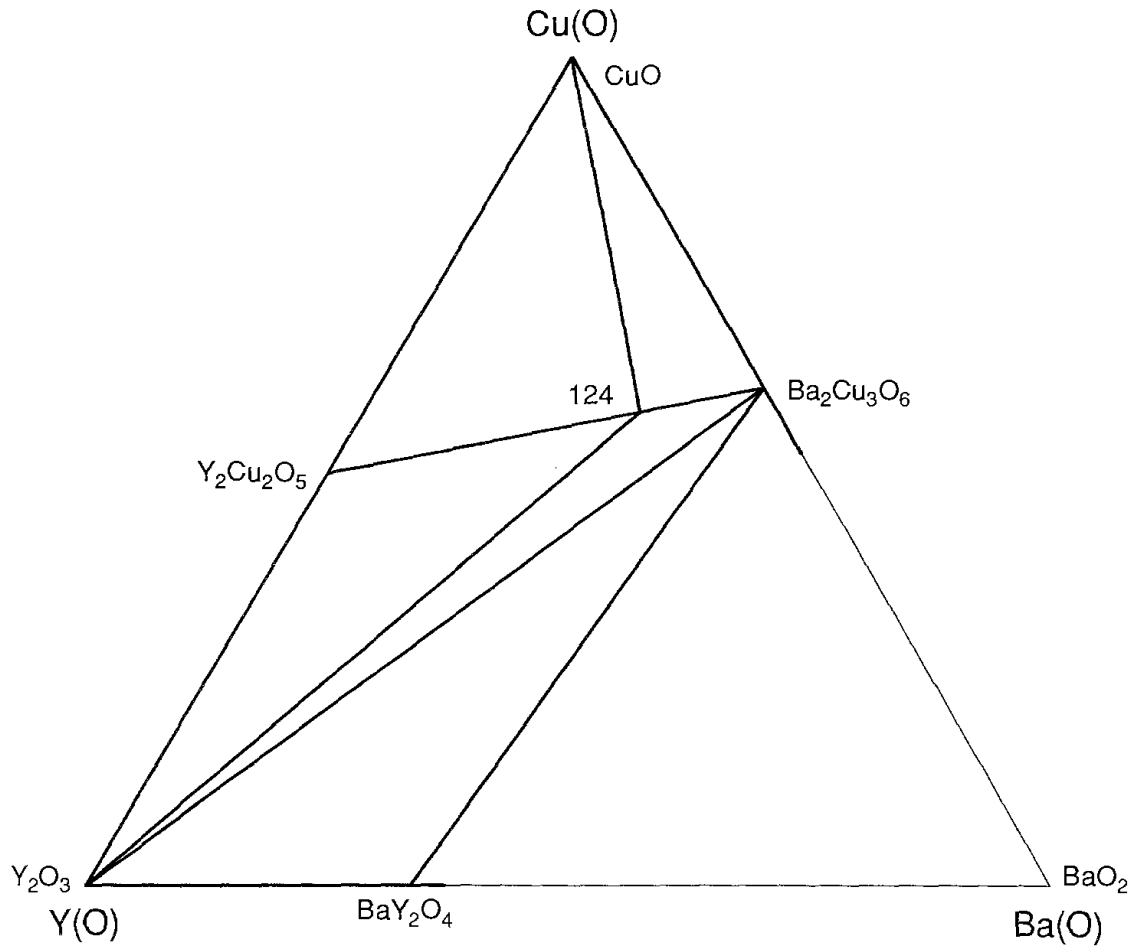

Fig. 43. Subsolidus Y(O)–Ba(O)–Cu(O) phase diagram at 700°C in oxygen at ambient pressure calculated from thermodynamic data (after Brosha et al. 1995). The Ba-rich region has been omitted.

13.3. *Low p_{O_2} or reducing conditions*

Upon decreasing partial pressures of oxygen, or increasing temperature, the analogous principle to the above governs the phase stability in the subsolidus region. Already moderately increased temperatures and moderately reduced partial pressures of oxygen are significant factors which lead to chemical reduction upon formation of other phases like Cu_2O, $BaCu_2O_2$ and $YCuO_2$, until the most reduced phases emerge, *viz.*, elemental Cu, coexisting with Y_2O_3, BaO and Y, Ba oxides (Karen et al. 1990a).

13.3.1. *Reduction by low p_{O_2}*

Isothermal subsolidus reductions in the Y- and Cu-rich portion of the Y(O)–Ba(O)–Cu(O) system have been studied with the help of EMF (coulometric) measurements. The oxygen- and Cu-richest phases decompose first, upon decrease in the partial pressure of oxygen.

$YBa_2Cu_4O_8$, which has $v_{Cu} = 2.25$, decomposes (Kale 1992) already at relatively high oxygen pressures into $Y_2Ba_4Cu_7O_{14+w}$, CuO and O_2: For the interval $850 < T_{dec} < 1100$ K,

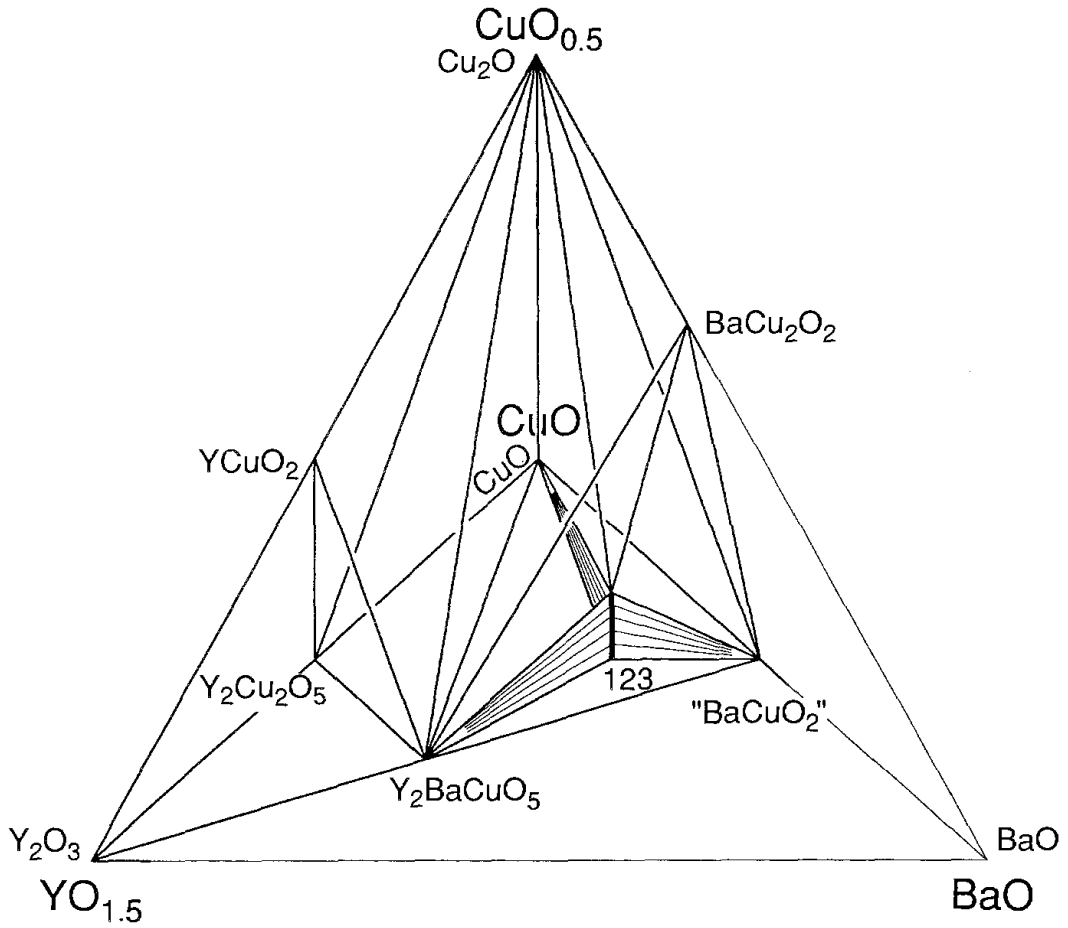

Fig. 44. Isothermal $YO_{1.5}$–BaO–CuO–$CuO_{0.5}$ diagram at 950°C (after Borowiec and Kolbrecka 1991). $YO_{1.5}$, BaO, and CuO form the base of the tetrahedron. The presence of L close to "$BaCuO_2$" and the small oxygen-solubility range of the latter phase are disregarded. The Ba-rich region has been omitted.

the following expression is obtained from the coulometric $\Delta\mu_{O_2}$ data of Kale (1992) (in Pa, K):

$$\log p_{O_2} = 16.62 - \frac{13\,090}{T_{dec}}, \tag{7}$$

where T_{dec} is the decomposition temperature.

The situation for $1 < v_{Cu} < 2$ is shown in the tetrahedral diagram in fig. 44, based on combined EMF+p,t-equilibrations data (Borowiec and Kolbrecka 1991). $YBa_2Cu_3O_{6+w}$ decomposes in the solid state when $w \approx 0$ (Karen et al. 1990a, Bormann and Nölting 1989, Nowotny et al. 1990, Porat et al. 1992, Kim and Gaskell 1994), defined by the partial pressure of oxygen at T_{dec}. For the interval $1023 < T_{dec} < 1148$ K, the following expression is valid (in Pa, K; calculated from data of Beyers and Ahn 1991):

$$\log p_{O_2} = 12.28(30) - \frac{11\,975(328)}{T_{dec}}. \tag{8}$$

For the continuation to higher temperatures, see MacManus-Driscoll et al. (1995). Very similar values were obtained by Kim and Gaskell (1994) for the interval $993 < T < 1222$ K. The sequence of subsequent redox reactions occurring upon the gradual removal of oxygen from various nominal compositions has been investigated by solid-state coulometric titration (Beyers and Ahn 1991, Ahn et al. 1988, 1990) and TGA in controlled atmospheres (Kim and Gaskell 1994) followed by PXD. Details for the isothermal pseudoternary Cu-rich subsystem according to Beyers and Ahn (1991) and Ahn et al. (1990) are shown in fig. 45, referring to the p_{O_2} plateaus "seen" by coulometric titration at 850°C (chosen in order to maintain acceptable kinetics of the solid-state reactions). Nevertheless, even then, a liquidus briefly appears as a function of the decreasing partial pressure of oxygen. Table 23 lists nine observed invariant reactions occurring between the ten individual situations drawn in fig. 45 and the respective partial pressures of oxygen ("plateaus") for each reaction. Unfortunately, the Ba-rich perovskite phase participating in these equilibria has only been identified as "132" by Ahn et al. (1990). This composition does not refer to an existing phase in this system and therefore it is replaced for our purpose by an "X". Since $YBa_4Cu_3O_{9+w}$ is not stable (Karen et al. 1990a) already at the partial pressure of the first plateau ($p_{O_2} = 560$ Pa), it is quite probable that the X phase actually is the Cu-rich composition of the $Ba_8[Cu_{4+z}R_{1+x}(CO_3)_{3-x-z}]O_{10+w}$ oxide carbonate (see sect. 13.5). Similarly, the "$BaCuO_2$" phase also possibly represents an oxide carbonate (see sect. 7). With these facts in mind, the data in table 23 and fig. 45 illustrate how a "real" Cu-rich system behaves upon removal of oxygen.

The nature of the solid-state decomposition products of the $YBa_2Cu_3O_6$ phase remains still somewhat ambiguous (Kim and Gaskell 1994). Three sets of decomposition products are generally reported: (1) Y_2BaCuO_5, "$BaCuO_2$" and Cu_2O have been considered by Bormann and Nölting (1989) and Porat et al. (1992), however, based on later unconfirmed citations. (2) Y_2BaCuO_5, "$BaCuO_2$" and $BaCu_2O_2$ have been observed by Borowiec and Kolbrecka (1991) and this situation is shown in fig. 44. (3) Y_2BaCuO_5, $BaCu_2O_2$ and the X phase have been identified by Beyers and Ahn (1991), Lindemer et al. (1991) and Kale (1992), and this situation appears in table 23 and fig. 45. The reason for these disagreements can be twofold: (i) An undefined degree of stabilization by oxide carbonates even while the values of p_{O_2} are well under control. (ii) The poor resolution in terms of p_{O_2} and temperature for the reaction proper of the decomposition of 123, the decomposition of "$BaCuO_2$" into $BaCu_2O_2$, and the formation of the phase X. Several indistinct TGA plateaus were observed by Kim and Gaskell (1994), following closely after each other, upon increased temperature at low partial pressures of oxygen, after the stability limit of the 123 phase has been crossed. This is suggested to indicate that the three sets of reaction products indeed occur in the said order upon the solid-state reduction of the nominal 123 composition. At the very first TGA plateau, before these profound reduction processes occur, a demixing of a small amount of Y_2BaCuO_5 from the 123 phase is seen by Kim and Gaskell (1994). This further increases the ambiguity as to the actual solid-state decomposition point of the 123 phase.

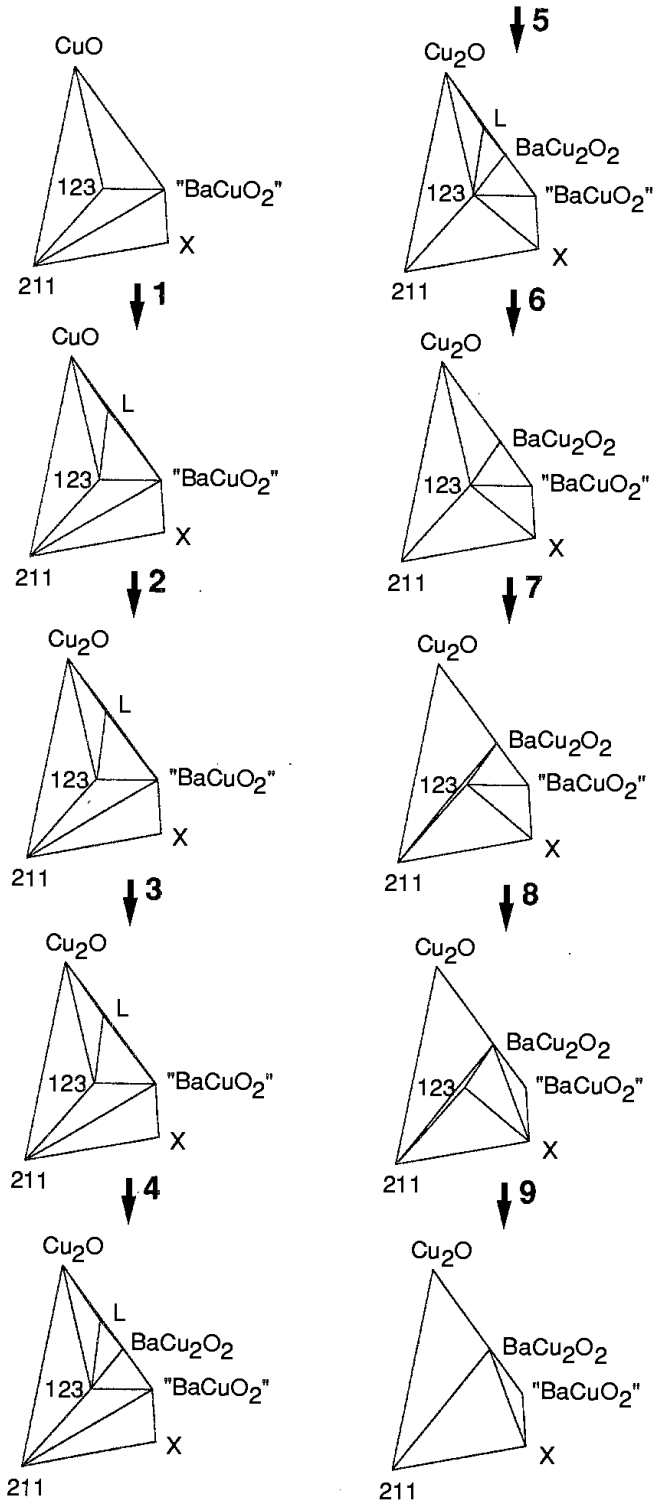

Fig. 45. Cu-rich sections of the pseudoternary Y(O)–Ba(O)–Cu(O) phase diagram upon reduction at 850°C by means of coulometric titration (after Beyers and Ahn 1991 and Ahn et al. 1990). Numbered arrows refer to table 23.

Table 23
Phases involved and oxygen partial pressures (in Pa) for invariant reactions (not balanced) near 123 at 850°C (Ahn et al. 1990)

R [a]	p_{O_2}	Reaction components [b]
1	560	$YBa_2Cu_3O_{6+w} + BaCuO_2 + CuO \rightleftharpoons L + O_2$
2	410	$CuO \rightleftharpoons Cu_2O + O_2$
3	300	$BaCuO_2 + L \rightleftharpoons BaCu_2O_2 + O_2$
4	300	$BaCuO_2 + L \rightleftharpoons YBa_2Cu_3O_{6+w} + BaCu_2O_2 + O_2$
5	270	$Y_2BaCuO_5 + BaCuO_2 \rightleftharpoons YBa_2Cu_3O_{6+w} + X + O_2$
6	150	$L \rightleftharpoons BaCu_2O_2 + Cu_2O + YBa_2Cu_3O_{6+w} + O_2$
7	100	$YBa_2Cu_3O_{6+w} + Cu_2O \rightleftharpoons Y_2BaCuO_5 + BaCu_2O_2 + O_2$
8	70	$YBa_2Cu_3O_{6+w} + BaCuO_2 \rightleftharpoons X + BaCu_2O_2 + O_2$
9	40	$YBa_2Cu_3O_{6+w} \rightleftharpoons X + Y_2BaCuO_5 + BaCu_2O_2 + O_2$

[a] Number refers to the pressure plateau in fig. 45.
[b] X denotes the reported Ba-rich perovskite, being most probably the 184 oxide carbonate.

13.3.2. *Reduction by high temperatures*

When the chemical reduction of the R(O)–Ba(O)–Cu(O) system is performed by means of increasing temperature, the oxide carbonate problem is somewhat alleviated. However, the solidus–liquidus equilibria are soon entering the picture.

The temperature-induced reduction and decomposition is characterized by the incongruent melting (upon formation of Y_2BaCuO_2 and a liquid, Lindemer et al. 1991) at the temperature T_m. T_m of $YBa_2Cu_3O_{6+w}$ decreases with w and in turn also with decreasing partial pressure of O_2 in the surrounding atmosphere. DTA-based data for T_m, obtained (Idemoto and Fueki 1989) in atmospheres with the oxygen partial pressure varied in the interval $10^2 < p_{O_2} < 10^5$ Pa, can be approximated linearly as follows (in Pa, K):

$$\log p_{O_2} = 37.6(9) - \frac{42256(1137)}{T_m}, \tag{9}$$

with T_m between some 900 and 1024°C (the latter in pure O_2). However, indications of the liquidus are often observed at lower temperatures than stated above. Examinations (Clarke et al. 1991) of cyclically annealed phase-pure $YBa_2Cu_3O_{6+w}$ indicated that already below the melting point of this phase copper atoms may have a tendency to migrate to the surface of the bulk particles. According to Clarke et al. (1991) this excess of copper on the grain boundaries causes the formation of a peritectic liquid which in turn results in a partial phase separation upon cooling. Vaporization studies (Wahlbeck et al. 1989, Sata et al. 1991) have shown measurable partial pressures of both copper and barium species over $YBa_2Cu_3O_{6+w}$ at temperatures around melting. At 890°C, *vapor pressure* values (in Pa) of $1.2 \cdot 10^{-4}$ for Cu, $2.2 \cdot 10^{-5}$ for CuO and $2.5 \cdot 10^{-5}$ for BaO under 21 kPa of oxygen were obtained by Sata et al. (1991). No Y-containing vapor is detected at this temperature.

13.4. *High-pressure phases*

Phase equilibria in the Y(O)–Ba(O)–Cu(O) system at 950°C under 1 MPa pressure were investigated (Lawanier et al. 1996) using a piston–cylinder-type apparatus and SEM analyses. The Y- and Cu-rich portions of the thus established phase diagram are identical with the situation seen at 900°C in ambient oxygen (fig. 35), whereas the rest of the diagram suffers from formation of oxide carbonates. The 124 phase is not found by Lawanier et al. (1996), and it would be interesting to see whether this can be rationalized by the fact that the molar volume of 124 is larger than the sum of molar volumes of CuO and $YBa_2Cu_3O_{6+w}$ for any w.

13.5. *Oxide carbonates*

As shown in sect. 3, the occurrence of the R oxide carbonates has been known for a long time. Their crystal structures can be derived from those of the pure oxides by replacing an appropriate portion of oxygen atoms by carbonate groups, accompanied by structural distortions. In a similar way, $CaCO_3$ is related to CaO. Also the Ba-rich ternary oxides of Ba and Rs form easily oxide carbonates (De Leeuw et al. 1988a). Apart from the structural relationship, a clear link is seen between the stability of oxide carbonates and the basicity of the oxides. Since the copper carbonate itself is instable, it took some time to acknowledge that also A,R cuprates may accommodate certain portion of carbonate groups in their crystal structures. Significant contents of CO_2 were found in the Cu-poor and Ba-rich perovskite-type phase from the Y(O)–Ba(O)–Cu(O) system (Fjellvåg et al. 1988c), and it was realized that CO_2 is built in this cuprate as structural carbonate ions (Roth et al. 1988). A similar history can be traced for the 123 phase which was also found to accommodate some carbonate ions (Karen et al. 1990a, Shaw et al. 1990, Lindemer et al. 1990). Later it was realized and confirmed that the carbonate groups do not occupy the oxygen atom positions, but the Cu sites (first shown for the $Sr_2CuO_2CO_3$ case by Miyazaki et al. 1992a). This meant that the cuprate coordination polyhedron is replaced by the carbonate triangle at the centre of the single-perovskite "cube". Generally, the tendency to form oxide carbonates increases with the overall basicity of the multicomponent oxide. This is illustrated in fig. 46, showing the $Y(O/CO_3)$–$Ba(O/CO_3)$–$Cu(O/CO_3)$ system at 800 and 900°C, as found from a large number of samples (Karen and Kjekshus 1991, Karen et al. 1990a, Fjellvåg et al. 1988c). The oxide carbonate phases in question are stable in a narrow shell defined by the degree of basicity for the constituents (notably the BaO content), and delimited by the concentration of CO_2 in the surrounding atmosphere and the temperature. At lower BaO contents and CO_2 concentrations, as well as at higher temperatures, pure oxide phases become stable. For larger BaO contents, higher CO_2 concentrations or lower temperatures, $BaCO_3$ is stabilized next to the oxides of the other metals. Except for the pseudoternary Y,Ba and Ba,Cu oxide carbonates, described in sects. 6 and 7, two quaternary oxide carbonates are seen in fig. 46:

$\mathbf{Ba_8[Cu_{4+z}Y_{1+x}(CO_3)_{3-x-z}]O_{10+w}}$ ($0.0 < x < 0.3$ and $0.0 < z < 0.4$) is the actual composition (Karen and Kjekshus 1991, 2000, Karen et al. 1990a, Fjellvåg et al. 1988c) of

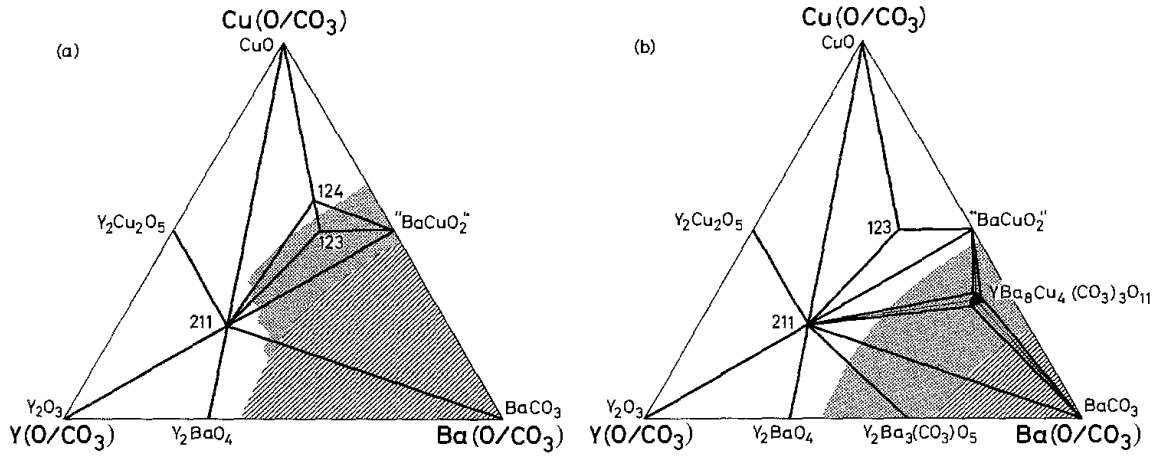

Fig. 46. Phase compatibilities in the $Y(O/CO_3)$–$Ba(O/CO_3)$–$Cu(O/CO_3)$ system, from Karen and Kjekshus (1991), as seen by PXD after repeated firings of citrate precursors at (a) 800°C and (b) 900°C in oxygen of ambient pressure containing ~40 ppm CO_2. Phenomenological frontiers of the oxide carbonate stability are shown by dotted shading, those of carbonate stability by line shading.

the elusive "other perovskite phase" in this system. The composition is remarkable in that carbonate groups can replace both Cu and Y in the centres of the perovskite-type cubes of Ba atoms. As a result of this, a distinct region of homogeneity occurs (Fjellvåg et al. 1988c) for this phase in the pseudoternary phase diagram $Y(O/CO_3)$–$Ba(O/CO_3)$–$Cu(O/CO_3)$ in fig. 46, extending towards both Y and Cu from the "184" formula $Ba_8[Cu_4Y(CO_3)_3]O_{10+w}$. Also the oxygen content is variable (Karen and Kjekshus 1991), as an example, in the interval $0.05 < w < 1.08$ for the 184 composition. This span is similar also for compositions with non-zero x and/or z, merely shifted due to the valence balance. The crystal structure of this oxide carbonate has been recently determined (Rodriguez et al. 1995) for one specific composition (a 142 oxide carbonate, Rodriguez et al. 1993), which lies reasonably close to the Y-rich end of the solid-solution region [$x = 1$, $z = 0$, w = unspecified; *P4/m*; 8.1973(4), 8.0360(5)]. The structure is similar to that suggested (Greaves and Slater 1991b) previously for the (as-refined) composition close to the Cu-rich end of the solid-solution region, indexed with a half-volume unit cell [$x = 1$, $z = 0.54$, $w = 4.08$; *P4/mmm*; 578, 800]. The $Ba_8[Cu_{4+z}R_{1+x}(CO_3)_{3-x-z}]O_{10+w}$ oxide carbonate solid solution is formed for all trivalent Rs smaller than Sm (including Sc) (Hodorowicz et al. 1992b) and these R atoms can be fully replaced by atoms of similar size like Ca or Cd (Calestani et al. 1996). Synthesis of well crystallized samples of this oxide carbonate is not straightforward. When the amount of carbonate ions is controlled via the starting mixture, the synthesis system must be kept closed and reacted at relatively low temperatures, and this causes problems with the homogeneity of the product. When the amount of carbonate ions is controlled via a controlled equilibrium content of CO_2 in the flowing atmosphere at a given temperature, problems with establishing the equilibrium and the narrow region of stability with respect to temperature may cause decompositions. The structural features are not easy to decipher in the only slightly deformed, nearly cubic $2a$ perovskite cell with random orientation of the carbonate groups. These problems are

also projected into the poor compositional resolution of the phase. This oxide carbonate was considered to be 132 oxide (Roth et al. 1987, Frase et al. 1987, Wang et al. 1987, Frase and Clarke 1987, Yang et al. 1988), 153 oxide (Koscheeva et al. 1990) or 163 oxide (Fjellvåg et al. 1987, Saltykova et al. 1990) (the latter composition lies on the border of the homogeneity range of the oxide carbonate). It is not clear whether the compositions 152 and 385 mentioned by De Leeuw et al. (1988a) represent single phases, oxides or oxide carbonates.

$YBa_2Cu_{3-u}(CO_3)_uO_{6+w-3u/2}$ is a solid solution where the carbonate content can be varied up to at least $u = 0.30$. The crystal structure (Karen et al. 2000) is very similar to that of the 123 (superconductor) oxide, and is derived by replacing the portion u of the Cu(1) atoms in the cuprate squares by the carbonate triangles. This leads to a rapid change to a tetragonal symmetry and a gradual decrease in the unit-cell parameter c with increasing u [$YBa_2Cu_{2.70}C_{0.30}O_{7.12}$; *P4/mmm*; 387.17, 1160.7; Karen et al. 2000]. The telltale sign for identifying the oxide carbonate against the pure 123 oxide (both being oxygen saturated but the latter having higher Cu valence) is the occurrence of tetragonal symmetry for the oxide carbonate, accompanied by a *decrease* in the unit-cell parameter c. The pure oxide, on the other hand, becomes tetragonal only upon a substantial chemical reduction, accompanied by an *increase* in the c parameter from some 1170 pm to around 1190 pm. At the oxygen-saturated conditions, the Cu valence in the oxide carbonate is around +2.20, which is somewhat lower than for the pure oxide 123 phase. Such a value lies between that expected for the structural model where the carbonate bridges the two Cu(2) sites along the c axis and that where it is situated within the a,b plane. This indicates a possible disorder. An interesting feature of this oxide carbonate is that it promotes accommodation of rather small "sized" cations at the Ba site. Atoms as small as Hg, Ca or Y can partially replace Ba in the structure; as an example: $Y(Ba_{0.8}Y_{0.2})_2Cu_{2.8}(CO_3)_{0.2}O_{6.77}$ [*P4/mmm*; 387.7(2), 1157.3(13); Karen and Kjekshus (1991, 2000)]. Similar Y-for-Ba substitutions have variously been reported in the literature (Iqbal et al. 1988, Umarji et al. 1988) before the existence of the cuprate carbonates was realized. Note the further contraction of c owing to the exchange of the large Ba with the smaller Y. It is not surprising that *vice-versa* also the accommodation of the carbonate ions in the 123-type structure is being promoted when Ba is replaced by the smaller Sr or Ca atoms (a partial replacement for the latter). Several such variants have been structurally characterized in detail (Hervieu et al. 1996, Miyazaki et al. 1992b,c, Domengès et al. 1993, 1994, Raveau et al. 1995) showing that the carbonate group acts as a bridge between the two Cu(2) sites. For an overview of the crystal chemistry of such oxide carbonates, see Raveau et al. (1995). Finally, also other oxoanions can function in place of carbonate groups in similar 123-type compounds, *e.g.*, nitrate (Maignan et al. 1993), borate (Li et al. 1994), phosphate (Nagarajan et al. 1994, Marimuthu et al. 1997) or sulphate (Krekels et al. 1993a).

The $YBa_2Cu_{3-u}(CO_3)_uO_{6+w-3u/2}$ oxide carbonate would appear as an intermediate phase upon an increased synthesis temperature of the 123 oxide from carbonaceous precursors (Karen and Kjekshus 1991, Gotor et al. 1995, Karen et al. 1990a, Karen and Kjekshus 1994a, Gotor et al. 1993). In O_2 atmosphere, the oxide carbonate would

be formed around some 780°C, together with the appropriate amount of CuO. Upon an increase in temperature, CuO would partially and temporarily react upon formation of the 124 phase, before the system is converted to the 123 phase (Karen and Kjekshus 2000, Karen et al. 2000, Cazy et al. 1997). Even at temperatures above 900°C, a part of the oxide carbonate can remain trapped inside the sample in cases when the release of CO_2 to the surrounding atmosphere is not fully facilitated, for example when the sample is densely sintered (Karen and Kjekshus 1994a). The accommodation of carbonate groups decreases T_c or even quenches the superconductivity of the 123 phase (Karen and Kjekshus 1991, Wang et al. 1996), and therefore the carbon pathway and the residual carbon contents upon the ceramic syntheses have been subject of considerable interest (Gotor et al. 1995, Wang et al. 1996, Maciejewski et al. 1994). The features typical of the oxide carbonate unit cell were first seen in some samples of the 123 phase synthesized in a special manner (closed system, Fjellvåg et al. 1987; plasma spraying, Gudmundsson et al. 1990; CO_2 atmosphere, Chang et al. 1990), and later attributed to oxide carbonate formation (Karen et al. 1990a, Shaw et al. 1990, Lindemer et al. 1990). Particularly syntheses in closed pressurized systems are prone to the formation of oxide carbonates. Any CO_2 inadvertently brought into the reaction chamber, either as a surface, atmosphere or carbonate-phase impurity, will not leave the system during the experiment, and the elevated pressures will increase the thermal stability of the oxide carbonates. For example, the typical structural features of the 123 oxide carbonate can be seen in the high-pressure studies by Chandrachood et al. (1990) and Dlyachkova et al. (1991). On the other hand, the synthesis of the pure oxide carbonate $YBa_2Cu_{3-u}(CO_3)_uO_{6+w-3u/2}$ is rather difficult to conduct under equilibrium conditions. When an open system is adopted, the equilibrium partial pressure of CO_2 is too low to be easily controlled in the narrow window of the low temperatures between the kinetic limitation of the synthesis proper and the formation of the 124 phase or melting. In a closed system, problems with the homogeneity arise.

When the BaO content is lowered below that of the 123 composition, the formation of the possible oxide carbonate is even more difficult. The possible existence of such a phase, derived from the 247 composition, is indicated in a high-pressure study by Ono and Horiuchi (1995). At ambient oxygen pressures, experiments with a parallel synthesis of the 123 and 124 oxide carbonates at 800°C yielded the desired phase only for the 123 composition, whereas a pure oxide was formed for the 124 composition (Karen et al. 1990a). In contrast, both 123 and 124 were found stable at the same temperature for at least 1000 hrs in pure (CO_2 free) oxygen of atmospheric pressure (Karen et al. 1990a).

13.6. *Thermodynamics*

Various aspects of materials chemistry of the R,Ba cuprates have been approached in the literature from a thermodynamic point of view. These reports are either general (MacManus-Driscoll 1997) or specialized to selective synthesis methods, either carbon-free (powders, Heintz and Dardant 1997; thin films by CVD, Ottosson et al. 1991; sputtering, Raven et al. 1992) or carbon-based (CVD, Vahlas and Besmann 1992). Also for these multicomponent cuprates, thermodynamics reflects well the underlying chemical properties. As an example, calorimetric data show clearly that the enthalpies of formation

from oxides and of the oxygen incorporation become increasingly exothermic when the electropositive character of the 'cations' increases (Navrotsky 1994). This complies with rules known to chemists. However, a detailed look on the published thermodynamic data reveals severe consistency problems. One reason lies undoubtedly in the combination of the chemical properties brought about by the individual component oxides, which makes it difficult to control the reactivity of these phases when the reactivity should be contained (BaO-related reactivity problems under EMF measurements) or utilized (Y_2O_3-related sluggish kinetics under calorimetry). In addition, lack of compositional definition (oxide carbonates) and wide nonstoichiometry (redox) contributions to the energetics emerge as problems for some phases.

In this situation, estimate and assessment techniques are often used to sort out the desired data. An extensive summary report on the assessments based on phase diagram equilibria in the Y(O)–Ba(O)–Cu(O) system is given by Boudéne et al. (1996), but, unfortunately, it contains no numerical data, only calculated phase diagrams. No effort is also made to display any variations associated with the variable oxygen content. The latter are reported in detail in a similar summary report by Hauck et al. (1998), again with no background data listed except for the calculated diagrams.

Similar levels of approximation with respect to the oxygen content are apparent also in the thermodynamic data which have been estimated or simulated. Data where only principal oxygen contents are considered have been summarized (not assessed) by Ilynych et al. (1995) based on previous reports on enthalpy (Moiseev et al. 1994a) entropy (Moiseev et al. 1994b) and heat-capacity (Moiseev et al. 1994c) estimates. A selection of these data is given in table 24, showing some notable differences with calorimetric data *vide infra*. When the estimates cover only selected regions of the R(O)–Ba(O)–Cu(O) phase diagram, it is easier to take into consideration also the energetics of the variable oxygen content and perform assessments based on equilibrium data. Such approach makes it also possible to include eventual order/disorder parameters, as done for $YBa_2Cu_3O_{6+w}$ by Voronin and Degterov (1991), Voronin (1994b), and, in a most comprehensible manner, by Rudnyi et al. (1998) and Voronin (2000). A self-consistent set of empirical equations is obtained by fitting evaluated data, which describes the dependence of $\Delta_r H^\circ$ and $\Delta_r S^\circ$ of formation from oxides on p_{O_2}, T, w and the degree of oxygen disorder in the a, b plane of Cu(1). The latter is entered as the fractional oxygen occupancy n of the site occurring between the square chains in the said plane ($w \geqslant 2n$):

$$\frac{\Delta_r H^\circ}{R} = A_1 + A_2 w + w(1-w)A_1^h + n(w-n)B_1^h, \tag{10}$$

$$\begin{aligned}\frac{\Delta_r S^\circ}{R} = {} & B_1 + B_2 + w(1-w)\left[A_1^s + A_2^s(1-w)\right] + n(w-n)B_1^s \\ & - [(w-n)\ln(w-n) + n\ln(n) + (1-n)\ln(1-n) \\ & \quad + (1-w+n)\ln(1-w+n) + (w)\ln(w) + (1-w)\ln(1-w)].\end{aligned} \tag{11}$$

The equilibrium p_{O_2}, w, n values are then related by

$$T\ln\left(\frac{(w-n)(1-n)}{n(1-w+n)}\right) = (w-2n)(B_1^h - TB_1^s) \tag{12}$$

Table 24
Simulated standard thermodynamic values[a] and virial heat-capacity coefficients for solid oxides from the Y(O)–Ba(O)–Cu(O) system selected from Ilynych et al. (1995); for units see the Introduction

Phase	S°	H°	A	B	C
$YBa_2Cu_3O_6$	319.86	−2587(8)	307.48	0.07628	0.00026213
$YBa_2Cu_3O_7$	323.06	−2706(2)	315.29	0.05447	0.0004245
$YBa_2Cu_{3.5}O_{7.5}$	345.15	−2794(4)	305.12	0.08456	0.00022064
$YBa_2Cu_4O_8$	367.24	−2881(6)	356.72	0.04574	0.0004247
$YBa_2Cu_5O_9$	411.41	−3055(10)	363.27	0.11467	0.00022064
$YBa_4Cu_3O_{8.5}$	454.15	−3828(14)	312.96	0.04107	0.0004281
Y_2BaCuO_5	223.00	−2712(3)	206.10	0.0352	0.00020925
$YCuO_2$	98.81	−1039(24)	092.90	0.01636	0.0000805
$Y_2Cu_2O_5$	200.83	−2215(5)	201.65	0.04185	0.00018155
Y_2BaO_4	178.81	−2533(1)	164.65	0.02053	0.0002032
$Y_4Ba_3O_9$	424.00	−5667(9)	393.75	0.04823	0.00044915
$BaCuO_2$	110.52	−782(21)	091.45	0.02442	0.00007245
$BaCu_2O_2$	151.51	−807(7)	118.30	0.02709	0.0000801
Ba_2CuO_3	176.87	−1409(29)	145.32	0.02877	0.00016594

[a] For recent data on $YBa_2Cu_{3.5}O_{7.46}$ see Monayenkova et al. (1998), on $YBa_2Cu_{3.5}O_{7.43}$ Zhou and Navrotsky (1999).

from which n is calculated, and

$$\ln\left(\frac{p_{O_2}}{p^\circ_{O_2}}\right) = \ln\left(\frac{n(w-n)\,w^2}{(1-w+n)(1-n)(1-w)^2}\right) + \frac{A_2 - TB_2 + (A_1^h - A_1^s T)(1-2w) - TA_2^s(1-w)(1-3w) + \frac{1}{2}w(B_1^h - TB_1^s)}{\frac{1}{2}T}, \tag{13}$$

where $p^\circ_{O_2} = 101325\,\text{Pa}$, $R = 8.314\,\text{J/mol K}$, and $A_1 = -4477.6\,\text{K}$, $B_1 = 4.117$, $A_2 = -10669.8\,\text{K}$, $B_2 = -10.4058$, $A_1^h = 886.731\,\text{K}$, $A_1^s = 0.4871$, $A_2^s = -1.4204$, $B_1^h = 1158.53\,\text{K}$, $B_1^s = -3.33514$ in eqs. (10)–(13). An extrapolation of this model to phases related by increasing the number of the copper oxygen chains where Cu has the square planar coordination makes it possible to predict stabilities of such phases (Voronin 1994a,b, Voronin and Degtyarev 1993). In absence of the o,t transition in these phases, n is no longer needed, whereas, for $Y_2Ba_4Cu_7O_{14+w}$ of Voronin and Degtyarev (1993), w still enters the expressions:

$$\frac{\Delta_r H^\circ}{R} = A_1 + A_2 w + w(1-w)(A_1^h - wA_2^h), \tag{14}$$

$$\frac{\Delta_r S^\circ}{R} = B_1 + B_2 + w(1-w)(B_1^s + B_2^s w) - [(w)\ln(w) + (1-w)\ln(1-w)], \tag{15}$$

Table 25
Some EMF-determined standard Gibbs-energy functions ($\Delta_r G°$; eq. 2) of formation of R_2BaCuO_5 from oxides; units have been omitted

R	A	B	T interval	Cell definition	Ref.
Yb	−54.9	−0.00485	973–1173	CaF_2 ellyte, 21 kPa O_2	[1]
Tm	−51.5	−0.005	973–1173	CaF_2 ellyte, 21 kPa O_2	[1]
Er	−59.3	−0.00166	973–1173	CaF_2 ellyte, 21 kPa O_2	[1]
Ho	−52.7	−0.00765	973–1173	CaF_2 ellyte, 21 kPa O_2	[1]
Dy	−51.2	−0.00906	973–1173	CaF_2 ellyte, 21 kPa O_2	[1]
Y	−48(12)	+0.0066(21)	973–1173	BaF_2 ellyte, 101 kPa O_2	[2]
Gd	−59.9	−0.00158	973–1173	CaF_2 ellyte, 21 kPa O_2	[1]
Eu	−82.53	+0.0165	973–1173	CaF_2 ellyte, 21 kPa O_2	[3]

References
[1] Kopyto and Fitzner (1997)
[2] Skolis et al. (1991)
[3] Przybyło et al. (1996)

and the equilibrium p_{O_2}, w values are related by

$$\ln\left(\frac{p_{O_2}}{p^{\circ}_{O_2}}\right) = 2\ln\left(\frac{w}{1-w}\right) + \frac{A_2 - TB_2 + A_1^h - B_1^s T + 2w\left[A_2^h - A_1^h - T(B_2^s - B_1^s)\right] - 3w^2(A_2^h - TB_2^s)}{\frac{1}{2}T}, \tag{16}$$

where, in eqs. (14)–(16), $A_1 = -22\,276$ K, $B_1 = 3.1236$, $A_2 = -10\,634.4$ K, $B_2 = -8.7515$, $A_1^h = 2340.3$ K, $A_2^h = 1769.7$ K, $B_1^s = 4.8136$, $B_2^s = -0.048$. For $YBa_2Cu_4O_8$, the variability in w can be neglected altogether:

$$\frac{\Delta_r G^{\circ}}{R} = -17\,156 + 4.338T + 0.265T\ln T. \tag{17}$$

When the stability field of $YBa_2Cu_3O_{6+w}$ versus other phases in the phase diagram is calculated using an analogous approach (Voronin 1994b), the results suggest that $YBa_2Cu_3O_{6+w}$ is thermodynamically stable only in its reduced form (*viz.*, that formed during the firing process) and instable against formation of Y_2BaCuO_5, $BaCuO_2$, $Y_2Ba_4Cu_7O_{14}$ when the oxygen content is increased at lower temperatures. The diffusion of oxygen is much faster than that of the metals under these conditions and this prevents the decomposition. The problem is, however, that the compositional definition of at least one of these alleged products is poor. Similar calculations with similar results are performed (Voronin 1994b) also for the system including carbon, considering formation of $BaCO_3$ only (*viz.*, oxide carbonates neglected).

Much of the data used in the above assessments originates from EMF measurements in solid-state cells. These data are best utilized through such assessments, given the variety

Table 26
Standard enthalpies of formation from oxides ($\Delta_f H°$) and from elements ($H°$), and partial molar enthalpy of oxygen, evaluated for 298 K and the listed exact compositions, according to drop-calorimetry; for units see the Introduction

Phase	$\Delta_f H°$	$H°$	$\Delta\bar{h}_O$ [a]	Ref.
$TmBa_2Cu_3O_7$	−123(5)	−2636(7)	−87(9)	[1]
$HoBa_2Cu_3O_7$	−129(6)	−2638(8)	−63(10)	[1]
$DyBa_2Cu_3O_7$	−124(5)	−2623(8)	−92(9)	[1]
$GdBa_2Cu_3O_7$	−131(5)	−2609(8)	−86(6)	[1]
$EuBa_2Cu_3O_7$	−134(5)	−2528(8)	−78(7)	[1]
$NdBa_2Cu_3O_7$ [b]	−142(6)	−2614(8)	−83(10)	[1]
$PrBa_2Cu_3O_7$ [b]	−138(11)	−2611(13)	−95(6)	[1]
$YBa_2Cu_3O_7$	−137(5)	−2658(8)	−107(8)	[1]
$HoBa_2Cu_4O_8$	−187(7)	−2853(10)		[1]
$DyBa_2Cu_4O_8$	−176(6)	−2833(9)		[1]
$GdBa_2Cu_4O_8$	−168(6)	−2803(9)		[1]
$EuBa_2Cu_4O_8$	−184(6)	−2735(9)		[1]
$SmBa_2Cu_4O_8$	−191(6)	−2828(8)		[1]
Y_2BaCuO_5	−48.6(3)			[2]
	−56(18) [c]			[3]

[a] Per mole O, refers to $w \approx 0.96$ samples as synthesized.
[b] Synthesis conditions may indicate that a minor presence of R at the Ba site could have been neglected. The samples are, however, reported phase pure.
[c] Refers to 650°C.

References
[1] Lamberti et al. (1997) [2] Zhou and Navrotsky (1992) [3] Rian (1992)

of sources of error in the EMF measurements discussed by Voronin and Degterov (1991) and Vigeland (1996) as an example. Several EMF studies have been conducted also for R other than Y, *e.g.*, R = Sm (Xing et al. 1996), R = Eu (Przybyło et al. 1996) and R = Dy–Yb (Kopyto and Fitzner 1999). A comparison of the Gibbs-energy functions (Kopyto and Fitzner 1997, Skolis et al. 1991) is shown in table 25 for R_2BaCuO_5 which is practically stoichiometric.

Calorimetry is generally a high-accuracy method for determination of thermodynamic properties. A particular variant is the high-temperature drop calorimetry where the oxide phase is dissolved in a suitable melt and enthalpies of formation from oxides are evaluated from the thermal effect. Drop-calorimetry data (Rian 1992, Zhou and Navrotsky 1992, Lamberti et al. 1997) obtained for phases from the R(O)–Ba(O)–Cu(O) phase diagram are summarized in table 26. Similar, but much more scattered data were obtained in numerous early studies by various aqueous-solution calorimetry techniques; for recent more precise data by the latter technique on $RBa_2Cu_3O_{6.9}$ (R = Gd, Ho, Y), see Matskevich and McCallum (1999). Only a few adiabatic calorimetry studies have focused on determination of thermodynamic properties of the superconducting phases.

As an example, for the oxygen-saturated $YBa_2Cu_3O_{6.9}$, the standard absolute entropy at 298.15 K is reported as S° = 318.1 and 321.85 J/molK by Atake et al. (1991) and Shaviv et al. (1990), respectively.

14. Solidus–liquidus systems R(O)–Ba(O)–Cu(O)

The question of the solidus–liquidus equilibria in the R(O)–Ba(O)–Cu(O) phase diagrams is dealt with in a special chapter of this Handbook, hence only a brief information is given here, relevant to the subsolidus-phase chemistry. It is typical for such multicomponent systems that a large number of isobaric and isothermal sections is necessary for a complete description of the occurring *s–l* relationships.

For R = Y, a combination of the available information into a spatial *x–y–t* pseudoternary diagram has been attempted (Kosmynin et al. 1990), but normally the experimental investigations are limited to various pseudobinary sections. A few such cuts (Roth et al. 1988, Kawabata et al. 1990, Mikirticheva et al. 1991, Šesták et al. 1991, Licci et al. 1989) are shown together in fig. 47. When interpreting these data, it should be borne in mind that

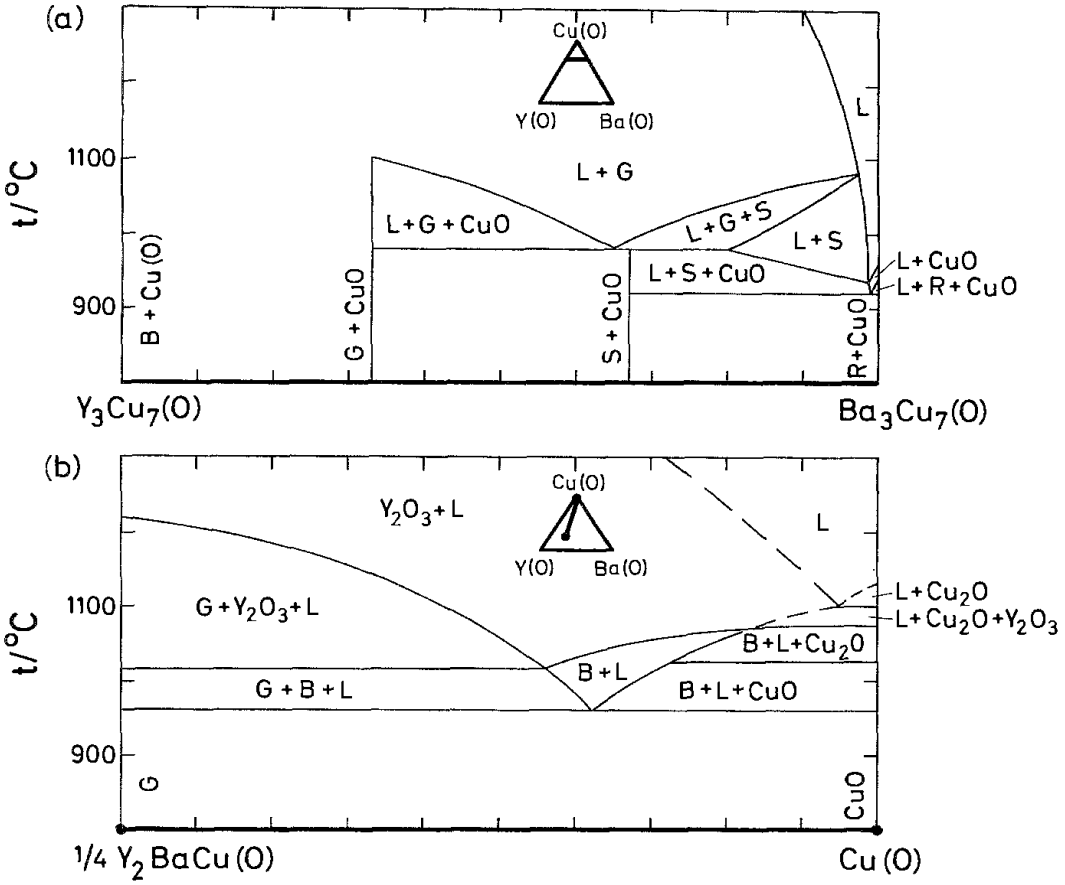

Fig. 47. Pseudobinary *x–t* diagrams for certain cuts (shown in the thick-line insets) of the Y(O)–Ba(O)–Cu(O) system, from (a) Kawabata et al. (1990) (in air); (b) Mikirticheva et al. (1991) (in air); (c) Licci et al. (1989) (in oxygen); (d) Roth et al. (1988) (in air), (e) Šesták et al. (1991) (in air). Ternary and quaternary phases are marked as follows: B, $Y_2Cu_2O_5$, G, Y_2BaCuO_5, R, $BaCuO_{2+w}$, S, $YBa_2Cu_3O_{6+w}$, W, BaY_2O_4.

the crucial problem concerning any phase diagram, *i.e.*, whether real equilibrium states are achieved or not, is considerably enhanced for *s–l* boundaries. In fact, each examination (microscopy, diffraction, thermal analysis, quenching, physical phase separation, *etc.*) provides a slightly different viewpoint. Mikirticheva et al. (1991) and Licci et al. (1989) give instructive examples for quenching versus DTA. Different primary crystallization

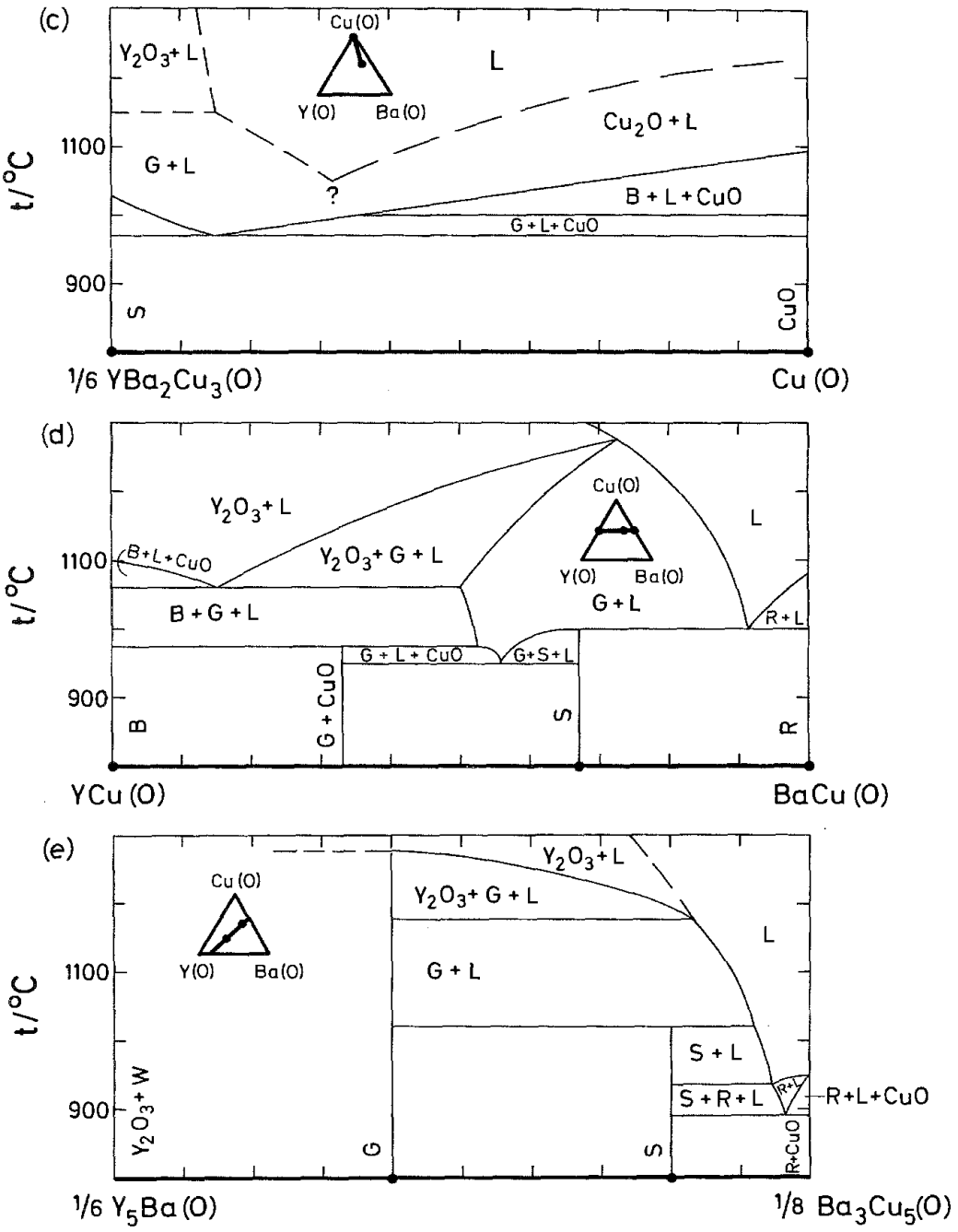

Fig. 47 (continued).

fields were found in a section of the pseudoternary system very close to Cu(O), resulting from the lack of equilibrium conditions during a DTA experiment. Hence, crystallizations of either $Y_2Cu_2O_5$ (DTA) or Cu_2O (quenching) are observed for one and the same composition in a certain composition interval. The liquidus surface for the Cu-rich portion of the system reaches relatively low temperatures (Aselage and Keefer 1988) and this can explain why the degree of sintering of the 123 samples varies from experiment to experiment (depending on whether or not a small excess of CuO is present), since a liquid phase is involved above 940°C and acts as a transport medium. An analogous explanation applies to the strong densification often observed upon the first firing since the intimate mixtures of the particles of the individual components may produce sufficient amounts of the lowest melting eutectic (890°C) to promote sintering. A detailed overview of the *s–l* situation around the $YBa_2Cu_3O_7$ phase field has appeared recently (Wong-Ng and Cook 1998). Perils of these systems, in particular with respect to p_{O_2}, are discussed by Alarco et al. (1999).

For R = Nd which came into focus owing to good superconducting properties of the Nd123 phase, solidus–liquidus equilibria, as well as temperature dependences of the composition limits of the $Nd(Ba_{1-y}Nd_y)_2Cu_3O_w$ phase have been studied in detail by Goodilin et al. (1997a,b); for R = Pr by Tagami et al. (1998).

15. R,R′(O)–Ba(O)–Cu(O)

15.1. *Trivalent R*

The presence of two trivalent Rs does not usually bring about enough difference in size and bond peculiarity to promote a new structure type. Instead, wide solid-solution ranges emerge within the structure types of the quaternary oxides:

$(R_{1-x}R'_x)(Ba_{1-y}R'_y)_2Cu_3O_7$. At conditions defined by firing at 910°C in a pure oxygen atmosphere and subsequent oxygen saturation at 340°C, full mutual miscibility occurs at the R site of $RBa_2Cu_3O_7$ for R = Y in combination with R′ = Yb–Dy, Gd, Eu and Sm (Karen et al. 1990b, Neukirch et al. 1988, Thomsen et al. 1988, Noto et al. 1987, Oota et al. 1987, Millet et al. 1988). Less compatibility is found for the potentially tetravalent Ce and Tb, whose solid solubility at the Y site does not exceed a few per cent for Ce and less than 25% for Tb (Karen et al. 1990b, Karen and Kjekshus 2000). Substitution of Y by the smallest lanthanide Lu is limited (Raychandhuri et al. 1987) and occurs up to some 30% (Karen et al. 1990b). For the large Nd, Pr and La atoms, an equilibrium distribution between the Y and Ba sites exists. This implies that Nd and larger Rs will not enter solely the Y site unless some R also finds its way to the Ba site (K. Zhang et al. 1987). When a partial or complete replacement of only Y is attempted by Nd and larger Rs, the "$BaCuO_{2+w}$" phase is formed to tie up the amount of Ba which has been replaced by R (Karen et al. 1990b). On the other hand, only La is large enough to participate at the Ba site alone, up to $y = 0.36(2)$ (Karen et al. 1990b, 1991a). When the just mentioned critical concentration is exceeded, a substitution of Y by La also occurs, and $Y_2Cu_2O_5$ appears as a second phase. This

situation and the relative difference between the size effect of Nd and La is illustrated in the selected parts of the tetrahedral diagrams (Karen et al. 1990a, 1991a) for the Y(O)–Nd(O)–Ba(O)–Cu(O) and Y(O)–La(O)–Ba(O)–Cu(O) systems in fig. 48. As seen in the previous sections with similar mixed-valence solid solutions, the average oxidation state of Cu is conserved upon substitution of the trivalent R for Ba. For the 123-type phase this means that its saturated oxygen content is increased by y per formula (Karen et al. 1991a). When the oxygen content exceeds seven, the additional oxygens are accommodated at the vacant sites adjacent to the copper–oxygen squares. This also turns the originally orthorhombic structure into tetragonal when y exceeds a certain value, as a combined effect of the oxygen insertion and a structural deformation due to the partial replacement of the large Ba by the smaller R (K. Zhang et al. 1987, Karen et al. 1991a, Segre et al. 1987, Takita et al. 1988, Newsam et al. 1989). For example, oxygen saturated $Y(Ba_{1-y}La_y)_2Cu_3O_{6.95(2)+y}$ is tetragonal at ambient temperatures for $y > 0.140(5)$ [$Y(Ba_{0.8}La_{0.2})_2Cu_3O_{7.15}$; *P4/mmm*; 385.46(2), 1156.6(1); Karen et al. (1991a)]. When the oxygen content is varied, T_c of the $Y(Ba_{1-y}La_y)_2Cu_3O_{6+y+w}$ solid solution is neither coupled to the orthorhombic feature nor to whether or not the oxygen content exceeds 7 per formula. A correlation occurs between T_c and the calculated Cu bond valence in the square-pyramidal sheets. The valence is influenced by the substitution-induced deformations of the bond lengths and by the introduction of the additional Cu–O bonds in the square-planar chains. Therefore, despite the constant overall Cu valence in $Y(Ba_{1-y}La_y)_2Cu_3O_{6.95(2)+y}$, T_c decreases with y. In addition, it also decreases with any reduction in the oxygen content (*viz.*, compared with oxygen saturated samples) (Karen et al. 1992a).

$(R_{1-x}R'_x)(Ba_{1-y}R'_y)_2Cu_4O_8$. As seen in sect. 13, the $RBa_2Cu_4O_8$ phase favours smaller R atoms than does the $RBa_2Cu_3O_7$-type phase (Morris et al. 1989c). This means that the larger Rs tend to favour the combination of 123 and CuO against 124. Obviously, large ranges of solid solubility exist between R and R′ of similar size. However, like in the 123 phase, La is large enough so that it can partially substitute for Ba (Sakurai et al. 1990) and $Y(Ba_{1-y}La_y)_2Cu_4O_8$ is formed for $0.0 < y < 0.1$ (Sakurai et al. 1990, Morris et al. 1990a). Above $y = 0.1$, the reported observation of CuO could indicate that La simultaneously enters the Y site. The La substitution does not bring about any change in the oxygen content and a rapid decrease in T_c is observed (Sakurai et al. 1990) with increasing y. This is in line with the rigid, double-square chains of the cuprate anions.

o-$(R_{1-x}R'_x)_2BaCuO_5$. An extended region of solid solubility is found (Karen et al. 1990a) for R = Y, reaching $x = 0.85$ for R′ = Nd and $x = 0.30$ for R′ = La.

t-$(R_{1-x-x'}Ba_xR'_{x'})_2BaCuO_5$. In addition to Ba present at the R site ($0 < x < 0.15$ for R = Nd and $0.04 < x < 0.40$ for R = La) some R′ = Y can be accommodated at this site, reaching $x' = 0.05$ for R = Nd and $x' = 0.10$ for R = La (Karen et al. 1990a, Abbattista et al. 1990).

The only examples of new structures as a consequence of the introduction of the trivalent R′ element come about when there is a large size difference between R and R′. Thus, La and Lu, the largest and smallest lanthanoid, give rise to a new structural arrangement:

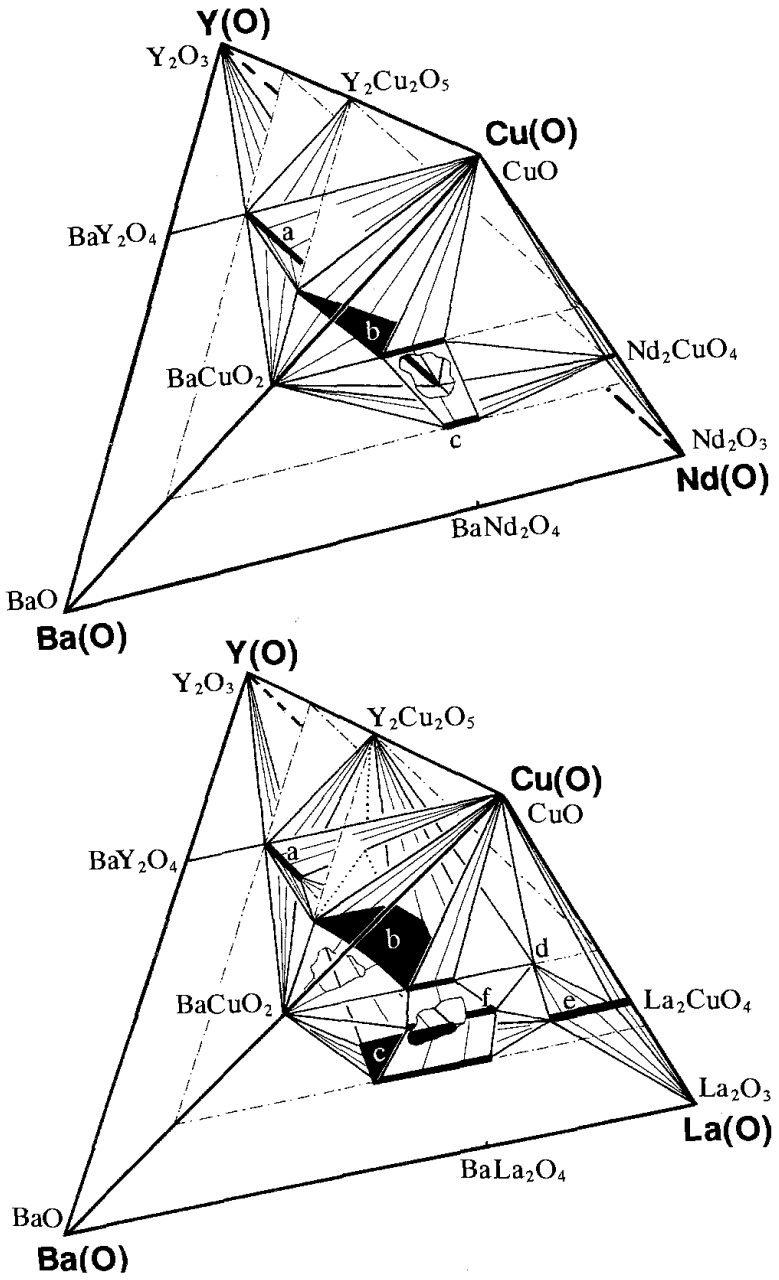

Fig. 48. Subsolidus (pseudoquaternary) tetrahedral phase diagrams of the Y(O)–Nd(O)–Ba(O)–Cu(O) and Y(O)–La(O)–Ba(O)–Cu(O) systems at 900°C in oxygen, covering the neighbourhood of the $YBa_2Cu_3O_{6+w}$-type phase and the Cu-rich corner (after Karen et al. 1990a, 1991a.) Phase designations: a, $(Y_{1-x}R_x)_2BaCuO_5$ (R=Nd: $0.00 < x < 0.85$; R=La: $0.00 < x < 0.30$; Karen et al. 1990a, 1991a); b, $(Y_{1-x}R_x)(Ba_{1-y}R_y)_2Cu_3O_{6+w+y}$ (R=Nd; Hodorowicz et al. 1990, Karen et al. 1990b, Skakle and West 1996): $y = 0.0$ for $x = 0$ and $0.03 < y < 0.33$ for $x = 1$; R=La: Karen and Kjekshus 2000, Karen et al. 1990b, 1991a): $0.0 < y < 0.36$ for $x = 0$ and $0.09 < y < 0.26$ for $x = 1$); c, $[(R_{1-x}Ba_x)_{1-x'}Y_{x'}]_2BaCuO_5$ (R=Nd: $0.00 < x < 0.15$ for $x' = 0$ and $0.0 < x' < 0.05$ for $x = 0$; R=La: $0.04 < x < 0.40$ for $x' = 0$ and $0.0 < x' < 0.15$ for $x = 0$, Karen and Kjekshus 2000, Karen et al. 1990a, Abbattista et al. 1990); d, $BaLa_4Cu_5O_{13}$; e, $(R_{1-x}Ba_x)_2CuO_4$ (R=Nd: $0.0 < x < 0.05$?; R=La: $0.0 < x < 0.15$?); f, $(La_{1-x}Ba_x)BaCu_2O_{6+w}$ ($0.10 < x < 0.40$, De Leeuw 1989).

$La_2LuBa_3Cu_6O_{14+w}$, with $w \approx 0.3$ and crystal structure (Watanabe et al. 1988) derived from that of the $YBa_2Cu_3O_7$ type by cation ordering. The oxygen saturated phase (at ambient oxygen pressure) is tetragonal (Watanabe et al. 1988) [*P4/mmm*; 546.6, 1161.5] but becomes orthorhombic upon oxidation at $p_{O_2} = 5$ MPa and also superconducting with $T_c = 40$ K (Watanabe et al. 1988).

Also other quintenary oxides are formed with R = La; based on other than 123 structures in the La(O)–Ba(O)–Cu(O) system:

$La_6R'BaCu_8O_{20}$, where R′ = Y or Dy, is related to $La_4BaCu_5O_{13}$. The monoclinic crystal structure (Cava et al. 1994) contains an ordered network of cuprate octahedra, square-pyramids and squares, and is considered as a first member of a structural series. The symmetry of the structure is described in terms of subcell–supercell relations based on an orthorhombic subcell [381.4(1), 386.9(1), 385.8(1)].

15.2. *Tetravalent R*

When tetravalent Ce is introduced as the R′ atom, genuine quintenary oxides appear in the R,R′(O)–Ba(O)–Cu(O) systems. Their structural features can generally be described as combinations of simpler structure types with the fluorite-type CeO_2 subunits, supplemented with degrees of solid-state miscibility:

$(R_{1-x}Ce_x)_2(Ba_{1-y}R_y)_2Cu_3O_{8-w}(O)_2$, which contains slabs of corner-sharing cuprate units (with some vacancies) reminiscent of those in $YBa_2Cu_3O_7$, except that the squares in the chains are partially filled up and disordered to form octahedra (Sawa et al. 1989b, Tsuda et al. 1989). These $[Cu_3O_{8-w}]_n$ slabs contain a Ba/R mixed-occupied site and are separated by fluorite-type layers of R/Ce and isolated oxygen atoms. As an example: $(Eu_{0.67}Ce_{0.33})_2(Ba_{0.67}R_{0.33})_2Cu_3O_{8-w}(O)_2$ [*I4/mmm*; 385.04(1), 2846.0(1); Sawa et al. (1989b)]. The oxygen content corresponds to $w \approx 1$ even after a high-pressure oxygen saturation, and the formal copper valence is relatively low, but still in excess of II (Nobumasa et al. 1989). The variations in the oxygen nonstoichiometry over the interval $1.0 < w < 1.2$ have been studied in detail by coulometric titration (on a Nd variant) (Patrakeev et al. 1995a). This structure is formed only for a narrow size-span of R = Nd, Sm and Eu and the phases in question are superconducting with $T_c \approx 43$ K (Sawa et al. 1989b). A large number of substituted variants has appeared (Wada et al. 1990b, Ichinose et al. 1990, Wada et al. 1990c).

There are certainly more phases to be expected upon increasing the number of components. Simultaneously, however, will their stability be only marginally distinct from the neighbouring phases and their characterization will therefore more and more rely on high-resolution methods.

16. Systems R(O)–A,A′(O)–Cu(O)

16.1. *R(O)–Ca,Sr(O)–Cu(O)*

Only certain significant compositions are studied in these rather specialized systems. Perhaps the most interesting example is the $La_2CaCu_2O_{6-w}$ phase, which becomes

superconducting ($T_c \approx 60$ K) upon partial substition of La by Sr (Cava et al. 1990c). The substitution increases both the Cu valence (hole-doping) and the content of oxygen vacancies [$(La_{0.8}Sr_{0.2})_2CaCu_2O_{5.94(2)}$; *I4/mmm*; 382.08(1), 1959.93(7)] which are located at the apical sites of the square-pyramidal coordinations in the crystal structure described in sect. 10. A variant with Nd instead of La is also described (Huang and Sleight 1990).

16.2. *R(O)–Ca,Ba(O)–Cu(O)*

In accordance with ionic size relations, no Ca/Ba mixing is observed. However, Ca shows solid solubility with the smaller Rs:

$(R_{1-x}Ca_x)Ba_2Cu_3O_7$, where the solid-solubility range reaches up to $x = 0.25$ for R = Y at common ceramic synthesis conditions (~900°C, ambient pressure). Substitutions up to $x = 0.5$ are reported when the pressure is enhanced as little as to $p_{O_2} = 400$ kPa (Morris et al. 1990b). The observation of a $BaCuO_2$-type impurity by Morris et al. (1990b) indicates a possibility for a simultaneous Ca-for-Ba substitution. The Ca/Ba occupancy would in particular be promoted by an eventual formation of an oxide carbonate (Karen and Kjekshus 1991), which is easily feasible in the closed system. This conjecture might be supported by the observed transition into tetragonal symmetry and a shortened c axis. A study where single crystals were grown from melts with different Ca concentrations, has indeed shown that above $x = 0.11$, calcium begins to partially replace barium (Böttger et al. 1997). As valid for other substitutions, the average valence state of Cu is maintained and the oxygen-saturated phase compensates for the aliovalent substitution by formation of oxygen vacancies according to $(Y_{1-x}Ca_x)Ba_2Cu_3O_{6.95-x/2}$, and, in line with this, T_c is not increased; actually a decrease is observed (Karen and Kjekshus 2000, Manthiram et al. 1988, Böttger et al. 1996). A detailed structural study by Böttger et al. (1996) shows that this decrease in T_c correlates with charge-transfer effects evaluated from bond valence. However, when the structure is appreciably deoxygenated ($YBa_2Cu_3O_{6.1}$, non-superconducting and also tetragonal) the energy of formation for oxygen vacancies becomes higher, and the Ca substitution causes a localized hole doping at the pyramidal sheets of the cuprate anion. Hence, superconductivity reappears with low T_c (Parise and McCarron III 1989, McCarron III et al. 1989). The structure then remains tetragonal, but the changes in the bond distances confirm the hole doping (Liu et al. 1990).

$(R_{1-x}Ca_x)Ba_2Cu_4O_8$ is interesting in that a hole doping as above causes an increase in T_c (Wada et al. 1990d, Miyatake et al. 1989). The reason is the structurally fixed oxygen content. Because formation of the oxygen vacancies is not possible, all the extra charge brought about by the aliovalent substitution is accumulated within the cuprate network, thus increasing the formal Cu valence (and in turn T_c, Miyatake et al. 1989). This acts against a high solid solubility of Ca at the Y site (Wada et al. 1990d). Also the stability region of the Ca-substituted 124 phase is shifted towards higher oxygen pressures and Ca substitution vanishes entirely for the 247-type structure (Wada et al. 1990d), perhaps similarly as it was decreased by the presence of the large early Rs at the Y site (Morris et al. 1989c). When the substitution of Ba by Ca in 124 is attempted, appearance of some Y_2BaCuO_5, CuO and $BaCuO_{2+w}$ indicates that also (or rather) the Y site has been at-

tacked. However, some presence of Ca at the Ba site in such samples is evidenced by NQR (Mangelschots et al. 1990a, Mangelschots et al. 1990b). The situation with Ca doping in 124 apparently involves an equlibrium distribution of Ca between the R and Ba sites.

$(Y_{1-x}Ca_x)Ba_4Cu_3O_9$: Whereas only negligible Ca–Y homogeneity region applies to stoichiometric phases like Y_2BaCuO_5, mixed valence phases can tolerate the necessary extent in the oxygen vacancy variation induced by the aliovalent substitution of R by Ca, and a wide solid miscibility is possible. One such example is expected to be $YBa_4Cu_3O_9$ (Kubat-Martin et al. 1990), where both Ca and Y variants exist.

When phases with large Rs are combined with Ca, new structures are formed rather than simple substitutions:

$R_{1-x}Ca_x(Ba_{1-y}La_y)_2Cu_3O_{6+w}$ is another important example for the replacement of R by Ca; the "Ca(BaLa)Cu_3O_{6+w}" superconductor (Fu et al. 1988, De Leeuw et al. 1988c, Murphy et al. 1987). These solid-solutions have non-zero lower limits of solubility for R=La, $0.22 < x < 0.5$ and $0.09 < y < 0.25$ (Skakle and West 1994c) in the crystal structure (Skakle and West 1994d) of the 123 type. The upper limits of solid solubility have integer fraction values, yet no conclusive evidence for structural ordering have been drawn from TEM investigations (Carim et al. 1988, Zandbergen et al. 1988). Contrary to the structure of $LaBa_2Cu_3O_7$ which is orthorhombic (Skakle and West 1994b), the symmetry of the unit cell is tetragonal throughout the solid-solution region, *e.g.*, $La_{0.5}Ca_{0.5}(Ba_{0.75}La_{0.25})_2Cu_3O_{7.01}$ [*P4/mmm*; 387.42(1), 1171.38(4); Skakle and West (1994d)]. The disordering on the oxygen sites which leads to the tetragonal symmetry is explained (Skakle and West 1994d) as a compression of the cuprate slab, in a similar manner as for the La-for-Ba substitution (Karen et al. 1992a, Karen et al. 1991a) in the 123 structure. Like in the latter case, the oxygen content may exceed 7 per formula unit. In contrast to this analogy, the variation in the saturated oxygen content shows that the substitution by Ca is compensated by formation of holes in the cuprate network (Skakle and West 1994d). In the oxygen saturated state, T_c follows the copper valence across the solid-solution region, with maximum T_c around 80 K (Skakle and West 1994d). When an individual composition is deoxidized, T_c shows a similar "double plateau" behaviour as the 123 phase in fig. 36 (Skakle et al. 1996). Since the substitution by Ca is always at least partially compensated by the presence of La at the Ba site, the saturated oxygen content at ambient pressure does not exceed the value of approximately 7 per formula. This probably provides the rationale for the extent of this solid-solution series, in addition to the mixed Ba–La occupancy features discused in sect. 13 for the Ca-free version. However, under high pressure of oxygen, w as large as 1.25 is achieved, accompanied by a decrease in T_c to 35 K, apparently due to overdoping (Skakle et al. 1997). It is also interesting to note that the original "CaBaLa" formula does not correspond to single phase and accordingly lies outside the solid-solution region (Keller-Berest et al. 1989). The extent of the solid solution is illustrated in fig. 49, drawn into the pseudoternary phase diagram CaCu(O)–BaCu(O)–LaCu(O) and compared with the situation seen (Karen et al. 1990b) when Ca in the phase diagram is exchanged with Y, having similar size, yet different valence. The reason behind this arrangement is to include the $YBa_2Cu_3O_7$ phase into the picture and illustrate the complex interplay between size and valence in the formation of the triple-

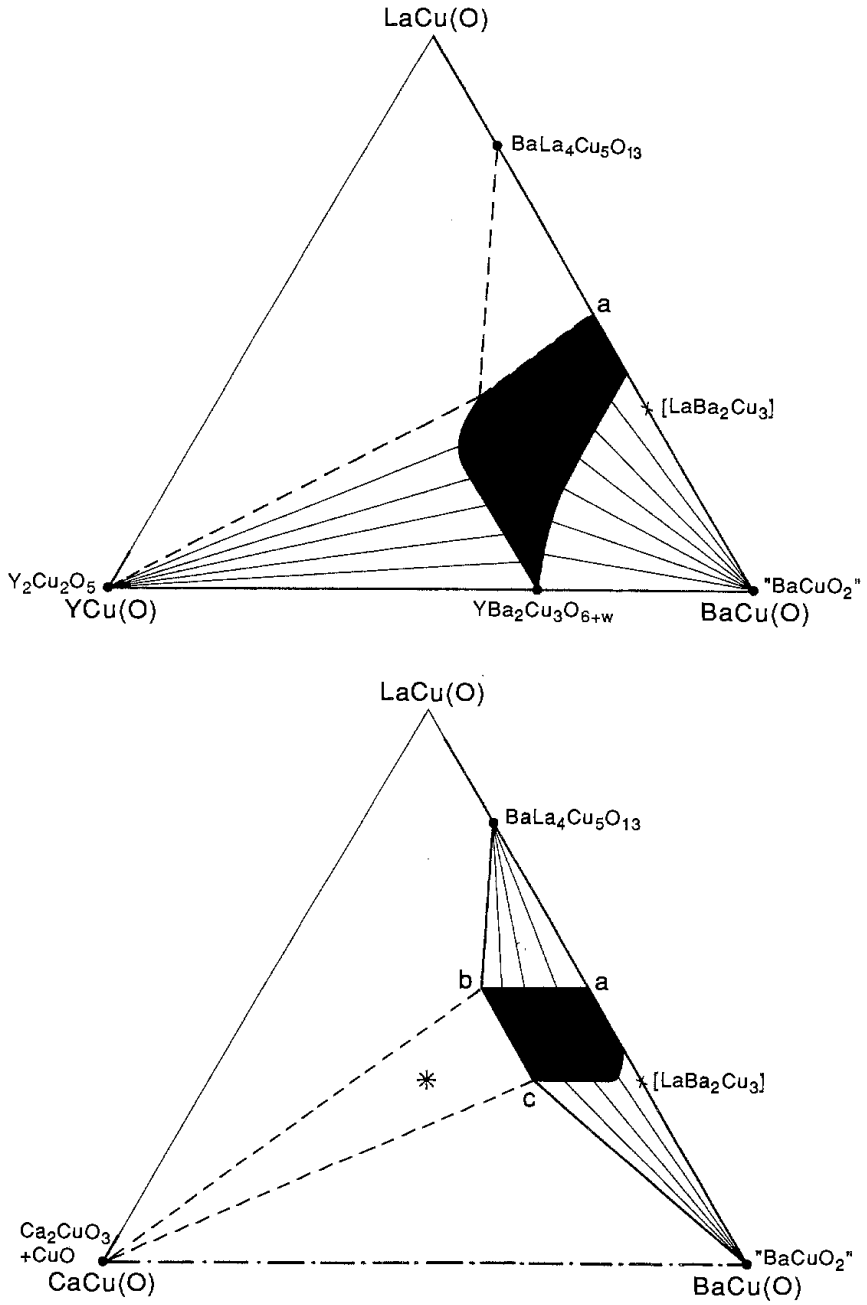

Fig. 49. Regions of stability for the 123 type structures, drawn into the MCu(O)–BaCu(O)–LaCu(O) phase diagrams for M = Y (Karen and Kjekshus 2000, Karen et al. 1990b; oxygen, 910°C) and M = Ca (Skakle and West 1994c; air, 950°C). The difference in conditions is believed to be unimportant for the overal picture. The "CaBaLa" composition is marked with a star. Other significant compositions: a, $La(Ba_{0.75}La_{0.25})_2Cu_3$; b, $La(Ba_{0.50}Ca_{0.25}La_{0.25})_2Cu_3$; c, $La(Ba_{0.75}Ca_{0.25})_2Cu_3$.

perovskite structure. A similar result has been obtained for R = Nd, the main difference being found in the solubility limits [$0.15 < x < 0.4$; $0.04 < y < 0.33$; Skakle and West (1996)].

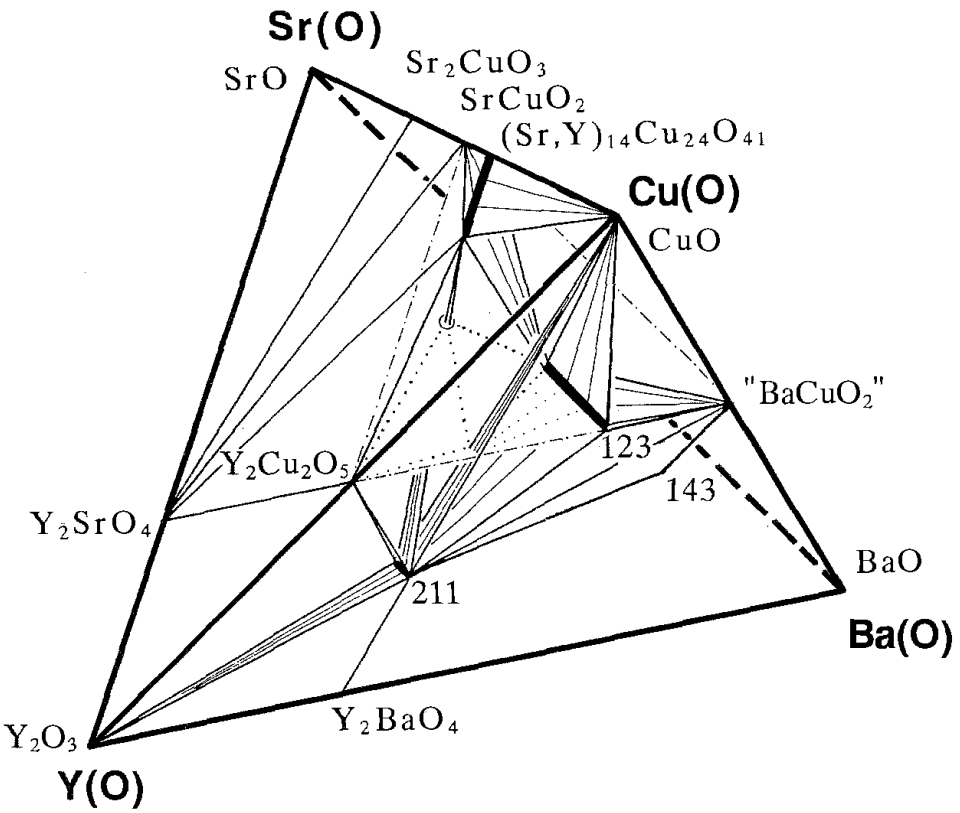

Fig. 50. Subsolidus (pseudoquaternary) tetrahedral phase diagram of the Y(O)–Sr(O)–Ba(O)–Cu(O) system at 900°C in oxygen, covering the neighbourhood of the $YBa_2Cu_3O_{6+w}$-type phase and the Cu-rich corner. (After Roth et al. 1989b and Karen et al. 1991b.)

16.3. *R(O)–Sr,Ba(O)–Cu(O)*

The pseudoquaternary Y(O)–Sr(O)–Ba(O)–Cu(O) system has been investigated to some extent in conjunction with effects of Sr substitution in the $RBa_2Cu_3O_{6+w}$ phase, particularly for R = Y (Roth et al. 1989b, Karen et al. 1991b) and R = La (Skakle and West 1995b). In the system with R = Y, mutual solid miscibility ranges are observed for Sr and Ba (see fig. 50):

$Y_2(Ba_{1-y}Sr_y)CuO_5$ with $0.00 < y < 0.10$ after equilibration in pure oxygen at 910°C, followed by oxidation at 340°C (Karen et al. 1991b).

$Y(Ba_{1-y}Sr_y)_2Cu_3O_{6.95}$ with $0.0 < y < 0.4$ under the same conditions as above (Karen et al. 1991b). Beyond the solid-solution limit, two other saturated solid solutions emerge: $Y_2(Ba_{0.9}Sr_{0.1})CuO_5$ and $(Sr_{2/3}Ba_{1/3})_{14}Cu_{24}O_{41}$. A practically zero substitution range is found for substitition of Y by Sr.

$Y(Ba_{1-y}Sr_y)_2Cu_4O_8$ allows rather low substitition levels of Sr, even when the Ba site is concerned. The reported substitution limit is $y = 0.10$, referring to 800°C in ambient oxygen (Tan et al. 1990).

A similar situation appears also for the larger trivalent Rs. It seems that a somewhat higher degree of solid solubility of Sr at the Ba site of $R(Ba_{1-y}Sr_y)_2Cu_3O_{6+w}$ is achieved

when the R size increases, apparently associated with the maintenance of the Cu bond valence. Various properties including superconductivity of such solid solutions have been studied in detail for R = Gd (Gunasekaran et al. 1996) R = Sm (Psycharis et al. 1996) both having $0.00 < y < 0.50$; similarly for R = Nd where the synthesis must be performed in a moderately reducing environment to prevent the simultaneous substitution of Nd at the Ba/Sr site (Fujihara et al. 1997) described in sect. 13.1.3. For R = La in particular, solid solubility based on both Ba, Sr or La is very distinct. As an example:

$\mathbf{La(Ba_{1-y-y'}Sr_yLa_{y'})_2Cu_3O_{6+w}}$, where the substition by Sr is limited to the Ba site. Both lower limits of solubility are non-zero, $0.16 < y < 0.25$ and $0.09 < y' < 0.25$, but the extent of the solid solution is quite significant, as it means that up to half of the barium can be replaced (Skakle and West 1995b). The solid-solubility region drawn into the phase diagram is practically identical with that for the Ca version in fig. 49, in spite of Ca entering the R site in the 123 structure, not the Ba site as it is the case for Sr. A similar result has been obtained for R = Nd, the limits of solubility being $0.06 < y < 0.20$ and $0.04 < y' < 0.33$ (Skakle and West 1996).

$\mathbf{(La_{1-x}Ba_x)_2SrCu_2O_{6+w}}$ is a solid solution where Ba partially ($0.000 < x < 0.125$) enters the R site, while the Sr site remains intact. The crystal structure (Currie et al. 1990) features, including the variability in oxygen content, remain essentially as those of the prototype (sect. 11). As an example: $x = 0.05, w = 0.30$ [*I4/mmm*; 385.43(1), 2021.55(3)]. However, the substitution by Ba is compensated by creation of oxygen vacancies, and the saturated oxygen content decreases with increasing x: $x = 0.125, w = 0.11$ [385.14(1), 2021.63(7); Currie et al. (1990)]. Despite the high and mixed Cu valence, no superconductivity is observed.

17. $RBa_2Cu_3O_7$, chemical behaviour

17.1. *Chemical properties*

The individual elements which constitute the components of $RBa_2Cu_3O_7$ each bring their own specific chemical properties to the phase. Most dominant is Ba which introduces an enhanced Lewis basicity to the oxygen atoms. As a result, $RBa_2Cu_3O_7$ is reactive towards Lewis acids (*e.g.*, Al_2O_3, SO_2, SiO_2, CO_2, H^+ – even from H_2O). Copper brings about its variable valence and easy reducibility, and has also an influence on the behaviour in aqueous systems (formation of complexes).

17.1.1. *Properties relevant to Cu*

The perovskite-type structure allows for extensive oxygen vacancies, and gives space for wide variations in the Cu valence upon exchange of oxygen with the surrounding atmosphere. This feature will be dealt with in detail in sect. 17.2. The reduced, oxygen vacant phase $RBa_2Cu_3O_6$ may be oxidized also by some non-oxygen agents like NF_3 (fluorination) and halogens. These processes will be described as chemical substitutions in sect. 18. The oxidative power of $RBa_2Cu_3O_{6+w}$ increases when w approaches 1.0.

In contact with acidic aqueous systems, the solid oxidizes H_2O into O_2, and Cl^- and Br^- into Cl_2 and Br_2, upon formation of Cu^{II}. Iodide ions are oxidized into I_2 upon formation of Cu^{I}. The latter reactions form the basis for several methods of wet chemical analyses of the oxygen content in the $RBa_2Cu_3O_{6+w}$ phase. In the solid state, the noble character of elemental copper causes $RBa_2Cu_3O_{6+w}$ to be (ultimately) reduced into metallic Cu already under moderately reducing conditions. The solid-state chemical equlibria associated with such a reduction of $YBa_2Cu_3O_6$ involve several intermediate compounds and are described in sect. 13.3.

The specifics of the copper chemistry in aqueous systems can be manifested in an interesting reaction when the mixed-valence phase dissolves in aqueous ammonia: (Fjellvåg et al. 1987)

$$2YBa_2Cu_3O_{6.5} \xrightarrow{11H_2O,\ 24NH_3} 2YO(OH) + 4Ba^{2+} + 6[Cu(NH_3)_4]^{2+} + 20OH^-. \tag{18}$$

Such a reaction does not occur for the stoichiometric cuprate Y_2BaCuO_5.

17.1.2. *Properties relevant to Ba*

Reactivity towards Lewis acids, including protons from "hydrogen acids" is strongly enhanced by the high content of barium. Possible reactions with the surrounding chemical environment are of the greatest concern. Solid-state reactions of $YBa_2Cu_3O_{6+w}$ with acidic transition-metal oxides (Cima et al. 1988, Filipczuk 1991) and analogous materials (Komatsu et al. 1988, Moiseev et al. 1993) are found to proceed readily upon formation of Ba containing oxides. Also the reaction with liquid H_2O is of particular importance. The reaction gives yttrium and copper oxides, barium hydroxide and barium copper hydroxide as main products. The real pathway is considerably more complex owing to the omnipresence of CO_2 (Yokota et al. 1990). Similar products are also obtained after exposition to the atmosphere (Thompson et al. 1987). For the possibility of incorporation of OH^- ions into $YBa_2Cu_3O_{6+w}$ in aqueous systems, see sect. 18. As an example of a gas-solid, Lewis-type reaction, an interaction with NO_2 at 200°C can be cited (Montzka et al. 1991), interesting in that both the acidic and oxidative properties of NO_2 are in effect when reduced 123 is involved. A mixture of oxidation and degradation products is formed, consisting mainly of oxidized 123 and barium nitrite.

The reaction with gaseous CO_2 is probably the most important of the degradation reactions of $RBa_2Cu_3O_{6+w}$, since CO_2 is present in the air and in traces in most of the chemical environments. This reaction is also the reverse of the commonly used carbonate synthese route for $RBa_2Cu_3O_{6+w}$. Depending on the temperature, several reaction products are observed (Fjellvåg et al. 1988b, Gao et al. 1990) when $YBa_2Cu_3O_{6+w}$ is exposed to a dry mixture of CO_2 and O_2:

$$2YBa_2Cu_3O_{6+w} \xrightarrow{4CO_2} Y_2O_3 + 4BaCO_3 + 6CuO + (w - \tfrac{1}{2})O_2, \quad \text{for } 400 < t < 730°C \tag{19}$$

$$2YBa_2Cu_3O_{6+w} \xrightarrow{4CO_2} Y_2Cu_2O_5 + 4BaCO_3 + 4CuO + (w - \tfrac{1}{2})O_2, \quad \text{for } 730 < t < 950°C \tag{20}$$

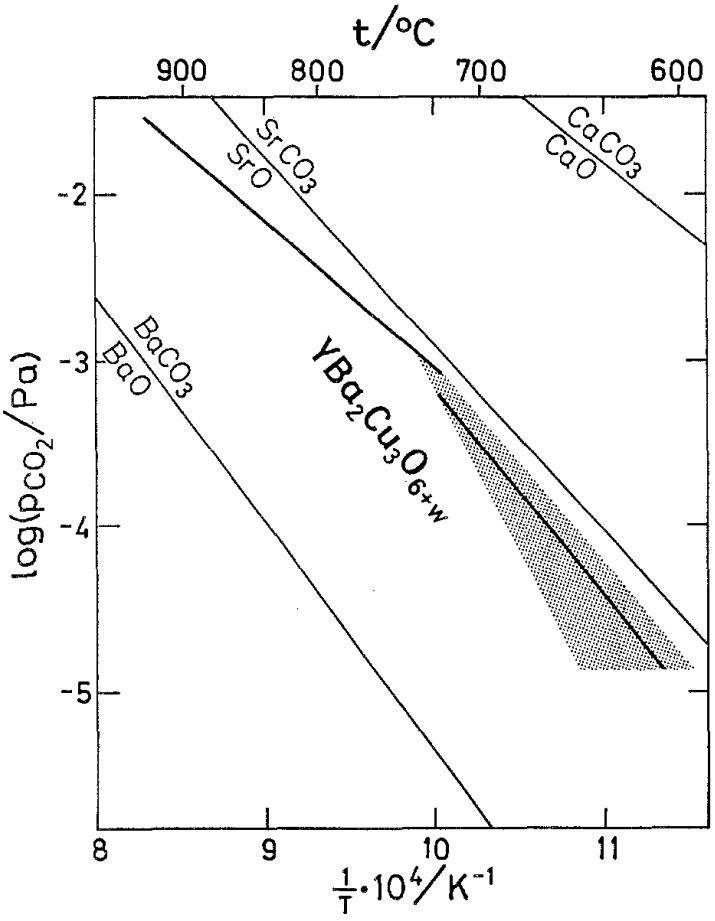

Fig. 51. $YBa_2Cu_3O_{6+w}$ stability with respect to carbonatization in O_2/CO_2 atmospheres at ambient pressure (after Fjellvåg et al. 1988b). Equilibrium according to eq. (19) is indicated by the shaded area, equilibrium according to eq. (20) by the solid lines. Data for A carbonates are given for comparison.

$$2YBa_2Cu_3O_{6+w} \xrightarrow{3CO_2} Y_2BaCuO_5 + 3BaCO_3 + 5CuO + (w - \tfrac{1}{2})O_2, \quad \text{for } t > 950°C \tag{21}$$

where w and the question whether CuO or Cu_2O is formed depend on p_{O_2} and temperature. The observed (Fjellvåg et al. 1988b) partial pressures of CO_2 at equilibrium with $YBa_2Cu_3O_{6+w}$ are shown in a van't Hoff plot in fig. 51, together with calculated (Barin and Knacke 1973, Barin et al. 1977) dissociation pressures of $CaCO_3$, $SrCO_3$ and $BaCO_3$. Using the original data from Fjellvåg et al. (1988b), the onsets of carbonatization or decarbonatization reaction of $YBa_2Cu_3O_{6+w}$ in oxygen-rich atmospheres according to eq. (20) can be expressed as follows (in Pa, K):

$$\log p_{CO_2} = 11.217(313) - \frac{9270(340)}{T}. \tag{22}$$

The kinetics of these carbonatization processes as a function of temperature and particle size has been investigated and an empirical rate equation with a 1.5 order dependence has been derived (Borowiec et al. 1991). The reaction with CO_2 has a very significant effect on the processing and superconducting properties of $YBa_2Cu_3O_{6+w}$ (Shaw et al. 1990,

Gallagher et al. 1988, Selvduray et al. 1992). Severe degradation in the critical current occurs before even a slight weight increase can be observed (Gallagher 1991).

17.2. *Oxygen-exchange equilibrium*

The variable valence of Cu in $RBa_2Cu_3O_7$ leads to a variable oxygen content in the solid state:

$$RBa_2Cu_3O_{(6+w)+\Delta w} \rightleftharpoons RBa_2Cu_3O_{6+w} + \tfrac{1}{2}\Delta w\, O_2. \tag{23}$$

The equilibrium is defined by p_{O_2}, T, and, in contrast to the reactions occurring between fixed compositions, also by the compositional variable w. Accordingly, when w is maintained constant, a normal, linear van't Hoff plot is valid. Such a plot is shown in fig. 52, obtained (Fjellvåg et al. 1988b) by actually varying p_{O_2} at different temperatures, under the thermogravimetric control of $w = 0.5$. The least-squares approximation of the data in fig. 52 gives for $YBa_2Cu_3O_{6.50}$ (in Pa, K):

$$\log p_{O_2} = 12.75(20) - \frac{8148(177)}{T}. \tag{24}$$

However, when p_{O_2} is maintained constant, a linear van't Hoff plot can no longer be extracted for the compositional variable. This illustrates the fact that w is a composite variable which, as such, does not represent an actual participant in the equilibrium in eq. (23). Two types of models are used to approach these real components: (i) a defect-chemistry model, based on solid-state equilibria among variously charged and clustered defects, and (ii) a lattice-gas model, based on structural features of the oxygen "sublattice" and statistical thermodynamics.

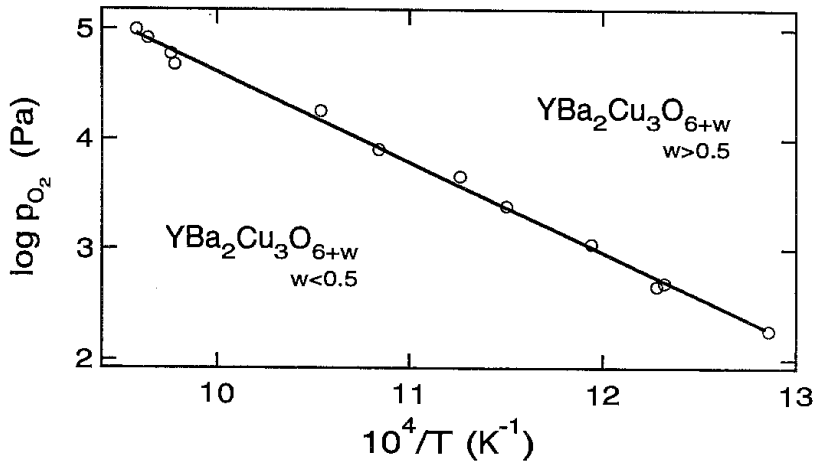

Fig. 52. $YBa_2Cu_3O_{6.50}$ stability with respect to oxygen uptake and release, according to Fjellvåg et al. (1988b).

17.2.1. *Experimental data*

A great number of studies report data on the oxygen-exchange equilibrium in eq. (23). However, only some cover a wide range in the p–t–w variables. Such data are obtained

by a variety of techniques: TGA accompanied by quenching of selected samples and by chemical and PXD analyses (R = Y, Gallagher 1987, Strobel et al. 1987, Kishio et al. 1987, 1989, Marucco et al. 1988, Yamaguchi et al. 1988, Lindemer et al. 1989; R = Er, Liang and Nakamura 1988), coulometric titration (R = Y, Porat et al. 1992, Mathews and Jacob 1992; R = Ho, Q.-Z. Zhang et al. 1992; R = Pr, Patrakeev et al. 1995b) and pressure/volume measurements (R = Y, Meuffels et al. 1989, Schleger et al. 1991; R = Er, Pörschke et al. 1992). At high pressures, equilibration and cooling techniques (R = Y, O'Bryan et al. 1989, Karpinski et al. 1989d) or gas-volume titrations (R = Y, Conder et al. 1992) have been used. As stated in several of the cited studies, a reliable determination of the oxygen content is crucial for the accuracy of the p–t–w data, especially when it concerns the reference composition for TGA or coulometry. In particular, hydrogen-reduction analyses can be burdened by systematic errors owing to the presence of a residual carbonate in the samples, resulting in somewhat higher-than-real oxygen contents. Even when these problems are eliminated, the resulting p–t–w data seem to have a non-ideal character, caused by the width of the homogeneity region with respect to w and the order/disorder phenomena related to the accommodation of oxygen in the crystal structure. As a consequence of these combined factors, a precise description of the nonstoichiometry of $YBa_2Cu_3O_{6+w}$ has not yet been satisfactorily worked out.

17.2.2. *The defect chemistry approach*

Defect chemistry models assume that there occur equilibria in the solid state between the point defects that participate in the oxygen-exchange reaction. During this reaction, formation of aliovalent atoms or atom clusters is the essence of the redox process in the solid state. However, when the span of the redox process covers an entire unit of valence, as for $RBa_2Cu_3O_{6+w}$, it may become less clear which oxidation state is the aliovalent one. In addition, a non-ideal behaviour can be expected at high defect concentrations. The usual approach is to identify the stoichiometric state and use this as the basis for the definition of the defects. The stoichiometric state appears at an integer composition where a n-to-p semiconducting transition occurs corresponding to the intrinsic situation with the Fermi energy in the middle of the gap (Maier and Tuller 1993). This situation also corresponds to a minimum in the oxygen ion diffusivity (Smyth 1989). Based on both these criteria, the stoichiometric situation occurs at the composition $RBa_2Cu_3O_6$, *i.e.*, having Cu^{I} with its typical linear coordination at the Cu(1) site and Cu^{II} at the two square-pyramidal Cu(2) sites (Chang et al. 1988, Kishio et al. 1989). Unfortunately, the phase stability boundary coincides with this composition, and this causes difficulty with unambiguous assignment of defect models.

One model follows the traditional dopant–compensator approach. Seemingly, either donor or acceptor doping could be chosen in this case, having oxygen interstitials or vacancies as compensators, respectively. However, as the homogeneity range extends as high as to $RBa_2Cu_3O_7$, there are not enough donor atoms and only the Ba'_Y acceptor can be considered. The stoichiometric composition $RBa_2Cu_3^{+5/3}O_6$ is then formally derived by the oxygen-vacancy compensation of an acceptor-doped $Y_3Cu_3^{+5/3}O_7$. Oxidation of the

stoichiometric composition proceeds according to the following equation (with associated equilibrium constant):

$$2V_O^{\cdot\cdot} + O_2 = 2O_O^{\times} + 4h^{\cdot}; \qquad K_{ox} = [h^{\cdot}]^4 [V_O^{\cdot\cdot}]^{-2} \left(\frac{p_{O_2}}{p^{\circ}_{O_2}}\right)^{-1}, \tag{25}$$

and, similarly, for reduction:

$$2O_O^{\times} = O_2 + 2V_O^{\cdot\cdot} + 4e'; \qquad K_{red} = [e']^4 [V_O^{\cdot\cdot}]^2 \frac{p_{O_2}}{p^{\circ}_{O_2}}. \tag{26}$$

Concentration of the uncharged species is unity and $p^{\circ}_{O_2}$ is the chosen standard pressure (here 101 325 Pa). Considering that $[Ba'_Y] = 2$ and $w = 1 - [V_O^{\cdot\cdot}]$ (any oxygen interstitials are neglected) and using the electroneutrality condition,

$$2[V_O^{\cdot\cdot}] + [h^{\cdot}] = [e'] + [Ba'_Y], \tag{27}$$

a polynomial is obtained for w and $\log p_{O_2}$, with K_{ox} and K_{red} as parameters. When the temperature dependences of the equilibrium constants are expressed via the van't Hoff approximation,

$$\ln K_j = \frac{\Delta s_j^{\circ}}{R} - \frac{\Delta h_j^{\circ}}{RT} \quad (j = \text{ox, red}), \tag{28}$$

the numerical solution of the polynomial can be fitted to the entire set of the experimental $w(p_{O_2}, T)$ data points. The result of such an approach to a selected series of literature data covering most of the relevant state conditions is illustrated in fig. 53. A good fit is obtained, in particular in the vicinity of the stoichiometric composition $RBa_2Cu_3^{+5/3}O_6$ where also the reduction reaction (eq. 26) contributes to the modelling. The fitted standard thermodynamic values for the latter reaction, as well as for oxidation (eq. 25), are listed in table 27. Since the compound is not stable in the region where $v_{Cu} < 5/3$, experimental data are not available for the situation where eq. (26) prevails. This is the reason for the relatively large standard deviations of Δh°_{red} and Δs°_{red}. Nevertheless, the model suggests that the reduction reaction under formation of electrons contributes to the redox behaviour of $RBa_2Cu_3O_{6+w}$.

Another model has often been applied to $RBa_2Cu_3O_{6+w}$, based on the S-shaped isotherms which become nearly linear when the composition is expressed as $\log[w/(1-w)]$. A mass-action term of the $w/(1-w)$ type appears when the number of the structure sites involved is considered constant (Maier and Tuller 1993). This means that for every defect on the product side of the formal defect reaction, there occurs one participating structural site, appearing at the left hand side of the equation. The slope of the $\log p_{O_2}$ vs. $\log[w/(1-w)]$ dependences then refers to the number of such defects corresponding to

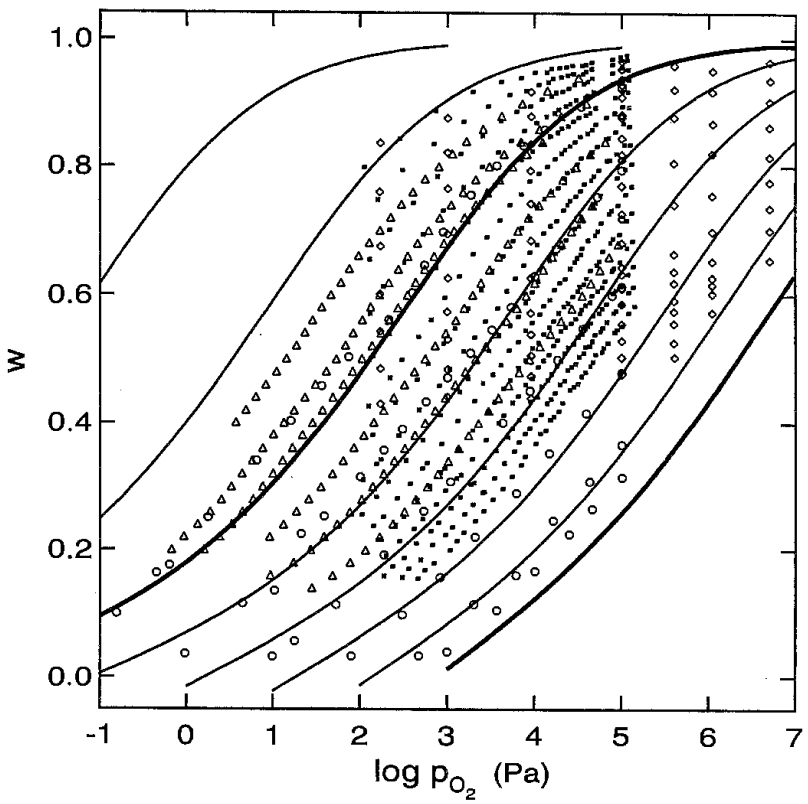

Fig. 53. Isotherms for $YBa_2Cu_3O_{6+w}$ compositions (500 and 1000°C isotherms drawn thick) according to fits of eqs. (25)–(28) to combined data from Meuffels et al. (1989) (square dots), Schleger et al. (1991) (triangles), Conder et al. (1992) (diamonds) and Mathews and Jacob (1992) (circles).

2 oxygen atoms (from the O_2 molecule). By choices of variously charged and clustered defects, various slopes can be modelled; ranging between 6 for the 'standard' charges,

$$O_2 + 2V_i + 4Cu_{Cu}^{\times} \rightleftharpoons 2O_i'' + 4Cu_{Cu}^{\cdot}, \tag{29}$$

and 2 for fully ionized defects (chosen for $YBa_2Cu_3O_{6+w}$ by Maier and Tuller 1993 and Maier et al. 1990):

$$O_2 + 2V_i \rightleftharpoons 2O_i^{\times}. \tag{30}$$

In general, the equilibrium-constant term for such defect reactions, introducing w as the variable under the condition of electroneutrality for the defects considered, leads to the following expression:

$$\log \frac{p_{O_2}}{p_{O_2}^{\circ}} = -\log K_{ox'} + n \log \frac{w}{1-w}, \tag{31}$$

where n is the said slope. Fitting selected wide-range experimental data with eq. (31) yields n close to 3, see table 28. As illustrated in fig. 54, the fit is reasonably good except

Table 27
Parameters describing the oxygen nonstoichiometry in $YBa_2Cu_3O_{6+w}$ according to eqs. (25)–(28) (referring to 1 mole of O_2), as fitted from selected literature data; for units see the Introduction

Δh°_{ox}	Δs°_{ox}	Δh°_{red}	Δs°_{red}	t	log p_{O_2}	Points	Method used	Ref.
−172(1)	−173(1)	309(31)	48(13)	450–650	0.6 to 5.0	186	Gas-volume titration	[1]
−153.4(6)	−151.1(8)	227(42)	29(42)	400–750	2.0 to 5.1	450	Gas-volume titration	[2]
−162(2)	−160(2)	213(77)	0(78)	300–900	0.0 to 5.0	66	TGA	[3]
−163(3)	−158(3)	228(21)	32(20)	500–950	−1.4 to 5.0	68	Coulometric titration	[4]
−149(1)	−143(2)	264(fixed)	58(fixed)	450–1000	3.2 to 6.7	82	Gas-volume titration	[5]
−157.0(6)	−154.3(8)	264(18)	58(17)			855	Above data combined	

References

[1] Schleger et al. (1991)
[2] Meuffels et al. (1989)
[3] Lindemer et al. (1989)
[4] Mathews and Jacob (1992)
[5] Conder et al. (1992)

Table 28
Parameters describing the oxygen nonstoichiometry in $YBa_2Cu_3O_{6+w}$ according to eqs. (28) and (31) (referring to 1 mole of O_2), as fitted from selected literature data; for units see the Introduction

$\Delta h^\circ_{ox'}$	$\Delta s^\circ_{ox'}$	n	t	$\log p_{O_2}$	Points	Method used	Ref.
−174(1)	−168(1)	3.02(1)	450–650	0.6 to 5.0	186	gas-volume titration	[1]
−163.3(6)	−155.2(7)	2.88(1)	400–750	2.0 to 5.1	450	gas-volume titration	[2]
−174(4)	−164(5)	2.76(6)	300–900	0.0 to 5.0	66	TGA	[3]
−169(4)	−159(5)	2.72(6)	500–950	−1.4 to 5.0	68	coulometric titration	[4]
−155(2)	−143(2)	2.67(4)	450–1000	3.2 to 6.7	82	gas-volume titration	[5]
−166(1)	−157(1)	2.82(1)			855	Above data combined	

References

[1] Schleger et al. (1991)
[2] Meuffels et al. (1989)
[3] Lindemer et al. (1989)
[4] Mathews and Jacob (1992)
[5] Conder et al. (1992)

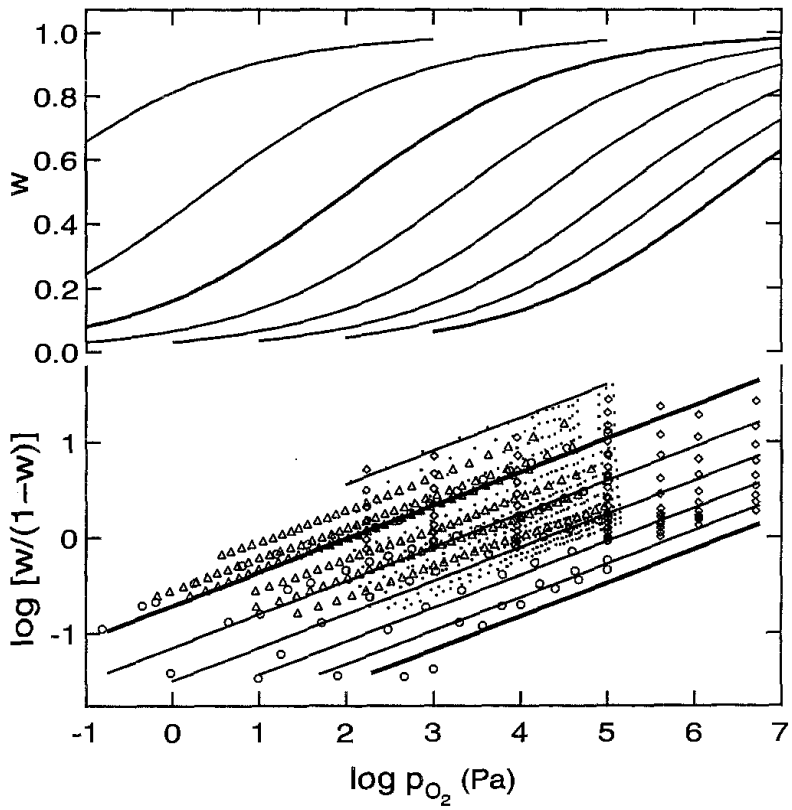

Fig. 54. Isotherms for $YBa_2Cu_3O_{6+w}$ compositions (500 and 1000°C isotherms drawn thick). Bottom plot: bivariate least squares fits to combined data from Meuffels et al. (1989) (dots), Schleger et al. (1991) (triangles), Conder et al. (1992) (diamonds) and Mathews and Jacob (1992) (circles) according to eqs. (31) and (28). Top plot: Drawn according to the fitted parameters.

for the most reduced compositions. It could be argued that those are the compositions where the contribution of eq. (26) in the previous (traditional) defect model is most significant. However, as an empirical approach, eq. (31) is quite attractive owing to its simplicity and robustness. As an example for the latter property, even when the defect equilibria are based on the incorrect stoichiometric state with $w = 1$ instead of $w = 0$ (Verweij 1988, Schwitzgebel and Junk 1989, Nowotny and Rekas 1990a,b, Lanckbeen et al. 1994), the term $w/(1-w)$ would merely be inverted and reasonably linear isotherms obtained. It is however clear that none of the fine variations in w occurring (Meuffels et al. 1989, Pörschke et al. 1992) around the structural o,t-transition can be modelled by any of the simple defect-chemistry approximations considered.

17.2.3. *The lattice-gas approach*

Lattice-gas models of thermodynamics of the oxygen exchange consider configuration and interaction between the oxygen atoms at the available sites. For $YBa_2Cu_3O_{6+w}$, a two-dimensional model is often applied, making use of the structurally well established fact that the oxygen absorption and desorption takes place exclusively in the a, b plane of Cu(1) (Verweij and Feiner 1990, Tétot et al. 1993). Whereas fairly precise predictions

are obtained (Shaked et al. 1989, Ceder et al. 1990) for the oxygen-related order–disorder phenomena like the p–t dependence of the orthorhombic to tetragonal (o,t) transition, discrepancies are seen in the description of the oxygen-exchange equilibria (McKinnon et al. 1988). In the most simple of these statistical models applied to evaluate experimental data (Meuffels et al. 1989, Pörschke et al. 1992) the oxygen-exchange reaction is assumed as follows:

$$\tfrac{1}{2}O_{2(g)} \rightleftharpoons O_{(s,\,YBa_2Cu_3O_{6+w})}, \tag{32}$$

with equilibrium constant expressed via chemical potentials as the partial molar free energy for incorporation of 1 mol oxygen atoms in the solid, Δg_O. Referring to the standard state $p^\circ_{O_2}$ and the actual temperature:

$$\Delta g_O = \Delta h_O - T\Delta s_O = \tfrac{1}{2}RT \ln\left(\frac{p_{O_2}}{p^\circ_{O_2}}\right). \tag{33}$$

Both enthalpy and entropy are further expressed by Meuffels et al. (1989) and Pörschke et al. (1992) as a sum of standard and excess values (to account for the apparent non-ideal behaviour)

$$\Delta h_O = \Delta h^\circ_O + h^E_O, \tag{34}$$

where w enters in the configurational entropy:

$$\Delta s_O = \Delta s^\circ_O + s^E_O + R \ln\left(\frac{2-w}{w}\right), \tag{35}$$

which assumes that structurally there are two oxygen sites, O(1) and O(5), to choose between.

However, when one expresses the partial pressure of oxygen from eqs. (33)–(35) as a function of the concentration term, the standard and excess values can be regrouped to give an equilibrium constant (related to the oxygen-exchange reaction in eq. 32)

$$\ln\left(\frac{p_{O_2}}{p^\circ_{O_2}}\right) = -2\ln K_{32} + 2\ln\left(\frac{w}{2-w}\right), \tag{36}$$

where $-\ln K_{32} = (\Delta h^\circ_O + \Delta h^E_O)/RT - (\Delta s^\circ_O + \Delta s^E_O)/R$. Equation 36 is hence similar to eq. (31) derived from the defect-model considerations. Two differences appear, *viz.*, in that the slope of the isotherms is 2 rather than ~3 (originating from eq. 32) and in that two sites are considered in the configurational entropy term. The detailed and accurate experimental data from Meuffels et al. (1989) and Pörschke et al. (1992) treated by the model behind eq. (36) give large excess values, and this reflects the said difference in the slope and in the composition term. Typically for the latter, it is even suggested by

Patrakeev et al. (1995b) that, with increasing w, the number of available sites in this configurational entropy term decreases to 1.

Nevertheless, the partial molar values play an important role. The composition w enters the configurational partial molar entropy, and the partial molar enthalpy of oxygen should be rather independent of w and the model adopted. Experimental data at constant w (like in fig. 52) across the homogeneity range give indeed only modestly varying $\Delta h^{\circ}_{O_2}$ (between 160 and 172 kJ/mol) whereas $\Delta s^{\circ}_{O_2}$ changes markedly (between some 100 and 210 J/mol K) when w is varied from 0.1 to 0.9 (H. Zhang et al. 1996, Prado et al. 1998). The scatter in the $\Delta h^{\circ}_{O_2}$ values summarized by Mathews and Jacob (1992) is much larger (between −160 and −220 kJ/mol) and should hence be attributed to the variations in the experimetal methods and models used rather than to the variable composition. Values in this range are also obtained for other nonstoichiometric cuprates. Direct calorimetric measurements (Gerdanian et al. 1989, Parks et al. 1989, H.-Z. Zhang et al. 1995) confirm that the w dependence is minor, but a λ feature is observed by Gerdanian et al. (1989) around the o,t-structural transition. Such a λ discontinuity is also evaluated from inflexion points of isotherms obtained by detailed coulometric titration meaurements (Mathews and Jacob 1992). This means that a precise modelling must take into account the change in the interactions accompanying this structural transition. The compositional dependences of $\Delta h^{\circ}_{O_2}$ and $\Delta s^{\circ}_{O_2}$ are usually expressed empirically. Perhaps the simplest approximation is suggested by H. Zhang et al. (1996) stating that the heat-capacity contribution of the w oxygen atoms is equal to that of $\frac{1}{2}wO_{2\,(g)}$ giving linear relationships for enthalpy and parabolic for entropy as a function of w. More detailed empirical approximations are able to take into account the order–disorder transition and one such approach (Voronin and Degterov 1991, Voronin 1994b, 2000, Rudnyi et al. 1998) is illustrated in sect. 13.6.

18. Structural and chemical variants of $YBa_2Cu_3O_7$

18.1. *Substitution by hydrogen, proton and hydroxyl*

For variety of reasons, the only path to the hydrogen-substituted variants of $YBa_2Cu_3O_{6+w}$ is the interaction of the master phase with gaseous H_2 or H_2O. The reactions involved have two main components, one redox and the other acidobasic, both causing easily a destruction of the phase, the former due to the reduction into the (ultimately) metallic Cu, the latter due to the hydrolysis. Both decompositions can be avoided by adopting low temperatures for the interactions, and, at higher temperatures, by maintaining the appropriate low partial pressures of the gaseous species.

Under such mild conditions, the reacting centres are the Lewis-base oxygens in $YBa_2Cu_3O_{6+w}$ which have strong affinity towards the Lewis-acid protons and form hydroxide defects. These hydroxide defects are the regular hydroxide groups occurring, *e.g.*, in the structures of various metal hydroxides, where they behave effectively as a spherical anion with a radius of some 153 pm (Evans 1964). This radius is only slightly larger than the generally accepted radius for O^{2-} (140 pm), since the covalent O–H bond

is short. However, the migrating hydrogen species in the solid state are not the hydroxide groups as such, but the protons alone (Norby 1990, Iwahara 1992, Sutija et al. 1995), and therefore the defects are often denoted in the literature simply as $H_i^{\cdot}$.

Adopting the same standard stoichiometric state as for the oxygen equilibria in sect. 17.2, and for simplicity formally assuming that the changes occur in the Cu(1) region, the formations of the hydroxide defects from H_2 and H_2O are expressed in terms of defect reactions in the following. The incorporation of n moles of H_2 into 1 mole of $YBa_2Cu_3O_{6+w}$ will create $2n$ mol hydroxide defects and reduce the overall formal Cu valence by $2n/3$, while the overall number of the occupied "oxygen" sites per formula remains constant at $6+w$. The span of the Cu-valence states compatible with the given structure type is then likely to be the limiting factor for the extent of the reaction:

$$H_2 + 2O_i'' + 2Cu_{Cu}^{\cdot} \rightleftharpoons 2(OH)_i' + 2Cu_{Cu}^{\times}. \tag{37}$$

The incorporation of n moles of H_2O into 1 mole of $YBa_2Cu_3O_{6+w}$ will create $2n$ mol hydroxide defects and maintain the Cu valence constant, while the overall occupancy of the "oxygen" sites increases by n per formula. The occupancy span for the "oxygen" sites is then likely to be the limiting factor for the extent of this reaction:

$$H_2O + V_i + O_i'' \rightleftharpoons 2(OH)_i'. \tag{38}$$

It is more or less a matter of formality that these equations can be rewritten to involve the $O_O^{\times}$ oxygens instead of the O_i'' (the latter being the w per formula oxygens), holes $h^{\cdot}$ instead of $Cu_{Cu}^{\cdot}$, or, for that matter, also $H_i^{\cdot}$ and O_i'' instead of $(OH)_i'$.

In a sensitive redox system like this, the acidobasic reaction in eq. (38) is expected to be significantly accompanied by the redox reaction in eq. (37) when the system contains H_2 in the atmosphere and by the redox reaction in eq. (29) for systems with O_2 atmospheres. Moreover, these equations can be combined with the equations for dissociation of water into the elements and for the intrinsic condition to achieve different combinations of the involved defects for expressing equilibrium constants.

It is experimentally established that some incorporation of hydrogen into $YBa_2Cu_3O_{6+w}$ takes place at moderately elevated temperatures, both by reaction with dihydrogen (Yang et al. 1987, Burger et al. 1989, Johnson et al. 1989, Hauck et al. 1993) and with water (Ikuma et al. 1990, Kobayashi 1990, Günther and Schöllhorn 1996). In fact, NMR analyses indicate that even the standard ceramic syntheses of $YBa_2Cu_3O_{6+w}$ may result in as much as 0.2 H atoms per formula, originating presumably from water vapour (Porath et al. 1994). Recently a hydrogenation at ambient temperature was reported by Weiss et al. (1998), facilitated electrochemically (a cathodic reduction).

The low-temperature hydrogenation of $YBa_2Cu_3O_{6+w}$ seems to be the most reproducible method for synthesis of the protonated phases. Their characterization, however, has proved extremely difficult, particularly due to the analytical problems with hydrogen being the lightest atom (TGA, PXD) and an incoherently scattering element (PND), as well as due to the inhomogeneities and the enhanced reactivity of the products. A somewhat clearer picture can be extracted from a combination of several recent studies

adopting special methods like the ^{15}N nuclear reaction method (Dortmann et al. 1994), HREM (Garrote et al. 1995) and PND at variable temperatures (Fruchart et al. 1990), as well as special substrates, like the thin film arrangement of Dortmann et al. (1994). The data show consistently that the incorporation of hydrogen proceeds in two steps. The first step occurs at low temperatures, below some 200°C (under 1 atm of H_2, the temperature being even lower under higher pressures, Fruchart et al. 1990, and *vice versa,* Garrote et al. 1995). Small amounts of hydrogen, up to some 0.3 per formula are absorbed (say, according to eq. 37) while some water is released (say, according to eq. 38). This results in rather insignificant changes in the lattice parameters and T_c of the matrix phase. According to other reports (Harrington et al. 1994, Kebukawa et al. 1994), a hydrogen content up to some 1 per formula can be achieved, accompanied by a structural change into tetragonal symmetry and a *decrease* in the *c* parameter. In the second step, occurring above 200°C, and up to, say, 300°C, this phase gradually disappears and another, yet closely related triple-perovskite phase is formed, containing at saturation approximately 2 H atoms per formula. The oxidation state of Cu is then the same as in $YBa_2Cu_3O_6$ having monovalent copper at the Cu(1) site. Typical for this now recognized perovskite structure is that the *c* axis is extended by almost 200 pm as compared with the original material (according to Dortmann et al. 1994), and this can be corroborated by the data of Garrote et al. (1995) (although probably erroneously referred to the 124 or 147 phases) and by Fruchart et al. (1990) (although giving an obviously misprinted value). During the formation of this phase, the release of water seen (Fruchart et al. 1990) by TGA is comparable with that during the first step, whereas the continuing reduction of copper, particularly at Cu(1), is manifested by the superstructure features seen by HREM (Garrote et al. 1995), by iodometry (Kebukawa et al. 1994) and apparently also by the appearance (Niedermayer et al. 1989, Glückler et al. 1993) of an antiferromagnetic ordering typical for the $w \rightarrow 0$ versions of the original phase. The additional hydrogen-containing defects are tentatively located (Dortmann et al. 1994) in the Cu(1) coordination sphere and this provides a good possible explanation for the *c*-axis extension: Whereas the Cu(1) atom is reduced to Cu^I and should presumably adopt the linear coordination in the *c* direction, there are now hydroxide groups OH^- located around Cu(1) at high concentrations. For bond-valence reasons and also owing to the size of the hydroxide groups, the *c*-axis bond distance at Cu(1) must then extend substantially. It should be mentioned that also the $YBa_2Cu_4O_8$ phase absorbs around 2H per formula unit and that this does not cause any such significant *c*-axis extension (Dortmann et al. 1994). It seems that a moderate hydrogenation is reversible in pure oxygen at 200 to 400°C (Garrote et al. 1995, Baikov 1995). The detailed compositional and structural characterization of the hydrogenated 123 phase is still missing. However, several computational studies (Prakash and Burger 1993, Cherry et al. 1995) are available, dealing with the location of protons and hydroxide groups in the perovskite-type structures. These atomistic simulations confirm the O–H bond distance (94 pm, Cherry et al. 1995), the location of the protons close to the direction of the adjacent oxide ion, and the occurrence of a low-energy barrier for the proton transport. For more recent structural models of the hydrogen and water intercalation into $YBa_2Cu_3O_{6+w}$ see Günther et al. (1999).

18.2. *Substitution by halogen*

The partial substitution of oxygens in $YBa_2Cu_3O_{6+w}$ by the lighter halogen atoms is structurally similar to the substitution by the hydroxide groups, both when ionic charge and radius are considered. Also here the feasible synthesis route is the direct halogenation of $YBa_2Cu_3O_{6+w}$ at slightly elevated temperatures, preferably by NF_3 in case of fluorine (LaGraff et al. 1989). Attempts to introduce halogens as Ba halogenides into the ceramic syntesis yield no reaction (Tyagi et al. 1988, Wang et al. 1988). However, an important difference between halogenation and hydrogenation is that halogenation oxidizes copper (formation of Cu–X bonds), whereas hydrogenation reduces it (formation of O–H bonds). The incorporation of n mol X_2 (X = halogen) into 1 mol $YBa_2Cu_3O_{6+w}$ will increase the overall formal Cu valence by $2n/3$ and will also increase the overall occupancy of the possible "oxygen" sites by $2n$ per formula. Both the valence and occupancy spans can restrict the extent of this reaction, which, in some similarity with eq. (37), can be expressed as follows:

$$X_2 + 2V_i + 2Cu_{Cu}^{\times} \rightleftharpoons 2X_i' + 2Cu_{Cu}^{\cdot}. \tag{39}$$

It is experimentally well established that fluorine (LaGraff et al. 1989, Perrin et al. 1989, MacManus et al. 1991), chlorine and even bromine (Mokhtari et al. 1995) enter the vacant oxygen sites in the Cu(1) coordination sphere, in concentrations decreasing in the said order. Quantum-chemical calculation (Mokhtari et al. 1995) of the alternative structures for the thus formed halogenide cuprate anions show that upon the reaction with the molecular halogens only the vacant oxygen sites are reasonable candidates for accommodation of the halogen atoms. Moreover, only the most electronegative of them, fluorine, should be able to enter also the normally empty sites between the copper oxygen square-chains, transforming them into octahedra. Chlorine and bromine, on the other hand, would only enter the vacancies inside the chains. This is in accordance with structural data from PND (LaGraff et al. 1989, Mokhtari et al. 1995).

Since the substitution of halogen (as well as hydroxyl) for oxygen is aliovalent, it can be used for fine tuning of the valence state and structural environment of copper. Both electron and hole doping (for superconductivity) can be achieved, by substituting for oxygens and vacancies, respectively. As the oxide halogenides are relatively stable, successful attempts have been made to synthesize halogenated versions of also other cuprates than 123, like $Sr_2CuO_2F_{2+\delta}$ with the o-La_2CuO_4-type structure (T phase) (Morosin et al. 1995), $A_2CuO_2F_2$ (A = Ca, Sr) with the t-Nd_2CuO_4-type structure (T′ phase, Al-Mamouri et al. 1995, Kissick et al. 1997), $(Ca,R)_2CuO_3Cl$ with the tetragonal T*-phase structure (Ramanujachary et al. 1991, Tatsuki et al. 1996), and $A_2CaCu_2O_4Cl_2$ with the $R_2CaCu_2O_6$-type (Ruddlesden–Popper-type) structure (Zenitani et al. 1995, Kawashima et al. 1996). For the phase diagram in the Ba(O)–Ba(Cl)–Cu(O) subsystem see Ruck et al. (1998).

18.3. *Substitution by metal except A and R*

The diversion brought into the R(O)–A(O)–Cu(O) systems through the introduction of a fourth kind of metal is much more drastic than when similar A or R are involved.

However, the problem is that not even the R(O)–A(O)–M(O) systems are known well. Only for specific cases concerning superconducting phases, there is relatively abundant information available about the solid solubility with respect to various metals M, but only rarely the phases occurring in equilibrium at the solubility limits are identified.

18.3.1. *Solid solubility at the R site*

Only few elements other than R and A are able to significantly enter these sites. Of the alkaline metals, sodium may apparently be present at the Y site up to a few atom percent, provided a matching amount is allotted to the Ba site (Karen et al. 1990a). Syntheses of homogeneous, single-phase oxides which contain the alkali metals are difficult owing to the high volatility of the alkali metal peroxides and superoxides. Usually, a deficiency in alkali metal is found in the subsequent analyses of the products, despite all precautions taken. A more straightforward situation occurs with the metals of the actinide series, which are chemically similar to R. Curium forms a non-superconducting $CmBa_2Cu_3O_7$ phase (Soderholm et al. 1989). Also an equiatomic Th,Ca mixture enters partially at the Y site of $YBa_2Cu_3O_{6+w}$, $x \leqslant 0.1$ (Andersson et al. 1989). Of the other metals, cadmium is reported (Chen et al. 1990) to substitute at the Y site in $YBa_2Cu_3O_{6+w}$ up to some $x = 0.5$, with a rather surprisingly negligible effect on T_c, despite the observed structural conversion from orthorhombic to tetragonal at $x = 0.4$. However, the presence of $BaCuO_2$ impurities suggests that Cd may also be entering the Ba site, although this possibility was not considered in Chen et al. (1990).

18.3.2. *Solid solubility at the Ba site*

Also this type of substitution occurs rarely for other elements than Sr (see sect. 16) and large Rs (see sect. 13). Alkali metals again are practically the only candidates, and minute amounts of K, Rb and Cs are reported either at the Ba site (Ausloos et al. 1988) or at both the Y and Ba sites in $YBa_2Cu_3O_{6+w}$ (Karen et al. 1990a, Tallon et al. 1990b). Somewhat surprisingly, no incorporation of Pb at the Ba site is found, and a different (although 123-related) structure is in fact formed when PbO is introduced into the Y(O)–Ba(O)–Cu(O) system (Fu et al. 1989, Zandbergen et al. 1990).

18.3.3. *Solid solubilities at the Cu sites*

The chemical and ionic-size similarity governs also here. For the $YBa_2(Cu_{1-z}M_z)_3O_{6+w}$-type substitution, an overview of candidates for substituents is presented in table 29, together with the phases involved in the equilibrium at the solid-solution limits. Despite the comprehensive literature on these substitution phases, such key data are not frequently reported, simply because the extra labour has not been undertaken to perform the tedious experimental work on poly-phase materials to ensure equilibrium. This statement is particularly valid for the investigations on substituents with very low limits of solid solubility (Andresen et al. 1991), where also the detection threshold for the adopted analytical method should be taken into consideration. With the high sensitivity PXD instrumentation used by Andresen et al. (1991), the detection limit is some 0.5 and 1 wt%

Table 29
Equilibrium phase compositions at the limit of solid solubility for M in $YBa_2(Cu_{1-z}M_z)_3O_{6+w}$ for samples fired at 910°C in pure oxygen and oxidized at 340°C, according to Andresen et al. (1991)

M	Y_2BaCuO_5	$BaCuO_{2+w}$	Other phases observed[a]	z_{lim}
Li	+	+	$BaCO_3$	0.04(1)
Mg	+	+	MgO	0.04(1)
Sc	+	–	$BaSc_2O_4$	0.01(1)
Ti	+	–	Ba titanates, TiO_2	0.00(2)
V	+	–	$Ba_3V_2O_8$	0.00(4)
Cr	+	–	$BaCrO_4$	0.02(1)
Mn	+	–	$Ba_3Mn_2O_8$	0.00(3)
Fe	–	+[b]	$YBa(Cu_{1-z}Fe_z)_2O_5$[c]	0.22(1)
Co	–	–	$YBa(Cu_{1-z}Co_z)_2O_5$[d]	
			$Ba(Co_{1-z}Cu_z)O_w$[e]	0.30(5)
Ni	+	+	NiO	0.08(1)
Zn	+	+	ZnO	0.09(1)

[a] A small amount of an additional phase is expected to occur for Li, Sc, V and Mn.
[b] [$Ba(Cu_{0.70(5)}Fe_{0.30(5)})O_{2+w}$; $Im\bar{3}m$; 1842.4(4)].
[c] [$z = 0.4$; *P4mm*; 387.0(1), 767.1(1)].
[d] [$z \approx 0.5$; *P4mm*; 387.2(1), 756.2(2)].
[e] [$z \approx 0.0$, $w = 2.80(3)$; h; 571.65(2), 444.00(2)].

for the nearest neighbour phases of Y_2BaCuO_5 and $BaCuO_{2+w}$, respectively. Therefore, substitution limits with $z < 0.01$ cannot be ascertained.

The solubility limits in table 29 agree reasonably well with other literature data, *viz.*, in those not very frequent cases where such data are explicitly stated. As an example for the further data: Fe ($z = 0.18$, Ullmann et al. 1988), Co ($z = 0.25$, Kiemel et al. 1988), Ni ($z = 0.04$, Qian et al. 1989; $z = 0.09$, Maeno et al. 1987; $0.10 < z < 0.17$, Tarascon et al. 1987), Zn ($z = 0.10$, Takabatake and Ishikawa 1988; $z = 0.12$, Xiao et al. 1988), Al ($z = 0.04$, Takabatake and Ishikawa 1988, Kirby et al. 1987, Siegrist et al. 1987), Ga ($z = 0.05$, Xu et al. 1988), Au ($z = 0.10$, Hepp et al. 1988, Cieplak et al. 1990, Renevier et al. 1990) and Pd ($z = 0.17$, Ferey et al. 1988). For the group of the most compatible substituents, Fe, Co, Ni, Zn and Mg, the three- or four-phase neighbourhoods occurring at the solid-solubility limits are illustrated in the tetrahedral diagrams in fig. 55; for thermochemical considerations, see Rodriguez et al. (2000). It should be noted, however, that under changed state conditions, the solid solubilities may change completely. As an example, under pressure of 1.8 GPa, a full replacement of the square-planar-coordinated Cu atoms by Au is observed and the phase even retains the superconductivity ($T_c = 80$ K) when doped by a Ca-for-Y substitution (Bordet et al. 1997).

For $YBa_2(Cu_{1-z}M_z)_3O_{6+w}$ oxygen saturated at a given p_{O_2}, the oxidation state of Cu according to iodometry equals that of the pure matrix phase. When the typical valence of a given substituent exceeds the valence of Cu, *e.g.*, Fe^{III}, Co^{III}, $Ni^{>II}$, Al^{III}, Ga^{III}, the oxygen content hence may exceed seven per formula (Andresen et al. 1991, Hiratani et al. 1987). These oxygen-saturated samples then often exhibit a crossover from orthorhombic

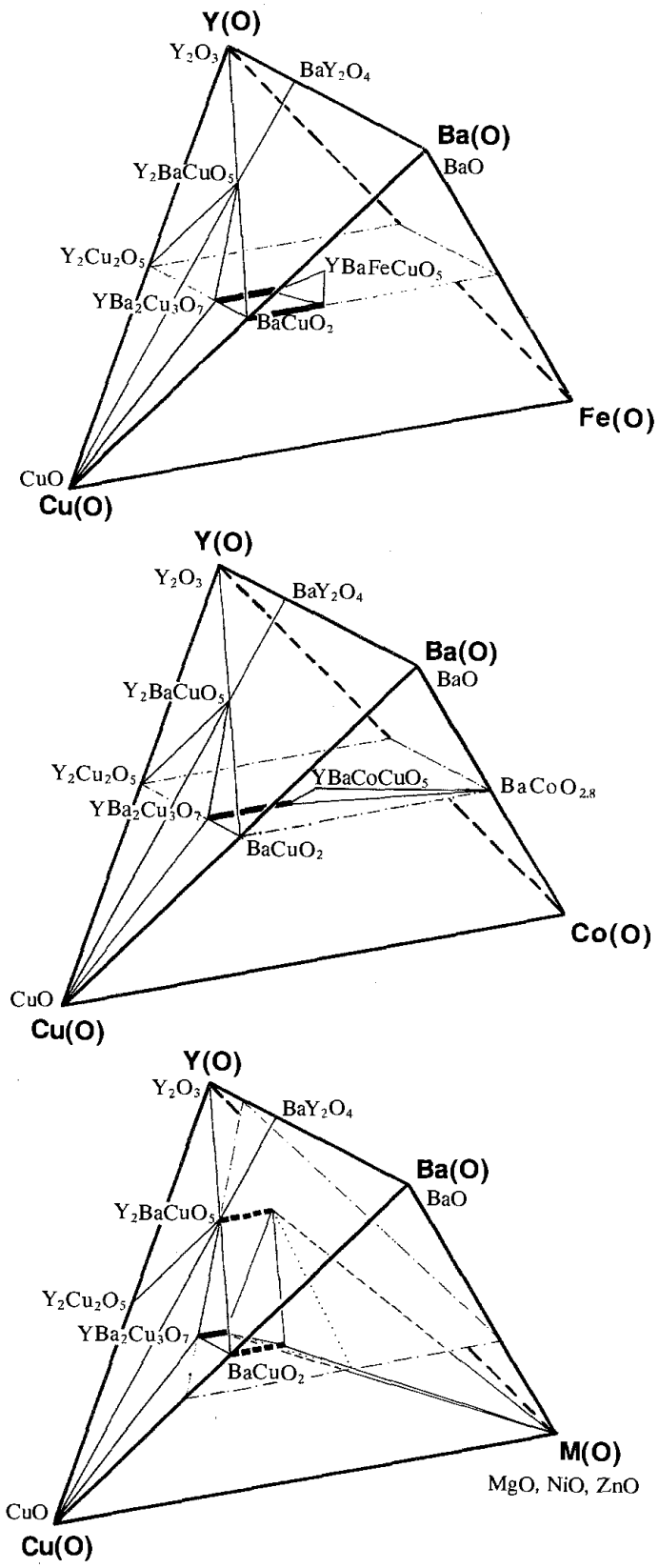

Fig. 55. Four-phase tetrahedral envelopes adjacent to the M-saturated $YBa_2(Cu_{1-z}M_z)_3O_{6+w}$ solid solutions for M = Fe, Co and Mg/Ni/Zn, in subsolidus (pseudoquaternary) tetrahedral phase diagrams, as seen by room-temperature PXD after firing at 900°C in oxygen.

to tetragonal symmetry, seen by PXD, which occurs at surprisingly low substitution levels, usually below $z = 0.05$ (Andresen et al. 1991, Takabatake and Ishikawa 1988, Xu et al. 1988). This behaviour coincides with the fact that Fe, Co, Al, and Ga introduce a tendency for non-planar coordination at the square-planar Cu(1) site and concentrate themselves at twin-domain boundaries (Bordet et al. 1988b, Kajitani et al. 1988, Miceli et al. 1988). With increasing z, the amount of such boundaries must increase at the expense of the bulk material and the domain size is reduced to a nanometer scale, below the PXD detection threshold, but observable by HREM (Renevier et al. 1989, Hiroi et al. 1988). However, the orthorhombic structure persists at quite high substitution levels of iron (and cobalt) if a reducing atmosphere is applied during the firing, and the samples are reoxidized at low temperatures (Katsuyama et al. 1989, 1990). The probable reason is that, under reducing conditions, these higher-valent substituents tend to be located primarily at the square-pyramidal Cu(2) sites where, due to the site symmetry, they are not coupled via twinning. The critical concentration for the o,t transition for the low-temperature reoxidized samples is increased to $z_{o,t} \approx 0.15$. This is about the same as found for the La-for-Ba substitution, where it is attributed to the linkage of the copper–oxygen chains by entering additional oxygens (Karen et al. 1991a).

It should be mentioned that also other phases in the Y(O)–Ba(O)–Cu(O) system are liable to similar substitutions. For example, $YBa_2(Cu_{1-z}Fe_z)_4O_8$ is prepared up to $z = 0.1$ and found tetragonal and non-superconducting above $z = 0.04$ in direct contrast to the relatively benign effect of Fe towards superconductivity in the 123 phase (Felner et al. 1991).

18.4. *Isostructural triple perovskites*

18.4.1. *R(O)–Ba(O)–M(O)*

A complete replacement of Cu in the $YBa_2Cu_3O_7$-type structure by the first-row transition metals and Au has been tested (Karen and Kjekshus 2000) under conditions (temperature, partial pressure of oxygen) appropriate to the presumed stabilization of di- or tri-valent ions of these metals (whichever applicable) in the oxide. With the notable exception of Fe, all systems yielded a disordered perovskite or mixtures of phases which are thus more stable than the triple-perovskite arrangement. As an example, Sc forms a disordered perovskite, Ti (at very low p_{O_2}'s) forms a (light-blue coloured) mixture of the $(Y_{0.2}Ba_{0.8})TiO_3$ perovskite and the $Y_2Ti_2O_7$ pyrochlore, *etc.*, up to Au, which gives an ordered Ba_2AuYO_6 perovskite and leaves the rest of the Au metal unreacted (Karen and Kjekshus 2000).

$YBa_2Fe_3O_{8+w}$, the exception, is a triple perovskite obtained phase pure (Huang et al. 1992a, Karen et al. 1992c) from citrate precursors by repeated prolonged annealing at around 1000°C. At lower temperatures, like those used for the syntheses of the $YBa_2Cu_3O_7$ cuprate counterpart, the ordering into the triple perovskite becomes very slow. In an oxygen atmosphere, the phase is stable only up to some 1250°C, and melts incongruently between 1250 and 1300°C. $Ba(Fe_{1-z}Y_z)O_3$ ($z \approx 0.1$, cubic), $YFeO_3$ and $BaFe_2O_4$, are seen after quenching (Karen and Kjekshus 2000). The oxygen content of

8 per formula represents a hypothetical oxygen-rich extension of the cuprate, where the square-chains are fully developed to octahedra, and the structure (Huang et al. 1992a) has tetragonal symmetry [$w = 0.01$; *P4/mmm*; 391.81(5), 1182.4(2); Karen and Kjekshus (1994b)]. Upon reduction, these octahedra begin to approach the square-planar situation for M = Cu, but long before it happens, the homogeneity range ends at $w = -0.25$ and Fe^{II} phases are formed (Karen and Kjekshus 1994b, 2000). Shortly before that (at some $w = -0.20$) the symmetry nevertheless turns orthorhombic, mirroring in this respect the behaviour of the tetragonal $YBa_2Cu_3O_6$ upon oxidation [$w = -0.24$; *Pmmm*; 390.98(4), 392.76(4), 1177.85(18); Karen and Kjekshus (2000)]. In line with the cuprate, indications are obtained by fine-focus Raman analyses of occurrences of domains with different oxygen content (Atanassova et al. 1994). The attempts to vary the oxygen content in $YBa_2Fe_3O_{8+w}$ show that the structure can also tolerate a small amount of extra oxygens. Some 0.1 per formula unit is achieved at 450°C under $p_{O_2} = 15$ MPa (Karen et al. 1992c, Karen and Kjekshus 1994b), and only slightly less under ambient-pressure oxidation [$w = 0.08$; *P4/mmm*; 391.51(2), 1181.35(9); Karen and Kjekshus (2000)]. The structural location of the extra oxygens was done by PND on a series of samples where the saturated oxygen content was controlled by a progressing Ca-for-Y substitution (Natali Sora et al. 1994). According to Natali Sora et al. (1994), these oxygen atoms in excess of 8 are present in the Y layer, imposing split-position crystallographic defects upon the neighbouring oxygen sites. Beyond this, the extra oxygens have only a negligible structural effect. It is the replacement of the coordination squares by the octahedra that alters profoundly the charge balance between the two M sites, manifested in a complete reversal of the two apical bond lengths M–O when going from M = Cu to Fe. This difference is so profound that, despite the otherwise similar unit-cell dimensions, only limited solid solubility occurs between the Cu and Fe variant. These solid solubilities are illustrated in fig. 56 showing the square section of the tetrahedral phase diagram of the YFe(O)–BaFe(O)–YCu(O)–BaCu(O) subsolidus system at (nearly) isothermal conditions (Karen et al. 1992c), which includes several relevant coexisting phases from both the Cu and Fe system. Considering that Co has the largest homogeneity range of all metals at the Cu site in $YBa_2Cu_3O_{6+w}$, it was not very surprising to find out that Co is also very much compatible with $YBa_2Fe_3O_{8+w}$, being able to replace almost one half of the present Fe atoms (Karen and Kjekshus 2000). The oxygen-saturated $YBa_2(Fe_{1-z}Co_z)_3O_{8+w}$ maintain their oxygen content roughly constant throughout the homogeneity range in z, showing that it is Co^{3+} that replaces Fe^{3+} in this structure. The triple-perovskite structure of $RBa_2Fe_3O_{8+w}$ is much less accommodative for various Rs than the corresponding cuprate. In fact, it has been obtained only in a narrow region of close R elements (around the size of Y, Dy and Er). For larger R atoms, which also introduce more of the extra oxygen atoms (as much as $w = 0.8$ for R = La), the atomic arrangement gradually acquires the character of the disordered perovskite type, whereas for smaller R = Yb and Lu the phase in question does not exist (Karen et al. 1998). The largest R, *viz.*, La, can also enter the Ba site in $YBa_2Fe_3O_{8+w}$, but only when a matching amount occurs at the Y site. This situation rapidly brings about the appearance of the disordered cubic perovskite instead of the triple perovskite (Karen and Kjekshus 2000). This is in interesting contrast to the

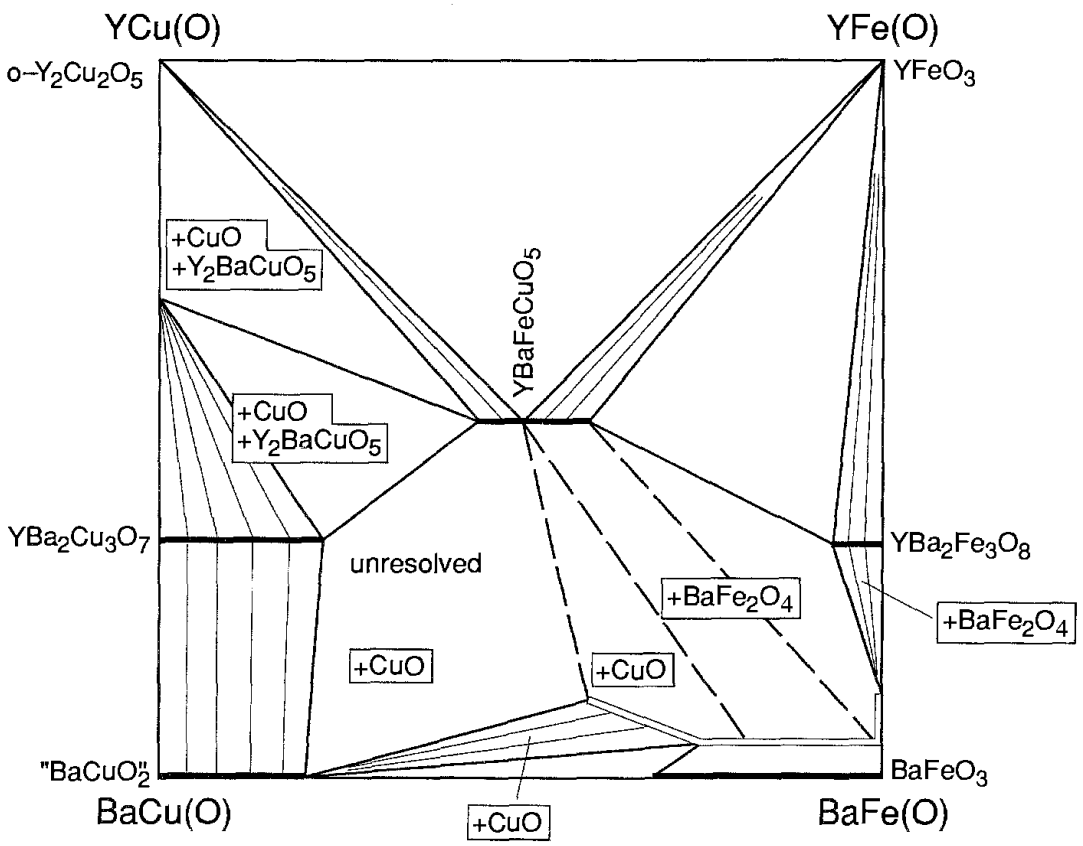

Fig. 56. Subsolidus phase compatibilites in the YCu(O)–BaCu(O)–YFe(O)–BaFe(O) system at 910–950°C in oxygen (after Karen et al. 1992c). The $(Ba_{1-y}Y_y)(Fe_{1-z}Y_z)O_3$ solid solution, located above the plane of the diagram, is shown by double lines, as seen by PXD.

cuprate where La is able to substitute solely for Ba (see sect. 15), probably in conjunction with the fact that the unit-cell volume is smaller for the cuprate than for the Fe version.

18.4.2. *R(O)–Ba(O)–M,M'(O)*

As apparent from the previous paragraph, Co is nearly, but not fully compatible with the 123 triple-perovskite structure. A full replacement by Co is reported under the condition (Geremia et al. 1989) that some barium is simultaneously substituted by potassium [$Y(Ba_{0.75}K_{0.25})_2Co_3O_8$; *P4/mmm*; 386.8(2), 1123.7(9)]. A special kind of M-for-Cu substitution occurs within the $RBa_2Cu_3O_{6+w}$-type family for large Rs. The introduction of M = Nb or Ta here leads to a complete conversion of the Cu–O coordination square chains to sheets of M-centered octahedra (Greaves and Slater 1989). An oxygen content of 8 per formula is thus obtained for the non-superconducting $La(Ba_{0.95}La_{0.05})_2(Cu_{0.1}Ta_{0.9})Cu_2O_8$ phase [*P4/mmm*; 396.58(1), 1203.04(3)]. A zig-zag folding of the transition-metal occupied octahedra is deduced from weak superstructure reflections [*I4/mcm*] observed by neutron diffraction (Rey et al. 1990). This indicates that an analogous tilt to that proposed (Wong-Ng et al. 1990b, François et al. 1988) for $YBa_2Cu_3O_7$ may be imagined.

Small Rs like Y do not allow such an arrangment of transition metals in the 123 structure and when such preparations are attempted, a different perovskite arrangement is obtained, despite the analogy in stoichiometry, *e.g.*, $YBa_2Cu_2WO_{9-w}$ [$Fm\bar{3}m$; 833.2; Yaron et al. (1990)]. Other substituents may introduce a completely different coordination at one of the Cu sites in $YBa_2Cu_3O_7$, leaving the other untouched. For example, non-superconducting $YBa_2TlCu_2O_7$ [*P4/mmm*; 386.87(1), 1247.3(1)] has a Tl–O monolayer sheet instead of the square chains (Manako et al. 1988), and is hence not isotypic with $YBa_2Cu_3O_7$. Also in other cases the reasons for the (in)compatibility represent an interplay of bond-valence (ionic size) and electronic band structure arguments. Thus, when Ba is replaced by Sr, other metals can be stabilized substituting for Cu.

18.4.3. *R(O)–Sr(O)–M,M′(O)*

The presence of the smaller Sr atoms stabilizes some degree of substitution by W as well as Mo and Re in the triple-perovskite structure (Harlow et al. 1996). Based on PND structure determinations, it is argued that these high-valent transition metals cause an increase of the average bond valence at the "copper" sites and hence shrink the "cuprate" network which then suits the Sr size better [$YSr_2Cu_{2.8}W_{0.2}O_{7.13}$; *P4/mmm*; 380.36(3), 1151.13(8); Harlow et al. (1996)]. After saturation by oxygen at high pressures, superconductivity is observed with T_c around 70 K (Dąbrovski et al. 1997). Also a replacement of a portion of Cu by substantially smaller atoms like Al has a similar effect in stabilizing Sr in the structure (and *vice versa*) (Stavola et al. 1989, Sunshine et al. 1989). Such small atoms must have tetrahedral coordination, and this can only be accommodated instead of the copper–oxygen squares in the chains. This location has been structurally well established for $YSr_2AlCu_2O_7$ [*P4/mmm*; 386.46(1), 1111.39(3); Huang et al. (1993)] and for the Ga (Vaughey et al. 1991, J.P. Zhang et al. 1994) and Co (Huang et al. 1992b, Krekels et al. 1993b) versions, differing in details on how the tetrahedral chains propagate in the *a*, *b* plane. HREM studies (Ramírez-Castellanos et al. 1997) reveal that such details also include ordering into a supestructure. Although these phases are not strictly isotypic with $YBa_2Cu_3O_7$, they are on equal footage with the oxide-carbonate, oxide-phosphate, *etc.*, variants, described in sect. 13.5.

References

Abalduev, B.V., and A.F. Bolchakov, 1972, Elektron. Tekh. 4, 7.

Abbattista, F., M. Vallino, C. Brisi and M. Lucco-Borlera, 1988a, Mater. Res. Bull. **23**, 1509.

Abbattista, F., M. Vallino, M. Lucco Bolera and C. Brisi, 1988b, Mater. Chem. Phys. **20**, 191.

Abbattista, F., M. Vallino and D. Mazza, 1989a, Mater. Chem. Phys. **21**, 521.

Abbattista, F., C. Brisi, S. Delmastro, M. Lucco-Bolera, D. Mazza and M. Vallino, 1989b, Mater. Chem. Phys. **24**, 147.

Abbattista, F., M. Vallino and D. Mazza, 1990, Mater. Chem. Phys. **24**, 363.

Abbattista, F., D. Mazza and M. Vallino, 1991, Eur. J. Solid State Inorg. Chem. **28**, 649.

Abrahams, S.C., and J. Kalnajs, 1954, Acta Crystallogr. **7**, 838.

Ahn, B.T., T.M. Gür, R. Huggins, R. Beyers and E.M.

Engler, 1988, Mater. Res. Soc. Symp. Proc. **99**, 171.

Ahn, B.T., V.Y. Lee, R. Beyers, T.M. Gür and R.A. Huggins, 1990, Physica C **167**, 529.

Ait-Hou, A., T. Rais, C. Chatillon and M. Allibert, 1995, Ann. Chim. Fr. **20**, 345.

Akimitsu, J., S. Suzuki, M. Watanabe and H. Sawa, 1988, Jpn. J. Appl. Phys. Part 2 **27**, L1859.

Al-Mamouri, M., P.P. Edwards, C. Greaves, P.R. Slater and M. Slaski, 1995, J. Mater. Chem. **5**, 913.

Alarco, J.A., J.D. Riches and J.C. Barry, 1999, Physica C **329**, 181.

Alario-Franco, M.A., C. Chaillout, J.J. Capponi, J. Chenavas and M. Marezio, 1989, J. Less-Common Met. **150**, 117.

Alcock, C.B., and B. Li, 1990, J. Am. Ceram. Soc. **73**, 1176.

Amitin, E.B., W.G. Bessergenev, Yu.A. Kovalevskaya and I.E. Paukov, 1983, J. Chem. Thermodyn. **15**, 181.

Ammamoto, Y., H. Yamane and T. Hirai, 1996, J. Solid State Chem. **125**, 117.

Andersen, N.H., B. Lebech and H.F. Poulsen, 1990a, Physica C **172**, 31.

Andersen, N.H., B. Lebech and H.F. Poulsen, 1990b, J. Less-Common Met. **164–165**, 124.

Andersson, M., Z. Hegedűs, M. Nygren and Ö. Rapp, 1989, Physica C **160**, 65.

Andresen, P.H., H. Fjellvåg, P. Karen and A. Kjekshus, 1991, Acta Chem. Scand. **45**, 698.

Antipov, E.V., L.I. Lykova and L.M. Kovba, 1984, Zh. Neorg. Khim. **29**, 1624.

Aranda, M.A.G., and J.P. Attfield, 1993, Angew. Chem. Int. Ed. Engl. **32**, 1454.

Aride, J., S. Flandrois, M. Taibi, A. Boukhari, M. Drillon and J.L. Soubeyroux, 1989, Solid State Commun. **72**, 459.

Arjomand, M., and D.J. Machin, 1975, J. Chem. Soc. Dalton Trans. **11**, 1061.

Armstrong, A.R., and P.P. Edwards, 1992, J. Solid State Chem. **98**, 432.

Armstrong, A.R., H.S. Obhi and P.P. Edwards, 1993, J. Solid State Chem. **106**, 120.

Åsbrink, S., and L.-J. Norrby, 1970, Acta Crystallogr. B **26**, 8.

Aselage, T., and K. Keefer, 1988, J. Mater. Res. **3**, 1279.

Atake, T., A. Honda and H. Kawaji, 1991, Physica C **190**, 70.

Atanassova, Y.K., V.G. Hadjiev, P. Karen and A. Kjekshus, 1994, Phys. Rev. B **50**, 586.

Attfield, J.P., and G. Férey, 1989, J. Solid State Chem. **82**, 132.

Ausloos, M., C. Laurent, H.W. Vanderschueren, A. Rulmont and P. Tarte, 1988, Solid State Commun. **68**, 539.

Ayoub, N.Y., C.C. Almasan, E.A. Early, J.T. Markert, C.L. Seaman and M.B. Maple, 1990, Physica C **170**, 211.

Azad, A.M., O.M. Sreedharan and K.T. Jacob, 1991, J. Mater. Sci. **26**, 3374.

Azuma, M., Z. Hiroi, M. Takano, Y. Bando and Y. Takeda, 1992, Nature London **356**, 775.

Babu, T.G.N., D.J. Fish and C. Greaves, 1991, J. Mater. Chem. **1**, 677.

Baenziger, N.C., H.A. Eick, H.S. Schuldt and L. Eyring, 1961, J. Am. Chem. Soc. **83**, 2219.

Baikov, Y.M., 1995, ISSI Lett. **6**, 1.

Banks, E., S.J. La Placa, W. Kunnmann, L.M. Corliss and J.M. Hastings, 1972, Acta Crystallogr. B **28**, 3429.

Barin, I., and O. Knacke, 1973, Thermochemical Properties of Inorganic Substances (Springer, Berlin) pp. 77, 79, 163, 174, 181, 711.

Barin, I., O. Knacke and O. Kubashevski, 1977, Thermochemical Properties of Inorganic Substances, Supplement (Springer, Berlin) p. 679.

Barin, I., F. Sauert, E. Schultze-Rhonhof and W. Shu Sheng, 1993, Thermochemical Data of Pure Substances (VCH, Weinheim).

Barker, W.W., and A.F. Wilson, 1968, J. Inorg. Nucl. Chem. **30**, 1415.

Bärninghausen, H., and G. Brauer, 1962, Acta Crystallogr. **15**, 1059.

Bazuev, G.V., and V.N. Krasilnikov, 1991, Zh. Neorg. Khim. **36**, 2195.

Bednorz, J.G., and K.A. Müller, 1986, Z. Phys. B **64**, 189.

Beno, M.A., L. Soderholm, D.W. Capone II, D.G. Hinks, J.D. Jorgensen, J.D. Grace, I.K. Schuller, C.U. Segre and K. Zhang, 1987, Appl. Phys. Lett. **51**, 57.

Bernal, J.D., E. Diatlowa, J. Kasarnowsky, S. Reichstein and A.G. Ward, 1935, Z. Kristallogr. A **92**, 344.

Bertinotti, A., J. Hamman, D. Luzet and E. Vincent, 1989, Physica C **160**, 227.

Bevan, D.J.M., and J. Kordis, 1964, J. Inorg. Nucl. Chem. **26**, 1509.

Bevan, D.J.M., W.W. Barker, R.L. Martin and T.C. Parks, 1964, in: Proc. 4th Conf. on Rare Earth Research, Phoenix, AZ, ed. L. Eyring, p. 441.

Beyers, R., and B.T. Ahn, 1991, Annu. Rev. Mater. Sci. **21**, 335.

Boebinger, G.S., Y. Ando, A. Passner, T. Kimura, M. Okuya, J. Shimoyama, K. Kishio, K. Tamasaku, N. Ichikawa and S. Uchida, 1996, Phys. Rev. Lett. **77**, 5417.

Bordet, P., C. Chaillout, J. Chenavas, J.L. Hodeau, M. Marezio, J. Karpinski and E. Kaldis, 1988a, Nature London **334**, 596.

Bordet, P., J.L. Hodeau, P. Strobel, M. Marezio and A. Santoro, 1988b, Solid State Commun. **66**, 435.

Bordet, P., J.L. Hodeau, R. Argoud, J. Muller, M. Marezio, J.C. Martinez, J.J. Prejean, J. Karpinski, E. Kaldis, S. Rusiecki and B. Bucher, 1989, Physica C **162–164**, 524.

Bordet, P., S. Le Floch, C. Chaillout, F. Duc, M.F. Gorius, M. Perroux, J.J. Capponi, P. Toulemonde and J.L. Tholence, 1997, Physica C **276**, 237.

Bormann, R., and J. Nölting, 1989, Appl. Phys. Lett. **54**, 2148.

Borowiec, K., and K. Kolbrecka, 1991, J. Solid State Chem. **92**, 170.

Borowiec, K., J. Przyluski and K. Kolbrecka, 1991, J. Am. Ceram. Soc. **74**, 2007.

Böttger, G., I. Mangelschots, E. Kaldis, P. Fischer, C. Krüger and F. Fauth, 1996, J. Phys.: Condens. Matter **8**, 8889.

Böttger, G., H. Schwer, E. Kaldis and K. Bente, 1997, Physica C **275**, 198.

Boudéne, A., K. Hack, A. Mohammad, D. Neuschütz, E. Zimmermann, G. Effenberg, S. Fries, H.L. Lukas, R.A. Konetzki, R. Schmid-Fetzer, W. Huang, B. Sundman, C. Bernard, C. Colinet, A. Pasturel, A. Pisch, F. Weiss, A. Rais, M. Ganteaume, J.C. Mathieu, J. Rogez, B.B. Argent, A.T. Dinsdale and A. Watson, 1996, High Temp. Mater. Sci. **35**, 159.

Brauer, G., and K.A. Gingerich, 1960, J. Inorg. Nucl. Chem. **16**, 87.

Brauer, G., and H. Gradinger, 1954, Z. Anorg. Allg. Chem. **276**, 209.

Brauer, G., and B. Pfeiffer, 1963, J. Less-Common Met. **5**, 171.

Brese, N.E., M. O'Keeffe, R.B. Von Dreele and V.G. Young Jr, 1989, J. Solid State Chem. **83**, 1.

Bringley, J.F., B.A. Scott, S.J. La Placa, R.F. Boehme, T.M. Shaw, M.W. McElfresh, S.S. Trail and D.E. Cox, 1990a, Nature London **347**, 263.

Bringley, J.F., S.S. Trail and B.A. Scott, 1990b, J. Solid State Chem. **86**, 310.

Bringley, J.F., S.S. Trail and B.A. Scott, 1990c, J. Solid State Chem. **88**, 590.

Brosha, E.L., F.H. Garzon and I.D. Raistrick, 1994, J. Am. Ceram. Soc. **77**, 1139.

Brosha, E.L., F.H. Garzon and I.D. Raistrick, 1995, J. Am. Ceram. Soc. **78**, 1745.

Brosha, E.L., F.H. Garzon, I.D. Raistrick and P.K. Davies, 1996, J. Solid State Chem. **122**, 176.

Brosset, C., and N.-G. Vannerberg, 1956, Nature London **177**, 238.

Burger, J.P., M. Nicolas, J.N. Daou, P. Vajda, L. Dumoulin and J. Lesueur, 1989, Z. Phys. Chem. **163**, 733.

Burgers, W.G., 1933, Z. Phys. **80**, 352.

Burnham, D.A., L. Eyring and J. Kordis, 1968, J. Phys. Chem. **72**, 4424.

Caignaert, V., N. Nguyen and B. Raveau, 1990a, Mater. Res. Bull. **25**, 199.

Caignaert, V., R. Retoux, C. Michel, M. Hervieu and B. Raveau, 1990b, Physica C **167**, 483.

Caignaert, V., R. Retoux, M. Hervieu, C. Michel and B. Raveau, 1991, J. Solid State Chem. **91**, 41.

Calestani, G., F.C. Matacotta, A. Migliori, P. Nozar, L. Righi and K.A. Thomas, 1996, Physica C **261**, 38.

Carim, A.H., A.F. De Jong and D.M. De Leeuw, 1988, Phys. Rev. B **38**, 7009.

Casalta, H., P. Schleger, P. Harris, B. Lebech, N.H. Andresen, R. Liang, P. Dosanjh and W.N. Hardy, 1996, Physica C **258**, 321.

Cava, R.J., B. Batlogg, C.H. Chen, E.A. Rietman, S.M. Zahurak and D. Werder, 1987a, Nature London **329**, 423.

Cava, R.J., B. Batlogg, C.H. Chen, E.A. Rietman, S.M. Zahurak and D. Werder, 1987b, Phys. Rev. B **36**, 5719.

Cava, R.J., J.J. Krajewski, W.F. Peck Jr, B. Batlogg and L.W. Rupp Jr, 1989, Physica C **159**, 372.

Cava, R.J., B. Batlogg, R.B. Van Dover, J.J. Krajewski, J.V. Waszczak, R.M. Fleming, W.F. Peck Jr, L.W. Rupp Jr, P. Marsh, A.C.W.P. James and L.F.Schneemeyer, 1990a, Nature London **345**, 602.

Cava, R.J., A.W. Hewat, E.A. Hewat, B. Batlogg, M. Marezio, K.M. Rabe, J.J. Krajewski, W.F. Peck Jr and L.W. Rupp Jr, 1990b, Physica C **165**, 419.

Cava, R.J., A. Santoro, J.J. Krajewski, R.M. Fleming, J.V. Waszczak, W.F. Peck Jr and P. Marsh, 1990c, Physica C **172**, 138.

Cava, R.J., T. Siegrist, B. Hessen, J.J. Krajewski, W.F. Peck, B. Batlogg, H. Takagi, J.V. Waszczak, L.F.

Schneemeyer and H.W. Zandbergen, 1991, J. Solid State Chem. **94**, 170.

Cava, R.J., H.W. Zandbergen, R.B. Van Dover, J.J. Krajewski, T. Siegrist, W.F. Peck, R.S. Roth and R.J. Felder, 1994, J. Solid State Chem. **109**, 345.

Cazy, E., A. Khalfi, D.S. Smith and J.P. Bonnet, 1997, J. Mater. Res. **12**, 1451.

Ceder, G., M. Asta, W.C. Carter, M. Kraitchman, D. De Fontaine, M.E. Mann and M. Sluiter, 1990, Phys. Rev. B **41**, 8698.

Chaillout, C., S.W. Cheong, Z. Fisk, M.S. Lehmann, M. Marezio, B. Morosin and J.E. Schirber, 1989, Phys. Scripta T **29**, 97.

Chaillout, C., J. Chenavas, S.W. Cheong, Z. Fisk, M. Marezio, B. Morosin and J.E. Schirber, 1990, Physica C **170**, 87.

Chandrachood, M.R., D.E. Morris and A.P.B. Sinha, 1990, Physica C **171**, 187.

Chang, E.K., D.J.L. Hong, A. Mehta and D.M. Smyth, 1988, Mater. Lett. **6**, 251.

Chang, E.K., E.F. Ezell and J.M. Kirschner, 1990, Supercond. Sci. Technol. **3**, 391.

Chang, H., Y.Y. Ren, Y.Q. Wang, Y.Y. Xue and C.W. Chu, 1994, Physica C **228**, 383.

Chen, B., D. Walker, E.Y. Suard and B.A. Scott, 1995a, Chem. Mater. **7**, 355.

Chen, B.-H., D. Walker, E. Suard, B.A. Scott, B. Mercey, M. Hervieu and B. Raveau, 1995b, Inorg. Chem. **34**, 2077.

Chen, B.-H., D. Walker, B.A. Scott and D.B. Mitzi, 1996, J. Solid State Chem. **121**, 498.

Chen, J.W., C.F. Chen, T.C. Chang and Y.D. Yao, 1990, Physica C **165**, 287.

Cheong, S.W., J.D. Thompson and Z. Fisk, 1989, Physica C **158**, 109.

Cherry, M., M.S. Islam, J.D. Gale and C.R.A. Catlow, 1995, J. Phys. Chem. **99**, 14614.

Chessin, H., and W.C. Hamilton, 1965, Acta Crystallogr. **18**, 689.

Chmaissem, O., Q. Huang, S.N. Putilin, M. Marezio and A. Santoro, 1993, Physica C **212**, 259.

Chou, F.C., and D.C. Johnston, 1996, Phys. Rev. B **54**, 572.

Christensen, A.N., 1970, Acta Chem. Scand. **24**, 2440.

Cieplak, M.Z., G. Xiao, C.L. Chien, A. Bakshai, D. Artymovicz, W. Bryden, J.K. Stalick and J.J. Rhyne, 1990, Phys. Rev. B **42**, 6200.

Cima, M.J., J.S. Schneider, S.C. Peterson and W. Coblenz, 1988, Appl. Phys. Lett. **53**, 710.

Clarke, A.P., R.B. Schwarz and J.D. Thompson, 1991, J. Less-Common Met. **168**, 1.

Collins, B.T., W. Desisto, R. Kershaw, K. Dwight and A. Wold, 1989, J. Less-Common Met. **156**, 341.

Conder, K., J. Karpinski, E. Kaldis, S. Rusiecki and E. Jilek, 1992, Physica C **196**, 164.

Cordfunke, E.H.P., A.S. Booij and M.E. Huntelaar, 1998, J. Chem. Thermodyn. **30**, 437.

Costa, G.A., M. Ferretti, E.A. Franceschi and G.L. Olcese, 1988, Thermochim. Acta **133**, 17.

Cox, D.E., A.I. Goldman, M.A. Subramanian, J. Gopalakrishnan and A.W. Sleight, 1989, Phys. Rev. B **40**, 6998.

Cromer, D.T., 1957, J. Phys. Chem. **61**, 753.

Currie, D.B., M.T. Weller, S. Rowles and D.H. Gregory, 1990, Mater. Res. Bull. **25**, 1279.

Dąbrovski, B., K. Rogacki, J.W. Koenitzer, K.R. Poeppelmeier and J.D. Jorgensen, 1997, Physica C **277**, 24.

Dąbrowski, B., D.G. Hinks, J.D. Jorgensen and D.R. Richards, 1989a, Mater. Res. Soc. Symp. Proc. **100**, 69.

Dąbrowski, B., J.D. Jorgensen, D.G. Hinks, S. Pei, D.R. Richards, H.B. Vanfleet and D.L. Decker, 1989b, Physica C **162–164**, 99.

Dann, S.E., and M.T. Weller, 1995, J. Solid State Chem. **115**, 499.

Darracq, S., S.G. Kang, J.H. Choy and G. Demazeau, 1995, J. Solid State Chem. **114**, 88.

Daturi, M., M. Ferreti, E.A. Franceschi and M. Minguzzi, 1996, Physica C **268**, 300.

Davies, P.K., and C.M. Katzan, 1990, J. Solid State Chem. **88**, 368.

Davies, P.K., E. Caignol and T. King, 1991, J. Am. Ceram. Soc. **74**, 569.

De Leeuw, D.M., 1989, J. Less-Common Met. **150**, 95.

De Leeuw, D.M., C.A.H.A. Mutsaers, C. Langereis, H.C.A. Smoorenburg and P.J. Rommers, 1988a, Physica C **152**, 39.

De Leeuw, D.M., C.A.H.A. Mutsaers, G.P.J. Geelen, H.C.A. Smoorenburg and C. Langereis, 1988b, Physica C **152**, 508.

De Leeuw, D.M., C.A.H.A. Mutsaers, H.A.M. Van Hal, H. Verweij, A.H. Carim and H.C.A. Smoorenburg, 1988c, Physica C **156**, 126.

De Leeuw, D.M., C.A.H.A. Mutsaers, G.P.J. Geelen and C. Langereis, 1989a, J. Solid State Chem. **80**, 276.

De Leeuw, D.M., C.A.H.A. Mutsaers, R.A. Steeman, E. Frikkee and H.W. Zandbergen, 1989b, Physica C **158**, 391.

De Villiers, J.P.R., 1971, Am. Mineral. **56**, 758.

Dinsdale, A.T., 1991, Calphad **15**, 317.

Dlyachkova, T.V., N.I. Kadyrova, N.V. Talashmanova, S.I. Alyamovskii and Yu.G. Zainulin, 1991, Zh. Neorg. Khim. **36**, 1091.

Domenges, B., F. Abbattista, C. Michel, M. Vallino, L. Barbey, N. Nguyen and B. Raveau, 1993, J. Solid State Chem. **106**, 271.

Domengès, B., M. Hervieu and B. Raveau, 1993, Physica C **207**, 65.

Domengès, B., Ph. Boullay, M. Hervieu and B. Raveau, 1994, J. Solid State Chem. **108**, 219.

Dortmann, G., J. Erxmayer, S. Blässer, J. Steiger, T. Paatsch, A. Weidinger, H. Karl and B. Stritzker, 1994, Phys. Rev. B **49**, 600.

Doverspike, K., J.-H. Liu, K. Dwight and A. Wold, 1989, J. Solid State Chem. **82**, 30.

Effenberger, H., K. Mereiter and J. Zemann, 1981, Z. Kristallogr. **156**, 233.

Eick, H.A., N.C. Baenziger and L. Eyring, 1967, J. Am. Chem. Soc. **78**, 5147.

Er-Rakho, L., C. Michel and B. Raveau, 1988, J. Solid State Chem. **73**, 514.

Evans, R.C., 1964, An Introduction to Crystal Chemistry (Cambridge University Press, Cambridge) p. 273.

Eyring, L., 1979, in: Handbook on the Physics and Chemistry of Rare Earths, Vol. 3, eds K.A. Gschneidner Jr and L. Eyring (North-Holland, Amsterdam) p. 337.

Felner, I., I. Nowik, B. Brosh, D. Hechel and E.R. Bauminger, 1991, Phys. Rev. B **43**, 8737.

Ferey, G., A. Le Bail, Y. Lalignant, M. Hervieu, B. Raveau, A. Sulpice and R. Tournier, 1988, J. Solid State Chem. **73**, 610.

Filipczuk, S.W., 1991, Physica C **173**, 1.

Fisk, Z., J.D. Thompson, M.F. Hundley, R.B. Schwarz, G.H. Kwei, J.E. Schirber, S.-W. Cheong, A.S. Cooper, P. Bordet and M. Marezio, 1991, J. Less-Common Met. **168**, 31.

Fjellvåg, H., P. Karen and A. Kjekshus, 1987, Acta Chem. Scand. Ser. A **41**, 283.

Fjellvåg, H., P. Karen and A. Kjekshus, 1988a, Acta Chem. Scand. Ser. A **42**, 144.

Fjellvåg, H., P. Karen, A. Kjekshus, P. Kofstad and T. Norby, 1988b, Acta Chem. Scand. Ser. A **42**, 178.

Fjellvåg, H., P. Karen, A. Kjekshus and J.K. Grepstad, 1988c, Acta Chem. Scand. Ser. A **42**, 171.

Foëx, M., 1961, Bull. Soc. Chim. France, p. 109.

Foëx, M., and J.-P. Traverse, 1966, Bull. Soc. Fr. Mineral. Cristallogr. **89**, 184.

Fotiev, A.A., G.E. Shter, A.S. Kosmynin, I.K. Garkuchin, V.L. Balachov and A.S. Trunin, 1990, Sverkhprovodimost Fiz. Khim. Tekh. **3**, 1071.

François, M., A. Junod, K. Yvon, A.W. Hewat, J.J. Capponi, P. Strobel, M. Marezio and P. Fischer, 1988, Solid State Commun. **66**, 1117.

Frase, K.G., and D.R. Clarke, 1987, Adv. Ceram. Mat. **2**, 295.

Frase, K.G., E.G. Liniger and D.R. Clarke, 1987, J. Am. Ceram. Soc. **70**, C204.

Freund, H.-R., and H. Müller-Buschbaum, 1977a, Z. Naturforsch. B **32**, 609.

Freund, H.-R., and H. Müller-Buschbaum, 1977b, Z. Naturforsch. B **32**, 1123.

Fruchart, D., J.L. Soubeyroux, D. Tran Qui, C. Pique, C. Rillo, F. Lera, V. Orera, J. Flokstra and D.H.A. Blank, 1990, J. Less-Common Met. **157**, 233.

Fu, W.T., H.W. Zandbergen, C.J. Van der Beek and L.J. De Jongh, 1988, Physica C **156**, 133.

Fu, W.T., H.W. Zandbergen, W.G. Haije and L.J. De Jongh, 1989, Physica C **159**, 210.

Fu, W.T., Q. Xu, A.A. Verheijen, H.W. Von Ruitenbeek, H.W. Zandbergen and L.J. De Jongh, 1990, Solid State Commun. **73**, 291.

Fuertes, A., X. Obradors, J.M. Navarro, P. Gomez-Romero, N. Casañ-Pastor, F. Pérez, J. Fontcuberta, C. Miravitlles, J. Rodríguez-Carvajal and B. Martínez, 1990, Physica C **170**, 153.

Fujihara, S., N. Yoshida and T. Kimura, 1997, Physica C **288**, 158.

Gadalla, A.M., and P. Kongkachuichay, 1991, J. Mater. Res. **6**, 450.

Gadalla, A.M.M., and J. White, 1966, Trans. Br. Ceram. Soc. **65**, 181.

Gai, P.L., and E.M. McCarron III, 1990, Science **247**, 553.

Gallagher, P.K., 1987, Adv. Ceram. Mater. **2**, 632.

Gallagher, P.K., 1991, Thermochim. Acta **174**, 85.

Gallagher, P.K., G.S. Grader and H.M. O'Bryan, 1988, Mater. Res. Bull. **23**, 1491.

Gao, Y., K.L. Merkle, C. Zhang, U. Balachandran and R.B. Poeppel, 1990, J. Mater. Res. **5**, 1363.

Garbauskas, M.F., R.W. Green, R.H. Arendt and J.S. Kasper, 1988, Inorg. Chem. **27**, 871.

García-Muñoz, J.L., and J. Rodríguez-Carvajal, 1990, Phys. Lett. A **149**, 319.

Garrote, I., E. Morán, M.A. Alario-Franco, J.M. Rojo and J. Sanz, 1995, J. Mater. Chem. **5**, 1171.

Garzon, F.H., I.D. Raistrick, D.S. Ginley and J.W. Halloran, 1991, J. Mater. Res. **6**, 885.

Genoud, J.-Y., A. Mirmelstein, G. Triscone, A. Junod and J. Muller, 1995, Phys. Rev. B **52**, 12833.

Geny, J., J.K. Meen and E. Don, 1996a, in: Proc. 10th Anniversary HTS Workshop; Physics, Materials and Applications, ed. B. Batlogg (World Scientific, Singapore) p. 125.

Geny, J., J.K. Meen and D. Elthon, 1996b, J. Am. Ceram. Soc. **79**, 3083.

Geny, J., J.K. Meen and D. Elthon, 1997, J. Am. Ceram. Soc. **80**, 176.

George, E., D. Elthon and J.K. Meen, 1995, J. Am. Ceram. Soc. **78**, 3309.

Gerdanian, P., C. Picard and J.F. Marucco, 1989, Physica C **157**, 180.

Geremia, S., G. Nardin, R. Mosca, L. Randaccio and E. Zangrando, 1989, Solid State Commun. **72**, 333.

Gleixner, R.A., and Y.A. Chang, 1985, Metall. Trans. B **16**, 743.

Glückler, H., U. Binninger, C. Niedermayer, E. Recknagel and A. Weidinger, 1993, Z. Phys. Chem. **179**, 389.

Goodenough, J.B., J.-S. Zhou and J. Chan, 1993, Phys. Rev. B **47**, 5275.

Goodilin, E.A., M. Kambara, T. Umeda and Y. Shiohara, 1997a, Physica C **289**, 251.

Goodilin, E.A., M. Kambara, T. Umeda and Y. Shiohara, 1997b, Physica C **289**, 37.

Gotor, F.J., P. Odier, M. Gervais, J. Choisnet and Ph. Monod, 1993, Physica C **218**, 429.

Gotor, F.J., N. Pellerin, P. Odier, E. Cazy, J.P. Bonnet, A.R. Fert and J. Ayache, 1995, Physica C **247**, 252.

Gottschall, R., and R. Schöllhorn, 1993, Solid State Ionics **59**, 93.

Graf, T., J.L. Jorda and J. Muller, 1989, J. Less-Common Met. **146**, 49.

Graf, T., G. Triscone and J. Muller, 1990, J. Less-Common Met. **159**, 349.

Graf, T., G. Triscone, A. Junod and J. Muller, 1991, J. Less-Common Met. **170**, 359.

Grande, B., H. Müller-Buschbaum and M. Schweizer, 1977, Z. Anorg. Allg. Chem. **428**, 120.

Grasmeder, J.R., and M.T. Weller, 1990, J. Solid State Chem. **85**, 88.

Greaves, C., and P.R. Slater, 1989, Physica C **161**, 245.

Greaves, C., and P.R. Slater, 1990, Solid State Commun. **73**, 629.

Greaves, C., and P.R. Slater, 1991a, J. Mater. Chem. **1**, 17.

Greaves, C., and P.R. Slater, 1991b, Physica C **175**, 172.

Grebenyuk, V.D., I.V. Kavich, A.G. Mikolaichuk and I.T. Romanchuk, 1967, Ukr. Fiz. Zh. **12**, 876.

Gruen, D.M., W.C. Koehler and J.J. Katz, 1951, J. Am. Chem. Soc. **73**, 1475.

Gschneidner Jr, K.A., 1997, private communication (Iowa State University, Ames, IA).

Gschneidner Jr, K.A., N. Kippenhan and O.D. McMasters, 1973, Thermochemistry of the Rare Earths, IS-RIC-6 (Rare-Earth Information Center, Ames Laboratory). Available from Molycorp.

Gudmundsson, B., H. Wang, R.A. Neiser, B. Katz and H. Herman, 1990, J. Appl. Phys. **67**, 2653.

Guha, J.P., and D. Kolar, 1971, J. Mater. Sci. **6**, 1174.

Guillatt, I.F., and N.H. Brett, 1970, J. Mater. Sci. Lett. **5**, 615.

Guillaume, M., P. Allenspach, J. Mesot, B. Roessli, U. Staub, P. Fischer and A. Furrer, 1993, Z. Phys. B **90**, 13.

Gunasekaran, R.A., B. Hellebrand and P.L. Steger, 1996, Physica C **270**, 25.

Gundermann, J., and C. Wagner, 1937, Z. Phys. Chem. B **37**, 155.

Günther, W., and R. Schöllhorn, 1996, Physica C **271**, 241.

Günther, W., R. Schöllhorn, M. Epple, H. Siegle, C. Thomsen, B. Kabius, U. Poppe, J. Schubert and W. Zander, 1999, Philos. Mag. A **79** 449.

Guskos, N., V. Likodimos, C.A. Londos, V. Psycharis, C. Mitros, A. Koufodakis, H. Gamari-Seale, W. Windsch and H. Metz, 1995, J. Solid State Chem. **119**, 50.

Gutau, W., and H. Müller-Buschbaum, 1989, J. Less-Common Met. **152**, L11.

Haas, H., and E. Kordes, 1969, Z. Kristallogr. **129**, 259.

Hahn, T., ed., 1995, International Tables for Crystallography, Volume A: Space-Group Symmetry, 4th Ed. (Kluwer Academic Publishers, Dordrecht) p. 13.

Hallstedt, B., D. Risold and L.J. Gauckler, 1994, J. Phase Equilib. **15**, 483.

Han, P.D., L. Chang and D.A. Payne, 1994, Physica C **228**, 129.

Harlow, R.L., G.H. Kwei, R. Suryanarayanan and M.A. Subramanian, 1996, Physica C **257**, 125.

Harrington, I., C. Korn, S.D. Goren, H. Shaked and G. Kimmel, 1994, Physica C **226**, 255.

Haskel, D., E.A. Stern, D.G. Hinks, A.W. Mitchell, J.D. Jorgensen and J.I. Budnick, 1996, Phys. Rev. Lett. **76**, 439.

Hauck, J., B. Bischof, K. Mika, E. Janning, H. Libutzki and J. Plewa, 1993, Physica C **212**, 435.

Hauck, J., K. Bickmann and K. Mika, 1998, Supercond. Sci. Technol. **11**, 63.

Hayri, E.A., and J.Z. Larese, 1990, Physica C **170**, 239.

Heinau, M., R. Baumann, B. Nick, M. Hartweg and L. Walz, 1994, Z. Kristallogr. **209**, 418.

Heintz, J.M., and A. Dardant, 1997, Physica C **290**, 132.

Hepp, A.F., J.R. Gaier, J.J. Pouch and P.D. Hambourger, 1988, J. Solid State Chem. **74**, 433.

Hervieu, M., V. Caignaert, C. Michel, R. Retoux and B. Raveau, 1990, Microsc. Microanal. Microstruct. **1**, 109.

Hervieu, M., B. Mercey, W. Prellier, J.L. Allen, J.-F. Hamet and B. Raveau, 1996, J. Mater. Chem. **6**, 165.

Hewat, A.W., J.J. Capponi, C. Chaillout, M. Marezio and E.A. Hewat, 1987, Solid State Commun. **64**, 301.

Hiratani, M., Y. Ito, K. Miyauchi and T. Kudo, 1987, Jpn. J. Appl. Phys. Part 2 **26**, L1997.

Hiratani, M., Y. Takeda, S. Saitoh and K. Miyauchi, 1989, Jpn. J. Appl. Phys. Part 2 **28**, L769.

Hiratani, M., S. Saito, M. Suga and T. Sowa, 1990, Solid State Commun. **75**, 425.

Hiroi, Z., 1996, J. Solid State Chem. **123**, 223.

Hiroi, Z., M. Takano, Y. Takeda, R. Kanno and Y. Bando, 1988, Jpn. J. Appl. Phys. Part 2 **27**, L580.

Hiroi, Z., M. Azuma, M. Takano and Y. Bando, 1991, J. Solid State Chem. **95**, 230.

Hiroi, Z., M. Takano, M. Azuma and Y. Takeda, 1993, Nature London **364**, 315.

Hjorth, M., and J. Hyldtoft, 1990, Acta Chem. Scand. **44**, 516.

Hodges, J.P., P.R. Slater, P.P. Edwards, C. Greaves, M. Slaski, G. Van Tendeloo and S. Amelinckx, 1996, Physica C **260**, 249.

Hodorowicz, E., S.A. Hodorowicz and H.A. Eick, 1989, Physica C **158**, 127.

Hodorowicz, E., S.A. Hodorowicz and H.A. Eick, 1992a, J. Alloys & Compounds **181**, 445.

Hodorowicz, E., S.A. Hodorowicz and H.A. Eick, 1992b, Physica C **198**, 19.

Hodorowicz, S.A., A. Lasocha, W. Lasocha and H.A. Eick, 1988, J. Solid State Chem. **75**, 270.

Hodorowicz, S.A., J. Czerwonka and H.A. Eick, 1990, J. Solid State Chem. **88**, 391.

Holtermann, C., and P. Laffitte, 1939, C.R. Acad. Sci. Paris **208**, 517.

Hor, P.H., R.L. Meng, Y.Q. Wang, L. Gao, Z.J. Huang, J. Bechtold, K. Forster and C.W. Chu, 1987, Phys. Rev. Lett. **58**, 1891.

Hor, P.H., H.H. Feng, Z.G. Li, J.F. DiCarlo, S. Bhavaraju and A.J. Jacobson, 1996, J. Phys. Chem. Solids **57**, 1061.

Hou, C.J., A. Manthiram, L. Rabenberg and J.B. Goodenough, 1990, J. Mater. Res. **5**, 9.

Huang, J., and W. Sleight, 1990, Physica C **169**, 169.

Huang, Q., P. Karen, V.L. Karen, A. Kjekshus, J.W. Lynn, A.D. Mighell, N. Rosov and A. Santoro, 1992a, Phys. Rev. B **45**, 9611.

Huang, Q., R.J. Cava, A. Santoro, J.J. Krajewski and W.F. Peck, 1992b, Physica C **193**, 196.

Huang, Q., S.A. Sunshine, R.J. Cava and A. Santoro, 1993, J. Solid State Chem. **102**, 534.

Huang, T.C., J.B. Torrance, A.I. Nazzal and Y. Tokura, 1989, Powder Diffr. 4, 152.

Hultgren, R., P.D. Desai, D.T. Hawkins, M. Gleiser, K.K. Kelley and D.D. Wagman, 1973, Selected Values of the Thermodynamic Properties of the Elements (ASM, Metals Park, OH).

Hundley, M.F., J.D. Thompson, S.-W. Cheong, Z. Fisk, R.B. Schwarz and J.E. Schirber, 1989, Phys. Rev. B **40**, 5251.

Hundley, M.F., J.D. Thompson, S.W. Cheong, Z. Fisk and J.E. Schirber, 1990, Phys. Rev. B **41**, 4062.

Ichihashi, T., S. Iijima, Y. Kubo and J. Tabuchi, 1988, Jpn. J. Appl. Phys. Part 2 **27**, L1187.

Ichinose, A., T. Wada, Y. Yaegashi, H. Yamauchi and S. Tanaka, 1990, Jpn. J. Appl. Phys. Part 2 **29**, L426.

Idemoto, Y., and K. Fueki, 1989, Jpn. J. Appl. Phys. Part 1 **29**, 2729.

Idemoto, Y., I. Oyagi and K. Fueki, 1992, Physica C **195**, 269.

Idemoto, Y., H. Tokue and K. Fueki, 1993, Denki Kagakuoyobi Kogyo Butsuri Kagaku **61**, 753.

Ikeda, N., Z. Hiroi, M. Azuma, M. Takano and Y. Bando, 1993, Physica C **210**, 367.

Ikuma, Y., M. Yoshimura and S. Kabe, 1990, J. Mater. Res. **5**, 17.

Ilynych, N., S. Zaitzeva, G. Moiseev, J. Šesták and N. Vatolin, 1995, Thermochim. Acta **266**, 285.

Iqbal, Z., F. Reidinger, A. Bose, N. Cipollini, T.J. Taylor, H. Eckhardt, B.L. Ramakrishna and E.W. Ong, 1988, Nature London **331**, 326.

Isawa, K., Y. Yaegashi, M. Komatsu, M. Nagano, S. Sudo, M. Karppinen and H. Yamauchi, 1997, Phys. Rev. B **56**, 3457.

Ivanov-Emin, B.N., and J.N. Medvedev, 1990, Zh. Neorg. Khim. **35**, 300.

Iwahara, H., 1992, in: Proton Conductors. Solids, membranes and gels – materials and devices, ed. P. Colomban (Cambridge University Press, Cambridge) p. 122.

Izakovich, E.N., N.A. Zheltova, Y.M. Korolev, Z.D. Sokolovskaya, V.N. Spector and M.L. Khidekel, 1989, Phys. Status Solidi **116**, K13.

Izumi, F., E. Takayama-Muromachi, A. Fujimori, T. Kamiyama, H. Asano, J. Akimitsu and H. Sawa, 1989, Physica C **158**, 440.

Jacob, K.T., and V. Varghese, 1995, J. Mater. Chem. **5**, 1059.

Jacob, K.T., and Y. Waseda, 1994, J. Phase Equilib. **15**, 401.

Jacob, K.T., T. Mathews and J.P. Harja, 1993, Metall. Trans. A **24**, 1655.

Jacob, K.T., P.M. Raj and Y. Waseda, 1995, J. Phase Equilib. **16**, 113.

Jacobson, A.J., B.C. Tofield and B.E.F. Fender, 1972, Acta Crystallogr. B **28**, 956.

James, A.C.W.P., S.M. Zahurak and D.W. Murphy, 1989, Nature London **338**, 240.

JANAF, 1971, JANAF Thermochemical Tables, 2nd Ed., NSRDS-NBS 37 (US Government Printing Office, Washington, DC).

Jin, S., H.M. O'Bryan, P.K. Gallagher, T.H. Tiefel, R.J. Cava, R.A. Fastnacht and G.W. Kammlott, 1990, Physica C **165**, 415.

Johnson, J.R., M. Suenaga, P. Thompson and J.J. Reilly, 1989, Z. Phys. Chem. **163**, 721.

Jorda, J.L., and M.T.S. Cohen-Adad, 1991, J. Less-Common Met. **171**, 127.

Jørgensen, C.K., R. Pappalardo and E. Rittershaus, 1965, Z. Naturforsch. A **20**, 54.

Jorgensen, J.D., H.-B. Schüttler, D.G. Hinks, D.W. Capone, H.K. Zhang, M.B. Brodsky and D.J. Scalapino, 1987, Phys. Rev. Lett. **58**, 1024.

Jorgensen, J.D., B.W. Veal, A.P. Paulikas, L.J. Nowicki, G.W. Crabtree, H. Claus and W.K. Kwok, 1990a, Phys. Rev. B **41**, 1863.

Jorgensen, J.D., S. Pei, P. Lightfoot, D.G. Hinks, B.W. Veal, B. Dąbrowski, A.P. Paulikas and R. Kleb, 1990b, Physica C **171**, 93.

Jorgensen, J.D., S. Pei, P. Lightfoot, H. Shi, A.P. Paulikas and B.W. Veal, 1990c, Physica C **167**, 571.

Kajitani, T., K. Kusaba, M. Kikuchi, Y. Syono and M. Hirabyashi, 1988, Jpn. J. Appl. Phys. Part 2 **27**, L354.

Kajitani, T., K. Hiraga, S. Hosoya, T. Fukuda, K. Oh-ishi, M. Kikuchi, Y. Syono, S. Tomiyoshi, M. Takahashi and Y. Muto, 1990, Physica C **169**, 227.

Kaldis, E., P. Fischer, A.W. Hewat, E.A. Hewat, J. Karpinski and S. Rusiecki, 1989, Physica C **159**, 668.

Kaldis, E., J. Röhler, E. Liarokapis, N. Poulakis, K. Conder and P.W. Loeffen, 1997, Phys. Rev. Lett. **79**, 4894.

Kale, G.M., 1992, Supercond. Sci. Technol. **5**, 333.

Kale, G.M., 1996, J. Solid State Chem. **125**, 13.

Kale, G.M., and D.J. Fray, 1995a, J. Am. Ceram. Soc. **78**, 1882.

Kale, G.M., and D.J. Fray, 1995b, J. Electron. Mater. **24**, 1981.

Kale, G.M., and K.T. Jacob, 1989a, Solid State Ionics **34**, 247.

Kale, G.M., and K.T. Jacob, 1989b, Chem. Mater. **1**, 515.

Kang, Z.C., and L. Eyring, 1997, J. Alloys & Compounds **249**, 206.

Karen, P., and A. Kjekshus, 1991, J. Solid State Chem. **94**, 298.

Karen, P., and A. Kjekshus, 1994a, J. Am. Ceram. Soc. **77**, 547.

Karen, P., and A. Kjekshus, 1994b, J. Solid State Chem. **112**, 73.

Karen, P., and A. Kjekshus, 2000, unpublished.

Karen, P., O. Braaten, H. Fjellvåg and A. Kjekshus, 1990a, in: AMSAHTS '90, NASA Conf. Publ. 3100, eds L.H. Bennett, Y. Flom and K. Moorjani (NASA) p. 117.

Karen, P., H. Fjellvåg, O. Braaten, A. Kjekshus and H. Bratsberg, 1990b, Acta Chem. Scand. **44**, 994.

Karen, P., H. Fjellvåg, A. Kjekshus and A.F. Andresen, 1991a, J. Solid State Chem. **93**, 163.

Karen, P., H. Fjellvåg, A. Kjekshus and A.F. Andresen, 1991b, J. Solid State Chem. **92**, 57.

Karen, P., H. Fjellvåg and A. Kjekshus, 1992a, J. Solid State Chem. **97**, 257.

Karen, P., A. Kjekshus and A.F. Andresen, 1992b, Acta Chem. Scand. **96**, 1059.

Karen, P., P.H. Andresen and A. Kjekshus, 1992c, J. Solid State Chem. **101**, 48.

Karen, P., A. Kjekshus, Q. Huang, J.W. Lynn, N. Rosov, I. Natali Sora, V.L. Karen, A.D. Mighell and A. Santoro, 1998, J. Solid State Chem. **136**, 21.

Karen, P., A. Kjekshus, Q. Huang, V. Karen, A.D. Mighell and A. Santoro, 2000, Physica C **336**, 279.
Karpinski, J., E. Kaldis, E. Jilek, S. Rusiecki and B. Bucher, 1988, Nature London **336**, 660.
Karpinski, J., E. Kaldis, S. Rusiecki, E. Jilek, P. Fischer, P. Bordet, C. Chaillout, J. Chenavas, J.L. Hodeau and M. Marezio, 1989a, J. Less-Common. Met. **150**, 129.
Karpinski, J., S. Rusiecki, B. Bucher, E. Kaldis and E. Jilek, 1989b, Physica C **161**, 618.
Karpinski, J., S. Rusiecki, E. Kaldis, B. Bucher and E. Jilek, 1989c, Physica C **160**, 449.
Karpinski, J., E. Kaldis and S. Rusiecki, 1989d, J. Less-Common Met. **150**, 207.
Karpinski, J., S. Rusiecki, E. Kaldis and E. Jilek, 1990, J. Less-Common. Met. **164–165**, 3.
Karpinski, J., H. Schwer, G.I. Meijer, K. Conder, E.M. Kopnin and C. Rossel, 1997, Physica C **274**, 99.
Karppinen, M., H. Yamauchi, H. Suematsu, K. Isawa, M. Nagano, R. Itti and O. Fukunaga, 1997, J. Solid State Chem. **130**, 213.
Katsuyama, S., Y. Ueda and K. Kosuge, 1989, Mater. Res. Bull. **24**, 603.
Katsuyama, S., Y. Ueda and K. Kosuge, 1990, Physica C **165**, 404.
Kawabata, S., H. Hoshizaki, N. Kawahara, H. Enami, T. Shinohara and T. Imura, 1990, Jpn. J. Appl. Phys. Part 2 **29**, L1490.
Kawashima, T., Y. Matsui and E. Takayama-Muromachi, 1996, Physica C **257**, 313.
Kazakov, S.M., S. Pachot, E.M. Kopnin, S.N. Putilin, J.J. Capponi, P.G. Radaelli and M. Marezio, 1997, Physica C **276**, 139.
Kebukawa, T., Y. Kumaki, K. Fujiwara, Y. Tatsumi, H. Taimatsu and H. Kaneko, 1994, Jpn. J. Appl. Phys. Part 2 **33**, L507.
Kedrovskii, O.V., I.V. Kovtunenko, E.V. Kiseleva and A.A. Bundel, 1967, Russ. J. Phys. Chem. **41**, 205.
Keller-Berest, F., S. Metgert, G. Collin, P. Monod and M. Ribault, 1989, Physica C **161**, 150.
Khasanova, N.R., F. Izumi, Z. Hiroi, M. Takano, Q. Huang and A. Santoro, 1996, Acta Crystallogr. C **52**, 2381.
Kiemel, R., W. Schäfer, S. Kemmler-Sack, G. Kruschel and B. Elschner, 1988, J. Less-Common Met. **143**, L11.
Kikkawa, S., N. Kato, N. Taya, M. Tada and F. Kanamaru, 1995, J. Am. Ceram. Soc. **78**, 1387.
Kikuchi, M., E. Ohshima, M. Kikuchi, T. Atou and Y. Syono, 1994, Physica C **232**, 263.
Kikuchi, M., F. Izumi, M. Kikuchi, E. Ohshima, Y. Morii, Y. Shimojo and Y. Syono, 1995, Physica C **247**, 183.
Kim, J.-S., and D.R. Gaskell, 1994, J. Am. Ceram. Soc. **77**, 753.
Kinoshita, K., and T. Yamada, 1992, Nature London **357**, 313.
Kinoshita, K., F. Izumi, T. Yamada and H. Asano, 1992, Phys. Rev. B **45**, 5558.
Kipka, R., and H. Müller-Buschbaum, 1977, Z. Naturforsch. B **32**, 121.
Kirby, P.B., M.R. Harrison, W.G. Freeman, I. Samuel and M.J. Haines, 1987, Phys. Rev. B **36**, 8315.
Kishio, K., J. Shimoyama, T. Hasegawa, K. Kitazawa and K. Fueki, 1987, Jpn. J. Appl. Phys. **26**(Part 2), L1228.
Kishio, K., K. Suzuki, T. Hasegawa, T. Yamamoto, K. Kitazawa and K. Fueki, 1989, J. Solid State Chem. **82**, 192.
Kissick, J.L., C. Greaves, P.P. Edwards, V.M. Cherkashenko, E.Z. Kurmayev, S. Bartkowski and M. Neumann, 1997, Phys. Rev. B **56**, 2831.
Klibanow, D., K. Sujata and T.O. Mason, 1988, J. Am. Ceram. Soc. **71**, C-267.
Klinkova, L.A., N.V. Barkovskii, D.I. Batova, A.I. Kolyubakin and S.A. Shevchenko, 1992, Supercond. Phys. Chem. Tech. **5**, 1247.
Kobayashi, K., 1990, J. Am. Ceram. Soc. **73**, 146.
Kobayashi, N., Z. Hiroi and M. Takano, 1997, J. Solid State Chem. **132**, 274.
Köhler, B.U., and M. Jansen, 1986, Z. Anorg. Allg. Chem. **543**, 73.
Komatsu, T., O. Tanaka, K. Matusita, M. Takata and T. Yamashita, 1988, Jpn. J. Appl. Phys. Part 2 **27**, L1025.
Konetzki, R., R. Schmid-Fetzer, S. Fries and H.L. Lukas, 1994, Z. Metallkd. **85**, 748.
Konetzki, R.A., and R. Schmid-Fetzer, 1992, J. Solid State Chem. **99**, 58.
Konetzki, R.A., and R. Schmid-Fetzer, 1995, J. Solid State Chem. **114**, 420.
Kopyto, M., and K. Fitzner, 1996, J. Mater. Sci. **31**, 2797.
Kopyto, M., and K. Fitzner, 1997, J. Solid State Chem. **134**, 85.
Kopyto, M., and K. Fitzner, 1999, J. Solid State Chem. **144**, 118.
Kordis, J., and L. Eyring, 1968, J. Phys. Chem. **72**, 2030.

Koscheeva, S.N., V.A. Fotiev, A.A. Fotiev and V.G. Zubkov, 1990, Izv. Akad. Nauk. S.S.S.R., Neorg. Mater. **26**, 1491.

Kosmynin, A.C., G.E. Shter, I.K. Garkushin, A.S. Trunin, V.A. Balashov and A.A. Fotiev, 1990, Sverkhprovodimost Fiz. Khim. Tekh. **3**, 1870.

Kovba, L.M., L.I. Lykova and E.V. Antipov, 1983, Zh. Neorg. Khim. **28**, 724.

Krekels, T., O. Milat, G. Van Tendeloo, J. Van Landuyt and S. Amelinckx, 1993a, Physica C **210**, 439.

Krekels, T., O. Milat, G. Van Tendeloo, S. Amelinckx, T.G.N. Babu, A.J. Wright and C. Greaves, 1993b, J. Solid State Chem. **105**, 313.

Krüger, C., W. Reichelt, A. Almes, U. König, H. Oppermann and H. Scheler, 1992, J. Solid State Chem. **96**, 67.

Kubat-Martin, K.A., E. Garcia and D.E. Peterson, 1990, Physica C **172**, 75.

Kubat-Martin, K.A., G.H. Kwei, A.C. Lawson and D.E. Peterson, 1992, J. Solid State Chem. **100**, 130.

Kuzmicheva, G.M., V.V. Luparev and E.P. Khlybov, 1996, Zh. Neorg. Khim. **41**, 181.

Kwestroo, W., H.A.M. Van Hal and C. Langereis, 1974, Mater. Res. Bull. **9**, 1631.

La Placa, S.J., J.F. Bringley, B.A. Scott and D.E. Cox, 1993, Acta Crystallogr. C **49**, 1415.

La Placa, S.J., J.F. Bringley, B.A. Scott and D.E. Cox, 1995, J. Solid State Chem. **118**, 170.

Laffez, P., X. Wu, S. Adachi, H. Yamauchi and N. Môri, 1994, Physica C **233**, 373.

LaGraff, J.R., E.C. Behrman, J.A.T. Taylor, F.J. Rotella, J.D. Jorgensen, L.Q. Wang and P.G. Mattocks, 1989, Phys. Rev. B **39**, 347.

Lamberti, V.E., M.A. Rodriguez, J.D. Trybulski, A. Navrotsky and H.B. Liu, 1997, Chem. Mater. **9**, 932.

Lamoreaux, R.H., D.L. Hildenbrand and L. Brewer, 1987, J. Phys. Chem. Ref. Data **16**, 419.

Lanckbeen, A., C. Legros, J.F. Marucco and R. Deltour, 1994, Physica C **221**, 53.

Lapinskas, S., E.E. Tornau, A. Rosengren and P. Schleger, 1995, Phys. Rev. B **52**, 15565.

Lappas, A., K. Prassides, A.R. Armstrong and P.P. Edwards, 1993, Inorg. Chem. **32**, 383.

Lawanier, J.P., J.K. Meen and D. Elthon, 1996, J. Am. Ceram. Soc. **79**, 533.

Lee, J.Y., J.S. Kim, J.S. Swinnea and H. Steinfink, 1990, J. Solid State Chem. **84**, 335.

Lenglet, M., K. Kartouni, J. Machefert, J.M. Claude, P. Steinmetz, E. Beauprez, J. Heinrich and N. Gelati, 1995, Mater. Res. Bull. **30**, 393.

Li, J.Q., H. Chen and Z.X. Zhao, 1994, Physica C **233**, 40.

Li, S., E.A. Hayri, K.V. Ramanujachary and M. Greenblatt, 1988, Phys. Rev. B **38**, 2450.

Liang, R., and T. Nakamura, 1988, Jpn. J. Appl. Phys. **27**(Part 2), L1277.

Licci, F., P. Tissot and H.J. Scheel, 1989, J. Less-Common Met. **150**, 201.

Lightfoot, P., S. Pei, J.D. Jorgensen, X.-X. Tang, A. Manthiram and J.B. Goodenough, 1990a, Physica C **169**, 15.

Lightfoot, P., S. Pei, J.D. Jorgensen, X.-X. Tang, A. Manthiram and J.B. Goodenough, 1990b, Physica C **169**, 464.

Lin, S.-H., and N.-L. Wu, 1996, Physica C **262**, 33.

Lin, Y.P., J.E. Greedan, A.H. O'Reilly, J.N. Reimers, C.V. Stager and M.L. Post, 1990, J. Solid State Chem. **84**, 226.

Lindemer, T.B., and E.D. Specht, 1995, Physica C **255**, 81.

Lindemer, T.B., J.F. Hunley, J.E. Gates, A.L. Sutton Jr, J. Brynestad, C.R. Hubbard and P.K. Gallagher, 1989, J. Am. Ceram. Soc. **72**, 1775.

Lindemer, T.B., C.R. Hubbard and J. Brynestad, 1990, Physica C **167**, 312.

Lindemer, T.B., F.A. Washburn, C.S. MacDougall, R. Feenstra and O.B. Cavin, 1991, Physica C **178**, 93.

Lindemer, T.B., E.D. Specht, C.S. MacDougall, G.M. Taylor and S.L. Pye, 1993, Physica C **216**, 99.

Lindemer, T.B., E.D. Specht, P.M. Martin and M.L. Flitcroft, 1995, Physica C **255**, 65.

Liu, R.S., J.R. Cooper, J.W. Loram, W. Zhou, W. Lo, P.P. Edwards, W.Y. Liang and L.S. Chen, 1990, Solid State Commun. **76**, 679.

Lobo, R.C., C. Greaves and F.J. Berry, 1990, J. Solid State Chem. **88**, 513.

Longo, J.M., and P.M. Raccah, 1973, J. Solid State Chem. **6**, 526.

Longo, V., D. Minichelli and F. Ricciardiello, 1981, Sci. Ceram. **11**, 171.

Lopato, L.M., 1976, Ceramurgia Int. **2**, 18.

Lopato, L.M., L.I. Lugin and A.V. Shevchenko, 1970, Dopov. Akad. Nauk Ukr.S.S.R., Ser. B, Ukr. Khim. Zh. **32**, 535.

Lopato, L.M., I.M. Maister and A.V. Shevchenko, 1972, Izvest. Akad. Nauk S.S.S.R., Ser. Neorg. Mater. **8**, 861.

Lopato, L.M., L.I. Lugin and A.V. Shevchenko, 1973, Ukr. Khim. Zh. **39**, 142.

Ludwig, H.A., W.H. Fietz and H. Wühl, 1992, Physica C **197**, 113.

Machida, M., K. Yasnoka, K. Equchi and H. Arai, 1991, J. Solid State Chem. **91**, 176.

Maciejewski, M., A. Baiker, K. Conder, C. Krüger, J. Karpinski and E. Kaldis, 1994, Physica C **227**, 343.

MacManus, J.L., D.J. Fray and J.E. Evetts, 1991, Physica C **184**, 172.

MacManus-Driscoll, J.L., 1997, Adv. Mater. **9**, 457.

MacManus-Driscoll, J.L., J.C. Bravman and R.B. Beyers, 1995, Physica C **241**, 401.

Maeno, Y., T. Nojima, Y. Aoki, M. Kato, K. Hoshino, A. Minami and T. Fujita, 1987, Jpn. J. Appl. Phys. Part 2 **26**, L774.

Maier, J., and H.L. Tuller, 1993, Phys. Rev. B **47**, 8105.

Maier, J., P. Murugaraj and G. Pfundtner, 1990, Solid State Ionics **40/41**, 802.

Maignan, A., M. Hervieu, C. Michel and B. Raveau, 1993, Physica C **208**, 116.

Maiorova, A.F., S.N. Mudretsova, M.L. Kovba, A.S. Monaenkova and A.A. Popova, 1993, Physica C **218**, 137.

Malik, S.K., R. Prasad, N.C. Soni, K. Adhikari and W.B. Yelon, 1996, Physica B **224**, 562.

Maljuk, A.N., G.A. Emelchenko and A.V. Kosenko, 1996, J. Alloys & Compounds **234**, 52.

Manako, T., Y. Shimakawa, Y. Kubo, T. Satoh and H. Igarashi, 1988, Physica C **156**, 315.

Mangelschots, I., M. Mali, J. Roos, H. Zimmermann, D. Brinkmann, S. Rusiecki, J. Karpinski, E. Kaldis and E. Jilek, 1990a, Physica C **172**, 57.

Mangelschots, I., M. Mali, J. Roos, H. Zimmermann, D. Brinkmann, J. Karpinski, E. Kaldis and S. Rusiecki, 1990b, J. Less-Common Met. **164–165**, 78.

Manthiram, A., S.-J. Lee and J.B. Goodenough, 1988, J. Solid State Chem. **73**, 278.

Marimuthu, K.N., M.S. Ramachandra Rao and U.V. Varadaraju, 1997, Physica C **280**, 327.

Martin, K.A.K., Z. Fisk and R.R. Ryan, 1988, Acta Crystallogr. C **44**, 1518.

Marucco, J.-F., P. Garoche and G. Collimu, 1988, Rev. Int. Hautes Temp. Refract. Fr. **24**, 231.

Massalski, T.B., ed., 1990, Binary Alloy Phase Diagrams, 2nd Ed. (ASM International).

Mastromonaco, M.D., I. Barbariol and A. Cocco, 1969, Ann. Chim. Rome **59**, 465.

Matacotta, F.C., G. Calestani, A. Migliori, P. Nozar, P. Scardi, O. Greco, P. Ricci, A. Tomasi and K.A. Thomas, 1997, J. Solid State Chem. **129**, 165.

Mathews, T., and K.T. Jacob, 1992, Metall. Trans. A **23**, 3325.

Mathews, T., J.P. Hajra and K.T. Jacob, 1993, Chem. Mater. **5**, 1669.

Matskevich, N.I., and R.W. McCallum, 1999, Thermochim. Acta **342**, 41.

Matsushita, Y., Y. Oyama, M. Hasegawa and H. Takei, 1994, J. Solid State Chem. **114**, 289.

Matveev, A.T., Y. Matsui, S. Yamaoka and E. Takayama-Muromachi, 1997, Physica C **288**, 185.

Mazza, D., M. Vallino, F. Abbattista and S. Delmastro, 1990, Mater. Chem. Phys. **25**, 385.

McCarron, E.M., M.A. Subramanian, J.C. Calabrese and R.L. Harlow, 1988, Mater. Res. Bull. **23**, 1355.

McCarron III, E.M., M.K. Crawford and J.B. Parise, 1989, J. Solid State Chem. **78**, 192.

McCarty, K.F., J.E. Schirber, S.W. Cheong and Z. Fisk, 1991, Phys. Rev. B **43**, 7883.

McGullough, J.D., 1950, J. Am. Chem. Soc. **72**, 1386.

McGullough, J.D., and J.D. Britton, 1952, J. Am. Chem. Soc. **74**, 5225.

McKinnon, W.R., M.L. Post, L.S. Selwyn and G. Pleizier, 1988, Phys. Rev. B **38**, 6543.

Meuffels, P., R. Naeven and H. Wenzl, 1989, Physica C **161**, 539.

Mey, S., K. Hack, K. Itagaki, P.J. Spencer and D. Neuschutz, 1990, Calphad **14**, 175.

Miceli, P.F., J.M. Tarascon, L.H. Greene, P. Barboux, F.J. Rotella and J.D. Jorgensen, 1988, Phys. Rev. B **37**, 5932.

Michel, C., and B. Raveau, 1982, J. Solid State Chem. **43**, 73.

Michel, C., and B. Raveau, 1984, Rev. Chim. Miner. **21**, 407.

Michel, C., L. Er-Rakho and B. Raveau, 1981, J. Solid State Chem. **39**, 161.

Michel, C., L. Er-Rakho, M. Hervieu, J. Pannetier and B. Raveau, 1987, J. Solid State Chem. **68**, 143.

Migliori, A., M. Gemmi, G. Calestani, D. Belletti, F.C. Matacotta, C. Dionigi and P. Nozar, 1999, Physica C **328**, 89.

Mikirticheva, G.A., V.I. Schitova, L.Yu. Grabovenko, D.I. Romanov and R.G. Grebenschikov, 1991, Zh. Neorg. Khim. **36**, 562.

Milat, O., G. Van Tendeloo, S. Amelinckx, T.G.N. Babu and C. Greaves, 1992, J. Solid State Chem. **101**, 92.

Millet, P., R. Enjalbert, J. Galy, C. Faulmann, P. Cassoux, H. Rakoto and S. Askénazy, 1988, C.R. Acad. Sci. Paris **306**, 407.

Minenkov, Yu.F., N.I. Matskevich, Yu.G. Stenin and P.P. Samoilov, 1996, Thermochim. Acta **278**, 1.

Mingmei, W., S. Qiang, H. Gang, R. Yufang and W. Hongyiang, 1994, J. Solid State Chem. **110**, 389.

Miyatake, T., S. Gotoh, N. Koshizuka and S. Tanaka, 1989, Nature London **341**, 41.

Miyazaki, Y., H. Yamane, T. Kajitani, Y. Oku, K. Hiraga, Y. Morii, K. Fuchizaki, S. Funahashi and T. Hirai, 1992a, Physica C **191**, 434.

Miyazaki, Y., H. Yamane, N. Ohnishi, Y. Kajitani, K. Hiraga, Y. Morii, S. Funahashi and T. Hirai, 1992b, Physica C **198**, 7.

Miyazaki, Y., H. Yamane and T. Hirai, 1992c, Physica C **198**, 53.

Mizuno, F., H. Masuda, I. Hirabayashi, S. Tanaka, M. Hasegawa and U. Mizutani, 1990, Nature London **345**, 788.

Mizusaki, J., H. Tagawa, K. Hayakawa and K. Hirano, 1995, J. Am. Ceram. Soc. **78**, 1781.

Moiseev, G.K., S.I. Zaitseva, J. Šesták and N.A. Vatolin, 1993, Thermochim. Acta **216**, 301.

Moiseev, G.K., N.A. Vatolin and J. Šesták, 1994a, Thermochim. Acta **237**, 391.

Moiseev, G.K., N.A. Vatolin and J. Šesták, 1994b, Thermochim. Acta **237**, 401.

Moiseev, G.K., N.A. Vatolin and J. Šesták, 1994c, Thermochim. Acta **237**, 409.

Mokhtari, M., C. Perrin, M. Sergent, E. Furet, J.-F. Halet, J.-Y. Saillard, E. Ressouche and P. Burlet, 1995, Solid State Commun. **93**, 487.

Monayenkova, A.S., A.A. Popova, V.V. Kuzmenko, J. Karpinski and K. Conder, 1998, J. Chem. Thermodyn. **30**, 81.

Montzka, S.A., B.M. Hybertson, R.M. Barkley and R.E. Sievers, 1991, J. Mater. Res. **6**, 891.

Moreau, J.M., 1968, Mater. Res. Bull. **3**, 427.

Moret, R., J.P. Pouget and G. Collin, 1987, Europhys. Lett. **4**, 365.

Morgan, P.E.D., D.E. Partin, B.L. Chamberland and M. O'Keeffe, 1996, J. Solid State Chem. **121**, 33.

Morosin, B., E.L. Venturini, J.E. Schirber, R.G. Dunn and P.P. Newcomer, 1995, Physica C **241**, 181.

Morris, D.E., N.G. Asmar, J.H. Nickel, R.L. Sid and J.Y.T. Wei, 1989a, Physica C **159**, 287.

Morris, D.E., J.H. Nickel, J.Y.T. Wei, N.G. Asmar, J.S. Scott, U.M. Scheven, C.T. Hultgren, A.G. Markelz, J.E. Post, P.J. Heaney, D.R. Veblen and R.M. Hazen, 1989b, Phys. Rev. B. **39**, 7347.

Morris, D.E., N.G. Asmar, J.Y.T. Wei, J.H. Nickel, R.L. Sid and J.S. Scott, 1989c, Phys. Rev. B **40**, 11406.

Morris, D.E., P.K. Narwankar, A.P.B. Sinha, K. Takano and V. Shum, 1990a, Appl. Phys. Lett. (USA) **57**, 715.

Morris, D.E., P.K. Narwankar and A.P.B. Sinha, 1990b, Physica C **169**, 7.

Müller-Buschbaum, H., 1968, Z. Anorg. Allg. Chem. **358**, 138.

Müller-Buschbaum, H., and A. Boehlke, 1987, Z. Anorg. Allg. Chem. **553**, 212.

Müller-Buschbaum, H., and P.-H. Graebner, 1971, Z. Anorg. Allg. Chem. **386**, 158.

Müller-Buschbaum, H., and M. Scheikowski, 1990, Z. Anorg. Allg. Chem. **591**, 181.

Müller-Buschbaum, H., and C. Teske, 1969, Z. Anorg. Allg. Chem. **369**, 255.

Müller-Buschbaum, H., and H.G. von Schnering, 1965, Z. Anorg. Allg. Chem. **340**, 232.

Müller-Buschbaum, H., and W. Wollschläger, 1975, Z. Anorg. Allg. Chem. **414**, 76.

Murphy, D.W., S. Sunshine, R.B. Van Dover, R.J. Cava, B. Batlogg, S.M. Zahurak and L.F. Schneemeyer, 1987, Phys. Rev. Lett. **58**, 1888.

Nagarajan, R., S. Ayyappan and C.N.R. Rao, 1994, Physica C **220**, 373.

Nakata, H., J. Akimitsu, S. Katano, T. Minami, N. Ogita and M. Udagawa, 1995, Physica C **255**, 157.

Nakazawa, Y., M. Ishikawa, T. Takabatake, K. Koga and K. Terakura, 1987, Jpn. J. Appl. Phys. Part 2 **26**, L796.

Natali Sora, I., Q. Huang, J.W. Lynn, N. Rosov, P. Karen, A. Kjekshus, V.L. Karen, A.D. Mighell and A. Santoro, 1994, Phys. Rev. B **49**, 3465.

Navrotsky, A., 1994, Pure Appl. Chem. **66**, 1759.

Neukirch, V., C.T. Simmons, P. Sladeczek, C. Laubschat, O. Strebel, G. Kaindl and D.D. Sarma, 1988, Europhys. Lett. **5**, 567.

Newsam, J.M., A.J. Jacobson, D.P. Goshorn, J.T. Lewandowski, D.B. Mitzi, A. Kapitulnik, D. Xie and W.B. Yelon, 1989, Solid State Ionics **32/33**, 1064.

Nguyen, N., L. Er-Rakho, C. Michel, J. Choisnet and B. Raveau, 1980, Mater. Res. Bull. **15**, 891.

Nguyen, N., J. Choisnet and B. Raveau, 1982, Mater. Res. Bull. **17**, 567.

Nguyen, N., F. Studer and B. Raveau, 1983, J. Phys. Chem. Solids **44**, 389.

Niedermayer, C., H. Glückler, R. Simon, A. Golnik, M. Rauer, E. Recknagel, A. Weidinger, J.I. Budnick, W. Paulus and R. Schöllhorn, 1989, Phys. Rev. B **40**, 11386.

Niggli, P., 1922, Z. Kristallogr. **57**, 253.

Nobumasa, H., K. Shimizu, Y. Kitano, M. Tanaka and T. Kawai, 1989, Jpn. J. Appl. Phys. Part 2 **28**, L1948.

Norby, T., 1990, Solid State Ionics **40/41**, 857.

Norrestam, R., M. Hjorth and J.-O. Bovin, 1988, Z. Kristallogr. **183**, 245.

Norrestam, R., M. Nygren and J.-O. Bovin, 1991, Angew. Chem. Int. Ed. Engl. **30**, 864.

Noto, K., H. Morita, K. Watanabe, T. Murakami, Y. Koyanagi, I. Yoshi, I. Sato, H. Sugawara, N. Kobyashi, H. Fujimori and Y. Muto, 1987, Physica B **148**, 239.

Nowotny, J., and M. Rekas, 1990a, J. Am. Ceram. Soc. **73**, 1048.

Nowotny, J., and M. Rekas, 1990b, J. Am. Ceram. Soc. **73**, 1054.

Nowotny, J., M. Rekas and W. Weppner, 1990, J. Am. Ceram. Soc. **73**, 1040.

O'Bryan, H.M., P.K. Gallagher, R.A. Laudise, A.J. Caporaso and R.C. Sherwood, 1989, J. Am. Ceram. Soc. **72**, 1298.

O'Connor, B.H., and T.M. Valentine, 1969, Acta Crystallogr. B **25**, 2140.

Oka, K., and H. Unoki, 1990, Jpn. J. Appl. Phys. Part 2 **29**, L909.

Okada, H., M. Takano and Y. Takeda, 1990, Physica C **166**, 111.

Okai, B., 1990, Jpn. J. Appl. Phys. Part 2 **29**, L2180.

Okamoto, H., 1997, J. Phase Equilib. **18**, 400.

O'Keeffe, M., and J.-O. Bovin, 1978, Am. Mineral. **63**, 180.

Olafsen, A., and H. Fjellvåg, 1999, J. Mater. Chem. **9**, 2697.

Oniyama, E., P.G. Wahlbeck, D.E. Peterson, J.Y. Coulter and E.J. Peterson, 1997, Physica C **288**, 151.

Ono, A., 1992, Physica C **198**, 287.

Ono, A., and S. Horiuchi, 1995, Physica C **247**, 319.

Oota, A., Y. Sasaki, Y. Kiyoshima, M. Ohkubo and T. Hioki, 1987, Jpn. J. Appl. Phys., Part 2 **26**, L2091.

Opila, E.J., and H.L. Tuller, 1994, J. Am. Ceram. Soc. **77**, 2727.

Ostapchenko, E.P., 1956, Izvest. Akad. Nauk S.S.S.R., Ser. Fiz. **20**, 1105.

Ottosson, M., A. Hårsta and J.-O. Carsson, 1991, J. Electrochem. Soc. **138**, 778.

Otzschi, K., and Y. Ueda, 1993, J. Solid State Chem. **107**, 149.

Otzschi, K., A. Hayashi, Y. Fujiwara and Y. Ueda, 1993, J. Solid State Chem. **105**, 573.

Otzschi, K., K. Koga and Y. Ueda, 1995, J. Solid State Chem. **115**, 490.

Ourmazd, A., and J.C.H. Spence, 1987, Nature London **329**, 425.

Paletta, E., and H. Müller-Buschbaum, 1968, J. Inorg. Nucl. Chem. **30**, 1425.

Pankajavalli, R., and O.M. Sreedharan, 1988, J. Mater. Sci. Lett. **7**, 714.

Pankajavalli, R., and O.M. Sreedharan, 1996, J. Mater. Sci. **31**, 3137.

Pankratz, L.B., 1982, Thermodynamic Properties of Elements and Oxides, Bulletin 672 (US Bureau of Mines).

Parise, J.B., and E.M. McCarron III, 1989, J. Solid State Chem. **83**, 188.

Park, M., M.J. Kramer, K.W. Dennis and R.W. McCallum, 1996, Physica C **259**, 43.

Parker, V.B., 1995, J. Phys. Chem. Ref. Data **24**, 1023.

Parks, M.E., A. Navrotsky, K. Mocala, E. Takayama-Muromachi, A. Jacobson and P.K. Davies, 1989, J. Solid State Chem. **83**, 218.

Patrakeev, M.V., I.A. Leonidov, A.A. Lakhtin and V.L. Kozhevnikov, 1995a, J. Solid State Chem. **120**, 146.

Patrakeev, M.V., I.A. Leonidov and V.L. Kozhevnikov, 1995b, Solid State Ionics **82**, 5.

Paulus, E.F., G. Miehe, H. Fuess, I. Yehia and V. Löchner, 1991, J. Solid State Chem. **90**, 17.

Paulus, E.F., G. Wltschek and H. Fuess, 1994, Z. Kristallogr. **209**, 586.

Pederzolli, D.R., and P. Attfield, 1998, J. Solid State Chem. **136**, 137.

Pei, S., A.P. Paulikas, B.W. Veal and J.D. Jorgensen, 1990, Acta Crystallogr. C **46**, 1986.

Peitola, K., M. Karppinen, H. Rundölf, R. Tellgren, H. Yamauchi and L. Niinistö, 1999, J. Mater. Chem. **9**, 2599.

Perrin, C., O. Peña, M. Sergent, P. Christensen, G. Fonteneau and J. Lucas, 1989, Supercond. Sci. Technol. **2**, 35.

Petriček, S., N. Bukovec and P. Bukovec, 1992, J. Solid State Chem. **99**, 58.

Petrů, F., F. Kůtek and J. Šatava, 1966, Collect. Czech. Chem. Commun. **31**, 4459.

Pieczulewski, C.N., J.E. McAdams and T.O. Mason, 1990, J. Am. Ceram. Soc. **73**, 3088.

Plackowski, T., C. Sułkovski, Z. Bukowski, D. Włosewicz and K. Rogacki, 1995, Physica C **254**, 331.

Porat, O., I. Riess and H.L. Tuller, 1992, Physica C **192**, 60.

Porath, D., A. Grayevsky, N. Kaplan, D. Shaltiel, U. Yaron and E. Walker, 1994, J. Alloys & Compounds **204**, 79.

Pörschke, E., P. Meuffels and H. Wenzl, 1992, J. Phys. Chem. Solids **53**, 73.

Poulsen, H.F., M. von Zimmermann, J.R. Schneider, N.H. Andersen, P. Schleger, J. Madsen, R. Hadfield, H. Casalta, R. Liang, P. Dosanjh and W. Hardy, 1996, Phys. Rev. B **53**, 15335.

Prado, F., A. Caneiro and A. Sequis, 1998, Physica C **295**, 235.

Prakash, S., and J.P. Burger, 1993, Z. Phys. Chem. **181**, 159.

Prandtl, W., and G. Rieder, 1938, Z. Anorg. Allg. Chem. **238**, 225.

Przybyło, W., and K. Fitzner, 1996, Arch. Metall. **41**, 141.

Przybyło, W., B. Onderka and K. Fitzner, 1996, J. Solid State Chem. **126**, 38.

Psycharis, V., C. Mitros, A. Koufoudakis, H. Gamari-Seale, D. Niarchos, N. Kalitsounakis, N. Poulakis, D. Palles and E. Liarokapis, 1996, Physica C **267**, 211.

Qian, M., E.A. Stern, Y. Ma, R. Ingalls, M. Sarikaya, B. Thiel, R. Kurosky, C. Han, L. Hutter and I. Aksay, 1989, Phys. Rev. B **39**, 9192.

Raghavan, S., 1996, J. Alloys & Compounds **232**, L20.

Ramanujachary, K.V., M. Greaney, R.L. Fuller and M. Greenblatt, 1991, J. Solid State Chem. **93**, 263.

Ramdas, S., K.C. Patil and C.N.R. Rao, 1970, J. Chem. Soc. A, p. 64.

Ramirez, A.P., R. Jager-Waldau and T. Siegrist, 1986, Z. Phys. B **64**, 189.

Ramírez-Castellanos, J., Y. Matsui, T. Kawashima, E. Takayama-Muromachi and A.I. Kirkland, 1996, Physica C **262**, 285.

Ramírez-Castellanos, J., Y. Matsui, M. Isobe and E. Takayama-Muromachi, 1997, J. Solid State Chem. **133**, 434.

Rangavittal, N., G.N. Subbana, T.N. Guru Row and C.N.R. Rao, 1995, J. Solid State Chem. **114**, 95.

Rapp, R.P., A. Mehta, J. DiCarlo and A. Navrotsky, 1994, J. Mater. Res. **9**, 8.

Raveau, B., C. Michel, B. Mercey, J.F. Hamet and M. Hervieu, 1995, J. Alloys & Compounds **229**, 134.

Raven, M.S., E.E. Inameti, Y.M. Wan and B.G. Murray, 1992, Vacuum **43**, 127.

Raychandhuri, A.K., K. Sreedhar, K.P. Rajeev, R.A. Mohan Ram, P.A. Ganguly and C.N.R. Rao, 1987, Philos. Mag. Lett. **56**, 29.

Renevier, H., J.L. Hodeau, P. Bordet, J.J. Capponi, M. Marezio, F. Baudelet, H. Tolentino, G. Tourillon, E. Dartige, A. Fontaine, J.C. Martinez and J.J. Prejean, 1989, Physica C **162–164**, 51.

Renevier, H., J.L. Hodeau, T. Fournier, P. Bordet and M. Marezio, 1990, Physica C **172**, 183.

Rey, M.-J., P. Dehaudt, J. Joubert and A.W. Hewat, 1990, Physica C **167**, 162.

Rial, C., E. Morán, M.A. Alario-Franco, U. Amador and N.H. Andersen, 1996, Physica C **270**, 51.

Rian, G., 1992, Dissertation (NTH Trondheim). IUK-report 1992:65.

Risold, D., B. Hallstedt and L.J. Gauckler, 1995, J. Am. Ceram. Soc. **78**, 2655.

Risold, D., B. Hallstedt and L.J. Gauckler, 1997a, J. Am. Ceram. Soc. **80**, 527.

Risold, D., B. Hallstedt and L.J. Gauckler, 1997b, J. Am. Ceram. Soc. **80**, 537.

Roberts, H.S., and F.H. Smyth, 1921, J. Am. Chem. Soc. **43**, 1061.

Robertson, A.D., P.V.P.S.S. Sastry and A.R. West, 1996, J. Eur. Ceram. Soc. **16**, 637.

Rodriguez, M.A., J.J. Simmins and R.L. Snyder, 1993, J. Mater. Res. **8**, 415.

Rodriguez, M.A., R.L. Snyder, J.J. Simmins, Y.M. Guo, R.A. Condrate Sr, F.J. Rotella and J.D. Jorgensen, 1995, J. Appl. Cryst. **28**, 429.

Rodriguez, M.A., A. Navrotsky and F. Licci, 2000, Physica C **329** 88.

Roth, R.S., and S.J. Schneider, 1960, J. Res. Natl. Bur. Stand., Sect. A **64**, 309.

Roth, R.S., K.L. Davis and J.R. Dennis, 1987, Adv. Ceram. Mater. **2**, 303.

Roth, R.S., C.J. Rawn, F. Beech, J.D. Whitler and J.O. Anderson, 1988, in: Ceramic Superconductors 2, Research Update, ed. M.F. Yan (American Ceramic Society, Westerville, OH) p. 13.

Roth, R.S., C.J. Rawn, J.J. Ritter and B.P. Burton, 1989a, J. Am. Ceram. Soc. **72**, 1545.

Roth, R.S., C.J. Rawn, J.D. Whitler, C.K. Chiang and W.K. Wong-Ng, 1989b, J. Am. Ceram. Soc. **72**, 395.

Roth, R.S., C.J. Rawn, B.P. Burton and F. Beech, 1990, J. Res. Natl. Bur. Stand. **95**, 291.

Roth, R.S., N.M. Hwang, C.J. Rawn, B.P. Burton and J.J. Ritter, 1991, J. Am. Ceram. Soc. **74**, 2148.

Ruck, K., D. Eckert, G. Krabbes, M. Wolf and H.-K. Müller, 1998, J. Solid State Chem. **141**, 378.

Rudenko, V.S., and A.G. Boganov, 1971, Izvest. Akad. Nauk S.S.S.R., Neorg. Mater. 7, 108.
Rudnyi, E.B., 1996, Russ. J. Phys. Chem. **70**, 913.
Rudnyi, E.B., and G.F. Voronin, 1996, Calphad **20**, 297.
Rudnyi, E.B., V.V. Kuzmenko and G.F. Voronin, 1998, J. Phys. Chem. Ref. Data **27**, 855.
Sakurai, T., T. Wada, N. Suziki, S. Koriyama, T. Miyatake, H. Yamauchi, N. Koshizuka and S. Tanaka, 1990, Phys. Rev. B **42**, 8030.
Saltykova, I.A., N.N. Baranova, V.P. Barchatov, I.N. Dubrovina and V.F. Balakirev, 1990, Sverkhprovodimost Fiz. Khim. Tekh. **3**, 1250.
Sastry, P.V.P.S.S., A.D. Robertson, E.E. Lachowski, A. Coats and A.R. West, 1995, J. Mater. Chem. **5**, 1931.
Sastry, R.L.N., P.N. Mehrotra and C.N.R. Rao, 1966, J. Inorg. Nucl. Chem. **28**, 2167.
Sata, T., K. Sakai and S. Tashiro, 1991, J. Am. Ceram. Soc. **74**, 1445.
Sato, S., and I. Nakada, 1989, Acta Crystallogr. C **45**, 523.
Satterfield, C.N., and T.W. Stein, 1954, Ind. Eng. Chem. **46**, 1734.
Sawa, H., K. Obara, J. Akimitsu, Y. Matsui and S. Horiuchi, 1989b, J. Phys. Soc. Jpn. **58**, 2252.
Sawa, K., S. Suzuki, M. Watanabe, J. Akimitsu, H. Matsubara, H. Watabe, S. Uchida, K. Kokusho, H. Asano, F. Izumi and E. Takayama-Muromachi, 1989a, Nature London **337**, 347.
Sawyer, J.O., B.G. Hyde and L. Eyring, 1965, Coll. Int. C.N.R.S., p. 1190.
Sawyer, J.O., P. Caro and L. Eyring, 1972, Monatsh. Chem. **102**, 333.
Scheel, H.J., and F. Licci, 1991, Thermochim. Acta **174**, 115.
Schleger, P., W.N. Hardy and B.X. Yang, 1991, Physica C **176**, 261.
Schleger, P., H.F. Hadfield, H. Casalta, N.H. Andresen, H.F. Poulsen, M. Zimmermann, J.R. Schneider, R. Liang, P. Dosanjh and W.N. Hardy, 1995, Phys. Rev. Lett. **74**, 1446.
Schmid, R., 1983, Metall. Trans. B **14**, 473.
Schneider, S.J., and R.S. Roth, 1960, J. Res. Natl. Bur. Stand. Ser. A **64**, 317.
Schulze, A.-R., and H. Müller-Buschbaum, 1980a, Z. Anorg. Allg. Chem. **471**, 59.
Schulze, A.-R., and H. Müller-Buschbaum, 1980b, Z. Anorg. Allg. Chem. **461**, 48.
Schulze, K., P. Majewski, B. Hettich and G. Petzow, 1990, Z. Metallk. **81**, 836.
Schumacher, E.E., 1926, J. Am. Chem. Soc. **48**, 396.
Schwitzgebel, G., and St. Junk, 1989, Ber. Bunsenges. Phys. Chem. **93**, 1356.
Segre, C.U., B. Dąbrowski, D.G. Hinks, K. Zhang, J.D. Jorgensen, M.A. Beno and I.K. Schuller, 1987, Nature London **329**, 227.
Seiji, N., S. Adachi and H. Yamauchi, 1994, Physica C **227**, 377.
Selvduray, G., C. Zhang, U. Balachandran, Y. Gao, K.L. Merkle, H. Shi and R.B. Poeppel, 1992, J. Mater. Res. 7, 283.
Señaris-Rodriguez, M.A., A.M. Chippindale, A. Várez, E. Morán and M.A. Alario-Franco, 1991, Physica C **172**, 477.
Serquis, A., F. Prado and A. Caneiro, 1996, Physica C **273**, 163.
Šesták, J., J. Kamarád, P. Holba, A. Tříska, E. Pollert and M. Nevřiva, 1991, Thermochim. Acta **174**, 99.
Shaked, H., J.D. Jorgensen, J. Faber Jr, D.G. Hinks and B. Dąbrowski, 1989, Phys. Rev. B **39**, 7363.
Shamrai, V.F., Y.V. Efimov, M.E. Saveleva, G.M. Leitus, E.A. Myasnikova, T.M. Frolova and A.M. Postnikov, 1992, Supercond. Phys. Chem. Tech. **5**, 1647.
Shaviv, R., E.F. Westrum Jr, R.J.C. Brown, M. Sayer, X. Yu and R.D. Weir, 1990, J. Chem. Phys. **92**, 6794.
Shaw, T.M., D. Dimos, P.E. Batson, A.G. Schrott, D.R. Clarke and P.R. Duncombe, 1990, J. Mater. Res. **5**, 1176.
Shen, L., P.A. Salvador and T.O. Mason, 1994, J. Am. Ceram. Soc. **77**, 81.
Shi, F., W.J. Bresser, M. Zhang, Y. Wu, D. McDaniel and P. Boolchand, 1996, Phys. Rev. B **54**, 6776.
Shibata, H., K. Kinoshita and T. Yamada, 1994, Physica C **232**, 181.
Shimakawa, Y., J.D. Jorgensen, J.F. Mitchell, B.A. Hunter, H. Shaked, D.G. Hinks, R.L. Hitterman, Z. Hiroi and M. Takano, 1994, Physica C **228**, 73.
Shimpo, R., and Y. Nakamura, 1990, J. Jpn Inst. Met. Sendai **54**, 549.
Sieglaff, C.L., and L. Eyring, 1957, J. Am. Chem. Soc. **79**, 3024.
Siegrist, T., L.F. Schneemeyer, J.V. Waszczak, N.P. Singh, R.L. Opila, B. Batlogg, L.W. Rupp and D.W. Murphy, 1987, Phys. Rev. B **36**, 8365.
Siegrist, T., S.M. Zahurak, D.W. Murphy and R.S. Roth, 1988, Nature London **334**, 231.
Siegrist, T., R.S. Roth, C.J. Rawn and J.J. Ritter, 1990, Chem. Mater. **2**, 192.

Simon, A., K. Trübenbach and H. Borrmann, 1993, J. Solid State Chem. **106**, 128.

Skakle, J.M.S., and A.R. West, 1994a, J. Am. Ceram. Soc. **77**, C2199.

Skakle, J.M.S., and A.R. West, 1994b, J. Mater. Chem. **4**, 1745.

Skakle, J.M.S., and A.R. West, 1994c, Physica C **220**, 187.

Skakle, J.M.S., and A.R. West, 1994d, Physica C **227**, 336.

Skakle, J.M.S., and A.R. West, 1995a, J. Mater. Chem. **5**, 765.

Skakle, J.M.S., and A.R. West, 1995b, Physica C **241**, 191.

Skakle, J.M.S., and A.R. West, 1996, Physica C **261**, 105.

Skakle, J.M.S., A. Tempelton, E.E. Lachowski and A.R. West, 1996, Physica C **260**, 137.

Skakle, J.M.S., E.E. Lachowski, R.I. Smith and A.R. West, 1997, Phys. Rev. B **55**, 15228.

Skolis, Yu.Ya., and S.V. Kitsenko, 1989, Zh. Fiz. Khim. **63**, 1132.

Skolis, Yu.Ya., F.S. Pashin, M.L. Kovba and S.V. Kitsenko, 1991, Zh. Fiz. Khim. **65**, 13.

Slater, P.R., P.P. Edwards, C. Greaves, I. Gameson, M.G. Francescomi, J.P. Hodges, M. Al-Mamouri and M. Slaski, 1995, Physica C **241**, 151.

Smith, A.J., and A.J.E. Welch, 1960, Acta Crystallogr. **13**, 653.

Smith, M.G., A. Manthiram, J. Zhou, J.B. Goodenough and J.T. Markert, 1991, Nature London **351**, 549.

Smyth, D.M., 1989, in: Selected Topics in High Temperature Chemistry, Defect Chemistry of Solids, eds O. Johannesen and A.G. Anderson (Elsevier, Amsterdam) p. 1.

Soderholm, L., G.L. Goodman, U. Welp, C.W. Williams and J. Bolender, 1989, Physica C **161**, 252.

Sonntag, R., D. Hohlwein, T. Brückel and G. Collin, 1991, Phys. Rev. Lett. **66**, 1497.

Stalick, J., and W. Wong-Ng, 1990, Mater. Lett. **9**, 401.

Stavola, M., D.M. Krol, L.F. Schneemeyer, S.A. Sunshine, J.V. Waszczak and S.G. Kosinski, 1989, Phys. Rev. B **39**, 287.

Steiner, C., M. Andratschke and K.-J. Range, 1996, Z. Anorg. Allg. Chem. **622**, 1314.

Steinfink, H., J.S. Swinnea, Z.T. Sui, H.M. Hsu and J.B. Goodenough, 1987, J. Am. Chem. Soc. **109**, 3348.

Straube, E., D. Hohlwein and F. Kubanek, 1998, Physica C **295**, 1.

Strobel, P., J.J. Capponi, M. Marezio and P. Monod, 1987, Solid State Commun. **64**, 513.

Subasri, R., and O.M. Sreedharan, 1998, J. Alloys & Compounds **274**, 153.

Subasri, R., R. Pankajavalli and O.M. Sreedharan, 1997, Physica C **281**, 85.

Sunshine, S.A., L.F. Schneemeyer, T. Siegrist, D.C. Douglass, J.V. Waszczak, R.J. Cava, E.M. Gyorgy and D.W. Murphy, 1989, Chem. Mater. **1**, 331.

Sutija, D.P., T. Norby and P. Björnbom, 1995, Solid State Ionics **77**, 167.

Suzuki, R.O., S. Okada, T. Oishi and K. Ono, 1990, Mater. Trans. JIM **31**, 1078.

Suzuki, R.O., P. Bohac and L.J. Gauckler, 1992, J. Am. Ceram. Soc. **75**, 2833.

Suzuki, R.O., P. Bohac and L.J. Gauckler, 1994, J. Am. Ceram. Soc. **77**, 41.

Tagami, M., M. Kambara, T. Umeda and Y. Shiohara, 1998, J. Mater. Res. **13**, 118.

Takabatake, T., and M. Ishikawa, 1988, Solid State Commun. **66**, 413.

Takano, M., Y. Takeda, H. Okada, M. Miyamoto and T. Kusaka, 1989, Physica C **159**, 375.

Takayama-Muromachi, E., and A. Navrotsky, 1993, J. Solid State Chem. **106**, 349.

Takayama-Muromachi, E., F. Izumi, Y. Uchida, K. Kato and H. Asano, 1989a, Physica C **159**, 634.

Takayama-Muromachi, E., Y. Uchida, M. Kobayashi and K. Kato, 1989b, Physica C **158**, 449.

Takita, K., H. Katoh, H. Akinaga, M. Nishino, T. Ishigaki and H. Asano, 1988, Jpn. J. Appl. Phys. Part 2 **27**, L57.

Tallon, J.L., D.M. Pooke, R.G. Buckley, M.R. Presland and F.J. Blunt, 1990a, Phys. Rev. B **41**, 7220.

Tallon, J.L., D.M. Pooke, M.P. Staines, M.E. Bowden, N.E. Flower, R.G. Buckley, M.R. Presland and R.L. Davis, 1990b, Physica C **171**, 61.

Tamaru, S., and K. Siomi, 1932, Z. Phys. Chem. Stoechiom. Verwandschaftsl. A **159**, 227.

Tan, Z., J.I. Budnick, W.Q. Chen and D.L. Brewe, 1990, Phys. Rev. B **42**, 4808.

Tarascon, J.M., L.H. Greene, P. Barrboux, W.R. McKinnon, G.W. Hull, T.P. Orlando, K.A. Delin, S. Foner and E.J. McNiff Jr, 1987, Phys. Rev. B **36**, 8393.

Tatsuki, T., T. Tamura, Y. Moriwaki, X.-J. Wu, S. Adachi and K. Tanabe, 1996, Physica C **270**, 327.

Teske, C.L., and H. Müller-Buschbaum, 1969a, Z. Anorg. Allg. Chem. **371**, 325.

Teske, C.L., and H. Müller-Buschbaum, 1969b, Z. Anorg. Allg. Chem. **370**, 134.
Teske, C.L., and H. Müller-Buschbaum, 1970a, Z. Anorg. Allg. Chem. **379**, 234.
Teske, C.L., and H. Müller-Buschbaum, 1970b, Z. Anorg. Allg. Chem. **379**, 113.
Teske, C.L., and H. Müller-Buschbaum, 1972, Z. Naturforsch. B **27**, 296.
Tétot, R., C. Giaconia, A. Finel and G. Boureau, 1993, Phys. Rev. B **48**, 10090.
Thiele, E., and P.K. Davies, 1991, J. Am. Ceram. Soc. **74**, 1011.
Thompson, J.G., B.G. Hyde, R.L. Withers, J.S. Anderson, J.D. Fitzgerald, J. Bitmead, M.S. Paterson and A.M. Stewart, 1987, Mater. Res. Bull. **22**, 1715.
Thompson, J.G., J.D. Fitz Gerald, R.L. Withers, P.J. Barlow and J.S. Anderson, 1989, Mater. Res. Bull. **24**, 505.
Thompson, J.G., T.J. White, R.L. Withers, J.D. Fitz Gerald, P.J. Barlow and S.J. Collcott, 1990, Mater. Forum **14**, 27.
Thomsen, C., R. Liu, A. Wittlin, L. Genzel, M. Cardona, W. König, M.V. Cabañas and E. García, 1988, Solid State Commun. **65**, 219.
Tokura, T., H. Takagi and S. Uchida, 1989, Nature London **337**, 345.
Tokura, Y., J.B. Torrance, A.I. Nazzal, T.C. Huang and C. Ortiz, 1987, J. Am. Chem. Soc. **109**, 7555.
Torkar, K., H. Krischner and E. Will, 1969, Monatsh. Chem. **100**, 825.
Trari, M., J. Toepfer, J.-P. Doumerc, M. Pouchard, A. Ammar and P. Hagenmuller, 1994, J. Solid State Chem. **111**, 104.
Tsang, C., J.K. Meen and D. Elthon, 1995, J. Am. Ceram. Soc. **78**, 1863.
Tsuda, K., M. Tanaka and J. Akimitsu, 1989, Jpn. J. Appl. Phys. Part 2 **28**, L1552.
Tyagi, A.K., S.J. Patwe, U.R.K. Rao and R.M. Iyer, 1988, Solid State Commun. **65**, 1149.
Uehara, M., H. Nakata and J. Akimitsu, 1993, Physica C **216**, 453.
Ukei, K., T. Shishido and T. Fukuda, 1994, Acta Crystallogr. B **50**, 42.
Ullmann, B., K. Heinemann, H.U. Krebs, H.C. Freyhardt and E. Schwarzmann, 1988, Physica C **153–155**, 872.
Umarji, A.M., P. Somasundaram, L. Ganapathi and C.N.R. Rao, 1988, Solid State Commun. **66**, 177.
Vahlas, C., and T. Besmann, 1992, J. Am. Ceram. Soc. **75**, 2679.
Vallino, M., D. Mazza and F. Abbattista, 1991, J. Less-Common Met. **170**, 83.
Valo, J., R. Matero, M. Leskelä, M. Karppinen, L. Niinistö and J. Lindén, 1995, J. Mater. Chem. **5**, 875.
Vaughey, J.T., J.P. Thiel, E.F. Hasty, D.A. Groenke, B. Dąbrowski, D.G. Hinks and A.W. Mitchell, 1991, Chem. Mater. **3**, 935.
Verweij, H., 1988, Solid State Commun. **67**, 109.
Verweij, H., and L.F. Feiner, 1990, Phys. Rev. B **41**, 4302.
Vettier, C., P. Burlet, J.Y. Henry, M.J. Jurgens, G. Lapertot, L.P. Regnault and J. Rossat-Mignod, 1989, Phys. Scripta T **29**, 110.
Vigeland, B.E., 1996, Dissertation (NTH Trondheim). IUK-report 1996:83.
Villars, P., A. Prince and H. Okamoto, 1995, Handbook of Ternary Alloy Phase Diagrams (ASM International).
Voronin, G.F., 1994a, Zh. Neorg. Khim. **39**, 1776.
Voronin, G.F., 1994b, in: Materials and Crystallographic Aspects of HT_c-Superconductivity, ed. E. Kaldis (Kluwer Academic Publishers, Dordrecht), p. 585.
Voronin, G.F., 2000, Pure Appl. Chem. **72**, 463.
Voronin, G.F., and S.A. Degterov, 1991, Physica C **176**, 387.
Voronin, G.F., and S.A. Degterov, 1994, J. Solid State Chem. **110**, 50.
Voronin, G.F., and S.A. Degtyarev, 1993, Zh. Phys. Khim. **67**, 1351.
Wada, T., A. Ichinose, H. Yamauchi and S. Tanaka, 1990a, Physica C **171**, 344.
Wada, T., A. Ichinose, Y. Yaegashi, H. Yamauchi and S. Tanaka, 1990b, Phys. Rev. B **41**, 1984.
Wada, T., T. Kaneko, A. Ichinose, Y. Yaegashi, S. Ikegawa, H. Yamauchi and S. Tanaka, 1990c, Jpn. J. Appl. Phys. Part 2 **29**, L43.
Wada, T., N. Suzuki, A. Ichinose, Y. Yaegashi, H. Yamauchi and S. Tanaka, 1990d, Jpn. J. Appl. Phys. Part 2 **29**, L915.
Wahlbeck, P.G., D.L. Myers and J.C. Ho, 1989, Physica C **161**, 175.
Wang, G., S.-J. Hwu, S.N. Song, J.B. Ketterson, L.D. Marks, K.R. Poeppelmeier and T.O. Mason, 1987, Adv. Ceram. Mat. **2**, 313.
Wang, H.H., A.M. Kini, H.-C.I. Kao, E.H. Appelman, A.R. Thompson, R.E. Botto, K.D. Carlson, J.M. Williams, M.Y. Chen, J.A. Schlueter, B.D. Gates, S.L. Hallenbeck and A.M. Despotes, 1988, Inorg. Chem. **27**, 5.

Wang, J., I. Monot, M. Hervieu, J. Provost and G. Desgardin, 1996, Supercond. Sci. Technol. **9**, 69.
Wang, Y., B.A. Scott, B.-H. Chen and D. Walker, 1997, Physica C **275**, 52.
Wang, Y.Y., H. Zhang, V.P. Dravid, L.D. Marks, P.D. Han and D.A. Payne, 1995, Physica C **255**, 247.
Watanabe, T., K. Kinoshita, H. Shibata, A. Matsuda, Y. Asano and T. Yamada, 1988, Jpn. J. Appl. Phys. Part 2 **27**, L1245.
Webb, A.W., E.F. Skelton, S.B. Qadri, E.R. Carpenter Jr, M.S. Osofsky, R.J. Soulen and V. LeTourneau, 1989, Physica C **162–164**, 899.
Webb, A.W., E.F. Skelton, S.B. Quadri and E.R. Carpenter, 1993, J. Solid State Chem. **102**, 519.
Weiss, M., W. Günther and R. Schöllhorn, 1998, Physica C **304** 156.
Weller, M.T., and D.R. Lines, 1989, J. Solid State Chem. **82**, 21.
Whitler, D.J., and R.S. Roth, eds, 1991, Phase Diagrams for High-T_c Superconductors (The American Ceramic Society, Westerwille, OH).
Wilhelm, H., C. Cros, F. Arrouy and G. Demazeau, 1996, C.R. Acad. Sci. Paris **322**, 437.
Williams, R.K., D.M. Kroeger, P.M. Martin, J.R. Mayotte, E.D. Specht and J. Brynestad, 1994, J. Appl. Phys. **76**, 3673.
Wolf, L., and H. Schwab, 1964, J. Prakt. Chem., 4. Reihe **24**, 293.
Wong-Ng, W., and L.P. Cook, 1996, Physica C **273**, 135.
Wong-Ng, W., and L.P. Cook, 1998, J. Res. Natl. Inst. Stand. Technol. **103**, 379.
Wong-Ng, W., and B. Paretzkin, 1991, Powder Diffr. **6**, 187.
Wong-Ng, W., and R.S. Roth, 1994, Physica C **233**, 97.
Wong-Ng, W., B. Paretzkin and E.R. Fuller Jr, 1990a, J. Solid State Chem. **85**, 117.
Wong-Ng, W., F.W. Gayle, D.L. Kaiser, S.F. Watkins and F.R. Fronczek, 1990b, Phys. Rev. B **41**, 4220.
Wong-Ng, W., L.P. Cook, B. Paretzkin, M.D. Hill and J.K. Stalick, 1994, J. Am. Ceram. Soc. **77**, 2354.
Wong-Ng, W., A. Melamud, L.H. Bennet and R.E. Watson, 1999, Physica C **322**, 177.
Wong-Ng, W., J. Dillingham and L.P. Cook, 2000, J. Solid State Chem. **149**, 333.
Wong-Ng, W.K., K.L. Davis and R.S. Roth, 1988, J. Am. Ceram. Soc. **71**, C64.
Wrigge, F.W., and K. Meisel, 1932, Z. Anorg. Allg. Chem. **203**, 312.
Wu, H., M.J. Kramer, K.W. Dennis and R.W. McCallum, 1997, Physica C **290**, 252.
Wu, X.-J., P. Laffez, H. Yamauchi and N. Môri, 1994, Physica C **228**, 292.
Xiao, G., M.Z. Cieplak, A. Gavrin, F.H. Streitz, A. Bakhshai and C.L. Chien, 1988, Phys. Rev. Lett. **60**, 1446.
Xing, X., Z. Qiao and S. Wei, 1996, Met. Mater. Trans. B**27**, 973.
Xiong, X., Q. Zhu, Z.G. Li, S.C. Moss, H.H. Feng, P.H. Hor, D.E. Cox, S. Bhavaraju and A.J. Jacobson, 1996, J. Mater. Res. **11**, 2121.
Xu, Y., R.L. Sabatini, A.R. Moodenbaugh and M. Suenaga, 1988, Phys. Rev. B **38**, 7084.
Yakhou, F., V. Plakhty, A. Stratilatov, P. Burlet, J.P. Lauriat, E. Elkaim, J.Y. Henry, M. Vlasov and S. Moshkin, 1996, Physica C **261**, 315.
Yamaguchi, S., K. Terabe, A. Saito, S. Yahagi and Y. Iguchi, 1988, Jpn. J. Appl. Phys. **27**(Part 2), L179.
Yamaura, K., Z. Hiroi and M. Takano, 1994, Physica C **229**, 183.
Yang, C.Y., X.-Q. Yang, S.M. Heald, J.J. Reilly, T. Skotheim, A.R. Moodenbaugh and M. Suenaga, 1987, Phys. Rev. B **36**, 8798.
Yang, K.Y., H. Homma, R. Lee, R. Bhadra, M. Grimsditch, S.D. Bader, J.P. Locquet, Y. Bruynseraede and I.K. Schuller, 1988, Appl. Phys. Lett. **53**, 808.
Yankin, A.M., Yu.B. Golikov, P.G. Zakharov, O.A. Vikhreva, I.N. Dubrovina and V.F. Balakirev, 1996, Zh. Neorg. Khim. **41**, 729.
Yaron, U., D. Kowal, J. Felner and M. Einav, 1990, Physica C **168**, 546.
Yazawa, I., R. Sugise, N. Terada, M. Jo, K. Oka, H. Hayakawa and H. Ihara, 1990, Jpn. J. Appl. Phys. Part 2 **29**, L1480.
Yokota, K., T. Kura, M. Ochi and S. Katayama, 1990, J. Mater. Res. **5**, 2790.
Yoo, S.I., and R.W. McCallum, 1993, Physica C **210**, 147.
Young, D.A., 1991, Phase Diagrams of the Elements (University of California Press).
Zandbergen, H.W., W.T. Fu and L.J. De Jongh, 1988, Physica C **156**, 307.
Zandbergen, H.W., W.T. Fu and J.M. Van Ruitenbeek, 1990, Physica C **166**, 502.
Zenitani, Y., K. Inari, S. Sahoda, M. Uehara, J. Akimitsu, N. Kubota and M. Ayabe, 1995, Physica C **248**, 167.
Zhang, H., Y.Y. Wang, L.D. Marks, V.P. Dravid, P.D. Han and D.A. Payne, 1995, Physica C **255**, 257.

Zhang, H., P. Zhang and X. Chen, 1996, J. Mater. Chem. **6**, 615.

Zhang, H.-Z., Z. Fang, P.-M. Zhang and X.-M. Chen, 1995, J. Solution Chem. **24**, 565.

Zhang, J.P., D.A. Groenke, B. Dąbrowski, K.R. Poeppelmeier and L.D. Marks, 1994, Physica C **227**, 259.

Zhang, K., B. Dąbrowski, C.U. Segre, D.G. Hinks, I.K. Schuller, J.D. Jorgensen and M. Slaski, 1987, J. Phys. C **20**, L935.

Zhang, Q.-Z., T. Atake and Y. Saito, 1992, Solid State Ionics **50**, 209.

Zhang, W., and K. Osamura, 1991, Mater. Trans. JIM **32**, 1048.

Zhang, W., and K. Osamura, 1992, Physica C **190**, 396.

Zhang, W., K. Osamura and S. Ochiai, 1990, J. Am. Ceram. Soc. **73**, 1958.

Zhanguo, F., J. Chunlin and Z. Zhongxian, 1990, J. Less-Common Met. **161**, 49.

Zhao, J., C. Dong, Y.X. Fan, F. Wu, H. Chen, G.C. Che and Z.X. Zhao, 1996, Physica C **264**, 19.

Zhong, Q., Y. Zhang, X. Chen, G. Rao and J. Liang, 1994, J. Alloys & Compounds **210**, 261.

Zhou, Z., and A. Navrotsky, 1992, J. Mater. Res. **7**, 2920.

Zhou, Z., and A. Navrotsky, 1993, J. Mater. Res. **8**, 3023.

Zhou, Z., and A. Navrotsky, 1999, J. Mater. Res. **14**, 3511.

Zhu, Y.T., E.J. Peterson, P.S. Baldonado, J.Y. Coulter, D.E. Peterson and F.M. Mueller, 1998a, J. Phys. Chem. Solids **59**, 1331.

Zhu, Y.T., P.S. Baldonado, E.J. Peterson, Y.S. Park, A. Manthiram, D.P. Butt, D.E. Peterson and F.M. Mueller, 1998b, Physica C **298**, 29.

Zhu, Y.T., E.J. Peterson, P.S. Baldonado, J.Y. Coulter, D.E. Peterson and F.M. Mueller, 1999, J. Mater. Res. **14**, 334.

Zimmermann, E., K. Hack and D. Neuschütz, 1995, Calphad **19**, 119.

Zolliker, P., D.E. Cox, J.B. Parise, E.M. McCarron III and W.E. Farneth, 1990, Phys. Rev. B **42**, 6332.

Handbook on the Physics and Chemistry of Rare Earths
Vol. 30
edited by K.A. Gschneidner, Jr., L. Eyring and M.B. Maple

Chapter 191

ELECTRON PARAMAGNETIC RESONANCE IN CUPRATE SUPERCONDUCTORS AND IN PARENT COMPOUNDS

B. ELSCHNER[1] and A. LOIDL[2]
[1]*Institut für Festkörperphysik, Technische Universität Darmstadt, 64289 Darmstadt, Germany;* [2]*Lehrstuhl für Experimentalphysik V, Elektronische Korrelationen und Magnetismus, Universität Augsburg, 86135 Augsburg, Germany*

Contents

List of symbols 375
1. Introduction 376
2. Experiments in cuprates without additional EPR probes 378
   2.1. EPR silence 378
   2.2. Investigations of related compounds 379
   2.3. Electronic phase separation 380
   2.4. EPR of polaronic origin in $La_{2-x}Sr_xCuO_{4+\delta}$ 381
   2.5. EPR of chain fragments in $YBa_2Cu_3O_{6+\delta}$ 384
   2.6. Low-field nonresonant microwave absorption 388
3. EPR experiments on paramagnetic centers doped into the 2:1:4 cuprates 388
   3.1. Doping with lanthanides 388
      3.1.1. Gadolinium 388
      3.1.2. Erbium 391
      3.1.3. Pure 2:1:4 lanthanide cuprates 393
   3.2. Doping with 3d transition metals 396
      3.2.1. Manganese 397
      3.2.2. Iron 399
4. EPR experiments on paramagnetic centers doped into the 1:2:3 compounds 403
   4.1. Doping with lanthanides 404
      4.1.1. Gadolinium 404
         4.1.1.1. Crystal-field effects 404
         4.1.1.2. Gd-exchange interactions 405
         4.1.1.3. Magnetic order, spin gaps and dynamic processes 406
      4.1.2. Other lanthanide ions 408
   4.2. Doping with 3d transition metals 409
5. Summary and outlook 410
Acknowledgement 411
References 411

List of symbols

A	hyperfine constant
b	$= d(\Delta H)/dT$: Korringa slope
b_n^m	crystal field parameters
g	ESR g-value
$\tilde{g}$	g-tensor
g_e	conduction-electron g-value
Δg	experimentally observed g-shift with respect to the g-value of an ion in an insulator
G	Gauss (unit)
H	external magnetic field
H_i	internal magnetic field
H_{cc}	lower critical field of a superconductor
H_{res}	magnetic field at resonance absorption
ΔH	ESR linewidth at resonance absorption
ΔH_0	residual linewidth $\Delta H(T \rightarrow 0\,\mathrm{K})$
J	exchange constant

k_B	Boltzmann constant	Γ_{ij}	magnetic relaxation rate from ion i to ion j
$N(E_F)$	electronic density of states at the Fermi energy	δ	oxygen concentration $6+\delta$
		θ	Curie–Weiss temperature
O_n^m	Stevens operators	θ	sometimes used as angle between a crystallographic axis and the external magnetic field
T	temperature		
T_c	superconducting to normal conducting phase-transition temperature	μ_B	Bohr magneton
		χ_0	static magnetic susceptibility
T_N	Néel temperature	ξ	magnetic correlation length
T_1	spin–lattice relaxation time	ω	angular frequency
T_2	spin–spin relaxation time	ω_{sf}	spin-fluctuation frequency
Γ	magnetic relaxation rate		
Γ_{iL}	magnetic relaxation rate from ion i to lattice		

1. Introduction

Electron-paramagnetic-resonance (EPR) techniques are a valuable tool to study the local electronic and magnetic properties in high-T_c superconductors and in the magnetically ordered and insulating parent compounds. Most EPR measurements are carried out on localized magnetic moments. Very often paramagnetic probe ions, like Mn^{2+} or Gd^{3+}, are used. In some cases EPR spectroscopy can be performed on a localized moment of a constituent ion of the material under consideration, i.e. Cu^{2+} or V^{4+}. In certain cases, mostly in organic compounds, even charge carriers (holes or electrons) serve as paramagnetic centers. Using standard techniques, EPR experiments are performed at microwave frequencies, from 9 GHz (X-band) to 36 GHz (Q-band) in external magnetic fields ranging from 0.2 T to 4 T. Recently a number of high-frequency (high magnetic field) experiments were conducted using frequencies up to 500 GHz and fields up to 12 T. Usually EPR operates in cw mode using magnetic field sweeps at a given microwave frequency. Pulsed experiments and pulse-echo techniques which are standard in nuclear magnetic resonance (NMR) studies have been developed but can only be employed in systems with very narrow and strong absorption lines, and definitely not in high-T_c compounds where the homogeneously broadened linewidth is much too large.

Through exchange narrowing effects, local magnetic moments in metallic hosts show a single absorption line, and three relevant parameters can be determined from the microwave absorption: the intensity, the resonance field and the linewidth. The intensity measures the magnetic susceptibility of the probe itself. For example, in the case of paramagnetic probe ions it follows a Curie or a Curie–Weiss law, while in the case of conduction electrons it shows the characteristics of a Pauli-spin susceptibility. The resonance field is mainly determined by the g-value of the probe. Analogous to the Knight shift in NMR experiments, in pure metals g-shifts, Δg, are observed due to exchange interactions of the localized spin with the conduction electrons, namely $\Delta g = J(0) \cdot N(E_F)$. Here $J(0)$ is the exchange integral at zero wave vector $J(q=0)$ and $N(E_F)$ is the density

of states at the Fermi energy. In addition, Δg is influenced by spin fluctuations of surrounding local moments which are transferred via indirect exchange interactions to the EPR probe. Hence, Δg is a direct measure of the local static susceptibility at the site of the EPR probe.

The exchange interactions with the conduction electrons also contribute to the linewidth. In metals with no localized moments and no spin fluctuations, the linewidth can be expressed as $\Delta H = \Delta H_0 + bT$, where ΔH_0 is a temperature-independent residual linewidth and b characterizes the Korringa relaxation; b is determined by $b = 4\pi N^2(E_F) \langle J(q) \rangle^2 k_B / g_e \mu_B$. In addition the linewidth is influenced by fluctuating localized spins surrounding the probing ion. The time scale of the spin dynamics of the probing EPR spin is determined by two relaxation times: T_1, the relaxation time of the longitudinal magnetization, and T_2, that of the transverse magnetization. The homogeneous EPR linewidth, characterized by a Lorentzian lineshape, is determined by the transverse relaxation T_2. In metals, which have high relaxation rates, the relation $T_2 = T_1$ generally holds (e.g. Barnes 1981). In compounds which are close to a metal–insulator transition this equality may be violated, and its validity has to be carefully checked in each case. Due to the large relaxation rates, also saturation effects are not important. In EPR experiments the relaxation rate $\Gamma_\perp$ is determined by a four-spin correlation function (Kawasaki 1968, Huber 1972). Recently Chakravarty and Orbach (1990) have calculated $\Gamma_\perp$ for La_2CuO_4 and predicted a very broad linewidth of the Cu^{2+} resonance which was expected to be unobservable at high temperatures. However, in high-frequency EPR experiments or at high temperatures there should be a chance to observe the Cu resonance in the 1:2:4 cuprates. It is important to note that the necessity of four-spin correlation functions to describe EPR results is in contrast with the situation in NMR experiments. The NMR linewidth is determined by local correlations, i.e. by the usual two-spin correlation functions.

In metals the EPR linewidth provides direct experimental access to the local density of states at the Fermi energy and to the spin dynamics which is transferred via indirect exchange interactions or via classical dipole–dipole interactions to the probing spin. Detailed reviews on EPR in metals have been given by Taylor (1975), Barnes (1981) and Elschner and Loidl (1997).

In semiconducting or insulating materials the g-shift provides valuable insights into the ground state of the EPR probe in the crystalline electric field of the host material. The linewidth includes relaxations via the phonon system but in magnetic systems is dominated by exchange interactions (Heisenberg exchange, anisotropic exchange, dipole–dipole interactions, superexchange interactions, Dzyaloshinskii–Moriya interactions; see e.g., Mehran and Stevens 1982).

Finally, in all compounds the EPR is a very sensitive probe of static short- or long-range magnetic order. In ordered magnets or in systems with frozen-in magnetic correlations the linewidth is considerably enhanced due to an inhomogeneous broadening introduced by the static local fields.

2. Experiments in cuprates without additional EPR probes

2.1. *EPR silence*

Soon after the discovery of the high-T_c compounds a great number of EPR experiments were performed, and most of this early EPR experiments on Y–Ba–Cu–O ceramic samples revealed the existence of a weak signal indicative for Cu^{2+} located in uniaxial symmetry ($g_{\|} \approx 2.20$; $g_{\perp} \approx 2.05$). Usually the signals were easy to detect, even at room temperature. As a function of temperature the EPR intensities revealed a Curie-like behavior while the linewidths remained almost constant down to the lowest temperatures (Blank et al. 1987, Castilho et al. 1987, Mehran et al. 1987, Rettori et al. 1987, Shrivastava 1987, Shaltiel et al. 1987, De 1988, Kanoda et al. 1988, Alekseevskii et al. 1988, 1989, Pechoniy et al. 1990). However, it soon became clear that most of the observed signals were probably due to impurity phases, mostly due to spurious amounts of the green phase Y_2BaCuO_5 or of $BaCuO_2$ (Bowden et al. 1987, Kohara et al. 1987, Vier et al. 1987, Albino et al. 1988a, 1988b, Amoretti et al. 1988, Deville et al. 1988, 1989, McKinnon et al. 1988, Mehran et al. 1988a, 1988b, Owens et al. 1988, Tyagi et al. 1988, Genossar et al. 1989, Yu et al. 1989, Barham and Doetschman 1992, Atsarkin et al. 1995). Complex defect states which could be responsible for the origin of the observed Cu EPR signal were proposed by Stankowski et al. (1991), and some experimental evidence that the observed EPR spectra in Y–Ba–Cu–O result from an atmospheric degradation of the material has been provided by Cywinski et al. (1988). Already in the late 1980s the Cu^{2+} signal of ceramic compounds was taken as a good measure of the amount of impurity phases in the material (Morimoto et al. 1988).

At that time a variety of models were proposed to explain the absence of an intrinsic EPR signal in the high-T_c compounds. Mehran and Anderson (1989) attributed the non-observability of the signals in the metallic state to very short spin–lattice relaxation times due to high spin–holon scattering rates. The absence of resonance absorption in the insulators supported conclusions, either about the formation of exchange pairs (Deville et al. 1989), or that the correlation lengths in these compounds have been grossly underestimated or that conventional theory of antiferromagnetism is not valid (Mehran et al. 1988a, McKinnon et al. 1988, Mehran and Anderson 1989).

A more recent experimental investigation (Simon et al. 1993) has demonstrated that a Cu^{2+}-EPR signal in high-temperature superconductors (HTSC) can not be observed up to 1150 K, neither in single crystals, nor in ceramic pellets of $La_2CuO_{4+\delta}$, with oxygen concentrations $0 \leqslant \delta < 0.12$. Chakravarty and Orbach (1990) and Lazuta (1991) suggested that the non-observability of an Cu^{2+}-EPR signal in $La_2CuO_{4+\delta}$ at room temperature can be explained by the enormous broadening of the absorption line due to an antisymmetric Dzyaloshinskii–Moriya exchange and due to the fact that the 2D-correlation length ξ_{2D} is still finite even at high temperatures. A linewidth of 190 kG at 380 K was calculated which is reduced to 13 kG at 500 K. Apparently, a comparison with the experimental results by Simon et al. (1993) shows that these calculated values still seem to be underestimated.

EPR studies of $La_{1.82}Sr_{0.18}(Cu_{1-x}Zn_x)O_4$ show that replacement of the copper ions by nonmagnetic Zn ions leads to the formation of complexes with localized magnetic moments (Kataev et al. 1990). Samples without Zn are EPR silent. This result is in clear contrast to the finding of Janes et al. (1991) and Janes and Edwards (1994) who tried to detect EPR signals in $La_2Cu_{1-x}Zn_xO_4$ and $Nd_2Cu_{1-x}Zn_xO_4$, at ambient and elevated temperatures. But both measurements did not show any EPR signals intrinsic to the bulk materials, although the authors tried to optimize x and T in order to reduce the correlation length to a minimum by simultaneously introducing the highest possible Zn^{2+} concentration.

Today it is generally believed that in all optimum-doped or slightly overdoped HTSC EPR signals originating from intrinsic Cu^{2+} ions are not observable. This fact is unexpected and amazing as the copper ions in HTSC are in the true Cu^{2+} state (Shirane et al. 1987, Aeppli et al. 1989). Commonly Cu^{2+} signals in isolating crystals are easy to observe by EPR owing to the fact that its ^{2}D-ground state in tetragonal, or even in lower symmetry, splits into $d_{x^2-y^2}$ and d_{z^2} orbital singlets (see e.g., Abragam and Bleaney 1970). We will not give further consideration to the details of all of the papers about "Cu^{2+} EPR" in HTSC material which appeared during the first years after the discovery of the HTSC. There are at least two survey articles (Hoffmann et al. 1990 and Punnoose and Singh 1995) where the reader can find many details about these early EPR investigations on HTSC. A short section dealing with EPR experiments in high-T_c materials can also be found in a review by Elschner and Loidl (1997) on EPR in metals. Our present review article deals in detail with further developments of EPR in HTSC since about 1993.

2.2. *Investigations of related compounds*

To shed some light on the unexpected EPR silence of the high-T_c cuprates a number of investigations have been performed on closely related compounds. Castner and Seehra (1993) investigated a 2-dimensional $S=1/2$ system similar to La_2CuO_4. They used single crystals of copper formate tetrahydrate [$Cu(HCOO)_2 \cdot 4H_2O$] which exhibits a Heisenberg-exchange interaction between planar Cu^{2+} ions of order 100 K and a Néel temperature $T_N \approx 17$ K. The EPR measurements were conducted at 9 GHz and 36 GHz. The EPR linewidth has been determined between 24 K and 300 K. Above the minimum ($T_{min} \approx 2T_N$) the linewidth shows a weak linear increase ($b \approx 1$ G/K). It is attributed to a phonon-modulated Dzyaloshinskii–Moriya (DM) interaction between the Cu ions. The rapid increase of the linewidth for $T < T_{min}$ results from critical spin fluctuations and is observed between $2T_N$ and $1.5T_N$. A comparison of $Cu(HCOO)_2 \cdot 4H_2O$ and La_2CuO_4 shows that both have comparable values of the ratio T_N/J but that the Heisenberg-exchange J and the antisymmetrical DM exchange are at least one order of magnitude larger in the lanthanum cuprate. In addition, the temperature has to be high enough to obtain a sufficiently small value of the magnetic correlation length ξ/a. Obviously, these facts make it difficult or even impossible to observe Cu^{2+}-EPR signals in pure La_2CuO_4.

Janes et al. (1994) tried to attack the problem of the EPR silence of the antiferromagnetic parent compounds of HTSC (e.g. La_2CuO_4 or YBa_2CuO_6) by measuring

$La_2Ni_{1-x}Cu_xO_4$ ($0 \leqslant x \leqslant 1$). For the whole series of Cu concentrations x, no intrinsic Cu^{2+} signal could be detected. Only weak EPR signals were observed in the $g \approx 2$ region, again pointing towards spurious impurity phases. However, the authors observed a remarkable degradation of the cavity-Q-factor due to the microwave absorption of free carriers. The absence of a Cu^{2+} bulk signal is attributed to antiferromagnetic couplings between Cu^{2+} moments in connection with inhomogeneously distributed Cu^{2+} ions yielding phase-separated clusters.

Gd^{3+} and Cu^{2+} EPR measurements were conducted by Mehran et al. (1988c) in the green-phase compounds Gd_2BaCuO_5 and Y_2BaCuO_5 and were compared to the corresponding measurements in the "black-phase" high-T_c materials $GdBa_2Cu_3O_7$ and $YBa_2Cu_3O_7$. The green-phase insulators reveal magnetic order at $T_N = 12$ K and 35 K, and the paramagnetic susceptibility was described with Curie–Weiss (CW) temperatures $\Theta = -26$ K and $\Theta = -38$ K for the Gd and the Y compound, respectively. The EPR spectra for both green phases reveal ideal Lorenztian lineshapes. Below 100 K, and with further decreasing temperatures in the Gd compound, the linewidth continuously increases, which is commonly observed in compounds close to magnetic order. The Gd-EPR intensity shows a sharp peak at 19 K, and a plot of the inverse intensity vs. temperature gives a CW temperature $\Theta = -20$ K. The divergence just above T_N has been explained by strong anisotropic dipolar interactions. In Gd_2BaCuO_5 the Gd signal is much stronger and the Cu-EPR signal is hidden below the strong Gd resonance absorption. In Y_2BaCuO_5 the intensity of the Cu^{2+} resonance reveals a broad maximum close to 60 K, and from the inverse susceptibility a CW temperature, $\Theta = -100$ K, was calculated, significantly different from the dc magnetization results. These discrepancies were not discussed in detail. It seems however, that the EPR intensity documents strongly two-dimensional character of the magnetic order and it seems highly interesting to conduct further EPR investigations in this direction.

2.3. *Electronic phase separation*

There exist a number of theoretical concepts and some experimental evidence that an electronic phase separation may exist in the cuprates (for a review see, e.g., Sigmund and Müller 1994). It is generally believed that holes doped into the CuO_2 planes are located close to the O2p orbitals. Assuming antiferromagnetic (AFM) order the holes are strongly localized. This is due to the fact that the holes, on their way through the lattice, have to flip every second Cu^{2+} spin. In addition, it has been argued (Aharony et al. 1988) that the direct exchange interaction between the spin of the hole and the neighboring Cu^{2+} spin is much stronger than the indirect Cu–O–Cu superexchange. Hence, it seems plausible that the hole induces a ferromagnetic (FM) polarization of the neighboring Cu spins. (At this point it has to be mentioned that on the basis of a t–J model AFM spin polarons were predicted by Martinez and Horsch 1991). This hole-induced FM cluster usually is called magnetic polaron. The holes can move freely within the FM cluster, however the clusters themselves have high effective masses corresponding to a low mobility. These magnetic polarons are the main reason for the occurrence of electronic phase separation.

Percolating clusters behave almost metallic while the surrounding material is insulating. However, a real electronic phase separation can only occur when also the hole dopants can move freely to establish charge compensation. Emery and Kivelson (1993) therefore proposed a frustrated phase separation. The Coulomb repulsion between the clusters and the Coulomb attraction of the clusters with the charge compensation centers hamper the process of long-range phase separation. Some EPR experiments were performed to detect this phase separation and some of those are reported here. It will become clear in the two following sections 2.4 and 2.5 that the observation of intrinsic EPR signals also seems to be directly related to this electronic phase separation. However, at present no clear answer concerning this last point can be given, and much more experimental work is needed to clarify these questions.

Experimental evidence, such as neutron scattering measurement on powders (Jorgensen et al. 1988) and single crystals (Chaillout et al. 1989), ^{139}La NMR (Hammel et al. 1990) and other methods (e.g. Kremer et al. 1992), has shown that $La_2CuO_{4+\delta}$ undergoes a phase separation on cooling below room temperature. This phase separation generates insulating, conducting and even superconducting domains in La_2CuO_4. It has been studied intensively by EPR techniques (Wübbeler et al. 1996, Wübbeler and Schirmer 1992, Schirmer et al. 1994). A paramagnetic center probing the phase-separation process has been found in ceramic or powdered specimen. It has been shown that the intensity of this resonance is directly related to the surface area of the specimen. The g-values, $g_{\|} = 2.28$ and $g_{\perp} = 2.06$, have been determined, values which are consistent with a Cu^{2+} resonance with a $(x^2 - y^2)$ orbital ground state. Linewidth and g-value were found to be independent of temperature. From systematic annealing and cooling investigations it has been concluded that the resonance absorption results from probes at surfaces and/or interfaces. Mechanically grounded single crystals, with well-defined diameters d of the microcrystallites, showed EPR intensities $I \sim d^2$. Obviously a large part of the Cu^{2+} ions at the surface of the microcrystallites of these oxygen-enriched samples contributed to the experimentally observed signal.

EPR experiments on $La_2CuO_{4+\delta}$ ($\delta \approx 0.015$) powders, obtained from crushed single crystals, were performed by Szymczak et al. (1995). The authors observed the typical powder spectrum of isolated Cu^{2+} centers with $g_{\|} = 2.355$ and $g_{\perp} = 2.098$. This resonance absorption was associated with Cu^{2+} ions located in domain walls and grain boundaries. The spectrum showed a "hyperfine-like structure" with a hyperfine constant $A = 1.4 \times 10^{-2}$ cm^{-1}, which is rather unusual for a Cu-hyperfine pattern (see, e.g., Abragam and Bleaney 1970).

2.4. *EPR of polaronic origin in $La_{2-x}Sr_xCuO_{4+\delta}$*

Recently Kochelaev et al. (1997) reported on intrinsic EPR in $La_{2-x}Sr_xCuO_{4+\delta}$ single crystals and powders (Kruschel 1993). For samples with Sr content $0 \leqslant x \leqslant 0.2$, broad but well-defined single Lorentzian EPR lines without any fine or hyperfine structure have been detected for temperatures $20\,\mathrm{K} \leqslant T \leqslant 300\,\mathrm{K}$. A typical derivative of an absorption spectrum observed in a crystal with $x = 0.075$ at 70 K is shown in the inset of fig. 1.

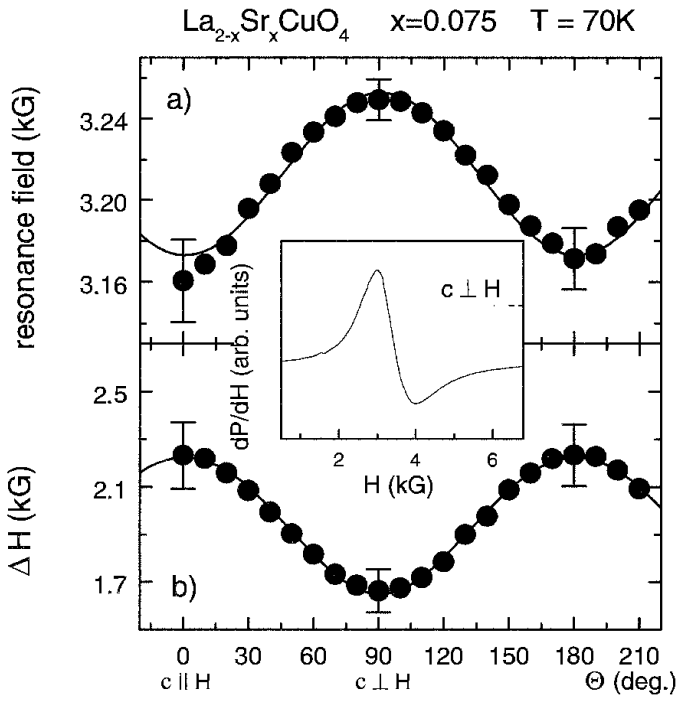

Fig. 1. Angular dependence (a) of the resonance field and (b) of the linewidth ΔH in $La_{1.925}Sr_{0.075}CuO_4$ at 70 K by rotating the c-axis with respect to the magnetic field. A purely axial symmetric behavior is indicated by the solid lines. The inset shows the absorption derivative indicating a Lorentzian lineshape of the EPR spectrum for the crystal orientation $c \perp H$. From Kochelaev et al. (1997).

The angular dependence of the resonance field for $c \parallel H$ ($\Theta = 0°$) to $c \perp H$ ($\Theta = 90°$) is shown in fig. 1. It can be well described by g-factors with uniaxial symmetry (solid line in fig. 1). When the a,b plane is rotated the resonance field and the linewidth are constant within experimental accuracy. This behavior of the resonance absorption is typical for a paramagnetic (pm) center with spin $S = \frac{1}{2}$. For a pm center with spin $S > \frac{1}{2}$ and an unresolved fine structure one expects a minimum in the angular dependence of the linewidth near the magic angle ($\Theta \approx 60°$) which has been not observed by Kochelaev et al. (1997). $g_{\parallel}$ decreases with decreasing temperature to a rather unusual value $g_{\parallel} < 2$, showing a crossover with $g_{\perp}$ at approximately 40 K. The cross-over temperature observed in different samples depends weakly on the Sr concentration x (fig. 2). Comparing these experimental observations with model calculations, Kochelaev et al. (1997) claim that these EPR measurements provide experimental evidence of a three-spin polaron, consisting of two Cu^{2+} ions coupled to one p hole as shown in fig. 3. This type of quasiparticle has been proposed by Emery and Reiter (1988) and was later considered in detail by Frenkel et al. (1990). The symmetry properties and the peculiar temperature dependence of the EPR line indicate the presence of dynamical Jahn–Teller distortions and the formation of a collective mode of polarons and strongly correlated Cu ions in a strong bottleneck regime. From the integral intensity of the EPR signal it can be concluded that approximately 1% of the total number of p holes are active EPR centers. This intensity consideration has been performed strictly for the sample with a Sr concentration of only $x = 0.075$.

Using the framework of the model of electronic phase separation, as outlined above, it can be speculated that isolated three-spin polarons which are EPR active are detected

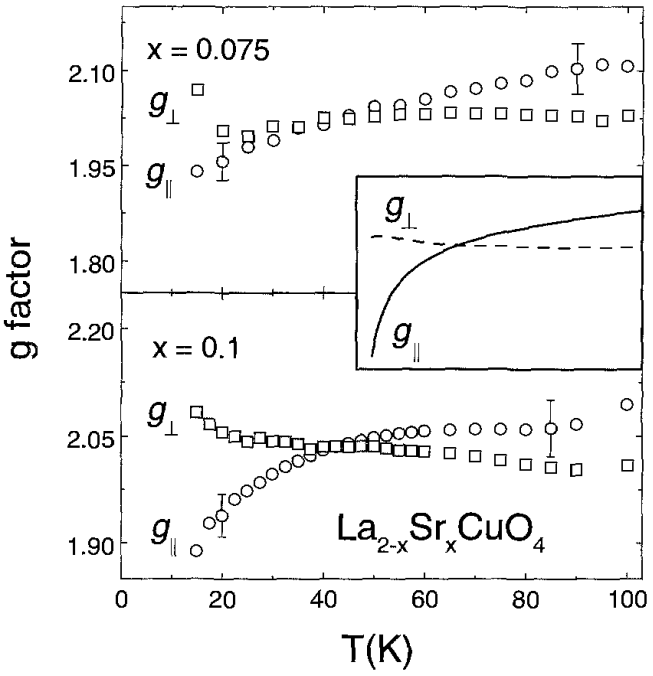

Fig. 2. Temperature dependence of the g-factors of $La_{2-x}Sr_xCuO_4$ as determined from the resonance field for two different crystals orientations $c \| H$ and $c \perp H$, respectively. The inset shows the temperature dependence of the g-values obtained from model calculations and demonstrates that the model describes the unusual crossover of the g-factors satisfactorily well. From Kochelaev et al. (1997).

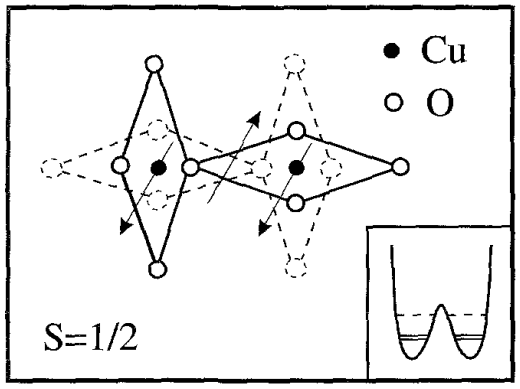

Fig. 3. Three-spin magnetic polaron which is regarded as the EPR active center in the CuO_2 plane. The Jahn–Teller distorted polaron has two degenerated configurations as indicated by the dashed lines. The inset shows the corresponding double-well potential with the excited vibronic state (dashed line) and the ground state split by tunneling (solid line). From Kochelaev et al. (1997).

in regions with low hole concentrations only. At higher hole concentrations the polarons coagulate and do not contribute to the EPR signal any further. At higher Sr concentrations all polarons are connected and can move freely. In this regime only a small fraction of polarons in highly hole-deficient regions can be detected.

Single crystals of high quality, i.e. with a sharp superconducting transition, do not show this EPR signal. In contrast, EPR-active crystals reveal a somewhat broader superconducting transition. Obviously the existence of the EPR signal observed from three-spin polarons presupposes electronic phase separation and possibly, because of thermodynamic stability considerations, also a separation of the charge compensation centers, i.e., inhomogeneities in the Sr concentration.

The temperature dependence of the linewidth is shown in fig. 4. All compounds reveal a steep increase of the linewidth towards the lowest temperatures, which seems to be a common feature of all doped and undoped cuprates investigated by EPR so

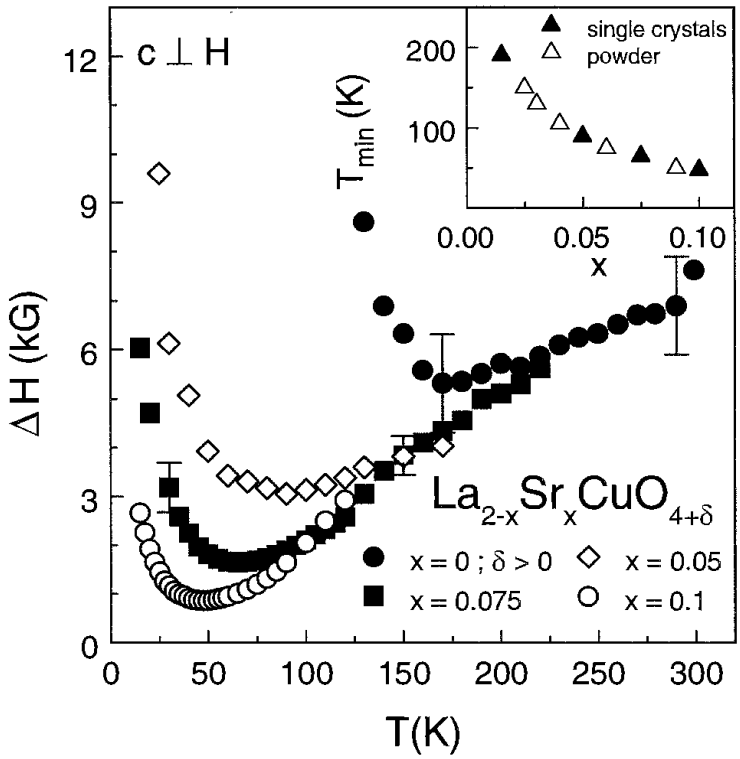

Fig. 4. Temperature dependence of the linewidth ΔH in $La_{2-x}Sr_xCuO_{4+\delta}$. The inset shows the temperature T_{min} of the linewidth minima vs. the Sr concentration x. The results of measurements with polycrystalline samples (open symbols) are also included for comparison. From Kochelaev et al. (1997).

far. With decreasing temperature the linewidth decreases, passes through a minimum and increases towards the lowest temperatures. The minimum strongly depends on the hole concentration which is shown separately in the inset of fig. 4. The envelope of the linewidth of all concentrations for $T > T_{min}$ decreases somewhat weaker than linear. It reconciles the dynamic susceptibility of the cuprates which reveals the opening of a pseudogap in the electronic density of states. The increase of the linewidth towards low temperatures seems to signal the freezing-in of spin fluctuations and the concomitant localization of charge carriers. The intensity of the resonance absorption, which reflects the static susceptibility of the EPR probe itself, shows a Curie-like temperature dependence at low temperatures, but is almost temperature independent and characteristic of a Pauli-spin susceptibility at higher temperatures (Kochelaev et al. 1997).

2.5. *EPR of chain fragments in $YBa_2Cu_3O_{6+\delta}$*

As noted in section 2.1, soon after the discovery of the high-T_c cuprates it became clear that in $YBa_2Cu_3O_{6+\delta}$ for $\delta = 1$ no intrinsic Cu EPR signal can be detected. However, clear experimental evidence for the existence of intrinsic EPR signals for $\delta < 1$ has been provided by different groups in single crystals (Mehran et al. 1988b, Shaltiel et al. 1989b,

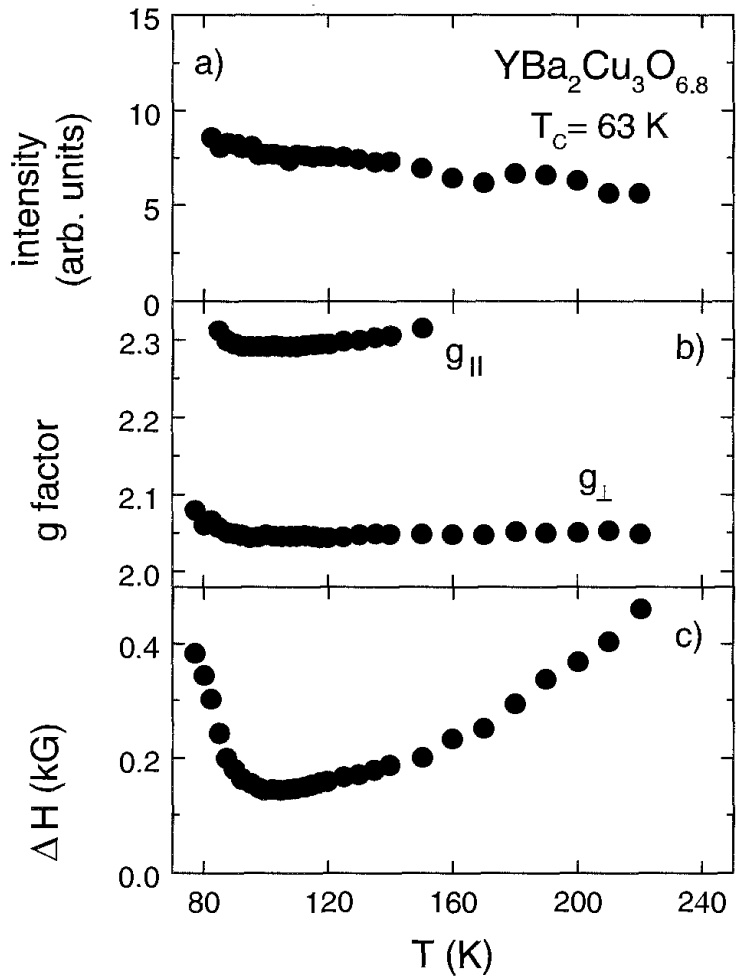

Fig. 5. Temperature dependence (a) of the intensity of the absorption line, (b) of the g-factors, $g_{||}$ and $g_\perp$, and (c) of the linewidth in $YBa_2Cu_3O_{6.8}$. Due to a strong increase of the linewidth the EPR signals are lost well above the superconducting phase transition temperature.

Kochelaev et al. 1990, Garifullin et al. 1991, Sichelschmidt et al. 1994, 1995a,b) and in polycrystalline samples (Owens et al. 1988, Garifullin et al. 1991). The general features of the observed "Cu-like" EPR signal are characterized for a sample with superconducting phase-transition temperature $T_c = 63$ K ($\delta = 0.8$) in fig. 5 (Sichelschmidt et al. 1995a). The intensity shows a weak temperature dependence. This observation rules out any paramagnetic defect state which should reveal a Curie-like increase. The g-factor is anisotropic within the a,c plane with $g_{||} = 2.05$ and $g_\perp = 2.3$. Here the subscripts $||$ and $\perp$ indicate directions of the c-axis of the crystal with respect to the external magnetic field. It is important to note that within the a,b plane which corresponds to the CuO_2 planes the g-value is isotropic within experimental uncertainty. Hence, the observed g-values were close to what one would expect for Cu^{2+} ($S = \frac{1}{2}$) in a crystal with uniaxial symmetry. The linewidth reveals a minimum around 100 K. It increases steeply towards T_c and becomes

too broad to be observed for temperatures still above T_c. With rising temperatures starting from the minimum linewidth, ΔH increases stronger than linear in T.

The first observation of an EPR signal in undoped (no additional electron paramagnetic center) $YBa_2Cu_3O_{6+\delta}$ was reported by Mehran et al. (1988b). They observed a slightly anisotropic signal only in as-grown crystals with T_c close to 40 K. The appearance of the signal has been explained in terms of a Jahn–Teller–Kondo effect. It was speculated that the conduction electrons mix the two states of the split Γ_3 doublet.

A similar signal has been observed by Shaltiel et al. (1989a), again in as-grown crystals. The authors claimed that the detected EPR signal is characteristic of a Cu^{2+} ion in tetragonal symmetry and presumably originates from copper-chain ions which are octahedrally coordinated by six oxygen neighbors. These authors gave an explanation of the observed temperature dependence of the signal in terms of the onset of local superconductivity. Similar observations have been reported by Alekseevskii et al. (1989), Kochelaev et al. (1990) and Garifullin et al. (1991). These authors gave a detailed report of the lineshape and of the observed intensities as a function of the heat treatment of the samples. Guided by the fully symmetrical lineshapes, they suggested that the signals result from insulating regions in the sample. In addition, the intensities of the signals decreased after a heat treatment and the authors argued that this observation also points towards an (electronic) phase separation.

A detailed experimental report on the temperature and oxygen dependence of the EPR resonance absorption in $YBa_2Cu_3O_{6+\delta}$ has been given by Sichelschmidt et al. (1994, 1995a,b). Intrinsic EPR signals could only be detected for oxygen concentrations $0.7 < \delta < 0.9$. The authors concluded that the signals are due to paramagnetic chain fragments along the Cu–O chains (Cu1 sites). The intensity of the observed resonance absorption is shown in fig. 6 together with the experimentally observed superconducting phase-transition temperatures. EPR signals were only detected on the borderline from the ortho–I to the ortho–II phase. Figure 6 demonstrates that at $\delta = 0.8$ approximately 15% of the Cu ions along the chains contribute to the paramagnetic chain fragments. The experimental results compare well with theoretical results utilizing modified lattice-gas models (inset of fig. 6: Uimin and Rossat-Mignod 1992, Uimin and Stepanov 1993). These calculations predict a maximum number of paramagnetic chain fragments close to $\delta = 0.8$, which is in perfect agreement with the experimental results.

The temperature dependence of the linewidth for different oxygen concentrations is shown in fig. 7 (Sichelschmidt et al. 1995a). All samples reveal a minimum at approximately 100 K and show an exponential increase towards low temperatures (Sichelschmidt et al. 1995b). At high temperatures the linewidth increases roughly with T^2 and shows a significant concentration dependence characteristic for a strong bottleneck regime. The experimental results of figs. 5–7 were consistently explained by assuming a strong collective motion of the paramagnetic chain fragments (Cu1 sites) with the Cu spin fluctuations in the CuO_2 planes (Cu2 sites) and only a weak coupling of the magnetic moments of the CuO_2 planes to the lattice and the exponential opening of a pseudogap at low temperatures. A gap value of 45 meV has been determined from all concentrations

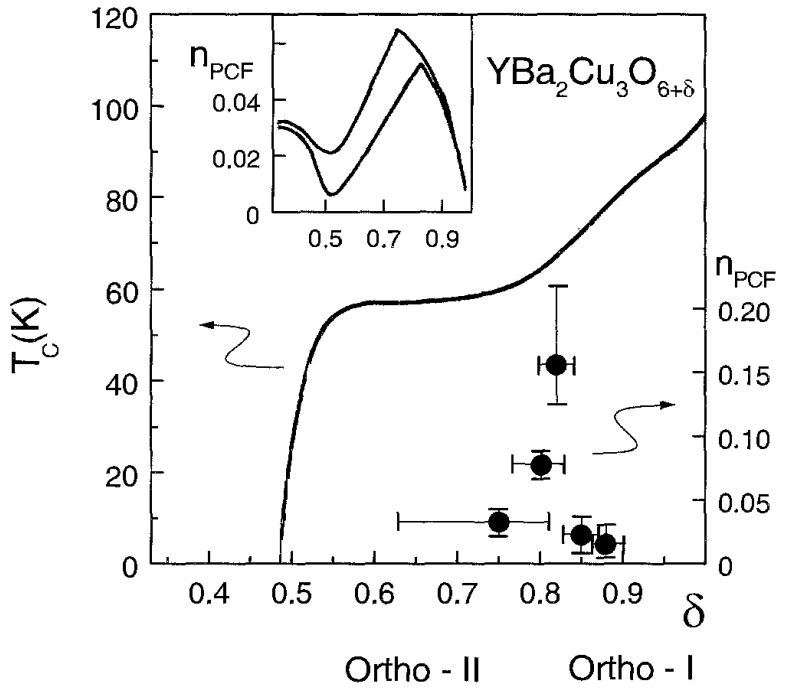

Fig. 6. Oxygen concentration dependence of the fraction of paramagnetic chain fragments n_{pcf} as calculated from the integrated intensity of the EPR signal in $YBa_2Cu_3O_{6+\delta}$ (solid symbols, right scale). The concentration dependence of the superconducting phase transition temperature T_c is also shown (solid lines, left scale). The inset shows the concentration dependence of paramagnetically active chain fragments for two different "sample-preparation" temperatures which has been calculated using a modified lattice-gas model. From Sichelschmidt et al. (1995a).

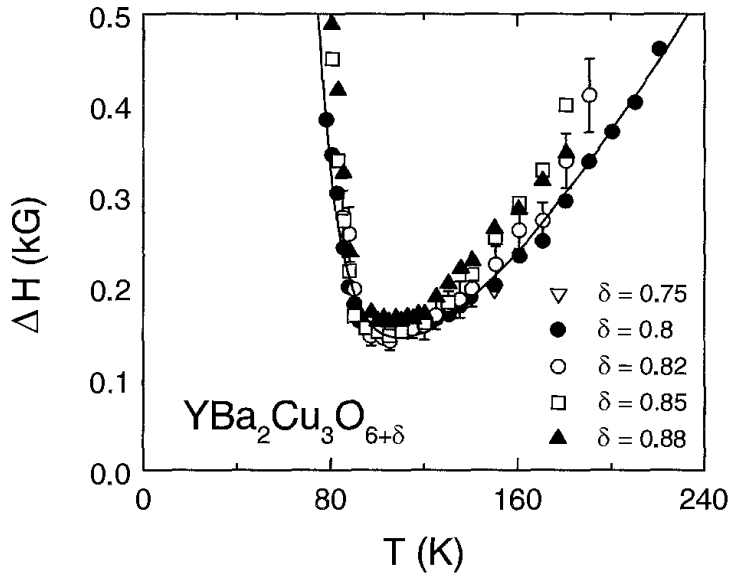

Fig. 7. Temperature dependence of the linewidth ΔH in $YBa_2Cu_3O_{6+\delta}$ for five samples with different oxygen concentrations $0.75 \leqslant \delta \leqslant 0.88$. The solid line represents the result of a fit to the data for the sample with an oxygen concentration $\vartheta = 0.8$ ($T_c = 63$ K). From Sichelschmidt et al. (1995a).

under investigation, significantly larger than the pseudogap as determined from NMR and neutron scattering results (Sichelschmidt et al. 1995b).

2.6. *Low-field nonresonant microwave absorption*

From early on it has been recognized that low-field nonresonant microwave absorption can be used to characterize the high-temperature superconductors. Type-II superconductors can be penetrated by the magnetic field via flux vortices, and thermal excitations of these vortices are responsible for microwave absorption. Hence, this kind of nonresonant EPR spectroscopy can provide some information on the vortex dynamics and on the lower critical field H_{c1}. A number of EPR experiments focusing on the low-field signals have been reported on HTSC. The nonresonant absorption yields a broad peak in the field derivative of the absorption spectrum, sometimes an additional fine structure has been observed, and in all experiments strong hysteresis effects were noted.

In the early work, Rettori et al. (1987) have suggested that the signal observed in YBCO ceramics is due to a transition from the Meissner state to a mixed state, while Durny et al. (1987), Blazey et al. (1987), Ramakrishna et al. (1988) and Rubins et al. (1988) have interpreted their experiments in 2:1:4 as well as in 1:2:3 compounds in the framework of the superconducting glass theory for weakly linked superconducting clusters given by Ebner and Stroud (1985). From the temperature dependence of the field-modulated microwave absorption of zero-field cooled samples Foukis et al. (1988) determined the lower critical field in YBCO ceramics. They found $H_{c1} = H_{c1}(0)[1-(T/T_c)^2]$, with $H_{c1}(0) = 190(20)$ G.

3. EPR experiments on paramagnetic centers doped into the 2:1:4 cuprates

3.1. *Doping with lanthanides*

3.1.1. *Gadolinium*

Rettori et al. (1993) measured the EPR of Gd^{3+} in single crystals of $La_{2-x}Sr_xCuO_{4+\delta}$ doped with 0.1–1% Gd as a function of temperature T and of angle Θ between the external magnetic field and the b-axis of the crystal. The experiments were conducted for Sr concentrations $0 \leqslant x \leqslant 0.024$. The single crystals were grown in air from CuO-rich flux by slow cooling in Pt crucibles. The oxygen content has been modified by annealing the crystals under vacuum (1.3×10^{-4} Pa) or oxygen pressure (1.52×10^{7} Pa) at $T = 800$ K. The measurements were carried out at 9 GHz (X-band) and at 35 GHz (Q-band) at temperatures between 1.5 K and 300 K. The results can be summarized as follows: For $T > T_N$ ($T_N \approx 250$ K for $x = 0$; $T_N \approx 20$ K for $x = 0.024$) they observed spectra from four magnetically nonequivalent crystallographic Gd^{3+} sites indicating a twinned crystal. At room temperature the individual fine-structure lines are broad (300–400 G). Depending on the angle Θ the spectra are more or less resolved. Particularly for $\Theta = 0°$ the four lines

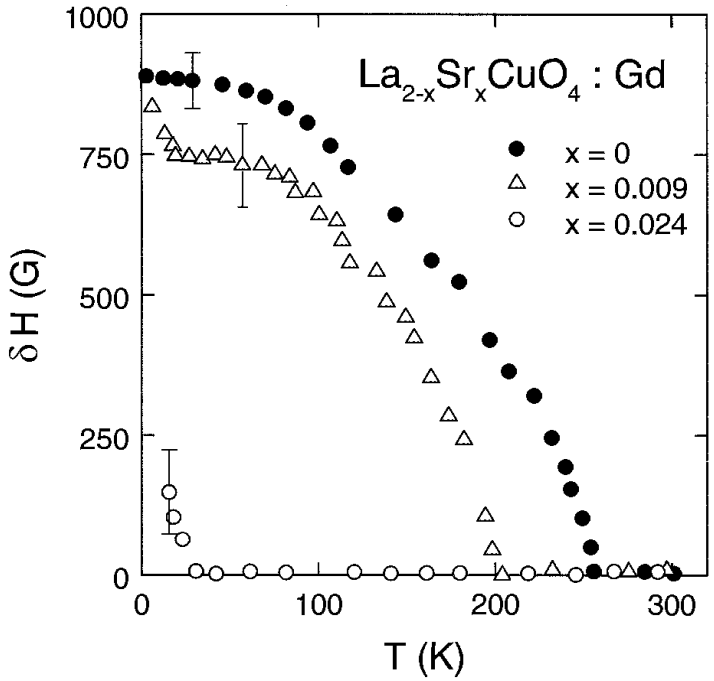

Fig. 8. Temperature dependence of the line splitting of the $-\frac{7}{2}$ to $-\frac{5}{2}$ transition of the Gd resonance in $La_{2-x}Sr_xCuO_4$:Gd for Sr concentrations $x=0$, 0.009 and 0.024 and with the external magnetic field $H \parallel b$. The splitting results from the AFM ordering of the Cu moments for $T < T_N$ and provides a direct measure of the ordered moments. From Rettori et al. (1993).

coalesce into one single resonance line. For the case of Gd^{3+} substituting for La^{3+} ions, an appropriate spin-Hamiltonian can be written as

$$H = \mu_B \vec{S} \tilde{g} \vec{H} + \sum_{n=2,4,6} \sum_{m}^{n} b_n^m O_n^m, \tag{1}$$

where $\tilde{g}$ is the g-tensor, O_n^m are the Stevens operators, and b_n^m are the corresponding crystal field parameters (see, e.g. Abragam and Bleaney, 1970). By a careful analysis the authors were able to extract the components of the $\tilde{g}$-tensor and the b_n^m parameters with $n=2$, 4 and 6 with high accuracy. For $T < T_N$ the spectra change dramatically. Each of the EPR lines is further split. To fit the spectra in this temperature range the authors had to add a further term to the spin-Hamiltonian describing an internal magnetic field. This internal field originates from the AFM ordering of the Cu moments for $T < T_N$. The temperature dependence of the additional splitting of the resonance lines allowed the calculation of the moments per Cu ion. From these EPR measurements it has been concluded that at 4 K the Cu moments are of the order of $0.6\mu_B$ per Cu^{2+} and the Cu spins are oriented within the b,c plane, canted by an angle of approximately 5° with respect to the c-axis. For external magnetic fields $H \parallel b$ the temperature dependence of the splitting of the $-\frac{7}{2}$ to $-\frac{5}{2}$ transition is shown in fig. 8 for different Sr concentrations x. This result is in a good agreement with the magnetic structure inferred from neutron scattering

experiments (K. Yamada et al. 1989). The internal magnetic field was estimated to amount to 650±30 G located in the *b,c* plane. For $T > T_N$ the EPR linewidths broaden by a factor 2–3 due to slow magnetic fluctuations. At an angle $\Theta \approx 30°$ there is a noticeable difference between the experimental data and the model fit, well beyond the experimental error. The authors claim that additional internal fields from neighboring Gd ions can explain these discrepancies.

Recently Kataev et al. (1996, 1997) studied the slow AFM spin dynamics in the low-temperature tetragonal phase (LTT) of $La_{2-x}Sr_xCuO_4$ with strontium concentrations $0.05 \leqslant x \leqslant 0.20$ by Gd EPR. They used polycrystalline samples in which La ions were substituted by the van-Vleck ions Eu^{3+} (up to 12% relative to La) in order to stabilize the LTT phase. The concentration of the Gd probe ions was 1% for all samples. Due to the fact that neither single crystals nor grain-oriented powder samples were used, the spectrum was only partly resolved. The authors measured the central component of the spectrum as a function of temperature and extracted a Korringa-like behavior of the linewidth for $T \geqslant 80$ K. The slope increases with Sr concentration x. The Korringa relaxation is attributed to small but finite exchange couplings between Gd^{3+} and mobile holes in the CuO_2 planes. The authors tried to gain qualitative insights into the low-frequency spin dynamics by using a simplified form of the generalized relation between the Gd spin relaxation and the dynamic susceptibility of the CuO_2 planes:

$$\left(\frac{1}{T_1}\right)_{Gd} = \frac{\gamma}{M^2}(\Delta H - \Delta H_0) \approx \frac{k_B J^2_{Gd-Cu}}{(g_{Cu}\mu_B\hbar)^2}\chi_0\frac{T}{\omega_{sf}}, \tag{2}$$

where χ_0 denotes the static susceptibility and ω_{sf} is the frequency of the spin fluctuations in the CuO_2 plane. M is a matrix element of the corresponding Zeeman transition in the Gd system, and ΔH_0 is the EPR linewidth for $T \to 0$ K. According to eq. (2) the spin–lattice relaxation time is directly related to the measured linewidth, and its temperature dependence is shown as inset in fig. 9. Using eq. (2) and assuming reasonable values for $J_{Gd-Cu} \approx 5$ K and $\chi_0 \approx 2 \times 10^{-4}$ emu/mole the authors calculated the temperature dependence of the spin-fluctuation frequency ω_{sf} as shown in fig. 9 (Kataev et al. 1997). The steep decrease of the fluctuation frequency below ~70 K is due to the slowing down of the spin fluctuation in the CuO_2 planes. This effect leads to the experimentally observed broadening of the Gd^{3+} EPR line. The authors argued that this extremely slow AF-spin dynamics is a characteristic property of the magnetism in the LTT phase of $La_{2-x}Sr_xCuO_4$. At low temperatures ω_{sf} slows down to 10^{10}–10^{11} s^{-1}, but the compound obviously does not exhibit a true "static" AFM order in the LTT phase.

In further papers Rameev et al. (1995), Teitel'baum et al. (1994) and Kataev et al. (1993) discussed results of EPR measurements on La–Sr–Cu–O or La–Ba–Cu–O ceramics doped with Gd^{3+}. Again the temperature dependence of a central component of the only partly resolved EPR spectrum has been measured. A linear, Korringa-like dependence, $\Delta H = H_0 + bT$, has been observed for all Sr concentrations ($0.08 \leqslant x \leqslant 0.25$) for $T > 60$ K. The authors discuss the relation between the Korringa slope b and the Sr (Rameev et al. 1995) or Ba (Teitel'baum et al. 1994) concentration x, and find a

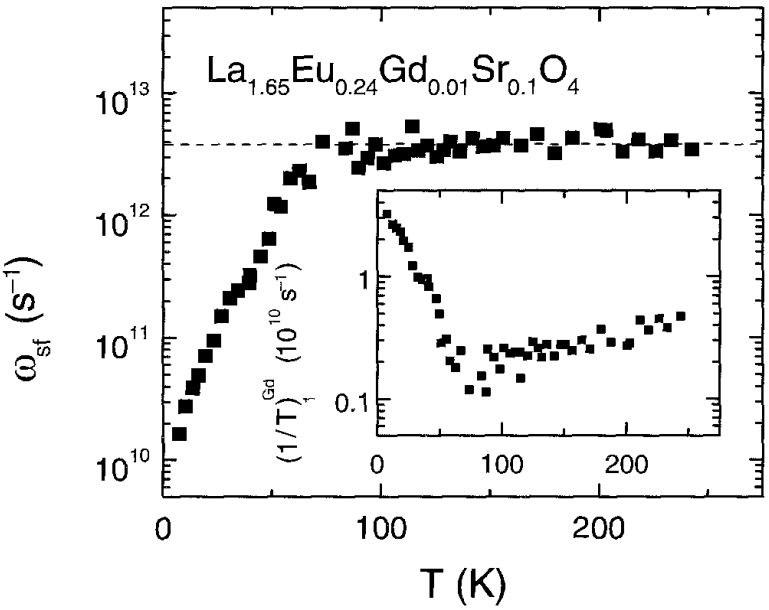

Fig. 9. Temperature dependence of the characteristic frequency of the AFM spin fluctuations in the CuO_2 planes in $La_{1.65}Eu_{0.24}Gd_{0.01}Sr_{0.1}Cu_4$. $\omega_{sf}(T)$ has been calculated from the spin–lattice relaxation rate of Gd which is shown in the inset. From Kataev et al. (1997).

behavior $b = 8.35(x - 0.06)$ G/K/% Sr. They interpret this result as proof for an increasing density of states with increasing x, i.e., with the concentration of charge carriers, independent of the dopant (Rameev et al. 1995).

A detailed analysis of the EPR linewidth and resistivity allowed the conclusion that the well-known anomalous suppression of superconductivity for Ba concentration around $x \approx 0.125$ probably is due the localization of charge carriers in combination with a structural instability. The resistivity data lead to the assumption that spatially separated superconduction and non-superconduction regions exist. Kataev et al. (1992) reported an experimental study on Gd^{3+} EPR in $La_{2-x-y}Gd_ySr_xCuO_4$ using powdered samples with $0 \leqslant x \leqslant 0.15$ and $y = 0.01$. The main experimental finding was a correlation between the Korringa slope b (i.e. the squared density of states at the Fermi-energy) and the superconducting phase-transition temperature. The experimental result were parameterized using $T_c = \alpha \exp(-\beta b^{-1/2})$, where α and β are adjustable parameters. This relation holds for all samples with superconducting transition temperatures $T_c > 16$ K.

3.1.2. *Erbium*

EPR, resistivity and magnetic susceptibility of $La_{2-x-y}Er_ySr_xCuO_{4+\delta}$ were investigated by Kan et al. (1991). Samples with lanthanum concentrations $0.15 \leqslant x \leqslant 35$ and erbium concentrations $y = 0.01$ were studied in the superconducting and in the normal state. Powdered samples were investigated yielding broad Er spectra. In order to follow the temperature dependence of the EPR linewidth the lineshapes were analyzed using the analytical expressions for polycrystalline samples (Searl et al. 1961). The authors found

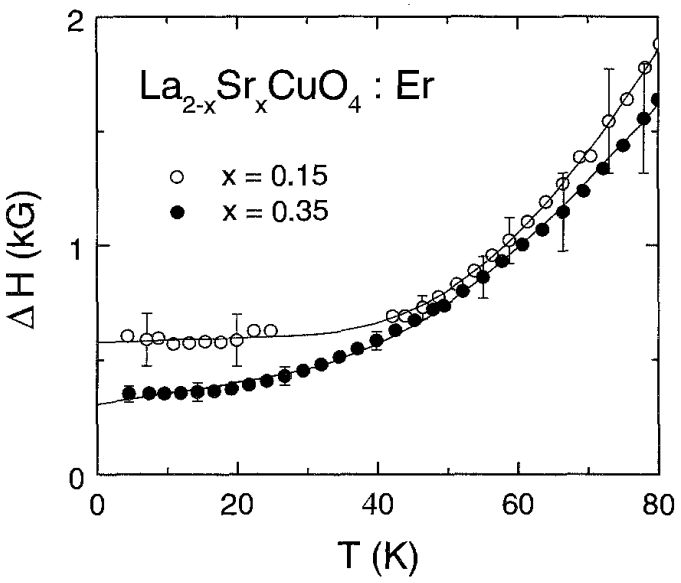

Fig. 10. Temperature dependence of the Er^{3+} EPR linewidth in $La_{2-x}Sr_xCuO_4$, doped with 1% Er. Results for Sr concentrations $x=0.15$ and $x=0.35$ are shown. The solid lines are fits as described in the text. From Kan et al. (1991).

$g_{\|}=1.3\pm0.1$ and $g_{\perp}=9.2\pm0.2$ with a spin Hamiltonian for Kramers doublets in a tetragonal crystalline field.

Figure 10 shows the temperature dependence of the Er^{3+}-EPR linewidth in erbium-doped 2 : 1 : 4 compounds with two different Sr concentrations, $x=0.15$ and 0.35 (Kan et al. 1991). In contrast to the finding of Kataev et al. (1997) for the Gd^{3+} resonance in the Eu-stabilized LTT phase of $La_{2-x-y}Eu_ySr_xCuO_4$, where due to the freezing of spin fluctuations the linewidth increased strongly, in superconducting $La_{2-x-y}Er_ySr_xCuO_{4+\delta}$ the linewidth remained approximately constant at low temperatures. The exponential increase of the Er^{3+}-EPR linewidth at higher temperatures ($T \geqslant 40$ K) was explained by a resonant phonon-relaxation process (Orbach process, see Abragam and Bleaney 1970). Although the Er ions are not located within CuO–planes they probe a finite carrier density on their sites which is clearly demonstrated by a finite Korringa slope b. The authors found $b=2.6$ G/K for $x=0.25$ and assumed a quadratic dependence of b, i.e., a linear dependence on the electronic density of states at the Fermi level on the strontium concentration x. The Er resonance in the tetragonal phase of $La_{2-x-y}Er_ySr_xCuO_4$ does not show any broadening at low temperatures. This fact provides clear experimental evidence that the spin fluctuations in the CuO_2 planes do not influence the resonance of the Er ions which are located outside these planes. Hence, any significant direct or indirect exchange interactions between Er and Cu can be excluded.

Er-EPR measurements have recently been published by Shimizu et al. (1997a). They studied samples with Sr concentrations $0 \leqslant x \leqslant 0.35$ doped with 2% erbium. Again, the broadening of the linewidth with rising temperature has been explained using the sum of a Korringa term and a phonon-induced Orbach process. The authors found a vanishing Korringa slope b for strontium concentrations $x \leqslant 0.1$ and a relation $b \propto x^2$ for concentrations $x > 0.1$, again indicating a linear increase of the electronic density of states with Sr content, beyond a critical concentration x_c. The crystal field splitting Δ was

determined from an analysis of the exponential increase of the linewidth due to Orbach processes. Shimizu et al. (1997a) found a concentration dependence $\Delta(x)/k_B$ ranging from 200 K to 100 K with a maximum value close to $x = 0.15$.

3.1.3. *Pure 2:1:4 lanthanide cuprates*

A systematic investigation of the magnetic properties (magnetization, microwave absorption, EPR and specific heat) of rare-earth copper oxides was carried out by Oseroff et al. (1990). They reported results on undoped R_2CuO_4 single crystals with R = Pr, Nd, Sm, Eu, and Gd, and on mixed crystals of the form $M_{2-x}N_xCuO_4$ with M = Pr, Nd, Sm, Eu, or Gd and N = Gd, Tb, or Dy. The measurements reveal two characteristic transition temperatures. The transition temperature at $T \approx 270$ K is associated with antiferromagnetic ordering of the Cu moments which are strongly coupled within the CuO_2 layers. The low-temperature anomaly ($T \leqslant 20$ K) was thought to arise from the onset of a spontaneous canting of the spins. The authors did not observe any EPR signal which they could identify with Cu^{2+} in these systems in the temperature range $2\text{ K} < T < 260\text{ K}$. The only EPR signal they had observed and identified was that due to Gd^{3+}, with its orbital singlet ground state. Apparently the Gd^{3+} resonance drastically changes at the three-dimensional (3D) Néel transition but it does not reflect the AFM ordering in the 2D CuO_2 planes.

EPR measurements were made on single crystals of Eu_2CuO_4 doped with 1% Gd by Zysler et al. (1991) and by Rao et al. (1988). They used conventional X-band and Q-band spectrometers at temperatures from 1.5 K to 300 K. The observed angular dependence of the Gd fine structure can be described by a conventional Hamiltonian as given in eq. (1). The authors determined the following g-shift and crystal-field parameters: $g_{\|} = 1.935$; $b_2^0 = -513 \times 10^{-4}\text{ cm}^{-1}$; $b_4^0 = -41 \times 10^{-4}\text{ cm}^{-1}$; $|b_4^4| = 235 \times 10^{-4}\text{ cm}^{-1}$. The splitting of the EPR lines was described by adding to eq. (1) additional crystal-field terms which are due to local distortions, and introducing an internal magnetic field $|H_i| \approx 350$ G. The origin of the internal field is associated with the onset of magnetic order of the Cu moments in the host lattice Eu_2CuO_4 ($T_N \approx 215$ K). The linewidth of the Gd resonance increases due to relaxations via thermally excited magnetic states of Eu^{3+}. This effect becomes significant for $T > 100$ K, but there is no increase of the linewidth towards the lowest temperatures (fig. 11). This finding seems to indicate that the Gd spins do not probe spin fluctuations, which is in agreement with the Er behavior in La_2CuO_4 (Kan et al. 1991). But it is certainly different from the observed temperature dependence of the Gd linewidth as observed in La–Eu–Sr–CuO_4 (Kataev et al. 1997).

Stepanov et al. (1994, 1995) investigated Gd_2CuO_4 to further illuminate the Cu^{2+}-EPR silence in La_2CuO_4. They used a new experimental technique, combining the far-infrared (FIR) method of Fourier-transform spectroscopy with high magnetic fields up to 13 Tesla. The Gd ions help to enhance the Cu resonance by coupling the two magnetic subsystems. And indeed, at 2 K the authors observed three antiferromagnetic-resonance (AFMR) branches. Infrared transmission spectra at 2 K are shown in fig. 12 as a function of magnetic field. In a complete set of measurements, with the external magnetic field

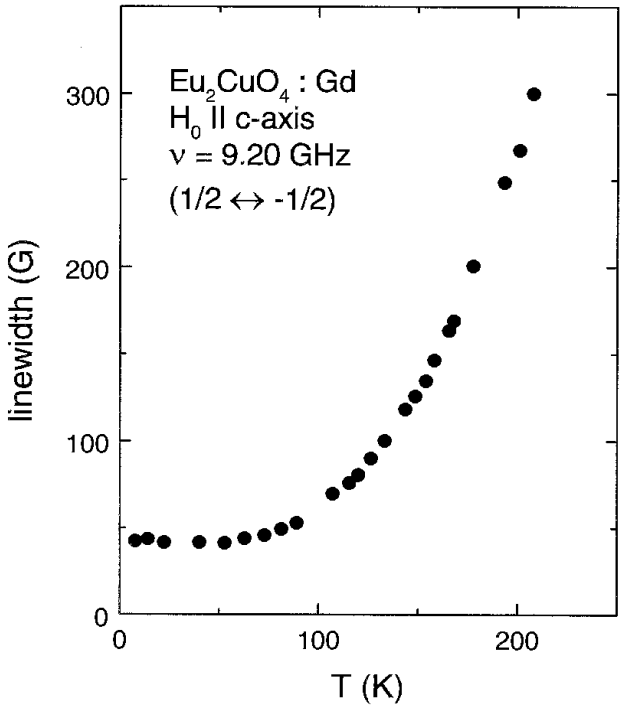

Fig. 11. Temperature dependence of the Gd^{3+} EPR linewidth of the $-\frac{1}{2}$ to $\frac{1}{2}$ transition in Eu_2CuO_4. The external magnetic field was directed along the crystallographic c-axis. From Zysler et al. (1991).

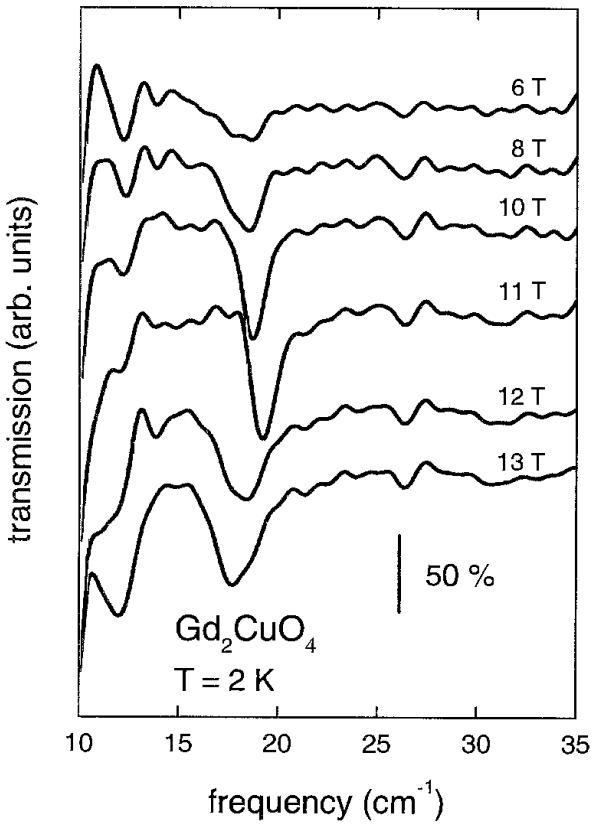

Fig. 12. FIR transmission for frequencies from $10\,cm^{-1}$ to $35\,cm^{-1}$ (30 GHz to 1000 GHz) in Gd_2CuO_4 as a function of magnetic field at 2 K. Transmission spectra for magnetic fields $6\,T \leqslant H \leqslant 13\,T$ are shown. From Stepanov et al. (1995).

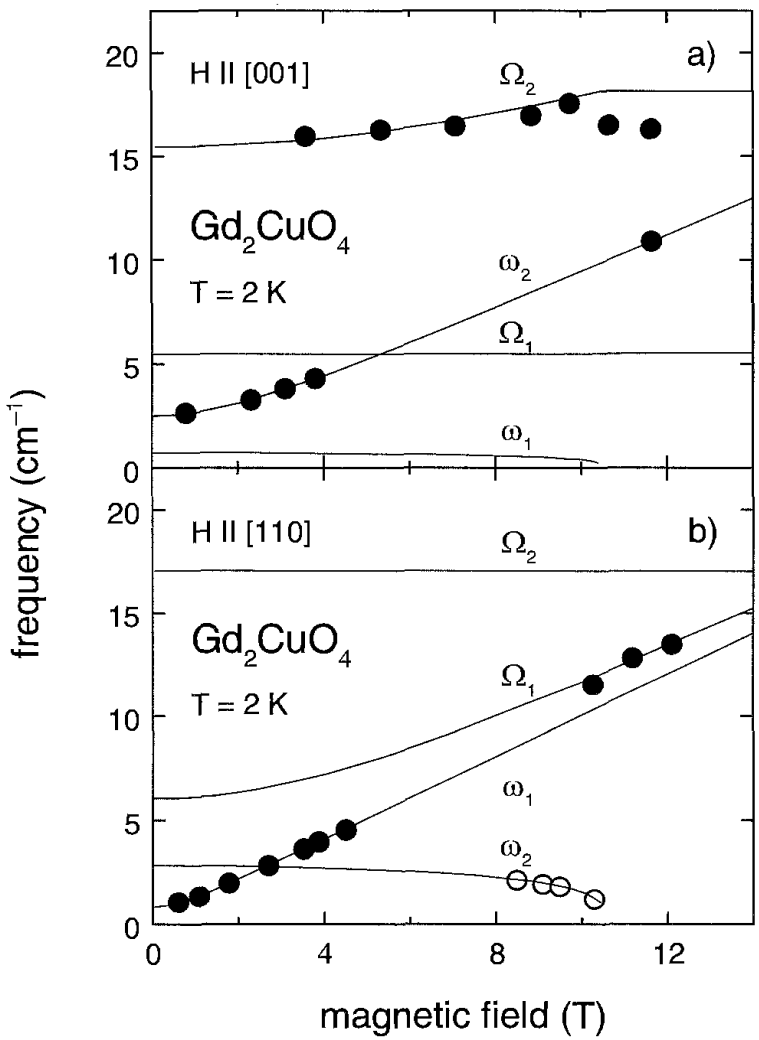

Fig. 13. Magnetic field dependence of the AFM resonances in Gd_2CuO_4 at 2 K. Branches ω_1 and ω_2 correspond to the Gd system, branches Ω_1 and Ω_2 to the Cu subsystem. The magnetic field is (a) along [001] and (b) along [110]. From Stepanov et al. (1995).

in two different crystallographic directions, the following frequencies could be identified: $\omega_1 = 0.8\,\mathrm{cm}^{-1}$, $\omega_2 = 2.8\,\mathrm{cm}^{-1}$, and $\Omega_2 = 17\,\mathrm{cm}^{-1}$ (figs. 13a,b). ω_1 and ω_2 correspond to the Gd magnetic subsystem, Ω_2 denotes the AFMR of the Cu^{2+} ions. The gap value for Ω_2 is $10\,\mathrm{cm}^{-1}$ at $T = 10\,\mathrm{K}$ and around 6–7 cm^{-1} at $T = 30\,\mathrm{K}$. Doping of Gd_2CuO_4 with another lanthanide ion, e.g. Nd, shifts the gap of Ω_2 to higher values, while the ω_1 and ω_2 modes remain unchanged. Intrinsic AFM order of the Gd magnetic subsystem is established at $T_N(\mathrm{Gd}) = 6.5\,\mathrm{K}$ and corresponds to a ferromagnetic (FM) propagation vector $\frac{1}{4}k = (0,0,0)$. The coupling between the Cu and Gd magnetic systems is determined by two main mechanisms: The first one consists in the staggered polarization with $\frac{1}{4}k = (\frac{1}{2},\frac{1}{2},0)$ imposed on the Gd subsystem by the ordered Cu-sublattices. The second coupling mechanism arises from the Cu–Gd exchange interaction and results in purely dynamic effects. In certain field directions (e.g. $H \parallel [001]$) the Gd subsystem enhances

the oscillator strength of the Cu-resonance mode. Utilizing this mechanism the authors were able to observe the Cu–AFMR mode directly.

Gd^{3+} EPR in $Nd_{2-x-y}Ce_xGd_yCuO_{4+\delta}$ was studied by Shimizu (1991). These compounds reveal superconductivity for Ce concentrations $0.14 < x < 0.18$. The author used powdered samples with $y = 0.005$ and $0.2 \leqslant x \leqslant 0.25$. Neutron scattering on single crystals of Nd_2CuO_4 (Matsuda et al. 1990) demonstrated different magnetically ordered phases (e.g. $T_N = 255\,K$ for the Cu spins). Again the EPR due to Cu^{2+} ions could not be detected in any of the samples investigated at any temperature. Around $T_N \approx 255\,K$, the Gd^{3+} resonance did not reveal changes in linewidth or resonance field. This finding can be expected, as the Gd^{3+} ions are substituted on Nd sites outside the CuO planes. T_N changes significantly with Ce concentration and disappears in the superconducting compounds. These results indicate that Ce doping (and/or oxygen reduction) is the reason for the disappearance of magnetic moments of the Cu ions. The linear dependence of the linewidth ΔH on the Ce concentration can be understood via a concentration-dependent variation of dipolar and exchange fields.

3.2. *Doping with 3d transition metals*

The EPR of 3d probes in metals is unusual. There are some exceptions: e.g. Cu:Mn (Owen et al. 1956), Pd:Mn (Alquie et al. 1978) and Pd:Fe (Devine 1976, 1977). But already in the last example the author pointed out that the observation of a resonance does not enable one to deduce whether this resonance simply originates from Fe or from Fe plus a spin-polarized cloud which is responsible for the formation of the well-known giant moment in the system Pd:Fe. The reader may find further examples of 3d EPR signals in metals in the review articles by Taylor (1975) and by Elschner and Loidl (1997).

Hirst (1972) gave an explanation for the observability or non-observability of resonance absorption for most of the 3d impurities. He related this problem to the appearance of a bottleneck situation (see Barnes 1979, 1981). To our knowledge the only 3d resonance, even with a resolved hyperfine structure, in a non-bottleneck case is $CePd_3:Mn$ (Schaeffer and Elschner 1985). $CePd_3$ is an intermediate-valence system with an extremely small conduction-electron density of states at the Fermi level.

The high-T_c cuprates La–Sr–Cu–O are very suitable host materials for Mn^{2+} or Fe^{3+} impurities. In the 2:1:4 compounds these 3d ions replace a Cu ion and hence are doped into the CuO_2 planes. A further advantage of these systems is that there exists only one Cu site in the unit cell. We notice that Fe ions are soluble in $La_{2-x}Sr_xCuO_4$ only in materials with $x \neq 0$ (Kemmler-Sack 1989). Fe^{3+} replaces Cu^{2+}, i.e. each Fe^{3+} compensates one charge carrier (hole). Hence, the density of charge carrier is determined by the sum of the Fe and Sr concentrations. Doping with Mn^{2+} leaves the concentration of charge carriers unaffected. In addition, Fe impurities influence the wave functions of the holes, inducing enhanced localization effects of the charge carriers. Unexpectedly, both Mn^{2+} and Fe^{3+} show a clear EPR signal which originates form the 3d ions. In all experimental reports, the intensity of the signal is proportional to the concentration of the dopants. The resonance absorption appears both in powders and in single crystals.

3.2.1. *Manganese*

Kikuchi and Ajiro (1988) investigated $(La_{1-x}Ba_x)_2CuO_4$ powdered samples with 0.1 and 1 at% Mn and Ba concentrations $0 \leqslant x \leqslant 0.1$, in the temperature range between 4.2 K and 300 K. Using a conventional X-band spectrometer they observed a well-defined Mn^{2+} signal corresponding to $g = 2.0$ without any hyperfine structures. The peak-to-peak linewidth is independent of temperature for $100\,K < T < 300\,K$ and approximately amounts to 400 G. It is strongly broadened towards lower temperatures which has been explained by a progressive freezing of spin fluctuations in the non-superconducting (nsc) samples. The corresponding behavior was not found in superconducting (sc) samples ($x = 0.1$). In addition, there is a remarkable shift of the resonance field towards lower fields. But linewidth and resonance field do not show any divergent behavior at a finite temperature, i.e. the slowing down of fluctuations persists down to 4.2 K. The authors (Kikuchi and Ajiro 1988) believe that these EPR measurements provide experimental evidence for a difference of the spin dynamics of sc and nsc La_2CuO_4-based compounds: The spin dynamics remains fast in sc samples, but considerably slows down in nsc samples, revealing the importance of magnetic fluctuations in the pairing process (Kikuchi and Ajiro 1988).

Onoda and Sato (1989) carried out EPR studies on powdered $(La_{1-x}Sr_x)CuO_{4-\delta}$ samples doped with 1% Mn. In contrast to Kikuchi and Ajiro (1988), they observed the magnetic slowing down associated with the progressive freezing of the Cu spins also for the superconducting samples $(La_{1-x}Sr_x)_2CuO_{4-\delta}$. The lineshape of their spectra is nearly Lorentzian, and the resonance fields correspond to $g \approx 2$ ($T \geqslant 50\,K$). The peak-to-peak linewidth remarkably depends on the heat treatment of the samples. Annealing in oxygen (2×10^7 Pa O_2 at 1350 K) suppressed the increase of linewidth at low temperatures.

These results show that it is difficult to compare EPR data of high-T_c cuprates from different laboratories. The number of parameters (i.e. annealing procedure, Sr content, oxygen stoichiometry, 3d-doping level, preparation procedure of the samples etc.) is too big, and hence the quality of the crystals, including effects like electronic phase separation, is too different in order to allow reliable comparisons. One way to avoid these difficulties is to carry out the investigation over a broad range of all these parameters and direct the attention to a well-defined preparation procedure for all samples used.

Recently the system $(La_{1-x}Sr_x)_2CuO_{4+\delta}$ doped with Mn has been studied carefully by Kochelaev et al. (1994). The aim of this detailed investigation was a systematic examination of the spin dynamics of this system. Mn-doped ceramic samples of $(La_{1-x}Sr_x)_2Cu_{1-y}Mn_yO_{4+\delta}$ with $0 \leqslant x \leqslant 0.3$ and $0 \leqslant y \leqslant 0.06$ were prepared by solid-state reaction from proper mixed powders of $SrCO_3$ and carefully dried La_2O_3, CuO and MnO. To avoid different oxygen contents all samples with the same manganese concentration were exposed to a common annealing procedure. Using a special annealing program the authors tried to keep the oxygen content close to 4 ($\delta \approx 0$). The EPR results of this study can be summarized as follows: (i) The EPR spectra are characterized by one unresolved Lorentzian linewith $g \approx 2.00$ ($30\,K \leqslant T \leqslant 300\,K$). A representative result of the Mn resonance absorption in $La_{1.8}Sr_{0.2}CuO_4$:Mn is shown in fig. 14. Remarkably

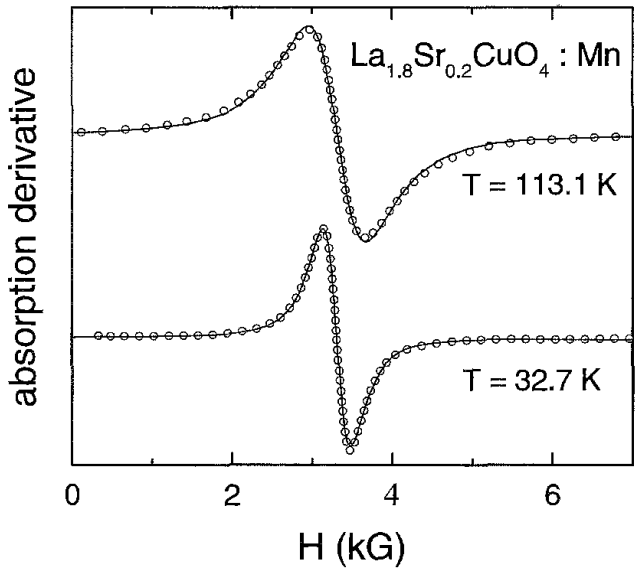

Fig. 14. Mn^{2+} in $La_{1.8}Sr_{0.2}Cu_{0.98}Mn_{0.02}O_4$: EPR spectrum at 32.7 K (lower curve) and 113.1 K (upper curve). The solid lines represent fits using Lorentzian lineshapes. From Kochelaev et al. (1994).

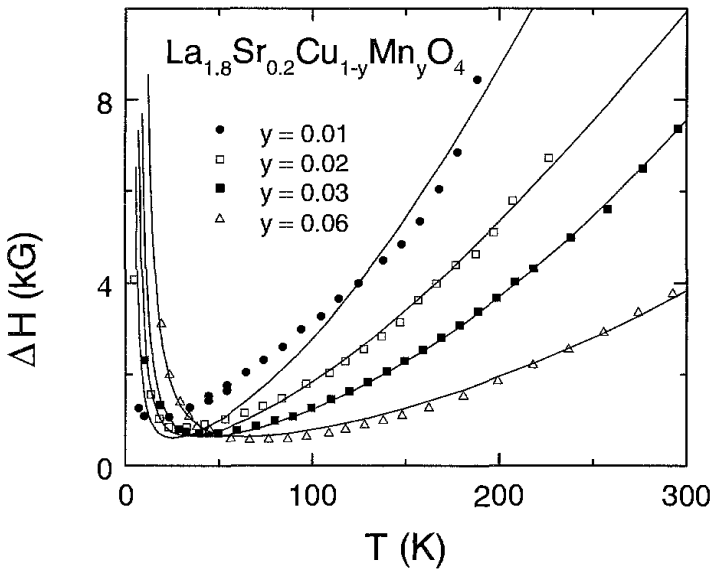

Fig. 15. Temperature dependence of Mn^{2+} linewidth for different Mn concentrations in $La_{1.7}Sr_{0.3}Cu_{1-y}Mn_yO_4$ ($0.01 \leqslant y \leqslant 0.06$). The solid lines represent the results of model fits. From Kochelaev et al. (1994).

the resonance field shifts to lower values for lower temperatures. (ii) The linewidth reveals a characteristic minimum between 20 K and 100 K, a value that depends both on Mn concentration and on Sr concentration. For yet higher temperatures the linewidth increases non-linearly, and (iii) the linewidth above the minimum depends inversely on the Mn concentration while it depends almost linearly on the Sr concentration. Representative results of the temperature dependence of the linewidth in $(La_{1-x}Sr_x)_2Cu_{1-y}Mn_yO_{4+\delta}$ for Sr concentration $x = 0.1$ and Mn concentrations $0 \leqslant y \leqslant 0.06$ are shown in fig. 15 (Kochelaev et al. 1994). From a detailed analysis of these results it became clear that the paramagnetic Curie constant seemed to be reduced almost by 60% as compared to a typical Mn^{2+} value.

Points (i) and (iii) are reminiscent of the so-called "bottleneck effect" for EPR of localized moments in metals (see e.g. Barnes 1981 and Elschner and Loidl 1997). As a consequence of the strong exchange coupling between Cu and Mn ions and of the close coincidence of their Larmor frequencies, the system displays a collective motion of the total magnetic moments of the Mn and Cu ions. Hence, it has been supposed that the relaxation of Cu or Mn ions to the lattice, $\Gamma_{\sigma L}$ and Γ_{sL} respectively, is ineffective to destroy this collective motion. This relaxation is negligible because both Mn^{2+} and Cu^{2+} have orbital-singlet ground states. Under these circumstances, i.e. with relaxation rates $\Gamma_{\sigma L}, \Gamma_{SL} \ll \Gamma_{\sigma S}, \Gamma_{S\sigma}$, the situation is similar to the well-known bottleneck effect and the authors could successfully fit their data with the well-known formula for a strong bottleneck system and using the measured dc susceptibility. Representative results of these fits are shown as solid lines in fig. 15 for $La_{1.7}Sr_{0.3}Cu_{1-y}Mn_yO_4$. It is important to note that $\Gamma_{S\sigma}$ between the two spin systems strongly depends on temperature and decreases with decreasing temperature, i.e. the bottleneck becomes weaker towards low temperatures (see e.g. Kochelaev et al. 1994). This entails that at low temperatures one has to take into account explicitly all contributions from local field distributions, e.g. crystal-field splitting, local magnetic field fluctuations, spin-glass behavior, dipolar interaction etc., which drive the rapid increase of the EPR linewidth at low temperatures.

It seems that the EPR measurements of S-state impurities in cuprates provide an effective tool for investigating the spin dynamics and for comparing different theoretical approaches concerning the nature of the spin correlations in the CuO_2 layers of the doped cuprates.

3.2.2. *Iron*

The other 3d S-state ion which is suitable as an EPR probe in the cuprates is Fe^{3+}. It substitutes Cu^{2+} in the CuO_2 planes and participates in the spin dynamics of these planes, too. As in the case of Mn^{2+}, there is substantial exchange between Fe^{3+} and Cu^{2+}, and again the coupled system, iron plus copper, is expected to be responsible for the EPR signal. But iron is trivalent and will annihilate one charge carrier created by Sr doping and thus the carrier density will depend on both the Sr and the Fe concentration. This fact is evidenced by the concentration dependence of the dc conductivity at room temperature, on both the Sr and the Fe concentration. Figure 16 shows the decrease of the conductivity in $La_{1-x}Sr_xCu_{1-y}Fe_yO_4$ at room temperature as a function of iron concentration y for a given set of strontium concentrations x (Kruschel 1993). With increasing Fe content an almost linear decrease of the conductivity is obtained for the three sample series investigated. Figure 16 demonstrates that a constant conductivity roughly depends on a constant carrier density, $n \sim x - y$. For instance, 200 Ωcm can be reached with $x = 0.1$, $y = 0.01$ and with $x = 0.2$, $y = 0.08$. Deviations from a constant carrier density and deviations from a constant slope on increasing Fe concentrations, which is observed for $x = 0.3$ (fig. 16), can be explained in terms of stronger localization processes induced by iron compared to strontium ions.

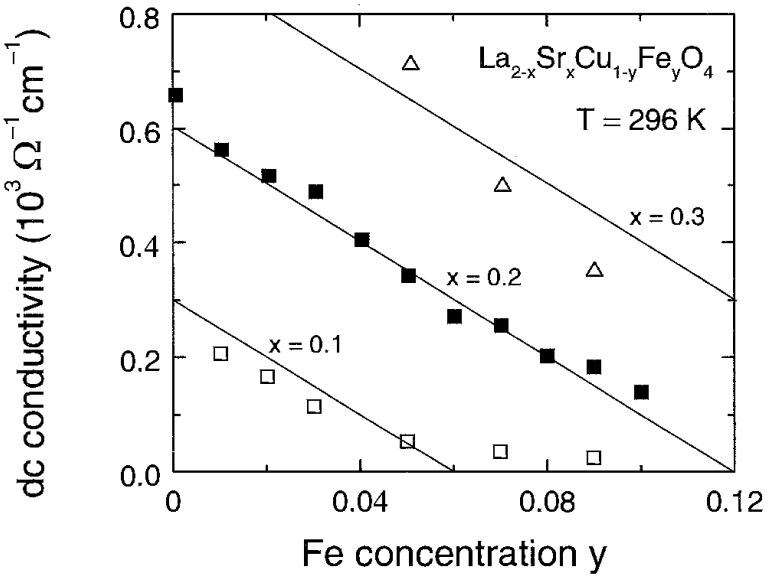

Fig. 16. Room temperature dc resistivity in $La_{2-x}Sr_xCu_{1-y}Fe_yO_4$ as a function of iron concentration y for samples with different strontium concentrations x. From Kruschel (1993).

Sienkiewicz et al. (1990) and Cieplak et al. (1993) reported on EPR measurements of $La_{1.85}Sr_{0.15}Cu_{1-y}Fe_yO_4$ with iron concentrations in the range $0 \leqslant y \leqslant 0.10$. The critical concentration y_c for the suppression of superconductivity is about 0.018. They reported on EPR measurements on polycrystalline samples as well as on powdered materials in order to reduce the skin effect. The EPR spectrum consisted of two absorption lines, with $g_1 \approx 2.07$ and $g_2 \approx 2.0$, the latter being very broad. Figure 17 shows the line with the g-value of 2, which is related to the Fe doping as a function of temperature. The EPR line is narrow only in a limited temperature range. It broadens at lower and higher temperatures. At low temperatures the line broadens progressively with increasing y, whereas at high temperatures ΔH is reduced by doping. Figure 18 shows the linewidth $\Delta H_{pp}(T)$ and the resistance $\rho(T)$. The respective temperatures where the curves reveal a minimum are given in the insert. There is a linear relation between $T_{min}(\Delta H)$ and $T_{min}(\rho)$. Sienkiewicz et al. (1990) interpret the low- and high-temperature behavior of the linewidth and its close correlation with the dc resistance as a consequence of a Fe–Fe dipole interaction at low temperatures and a Fe–Fe RKKY interaction at high temperatures. The RKKY interaction is supposed to be strongly influenced by localization effects. One can imagine that localization effects might be enhanced in the vicinity of impurities. This would be quite reasonable since Fe impurities have a valence of 3+ and may therefore attract negative charges.

Later on Cieplak et al. (1993) explained the increase of the linewidth towards low temperatures in terms of critical phenomena which are expected close to a spin-glass phase, and the broadening of the Fe EPR line was attributed to the freezing-in of spin fluctuations. The broadening of ΔH towards high temperatures was attributed to Korringa relaxation processes. Cieplak et al. (1993) reported a Korringa slope which is almost independent of the Fe concentration for $0.004 \leqslant y \leqslant 0.03$, which is hard to understand

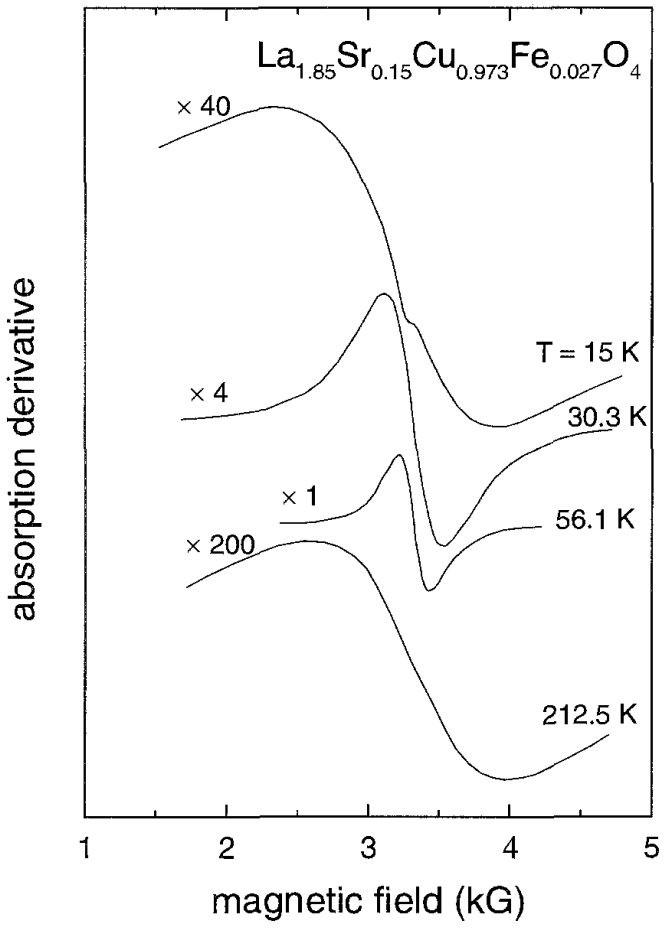

Fig. 17. Derivative of the EPR absorption vs. external magnetic field in $La_{1.85}Sr_{0.15}Cu_{0.973}Fe_{0.027}O_4$ for different temperatures from 15 K to 212.5 K. This figure nicely documents that a narrow EPR line can only be observed at intermediate temperatures. From Sienkiewicz et al. (1990).

in view of fig. 16. A similar behavior of the linewidth has been reported in samples with $0.2 \leqslant x \leqslant 0.3$ and $y = 0.03$ by Coldea (1991) and in samples with $0.03 \leqslant x \leqslant 0.12$ and $y = 0.01$ by Arai et al. (1994, 1996).

Shengelaya et al. (1994) investigated $La_{2-x}Sr_xCu_{1-y}Fe_yO_{4+\delta}$ with $y = 0.005$ and Sr concentrations $0.1 \leqslant x \leqslant 0.2$ over a limited temperature range of $20\,K < T < 110\,K$. The authors reported on the observation of Lorentzian lineshapes at all temperatures. They determined the peak-to-peak linewidth as a function of temperature for samples with various Sr concentrations. A characteristic linear increase of ΔH_{pp} (i.e., a Korringa-like increase) is observed at high temperatures ($60\,K \leqslant T \leqslant 110\,K$). The lines become broader with increasing Sr concentrations and the Korringa slope b was found to depend linearly on the Sr concentration, namely $b(x) = 227.3(x - 0.058)$. The Korringa slope depends quadratically on the density of states at the Fermi energy and hence, this behavior indicates a strongly sublinear dependence of the density of states on the Sr concentration beyond the metal–insulator transition at $x = 0.06$.

It has to be noticed that this Korringa-like behavior was found only in a rather narrow temperature range. Measurements which were extended to higher temperatures (see, e.g.. Kruschel 1993) show a significant nonlinear behavior. Furthermore $La_{2-x}Sr_xCu_{1-y}Fe_yO_4$

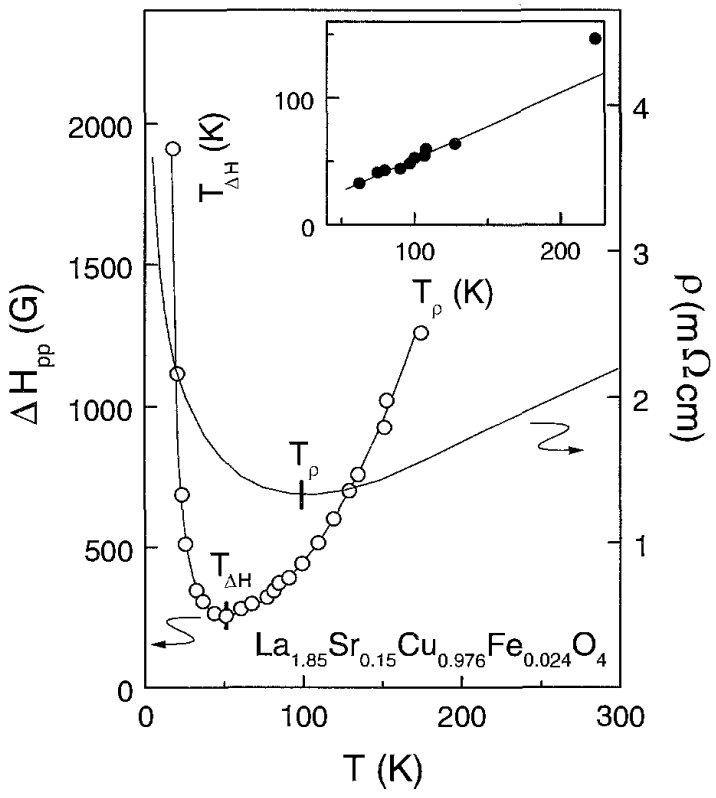

Fig. 18. EPR linewidth (left scale) and dc resistivity (right scale) for $La_{1.85}Sr_{0.15}Cu_{0.976}Fe_{0.024}O_4$. The inset shows the relation between $T_{min}(\Delta H)$ and $T_{min}(\rho)$ for samples with different Fe concentrations. From Sienkiewicz et al. (1990).

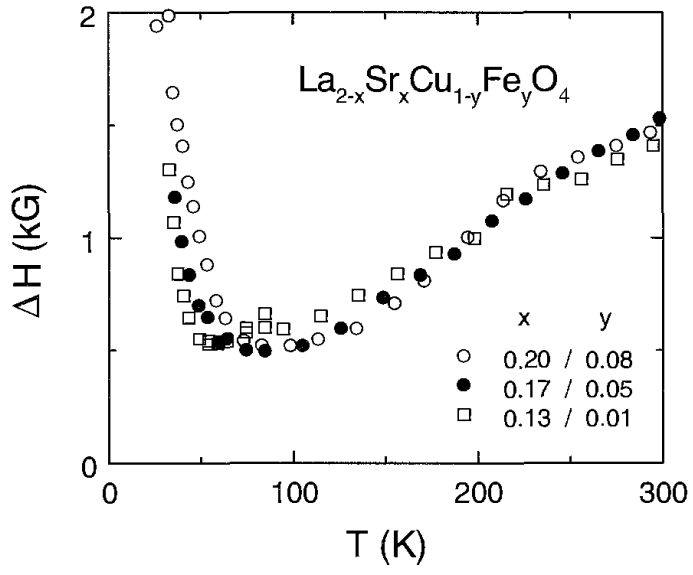

Fig. 19. Temperature dependence of EPR absorption linewidth for constant hole concentrations in $La_{2-x}Sr_xCu_{1-y}Fe_yO_4$, i.e. $x-y=$ const. From Kruschel (1993).

samples with $x=0.20$, 0.17 and 0.13 and $y=0.08$, 0.05 and 0.01 show the same linewidths (fig. 19), which confirms the assumption that $p=x-y$, i.e. the true number of charge carriers is the essential parameter to describe the EPR linewidth. Kruschel (1993) provided experimental evidence on many samples confirming this statement, e.g. $\Delta H(100\,\mathrm{K})$ for samples with $x=0.1$, $y=0.01$ and $x=0.2$, $y=0.09$ are practically

the same (~500 G). Figure 19 also reveals significant deviations from a linear increase of ΔH towards higher temperatures as outlined above. The steep increase of the linewidth below T_{min} seems to be a common feature of all 3d-doped and undoped cuprates investigated by EPR so far (Shengelaya et al. 1994, Kochelaev et al. 1994, 1997, Sienkiewicz et al. 1990, Cieplak et al. 1993, etc.). This increase signals the freezing of spin fluctuations and the concomitant localization of the charge carriers.

Shengelaya et al. (1994) and Kruschel (1993) draw attention to the fact that the dc resistance $R(T)$ in doped and undoped cuprates has an upturn below $T_{min}(R)$. The temperatures for $T_{min}(R)$ and $T_{min}(\Delta H)$ are almost the same and are strongly correlated. This suggests the conclusion that carrier localization is at least partially responsible for the steep increase of the EPR linewidth at low temperatures. This experimental observation seems to support models which assume that the AFM order is suppressed by mobile holes and that at low temperatures the freezing-in of charge carriers and the freezing-in of disordered spin configurations are closely connected.

In addition, Shengelaya et al. (1994) paid special attention to the EPR resonance absorption close to Sr concentration $x=0.125$. This concentration corresponds to the so-called 1/8 problem (see e.g., Tranquada et al. 1995), where superconductivity is suppressed in $La_{1-x}Ba_xCuO_4$. This anomaly is only weakly developed in the Sr compounds, but is strongly enhanced in Fe-doped samples. For concentrations close to $x=0.0125$, Shengelaya et al. found a strong increase of the linewidth towards low temperatures, indicating that this anomaly can be explained in terms of carrier-localization processes. And indeed, strip correlations of the spins and hole localization in domains in between has been experimentally verified by Tranquada et al. (1995) using neutron scattering techniques.

Concluding this section, we want to mention that an Fe-EPR study on overdoped $La_{2-x}Sr_xCuO_4$ with $x>0.5$ has been performed by Felner et al. (1996), and the phase separation which is induced by hydrogen doping has been observed in $La_{1.89}Sr_{0.11}CuO_4$ using Fe spin probes by Shengelaya et al. (1996).

4. EPR experiments on paramagnetic centers doped into the 1:2:3 compounds

There exists a large amount of work on either 1:2:3 compounds doped with rare-earth (R) ions or materials where yttrium has been fully substituted by an R ion. Y can be substituted by any other rare-earth species, except Ce or Pr, without any significant influence on the superconducting properties (Ho et al. 1987). Furthermore it has been shown that independent of the oxygen concentration very similar magnetic properties of the R subsystem are observed (Thompson et al. 1988). On passing we will also mention some attempts to observe EPR from 3d ions which were substituted for Cu. However, at present it is unclear which lattice sites are occupied, and it is even unclear whether Mn or Fe can be substituted into the 1:2:3 compounds at all.

4.1. *Doping with lanthanides*

4.1.1. *Gadolinium*

The largest body of EPR work in the 1:2:3 cuprates exists in Gd substituted samples. Gd reveals a pure S-state configuration without any orbital contributions, and it substitutes for Y at any amount and in all cases well-defined EPR signals were observed. This is true for metallic as well as for insulating samples. Like other R ions Gd does not perturb the superconducting properties. For instance, as in the Y compound, the superconducting phase-transition temperature in $GdBa_2Cu_3O_7$ is 92 K. Three-dimensional antiferromagnetic (AFM) order of the Gd sublattice is established at $T_N = 2.3$ K, with the magnetic moments perpendicular to the basal plane. In insulating $GdBa_2Cu_3O_{6.05}$, AFM order was found at $T_N = 2.4$ K (Thompson et al. 1988). Obviously, in both compounds the Gd–Gd exchange is small and of the same magnitude. From the very beginning it was interesting to clarify the exchange mechanism within the Gd sublattice. Obviously, dipolar interactions alone cannot account for the observed magnetic properties, and electron-mediated exchange can also be excluded as dominant mechanism, as the AFM ordering temperatures are identical for metallic and insulating compounds within experimental uncertainty. It was speculated that Gd–Gd interactions via a virtual exchange with electrons away from the Fermi energy may provide a possible mechanism (Liu 1988). A large amount of Gd-EPR work focused especially on this point of the Gd–Gd exchange interactions.

4.1.1.1. *Crystal-field effects.* The first EPR experiments on $GdBa_2Cu_3O_{6+\delta}$ were conducted by Schwartz et al. (1987) on ceramic samples at X-band frequencies. They observed the Gd resonance absorption close to the spin-only value $g = 2$, at room temperature as well as at 77 K in the superconducting phase. These experiments provided a direct experimental proof that the R ions are decoupled from the sc CuO_2 planes. EPR measurements on Gd-doped $YBa_2Cu_3O_{6+\delta}$ single crystals have been performed by Shaltiel et al. (1989b). These measurements were conducted at 9 GHz and at 36 GHz in insulating ($\delta = 0.1$) and in sc compounds ($\delta = 1$). From detailed measurements of the angular dependence of the resonance field within the *a,c* plane, the crystal-field (CF) parameters of Gd in its crystalline electric field were determined: $b_2^0 = 436$ MHz, $b_4^0 = 3.014$ MHz and $b_4^4 = -11.43$ MHz. The *g*-value was found to be 1.989(5). These values differ only slightly between the insulating and metallic samples. The authors also observed clear evidence for exchange-narrowing processes which were similar in the insulating and in the metallic samples. Janossy et al. (1990a,b) also studied Gd-doped $YBa_2Cu_3O_{6+\delta}$ ceramic samples. From the well-resolved fine structure, CF parameters similar to those observed by Shaltiel et al. (1989b) were derived. Later on Janossy et al. (1990a,b) performed a systematic study of the Gd resonance absorption as a function of the oxygen concentration. The occurrence of narrow lines in an intermediate concentration regime was interpreted by oxygen ordering processes within the chains.

4.1.1.2. *Gd-exchange interactions.* Nakamura et al. (1990a,b) investigated ceramic samples of $GdBa_2(Cu_{1-x}Ni_x)_3O_7$ using X-, K- and Q-band frequencies. They found that the linewidth of the Gd resonance absorption depends on the probing frequency and on the Ni concentration, and increases with increasing x. They concluded that the broadening of the Gd absorption is caused by dipolar interactions and in addition by exchange interactions, possibly superexchange interactions between Gd ions via the CuO_2 planes.

Deville et al. (1990, 1993) studied the Gd-EPR linewidth in $GdBa_2Cu_3O_{6+\delta}$ at X- and Q-band frequencies in ceramic samples and in single crystals at room temperature. The authors observed asymmetrical lineshapes due to the skin effect, which is characteristic of metallic samples. The linewidths amounted to 100 mT in single crystals and 300 mT in polycrystalline samples. The g-value was found to be 2.01(1), with a positive g-shift as compared to the free-electron value. The Lorentzian lineshapes indicated the presence of exchange-narrowing processes, which have their origin in the coupling between the Gd ions (Van Vleck–Anderson narrowing mechanism) (Van Vleck 1948, Anderson and Weiss 1953), but not in the coupling between Gd and the conduction electrons (Plefka–Barnes mechanism) (Plefka 1972, 1973, Barnes 1974). The Gd^{3+} ions are thought to be coupled by dipolar and AFM exchange couplings, with an effective exchange constant between next-nearest neighbors of $2J/k_B = -0.33$ K.

A detailed Gd-EPR experiment was conducted by Shaltiel et al. (1996) in Gd-doped $EuBa_2Cu_3O_{6+\delta}$ single crystals with an oxygen concentration $\delta \approx 0.85$ ($T_c = 80$ K). Just above the superconducting phase-transition temperature the Gd crystal-field spectrum is fully resolved, similar to the observations in the yttrium compounds. With increasing temperatures, exchange interactions narrow most of the EPR spectrum except the $\frac{7}{2}$ to $\frac{5}{2}$ transition. The latter reveals a pure Dysonian lineshape and exhibits a Korringa-like increase of the linewidth as a function of temperature. Using the Plefka–Barnes theory (Plefka 1972, 1973, Barnes 1974) they obtained a Korringa constant $b = 0.5$ G/K. This value yields an exchange interaction constant between the Gd spin and the conduction electrons of 0.5 meV, a value three orders of magnitude smaller than those observed in normal metals. The authors concluded (Shaltiel et al. 1996) that this fact explains the small effect of the R ions on the superconducting properties of the $RBa_2Cu_3O_{6+\delta}$ compounds.

Filip et al. (1994, 1996) analyzed the Gd-EPR linewidth in $Gd_xY_{1-x}Ba_2Cu_3O_{6+\delta}$ as a function of the Gd concentration x in the normal state at X-band frequencies in oriented powder samples. A Korringa-like broadening of the linewidth provided experimental evidence that in addition to the Gd–Gd exchange an exchange interaction between the Gd spins and the conduction electrons exists. It implies that part of the exchange interaction between the R ions could also be mediated via the conduction electrons. An effective exchange coupling constant $2J_{Gd-Gd} \approx 5$ μeV was determined by the authors via a comparison of the exchange-narrowed linewidth as a function of Gd concentration x. A further investigation on oriented powder samples of $Gd_xY_{1-x}Ba_2Cu_3O_{6+\delta}$ for concentrations $x = 0.25$, 0.5 and 0.75 has been presented by Kessler et al. (1997). The EPR absorption lines in all samples revealed Lorentzian lineshapes at all temperatures. For $T > T_c$ no temperature dependence of the g-values could be observed and the linewidth

revealed a Korringa-like broadening with a slope independent of the Gd concentration which amounts to $b = 0.035(2)\,\mathrm{mT/K}$. The g-shift was found to be positive and was associated with the dominance of the s(p)–f exchange over the d–f transferred exchange interactions. The effective exchange interaction between the Gd^{3+} ions and the conduction electrons was determined from the g-shift ($J_g = 3.2\,\mathrm{meV}$) and from the Korringa broadening ($J_K = 1.5\,\mathrm{meV}$). The size of this exchange coupling implies that a small part of the Gd–Gd interaction indeed may be mediated via the conduction electrons.

4.1.1.3. *Magnetic order, spin gaps and dynamic processes.* Badalyan et al. (1989) and Baranov and Badalyan (1993) studied Gd EPR on $GdBa_2Cu_3O_{6+\delta}$ with $\delta \geqslant 0.5$ at X-band frequencies. An intrinsic EPR signal was observed only for oxygen-deficient samples which are metallic and become superconducting. Below 50 K a signal appeared with a Curie-like increase of the intensity. With decreasing temperature the linewidth strongly decreases, passes through a minimum and, close to 10 K, shows a step-like increase at low temperatures possibly due the onset of magnetic order.

In a series of high-field EPR experiments, Janossy et al. (1995–1997) and Rockenbauer et al. (1997) studied $Gd_xY_{1-x}Ba_2Cu_3O_{6+\delta}$ compounds. These experiments were performed on oriented powder samples with oxygen concentrations $0 < \delta < 1$. In these high-frequency EPR experiments the magnetic-field dependent absorption of far-infrared light was measured with the sample placed in an oversized wave guide. Detailed studies of the temperature dependence of the g-shift and of the linewidth were performed. Typical EPR spectra at 245 GHz are shown in fig. 20 (Janossy et al. 1996). Here the central $-\frac{1}{2}$ to $+\frac{1}{2}$ transition at 8.8 T is well resolved at 40 K. With rising temperature it broadens considerably and shifts to higher resonance fields. Owing to the high frequencies the g-shifts can be resolved with much higher accuracy compared to standard (X- or Q-band) EPR experiments. The temperature dependence of the g-shift in $Gd{:}YBa_2Cu_3O_{6.76}$ is shown in fig. 21 (Janossy et al. 1996) and is compared to the ^{89}Y Knight shift as obtained

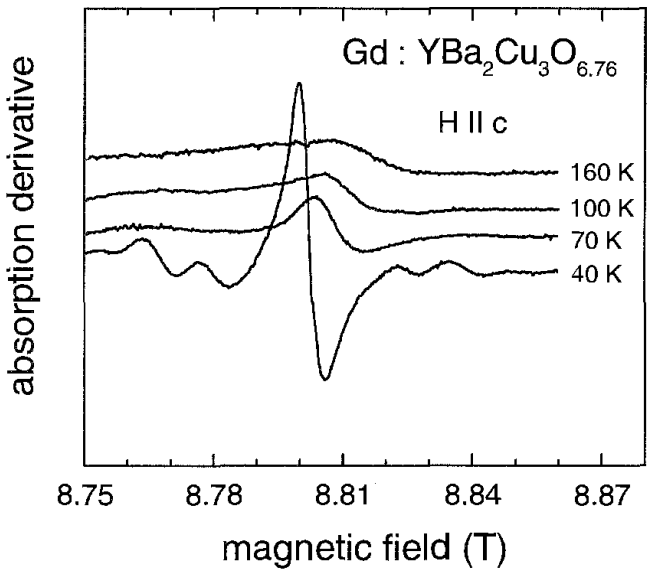

Fig. 20. Typical Gd^{3+} spectrum in gadolinium-doped $YBa_2Cu_3O_{6.76}$ at 245 GHz and 20 K. At 40 K besides the strong central line the fine structure becomes partially visible. From Janossy et al. (1996).

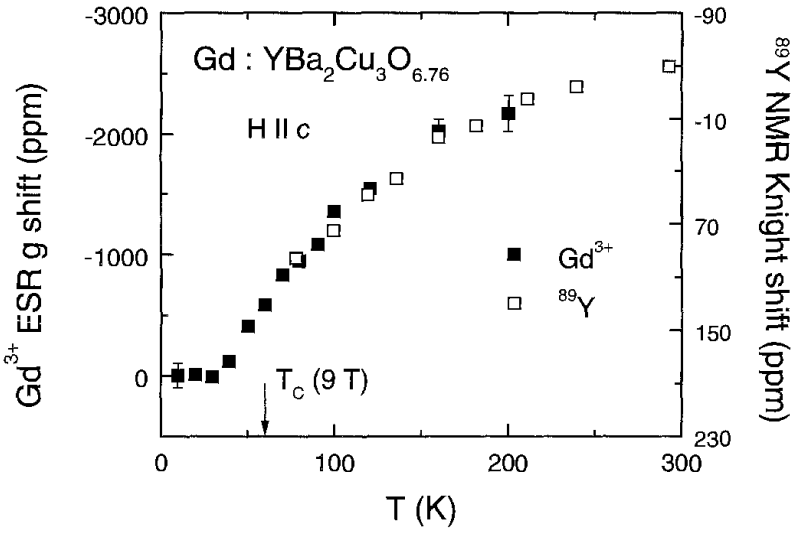

Fig. 21. Temperature dependence of the Gd^{3+} g-shift observed at 245 GHz. The EPR g-shift is compared with the ^{89}Y Knight shift as observed in NMR experiments. From Janossy et al. (1996).

in NMR experiments (Alloul et al. 1989). The temperature dependence of the g-value is in excellent agreement with the NMR Knight shift. The continuous decrease for $T > T_c$ can be interpreted as being due to the opening of a pseudo spin gap. The suppression of the superconducting state in Zn-doped YBCO ceramics with oxygen concentrations 6.76 and 7.0 and Zn concentrations of 3% has been investigated by high-field Gd-EPR studies by Janossy et al. (1994). From these experiments it has been concluded that the superconducting gap and the spin-fluctuation gap are concomitantly suppressed by Zn substitution.

Results of high-field Gd-EPR experiments on $YBa_2Cu_4O_8$ ($T_c = 82$ K) have been published by Williams et al. (1995) and Janossy et al. (1997). From the EPR g-shift the uniform spin susceptibility χ has been calculated with high precision. At low temperatures, in the range from $0.1T_c$ to $0.4T_c$ a linear temperature dependence of χ was observed. The temperature dependence of the normalized susceptibility is shown in fig. 22 and is compared to fits using a d-wave (solid line) and an s-wave (dashed line) coupling model. The results provide experimental evidence that $YBa_2Cu_3O_8$ reveals a d-wave sc gap with a maximum value $\Delta(0) = 190$ K, which seems to indicate the weak coupling limit (Janossy et al. 1997).

Finally, Atsarkin et al. (1996) developed a new method to measure the true spin–lattice relaxation time T_1 by EPR techniques. This technique measures the oscillating longitudinal magnetization of the sample by an amplitude-modulated microwave field under the condition of weak EPR saturation. Using this technique Gd-EPR measurements at X-band frequencies have been conducted on $GdBa_2Cu_3O_{6+\delta}$ samples with oxygen concentrations $\delta = 0.84$ ($T_c = 79$ K), 0.49 ($T_c = 48$ K) and 0.4 ($T_c = 48$ K). The observed spin–lattice relaxation rates are shown in fig. 23, using a representation $(T_1T)^{-1}$ vs. temperature (Atsarkin et al. 1996). The behavior as shown in fig. 23 is characteristic for the nuclear spin–lattice relaxation rate of ^{17}O or ^{89}Y nuclei in underdoped 1:2:3

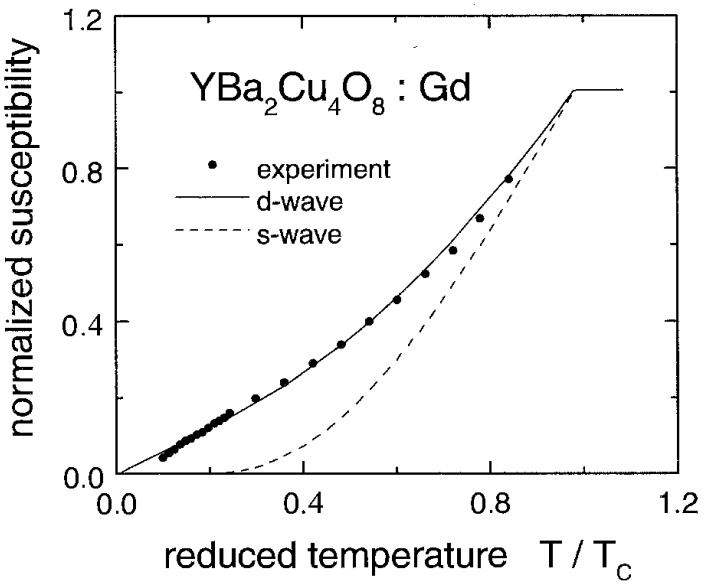

Fig. 22. Temperature dependence of the normalized spin susceptibility in gadolinium-doped $YBa_2Cu_4O_8$ vs. the reduced temperature. The spin susceptibility has been determined from Gd g-shift measurements at high frequencies. The solid line indicates a fit to a model assuming d-wave pairing symmetry. The dashed lines represents the results for s-wave superconductivity in the weak coupling limit. From Janossy et al. (1997).

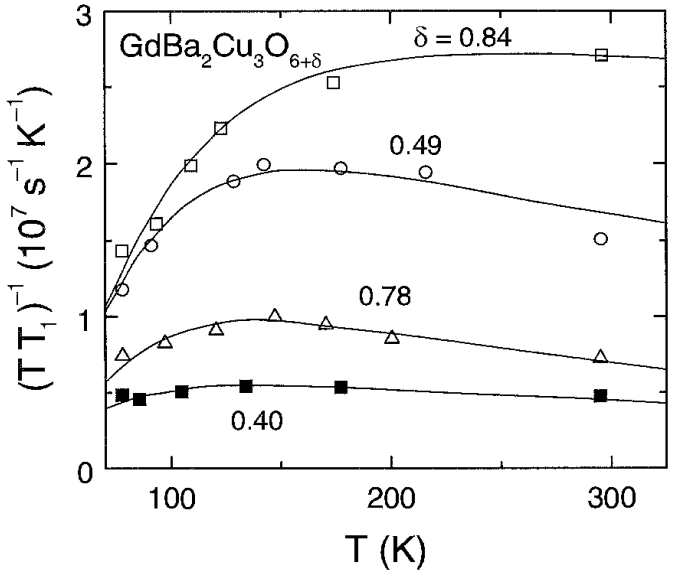

Fig. 23. Spin–lattice relaxation rate $(TT_1)^{-1}$ vs. temperature for various oxygen concentrations $\delta = 0.4$, 0.49, 0.78 and 0.84 in $GdBa_2Cu_3O_{6+\delta}$. T_1 has been measured using EPR techniques (see text). The solid lines have been calculated assuming a phenomenological spin-gap model. From Atsarkin et al. (1996).

systems, and can be explained by assuming the opening of a spin-gap well above the superconducting phase-transition temperature. The solid lines in fig. 23 were calculated assuming that the spin–lattice relaxation rate is determined by a dynamic susceptibility which shows the opening of the spin-gap according to $[1-\tanh^2(\Delta/2k_BT)]$. This expression is a purely phenomenological ansatz but has been successfully applied in the analysis of neutron scattering data (Tranquada et al. 1992).

4.1.2. *Other lanthanide ions*

The crystal-field interaction splits the ground-state J multiplet of the lanthanide ions. The splitting is determined by the charge distribution at the site of the lanthanide ion and by

the site symmetry. Usually these crystal-field excitations can be studied in detail using neutron scattering techniques, and a number of neutron experiments on $RBa_2Cu_3O_{6+\delta}$ and on $Y_{1-x}R_xBa_2Cu_3O_{6+\delta}$ compounds have been reported (e.g., Furrer 1993, Mukherjee et al. 1994, Allenspach et al. 1995). Using crystal-field spectroscopy, attempts have been made to probe the charge distribution and to monitor directly the changes of the carrier concentration on doping (Allenspach et al. 1995). The lowest crystal-field excitations can also be determined using EPR techniques. EPR experiments have been performed on Er^{3+} ions by Huang et al. (1991), Kurkin et al. (1993) and Shimizu et al. (1997b), and on Yb^{3+} ions by Kurkin et al. (1993).

Using 1:2:3 compounds with an oxygen concentration of 6.85, Kurkin et al. investigated the Er and Yb EPR in oriented powders, using 1% Er or Yb substituted for Y. The samples were characterized by a superconducting phase-transition temperature of 85 K. At low temperatures the g-values for Er and Yb amounted to $g_\perp = 4.56$ and 3.50 and $g_\parallel = 3.93$ and 2.95, respectively. For low temperatures ($T < 6$ K) the linewidths for both R ions remain almost constant. However, with rising temperature the linewidths decrease, pass through a minimum and exponentially increase with further increasing temperatures. The strong increase towards high temperatures is due to an Orbach spin–lattice relaxation process which has not been considered in this review. The minimum linewidth has been detected close to 30 K in the Er compounds and close to 60 K in the Yb compounds. The increase towards low temperatures has been analyzed assuming an exponential decrease of the relaxation rates which are thought to arise from the spin fluctuations in the CuO_2 planes. In a recent study Shimizu et al. (1997b) studied the lowest crystal-field excitation of Er^{3+} in $Y_{0.97}Er_{0.03}Ba_2Cu_3O_{6+\delta}$ as a function of oxygen concentration. The linewidth as a function of temperature has been analyzed using a sum of a Korringa term and Orbach relaxation. The crystal-field excitation energy was found to decrease smoothly with increasing oxygen concentration, from 140 K at 6.2 to approximately 110 K close to oxygen concentrations of 7. From neutron-scattering results in $ErBa_2Cu_3O_{6+\delta}$ just the opposite correlation of crystal-field excitation and oxygen concentration has been detected. In addition, the neutron-scattering results provided experimental evidence that the crystal-field transitions are composed of different components, indicating local phase separation (Allenspach et al. 1995). The Korringa slope, which is a direct measure of the density of states at the Fermi energy, was found to be zero for oxygen concentrations $\delta < 0.2$, increased up to $\delta \approx 0.4$, and saturated for higher oxygen concentrations. From this observation it has been concluded that the carrier concentrations roughly remains constant for $\delta > 0.4$.

4.2. *Doping with 3d transition metals*

In passing we want to mention that there have been some attempts to use Fe^{3+} or Mn^{2+} ions as EPR probes in $YBa_2Cu_3O_{6+\delta}$. At present it seems still unclear to what extent these dopants can be substituted while maintaining single-phase material. Up to now, not one convincing experiment exists that shows an intrinsic EPR signal from these dopants. Manganese-substituted 1:2:3 compounds were investigated by Kaise et al. (1990),

Moto et al. (1990), Y. Yamada et al. (1990) and Skrzypek et al. (1991). No manganese EPR signals have been found by Kaise et al. (1990) and by Skrzypek et al. (1991). The observation of Mn signals from phase-separated clusters was reported by Moto et al. (1990), and Mn signals of unclear origin were published by Y. Yamada et al. (1990). Attempts to use the trivalent magnetic Fe as EPR probe have been performed by Albino et al. (1988a) and by Romanyukha et al. (1990). While the former authors observed no EPR signals some evidence for Fe EPR signals has been reported by the latter.

5. Summary and outlook

After the discovery of high-T_c superconductivity by Bednorz and Müller (1986), up to now an enormous number of EPR investigations has been performed on this new class of materials. And while in the beginning it seemed that EPR can only be used to characterize the purity of the material under investigation, in time it has been established that a large amount of fundamental knowledge, especially about the physics of spin fluctuations, can be obtained from EPR experiments. Partly this success became possible with the highly improved sample preparation techniques and the availability of pure single-crystalline materials. With this short review we have tried to summarize the information that has been collected in HTSC during the last few years, but at the same time we want to emphasize that we are still lacking a deeper understanding of the different phenomena that were observed, and a lot of work, theoretical and experimental, will be necessary to arrive at definite conclusions.

First of all it became evident that a great number of different EPR probes can be used in HTSC. Neglecting defect states these are, amongst others: charge carriers doped into the CuO_2 planes, i.e. polarons which have been detected in the 1:2:4 compounds; paramagnetic chain fragments in the 1:2:3 compounds which are located in the Cu–O chains; 3d transition-metal ions, like Fe and Mn, which can be doped into the superconducting planes in the 1:2:4 compounds and rare-earth ions which can be used in the 1:2:3 compounds as well as in the 2:1:4 compounds and which are only weakly coupled to the spin fluctuations in the CuO_2 planes, but nevertheless provide important information about these excitations. At this point it is important to mention that it has now become clear that all EPR probes within the CuO_2 planes exhibit a strong bottleneck behavior. This means that the probing ions, like Mn, Fe, polarons, etc., are intimately coupled to the spin fluctuations undergoing a highly collective motion with the Cu spins, while both spin species are only weakly coupled to the lattice.

The second important piece of information from EPR experiments was collected about the slowing down of the spin fluctuations. Most of the EPR experiments, at least in slightly underdoped materials, show a strong increase of the linewidth towards low temperatures. This behavior seems to be compatible with the slowing down of the characteristic frequencies of the spin fluctuations. These EPR results have to be compared with NMR results which can be interpreted by the opening of a spin-gap well above the superconducting phase-transition temperature in the underdoped samples. In this

field systematic studies in high-quality samples, especially across the metal–insulator transition, are needed to provide experimental evidence if the slowing down of spin fluctuations can be observed in metallic and in insulating samples. These studies also have to take into account possible phase separation processes.

Of course EPR investigations allow a detailed analysis of the magnetic interactions. Paramount examples of this kind of investigation are the Gd-EPR experiments which yield detailed information about the nature of the Gd–Gd interactions in the lanthanide-doped superconductors.

A lot of information can be gained from the Korringa or Korringa-like increase of the linewidth towards high temperatures with respect to the density of states at the Fermi energy. This seems also to be important for the so-called 1/8 problem which, on the basis of the EPR results, seems to be due to charge localization processes. Tranquada et al. (1995) reported the appearance of an ordered stripe phase in $La_{1.48}Nd_{0.4}Sr_{0.12}CuO_4$ in which regions of ordered copper spins are separated by stripes with segregated holes. However, in this field a lot of controversial results exist, and careful and systematic further EPR experiments and detailed analyses will be necessary to arrive at final conclusions.

Finally, high-frequency and high magnetic-field EPR experiments seem to be a powerful tool to study the static and dynamic susceptibilities in HTSC. In this newly opened area of research important contributions have been published and further exciting experiments can be expected in the near future.

Acknowledgement

We acknowledge enlightening and stimulating discussions with B.I. Kochelaev and K.A. Müller. This review would not have been possible without the detailed and careful experimental work of L. Kan, G. Kruschel and J. Sichelschmidt. This work was partly supported by the BMBF under the contract number 13N6917/Elektronische Korrelationen und Magnetismus.

References

Abragam, A., and B. Bleaney, 1970, in: Electron Paramagnetic Resonance of Transition Ions (Clarendon Press, Oxford) p. 459.

Aeppli, G., S.M. Hayden, H.A. Mook, Z. Fisk, S.-W. Cheong, D. Rytz, J.P. Remeika, G.P. Espinosa and A.S. Cooper, 1989, Phys. Rev. Lett. **62**, 2052.

Aharony, A., R.J. Birgeneau, A. Conglio, M.A. Kastner and H.E. Stanley, 1988, Phys. Rev. Lett. **60**, 1330.

Albino, J., O. de Aguiar, J. van den Berg, H.B. Brom, G.J. Nieuwenhuys, J.A. Mydosh, F.P.F. van Berkel and H.W. Zandbergen, 1988a, Physica C **156**, 571.

Albino, J., O. de Aguiar, A.A. Menovsky, J. van den Berg and H.B. Brom, 1988b, J. Phys. C **21**, L237.

Alekseevskii, N.E., I.A. Garifullin, N.N. Garif'yanov, B.I. Kochelaev, A.V. Mitin, V.I. Nizhankovskii, L.R. Tagirov and E.P. Khylbov, 1988, Sov. Phys.-JETP **67**, 805.

Alekseevskii, N.E., A.V. Mitin, V.I. Nizhankovskii, I.A. Garfullin, N.N. Garif'yanov, G.G. Khaliullin, E.P. Khylbov, B.I. Kochelaev and L.R. Tagirov, 1989, J. Low Temp. Phys. 77, 87.

Allenspach, P., A. Furrer, F. Fauth, M. Gauillome,

W. Henggeler, J. Mesot and S. Rosenkranz, 1995, Physica B **213&214**, 78.

Alloul, H., T. Ohno and P. Mendels, 1989, Phys. Rev. Lett. **63**, 1700.

Alquie, G., A. Kreisler and J.P. Burger, 1978, Solid State Commun. **26**, 265.

Amoretti, G., E. Buluggiu, A. Vera, G. Calestani and F.C. Matacotta, 1988, Z. Phys. B **72**, 17.

Anderson, P.W., and P.R. Weiss, 1953, Rev. Mod. Phys. **25**, 269.

Arai, J., T. Nitta and N. Mori, 1994, Physica C **235–240**, 1649.

Arai, J., K. Kojima and N. Mori, 1996, J. Low Temp. Phys. **105**, 455.

Atsarkin, V.A., G.A. Vasneva and V.V. Demidov, 1995, JETP Lett. **81**, 509.

Atsarkin, V.A., V.V. Demidov and G.A. Vasneva, 1996, J. Low Temp. Phys. **105**, 443.

Badalyan, A.G., P.G. Baranov, V.I. Aleksandrov, M.A. Borik and V.V. Osiko, 1989, JETP Lett. **49**, 697.

Baranov, P.G., and A.G. Badalyan, 1993, Solid State Commun. **85**, 987.

Barham, P.J., and D.C. Doetschman, 1992, J. Mater. Res. 7, 565.

Barnes, R.G., 1979, NMR, EPR and Mössbauer effect: metals, alloys and compounds, in: Handbook on the Physics and Chemistry of Rare Earths, Vol. 2, eds K.A. Gschneidner Jr and L. Eyring (North-Holland, Amsterdam) p. 387.

Barnes, S.E., 1974, Phys. Rev. B **9**, 4789.

Barnes, S.E., 1981, Adv. Phys. **30**, 801.

Bednorz, J.G., and K.A. Müller, 1986, Z. Phys. B **64**, 189.

Blank, D.H.A., J. Flokstra, G.J. Gerritsma, L.J.M. van de Klundert and G.J.M. Velders, 1987, Physica B **145**, 222.

Blazey, K.W., K.A. Müller, J.G. Bednorz, W. Berlinger, G. Amoretti, E. Buluggiu, A. Vera and F.C. Matacotta, 1987, Phys. Rev. B **36**, 7241.

Bowden, G.J., P.R. Elliston, K.T. Wan, S.X. Dou, K.E. Easterling, A. Bourdillon, C.C. Sorrell, B.A. Cornell and F. Separovic, 1987, J. Phys. C **20**, L545.

Castilho, J.H., P.A. Venegas, G.E. Barberis, C. Rettori, R.F. Jardim, S. Gama, D. Davidov and I. Felner, 1987, Solid State Commun. **64**, 1043.

Castner, T.G., and M.S. Seehra, 1993, Phys. Rev. B 47, 578.

Chaillout, C., S.W. Cheong, Z. Fisk, M.S. Lehmann, M. Marezio, B. Morosin and J.E. Schirber, 1989, Phys. Scr. T **29**, 97.

Chakravarty, S., and R. Orbach, 1990, Phys. Rev. Lett. **64**, 224.

Cieplak, M.Z., A. Sienkiewicz, F. Mila, S. Guha, G. Xiao, J.Q. Xiao and C.L. Chien, 1993, Phys. Rev. B **48**, 4019.

Coldea, M., 1991, Physica C **185–189**, 1197.

Cywinski, R., S.H. Kilcoyne and J.N. Lomer, 1988, Solid State Commun. **67**, 355.

De, D.K., 1988, J. Phys. C **21**, 4481.

Deville, A., B. Gaillard, H. Noel, M. Potel, P. Gougeon and J.C. Levet, 1988, Physica C **153–155**, 669.

Deville, A., B. Gaillard, H. Noel, M. Potel, P. Gougeon and J.C. Levet, 1989, J. Phys. (Paris) **50**, 2357.

Deville, A., B. Gaillard, L. Bejjit, O. Monnereau, H. Noel and M. Potel, 1990, Physica B **165–166**, 1319.

Deville, A., L. Bejjit, B. Gaillard, J.P. Sorbier, O. Monnereau, H. Noel and M. Potel, 1993, Phys. Rev. B **47**, 2840.

Devine, R.A.B., 1976, Solid State Commun. **19**, 351.

Devine, R.A.B., 1977, J. Phys. F 7, 461.

Durny, R., J. Hautala, S. Ducharme, B. Lee, O.G. Symko, P.C. Taylor, D.J. Zheng and J.A. Xu, 1987, Phys. Rev. B **36**, 2361.

Ebner, C., and D. Stroud, 1985, Phys. Rev. B **31**, 165.

Elschner, B., and A. Loidl, 1997, in: Handbook on the Physics and Chemistry of Rare Earths, Vol. 24, eds K.A. Gschneidner Jr and L. Eyring (North-Holland, Amsterdam) p. 221.

Emery, V.J., and S.A. Kivelson, 1993, Physica C **209**, 597.

Emery, V.J., and G. Reiter, 1988, Phys. Rev. B **38**, 4547.

Felner, I., J. Gersten, A. Minakov, M. Merzlyakov and Yu. Bugoslavsky, 1996, Physica C **261**, 207.

Filip, C., C. Kessler, F. Balibanu, P. Kleeman, A. Darabont, L.V. Giurgiu and M. Mehring, 1994, Physica C **235–240**, 1645.

Filip, C., C. Kessler, F. Balibanu, P. Kleeman, A. Darabont, L.V. Giurgiu and M. Mehring, 1996, Physica B **222**, 16.

Foukis, V., O. Dobbert, K.-P. Dinse, M. Lehnig, T. Wolf and W. Goldacker, 1988, Physica C **156**, 467.

Frenkel, D.M., R.J. Gooding, B.I. Shraiman and E.D. Siggia, 1990, Phys. Rev. B **41**, 350.

Furrer, A., 1993, in: Selected Topics in Superconductivity, eds L.C. Gupta and M.S. Multani (World Scientific, Singapore) p. 349.

Garifullin, I.A., N.N. Garif'yanov, N.E. Alekseevskii and S.F. Kim, 1991, Physica C **179**, 9.

Genossar, J., D. Shaltiel, V. Zevin, A. Grayevsky and B. Fisher, 1989, J. Phys.: Condens. Matter **1**, 9471.

Hammel, P.Ch., A.P. Reyes, Z. Fisk, M. Takigawa, J.D. Thompson, R.H. Haffner, S.-W. Cheong and J.E. Schirber, 1990, Phys. Rev. B **42**, 6781.

Hirst, L.L., 1972, Adv. Phys. **21**, 759.

Ho, J.C., P.H. Hor, R.L. Meng, C.W. Chu and C.Y. Huang, 1987, Solid State Commun. **63**, 711.

Hoffmann, S.K., B. Czyzak and J. Stankowski, 1990, Acta Phys. Pol. A 77, 621.

Huang, M.X., J. Barak, S.M. Bhagat, L.C. Gupta, A.K. Rajarajan and R. Vijayaraghavan, 1991, J. Appl. Phys. 70, 5754.

Huber, D.L., 1972, Phys. Rev. B **6**, 3180.

Janes, R., and P.P. Edwards, 1994, J. Phys.: Condens. Matter **6**, L315.

Janes, R., K.K. Singh, S.D. Burnside and P.P. Edwards, 1991, Solid State Commun. 79, 241.

Janes, R., M.R. Little, M. Parker and N. Akther, 1994, J. Magn. Magn. Mater. **136**, L13.

Janossy, A., A. Rockenbauer and S. Pekker, 1990a, Physica C **167**, 301.

Janossy, A., A. Rockenbauer, S. Pekker, G. Oszlanyi, G. Faigel and L. Korecz, 1990b, Physica C **171**, 457.

Janossy, A., J.R. Cooper, L.-C. Brunel and A. Carrington, 1994, Phys. Rev. B **50**, 3442.

Janossy, A., L.-C. Brunel, G.V.M. Williams, J.R. Cooper and W.Y. Liang, 1995, in: Proc. Physical Phenomena at High Magnetic Fields – II, eds Z. Fisk, L. Gor'kov, D. Meltzer and R. Schrieffer (World Scientific, Singapore) pp. 525–530.

Janossy, A., L.-C. Brunel and J.R. Cooper, 1996, Phys. Rev. B **54**, 13.

Janossy, A., T. Feher, G. Oszlany and G.V.M. Williams, 1997, Phys. Rev. Lett. 79, 2762.

Jorgensen, J.D., B. Dabrowski, S. Pei, D.G. Hinks and L. Soderholm, 1988, Phys. Rev. B **38**, 11337.

Kaise, M., M. Mizuno, C. Nishihara, H. Nozoye and H. Shindo, 1990, in: Advances of Superconductivity II, Proc. 2nd Int. Symp. on Superconductivity, Tsukuba, 1989, eds T. Ishiguro and K. Kajimura (Springer, Tokyo) p. 543.

Kan, L., S. Elschner and B. Elschner, 1991, Solid State Commun. 79, 61.

Kanoda, K., T. Takahashi, T. Kawagoe, T. Mizoguchi, M. Hasumi and S. Kagoshima, 1988, Physica C **153–155**, 749–750.

Kataev, V.E., E.F. Kukovitskii, G.B. Teitelbaum and A.M. Finkelstein, 1990, J. Exp. Theor. Phys. Letters **51**, 129.

Kataev, V.E., Yu.S. Greznev, E.F. Kukovitskii, G.B. Teitelbaum, M. Breuer and N. Knauf, 1992, J. Exp. Theor. Phys. Lett. **56**, 385.

Kataev, V.E., Yu.S. Greznev, G.B. Teitelbaum, M. Breuer and N. Knauf, 1993, Phys. Rev. B **48**, 13042.

Kataev, V.E., B. Rameev, B. Büchner and R. Borowski, 1996, J. Low Temp. Phys. **105**, 449.

Kataev, V.E., B. Rameev, B. Büchner, M. Hücker and R. Borowski, 1997, Phys. Rev. B **55**, R3394.

Kawasaki, K., 1968, Progr. Theor. Phys. (Kyoto) **39**, 285.

Kemmler-Sack, S., 1989, private communication.

Kessler, C., M. Mehring, P. Castellaz, G. Borodi, C. Filip, A. Darabont and L.V. Giurgiu, 1997, Physica B **229**, 113.

Kikuchi, H., and Y. Ajiro, 1988, J. Phys. Soc. Jpn. **57**, 2628.

Kochelaev, B.I., L.R. Tagirov, I.A. Garifullin, N.N. Garif'yanov, G.G. Khalliullin, N.E. Alekseevskii, A.V. Mitin, V.I. Nizhanovskii and E.P. Khlybov, 1990, Exp. Technik Phys. **38**, 359.

Kochelaev, B.I., L. Kan, B. Elschner and S. Elschner, 1994, Phys. Rev. B **49**, 13106.

Kochelaev, B.I., J. Sichelschmidt, B. Elschner, W. Lemor and A. Loidl, 1997, Phys. Rev. Lett. 79, 4274.

Kohara, K., H. Yamagata, M. Matsumura, Y. Yamada, I. Nakada, E. Sakagami, Y. Oda and K. Asayama, 1987, Physica B **148**, 459.

Kremer, R.K., V. Hizhnyakov, E. Sigmund, F. Hensch, A. Simon, K.A. Müller and M. Mehring, 1992, Z. Phys. B **86**, 319.

Kruschel, G., 1993, PhD Thesis (TU Darmstadt).

Kurkin, I.N., I.Kh. Salikhov, M.A. Teplov and R.Sh. Zhdanov, 1993, Sov. Phys.-JETP 76, 657.

Lazuta, A.V., 1991, Physica C **181**, 127.

Liu, S.H., 1988, Phys. Rev. B 37, 7470.

Martinez, G., and P. Horsch, 1991, Phys. Rev. B **44**, 317.

Matsuda, M., K. Yamada, K. Kakurai, H. Kadowaki, T.R. Thurston, Y. Endoh, Y. Hidaka, R.J. Birgeneau, M.A. Kastner, P.M. Gehring, A.H. Moudden and G. Shirane, 1990, Phys. Rev. B **42**, 10098.

McKinnon, W.R., J.R. Morton, K.F. Preston and L.S. Selwyn, 1988, Solid State Commun. **65**, 855.

Mehran, F., and P.W. Anderson, 1989, Solid State Commun. 71, 29.

Mehran, F., and K.W.H. Stevens, 1982, Phys. Rep. **85**, 124.

Mehran, F., S.E. Barnes, T.R. McGuire, W.J. Gallagher, R.L. Sandstrom, T.R. Dinger and D.A. Chance, 1987, Phys. Rev. B **36**, 740.

Mehran, F., S.E. Barnes, G.V. Chandrashekhar, T.R. McGuire and M.W. Shafer, 1988a, Solid State Commun. **67**, 1187.

Mehran, F., S.E. Barnes, T.R. McGuire, T.R. Dinger, D.L. Kaiser and F. Holtzberg, 1988b, Solid State Commun. **66**, 299.

Mehran, F., S.E. Barnes, E.A. Giess and T.R. McGuire, 1988c, Solid State Commun. **67**, 55.

Morimoto, A., T. Maeda, A. Moto, M. Kumeda and T. Shimizu, 1988, Jpn. J. Appl. Phys. **27**, L407.

Moto, A., A. Morimoto, M. Kumeda and T. Shimizu, 1990, Supercond. Sci. Technol. **3**, 579.

Mukherjee, A., A.T. Boothroyd and J.S. Gardner, 1994, Physica C **235–240**, 1707.

Nakamura, F., Y. Ochiai, H. Shimizu and Y. Narahara, 1990a, Phys. Rev. B **42**, 2558.

Nakamura, F., Y. Ochiai, H. Shimizu and Y. Narahara, 1990b, Physica B **165&166**, 1315.

Onoda, M., and M. Sato, 1989, Solid State Commun. **70**, 309.

Oseroff, S.B., D. Rao, F. Wrigth, D.C. Vier, S. Schultz, J.D. Thompson, Z. Fisk, S.W. Cheong, M.F. Hundley and M. Tovar, 1990, Phys. Rev. B **41**, 1934.

Owen, J., M.E. Brown, W.D. Knight and C. Kittel, 1956, Phys. Rev. **102**, 1501.

Owens, F.J., B.L. Ramakrishna and Z. Iqbal, 1988, Physica C **156**, 221.

Pechoniy, A.P., M.D. Glinchuk, V.A. Miheev and I.G. Babich, 1990, Phase Transitions **29**, 105.

Plefka, T., 1972, Phys. Status Solidi b **51**, K113.

Plefka, T., 1973, Phys. Status Solidi b **55**, 129.

Punnoose, A., and R.J. Singh, 1995, Int. J. Mod. Phys. B **9**, 1123.

Ramakrishna, B.L., E.W. Ong and Z. Iqbal, 1988, J. Appl. Phys. **64**, 5803.

Rameev, B., E.F. Kukovitskii, V.E. Kataev and G.B. Teitelbaum, 1995, Physica C **246**, 309.

Rao, D., M. Tovar, S.B. Oseroff, D.C. Vier, S. Schultz, J.D. Thompson, S.W. Cheong and Z. Fisk, 1988, Phys. Rev. B **38**, 8920.

Rettori, C., D. Davidov, I. Belaish and I. Felner, 1987, Phys. Rev. **36**, 4028.

Rettori, C., D. Rao, S.B. Oseroff, G. Amoretti, Z. Fisk, S.W. Cheong, D. Vier, S. Schultz, M. Tovar, R.D. Zysler and J.E. Schirber, 1993, Phys. Rev. B **47**, 8156.

Rockenbauer, A., T. Feher, A. Janossy and J. Hodby, 1997, Appl. Magn. Reson. **12**, to be published.

Romanyukha, A.A., Yu.N. Shvachko, V.Yu. Irkhin, M.I. Katsnelson, A.A. Koshta and V.V. Ustinov, 1990, Physica B **171**, 276.

Rubins, R.S., J.E. Drumheller, S.L. Hutton, G.V. Rubenacker, D.Y. Jeong and T.D. Black, 1988, J. Appl. Phys. **64**, 1312.

Schaeffer, H., and B. Elschner, 1985, Solid State Commun. **53**, 611.

Schirmer, O.F., G. Wübbeler and Th. Walbrink, 1994, in: Proc. Workshop on Phase Separation in Cuprate Superconductors, eds E. Sigmund and K.A. Müller (Springer, Berlin) p. 133.

Schwartz, R.N., A.C. Pastor, R.C. Pastor, K.W. Kirby and D. Rytz, 1987, Phys. Rev. B **36**, 8858.

Searl, J.W., R.G. Smith and S.J. Wyard, 1961, Proc. Phys. Soc. London A **78**, 1174.

Shaltiel, D., J. Genossar, A. Grayevsky, Z.H. Kalman, B. Fisher and N. Kaplan, 1987, Solid State Commun. **63**, 987.

Shaltiel, D., H. Bill, P. Fischer, M. Francois, H. Hagemann, M. Peter, Y. Ravi Sekhar, W. Sadowski, H.J. Scheel, G. Triscone, E. Walker and K. Yvon, 1989a, Physica C **158**, 424.

Shaltiel, D., S.E. Barnes, H. Bill, M. Francois, H. Hagemann, J. Jegondaz, D. Lovy, P. Monod, M. Peter, A. Revcolevschi, W. Sadowski and E. Walker, 1989b, Physica C **161**, 13.

Shaltiel, D., C. Noble, J. Pilbrow, D. Hutton and E. Walker, 1996, Phys. Rev. B **53**, 12430.

Shengelaya, A.D., J. Olejniczak and H. Drulis, 1994, Physica C **233**, 124.

Shengelaya, A.D., J. Olejniczak, H. Drulis and N.M. Suleimanov, 1996, Solid State Commun. **99**, 779.

Shimizu, H., 1991, J. Phys. Soc. Jpn. **60**, 3842.

Shimizu, H., K. Fujiwara and K. Hatada, 1997a, Physica C **288**, 190.

Shimizu, H., K. Fujiwara and K. Hatada, 1997b, Physica C **282–287**, 1349.

Shirane, G., Y. Endoh, R.J. Birgeneau, M.A. Kastner, Y. Hidaka, M. Oda, M. Suzuki and T. Murakami, 1987, Phys. Rev. Lett. **59**, 1613.

Shrivastava, K.N., 1987, J. Phys. C **20**, L789.

Sichelschmidt, J., B. Elschner, A. Loidl and K. Fischer, 1994, Z. Physik B **93**, 407.

Sichelschmidt, J., B. Elschner, A. Loidl and B.I. Kochelaev, 1995a, Phys. Rev. B **51**, 9199.

Sichelschmidt, J., B. Elschner, A. Loidl and B.I. Kochelaev, 1995b, Physica B **206&207**, 742.

Sienkiewicz, A., M.-Z. Cieplak, G. Xiao and C.L. Chien, 1990, J. Less-Common. Met. **164&165**, 870.

Sigmund, E., and K.A. Müller, eds, 1994, Phase Separation in Cuprate Superconductors (Springer, Berlin) 401 pp.

Simon, P., J.M. Basset, S.B. Oseroff, Z. Fisk, S.W. Cheong, A. Wattiaux and S. Schultz, 1993, Phys. Rev. B **48**, 4216.

Skrzypek, D., K. Majewska and A. Ratuszna, 1991, Phys. Scr. **44**, 624.

Stankowski, J., W. Hilczer, J. Baszynski, B. Czyzk and L. Szczepanka, 1991, Solid State Commun. 77, 125.

Stepanov, A.A., S. Huant, I.M. Vitebsky, A. Chabanov and P. Wyder, 1994, Physica C **235–240**, 1643.

Stepanov, A.A., S. Huant, I.M. Vitebsky, P. Wyder, A. Chabanov, M.I. Kobets, V.A. Pashchenko, S.N. Barilo and D.I. Zhigunov, 1995, Phys. Rev. B **51**, 15596.

Szymczak, R., H. Szymczak and P. Piechota, 1995, Z. Phys. B **99**, 2.

Taylor, R.H., 1975, Adv. Phys. **24**, 681.

Teitel'baum, G.B., V.E. Kataev, Yu.S. Greznev, M. Breuer and N. Knauf, 1994, Physica B **194–196**, 1437.

Thompson, J.R., B.C. Sales, Y.C. Kim, S.T. Sekula, L.A. Boatner, J. Brynestad and D.K. Christen, 1988, Phys. Rev. B **37**, 9395.

Tranquada, J.M., P.M. Gehring, G. Shirane, S. Shamoto and M. Sato, 1992, Phys. Rev. B **46**, 5561.

Tranquada, J.M., B.J. Sternlieb, J.D. Axe, Y. Nakamura and S. Uchida, 1995, Nature **375**, 561.

Tyagi, S., M. Barsoum and K.V. Rao, 1988, Phys. Lett. A **128**, 225.

Uimin, G., and J. Rossat-Mignod, 1992, Physica C **199**, 251.

Uimin, G., and V. Stepanov, 1993, Ann. Phys. (Germany) **2**, 284.

Van Vleck, J.H., 1948, Phys. Rev. **74**, 1168.

Vier, D.C., S.B. Oseroff, C.T. Salling, J.F. Smyth, S. Schultz, Y. Dalichaouch, B.W. Lee, M.B. Maple, Z. Fisk and J.D. Thompson, 1987, Phys. Rev. B **36**, 8888.

Williams, G.V.M., J.L. Tallon, R. Meinhold and A. Janossy, 1995, Phys. Rev. B **51**, 16503.

Wübbeler, G., and O.F. Schirmer, 1992, Phys. Status Solidi b **174**, K21.

Wübbeler, G., O.F. Schirmer and S. Köhne, 1996, Phys. Rev. B **54**, 9054.

Yamada, K., K. Kakurai, Y. Endoh, T.R. Thurston, M.A. Kastner, R.J. Birgeneau, G. Shirane, Y. Hidaka and T. Murakami, 1989, Phys. Rev. B **40**, 4557.

Yamada, Y., K. Sugawara and Y. Shiohara, 1990, in: Advances in Superconductivity II, Proc. 2nd Int. Symp. on Superconductivity, Tsukuba 1989 (Springer, Tokio) p. 547.

Yu, J.-T., J.G. Hwang, C.-C. Tsai and K.H. Lii, 1989, Solid State Commun. **70**, 167.

Zysler, R.D., M. Tovar, C. Rettori, D. Rao, H. Shore, S.B. Oseroff, D.C. Vier, S. Schultz, Z. Fisk and S.W. Cheong, 1991, Phys. Rev. B **44**, 9467.

Handbook on the Physics and Chemistry of Rare Earths
Vol. 30
edited by K.A. Gschneidner, Jr., L. Eyring and M.B. Maple

Chapter 192

POSITRON ANNIHILATION IN HIGH-TEMPERATURE SUPERCONDUCTORS

Alfred A. MANUEL
Université de Genève, Département de Physique de la Matière Condensée, 24 quai E. Ansermet, 1211 Geneva 4, Switzerland;
Alfred.Manuel@physics.unige.ch

Contents

List of symbols and abbreviations 417
1. Introduction 418
2. Principles 418
   2.1. Positron in a perfect crystal 418
   2.2. Positron in a structural defect 419
   2.3. Positron in a superconductor 421
3. Experimental aspects 422
   3.1. ACAR spectroscopy 423
   3.2. Lifetime spectroscopy 424
   3.3. Lineshape spectroscopy 425
4. The study of $YBa_2Cu_3O_{7-\delta}$ 426
   4.1. Electron momentum density and Fermi surface 426
      4.1.1. Theoretical study 426
      4.1.2. Experimental study 429
   4.2. Defect spectroscopy 433
      4.2.1. Lifetime 433
      4.2.2. Lineshape 436
   4.3. Superconducting phase transition 438
5. Atomic substitutions in $YBa_2Cu_3O_{7-\delta}$ 440
   5.1. Cu substitution: $YBa_2(Cu_{3-x}M_x)O_{7-\delta}$ 440
   5.2. Y substitution: $(Y_{1-x}R_x)Ba_2Cu_3O_{7-\delta}$ 440
6. Other compounds 441
   6.1. $(La_{2-x}Sr_x)CuO_4$ and $(Nd_{2-x}Ce_x)CuO_4$ 441
   6.2. $Tl_2Ba_2CaCu_2O_8$ 442
   6.3. $Bi_2Sr_2CaCu_2O_{8+x}$ 443
   6.4. $Ba_{1-x}K_xBiO_3$ 444
7. Concluding remarks 444
Acknowledgement 445
References 445

List of symbols and abbreviations

ACAR	angular correlation of the annihilation radiation	$h(\vec{k})$	the reduced momentum distribution (LCW function)
$A(r,\theta)$	anisotropy of the 2D-ACAR distribution $N(p_x,p_y)$	I_i	intensities of the lifetime components $i=1,2,3$
BCS	Bardeen–Cooper–Schrieffer	$\vec{K}$	reciprocal lattice vector
$D(p_z)$	lineshape of the annihilation radiation	KKR	Korringa–Kohn–Rostoker
FLAPW	full-potential linearized amplified plane wave	LCAO	linear combination of atomic orbitals
FWHM	full width at half maximum	LDA	local density approximation
$\vec{G}$	reciprocal lattice vector	LCW	Lock–Crisp–West
GGA	generalized gradient approximation	LMTO	linear muffin-tin orbital
		MO	molecular orbital

$n_l(\vec{k})$	occupation number of electronic state $\vec{k}$ of band l	$\rho^{2\gamma}(\vec{p})$	electron momentum distribution sampled by positron
$N(p_x,p_y)$	2D-ACAR distribution	τ_m	mean lifetime
S	shape parameter of the annihilation line	τ_i	lifetime components $i=1,2,3$
W	wing parameter of the annihilation line	τ_B	bulk lifetime
Y-123	$YBa_2Cu_3O_{7-\delta}$	$\Psi_{l,\vec{k}}(\vec{r})$	wave function of an electron in state $\vec{k}$ of band l
$\gamma(\vec{r})$	enhancement factor due to the electron–positron interaction	$\Psi^+(\vec{r})$	wave function of a thermalized ($\vec{k}=0$) positron
λ	annihilation rate		

1. Introduction

When a positron enters a solid, it thermalizes in a time much shorter (few picoseconds) than its lifetime (few hundred of picoseconds). At the time of annihilation, the positron has diffused over a certain distance (few hundreds of nm). This diffusion process is critical to determine the state of the electron–positron pair at the time of annihilation: the positron migrates in a region energetically favorable, namely the interstitial region of the lattice. The positron might also be trapped if it reaches a defect and experiences a longer lifetime. Otherwise, it annihilates with an electron in the valence or conduction band. Observing the annihilation radiation provides information on the electronic structure in momentum space.

Positron annihilation is widely applied to study high-T_c superconductors. After presenting the basic concepts (sect. 2) and discussing some experimental aspects (sect. 3), there is an overview of the results obtained so far in $YBa_2Cu_3O_{7-\delta}$ (sect. 4), in $YBa_2Cu_3O_{7-\delta}$ with substitutions (sect. 5), and in other high-temperature superconducting oxides (sect. 6).

2. Principles

2.1. *Positron in a perfect crystal*

The general form of the electron momentum distribution $\rho^{2\gamma}(\vec{p})$ sampled by thermalized positrons is given by[1]

$$\rho^{2\gamma}(\vec{p}) = \sum_{l,\vec{k}} n_l(\vec{k}) \left| \int e^{i\vec{p}\,\vec{r}} \Psi_{l,\vec{k}}(\vec{r})\, \Psi^+(\vec{r}) \sqrt{\gamma(\vec{r})}\, d^3r \right|^2, \tag{1}$$

where $n_l(\vec{k})$ is the occupation number of state $\vec{k}$ of band l, $\Psi_{l,\vec{k}}(\vec{r})$ and $\Psi^+(\vec{r})$ are the electron and positron wave functions, and $\gamma(\vec{r})$ is the enhancement factor to account

[1] A complete theory of positrons in solids has been presented by Puska and Nieminen (1994).

for the many-body correlations not included in the local density approximation used to perform calculations of $\Psi_{l,\vec{k}}$ and Ψ^{+}. $\gamma(\vec{r})$ is a critical parameter and has a large effect on the annihilation rate (Barbiellini et al. 1992, Jarlborg et al. 1991, Mijnarends and Bansil 1995). The evaluation of $\gamma(\vec{r})$ has been investigated in great detail, and today one can use parametrizations which lead to a satisfactory agreement with the annihilation rate measured in a large number of solids (Boronski and Nieminen 1986, Jarlborg and Singh 1987, Barbiellini et al. 1995b).

The quantity $\rho^{2\gamma}(\vec{p})$ is the electron momentum distribution as seen by the positron. This basic quantity may be related to the true electron momentum distribution when the positron wave function is known through calculations. The many-body factor $\gamma(\vec{r})$ is known to play some role but it has been established that the correlations have no effect on the position of the Fermi surface breaks (Majumdar 1965). Equation (1) shows that positron annihilation is well suited for Fermi surface studies as only $n_l(\vec{k})$ has breaks. This can be further seen if one expresses the positron and electron wave functions as Bloch wave functions. One obtains

$$\rho^{2\gamma}(\vec{p}) = \sum_{l} n_l(\vec{k}) \sum_{\vec{K}} \delta(\vec{p} - \vec{k} - \vec{K}) \left| \sum a_{\vec{G}}(\vec{k})\, b_{\vec{K}-\vec{G}} \right|^2, \tag{2}$$

where $a_{\vec{G}}(\vec{k})$ and $b_{\vec{K}-\vec{G}}$ are, respectively, the coefficients of the electron and positron wave functions (the positron being thermalized, it is in a state $\vec{k}=0$). This equation, where $\vec{K}$ and $\vec{G}$ are reciprocal lattice vectors, shows also that the breaks in $n_l(\vec{k})$ are periodically repeated in momentum space.

If one assumes that the positron wave function is a constant, i.e. $b_{\vec{K}-\vec{G}} = \delta(\vec{K}, \vec{G})$, one can construct (Lock et al. 1973) the reduced momentum density $h(\vec{k})$:

$$h(\vec{k}) = \sum_{\vec{k}} \rho^{2\gamma}(\vec{k} + \vec{K}) = \sum_{l} n_l(\vec{k}) \tag{3}$$

which is periodic and contains only variations due to the Fermi surface through the step-like occupation function $n_l(\vec{k})$. For more details, see West (1995). Friedel and Peter (1989) have discussed this function, usually known as the LCW function, in the case of a weak charge or spin density waves and have pointed out that it must give the new Brillouin zone boundaries created by the lattice of spin modulations.

2.2. *Positron in a structural defect*

In order to be trapped by a structural defect, the positron must first diffuse to the defect and then make the transition from the free Bloch state to the localized trapped state. One

can write an equation similar to eq. (1) to describe the annihilation of a positron trapped in a defect, where the lattice periodicity is lost:

$$\rho^{2\gamma}(\vec{p}) = \sum_i \left| \int e^{i\vec{p}\,\vec{r}} \Psi_i(\vec{r}) \sqrt{\gamma(\vec{r})}\, \mathrm{d}^3 r \right|^2 . \tag{4}$$

Due to the nature of the electron wave functions involved in this case, $\rho^{2\gamma}(\vec{p})$ is not periodic, but its shape carries information on the electronic structure of the defect. This can be measured by 2D-ACAR and lineshape spectroscopies. Another important quantity to consider in this case is the total annihilation rate λ:

$$\lambda = \frac{\pi r_0^2 c}{(2\pi)^3} \int \rho^{2\gamma}(\vec{p})\, \mathrm{d}\vec{p} = \pi r_0^2 c \int |\Psi^+(\vec{r})|^2\, n(\vec{r})\, \gamma[n(\vec{r})]\, \mathrm{d}\vec{r}, \tag{5}$$

where r_0 is the classical radius of the electron, c the velocity of light and $n(\vec{r})$ the electron density. The annihilation rate λ is studied by positron lifetime spectroscopy.

In a real system, the positron exists in different states. It may annihilate either with valence or conduction electrons of the bulk. These processes give rise to a "bulk" annihilation rate λ_B. It may also be trapped in various defect states D_j where the electron density is smaller than in the bulk, i.e. a single vacancy, a cluster of vacancies, dislocations, impurities etc. Each defect state will be characterized by an annihilation rate λ_{D_j}. In a vacancy-like defect the trapped-positron lifetime is increased compared to free positrons annihilating in the bulk, as the electron density is locally reduced. Each defect state leads to a different lifetime $\tau_{D_j} = 1/\lambda_{D_j}$.

The trapping model introduced by Brandt (1967) describes the dynamics of the positron behavior in solids. It is governed by kinetic equations. Here we give a brief outline, and we refer to Hautojärvi and Corbel (1995) for an extensive discussion. The trapping model supposes that all positrons are free in Bloch states at $t=0$, and that the trapping rate κ_{D_j} of each defect D_j is proportional to the defect concentration C_{D_j}:

$$\kappa_{D_j} = \mu_{D_j} c_{D_j}, \tag{6}$$

where μ_{D_j} are the trapping coefficients. One has also to assume that the positron may escape from the trap: this process is characterized by the detrapping rate δ_{D_j}. The probabilities n_B and n_{D_j} for the positron to be in a free (bulk) state or trapped in the defect D_j is given by a set of linear differential equations:

$$\frac{\mathrm{d}n_B}{\mathrm{d}t} = -\left(\lambda^B + \sum_{j=1}^{N} \kappa_{D_j}\right) n_B + \sum_{j=1}^{N} \delta_{D_j} n_{D_j}, \tag{7}$$

$$\frac{\mathrm{d}n_{D_j}}{\mathrm{d}t} = \kappa_{D_j} n_B - (\lambda_{D_j} + \delta_{D_j}) n_{D_j}, \quad j = 1, \ldots, N. \tag{8}$$

The probability for a positron to exist at time t is of an exponential form:

$$n(t) = n_B(t) + \sum_{j=1}^{N} n_{D_j}(t) = \sum_{j=1}^{N+1} I_i e^{-\lambda_i t}, \tag{9}$$

where the decay constants λ_i and intensities I_i are found by solving eqs. (7)–(8). Solutions for simple cases will be considered in sect. 3.2.

2.3. *Positron in a superconductor*

Perkins and Woll (1969) have investigated the possibility of observing the effects of superconductivity on positron thermalisation. If the positron lifetime in the superconducting compound is small, they conclude that a lack of thermalisation of the positron may be observed. This would be reflected, for example, in a loss of resolution in an ACAR experiment. But the effect is small and has never been reported in low-T_c superconductors. It is doubtful that it might be observed in high-T_c superconductors because positron lifetimes are rather long in cuprates.

The simplest considerations on positron annihilation in a superconducing free electron gas were made by de Gennes (1966) who observed that the probability of finding an electron in a state with a wave vector $\vec{k}$, in the BCS ground state, is

$$v_{\vec{k}}^2 = \frac{1}{2}\left(1 - \frac{\xi_{\vec{k}}}{E_{\vec{k}}}\right), \tag{10}$$

where $E_{\vec{k}} = (\xi_{\vec{k}}^2 + \Delta^2)^{1/2}$, $\xi_{\vec{k}}$ is electronic energy and Δ is the superconducting gap. De Gennes concluded that, in the superconducting state, this implies a smearing of the Fermi distribution of

$$\delta k \sim \frac{1}{\xi_0} \sim \frac{\Delta}{\vec{h} v_F}, \tag{11}$$

where ξ_0 is the coherence length and v_F the Fermi velocity. Finally, de Gennes pointed out that, ideally, $v^2{}_{\vec{k}}$ can be measured by Compton and positron annihilation spectroscopies. If the smearing is small in low-T_c superconductors ($\delta k/k_F \approx 2/\pi\xi_0 k_F \approx 0.01$), it is, in principle, large enough ($\delta k/k_F \sim 0.1$) in high-T_c superconductors to be observed experimentally.

Barnes and Peter (1989) presented a formal theory of positron annihilation in superconductors. They showed that, in a superconducting state arising through pair formation in a non-interacting electron gas, the two-photon momentum density $\rho_{SC}^{2\gamma}(\vec{p})$, in the absence of electron–positron correlations, is described by

$$\rho_{SC}^{2\gamma}(\vec{p}) = \sum_{\vec{k},\vec{G},\sigma} \left|\Phi(\vec{p} - \vec{k} + \vec{G})\right|^2 \left|a_{\vec{G}}(\vec{k})\right|^2 [u_{\vec{k}}^2(1 - n_{\vec{k}}) + v_{\vec{k}}^2 n_{\vec{k}}]. \tag{12}$$

In this equation, Φ is the Fourier transform of the positron wave function, a is the coefficient of the Bloch electron wave function, and $n_k \equiv [1/(e^{-\beta E_{\vec{k}}} + 1)]$ is the thermal

distribution function for quasiparticles in the superconductor. This result shows that, in the momentum space mapped by positron annihilation, the sharp Fermi edge is lost in the superconducting state. This conclusion was also drawn by Györffy et al. (1989, 1995) from similar considerations.

These theoretical approaches do not include the electron–positron correlations. This is, most probably, a drastic approximation. One may wonder if the correlations may perturb the superconducting interaction sufficiently to suppress all kinds of pairing over the correlation distance. In this case, the positron would only probe the electronic structure of the normal state. Some authors have addressed the question of the superconductivity in an interacting electron–positron system. Benedek and Schüttler (1990) have considered the Cooper pairing and derived an approximate formulation of the positron characteristics in a BCS superconductor. They conclude that the momentum density in the normal and superconducting states does not differ sufficiently to explain the effects experimentally observed at T_c by positron spectroscopy (see sect. 4.3). Chakraborty (1989) has considered the effect of pairing on the positron for strongly interacting bound core-like electrons in a simple model including holes. She concludes that the overlap of the positron wave function with core electrons decreases with temperature below T_c and consequently expects an increase of the positron lifetime in the superconducting state. In a subsequent study (Chakraborty 1991), she analyzed the effect of different pairings on the positron annihilation characteristics and concluded that it should be possible to probe the pairing by positron spectroscopy. This statement has to be put in perspective with the fact that, in numerous high-T_c superconductors, the positron density is low in the CuO_2 planes. McMullen (1990) has investigated the lifetime of extended positron states in CuO_2 planes within the picture of the paired-boson resonating valence bond. Suvasini et al. (1992) have introduced a phenomenological term for treating the exchange correlation energy in the density functional theory for superconductors. It has been implemented within the LMTO formalism and the authors have obtained some results for Nb.

Finally, there are also four additional theoretical approaches. Tripathy and Bhuyan (1985) have briefly presented a formalism to describe the positron annihilation rate in a superconductor. Kresin and Morawitz (1990) have investigated the screening of a positron in superconductors and emphasize the consequence of the small values of the Fermi energy E_F in high-T_c materials. Sedov and Kuznetsov (1994) suggest that the transition to the superconducting state may inhibit the processes of ortho–para conversion of the positronium in voids. The positron trapping in superconductors has been described by Nieminen (1991) who considered the effect of various defects as well as the effect of pairing.

3. Experimental aspects

A schematic description of positron spectroscopy is shown in fig. 1. The positron e^+, emitted from the source, is sent into the sample. Some isotopes emit a γ-ray γ_s simultaneously with the positron. γ_s is useful for lifetime spectroscopy as it is a time

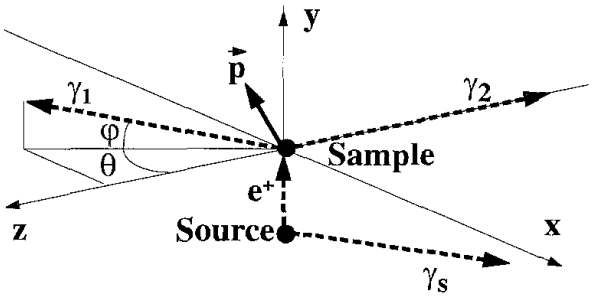

Fig. 1. Schematic representation of positron annihilation spectroscopy. The positron e^+ is emitted from the source simultaneously with the γ-ray γ_s. When it annihilates after thermalisation with an electron of momentum $\vec{p}$, the two γ-rays γ_1 and γ_2 are emitted.

marker for the birth of the positron. After thermalisation and diffusion in the sample, the positron annihilates with an electron of momentum $\vec{p}$. Most of the annihilation processes (for a detailed discussion see West 1974 and Brandt 1983) lead to the emission of two γ-rays γ_1 and γ_2 carrying out 511 keV each, the rest-mass energy of the annihilated particles. Three positron spectroscopies are currently used: ACAR, lifetime and lineshape (or Doppler broadening).

3.1. *ACAR spectroscopy*

ACAR stands for Angular Correlation of the Positron Annihilation Radiation. At the present time, this spectroscopy is two-dimensional, therefore we often use the term 2D-ACAR. It has been described in detail by West (1995). Briefly, it detects in coincidence the two annihilation γ-rays γ_1 and γ_2 (see fig. 1) using two position-sensitive detectors of high spatial resolution sitting at large distance on both sides of the sample, the detectors and the sample being aligned on the z-axis. By evaluating the angles θ and ϕ determined by the directions of γ_1 and γ_2, one obtains the two components p_x and p_y of the momentum $\vec{p}$ of the annihilated electron–positron pair:

$$p_x = mc\theta, \qquad p_y = mc\varphi. \tag{13}$$

θ and φ are of the order of 10–20 mrad. These relations fix the momentum scale: 1 mrad $= 10^{-3}\, mc = 0.137$ a.u. of momentum.

As the positron is thermalized, p_x and p_y are, to a good approximation, momentum components of the annihilated electron. The 2D-ACAR measurement yields $N(p_x,p_y)$, the projection of the two-photon momentum density $\rho^{2\gamma}(\vec{p})$:

$$N(p_x, p_y) = \int \rho^{2\gamma}(\vec{p})\, \mathrm{d}p_z. \tag{14}$$

The typical value for the resolution of a 2D-ACAR measurement is 0.03–0.05 a.u. of momentum on both p_x and p_y. Compared to 0.35 a.u., the Γ–X length of the Brillouin zone of $YBa_2Cu_3O_7$, one notices that 2D-ACAR spectroscopy has an excellent resolution. This high resolution and the 2D character of $N(p_x,p_y)$ are the main advantages of this technique. The main limitation of the 2D-ACAR is the long time (several days) required to complete one $N(p_x,p_y)$. This is due to the small ($\sim 10^{-4}$) solid angle covered

by the position-sensitive detectors and the limited intensity of the positron sources ($\sim 4\times 10^9$ Bq).

Anisotropies in the 2D-ACAR are often considered to enhance the interesting structures. If $N(r,\theta)$ denotes the 2D-ACAR in polar coordinates, the anisotropy $A(r,\theta)$ is given by

$$A(r,\theta) = N(r,\theta) - M(r), \tag{15}$$

where $M(r)$ is the mean value of $N(r,\theta)$ over θ for a given r:

$$M(r) = \tfrac{1}{2}\pi \int_0^{2\pi} N(r,\theta)\,\mathrm{d}\theta. \tag{16}$$

3.2. *Lifetime spectroscopy*

We have outlined the trapping model in sect. 2.2. The lifetime spectrum is the probability for annihilation at each time t. Following eq. (9), it is given by

$$-\frac{\mathrm{d}n(t)}{\mathrm{d}t} = \sum_{j=1}^{N+1} I_i \lambda_i \mathrm{e}^{-\lambda_i t} \tag{17}$$

with

$$\sum_{j=1}^{N+1} I_i = 1. \tag{18}$$

It is composed of several components with characteristic lifetimes $\tau_i = 1/\lambda_i$ and relative amplitudes I_i.

The positron lifetime spectrum is measured by recording time delays between the birth of positrons and their annihilation. The birth is usually detected through γ_s, the γ-ray emitted simultaneously with the positron during the β decay (see fig. 1). The typical isotope is ^{22}Na; it emits a γ-ray of 1.28 MeV simultaneously with the positron. The annihilation is detected by recording one of the two annihilation γ-rays of 511 keV, γ_1 or γ_2 of fig. 1. Practically, the positron source, contained within very thin solid layers (nickel, teflon, etc.), is sandwiched between two pieces of the material to be investigated.

The typical resolution of the lifetime spectrometers is 200–250 ps, FWHM. This value is of the order of magnitude of the positron lifetimes in solids. Therefore the determination of the lifetime components τ_i is a delicate operation. Various methods are available: (1) least-squares fit of a model spectrum convoluted with the resolution function of the spectrometer (Kirkegaard and Eldrup 1974); (2) Laplace transform (Gregory and Zhu 1990); and (3) maximum entropy (Shukla et al. 1993, 1997). The last two methods provide

a continuous distribution of lifetimes while the first performs the fit to a fixed number (two or three) of lifetime components. Both approaches are of interest and find their applications.

The least-squares fit method is useful if one wants to obtain the bulk lifetime $\tau_B = 1/\lambda_B$, within the hypothesis that there is only one trapping center D from which the positron can not be detrapped. In this case, known as the two-state trapping model, one can get an exact solution of the form:

$$n(t) = \frac{\lambda_B - \lambda_D}{\lambda_B - \lambda_D + \kappa} \exp[-(\lambda_B + \kappa)t] + \frac{\kappa}{\lambda_B - \lambda_D + \kappa} \exp[-\lambda D t]. \tag{19}$$

If τ_1 and τ_2 are the two lifetime components of intensities I_1 and I_2 fitted to the lifetime spectrum, one obtains by identification:

$$\frac{1}{\tau_B} = \frac{I_1}{\tau_1} + \frac{I_2}{\tau_2}. \tag{20}$$

Another frequently used quantity to analyze positron lifetime experiments is the mean lifetime τ_m:

$$\tau_m = I_1 \tau_1 + I_2 \tau_2. \tag{21}$$

3.3. *Lineshape spectroscopy*

Lineshape spectroscopy is based on the Doppler shift of the energy of the annihilation radiation γ_2 (see fig. 1). The origin of this shift ΔE is the finite momentum $\vec{p}$ of the annihilated electron–positron pair in the direction of the emitted γ-ray:

$$\Delta E = \tfrac{1}{2} c p_z. \tag{22}$$

In a way similar to ACAR, lineshape spectroscopy reflects also the momentum distribution of electrons in matter. As p_z can be determined by inverting eq. (22), the lineshape $D(p_z)$ is a one-dimensional profile of $\rho^{2\gamma}(\vec{p})$, the electron momentum distribution seen by the positron:

$$D(p_z) = \int \rho^{2\gamma}(\vec{p})\, \mathrm{d}p_x\, \mathrm{d}p_y. \tag{23}$$

One may wonder why $D(p_z)$ is interesting as it gives a less direct access to $\rho^{2\gamma}(\vec{p})$ than 2D-ACAR spectroscopy, eq. (14)? Lineshape spectroscopy has two advantages: (1) it is rapid: a profile is obtained in less than one hour; (2) it is technically simple, making use either of one (Hautojärvi and Vehanen 1979) or two (Ashoka-Kumar et al. 1996) high-purity Ge detectors. The rather low resolution of lineshape spectroscopy (0.4–0.6 a.u.)

prevents its use for fermiology (2D-ACAR spectroscopy is more appropriate in this case) but is not a handicap for defect studies.

Let us mention finally, though it is obsolete, that 1D angular correlation of the annihilation radiation (1D-ACAR) also provides lineshape profiles. The 1D-ACAR technique consists of performing an angular correlation by resolving one of the two angles θ and φ (see fig. 1). For example, if θ is resolved, 1D-ACAR provides the one-dimensional distribution $N(p_x)$ as

$$N(p_x) = \int \rho^{2\gamma}(\vec{p})\, \mathrm{d}p_y\, \mathrm{d}p_z. \tag{24}$$

The shape (S) and wing (W) parameters are commonly used to characterize the annihilation line. S is defined as the ratio of the surface of the central region to the total area. Similarly, W is the relative fraction of the wings of the line. These parameters have characteristic values for each material, depending on the electron momentum distribution. In a vacancy, the density of valence electrons is reduced, leading to a narrowing of the annihilation line and, consequently, to a larger S parameter.

4. The study of $YBa_2Cu_3O_{7-\delta}$

4.1. *Electron momentum density and Fermi surface*

4.1.1. *Theoretical study*

As the study of the electron momentum density and the Fermi surface by the positron annihilation techniques is rather indirect, it is important to perform the experimental investigations in close relation with a strong computational approach. The first valuable quantity to estimate is the positron density distribution in the lattice unit cell: it will indicate which electronic states might be observed experimentally. One has then to evaluate $\rho^{2\gamma}(\vec{p})$, the electron momentum density as seen by the positron. From this, the positron lifetime τ, the 2D-ACAR distribution $N(p_x,p_y)$ and the Doppler profile $D(p_z)$ can be easily deduced.

In $YBa_2Cu_3O_{7-\delta}$ the positron density $|\Psi^+(\vec{r})|^2$ is large between the Cu–O chains and very small in the other parts of the lattice cell. All the calculations agree on this fact, independently of the method: FLAPW (Massidda 1990, Massidda et al. 1991, Singh et al. 1989, Von Stetten et al. 1988), KKR (Mijnarends and Bansil 1995), atomic superposition (Bharathi et al. 1989, 1990, Jensen et al. 1989, McMullen et al. 1991), and LCAO-MO (Chiba 1992, Turchi et al. 1988, 1990). This behavior can be understood rather intuitively: the positron avoids positively charged regions of the lattice cell and migrates to the mostly open space in the cell. This general conduct is found in all the high-T_c compounds (see sect. 6), including $YBa_2Cu_3O_8$ (Barbiellini and Jarlborg 1992) and $HgBa_2CuO_4$ (Barbiellini and Jarlborg 1994).

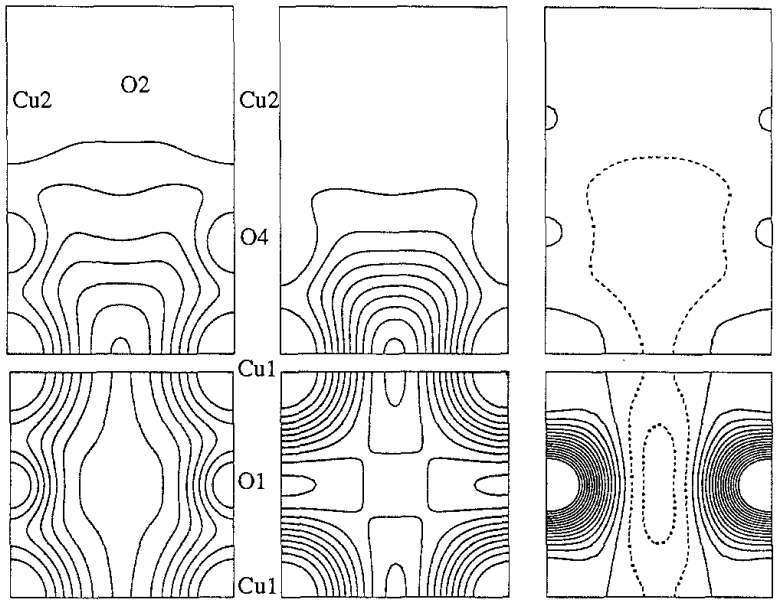

Fig. 2. (a) Positron density in $YBa_2Cu_3O_7$ in a vertical (100) plane (upper frame) and in a horizontal plane cutting the Cu–O chains (lower frame). (b) Same for $YBa_2Cu_3O_6$. (c) Difference between $YBa_2Cu_3O_6$ and $YBa_2Cu_3O_7$, on the same planes. (From Massidda 1990).

A map of the positron density $|\Psi^+(\vec{r})|^2$ in $YBa_2Cu_3O_{7-\delta}$ is shown in fig. 2. The fact that it is extremely small in the Cu–O planes has as a consequence that the study of the electronic structure in the Cu–O planes of $YBa_2Cu_3O_{7-\delta}$ is limited. There are other compounds where the electronic structure of the Cu–O planes can be sampled by positron annihilation: $Bi_2Sr_2CaCu_2O_{8+x}$, $Nd_{2-x}Ce_xCuO_4$ and $La_{2-x}Sr_xCuO_4$ for example.

Since positrons are highly sensitive to oxygen vacancies in $YBa_2Cu_3O_7$ (Von Stetten et al. 1988), it is important to investigate the positron wave function in some vacancy-like defects. It has been calculated in the O(1) single vacancy (Bharathi et al. 1989, Jensen et al. 1989), various O(1) vacancy clusters (Ishibashi et al. 1991, 1992), and the Cu(1) vacancy (Jensen et al. 1989). The localization of the positron wave function in the O(1) and Cu(1) single vacancies is shown in fig. 3. The Cu(1) vacancy induces a strong positron localization (deep trapping) while the O(1) vacancy acts as a shallow trap and a weak localization of the positron occurs.

After investigating the positron behavior, the next step is to solve the band structure and to calculate the momentum density $\rho^{2\gamma}(\vec{p})$. It is rather controversial to describe the electronic structure of high-T_c superconductors by band structure. But it is almost the only way to obtain a calculated momentum density in order to interpret the positron measurements. We refer to the chapter by Pickett and Mazin in this volume (ch. 193) for a general discussion of band-structure calculations in superconducting cuprates. Studies in relation with positron annihilation have been made using different methods: FLAPW (Massidda 1990, Massidda et al. 1991), LMTO (Bansil et al. 1988, Barbiellini et al. 1992,

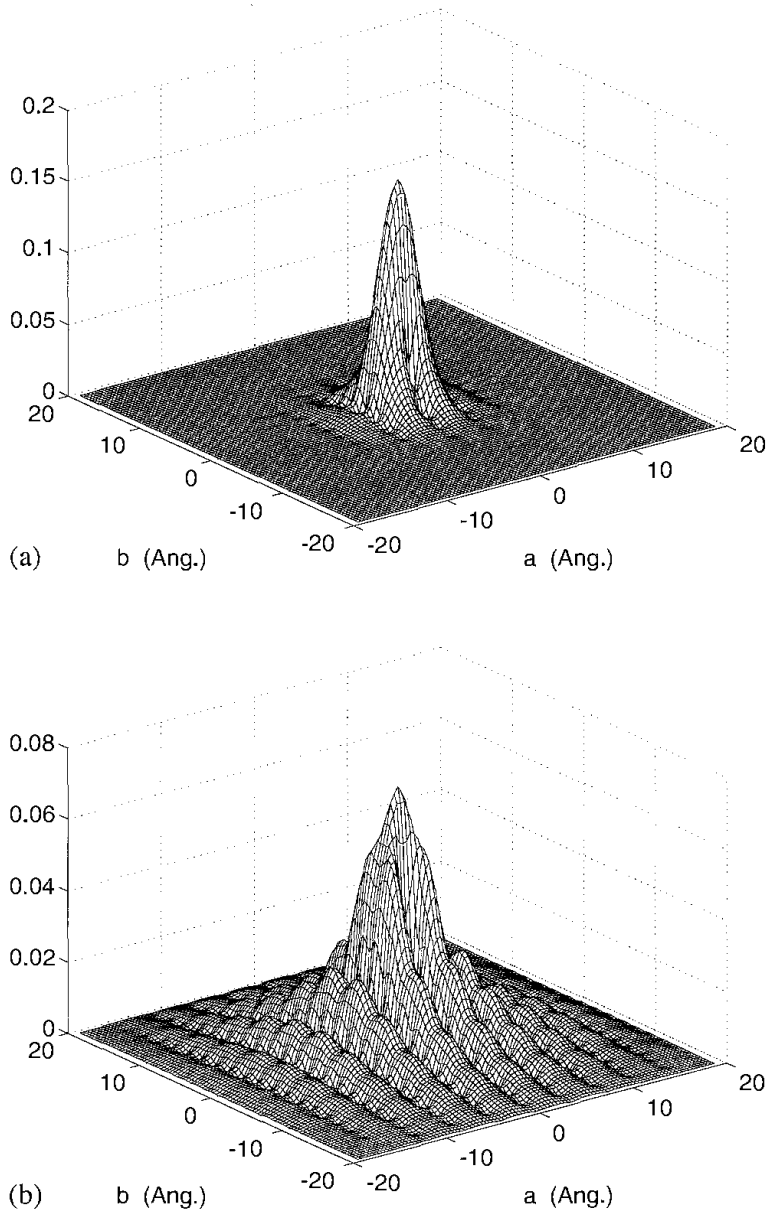

Fig. 3. The wave function of a positron in $YBa_2Cu_3O_7$ when trapped by (a) a Cu(1) vacancy and (b) an O(1) vacancy. The plots are in the a–b plane. (Recalculated by S. Ishibashi, according to Jensen et al. 1989.)

1996, Jarlborg et al. 1989, 1991), and KKR (Bansil et al. 1988, 1990, 1991, Bansil 1991, Bansil and Smedskjaer 1992). Simpler approaches which have considered only the Fermi surface also have to be mentioned (Antonov et al. 1988, 1989, Prasad and Srinivas 1989).

The Fermi surface is described in the Brillouin zone which for orthorhombic $YBa_2Cu_3O_7$ is a flat parallelepiped box. The short Γ–Z edge results in the Fermi surface having little dispersion in this direction. It is therefore made of almost cylindrical sheets. Most of the band-structure calculations show that the Fermi surface of $YBa_2Cu_3O_7$ consists of the five main sheets shown in fig. 4. Following Bansil et al. (1991) we shall

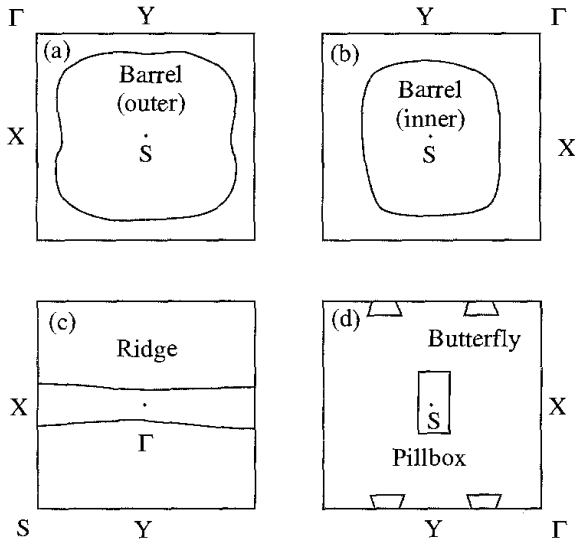

Fig. 4. The calculated Fermi surface of $YBa_2Cu_3O_7$ in the Γ–X–S–Y plane (From Bansil et al. 1991.)

refer frequently to (1) the outer and inner "barrels" (figs. 4a,b) which are a pair of closely spaced S-centered hole sheets, (2) an electron "ridge" running along Γ–X (fig. 4c), (3) a "pillbox" hole sheet around S, and (4) "butterflies" (fig. 4d). These last two sheets have heavy masses and are, therefore, quite sensitive, in size and shape, to computational details.

Some alternative approaches have been taken to study the positron annihilation characteristics without explicit band-structure calculations. As far as $YBa_2Cu_3O_7$ is concerned, the LCAO-MO approach developed by Chiba (1976) for oxides has been applied by Chiba (1992), Turchi et al. (1988, 1990) and Saul and Weissmann (1990). Although the Fermi surface is not a concept in the LCAO-MO description, this method is quite appropriate for the direct physical insights it provides for the analysis of the anisotropies $A(r, \theta)$ of the 2D-ACAR distribution, eq. (15).

4.1.2. *Experimental study*

The main question underlying the work performed by 2D-ACAR in Y-123 is the following: Is there a Fermi surface in high-T_c superconductors? (Berko 1989). Therefore, most of the efforts have been devoted to investigate the fermiology of Y-123. Another factor has to be mentioned: photoemission is more difficult in Y-123 than in other high-T_c superconductors because it is not easy to obtain clean and flat surfaces. Positron annihilation does not suffer from this limitation; it is therefore an attractive technique to study the topology of the Fermi surface of $YBa_2Cu_3O_{7-\delta}$.

The work in this field has been previously reviewed by Bansil (1995), Berko et al. (1991), Chan et al. (1992), Howell et al. (1992), Manuel (1989), Peter (1989, 1991, 1995), Peter et al. (1990, 1992a, 1993, 1998), Smedskjaer and Bansil (1992), Smedskjaer et al. (1993), and West (1992). These references outline the difficulties which had to be overcome to obtain unambiguous results on the size and shape of the Fermi surface. This effort took many years, and early works suffer from a number of biases: single

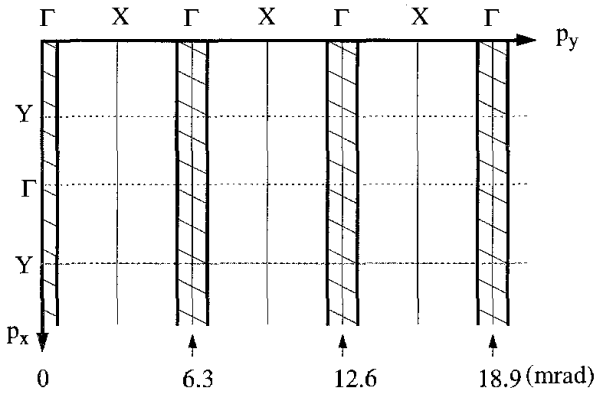

Fig. 5. The position of the ridge in momentum space, as seen in a 2D-ACAR projection along the Γ–Z direction. (From Manuel 1995.)

crystals of rather poor quality, the lack of understanding of the behavior of the positron in oxides, the lack of powerful tools to analyze the data, and the lack of awareness of the effect of positron trapping in defects. It is nevertheless worth mentioning that during this early phase, much valuable information has been gathered by the groups involved in this research.

These early works have shown that the ridge is the Fermi surface sheet most likely to be calipered by positron annihilation (Bansil et al. 1988, Smedskjaer et al. 1988a). They have also shown that measurements at room temperature, instead of low temperatures, provide larger signals (Smedskjaer et al. 1992a,b, Von Stetten et al. 1989). They have shown the existence of a background contribution of undetermined origin (Bansil et al. 1990), which was later clearly ascribed to partial positron trapping. Another lesson from these early works is the important role of the positron wave function which contrasts strongly with the study of traditional metals performed up to that time. Due to the non-uniformity of $\Psi^+(\vec{r})$, the momentum density $\rho^{2\gamma}(\vec{p})$ is different from the purely electronic momentum density. A consequence is the failure of the LCW theorem stating that the function $h(\vec{k})$ defined in eq. (3) is periodic and uniquely dependent on the occupation number in the Brillouin zone. A clear demonstration of this failure has been made with NiO, an insulator. In NiO, the projection of $h(\vec{k})$, obtained by 2D-ACAR measurements, shows modulations similar in amplitude and sharpness to the one observed in metallic $YBa_2Cu_3O_{7-\delta}$, prohibiting firm conclusions concerning the existence of the Fermi surface (Bansil et al. 1991, Haghighi et al. 1990), and suggesting that a careful analysis of the positron effect in the LCW maps has to be performed (Campuzano et al. 1991, Hoffmann et al. 1988a, 1991). As a consequence, a simple interpretation of LCW maps on the basis of the Fermi surface (Smedskjaer et al. 1988a, Hoffmann et al. 1988a,b) and the reconstruction of the Fermi surface using the LCW maps (Peter et al. 1988, Tanigawa 1989) have to be taken with care. Apart from these exceptions, early comparisons of the 2D-ACAR results with band-structure calculations (Bansil et al. 1990) have seen their results confirmed by the further studies.

The turning point in the study of the Fermi surface of $YBa_2Cu_3O_{7-\delta}$ was the availability of high-quality untwinned single crystals. It provided the possibility to obtain 2D-ACAR distributions of lower symmetry (c_{2v} instead of c_{4v}) and hence to differentiate

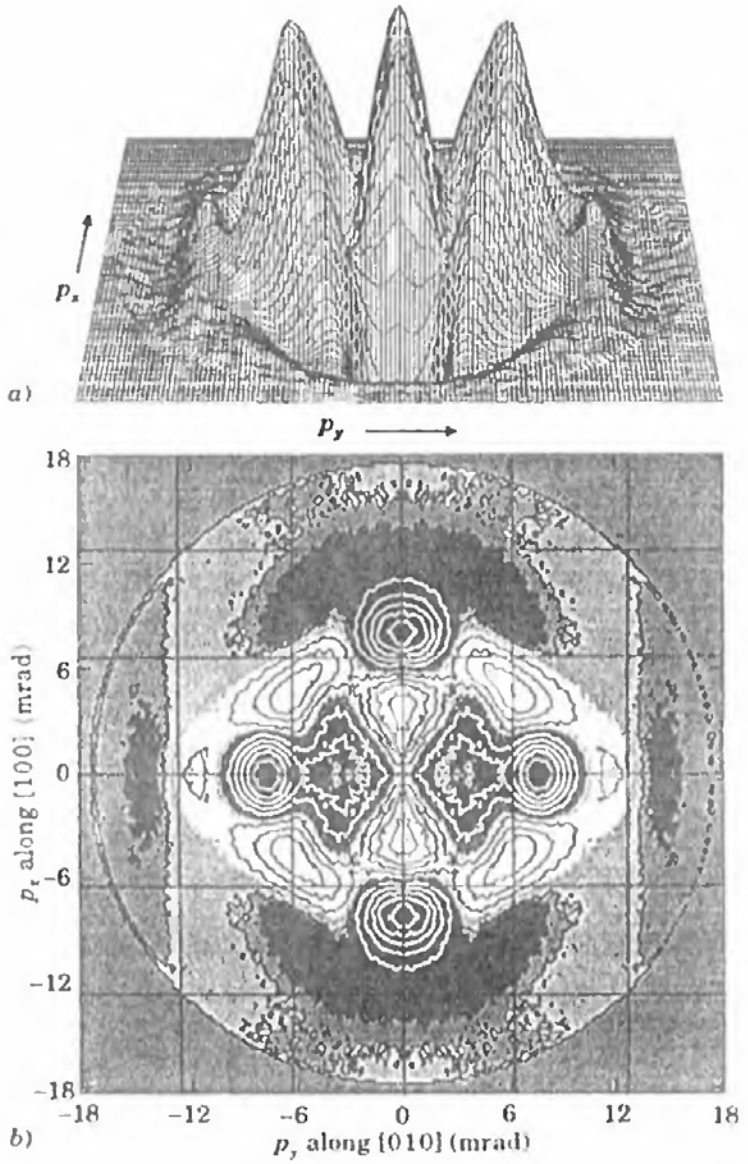

Fig. 6. (a) Isometric and (b) contour plots of the anisotropy of the Γ–Z-projected 2D-ACAR obtained with an untwinned $YBa_2Cu_3O_7$ sample. (From Haghighi et al. 1991.)

between the directions Γ–X and Γ–Y in the Brillouin zone. This has proved to be important to detect the ridge, the planar Fermi surface running along Γ–X. The first measurements were immediately successful (Smedskjaer et al. 1991, 1992c).

How is the Fermi surface reflected in the 2D-ACAR distribution? Consider $N(p_x,p_y)$ to be a projection along the Γ–Z direction. As the 2D-ACAR spectroscopy provides density distributions in momentum space, there will be periodical contributions of the Fermi surface, whose intensities are determined by the coefficients of the wave functions, as seen in eq. (2). For this particular projection, the sequence of the ridges is shown schematically in fig. 5. Some of them are directly observed in the measured distributions. Figure 6

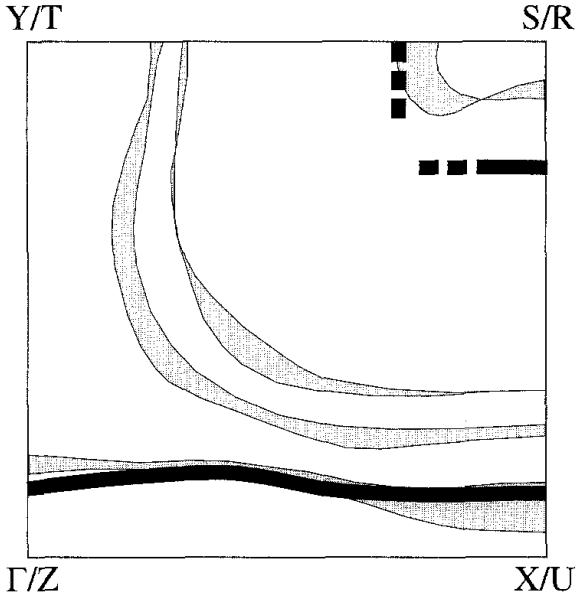

Fig. 7. Fermi surface of $YBa_2Cu_3O_7$. Calculations are from Yu et al. (1987). The thick lines are the 2D-ACAR results (From Shukla et al. 1995a.)

shows the anisotropy $A(r,\theta)$, defined in eq. (15), for the Γ–Z projection, measured with an untwinned single crystal (Haghighi et al. 1991). The second Umklapp of the ridge induces the remarkable close-to-straight lines running parallel to the Γ–X direction and symmetrically disposed close to $p_y = \pm 4\pi/b$ (12.6 mrad). The third Umklapp of the ridge at $p_y = 6\pi/b$ (18.9 mrad) has also been observed (Adam et al. 1993, Hoffmann et al. 1993a), as well as the ridge in the central Brillouin zone (Smedskjaer et al. 1992b, Pankaluoto et al. 1994). The S-centered pillbox has long been tracked (Smedskjaer et al. 1992b) and finally also clearly observed (Shukla et al. 1995a). And what about the barrels? They are extremely difficult to observe by positron annihilation, as the positron wave function is very small in the CuO_2 planes of $YBa_2Cu_3O_{7-\delta}$. West (1995) has obtained results in agreement with band calculations (Singh et al. 1990) by fitting LCW reduced distributions with arbitrary parameters to take into account the effect of the positron trapping in the oxygen vacancies, but these results do not conclude explicitly the detection of the barrels.

To summarize these results, the Fermi surface observed by 2D-ACAR in metallic $YBa_2Cu_3O_{7-\delta}$ is shown in fig. 7, along with the Fermi surface obtained by band-structure calculations. This figure shows that the ACAR experiments have provided a significant body of evidence suggesting that many aspects of the electronic structures of $YBa_2Cu_3O_{7-\delta}$ in its normal state are satisfactorily described by conventional LDA band theory. Taken together, these observations do not support the localization of electronic states, at least not strongly, along the $\vec{c}$-axis in $YBa_2Cu_3O_7$ (Pankaluoto et al. 1994). The progress in data analysis has been an important factor in achieving these results (Manuel 1995). Large improvements have been made in various directions: differential analysis (Bansil et al. 1988, Peter et al. 1992b), optimal linear filtering (Hoffmann et al. 1993b, Peter et al. 1996), partial deconvolution of the experimental resolution by the principle of maximum entropy (Hoffmann et al. 1991), partial deconvolution of the

positron wave function (West 1995), and statistical analysis of the data progression during the measurement (Barnes et al. 1994).

The insulating $YBa_2Cu_3O_{6+x}$ brings an extra confirmation of the Fermi surface observed in $YBa_2Cu_3O_{7-\delta}$: all the 2D-ACAR signals ascribed to the ridge and the pillbox in the metallic compound are lacking in the non-conducting compound (Smedskjaer et al. 1992a, Manuel et al. 1993). Beyond Fermi surface signatures, the metal–insulator transition induces another substantial change in the 2D-ACAR characteristics: the 2D-ACAR of the insulator is significantly narrower than that of the metal (Von Stetten et al. 1988, Barbiellini et al. 1991, Smedskjaer et al. 1992a). The calculation of the 2D-ACAR distributions for the metallic and the insulating phase shows that this is the consequence of the relaxation of the positron wave function (Massidda 1990) shown in fig. 2. The narrower 2D-ACAR of $YBa_2Cu_3O_6$ has led Erb et al. (1999) to ascribe the "fishtail" anomaly of the magnetic susceptibility in the superconducting state to large clusters of oxygen vacancies located in the Cu–O chains of $YBa_2Cu_3O_{6.9}$, and to interpret the fishtail anomaly as a peak effect due to the pinning of the magnetic vortices by these extended structural defects.

4.2. *Defect spectroscopy*

4.2.1. *Lifetime*

The mean lifetime τ_m, eq. (21), is the basic quantity obtained with positron lifetime spectroscopy. It does not depend on the analysis of the recorded lifetime spectra, as τ_1 and τ_2 do. It is therefore a reliable quantity but it lacks of physical insight. In this regard, τ_1 and τ_2 are more closely related to the annihilation processes competing in a real solid, but they are most of the time obtained on the basis of the two-state trapping model, neglecting a possible detrapping of the positron. τ_m provides a good basis to compare the different experiments performed on $YBa_2Cu_3O_{7-\delta}$, and it is therefore interesting to discuss it first.

Numerous results have been published and the dispersion of the results is rather large. The main reason for this dispersion is the quality of the materials investigated. We have made a statistical analysis of the lifetimes published since 1987. We find that the mean value of τ_m at room temperature is 190 ± 22 ps for the metallic phase and 210 ± 11 ps for the insulating phase[2]. These values are quite stable: they do not change by more than 2 ps if we restrict ourselves to the results published since 1991.

[2] The positron lifetimes given in this section have been established from data published in the following references: Balogh et al. (1988), Barbiellini et al. (1991), Bharathi et al. (1988a), Chu et al. (1991), Corbel et al. (1989), Gauthier (1991), Gopalan et al. (1992), Gou et al. (1995), Harshman et al. (1988), Hentrich et al. (1992a), Hermes et al. (1991), Hill et al. (1991), Ishibashi et al. (1988, 1990a,b), Jean et al. (1987, 1988, 1990), Jung et al. (1995), Lagouri et al. (1997a), Lam et al. (1996), Li Anli et al. (1989), Liolios et al. (1989, 1992), Mandal et al. (1988), Lu et al. (1992), Moser and Henry (1989), Peter et al. (1992a), Sausa et al. (1992), Sedov et al. (1990, 1995), Sen and Majumdar (1989), Shukla et al. (1995a), Smedskjaer et al. (1988b), Sundar et al. (1988a), C.Q. Tang et al. (1990), Teng et al. (1987), Usmar et al. (1987, 1988, 1992), Vasumathi et al. (1990), Wang et al. (1988, 1989), H. Zhang et al. (1988), J.C. Zhang et al. (1993a,b, 1995), Zhao et al. (1995), Zhi et al. (1993), and Zhou et al. (1988, 1997a).

Most of the lifetime spectra can be decomposed, after correction for the annihilation occurring in the positron source itself, into two or three components. Statistical analysis of the results found in the literature gives the following results for the metallic phase of $YBa_2Cu_3O_{7-\delta}$ at room temperature: $\tau_1 = 170 \pm 30$ ps ($I_1 = 85 \pm 23\%$), $\tau_2 = 358 \pm 166$ ps ($I_2 = 30 \pm 26\%$), and $\tau_3 = 1809 \pm 677$ ps ($I_3 = 2 \pm 2\%$). In the insulating phase, the compilation of the results gives: $\tau_1 = 195 \pm 30$ps ($I_1 = 81 \pm 23\%$), $\tau_2 = 380 \pm 261$ ps ($I_2 = 34 \pm 26\%$), and $\tau_3 = 2120 \pm 425$ ps ($I_3 = 1 \pm 1\%$). The dependence of the lifetime on oxygen concentration has been studied by Aravin et al. (1990, 1992), Smedskjaer et al. (1988b), Gopalan et al. (1992), C.Q. Tang et al. (1990), H. Zhang et al. (1988), J.C. Zhang et al. 1993b, 1994), Zhou et al. (1988), Hentrich et al. (1992a,b), Bharathi et al. (1988a,b), Vasumathi et al. (1990), Hermes et al. (1991) and Lagouri et al. (1997b). The oxygen dependence is usually found to be continuous from $YBa_2Cu_3O_7$ to $YBa_2Cu_3O_6$ at room temperature, although the temperature dependences are different in the conducting and insulating regimes.

As I_3 has a small intensity, it is subtracted from the spectra and the two-state trapping model is used to determine the bulk lifetime τ_B, according to eq. (20). The compilation of the results found in the literature gives $\tau_B = 184 \pm 11$ ps and 215 ± 4 ps for the metallic and insulating phase, respectively. These values are statistically different, contrary to τ_m, τ_1 and τ_2. The interpretation of this difference can be based on the calculated annihilation rates which depend on the positron density distribution in the lattice unit cell.

How do these results compare with calculations? The positron lifetime can be estimated from eq. (5) as $\tau = 1/\lambda$. For $YBa_2Cu_3O_7$ the calculated bulk lifetime is 160 ± 5 ps, and is independent of the method used: LMTO-LDA (Barbiellini et al. 1992, Peter et al. 1992a), LMTO-GGA (Barbiellini et al. 1996) or atomic models (Jensen et al. 1989, Ishibashi et al. 1991, 1992, McMullen et al. 1991). Let us mention that a few calculations give slightly different values (Jarlborg et al. 1991, Barbiellini et al. 1996, Bharathi et al. 1989). In $YBa_2Cu_3O_6$, the calculated bulk lifetime is significantly larger: 201 ps by LMTO in the LDA (Barbiellini et al. 1992, Peter et al. 1992a), 207 ps (Jensen et al. 1989) or 234 ps (Bharathi et al. 1989) by the atomic model of Puska and Nieminen (1983). It is also interesting to mention calculated positron lifetimes for $YBa_2Cu_3O_7$ with some defects present: oxygen vacancy: 159–180 ps; Cu(1) vacancy: 197–207 ps; Cu(2) vacancy: 182–200 ps; Y vacancy: 206–235 ps; Ba vacancy: 263–265 ps; Cu(1)–O(1) divacancy: 236 ps; twin boundary: 177–189 ps (Jensen et al. 1989, Ishibashi et al. 1991, 1992, McMullen et al. 1991, Howell et al. 1991); clusters of O(1) vacancies: 181–190 ps (Ishibashi et al. 1991, 1992).

The temperature dependence of the lifetime has been extensively investigated. In this section, we focus on temperatures above T_c. The temperature dependence around the superconducting transition is discussed in sect. 4.3. There is a large spread in the results, therefore it is difficult to give a precise description of the temperature dependence. This spread is mainly due to the difficulty in characterizing the samples. It has been observed, for example, that the positron lifetime depends on the twin density (Usmar et al. 1988). The sensitivity of positron spectroscopies to defects is so high that defects very often dominate the observed temperature dependencies. As it is not easy to characterize precisely the defects in the samples under investigation, one has to take

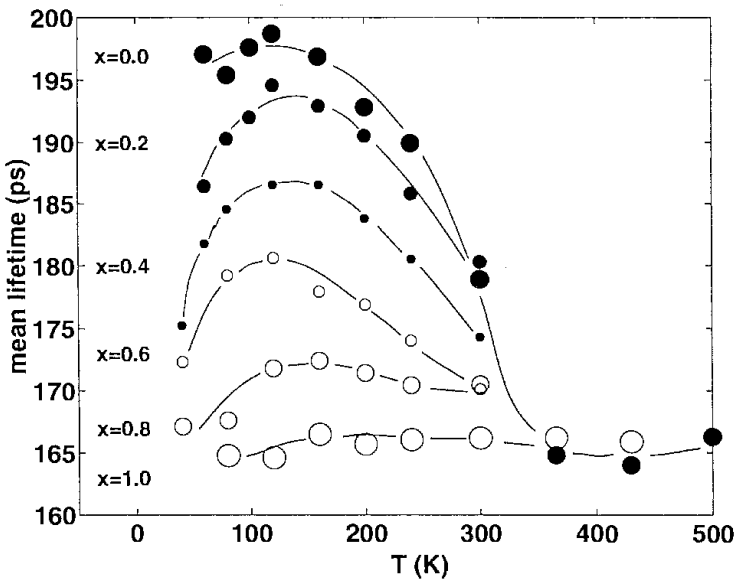

Fig. 8. Temperature dependence of the mean positron lifetime in $(Y_{1-x}Pr_x)Ba_2Cu_3O_{7-\delta}$. (From Peter et al. 1996.)

great care in interpreting the results. As considerable progress has been made in sample preparation, mainly in the growth of single crystals of high purity and high crystalline ordering, we restrict ourselves to some results which, at the present time, seem the most representative.

The typical temperature dependence of the positron lifetime in $YBa_2Cu_3O_{7-\delta}$ is represented by the upper curve in fig. 8 It shows a "bell-shaped" temperature dependence, i.e. lower values at low and high temperatures than in the intermediate range of temperatures. This dependence is frequently observed (Corbel et al. 1989, Gauthier 1991, Ishibashi et al. 1990a,b, 1991, 1992, Moser and Henry 1989, Peter 1995, Peter et al. 1995, 1996, Sundar et al. 1988b, Shukla et al. 1995a,b and Wang et al. 1988). When the temperature rises from 4 K, the mean positron lifetime increases from 170–180 ps to reach a maximum value of 200 ps around 150 K, then decreases to 165 ps up to a temperature of 350–400 K, then remains constant up to 500 K. Few measurements have been performed above 500 K, and they suggest that the positron lifetime increases monotonically from 600 to 1000 K (Hentrich et al. 1992a,b) as the density of structural defects increases.

The "bell-shaped" temperature dependence observed in $YBa_2Cu_3O_{7-\delta}$ between 10 to 500 K is the consequence of two different trapping centers: C1 with a high concentration and a low binding energy and C2 with a lower concentration, a higher binding energy and a positron lifetime longer than in C1. The trapping center C1 is more efficient at low temperatures since it is present at a higher concentration. But, as the temperature is raised, the positron can be thermally expelled from C1 and trapped in C2. The lifetime therefore increases. When the temperature is raised still further, the positron can be detrapped from C2, and the lifetime decreases down to the bulk value. The trapping center C1 is usually identified as oxygen vacancies located in the Cu–O chains. The identification of C2 is less

obvious. In a detailed discussion, Peter et al. (1996) reach the conclusion that the trapping center C2 consists of clusters of oxygen vacancies. The rise of lifetime which has been observed is in agreement with the lifetime calculated by Ishibashi et al. (1991). Some other identifications have also been proposed: metallic vacancies (Jensen et al. 1989) or twin boundaries (Usmar et al. 1994, Hentrich et al. 1992a). Smedskjaer et al. (1988b) have concluded that the trapping coefficient in oxygen vacancies is 4 orders of magnitude smaller than for vacancies in metals. Nevertheless, oxygen vacancies play a major role because of their large concentration.

The temperature dependence of the positron lifetime in $YBa_2Cu_3O_{7-\delta}$ can differ from "bell-shaped", and can show a continuous increase (Corbel et al. 1989, Kajcsos et al. 1989, Liolios et al. 1989), a continuous decrease (Corbel et al. 1989, Harshman et al. 1988, Kajcsos et al. 1989), or no temperature dependence at all (Ishibashi et al. 1989). Some different, more complicated, temperature dependences have also been reported (Sundar et al. 1988a,b, D.M. Zhang et al. 1993c). The fact that different kinds of temperature dependences have been observed by the same authors indicates clearly that the large variety of results is related to the samples and not to experimental difficulties. The different dependences observed are not all well understood. It seems that the positron lifetime remains constant with temperature in two cases: when the positrons are trapped by deep traps and when there is no significant trapping, as seems to be the case in $PrBa_2Cu_3O_7$ (fig. 8, lower curve). The two cases can be distinguished by the value of the mean lifetime, which is higher in the former case.

We have discussed mostly the temperature dependence of the positron mean lifetime τ_m. The temperature dependence of each separate lifetime component is more complex to review because the extraction of different lifetime components present in a spectrum is a delicate process. Using the two-state trapping model, most of the authors have limited the analysis of positron lifetime spectra to two lifetime components, after subtracting for source components and a low-intensity long component related to positronium formation at the surfaces. The first component, τ_1, is ascribed usually to annihilation of free positrons and the second, τ_2, to positrons trapped by defects. It should be pointed out that the relations frequently used to interpret the lifetime are based on the hypothesis that there is no positron detrapping, which is questionable at temperatures above 200 K.

To end this section, let us mention that, using a pulsed beam of monoenergetic positrons, Zhou et al. (1996, 1997a,b) have measured the positron lifetime as function of the implantation of the positrons in epitaxial thin films of $YBa_2Cu_3O_{7-\delta}$ and $GdBa_2Cu_3O_{7-\delta}$. This new approach is promising for various investigations such as, for example, the depth profiling of the oxygen concentration, the structural quality of the films or the detection of free volume holes near the surface.

4.2.2. *Lineshape*

The temperature dependence of the lineshape parameter S has been extensively investigated. In this section, we consider the temperature dependence in the normal state.

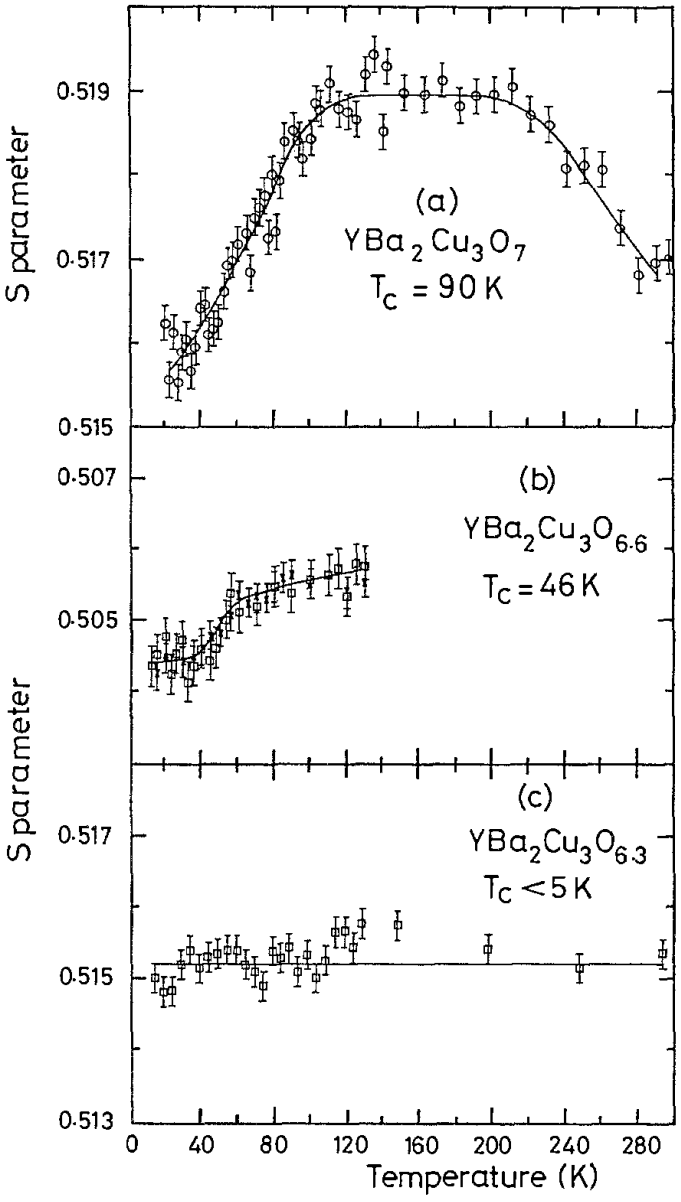

Fig. 9. Temperature dependence of the annihilation line parameter S in $YBa_2Cu_3O_{7-\delta}$ for three different oxygen concentrations. (From Lynn et al. 1988.)

The superconducting state will be discussed in sect. 4.3. The general trends presented in sect. 4.2.1 for the temperature dependence of the positron mean lifetime have also been observed by lineshape spectroscopy. A typical result is shown in fig. 9 for three different oxygen concentrations. The bell-shaped temperature dependence for optimally doped $YBa_2Cu_3O_{7-\delta}$ in fig. 9a is similar to what has been observed by lifetime spectroscopy (see sect. 4.2.1). The same conclusion is reached: oxygen vacancies in the Cu–O chains explain this temperature dependence. The same temperature dependence of the S parameter has been observed by Barbiellini et al. (1991), Brusa et al. (1989), Dryzek and Romek (1990), Smedskjaer et al. (1988b,c), and Usmar et al. (1988, 1994). As was found for the lifetime measurements, the temperature dependence depends critically

on the sample. The types of temperature dependences observed for $YBa_2Cu_3O_{7-\delta}$ are: an increase of the S parameter as the temperature increases up to 120 K and then a temperature-independent behavior (Liolios et al. 1989, Wang et al. 1988); a decrease (Lynn et al. 1988); a complex temperature dependence above 200 K (Balogh et al. 1988, Ilyasov et al. 1991, 1992, Smedskjaer et al. 1988b, Wang et al. 1989, Yang et al. 1987); and no temperature dependence at all (Belyaev et al. 1990b, Bezakova et al. 1989, Kajcsos et al. 1989, Lagouri et al. 1997a, Wang et al. 1989), which seems to be the trend for insulating $YBa_2Cu_3O_{6+x}$, see fig. 9c (Usmar et al. 1987).

The temperature dependence has been studied at higher temperatures (Hermes et al. 1991), providing another demonstration that the positron density in $YBa_2Cu_3O_7$ is large around the Cu–O chains. The oxygen dependence of the lineshape parameter S has been reported by Mikhalenkov et al. (1991), Smedskjaer et al. (1988b) and H. Zhang et al. (1988). It can be related to what has been observed by lifetime spectroscopy. Determination of S has also been performed with beams of monoenergetic positrons to correlate the depth variation of oxygen content with the history of thin-film or single-crystal samples (Anwand et al. 1995, Lynn et al. 1988).

4.3. *Superconducting phase transition*

Equation (11) provides a guideline of what is to be expected in the superconducting state. The gap induces a blurring of the Fermi breaks in the 2D-ACAR distributions. As seen in sect. 2.3, this effect should be visible in high-T_c superconductors. No smearing of the Fermi surface has been observed in $YBa_2Cu_3O_7$ until now. Two reasons may explain this result: (1) as the positron density is small in the CuO_2 planes, a superconducting gap in this region of the lattice cell cannot be observed; and (2) the positron–electron correlations destroy the superconductivity in the correlation hole surrounding the positron which, therefore, probes only the normal state.

As discussed in the previous subsections, both the positron lifetime and the lineshape parameter exhibit a temperature dependence. But it seems that these dependences can be very different without a clear reason. One fact without exception is that there is no discontinuity in the temperature dependence of lifetime or lineshape parameter around $T = 90$ K in the insulating samples, although the metallic ones show a variety of effects around T_c.

Apart from the smooth increase of the lifetime at low temperature, discussed in sect. 4.2.1 and attributed to detrapping mechanisms, sharp changes in the positron mean lifetime around the superconducting transition have been observed (Ishibashi et al. 1988, 1989, Jung et al. 1995, Kajcsos et al. 1989, Liolios et al. 1989, Sundar et al. 1988a,b, Sedov et al. 1990, 1991, 1992, Teng et al. 1987, D.M. Zhang et al. 1993c). It is difficult to give a simple picture of this phenomenon because the observed variations are very different from each other and even sometimes the subject of controversy (Usmar et al. 1992). More interesting is to report the conclusions of these studies.

A number of authors have observed that τ_2 increases when the temperature is raised up to T_c and that the temperature dependence of τ_2 is different above T_c: Jean et al.

(1987, 1988, 1989b), Jung et al. (1995), Sundar et al. (1988b), Usmar et al. (1987, 1988), Von Stetten et al. (1988). Jean et al. (1987, 1989b) conclude that O vacancies play a significant role in the superconductivity, and that the electronic structure changes at T_c, i.e. the electron density near the oxygen vacancies is larger in the superconducting state than in the normal state. Another explanation for the abrupt changes at T_c is that lattice relaxation occurs (Teng et al. 1987). But studies of Fe-doped $YBa_2Cu_3O_7$ show that there is no correlation between T_c and the change in the temperature dependence of the positron lifetime (Usmar et al. 1992, 1994, Ishibashi et al. 1991, 1992), and hence that the claim of positron spectroscopy being sensitive to superconductivity is completely erroneous. Still other authors have observed a reversed trend of τ_2 at T_c (Wang et al. 1988). Other authors have observed a sharp change of τ_1 at T_c (Liolios et al. 1989) or instabilities (Hill et al. 1991). Changes of τ_1 or τ_2 have also been observed around 250 K (Balogh et al. 1988). It is therefore difficult to draw a firm conclusion, and one should remain cautious about the interpretations of these results.

In addition, variations in the temperature dependence of the lineshape parameter S in a narrow temperature range around T_c have been reported (Arutyunov and Trashchakov 1992, Brusa et al. 1989, Ilyasov et al. 1991, 1992, Ishibashi et al. 1987, Jean et al. 1987, Kristiakova et al. 1989, Li Anli et al. 1989, Mandal et al. 1988, Matsui et al. 1989, Sen and Majumdar 1989, Smedskjaer et al. 1988b,c, Yang et al. 1987). Similarly, strong variations around T_c have also been observed in Bi-2223 (De et al. 1996a) but, here also, other measurements do not show anything (Lim and Byrne 1997). What is puzzling is the large variety of topologies of the localized discontinuities observed in $YBa_2Cu_3O_7$. Other authors have reported abrupt changes of the temperature dependence occurring at T_c (Bharathi et al. 1988a,b, Doyama et al. 1987, Huang et al. 1990, Jung et al. 1995, Liolios et al. 1989, Pujari et al. 1991, Sundar et al. 1988a,b, Usmar et al. 1987, 1988, 1994, Vasumathi et al. 1990). Finally, absence of a change in $S(T)$ at T_c has also been reported (Belyaev et al. 1990a,b,c, Lagouri et al. 1997a).

Various interpretations of the effects observed at, or around, T_c have been proposed: a significant redistribution of the electrons (Huang et al. 1990, Usmar et al. 1987, Zhu et al. 1988); an indirect indication for an electronic mechanism of the superconductivity (Mandal et al. 1988); a change of the lattice parameter at, or near, T_c (Kristiakova et al. 1989); a structural instability (Li Anli et al. 1989, Pujari et al. 1988, Wang et al. 1989); a lattice distortion (Wang et al. 1988); an adjustment of the position of the oxygen atoms (Arutyunov and Trashchakov 1992, Zhu et al. 1988); and a new mechanism of superconductivity (Yang et al. 1987). The frequently observed lower value of S in the superconducting state compared to the normal state is in agreement with the theory of Barnes and Peter (Barnes and Peter, 1989). However, the magnitude of this effect is much larger than the predicted one. This may be due to the fact that the theory has made the approximation that electrons do not interact with the positron. Also, it might well be that the observed effects in the positron characteristics are not related to superconductivity but are the result of positron dynamics in the presence of different trapping centers (Usmar et al. 1992, 1994).

5. Atomic substitutions in $YBa_2Cu_3O_{7-\delta}$

5.1. *Cu substitution:* $YBa_2(Cu_{3-x}M_x)O_{7-\delta}$

The 2D-ACAR spectrum is affected by the partial substitution of Cu atoms by Al atoms, while it remains almost the same when Cu is partly substituted by Ni and Zn (Barbiellini et al. 1993, Hoffmann et al. 1993a, Manuel et al. 1993). 2.1 at.% Al on the chains reduce T_c to 77 K and the Fermi surface ridge due to the electronic states of the Cu–O chains disappears. This strong effect points out that the electronic properties of the chains are heavily affected by the chemical disorder while it has only a minor effect on the superconducting properties. These observations suggest that the Al atoms are substituted for the Cu atoms of the chains and the superconductivity is mainly an effect related to the electronic properties of the CuO_2 planes. These statements are in agreement with what is observed when one substitutes about 3 at.% Cu by Zn or Ni. In these cases, T_c is reduced to 25 K and 73 K, respectively, but the 2D-ACAR spectroscopy provides clear signals from a linear ridge Fermi surface sheet due to the chains. Therefore, the Zn or Ni atoms, lying in the CuO_2 planes, do not affect the electronic structure of the Cu–O chains but do affect the superconducting properties, which are more sensitive to the CuO_2 planes.

In addition, the following observations have been made. Positron lifetime in Al-doped $YBa_2Cu_3O_7$ suggests that the Al atoms are probably in the Y sites (Sausa et al. 1992). Cd fills Ba vacancies and has no essential effect on the CuO_2 planes (Liolios et al. 1992). Fe substitutes for Cu(1), mainly at low Fe concentrations (H. Zhang 1990). As seen in sect. 4.3, analysis of lifetime spectra in Fe-doped samples suggests that claims of positron spectroscopy being sensitive to superconductivity have to be taken with care (Usmar et al. 1992, 1994, Ishibashi et al. 1991, 1992). Hf atoms substitute for Cu atoms of the Cu–O chains (Gopalan et al. 1992), as do the Sn atoms (J.C. Zhang et al. 1993a, Chen et al. 1992a,b). Sr doping supports the conjecture that the chemical doping induces additional oxygen defects (Huang et al. 1988). Zn doping changes the local charge density associated with the superconducting transition (Jean et al. 1990). It has also been found that hydrogenation of $YBa_2Cu_3O_{7-\delta}$ influences positron lifetimes, as the hydrogen atoms fill in vacancies and microvoids (J.Q. Li et al. 1997).

5.2. *Y substitution:* $(Y_{1-x}R_x)Ba_2Cu_3O_{7-\delta}$

Besides $YBa_2Cu_3O_7$, 2D-ACAR has been measured in compounds of the same structure but with different rare earths: R = Dy, Ho and Pr (Hoffmann et al. 1993a, 1995). It has been concluded that the electronic structure of these compounds is similar to that of $YBa_2Cu_3O_7$, as suggested by band-structure calculations. The ridge, i.e. the Fermi surface sheet originating from the Cu–O chains, is almost unchanged, as probably are the other sheets of the Fermi surface.

One striking fact is that the ridge, predicted for the metallic $PrBa_2Cu_3O_7$ (Singh 1994), is observed by 2D-ACAR, despite the insulating behavior of the crystal. The existence of the Fermi surface in this case is supported by the model of Fehrenbacher and Rice (1993).

We can ascribe the macroscopic insulating behavior of this compound to its extreme sensitivity to disorder on the chains, which themselves remain metallic at the microscopic level, until their 1D character is strongly damaged by defects and impurities. The recent observation of metallicity in $PrBa_2Cu_3O_7$ (Blackstead et al. 1995, Zhou Zhigang et al. 1997) is not in opposition with the conclusions drawn from the positron 2D-ACAR study.

In general, lifetime and lineshape studies conclude that the substitution of Y by a rare-earth element (La, Nd, Sm, Eu, Gd, Dy, Ho and Er) does not appreciably alter the annihilation characteristics (Lagouri et al. 1997a, Nagarajan et al. 1991). The substitution of Y by Ca atoms causes a transfer of hole carriers from the chains to the planes (Han et al. 1995). Equivalently, Dy substitution for Y induces a transfer of electrons from the CuO_2 planes to the Cu–O chains (Jung et al. 1996). Zhao et al. (1995) conclude that this charge transfer does not exist when Pr is substituted for Y (Zhao et al. 1995). Y. Li et al. (1997) point out a stress pinning in Eu-doped $YBa_2Cu_3O_7$. Pujari et al. 1996 have observed a clear discontinuity in the temperature dependence of the S-parameter at the onset of superconductivity in the tetragonal $CaLaBaCu_3O_{6.85}$ superconductor, a clone of $YBa_2Cu_3O_7$.

6. Other compounds

6.1. *$(La_{2-x}Sr_x)CuO_4$ and $(Nd_{2-x}Ce_x)CuO_4$*

The positron charge distribution calculated for La_2CuO_4 (Blandin et al. 1992, Kubo and Asano 1992, McMullen et al. 1991, Sundar et al. 1992, Turchi et al. 1990) and Nd_2CuO_4 (Blandin et al. 1992, Sundar et al. 1990b) overlaps substantially with the CuO_2 planes, leading to sizable contributions from the corresponding electronic states. The electronic momentum density sampled by the positrons exhibits substantial structure. It is well described by a localized ion scheme (Chiba, 1976) in La_2CuO_4 (Turchi et al. 1990, Wachs et al. 1988) or by band-structure approaches, both in La_2CuO_4 (Howell et al. 1994, Blandin et al. 1992) and in Nd_2CuO_4 (Blandin et al. 1992).

The Fermi surface has been studied in these two compounds. In $La_{2-x}Sr_xCuO_4$, the 2D-ACAR has been measured (Sterne et al. 1993, Howell et al. 1994) for various Sr concentrations ($x=0$, 0.1, 0.13 and 0.2). Unlike $YBa_2Cu_3O_7$, the Fermi surface features are not strongly reflected in the anisotropy $A(r,\theta)$ of eq. (15). Therefore, the analysis has been made on the measured and calculated projections of the reduced distributions $h(\vec{k})$, eq. (3). They are shown in fig. 10 for $x=0.13$. Discontinuities typical of a Fermi surface are seen in the doped samples. The form and position of these features are in general agreement with the Fermi surface predicted by band theory and are identified as a hole sheet located at the zone boundary and resulting from the Fermi surface of the CuO_2 planes. However, the evolution of the Fermi surface with Sr doping differs significantly from expectations based on single electron band theory. If the general filling of the Brillouin zone is consistent with the band picture, an apparent smearing of the Fermi surface is observed. Several effects can lead to this apparent smearing: (1) imperfections

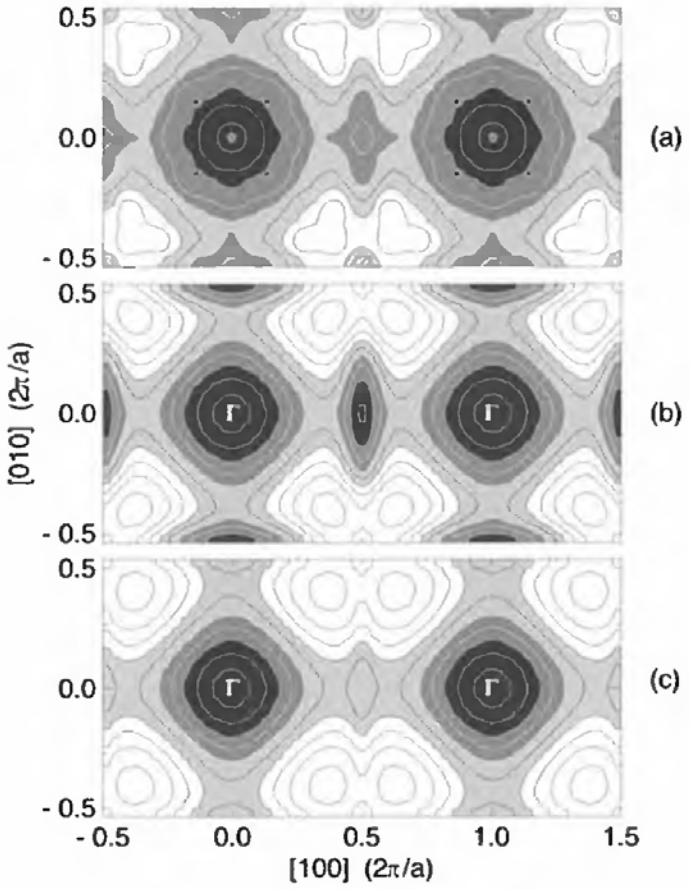

Fig. 10. Electron–positron k-space densities in an orthorhombic $La_{2-x}Sr_xCuO_4$ zone: (a) experimental results for $x=0.13$; (b) calculations for $x=0.15$; (c) calculation for an antiferromagnetic insulator. (From Howell et al. 1994.)

in the crystal structure, (2) scattering from a defect or from the disordered distribution of Sr atoms, (3) doping-dependent distortions of the positron distribution, or (4) electron correlations. This latter hypothesis is thought to be the most probable (Howell et al. 1994).

The Fermi surface of $Nd_{2-x}Ce_xCuO_4$ also induces signals in the 2D-ACAR distributions (Shukla et al. 1996). They have been observed at 400 K where shallow trapping by oxygen vacancies should be negligible according to the studies performed on $YBa_2Cu_3O_7$ (see sect. 4.2), although comparison of the shape of the 2D-ACAR with LMTO calculations does not exclude a partial deep trapping of the positron in metallic vacancies, as also suggested by the analysis of the positron lifetime. The Fermi surface observed in $Nd_{2-x}Ce_xCuO_4$, although the signals are weak, comes from the electronic states in the CuO_2 planes. It has the simple form described by band theory (Mattheiss 1987).

6.2. *$Tl_2Ba_2CaCu_2O_8$*

Tl-2212 is an other interesting candidate for investigating the electronic and superconducting properties of CuO_2 planes by positron spectroscopy. Calculations (Barbiellini et al. 1994, 1995a, Singh et al. 1989) show that the positron density distribution is large in

these planes. This is also the case for the other Tl-based compounds, Tl-2223 (Pickett and Singh 1992) and Tl-2201 (Singh and Pickett 1992).

Only a little work has been done on $Tl_2Ba_2CaCu_2O_8$, mainly due to difficulties encountered in the metallurgy. High-quality and well-characterized single crystals are needed. The anisotropy of the 2D-ACAR (Barbiellini et al. 1994) can be described by FLAPW or LCAO-MO calculations, while an uncharacterized contribution from localized positrons induces discrepancies in the general shape. The LCW remapping is, until now, inconclusive about the Fermi surface because the breaks are either strongly modulated by positron wave function effects or by positron trapping.

The trapping of positrons by lattice defects is clearly established in $Tl_2Ba_2CaCu_2O_8$ by the occurrence of multi components in the lifetime spectra (Sundar et al. 1990a, Jean et al. 1989a) and in the lineshape (Pujari et al. 1989), and by deviations from the lifetime calculated for the defect-free structure (Barbiellini et al. 1994).

6.3. $Bi_2Sr_2CaCu_2O_{8+x}$

The electronic properties of $Bi_2Sr_2CaCu_2O_{8+x}$ are more complicated to study than those of $YBa_2Cu_3O_7$ because the crystal structure is complicated by the occurrence of an incommensurate lattice modulation caused by the insertion of extra oxygen atoms in the BiO_2 layers.

Positron spectroscopy, as usual, depends on the positron density distribution. Unlike $YBa_2Cu_3O_7$, it seems to be more homogeneously distributed in the Bi compounds, and significantly overlapping with the electronic states in the charge reservoir Bi–O layers (Sundar et al. 1991) and the Cu–O sheets (Singh et al. 1989). Unfortunately, this favorable situation is largely cancelled by the incommensurate lattice modulation which includes an extra complication. Mijnarends et al. (1991a,b) have shown theoretically that the modulation should cause displacements of the image of the Fermi surface in the 2D-ACAR distributions. Their analysis shows the existence of a considerable fine structure but, in the absence of momentum density calculations, it is difficult to interpret the observed structure in terms of a Fermi surface. In another study (Chan et al. 1991a,b), the structure which is, in 2D-ACAR, due to the superlattice modulation along the *b*-axis of the BiO_2 layers is subtracted and the remaining part is compared with theoretical calculations of the $e^- - e^+$ momentum density using the FLAPW method. The measured 2D-ACAR distribution contains features consistent with both the CuO_2 and BiO_2 Fermi surfaces, in reasonable agreement with the calculations, as shown in fig. 11. The 2D-ACAR measured by the two groups shows temperature-dependent fine structure, but it is difficult to connect these observations with the occurrence of superconductivity.

Positron lifetime studies have revealed the existence of a large variety of defects in $Bi_2Sr_2CaCu_2O_{8+x}$. Trapping of positrons by vacancies, clusters of vacancies and voids has been observed (Pujari et al. 1991, 1994, Sanyal et al. 1995, Sundar et al. 1991, Z. Tang et al. 1993, D.M. Zhang et al. 1993a–c), outlining the need to improve the quality of sample preparation. (Bi,Pb)-2223 has also been investigated (Gao et al. 1994, Z. Tang et al. 1994, Wang et al. 1994). Z. Tang et al. (1994) conclude to the existence of Bi vacancies

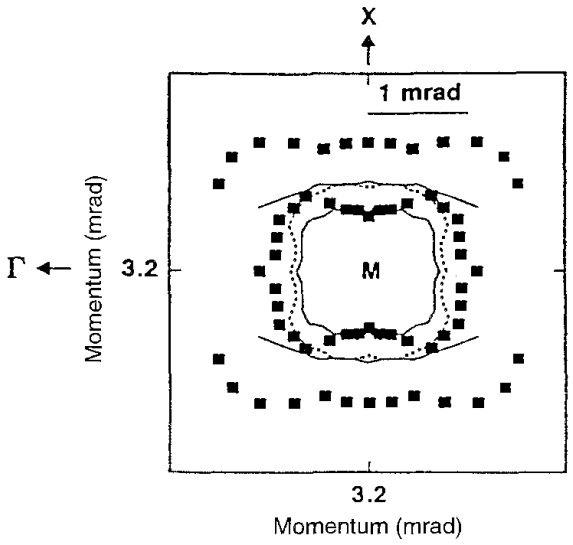

Fig. 11. The BiO_2 and CuO_2 Fermi surfaces near the M point in $Bi_2Sr_2CaCu_2O_{8+x}$. (From Chan et al. 1991a.)

in the Bi–O layers and also discuss the effect of F doping. Sedov et al. (1996) outline the influence of superconducting fluctuations upon the lifetime of the positron in voids in the same (Bi,Pb)-2223.

Some anomalies in the temperature dependence of the positron lifetime (Pujari et al. 1991, 1994) and in the lineshape (De et al. 1996b, 1997, Doyama et al. 1989, Sen and Majumdar 1989, Pujari et al. 1990, 1991) spectroscopies have been observed around T_c. As discussed for $YBa_2Cu_3O_7$ in sect. 4.3, the origin of these effects, which vary from sample to sample, is not clearly identified. They are ascribed to charge transfer from CuO_2 to BiO_2 planes at the onset of the superconductivity (Pujari et al. 1991, 1994) but may also be only indirectly coupled to superconductivity (Zhu et al. 1992).

6.4. $Ba_{1-x}K_xBiO_3$

2D-ACAR measurements (Mosley et al. 1994) have led to the identification of a Fermi surface in $Ba_{1-x}K_xBiO_3$. It is a cubic structure, centered around Γ, with rounded corners. Its location is in excellent agreement with that predicted by band-structure calculations. The observed large, parallel sheets of Fermi surface suggest the presence of effects due to Fermi surface nesting which may drive the superconducting state.

7. Concluding remarks

Positron annihilation has provided two significant contributions in the study of high-T_c superconductors. First, it has established the existence of Fermi surfaces in $YBa_2Cu_3O_{7-\delta}$ and has provided precise calipering of two sheets which are difficult to observe by any other method. The Fermi surface of the CuO_2 planes has been observed in other compounds: $RBa_2Cu_3O_{7-\delta}$ with R = Dy, Ho or Pr; $Ba_{1-x}K_xBiO_3$; $La_{2-x}Sr_xCuO_4$; and

$Nd_{2-x}Ce_xCuO_4$. It appears that the electronic structure observed with positrons in high-T_c superconductors is in amazingly good agreement with the prediction of band structure theory. Attempts to explain high-T_c superconductivity will have to take this fact very seriously.

Taking advantage of its large sensitivity to positron trapping, positron spectroscopy has also provided a large amount of information about the structural and compositional defects in the superconducting oxides, including the identification of the defects at the origin of the fishtail anomaly of the magnetic susceptibility of $YBa_2Cu_3O_{7-\delta}$ in the superconducting state, i.e. large clusters of oxygen vacancies located in the Cu–O chains (Erb et al. 1999). The knowledge accumulated in defect spectroscopy could be used to improve the quality of the materials, specifically single crystals, and to optimize the superconducting properties. This knowledge could also benefit the characterization of thin films. For this, intense beams of mono-energetic positrons shall inaugurate a number of new possibilities.

The superconducting state has not been yet observed directly by positron annihilation, and more theoretical investigations are required to state whether this will be possible or not. However, indirect effects have been observed, but the spread in the results prohibits a firm conclusion at the present time. These results are nevertheless stimulating for future research.

Acknowledgement

This work would not have been possible without the friendly support of B. Barbiellini, Ø. Fischer, L. Hoffmann, T. Jarlborg, R.C. Lodwick, M. Peter, A. Shukla, D. Vasumathi and E. Walker. I am also grateful to A. Bansil, T. Chiba, C. Corbel, P. Hautojärvi, R.H. Howell, S. Ishibashi, P. Mijnarends, S.G. Usmar, R.M. Singru and R.N. West for enlightening discussions.

References[3]

Adam, G., S. Adam, B. Barbiellini, L. Hoffmann, A.A. Manuel, M. Peter and S. Massidda, 1993, Solid State Commun. **88**, 739.

Antonov, V.N., V.L. Antonov, V.G. Bar'yakhtar, A.I. Baglyuk, E.G. Maximov, V.V. Nemoshkalenko, A.Ya. Perlov, S.Yu. Savrasov and Yu.A. Uspenskii, 1988, Int. J. Mod. Phys. B **1**, 1053.

Antonov, V.N., V.L. Antonov, V.G. Bar'yakhtar, A.I. Baglyuk, E.G. Maksimov, V.V. Nemoshkalenko, A.Ya. Perlov, S.Yu. Savrasov and Yu.A. Uspenskii, 1989, Sov. Phys.-JETP **68**, 415.

Anwand, W., G. Brauer, P.G. Coleman, A.P. Knights, K. Teske, G. Gschuster and K. Rudolph, 1995, Mater. Sci. Forum **175–178**, 133.

Aravin, L.G., A.V. Bobolev, V.V. Gustov, A.I. Rykzhkov, V.P. Shantarovich, S.N. Vydrin and R.N. Zainullin, 1990, Position and TSL-studies of superconducting ceramics $YBa_2Cu_3O_y$ for

[3] An extended list of references on positron annihilation in high-T_c superconductors (1987–1997) is located at http://www.unige.ch/sciences/DPMC/positrons/HTC.html. Classification by materials and by spectroscopies is provided.

various y, in: Proc. Int. Seminar on High Temperature Superconductivity, Dubna, USSR, 28 June–1 July 1989 (World Scientific, Singapore) pp. 385–391.

Aravin, L.G., A.V. Bobolev, M.K. Filimonov, V.V. Gustov, A.I. Rykzhkov, V.P. Shantarovich, S.N. Vydrin and A.R. Zainullin, 1992, Mater. Sci. Forum **105–110**, 893.

Arutyunov, N.Yu., and V.Yu. Trashchakov, 1992, Mater. Sci. Forum **105–110**, 587.

Ashoka-Kumar, P., M. Alatalo, V.J. Ghosh, A.C. Kruseman, B. Nielsen and K.G. Lynn, 1996, Phys. Rev. Lett. **77**, 2097.

Balogh, A.G., W. Puff, L. Liszkay and B. Molnar, 1988, Phys. Rev. B **38**, 2883.

Bansil, A., 1991, J. Phys. Chem. Solids **52**, 1493.

Bansil, A., 1995, Mater. Sci. Forum **175–178**, 819.

Bansil, A., and L.C. Smedskjaer, 1992, Mater. Sci. Forum **105–110**, 171.

Bansil, A., R. Pankaluoto, R.S. Rao, P.E. Mijnarends, W. Dlugosz, R. Prasad and L.C. Smedskjaer, 1988, Phys. Rev. Lett. **61**, 2480.

Bansil, A., P.E. Mijnarends and L.C. Smedskjaer, 1990, Physica C **172**, 175.

Bansil, A., P.E. Mijnarends and L.C. Smedskjaer, 1991, Phys. Rev. B **43**, 3667.

Barbiellini, B., and T. Jarlborg, 1992, J. Phys.: Condens. Matter **4**, 9015.

Barbiellini, B., and T. Jarlborg, 1994, Phys. Rev. B **50**, 3239.

Barbiellini, B., P. Genoud, J.Y. Henry, L. Hoffmann, T. Jarlborg, A.A. Manuel, S. Massidda, M. Peter, W. Sadowski, H.J. Scheel, A. Shukla, A.K. Singh and E. Walker, 1991, Phys. Rev. B **43**, 7810.

Barbiellini, B., P. Genoud, P. Lerch, T. Jarlborg and M. Peter, 1992, Mater. Sci. Forum **105–110**, 599.

Barbiellini, B., M. Gauthier, L. Hoffmann, T. Jarlborg, A.A. Manuel, S. Massidda, M. Peter, W. Sadowski, A. Shukla and E. Walker, 1993, Physica C **209**, 75.

Barbiellini, B., M. Gauthier, L. Hoffmann, T. Jarlborg, A.A. Manuel, S. Massidda, M. Peter and G. Triscone, 1994, Physica C **229**, 113.

Barbiellini, B., T. Jarlborg, S. Massidda and M. Peter, 1995a, Mater. Sci. Forum **175–178**, 879.

Barbiellini, B., M.J. Puska, T. Torsti and R.M. Nieminen, 1995b, Phys. Rev. B **51**, 7341.

Barbiellini, B., M.J. Puska, T. Korhonen, A. Harju, T. Torsti and R.M. Nieminen, 1996, Phys. Rev. B **53**, 16201.

Barnes, S.E., and M. Peter, 1989, Phys. Rev. B, **40**, 10958.

Barnes, S.E., M. Peter, L. Hoffmann, A.A. Manuel and A. Shukla, 1994, J. Stat. Phys. **76**, 679.

Belyaev, V.N., A.V. Kuznetsov, A.N. Mikheev, P.N. Sukharev and Yu.V. Shtotsky, 1990a, Positron annihilation in Y–Ba–Cu–O ceramics at temperatures around T_c, in: Proc. Int. Seminar on High Temperature Superconductivity, Dubna, USSR, 28 June–1 July 1989 (World Scientific, Singapore) pp. 392–396.

Belyaev, V.N., A.N. Mikheev, P.N. Sukharev and Yu.V. Shtotsky, 1990b, J. Phys.: Condens. Matter **2**, 4153–9.

Belyaev, V.N., V.N. Zakharchenko, A.N. Mikheev, P.N. Sukharev, S.V. Shavkin and Yu.V. Stotskii, 1990c, Supercond. Phys. Chem. Tech. **3**, 817.

Benedek, R., and H.B. Schüttler, 1990, Phys. Rev. B **41**, 1789.

Berko, S., 1989, Is there a Fermi surface in high T_c superconductors? A brief review of positron annihilation results, in: Proc. High-T_c Superconductivity: Magnetic Interactions, eds L.H. Bennett, Y. Flow and G.C. Vezzoli (World Scientific, Singapore) pp. 196–205.

Berko, S., D.J. Singh and E.C. Von Stetten, 1991, J. Phys. Chem. Solids **52**, 1485.

Bezakova, E., O. Sausa, J. Kristiak and M. Polak, 1989, Acta Phys. Slovaca, **39**, 314.

Bharathi, A., Y. Hariharan, A.K. Sood, V. Sankara Sastry, M.P. Janawadkar and C.S. Sundar, 1988a, Europhys Lett. **6**, 369.

Bharathi, A., Y. Hariharan, A.K. Sood, V. Sankara Sastry, M.P. Janawadkar and C.S. Sundar, 1988b, Physica C **153**, 111.

Bharathi, A., C.S. Sundar and Y. Hariharan, 1989, J. Phys. C **1**, 1467.

Bharathi, A., C.S. Sundar, W.Y. Ching, Y.C. Jean, P.H. Hor, Y.Y. Xue and C.W. Chu, 1990, Phys. Rev. B **42**, 10199.

Blackstead, H.A., D.B. Chrisey, J.D. Dow, J.S. Horowitz, A.E. Klunzinger and D.B. Pulling, 1995, Phys. Lett. A **207**, 109.

Blandin, P., S. Massidda, B. Barbiellini, T. Jarlborg, P. Lerch, A.A. Manuel, L. Hoffmann, M. Gauthier, W. Sadowski, E. Walker, M. Peter, J.J. Yu and A.J. Freeman, 1992, Phys. Rev. B **46**, 390.

Boronski, E., and R.M. Nieminen, 1986, Phys. Rev. B **34**, 3820.

Brandt, W., 1967, Positron annihilation in molecular substances and ionic crystals, in: Positron Annihila-

tion, eds A.T. Stewart and L.O. Roellig (Academic Press, New York) pp. 155–182.

Brandt, W., 1983, Statistical Dynamics of Positrons in Solids, in: Positron Solid-State Physics, eds W. Brandt and A. Dupasquier (North-Holland, Amsterdam) pp. 1–31.

Brusa, R.S., A. Dupasquier, R. Grisenti, S. Liu, S. Oss and A. Zecca, 1989, Positron trapping in sintered YBCO, in: Proc. Conf. on Positron Annihilation, Gent, Belgium, 1988, eds L. Dorikens, M. Dorikens and D. Segers (World Scientific, Singapore) pp. 907–909.

Campuzano, J.C., L.C. Smedskjaer, R. Benedek, G. Jennings and A. Bansil, 1991, Phys. Rev. B **43**, 2788.

Chakraborty, B., 1989, Phys. Rev. B **39**, 215.

Chakraborty, B., 1991, Phys. Rev. B **43**, 378.

Chan, L.P., D.R. Harshman, K.G. Lynn, S. Massidda and D.B. Mitzi, 1991a, Phys. Rev. Lett. **67**, 1350.

Chan, L.P., D.R. Harshman, K.G. Lynn, S. Massidda and D.B. Mitzi, 1991b, J. Phys. Chem. Solids **52**, 1557.

Chan, L.P., K.G. Lynn and D.R. Harshman, 1992, Mod. Phys. Lett. B **6**, 617.

Chen, A., Y. Zhi, B.R. Li, S.J. Wang and Y.L. Chen, 1992a, J. Phys.: Condens. Matter **4**, 4981.

Chen, A., Y. Zhi, B.R. Li and S.J. Wang, 1992b, Phys. Lett. A **165**, 171.

Chiba, T., 1976, J. Chem. Phys. **64**, 1182.

Chiba, T., 1992, J. Phys. Chem. Solids **53**, 1677.

Chu, C.W., P.H. Hor, Y.Y. Xue, G. Lin, R.L. Meng, K. Matsuishi, Z.J. Huang, C. Diaz and Y.C. Jean, 1991, Physica C **185–189**, 701.

Corbel, C., P. Bernede, H. Pascard, F. Rullier-Albenque, R. Korman and J.F. Marucco, 1989, Appl. Phys. A **48**, 335.

De, U.Y., P.M.G. Nambissan, D. Sanyal and D. Banerjee, 1996a, Physica B **224**, 544.

De, U.Y., P.M.G. Nambissan, D. Sanyal and D. Banerjee, 1996b, Phys. Lett. A **222**, 119.

De, U.Y., P.M.G. Nambissan, S. Chaudhuri, D. Sanyal and D. Banerjee, 1997, Physica B **230**, 856.

de Gennes, P.G., 1966, Superconductivity of Metals and Alloys (Benjamin, New York) pp. 109–114.

Doyama, M., R. Yamamoto, Y. Suzuki, S. Ishibashi, A. Yamaguchi, H. Kumakura and K. Togano, 1987, Physica B&C **148**, 497.

Doyama, M., M. Matsui, H. Numata, J. Liu, H. Matsuoka and T. Shimizu, 1989, Positron annihilation in Bi–Sr–Ca–Cu–O high T_c superconductors, in: Proc. Conf. on Positron Annihilation, Gent, Belgium, 1988, eds L. Dorikens, M. Dorikens and D. Segers (World Scientific, Singapore) pp. 931–932.

Dryzek, J., and M. Romek, 1990, Phys. Status Solidi A **121**, K159.

Erb, A., A.A. Manuel, R. Pozzi, M. Mali, M. Dhalle, F. Martin, J.Y. Genoud, B. Revaz, A. Junod, D. Vasumathi, S. Ishibashi, A. Shukla, O. Fischer, D. Brinkmann and R. Flükiger, 1999, Solid State Commun. **112**, 245.

Fehrenbacher, R., and T.M. Rice, 1993, Phys. Rev. Lett. **70**, 3471.

Friedel, J., and M. Peter, 1989, Europhys. Lett. **8**, 79.

Gao, X.H., X.G. Wang, S.F. Jiang, J. Li, S. Gao and G.D. Zheng, 1994, Phys. Rev. B **50**, 1237.

Gauthier, M., 1991, Arch. Sci. (Switzerland) **44**, 341.

Gopalan, P., E. Rajyashree-Prya, M. Premila, C.S. Sundar and K.P. Gopinathan, 1992, Mater. Sci. Forum **105–110**, 1033.

Gou, Z.H., F. Chen, S.G. Zheng, Z.X. Zhao and S.G. Zhu, 1995, Mater. Sci. Forum **175–178**, 367.

Gregory, R.B., and Y. Zhu, 1990, Nucl. Instrum. Methods Phys. Res. A **290**, 172.

Györffy, B.L., Z. Szoteck, W.M. Temmerman and G.M. Stocks, 1989, J. Phys.: Condens. Matter **1**(Suppl. A), 119.

Györffy, B.L., J. Maisnerowski, M.B. Suvasini, Z. Szoteck and W. Temmerman, 1995, Positron annihilation in the superconducting state, in: Positron Spectroscopy of Solids, eds A. Dupasquier and A.P. Mills Jr (IOS Press, Amsterdam) pp. 145–154.

Haghighi, H., J.H. Kaiser, S. Rayner, R.N. West, M.J. Fluss, R.H. Howell, P.E.A. Turchi, A.L. Wachs, Y.C. Jean and Z.Z. Wang, 1990, J. Phys.: Condens. Matter **2**, 1911.

Haghighi, H., J.H. Kaiser, S. Rayner, R.N. West, J.Z. Liu, R. Shelton, R.H. Howell, F. Solal and M.J. Fluss, 1991, Phys. Rev. Lett. **67**, 382.

Han, T.D., Z.A. Xu, Q.R. Zhang and X.Y. Zhou, 1995, Mater. Sci. Forum **175–178**, 371.

Harshman, D.R., L.F. Schneemeyer, J.V. Waszczak, Y.C. Jean, M.J. Fluss, R.H. Howell and A.L. Wachs, 1988, Phys. Rev. B **38**, 848.

Hautojärvi, P., and C. Corbel, 1995, Positron spectroscopy of defects in metals and semiconductors, in: Positron Spectroscopy of Solids, eds A. Dupasquier and A.P. Mills Jr (IOS Press, Amsterdam) pp. 491–532.

Hautojärvi, P., and A. Vehanen, 1979, Introduction of Positron Annihilation, in: Positrons in Solids, ed.

P. Hautojärvi, Vol. 12 of Topics in Current Physics (Springer, Berlin) pp. 1–23.

Hentrich, D., J.E. Kluin and T. Hehenkamp, 1992a, Phys. Status Solidi B **172**, 99.

Hentrich, D., J.E. Kluin and T. Hehenkamp, 1992b, Mater. Sci. Forum **105–110**, 1053.

Hermes, H., M. Forster and H.E. Schaefer, 1991, Phys. Rev. B **43**, 10399.

Hill, A.J., I.M. Katz, P.L. Jones and R.P. Pagano, 1991, Physica C **176**, 64.

Hoffmann, L., A.A. Manuel, M. Peter and E. Walker, 1988a, Europhys. Lett. **6**, 61.

Hoffmann, L., A.A. Manuel, M. Peter, E. Walker and M.A. Damento, 1988b, Physica C **153–155**, 129.

Hoffmann, L., W. Sadowski, A. Shukla, G. Adam, B. Barbiellini and M. Peter, 1991, J. Phys. Chem. Solids **52**, 1551.

Hoffmann, L., A.A. Manuel, M. Peter, E. Walker, M. Gauthier, A. Shukla, B. Barbiellini, S. Massidda, G. Adam, S. Adam, W.N. Hardy and R.X. Liang, 1993a, Phys. Rev. Lett. **71**, 4047.

Hoffmann, L., A. Shukla, M. Peter, B. Barbiellini and A.A. Manuel, 1993b, Nucl. Instrum. Methods Phys. Res. A **335**, 276.

Hoffmann, L., A.A. Manuel, B. Barbiellini, M. Peter, A. Shukla and E. Walker, 1995, Acta Phys. Pol. A **88**, 147.

Howell, R.H., F.A. Sterne, F. Solal, M.J. Fluss, H. Haghighi, J.H. Kaiser, S.L. Rayner, R.N. West, J.Z. Liu, P. Shelton, H. Kojima and K. Kitazawa, 1991, Physica C **185**, 735.

Howell, R.H., P. Sterne, F. Solal, M.J. Fluss, J. Tobin, J. O'Brien, H.B. Radousky, H. Haghighi, J.H. Kaiser, S.L. Rayner, R.N. West, J.Z. Liu, R. Shelton, C.G. Olsen, C. Gu, K. Katazawa and H. Kojima, 1992, Mater. Sci. Forum **105–110**, 265.

Howell, R.H., P.A. Sterne, M.J. Fluss, J.H. Kaiser, K. Kitazawa and H. Kojima, 1994, Phys. Rev. B **49**, 13127.

Huang, W.F., P.J. Ouseph, K. Fang and Z.J. Xu, 1988, Solid State Commun. **66**, 283.

Huang, W.F., Z.J. Xu, S.H. Liu and M.K. Wu, 1990, Phys. Rev. B, **41**, 2052.

Ilyasov, A.Z., A.V. Mikhailin, T.S. Orlova, B.I. Smirnov and R.A. Saykov, 1991, Sov. Phys. Solid State **33**, 1703.

Ilyasov, A.Z., A.V. Mikhailin, H.J. Kaufmann and V.I. Smirnov, 1992, Fiz. Tverd. Tela **34**, 1502.

Ishibashi, S., A. Yamaguchi, Y. Suzuki, M. Doyama, H. Kumakura and K. Togano, 1987, Jpn. J. Appl. Phys. **2**, L688.

Ishibashi, S., Y. Suzuki, T. Hatano, K. Ogawa, M. Doyama and R. Yamamoto, 1988, Phys. Lett. A **128**, 387.

Ishibashi, S., Y. Suzuki, H. Maruyama, R. Yamamoto and M. Doyama, 1989, Positron lifetime spectroscopy on high-T_c superconductor $ABa_2Cu_3O_{7-\delta}$ (A = Y, Eu), in: Proc. Conf. on Positron Annihilation, Gent, Belgium, 1988, eds L. Dorikens, M. Dorikens and D. Segers (World Scientific, Singapore) pp. 925–927.

Ishibashi, S., K. Suenuga, R. Yamamoto, M. Doyama and T. Matsumoto, 1990a, J. Phys.: Condens. Matter **2**, 3691.

Ishibashi, S., R. Yamamoto, M. Doyama and T. Matsumoto, 1990b, J. Less-Common Met. **164–165**, Part B, 1113.

Ishibashi, S., R. Yamamoto, M. Doyama and T. Matsumoto, 1991, J. Phys.: Condens. Matter **3**, 9169.

Ishibashi, S., R. Yamamoto, M. Doyama and T. Matsumoto, 1992, Mater. Sci. Forum **105–110**, 1081.

Jarlborg, T., and A.K. Singh, 1987, Phys. Rev. B **36**, 4660.

Jarlborg, T., A.A. Manuel, M. Peter and A.K. Singh, 1989, Positron annihilation in $YBa_2Cu_3O_7$ 2D-ACAR calculations, in: Proc. Conf. on Positron Annihilation, Gent, Belgium, 1988, eds L. Dorikens, M. Dorikens and D. Segers (World Scientific, Singapore) pp. 898–900.

Jarlborg, T., B. Barbiellini, E. Boronski, P. Genoud and M. Peter, 1991, J. Phys. Chem. Solids **52**, 1515.

Jean, Y.C., H. Nakanishi, S.J. Wang, W.N. Hardy, M.E. Hayden, R.F. Kief, R.L. Meng, H.P. Hor, J.Z. Huang and C.W. Chu, 1987, Phys. Rev. B **36**, 3994.

Jean, Y.C., J. Kyle, H. Nakanishi, P.E.A. Turchi, R.H. Howell, A.L. Wachs, M.J. Fluss, R.L. Meng, H.P. Hor, J.Z. Huang and C.W. Chu, 1988, Phys. Rev. Lett. **60**, 1069.

Jean, Y.C., H. Nakanishi, M.J. Fluss, A.L. Wachs, P.E.A. Turchi, R.H. Howell, Z.Z. Wang, R.L. Meng, P.H. Hor, Z.J. Huang and C.W. Chu, 1989a, J. Phys.: Condens. Matter **1**, 2989.

Jean, Y.C., H. Nakanishi, J. Kyle, S.J. Wang, P.E.A. Turchi, R.H. Howell, A.L. Wachs, M.J. Fluss, R.L. Meng, H.P. Hor, J.Z. Huang and C.W. Chu, 1989b, A systematic study of high temperature superconductivity by positron annihilation spectroscopy, in: Proc. Conf. on Positron Annihilation, Gent, Belgium, 1988, eds L. Dorikens, M. Dorikens

and D. Segers (World Scientific, Singapore) pp. 922–924.

Jean, Y.C., C.S. Sundar, A. Bharathi, J. Kyle, H. Nakanishi, P.K. Tseng, Z.Z. Wang, P.E.A. Turchi, R.H. Howell, A.L. Wachs and M.J. Fluss, 1990, Phys. Rev. Lett. **64**, 1593.

Jensen, K.O., R.M. Nieminen and M.J. Puska, 1989, J. Phys.: Condens. Matter **1**, 3727.

Jung, K., J.G. Byrne, M.C. Deandrade and M.B. Maple, 1995, J. Appl. Phys. **78**, 5534.

Jung, K., J.G. Byrne, M.C. Deandrade and M.B. Maple, 1996, Physica B **217**, 23.

Kajcsos, Z., K. Suvegh, A. Vertes, T. Porjesz, J. Kirschner, I. Herlasz, K. Fischer and W. Zinn, 1989, High-T_c superconductors studied by positron lifetime measurements, in: Proc. Conf. on Positron Annihilation, Gent, Belgium, 1988, eds L. Dorikens, M. Dorikens and D. Segers (World Scientific, Singapore) pp. 889–891.

Kirkegaard, P., and M. Eldrup, 1974, Comput. Phys. Commun. **7**, 401.

Kresin, B.V.Z., and H. Morawitz, 1990, J. Supercond. **3**, 227.

Kristiakova, K., O. Sausa, J. Kristiak and S. Janos, 1989, Z. Phys. B **77**, 197.

Kubo, Y., and S. Asano, 1992, Mater. Sci. Forum **105–110**, 711.

Lagouri, T., S. Dedoussis, M. Chardalas and A. Liolios, 1997a, Phys. Lett. A **229**, 259.

Lagouri, Th., S. Dedoussis, M. Chardalas and A. Liolios, 1997b, J. Radioanal. Nucl. Chem. **211**, 187.

Lam, C.C., L.W. Shao, X. Jin, W.M. Chen, H.Q. Xiong, J. Feng, S.R. Qi and K.C. Hung, 1996, Physica C **270**, 333.

Li, J.Q., C.C. Lam, H.Q. Xiong, W.M. Chen, L.W. Shao, X. Jin, J. Feng, S.R. Qi and K.C. Hung, 1997, Physica C **282–287**, 1611.

Li, Y., Y. Wang, C. Tang, Q. Ma, G. Cao, L. Wei, W. Wang and T. Zhang, 1997, Sci. China, **40**, 978.

Li Anli, Zheng Shengnan, Huang Hanchen, Li Donghong, Du Hongshan, Din Honglin, Sun Hancheng and Zhu Sheng Yu N., 1989, Chin. Phys. Lett. **6**, 549.

Lim, H.J., and J.G. Byrne, 1997, Physica B **229**, 294.

Liolios, A.K., S. Dedoussis, M. Chardalas, C.A. Eleftheriadis, D. Niarchos and S. Charalambous, 1989, Positron annihilation study of the YBaCuO high T_c superconductor, in: Proc. Conf. on Positron Annihilation, Gent, Belgium, 1988, eds L. Dorikens, M. Dorikens and D. Segers (World Scientific, Singapore) pp. 895–897.

Liolios, A.K., M. Chardalas, S. Dedoussis, C.A. Eleftheriadis, L. Papadimitriou, E. Mouhtari, C. Nikolopoulos and S. Charalambous, 1992, Mater. Sci. Forum **105–110**, 1129.

Lock, D.G., V.H.C. Crisp and R.N. West, 1973, J. Phys. F **3**, 561.

Lu, X., S.J. Wang, Y.C. Jean, P.H. Hor, Y.Y. Xue, Z.J. Huang and C.W. Chu, 1992, Phys. Rev. B **45**, 7989.

Lynn, K.G., S.G. Usmar, B. Nielsen, G.J. Van der Kolk, I. Kanazawa, P. Sferlazzo and A.R. Moodenbaugh, 1988, Temperature and depth dependence of positron annihilation parameters in $YBa_2Cu_3O_{7-x}$ and $La_{1.85}Sr_{0.15}CuO_4$, in: Proc. American Vacuum Soc. Topical Conf. (American Institute of Physics, New York) pp. 435–442.

Majumdar, C.K., 1965, Phys. Rev. A **140**, 227.

Mandal, P., A. Podd, P.M.G. Nambissan, P. Choudhury, B. Ghosh, P. Sen and C.K. Majumdar, 1988, J. Phys. C **21**, 3151.

Manuel, A.A., 1989, J. Phys.: Condens. Matter **1**(Suppl. A), 107.

Manuel, A.A., 1995, 2D-ACAR studies and positron beam developements in Switzerland, in: Positron Spectroscopy of Solids, eds A. Dupasquier and A.P. Mills Jr (IOS Press, Amsterdam) pp. 155–178.

Manuel, A.A., B. Barbiellini, M. Gauthier, L. Hoffmann, T. Jarlborg, S. Massidda, M. Peter, W. Sadowski, A. Shukla and E.J. Walker, 1993, J. Phys. Chem. Solids **54**, 1223.

Massidda, S., 1990, Physica C **169**, 137.

Massidda, S., J.J. Yu, A.J. Freeman, L. Hoffmann, P. Genoud and A.A. Manuel, 1991, J. Phys. Chem. Solids **52** 1503.

Matsui, M., H. Numata, H. Matsuoka, T. Shimizu, M. Doyama, S. Ishibashi and Y. Suzuki, 1989, Positron annihilation in high-T_c Ba–Y–Cu–O, in: Proc. Conf. on Positron Annihilation, Gent, Belgium, 1988, eds L. Dorikens, M. Dorikens and D. Segers (World Scientific, Singapore) pp. 928–930.

Mattheiss, L.F., 1987, Phys. Rev. Lett. **58**, 1028.

McMullen, T., 1990, Phys. Rev. B **41**, 877.

McMullen, T., P. Jena, S.N. Khanna, Y. Li and K.O. Jensen, 1991, Phys. Rev. B **43**, 10422.

Mijnarends, P.E., and A. Bansil, 1995, Theory of electron and positron momentum distributions in solids, in: Positron Spectroscopy of Solids, eds

A. Dupasquier and A.P. Mills Jr (IOS Press, Amsterdam) pp. 25–74.

Mijnarends, P.E., A.F.J. Melis and A.W. Weeber, 1991a, J. Phys. Chem. Solids **52**, 1569.

Mijnarends, P.E., A.F.J. Melis, A.W. Weeber, A.A. Menovsky and K. Kadowaki, 1991b, Physica C **176**, 113.

Mikhalenkov, V.S., E.A. Tsapko and A.V. Chernyashevskii, 1991, Fiz. Nizk. Temp. **17**, 1275.

Moser, P., and J.Y. Henry, 1989, Positron studies in as received and electron irradiated $YBa_2Cu_3O_{6.9}$, $DyBa_2Cu_3O_{6.9}$ and $CaSr_2Bi_2Cu_2O_{8-\delta}$, in: Proc. Conf. on Positron Annihilation, Gent, Belgium, 1988, eds L. Dorikens, M. Dorikens and D. Segers (World Scientific, Singapore) pp. 904–906.

Mosley, W.D., J.W. Dykes, R.N. Shelton, P.A. Sterne and R.H. Howell, 1994, Phys. Rev. Lett. **73**, 1271.

Nagarajan, T., S. Srinivasan, V. Sridharan, V. Prabha, R. Usha, B. Jayamala, K. Nandhini and A. Stephen, 1991, J. Phys. Chem. Solids **52**, 1591.

Nieminen, R.M., 1991, J. Phys. Chem. Solids **52**, 1577.

Pankaluoto, R., A. Bansil, L.C. Smedskjaer and P.E. Mijnarends, 1994, Phys. Rev. B **50**, 6408.

Perkins, A., and E.J. Woll Jr, 1969, Phys. Rev. **178**, 530.

Peter, M., 1989, IBM J. Res. Dev. **33**, 333.

Peter, M., 1991, J. Phys. Chem. Solids **52**, 1599.

Peter, M., 1995, Arch. Sci. **48**, 105.

Peter, M., L. Hoffmann and A.A. Manuel, 1988, Physica C **153–155**, 1724.

Peter, M., A.A. Manuel and L. Hoffmann, 1990, Key Eng. Mater. **48**, 117.

Peter, M., T. Jarlborg, B. Barbiellini, A.A. Manuel, L. Hoffmann, A. Shukla, E. Walker, P. Lerch and W. Sadowski, 1992a, Mater. Sci. Forum **105–110**, 411.

Peter, M., A.A. Manuel, L. Hoffmann and W. Sadowski, 1992b, Europhys. Lett. **18**, 313.

Peter, M., T. Jarlborg, A.A. Manuel, B. Barbiellini and S.E. Barnes, 1993, Z. Naturforsch. A **48**, 390.

Peter, M., A.A. Manuel, L. Hoffmann and A. Shukla, 1995, Mater. Sci. Forum **175–178**, 71.

Peter, M., A. Shukla, L. Hoffmann and A.A. Manuel, 1996, Nuova Acta Leopoldina NF **72**, Nr. 294, p. 257.

Peter, M., A.A. Manuel and A. Erb, 1998, Int. J. Modern Phys. B **12**, 3187.

Pickett, W.E., and D.J. Singh, 1992, Mater. Sci. Forum **105–110**, 125.

Prasad, R., and S. Srinivas, 1989, Momentum density and Fermi surface of $YBa_2Cu_3O_7$. In: Proc. of M2S-HTSC Conference, Stanford. Preprint.

Pujari, P.K., S.B. Manohar, T. Datta, S. Prakash, I.K. Gopalakrishnan, P.V.P.S.S. Sastry, G.M. Phatak and R.M. Iver, 1988, Physica C **156**, 769.

Pujari, P.K., T. Datta, S. Prakash, S.B. Manohar, I.K. Gopalakrishnan, G.M. Phatak, J.V. Yakhmi, P.V.P.S.S. Sastry and R.M. Iyer, 1989, Physica C **159**, 75.

Pujari, P.K., T. Datta, S.B. Manohar, S. Prakash, P.V.P.S.S. Sastry, J.V. Yakhmi and R.M. Iyer, 1990, Solid State Commun. **73**, 623.

Pujari, P.K., T. Datta, S. Prakash, S.B. Manohar, I.K. Gopalakrishnan, G.M. Phatak, J.V. Yakhmi, P.V.P.S.S. Sastry and R.M. Iyer, 1991, Bull. Mater. Sci. **14**, 681.

Pujari, P.K., T. Datta, U.Y. De and B. Ghosh, 1994, Phys. Rev. B **50**, 3438.

Pujari, P.K., R.A. Gunasekaran and J.V. Yakhmi, 1996, Phys. Lett. A **219**, 117.

Puska, M.J., and R.M. Nieminen, 1983, J. Phys. F **13**, 333.

Puska, M.J., and R.M. Nieminen, 1994, Rev. Mod. Phys. **66**, 841.

Sanyal, D., U.Y. De, K. Mandal, D. Banerjee and R. Bhattacharya, 1995, Phys. Lett. A **204**, 305.

Saul, A., and M. Weissmann, 1990, J. Phys.: Condens. Matter **2**, 9603.

Sausa, O., J. Kristiak, K. Kristiakova, G. Plesch and F. Hanic, 1992, Mater. Sci. Forum **105–110**, 1271.

Sedov, V.L., and S.N. Kuznetsov, 1994, Phys. Lett. A **193**, 413.

Sedov, V.L., M.A. Hafiz, I.E. Graboy, A.R. Kaul and V.P. Shabatin, 1990, Phys. Lett. A **151**, 93.

Sedov, V.L., M.A. Khafiz and V.P. Shabatin, 1991, Fiz. Nizk. Temp. **17**, 1558.

Sedov, V.L., M.A. Hafiz, I.E. Grabox, A.R. Kaul and V.P. Shabatin, 1992, Mater. Sci. Forum **105–110**, 1217.

Sedov, V.L., S.N. Kuznetsov, M.A. Hafiz and A.M. Mussalitin, 1995, Phys. Atomic Nuclei **58**, 1121.

Sedov, V.L., S.N. Kuznetsov, O.A. Tsigelnik, N.N. Oleynikov and D.I. Grigorashev, 1996, Phys. Lett. A **222**, 455.

Sen, P., and C.K. Majumdar, 1989, Positron annihilation studies in high temperature superconductors. In: Proc. Int. Symp. on High Temperature Superconductivity, Jaipur (Oxford & IBH Publishing, New Delhi) pp. 295–300.

Shukla, A., M. Peter and L. Hoffmann, 1993, Nucl. Instrum. Methods Phys. Res. A **335**, 310.

Shukla, A., L. Hoffmann, A.A. Manuel, E. Walker, B. Barbiellini and M. Peter, 1995a, Phys. Rev. B **51**, 6028.

Shukla, A., L. Hoffmann, A.A. Manuel, B. Barbiellini, M. Peter and E. Walker, 1995b, Mater. Sci. Forum **175–178**, 929.

Shukla, A., B. Barbiellini, L. Hoffmann, A.A. Manuel, W. Sadowski, E. Walker and M. Peter, 1996, Phys. Rev. B **53**, 3613.

Shukla, A., L. Hoffmann, A.A. Manuel and M. Peter, 1997, Mat. Sci. Forum **255–257**, 233.

Singh, D.J., 1994, Phys. Rev. B **50**, 4106.

Singh, D.J., and W.E. Pickett, 1992, Physica C **203**, 193.

Singh, D.J., W.E. Pickett, R.E. Cohen, H. Krakauer and S. Berko, 1989, Phys. Rev. B **39**, 9667.

Singh, D.J., W.E. Pickett, E.C. Von Stetten and S. Berko, 1990, Phys. Rev. B **42**, 2696.

Smedskjaer, L.C., and A. Bansil, 1992, J. Phys. Chem. Solids **53**, 1657.

Smedskjaer, L.C., J.Z. Liu, R. Benedek, D.G. Legnini, D.J. Lam, M.D. Stahulak, H. Claus and A. Bansil, 1988a, Physica C **156**, 269.

Smedskjaer, L.C., B.W. Veal, D.G. Legnini, A.P. Paulikas and L.J. Nowicki, 1988b, Physica B&C **150**, 56.

Smedskjaer, L.C., B.W. Veal, D.G. Legnini, A.P. Paulikas and L.J. Nowicki, 1988c, Phys. Rev. B **37**, 2330.

Smedskjaer, L.C., A. Bansil, U. Welp, Y. Fang and K.G. Bailey, 1991, J. Phys. Chem. Solids **52**, 1541.

Smedskjaer, L.C., A. Bansil, A.P. Paulikas, B.W. Veal, D.G. Legnini and K.G. Bailey, 1992a, Physica C **199**, 393.

Smedskjaer, L.C., A. Bansil, U. Welp, Y. Fang and K.G. Bailey, 1992b, Physica C **192**, 259.

Smedskjaer, L.C., A. Bansil, U. Welp, Y. Fang and K.G. Bailey, 1992c, Phys. Rev. B **46** 5868.

Smedskjaer, L.C., R. Pankaluoto, A. Bansil and P.E. Mijnarends, 1993, J. Phys. Chem. Solids **54**, 1239.

Sterne, P.A., R.H. Howell, M.J. Fluss, J.H. Kaiser, K. Kitazawa and H.J. Kojima, 1993, J. Phys. Chem. Solids **54**, 1231.

Sundar, C.S., A.K. Sood, A. Bharathi and Y. Hariharan, 1988a, Pramana **30**, L161.

Sundar, C.S., A.K. Sood, A. Bharathi and Y. Hariharan, 1988b, Physica C **153**, 155.

Sundar, C.S., A. Bharathi, W.Y. Ching, Y.C. Jean, P.H. Hor, R.L. Meng, Z.J. Huang and C.W. Chu, 1990a, Phys. Rev. B **42**, 2193.

Sundar, C.S., A. Bharathi, Y.C. Jean, P.H. Hor, R.L. Meng, Z.J. Huang and C.W. Chu, 1990b, Phys. Rev. B **42**, 426.

Sundar, C.S., A. Bharathi, W.Y. Ching, Y.C. Jean, P.H. Hor, R.L. Meng, Z.J. Huang and C.W. Chu, 1991, Phys. Rev. B **43**, 13019.

Sundar, C.S., A. Bharathi, D. Vasumathi and Y. Hariharan, 1992, Mater. Sci. Forum **105–110**, 1253.

Suvasini, M.B., B.L. Györffy and W.M. Temmerman, 1992, Mater. Sci. Forum **105–110**, 485.

Tang, C.Q., B.R. Li and A. Chen, 1990, Phys. Rev. B **42**, 8078.

Tang, Z., Z.Q. Chen, S.J. Wang, G.C. CE and Z.X. Zhao, 1993, J. Phys.: Condens. Matter **5**, 345.

Tang, Z., S.J. Wang and X.H. Gao, 1994, Phys. Rev. B **50**, 3209.

Tanigawa, S., 1989, Recent 2D-ACAR results in highly scattered electron systems from Tsukuba, in: Proc. Conf. on Positron Annihilation, Gent, Belgium, 1988, eds L. Dorikens, M. Dorikens and D. Segers (World Scientific, Singapore) pp. 119–121.

Teng, M.K., D.X. Shen, L. Chen, C.Y. Yi and G.H. Wang, 1987, Phys. Lett. A **124**, 363.

Tripathy, D.N., and M. Bhuyan, 1985, Positron annihilation in superconductors, in: Positron Annihilation, eds P.C. Jain, R.M. Singru and K.P. Gopinathan (World Scientific, Singapore) pp. 91–92.

Turchi, P.E.A., A.L. Wachs, Y.C. Jean, R.H. Howell, K.H. Wetzler and M.J. Fluss, 1988, Physica C **153**, 157.

Turchi, P.E.A., A.L. Wachs, K.H. Wetzler, J.H. Kaiser, R.N. West, Y.C. Jean, R.H. Howell and M.J. Fluss, 1990, J. Phys.: Condens. Matter **2**, 1635.

Usmar, S.G., P. Sferlazzo, K.G. Lynn and A.R. Moodenbaugh, 1987, Phys. Rev. B **36**, 8854.

Usmar, S.G., K.G. Lynn, A.R. Moodenbaugh, M. Suenaga and R.L. Sabatini, 1988, Phys. Rev. B **38**, 5126.

Usmar, S.G., Y. Xu, A.R. Moodenbaugh and M. Suenaga, 1992, Mater. Sci. Forum **105–110**, 1313.

Usmar, S.G., M. Biasini, A.R. Moodenbaugh, Y. Xu and H.M. Fretwell, 1994, J. Phys.: Condens. Matter **6**, 10487.

Vasumathi, D., C.S. Sundar, A. Bharathi, A.K. Sood and Y. Hariharan, 1990, Physica C **167**, 149.

Von Stetten, E.C., S. Berko, X.S. Li, R.R. Lee, J. Brynestad, D. Singh, H. Krakauer, W.E. Pickett and R.E. Cohen, 1988, Phys. Rev. Lett. **60**, 2198.

Von Stetten, E.C., S. Berko, X.S. Li, L.F. Schneemeyer, J. Brynestad, D. Singh, H. Krakauer, W.E. Pickett and R.E. Cohen, 1989, Temperature dependent positron–electron momentum densities in $YBa_2Cu_3O_{7-x}$ by 2D-ACAR, in: Proc. Conf. on Positron Annihilation, Gent, Belgium, 1988, eds L. Dorikens, M. Dorikens and D. Segers (World Scientific, Singapore) pp. 913–915.

Wachs, A.L., P.E.A. Turchi, Y.C. Jean, K.H. Wetzler, R.H. Howell, M.J. Fluss, D.R. Harshman, J.P. Remeika, A.S. Cooper and R.M. Fleming, 1988, Phys. Rev. B **38**, 913.

Wang, S.J., S.V. Naidu, S.C. Sharma, D.K. De, D.Y. Jeong, T.D. Black, S. Krichene, J.R. Reynolds and J.M. Owens, 1988, Phys. Rev. B **37**, 603.

Wang, S.J., X.H. Li, Y.L. Chen, S.Q. Li, G.H. Fong, Z. Wang, A. Chen and B.R. Li, 1989, Phys. Status Solidi A **114**, 273.

Wang, S.J., Z. Tang, Z.Q. Chen, X.H. Gao, S.F. Jian and J. Li, 1994, Phys. Rev. B **49**, 4319.

West, R.N., 1974, Positron Studies of Condensed Matter (Taylor and Francis, London) pp. 1–122.

West, R.N., 1992, J. Phys. Chem. Solids **53**, 1669.

West, R.N., 1995, Positron studies of the electronic structure of solids, in: Positron Spectroscopy of Solids, eds A. Dupasquier and A.P. Mills Jr (IOS Press, Amsterdam) pp. 75–134.

Yang, Z., J. Song, J. Zhu, J. Zhu and C.W. Lung, 1987, J. Phys. C **20**, L923.

Yu, J., S. Massidda, A.J. Freeman and D.D. Koelling, 1987, Phys. Lett. A **122**, 203.

Zhang, D.M., C.Q. Tang, T. Gen and and G.Y. Li, 1993a, Phys. Rev. B **47**, 3435.

Zhang, D.M., C.Q. Tang, T. Gen and G.Y. Li, 1993b, Phys. Status Solidi A **136**, K51.

Zhang, D.M., C.Q. Tang, T. Gen and G.Y. Li, 1993c, Cryst. Res. Technol. **28**, 225.

Zhang, H., 1990, Phys. Status Solidi A **121**, K207.

Zhang, H., X.-G. Wang and Y.-X. Fu, 1988, Phys. Status Solidi A **109**, K133.

Zhang, J.C., S.X. Cao, F.Q. Liu and J.Z. Liu, 1993a, Phys. Rev. B **48**, 16830.

Zhang, J.C., F.Q. Liu, J.Z. Liu, S.X. Cao and H.S. Guo, 1993b, Appl. Supercond. **1**, 1055.

Zhang, J.C., G.S. Cheng, J.Z. Liu, S.X. Cao and F.Q. Liu, 1994, Physica C **235**, 1345.

Zhang, J.C., F.Q. Liu, G.S. Cheng, J.X. Shang, J.Z. Liu, S.X. Cao and Z.X. Liu, 1995, Phys. Lett. A **201**, 70–76.

Zhao, Y.G., B.S. Cao, W.Z. Yu, Z.H. Du, Y.J. Wang, C.Y. Luo, H. Hu, S. Wang, J.H. Yang, A.S. He and B.L. Gu, 1995, Physica C **241**, 311.

Zhi, Y., A. Chen, B.R. Li, X.L. Zhang, X.H. Li and S.J. Wang, 1993, Chin. Sci. Bull. **38**, 769.

Zhou, X.Y., H. Jiang, Q. Zhang, G. Pan and Q. Long, 1988, Phys. Status Solidi A **109**, K129.

Zhou, X.Y., J. Stormer, R.L. Wang, J. Keimel, H.C. Li, G. Kögel and W. Triftshäuser, 1996, Phys. Rev. B **54**, 1398.

Zhou, X.Y., W. Bauer-Kugelmann, J. Störmer, G. Kögel and W. Triftshäuser, 1997a, Phys. Lett. A **225**, 143.

Zhou, X.Y., Xuekun Lu, H. Jiang, W. Bauer-Kugelmann, J.A. Duffy, G. Kögel and W. Triftshaüser, 1997b, J. Phys.: Condens. Matter **9**, L61.

Zhou, Zhigang, K. Oka, T. Ito and Y. Nishihara, 1997, Jpn. J. Appl. Phys. **36**, L18.

Zhu, J., J. Song, J. Wang, Z. Yang, Y. Zhang and C.W. Lung, 1988, J. Phys. C **21**, L281.

Zhu, J.S., X.Y. Zhou, Q.W. Long, G.D. Gu, W.L. Cai, Y.Z. Ruan and Y.H. Zhang, 1992, Chin. Sci. Bull. **37**, 646.

Handbook on the Physics and Chemistry of Rare Earths
Vol. 30
edited by K.A. Gschneidner, Jr., L. Eyring and M.B. Maple

Chapter 193

$RBa_2Cu_3O_7$ COMPOUNDS: ELECTRONIC THEORY AND PHYSICAL PROPERTIES*

W.E. PICKETT
Department of Physics, University of California Davis, Davis, CA 95616, USA

I.I. MAZIN
Code 6391, Naval Research Laboratory, Washington, DC 20375-5345, USA

Contents

Acronyms 453
Symbols 454
1. Introduction 454
1.1. CuO_2 planes and blocking layers 455
1.2. Band picture vs. correlated electron picture 456
1.3. Spectroscopies: Fermi surfaces and quasiparticle bands 457
1.4. Rare-earth substitutions 458
1.5. Characteristic features of cuprates: Why is T_c so high? 458
2. Reduction of full band structure to tight-binding "minimal basis" form 459
2.1. Single-plane tight-binding models 460
2.2. Single-chain tight-binding bands 463
2.3. Incorporating the third dimension 464
3. First-principles studies of uniaxial strain effects 466
3.1. Motivation 466
3.2. Efforts to understand T_c^{max} 467
3.3. Experimental data on uniaxial strains 468
3.4. First-principles studies of uniaxial strain effects 470
3.5. Effects of strain on many-body corrections 476
3.6. Implications for models of pairing 476
4. $PrBa_2Cu_3O_7$: How well is its unusual behavior understood? 477
4.1. Observed behavior of $Y_{1-x}Pr_xBa_2Cu_3O_7$ 477
4.2. Models for T_c suppression 478
4.3. Fehrenbacher–Rice model 480
4.4. First-principles electronic structure studies 481
5. Summary 486
Acknowledgments 487
References 487

Acronyms

1D, 2D	one-dimensional, two-dimensional
ACAR	angular correlation of annihilation radiation
ARPES	angle-resolved photoelectron emission spectroscopy
BCS	Bardeen–Cooper–Schrieffer (theory of superconductivity)
DC	direct current
FR	Fehrenbacher–Rice
FS	Fermi surface
GGA	generalized gradient approximation
HTS	high-temperature superconductor
LAPW	linearized augmented plane wave

* Supported by the Office of Naval Research.

LDA	local density approximation	QP	quasiparticle
LDA+U	LDA plus mean field treatment of Hubbard U	TB	tight binding
		vHs	van Hove singularity

Symbols

a.u.	atomic units, where $\hbar = 1$, electron mass and charge $m = \mathrm{I}$, $e = 1$	p_x, p_y, p_z	uniaxial stresses
		T_c	superconducting critical temperature
A_{1g}	fully symmetric phonons at $\vec{k} = 0$		
c_{ij}	elastic constants	T_c^{max}	maximal critical temperature as a function of doping
C_p	heat capacity		
Cu1, Cu2	chain, plane Cu sites in $YBa_2Cu_3O_7$and $PrBa_2Cu_3O_7$	T_N	Néel temperature for antiferromagnetic ordering
D	surface dipole moment	$pd\sigma^*$, $pd\pi^*$, $pf\sigma^*$	antibonding states of the specified type
E_F	=Fermi energy		
n, n_{opt}	hole 'carriers' per planar Cu; optimum value	U, U_d, U_p	on-site Hubbard repulsion energy
		$\alpha_x, \alpha_y, \alpha_z$	linear expansivities
$n(\vec{k})$	electronic momentum density	**Γ, X, Y, Z, S**	$\vec{k}$ points $(0,0,0)$, $(\pi,0,0)$, $(0,\pi,0)$, $(0,0,\pi)$, $(\pi,\pi,0)$
O1, O2, O3, O4	chain (O1), plane (O2,3) and bridging (O4) oxygen sites in $YBa_2Cu_3O_7$and $PrBa_2Cu_3O_7$		
		σ	planar charge density

"And I asked myself," said O'Hare,
"what does it mean?
What's the point of any of it?"
K. Vonnegut, Jr., *Mother Night*

1. Introduction

Of all of the high temperature superconductors (HTS) based on Cu–O layers, $YBa_2Cu_3O_7$ is by far the most widely studied, and arguably the second most studied solid material after silicon. It was discovered (Wu et al. 1987) shortly after superconductivity was reported for $(La,Ba)_2CuO_4$ (Bednorz and Müller 1986) whose critical temperature T_c was then only known to be around 30 K. The value of $T_c \approx 92$ K for $YBa_2Cu_3O_7$ was *really* high, four times higher than those of known superconductors, prior to Bednorz and Müller's discovery. Significantly, T_c was higher than the boiling point of liquid nitrogen (77 K), which raised the spectre of applications that had previously only been dreamt of (Ginzburg and Kirzhnits 1977). Although most of those applications still remain for the future, the intense scrutiny of $YBa_2Cu_3O_7$ – its structure and electronic properties, its magnetic response, and its behavior in the superconducting mixed state – has led to a good

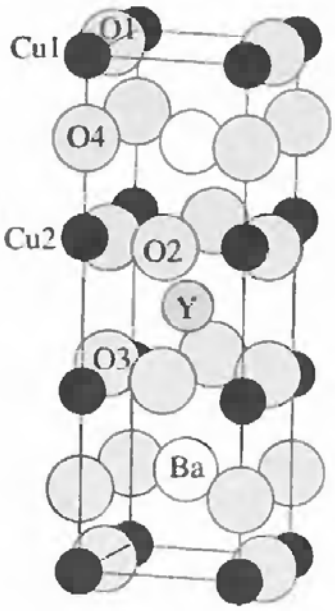

Fig. 1. Crystal structure of $YBa_2Cu_3O_7$, illustrating the two CuO_2 layers with Y ion between, and the blocking layer consisting of the Cu–O chain and the Ba–O layers on either side of the chain.

understanding of much of its behavior. As we will discuss in sect. 3, this understanding does not extend to the mechanism underlying the superconducting pairing itself.

$YBa_2Cu_3O_7$, whose structure is displayed in fig. 1, has been implicitly adopted as the paradigm for HTS, hence the huge amount of both experimental and theoretical work. More recently it has been decried as atypical and unnecessarily complicated: it is intrinsically orthorhombic rather than (quasi)tetragonal as most HTS are, it has two Cu–O layers rather than only one which introduces additional flexibility which is peripheral to superconductivity, and it has another subsystem beside the layers (the Cu–O chains) which is metallic in the normal state and superconducting below T_c. On the other hand, it is self-doped and stoichiometric. In any event, the fact that this material is in many respects well understood keeps it at the acme of the study of HTS.

In this chapter we review selected developments in the understanding and description of HTS cuprates, confining our applications to $YBa_2Cu_3O_7$. We address three topics. Section 2 provides the link between full first principles band structure theory and the description in terms of a minimal basis set. The question of what uniaxial strains may reveal about the microscopic cause of high T_c *per se* is probed in sect. 3. Introduction of Pr, with its loosely bound 4f electrons, into the $YBa_2Cu_3O_7$ HTS system is discussed in sect. 4, and a theoretical picture of the unusual properties of $PrBa_2Cu_3O_7$ is presented. In the remainder of this Introduction we lay the background for the following sections.

1.1. *CuO_2 planes and blocking layers*

The structures of all families of cuprate HTS have in common two features. The first substructure consists of a few (one to four) CuO_2 (nearly) square planar layers separated by divalent (most commonly Ca) or trivalent cations (Y, for example, or other rare-earth cations). The second substructure, called the 'blocking layer', consists of a set of cations

and O anions that can take on a wide variety of forms. Several examples were discussed in a review (Pickett 1989) and now there are many additional examples. While it is difficult to identify common characteristics among the blocking layers – some compounds (*viz.* $La_{2-x}Sr_xCuO_4$) have electronically inert blocking layers while others ($YBa_2Cu_3O_7$) have conducting blocking layers – it seems that the primary function of the blocking layers is to dope the CuO_2 layers with carriers (most commonly hole-type carriers). The reduction of the band structure to minimal basis form described in sect. 2 will illustrate how the blocking layer affects the band structure in the low excitation energy region. In sect. 3 we will discuss another apparent function of the blocking layer – setting the scale of T_c for a given hole doping – although just how this is done is not yet understood.

The blocking layer can extract electrons from (equivalently, dope holes into) the reference $Cu^{2+}(O^{2-})_2$ layer. In addition to determining its doping level, it completes the environment of the superconducting subsystem. It strains the CuO_2 layer, it warps or corrugates it, and it produces Madelung fields that shift the relative site potentials of the Cu and O ions. Rare earth ions between the layers of $YBa_2Cu_3O_7$ provide a probe of the system by varying the CuO_2 layer separation, by contributing a magnetic lattice that interacts with the superconducting state, and in the case of Pr it leads to entirely new physical phenomena that are discussed in sect. 4.

1.2. *Band picture vs. correlated electron picture*

Since the discovery of HTS, there has been active discussion about how to describe the electronic structure. The "strongly correlated" viewpoint has been that the strong intra-atomic repulsion (Hubbard U term) is so important, and the two-dimensionality so clear, that a 2D Hubbard model on a square lattice will provide the basic behavior that must be understood. A secondary question is whether a single band is sufficient, or other degrees of freedom present only in a several-band model are necessary. The "band structure" viewpoint might be said to be based on the presumption that it is necessary to consider the full complexity of the multi-atom, multiband character of the system, even at the cost of neglecting important correlations.

It hardly needs saying that neither picture is sufficient by itself. Evidently correlation effects are substantial, especially in the underdoped regime. The specific nature of the transition from antiferromagnetic insulator to underdoped superconductor is still an enigma in many respects. A square lattice Hubbard model however fails to be able to address most of the existing data for many HTS, and especially for $YBa_2Cu_3O_7$, because the properties within the $\hat{a}$–$\hat{b}$ plane are intrinsically anisotropic due to the presence of the Cu–O chains. In this chapter we will discuss data primarily from the viewpoint that one first considers the full multi-atom, multiband (but uncorrelated) band structure, energy, *etc.*, and then considers the effect of correlations. We will concentrate on only a few specific issues and address the various viewpoints as appropriate.

1.3. *Spectroscopies: Fermi surfaces and quasiparticle bands*

In this subsection we will provide a brief description of the current understanding of the band structure of the quasiparticles (QP) in the region of the Fermi level (E_F). Although there are dozens of cuprate superconductors known, nearly all investigations of the QP band structure has been devoted to $YBa_2Cu_3O_7$ and $Bi_2CaSr_2Cu_2O_{8+\delta}$, due to experience with and ease of preparing surfaces.

Fermi surface of $YBa_2Cu_3O_7$. The Fermi surface of $YBa_2Cu_3O_7$ as predicted from band theory in the local density approximation (LDA) has been presented and described in detail (Pickett et al. 1990, 1992, Andersen et al. 1991, Massidda et al. 1991, Mazin et al. 1993, Rodriguez et al. 1994) and is reproduced in fig. 2. It consists of two large 'barrel' surfaces with strong Cu–O character, centered on the Brillouin zone corner and having large rather flat portions perpendicular to the (100) and (010) directions. In addition, there is an additional flat, quasi-one-dimensional sheet arising from the Cu–O chains. Finally, there is a small 'stick' surrounding the zone corner, which like the sheets is also a consequence of the blocking layer, although a less direct one.

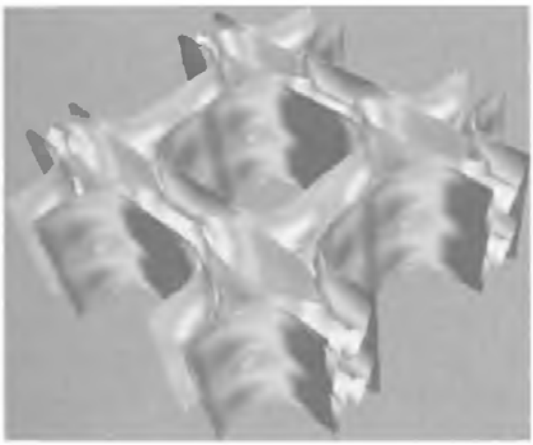

Fig. 2. Calculated Fermi surface of $YBa_2Cu_3O_7$.

Of these four predicted Fermi surfaces, three have been clearly identified. The most extensive studies have been carried out by Campuzano and coworkers (Gofron et al. 1993) and by Shen and Dessau (1995) using angle-resolved photoelectron emission spectroscopy (ARPES). The clearest observation of two distinct barrel surfaces was reported by Schabel et al. (1998). They used two independent photon polarizations on untwinned single crystals. A new feature is that they checked for Fermi surface signatures both by observing dispersing bands vanish as the angle of emission is varied (the conventional method) and by watching the momentum density $n(\vec{k})$ change rapidly with angle as proposed by Randeria (1996). They concluded that each method of identification of Fermi surfaces emphasized one of the two barrel surfaces. The nearly flat, chain-derived Fermi surface sheet, which shows up vividly in two-dimensional angular correlation of annihilation radiation (2D-ACAR) maps from positron annihilation studies, (Haghighi et al. 1991, West 1992, Smedskjaer and Bansil 1992, Manuel et al. 1995) is also seen

in ARPES spectra. Evidence for the fourth 'stick' surface was obtained in de Haas–van Alphen experiments (Fowler et al. 1992, Mueller et al. 1992, Mazin et al. 1992b). These surfaces result from a rather complex band structure involving orbitals on all Cu and O atoms in the unit cell, ten atoms in all. Section 2 is devoted to outlining how the essential characteristics can be parametrized in a physical fashion.

Quasiparticle bands. The excitation spectra of $YBa_2Cu_3O_7$ and $Bi_2CaSr_2Cu_2O_{8+\delta}$, primarily as measured by ARPES, have been studied extensively and are discussed by Schabel and Shen in Vol. 31 of this Handbook, ch. 201. In a new development, Fujimori et al. (1997) have reported ARPES studies on underdoped ($x = 0.1$), optimally doped ($x = 0.15$), and overdoped ($x = 0.3$) samples of $La_{2-x}Sr_xCuO_4$. Study of this system has been held up by difficulty in producing clean, reproducible surfaces. Although only a few selected directions were studied, dispersing bands were observed for all dopings. Crossings were indicative of the behavior obtained from band structure calculations (Allen et al. 1987, Krakauer et al. 1993): a (π, π) centered hole surface for the underdoped case, changing to a Γ-centered electron surface in the overdoped regime. Unlike in $YBa_2Cu_3O_7$ and $Bi_2CaSr_2Cu_2O_{8+\delta}$ the band crossing along the (π, π) direction is broad.

The undoped or slightly doped compound La_2CuO_{4+x}, $x \leqslant 0.03$, was studied by ARPES by Zakharov et al. (1997). They observed that this compound has no natural cleavage planes, so cleavage probably results in non-uniform surfaces, and at the very least it results in broken covalent or ionic bonds that may redistribute electronic charge compared to the underlying crystalline compound. Until confirmation from more extensive mapping of the Brillouin zone, results on this system should be considered tentative.

1.4. *Rare-earth substitutions*

At the beginning of "high T_c" Wu et al. (1987) introduced Y into the process and immediately produced $YBa_2Cu_3O_7$, nearly tripling T_c. Since that time there has been considerable study of the behavior of the $YBa_2Cu_3O_7$ system when Y is substituted with other rare-earth ions. For the strongly magnetic trivalent lanthanides, the magnetism on the lanthanide ions does not disrupt superconductivity (T_c remains above 90 K), and the magnetic ions order at low temperature. For Ce and especially for Pr, however, the behavior is much more complex.

The work on the $Pr_{1-x}R_xBa_2Cu_3O_{7-\delta}$ system up to 1992 was reviewed thoroughly by Radousky (1992). At that time theoretical work on the system was sparse. In the interim, more data and substantial theoretical work have led to considerably more insight in the complex behavior that arises upon introduction of Pr. This work forms the topic of sect. 4.

1.5. *Characteristic features of cuprates: Why is T_c so high?*

Although the bismuthate $Ba_{1-x}K_xBiO_3$ and fullerene-based materials have been discovered with T_c above 30 K, the HTS cuprates remain the only materials where T_c is above 40 K, and reaching as high as 135 K. Moreover, there are dozens of examples of such

cuprates. There is still, after nearly eleven years of intense study on these materials, no convincing picture that accounts for superconductivity that reaches half way to room temperature.

In sect. 3 we will discuss the correlation of the measured uniaxial strain dependence of T_c in $YBa_2Cu_3O_7$ with changes in the crystal structure and the electronic structure. It is worthwhile to list characteristic features of the HTS cuprates that may underpin the ability to become superconducting at high temperature:

- Square (or nearly so) CuO_2 layers: 1, 2, 3, or 4 of them. However, the number of layers is not necessarily crucial: in the Hg-based systems T_c is optimal between 100 K and 135 K for 1, 2, 3, and 4 layer members.
- Quasi-two-dimensional conductivity: extreme anisotropy of transport and low energy excitations. However, the least anisotropic material $YBa_2Cu_3O_7$, has a T_c much higher than other more 2D cuprates.
- Peculiar low-temperature and low-energy behavior, often characterized as 'non-Fermi-liquid'.
- Nearness to a 2D spin $\frac{1}{2}$ antiferromagnetic insulator phase for undoped members.
- Nearness (even more so) to a conventional Fermi liquid phase upon overdoping, also with rather high T_c.
- High T_c is specific to Cu, whose d states overlap in energy more strongly the O p bands than would other 3d transition metal d states in the same environment.
- A blocking layer is necessary: the "infinite layer" cuprate system is not superconducting (unless doped by cation substitution, in which case the cation layer would itself be the blocking layer). However, the blocking layer can be either insulating or metallic.
- Hole-doped cuprates inevitably have an apical oxygen coordinated with the planar Cu, in addition to the two planar oxygens.

In addition, characteristics of the CuO_2 layer, especially deviations from tetragonality and 'dimpling' of the CuO_2 network, have attracted considerable notice.

The discussion in sect. 3 is based on the observation that, while the *relative* value of T_c within a structure is governed in a systematic way by the carrier concentration, the value of the optimal T_c, denoted T_c^{max}, varies widely within the family of cuprates that all have the characteristics listed above. It is some variation of one or more of these characteristics, or possibly some unforeseen variable, that must control the value of T_c^{max}.

2. Reduction of full band structure to tight-binding "minimal basis" form

Although there is by no means a consensus regarding the relevance of the local density approximation (LDA) band structure for superconducting cuprates, a point of view that becomes increasingly more popular is that the LDA calculations provide a reasonable starting approximation for the fully doped systems, with some renormalization that can be incorporated on top of an LDA calculation. Both experimentalists trying to rationalize their data and theorists trying to base their models on something more realistic than a circular cylindrical Fermi surface are intensely interested in a tight-binding description

of the electronic structure of $YBa_2Cu_3O_7$ and its family. Similarly, the theories aiming at improving LDA by incorporating many-body corrections in some form or by modelling the paired state itself (Temmerman et al. 1996) are often much easier when applied to a realistic tight-binding model instead of the actual LDA band structure. The same applies to analysis of experimental results (see, *e.g.*, Krantz and Cardona 1995). In this section, we will discuss tight-binding models for the band structure of $YBa_2Cu_3O_7$, mainly following the folding down scheme of Andersen et al. (1994, 1995) to obtain a minimal basis description. A tight-binding parametrization of the full valence–conduction band structure was presented earlier by DeWeert, Papaconstantopoulos and Pickett (1989a,b).

As discussed in the previous section, the quasi-two-dimensional crystal structure of $YBa_2Cu_3O_7$ is most physically described as a stack of layers, of which two are CuO_2 perovskite planes, separated by an open layer of rare-earth ions (across which there is only small inter-CuO_2 layer hopping) a chain layer consisting of parallel CuO chains, and of two intermediate layers of apical oxygens O4 together with Ba ions. The CuO_2 layers are dimpled so that the interlayer distance measured between the neighboring Cu ions is 3.3 Å, while the distance between the oxygens in the neighboring layers is only 2.8 Å. The BaO layers are also warped, by about the same amount, apical oxygen being 0.3 Å closer to the chain layer than is Ba. The apical oxygen is substantially closer to the chain copper (1.85 Å) than to the plane copper (2.3 Å). Thus apical oxygen to some extent belongs to the chains but actually provides interaction between the chain and the layer states. The lattice constants are $a = 3.82$ Å, $b = 3.88$ Å, $c = 11.68$ Å.

2.1. *Single-plane tight-binding models*

It was mentioned in the previous section that the Fermi surface of $YBa_2Cu_3O_7$ has four sheets. We denote these as *a, b, c,* and *s*, which correspond to the four atomic layers mentioned above: *a* and *b* are, respectively, the odd (antibonding) and even (bonding) combinations of the pdσ states in two CuO_2 layers, *c* is the chain pdσ band, and *s* is formed predominantly by the apical oxygen p_y orbitals. We shall now discuss in more detail how these bands are formed. Let us start from a single CuO_2 plane. In the energy range of interest the bands are formed predominantly from Cu $d_{x^2-y^2}$ and O p orbitals. According to LDA calculations, the corresponding energy levels are separated by approximately 1 eV, that is, less than the calculated hopping amplitude. This accounts for the strong Cu–O hybridization found in LDA calculations. The band that forms the Fermi surface is the antibonding $O2_x$–$Cu2_{x^2-y^2}$–$O3_y$ pdσ* band (the * denotes an antibonding band). The nearest-neighbor tight-binding (TB) Hamiltonian for this band is (we use shorthand notations $x^2 - y^2 \equiv Cu2_{x^2-y^2}$, $x \equiv O2_x$, $y \equiv O3_y$):

$$H^0_{\mathrm{pd}\sigma} = \begin{array}{c} \\ \langle x^2-y^2| \\ \langle x| \\ \langle y| \end{array} \begin{array}{c} \begin{array}{cccc} |x^2-y^2\rangle & |x\rangle & |y\rangle \end{array} \\ \begin{pmatrix} \epsilon_{x^2-y^2} & ts_x & -ts_y \\ ts_x & \epsilon_{\mathrm{p}} & 0 \\ -ts_y & 0 & \epsilon_{\mathrm{p}} \end{pmatrix} \end{array}, \tag{1}$$

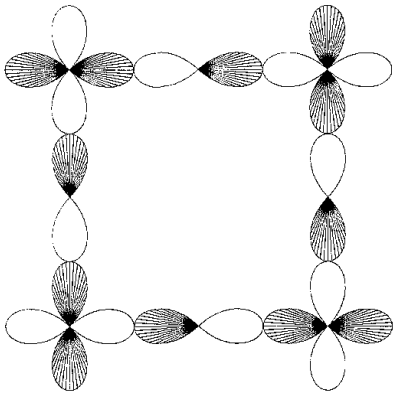

Fig. 3. Tight-binding orbitals corresponding to the antibonding state of the pdσ band at the point $\mathbf{S}(\pi,\pi)$. Cu2 are in the corners of the 2D unit cell.

where $s_x = 2\sin(ak_x/2)$, $c_x = 2\cos(ak_x/2)$, and similarly for y. A cartoon of the TB orbitals forming the highest state of this Hamiltonian at the point $\mathbf{S}=(\pi/a,\pi/b,0)$ is shown in fig. 3. The eigenenergies of the Hamiltonian (1) are the solutions of[1]

$$E = \epsilon_{x^2-y^2} + \frac{t^2 s_x^2}{E-\epsilon_p} + \frac{t^2 s_y^2}{E-\epsilon_p}. \tag{2}$$

Close to E_F one can assume $|E-E_F| \ll E_F - \epsilon_p = \Delta_p \approx 3$ eV, and derive an approximate dispersion law for the band crossing E_F,

$$E \approx \epsilon_{x^2-y^2} + \frac{t^2(s_x^2+s_y^2)}{\Delta_p} = \left(\epsilon_{x^2-y^2} + \frac{4t^2}{\Delta_p}\right) - \frac{2t^2}{\Delta_p}(\cos ak_x + \cos ak_y). \tag{3}$$

This is the TB dispersion law for a Cu $d_{x^2-y^2}$ ddσ-like nearest neighbor band. The effective Cu–Cu hopping amplitude is $\tilde{t} = -t^2/\Delta_p$. Such a dispersion yields, at half

[1] In this chapter we will use extensively the so-called Löwdin perturbation theory, which can be formulated like this: If a real symmetric matrix H can be written in form of two blocks

$$H = \begin{pmatrix} A & C \\ C & B \end{pmatrix},$$

the characteristic equation

$$\det(H-E) = 0,$$

can be equivalently written in form of a characteristic equation

$$\det(H'(E)-E) = 0$$

of a matrix H′ with the same dimension as A, defined by

$$H' = A + C^T \cdot (B-E)^{-1} \cdot C.$$

filling, a square rotated by 45° with respect to the crystallographic axes. This orientation is contrary to both calculation (see fig. 1) and experiment in $YBa_2Cu_3O_7$, where the Fermi surface (FS) is rather a square oriented parallel to the crystallographic axes with rounded corners. It was noticed long ago that such a difference is most likely coming from neglect in the Hamiltonian (1) of the O–O hopping. Including this hopping t', one gets

$$H_{\mathrm{pd}\sigma} = \begin{array}{c|ccc} & |x^2-y^2\rangle & |x\rangle & |y\rangle \\ \langle x^2-y^2| & \epsilon_{x^2-y^2} & ts_x & -ts_y \\ \langle x| & ts_x & \epsilon_{\mathrm{p}} & t's_xs_y \\ \langle y| & -ts_y & t's_xs_y & \epsilon_{\mathrm{p}} \end{array}, \tag{4}$$

and the bands are the solutions of the equation

$$E = \epsilon_{x^2-y^2} + t^2 \frac{(E-\epsilon_{\mathrm{p}})(s_x^2+s_y^2) - 2t's_x^2s_y^2}{(E-\epsilon_{\mathrm{p}})^2 - (t')^2 s_x^2 s_y^2}. \tag{5}$$

Making the same approximation as in eq. (3), and retaining terms linear in t', we obtain for the pdσ* band

$$E \approx \left(\epsilon_{x^2-y^2} + \frac{4t^2}{\Delta_{\mathrm{p}}} - \frac{8t't^2}{\Delta_{\mathrm{p}}^2}\right) - \left(\frac{2t^2}{\Delta_{\mathrm{p}}} - \frac{8t't^2}{\Delta_{\mathrm{p}}^2}\right)(\cos ak_x + \cos ak_y) - \frac{8t't^2}{\Delta_{\mathrm{p}}^2}\cos ak_x \cos ak_y. \tag{6}$$

This approximation corresponds to the one-band Cu $d_{x^2-y^2}$ model where now nearest neighbor and next-nearest neighbor coupling between Cu ions is taken into account. The last term appears as a result of the three-step hopping Cu–O–O–Cu, and thus the effective next-nearest neighbor Cu–Cu hopping magnitude is $\tilde{t}' = 2t't^2/\Delta_{\mathrm{p}}^2$. Note that *a priori* one does *not* expect to find an appreciable O–O hopping, because of the relatively large O–O distance. In fact, this hopping appears to be, in turn, assisted by the diffuse Cu s orbital, and essentially is $t' = -t_{\mathrm{sp}\sigma}^2/(\epsilon_{\mathrm{s}} - E)$. The role of the O s orbital has been discussed in detail by Andersen et al. (1994, 1995).

Equation (6) is the most popular analytical model for the band structure of $YBa_2Cu_3O_7$. It is usually written in the form

$$E - E_{\mathrm{F}} = 2\tilde{t}(\cos ak_x + \cos ak_y) + 4\tilde{t}' \cos ak_x \cos ak_y + \mu, \tag{7}$$

where the parameters are chosen to reproduce the experimental (ARPES) antibonding band dispersion,

$$\tilde{t} = -0.25\ \mathrm{eV}, \qquad \frac{\tilde{t}'}{\tilde{t}} = -0.45, \qquad \mu = 0.44\ \mathrm{eV}.$$

In many cases this simplified description is sufficient, although it is missing several important characteristics of the band structure, present both in the experiment and in

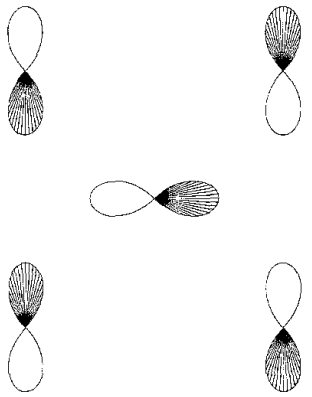

Fig. 4. Tight-binding orbitals corresponding to the "stick" band at the point $\mathbf{S}(\pi, \pi)$. O4 atoms are in the corners, Ba is in the center.

the LDA calculations. For example, the observed extended van Hove singularities at the points **X** and **Y** of the Brillouin zone. We shall return to these characteristics later in this section, but first we discuss the two chain-related bands.

2.2. *Single-chain tight-binding bands*

The *c*-band is the one-dimensional analogue of the pdσ band described above. Correspondingly, its dispersion is described by the same eq. (3), but with $s_x = 0$. More interesting is the apical oxygen band, *s*. In fact, these are two separate bands, one being predominantly p_x and another p_y in character. The lower one is entirely under the Fermi level, while the higher one crosses E_F near the **S** point. The two bands are split (by ~50 meV at the **S** point), due to orthorhombicity: the O4 p_y state, but not O4 p_x state, is hybridized with the Cu1 d_{yz}–O1 p_z band, which pushes the corresponding band slightly up, compared to the O4(p_x) band. Hopping between the O4 orbitals occurs via Ba orbitals, of which the most important are Ba p_x and p_y. The nearest neighbor TB Hamiltonian looks like

$$H_{\mathrm{BaO}} = \begin{array}{c|cccc} & |\mathrm{O4}(x)\rangle & |\mathrm{O4}(y)\rangle & |\mathrm{Ba}(x)\rangle & |\mathrm{Ba}(y)\rangle \\ \hline \langle \mathrm{O4}(x)| & \epsilon_x & 0 & -t_- c_x c_y & t_+ s_x s_y \\ \langle \mathrm{O4}(y)| & 0 & \epsilon_y & t_+ s_x s_y & -t_- c_x c_y \\ \langle \mathrm{Ba}(x)| & -t_- c_x c_y & t_+ s_x s_y & \epsilon_{\mathrm{Ba}} & 0 \\ \langle \mathrm{Ba}(y)| & t_+ s_x s_y & -t_- c_x c_y & 0 & \epsilon_{\mathrm{Ba}} \end{array}, \tag{8}$$

where $2t_\pm = t_{\mathrm{pp}\sigma} \pm t_{\mathrm{pp}\pi}$ (cf. fig. 4). Since the Ba p orbitals are far from the Fermi energy, we can fold them down in the same manner we did above, and get the following O4-only Hamiltonian:

$$H_{\mathrm{O4\ pp}} = \begin{array}{c|cc} & |\mathrm{O4}(x)\rangle & |\mathrm{O4}(y)\rangle \\ \hline \langle \mathrm{O4}(x)| & \left(\epsilon_x + \frac{t_-^2 c_x^2 c_y^2 + t_+^2 s_x^2 s_y^2}{E_F - \epsilon_{\mathrm{Ba}}}\right) & \frac{2t_+ t_- c_x c_y s_x s_y}{E_F - \epsilon_{\mathrm{Ba}}} \\ \langle \mathrm{O4}(y)| & \frac{2t_+ t_- c_x c_y s_x s_y}{E_F - \epsilon_{\mathrm{Ba}}} & \left(\epsilon_y + \frac{t_-^2 c_x^2 c_y^2 + t_+^2 s_x^2 s_y^2}{E_F - \epsilon_{\mathrm{Ba}}}\right) \end{array}, \tag{9}$$

which can be equivalently written in terms of effective O–O nearest neighbor hoppings

$$\tilde{t}_\sigma = -\tilde{t}_\pi = \frac{2t_\sigma t_\pi}{E_F - \epsilon_{Ba}},$$

and next-nearest neighbor hoppings

$$\tilde{t}'_\sigma = -\frac{t_\sigma^2}{E_F - \epsilon_{Ba}}, \qquad \tilde{t}'_\pi = \frac{t_\pi^2}{E_F - \epsilon_{Ba}}.$$

The expression is

$$H_{O\ pp} = \begin{array}{c} \\ \langle O(x)| \\ \langle O(y)| \end{array} \begin{array}{c} |O(x)\rangle \\ \left(\tilde{\epsilon}_x - 2\tilde{t}_\sigma C_x + 2\tilde{t}_\pi C_y - 4\tilde{t}'_- C_x C_y\right) \\ 4\tilde{t}'_+ S_x S_y \end{array} \begin{array}{c} |O(y)\rangle \\ 4\tilde{t}'_+ S_x S_y \\ \left(\tilde{\epsilon}_y - 2\tilde{t}_\sigma C_y + 2\tilde{t}_\pi C_x - 4\tilde{t}'_- C_x C_y\right) \end{array}, \tag{10}$$

where $C_x = \cos ak_x$, etc.

From either of these formulas one can see that hybridization between the two bands vanishes along the lines **X–S** and **Y–S**, and is maximal along **Γ–S**. To be complete, let us note that there is also a smaller O–O hopping via Ba d_{xy} orbitals. The most important effect of this is that the symmetry $\tilde{t}_\sigma = -\tilde{t}_\pi$ becomes violated, because both $\tilde{t}_\sigma$ and $\tilde{t}_\pi$ are reduced by $\frac{3}{4}t_{pd\sigma}^2/(E_F - \epsilon_{Ba\ d})$.

2.3. *Incorporating the third dimension*

At this point we have some basic understanding in tight-binding language of the band structure of $YBa_2Cu_3O_7$. Full understanding requires including the third dimension. There are a number of effects that the third dimension introduces, namely, (1) splitting of the CuO_2 pdσ bands in a (CuO_2) bilayer into a bonding (even) and antibonding (odd) combination, (2) k_z dispersion, and (3) dimpling of CuO_2 planes. Let us discuss them in this order.

Bilayer splitting. As long as one-electron hopping between the two CuO_2 planes is allowed, they necessarily split by $2t_\perp(k_x, k_y)$, where $t_\perp$ is the k-dependent interplanar hopping amplitude. Although there has been vigorous discussion about whether or not such hopping is allowed in the normal state, the question now seems to be settled experimentally (see Schabel and Shen, Vol. 31 of this Handbook, ch. 201). The bonding–antibonding splitting exists, although it may be overestimated in LDA. Symmetry of the interlayer hopping is important for many applications, so we discuss it in some detail now. For an even more thorough discussion the reader is referred to the paper of Andersen et al. (1995).

The first interesting question is whether the interlayer hopping occurs directly across the Y layer (the hopping distance is small, but lack of the bridging oxygen in the Y layers hinders hopping) or via a longer path Cu2–O4–Cu1–O4–Cu2, where each step is easier

than in the former case, but too many intermediate hoppings may reduce the effective amplitude considerably. Analysis of the band structure (Andersen et al. 1994, 1995) suggests that the main process in the interlayer interaction is hopping between the diffuse Cu s orbitals[2] directly across Y planes. Its magnitude had been estimated by Andersen et al. (1995) to be 0.75 eV, and is translated by means of the perturbation theory into the following addition to the Hamiltonian (1):

$$H^{\pm}_{\mathrm{pd}\sigma} = H^{0}_{\mathrm{pd}\sigma} \pm \begin{array}{c} \\ \langle x^2-y^2| \\ \langle x| \\ \langle y| \end{array} \begin{array}{c} \begin{array}{ccc} |x^2-y^2\rangle & |x\rangle & |y\rangle \end{array} \\ \begin{array}{ccc} 0 & 0 & 0 \\ 0 & t_{s\perp}s_x^2 & t_{s\perp}s_xs_y \\ 0 & t_{s\perp}s_xs_y & t_{s\perp}s_y^2 \end{array} \end{array} . \tag{11}$$

A remarkable property of this Hamiltonian is that the $\pm$ splitting of the highest of its eigenvalues is proportional to $(s_x^2 - s_y^2)^2 \equiv (\cos ak_x - \cos ak_y)^2$, and vanishes along the **Γ–S** line. This is true in both first and second order in $t_{s\perp}$. In the same approximation as used in eqs. (3)–(7):

$$E_k - E_{\mathrm{F}} = 2\tilde{t}(\cos ak_x + \cos ak_y) + 4\tilde{t}' \cos ak_x \cos ak_y + \mu \pm \frac{t_{s\perp}t^2}{\Delta_{\mathrm{p}}^2}(\cos ak_x - \cos ak_y)^2. \tag{12}$$

This form had been conjectured by Chakravarty before it was derived by Andersen et al. (1995) and had been intensively used by Chakravarty et al. (1993) and in other papers on the interlayer pair tunneling model.

Dispersion perpendicular to the layers. z-dispersion of the bonding band, as well as of the band s of the apical oxygen, is negligible. The two other bands show appreciable dispersion, which is due to their hybridization with each other. Consider the basal plane **ΓXSY** in the Brillouin zone (*i.e.*, $k_z = 0$); the chain-band states in this plane are even with respect to $k_z \to -k_z$ reflection, while the antibonding plane band is odd. Thus they do not hybridize (unless spin–orbit interaction is included), and they actually cross near the point $\mathbf{k} = (0.5\pi/a, 0.2\pi/b, 0)$. However this condition holds solely in the $k_z = 0$ plane, and the degeneracy at the crossing point is lifted for all non-zero k_z. The induced splitting is proportional to the plane-chain hopping amplitude τ_{c}, and is $4\tau_{\mathrm{c}} \sin(ck_z/2)$. From LDA calculations by Mazin et al. (1992c), $\tau_{\mathrm{c}} \approx 0.09$ eV. The maximal splitting of 0.35 eV occurs in the $k_z = \pi/c$ plane.

Dimpling of the CuO_2 layers. Last but not least, the CuO_2 planes in $YBa_2Cu_3O_7$ are dimpled, and this is the feature that leads to extended van Hove singularities near the **X** and **Y** points in the LDA calculations. The reason is that because of dimpling there is weak coupling between the plane O2 and O3 z-orbitals and the Cu2 $d_{x^2-y^2}$ orbital. This

[2] In this analysis the so-called Cu s is in fact a linear combination of the high-lying Cu s and low-lying Cu $d_{3z^2-r^2}$ orbitals, since both have the same symmetry with respect to the processes discussed in this chapter. We call it s, as did Andersen et al. (1994, 1995) because this character quantitatively dominates.

provides a coupling to the pdσ and two pdπ bands (the latter are formed by Cu2 d_{zx}, Cu2 d_{zy}, and O p_z orbitals) that otherwise are decoupled. The dispersion the pdπ bands along **ΓX** and **ΓY** directions is stronger than of the pdσ band (the latter is suppressed by interaction with Cu s (Andersen et al. 1995). As a result, although the pdπ bands occur well below the Fermi level and below the antibonding pdσ band *a* at the **Γ** point, they come close to the band *a* and the Fermi level near **X** and **Y**, and push this band up. *Exactly* at **X** and **Y**, however, the hybridization between pdσ and pdπ states *via* O *z*–Cu $d_{x^2-y^2}$ hopping is forbidden by symmetry. Thus, this hybridization flattens the dispersion of the antibonding pdσ band, causing what is known as extended van Hove singularities. In fact, in the calculated LDA band structure of $YBa_2Cu_3O_7$ this effect is so strong that instead of the flat band, extending from about $0.7\pi/a$ to $1.3\pi/a$, the calculated bands develop maxima ("bifurcated saddle points") at about $0.7\pi/a$ and $1.3\pi/a$, and a local minimum at π/a (**X**-point). Again, detailed discussion of the formation of extended saddle points in the framework of a nearest neighbor pdπ + pdσ TB model can be found in the work of Andersen et al. (1994,1995).

3. First-principles studies of uniaxial strain effects

3.1. *Motivation*

In the Introduction it was noted that, in spite of the vast amount of study of $YBa_2Cu_3O_7$ and other HTSs, there is no consensus at all on the microscopic mechanism responsible for pairing. It is widely accepted that the general picture of pairing introduced by BCS (Bardeen et al. 1957) is followed: two opposite spin electrons on opposite sides of the Fermi surface undergo an attractive effective interaction due to the virtual exchange of some intermediate boson (spin fluctuation, phonon, exciton, polaron, or generalizations and combinations thereof) and the system undergoes superconducting coherence below T_c. Beyond this general scenario, there is little agreement. The very short coherence length leads to at least a general picture of local pairs, and the implications are severe enough that applications of simple BCS theory are not reliable.

One feature which has achieved a consensus is the behavior of T_c versus level of doping *n* (hole 'carriers' per planar Cu) as determined from systematic regularities of the thermopower. As the sister antiferromagnetic phase is doped, superconductivity appears at a non-zero doping level. In many cases it is said to follow an inverted parabolic form (Schneider and Keller 1992, Tallon et al. 1995):

$$\frac{T_c}{T_c^{\max}} = 1 - \left(\frac{n - n_{\text{opt}}}{\Delta n}\right)^2, \tag{13}$$

where $T_c^{\max}$ is the maximum T_c achieved within the family in question (*viz.* $La_{2-x}Sr_xCuO_4$ with $n \approx x$, $YBa_2Cu_3O_{7-x}$ with *n* a more complex function of *x*, *etc*). $n_{\text{opt}} \approx 0.16$–$0.20$ is the optimal doping, that is, where T_c peaks, and the doping half-range is $\Delta n \approx 0.10$–0.13.

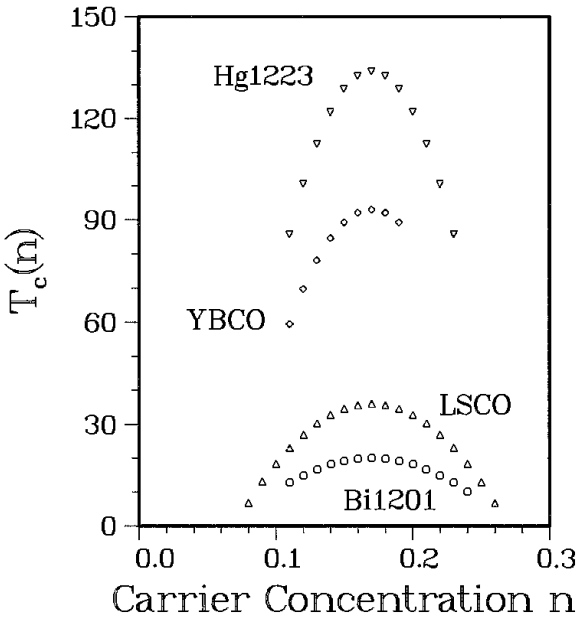

Fig. 5. Schematic inverted parabola behavior of four cuprate systems: Bi1201 = $BiSr_2CuO_{5+\delta}$, LSCO = $La_{2-x}Sr_xCuO_4$, YBCO = $YBa_2Cu_3O_{7-\delta}$, Hg1223 = $HgBa_2Sr_2Cu_3O_{10}$. The magnitude of the critical temperature varies dramatically, while the behavior with doping is similar.

Other interpretations of the data lead to a plateau in the region of optimal doping (Zhang and Sato 1993). This difference will not concern us here.

This relation has been the focus of both experimental efforts to establish its persistence in other families (it appears to be general) and theoretical studies to model and understand it. It is often presumed to encode the "essential physics" of HTS. What is more directly arguable is that it indicates the general way in which this doped 2D antiferromagnetic system metamorphizes into a superconductor. The ratio T_c/T_c^{max} itself is specifically normalized so that it does not address the magnitude of T_c^{max} itself. There are cuprate superconductors with very high T_c such as $HgBa_2Ca_2Cu_3O_{8+\delta}$ with $T_c^{max} = 135\,K$ (Schilling et al. 1993) (or 160 K under pressure), and there are members with very modest values such as $Bi_2Sr_{2-x}La_xCuO_{4+\delta}$ with $T_c^{max} = 20\,K$ (Wang et al. 1993). Their transformations from magnetic insulator to unusual superconductor seem extremely similar, while the value of T_c^{max} differs by a factor of seven. This distinction is pictured schematically in fig. 5. The distinction is not due primarily to differing numbers of Cu–O layers, since the Hg-based system T_c^{max} lies between 100 K and 135 K for members with one, two, three, or four layers.

Since the Cu–O layers appear very similar between the families of HTS, the underlying factors that determine T_c^{max} must lie outside the plane, that is, in the blocking layers, in spite of the fact that the basic superconductivity lies within the CuO_2 plane. Just what these factors might be is a crucial question that has only been given a modest amount of study.

3.2. *Efforts to understand* T_c^{max}

A compilation and analysis of structural families known up to 1994 to find correlations between T_c^{max} and some material property was presented by Ohta et al. (1991), with newer

developments presented by Tanaka (1994). Cu–O bondlengths, both within the layer and to the apical oxygen, have received much attention. Madelung site potentials in the parent insulators have also been analyzed thoroughly. This work built on analysis by Torrance et al. (1991) that indicated that metallic versus insulating behavior in a wide variety of transition metal oxides correlates with site energy difference between cation and anion, rather than with other parameters such as the strength of the on-site Coulomb repulsion. Ohta et al. presented correlation (with considerable spread) between the observed T_c and the difference in site potential between the planar O and apical O ions. They found a similar general positive correlation between T_c and an effective bandwidth. Their analysis suggested the apical O site energy is important, because of its effect on the Cu-centered singlet in the CuO_2 plane. Valence bond sums, which are related to the bondlengths mentioned above, also show some correlation with T_c^{max}. It has been suggested that the degree of itineracy, such as can be parametrized by second and third neighbor hopping amplitudes, correlates with T_c^{max} (Feiner et al. 1996). Whether these correlations point to a microscopic mechanism is a rather subjective matter.

3.3. *Experimental data on uniaxial strains*

The low symmetry of cuprate compounds, tetragonal or lower, renders the hydrostatic pressure dependence of physical properties ambiguous, since it is the sum of two (tetragonal) or three (orthorhombic) uniaxial stress dependences that may be very different. To obtain uniaxial data most directly, it is necessary to strain the crystal uniaxially so that only one lattice parameter changes, rather than simply apply uniaxial stress which alters all lattice parameters (via Poisson's ratio) due to the response of the crystal. Direct uniaxial strains are quite difficult to impose on a crystal. It can be done in principal to a cubic, tetragonal, or hexagonal crystal by applying a uniaxial stress along the $\hat{c}$ axis (or also the (111) axis in a cubic crystal) and then opposing the bulging in the perpendicular directions that is proportional to Poisson's ratio by an independent hydrostatic pressure adjusted to zero the lateral strain. This has never been done in cuprates.

An alternative is to make use of the thermodynamic Ehrenfest relation connecting the uniaxial stress (p_i, $i = x$, y, or z) dependence of T_c with the discontinuity in the linear expansivity at T_c:

$$\frac{dT_c}{dp_i} = VT_c\frac{\Delta\alpha_i}{\Delta C_p}. \tag{14}$$

Here ΔC_p is the discontinuity of the heat capacity across the superconducting transition, V is the volume, and $\Delta\alpha_i$ denotes the change in the linear expansivity along the ith Cartesian axis of the crystal. The uniaxial pressure dependences obtained by Meingast and collaborators (Meingast et al. 1991, 1993, Kraut et al. 1993, Welp et al. (1992,1994), and Kund and Andres (1993) are consistent with

$$\frac{dT_c}{dp_a} = -2.0\frac{K}{GPa}, \qquad \frac{dT_c}{dp_b} = +2.0\frac{K}{GPa}, \qquad \frac{dT_c}{dp_c} = +0.2\frac{K}{GPa}. \tag{15}$$

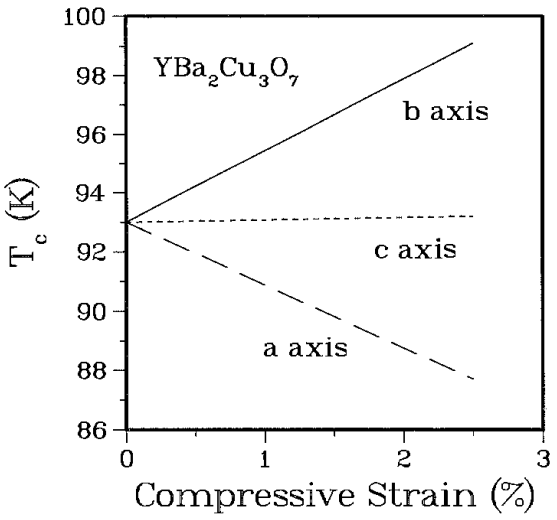

Fig. 6. Illustration of the uniaxial strain dependence of T_c in $YBa_2Cu_3O_7$. Only the known linear term (discussed in the text) is plotted; nonlinearity likely would be visible for the larger strains.

Lei et al. (1993) have obtained all elastic constants c_{ij}, which allow conversion from uniaxial stress to uniaxial strain (ϵ_j) using

$$\frac{dT_c}{d\epsilon_i} = -\sum_j c_{ij} \frac{dT_c}{dp_j}.$$

The results are

$$\frac{dT_c}{d\epsilon_a} = +212\,\mathrm{K}, \qquad \frac{dT_c}{d\epsilon_b} = -244\,\mathrm{K}, \qquad \frac{dT_c}{d\epsilon_c} = -8\,\mathrm{K}. \tag{16}$$

Note that the $\hat{c}$-axis value is indistinguishable from zero, while the $\hat{a}$- and $\hat{b}$-axis values are large, comparable in size, and opposite in sign. For emphasis we have plotted this behavior in fig. 6. Crommie et al. (1989) applied uniaxial *stress* along the $\hat{c}$-axis of a crystal of $YBa_2Cu_3O_7$. They attributed the observed rise in T_c (1 K/GPa) to an increase in $\hat{c}$-axis coupling. In light of the uniaxial *strain* data (above) obtained since this work, it is apparent that the change in T_c is the result of induced strains along the $\hat{a}$- and $\hat{b}$-axes that have partially but not totally cancelling effects. Sanfilippo et al. (1995) reported uniaxial stress studies of $YBa_2Cu_3O_7$ films, confirming the small stress dependence for $\hat{c}$-axis strain. Results for $\hat{a}$-axis strains were too dependent on the microstructure to determine intrinsic effects.

From many viewpoints one would expect that T_c will likely be sensitive to the $\hat{c}$-axis lattice parameter that governs the coupling between unit cells along $\hat{c}$, and that has been a foundation of the interlayer tunneling layer model of Chakravarty et al. (1993). Obviously that is not the case for $YBa_2Cu_3O_7$, at least at optimal doping. Klein and Simanovsky (1997) have suggested a model based on tunneling of the chain O between two off-chain sites. Carrier scattering from this tunneling unit is affected differently by uniaxial strains along the $\hat{a}$ and $\hat{b}$ directions. As presented, this model is specific to $YBa_2Cu_3O_7$ and does not shed light on the behavior of T_c^{max} across families of cuprates. Gvozdikov (1993)

suggested that the Fermi level lies between the van Hove singularities near the **X** and **Y** points, so that strain along $\hat{a}$ and $\hat{b}$ decreases and increases, respectively, the density of states at the Fermi level. This placement of the Fermi level, although consistent with the calculations, is not supported by experiment (see Schabel and Shen, Vol. 31 of this Handbook, ch. 201).

As mentioned above, there is nowhere near any consensus on the mechanism of pairing in the HTSs. Given the tremendous amount of experimental data and theoretical study on $YBa_2Cu_3O_7$, its properties are better understood than any other HTS. This striking behavior of the uniaxial stress dependence of T_c must contain pertinent information on the pairing mechanism. Note that this effect can hardly be due to change in carrier density: $YBa_2Cu_3O_7$ is already at or very near optimal doping, which means that *any* change will drive it away from optimum and thereby lower T_c. That is not the case. The increase in T_c with $\hat{b}$-axis compression either occurs at optimal doping, or occurs in spite of being driven away from optimal doping by strain.

3.4. *First-principles studies of uniaxial strain effects*

The all-electron, full potential linearized augmented plane wave (LAPW) method (Wei and Krakauer 1985, Singh 1991, 1995) was used to study changes in the lattice and electronic structure in $YBa_2Cu_3O_7$. In this method, the one-electron wavefunctions are expanded in plane waves in the regions between atoms, and the plane waves are connected smoothly to an angular momentum expansion inside of atom-centered non-overlapping spheres. This form leads to a natural form for the wavefunction both in the atomic regions and between atoms.

Structure and internal strains. Since the objective is to compare as closely as possible with trends in experimental data, we used the experimental lattice constants $a = 3.821$ Å, $b = 3.884$ Å, $c = 11.676$ Å rather than those that would minimize the energy, which would be about 1% smaller. The compressive uniaxial strains were chosen to be 2%, small enough that most physical properties will be in the linear regime at this value, yet large enough that numerical differences will be well above any procedural 'noise.'

The structure and labelling of atoms was shown in fig. 1. By convention, the Cu–O chains lie along the $\hat{b}$ direction. There are five atoms (Cu2, O2, O3, O4, Ba) whose z-component is not constrained by symmetry. Under uniaxial strain these internal coordinates will change; these changes are called internal strains. These internal coordinates were calculated for the unstrained crystal and for each of the uniaxial strains by calculating the energy $E[\{z_\alpha\}]$ and z-component of force $F_z[\{z_\alpha\}]$ for seven or eight sets of positions $\{z_\alpha, \alpha = \text{Cu2, O2, O3, O4, Ba}\}$. This set of data was fit to a polynomial to determine the position of the minimum of energy in the five-dimensional space, and the 5×5 dynamical matrix of force constants was also determined. Diagonalizing this matrix gives the corresponding phonon frequencies, which for this symmetry of displacements are the five zone-center fully symmetric A_{1g} phonons.

The results for the structural changes were given by Pickett (1997a) and are shown pictorially in fig. 7. It is instructive to consider whether the plane atoms Cu2, O2, O3

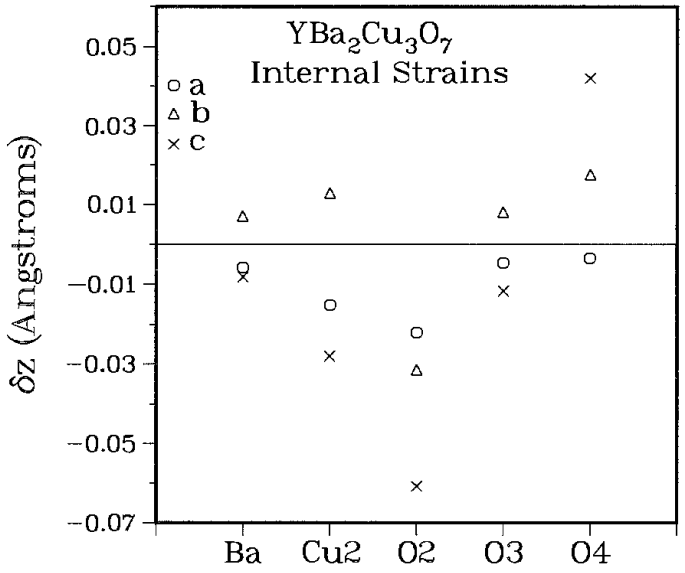

Fig. 7. Calculated internal strains due to uniaxial external strains of 2% along each of the crystal axes in $YBa_2Cu_3O_7$. Note that, except for O2, the $\hat{a}$- and $\hat{b}$-axis responses are opposite in sign.

and blocking layer atoms Ba and O4 behave collectively as different units. This seems not to be so. The Ba atom relaxes very little; note that this is not a mass effect since only static positions are being considered. The apical O4 atom, on the other hand, relaxes very strongly for $\hat{c}$-axis strain. This effect is easily attributed to the well established fact that the Cu1–O4 bond is much stronger than the Cu2–O4 bond, and $\hat{c}$-axis compression mainly shortens only the latter distance.

Comparison of internal strains for $\hat{a}$- and $\hat{b}$-axis strains is most revealing. For $\hat{a}$-axis strain, all internal strains are negative (toward the chain). For $\hat{b}$-axis strain, all except the O2 internal strain are positive. Thus these internal strains show a strong correlation with dT_c/dp_i: opposite for $\hat{a}$- and $\hat{b}$-axis strains. The O2 position is unique, in that each of the three uniaxial strains gives a negative internal strain. The striking result is that $\hat{b}$-axis strain makes the geometric structure of the CuO_2 layer nearer square symmetry, both by decreasing the longer b lattice parameter and by moving the height of the O2 atom nearer that of the O3 atom. $\hat{a}$-axis strain, on the other hand, drives the CuO_2 layer farther from square symmetry. The effect of tetragonal vs. orthorhombic symmetry upon T_c in the $(La,Sr)_2CuO_4$ system has been a point of much discussion. In that system, it seems likely that orthorhombic long-range order may open a pseudogap in the spectrum at the Fermi level, (Pickett et al. 1991, Cohen et al. 1989, 1992) thus accounting for the observed sharp drop in T_c.

There are no data on internal strains due to uniaxial strain or uniaxial stress. Some indication of changes in the structure for hydrostatic pressure up to 0.58 GPa was obtained by Jorgensen et al. (1990). They reported very small increases of z/c for all atoms, however, they were near the limit of their experimental uncertainty. Their conclusion was that the CuO_2 planes decreased in separation more rapidly than uniform scaling by $\Delta c/c$

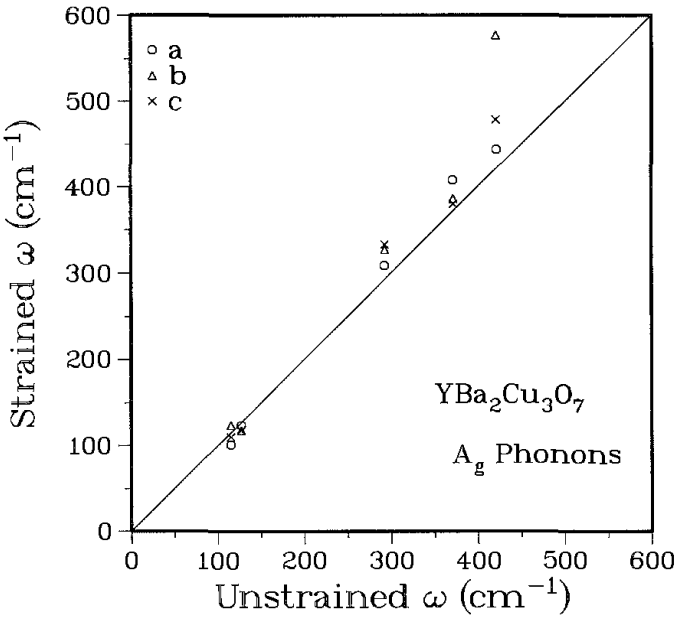

Fig. 8. Calculated frequencies of the A_{1g} optical phonons for uniaxially strained $YBa_2Cu_3O_7$, plotted versus the frequencies for the unstrained crystal. All responses are normal except for the highest frequency mode, for $\hat{b}$-axis strain.

would suggest. Our results can be converted to hydrostatic pressure values by using the relation

$$\frac{\mathrm{d}(\frac{z}{c})}{\mathrm{d}P} = \sum_i \frac{\mathrm{d}(\frac{z}{c})}{\mathrm{d}p_i} = -\sum_{ij}(c^{-1})_{ij}\frac{\mathrm{d}(\frac{z}{c})}{\mathrm{d}\epsilon_j}, \tag{17}$$

where c_{ij} are the elastic constants of Lei et al. (1993). Our results, in units of 10^{-4} GPa^{-1}, are −1.7, −6.8, −21.4, −3.2 and +12.2 for Ba, Cu2, O2, O3, and O4, respectively. The first four are opposite in sign to those reported by Jorgensen et al. (roughly 10, 7, 7, 6, 7 respectively). Our values for the relative changes in Cu1–O4 and Cu2–O4 bond lengths are, however, consistent with those reported by Jorgensen et al. In light of the experimental uncertainty and that it was assumed in the calculation that linearity extends to 2% strains, this discrepancy may not be very meaningful.

Phonon frequencies. The A_{1g} phonon frequencies that we obtain are shown graphically in fig. 8 as the frequency of the strained crystal *vs.* the frequency without strain. For the two low-frequency modes (around 110 cm^{-1} and 125 cm^{-1}, and due to Cu and Ba motion) the change is small and is within the uncertainty of our methods. The three higher frequencies, arising from oxygen motion, show the expected modest hardening under uniaxial strain, with one exception. For the $\hat{b}$-axis strain the highest frequency mode hardens by 140 cm^{-1} (70 cm^{-1} per % strain) a huge relative increase. This hardened mode has much stronger O3 character than the high frequency mode under $\hat{a}$- and $\hat{c}$-axis strains. O3 is distinguished from the O2 atom by virtue of being situated directly below/above the chain O1 atom. However, direct Coulomb repulsion between these negatively charged ions cannot be responsible for the increased frequency, because the distance between these two atoms is decreased much more by the $\hat{c}$-axis strain than by $\hat{b}$-axis strain.

We digress briefly to mention another aspect of A_{1g} phonons in $YBa_2Cu_3O_7$. Local density approximation calculations have consistently predicted that the two low-frequency

A_{1g} modes have strongly mixed Cu2 and Ba character (Rodriguez et al. 1990, Cohen et al. 1990). Isotope substitution (Henn et al. 1997, and references therein) indicates, however, that the low-frequency mode is almost entirely Ba in character, while the next higher mode is primarily Cu. Ambrosch–Draxl and collaborators (Kouba et al. 1996, Kouba and Ambrosch-Draxl 1997a,b) have refined the calculations by using an exchange-correlation energy functional that incorporates a dependence on the gradient of the density in addition to the usual density dependence, the so-called Generalized Gradient Approximation (GGA) of Perdew and coworkers (1992). Overall the corrections are quite small. The mixing of the two nearly degenerate low-frequency A_{1g} modes is quite sensitive to the energy surface, however, and the GGA results are in much better agreement with the isotope substitution studies. Even using the GGA, however, the frequencies of the three high-frequency modes remain 10–15% lower than measured values. This discrepancy may not be entirely a shortcoming of the LDA–GGA exchange-correlation functional, since calculated frequencies in other compounds are in much better agreement with observed values. The oxygen content of samples is at most 6.93; vacancies on one out of fourteen of the chain oxygen sites will allow local atomic relaxation that could affect frequencies.

Charge distribution. In analyzing the pressure dependence of T_c in cuprates, a 'prime suspect' has been the redistribution of charge ("holes") between the CuO_2 planes and the blocking layer, which in $YBa_2Cu_3O_7$ is the CuO chain and the two Ba–O layers. Due to the crossing of the CuO chain-derived Fermi surface sheet with the CuO_2 layer-derived barrel Fermi surfaces, identifying the "hole transfer" from the filled (or unfilled) bands is not an objective procedure. Moreover, since $YBa_2Cu_3O_7$ is already at optimal doping, changing the doping level in either direction can only decrease T_c, whereas $\hat{b}$-axis strain strongly increases T_c. For perspective on this question, we have looked at the redistribution of the actual electronic charge from three viewpoints: charges within the inscribed spheres, which are rough indicators of an atomic charge; core-level positions relative to the Fermi level, whose shifts give a different measure of the charge rearrangement; and a more direct indication, the a–b plane averaged density $\bar{\rho}(z)$.

Uniaxial-strain induced changes in the inscribed (muffin-tin) sphere charges and the core-levels are described in detail elsewhere (Pickett 1997b) so we only summarize the results here. Sphere charge shifts are generally similar for $\hat{a}$- and $\hat{b}$-axis strains, while $\hat{c}$-axis compression does seem to induce some plane $\rightarrow$ chain transfer of charge. Core-level shifts are somewhat difficult to interpret. A lowering of the Madelung energy on an atom will increase the charge, but then this increase in charge will raise the atom's potential. The resulting core-level shifts are not very instructive; for example, $\hat{a}$- and $\hat{b}$-axis strains give rather similar shifts overall, and the most evident aspect is that the shifts on the Ba atom are strongly positive while other atoms show smaller and usually negative shifts.

We focus then on the plane averaged change in valence electron density $\delta\bar{\rho}(z)$. It is necessary to keep in mind that the internal strains are included in this analysis. In addition, the average density is increased by 1/0.98 by the 2% compressive strain, and this is accounted for by renormalizing similarly the unstrained density before taking the difference. For the $\hat{c}$-axis strain the c-axis itself is compressed by the strain; the best that

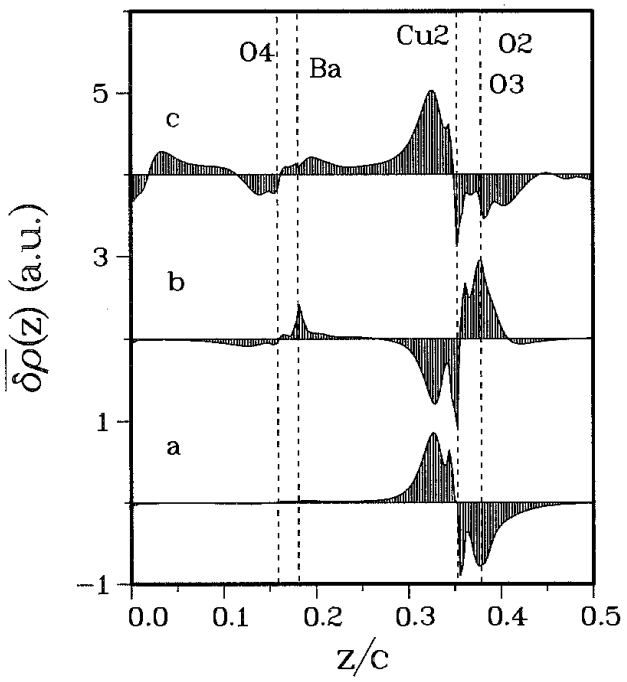

Fig. 9. Change in the planar-averaged valence charge density of $YBa_2Cu_3O_7$ due to uniaxial strains along each of the crystal axes. Note that the shifts for $\hat{a}$- and $\hat{b}$-axis strains are nearly equal and opposite.

can be done is to rescale strained and unstrained cells uniformly onto a common c-axis. As a result the interpretation becomes less straightforward.

The behavior of $\delta\bar{\rho}(z)$ is shown in fig. 9. For $\hat{c}$-axis strain there is some change in the density in the CuO chain region ($z \approx 0$ in the figure), whereas for both $\hat{a}$- and $\hat{b}$-axis strain there is no change in $\bar{\rho}$ near the chain. Thus there is no appreciable plane-to-chain charge transfer for either in-plane strain, while there is small but somewhat ambiguous (because of the rescaling) transfer for $\hat{c}$-axis strain. This is the first significant result: for both $\hat{a}$- and $\hat{b}$-axis strain, the CuO chain and indeed the entire blocking layer is decoupled from the important charge redistribution.

The charge rearrangements for $\hat{a}$- and $\hat{b}$-axis strains are, on average, of the sheet dipole type. Significantly, they are opposite and nearly equal, like the experimental observations for $dT_c/d\epsilon_a$ and $dT_c/d\epsilon_b$. The charge rearrangement is a combination of the relative displacement of positive Cu ions and negative O ions, as well as a change in charge of each of the ions. This dipolar shift of charge is only allowed because there are two CuO_2 layers in the $YBa_2Cu_3O_7$ structure, so they do not sit in a plane of z reflection as is the case for single CuO_2 layer compounds.

The charge rearrangement giving rise to this sheet dipole can be treated in terms of a planar sheet charge densities, obtained by integrating the curves of fig. 9, of $\sigma_{+,-} = \pm 0.2e/ab$ (or 2% strain) displaced from one another by $d = 0.05c \approx 1$ a.u. This corresponds to a surface dipole moment of $D = (\sigma_+ - \sigma_-)d \approx 4\times10^{-3}e$/a.u. The resulting shift in potential between the two sides of the sheet dipole (*i.e.* the blocking layer and the Y layer) by $\Delta V = 4\pi eD = 1.2$ eV, or 0.6 eV/% uniaxial strain. The sign of the dipole is such that for $\hat{b}$-axis strain this dipole tends to cancel the dipole that is already present

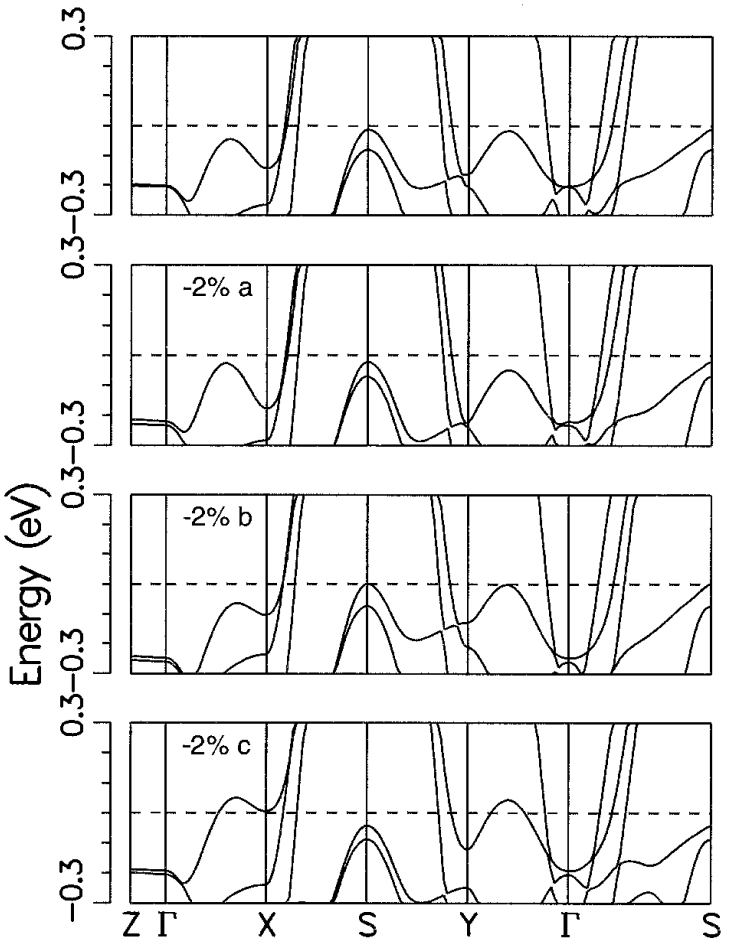

Fig. 10. Local density approximation band structure of $YBa_2Cu_3O_7$ near the Fermi level (horizontal line) for the unstrained crystal (top) and for uniaxial strains along each of the crystal axes. The shifts of critical points near the Fermi level are discussed in the text.

due to the corrugation of the Cu2 and O2, O3 atoms; for $\hat{a}$-axis strain the induced dipole adds to the intrinsic one.

LDA band structure. To evaluate the internal strains by minimization of the energy, it was necessary to use for the unstrained crystal the calculated internal positions. Although these predictions are quite close to the measured values, the small differences do result in one noticeable difference in the band structure: the band that just crosses the Fermi level from below and gives rise to the 'stick' Fermi surface does not quite reach the Fermi level when the theoretical internal parameters are used for atomic positions. The apical oxygen O4 position is the critical one. However, it is only the trends (finite differences) in band structure that we will report, and these changes will be insensitive to the reference point.

In fig. 10 we show the bands along the **Z–Γ–X–S–Y–Γ–S** lines. The focus of attention on the band structure has been on the regions of the extended van Hove singularities (vHs) seen in ARPES data. These vHs occur in the region of the **X** and **Y** points, and are extended along the **X–Γ** and **Y–Γ** directions, respectively. This behavior is discussed by Schabel and Shen in Vol. 31 of this Handbook, ch. 201. The origin of these vHs have been investigated in detail by Andersen and coworkers (1994, 1995). They arise from

saddle points in the bands associated with an antibonding pdσ CuO_2 plane band whose wavefunction is antisymmetric with respect to the mirror plane between the CuO_2 layers.

The compressive strain along the $\hat{b}$-axis leaves the separation of the two CuO_2 layers relatively unchanged but tends to align the heights of the O2 and O3 atoms, as noted above. The $\hat{a}$-axis strain pushes the two layers apart, thereby reducing the even-odd splitting of the layer bands. In the bands of fig. 10, it can be seen that $\hat{a}$- and $\hat{b}$-axis strains each shift the two saddle points in opposite directions, and these shifts are opposite for $\hat{a}$ and $\hat{b}$ strains. Since the saddle point near **Y** is closer to the Fermi level, and is shifted toward E_F by $\hat{b}$-axis strain (which is the one that increases T_c), this may be related to the superconducting character and critical temperature. The distinctions between $\hat{a}$- and $\hat{b}$-axis strain effects on the band structure do not seem striking, however.

3.5. *Effects of strain on many-body corrections*

We are not aware of work directly addressing the question of how effects of uniaxial strains should be included in many-body models. In terms of the TB band model presented in sect. 2, one can anticipate that hopping amplitudes should increase (decrease) as atoms are squeezed together (apart). Neglecting internal strain the effect of $\hat{a}$- and $\hat{b}$-axis strains will be similar. Likewise, changes in the on-site Coulomb repulsion U_d and U on Cu and O respectively will be identical for the two strains. The behavior of interatomic O2–O2 interaction V_{pp} likewise will not discriminate between $\hat{a}$- and $\hat{b}$-axis strains. Distinction between the two in-plane strains must be due to characteristics of orthorhombicity – either interactions related directly to the chain atoms, or indirectly to the presence of the chains, such as the internal strains discussed above.

There has been study of how model parameters affect T_c within several models. Di Castro, Feiner and Grilli (1991) treated a multiband model with hopping between Cu and all neighboring O ions, O–O hopping, on-Cu-site repulsion and Cu–O off-site repulsion. They concluded that the apical O ions have a strong effect on the character of the hole states in the CuO_2 layer, and thereby influence T_c^{max}.

On a phenomenological level, Monthoux et al. (1992) have touched on the question of what determines the value of T_c within their model of pairing due to a spectrum of spin fluctuations. Monthoux (1993) presented results at fixed carrier concentration and fixed coupling constant that indicated that T_c depends strongly on the spin fluctuation energy scale, but also shows some sensitivity to the general wavevector and frequency dependence of the spin fluctuation spectrum. The manner in which such variations are related to the blocking layer have not been studied.

3.6. *Implications for models of pairing*

It is not easy to relate the regularities we have found to any specific pairing mechanism in an objective way. The first clear and important result is that it is essential to account for internal strain in any consideration of the uniaxial strain dependence of properties, and hence any pressure dependence as well. It is, however, quite provocative that the

internal strains are more or less opposite in $YBa_2Cu_3O_7$, as are the observed shifts in T_c. The second noteworthy feature is that an increasing degree of tetragonality (*i.e.* square symmetry in the plane) of the CuO_2 layers correlates positively with T_c. Increasing tetragonality of the geometry does not increase the tetragonality of the electronic structure near the Fermi level in every respect, however, because the $\hat{b}$-axis strain that increases T_c actually results in more (rather than less) asymmetry between the saddle points near the Fermi level. The innate non-tetragonality that gave the intriguing uniaxial strain shifts of T_c that motivated this work comes back to complicate the interpretation of the results. The third clear result is that the dominant charge rearrangement that occurs due to uniaxial strain is an *intra*layer redistribution of charge between the Cu2 atom and the O2 and O3 atoms within the CuO_2 layers. This charge flow is in turn primarily a response to the internal strains. The relative amount of oxygen and copper character of the charge carriers appears to be closely linked to the value of T_c.

4. $PrBa_2Cu_3O_7$: How well is its unusual behavior understood?

4.1. *Observed behavior of* $Y_{1-x}Pr_xBa_2Cu_3O_7$

As mentioned above, the normal and superconducting properties of $RBa_2Cu_3O_7$ are essentially the same as those of $YBa_2Cu_3O_7$ for most lanthanides from Nd to Yb. Exceptions are Ce and Tb, which do not form $RBa_2Cu_3O_7$ compounds, and Pr, which does form crystallographically the same compound but with distinctively different physical properties. As soon as the lack of superconductivity in $PrBa_2Cu_3O_7$ was discovered it was established that there are no appreciable structural differences between $PrBa_2Cu_3O_7$ and other $RBa_2Cu_3O_7$ compounds.

The lack of superconductivity is not the only feature of $PrBa_2Cu_3O_7$ that singles it out. For instance, while in the other magnetic $RBa_2Cu_3O_7$ compounds the lanthanide ions order magnetically at $T \lesssim 1\,K$, Pr ions order at $T_N \approx 14\,K$. Another notable difference is that at room temperature $PrBa_2Cu_3O_{7-x}$ is insulating at all x, contrary to all other rare-earth compounds. Not only is pure $PrBa_2Cu_3O_7$ qualitatively different from the other $RBa_2Cu_3O_7$ compounds, doping with Pr makes $RBa_2Cu_3O_7$ with different rare earths behave differently, although in the absence of Pr the electronic properties of all $RBa_2Cu_3O_7$ including R = Y, Nd, Eu, Gd, Dy, Er, Yb, are essentially the same. For instance, the suppression rate $d \ln T_c/dx$ in $R_{1-x}Pr_xBa_2Cu_3O_7$ changes from 3 for Nd to about 0.5 for Y, Yb and Er. At the same time T_c without Pr differs by less than 4%. Not surprisingly, $PrBa_2Cu_3O_{7-x}$ attracted particular attention of researchers and gave rise to a variety of theoretical models, which will be discussed in the following sections. Experimental data are discussed in the detailed review of Radousky (1992), and below we shall mention mostly more recent experiments, keeping in mind that exhaustive information about the earlier experiments can be found in this review.

4.2. *Models for T_c suppression*

Since the transition temperature in high-T_c cuprates is strongly dependent on the carrier concentration, it is natural to assume that doping with Pr changes the hole concentration. This sounds reasonable because Pr does occur in the Pr^{IV} oxidation state. However, the Pr^{III} is not uncommon either. The usual technique for assigning a valency to an ion is from its spectroscopic signature. Local spectra for a given ion, for example, the Mössbauer isomer shift, are compared with those for the same ion in compounds where its oxidation state is not in doubt. For Pr such oxides are PrO_2, Pr_2O_3, and Pr_6O_{11}. The problem with such spectroscopic definition of valency is that it assumes purely ionic character for Pr ions, while for instance PrO_2 is known to have substantial Pr–O hybridization. As we will see below, the same is true for $PrBa_2Cu_3O_7$. An illuminating example is the above mentioned isomer shift (Moolenaar et al. 1996). While Pr in PrO_2 and $CsPrF_5$ has the same valency 4, the isomer shift is different, reflecting the fact that Pr in oxides is not purely ionic. If one assigns valency 4 to Pr in $CsPrF_5$, and valency 3 to Pr in PrF_3, then interpolation of their isomer shifts yields for $PrBa_2Cu_3O_7$ valency 3.3 (Moolenaar et al. argue that pure ionicity is only 3.2), while if PrO_2 is used as the reference for Pr^{IV} it is 3.4–3.5 instead. Keeping in mind that Y in $YBa_2Cu_3O_7$ is ionic and trivalent, we should accept the former number (3.2–3.3) for Pr valency. It is clear, however, why so different numbers are quoted in the literature. More references on spectroscopic valency can be found in the review of Radousky (1992) and in the discussion by Moolenaar et al. (1996).

In any event, the spectroscopically determined Pr valency in $PrBa_2Cu_3O_7$ does not deviate enough from 3 to explain the superconductivity suppression. Furthermore, the superconductivity is fully suppressed at as little as 60% substitution of Y by Pr, or 30% substitution of Nd by Pr in $Nd_{1-x}PrBa_2Cu_3O_7$, which is not consistent with the idea of hole depletion due to higher Pr valency: 30% Pr even with effective Pr ionicity 3.4 corresponds to the hole depletion of 0.12/cell, or the oxygen reduction of 0.06. The chain reservoir effect delays superconductivity suppression by oxygen reduction, but it remains clear that 0.12 holes/cell is an insufficient number. Moreover, the very fact that the suppression rate depends strongly on the host rare earth requires an assumption that the Pr valency depends on the host rare earth, which is hard to justify.

Another popular explanation of the T_c suppression utilizes the Abrikosov–Gor'kov mechanism of superconductivity suppression due to magnetic impurities. Note that if superconductivity in $YBa_2Cu_3O_7$ is d-wave, as widely believed, both magnetic and nonmagnetic impurities suppress T_c in the same manner; the resulting equations differ from those in the isotropic case merely by a factor of two. The high value of the Néel temperature for Pr spin ordering suggests larger admixture of the Pr f states to the valence $pd\sigma^*$ band, which should provide for the stronger scattering of the conduction electrons by Pr impurities compared with the other lanthanides. On the other hand, this argument explains why T_c suppression by Pr should be stronger, probably even much stronger than by Nd, but does not explain why Nd does not suppress T_c at all. Restoring superconductivity in $Y_{1-x}Pr_xBa_2Cu_3O_7$ upon doping with Ca does not square with the

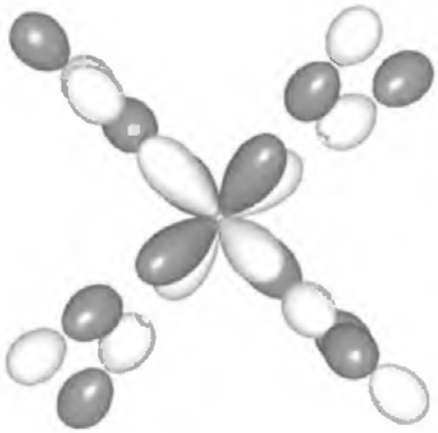

Fig. 11. Antibonding interaction between a Pr f $z(x^2-y^2)$ orbital and O p orbitals. The Pr atom, in the center, is surrounded octahedrally by eight oxygen ions. Light and dark shadings indicates different signs of the lobes.

pair-breaking model either. Finally, the dependence of T_c on the Pr concentration does not obey the Abrikosov–Gor'kov formula, which casts additional doubt on this mechanism. Still, occasionally some papers resuggesting the Abrikosov–Gor'kov impurity-induced suppression in $PrBa_2Cu_3O_7$ appear; the latest one, to our knowledge, is by Staub et al. (1997). An earlier and more detailed discussion of a pair-breaking explanation of T_c suppression in $PrBa_2Cu_3O_7$ was by Japha and Zevin (1992).

So, the two most obvious explanations of the anomalous behavior of $PrBa_2Cu_3O_7$ appear to be inconsistent with experimental observations. The idea of the hole depletion of the pdσ* band, responsible for superconductivity, was still appealing to theorists. Indeed, if Pr cannot serve as hole stealer, can it perhaps induce a redistribution of holes between the pdσ* band, and another band, not relevant for the superconductivity? A natural candidate was the chain band, as suggested by Khomskii (1993). Unfortunately, no microscopic mechanism to arrange hole transfer from planes to chains was suggested and even less was it clear why things depend on the host rare earth.

Yet another model was suggested by Fehrenbacher and Rice (1993a). They noticed that a rare-earth ion and four nearest oxygens form a nearly perfect cube. Moreover, among 7 orbitals of f symmetry there is one, xyz, which has eight equivalent lobes directed along eight directions $[\pm1, \pm1, \pm1]$. In the standard coordinate system where x, y correspond to the CuO bond directions the same orbital is $(x^2-y^2)z$. It is apparent that this f orbital will be most liable to formation of pfσ bonds. Fehrenbacher and Rice took a cluster of one Pr and eight surrounding oxygens and considered formation of an antibonding state of the $f_{(x^2-y^2)z}$ Pr orbital and eight oxygen p orbitals pointing directly towards Pr, as shown in fig. 11. If the energy difference between the bare O p level and bare Pr f level is not too large, the energy of this antibonding state may become higher than that of the pdσ* Cu–O state and will pull some holes out of the latter. Whether or not this will happen depends on the p–f energy separation and the p–f hopping integral. Both are difficult to estimate without detailed numerical calculations. Fehrenbacher and Rice, however, offered arguments of a semiquantitive character that suggested that in $PrBa_2Cu_3O_7$, and only in it among other $RBa_2Cu_3O_7$, the p–f energy distance is sufficiently small to initiate charge transfer.

4.3. *Fehrenbacher–Rice model*

The Fehrenbacher and Rice model had clear advantages over the other models put forward, however it had a number of difficulties. Some of these problems have been addressed, and in the remainder of this section we shall concentrate on this model and its more modern versions.

First of all, the insulating state of $PrBa_2Cu_3O_7$ is clearly different from the well studied insulating state of $YBa_2Cu_3O_{6+x}$ at $x < 0.34$. One of the important differences is in the optical conductivity. The optical conductivity of the pure $YBa_2Cu_3O_7$ shows substantial x–y anisotropy. The difference between x and y conductivity is ascribed to the metallic chain contribution. This contribution gradually decreases and eventually vanishes upon oxygen reduction. Contrary to that, $PrBa_2Cu_3O_7$ retains substantial difference between the y and x polarizations. Furthermore, this difference is more or less the same in $PrBa_2Cu_3O_7$ and in $YBa_2Cu_3O_7$ except for very low frequencies, $\omega \lesssim 0.1$ eV (Takenaka et al. 1992). This observation led Fehrenbacher and Rice (1993b) to a model which became known as "the Fehrenbacher–Rice model" in the narrow sense. Unlike the original model (Fehrenbacher and Rice 1993a) it does not assume that all conducting holes are trapped by the Pr–O clusters, but rather that only holes in planes are subject to such trapping. The holes in chains, to the contrary, remain metallic. This does not mean that the sample as a whole behaves as a metal, because an infinitesimally small number of defects leads to full localization in the 1D systems – of which the CuO chains in YBCO are an example. In $YBa_2Cu_3O_7$ chain-plane hopping effectively removes 1D character of the chain conductivity and makes it less prone to localization. In $PrBa_2Cu_3O_7$ metallic chains between the insulating planes would show 1D localization for static conductivity, as well as for the dynamic (optical) conductivity for the frequencies such that the corresponding wave length is much larger than the average distance between the chain defects. This is exactly what is observed in the experiment.

The Fehrenbacher–Rice model, with all its attractiveness, suffers from two remaining problems. First, the model relies upon detailed numerical balance between the Pr–O $pf\sigma^*$ state and the Cu–O $pd\sigma$ band. Such parameters as the $pf\sigma$ hopping amplitude cannot be measured experimentally, nor estimated with reasonable accuracy from general considerations; accurate first-principle calculations are needed. Second, the Fehrenbacher–Rice model predicts an unambiguous pressure effect: as long as the Pr–O bond length decreases, the corresponding hybridization increases and the hole depletion effect gets stronger. Indeed, while the pressure coefficient of T_c of $YBa_2Cu_3O_7$ is positive, upon Pr doping it decreases and eventually becomes negative. However, applying pressure is not the only way to change the Pr–O bond length. Substituting the host rare earth by another, with a different ionic radius, changes the distance between the CuO_2 planes and thus the R–O distance. The smallest radius and correspondingly the shortest R–O bond have Y and Yb, the longest one has Nd. Correspondingly, one would expect that if the effect of Pr doping on T_c will be different for the different rare earths, it would be the strongest in Y and Yb, and the weakest in Nd. The opposite is what is observed.

This problem had to be addressed with quantitative calculation. Such calculations, based on the so-called LDA+U approach, are subject of the next section.

4.4. *First-principles electronic structure studies*

A number of papers devoted to the electronic structure of $PrBa_2Cu_3O_7$ and based on the conventional Local Density Approximation (LDA) were published in 1990–1994. The LDA method itself is discussed in the context of cuprate superconductors by Pickett (1989). The only way to deal with the localized f electrons in LDA is to consider them as core states, otherwise the Fermi level is pinned inside the narrow f band and resulting band structure is unphysical. Without going into details, these studies did not discover any interesting difference between the $PrBa_2Cu_3O_7$ and other $RBa_2Cu_3O_7$. If one takes as the starting point the Fehrenbacher–Rice model, such an approach is completely unsatisfactory, because it cannot describe properly the p–f hybridization. Fortunately, a method had been developed that allows treating localized states like f states in the lanthanides as bands, fully including hybridization effects, and yet retains the onsite Coulomb repulsion leading to splitting between the lower and the upper Hubbard bands. This method includes the Hubbard U explicitly and is therefore called LDA+U. An extensive literature exists on this method; see Anisimov et al. (1997) for a review.

For application to $PrBa_2Cu_3O_7$, described below, two features are of importance. First, in the LDA+U method the Hubbard repulsion U is applied only inside the corresponding atomic sphere. For instance, the Cu d states, which are somewhat too localized to be describable in the quasi-one-electron framework, still extend substantially outside of the Cu atomic sphere. That is why LDA+U is questionable when applied to the Cu d orbitals in the HTSC cuprates. On the other hand, f states of the lanthanides in HTSC are well localized and LDA+U is an excellent approach. Second, state-of-art LDA+U programs use the so-called rotationally invariant formulation of the LDA+U (Liechtenstein et al. 1994). The physical result of this formalism is that the Hubbard operator acting on (in our case) seven f orbitals is a 7×7 matrix which depends on the occupation matrix of f orbitals. During the self-consistency loop both the occupation matrix and the U-matrix change ("rotate") until the true ground state is reached. For example one can start in the spherical harmonics representation and occupy, in case of Pr in $PrBa_2Cu_3O_7$, the orbital with $m = 2$, which is $z(x + iy)^2$. After reaching the self-consistency, one finds in LDA+U both $m = 2$ and $m = -2$ equally occupied. This signals that the initial guess was unlucky and the real ground state corresponds to a cubic harmonic, namely $z(x^2 - y^2)$.

These two features make rotationally invariant LDA+U ideally suited for testing the Fehrenbacher–Rice hypothesis. Such calculations were performed (Liechtenstein and Mazin 1995) and led to further development of this model. First, the calculations were done for pure $PrBa_2Cu_3O_7$. Pr in this compound has one occupied f orbital; several different starting configurations were chosen, but all runs converged to the same configuration. The f orbital, occupied in the ground state, is indeed $z(x^2 - y^2)$, as conjectured by Fehrenbacher and Rice. Since the crystal-field splittings of the f states are small, the only mechanism which would provide for such a clear discrimination

between this and the other orbitals is hybridization with the other states. In fact, one can identify these states by locating among the manifold of the Cu–O bands those which have noticeable admixture of the Pr f character. Indeed, Liechtenstein and Mazin (1995) found one band that did hybridize with the Pr $z(x^2-y^2)$ orbital and had visible admixture of its character. In accord with the Fehrenbacher–Rice model this band was formed mostly by the oxygen π orbitals: O2 y and z and O3 x and z (note that the pdσ^* Cu–O band is formed by the O2 x and the O3 y orbitals). However, further analysis of the first-principle calculations reveals interesting deviations from the predictions of the Fehrenbacher–Rice model. According to this model, each Pr forms a hybridized state with eight surrounding oxygen ions. These states are localized and independent of each other. Hopping between these cluster states is small and the dispersion of the corresponding band is negligible[3].

A surprising result of the LDA+U calculations was that the O π orbitals formed a band with a substantial dispersion. Furthermore, this very same band was present in the calculation even in $YBa_2Cu_3O_7$, where no f orbitals are occupied. More detailed analysis showed that this dispersion is due to pdπ hopping between oxygen and copper. Upon second thought, this does not seem strange: analysis of the dispersion of the Cu–O bands in the vicinity of the Fermi level (Andersen et al. 1994) gives for the pdπ hopping amplitude $t_{pd} \approx$ 0.83 eV, half that of the pdσ hopping. It should be noted that this ratio determines the Fermi surface geometry, which agrees with the experiment. Correspondingly, the antibonding pdπ band, the one which interacts with the Pr f electrons, has dispersion comparable to the pdσ^* band (a factor of two less). The question now is, how does this affect the Fehrenbacher–Rice model?

First of all, with this new information we see that the reservoir that can exchange holes with the superconducting pdσ band is not a collection of localized levels, but rather a band. This band should be fully occupied (*i.e.* not containing any holes) in all $RBa_2Cu_3O_7$ compounds except for $PrBa_2Cu_3O_7$. Since the calculations do not include any adjustable parameter, this is actually a good test for the model. LDA+U calculations, reported by Liechtenstein and Mazin (1995) found this band to be fully occupied both in $YBa_2Cu_3O_7$ and in $NdBa_2Cu_3O_7$, and to be partially empty in $PrBa_2Cu_3O_7$. Importantly, although the band is entirely below the Fermi level in $NdBa_2Cu_3O_7$, its top is only 0.2 eV from the Fermi level. One can believe that it should be relatively easy to modify the $NdBa_2Cu_3O_7$ system to shift this band (which we shall call below the FR band) up by a few tenths of an eV to make it cross the Fermi level. As the band crosses the Fermi level, the number of holes in the FR band – and thus the hole concentration in the CuO_2 bands – can vary continuously. The above mentioned observation of superconductivity suppression under the pressure in $NdBa_2Cu_3O_7$ is a clear manifestation of such an effect.

---

[3] An interesting complication is that, contrary to the assumption in the original paper, these cluster states, centered at neighboring Pr atoms, are not orthogonal. The reason is that, as discussed below, the Pr–O bond forms an angle (~35°) with the CuO_2 plane, which is smaller than 45°. As a result, the two p orbitals of the same oxygen, pointing towards two different Pr, are not orthogonal, the overlap being as large as 1/3. Consequences of this nonorthogonality in the framework of the Fehrenbacher–Rice model have been investigated (Mazin 1999). Below we briefly address this issue.

Results put into the tight-binding picture. Before going into quantitative details, let us discuss how this band is formed. First, we neglect the (very small) z-dispersion. (This means that all orbitals we consider are antisymmetric with respect to $z \to -z$ reflection, like the FR orbital.) Then the two plane problem is equivalent to a single plane one. In principle, the following orbitals contribute to the FR band: (1) Pr $z(x^2 - y^2)$, (2) O2 z, (3) O3 z, (4) O2 y, (5) O3 x, (6) Cu xy, (7) Cu yz, and (8) Cu zx. Their in-plane 2D symmetries are, respectively, $x^2 - y^2$, s, s, y, x, xy, y, and x, which simplifies the task of the tight-binding description of the band structure. Let us now identify the largest hopping amplitudes between these orbitals. One is pfσ, which we shall denote t_{pf}. It controls the following hoppings: $t_{12} = t_{13} = \sqrt{\frac{5}{27}}t_{\mathrm{pf}}$, $t_{14} = t_{15} = \sqrt{\frac{10}{27}}t_{\mathrm{pf}} = \sqrt{2}t_{12}$. This parameter defines the effect of the rare-earth substitution on the FR band. The second hopping is of pdπ type, denoted t_{pd}. The hopping amplitudes t_{28}, t_{37}, t_{46}, and t_{56} all are equal to t_{pd}. This parameter defines the dispersion of the FR band in the absence of the f states, *e.g.*, in $YBa_2Cu_3O_7$, or in the spin-minority channel in $PrBa_2Cu_3O_7$. It is instructive to consider these two hoppings separately.

Let us first set t_{pd} to zero. This corresponds to the original Fehrenbacher–Rice (1993b) model. Dispersion of the oxygen pπ states is completely neglected; an isolated Pr impurity forms a localized antibonding state, shifted up with respect to the bare O p level by

$$\epsilon_{\mathbf{k}} - E_{\mathrm{p}} = \delta\epsilon = \frac{5}{9}\frac{8t_{\mathrm{pf}}^2}{E_{\mathrm{p}} - E_{\mathrm{f}}}, \tag{18}$$

where 8 stands for the eight neighboring oxygens, and it is assumed that $t_{\mathrm{pf}} \ll E_{\mathrm{p}} - E_{\mathrm{f}}$. In the opposite limit, when all rare-earth sites are occupied by Pr, a narrow band is formed with the dispersion $\epsilon_{\mathbf{k}} - E_{\mathrm{p}} = \delta\epsilon - \delta\epsilon \cos 2\varphi(\cos ak_x + \cos bk_y)/2$, where $\varphi = \arctan(1/\sqrt{2}) \approx 35°$ is the angle that the Pr–O bond forms with the xy plane. Had this angle been 45°, as assumed by Fehrenbacher and Rice (1993b), this band would be dispersionless and thus fully localized. In reality, it should acquire a finite bandwidth $W = \delta\epsilon \cos 2\varphi = \delta\epsilon/3$ even if it had not had any without Pr. This is an example of dispersion due to nonorthogonality: the Hamiltonian written in terms of the oxygen orbitals pointing towards Pr is diagonal, but such a basis is nonorthogonal and that results in dispersion. Note that the top of the band occurs at the (π, π) point and that is where the holes go from the pdσ superconducting band. Figure 12 shows that indeed at this point pfσ interaction is antibonding along all bonds.

Now we consider the case of finite t_{pd} and no f states. For simplicity, we let the energy of the Cu d level be the same as the energy of the O p level. Then four O p orbitals and three Cu d orbitals form three antibonding bands (besides the bonding and nonbonding bands):

$$\epsilon_{\mathbf{k}} - E_{\mathrm{p}} = 2t_{\mathrm{pd}} \sin \tfrac{1}{2}ak_x, \tag{19}$$

$$\epsilon_{\mathbf{k}} - E_{\mathrm{p}} = 2t_{\mathrm{pd}} \sin \tfrac{1}{2}bk_y, \tag{20}$$

$$\epsilon_{\mathbf{k}} - E_{\mathrm{p}} = 2t_{\mathrm{pd}} \sqrt{\sin^2 \tfrac{1}{2}ak_x + \sin^2 \tfrac{1}{2}bk_y}. \tag{21}$$

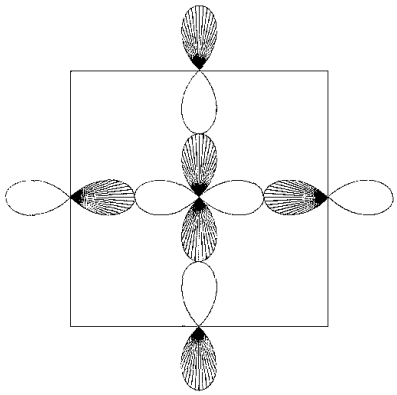

Fig. 12. Tight-binding orbitals corresponding to the Fehrenbacher–Rice (1993b) model (projected onto the x–y-plane). The Pr $z(x^2-y^2)$ orbital is in the center.

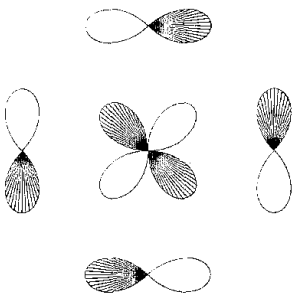

Fig. 13. Tight-binding orbitals corresponding to the antibonding combination of O2 y and O3 x with the Cu2 xy at the point $\mathbf{S}=(\pi,\pi)$. Cu2 ions are in the corners.

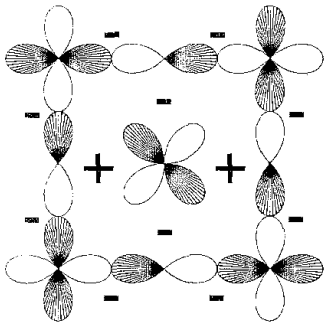

Fig. 14. Illustration of inability of the O2 y and O3 x orbitals to make an antibonding combination simultaneously with the Cu2 xy orbital (in the corners) and Pr f orbital (in the center).

The top of the highest (third) band is again at (π,π), as illustrated in fig. 13, showing again the antibonding interactions for all bonds.

The case of pdπ and pfσ interactions together cannot be solved analytically. Before reporting the numerical results, we make one additional observation: since both cases separately produce dispersive bands with the maximum at (π,π), one might expect this effect (band dispersion) to be enhanced when both interaction are included. One can easily see (fig. 14), that this is not true: the configuration of the O p orbitals, which is antibonding in the first case, is nonbonding in the second case, and vice versa.

The main shortcoming of the original Fehrenbacher–Rice (1993b) model was its inability to describe the different rate of T_c suppression with the different rare-earth hosts. The modification in the Liechtenstein–Mazin (1995) model, derived from LDA+U calculation, explained this phenomenon naturally. Unlike the Fehrenbacher–Rice model, the LDA+U treatment expresses the FR state in a band form. The position of the band

in pure $RBa_2Cu_3O_7$ compounds is different depending on the rare earth, the larger the atomic number the lower the position of the FR band. Since the *initial* band is located at different energies, its *final* position after introducing Pr impurities is also different. In order to estimate the effect of Pr doping quantitatively, one needs a model allowing one to deal with a disordered system. Liechtenstein and Mazin (1995) dealt with this problem by direct diagonalization of a tight-binding Hamiltonian which was a subset of the 8×8 Hamiltonian described above. The idea was that at small Pr concentration it is only a small region around the (π, π) point that participates in the hole depletion process. The structure of the Hamiltonian is such that at (π, π) the O z orbitals are not hybridized with the Pr f states and thus do not contribute to formation of the FR band. For the same reason one can drop the Cu xz and yz orbitals near the (π, π) point.

Finally, the effect of the Cu xy band can be taken into account by introducing effective p–p hopping between O2 and O3. This leads to an 2D Hamiltonian with 3 orbitals per unit cell. The parameters of this Hamiltonian were determined by fitting the LDA+U band structure near the Fermi level. Within this model, the difference between $Pr_xY_{1-x}Ba_2Cu_3O_7$ and $Pr_xNd_{1-x}Ba_2Cu_3O_7$ is in the on-site energy of the f level. For Y it is essentially infinity, for Pr it is the same as the bare p level energy, and for Nd it is 2.4 eV lower. Then one can calculate the density of states of the FR band for arbitrary x using a sufficiently large cluster and directly diagonalizing the Hamiltonian. The calculations resulted in two dependencies of the number of holes transferred from the pdσ band to the FR band, on the Pr concentration x. Using the known dependence of T_c on the hole concentration, as deduced from the oxygen-reduced $YBa_2Cu_3O_7$, one can then calculate the T_c suppression as a function of Pr concentration. In fact, the numerical results were qualitatively encouraging (correct trend between Y and Nd was found), but quantitatively the suppression was underestimated. It was attributed to possible underestimation of the p–f hopping amplitude. Increasing this parameter by 0.1 eV, or by 15%, brought the results in a good agreement with the experiment.

Several caveats can be pointed out. First, in the calculations of Liechtenstein and Mazin no correlation effects on the Cu site were taken into account. In the metallic regime of low Pr doping this may be a sensible approximation. However, near and beyond the metal-insulator transition it is qualitatively wrong. While the "band model" of Liechtenstein and Mazin correctly describes the T_c suppression, it cannot be applied to the insulating compositions and in particular to the pure $PrBa_2Cu_3O_7$. In fact, if one tries to do so one formally gets a metal with the total carrier concentration in the FR band only 5 times smaller than the carrier concentration in pure YBCO. To explain the nonmetallic DC conductivity in $PrBa_2Cu_3O_7$ one then needs an impurity scattering rate of the order of a few tenths of eV, which is rather large. The original Fehrenbacher–Rice model seemed to be more able to produce localization in the FR band, because they believed that width of the FR band will be very small "due to the orthogonality of the involved orbitals on shared O sites of neighboring Pr cubes". In reality, however, these orbitals are substantially nonorthogonal, as discussed above, and this argument does not really work. The issue of the nonmetallic conductivity in pure $PrBa_2Cu_3O_7$ is still puzzling. It is worth noting in this context that there were recently two reports of metallic (actually, superconducting)

behavior in specially prepared samples of pure stoichiometric $PrBa_2Cu_3O_7$ (Blackstead and Dow 1995, Zou et al. 1997). Although the experimentalists are sceptical (see, e.g., Narozhnyi and Drechsler 1999) about these results, they probably indicate that that the insulating state routinely obtained in $PrBa_2Cu_3O_7$ is nontrivial.

Another caveat associated with the calculations of Liechtenstein and Mazin is that LDA generally overestimates the spatial extent of the Cu d orbitals, so one may expect that the pdπ hopping amplitude is also overestimated, and most importantly, so is its ratio to the pfσ hopping amplitude. This is probably why it was necessary to increase the latter by 15% to achieve an agreement with the experiment.

Our final comment is that recently a direct experimental probe of the number of the p_z holes in CuO_2 planes in $Pr_xY_{1-x}Ba_2Cu_3O_7$ was reported (Merz et al. 1997). Since such holes do not exist in pure $YBa_2Cu_3O_7$, this experiment provides a direct measure of the hole concentration in the FR band. The results were quite convincing: substantial number of holes in the FR band was found at finite Pr dopings, accompanied by a decrease in the concentration of the pdσ holes. From the number of the p_z holes Mertz et al. computed the average angle that the FR orbitals make to the CuO_2 plane, and for the doping level $x = 0.8$ they found it to be 20–25°, to be compared with 15–18° in the model of Liechtenstein and Mazin (1995) and 35–37° in the original Fehrenbacher–Rice (1993b) model. More discussion of this experiment and its relation to the theoretical models is given by Mazin and Liechtenstein (1998).

5. Summary

In this article we have focussed on selected topics of current interest in theoretical studies of the $YBa_2Cu_3O_7$ and $PrBa_2Cu_3O_7$ systems. It has been clear for some time that, to address seriously the observed properties of this system, it is necessary to include the full complexity of the cell. The reduction of the elaborate first-principles description to minimal basis tight-binding form described in sect. 2 is a necessary component of forthcoming work on this system.

The material in sect. 3 and 4 illustrates clearly that it is the *character* of the charge carriers, as well as their concentration, that is a determining factor in how high T_c is in a given cuprate compound. In the case of the effect of uniaxial strain, the analysis suggest that the relative amounts of Cu and O character of the holes is an important factor determining T_c^{max}. For $PrBa_2Cu_3O_7$, the lack of superconductivity is due to a transfer of holes from the superconducting Cu–O band to a non-superconducting Pr–O band. Remarkably, these bands are very close both in real space – each are intimately connected to the planar O2 and O3 atoms – and in energy.

The uniaxial pressure and/or strain dependence of T_c differs among the various cuprates; see Meingast et al. (1994). This dependence, which as was emphasized above is an indirect but clear reflection of the effect of the blocking layer, provides a promising avenue of further research into specifically what makes T_c high, and therefore what the pairing mechanism is.

Acknowledgments

The authors have benefitted from discussions with D.J. Singh on a number of questions related to the content of this article. W.E.P. acknowledges a contract from the U.S. Office of Naval Research, and the work of I.I.M. at the Naval Research Laboratory is also supported by the Office of Naval Research.

References

Allen, P.B., W.E. Pickett and H. Krakauer, 1987, Phys. Rev. B **36**, 3926.

Andersen, O.K., A.I. Liechtenstein, C.O. Rodriguez, I.I. Mazin, O. Jepsen, V.P. Antropov, O. Gunnarsson and S. Gopalan, 1991, Physica C **185–189**, 147.

Andersen, O.K., O. Jepsen, A.I. Liechtenstein and I.I. Mazin, 1994, Phys. Rev. B **49**, 4145.

Andersen, O.K., A.I. Liechtenstein, O. Jepsen and F. Paulsen, 1995, J. Phys. Chem. Solids **56**, 1537.

Anisimov, V.I., F. Aryasetiawan and A.I. Lichtenstein, 1997, J. Phys.: Condens. Matter **9**, 767.

Bardeen, J., L.N. Cooper and J.R. Schrieffer, 1957, Phys. Rev. **106**, 162; **108**, 1175.

Bednorz, G., and K.A. Müller, 1986, Z. Phys. B **64**, 189.

Blackstead, H.A., and J.D. Dow, 1995, Phys. Rev. B **51**, 11830.

Chakravarty, S., A. Subdo, P.W. Anderson and S. Strong, 1993, Science **261**, 337.

Cohen, R.E., W.E. Pickett and H. Krakauer, 1989, Phys. Rev. Lett. **62**, 831.

Cohen, R.E., W.E. Pickett and H. Krakauer, 1990, Phys. Rev. Lett. **64**, 2575.

Cohen, R.E., W.E. Pickett and H. Krakauer, 1992, in: Proc. Lattice Effects in High T_c Superconductors, eds Y. Bar-Yam, T. Egami, J. Mustre-de Leon and A. Bishop (World Scientific, Singapore) p. 223.

Crommie, M.F., A.Y. Liu, A. Zettl, M.L. Cohen, P. Parilla, M.F. Hundley, W.N. Creager, S. Hoen and M.S. Sherwin, 1989, Phys. Rev. B **39**, 4231.

DeWeert, M.J., D.A. Papaconstantopoulos and W.E. Pickett, 1989a, Phys. Rev. B **39**, 4235.

DeWeert, M.J., D.A. Papaconstantopoulos and W.E. Pickett, 1989b, in: Atomic Scale Calculations in Materials Science, eds J. Tersoff, D. Vanderbilt and V. Vitek, MRS Symp. Proc. **141**, 103.

Di Castro, C., L.F. Feiner and M. Grilli, 1991, Phys. Rev. Lett. **66**, 3209.

Fehrenbacher, R., and T.M. Rice, 1993a, in: Proc. Int. Winter School, Kirchberg, 1992, Vol. 113 of Springer Series in Solid State Sciences (Springer, Berlin).

Fehrenbacher, R., and T.M. Rice, 1993b, Phys. Rev. Lett. **70**, 3471.

Feiner, L.F., J.H. Jefferson and R. Raimondi, 1996, Phys. Rev. Lett. **76**, 4939.

Fowler, C.M., B.L. Freeman, W.L. Hults, J.C. King, F.M. Mueller and J.L. Smith, 1992, Phys. Rev. Lett. **68**, 534.

Fujimori, A., A. Ino, T. Mizokawa, C. Kim, Z.-X. Shen, T. Sasagawa, T. Kimura, K. Kishio, M. Takaba, K. Tamasaku, H. Eisake and S. Uchida, 1997, J. Phys. Chem. Solids **59**, 1892.

Ginzburg, V.L., and D.A. Kirzhnits, eds, 1977, High-Temperature Superconductivity (Nauka, Moscow). English translation: 1982 (Consultants Bureau, New York).

Gofron, K., J.C. Campuzano, H. Ding, C. Gu, R.L. Liu, B. Dabrowski, B.W. Veal, W. Cramer and G. Jennings, 1993, J. Phys. Chem. Solids **54**, 1193.

Gvozdikov, V.M., 1993, J. Low Temp. Phys. **19**, 914.

Haghighi, H., J.H. Kaiser, S. Rayner, R.N. West, J.Z. Liu, R. Shelton, R.H. Howell, F.R. Solal and M.J. Fluss, 1991, Phys. Rev. Lett. **67**, 382.

Henn, R., T. Strach, E. Schonherr and M. Cardona, 1997, Phys. Rev. B **55**, 3285.

Japha, Y., and V. Zevin, 1992, Phys. Rev. **46**, 9240.

Jorgensen, J.D., S.P. Lightfoot, D.G. Hinks, B.W. Veal, B. Dabrowski, A.P. Paulikas, R. Kleb and I.D. Brown, 1990, Physica C**171**, 93.

Khomskii, D., 1993, J. Supercond. **6**, 69.

Klein, M.W., and S.B. Simanovsky, 1997, Phys. Rev. Lett. **78**, 3927.

Kouba, R., and C. Ambrosch-Draxl, 1997a, Physica C **282–287**, 1635.

Kouba, R., and C. Ambrosch-Draxl, 1997b, Phys. Rev. B **56**, 14766.

Kouba, R., R. Abt and C. Ambrosch-Draxl, 1996, Czech. J. Phys. **46**, 923.

Krakauer, H., W.E. Pickett and R.E. Cohen, 1993, Phys. Rev. B **47**, 1002.

Krantz, M., and M. Cardona, 1995, J. Low Temp. Phys. **99**, 205.

Kraut, O., C. Meingast, G. Bräuchle, H. Claus, A. Erb, G. Müller-Vogt and H. Wühl, 1993, Physica C **205**, 139.

Kund, M., and K. Andres, 1993, Physica C **205**, 32.

Lei, M., J.L. Sarrao, W.M. Visscher, T.M. Bell, J.D. Thompson, A. Migliori, U.W. Welp and B.W. Veal, 1993, Phys. Rev. B **47**, 6154.

Liechtenstein, A.I., and I.I. Mazin, 1995, Phys. Rev. Lett. **74**, 1000.

Liechtenstein, A.I., V.I. Anisimov and J. Zaanen, 1994, Phys. Rev. B **52**, R5467.

Manuel, A.A., A. Shukla, L. Hoffmann, T. Jarlborg, B. Barbiellini, S. Massidda, W. Sadowski, E. Walker, A. Erb and M. Peter, 1995, J. Phys. Chem. Solids **56**, 1951.

Massidda, S., Jaejun Yu, Key Taeck Park and A.J. Freeman, 1991, Physica C **176**, 159.

Mazin, I.I., 1999, Phys. Rev. B **60**, 92.

Mazin, I.I., and A.I. Liechtenstein, 1998, Phys. Rev. B **57**, 150.

Mazin, I.I., O. Jepsen, O.K. Andersen and A.I. Liechtenstein, 1992b, Phys. Rev. Lett. **68**, 3936.

Mazin, I.I., S.N. Rashkeev, A.I. Liechtenstein and O.K. Andersen, 1992c, Phys. Rev. B **46**, 11232.

Mazin, I.I., O.K. Andersen, A.I. Liechtenstein, O. Jepsen, V.P. Antropov, S.N. Rashkeev, V.I. Anisimov, J. Zaanen, C.O. Rodriguez and M. Methfessel, 1993, in: Lattice Effects in High-Temperature Superconductors, eds Y. Bar-Yam, T. Egami, J. Mustre-de Leon and A.R. Bishop (World Scientific, Singapore) p. 235.

Meingast, C., O. Kraut, T. Wolf, H. Wühl, A. Erb and G. Müller-Vogt, 1991, Phys. Rev. Lett. **67**, 1634.

Meingast, C., J. Karpinski, E. Jilek and E. Kaldis, 1993, Physica C **209**, 591.

Meingast, C., F. Gugenberger, O. Kraut and H. Wühl, 1994, Physica C **235–240**, 1313.

Merz, M., N. Nücker, E. Pellegrin, P. Schweiss, S. Schuppler, M. Kielwein, M. Knupfer, M.S. Golden, J. Fink, C.T. Chen, V. Chakarian, Y.U. Idzerda and A. Erb, 1997, Phys. Rev. B **55**, 9160.

Monthoux, P., 1993, J. Phys. Chem. Solids **54**, 1093.

Monthoux, P., A. Balatsky and D. Pines, 1992, Phys. Rev. B **46**, 14803.

Moolenaar, A.A., P.C.M. Gubbens, J.J. van Loef, M.J.V. Menken and A.A. Menovsky, 1996, Physica C **267**, 279.

Mueller, F.M., C.M. Fowler, B.L. Freeman, W.L. Hults, J.C. King and J.L. Smith, 1992, Phys. Rev. Lett. **68**, 3937.

Narozhnyi, V.N., and S.-L. Drechsler, 1999, Phys. Rev. Lett. **82**, 461.

Ohta, Y., T. Tohyama and S. Maekawa, 1991, Phys. Rev. B **43**, 2968.

Perdew, J.P., J.A. Chevary, S.H. Vosko, K.A. Jackson, M.R. Pederson, D.J. Singh and C. Fiolhais, 1992, Phys. Rev. B **46**, 6671.

Pickett, W.E., 1989, Rev. Mod. Phys. **61**, 115.

Pickett, W.E., 1997a, Phys. Rev. Lett. **78**, 1960.

Pickett, W.E., 1997b, Physica C **289**, 51.

Pickett, W.E., R.E. Cohen and H. Krakauer, 1990, Phys. Rev. B **42**, 8764.

Pickett, W.E., R.E. Cohen and H. Krakauer, 1991, Phys. Rev. Lett. **67**, 228.

Pickett, W.E., H. Krakauer, R.E. Cohen and D.J. Singh, 1992, Science **255**, 46.

Radousky, H., 1992, J. Mater. Res. **7**, 1917.

Randeria, M., 1996, J. Supercond. **9**, 471.

Rodriguez, C.O., A.I. Liechtenstein, I.I. Mazin, O. Jepsen, O.K. Andersen and M. Methfessel, 1990, Phys. Rev. B **42**, 2692.

Rodriguez, C.O., A.I. Liechtenstein, O. Jepsen, I.I. Mazin and O.K. Andersen, 1994, Comp. Mater. Sci. **2**, 39.

Sanfilippo, S., J. Beille, F. Pourtier, J.C. Villigier, D. Chateigner, P. Germi, M. Pernet and H. Noël, 1995, Solid State Commun. **96**, 391.

Schabel, M.C., C.-H. Park, A. Matsuura, Z.-X. Chen, D.A. Bonn, R.X. Liang and W.N. Hardy, 1998, Phys. Rev. B **57**, 6107.

Schilling, A., M. Cantoni, J.D. Guo and H.R. Ott, 1993, Nature **363**, 56.

Schneider, T., and H. Keller, 1992, Phys. Rev. Lett. **69**, 3374.

Shen, Z.-X., and D.S. Dessau, 1995, Phys. Rep. **253**, 1.

Singh, D.J., 1991, Phys. Rev. B **43**, 6388.

Singh, D.J., 1995, Plane waves, Pseudopotentials, and the LAPW Method (Kluwer Academic, Boston).

Smedskjaer, L.C., and A. Bansil, 1992, J. Phys. Chem. Solids **53**, 1657.

Staub, U., L. Soderholm, S.S. Kanthakumar, R. Osborn and F. Fauth, 1997, Europhys. Lett. **39**, 663.

Takenaka, K., Y. Imanaka, K. Tamasaku, T. Ito and S. Uchida, 1992, Phys. Rev. B **46**, 5833.

Tallon, J.L., C. Bernhard, H. Shaked, R.L. Hitterman and J.D. Jorgensen, 1995, Phys. Rev. B **51**, 12911.

Tanaka, S., 1994, Jpn. J. Appl. Phys. **33**, 1004.

Temmerman, W.M., Z. Szotek, B.L. Gyorffy, O.K. Andersen and O. Jepsen, 1996, Phys. Rev. Lett. **76**, 307.

Torrance, J.B., P. Lacorro, C. Asavaroenghcai and R. Metzger, 1991, J. Solid State Commun. **90**, 168.

Wang, N.L., Y. Chong, C.Y. Wang, D.J. Huang, Z.Q. Mao, L.Z. Cao and Z.J. Chen, 1993, Phys. Rev. B **47**, 3347.

Wei, S.-H., and H. Krakauer, 1985, Phys. Rev. Lett. **55**, 1200.

Welp, U., M. Grimsditch, S. Flechler, W. Nessler, J. Downey, G.W. Crabtree and J. Guimpel, 1992, Phys. Rev. Lett. **69**, 2130.

Welp, U., M. Grimsditch, S. Flechler, W. Nessler, B. Veal and G.W. Crabtree, 1994, J. Supercond. **7**, 159.

West, R.N., 1992, J. Phys. Chem Solids **53**, 1669.

Wu, M.K., J.R. Ashburn, C.J. Torng, P.H. Hor, R.L. Meng, L. Gao, Z.J. Huang, Y.Q. Wang and and C.W. Chu, 1987, Phys. Rev. Lett. **58**, 908.

Zakharov, A.A., H. Hylén, M. Qvarford, I. Lindau, M. Leandersson, M.B. Tsetlin and M.N. Mikheeva, 1997, Phys. Rev. B **56**, 9030.

Zhang, H., and H. Sato, 1993, Phys. Rev. Lett. **70**, 1697.

Zou, Z., K. Oka, T. Ito and Y. Nishihara, 1997, Jpn. J. Appl. Phys. Lett. **36**, L18.

Handbook on the Physics and Chemistry of Rare Earths
Vol. 30
edited by K.A. Gschneidner, Jr., L. Eyring and M.B. Maple

Chapter 194

ELECTRONIC 4f STATE SPLITTINGS IN CUPRATES

U. STAUB
Swiss Light Source, Paul Scherrer Institute, 5232 Villigen PSI, Switzerland

L. SODERHOLM
Chemistry Division, Argonne National Laboratory, Argonne, IL 60439, USA

Contents

List of symbols 491
List of abbreviations 492
1. Introduction 492
2. Formalism of the crystal field potential 494
2.1. Free-ion interactions 494
2.2. Crystal-field interactions: tensor formalism 495
2.3. Stevens equivalent operator method 496
2.4. Symmetry 497
2.5. Mean-field description 497
2.6. Parameter modeling 498
3. Rare-earth energy levels and wavefunctions 499
3.1. Experiments 499
3.2. Determination of CEF parameters 500
3.3. Experimental data: examples 502
3.3.1. $R_{2-x}Ce_xCuO_4$ 502
3.3.2. $RBa_2Cu_3O_x$ 504
3.4. Wavefunctions and transition probabilities 511
3.5. Calculated magnetic properties 514
4. Applications to high-T_c superconductors 516
4.1. Effect of superconductivity 516
4.1.1. Charge transfer 516
4.1.2. Local (in)homogeneities 518
4.2. s–f interactions 520
4.2.1. Relaxation measurements on CEF transitions 520
4.2.2. The exceptional influence of Pr 523
4.3. f–f interactions 528
4.3.1. Grain-aligned $HoBa_2Cu_3O_x$ 528
4.3.2. Ho^{3+} dimer excitations in $Y_{1-x}Ho_xBa_2Cu_3O_7$ 530
4.3.3. $R_{2-x}Ce_xCuO_4$ 532
4.4. f–phonon interactions 534
4.5. Tb^{3+} magnetic correlations: a perfect two-level system? 537
Acknowledgments 541
References 541

List of symbols

$a_M^{(i)}$	wave function coefficient of the CEF state
B_m^n	CEF parameters in tensor notation
B_n^m	CEF parameter in Stevens' notation
c	speed of light
C_m^n	tensor operator
e	charge of electron
e^{-2W}	Debye–Waller factor
$E_n, \hbar\omega_n$	energy of state n
F	magnetic form factor
f_k	Slater–Condon electrostatic integral
g	Landé splitting factor
H	magnetic field
$\hbar$	Planck's constant
H_{CEF}	crystal electric field Hamiltonian
I_{s-f}^{α}	anisotropic indirect exchange integral

J	total magnetic angular momentum	T_N	Neél temperature
J_{ex}, J_i^α	exchange coupling parameters	V	coupling matrix element between phonon and CEF excitation
$J(Q)$	Fourier transformed exchange coupling function	Δ	energy separation between two CEF states
k_B	Boltzmann's constant	δ	Dirac's delta function
L	orbital magnetic momentum	Γ	full width at half maximum of CEF transition
M	Projection of the total angular momentum on the z-axis	Γ_i	irreducible representation of ith CEF state
m_e	mass of electron	γ	gyromagnetic ratio
M^2	transition matrix element	γ_m^n, f_m^n	geometrical factors
$N(0)$	density of states at the Fermi surface	λ	mean field parameter
O_n^m	Stevens operator	μ_B	Bohr magneton
Q_α	αth component momentum transfer	ρ_n	probability that state Γ_n is occupied
$\langle r^n \rangle$	2nd moment of the 4f electron radial distribution	$\rho(r)$	charge distribution
S	spin magnetic momentum	ς_f	spin–orbit integral
$\frac{d^2\sigma}{d\Omega d\omega}$	double-differential neutron cross section	χ	susceptibility
T	temperature		
T_c	superconducting transition temperature		

List of abbreviations

R	Rare earth or yttrium	HF	Hartree–Fock
BCS	Bardeen–Cooper–Schrieffer	NQR	Nuclear quadrupolar resonance
INS	Inelastic neutron scattering	RKKY	Ruderman–Kittel–Kasuya–Yosida
CEF	Crystalline electric field		

1. Introduction

A fundamental understanding of the electronic properties of the CuO states in high-temperature superconductors has been the subject of intense experimental and theoretical efforts. Comparatively little work has been done to understand the electronic behavior of the rare-earth ions (R) that are often incorporated into these materials. In part this is because the R ion usually does not significantly influence the superconducting properties of the material, even though ions such as Gd or Dy have large magnetic moments. This behavior is in contrast to BCS-type superconductors in which even small concentrations of magnetic impurities suppress superconductivity.

Despite this lack of influence on superconductivity, the rare-earth sublattices often exhibit interesting magnetic behavior, including three-dimensional long-range ordering and two-dimensional and quasi two-dimensional ordering with finite correlation lengths. Magnetic ordering usually occurs only at temperatures lower than about 2.5 K. Unlike the conventional superconductors, in which the magnetic ordering and superconductivity

occur at similar temperatures, the copper oxides exhibit magnetic ordering on the rare-earth sublattice at temperatures typically 0.5–5% of the superconducting critical temperature. Therefore, these materials provide an opportunity to study the interactions and co-existence of superconductivity and magnetism from a different perspective.

In order to attain a fundamental understanding of the rare-earth magnetic properties, and also the interactions of the magnetic f states with the superconducting states, it is necessary to have a basic knowledge of the single-ion electronic properties of the f states. A knowledge of the f–state energies and wavefunctions provides the basis for the modeling of a variety of measurable properties, including magnetic susceptibilities, ordered moments and their directions. It is also possible to compare with experiment modeled g-values, Mössbauer and specific-heat spectra.

This review summarizes studies undertaken to characterize the electronic splittings of the rare-earth 4f states in high–T_c superconductors. A full crystal-electric-field (CEF) analysis is presented for R ions in two exemplary series of high-temperature superconductors, the electron superconductors R_2CuO_4 and the $RBa_2Cu_3O_7$ series. Most of the other known series, including $RBa_2Cu_4O_8$, $TlSr_2RCu_2O_7$ and $Pb_2Sr_2RCu_3O_8$, have R-site symmetries similar to that found in $RBa_2Cu_3O_7$. Therefore the single-ion CEF parametrization described herein can effectively be used to model R-ion electronic behaviors in these materials as well. In contrast, the R-site symmetries in R_2CuO_4 and $(Pr_{1.5}Ce_{.5})Sr_2Cu_2NbO_{10}$ are significantly different and therefore their electronic properties require an independent CEF analysis.

Whereas optical spectroscopy is the technique most often used to provide data about the splitting of the 4f configuration in a solid material, the conductivity of the high-temperature superconductors renders them opaque to optical photons. Most of the data available for analysis are obtained from inelastic neutron scattering (INS). INS is usually limited to energies less than about 150 meV, therefore most of the published data involve states within the Russell–Saunders ground level. Limited information about splitting of the free-ion terms is obtained from intermultiplet INS data, Raman spectroscopy, or from published work on R in LaF_3. The trends established in the CEF parametrization across a series, and the success with which the calculated energy levels and wavefunctions reproduce other electronic and magnetic data, provide confidence in the analysis.

This review is divided into two main parts. The first part introduces the CEF formalism used in the analysis, together with an overview of the method by which the potentials were determined. Systematic sets of CEF parameters are presented in tables, together with the energies, wavefunctions, and transition-matrix elements for each R in the series. These representations of the R-ion energetics form the basis from which to build an understanding of the magnetic properties of high-T_c superconductors.

The second part reviews published applications of CEF parametrization to the understanding of superconductivity. The use of the rare-earth f states as a local probe to monitor changes of the local charge distribution, and resulting models of clustering and percolative superconductivity, are discussed. Also discussed are s–f, f–f, and f–phonon interactions. Quantification of these interactions is important to the overall understanding of these unusual complex oxides.

2. Formalism of the crystal field potential

2.1. *Free-ion interactions*

The R-ion's valence f electrons are unavailable for bonding because they are buried within the outer s-, p- and d electron shells. As a consequence, the electronic properties exhibited by an R ion are well described by simple electrostatic, single-ion modeling. There are several excellent reviews in the literature about the treatment of the f-ion electronic properties (e.g. Judd 1963, Wybourne 1965, Newman 1971). We present here a brief introduction to establish the formalisms, nomenclature, and conventions used in this review.

Realizing that the core-electron shells are spherically symmetric, the non-relativistic Hamiltonian for a rare-earth free ion is represented by:

$$H = \sum_{i=1}^{N} \left(\frac{p_i^2}{2m} + \frac{Ze^2}{r_i} \right) + \sum_{i<j}^{N} \frac{e^2}{r_{ij}}. \tag{1}$$

A point nucleus of charge Ze is surrounded by N electrons with mass m and charge $-e$. The distance of the ith electron from the point nucleus is r_i and the distance of the ith to the jth electron is r_{ij}. The first summation in eq. (1) is spherically symmetric and does not remove any degeneracy within the f^N configuration, therefore it is neglected in our crystal-field treatment. The second summation represents the electrostatic repulsion between the f^N electrons and the coupling between their spin- and orbit-angular momenta. This term cannot be solved exactly, except for the one-electron case; a problem that is overcome by assuming that each electron is moving independently in a spherically averaged potential field, $U(r_i)$. Variables can be separated as for the hydrogen atom, and the angular terms can be evaluated explicitly. However, because the central-field potential $U(r_i)$ is undefined in the effective-operator or parametric approach, the radial integrals must be determined by fitting experimental data. The Hamiltonian for the free-ion interaction H_{FI} can be written as (Crosswhite and Crosswhite 1984):

$$H_{\mathrm{FI}} = H_{\mathrm{EI}} + H_{\mathrm{SO}} (+H_{\mathrm{IN}}), \tag{2}$$

with

$$H_{\mathrm{EI}} = \sum_{k=0,2,4,6} f_k F^k, \qquad H_{\mathrm{SO}} = A_{\mathrm{SO}} \zeta_{\mathrm{f}}. \tag{3,4}$$

The parameters F^k and ζ_{f} correspond to Slater–Condon electrostatic and spin–orbit integrals, respectively, and f_k and A_{SO} represents matrix elements for the angular parts of these electrostatic and spin–orbit interactions. The F^k integrals as used in the effective-operator approach are different from those used in the Hartree–Fock (HF) approach because they absorb some effects of configuration interaction that are not included in the

HF definition. H_{IN} includes higher order corrections, such as those representing two- and three-body interactions (Morrison and Rajnak 1971, Crosswhite and Crosswhite 1984).

Whereas the total orbital (L) and spin (S) angular momenta commute with H_{EI}, H_{SO} commutes only with the resultant, J ($=L+S$). Therefore, the free-ion Hamiltonian (2.1.2) is diagonal in J, and splits the 4f configuration into levels that remain degenerate in M_J.

2.2. *Crystal-field interactions: tensor formalism*

When an f ion is situated in a crystalline lattice the free-ion energy levels are perturbed by the electrostatic potential arising from the neighboring charges. The Hamiltonian that includes the crystal field (CEF) potential can be written as

$$H = H_{FI} + H_{CEF}, \tag{5}$$

where

$$H_{CEF} = V_{CEF}(r) = \int \frac{\rho(\boldsymbol{R})}{|\boldsymbol{R}-\boldsymbol{r}|}\,\mathrm{d}\boldsymbol{R}, \tag{6}$$

and $\rho(\boldsymbol{R})$ corresponds to the charge distribution around the rare-earth ion. This potential partly lifts the $(2J+1)$ degeneracy of the free-ion levels. The wavefunction for the state (i) has the form

$$\sum_{L,S,J,M} a^{(i)}_{L,S,J,M}\,|L,S,J,M\rangle\,. \tag{7}$$

These states do not have integer values of quantum numbers L, S and J, which necessitates the use of operator techniques for a complete description of the free-ion and crystal-field interactions. An elegant description using tensor operators (see e.g. Judd 1963) is expressed as

$$H_{CEF} = \sum_{n,m,i} B^n_m\,(C^n_m(i) + C^n_{-m}(i))\,. \tag{8}$$

B^n_m can be regarded as coefficients of expansion (CEF parameters) to be determined empirically from the data. When considering f electrons, the only non-zero contributions to the summation correspond to the even values of $n \leqslant 6$. $C^n_m(i)$ correspond to the mth component of a spherical tensor operator of rank n, which is dependent on the ith electron. These components are defined in terms of spherical harmonics $Y_{nm}(\theta_i\phi_i)$ such that

$$C^n_m(i) = \sqrt{\frac{4\pi}{2k+1}}\,Y_{nm}(\theta_i\phi_i). \tag{9}$$

$\theta_i\phi_i$ are the angular positions of the ith electron. The non-zero values of $C^n_m(i)$ are further limited by the point symmetry of the rare-earth site. Specifically, the presence

of a reflection plane, σ_v, which is present for all the structures discussed herein, restricts the B_m^n's to their real components; i.e. the imaginary CEF parameters are equal to zero by symmetry.

2.3. *Stevens equivalent operator method*

As outlined by Stevens (Stevens 1952), simple relations exist between the matrix elements of the potential operators and the appropriate angular momentum operators for states with $2J$ integer. The CEF potentials are described as a perturbation of the $^{2S+1}L_J$ ground level. This is a good approximation if the CEF potential is small compared to the free-ion interaction, that is, when the overall CEF splitting of the level is small compared to the splitting between the next higher J multiplets. By writing the potential in momentum space the corresponding Hamiltonian operator for the crystal field is written as

$$H_{\mathrm{CEF}} = \sum_{n=0}^{6} \sum_{m=0}^{n} B_n^m O_n^m. \tag{10}$$

Here the B_n^m are the CEF parameters determined experimentally, and the O_n^m are the Stevens operators (Stevens 1952). In order to compare directly the crystal-field parameters for different rare-earth ions in an isostructural series, it is more convenient to express these parameters in terms of A_n^m's, which are related to the B_n^m's through:

$$B_n^m = A_n^m \langle r^n \rangle \theta_j^n, \tag{11}$$

with the proportionality constants $\theta_j^n = \alpha, \beta, \gamma$ for $n = 1, 2, 3$ respectively. Values of $\langle r^n \rangle$, the 2nd moment of the 4f electron radial distribution, have been previously tabulated (Freeman and Watson 1962, Abragam and Bleaney 1970, Taylor and Darby 1972). The wavefunction for state (i) is described by

$$\sum_{M=-J}^{J} a_M^{(i)} |J, M\rangle, \tag{12}$$

with $\sum_M (a_M^{(i)})^2 = 1$ to satisfy the normalization condition.

The Stevens operator method represents a convenient simplification for evaluating the matrix elements of the CEF potential between wavefunctions specified by a single value of the angular momentum, J. It eliminates the necessity to go back to single-electron wavefunctions, and information about the higher J levels is not required for this treatment. Whereas the assumption of an isolated ground level may be appropriate for simple metallic systems, where the energy splitting is usually in the order of a few tens of meV, the rare-earth superconductors under consideration herein exhibit crystal-field splittings of the order of 100 meV. Therefore, admixing between different levels is significant, particularly for the light R ions. This admixture vitiates calculations based on

Table 1
Conversion between D^n_m and B^m_n [a]

D^n_m	D^2_0	D^2_2	D^4_0	D^4_2	D^4_4	D^6_0	D^6_2	D^6_4	D^6_6
Factor	2	0.813	8	1.265	0.956	16	1.561	1.426	1.053

[a] $B^m_n = B^n_m \theta^n_j / D^n_m = B^{n\,*}_m \theta^n_j$ where $\theta^n_j = \alpha, \beta, \gamma$ for $n = 1, 2, 3$ are proportional constants depending on the J level of the R under consideration. (B^m_n, Stevens formalism; B^n_m, tensor formalism; $B^{n\,*}_m$, notation by ETH group (Mesot et al. 1993b). Further details can be found elsewhere (Taylor and Darby 1972).

a simple Stevens CEF treatment. Therefore, in order to compare the effect of the crystal field across all the R ions within the various series of high-T_c oxides, **we utilize a full tensor treatment for all work presented in this review.**

A comparison between CEF parameters obtained using tensor operators and the commonly used Stevens formalism can be made by a numerical conversion (see table 1). We follow the common convention of writing the tensor parameters as B^n_m and inverting the indices for the Stevens parameters, B^m_n. Table 1 also contains the conversation factors for a comparison with parameters used by a group at the ETH Zurich. Further details about conversions between various formalisms are available elsewhere (Bleaney and Stevens 1953, Hutchings 1964, Kassman 1970). We stress that care is necessary when comparing parameters obtained by different groups and different techniques.

2.4. *Symmetry*

Irrespective of the formalism used to describe the crystal field, the point symmetry of the electrostatic potential exerted at the R site significantly restricts the non-zero matrix elements that need to be evaluated. The number of non-vanishing B^n_m's depends on the crystal-site symmetry of the paramagnetic ion because the Hamiltonian must be invariant with respect to site-symmetry operations. Detailed descriptions of these symmetry restrictions, and their derivations, can be found in the literature (Wybourne 1965, Dieke 1968).

2.5. *Mean-field description*

For a description of effects of rare-earth exchange interactions (including superexchange and dipole exchange) on the CEF, a mean-field term is added as a perturbation to the crystal-field Hamiltonian. The mean-field term is expressed as

$$H_{\mathrm{MF}} = -\lambda \mu_B \boldsymbol{H} \langle \boldsymbol{L} + 2\boldsymbol{S} \rangle = -\lambda \langle \boldsymbol{L} + 2\boldsymbol{S} \rangle (\boldsymbol{L} + 2\boldsymbol{S}). \tag{13}$$

Here $\boldsymbol{H}$ corresponds to the magnetic field at the R site, which may originate from cooperative ordering, i.e. an internal field, or from an applied, external field. λ represents the mean-field parameter. The mean-field approximation leads to a reasonable description of the influence of magnetic ordering on the CEF splitting when the exchange

interaction is small. This treatment remains a single-ion approximation, and therefore it is not sufficient to describe collective excitations (correlation between magnetic moments). Instead, collective excitations are usually described using the random-phase approximation formalism as discussed in sect. 4.3.

2.6. *Parameter modeling*

A parametric description of the energy states arising from a rare-earth f^n configuration in a crystal lattice must account for the electron–electron repulsion, spin–orbit coupling, and crystal-field interactions. In a classic study of R ions doped into LaF_3 (Carnall et al. 1988, 1989), optical data, obtained over an energy range of 0–5000 meV (0–40 000 cm^{-1}), were fit using 20 parameters to determine the free-ion levels, and an additional 9 CEF parameters appropriate to the C_{2v} site symmetry. Thus, 29 parameters were fit systematically to the optical data from 10 different R ions. Unfortunately, high-T_c oxides are opaque to optical radiation, therefore the data used for fitting are limited to those obtained by inelastic neutron scattering, and to a limited extent, Raman spectroscopy. Inelastic neutron scattering data cover an energy to less than about 200 meV, which usually limits the observable transitions to those within the ground multiplet. Depending on the multiplicity of the ground J multiplet, and the transition probabilities between the various states, there may be a very restricted set of data available to model the crystal field. More data can be used if it is assumed that the CEF potential is similar for all the rare earths in an isostructural series of compounds, and then fitting spectra obtained from more than one rare earth. Nonetheless, modeling of the CEF is often used to determine a set of crystal-field parameters to serve as a starting point for fitting the data, and determining scaling between data from different rare earths. The modeling can also serve to restrict the ratios of the various components of a specific rank tensor.

Crystal-field parameters are determined from a simple point-charge approximation using

$$B_m^n = e\,|e| \sum_i Z_i \frac{f_n^m(\theta_i, \phi_i)}{(|\boldsymbol{R}_i - \boldsymbol{r}|)^{2n+1}} \langle r^n \rangle , \tag{14}$$

where $f_m^n(\theta_i,\phi_i)$ are geometric factors (Hutchings and Wolf 1964). This modeling generally gives good ratios of $B_m^n/B_{m'}^n$ for a given n, even though the magnitude of the individual parameters may be unrealistic. In order to overcome this problem, superposition modeling was used. This modeling is based on the idea of separating the geometrical and physical information contained in the crystal-field parameters (Bradbury and Newman 1967, Newman and Ng 1989). The crystal-field parameters for superposition modeling are expressed as

$$B_m^n = \sum_i \bar{B}_n(R_i)\, K_{nm}(\theta_i, \phi_i) \langle r^n \rangle , \tag{15}$$

where $\bar{B}_n(R_i)$ are intrinsic parameters, which are assumed to have a power-law dependence to the ligand distances:

$$\bar{B}_n(R_L) = \bar{B}_n(R_0)\left(\frac{R_0}{R}\right)^{t_n}. \tag{16}$$

$\bar{B}_n(R_0)$ and the exponent t_n are obtained from a set of well-determined crystal-field parameters, and then corrected for ligand distance in the system of interest. $K_{kq}(\theta_L,\phi_L)$ are coordination factors similar to $f_n^m(\theta_i,\phi_i)$ in eq. (14), which are determined only by the angular coordinates of the surrounding ligands. These factors are essentially tesseral harmonics, and have been tabulated by Newman and Ng (1989) and Hutchings (1964). The parameters t_n compensate in a simple phenomenological way the inaccuracies of the point-charge model, which would lead to $t_n = 3$, 5 and 7 for $n = 2$, 4 and 6, respectively. This modeling has demonstrated success in the analysis of optical data across the rare-earth garnet series (Newman and Stedman 1969).

3. Rare-earth energy levels and wavefunctions

3.1. *Experiments*

An understanding of the single-ion properties of rare-earth ions in high-T_c compounds requires a fundamental understanding of the electronic structure of the f ion. The energies and wavefunctions of the states that arise from an f^n configuration under site-specific conditions can be used to model a variety of single-ion and cooperative phenomena. Details about the f-ion configuration splitting can be obtained from a crystal-field analysis as discussed in sect. 2. Most of the published data used for this analysis have been obtained from Raman spectroscopy or inelastic neutron scattering (INS). Raman scattering can probe magnetic transitions, but selection rules only allow f–f transitions when the absorbing ion sits on an acentric lattice site. Such is the case for R in the electron superconductor series, $R_{2-x}Ce_xCuO_4$ (R = Sm, Pr, Nd). Limited studies have been conducted for this purpose, e.g. by Jandl et al. (1995), Sanjurjo et al. (1995) and Strach et al. (1996). INS does not carry the same symmetry restrictions for magnetic transitions and therefore it has been the most widely used technique for the study of fundamental f-ion electronic and magnetic excitations for these optically opaque materials. Recently, an infrared study on $NdBa_2Cu_3O_6$ has been reported, which observed a relatively large number of f–f transitions (Martin et al. 1999).

Neutrons are nuclear particles with half-integral spins which can easily interact with magnetic moments in materials. The neutron scatters inelastically as a result of either magnetic or structural excitations, e.g. phonons. Distinguishing between scattering from magnetic versus vibrational processes requires temperature- and/or Q-dependent information. The Q dependence of a magnetic excitation is governed by the square of its magnetic form factor, which for most rare earths decreases with increasing Q. The

temperature dependence of magnetic excitations is governed by Boltzmann statistics. For example, ground-state transitions decrease in intensity with increasing temperature as the ground state is depopulated. In contrast, vibronic excitations increase with increasing Q and temperature and therefore can be separated from the CEF excitations.

The INS cross section for a magnetic excitation between the CEF states Γ_n and Γ_m of an isolated rare-earth ion is given in the dipole approximation by (Marshall and Lovesey 1971)

$$\frac{\mathrm{d}\sigma}{\mathrm{d}\Omega\,\mathrm{d}\omega} = \left(\frac{\gamma e^2}{m_e c^2}\right)\frac{k_f}{k_i}\,\tfrac{1}{2}\,|F(Q)|^2\,\mathrm{e}^{-2W}\rho_n \times \sum_{\alpha,\beta}(\delta_{\alpha,\beta}-Q_\alpha Q_\beta)\,\langle\Gamma_n\,|L_\alpha+2S_\alpha|\,\Gamma_m\rangle\,\langle\Gamma_m\,|L_\beta+2S_\beta|\,\Gamma_n\rangle\,\delta(\hbar\omega+E_n-E_m), \tag{17}$$

with $\alpha,\beta=x,y,z$; $\gamma e^2/m_e c^2$ is a prefactor; k_f and k_i are the final and incident neutron wavevectors, respectively; $F(Q)$ is the magnetic form factor; e^{-2W} is the Debye–Waller factor; ρ_n is the probability that the state Γ_n is occupied; L_α and S_α are the α components of angular and spin operator; and E_n (E_m) corresponds to the energy of state Γ_n (Γ_m). The function $(\delta_{\alpha,\beta}-Q_\alpha Q_\beta)$ ensures that only components of the spin systems perpendicular to the momentum transfer $\boldsymbol{Q}$ contribute to the cross section. This factor reduces to $\frac{2}{3}$ when using a polycrystalline average (powder samples) $\boldsymbol{Q}\rightarrow Q$. When using Stevens' formalism to describe the CEF potential then $L_\alpha+2S_\alpha$ reduces to $g_J J_\alpha$. Further details can be found elsewhere (Marshall and Lovesey 1971, Squires 1978). We note that for transitions between CEF-split states from the ground to excited J-levels, the Q dependence is not described by a simple form factor, and may even differ for transitions with different final states within the same J-level (fig. 1) (Staub et al. 1997b).

Transitions between crystal-field states are observed as peaks in the INS data, thus providing information about the relative energies of the states within the Russell–Saunders ground level. These data normally have an energy resolution of some fraction of a meV. The intensities of the peaks provide direct information about the magnetic strength coupling the states. However, to obtain absolute values for the observed intensities, a careful data calibration and correction procedure has to be applied, which leads to an overall accuracy of not better than 5%. In addition, multiple peaks may not be fully resolved or they may have asymmetric line shapes, further complicating the extraction of accurate intensities or intensity ratios. A successful parametrization of these data requires correct symmetry and state assignments to all observed transitions. These assignments for a given material are sometimes neither straightforward nor unique.

3.2. *Determination of CEF parameters*

Herein we present a set of crystal-field parameters for R ions in the two representative sites most commonly found in high-T_c superconductors. We focus on the R sites in $R_{2-x}Ce_xCuO_4$ and $RBa_2Cu_3O_x$ because they represent two distinctly different crystal-field environments. Most of the other series, including the $Pb_2Sr_2R_{1-x}Ca_xCu_3O_8$,

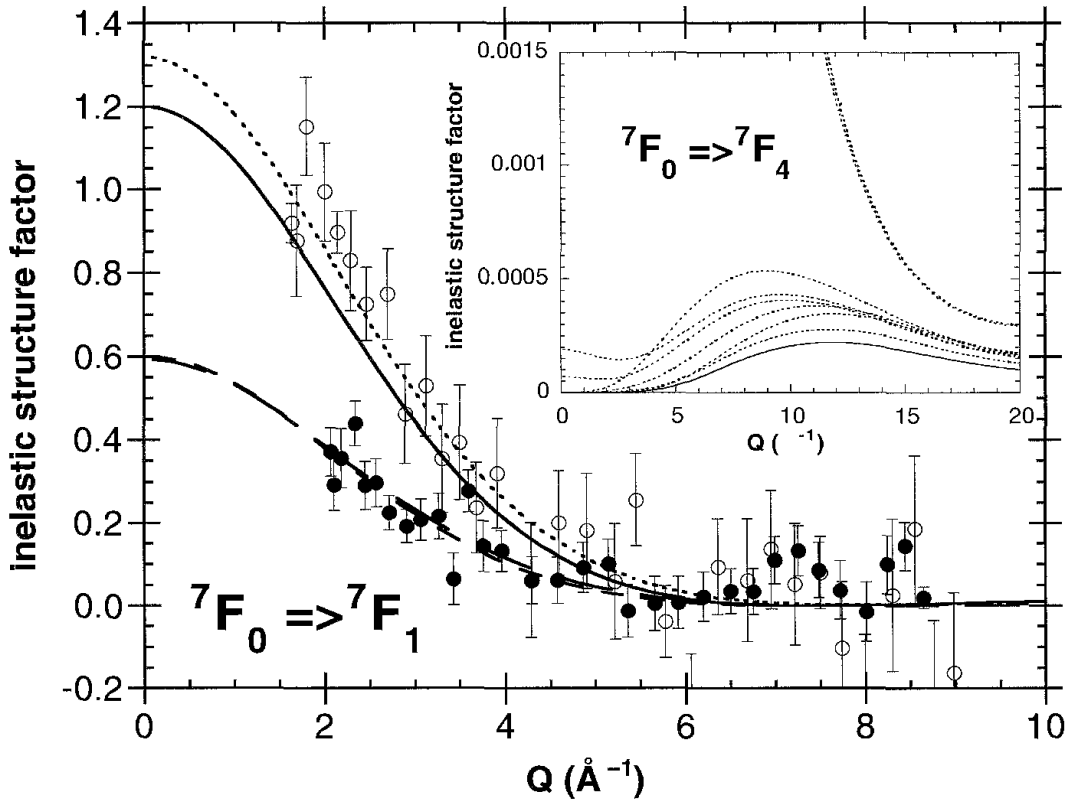

Fig. 1. Calculated and observed Q-dependence of transitions from the $^7F_0$ to the CEF split $^7F_1$ multiplet of Eu^{3+} in $EuBa_2Cu_3O_7$ (Staub et al. 1997b). Inset: Calculation for transitions into the $^7F_4$ multiplet. The solid lines correspond to the intensities into the unsplit multiplets and the dotted lines to individual transitions.

$Bi_2Sr_2R_{1-x}Ca_xCu_3O_8$, $RBa_2Cu_4O_8$ and $R_2Ba_4Cu_7O_{14+x}$ systems exhibit a very similar electrostatic environment to that found for $RBa_2Cu_3O_x$. We use these representative sets of parameters to derive energy-level schemes, transition probabilities, and single-ion magnetic properties. These results are presented in tabular form in order to provide a basis for the calculation of a variety of single-ion or cooperative properties of an R ion in these high-T_c materials.

The determination of a reliable set of CEF parameters from the available data is a non-trivial problem. In addition to the free-ion parameters, five independent CEF parameters are needed for tetragonal symmetry, and nine for orthorhombic symmetry. Because of the non-linearity of the parameter space, good starting estimates are indispensable. Once a reliable set of crystal-field parameters has been determined for one R within an isostructural series, these values can be extrapolated to other members of the same series (Goodman et al. 1991). We have used free-ion parameters from an independent optical study of the series LaF_3:R (Carnall et al. 1989), except for R = Eu, where some limited information is available from the observed transitions into excited J-multiplets (Staub et al. 1997b). It is clear that the use of these fluoride parameters in an intermediate-coupling treatment results in a significant improvement over the treatment of isolated ground levels following the procedures outlined by Stevens (1952).

Point-charge and/or superposition modeling have been used both to provide initial estimates of CEF parameters for refinement, and to provide an independent check that the parameters obtained from the fitting procedure are physically meaningful. The reproduction of the energies and intensities of magnetic transitions for several R from an isostructural series provides further confidence in the CEF parametrization.

3.3. *Experimental data: examples*

3.3.1. $R_{2-x}Ce_xCuO_4$

Compounds with the stoichiometry R_2CuO_4 crystallize in the space group I_4/mmm, with the rare earth on a tetragonal site with D_{4h} symmetry. Many studies have been performed on these compounds (see, e.g., Boothroyd et al. 1990, 1992, Staub et al. 1990, Loong and Soderholm 1992, 1993, Muzichka et al. 1992, Dufour et al. 1995, Jandl et al. 1995). Example energy spectra, obtained from the parent compound Nd_2CuO_4, are shown in fig. 2 (Loong and Soderholm 1993). The Nd^{3+} $J=9/2$ ground multiplet is split into five Kramers doublets ($3\Gamma_6$ and $2\Gamma_7$). All the ground-state transitions are observed because

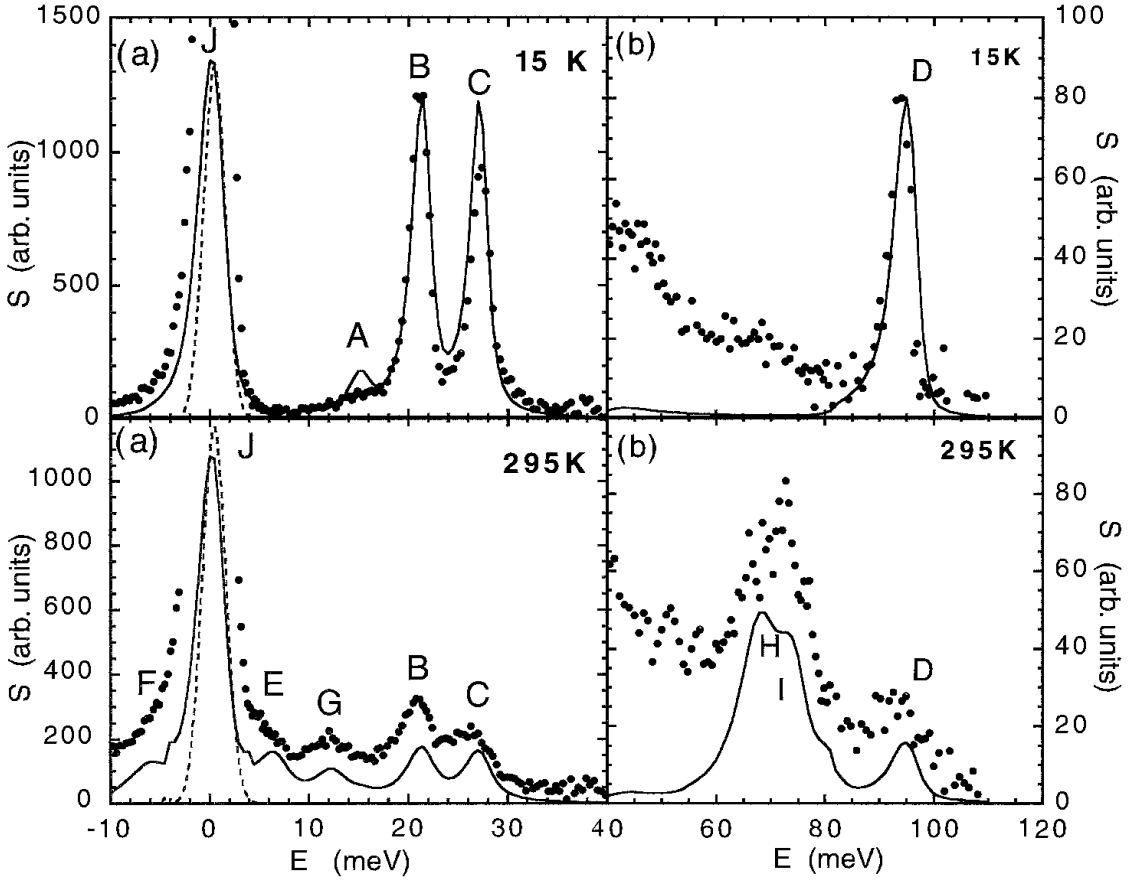

Fig. 2. INS spectra obtained from Nd_2CuO_4 (Loong and Soderholm 1993). The labels correspond to assigned CEF transitions and the solid line represents the spectrum calculated from the CEF fit.

Table 2
Observed energies and representations of the CEF states of the ground-state, first*, second**, and third*** excited multiplets of R^{3+} in R_2CuO_4

	E_n [a] (meV)		E_n [b] (meV)		E_n [c] (meV)	
R	Pr	i	Nd	i	Sm	i
(J)	(4)	Γ_i	(9/2)	Γ_i	(5/2)	Γ_i
$n=0$	0	4	0	6	0	7
1	18.1	5	14.9	7	–	
2	–	5	20.8	6	24.3	7
3	84		25.5	7	–	
4	88	5	93.2	6	146*	7
5	–	5	246*	6	–	
6	92		248*	6	170*	7
7	292**		249*	7	–	
8	292**		–		294**	7
9	292**		295*	6	–	
10	–		299*	7	–	
11	–		486**	6	318**	7
12	–		–		–	
13	335**		490**	6	–	
14			–		466***	7
15			538**	6	–	
16			–		483***	7
17			–			
18			–			
19			–			
20			–			
21			734***	6		
22			794***	6		
23			–			
24			–			
25			819***	6		

[a] Boothroyd et al. (1992), Sanjuán and Laguna (1995).
[b] Boothroyd et al. (1992), Jandl et al. (1995).
[c] Strach et al. (1996).

they have non-zero transition probabilities. There are three peaks at 21, 26 and 93 meV. In addition, there are transitions observable between excited states at elevated temperatures. These limited data are augmented with results from interlevel transitions observed by INS (Boothroyd et al. 1992) and from Raman spectroscopy (Dufour et al. 1995, Jandl et al. 1995). Taken together, there are sufficient data to determine the 5 CEF parameters. The parameters obtained from this analysis extrapolate well to represent the spectra obtained from Pr_2CuO_4 and Sm_2CuO_4, the only other R_2CuO_4 compounds for which data are available. The ability of the CEF model to reproduce the available neutron and Raman data from across the R_2CuO_4 series provides confidence in the analysis.

Table 2 lists the state energies and symmetries for the R_2CuO_4 system (R = Nd, Pr, Sm) system. The best set of CEF parameters derived from these data is listed in table 3.

Table 3
Crystal-field parameters in Wybourne notation (Wybourne 1965) for the R^{3+} ions in the R_2CuO_4 series judged to be the most accurate presented in the literature.

Species	B_0^2 (meV)	B_0^4 (meV)	B_4^4 (meV)	B_0^6 (meV)	B_4^6 (meV)	Reference
Sm	−40.8	−189	206	29.6	166.8	(Strach et al. 1996)
Nd	−40.5	−280.7	204.5	26.7	183.1	(Jandl et al. 1995)
Pr	−70.3	−211.1	191.7	53.9	229.2	(Loong and Soderholm 1993)
	−28	−301	228	26	224	(Boothroyd et al. 1992)

3.3.2. $RBa_2Cu_3O_x$

Isostructural compounds within the series $RBa_2Cu_3O_x$ are reported for R = Y, La–Yb (except Ce and Tb). The oxygenated samples ($x \geqslant 6.5$) crystallize in the orthorhombic space group Pmmm, with the rare earth on a site of D_{2h} symmetry. At lower oxygen content ($x \leqslant 6.45$) the samples are tetragonal (space group P4/mmm) with the rare earth on the site of D_{4h} symmetry.

Historically, the initial determination of a set of crystal-field parameters for the $RBa_2Cu_3O_x$ system was based on the assumption that the R site symmetry was only slightly distorted from cubic (Furrer et al. 1988). This assumption significantly simplified the problem because a cubic CEF potential has only two independent parameters. By judiciously choosing the Ho^{3+} ion, which has a high multiplicity ($J = 8$), and by utilizing the relationships in the CEF parameters outlined by Lea, Leask and Wolf (1962), the magnitude of the fourth- and sixth-order crystal-field parameters are successfully estimated. These estimates were very close to the values determined independently by superposition modeling (Nekvasil 1988). An estimate of a second-order, B_0^2 parameter, is also required. This value is derived from either Gd Mössbauer data (Alp et al. 1987) or from the CEF splitting of the Eu $J = 1$ first excited multiplet (Staub et al. 1995a). An independent check of the sign of B_0^2 is obtained by calculating the single-ion susceptibility and determining the mean direction, because the sign of B_0^2 often defines the mean direction of the magnetization (in or out of plane).

As an example for data from the $RBa_2Cu_3O_x$ series, we have selected the R = Yb analog because of its well-resolved, high-energy CEF states. The eight-fold degeneracy of the ground multiplet $^2F_{7/2}$ of Yb^{3+} in $YbBa_2Cu_3O_7$ is split by an orthorhombic CEF into four Kramers doublets with Γ_5 symmetry. Therefore, all three ground-state CEF transitions have a non-zero transition probability. Figure 3 shows the characteristic energy spectrum of neutrons scattered from $YbBa_2Cu_3O_7$ (Guillaume et al. 1992). The intensity distribution below 80 meV is reminiscent of the phonon scattering seen in the $RBa_2Cu_3O_x$ compounds. At higher energies three well-defined ground-state CEF transitions are observable.

The plots in fig. 4 show the main CEF parameters found in the literature. These plots include mainly one experimental parameter set for each R^{3+} per research group (see also table 5). The two open circles, corresponding to CEF parameter for Sm and Dy, were

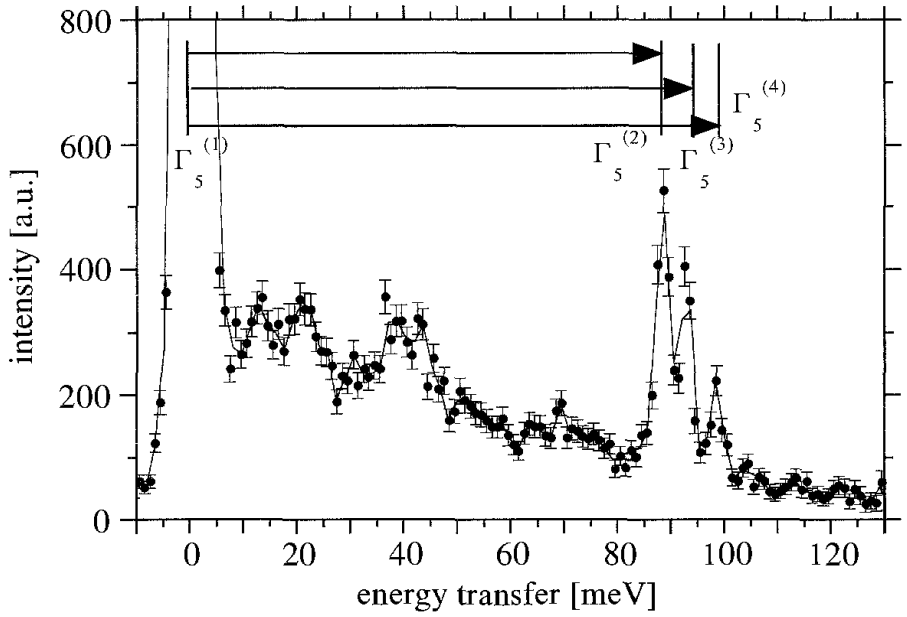

Fig. 3. INS spectra obtained from $YbBa_2Cu_3O_7$ (Guillaume et al. 1992). The energy level scheme determined from these data is indicated above the data.

obtained by refitting the published experimental data. For the Sm fit, the second excited CEF state within the ground level has been reassigned to higher energies than previously reported (Guillaume et al. 1995). This reassignment is based on new data obtained from Raman spectroscopy (Strach et al., personal communication). For the Dy fit, the previously published CEF parameters (Allenspach et al. 1989b) did not follow the trend established for the entire R series.

Independent data on the CEF potential at the R site in the $RBa_2Cu_3O_x$ and related series have been obtained from studies on $Pb_2Sr_2R_{1-x}Ca_xCu_3O_8$ compounds. Whereas the true crystal structure is rather complex (Marezio et al. 1990, Xue et al. 1993), the R near neighbors are tetragonally coordinated and the overall CEF is very similar to that observed in the $RBa_2Cu_3O_x$ series. Within the Pb-based series, single-phase samples have been reported for R = Y, La–Lu (Schneemeyer et al. 1989). As an example of experimental results for the $Pb_2Sr_2R_{1-x}Ca_xCu_3O_8$ series, we chose the non-Kramers ion $R = Ho^{3+}$ and $x = 0$, which is the non-superconducting parent compound (undoped). The $^5I_8$ ground-multiplet of Ho^{3+} is split under the pseudo-tetragonal site symmetry of the CEF into four doublets and nine singlets. Excitations between many of these states are allowed, e.g., eight ground-state transitions are observed at low temperatures as shown in fig. 5 (Soderholm et al. 1995). We note that Ho^{3+} in $Bi_2Sr_2(R/Ca)Cu_2O_8$ exhibits a very similar splitting (Staub et al. 1991). The true R-site symmetry in $Pb_2Sr_2(R/Ca)Cu_3O_8$ is lower than tetragonal (Skanthakumar and Soderholm 1996, Staub et al. 1998a). The result of this lower symmetry is a very slight splitting of some of the magnetic peaks, as shown in fig. 5. This splitting provides corroborating evidence for the symmetry assignments to these peaks.

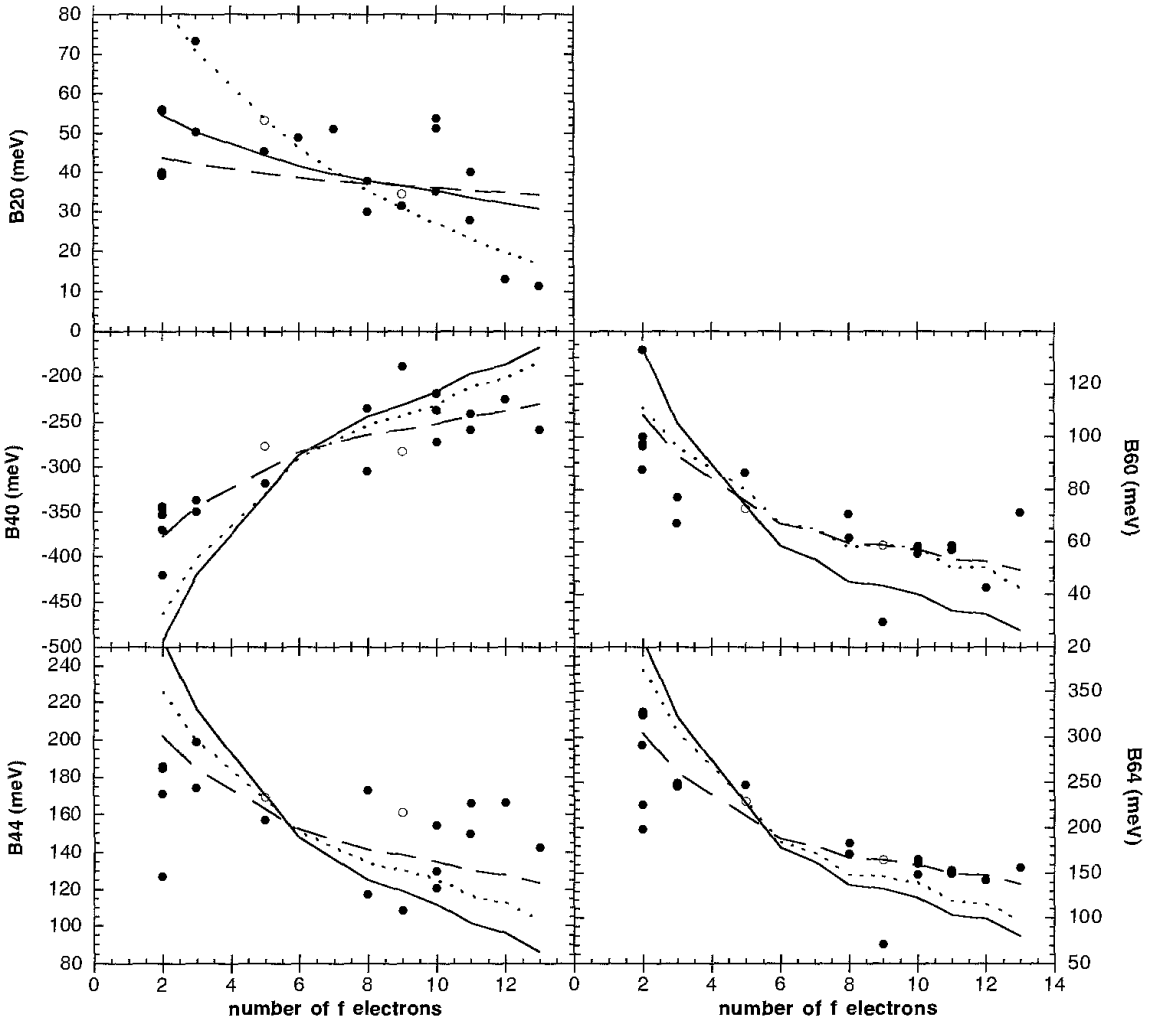

Fig. 4. Main CEF parameters from the $RBa_2Cu_3O_7$ series taken from table 5 (solid circles from the literature, open circles from the fit). The lines represent the R-dependence modeled with an $\langle r^n \rangle$ contribution (solid line), structural and $\langle r^n \rangle$ contribution (dotted line) and $0.61\langle r^n \rangle$ contribution (dashed line).

The absolute values of the CEF parameters obtained from the CEF analysis of the R^{3+} site in $RBa_2Cu_3O_x$ are seen to increase for increasing ionic size (decreasing number of f electrons) across the R series. This result is generally expected from the behavior of the second moment of the radial distribution $\langle r^n \rangle$. Of the general trends established for the individual parameters, the most poorly defined is that for the second-order parameters (fig. 4). This result is expected because the second-order parameters are strongly influenced by longer-range interactions and hybridization, which are most poorly modeled within the simple approximation used here. The second-order parameter is best defined for Eu.

Three simple extrapolation schemes have been applied to describe the R-dependence of the CEF parameters. First, if the changes in CEF parameters are attributed to the systematic variation of $\langle r^n \rangle$ (eq. 11) (Freeman and Watson 1962) the changes are

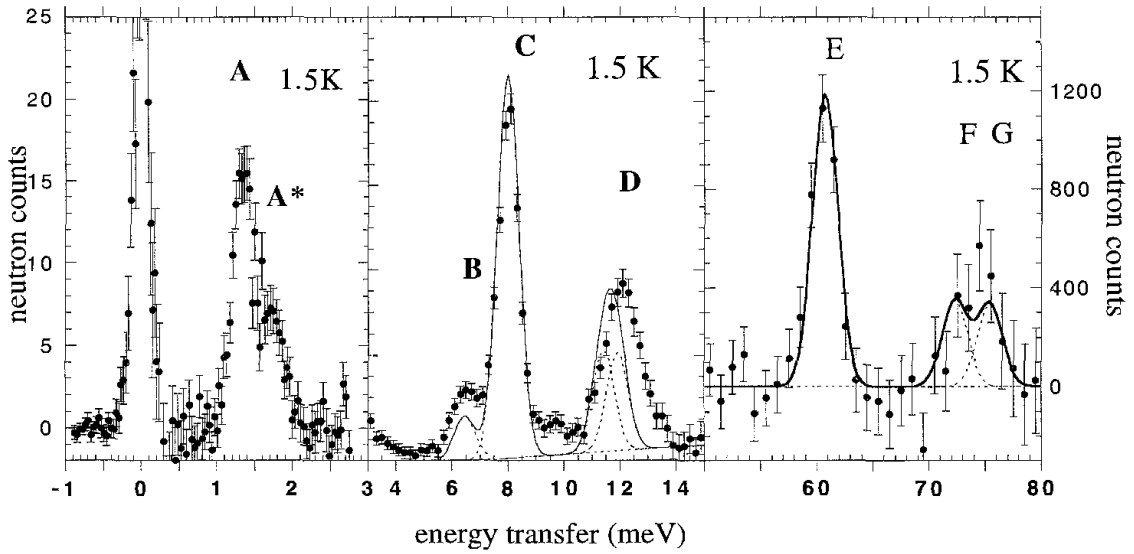

Fig. 5. INS energy spectra from $Pb_2Sr_2HoCu_3O_8$ (1.5 K) (Soderholm et al. 1995). The labels correspond to assigned CEF excitations and the lines represent the best CEF calculations.

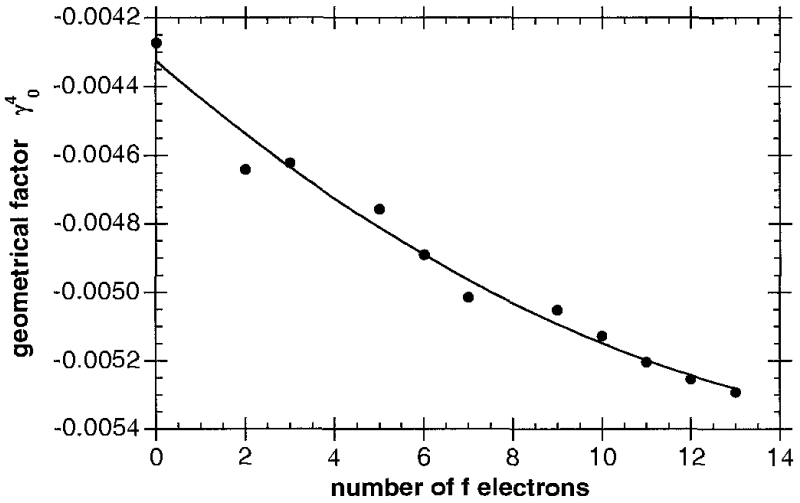

Fig. 6. Example of a geometrical factor (γ_0^4) calculated for $RBa_2Cu_3O_7$ from the structural data of (Guillaume et al. 1993). The line corresponds to a smoothed function used for the model in fig. 4.

overestimated (full line in fig. 4). Second, if the influence of the changing local-site structure (eq. 16) is added to the $\langle r^n \rangle$ dependence (dotted line) the agreement improves for the 4th and 6th order parameters, however, the changes in B_0^2 are overestimated. The structural (Guillaume et al. 1993) influence alone is exemplified for B_0^4 in fig. 6. Third, if only 61% of the changes from $\langle r^n \rangle$ alone are used, as proposed by Goodman et al. (Goodman et al. 1991), the result is shown as the broken line in fig. 4. This is by far the best approximation except for the second-order term, for which the full contribution of the $\langle r^n \rangle$ dependence best describes the systematic variation of the observed parameters. This

Table 4

Observed energies and representations of the CEF states of the ground-state, first (*) and second (**) excited multiplets of R^{3+} in $RBa_2Cu_3O_7$. For R = Pr and Tb, the values of the CEF energies (within the ground state multiplet) in the very similar $Pb_2Sr_2RCu_3O_8$ series were taken.

	E_n[b]	i	E_n[c]	i	E_n[d]	i	E_n[e]	i	E_n[f]	i	E_n[g]	i	E_n[h]	i	E_n[i]	i	E_n[j]	i	E_n[k]	i
R	Pr	Γ_i	Nd	Γ_i	Sm	Γ_i	Eu	Γ_i	Tb	Γ_i	Dy	Γ_i	Ho	Γ_i	Er	Γ_i	Tm	Γ_i	Yb	Γ_i
(J)	(4)		(9/2)		(5/2)		(0)		(6)		(15/2)		(8)		(15/2)		(6)		(7/2)	
$n=0$	0	4	0	5	0	5	0	1	0	3	0	5	0	3	0	5	0	3	0	5
1	1.5	2	12	5	12	5	35.7*	2	<0.05	1	3.3	5	0.51	2	9.3	5	11.8	2	88.5	5
2	3	1	20.3	5	34[a]	5	38.5*	4	–		5.9	5	1.78	4	9.8	5	14.3	4	92.8	5
3	–		37.7	5	124*	5	44.4*	3	30.2	4	14	5	3.83	1	10.8	5	24.5	1	98.5	5
4	61		115.6	5	154*	5	86**	1	30.2	2	17	5	4.5	3	68.9	5	25	1		
5	–				168*	5	86**	2	–		–		8.4	1	72.5	5	34	3		
6	–				185*	5	87**	4	36.7	4	–		10.7	4	76.5	5	–			
7	77								36.7	2	–		11.8	2	80.2	5	–			
8	89								–				–	3			80			
9	–*								–				57.6	1			–			
10	282*								–				–	3			–			
11									–				60.	2			91.4			
12									59.9	1			60.7	4			–			
13													–	3						
14													70.5	4						
15													71.1	2						
16													73.6	1						

[a] From Strach et al., personal communication.
[b] Soderholm et al. (1991a), Boothroyd et al. (1993), Staub et al. (2000).
[c] Allenspach et al. (1994)
[d] Guillaume et al. (1995)
[e] Staub et al. (1997b)
[f] Staub et al. (1995b)
[g] Allenspach et al. (1989b)
[h] Staub et al. (1994a)
[i] Mesot et al. (1993b)
[j] Osborn and Goremychkin (1991), Amoretti et al. (1994)
[k] Guillaume et al. (1992)

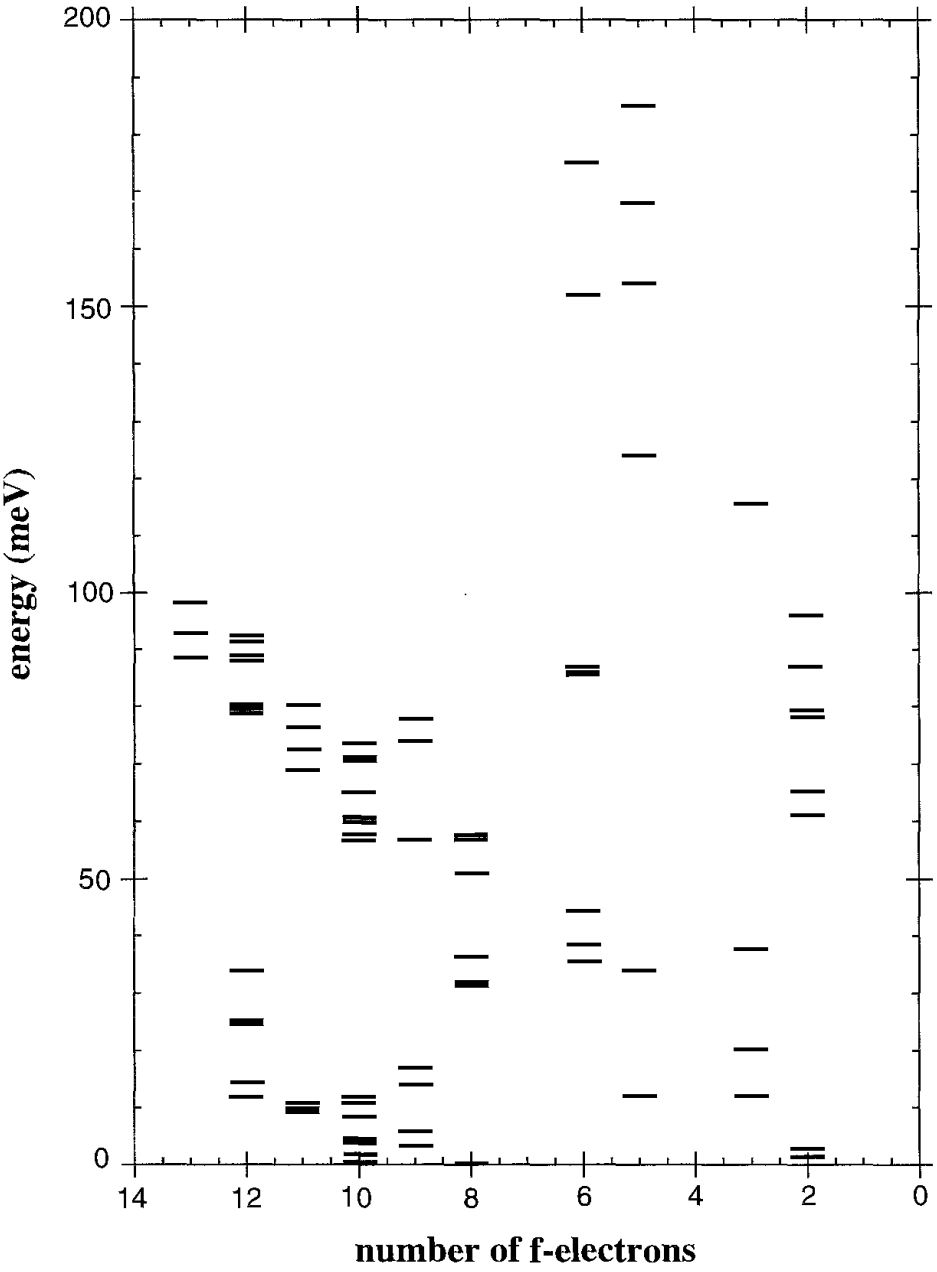

Fig. 7. Energy level schemes of R^{3+} ions in $RBa_2Cu_3O_7$.

is the same result as previously found for the approximation of the trends in higher-order parameters seen for the R:LaF_3 series (Carnall et al. 1989).

Table 4 lists the state energies, which are displayed in fig. 7 and symmetries in $RBa_2Cu_3O_7$ of the trivalent rare-earth ions Pr–Tm (excluding Gd, which is an s-state ion, and Pm, which is not a stable isotope). The CEF parameters derived from these data are listed in table 5.

Table 5
Crystal field parameters in Wybourne notation (Wybourne 1965)[a]

R	B_0^2 (meV)	B_2^2 (meV)	B_0^4 (meV)	B_2^4 (meV)	B_4^4 (meV)	B_0^6 (meV)	B_2^6 (meV)	B_4^6 (meV)	B_6^6 (meV)	Ref.
Yb[b]	***11.3***	*1.62*	***−258.7***	*10.2*	*142.3*	***71.35***	*−1.0*	*156.3*	*0.7*	[1]
Tm[b,c]	**(12.9)**	**(−8.05)**	**−225.4**	**7.8**	**166.5**	**42.8**	**0.6**	**142.4**	**−13.1**	[2]
Tm[b,c] (*"fit"*)	***(12.9)***	***(8.05)***	***−225.4***	***7.8***	***166.5***	***42.8***	***0.6***	***142.4***	***0.4***	
Er	***27.9***	***9.5***	***−258.0***	***13.0***	***149.9***	***58.7***	***−0.9***	***149.1***	***0.7***	[3]
Er	**40.2**	**18.6**	**−240.8**	**−0.5**	**165.9**	**56.8**	**−6.9**	**153.4**	0	[4]
Ho[b]	**41.4**	**7.3**	**−218.6**	**2.3**	**120.6**	**55.7**	**−3.3**	**148.8**	**−1.5**	[5]
Ho	***35.2***	***9.8***	***−272.0***	***4.5***	***154.2***	***63.5***	***−3.9***	***166.1***	***−0.4***	[6]
Ho[7]	**53.9**	**9.5**	**−236.5**	**−36.9**	**130.2**	**58.5**	**−31.3**	**161.8**	**−1.8**	[7]
Dy[b]	**31.5**	4.0	**−189.2**	7.2	**108.2**	**29.4**	−0.6	**71.6**	0.4	[8]
Dy (fit)	***34.4***	*5.5*	***−283.3***	***7.6***	***160.9***	*58.6*	*−0.6*	*164.8*	*0.4*	
Tb	37.8	9.8	−304.8	4.6	172.8	70.6	−3.9	184.2	−0.5	[9]
Tb[d]	***(60)***	–	***−235***	–	*117.5*	***61.5***	–	*171.6*	–	[10]
Gd[e]	***51***	***11***								[11]
Eu[f]	***49***	***5***	*−332*	*4.5*	*185*	*53.2*	*−3.9*	*213.2*	*−0.4*	[12]
Sm[13]	**45.6**	2.6	**−317.6**	8.0	**156.6**	**86.4**	1.7	**247.1**	1.3	[13]
Sm[f] *(fit)*	***53.4***	*2.1*	*−277.1*	*11.3*	***169.1***	***72.9***	*0.1*	***229.1***	*0.7*	
Nd	***73.4***	*3.6*	***−349.6***	*10.5*	***198.8***	***66.9***	*−0.6*	***248.6***	*0.8*	[14]
Nd	**50.4**	**18.4**	**−336.3**	**1.45**	**207.0**	**77**	**−33.3**	**245.3**	**10.2**	[15]
Nd	51.4	22.2	**−327.4**	−2.5	**210.5**	74.9	−31.8	**247**	−0.5	[16]
Pr	**56.0**	**19.9**	**−343.9**	**1.7**	**184.9**	**97.5**	**−42.2**	**323.9**	**13**	[17]
Pr	**55.7**	**26.4**	**−345.3**	**1.9**	**185.7**	**100.2**	**−40.3**	**327.2**	**−0.6**	[18]
Pr	**−28.8**	**6.8**	**−420.2**	**20.0**	**127.0**	**87.8**	0	**198.3**	0	[19]
Pr	**40**	**16**	**−370**	**−49**	**171**	**133**	**13**	**291**	**29**	[20]
Pr[d]	***(39.1)***	***(5.3)***	***−352.9***	–	***185.9***	***96.5***	–	***225.7***	–	[21]

[a] The bold parameters are the parameters effectively fitted, the italic are judged to be the most accurate and are used for table 7, 9 and 10, whereas the others were fixed from extrapolation procedures. (For R = Tm, the "fit" corresponds to the inversion of B_2^2 (which is required to obtain the correct easy axis of the magnetization (Nichols et al. 1994) and a reasonable B_2^2.

[b] Used Stevens formalism.

[c] CEF parameters from the $RBa_2Cu_4O_8$ structure.

[d] CEF parameters from the $Pb_2Sr_2RCu_3O_8$ structure

[e] Mössbauer data.

[f] Sm; change of spin orbit parameter from 1176 to 1183 cm^{-1}; For Eu see Staub et al. (1997b).

References

[1] (Guillaume et al. 1992)
[2] (Amoretti et al. 1994)
[3] (Mesot et al. 1993b)
[4] (Soderholm et al. 1992b)
[5] (Furrer et al. 1988)
[6] (Staub et al. 1994c)
[7] (Goodman et al. 1991, Soderholm et al. 1991a)
[8] (Allenspach et al. 1989b)
[9] (Staub et al. 1994a)
[10] (Staub et al. 1995b)
[11] (Alp et al. 1987)
[12] (Staub et al. 1997b)
[13] (Guillaume et al. 1995)
[14] (Allenspach et al. 1994)
[15] (Goodman et al. 1991)
[16] (Soderholm et al. 1991a)
[17] (Goodman et al. 1991)
[18] (Soderholm et al. 1991a)
[19] (Hilscher et al. 1994)
[20] (Boothroyd et al. 1993)
[21] (Staub et al. 1997c)

Table 6
Wavefunction components of the ground state for the R_2CuO_4 series (and first excited state for Pr, Boothroyd et al. 1992)[a]

R	$a^1_{9/2}$	$a^1_{7/2}$	$a^1_{5/2}$	$a^1_{3/2}$	$a^1_{1/2}$		
Nd	−0.49	0.58	–	–	−0.64		
Sm			−0.92	−0.36	–		
R	Γ	E (meV)	$a^{(i)}_4$	$a^{(i)}_3$	$a^{(i)}_2$	$a^{(i)}_1$	$a^{(i)}_0$
Pr	4	0	–	–	0.70	–	–
	5	18.1	–	−0.84	–	0.50	–

[a] Calculated from parameters of table 3 including free ion interactions. Wave functions are not renormalized to 1.

3.4. *Wavefunctions and transition probabilities*

The wavefunctions derived from the CEF treatment outlined above are tabulated as a function of R for the R_2CuO_4 series in table 6. Table 7 includes the same results for the $RBa_2Cu_3O_7$. Only the strongest wavefunction coefficients with L and S quantum numbers of the ground level are included. We note that the wavefunctions have not been renormalized to 1.

For the $RBa_2Cu_3O_7$ series, these wavefunctions obey the relations for orthorhombic symmetry, which for Kramers ions are given as

$$\left|\Gamma^{(i)}_5\right\rangle = a^{(i)}_{\pm 15/2}\,|\pm 15/2\rangle + a^{(i)}_{\pm 13/2}\,|\pm 13/2\rangle + a^{(i)}_{\pm 11/2}\,|\pm 11/2\rangle + a^{(i)}_{\pm 9/2}\,|\pm 9/2\rangle + a^{(i)}_{\pm 7/2}\,|\pm 7/2\rangle + a^{(i)}_{\pm 5/2}\,|\pm 5/2\rangle + a^{(i)}_{\pm 3/2}\,|\pm 3/2\rangle + a^{(i)}_{\pm 1/2}\,|\pm 1/2\rangle\,,$$

and for non-Kramers ions as

$$\left|\Gamma^{(i)}_1\right\rangle = a^{(i)}_8\,|8\rangle + a^{(i)}_6\,|6\rangle + a^{(i)}_4\,|4\rangle + a^{(i)}_2\,|2\rangle + a^{(i)}_0\,|0\rangle + a^{(i)}_2\,|-2\rangle + a^{(i)}_4\,|-4\rangle + a^{(i)}_6\,|-6\rangle + a^{(i)}_8\,|-8\rangle\,,$$

$$\left|\Gamma^{(i)}_2\right\rangle = a^{(i)}_7\,|7\rangle + a^{(i)}_5\,|5\rangle + a^{(i)}_3\,|3\rangle + a^{(i)}_1\,|1\rangle - a^{(i)}_1\,|-1\rangle - a^{(i)}_3\,|-3\rangle - a^{(i)}_5\,|-5\rangle - a^{(i)}_7\,|-7\rangle\,,$$

$$\left|\Gamma^{(i)}_3\right\rangle = a^{(i)}_8\,|8\rangle + a^{(i)}_6\,|6\rangle + a^{(i)}_4\,|4\rangle + a^{(i)}_2\,|2\rangle - a^{(i)}_2\,|-2\rangle - a^{(i)}_4\,|-4\rangle - a^{(i)}_6\,|-6\rangle - a^{(i)}_8\,|-8\rangle\,,$$

$$\left|\Gamma^{(i)}_4\right\rangle = a^{(i)}_7\,|7\rangle + a^{(i)}_5\,|5\rangle + a^{(i)}_3\,|3\rangle + a^{(i)}_1\,|1\rangle + a^{(i)}_1\,|-1\rangle + a^{(i)}_3\,|-3\rangle + a^{(i)}_5\,|-5\rangle + a^{(i)}_7\,|-7\rangle\,.$$

Tables 8 and 9 list the calculated transition probabilities of the ground-state transitions for the R^{3+} ions in the R_2CuO_4 and $RBa_2Cu_3O_7$ systems, respectively. We note that the

Table 7
Wavefunction components of the ground state for the $RBa_2Cu_3O_7$ series (and first excited states for non-Kramers ions)[a]

Only ground state for Kramers ions

R	$a^1_{15/2}$	$a^1_{13/2}$	$a^1_{11/2}$	$a^1_{9/2}$	$a^1_{7/2}$	$a^1_{5/2}$	$a^1_{3/2}$	$a^1_{1/2}$
Nd				–0.70	–0.34	–0.06	0.01	–0.62
Sm					(–0.15)	0.03	0.01	–0.98
Dy	0.00	–0.01	0.98	0.09	0.13	0.05	0.07	0.07
Er	0.03	–0.54	–0.28	0.00	–0.01	0.58	0.54	–0.01
Yb					–0.01	–0.51	0.01	–0.86

Non-Kramers ion

R	Γ	E [meV]	$a^{(i)}_8$	$a^{(i)}_7$	$a^{(i)}_6$	$a^{(i)}_5$	$a^{(i)}_4$	$a^{(i)}_3$	$a^{(i)}_2$	$a^{(i)}_1$	$a^{(i)}_0$
Pr[b]	4	0					–	0.66	–	–0.20	
Pr[b]	2	2					–	–0.66	–	–0.19	
Pr[b]	1	4					0.00	–	0.70	–	–0.02
Eu	1	0					(–0.18)				0.93
Eu	2	35.7								–0.65	–
Eu	4	38.5								0.65	–
Eu	3	44.4								–	0.90
Tb	3	0			–0.71	–	0.00	–	0.02	–	0.00
Tb	1	0.007			–0.70	–	–0.01	–	0.01	–	0.01
Ho	3	0	–0.10	–	–0.52	–	-0.19	–	–0.52	–	0
Ho	2	0.5	–	0.43	–	0.20	–	0.51	–	0.13	–
Ho	4	1.78	–	0.46	–	-0.01	–	0.53	–	–0.06	–
Tm	3	0			0.30		–0.03	–	0.64	–	0
Tm	4	11.8			–	–0.04	–	0.42	–	–0.58	–
Tm	2	14.1			–	–0.02	–	–0.39	–	–0.60	–

[a] Calculated using italic parameters from table 5 including free-ion interactions. In the case of Eu and Sm, we added the strongest admixture coefficient of the $J=4$ and 9/2 in parentheses, respectively. The wave functions are not renormalized to 1.
[b] From $Pb_2Sr_2PrCu_3O_8$.

Hamiltonian used to determine the wavefunctions, from which the transition probabilities are derived, does not include an exchange (mean-field) term. In selected cases, a good representation of the data requires this additional term.

Table 8
Transition probabilities of ground-state CEF transitions for R^{3+} in R_2CuO_4 [a]

n	R			n	R		
	Pr	Nd	Sm		Pr	Nd	Sm
0	0	3.5	0.3	8	1.4*	0.4*	
1	$8.9_{\perp}$	$0.4_{\perp}$	$<0.1_{\perp}$	9	<0.1	0.5*	
2	0	$4.2_{(z)}$	0.06	10	<0.1	0.2*	
3	<0.1	$3.3_{\perp}$	2.5*	11	<0.1		
4	2_z	0.4	0.3*	12	<0.1		
5	0	1.7*	0.6*	13	<0.1		
6	0	0.2*	1.3*	14	0.0		
7	1.2*	0.3*					

[a] $\sum_{\alpha=x,y,z} |\langle 0|L^{\alpha}+2S^{\alpha}|n\rangle|^2$, calculated using parameters from table 3 (Pr, Boothroyd et al. 1992) numbered as a function of increasing energies. The major component α is shown as a subscript. We note that the CEF transitions of the Kramers ions have in general mixed polarization in tetragonal symmetry. * corresponds to transitions into states within the first excited J-multiplet. The entry 0 is by symmetry exact.

Table 9
Transition probabilities of ground-state CEF transitions for R^{3+} in $RBa_2Cu_3O_7$ [a]

n	R									
	Pr_{α}	Nd_{α}	Sm_{α}	Eu_{α}	Tb_{α}	Dy_{α}	Ho_{α}	Er_{α}	Tm_{α}	Yb_{α}
0	0	4.6	0.24	0	0	51_z	0	36	0	9
1	4.5_z	0.1	0.05	4.7^*_y	81_z	$31_{\perp}$	40.5_x	24.5	22.5_x	5.7
2	3.9_y	2.6	0.00	4.4^*_x	–	$15.5_{\perp}$	8_y	6	20_y	4.3
3	0.4	2.2	2.5*	3.9^*_z	–	$7.5_{\perp}$	11_z	17.5	10_z	2.1
4	0.8	1.4	1.0*	0**	–	$6._{\perp}$	0	0.4	1	
5	0.8		0.65*	0**	–	–	19.5_z	1.5	0	
6	0		0.61*	0**	7_y	$0.5_{\perp}$	5.5_y	3.8	<0.1	
7	0.5				6.5_x	–	7.5_x	4.5	0	
8	0.9				–		0		1	
9					–		0.5_z		<0.1	
10					–		0		0.5	
11					–		1.5_x		0.5	
12							2_y		0.5	
13							0			
14							2.5_y			
15							<0.1			
16							1.5_z			

[a] $\sum_{\alpha=x,y,z} |\langle 0|L^{\alpha}+2S^{\alpha}|n\rangle|^2$, calculated using parameters from table 5 numbered as a function of increasing energies. The major component α is shown as a subscript. * and ** correspond to transitions into states within the first and second excited J multiplets, respectively. Asterisks indicate transitions within the first excited J-multiplet. The entry 0 is by symmetry exact.

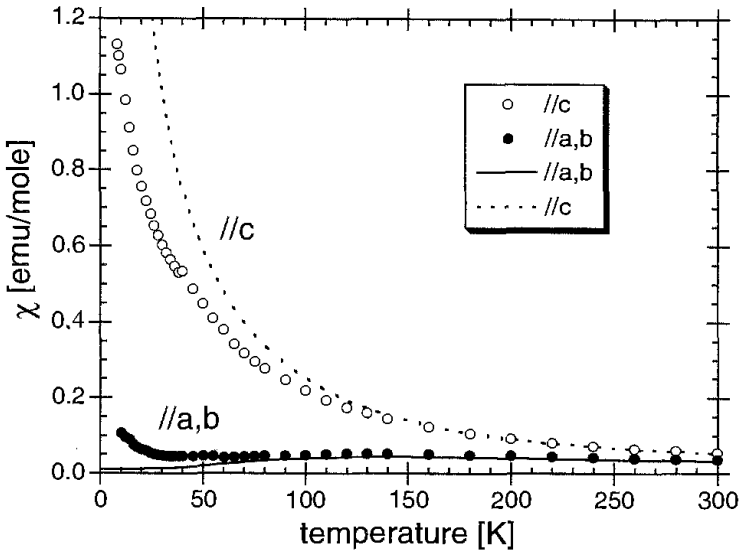

Fig. 8. A comparison of the observed and calculated (lines) single-crystal susceptibilities of $Pb_2Sr_2TbCu_3O_8$ (Staub et al. 1995b).

3.5. *Calculated magnetic properties*

Macroscopic magnetic properties can be calculated from the determined energy states and transition strengths. The comparison of these calculated quantities with experimental observations is a useful test of the reliability of the CEF parametrization. For example, the magnetic contribution in the specific heat (Schottky anomalies) or the paramagnetic single-ion susceptibilities can be calculated directly from the energy of the states and the calculated transition probabilities. The susceptibilities are given by

$$\chi_0^\alpha = \frac{g^2\mu_B^2}{k_B T} \sum_{\substack{m,n \\ E_m = E_n}} |\langle n|J^\alpha|m\rangle|^2 \rho_n - \frac{g^2\mu_B^2}{k_B T} \left(\sum_{\substack{m,n \\ E_m = E_n}} \langle n|J^\alpha|m\rangle \rho_n \right)^2 + 2g^2\mu_B^2 \sum_{\substack{m,n \\ E_m \neq E_n}} \frac{|\langle n|J^\alpha|m\rangle|^2}{E_m - E_n} \rho_n. \tag{18}$$

As an example, fig. 8 shows a comparison of the calculated paramagnetic single-ion susceptibilities with the experimental results obtained from a single crystal of $Pb_2Sr_2TbCu_3O_8$ (Staub et al. 1995b). The calculations are in reasonable agreement with the observations. The discrepancies between the calculations and the data are due to the R–R interactions. Less common is the comparison of the calculated high-field magnetization with experiments on single crystals as e.g. performed for $HoBa_2Cu_3O_7$ (Furrer et al. 1988).

Table 10
g-factors or paramagnetic single-ion susceptibilities χ_α (at 1.5 K in emu/mole), calculated (μ_{CEF}^{sat}) and observed (μ_{obs}^{sat}) saturation magnetic moments including moment direction for the rare earths in the $RBa_2Cu_3O_7$ series.

	Pr[a] (χ)	Nd (g)	Sm (g)	Eu (χ)	Gd (g)	Tb[a] (g)	Dy (g)	Ho (χ)	Er (g)	Tm (χ)	Yb (g)
χ_x/g_x	0.0731	3.28	2.85	0.0082	2	0.01	1.45	5.07	6.23	0.091	0.982
χ_y/g_y	0.0012	3.01	2.94	0.0094	2	0	0.93	0.321	6.91	0.112	0.992
χ_z/g_z	0.235	3.97	0.88	0.0063	2	12.0	10.5	0.342	3.80	0.021	0.963
μ_{CEF}^{sat} (μ_B)	1.55 $\parallel c$	1.29 $\parallel c$[c]	0.33 $\parallel b$	0 $\parallel b$	7.94	9 $\parallel c$[f]	7 $\parallel c$[g]	2.68 $\parallel a$[i]	4.19 $\parallel b$[j]	0 $\parallel b$	1.74 $\parallel b$[l]
μ_{obs}^{sat} (μ_B)	1.45 $\parallel c$[b]	1.1 $\parallel c$[d]	–	–	6.9 $\parallel c$[e]	9.1 $\parallel c$[f]	7.2 $\parallel c$[h]	2.8 $\parallel a$[i]	4.8 $\parallel b$[k]	–	1.4 $\parallel b$[m]

[a] For the $Pb_2Sr_2RCu_3O_8$ series.
[b] (Staub et al. 2000)
[c] (Allenspach et al. 1994)
[d] (Fischer et al. 1989, Yang et al. 1989)
[e] (Chattopadhyay et al. 1988)
[f] (Staub et al. 1997e)
[g] (Allenspach et al. 1989b)
[h] (Goldman et al. 1987)
[i] (Roessli et al. 1993)
[j] (Mesot et al. 1993b)
[k] (Maletta et al. 1990)
[l] (Guillaume et al. 1992)
[m] (Roessli et al. 1992)

An additional test of the wavefunctions is to compare the observed magnitude and direction of the saturated zero-field magnetic moment with the self-consistent calculation in the mean-field approximation (eq. 10). The saturation magnetic moment is defined as the magnetic moment for $T \rightarrow 0$. The results of such a comparison are listed in table 10. Magnetic ordering on the R sublattice is observed for most of the rare earths in the $RBa_2Cu_3O_7$ series, except R = Eu and Tm, where the singlet ground state is well separated from the higher-lying CEF states. The direction of the moment is given by the mean direction of the susceptibility at low temperatures. This quantity cannot be determined directly by a macroscopic magnetization experiment because of the Meissner effect resulting from superconductivity. Paramagnetic single-ion susceptibilities (calculated at 1.5 K) and g-factors for R ions with doublet ground states from which the easy axis can be obtained are listed in table 10.

As an example, for $YbBa_2Cu_3O_7$, an antiferromagnetic Néel temperature of 0.35 K of the Yb sublattice was observed (Hodges et al. 1987). Neutron diffraction was used to determine a magnetic zero-field saturation moment of $1.44\mu_B$, parallel to the crystallographic b direction (Roessli et al. 1992). In contrast, a Mössbauer study found a zero-field moment of $1.7\mu_B$ (Hodges et al. 1987). The moment calculated self-consistently in the mean-field approximation is $1.74\mu_B$ parallel to b (Guillaume et al. 1992).

4. Applications to high-T_c superconductors

4.1. *Effect of superconductivity*

4.1.1. *Charge transfer*

The variable oxygen stoichiometry, x, has been shown to have a drastic influence on the physical properties exhibited by the $RBa_2Cu_3O_x$ series. The oxygen content, which varies $6 \leqslant x \leqslant 7$, influences the structure, the superconducting transition temperature T_c, and the conductivity. It has been argued that as oxygen is added to $RBa_2Cu_3O_6$, holes are introduced into the CuO_2 band which, at a critical concentration, result in a transition from the semiconducting (antiferromagnetic) into the superconducting (metallic) state. A metal-to-semiconductor transition is observed at $x \approx 6.5$. In general, it is believed that the superconducting properties are controlled by the carrier concentration in the CuO_2 planes, which are transferred from the block layers (for the $RBa_2Cu_3O_{7-\delta}$ systems the chains) to the CuO_2 planes. For most of the rare-earth substituted compounds, a two–plateau structure is observed in the superconducting critical temperature as a function of x, for which $T_c \approx 90$ K for $7 > x > 6.8$, $T_c \approx 60$ K for $6.8 > x > 6.4$ and $T_c = 0$ K for $6.4 > x > 6$ (Cava et al. 1987). In 1987, Cava et al. proposed that the plateau effect was the result of local ordering in the CuO chains. However, it was shown that the situation is more complicated due to the occurrence of several local oxygen ordering schemes in the chains, even within the plateau where changes in T_c are small (Beyers et al. 1989).

The CEF splitting of the R levels is dependent on the neighboring charge distribution, and therefore should be sensitive to changes in the charge distribution on the CuO_2 planes. It has been shown that select CEF transitions shift their energies and intensities with changing oxygen content (Mesot et al. 1993b, Staub et al. 1994c). These data have been used to model the charge distribution around the R ion. Only the leading CEF parameters (B_0^4, B_4^4, B_0^6 and B_4^6) were used in the analysis because the other parameters are not as well determined, as evidenced by their larger error bars (see sect. 3). B_0^2 was also not included because it is sensitive to changes in the long-range part of the CEF potential. The experimental data are compared to a structurally based set of parameters that are derived from a modified point-charge model. In order to overcome the problem of how to assign charges in the simple point-charge model, the crystal-field parameters in eq. (14) were ratioed to their fully oxygenated counterpart (Mesot et al. 1993b, Staub et al. 1994c),

$$\frac{B_m^n(x)}{B_m^n(7)} = \frac{\gamma_m^n(x)}{\gamma_m^n(7)} \leqslant 1 \quad \text{for} \quad 6 \leqslant x \leqslant 7, \tag{19}$$

where $\gamma_m^n(\boldsymbol{R}_i) = f_m^n(\theta_i, \phi_i)/(|\boldsymbol{R}_i - \boldsymbol{r}|)^{2n+1}$. This model assumes that the charge on the oxygen in the CuO_2 planes is a constant, and that only structural modifications are responsible for the observed changes in the CEF parameters. From the calculation of the geometrical factors, it is expected that the CEF parameters decrease as a function of decreasing oxygen content x. This expectation is not changed if the $\langle r^n \rangle$ dependence of the superposition model (eq. 15) is included in the calculation. The calculated changes

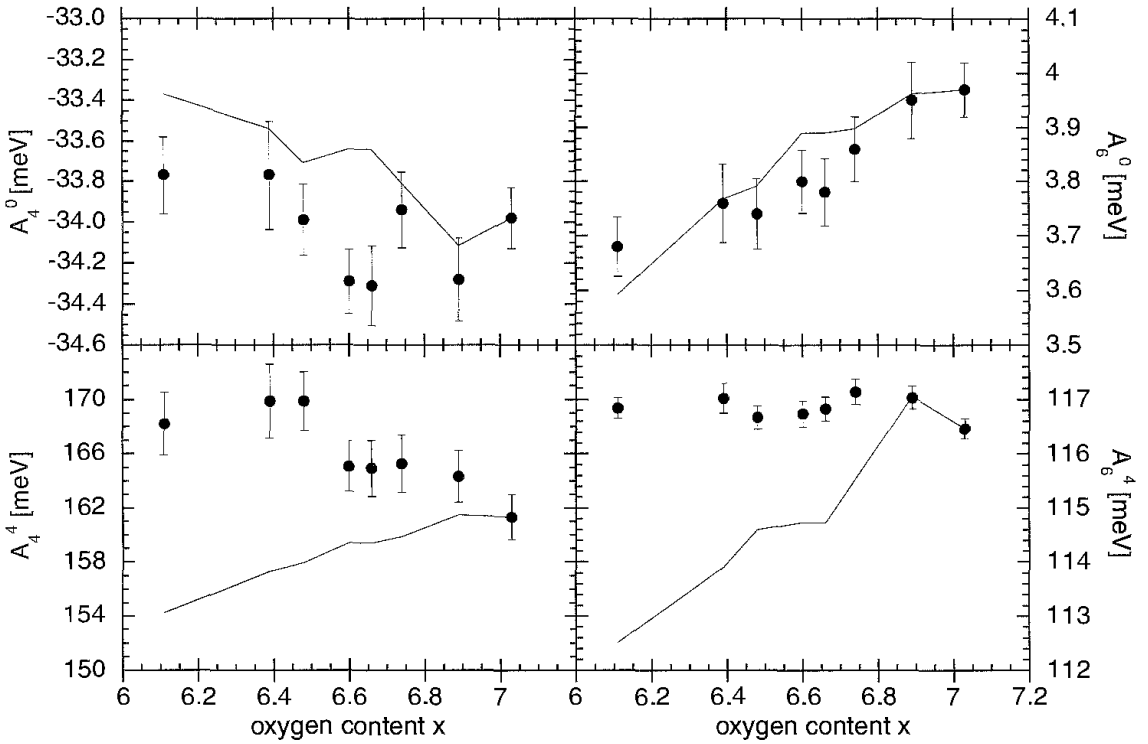

Fig. 9. Main CEF parameters (solid dots) compared with structural expectations values (lines) for $HoBa_2Cu_3O_x$ (Staub et al. 1994c).

in the CEF parameters for R=Ho, as a function of x, are compared with experiment in fig. 9 (Staub et al. 1994c). By slightly modifying the point-charge relation, a quantified charge distribution was obtained in the $RBa_2Cu_3O_x$ series for R=Er (Mesot et al. 1993b), Ho (Staub et al. 1994c) and Nd (Allenspach et al. 1994). Assuming that the Z(O) for the planar oxygens in the fully oxygenated sample is –2, a charge difference was determined of 0.08 $|e|$/O between the $x=6$ and $x=7$ samples of the R=Ho series (Staub et al. 1994c) as shown in fig. 10. A value of 0.07 $|e|$/O was found by a similar analysis of data on the Er analog (Mesot et al. 1993b), also shown in fig. 10. This result implies that about 30% of the added charge goes into the planes. This result is less than the value of 40% derived from resistivity measurements (Welp et al. 1990), and slightly more than the charge transfer 0.04 $|e|$/O (0.08 $|e|$/Cu) derived from diffraction data by means of the bond valence sum formalism (Cava et al. 1990) for the related $YBa_2Cu_3O_x$ compound. Recent soft X-ray spectroscopic experiments on the O K-edge obtained similar results (Nücker et al. 1995).

In a similar study on $Nd_{2-x}Ce_xCuO_4$ (Furrer et al. 1990a), an effective charge modification on the oxygen ligands was derived as a function of Ce doping. An associated charge enhancement of 0.07 $|e|$/O was derived using the same extrapolation of the 4th- and 6th-order CEF parameters between Nd_2CuO_4 and a 15% Ce-doped compound.

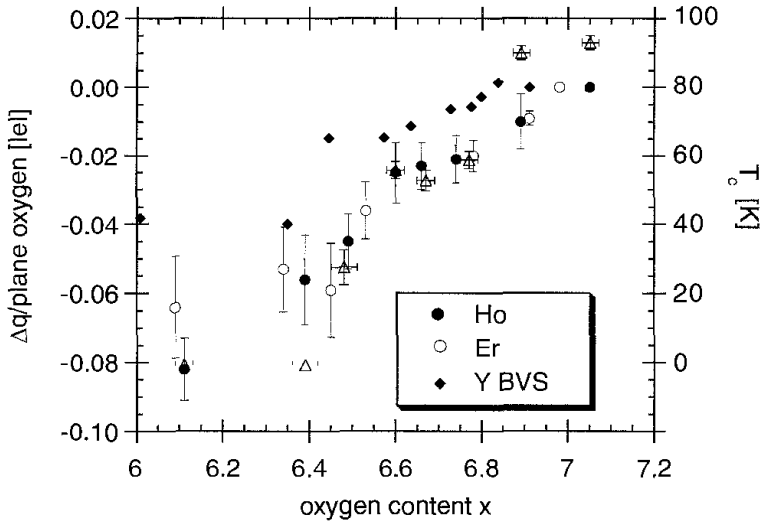

Fig. 10. Charge transfers as a function of oxygen content x derived for Ho (Staub et al. 1994c) and Er (Mesot et al. 1993b) by CEF spectroscopy and for Y by bond valence calculations (BVS) (Cava et al. 1990) and T_c (triangles) as a function of x (left scale) for R = Ho (Staub et al. 1994c).

Overall, these results support the general idea of charge transfer, if the increasingly negative charge on the planar oxygen is interpreted as an increase of the hole concentration in the CuO_2 planes.

4.1.2. *Local (in)homogeneities*

The sensitivity of the R-ion's level splittings to structural and electronic changes has also been exploited to determine details about the local chemical inhomogeneities in $ErBa_2Cu_3O_x$. High-resolution INS data from the lowest three transitions of Er^{3+} are shown in fig. 10 (Mesot et al. 1993a) exemplified for $x = 6.78$. A substructure is observed for peak A, which has been interpreted as three individual transitions (A_1, A_2 and A_3), whose spectral weights depend on the oxygen content of the sample. The observed spectrum is decomposed into Gaussians whose intensities and positions are optimized by CEF modeling, as depicted by the dashed lines in fig. 11. The intensities of the transitions A_1, A_2 and A_3 are found to vary smoothly with oxygen content, from which it was concluded that the hole concentration in the CuO_2 planes is linearly related to the oxygen content. The three subpeaks under A have maximum spectral weights at $x = 7.0$ (A_1), $x = 6.5$ (A_2), and $x = 6.0$ (A_3) (see fig. 12) (Mesot et al. 1993a). The three subpeaks were attributed to two different superconducting local regions, A_1 ($T_c \approx 90$ K) and A_2 ($T_c \approx 60$ K), and an insulating phase (A_3). The observed behavior of T_c versus x, discussed in sect. 4.1.1, is then proposed to originate from the changing relative maximum concentrations of the three local regions. The plateau effect is attributed to a percolation mechanism of electrical conductivity, as discussed from both a theoretical (Hizhnyakov et al. 1989) and an experimental (Kremer et al. 1992) standpoint. We note that this model is based on a linear charge transfer as a function of oxygen and the interpretation does not include any effects of oxygen ordering in the chains as seen by electron diffraction (Beyers et al.

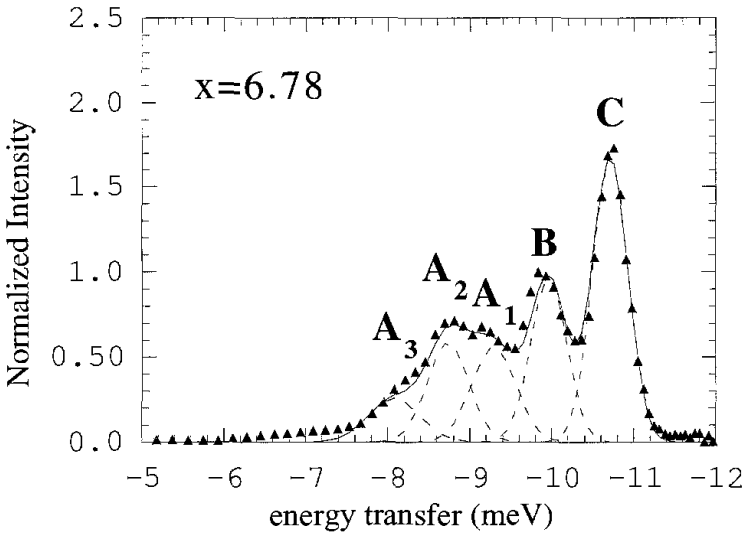

Fig. 11. INS energy spectra from $ErBa_2Cu_3O_{6.78}$ (Mesot et al. 1993a). The labels are explained in the text.

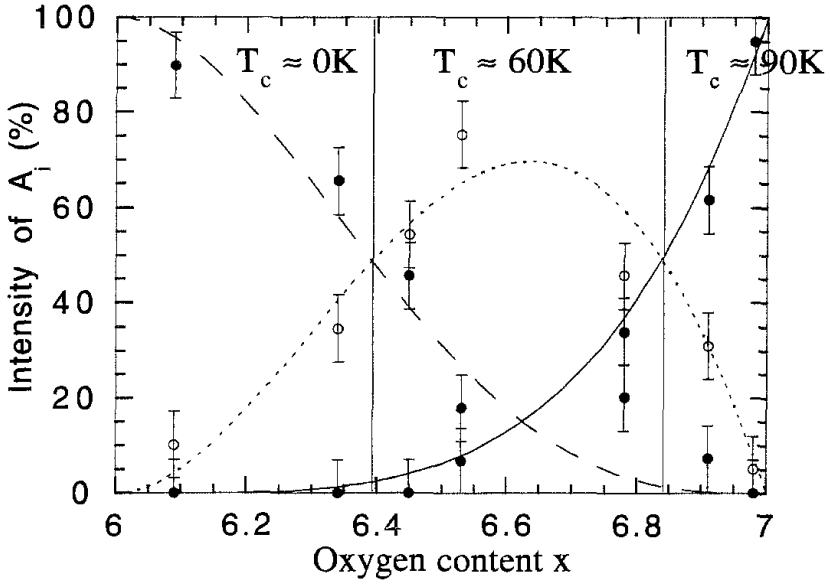

Fig. 12. Proportions of the CEF transition A_i as a function of oxygen content. The lines corresponds to geometrical probability functions (solid line, solid circles: A_1; dotted line, open circles: A_2; dashed line, triangles: A_3) (Mesot et al. 1993a). The vertical lines separate regions where different A_i components dominate, which are associated with the two-plateau structure of T_c.

1989). However, it is also possible that the INS data reflect the local oxygen distribution in the chains because the changes in transition A energy are sensitive to the second-order CEF parameters, which are most strongly influenced by the long-range CEF potential.

The INS data have been independently analyzed by a different group (Muroi and Street 1995). In this interpretation, it is postulated that the CuO_2 planes are either hole-free (insulating) or hole-rich (metallic, superconducting). The three local

environments determined from the substructure of A are associated with the three different R environments that would be created by the combination of two adjacent CuO_2 planes with two possible CuO_2 electronic phases. In phase (a), the two CuO_2 planes adjacent to R are both metallic, in phase (b) one of the two planes is metallic whereas the other is insulating, and in phase (c) the two adjacent planes are both insulating. This model is used to explain a variety of data in addition to the INS data discussed herein. Muroi and Street (1995) conclude that the primary factor controlling T_c is the 1D ordering of the chain oxygens, which was studied in great detail by e.g. Lütgemeier et al. (Lütgemeier et al. 1996) with Cu NQR.

INS results similar to those from $ErBa_2Cu_3O_x$ were also found in the electron-doped superconductor $Pr_{2-x}Ce_xCuO_{4-\delta}$ (Henggeler et al. 1996). Here the dopant is Ce^{4+}, which replaces Pr^{3+} and dopes electrons into the system. However, by introducing a tetravalent ion, the CEF potential is inherently distorted by the additional positive charge at the R site as well as by the introduction of carriers and therefore does not directly support a percolation mechanism of the conductivity by cluster formation. For example, different local CEF potentials were observed in $Pb_2Sr_2Er_{0.5}Ca_{0.5}Cu_3O_8$ (Soderholm et al. 1995) ($T_c \approx 70$ K) where they were attributed entirely to the replacement of Er^{3+} by Ca^{2+} ions.

4.2. *s–f interactions*

4.2.1. *Relaxation measurements on CEF transitions*

Interactions between CuO conduction states and the rare-earth localized f states are expected to be small in these oxide systems because their superconducting properties are generally insensitive to R substitutions. Nonetheless, because of the importance of understanding all electronic interactions in these materials, several INS studies have been reported on s–f interactions in $RBa_2Cu_3O_x$ [R = Tm (Goremychkin et al. 1989, Osborn and Goremychkin 1991) Ho (Mukherjee et al. 1994, Boothroyd et al. 1996), Nd (Allenspach et al. 1989a), Tb (Staub et al. 1997a, 1999)] as well as Ho and Tm in $RBa_2Cu_4O_8$ (Amoretti et al. 1994, Furrer et al. 1997, Mesot et al. 1998), $Er_2Ba_4Cu_7O_{15+\delta}$ (Furrer et al. 1997, Mesot et al. 1998) and $Pb_2Sr_2R_{0.5}Ca_{0.5}Cu_3O_8$ (Staub et al. 1996b). In addition, there are three theoretical studies that attempt to model the observed temperature dependence of the INS linewidths in $RBa_2Cu_3O_x$ (Aksenov and Kabanov 1994, Kovacevic and Plakida 1994, Lovesey and Staub 2000). Whereas most of these studies interpreted their data on the basis of the s–f interaction, very recent studies have shown that these data can be described more coherently by the magneto-elastic interaction with lattice vibrations (Staub et al. 1999, Lovesey and Staub 2000).

Any temperature dependence of the CEF halfwidth can be attributed to either s–f interaction or the interaction of f states with phonons. s–f line broadening for simple metals has been attributed to the effects of the carrier spin dynamics on the CEF-state lifetimes and has been described by the Fermi liquid theory, introduced by Becker et al. (1977). The s–f interaction Hamiltonian describing the coupling between the 4f electrons and the conduction electrons can be written as

$$H_{\text{int}} = \sum_{\alpha} I^{\alpha}_{\text{s-f}} \boldsymbol{J}^{\alpha}_{i} \boldsymbol{S}^{\alpha}_{j}, \tag{20}$$

where $\boldsymbol{J}_i$ is the operator of the total angular momentum of the rare-earth ion at site i, $\boldsymbol{S}_j$ is the spin operator at site j, nearest to site i, and $I^{\alpha}_{\text{s-f}}$ is the anisotropic indirect-exchange integral for which $\alpha = x, y, z$. The temperature dependence of the halfwidth Γ for the transitions between two singlets, the ground state and an excited state separated by an energy ω_1, is given as (Boothroyd et al. 1996)

$$\Gamma = \Gamma_0 + 2J_{\text{ex}}^2 M_{01}^2 \coth\left(\frac{\beta\hbar\omega_1}{2}\right)\chi''(\omega_1) + 2J_{\text{ex}}^2 \sum_{t>1}\left(M_{0t}^2 \frac{\chi''(\omega_t)}{e^{\beta\hbar\omega_t}-1} + M_{1t}^2 \frac{\chi''(\omega_t-\omega_1)}{e^{\beta\hbar(\omega_t-\omega_1)}-1}\right). \tag{21}$$

Here, J_{ex} is the exchange coupling between states of the rare-earth ion and those of the CuO_2 planes with local susceptibility $\chi(\omega)$, M is the dipole transition-matrix element of the corresponding CEF transition, and $\beta = 1/k_B T$. The local magnetic susceptibility (Becker et al. 1977) is defined as

$$\chi(\omega_{\text{CEF}}) = \sum_{q \in BZ} \chi(\boldsymbol{q}, \omega). \tag{22}$$

Therefore, INS spectroscopy probes $\text{Im}(\chi(\boldsymbol{q},\omega))$ at $\omega \approx \omega_{\text{CEF}}$. This information is complementary to ^{89}Y and ^{17}O NMR spectroscopy, which probe the dynamic susceptibility for $\omega \to 0$.

An in-depth study on the temperature dependence of CEF linewidths has been reported for Tm^{3+} in $TmBa_2Cu_3O_7$ (Goremychkin et al. 1989, Osborn and Goremychkin 1991). There is a relatively large separation between the singlet ground state and the lowest excited states (two singlets at about 12 and 14 meV). Whereas the depopulation of the ground state is relatively small at higher temperatures, some of the transitions between excited states have energies similar to those originating from the ground state. The resulting peak overlap significantly complicates the data analysis. The observed temperature dependence of the intrinsic Tm CEF transition halfwidth Γ (after convolving with the instrumental resolution) is shown in fig. 13 for $x = 6.1$ and 7 (Osborn and Goremychkin 1991). The linewidth is not resolution limited, even at very low temperature. The residual broadening may originate from a very small hybridization and/or from structural defects such as distributions in oxygen stoichiometry, even in highly oxygenated samples. Γ decreases strongly below $T = 120$ K, which is about 30 K above T_c. This change in slope has been interpreted as an indication of a gap opening in the spin-excitation spectrum of the CuO_2 planes. A study on the lowest-lying CEF transition in $Y_{0.9}Ho_{0.1}Ba_2Cu_3O_7$ reveals an anomaly in Γ around 115 K (Boothroyd et al. 1996). The ratio of Γ/Γ_N shows an increase with temperature well below T_c, which has been interpreted as characteristic of a high degree of gap anisotropy. In addition, another recent study on $HoBa_2Cu_4O_8$ and $Er_2Ba_4Cu_7O_{15+\delta}$ has reported deviations from the Fermi liquid behavior of $\Gamma(T)$, which was interpreted as an indication of the opening of the pseudogap far above T_c (Furrer et al. 1997, Mesot et al. 1998).

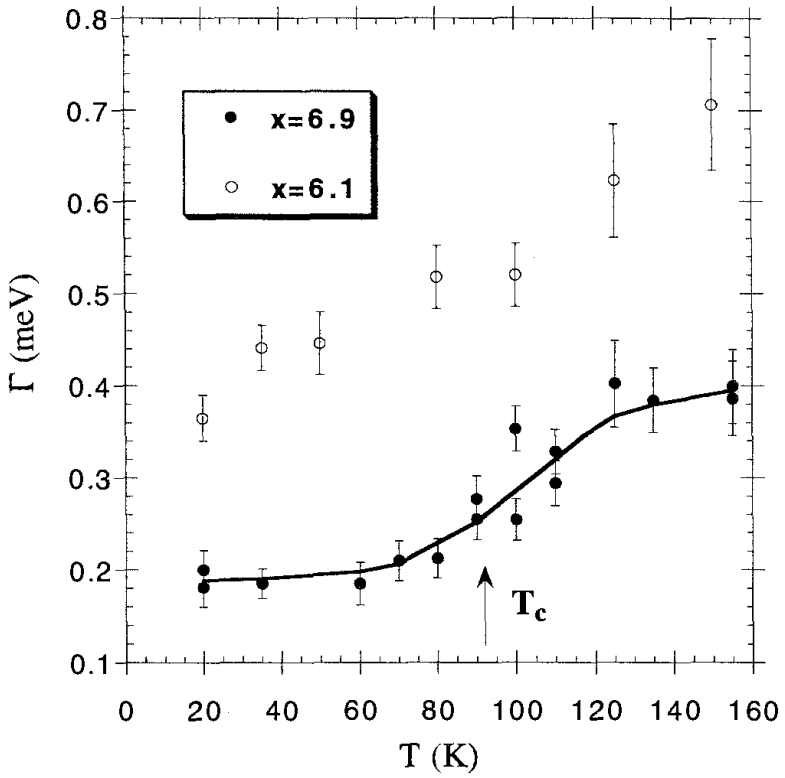

Fig. 13. Halfwidth Γ of the lowest-lying CEF transition of Tm in $TmBa_2Cu_3O_x$ as function of temperature (Osborn and Goremychkin 1991).

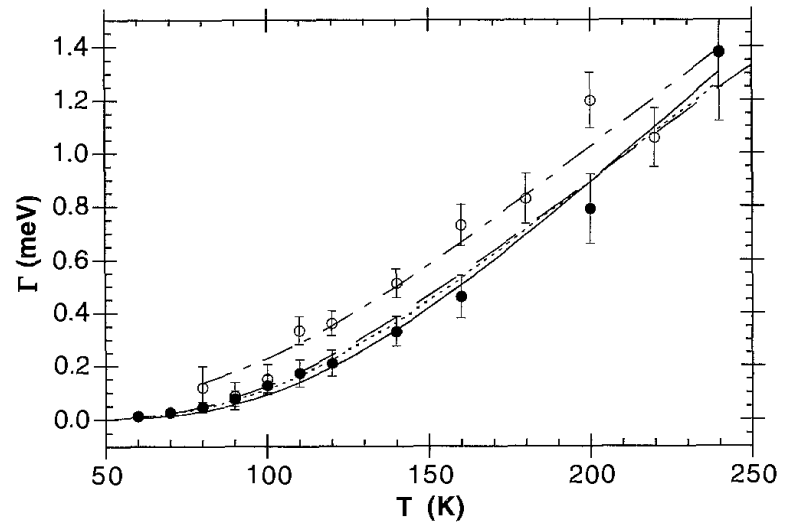

Fig. 14. Temperature dependence of the full width at half maximum of the quasi-elastic contribution of Tb in $Y_{0.9}Tb_{0.1}Ba_2Cu_3O_{7-\delta}$ for the metallic ($\delta = 0.1$) and insulating ($\delta = 0.9$) material. The lines correspond to calculation, based on an interaction with phonons (Staub et al. 1999).

The temperature dependence of the full width at half maximum Γ of the quasi-elastic (QE) component in $Y_{0.9}Tb_{0.1}Ba_2Cu_3O_{7-\delta}$is shown in fig. 14. The temperature

dependence can described by a $1/(e^{\Delta/k_B T}-1)$ function and has previously been fitted with a power law $(T)^{\nu}$ obtaining a critical exponent of $\nu=2.6$ (Staub et al. 1997a). Because the halfwidth of the quasi-elastic component is directly related to the frequency of the spin fluctuations, the results indicate that the characteristic frequency of the Tb spins decreases with decreasing temperature according to a $1/(e^{\Delta/k_B T}-1)$ function. Similar results were also found for $Pb_2Sr_2Tb_{0.5}Ca_{0.5}Cu_3O_{7-\delta}$ (Staub et al. 1996b). The temperature dependence of Γ does not arise from Tb–Tb interactions, because it does not significantly change with the concentration of the magnetic Tb ions as has been previously suggested (Staub et al. 1997a). There was no anomaly observed in the Γ vs T behavior for either of these compounds to indicate an opening of a spin gap. Taken together with the result on the non-superconducting $Y_{0.9}Tb_{0.1}Ba_2Cu_3O_{6.25}$ compound, these results imply that the $1/(e^{\Delta/k_B T}-1)$ dependence of linewidth with temperature is not dominated by the s–f interaction.

Taken as a whole, the INS-linewidth studies on these high-T_c materials do not present any cohesive insight. The results on Ho and Tm, $J_{ex}^2 N(0)^2$ differ by a factor of three, and a recent EPR study on Gd found a value of 20 times smaller (Shaltiel et al. 1996), where for simple metals this value is roughly constant between R=Gd and R=Er (Fulde and Loewenhaupt 1985). Similar linewidth dependencies were observed for $TmBa_2Cu_3O_7$ and the insulator $TmBa_2Cu_3O_{6.1}$, even though the Fermi Liquid theory, assumed in the data analyses, should not be valid for the latter compound because it is an insulator. These problems arises because the effect of the phonon contribution on the relaxation rate of inelastic CEF transitions was neglected in these studies. As has been shown very recently, the temperature dependence of the linewidth of Tb, Ho and Tm can be accurately described by the magneto-elastic interaction with lattice vibrations (phonons) involving excited CEF states (fig. 14) (Staub et al. 1999, Lovesey and Staub 2000). The occurrence of a deviation in $\Gamma(T)$ from the description with the s–f interaction as previously interpreted in terms of the opening of a gap, is not obtained by the comparison with a model based on the magneto-elastic interaction (quadrupole coupling with lattice vibration). Therefore, CEF relaxation measurements cannot be used to obtain meaningful information on the dynamical susceptibility of the CuO_2 planes because the CEF relaxation is dominated by the interaction with phonons.

4.2.2. *The exceptional influence of Pr*

Shortly after the discovery of superconductivity at about 92 K in the $RBa_2Cu_3O_7$ series (Brown et al. 1987, Hor et al. 1987), it was demonstrated that Pr uniquely suppresses superconductivity (Soderholm et al. 1987, Dalichaouch et al. 1988). Initially it was argued that T_c was suppressed through a charge transfer from Pr to the CuO planes, and that Pr was intermediate and tetravalent in this material. Part of the support for this hypothesis came from the observation that the effective moment on Pr was intermediate between those expected for a trivalent and for a tetravalent free ion. Subsequent work has shown that Pr is close to trivalent in $PrBa_2Cu_3O_7$ (Radousky 1992) and that simple charge-transfer or hole-filling mechanisms are not primarily responsible for T_c suppression.

A variety of other mechanisms, including hole localization, magnetic-pair breaking, or hybridization, have since been suggested (Guo and Temmerman 1990, Radousky 1992, Fehrenbacher and Rice 1993, Liechtenstein et al. 1995).

INS studies have been used extensively to characterize the electronic properties of Pr in $PrBa_2Cu_3O_x$ (Skanthakumar et al. 1990, Goodman et al. 1991, Soderholm et al. 1991a, Jostarndt et al. 1992, Nekvasil et al. 1992, Boothroyd et al. 1993, Hilscher et al. 1994). Whereas there are discrepancies in some peak assignments, the overall conclusions are clear. Using the CEF modeling outlined in sect. 3, the observed peaks can be assigned as transitions within a Pr^{3+} $^3H_4$ ground level. Whereas the ground state is a singlet in orthorhombic symmetry, the splitting between it and the first two excited states is only about 4 meV, with the next excited state above 45 meV. The result of this unusual splitting is that the bulk magnetic properties of Pr are described as if it has an isolated pseudo-triplet ground state, with an effective moment of about $2.8\mu_B$ (Soderholm et al. 1991a), reduced from the free-ion value of $3.58\mu_B$. A slight mixing coefficient for the calculated wavefunctions is sufficient to explain the saturation moment observed experimentally (Goodman et al. 1991). The CEF parameters fit to the data follow the trends established by the other R ions (see sect. 3).

One notable feature of the INS spectral response from $PrBa_2Cu_3O_x$ is that the CEF transitions are all very broad, as demonstrated in fig. 15 (Jostarndt et al. 1992). In addition, the low-energy transitions exhibit a pronounced tail on the high-energy side which continues up to at least 10 meV. The low-energy response of the deoxygenated sample, $PrBa_2Cu_3O_6$, has much sharper CEF transitions than seen from $PrBa_2Cu_3O_7$ (fig. 15), however, they are still much broader than the transitions observed from other $RBa_2Cu_3O_x$ compounds. The spectra from the deoxygenated samples still show the asymmetric tails to the high-energy side of the peaks. A dilution with non-magnetic Y ions (Y partially replacing Pr) significantly affects the low energy response (Jostarndt et al. 1992). Therefore, it appears that Pr–Pr interactions may account for some of the broadening of the CEF transitions, but they are not able to explain the high-energy tails seen in the spectra. Also for $(Pr_{1.5}Ce_{0.5})Sr_2Cu_2NbO_{10-\delta}$, superconductivity is suppressed and there is a very broad CEF response in the INS data (Staub et al. 1998b). Other related Pr oxides, such as $BaPrO_3$, PrO_2 (Kern et al. 1985), $PrScO_3$ (Soderholm et al. 1990) and the superconductor-parent compound Pr_2CuO_4 (Soderholm 1992) do not show the significant INS peak broadening observed from $PrBa_2Cu_3O_7$.

Unlike the peak broadenings observed in the INS data from $RBa_2Cu_3O_7$ (R = Tm, Ho), discussed in the previous section, the peak broadening observed for the Pr transitions is not temperature dependent. As a result, the interactions responsible are expected to be static, as opposed to the dynamic processes proposed for the Tm and Ho interactions. This interaction for Pr may involve a stronger hybridization of the 4f states with the CuO_2 band states, which would be consistent with the known f-state bonding behavior established across the R series.

The magnetic behavior of non-superconducting analogs of high-T_c series provides additional evidence that Pr f states interact strongly with the CuO states. From table 11, it can be seen that when T_c is suppressed, as it is for $PrBa_2Cu_3O_7$,

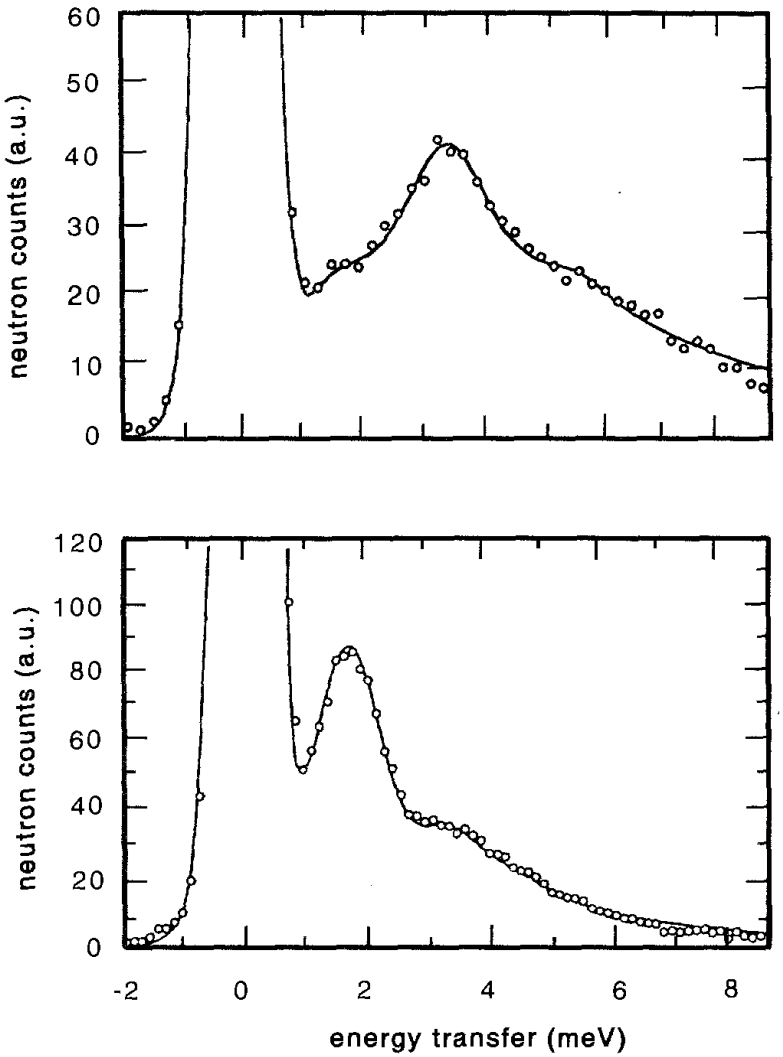

Fig. 15. INS spectra from $PrBa_2Cu_3O_x$ ($x=7$, upper part; $x=6$, lower part, 1.5 K). Data and lines as in (Jostarndt et al. 1992).

$(Pr_{1.5}Ce_{0.5})Sr_2Cu_2NbO_{10-\delta}$, $CmBa_2Cu_3O_7$, and Cm_2CuO_4, the R moments order at an unusually high temperature. Only when the samples are not superconducting is the T_N anomalously high. Pr in $PrBa_2Cu_3O_7$ and Cm both have local moments in radially extended f states. In contrast, the CEF splitting for Pr in Pr_2CuO_4 results in an isolated singlet ground state, and there is no local moment available on the R ion to interact with the CuO states, irrespective of the degree of s–f hybridization.

The Pr analog of the $Pb_2Sr_2R_{1-x}Ca_xCu_3O_8$ series provides further insight into these interactions. As seen from table 11, the behaviors of $Pb_2Sr_2Pr_{1-x}Ca_xCu_3O_8$ ($x=0$ and 0.5) are intermediate between those observed for $Pr_{2-x}Ce_xCuO_4$ and $PrBa_2Cu_3O_7$. The T_N of the Pb-based parent compound ($x=0$) is slightly higher than seen for the other members of the same series, whereas the T_c for the superconductor ($x=0.5$) is suppressed by about 10 K (Skanthakumar and Soderholm 1996). Figure 16 contrasts the high-resolution,

Table 11
Superconducting transition temperatures (T_c) and magnetic properties of selected compounds from the R_2CuO_4, $RBa_2Cu_3O_7$, $(Pr_{1.5}Ce_{0.5})Sr_2Cu_2NbO_{10-\delta}$, and $Pb_2Sr_2RCu_3O_8$ series[a]

Compound	T_c (K)	T_N^R (K)	μ_{sat} (μ_B)	Reference
Pr_2CuO_4	–[b]	–	0.08	Matsuda et al. (1990), Sumarlin et al. (1995)
Gd_2CuO_4	–	8.8	7.9[c]	Oseroff et al. (1990)
Cm_2CuO_4	–	25	7.9[c]	Soderholm et al. (1991b)
$Pr_{1.85}Ce_{0.15}CuO_4$	24	–		Takagi et al. (1989)
$Sm_{1.85}Ce_{0.15}CuO_4$	24	–		Takagi et al. (1989)
$Cm_{1.85}Ce_{0.15}CuO_4$	–	13	7.9[c]	Soderholm et al. (1991b)
$PrBa_2Cu_3O_7$	–	17	0.74	Li et al. (1989)
$Pr_{0.5}Ca_{0.5}Ba_2Cu_3O_7$	43	–		Norton et al. (1991)
$GdBa_2Cu_3O_7$	92	2.2	7.9[c]	Brown et al. (1987)
$CmBa_2Cu_3O_7$	–	22	7.9[c]	Soderholm et al. (1989)
$Pb_2Sr_2PrCu_3O_8$	–	6	1.45	Shieh et al. (1994), Staub et al. (2000)
$Pb_2Sr_2Pr_{0.5}Ca_{0.5}Cu_3O_8$	61	–		Soderholm et al. (1997)
$Pb_2Sr_2GdCu_3O_8$	–	2.5	7.9[c]	Lai et al. (1994)
$Pb_2Sr_2Gd_{0.5}Ca_{0.5}Cu_3O_8$	70	–		Cava et al. (1988)
$(Pr_{1.5}Ce_{0.5})Sr_2Cu_2NbO_{10-\delta}$	–	10	?	Goodwin et al. (1997)

[a] The magnetic ordering temperatures (T_N^R) are reported for the rare-earth sublattice.
[b] –, No transition observed.
[c] Moment estimated as free ion value for spherically symmetric ground state.

low-energy inelastic neutron scattering spectra obtained from $Pb_2Sr_2Pr_{1-x}Ca_xCu_3O_8$ for $x=0$ and 0.5 (Staub et al. 1997d). The positions and intensities of the INS peaks from the parent compound confirm the similarity of the CEF splitting to that of the $RBa_2Cu_3O_7$. The pseudo-triplet ground state, with an overall splitting only slightly smaller than the 4 meV observed for $PrBa_2Cu_3O_7$, is isolated from the other states, which are at energies above 50 meV (Staub et al. 1997c). The peaks are broader than expected from the instrument resolution. In contrast, the spectra obtained from the $x=0.5$ compound show no evidence of the well-defined features observed for the $x=0$ sample. Instead, these features have been replaced by a very broad magnetic intensity that results from a static distribution in the CEF generated by Ca doping (Staub et al. 1997d). In addition, the magnetic scattering from the Ca-doped compound shows a decreased intensity at low-energy transfer. The magnetic scattering is displaced to higher-energy transfers relative to the parent compound, with significant magnetic intensity observed in the range of 10–15 meV. This increase in energy of the magnetic scattering indicates that the ground-state "triplet" is further split by the incorporation of Ca into the lattice.

It appears that Ca substitution plays more than one role in the electronic behavior of this material. In addition to modifying the hole doping on the CuO sublattice, the replacement of R^{3+} by Ca^{2+} modifies the electronic ground-state properties of the Pr^{3+} ion. It does so

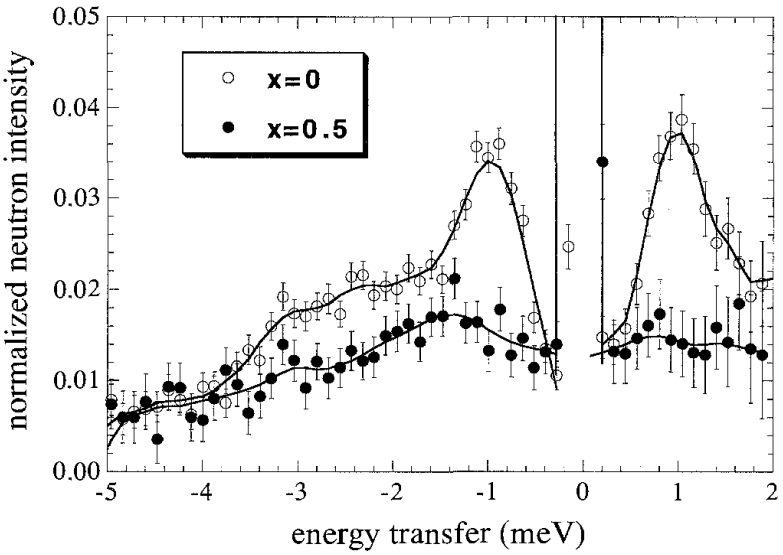

Fig. 16. Low-energy INS spectra corrected with detailed balance from $Pb_2Sr_2Pr_{1-x}Ca_xCu_3O_8$ (Staub et al. 1997d). Data are normalized per mole Pr ions (20 K).

by distorting the pseudo-cubic environment of the Pr ion, which results in an increased average splitting of the ground-state triplet. The importance of this increased splitting lies in the reduced ability of the Pr ion to renormalize the low-energy singlets to form a magnetic ground state. As the splitting increases, the Pr ion acts more like a singlet, non-Kramers ion. When Ca replaces some Pr in the Pb-based compound, the average splitting of the Pr^{3+} pseudo-triplet is increased, therefore $Pb_2Sr_2Pr_{0.5}Ca_{0.5}Cu_3O_8$ superconducts, but T_c remains slightly suppressed, because the triplet splitting is not large enough to remove all moment from the ground state. This same increase in the average splitting by Ca of the Pr pseudo-triplet ground state is expected to apply in $(Y_{1-x-y}Ca_yPr_x)Ba_2Cu_3O_7$ (Neumeier et al. 1989) and in $Pr_{0.5}Ca_{0.5}Ba_2Cu_3O_7$ thin films (Norton et al. 1991, 1994).

This analysis of the electronic and magnetic properties of Pr in the $RBa_2Cu_3O_7$, $R_{2-x}Ce_xCuO_4$, $(Pr_{1.5}Ce_{0.5})Sr_2Cu_2NbO_{10-\delta}$, and $Pb_2Sr_2R_{1-x}Ca_xCu_3O_8$, taken together with the data on the Cm analogs of these materials, provide a platform on which to base a fundamental understanding of the selective suppression of high-T_c superconductivity. These data suggest that it is the localized magnetic moments on the R sites that interact with the CuO states to suppress T_c. The restriction of this magnetic interaction to R = Pr and Cm, but not the heavier lanthanides such as Gd, may lie in the extended f orbitals of the lighter lanthanides and actinides, and their known ability to hybridize (Soderholm 1992). The relevance of the magnetic ground state, specifically the size of the quasi-triplet ground-state splitting, to T_c suppression may affect the f-state hybridization with the CuO_2 band states. A non-magnetic singlet ground state may not be able to hybridize effectively with the CuO_2 states. Such effects are well known in Kondo systems, in which the CEF energy splitting can compete with the Kondo hybridization (Watanabe and Kuramoto 1997).

Whereas the theory of Fehrenbacher and Rice (Fehrenbacher and Rice 1993) can explain selected X-ray absorption and optical reflectivity data, the proposed admixture of 50% Pr^{3+} ($4f^2$) and 50% magnetically Pr^{4+} ($4f^1$) is not consistent with the overall INS results. The magnetic data from Pr are well understood in terms of Pr^{3+} ions only. The Cm data are even more definitive in this regard ($\mu_{eff}(Cm^{3+}) = 7.94\mu_B$; $\mu_{eff}(Cm^{4+}) = 0\mu_B$). Certainly it has not been demonstrated how a mixing of Pr^{3+} and Pr^{4+} can explain the high ordering temperatures of the Pr and Cm moments. In contrast, the theory developed by Guo and Temmerman (Guo and Temmerman 1990) is consistent with the results discussed herein. The band-structure calculations by Liechtenstein and Mazin (Liechtenstein et al. 1995) can be consistent with these findings, however, they do not include or predict unusual magnetic properties.

Further progress on this problem may necessitate an understanding of interactions responsible for high-temperature superconductivity.

4.3. *f–f interactions*

4.3.1. *Grain-aligned $HoBa_2Cu_3O_x$*

A variety of data and calculations have been reported that focus on the contributions of Ruderman–Kittel–Kasuya–Yosida (RKKY), dipolar or (super-) exchange mechanisms to the f–f interactions that result in antiferromagnetic ordering of the R sublattice at low temperatures. For example, $^{155}Gd^{3+}$ Mössbauer spectroscopy data from $GdBa_2Cu_3O_7$ did not provide evidence for the presence of conduction electrons at the Gd^{3+} site (Alp et al. 1987), implying only very weak RKKY interactions. Low-temperature specific-heat and magnetization measurements indicate large anisotropies of the exchange interaction in the (a,b) plane (Yang et al. 1989) (chapter 200, this Handbook). Extensive neutron diffraction studies have been performed to understand the low-temperature magnetic ordering of the R sublattices (see chapter 199, this Handbook). Insight into the R–R coupling mechanism has been obtained from studying the spin dynamics using INS. Measurements of the collective magnetic excitations or spin waves inherently contain microscopic information about the nature and size of the magnetic f–f interaction. INS experiments on the wavevector ($\boldsymbol{Q}$) dependence of a particular CEF transition provides a measure of exchange parameters. Only a few studies are reported in the literature because of the lack of large, perfect single crystals needed for this kind of experiments. Experimental results are available on $R_{2-x}Ce_xCuO_4$ for R = Pr (Sumarlin et al. 1995) R = Nd (Casalta et al. 1996, Henggeler et al. 1996, 1997, Loewenhaupt et al. 1996) and for $RBa_2Cu_3O_7$ [R = Ho (Staub et al. 1993, 1994b, Fauth et al. 1995) and Er (Fauth et al. 1995, Skanthakumar et al. 1997)]. Limited theoretical studies have also been reported (Thalmeier 1996, Sachidanandam et al. 1997, Rastelli and Tassi 1998, Pyttlik and Becker 1998).

The results from $HoBa_2Cu_3O_x$ are chosen as an example because the CEF level scheme of Ho in this CEF is characterized by a series of low-lying states (Furrer et al. 1988, Staub et al. 1994c) which can be sufficiently resolved within the small range of energy

dispersion anticipated for these systems. The f–f interaction Hamiltonian can be written as

$$H = H_{\mathrm{CEF}} - \tfrac{1}{2}\sum_{i,j,\alpha} J_{ij}^{\alpha\alpha} \boldsymbol{J}_j^{\alpha} \boldsymbol{J}_i^{\alpha} \quad (\alpha = x, y, z). \tag{23}$$

Because the energy of the first ground-state transition in $HoBa_2Cu_3O_x$ is sufficiently small compared to the energies of the other CEF transitions, the energy dispersion of the excitation can be expressed in an effective two-level system as

$$\omega^{\alpha}(\boldsymbol{Q}) = \Delta\sqrt{1 - \frac{2M_{\alpha}^2 J^{\alpha}(\boldsymbol{Q})}{\Delta}\tanh\left(\frac{\Delta}{2k_{\mathrm{B}}T}\right)}. \tag{24}$$

Here, Δ corresponds to the energy separation of the two lowest CEF states Γ_3 and Γ_4, and $M_{\alpha} = \langle\Gamma_4|J^{\alpha}|\Gamma_3\rangle$ $(\alpha = x, y, z)$ are the components of the dipole transition matrix element between these two states. M_{α} and Δ are the characteristic parameters derived from the single-ion susceptibility which is deduced from the INS experiments on the CEF on polycrystalline samples (tables 6 and 8). For a determination of the exchange integrals $J^{\alpha}(\boldsymbol{Q})$, exchange parameters J_a^{α}, J_b^{α} and J_c^{α} were introduced that couple the central Ho^{3+} ion with the rare-earth ions at the nearest-neighbor positions. The absence of dispersion along the z-axis leads to the conclusion that there is no significant coupling along the c-axis ($J_c^{\alpha} \approx 0$). This result is consistent with the large separation of Ho^{3+} ions along that direction. Information on J_a^{α} and J_b^{α} is difficult to obtain because of the random orientation of the x- and y-axes in the grain-aligned samples used in the experiments. Therefore, the magnetic-excitation spectrum (fig. 17) is a superposition of $\omega^{\alpha}(\boldsymbol{Q})$ for all possible $\boldsymbol{Q} \perp c$ ($Q^{\perp}$). To overcome this problem, a pseudo-tetragonal model was used, in which $J_a^{\perp} = J_a^x = J_a^y$, $J_b^{\perp} = J_b^x = J_b^y$, and $M^{\perp} = M^x = M^y$. This notation leads naturally to $J\|_a = J_a^z$, $J\|_b = J_b^z$, and $M\| = M^z$. The exchange-coupling constants obtained from this model are listed in table 12.

Several conclusions can be drawn from this analysis. Firstly, the observed dispersion effects indicate that a 2D Ising system cannot represent the magnetic interactions for R = Ho. The exchange coupling with an antiferromagnetic coupling along b, a weak ferromagnetic coupling along a and no observable coupling within the accuracy of the experiment along c, has an almost 1D character. Such a coupling scheme is actually expected from dipolar considerations. Detailed, first-principle calculations are required for comparison with the nearest-neighbor coupling constants obtained from INS experiments. The coupling constants determined from INS can be used to obtain a mean-field parameter of 6.5 μeV (Roessli et al. 1993), which is not sufficient to induce magnetic ordering in the R sublattice for Ho. An additional hyperfine interaction is required for the system to induce magnetic ordering of the R sublattice at 190 mK, as previously found for HoF_3 (Leask et al. 1994). At 1.5 K, far above the Neél temperature, short-range order of the Ho^{3+} sublattice has been observed and attributed to the peculiarities of the singlet ground state system (Staub and Ritter 1996).

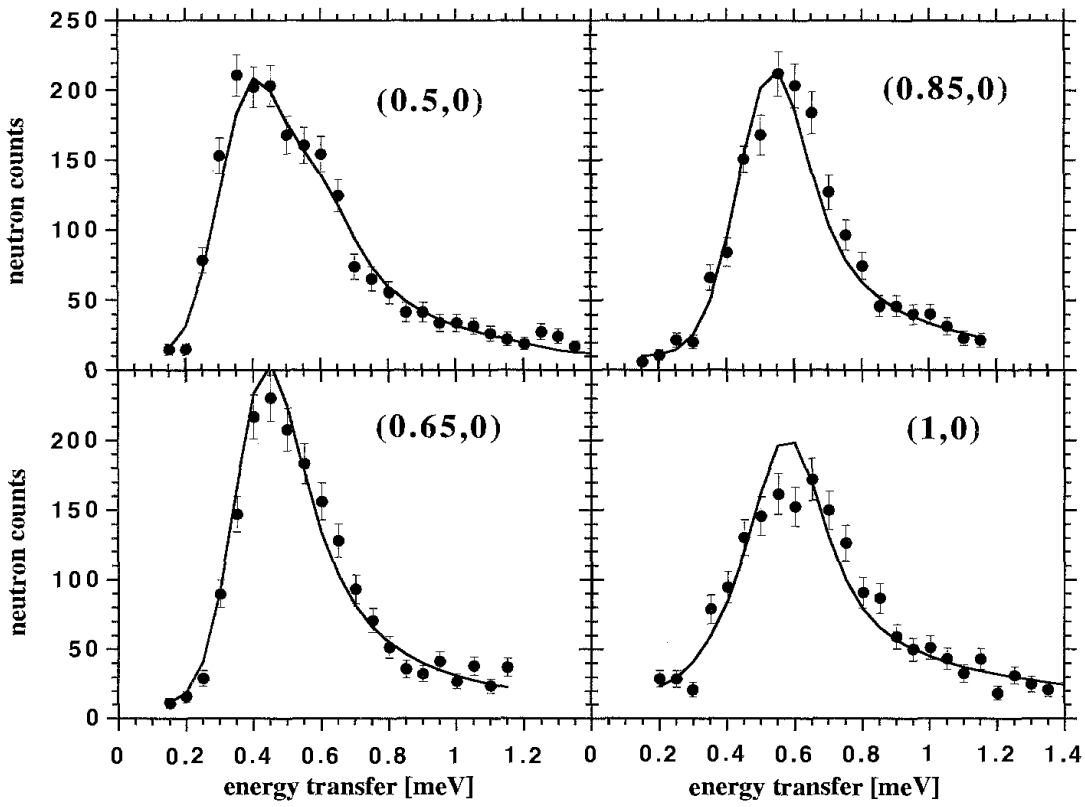

Fig. 17. INS data obtained from grain-aligned $HoBa_2Cu_3O_7$ for propagation within the a,c plane (1.5 K) (Staub et al. 1994b). The line represents the model as explained in the text.

Table 12
Exchange coupling parameters and anisotropic matrix elements for Ho^{3+} in $RBa_2Cu_3O_7$.

Parameter	Pure Ho models			$Y_{0.9}Ho_{0.1}Ba_2Cu_3O_7$ (Guillaume et al. 1994)
	$J_\alpha^\perp = J_\alpha^\parallel$ (Staub et al. 1993)	$M^{x2} = M^{y2}$ (Staub et al. 1994b)	$M^{y2} = M^{z2}$ (Fauth et al. 1995)	
$J_a^\perp$ (μeV)	0.5	3.3±0.8	3.2±0.7	2.6±0.4
$J_a^\parallel$ (μeV)	0.5	0±0.4	0±0.2	
$J_b^\perp$ (μeV)	−2.8	−2.6±0.3	−2.4±0.8	−2.6±0.4
$J_b^\parallel$ (μeV)	−2.8	−6.9±0.7	−6.9±1.6	
$M^{\alpha 2}$	$M^2 = 27$	$M^{\perp 2} = 19.2 \pm 0.4$ $M^{\parallel 2} = 7.8 \pm 0.6$	$M^{x2} = 11.4 \pm 0.2$ $M^{z2} = 8.8 \pm 0.7$	

4.3.2. *Ho^{3+} dimer excitations in $Y_{1-x}Ho_xBa_2Cu_3O_7$*

Another approach to gain information about the f–f interaction is to study magnetic dimer excitations as was performed e.g. in the $Cs_3R_2Br_9$ systems where the rare earth naturally forms dimers (Furrer et al. 1985, 1990b). Dimers and small clusters can be formed in all compounds in which solid solutions of rare-earth and non-magnetic ions (e.g.

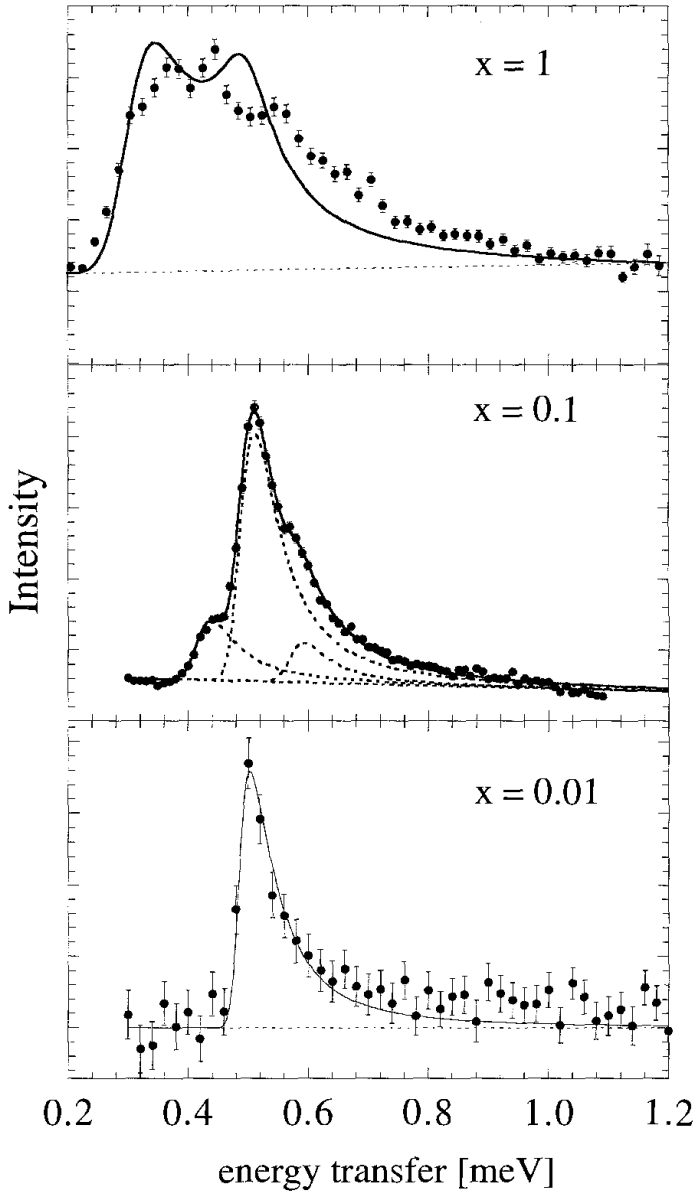

Fig. 18. $Y_{1-x}Ho_xBa_2Cu_3O_7$ INS spectra as a function of Ho content, x: upper panel, $x=1$; middle panel, $x=0.1$ (Guillaume et al. 1994); lower panel, $x=0.01$ (Henggeler et al. 1999).

Y or La) are possible without structural phase transitions as e.g. the $RBa_2Cu_3O_x$ series. An Y/R ratio of 9 results in 66% single R^{3+} ions, 29% dimers and 5% higher clusters. INS experiments allow a straightforward determination of the magnetic-coupling parameters, as demonstrated by the work on $Y_{0.9}Ho_{0.1}Ba_2Cu_3O_x$ (Guillaume et al. 1994).

The spectral response of the Ho^{3+} monomers corresponds to the CEF energy level sequence of $HoBa_2Cu_3O_x$ (table 4). The coupling between the Ho^{3+} spins in the dimers produces a splitting of the CEF states. The influence of the magnetic-exchange interaction on the INS spectra for polycrystalline samples and different Ho/Y ratios is exemplified in fig. 18. Spectra of the strongly diluted (1% Ho) sample exhibit only a narrow CEF excitation (pure single ion) whereas spectra of the 10% Ho compound exhibit the dimer

and single-ion excitations. Spectra of the 100% Ho analog exhibit a broad excitation, broadened by the averaging of the dispersive excitation, which can be reasonably described by the exchange coupling of model 1 in sect. 4.3.1. The exchange Hamiltonian of the Ho^{3+} dimer can be written as

$$H_{ex} = -J^{\perp}\left(\boldsymbol{J}_1^x \cdot \boldsymbol{J}_2^x + \boldsymbol{J}_1^y \cdot \boldsymbol{J}_2^y\right) - \boldsymbol{J}^{\parallel}\left(\boldsymbol{J}_1^z \cdot \boldsymbol{J}_2^z\right). \tag{25}$$

The term with $J^{\parallel}$ does not have an influence on the dimer splitting of the lowest-lying states (due to the particular symmetry of these states) and can therefore be neglected. However, it is not zero as can be seen from the results of the previous section. A convenient basis set for the calculation is given by the functions $|J_1 J_2 JM\rangle$ with $J = J_1 + J_2$ and $-J \leqslant M \leqslant J$.

The exchange-coupling parameters are similar to those obtained from the INS experiments on the grain-aligned samples (table 12). As can be seen from this study crucial information on the exchange-coupling constants can be obtained by studying dimer excitations on dilute systems. Such investigations could be performed in any systems for which large, high-quality single crystals are not available.

4.3.3. $R_{2-x}Ce_xCuO_4$

The observation of a large linear coefficient of the specific heat for $Nd_{2-x}Ce_xCuO_4$ has been used to argue for a novel heavy-fermion material (Brugger et al. 1993), supported by theoretical considerations (Fulde 1997). This interpretation has been brought into question by recent measurements on collective magnetic excitations (Henggeler et al. 1998). The f–f and R–Cu interactions lead to an interpretation of the specific-heat data (Henggeler et al. 1998). The two-ion basis required for the R_2CuO_4 structure leads to the energy dispersion relation (simplified two level system)

$$\omega(\boldsymbol{Q}) = \Delta\sqrt{1 - \frac{2M^2\{J(\boldsymbol{Q}) \pm |J'(\boldsymbol{Q})|\}}{\Delta}\tanh\left(\frac{\Delta}{2k_B T}\right)}. \tag{26}$$

This dispersion relation contains two different branches (in the antiferromagnetic phase, more branches have to be considered) of spin waves. These branches are similar to the different branches in the phonon dispersion relation, however, in this case they exhibit energy gaps caused by the CEF interaction (Δ). Exchange parameters, J_i, correspond to exchange constants between the ith neighboring R ions perpendicular (J_1), diagonal (J_2) and within the plane (J_3,J_4) (see fig. 19).

For Pr_2CuO_4 the dispersion of the Γ_4–Γ_5 CEF transition located at 18.1 meV exhibit a dispersion of 1.2 meV (Sumarlin et al. 1995) that corresponds to an exchange coupling between Pr ions which is more than an order of magnitude stronger than the coupling found between Ho ions in $HoBa_2Cu_3O_x$ (Staub et al. 1993). The exchange-coupling constants derived from the dispersion of the excitations are tabulated in table 13. The results indicate that there is also a dispersion in the (0,0,1) direction, which reflects the

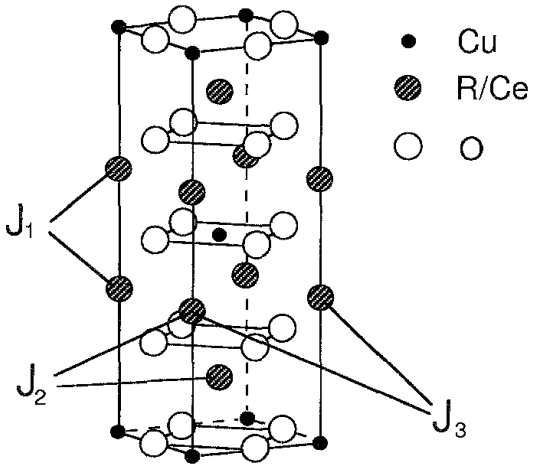

Fig. 19. Crystal structure of $R_{2-x}Ce_xCuO_4$ with the different exchange coupling constants listed in table 13.

Table 13
Exchange coupling parameters in $R_{2-x}Ce_xCuO_4$ derived from the dispersion of the CEF excitations

	Nd[a]	Nd[a]	$Nd_{1.85}Ce_{0.15}$[b]	Pr[c]	$Pr_{1.85}Ce_{0.15}$[a]
J_1 (μeV)	−32±3	−7±2	−32[d]	−50±5	−30±10
J_2 (μeV)	18±3[e]	−19±1	18[e]	−15±2	−10±2
J_3 (μeV)	−5±2	−2.5±1	−5[d]	−15±2	−16±2
J_4 (μeV)	−3±2		−3[d]		
h_{Cu}(meV)	0.52±0.03		0.38±0.04		
Δ/Δ_{CEF} (meV)	0.49	21	0.34	18.1	18.1

[a] From Henggeler et al. (1997).
[b] From Henggeler et al. (1998).
[c] From Sumarlin et al. (1995).
[d] Assumed to be the same as for pure Nd.
[e] From Henggeler, personal communications.

coupling through the CuO_2 planes. The Cu spins in this material order at $T_N = 251$ K (Sumarlin et al. 1995) and because of the crystal symmetry, a small magnetic moment is induced at the Pr site. This interaction will lift the degeneracy of the doublet, however, this splitting is too small to be resolved.

For Nd_2CuO_4, the R–Cu exchange interaction is a relevant quantity for the description of the low-energetic collective magnetic excitations. Collective excitations were studied on the $\Gamma_6^{(1)} \rightarrow \Gamma_6^{(2)}$ ($\Delta = 21$ meV) transition as well as within the $\Gamma_6^{(1)}$ doublet (Henggeler et al. 1996, 1997), which split by the R–Cu exchange interaction. Splittings of higher lying doublets has been observed by Raman spectroscopy (Jandl et al. 1995). The relevant exchange-coupling constants and splittings are listed in table 13. We note that the splitting induced by the molecular field of the Nd magnetic ordering is negligible. It is interesting to note that these coupling constants are similar except J_2 obtained from the low-energetic excitations.

For $Nd_{2-x}Ce_xCuO_4$ the magnetic excitations are shifted to lower energy transfers for increasing Ce concentrations, which directly reflect the weaker R–Cu exchange interaction

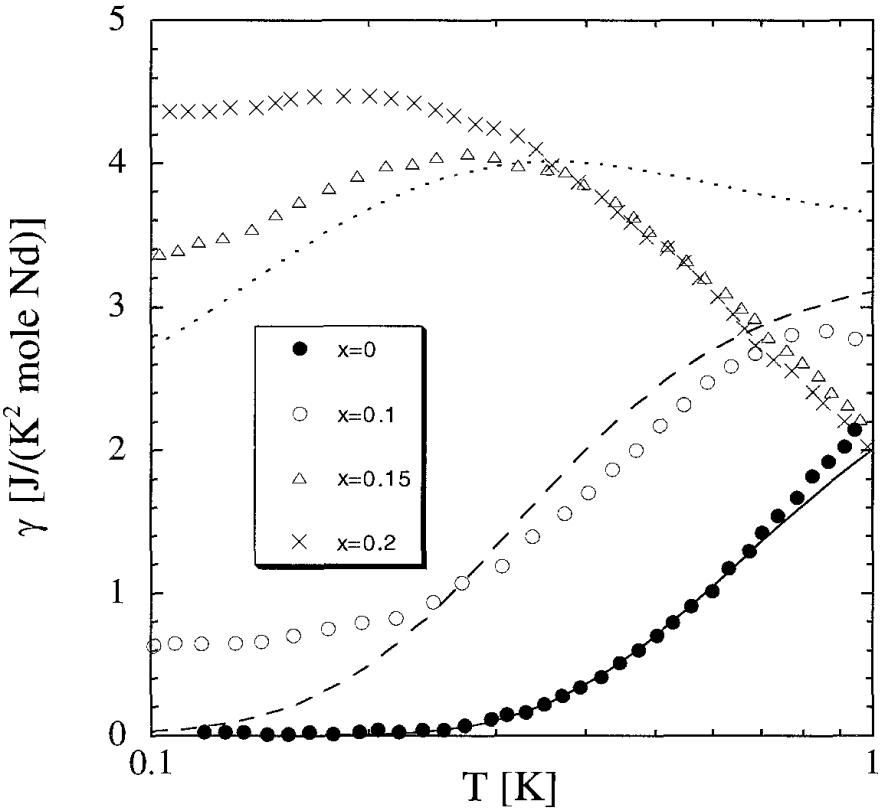

Fig. 20. Observed (Brugger et al. 1993) and calculated specific heat (Henggeler et al. 1998) of $Nd_{2-x}Ce_xCuO_4$ (solid line, $h_{Cu}=0.52$; broken line, $h_{Cu}=0.42$; dotted line, $h_{Cu}=0.38$ meV).

due to the reduced ordered magnetic moment on the Cu site. The low-lying collective excitations can be modeled by the same f–f interaction constants and a smaller R–Cu (h_{Cu}) interaction (see table 13). From this model, the magnetic contribution to the specific heat can be calculated and it is found to be in excellent agreement with the experimental data (fig. 20), Henggeler et al. 1998). These results argue strongly against the hypothesis that $Nd_{2-x}Ce_xCuO_4$ is another novel heavy-fermion system (Fulde 1997).

4.4. *f–phonon interactions*

Under specific conditions, a rare-earth crystal-field excitation may couple with a lattice-vibrational mode, leading to a renormalization of the two excitations with resulting changes in wavefunctions, energies and linewidths of the associated transitions (bound state). The degree to which these two excitations can couple is a function of their symmetry, spatial orientation and energy differences. For R-containing high-T_c superconductors, phonons that correspond to the motion of the nearest-neighbor oxygen ions are the most likely to couple with the CEF excitations. Therefore, observable effects may be expected if a crystal-field transition has an energy similar to that of one of the two Raman-active modes that involve the oxygens from the CuO_2 planes.

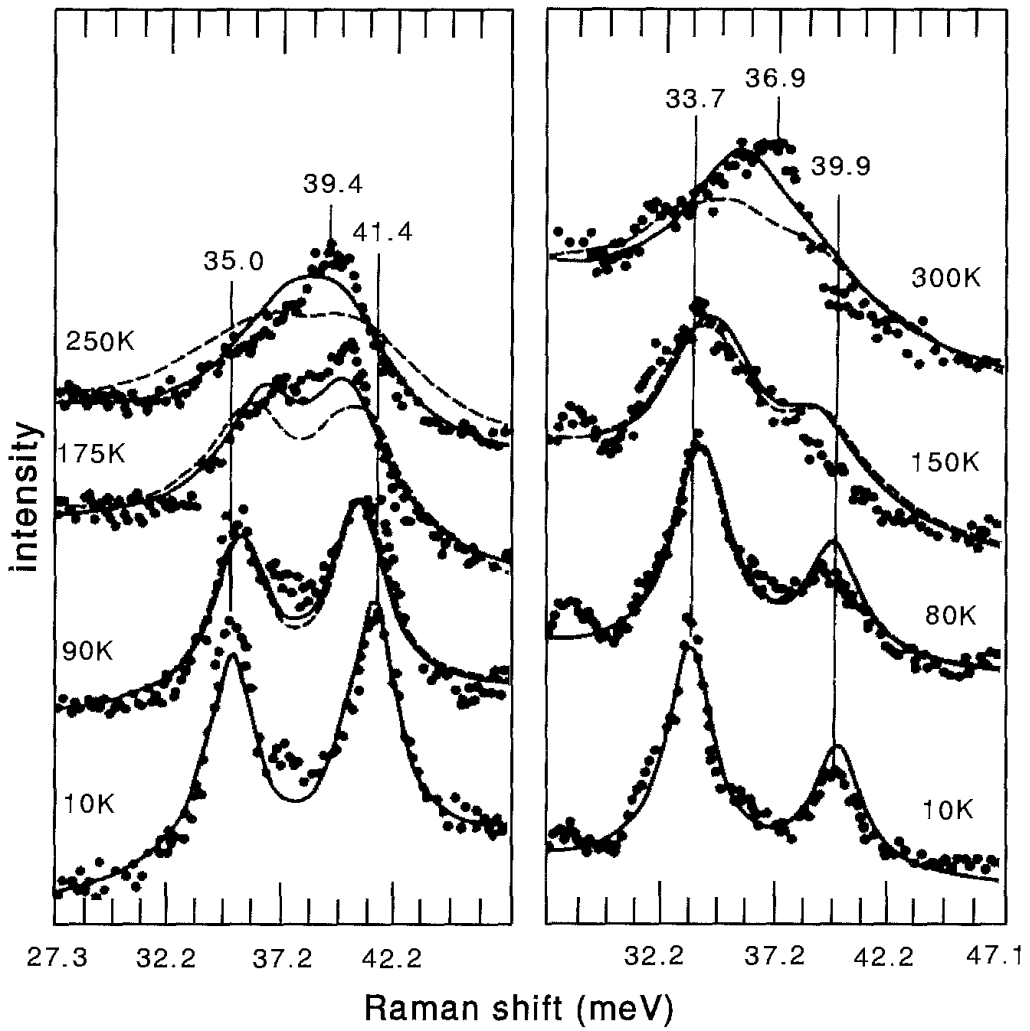

Fig. 21. Raman spectra of $NdBa_2Cu_3O_7$ with isotopic enrichment ^{16}O (left panel) and ^{18}O (right panel). Data and fit are taken from (Heyen et al. 1991b).

This coupling has been observed in both $NdBa_2Cu_3O_{7-\delta}$ and $Pb_2Sr_2NdCu_3O_8$ (Heyen et al. 1991a,b, Wegerer et al. 1993). The R ion occupies a site with an inversion center in both these materials, and therefore Raman-active transitions between the CEF states are forbidden. The Nd^{3+} crystal-field transition, expected near 36 meV for both these compounds (Soderholm et al. 1991a), has Γ_5 (B_{1g}) symmetry in a tetragonal (or in these cases pseudo-tetragonal) unit cell, and therefore it can couple with the planar oxygen out-of-phase phonon mode with the same symmetry, which is expected at about 38 meV. Indeed, a double-peaked feature is observed near 37 meV by both neutron scattering (Allenspach et al. 1989a), which is sensitive to the CEF transition, and Raman spectroscopy, which is sensitive to the phonon (Ruf 1996).

Figure 21 shows the temperature dependence of the Raman spectra for different oxygen isotopes (O^{16} and O^{18}) in $NdBa_2Cu_3O_7$ (Heyen et al. 1991b). The two peaks observed in the Raman experiment correspond to only the phononic character of the coupled

excitation. At low temperatures both isotopic samples show relatively strong and well-separated peaks. For rising temperatures, one peak is decreasing in intensity and the energy separation of the excitations is decreasing too. Above 50 K the population of the magnetic ground state is decreasing and therefore the phonon, with a temperature dependence that follows Bose statistics, is less able to couple with the magnetic ground-state excitation. This is manifested in the Raman spectra by the observed energy separation between the excitations, which decreases due to this decoupling. In addition, the decoupling accounts for the decreasing intensity upon rising temperature of one peak, because the decoupling separates the transitions, one of which has more phononic character than the other, which has more magnetic character. The comparison of the temperature dependence between the O^{16} and the O^{18} isotopic samples reveals the fundamental physics of the coupling between these two excitations. In $NdBa_2Cu_3O_7^{18}$ the energy of the unaffected B_{1g} phonon mode is expected to be 6% smaller than for $NdBa_2Cu_3O_7^{16}$, because the pure energies of the two excitations are interchanged by replacing O^{18} by O^{16}. Therefore, the higher-energy peak in $NdBa_2Cu_3O_7^{18}$ decreases in intensity with rising temperature, corresponding more and more to the pure CEF excitation, whereas for the O^{16} compound this behavior is reversed.

The renormalized energies of the two-coupled excitations are given by (Thalmeier and Fulde 1982)

$$E_{1,2} = \frac{\hbar\omega_{\mathrm{ph}} + \hbar\omega_{\mathrm{CEF}}}{2} \pm \sqrt{\left(\frac{\hbar\omega_{\mathrm{ph}} + \hbar\omega_{\mathrm{CEF}}}{2}\right)^2 + \frac{V^2}{2}}, \tag{27}$$

assuming that other CEF levels are not significantly affected by this renormalization. Here, $\hbar\omega_{\mathrm{ph}}$ and $\hbar\omega_{\mathrm{CEF}}$ correspond to the pure phonon and CEF energies, respectively, and V corresponds to the coupling matrix element between the two excitations. Thalmeier and Fulde (Thalmeier and Fulde 1982, Thalmeier 1984) have shown that this picture remains unchanged even when phonon dispersion is taken into account, provided that the phonon band width (dispersion of the branch) $\hbar\omega_{\mathrm{ph}}(q)$ is smaller than V. This condition is most likely fulfilled for $NdBa_2Cu_3O_x$, where the splitting is about 6 meV at low temperature, and the width for this particular phonon band is expected to be approximately 2 meV.

The splitting of the 38 meV peak was also observed by an INS experiment (Allenspach et al. 1989a) which is much more sensitive to the magnetic character of the coupled transitions in the particular Q range chosen for the experiment. The main difference between the two experiments is that the INS experiment on a polycrystalline material is averaged in Q over the whole Brillouin zone whereas the Raman experiment probes the zone center alone. The Q dependence in the INS experiment confirms the magnetic origin of these two transitions, in agreement with expectation.

The observed splitting of these two transitions allows the determination of the coupling matrix element, V, as well as the unperturbed energies of the B_{1g} phonon and CEF excitation. The values obtained by E.T. Heyen et al. (1991b) at 10 K are $V = 4.3$ meV for the coupling matrix element, and $\hbar\omega_{\mathrm{ph}} = 38.2$ and $\hbar\omega_{\mathrm{CEF}} = 37.7$ meV for the pure energies of the phonon and CEF excitations, respectively. There is a temperature dependence

to these parameters (Wegerer et al. 1993) that is conjectured to originate from phonon dispersion, which may not have been adequately treated. An anomaly in the temperature dependence of both $\hbar\omega_{ph}$ and $\hbar\omega_{CEF}$ is observed at T_c.

A Raman study on $Pb_2Sr_2NdCu_3O_8$, (Wegerer et al. 1993) in which the Nd has a very similar local environment to that observed in $NdBa_2Cu_3O_7$ (Marezio et al. 1990) also revealed a coupling between the phonon and crystal-field excitations with B_{1g} symmetry. A fit of the $Pb_2Sr_2NdCu_3O_8$ data using the same procedures as those employed for the $NdBa_2Cu_3O_7$ data, results in a value of $V = 2.8$ meV. No anomaly is observed in the temperature dependence of $\hbar\omega_{ph}$, in agreement with the absence of superconductivity in the parent $Pb_2Sr_2Nd_{1-x}Ca_xCu_3O_8$ ($x = 0$) compound.

These Raman results raise an interesting question. A strong coupling has been reported between the Nd crystal-field transition and the phonon mode with B_{1g} symmetry in two superconducting series. The result of this coupling is the admixture of some crystal-field character into the oxygen out-of-phase phonon mode with the same symmetry. This phonon mode involves oxygens in the CuO planes that support the superconductivity. There is even an anomaly observed in the temperature dependence of both $\hbar\omega_{ph}$ and $\hbar\omega_{CEF}$ at T_c and yet there is no observed effect on T_c for the Nd analog of either $RBa_2Cu_3O_7$ or the $Pb_2Sr_2R_{.5}Ca_{.5}Cu_3O_8$ series. Both $NdBa_2Cu_3O_7$ and $Pb_2Sr_2Nd_{.5}Ca_{.5}Cu_3O_8$ have T_c's that follow the trends established by their respective series, despite the fact that Nd has a rather large magnetic moment. These results appear to support the current belief that phonons (at least this particular branch) are not a major player in the mechanism responsible for high-T_c superconductivity. Otherwise a large anomaly would be expected in the variation of T_c with R at Nd. Such an anomaly is not observed.

4.5. *Tb^{3+} magnetic correlations: a perfect two-level system?*

The Tb analog is one of the $RBa_2Cu_3O_x$ series that does not form, although partial substitution of Y with Tb results in single-phase samples up to Y:Tb 1:1 (thin films) (Fincher and Blanchet 1991). No adverse effect on the superconducting properties of these doped samples was observed as a function of Tb concentration. The Tb member of the $Pb_2Sr_2R_{1-x}Ca_xCu_3O_8$ series does form, and the $x = 0.5$ compound is a high-T_c superconductor.

X-ray absorption studies demonstrate a trivalent oxidation state for Tb in both series (Staub et al. 1994a, 1995b). Whereas Tb does not appear to influence the superconducting properties of either $Y_{1-x}Tb_xBa_2Cu_3O_\delta$ (Fincher and Blanchet 1991, Staub et al. 1994a) or $Pb_2Sr_2Tb_{1-x}Ca_xCu_3O_8$ (Staub et al. 1995b, Soderholm et al. 1997), it does appear to have a marked effect on the magnetic properties exhibited by these materials. In the double-layer compounds that form R = Tb analogs, the Tb sublattices exhibit high magnetic-ordering temperatures (T_N). For example, $TlSr_2TbCu_2O_7$ has $T_N = 7$ K (Sundaresan et al. 1995) and $Pb_2Sr_2Tb_{1-x}Ca_xCu_3O_8$ has $T_N = 5.3$ K for $x = 0$ (Shih et al. 1994) and $T_N = 4$ K for $x = 0.5$ (Staub et al. 1997e). In addition, short-range Tb–Tb magnetic correlations have

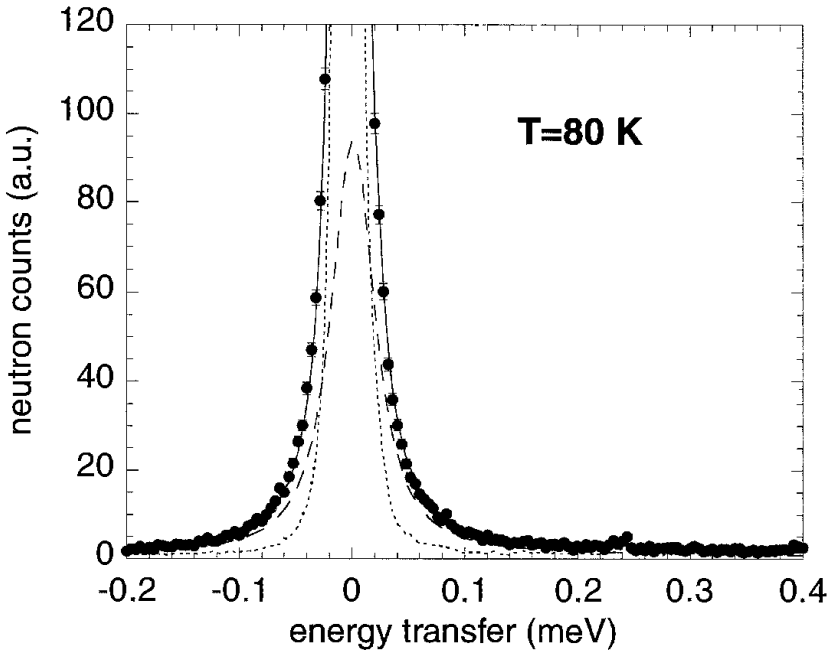

Fig. 22. INS energy spectra from $Pb_2Sr_2Tb_{0.5}Ca_{0.5}Cu_3O_8$. The dotted line corresponds to the fit of the elastic component, the broken line to the fit of the quasi-elastic component (Lorentzian) and the solid line to the total fit (Staub et al. 1996b).

been observed up to temperatures more than an order of magnitude above T_N (Staub et al. 1996b).

Insight into the mechanism responsible for such apparently strong Tb–Tb correlations has been gained from a detailed analysis of the electronic properties of Tb in these compounds. In $Y_{1-x}Tb_xBa_2Cu_3O_{7-\delta}$ and $Pb_2Sr_2Tb_{1-x}Ca_xCu_3O_8$, Tb exhibits a quasi-doublet ground-state, two singlets separated by only a few μeV (Staub et al. 1994a, 1996b), which are in turn separated by about 20 meV from the higher-lying CEF states. The two states forming the quasi-doublet do not merge, even when the symmetry is formally raised to cubic (Lea et al. 1962). Therefore, this system has been modeled as a two-level system.

Typical low-energy INS spectra of $Pb_2Sr_2Tb_{0.5}Ca_{0.5}Cu_3O_8$, a superconductor with $T_c = 71$ K and T_N(Tb sublattice) of 4 K, taken with 15 μeV resolution, are shown in fig. 22 for 80 K. The peak at the origin of the energy spectrum is decomposed for analysis into two magnetic components: (i) a static, resolution-limited component and (ii) a dynamic, quasi-elastic component with a Lorentzian lineshape. Static effects are attributed to the elastic contribution (Γ resolution is 15 μeV). They include coherent and incoherent nuclear scattering as well as coherent magnetic scattering because the data cover a Q range that includes a two-dimensional magnetic Bragg reflection (below T_N) or spin correlations (above T_N) slower than $\nu < 10^{11}$ Hz.

In order to analyze the data, the Tb^{3+} paramagnetic ground state is described using the CEF Hamiltonian, and the ordered ground state, including short-range order, is described

using the MF approximation (eqs. 8, 13). The evolution of the magnetic moment and the corresponding splitting is given analytically by (Lovesey 1996)

$$|\langle a|J^z|a\rangle|^2 = |\langle b|J^z|b\rangle|^2 \propto \left[1-\left(\frac{\Delta}{\varepsilon}\right)^2\right]|\langle 0|J^z|1\rangle|^2,$$
$$|\langle b|J^z|a\rangle|^2 = |\langle a|J^z|b\rangle|^2 \propto \left(\frac{\Delta}{\varepsilon}\right)^2|\langle 0|J^z|1\rangle|^2, \tag{28}$$

where $|a\rangle$, $|b\rangle$ and $|0\rangle$, $|1\rangle$ correspond to the wavefunctions of the MF and pure CEF states labeled with a, b and 0, 1, respectively. $\Delta = E_1 - E_0$ (7 μeV) is the energy splitting of the pure CEF states, $\varepsilon = E_b - E_a$ (0.6 meV) is the energy differences between the two lowest states in the MF model, and $\beta = 1/k_B T$, where k_B is the Boltzmann constant. The energy splitting of the MF states is given by

$$\varepsilon = \sqrt{\Delta^2 + 4g_J^2\lambda^2|\langle 1|J^z|0\rangle|^2}. \tag{29}$$

Here, λ is the mean-field constant and can be directly calculated from the susceptibility at T_N [$\lambda/g_J^2 = \chi(T_N)^{-1}$] and is found to be 6.4 μeV (Staub et al. 1995b).

The CEF wavefunctions (without MF), calculated by assuming the pure CEF wavefunctions in eqs. (28) and (29), are almost pure $|6\rangle$ and $|-6\rangle$ (see table 7). The Tb^{3+} saturation moment is calculated using these wavefunctions in eqs. (28) and (29), together with an exchange-interaction strength λ. The value obtained for the saturation moment, $9\mu_B$, is in excellent agreement with the magnetic-neutron diffraction results of $9.1\mu_B$ for the pure Tb sample, or the $8.8\mu_B$ for the Tb/Ca sample (Staub et al. 1997e).

The value obtained for λ (6.4 μeV, Staub et al. 1995b) is roughly the same as that found in $HoBa_2Cu_3O_7$, which has a T_N of only 0.19 K (Roessli et al. 1993) compared to the T_N of 5.3 K found for $Pb_2Sr_2TbCu_3O_8$. These results demonstrate that a small interaction strength leads to a moderate splitting of the Tb quasi-doublet ground-state and an interchange of the transition strengths. The small value of λ results in such a high T_N for the Pb-based compound because of the extremely small ratio of Δ/ε. The particular details of the wavefunctions result in $g_J^2|\langle 1|J^z|0\rangle|^2 \approx g_J^2 J^2 \approx 81$, which leads to a squared saturation moment of $g_J^2 J^2(1-(\Delta/\varepsilon)^2) \approx g_J^2 J^2 \approx 81$. The total magnetic scattering is $g_J^2 J(J+1)$. The remaining magnetic scattering is of the order of $g_J^2 J$ and can be found in the transverse CEF transition between the ground state and states with components of $m = \pm 5$ (Staub et al. 1995b).

The integrated magnetic intensities of the $Pb_2Sr_2Tb_{1-x}Ca_xCu_3O_8$ INS elastic line are shown in fig. 23 as a function of temperature. At elevated temperatures ($T = 200$ K) only a quasi-elastic component was observed, whereas at low temperature ($T < 40$ K) only the static, elastic component was observed. The same was found in $Y_{0.9}Tb_{0.1}Ba_2Cu_3O_x$. Similar behavior has been observed previously in spin-glass systems such as the Cu–Mn alloys (Murani 1985). The temperature dependence observed in the Pb-based system is interpreted as follows. At low temperatures (1.5 K) the Tb spins are ordered

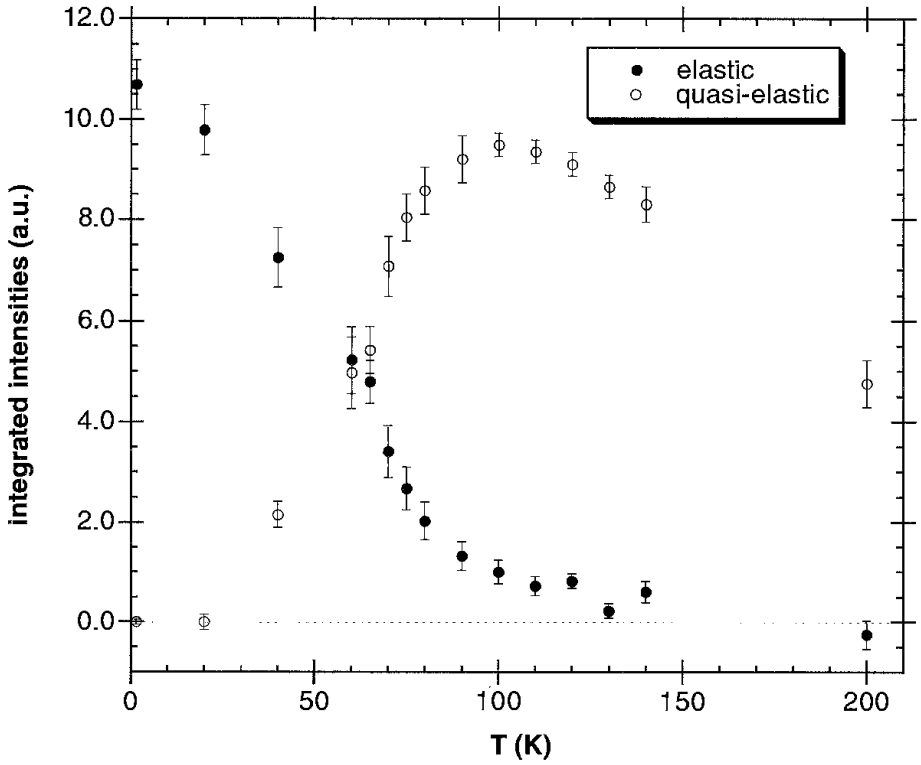

Fig. 23. Temperature dependence of the integrated magnetic intensities of the quasi-elastic and elastic components (Staub et al. 1996b).

antiferromagnetically ($T_N \approx 4$ K (Staub et al. 1997e) and only the elastic contribution is observed. The elastic component to the intensity starts to decrease and the quasi-elastic component to increase between 20 K to 40 K, which indicates that the magnetic moments of the correlated spins are decreasing with rising temperature. Above 100 K, the quasi-elastic intensity also decreases, which is the result of the thermal depopulation of the ground state. At 200 K the magnetic-elastic intensity has vanished, and the system is well described by a paramagnetic model with two singlets acting as a doublet because $\Gamma \gg \Delta$. This doublet carries the large transition probability of the $|0\rangle \rightarrow |1\rangle$ CEF transition.

These results can be compared to those found for $NdBa_2Cu_3O_x$ (Drössler et al. 1996). In $NdBa_2Cu_3O_{6.9\ (6.4)}$, a magnetic quasi-elastic component was observed with a Gaussian lineshape that persisted at temperatures up to 5 K (10 K), which is well above T_N of 0.5 (1.5) K. The Gaussian type of magnetic intensity observed in $NdBa_2Cu_3O_x$ and the elastic-magnetic contribution in the Tb analogs may have the same basic origin. Both could be explained by a distribution of magnetic fields acting at the R site induced by the Cu sublattice due to the R–Cu interaction, which is mediated over the plane-oxygen ions. Such a R–Cu interaction could explain the higher T_N of $NdBa_2Cu_3O_x$ for the low oxygen compounds, in which the Cu sublattice is ordered antiferromagnetically even at high temperatures, whereas in the superconductor only copper dynamics exist. The fact that such an effect is observed for Tb, for which a much smaller R–Cu exchange interaction is expected, can be explained by the particulars of the two-level system, with

the very small energy separation, discussed herein. In the latter case, very small changes in interactions may change the magnetic properties significantly. Even though such a scenario is likely there may be other possible interpretations (e.g. elastic component as precursor of magnetic order) that cannot be ruled out based on the available data.

Acknowledgments

This work was supported by DOE-BES, Chemical Sciences, under contract W-31-109-ENG-38.

References

Abragam, A., and B. Bleaney, 1970, Electron Paramagnetic Resonance of Transition Ions (Clarendon Press, Oxford) 911 pp.

Aksenov, V.L., and V.V. Kabanov, 1994, Phys. Rev. B **49**, 3524.

Allenspach, P., A. Furrer, P. Brüesch and P. Unternährer, 1989a, Physica B **156–157**, 864.

Allenspach, P., F. Hulliger and A. Furrer, 1989b, Phys. Rev. B **39**, 2226.

Allenspach, P., J. Mesot, U. Staub, M. Guillaume, A. Furrer, S.-I. Yoo, M.J. Kramer, R.W. McCallum, H. Maletta, H. Blank, H. Mutka, R. Osborn, M. Arai, Z. Bowden and A.D. Taylor, 1994, Z. Phys. B **95**, 301.

Alp, E.E., L. Soderholm, G.K. Shenoy, D.G. Hinks, D.W. Capone, K. Zhang and B.D. Dunlap, 1987, Phys. Rev. B **36**, 8910.

Amoretti, G., R. Caciuffo, P. Santini, O. Francescangeli, E.A. Goremychkin, R. Osborn, G. Calestani, M. Sparpaglione and L. Bonoldi, 1994, Physica C **221**, 227.

Becker, K.W., P. Fulde and J. Keller, 1977, Z. Phys. B **28**, 9.

Beyers, R., B.T. Ahn, G. Gorman, V.Y. Lee, S.S.P. Parkin, M.L. Ramirez, K.P. Roche, J.E. Vazquez, T.M. Gür and R.A. Huggins, 1989, Nature **340**, 619.

Bleaney, B., and K.W.H. Stevens, 1953, Rep. Prog. Phys. **16**, 108.

Boothroyd, A.T., S.M. Doyle, D.M. Paul, D.S. Misra and R. Osborn, 1990, Physica C **165**, 17.

Boothroyd, A.T., S.M. Doyle, D.M. Paul and R. Osborn, 1992, Phys. Rev. B **45**, 10075.

Boothroyd, A.T., S.M. Doyle and R. Osborn, 1993, Physica C **217**, 425.

Boothroyd, A.T., A. Mukherjee and A.P. Murani, 1996, Phys. Rev. Lett. **77**, 1600.

Bradbury, M.I., and D.J. Newman, 1967, Chem. Phys. Lett. **1**, 44.

Brown, S.E., J.D. Thompson, J.O. Willis, R.M. Aikin, E. Zirngiebl, J.L. Smith, Z. Fisk and R.B. Schwarz, 1987, Phys. Rev. B **36**, 2298.

Brugger, T., T. Schreiner, G. Roth, P. Adelmann and G. Czjzek, 1993, Phys. Rev. Lett. **71**, 2481.

Carnall, W.T., G.L. Goodman, K. Rajnak and R.S. Rana, 1988, A systematic analysis of the spectra of the lanthanides doped into single crystal LaF_3 (Argonne National Laboratory) 143 pp.

Carnall, W.T., G.L. Goodman, K. Rajnak and R.S. Rana, 1989, J. Chem. Phys. **90**, 3443.

Casalta, H., P. Bourges, D. Petitgrand and A. Ivanov, 1996, Solid State Commun. **100**, 683.

Cava, R.J., B. Batlogg, C.H. Chen, E.A. Rietman, S.M. Zahurak and D. Werder, 1987, Nature **329**, 423.

Cava, R.J., B. Batlogg, J.J. Krajewski, L.W. Rupp, L.F. Schneemeyer, T. Siegrest, R.B. vanDover, P. Marsh and W.F. Peck, 1988, Nature **336**, 211.

Cava, R.J., A.W. Hewat, E.A. Hewat, B. Battlog, M. Marezio, K.M. Rabe, J.J. Krajewski, W.F. Peck Jr, L.W. Rupp, P.K. Gallagher, S.H. Glarum, J.H. Marshall, R.C. Farrow, J.V. Waszczak, R. Hull and P. Treror, 1990, Physica C **165**, 419.

Chattopadhyay, T., H. Maletta, W. Wirges, K. Fischer and P.J. Brown, 1988, Phys. Rev. B **38**, 838.

Crosswhite, H.M., and H. Crosswhite, 1984, J. Opt. Soc. Am. B **1**, 246.

Dalichaouch, Y., M.S. Torikachvili, E.A. Early, B.W. Lee, C.L. Seaman, K.N. Yang, H. Zhou and M.B. Maple, 1988, Solid State Commun. **65**, 1001.

Dieke, G.H., 1968, Spectra and Energy Levels of Rare Earth Ions in Crystals (Interscience Publishers, New York) 401 pp.

Drössler, H., H.D. Jostarndt, J. Harnischmacher, J. Kalenborn, U. Walter, A. Severing, W. Schlabitz and E. Holland-Moritz, 1996, Z. Phys. B **100**, 1.

Dufour, P., S. Jandl, C. Thomsen, M. Cardona, B.M. Wanklyn and C. Changkang, 1995, Phys. Rev. B **51**, 1053.

Fauth, F., U. Staub, M. Guillaume, J. Mesot, A. Furrer, P. Dosanjh, H. Zhou and P. Vorderwisch, 1995, J. Phys.: Condens. Matter **7**, 4215.

Fehrenbacher, R., and T.M. Rice, 1993, Phys. Rev. Lett. **70**, 3471.

Fincher Jr, C.R., and G.B. Blanchet, 1991, Phys. Rev. Lett. **67**, 2902.

Fischer, P., B. Schmid, P. Brüesch, F. Stucki and P. Unternährer, 1989, Z. Phys. B **74**, 183.

Freeman, A.J., and R.E. Watson, 1962, Phys. Rev. **127**, 2058.

Fulde, P., 1997, Physica B, **230–232**, 1.

Fulde, P., and M. Loewenhaupt, 1985, Adv. Phys. **34**, 589.

Furrer, A., H.U. Güdel and J. Darriet, 1985, J. Less-Common Met. **111**, 223.

Furrer, A., P. Brüesch and P. Unternährer, 1988, Phys. Rev. B **38**, 4616.

Furrer, A., P. Allenspach, J. Mesot and U. Staub, 1990a, Physica C **168**, 609.

Furrer, A., H.U. Güdel, E.R. Krausz and H. Blank, 1990b, Phys. Rev. Lett. **64**, 68.

Furrer, A., J. Mesot, W. Henggeler and G. Bottger, 1997, J. Supercond. **10**, 273.

Goldman, A.I., B.X. Yang, J. Tranquada, J.E. Crow and Chan-See Jee, 1987, Phys. Rev. B **36**, 7234.

Goodman, G.L., C.-K. Loong and L. Soderholm, 1991, J. Phys.: Condens. Matter **3**, 49.

Goodwin, T.J., R.N. Shelton, H.B. Radousky, N. Rosov and J.W. Lynn, 1997, Phys. Rev. B **55**, 3297.

Goremychkin, E.A., R. Osborn and A.D. Taylor, 1989, JETP Lett. **50**, 380.

Guillaume, M., P. Allenspach, J. Mesot, U. Staub, A. Furrer, R. Osborn, A.D. Taylor, F. Stucki and P. Unternährer, 1992, Solid State Commun. **81**, 999–1002.

Guillaume, M., P. Allenspach, J. Mesot, B. Roessli, U. Staub, P. Fischer and A. Furrer, 1993, Z. Phys. B **90**, 13.

Guillaume, M., U. Staub, F. Fauth, J. Mesot, A. Furrer and C.J. Carlile, 1994, Physica C **223**, 333.

Guillaume, M., W. Henggeler, A. Furrer, R.S. Eccleston and V. Trounov, 1995, Phys. Rev. Lett. **74**, 3423.

Guo, G.Y., and W.M. Temmerman, 1990, Phys. Rev. B **41**, 6372.

Henggeler, W., T. Chattopadhyay, P. Thalmeier, P. Vorderwisch and A. Furrer, 1996, Europhys. Lett. **34**, 537.

Henggeler, W., T. Chattopadhyay, B. Roessli, P. Vorderwisch, P. Thalmeier, D.I. Zhigunov, S.N. Barilo and A. Furrer, 1997, Phys. Rev. B **55**, 1269.

Henggeler, W., B. Roessli, A. Furrer, P. Vorderwisch and T. Chatterij, 1998, Phys. Rev. Lett. **80**, 1300.

Henggeler, W., M. Guillaume, P. Allenspach, J. Mesot, A. Furrer and M. Adams, 1999, J. Phys.: Condens. Matter **11**, 2921.

Heyen, E.T., R. Wegerer and M. Cardona, 1991a, Phys. Rev. Lett. **67**, 144.

Heyen, E.T., R. Wegerer, E. Schönherr and M. Cardona, 1991b, Phys. Rev. B **44**, 10195.

Hilscher, G., E. Holland-Moritz, T. Holubar, H.-D. Jostarndt, V. Nekvasil, G. Schaudy, U. Walter and G. Fillion, 1994, Phys. Rev. B **49**, 535.

Hizhnyakov, V., N. Kristoffel and E. Sigmund, 1989, Physica C **161**, 435.

Hodges, J.A., P. Impert and G. Jéhanno, 1987, Solid State Commun. **64**, 1209.

Hor, P.H., R.L. Meng, Y.Q. Wang, L. Gao, Z.J. Huang, J. Bechtold, K. Forster and C.W. Chu, 1987, Phys. Rev. Lett. **58**, 1891.

Hutchings, M.T., 1964, Point-charge calculations of energy levels of magnetic ions in crystalline electric fields, in: Solid State Physics: Advances in Research and Applications, eds F. Seitz and D. Turnbull (Academic Press, New York) Vol. 16, p. 227.

Hutchings, M.T., and W.P. Wolf, 1964, J. Chem. Phys. **41**, 617.

Jandl, S., P. Dufour, T. Strach, T. Ruf, M. Cardona, V. Nekvasil, C. Chen and B.M. Wanklyn, 1995, Phys. Rev. B **52**, 15558.

Jostarndt, H.-D., U. Walter, J. Harnischmacher, J. Kalenborn, A. Severing and E. Holland-Moritz, 1992, Phys. Rev. B **46**, 14872.

Judd, B.R., 1963, Operator Techniques in Atomic Spectroscopy (McGraw-Hill, New York) 242 pp.

Kassman, A.J., 1970, J. Chem. Phys. **53**, 4118.

Kern, S., C.K. Loong and G.H. Lander, 1985, Phys. Rev. B **32**, 3051.

Kovacevic, Z., and N.M. Plakida, 1994, Physica C **228**, 15.

Kremer, R.K., E. Sigmund, V. Hizhnyakov, F. Hentsch, A. Simon, K.A. Müller and M. Mehring, 1992, Z. Phys. B **86**, 319.

Lai, C.C., J.H. Shieh, B.S. Chiou, J.C. Ho and H.C. Ku, 1994, Phys. Rev. B **49**, 1499.

Lea, K.R., M.J.M. Leask and W.P. Wolf, 1962, J. Phys. Chem. Solids **23**, 1381.

Leask, M.J.M., M.R. Wells, R.C.C. Ward, S.M. Hayden and J. Jensen, 1994, J. Phys.: Condens. Matter **6**, 505.

Li, W.-H., J.W. Lynn, S. Skanthakumar and T.W. Clinton, 1989, Phys. Rev. B **40**, 5300.

Liechtenstein, A.I., I.I. Mazin and O.K. Andersen, 1995, Phys. Rev. Lett. **74**, 2303.

Loewenhaupt, M., A. Metz, N.M. Pyka, D.M. Paul, J. Martin, V.H.M. Duijn, J.J.M. Franse, H. Mutka and W. Schmidt, 1996, Ann. Phys. **5**, 197.

Loong, C.-K., and L. Soderholm, 1992, J. Alloys & Compounds **181**, 241.

Loong, C.K., and L. Soderholm, 1993, Phys. Rev. B **48**, 14001.

Lovesey, S.W., 1996, J. Phys.: Condens. Matter **8**, 5915.

Lovesey, S.W., and U. Staub, 2000, Phys. Rev. B **61**, 9130.

Lütgemeier, H., S. Schmenn, P. Meuffels, O. Storz, R. Schöllhorn, C. Niedarmeyer, I. Heinmaa and Y. Baikov, 1996, Physica C **267**, 191.

Maletta, H., E. Pörschke, T. Chattopadahyay and P.J. Brown, 1990, Physica C **166**, 9.

Marezio, M., A. Santoro, J.J. Capponi, E.A. Hewat, R.J. Cava and F. Beech, 1990, Physica C **169**, 401.

Marshall, W., and S.W. Lovesey, 1971, Theory of Thermal Neutron Scattering (Oxford University Press, Oxford) 623 pp.

Martin, A.A., T. Ruf, M. Cardona, S. Jandl, D. Barba, V. Nekvasil, M. Diviš and T. Wolf, 1999, Phys. Rev. B **59**, 6528.

Matsuda, M., K. Yamada, K. Kakurai, H. Kadowaki, T.R. Thurston, Y. Endoh, Y. Hidaka, R.J. Birgeneau, M.A. Kastner, P.M. Gehring, A.H. Moudden and G. Shirane, 1990, Phys. Rev. B **42**, 10098.

Mesot, J., P. Allenspach, U. Staub, A. Furrer and H. Mutka, 1993a, Phys. Rev. Lett. **70**, 865.

Mesot, J., P. Allenspach, U. Staub, A. Furrer, H. Mutka, R. Osborn and A. Taylor, 1993b, Phys. Rev. B **47**, 6027.

Mesot, J., G. Böttger, H. Mutka and A. Furrer, 1998, Europhys. Lett. **44**, 498.

Morrison, J.C., and K. Rajnak, 1971, Phys. Rev. A **3**, 536.

Mukherjee, A., A.T. Boothroyd, D.M. Paul, M.P.S. Kumar and M.A. Adams, 1994, Phys. Rev. B **49**, 13089.

Murani, A.P., 1985, J. Phys. F **15**, 417.

Muroi, M., and R. Street, 1995, Physica C **246**, 357.

Muzichka, Y.U., E.A. Goremychkin, I.V. Sashin, M. Divis, V. Nekvasil, M. Nevriva and G. Fillion, 1992, Solid State Commun. **82**, 461.

Nekvasil, V., 1988, Solid State Commun. **65**, 1103.

Nekvasil, V., E. Holland-Moritz, H.-D. Jostarndt, U. Walter and G. Hilscher, 1992, J. Magn. Magn. Mater. **117**, 11.

Neumeier, J.J., T. Bjornholm, M.B. Maple and I.K. Schuller, 1989, Phys. Rev. Lett. **63**, 2516.

Newman, D.J., 1971, Adv. Phys. **20**, 197.

Newman, D.J., and B. Ng, 1989, Rep. Prog. Phys. **52**, 699.

Newman, D.J., and G.E. Stedman, 1969, J. Chem. Phys. **51**, 3013.

Nichols, D.H., B. Dabrowski, U. Welp and J.E. Crow, 1994, Phys. Rev. B **49**, 9150.

Norton, D.P., D.H. Lowndes, B.C. Sales, J.D. Budai, B.C. Chakoumakos and H.R. Kerchner, 1991, Phys. Rev. Lett. **66**, 1537.

Norton, D.P., D.H. Lowndes, B.C. Sales, J.D. Budai, E.C. Jones and B.C. Chakoumakos, 1994, Phys. Rev. B **49**, 4182.

Nücker, N., E. Pellegrin, P. Schweiss, J. Fink, W. Frentup, A. Erb and G. Müller-Vogt, 1995, Phys. Rev. B **51**, 8529.

Osborn, R., and E.A. Goremychkin, 1991, Physica C **185**, 1179.

Oseroff, S.B., D. Rao, F. Wright, D.C. Vier, S. Schultz, J.D. Thompson, Z. Fisk, S.W. Cheong, M.F. Hundley and M. Tovar, 1990, Phys. Rev. B **41**, 1934.

Pyttlik, T., and K.W. Becker, 1998, Z. Phys. B **3**, 333.

Radousky, H.B., 1992, J. Mater. Res. **7**, 1917.

Rastelli, E., and A. Tassi, 1998, Z. Phys. B **4**, 285.

Roessli, B., P. Allenspach, P. Fischer, J. Mesot, U. Staub, H. Maletta, P. Brüesch, C. Ritter and A.W. Hewat, 1992, Physica B **180–181**, 396.

Roessli, B., P. Fischer, U. Staub, M. Zolliker and A. Furrer, 1993, Europhys. Lett. **23**, 511.

Ruf, T., 1996, Physica B **219–220**, 132.

Sachidanandam, R., T. Yildirim, A.B. Harris, A. Aharony and O. Entin-Wohlman, 1997, Phys. Rev. B **56**, 260.

Sanjuán, M.L., and M.A. Laguna, 1995, Phys. Rev. B **52**, 13000.

Sanjurjo, J.A., G.B. Martins, P.G. Pagliuso, E. Granado, I. Torriani, C. Rettori, S. Oseroff and Z. Fisk, 1995, Phys. Rev. B **51**, 1185.

Schneemeyer, L.F., R.J. Cava, A.C.W.P. James, P. Marsh, T. Siegrist, J.V. Waszczak, J.J. Krajewski, W.P. Peck Jr, R.L. Opila, S.H. Glarum, J.H. Marshall, R. Hull and J.M. Bonar, 1989, Chem. Mater. **1**, 548.

Shaltiel, D., C. Noble, J. Pilbrow, D. Hutton and E. Walker, 1996, Phys. Rev. B **53**, 12430.

Shieh, J.H., H.C. Ku and J.C. Ho, 1994, Phys. Rev. B **50**, 3288.

Shih, C.R., T.H. Meen, Y.C. Chen and H.D. Yang, 1994, Phys. Rev. B **50**, 9619.

Skanthakumar, S., and L. Soderholm, 1996, Phys. Rev. B **53**, 920.

Skanthakumar, S., W.-H. Li, J.W. Lynn, A. Kebede, J.E. Crow and T. Mihalisin, 1990, Physica B **163**, 239.

Skanthakumar, S., J.W. Lynn and F. Dogan, 1997, J. Appl. Phys. **81**, 4934.

Soderholm, L., 1992, J. Alloys & Compounds **181**, 13.

Soderholm, L., K. Zhang, D.G. Hinks, M.A. Beno, J.D. Jorgenson, C.U. Segre and I.K. Schuller, 1987, Nature **328**, 604.

Soderholm, L., G.L. Goodman, U. Welp, C.W. Williams and J. Bolender, 1989, Physica C **161**, 252.

Soderholm, L., C.-K. Loong, G.L. Goodman, U. Welp, J. Bolender and C.W. Williams, 1990, Physica B **163**, 655.

Soderholm, L., C.-K. Loong, G.L. Goodman and B.D. Dabrowski, 1991a, Phys. Rev. B **43**, 7923.

Soderholm, L., C.W. Williams and U. Welp, 1991b, Physica C **179**, 440.

Soderholm, L., C.-K. Loong and S. Kern, 1992b, Phys. Rev. B. **45**, 10062.

Soderholm, L., C.-K. Loong, U. Staub, S. Skanthakumar, J.S. Xue, J.P. Hammonds, J.E. Greedan and M. Maric, 1995, Physica C **246**, 11.

Soderholm, L., S. Skanthakumar, U. Staub, M.R. Antonio and C.W. Williams, 1997, J. Alloys & Compounds **250**, 623.

Squires, G.L., 1978, Introduction to the Theory of Thermal Neutron Scattering (Cambridge University Press, Cambridge) 260 pp.

Staub, U., and C. Ritter, 1996, Phys. Rev. B **54**, 7279.

Staub, U., P. Allenspach, A. Furrer, H.R. Ott, S.-W. Cheong and Z. Fisk, 1990, Solid State Commun. **75**, 431.

Staub, U., P. Allenspach, J. Mesot, A. Furrer, R. Müller, T. Schweizer, L.J. Gauckler, H. Blank and H. Mutka, 1991, Z. Phys. B **85**, 35–41.

Staub, U., F. Fauth, M. Guillaume, J. Mesot, A. Furrer, P. Dosanjh and H. Zhou, 1993, Europhys. Lett. **21**, 845.

Staub, U., M.R. Antonio, L. Soderholm, M. Guillaume, W. Henggeler and A. Furrer, 1994a, Phys. Rev. B **50**, 7085.

Staub, U., F. Fauth, M. Guillaume, J. Mesot, A. Furrer, P. Dosanjh, H. Zhou and P. Vorderwisch, 1994b, J. Appl. Phys. **75**, 6334.

Staub, U., J. Mesot, M. Guillaume, P. Allenspach, A. Furrer, H. Mutka, Z. Bowden and A.D. Taylor, 1994c, Phys. Rev. B **50**, 4068.

Staub, U., R. Osborn, E. Balcar, L. Soderholm and V. Trounov, 1995a, Europhys. Lett. **31**, 175.

Staub, U., L. Soderholm, S. Skanthakumar and M.R. Antonio, 1995b, Phys. Rev. B **52**, 9736.

Staub, U., L. Soderholm, S. Skanthakumar, S. Rosenkranz, C. Ritter and W. Kagunya, 1996b, Europhys. Lett. **34**, 447.

Staub, U., F. Fauth, M. Gutmann and W. Kagunya, 1997a, Physica B **234–236**, 841.

Staub, U., R. Osborn, E. Balcar, L. Soderholm and V. Trounov, 1997b, Phys. Rev. B **55**, 11629.

Staub, U., S. Skanthakumar, L. Soderholm and R. Osborn, 1997c, J. Alloys Compd. **250**, 581.

Staub, U., L. Soderholm, S. Skanthakumar, R. Osborn and F. Fauth, 1997d, Europhys. Lett. **39**, 663.

Staub, U., L. Soderholm, S. Skanthakumar, S. Rosenkranz, C. Ritter and W. Kagunya, 1997e, Z. Phys. B **104**, 37.

Staub, U., L. Soderholm, S. Skanthakumar, P. Pattison and K. Conder, 1998a, Phys. Rev. B **57**, 5535.

Staub, U., L. Soderholm, R. Osborn, T.J. Goodwin, H.B. Radousky and R.N. Shelton, 1998b, J. Phys.: Condens. Matter **10**, 4637.

Staub, U., M. Gutmann, F. Fauth and W. Kagunya, 1999, J. Phys.: Condens. Matter **11**, L59.

Staub, U., L. Soderholm, S. Skanthakumar, R. Osborn, F. Fauth and C. Ritter, 2000, Physica C **333**, 13.

Stevens, K.W.H., 1952, Proc. Phys. Soc. London Sect. A **65**, 209.

Strach, T., T. Ruf, M. Cardona, C.T. Lin, S. Jandl, V. Nekvasil, D.I. Zhigunov, S.N. Barilo and S.V. Shiryaev, 1996, Phys. Rev. B **54**, 4276.

Sumarlin, I.W., J.W. Lynn, T. Chattopadyhay, S.N. Barilo, D.I. Zhigunov and J.L. Peng, 1995, Phys. Rev. B **51**, 5824.

Sundaresan, A., A.D. Chinchure, K. Ghosh, S. Ramakrishnan, V.R. Marathe, L.C. Gupta, M. Sharon and S.S. Shah, 1995, Phys. Rev. B **51**, 3893.

Takagi, H., S. Uchida and Y. Tokura, 1989, Phys. Rev. Lett. **62**, 1197.

Taylor, K.N.R., and M.I. Darby, 1972, Physics of Rare Earth Solids (Chapman and Hall, London) 308 pp.

Thalmeier, P., 1984, J. Phys. C **17**, 4153.

Thalmeier, P., 1996, Physica C **266**, 89.

Thalmeier, P., and P. Fulde, 1982, Phys. Rev. Lett. **49**, 1588.

Watanabe, S., and Y. Kuramoto, 1997, Z. Phys. B **104**, 535.

Wegerer, R., C. Thomsen, T. Ruf, E. Schönherr, M. Cardona, M. Reedyk, J.S. Xue, J.E. Greedan and A. Furrer, 1993, Phys. Rev. B **48**, 6413.

Welp, U., S. Flesher, W.K. Kwok, J. Downey, Y. Fang, G.W. Crabtree and J.Z. Liu, 1990, Phys. Rev. B **42**, 10189.

Wybourne, B.G., 1965, Spectroscopic Properties of Rare Earths (Interscience, New York) 236 pp.

Xue, J.S., J.E. Greedan and M. Maric, 1993, J. Solid State Chem. **102**, 501.

Yang, K.N., J.M. Ferreira, B.W. Lee, M.B. Maple, W.-H. Li, J.W. Lynn and R.W. Erwin, 1989, Phys. Rev. B **40**, 10963.

AUTHOR INDEX

Abalduev, B.V. 245
Abbattista, F. 93, 264, 297, 298, 301, 303–307, 327, 328
Abbattista, F., see Domenges, B. 304, 305
Abbattista, F., see Mazza, D. 262, 272
Abbattista, F., see Vallino, M. 295–297, 301, 303–306
Abe, K., see Kuroda, K. 94, 101, 155, 172, 183
Abe, K., see Watanabe, N. 104, 192
Abell, J.S., see Gencer, F. 147
Abell, J.S., see Yang, G. 169
Abragam, A. 379, 381, 389, 392, 496
Abrahams, E., see Varma, C.M. 15
Abrahams, S.C. 245
Abrosimov, N.V., see Emelchenko, G.A. 94
Abrosimov, N.V., see Tatarchenko, V.A. 148
Abt, R., see Kouba, R. 473
Adachi, M., see Tsukui, S. 202
Adachi, S., see Laffez, P. 264–266
Adachi, S., see Seiji, N. 308
Adachi, S., see Tatsuki, T. 348
Adam, G. 432
Adam, G., see Hoffmann, L. 430, 432, 440
Adam, S., see Adam, G. 432
Adam, S., see Hoffmann, L. 432, 440
Adams, C., see Wu, X.D. 25
Adams, M., see Henggeler, W. 531
Adams, M.A., see Mukherjee, A. 520
Adelmann, P., see Brugger, T. 532, 534
Adhikari, K., see Malik, S.K. 302
Aeppli, G. 379
Aeppli, G., see Cheong, S.-W. 24
Aeppli, G., see Mason, T.E. 24
Agarwal, S.K. 69, 70
Aharony, A. 380
Aharony, A., see Sachidanandam, R. 528
Ahn, B.T. 91, 112, 313–315
Ahn, B.T., see Beyers, R. 91, 312–314, 516, 518
Aichele, T. 163
Aikin, R.M., see Brown, S.E. 523, 526
Ait-Hou, A. 248
Aizu, K. 208
Ajiro, Y., see Kikuchi, H. 397
Akao, T., see Lee, S. 169
Akimitsu, J. 59, 62, 295
Akimitsu, J., see Izumi, F. 295
Akimitsu, J., see Nakata, H. 261
Akimitsu, J., see Sawa, H. 59, 329
Akimitsu, J., see Sawa, K. 285
Akimitsu, J., see Tsuda, K. 329
Akimitsu, J., see Uehara, M. 9, 261
Akimitsu, J., see Zenitani, Y. 348
Akinaga, H. 111
Akinaga, H., see Takita, K. 101, 111, 204, 327
Aksay, A., see Sarikaya, M. 175
Aksay, I., see Qian, M. 350
Aksenov, V.L. 520
Akther, N., see Janes, R. 379
Al-Mamouri, M. 348
Al-Mamouri, M., see Slater, P.R. 272
Alarco, J.A. 326
Alario Franco, M. 41
Alario-Franco, M.A. 300
Alario-Franco, M.A., see Garrote, I. 347
Alario-Franco, M.A., see Rial, C. 303
Alario-Franco, M.A., see Señaris-Rodriguez, M.A. 307
Alatalo, M., see Ashoka-Kumar, P. 425
Albino, J. 378, 410
Alcock, C.B. 257–259
Aleksandrov, V.I., see Badalyan, A.G. 406
Alekseevskii, N.E. 378, 386
Alekseevskii, N.E., see Garifullin, I.A. 385, 386
Alekseevskii, N.E., see Kochelaev, B.I. 385, 386
Aleshina, N.N. 90
Alex, V., see Uecker, R. 177
Alexander, K.B., see Goyal, A. 142, 180
Alexander, K.B., see Williams, R.K. 89, 92
Allen, J.L., see Hervieu, M. 272, 318
Allen, P.B. 458

Allenspach, P. 409, 505, 508, 510, 515, 517, 520, 535, 536
Allenspach, P., see Furrer, A. 517
Allenspach, P., see Guillaume, M. 299, 504, 505, 507, 508, 510, 515
Allenspach, P., see Henggeler, W. 531
Allenspach, P., see Mesot, J. 497, 508, 510, 515–519
Allenspach, P., see Roessli, B. 515
Allenspach, P., see Staub, U. 502, 505, 510, 516–518, 528
Allibert, M., see Ait-Hou, A. 248
Alloul, H. 20, 407
Almasan, C.C., see Ayoub, N.Y. 285
Almasan, C.C., see Dalichaouch, Y. 17
Almasan, C.C., see Jiang, C.N. 19, 20
Almasan, C.C., see Maple, M.B. 5, 16, 17
Almes, A., see Krüger, C. 254, 268
Alonso, J.A., see Puig, T. 208
Alp, E.E. 504, 510, 528
Alp, E.E., see Guo, J. 121
Alquie, G. 396
Altorfer, F., see Marti, W. 162, 177
Alyamovskii, S.I., see Dlyachkova, T.V. 319
Amador, U., see Rial, C. 303
Amar, A., see Mathai, A. 14
Ambrosch-Draxl, C., see Kouba, R. 473
Amelinckx, S., see Hodges, J.P. 272
Amelinckx, S., see Krekels, T. 41, 318, 355
Amelinckx, S., see Milat, O. 255, 260
Amelinckx, S., see Reyes-Casga, J. 41
Amelinckx, S., see Van Tendeloo, G. 190
Amelinckx, S., see Zandbergen, H.W. 50
Amitin, E.B. 235
Ammamoto, Y. 293
Ammar, A., see Trari, M. 279
Amoretti, G. 378, 508, 510, 520
Amoretti, G., see Blazey, K.W. 388
Amoretti, G., see Rettori, C. 388, 389
Andersen, N.H. 299–301
Andersen, N.H., see Lister, S.J.S. 192
Andersen, N.H., see Poulsen, H.F. 300
Andersen, N.H., see Rial, C. 303
Andersen, N.H., see v. Zimmermann, M. 24
Andersen, O.K. 457, 460, 462, 464–466, 475, 482
Andersen, O.K., see Liechtenstein, A.I. 524, 528
Andersen, O.K., see Mazin, I.I. 457, 458, 465
Andersen, O.K., see Rodriguez, C.O. 457, 473
Andersen, O.K., see Temmerman, W.M. 460
Anderson, J.O., see Roth, R.S. 297, 316, 324
Anderson, J.S., see Thompson, J.G. 264, 266, 335
Anderson, P.W. 15, 16, 23, 405
Anderson, P.W., see Chakravarty, S. 465, 469
Anderson, P.W., see Mehran, F. 378
Andersson, M. 349
Ando, Y. 18
Ando, Y., see Boebinger, G.S. 18, 291
Andratschke, M., see Steiner, C. 281
Andre, M.O., see D'Anna, G. 205
Andres, K., see Kund, M. 468
Andresen, A.F., see Karen, P. 307, 326–328, 331, 333, 352
Andresen, N.H., see Casalta, H. 299
Andresen, N.H., see Schleger, P. 300
Andresen, P.H. 349, 350, 352
Andresen, P.H., see Karen, P. 352–354
Andrianov, V.A. 153, 192
Angadi, M.A. 205
Anisimov, V.I. 481
Anisimov, V.I., see Liechtenstein, A.I. 481
Anisimov, V.I., see Mazin, I.I. 457
Anisimova, O.L., see Andrianov, V.A. 153, 192
Anlage, S.M. 11, 13
Anlage, S.M., see Wu, D.-H. 13
Ansaldo, E.J., see Bernard, C. 6
Antipov, E.V. 253
Antipov, E.V., see Fomichev, D.V. 101
Antipov, E.V., see Kovba, L.M. 253
Antipov, E.V., see Nuñez-Regueiro, M. 4
Antipov, E.V., see Putilin, S.N. 4
Antonio, M.R., see Soderholm, L. 526, 537
Antonio, M.R., see Staub, U. 508, 510, 514, 537–539
Antonov, V.L., see Antonov, V.N. 428
Antonov, V.N. 428
Antropov, V.P., see Andersen, O.K. 457
Antropov, V.P., see Mazin, I.I. 457
Anwand, W. 438
Aoki, Y., see Fujiita, T. 32
Aoki, Y., see Maeno, Y. 350
Appelman, E.H., see Wang, H.H. 348
Aprili, M., see Lesueur, J. 14
Arai, H., see Machida, M. 264
Arai, J. 401
Arai, M., see Allenspach, P. 508, 510, 515, 517
Arakcheeva, A., see Leonyuk, L. 149
Aranda, M.A.G. 263
Aravin, L.G. 434
Arendt, P., see Wu, X.D. 25

Arendt, R.H., see Garbauskas, M.F. 299
Argent, B.B., see Boudéne, A. 320
Argoud, R., see Bordet, P. 307
Aride, J. 275
Arjomand, M. 264
Arko, A.J., see Shen, Z.-X. 13
Armstrong, A.R. 267, 272
Armstrong, A.R., see Lappas, A. 272
Arnott, M. 91, 199
Arrouy, F., see Wilhelm, H. 281
Artymovicz, D., see Cieplak, M.Z. 350
Arutyunov, N.Yu. 439
Aryasetiawan, F., see Anisimov, V.I. 481
Asaf, U., see Felner, I. 6
Asano, H., see Izumi, F. 295
Asano, H., see Kinoshita, K. 287
Asano, H., see Sawa, H. 59
Asano, H., see Sawa, K. 285
Asano, H., see Takayama-Muromachi, E. 285
Asano, H., see Takita, K. 327
Asano, S., see Kubo, Y. 441
Asano, Y., see Watanabe, T. 329
Asaoka, H. 147–150, 205, 208
Asaoka, H., see Takei, H. 149
Asavaroenghcai, C., see Torrance, J.B. 468
Asayama, K., see Kohara, K. 378
Åsbrink, S. 248
Aselage, T. 89, 102, 296, 326
Ashburn, J.R., see Wu, M.K. 5, 35, 454, 458
Ashoka-Kumar, P. 425
Askénazy, S., see Millet, P. 326
Askew, T.R., see Subramanian, M.A. 5
Asmar, N.G., see Morris, D.E. 308, 327, 330
Assmus, W. 72, 90, 146–148, 170
Assmus, W., see Frieling, T. 147
Assmus, W., see Kowalewski, J. 149
Asta, M., see Ceder, G. 300, 301, 344
Asta, M., see de Fontaine, D. 192
Astle, M.J., see Weast, R.C. 72
Aswal, D.K. 94, 112, 134, 147, 149, 150, 153, 177
Aswal, D.K., see Gupta, S.K. 203
Atake, T. 324
Atake, T., see Zhang, Q.-Z. 338
Atanassova, Y.K. 353
Atou, T., see Kikuchi, M. 272
Atsarkin, V.A. 378, 407, 408
Attfield, J.P. 242
Attfield, J.P., see Aranda, M.A.G. 263
Attfield, P., see Pederzolli, D.R. 279
Aubin, H. 13
Auguste, F. 152
Ausloos, M. 349
Ausloos, M., see Auguste, F. 152
Ausloos, M., see Vandewalle, N. 142
Axe, J.D., see Tranquada, J.M. 24, 403, 411
Ayabe, M., see Zenitani, Y. 348
Ayache, J., see Gotor, F.J. 250, 318, 319
Ayache, J., see Odier, P. 190
Ayoub, N.Y. 285
Ayoub, N.Y., see Early, E.A. 5
Ayyappan, S., see Nagarajan, R. 318
Azad, A.M. 282, 283
Azano, H., see Izumi, F. 37
Azuma, M. 269
Azuma, M., see Hiroi, Z. 259, 260
Azuma, M., see Ikeda, N. 293

Baar, D.J., see Bonn, D.A. 13
Baar, D.J., see Liang, R. 147, 148, 150
Baar, D.J., see Moler, K.A. 13
Babcock, S.E., see Vargas, J.L. 181, 189
Babich, I.G., see Pechoniy, A.P. 378
Babonas, G.J., see Leonyuk, L. 149, 190
Babonas, G.J., see Shvanskaya, L. 153
Babu, T.G.N. 159, 260
Babu, T.G.N., see Krekels, T. 355
Babu, T.G.N., see Milat, O. 255, 260
Badalyan, A.G. 406
Badalyan, A.G., see Baranov, P.G. 406
Bader, S.D., see Yang, K.Y. 297, 318
Baenziger, N.C. 240
Baenziger, N.C., see Eick, H.A. 235
Bagley, B.G., see Tarascon, J.M. 39
Baglyuk, A.I., see Antonov, V.N. 428
Bahcall, S.R., see Kouznetsov, K.A. 15
Baiker, A., see Maciejewski, M. 319
Baikov, Y., see Lütgemeier, H. 520
Baikov, Y.M. 347
Bailey, K.G., see Smedskjaer, L.C. 430–433
Bakhshai, A., see Xiao, G. 350
Bakshai, A., see Cieplak, M.Z. 350
Balachadran, U., see McGinn, P.J. 153
Balachandran, U., see Gao, Y. 335
Balachandran, U., see Selvduray, G. 337
Balachov, V.L., see Fotiev, A.A. 274
Balakirev, V.F., see Saltykova, I.A. 297, 318
Balakirev, V.F., see Yankin, A.M. 256
Balashov, V.A., see Kosmynin, A.C. 324
Balatsky, A., see Monthoux, P. 476
Balatsky, A.V., see Movshovich, R. 15

Balcar, E., see Staub, U. 500, 501, 504, 508, 510
Baldonado, P.S., see Zhu, Y.T. 297
Baldwin, A.R., see Jiang, C.N. 19, 20
Balestrino, G. 148, 169
Balibanu, F., see Filip, C. 405
Balogh, A.G. 433, 438, 439
Bando, Y., see Azuma, M. 269
Bando, Y., see Hiroi, Z. 260, 352
Bando, Y., see Ikeda, N. 293
Banerjee, D., see De, U.Y. 439, 444
Banerjee, D., see Sanyal, D. 443
Banks, E. 253
Bansil, A. 427–430, 432
Bansil, A., see Campuzano, J.C. 430
Bansil, A., see Mijnarends, P.E. 419, 426
Bansil, A., see Pankaluoto, R. 432
Bansil, A., see Smedskjaer, L.C. 429–433, 457
Barak, J., see Huang, M.X. 409
Baranov, P.G. 406
Baranov, P.G., see Badalyan, A.G. 406
Baranova, N.N., see Saltykova, I.A. 297, 318
Barba, D., see Martin, A.A. 499
Barbanera, S., see Balestrino, G. 148
Barbariol, I., see Mastromonaco, M.D. 252
Barberis, G.E., see Castilho, J.H. 378
Barbey, L., see Domenges, B. 304, 305
Barbiellini, B. 419, 426, 427, 433, 434, 437, 440, 442, 443
Barbiellini, B., see Adam, G. 432
Barbiellini, B., see Blandin, P. 441
Barbiellini, B., see Hoffmann, L. 430, 432, 440
Barbiellini, B., see Jarlborg, T. 419, 428, 434
Barbiellini, B., see Manuel, A.A. 433, 440, 457
Barbiellini, B., see Peter, M. 429, 433, 434
Barbiellini, B., see Shukla, A. 156, 432, 433, 435, 442
Barboux, P., see Miceli, P.F. 352
Barboux, P., see Tarascon, J.M. 39
Barchatov, V.P., see Saltykova, I.A. 297, 318
Bardeen, J. 466
Barham, P.J. 378
Barilo, S.N., see Henggeler, W. 528, 533
Barilo, S.N., see Stepanov, A.A. 393–395
Barilo, S.N., see Strach, T. 499, 503, 504
Barilo, S.N., see Sumarlin, I.W. 526, 528, 532, 533
Barin, I. 231, 247, 248, 336
Barkatt, A., see Hu, S. 91
Barker, W.W. 241
Barker, W.W., see Bevan, D.J.M. 241, 242
Barkley, R.M., see Montzka, S.A. 335
Barkovskii, N.V., see Klinkova, L.A. 265
Barlow, P.J., see Thompson, J.G. 264, 266
Barnes, R.G. 396
Barnes, S.E. 377, 396, 399, 405, 421, 433, 439
Barnes, S.E., see Mehran, F. 378, 380, 384, 386
Barnes, S.E., see Peter, M. 429
Barnes, S.E., see Shaltiel, D. 384, 404
Bärninghausen, H. 235
Barrboux, P., see Tarascon, J.M. 350
Barrett, S.E., see Martindale, J.A. 13
Barry, J.C., see Alarco, J.A. 326
Barsoum, M., see Tyagi, S. 378
Bartkowski, S., see Kissick, J.L. 348
Bartosch, K., see Mersmann, A. 75
Bar'yakhtar, V.G., see Antonov, V.N. 428
Basov, D.N. 11, 12, 20
Basov, D.N., see Puchkov, A.V. 20
Basset, J.M., see Simon, P. 378
Baszynski, J., see Stankowski, J. 378
Batlogg, B. 13, 20
Batlogg, B., see Cava, R.J. 5, 6, 9, 191, 192, 275, 287, 288, 299–301, 307, 308, 516, 526
Batlogg, B., see Hwang, H.Y. 20
Batlogg, B., see Murphy, D.W. 331
Batlogg, B., see Siegrist, T. 350
Batlogg, B.J. 69, 71, 72, 203, 209, 210
Batova, D.I., see Klinkova, L.A. 265
Batson, P.E., see Shaw, T.M. 316, 319, 336
Battlog, B., see Cava, R.J. 34, 35, 49, 517, 518
Baudelet, F. 38
Baudelet, F., see Renevier, H. 352
Bauer-Kugelmann, W., see Zhou, X.Y. 433, 436
Bauerle, D., see Hellebrand, B. 209
Bauerle, D., see Wang, X.Z. 159, 209
Bauernfeind, L. 6
Baumann, R., see Heinau, M. 268
Bauminger, E.R., see Felner, I. 352
Bauser, E. 83, 85, 144
Bayuzick, R.J., see Olive, J.R. 196, 212
Bazhenov, A.V., see Emelchenko, G.A. 94
Bazuev, G.V. 265
Beahm, E.C., see Hunt, R.D. 114, 121
Béal-Monod, M.T. 15
Beauprez, E., see Lenglet, M. 248
Becht, M. 73, 156, 159
Bechtold, J., see Hor, P.H. 298, 523
Becker, K.W. 520, 521
Becker, K.W., see Pyttlik, T. 528
Becker, R. 83

Becker, W., see Elschner, S. 202
Bednorz, G. 454
Bednorz, J.G. 2, 4, 31, 69, 303, 410
Bednorz, J.G., see Blazey, K.W. 388
Bednorz, J.G., see Maeno, Y. 9
Beech, F., see Marezio, M. 505, 537
Beech, F., see Roth, R.S. 257, 258, 297, 316, 324
Beech, F., see Santoro, A. 37
Beeli, C., see Karpinski, J. 89
Beeli, C., see Saito, K. 205
Behnia, K., see Aubin, H. 13
Behrman, E.C., see LaGraff, J.R. 348
Beille, J. 32
Beille, J., see Early, E.A. 5
Beille, J., see Sanfilippo, S. 469
Bejjit, L., see Deville, A. 405
Belaish, I., see Rettori, C. 378, 388
Bell, R.F., see Warren Jr, W.W. 20
Bell, T.M., see Lei, M. 469, 472
Belletti, D., see Migliori, A. 264
Beluj, A.V., see Makarova, N.G. 90, 126
Belyaev, V.N. 438, 439
Bender, H., see Lin, C.T. 104, 114, 147, 151, 168, 175
Benedek, R. 422
Benedek, R., see Campuzano, J.C. 430
Benedek, R., see Smedskjaer, L.C. 430
Bennema, P. 80
Bennema, P., see Liu, X.Y. 80
Bennet, L.H., see Wong-Ng, W. 299
Beno, M., see Jorgensen, J.D. 37
Beno, M.A. 35, 299
Beno, M.A., see Segre, C.U. 327
Beno, M.A., see Soderholm, L. 523
Benoit, W., see D'Anna, G. 205
Bente, K., see Böttger, G. 330
Benz, K.W., see Danilewsky, A.N. 88
Berastegui, P., see Petrykin, V.V. 93, 102, 111
Bergemann, C., see Julian, S.R. 9
Berko, S. 429
Berko, S., see Singh, D.J. 426, 432, 442, 443
Berko, S., see Von Stetten, E.C. 426, 427, 430, 433, 439
Berkowski, M., see Scheel, H.J. 156, 157
Berkstresser, G.W., see O'Bryan, H.M. 157
Berlinger, W., see Blazey, K.W. 388
Berlinsky, A.J., see Bonn, D.A. 13
Bernal, J.D. 245
Bernard, C. 6
Bernard, C., see Boudéne, A. 320
Bernede, P., see Corbel, C. 433, 435, 436
Bernhard, C., see Tallon, J.L. 466
Berry, F.J., see Lobo, R.C. 259
Berthier, Y., see Grevin, B. 156
Bertinotti, A. 263
Bertrand, C. 93
Besmann, T., see Vahlas, C. 319
Bessergenev, W.G., see Amitin, E.B. 235
Bestgen, H., see Elschner, S. 202
Bevan, D.J.M. 238, 241, 242
Beyer, W.H., see Weast, R.C. 72
Beyers, R. 91, 312–314, 516, 518
Beyers, R., see Ahn, B.T. 91, 112, 313–315
Beyers, R.B., see MacManus-Driscoll, J.L. 313
Bezakova, E. 438
Bhadra, R., see Shi, D. 202
Bhadra, R., see Yang, K.Y. 297, 318
Bhagat, S.M., see Huang, M.X. 409
Bharathi, A. 426, 427, 433, 434, 439
Bharathi, A., see Jean, Y.C. 433, 440
Bharathi, A., see Sundar, C.S. 433, 435, 436, 438, 439, 441, 443
Bharathi, A., see Vasumathi, D. 433, 434, 439
Bhattacharya, D., see Pathak, L.C. 153
Bhattacharya, R., see Sanyal, D. 443
Bhavaraju, S., see Hor, P.H. 277
Bhavaraju, S., see Xiong, X. 277
Bhushan, M., see Tsuei, C.C. 14
Bhuyan, M., see Tripathy, D.N. 422
Biasini, M., see Usmar, S.G. 436, 437, 439, 440
Bickmann, K., see Hauck, J. 201, 238, 241, 242, 320
Bieger, W. 102, 105, 166
Bieger, W., see Krabbes, G. 89, 166
Bieger, W., see Schatzle, P. 166
Bieger, W., see Wiesner, U. 90
Biernath, T., see Erb, A. 89
Bill, H., see Shaltiel, D. 384, 386, 404
Binninger, U., see Glückler, H. 347
Birgeneau, R.J., see Aharony, A. 380
Birgeneau, R.J., see Matsuda, M. 396, 526
Birgeneau, R.J., see Shirane, G. 379
Birgeneau, R.J., see Thurston, T.R. 24
Birgeneau, R.J., see Yamada, K. 390
Bischof, B., see Hauck, J. 346
Bitmead, J., see Thompson, J.G. 335
Björnbom, P., see Sutija, D.P. 346
Bjørnholm, T., see Markert, J.T. 5
Bjornholm, T., see Neumeier, J.J. 527
Bjørnholm, T., see Neumeier, J.J. 17

Black, R.C., see Mathai, A. 14
Black, T.D., see Rubins, R.S. 388
Black, T.D., see Wang, S.J. 433, 435, 438, 439
Blackstead, H.A. 441, 486
Blanchet, G.B., see Fincher Jr, C.R. 537
Blanchet, G.B., see Maple, M.B. 5, 16, 17
Blandin, P. 441
Blank, D.H.A. 378
Blank, D.H.A., see Fruchart, D. 347
Blank, H., see Allenspach, P. 508, 510, 515, 517
Blank, H., see Furrer, A. 530
Blank, H., see Staub, U. 505
Blasius, Th., see Bernard, C. 6
Blässer, S., see Dortmann, G. 347
Blatter, G. 12
Blazey, K.W. 388
Bleaney, B. 497
Bleaney, B., see Abragam, A. 379, 381, 389, 392, 496
Blunt, F.J., see Tallon, J.L. 308
Boatner, L.A., see Thompson, J.R. 403, 404
Bobolev, A.V., see Aravin, L.G. 434
Boebinger, G.S. 18, 291
Boebinger, G.S., see Ando, Y. 18
Boehlke, A., see Müller-Buschbaum, H. 250
Boehme, R.F., see Bringley, J.F. 260, 280, 281
Boehnke, U.-C., see Herrmann, J. 6
Boganov, A.G., see Rudenko, V.S. 240
Bohac, P., see Suzuki, R.O. 254, 257, 258
Bohm, J. 130, 144
Bok, J., see Labbé, J. 37
Bokshtein, B.S. 201
Bokshtein, S.Z., see Bokshtein, B.S. 201
Bolchakov, A.F., see Abalduev, B.V. 245
Bolender, J., see Soderholm, L. 349, 524, 526
Bonar, J.M., see Schneemeyer, L.F. 505
Bonn, D.A. 13
Bonn, D.A., see Hardy, W.N. 13
Bonn, D.A., see Homes, C.C. 20
Bonn, D.A., see Liang, R. 147, 148, 150
Bonn, D.A., see Liang, R.X. 148, 171, 196
Bonn, D.A., see Schabel, M.C. 457
Bonnet, J.P., see Cazy, E. 319
Bonnet, J.P., see Gotor, F.J. 250, 318, 319
Bonoldi, L., see Amoretti, G. 508, 510, 520
Booij, A.S., see Cordfunke, E.H.P. 253
Boolchand, P., see Shi, F. 293
Boothroyd, A.T. 502–504, 508, 510, 511, 513, 520, 521, 524
Boothroyd, A.T., see Chen, C.K. 112, 156
Boothroyd, A.T., see Lister, S.J.S. 192
Boothroyd, A.T., see Mukherjee, A. 409, 520
Borchardt, G., see Claus, J. 201, 202
Bordet, P. 44, 47, 48, 307, 308, 350, 352
Bordet, P., see Chaillout, C. 48
Bordet, P., see Fisk, Z. 285
Bordet, P., see Karpinski, J. 307
Bordet, P., see Renevier, H. 350, 352
Borik, M.A., see Badalyan, A.G. 406
Bormann, R. 312, 313
Bornarel, A.-C., see Wolf, Th. 150, 152, 200, 203, 205
Bornmann, S., see Aichele, T. 163
Bornmann, S., see Dubs, C. 161, 190
Borodi, G., see Kessler, C. 405
Boronski, E. 419
Boronski, E., see Jarlborg, T. 419, 428, 434
Borowiec, K. 312, 313, 336
Borowski, R., see Kataev, V.E. 390–393
Borrmann, H., see Simon, A. 300
Bose, A., see Iqbal, Z. 318
Bossy, J., see Rossat-Mignod, J. 20
Boterel, F., see Caignaert, V. 38
Böttger, G. 330
Bottger, G., see Furrer, A. 520, 521
Böttger, G., see Mesot, J. 520, 521
Botto, R.E., see Wang, H.H. 348
Boudene, A. 90
Boudéne, A. 320
Boukhari, A., see Aride, J. 275
Boullay, Ph., see Domengès, B. 318
Bourdillon, A., see Bowden, G.J. 378
Boureau, G., see Tétot, R. 343
Bourgault, B. 52
Bourgault, D., see Martin, C. 53
Bourgault, D., see Porcar, L. 194
Bourges, P., see Casalta, H. 528
Bourges, P., see Rossat-Mignod, J. 20
Boutellier, R., see Sun, B.N. 147
Bovin, J.-O., see Norrestam, R. 275, 296
Bovin, J.-O., see O'Keeffe, M. 248
Bowden, G.J. 378
Bowden, M.E., see Tallon, J.L. 349
Bowden, Z., see Allenspach, P. 508, 510, 515, 517
Bowden, Z., see Staub, U. 510, 516–518, 528
Braaten, O., see Karen, P. 90, 93, 253, 262, 297–299, 302–307, 311–313, 316, 318, 319, 326–328, 331, 332, 349
Bradbury, M.I. 498
Brand, M., see Elschner, S. 202

Brandle, C.D., see O'Bryan, H.M. 157
Brandstatter, G. 191
Brandt, C., see Krauns, C. 148, 166, 200
Brandt, E.H. 12
Brandt, W. 420, 423
Bratsberg, H., see Karen, P. 297, 298, 302, 304–306, 326, 328, 331, 332
Bräuchle, G., see Kraut, O. 468
Brauer, G. 238, 240, 241
Brauer, G., see Anwand, W. 438
Brauer, G., see Bärninghausen, H. 235
Braun, H.F., see Bauernfeind, L. 6
Brauner, D.A. 14
Bravman, J.C., see MacManus-Driscoll, J.L. 313
Bredikhin, S.I. 201, 202
Breit, V., see Hauff, R. 203
Brennert, G.F., see Warren Jr, W.W. 20
Brese, N.E. 264
Bresser, W.J., see Shi, F. 293
Brett, N.H., see Guillatt, I.F. 245
Breuer, M., see Kataev, V.E. 390, 391
Breuer, M., see Teitel'baum, G.B. 390
Brewe, D.L., see Tan, Z. 295, 333
Brewer, J.H., see Bonn, D.A. 13
Brewer, L., see Lamoreaux, R.H. 243
Bringley, J.F. 260, 280, 281, 284
Bringley, J.F., see La Placa, S.J. 280, 281
Bringmann, B., see Krauns, C. 148, 166, 200
Brinkmann, D., see Erb, A. 433, 445
Brinkmann, D., see Mangelschots, I. 331
Brisi, C., see Abbattista, F. 264, 297, 301, 303, 305, 306
Britton, J.D., see McGullough, J.D. 242
Brodsky, M.B., see Jorgensen, J.D. 303
Brom, H.B., see Albino, J. 378, 410
Brosh, B., see Felner, I. 352
Brosha, E.L. 89, 90, 264, 265, 275, 306, 307, 310, 311
Brosset, C. 245
Brown, I.D., see Jorgensen, J.D. 471
Brown, M.E., see Owen, J. 396
Brown, P.J., see Chattopadhyay, T. 515
Brown, P.J., see Maletta, H. 515
Brown, R.J.C., see Shaviv, R. 324
Brown, S.E. 523, 526
Brücher, E., see Bernard, C. 6
Brückel, T., see Sonntag, R. 300
Brüesch, P., see Allenspach, P. 520, 535, 536
Brüesch, P., see Fischer, P. 515
Brüesch, P., see Furrer, A. 504, 510, 514, 528
Brüesch, P., see Roessli, B. 515
Brugger, T. 532, 534
Bruggink, W.H., see Reyes-Casga, J. 41
Brunel, L.-C., see Janossy, A. 406, 407
Brusa, R.S. 437, 439
Bruynseraede, Y., see Yang, K.Y. 297, 318
Bryden, W., see Cieplak, M.Z. 350
Brynestad, J., see Lindemer, T.B. 316, 319, 338, 341, 342
Brynestad, J., see Thompson, J.R. 403, 404
Brynestad, J., see Von Stetten, E.C. 426, 427, 430, 433, 439
Brynestad, J., see Williams, R.K. 89, 92, 310
Bucher, B. 20
Bucher, B., see Bordet, P. 307
Bucher, B., see Karpinski, J. 168, 307–309
Buchgeister, M., see Maple, M.B. 5, 16, 17
Büchner, B., see Kataev, V.E. 390–393
Buckley, R.G., see Tallon, J.L. 308, 349
Budai, J.D., see Goyal, A. 25
Budai, J.D., see Norton, D.P. 526, 527
Budnick, J.I., see Haskel, D. 290
Budnick, J.I., see Niedermayer, C. 347
Budnick, J.I., see Tan, Z. 295, 333
Bugoslavsky, Yu., see Felner, I. 403
Buhrman, R., see Batlogg, B.J. 69, 71, 72, 203, 209, 210
Buhrman, R.A., see Moeckly, B.H. 159
Bukovec, N., see Petriček, S. 264, 265
Bukovec, P., see Petriček, S. 264, 265
Bukowski, Z., see Plackowski, T. 302
Buluggiu, E., see Amoretti, G. 378
Buluggiu, E., see Blazey, K.W. 388
Bundel, A.A., see Kedrovskii, O.V. 245, 246
Burger, J.P. 346
Burger, J.P., see Alquie, G. 396
Burger, J.P., see Prakash, S. 347
Burgers, W.G. 245
Burkhardt, E., see Schmid, H. 208
Burlet, P., see Mokhtari, M. 348
Burlet, P., see Rossat-Mignod, J. 20
Burlet, P., see Vettier, C. 300, 301
Burlet, P., see Yakhou, F. 263
Burnham, D.A. 240
Burnside, S.D., see Janes, R. 379
Burton, B.P., see Roth, R.S. 254, 255, 257, 258, 267, 268
Burton, J.A. 123
Burton, W.K. 83
Butt, D.P., see Zhu, Y.T. 297
Bykov, A.B. 89

Byrne, J.G., see Jung, K. 433, 438, 439, 441
Byrne, J.G., see Lim, H.J. 439

Cabañas, M.V., see Thomsen, C. 326
Cabanel, R., see Beille, J. 32
Cabre, R. 134, 144, 153, 155
Cabrera, N. 84
Cabrera, N., see Burton, W.K. 83
Caciuffo, R., see Amoretti, G. 508, 510, 520
Cai, C., see Gong, S. 152
Cai, W.L., see Zhu, J.S. 444
Caignaert, V. 38, 286, 292
Caignaert, V., see Domengès, B. 37
Caignaert, V., see Hervieu, M. 292
Caignol, E., see Davies, P.K. 285–287
Calabrese, J.C., see McCarron, E.M. 258, 268
Calestani, G. 317
Calestani, G., see Amoretti, G. 378, 508, 510, 520
Calestani, G., see Dimesso, L. 166, 189
Calestani, G., see Matacotta, F.C. 267
Calestani, G., see Migliori, A. 264
Campbell, I.H., see Wu, X.D. 25
Campuzano, J.C. 430
Campuzano, J.C., see Ding, H. 20–22
Campuzano, J.C., see Gofron, K. 457
Caneiro, A., see Prado, F. 345
Caneiro, A., see Serquis, A. 285
Canfield, P.C., see Cheong, S.-W. 24
Cantoni, M., see Schilling, A. 4, 467
Cao, B.S., see Zhao, Y.G. 433, 441
Cao, G. 152
Cao, G., see Li, Y. 441
Cao, L.Z., see Wang, N.L. 467
Cao, S.X., see Zhang, J.C. 433, 434, 440
Cao, X.W., see Lin, J.G. 156, 204
Caplin, A.D., see Angadi, M.A. 205
Caplin, A.D., see Crossley, A.L. 189
Capone, D.W., see Alp, E.E. 504, 510, 528
Capone, D.W., see Beno, M.A. 35
Capone, D.W., see Jorgensen, J.D. 303
Capone II, D.W., see Beno, M.A. 299
Caporaso, A.J., see O'Bryan, H.M. 338
Capponi, J.J. 35
Capponi, J.J., see Alario Franco, M. 41
Capponi, J.J., see Alario-Franco, M.A. 300
Capponi, J.J., see Bordet, P. 44, 350
Capponi, J.J., see François, M. 299, 354
Capponi, J.J., see Hewat, A.W. 299
Capponi, J.J., see Kazakov, S.M. 260
Capponi, J.J., see Marezio, M. 505, 537
Capponi, J.J., see Renevier, H. 352
Capponi, J.J., see Strobel, P. 338
Capponi, J.-J., see Nuñez-Regueiro, M. 4
Cardona, M., see Dufour, P. 502, 503
Cardona, M., see Henn, R. 473
Cardona, M., see Heyen, E.T. 535, 536
Cardona, M., see Jandl, S. 499, 502–504, 533
Cardona, M., see Krantz, M. 460
Cardona, M., see Martin, A.A. 192, 499
Cardona, M., see Strach, T. 499, 503, 504
Cardona, M., see Thomsen, C. 326
Cardona, M., see Wegerer, R. 535, 537
Cardwell, D.A. 142
Cardwell, D.A., see Lo, W. 140, 142
Carim, A.H. 331
Carim, A.H., see De Leeuw, D.M. 331
Carlile, C.J., see Guillaume, M. 530, 531
Carlson, K.D., see Wang, H.H. 348
Carnall, W.T. 498, 501, 509
Caro, P., see Sawyer, J.O. 242, 243
Carolan, J.F., see Liang, R. 147, 148, 150
Carpenter, E.R., see Webb, A.W. 280
Carpenter Jr, E.R., see Webb, A.W. 280
Carrington, A., see Janossy, A. 407
Carsson, J.-O., see Ottosson, M. 319
Carter, W.C., see Ceder, G. 300, 301, 344
Casalta, H. 190–192, 299, 528
Casalta, H., see Alloul, H. 20
Casalta, H., see Poulsen, H.F. 300
Casalta, H., see Schleger, P. 300
Casañ-Pastor, N., see Fuertes, A. 286
Cassoux, P., see Millet, P. 326
Castellani, C. 23
Castellano, G., see Balestrino, G. 148
Castellaz, P., see Kessler, C. 405
Castilho, J.H. 378
Castner, T.G. 379
Catlow, C.R.A., see Cherry, M. 347
Cava, R.J. 5, 6, 9, 34, 35, 49, 69, 70, 191, 192, 275, 287, 288, 299–301, 307, 308, 329, 330, 516–518, 526
Cava, R.J., see Batlogg, B. 20
Cava, R.J., see Huang, Q. 355
Cava, R.J., see Hwang, H.Y. 20
Cava, R.J., see Jin, S. 307
Cava, R.J., see Marezio, M. 505, 537
Cava, R.J., see Murphy, D.W. 331
Cava, R.J., see Schneemeyer, L.F. 505
Cava, R.J., see Sunshine, S.A. 355
Cava, R.J., see Warren Jr, W.W. 20
Cavin, O.B., see Lindemer, T.B. 313, 315

Cazy, E. 319
Cazy, E., see Gotor, F.J. 250, 318, 319
CE, G.C., see Tang, Z. 443
Ceder, G. 300, 301, 344
Ceder, G., see de Fontaine, D. 192
Chabanov, A., see Stepanov, A.A. 393–395
Chabot, B., see Scheel, H.J. 156, 157
Chaillout, C. 48, 277, 381
Chaillout, C., see Alario Franco, M. 41
Chaillout, C., see Alario-Franco, M.A. 300
Chaillout, C., see Beille, J. 32
Chaillout, C., see Bordet, P. 44, 47, 48, 308, 350
Chaillout, C., see Capponi, J.J. 35
Chaillout, C., see Hewat, A.W. 299
Chaillout, C., see Karpinski, J. 307
Chakarian, V., see Merz, M. 486
Chakoumakos, B.C., see Lindemer, T.B. 92, 93, 108, 199, 204
Chakoumakos, B.C., see Norton, D.P. 526, 527
Chakraborty, B. 422
Chakravarty, S. 377, 378, 465, 469
Chalmers, B., see Rutter, J.W. 77
Chamberland, B.L., see Morgan, P.E.D. 248
Chaminade, J.P., see Grenier, J.C. 33
Chan, J., see Goodenough, J.B. 277
Chan, L.P. 429, 443, 444
Chan, W.C. 194
Chance, D.A., see Mehran, F. 378
Chandrachood, M.R. 90, 91, 280, 308, 319
Chandrashekhar, G.V., see Mehran, F. 378
Chang, B.P., see O'Sullivan, E.J.M. 201
Chang, E.K. 319, 338
Chang, H. 265
Chang, L., see Han, P.D. 259
Chang, T.C., see Chen, J.W. 349
Chang, Y.A., see Gleixner, R.A. 247
Changkang, C., see Dufour, P. 502, 503
Changkang, Ch. 149, 150
Char, K., see Kleiner, R. 14
Charalambous, S., see Liolios, A.K. 433, 436, 438–440
Chardalas, M., see Lagouri, T. 433, 438, 439, 441
Chardalas, M., see Lagouri, Th. 434
Chardalas, M., see Liolios, A.K. 433, 436, 438–440
Chateigner, D., see Sanfilippo, S. 469
Chatillon, C., see Ait-Hou, A. 248
Chatterij, T., see Henggeler, W. 532–534
Chattopadahyay, T., see Maletta, H. 515
Chattopadhyay, T. 515
Chattopadhyay, T., see Henggeler, W. 520, 528, 533
Chattopadyhay, T., see Sumarlin, I.W. 526, 528, 532, 533
Chaud, X., see Porcar, L. 194
Chaudhari, P. 10, 14
Chaudhuri, S., see De, U.Y. 444
Chauhan, H.S. 120, 121
Chauhan, H.S., see Endo, A. 134, 135
Chauhan, H.S., see Kambara, M. 120, 121
Che, G.C., see Zhao, J. 268
Chebotarev, N.M., see Fischer, K. 91, 114, 150, 199
Chen, A. 440
Chen, A., see Tang, C.Q. 433, 434
Chen, A., see Wang, S.J. 433, 438, 439
Chen, A., see Zhi, Y. 433
Chen, B. 281
Chen, B., see Kleiner, R. 14
Chen, B., see Kouznetsov, K.A. 15
Chen, B., see Pradhan, A.K. 72, 205
Chen, B.-H. 260, 281
Chen, B.-H., see Wang, Y. 256, 261
Chen, C., see Jandl, S. 499, 502–504, 533
Chen, C., see Wanklyn, B.M. 147
Chen, C.F., see Chen, J.W. 349
Chen, C.H., see Cava, R.J. 299, 300, 516
Chen, C.K. 69, 72, 90, 91, 93–95, 112, 114, 116, 139, 146–149, 152, 156, 170, 196
Chen, C.T., see Merz, M. 486
Chen, F., see Chu, C.W. 4
Chen, F., see Gou, Z.H. 433
Chen, H., see Li, J.Q. 318
Chen, H., see Zhao, J. 268
Chen, J.W. 349
Chen, L. 149
Chen, L., see Teng, M.K. 433, 438, 439
Chen, L.S., see Liu, R.S. 330
Chen, M.Y., see Wang, H.H. 348
Chen, N., see Shi, D. 202
Chen, T.G. 149
Chen, T.G., see Xie, X.M. 201, 202
Chen, W., see McGinn, P.J. 153
Chen, W.M., see Lam, C.C. 433
Chen, W.M., see Li, J.Q. 440
Chen, W.Q., see Tan, Z. 295, 333
Chen, X., see Zhang, H. 345
Chen, X., see Zhong, Q. 286, 288
Chen, X.-M., see Zhang, H.-Z. 345
Chen, Y.C., see Shih, C.R. 537

Chen, Y.L., see Chen, A. 440
Chen, Y.L., see Wang, S.J. 433, 438, 439
Chen, Y.M., see Ignatiev, A. 159
Chen, Z.J., see Wang, N.L. 467
Chen, Z.Q., see Tang, Z. 443
Chen, Z.Q., see Wang, S.J. 443
Chen, Z.-X., see Schabel, M.C. 457
Chenavas, J., see Alario Franco, M. 41
Chenavas, J., see Alario-Franco, M.A. 300
Chenavas, J., see Bordet, P. 308
Chenavas, J., see Chaillout, C. 277
Chenavas, J., see Karpinski, J. 307
Chenevas, J., see Bordet, P. 47, 48
Chenevas, J., see Chaillout, C. 48
Cheng, G.S., see Zhang, J.C. 433, 434
Cheong, S.W. 273
Cheong, S.W., see Chaillout, C. 277, 381
Cheong, S.W., see Hundley, M.F. 277
Cheong, S.W., see McCarty, K.F. 277
Cheong, S.W., see Oseroff, S.B. 393, 526
Cheong, S.W., see Rao, D. 393
Cheong, S.W., see Rettori, C. 388, 389
Cheong, S.W., see Simon, P. 378
Cheong, S.W., see Zysler, R.D. 393, 394
Cheong, S.-W. 24
Cheong, S.-W., see Aeppli, G. 379
Cheong, S.-W., see Fisk, Z. 285
Cheong, S.-W., see Hammel, P.Ch. 381
Cheong, S.-W., see Hundley, M.F. 285
Cheong, S.-W., see Staub, U. 502
Cherkashenko, V.M., see Kissick, J.L. 348
Chernov, A.A., see Coriell, S.R. 88
Chernyaev, S.V., see Mozhaev, A.P. 202
Chernyashevskii, A.V., see Mikhalenkov, V.S. 438
Cheronov, A.A. 77, 79, 88
Cherry, M. 347
Chessin, H. 247
Chevalier, B., see Beille, J. 32
Chevary, J.A., see Perdew, J.P. 473
Chi, C.C., see Kirtley, J.R. 14
Chi, C.C., see Tsuei, C.C. 14
Chiang, C.K., see Roth, R.S. 272, 273, 289, 290, 333
Chiang, H.C., see Luo, H.M. 93
Chiba, T. 426, 429, 441
Chicherin, D.S., see Rebane, J.A. 203
Chien, C.L., see Cieplak, M.Z. 350, 400, 403
Chien, C.L., see Sienkiewicz, A. 400–403
Chien, C.L., see Xiao, G. 350
Chien, T.R. 16
Chikumoto, N. 189, 200, 208
Chinchure, A.D., see Sundaresan, A. 537
Ching, W.Y., see Bharathi, A. 426
Ching, W.Y., see Sundar, C.S. 443
Chiou, B.S., see Lai, C.C. 526
Chippindale, A.M., see Señaris-Rodriguez, M.A. 307
Chisholm, M.F., see Kaiser, D.L. 148
Chmaissem, O. 264
Chmaissem, O., see Putilin, S.N. 4
Chodorowiczbak, A. 92
Choi, I., see Kuroda, K. 94, 101, 155, 183
Choi, I.H., see Kuroda, K. 94, 101, 151
Choisnet, J., see Gotor, F.J. 318
Choisnet, J., see Nguyen, N. 34, 286, 289–292
Chong, I., see Hiroi, Z. 189
Chong, Y., see Wang, N.L. 467
Chou, F.C. 277
Chou, P.C., see Ignatiev, A. 159
Choudhury, P., see Mandal, P. 433, 439
Chow, J.C.L., see Lo, W. 140
Chowdhury, A.J.S., see Changkang, Ch. 149, 150
Choy, J.H., see Darracq, S. 293
Chrisey, D.B., see Blackstead, H.A. 441
Christen, D.K., see Goyal, A. 25, 71, 73, 159
Christen, D.K., see Thompson, J.R. 403, 404
Christensen, A.N. 147, 153, 191, 242
Christensen, A.N., see Zhokhov, A.A. 147, 156
Christensen, P., see Perrin, C. 348
Chrosch, J., see Lin, C.T. 175
Chu, and C.W., see Wu, M.K. 454, 458
Chu, C.W. 4, 433
Chu, C.W., see Bharathi, A. 426
Chu, C.W., see Chang, H. 265
Chu, C.W., see Ho, J.C. 403
Chu, C.W., see Hor, P.H. 298, 523
Chu, C.W., see Jean, Y.C. 433, 438, 439, 443
Chu, C.W., see Lin, J.G. 156, 204
Chu, C.W., see Lu, X. 433
Chu, C.W., see Sundar, C.S. 441, 443
Chu, C.W., see Wu, M.K. 5, 35
Chunlin, J. 153
Chunlin, J., see Zhanguo, F. 282, 283
Cieplak, M.Z. 350, 400, 403
Cieplak, M.Z., see Xiao, G. 350
Cieplak, M.-Z., see Sienkiewicz, A. 400–403
Cima, M.J. 77, 154, 335
Cima, M.J., see Figueredo, A.M. 153
Cipollini, N., see Iqbal, Z. 318
Clarke, A.P. 315

Clarke, D.R., see Frase, K.G. 297, 318
Clarke, D.R., see Fraze, K.G. 89
Clarke, D.R., see Shaw, T.M. 316, 319, 336
Clarke, J., see Kleiner, R. 14
Clarke, J., see Kouznetsov, K.A. 15
Claude, J.M., see Lenglet, M. 248
Claus, H. 189
Claus, H., see Hauff, R. 203
Claus, H., see Jorgensen, J.D. 299
Claus, H., see Kraut, O. 468
Claus, H., see Smedskjaer, L.C. 430
Claus, H., see Veal, B.W. 39
Claus, J. 201, 202
Clausen, K.N., see Cheong, S.-W. 24
Clem, J.R., see Batlogg, B.J. 69, 71, 72, 203, 209, 210
Clinton, T.W., see Li, W.-H. 526
Cloots, R., see Vandewalle, N. 142
Coats, A., see Sastry, P.V.P.S.S. 259, 260
Cobb, J.L., see Stadloper, B. 11, 13
Coblenz, W., see Cima, M.J. 335
Cocco, A., see Mastromonaco, M.D. 252
Cochran, W.G. 123
Cockayne, B., see Hurle, D.T.J. 145
Coffey, D. 13
Coffey, L., see Coffey, D. 13
Cohen, M.L., see Crommie, M.F. 469
Cohen, R.E. 471, 473
Cohen, R.E., see Krakauer, H. 458
Cohen, R.E., see Pickett, W.E. 457, 471
Cohen, R.E., see Singh, D.J. 426, 442, 443
Cohen, R.E., see Von Stetten, E.C. 426, 427, 430, 433, 439
Cohen-Adad, M.T.S., see Jorda, J.L. 273–275, 278, 284, 285
Coldea, M. 401
Coleman, P.G., see Anwand, W. 438
Colinet, C., see Boudéne, A. 320
Collcott, S.J., see Thompson, J.G. 264
Collin, G., see Baudelet, F. 38
Collin, G., see Grevin, B. 156
Collin, G., see Keller-Berest, F. 331
Collin, G., see Monod, Ph. 39
Collin, G., see Moret, R. 290
Collin, G., see Sonntag, R. 300
Collins, B.T. 248
Collinu, G., see Marucco, J.-F. 338
Conder, K. 338, 340–343
Conder, K., see Kaldis, E. 299
Conder, K., see Karpinski, J. 168, 260
Conder, K., see Kruger, Ch. 192, 201
Conder, K., see Maciejewski, M. 319
Conder, K., see Monayenkova, A.S. 321
Conder, K., see Staub, U. 505
Condrate Sr, R.A., see Rodriguez, M.A. 317
Conglio, A., see Aharony, A. 380
Connor, D.A.O., see Darlington, C.N.W. 148
Cook, L.P., see Wong-Ng, W. 90, 92, 93, 101, 262, 274, 289, 303, 304, 326
Cooper, A.S., see Aeppli, G. 379
Cooper, A.S., see Fisk, Z. 285
Cooper, A.S., see Wachs, A.L. 441
Cooper, J.R., see Janossy, A. 406, 407
Cooper, J.R., see Liu, R.S. 330
Cooper, J.R., see Loram, J.W. 20, 203
Cooper, J.R., see Tallon, J.L. 20
Cooper, L.N., see Bardeen, J. 466
Cooper, S.L. 18
Corbel, C. 433, 435, 436
Corbel, C., see Hautojärvi, P. 420
Cordfunke, E.H.P. 253
Coriell, S.R. 88
Corliss, L.M., see Banks, E. 253
Cornell, B.A., see Bowden, G.J. 378
Costa, G.A. 251
Coulter, J.Y., see Oniyama, E. 114, 297
Coulter, J.Y., see Zhu, Y.T. 297
Coulter, Y., see Wu, X.D. 25
Coutures, J.P., see Dembinski, D. 89, 147
Cox, D.E. 276
Cox, D.E., see Bringley, J.F. 260, 280, 281
Cox, D.E., see La Placa, S.J. 280, 281
Cox, D.E., see Xiong, X. 277
Cox, D.E., see Zolliker, P. 277
Cox, D.L. 13, 14
Crabtree, G.W. 12
Crabtree, G.W., see Jorgensen, J.D. 299
Crabtree, G.W., see Sinha, S.K. 6
Crabtree, G.W., see Welp, U. 468, 517
Cramer, W., see Gofron, K. 457
Crawford, M.K., see McCarron III, E.M. 330
Creager, W.N., see Crommie, M.F. 469
Crisp, V.H.C., see Lock, D.G. 419
Cromer, D.T. 238
Crommie, M.F. 469
Cros, C., see Wilhelm, H. 281
Crossley, A.L. 189
Crosswhite, H., see Crosswhite, H.M. 494, 495
Crosswhite, H.M. 494, 495
Crow, J.E., see Goldman, A.I. 515
Crow, J.E., see Nichols, D.H. 510
Crow, J.E., see Skanthakumar, S. 524

Currie, D.B. 334
Cywinski, R. 378
Czerwonka, J. 92
Czerwonka, J., see Hodorowicz, S.A. 92, 253, 276, 302–305, 328
Czjzek, G., see Brugger, T. 532, 534
Czyzak, B., see Hoffmann, S.K. 379
Czyzk, B., see Stankowski, J. 378

Dabbagh, G., see Warren Jr, W.W. 20
Daborwski, B., see Zhang, K. 101
Dąbrovski, B. 355
Dabrowski, B. 169
Dąbrowski, B. 277
Dabrowski, B., see Basov, D.N. 20
Dabrowski, B., see Gofron, K. 457
Dabrowski, B., see Jorgensen, J.D. 33, 177, 381, 471
Dąbrowski, B., see Jorgensen, J.D. 299
Dabrowski, B., see Nichols, D.H. 510
Dabrowski, B., see Segre, C.U. 101
Dąbrowski, B., see Segre, C.U. 327
Dąbrowski, B., see Shaked, H. 299, 344
Dąbrowski, B., see Vaughey, J.T. 355
Dąbrowski, B., see Zhang, J.P. 355
Dąbrowski, B., see Zhang, K. 302, 326, 327
Dabrowski, B.D., see Soderholm, L. 508, 510, 524, 535
Dalen, A.J.J., see Koblischka, M.R. 72
Dalichaouch, Y. 17, 523
Dalichaouch, Y., see Maple, M.B. 5, 6, 10
Dalichaouch, Y., see Markert, J.T. 4, 6, 7, 10, 11
Dalichaouch, Y., see Vier, D.C. 378
Damento, M.A. 148
Damento, M.A., see Hoffmann, L. 430
Daniel, P., see Goutenoire, F. 54
Danilewsky, A.N. 88
Dann, S.E. 292
D'Anna, G. 205
Dantsker, E., see Kleiner, R. 14
Daou, J.N., see Burger, J.P. 346
Darabont, A., see Filip, C. 405
Darabont, A., see Kessler, C. 405
Darby, M.I., see Taylor, K.N.R. 496, 497
Dardant, A., see Heintz, J.M. 319
Darlington, C.N.W. 148
Darracq, S. 293
Darriet, J., see Furrer, A. 530
Dartige, E., see Renevier, H. 352
Dartyge, E., see Baudelet, F. 38
Dartyge, E., see Maurer, M. 38
Dash, S. 147
Datta, T., see Pujari, P.K. 439, 443, 444
Daturi, M. 285
Davidov, D., see Castilho, J.H. 378
Davidov, D., see Rettori, C. 378, 388
Davies, P.K. 285–287, 305, 306
Davies, P.K., see Brosha, E.L. 264, 265
Davies, P.K., see Parks, M.E. 345
Davies, P.K., see Thiele, E. 305
Davis, K.L., see Roth, R.S. 89, 147, 297, 318
Davis, K.L., see Wong-Ng, W.K. 261, 262
Davis, M.E., see Jin, S. 11
Davis, M.F., see Miller, J.H. 14
Davis, R.L., see Tallon, J.L. 349
De, D.K. 378
De, D.K., see Wang, S.J. 433, 435, 438, 439
De, U.Y. 439, 444
De, U.Y., see Pujari, P.K. 443, 444
De, U.Y., see Sanyal, D. 443
de Aguiar, O., see Albino, J. 378, 410
de Andrade, M.C., see Dalichaouch, Y. 17
de Brion, S., see Radaelli, P.G. 59
de Fontaine, D. 192
De Fontaine, D., see Ceder, G. 300, 301, 344
de Gennes, P.G. 421
De Jong, A.F., see Carim, A.H. 331
De Jongh, L.J., see Fu, W.T. 291, 331, 349
De Jongh, L.J., see Zandbergen, H.W. 331
de Jongh, L.J., see Zandbergen, H.W. 50
De Leeuw, D.M. 250, 253, 288–292, 297, 305, 306, 316, 318, 328, 331
De Leeuw, D.M., see Carim, A.H. 331
De Villiers, J.P.R. 247
Deandrade, M.C., see Jung, K. 433, 438, 439, 441
Decker, D.L., see Dąbrowski, B. 277
Dedoussis, S., see Lagouri, T. 433, 438, 439, 441
Dedoussis, S., see Lagouri, Th. 434
Dedoussis, S., see Liolios, A.K. 433, 436, 438–440
Degterov, S.A. 89, 92
Degterov, S.A., see Voronin, G.F. 89, 91, 261–264, 266, 267, 308, 320, 323, 345
Degtyarev, S.A., see Voronin, G.F. 321
Dehaudt, P., see Rey, M.-J. 354
Delin, K.A., see Orlando, T.P. 10
Delin, K.A., see Tarascon, J.M. 350
Delmastro, S., see Abbattista, F. 303, 305, 306
Delmastro, S., see Mazza, D. 262, 272

Delong, L.E., see Fertig, W.A. 6
Deltour, R., see Lanckbeen, A. 343
Demazeau, G., see Beille, J. 32
Demazeau, G., see Darracq, S. 293
Demazeau, G., see Wilhelm, H. 281
Dembinski, D. 89, 147
Dembinski, K., see Odier, P. 190
Demiannets, L.N., see Bykov, A.B. 89
Demidov, V.V., see Atsarkin, V.A. 378, 407, 408
Demyanets, L.N. 72, 146
Dennis, J.R., see Roth, R.S. 89, 147, 297, 318
Dennis, K.W., see Kramer, M.J. 105, 199, 200
Dennis, K.W., see Park, M. 112, 114, 305
Dennis, K.W., see Wu, H. 104, 105, 208, 302
Desai, P.D., see Hultgren, R. 231, 235, 237–239
Desgardin, G. 140, 212
Desgardin, G., see Caignaert, V. 38
Desgardin, G., see Marinel, S. 134
Desgardin, G., see Wang, J. 319
deSilva, P., see Tallon, J.L. 20
Desisto, W., see Collins, B.T. 248
Deslandes, F., see Beille, J. 32
Deslandes, F., see Michel, C. 35
Despotes, A.M., see Wang, H.H. 348
Dessau, D.S., see Loeser, A.G. 20
Dessau, D.S., see Shen, Z.-X. 13, 457
Deveraux, T.P. 13
Deville, A. 378, 405
Devine, R.A.B. 396
DeWeert, M.J. 460
Dewhurst, C.D., see Lo, W. 142
Dhalle, M., see Erb, A. 433, 445
Di Castro, C. 476
Di Castro, C., see Castellani, C. 23
Diatlowa, E., see Bernal, J.D. 245
Diaz, C., see Chu, C.W. 433
DiCarlo, J., see Rapp, R.P. 281
DiCarlo, J., see Shen, Z.-X. 13
DiCarlo, J.F., see Hor, P.H. 277
Dickenson, P., see Shen, Z.-X. 13
Diederich, F., see Holczer, K. 9
Dieke, G.H. 497
Diko, P. 182, 198
Dillingham, J., see Wong-Ng, W. 289
Dimesso, L. 166, 189
Dimos, D., see Shaw, T.M. 175, 316, 319, 336
Din Honglin, see Li Anli 433, 439
Ding, H. 20–22
Ding, H., see Gofron, K. 457
Dinger, T.R., see Mehran, F. 378, 384, 386
Dinsdale, A.T. 231
Dinsdale, A.T., see Boudéne, A. 320
Dinse, K.-P., see Foukis, V. 388
Dionigi, C., see Migliori, A. 264
Diviš, M., see Martin, A.A. 499
Divis, M., see Muzichka, Y.U. 502
Dlugosz, W., see Bansil, A. 427, 428, 430, 432
Dlyachkova, T.V. 319
Dmitruk, T.M., see Makarova, N.G. 90, 126
Dobbert, O., see Foukis, V. 388
Doetschman, D.C., see Barham, P.J. 378
Dogan, F., see Skanthakumar, S. 528
Domenges, B. 304, 305
Domengès, B. 37, 47, 48, 62, 190, 318
Domengès, B., see Hervieu, M. 39, 41
Domengès, B., see Roth, G. 37
Domengès, D., see Hervieu, M. 46, 47
Don, E., see Geny, J. 281
Dong, C., see Zhao, J. 268
Doniach, S., see Shen, Z.-X. 13
Dordor, P., see Grenier, J.C. 33
Doring, W., see Becker, R. 83
Doroshenko, N., see Dyakonov, V. 204
Dortmann, G. 347
Dosanjh, P., see Bonn, D.A. 13
Dosanjh, P., see Casalta, H. 299
Dosanjh, P., see Fauth, F. 528, 530
Dosanjh, P., see Liang, R. 147, 148, 150
Dosanjh, P., see Poulsen, H.F. 300
Dosanjh, P., see Schleger, P. 300
Dosanjh, P., see Staub, U. 528, 530, 532
Dou, S.X., see Bowden, G.J. 378
Douglass, D.C., see Sunshine, S.A. 355
Doumerc, J.P., see Grenier, J.C. 33
Doumerc, J.-P., see Trari, M. 279
Doverspike, K. 286, 292
Dow, J.D., see Blackstead, H.A. 441, 486
Downey, J., see Welp, U. 468, 517
Downey, J.W., see Veal, B.W. 39
Doyama, M. 439, 444
Doyama, M., see Ishibashi, S. 427, 433–436, 438–440
Doyama, M., see Matsui, M. 439
Doyle, S.M., see Boothroyd, A.T. 502–504, 508, 510, 511, 513, 524
Dravid, V.P., see Wang, Y.Y. 259
Dravid, V.P., see Zhang, H. 259
Drechsler, S.-L., see Narozhnyi, V.N. 486
Dreysse, H. 81
Driessen, F.A.J.M., see van de Leemput, L.E.C. 133

Drillon, M., see Aride, J. 275
Drössler, H. 540
Drulis, H., see Shengelaya, A.D. 401, 403
Drunheller, J.E., see Rubins, R.S. 388
Dryzek, J. 437
Du Hongshan, see Li Anli 433, 439
Du, Z.H., see Zhao, Y.G. 433, 441
Dubrovina, I.N., see Saltykova, I.A. 297, 318
Dubrovina, I.N., see Yankin, A.M. 256
Dubs, C. 161, 190
Dubs, C., see Aichele, T. 163
Duc, F., see Bordet, P. 350
Ducharme, S., see Durny, R. 388
Duffy, J.A., see Zhou, X.Y. 436
Dufour, P. 502, 503
Dufour, P., see Jandl, S. 499, 502–504, 533
Duijn, V.H.M., see Loewenhaupt, M. 528
Dumoulin, L., see Burger, J.P. 346
Dumoulm, L., see Lesueur, J. 14
Dumschat, J., see Hilscher, G. 72
Duncombe, P.R., see Shaw, T.M. 316, 319, 336
Dunlap, B.D., see Alp, E.E. 504, 510, 528
Dunn, R.G., see Morosin, B. 348
Dupasquier, A., see Brusa, R.S. 437, 439
Dupret, F. 125
Durbin, S.D., see Nishimura, Y. 94, 112, 199
Durcok, S., see Nevriva, M. 114, 147, 153, 194
Durny, R. 388
Duty, T.L., see Bonn, D.A. 13
Dwight, K., see Collins, B.T. 248
Dwight, K., see Doverspike, K. 286, 292
Dyachenko, O.G., see Fomichev, D.V. 101
Dyakonov, V. 204
Dykes, J.W., see Mosley, W.D. 444
Dynes, R.C., see Basov, D.N. 11, 12
Dynes, R.C., see Kleiner, R. 14
Dynes, R.C., see Kouznetsov, K.A. 15
Dynes, R.C., see Sun, A.G. 14, 15
d'Yvoire, F., see Monod, Ph. 39
Dzhafarov, T.D. 203
Dzick, J., see Freyhardt, H.C. 159

Early, E.A. 5
Early, E.A., see Ayoub, N.Y. 285
Early, E.A., see Dalichaouch, Y. 523
Early, E.A., see Markert, J.T. 5
Easterling, K.E., see Bowden, G.J. 378
Ebbing, G., see Schatzle, P. 166
Ebner, C. 388
Eccleston, R.S., see Guillaume, M. 505, 508, 510
Eckert, D., see Narozhnyi, V.N. 155
Eckert, D., see Ruck, K. 348
Eckhardt, H., see Iqbal, Z. 318
Edwards, P.P., see Al-Mamouri, M. 348
Edwards, P.P., see Armstrong, A.R. 267, 272
Edwards, P.P., see Hodges, J.P. 272
Edwards, P.P., see Janes, R. 379
Edwards, P.P., see Kissick, J.L. 348
Edwards, P.P., see Lappas, A. 272
Edwards, P.P., see Liu, R.S. 330
Edwards, P.P., see Slater, P.R. 272
Effenberg, G., see Boudéne, A. 320
Effenberger, H. 247
Efimov, Y.V., see Shamrai, V.F. 297
Egami, M. 128, 130, 138, 172
Egami, M., see Kusao, T. 131, 179
Egami, M., see Namikawa, Y. 123, 127–129, 136, 137, 151, 172, 177–180, 198
Egami, N., see Yao, X. 136, 151, 165, 172, 199
Egi, T. 153, 155, 173, 189, 205, 206
Egi, T., see Chikumoto, N. 208
Egi, T., see Gu, G.D. 169
Egi, T., see Kuroda, K. 94, 101, 151
Egi, T., see Ting, W. 161, 190
Eick, H.A. 235
Eick, H.A., see Baenziger, N.C. 240
Eick, H.A., see Czerwonka, J. 92
Eick, H.A., see Hodorowicz, E. 295–298, 317
Eick, H.A., see Hodorowicz, S.A. 92, 253, 276, 301–305, 328
Einav, M., see Yaron, U. 355
Einzel, D., see Deveraux, T.P. 13
Eisake, H., see Fujimori, A. 458
Eldrup, M., see Kirkegaard, P. 424
Eleftheriadis, C.A., see Liolios, A.K. 433, 436, 438–440
Elkaim, E., see Yakhou, F. 263
Ellis, D.E., see Guo, J. 121
Elliston, P.R., see Bowden, G.J. 378
Elschner, B. 377, 379, 396, 399
Elschner, B., see Kan, L. 391–393
Elschner, B., see Kiemel, R. 350
Elschner, B., see Kochelaev, B.I. 381–384, 397–399, 403
Elschner, B., see Schaeffer, H. 396
Elschner, B., see Sichelschmidt, J. 385–388
Elschner, S. 202
Elschner, S., see Kan, L. 391–393
Elschner, S., see Kochelaev, B.I. 397–399, 403
Elthon, D., see Geny, J. 293, 294
Elthon, D., see George, E. 265, 267–269

Elthon, D., see Lawanier, J.P. 316
Elthon, D., see Tsang, C. 254–256
Elwell, D. 75, 86, 89, 121, 139, 143, 171
Emelchenko, G.A. 94, 108, 150, 165, 174
Emelchenko, G.A., see Bredikhin, S.I. 201, 202
Emelchenko, G.A., see Maljuk, A.N. 285
Emel'chenko, G.A., see Maljuk, A.N. 94
Emel'chenko, G.A., see Tatarchenko, V.A. 148
Emelchenko, G.A., see Zhokhlov, A.A. 165
Emelyanov, D.A., see Lee, S. 169
Emery, V.J. 23, 381, 382
Enami, H., see Kawabata, S. 89, 324
Endo, A. 134, 135
Endo, A., see Chauhan, H.S. 120, 121
Endo, A., see Kambara, M. 120, 121, 166
Endo, A., see Shiohara, Y. 69–72, 77, 95, 133, 139, 142, 146, 154, 159, 164, 166, 194, 195, 205, 206, 212
Endo, A., see Watanabe, Y. 166
Endo, A., see Yao, X. 155
Endo, U., see Koyama, S. 53
Endoh, Y., see Matsuda, M. 396, 526
Endoh, Y., see Shirane, G. 379
Endoh, Y., see Thurston, T.R. 24
Endoh, Y., see Yamada, K. 390
Engler, E.M., see Ahn, B.T. 313
Enjalbert, R., see Millet, P. 326
Enomoto, Y., see Goodilin, E.A. 108
Enomoto, Y., see Konishi, M. 161
Enomoto, Y., see Saba, F. 71, 159
Enomoto, Y., see Usagawa, T. 160
Entin-Wohlman, O., see Sachidanandam, R. 528
Epple, M., see Günther, W. 347
Equchi, K., see Machida, M. 264
Er-Rakho, L. 289–291
Er-Rakho, L., see Michel, C. 304–306
Er-rakho, L., see Michel, C. 31
Er-Rakho, L., see Nguyen, N. 286, 289–291
Er-rakho, L., see Nguyen, N. 34
Erb, A. 89, 145, 147, 148, 150, 171, 201–203, 205, 433, 445
Erb, A., see Genoud, J.-Y. 169
Erb, A., see Klein, L. 205
Erb, A., see Kraut, O. 468
Erb, A., see Manuel, A.A. 457
Erb, A., see Meingast, C. 468
Erb, A., see Merz, M. 486
Erb, A., see Nücker, N. 517
Erb, A., see Peter, M. 429
Erb, A., see Shukla, A. 156
Erwin, R.W., see Yang, K.N. 515, 528
Erxmayer, J., see Dortmann, G. 347
Espinosa, G.P., see Aeppli, G. 379
Espinosa, G.P., see Cava, R.J. 35
Etourneau, J., see Beille, J. 32
Evans, R.C. 345
Evetts, J.E., see MacManus, J.L. 348
Eyring, L. 235
Eyring, L., see Baenziger, N.C. 240
Eyring, L., see Burnham, D.A. 240
Eyring, L., see Eick, H.A. 235
Eyring, L., see Kang, Z.C. 238
Eyring, L., see Kordis, J. 238
Eyring, L., see Sawyer, J.O. 238, 242, 243
Eyring, L., see Sieglaff, C.L. 238
Ezell, E.F., see Chang, E.K. 319

Faber Jr, J., see Shaked, H. 177, 191, 192, 299, 344
Fabris, B.B., see Marella, M. 142
Fahrenbacher, R. 5
Faigel, G., see Janossy, A. 404
Fan, N.Q., see Miller, J.H. 14
Fan, Y.X., see Zhao, J. 268
Fang, K., see Huang, W.F. 440
Fang, Y., see Smedskjaer, L.C. 430–432
Fang, Y., see Welp, U. 517
Fang, Z., see Zhang, H.-Z. 345
Farneth, W.E., see Zolliker, P. 277
Farrell, D.E. 12
Farrow, R., see Cava, R.J. 9
Farrow, R.C., see Cava, R.J. 517, 518
Fastnacht, R.A., see Jin, S. 11, 307
Faulmann, C., see Millet, P. 326
Fauth, F. 528, 530
Fauth, F., see Allenspach, P. 409
Fauth, F., see Böttger, G. 330
Fauth, F., see Guillaume, M. 530, 531
Fauth, F., see Staub, U. 479, 508, 515, 520, 522, 523, 526–528, 530, 532
Feenstra, R., see Lindemer, T.B. 313, 315
Feher, T., see Janossy, A. 406–408
Feher, T., see Rockenbauer, A. 406
Fehrenbacher, R. 440, 479, 480, 483, 484, 486, 524, 528
Feigel'man, M.V., see Blatter, G. 12
Feiner, L.F. 468
Feiner, L.F., see Di Castro, C. 476
Feiner, L.F., see Verweij, H. 343
Felder, R.J., see Cava, R.J. 329
Felner, I. 6, 352, 403

Felner, I., see Castilho, J.H. 378
Felner, I., see Rettori, C. 378, 388
Felner, J., see Yaron, U. 355
Fender, B.E.F., see Jacobson, A.J. 253
Feng, H.H., see Hor, P.H. 277
Feng, H.H., see Xiong, X. 277
Feng, J., see Lam, C.C. 433
Feng, J., see Li, J.Q. 440
Ferey, G. 350
Férey, G., see Attfield, J.P. 242
Ferreira, J.M., see Maple, M.B. 5, 6, 10
Ferreira, J.M., see Tellez, D.A.L. 94
Ferreira, J.M., see Yadava, Y.P. 159
Ferreira, J.M., see Yang, K.N. 515, 528
Ferreti, M., see Daturi, M. 285
Ferretti, M., see Costa, G.A. 251
Ferretti, M., see Magnone, E. 152
Fert, A.R., see Gotor, F.J. 250, 318, 319
Fertig, W.A. 6
Fietz, W.H., see Ludwig, H.A. 299
Figueredo, A.M. 153
Figueredo, A.M., see Cima, M.J. 77, 154
Filimonov, M.K., see Aravin, L.G. 434
Filip, C. 405
Filip, C., see Kessler, C. 405
Filipczuk, S.W. 335
Fillion, G., see Hilscher, G. 510, 524
Fillion, G., see Muzichka, Y.U. 502
Fincher Jr, C.R. 537
Fincher Jr, C.R., see Maple, M.B. 5, 16, 17
Finel, A., see Tétot, R. 343
Fink, J., see Merz, M. 486
Fink, J., see Nücker, N. 517
Finkelstein, A.M., see Kataev, V.E. 379
Fiolhais, C., see Perdew, J.P. 473
Fiory, A.T. 203
Fischer, K. 89, 91, 114, 148, 150, 199
Fischer, K., see Chattopadhyay, T. 515
Fischer, K., see Kajcsos, Z. 436, 438
Fischer, K., see Sichelschmidt, J. 385, 386
Fischer, O., see Erb, A. 433, 445
Fischer, Ø., see Ishikawa, M. 6
Fischer, Ø., see Renner, C.H. 22
Fischer, P. 515
Fischer, P., see Böttger, G. 330
Fischer, P., see François, M. 299, 354
Fischer, P., see Guillaume, M. 299, 507
Fischer, P., see Kaldis, E. 307
Fischer, P., see Karpinski, J. 307
Fischer, P., see Roessli, B. 515, 529, 539
Fischer, P., see Shaltiel, D. 386
Fish, D.J., see Babu, T.G.N. 260
Fisher, B., see Genossar, J. 378
Fisher, B., see Shaltiel, D. 378
Fisher, D.S., see Huse, D.A. 12
Fisher, L.M., see Aleshina, N.N. 90
Fisher, M.P.A., see Huse, D.A. 12
Fisher, P., see Marti, W. 162, 177
Fisk, Z. 285
Fisk, Z., see Aeppli, G. 379
Fisk, Z., see Brown, S.E. 523, 526
Fisk, Z., see Chaillout, C. 277, 381
Fisk, Z., see Cheong, S.-W. 24
Fisk, Z., see Cheong, S.W. 273
Fisk, Z., see Hammel, P.Ch. 381
Fisk, Z., see Hundley, M.F. 277, 285
Fisk, Z., see Martin, K.A.K. 276
Fisk, Z., see McCarty, K.F. 277
Fisk, Z., see Moncton, D.E. 6
Fisk, Z., see Oseroff, S.B. 393, 526
Fisk, Z., see Rao, D. 393
Fisk, Z., see Rettori, C. 388, 389
Fisk, Z., see Sanjurjo, J.A. 499
Fisk, Z., see Simon, P. 378
Fisk, Z., see Staub, U. 502
Fisk, Z., see Takigawa, M.A. 20
Fisk, Z., see Vier, D.C. 378
Fisk, Z., see Zysler, R.D. 393, 394
Fita, I., see Dyakonov, V. 204
Fitz Gerald, J.D., see Thompson, J.G. 264, 266
Fitzgerald, J.D., see Thompson, J.G. 335
Fitzner, K., see Kopyto, M. 282, 283, 322, 323
Fitzner, K., see Przybylo, W. 92
Fitzner, K., see Przybyło, W. 273, 282, 283, 322, 323
Fjellvåg, H. 275, 296–299, 316–319, 335–337
Fjellvåg, H., see Andresen, P.H. 349, 350, 352
Fjellvåg, H., see Karen, P. 209, 253, 262, 297–299, 302–307, 311–313, 316, 318, 319, 326–328, 331–333, 349, 352
Fjellvåg, H., see Olafsen, A. 243
Flandrois, S., see Aride, J. 275
Flechler, S., see Welp, U. 468
Fleming, R.M., see Cava, R.J. 34, 287, 288, 330
Fleming, R.M., see Fiory, A.T. 203
Fleming, R.M., see Wachs, A.L. 441
Flemings, M.C. 77
Flemings, M.C., see Cima, M.J. 77, 154
Flemings, M.C., see Figueredo, A.M. 153
Flesher, S., see Welp, U. 517
Flewitt, D.E.J. 171

Flippen, R.B., see Subramanian, M.A. 5
Flitcroft, M.L., see Lindemer, T.B. 92, 93, 104, 105, 108, 199, 302
Flokstra, J., see Blank, D.H.A. 378
Flokstra, J., see Fruchart, D. 347
Flower, N.E., see Tallon, J.L. 203, 204, 349
Flukiger, R., see Erb, A. 145, 147, 148, 150, 171, 205
Flükiger, R., see Erb, A. 433, 445
Fluss, M.J., see Haghighi, H. 430–432, 457
Fluss, M.J., see Harshman, D.R. 433, 436
Fluss, M.J., see Howell, R.H. 429, 434, 441, 442
Fluss, M.J., see Jean, Y.C. 433, 438–440, 443
Fluss, M.J., see Sterne, P.A. 441
Fluss, M.J., see Turchi, P.E.A. 426, 429, 441
Fluss, M.J., see Wachs, A.L. 441
Foëx, M. 235, 241, 242, 250
Folkerts, T.Y. 148
Foltyn, S.R., see Wu, X.D. 25
Fomichev, D.V. 101
Foner, S., see Orlando, T.P. 10
Foner, S., see Tarascon, J.M. 350
Fong, G.H., see Wang, S.J. 433, 438, 439
Fontaine, A., see Baudelet, F. 38
Fontaine, A., see Maurer, M. 38
Fontaine, A., see Renevier, H. 352
Fontcuberta, J., see Fuertes, A. 286
Fonteneau, G., see Perrin, C. 348
Forro, L., see Mandrus, D. 13
Forster, K., see Hor, P.H. 298, 523
Forster, M., see Hermes, H. 433, 434, 438
Fotiev, A.A. 274
Fotiev, A.A., see Koscheeva, S.N. 297, 318
Fotiev, A.A., see Kosmynin, A.C. 324
Fotiev, V.A., see Koscheeva, S.N. 297, 318
Foukis, V. 388
Fournès, L., see Grenier, J.C. 33
Fournier, P., see Loeser, A.G. 20
Fournier, P., see Puchkov, A.V. 20
Fournier, T., see Renevier, H. 350
Fowler, C.M. 458
Fowler, C.M., see Mueller, F.M. 458
Francescangeli, O., see Amoretti, G. 508, 510, 520
Franceschi, E.A., see Costa, G.A. 251
Franceschi, E.A., see Daturi, M. 285
Francesconi, M.G., see Slater, P.R. 272
Franck, J.P. 11
François, M. 299, 354
Francois, M., see Shaltiel, D. 384, 386, 404
Frank, F.C. 84
Frank, F.C., see Burton, W.K. 83
Franse, J.J.M., see Loewenhaupt, M. 528
Frase, K.G. 297, 318
Fray, D.J., see Kale, G.M. 273, 276, 278–280, 282, 283
Fray, D.J., see MacManus, J.L. 348
Fraze, K.G. 89
Freeman, A.J. 496, 506
Freeman, A.J., see Blandin, P. 441
Freeman, A.J., see Massidda, S. 426, 427, 457
Freeman, A.J., see Yu, J. 432
Freeman, B.L., see Fowler, C.M. 458
Freeman, B.L., see Mueller, F.M. 458
Freeman, W.G., see Kirby, P.B. 350
Frello, T., see v. Zimmermann, M. 24
Frenkel, D.M. 382
Frentup, W., see Nücker, N. 517
Fretwell, H.M., see Usmar, S.G. 436, 437, 439, 440
Freund, H.-R. 275
Freyhardt, H.C. 159
Freyhardt, H.C., see Muller, D. 134
Freyhardt, H.C., see Ullmann, B. 350
Friedel, J. 37, 419
Frieling, T. 147
Fries, S., see Boudéne, A. 320
Fries, S., see Konetzki, R. 235
Frikkee, E., see De Leeuw, D.M. 297
Frolova, T.M., see Shamrai, V.F. 297
Fronczek, F.R., see Wong-Ng, W. 299, 354
Fruchart, D. 347
Fu, K.-J., see Holczer, K. 9
Fu, W.T. 291, 331, 349
Fu, W.T., see Zandbergen, H.W. 50, 331, 349
Fu, Y., see Gong, S. 152
Fu, Y.-X., see Zhang, H. 433, 434, 438
Fuchizaki, K., see Miyazaki, Y. 260, 316
Fuchs, G., see Narozhnyi, V.N. 155
Fueki, K. 209
Fueki, K., see Idemoto, Y. 91, 199, 282, 283, 294, 315
Fueki, K., see Kishio, K. 5, 338
Fuertes, A. 286
Fuess, H., see Paulus, E.F. 263
Fujihara, S. 166, 334
Fujii, H., see Fujiita, T. 32
Fujiita, T. 32
Fujimori, A. 458
Fujimori, A., see Izumi, F. 295
Fujimori, H., see Noto, K. 326

Fujimoto, H., see Nakamura, Y. 149
Fujimoto, H., see Yamaguchi, K. 182
Fujinami, K., see Kawano, M. 205
Fujino, K., see Hasegawa, K. 159
Fujita, T., see Julian, S.R. 9
Fujita, T., see Maeno, Y. 9, 350
Fujiwara, K., see Kebukawa, T. 347
Fujiwara, K., see Shimizu, H. 392, 393, 409
Fujiwara, Y., see Otzschi, K. 291
Fukuba, H., see Fujiita, T. 32
Fukuda, T., see Kajitani, T. 285
Fukuda, T., see Ukei, K. 258
Fukunaga, O., see Karppinen, M. 281
Fukuyama, H. 23
Fukuyama, H., see Suzumura, Y. 23
Fulde, P. 523, 532, 534
Fulde, P., see Becker, K.W. 520, 521
Fulde, P., see Thalmeier, P. 536
Fuler, E.R., see Wong-Ng, W. 92, 93
Fuller Jr, E.R., see Wong-Ng, W. 275, 297, 301, 302
Fuller, R.L., see Ramanujachary, K.V. 348
Funahashi, S., see Miyazaki, Y. 62, 260, 316, 318
Funkenbusch, P.D., see Goyal, A. 142, 180
Furet, E., see Mokhtari, M. 348
Furrer, A. 409, 504, 510, 514, 517, 520, 521, 528, 530
Furrer, A., see Allenspach, P. 409, 505, 508, 510, 515, 517, 520, 535, 536
Furrer, A., see Fauth, F. 528, 530
Furrer, A., see Guillaume, M. 299, 504, 505, 507, 508, 510, 515, 530, 531
Furrer, A., see Henggeler, W. 520, 528, 531–534
Furrer, A., see Mesot, J. 72, 497, 508, 510, 515–521
Furrer, A., see Roessli, B. 515, 529, 539
Furrer, A., see Staub, U. 502, 505, 508, 510, 516–518, 528, 530, 532, 537, 538
Furrer, A., see Wegerer, R. 535, 537
Furuya, K. 149
Furuya, K., see Nakamura, Y. 134, 153
Furuya, K., see Yao, X. 155

Gadalla, A.M. 274, 277
Gadalla, A.M.M. 254
Gadkari, S.C., see Aswal, D.K. 147, 149, 150
Gagnon, R., see Aubin, H. 13
Gai, P.L. 290
Gaier, J.R., see Hepp, A.F. 350
Gaillard, B., see Deville, A. 378, 405
Gajewski, D.A., see Jiang, C.N. 19, 20
Gajewski, D.A., see Kleiner, R. 14
Gajewski, D.A., see Kouznetsov, K.A. 15
Gajewski, D.A., see Maple, M.B. 5, 16, 17
Gajewski, D.A., see Sun, A.G. 14, 15
Gale, J.D., see Cherry, M. 347
Galez, P., see Bertrand, C. 93
Galkin, A.A., see Kemnitz, E. 201
Galkin, A.A., see Mozhaev, A.P. 202
Gallagher, P.K. 337, 338
Gallagher, P.K., see Cava, R.J. 517, 518
Gallagher, P.K., see Jin, S. 307
Gallagher, P.K., see Lindemer, T.B. 338, 341, 342
Gallagher, P.K., see O'Bryan, H.M. 157, 338
Gallagher, W.J., see Mehran, F. 378
Galy, J., see Millet, P. 326
Gama, S., see Castilho, J.H. 378
Gamari-Seale, H., see Guskos, N. 263
Gamari-Seale, H., see Psycharis, V. 334
Gambino, R.J., see Chaudhari, P. 10
Gameson, I., see Slater, P.R. 272
Ganapathi, L., see Umarji, A.M. 318
Gang, H., see Mingmei, W. 264
Ganguli, A.K. 53
Ganguly, P.A., see Raychandhuri, A.K. 326
Ganteaume, M., see Boudéne, A. 320
Gao, L., see Chu, C.W. 4
Gao, L., see Hor, P.H. 298, 523
Gao, L., see Wu, M.K. 5, 35, 454, 458
Gao, S., see Gao, X.H. 443
Gao, W., see Chen, T.G. 149
Gao, X.H. 443
Gao, X.H., see Tang, Z. 443
Gao, X.H., see Wang, S.J. 443
Gao, Y. 335
Gao, Y., see Selvduray, G. 337
Garbauskas, M.F. 299
Garcia, E., see Kubat-Martin, K.A. 270, 271, 331
García, E., see Thomsen, C. 326
García-Muñoz, J.L. 275
Gardner, J.S., see Mukherjee, A. 409
Garfullin, I.A., see Alekseevskii, N.E. 378, 386
Garifullin, I.A. 385, 386
Garifullin, I.A., see Alekseevskii, N.E. 378
Garifullin, I.A., see Kochelaev, B.I. 385, 386
Garif'yanov, N.N., see Alekseevskii, N.E. 378, 386

Garif'yanov, N.N., see Garifullin, I.A. 385, 386
Garif'yanov, N.N., see Kochelaev, B.I. 385, 386
Garkuchin, I.K., see Fotiev, A.A. 274
Garkushin, I.K., see Kosmynin, A.C. 324
Garoche, P., see Marucco, J.-F. 338
Garrote, I. 347
Garzon, F.H. 310
Garzon, F.H., see Brosha, E.L. 264, 265, 275, 306, 307, 310, 311
Garzon, F.N., see Brosha, E.L. 89, 90
Gaskell, D.R., see Kim, J.-S. 89, 312, 313
Gates, B.D., see Wang, H.H. 348
Gates, J.E., see Lindemer, T.B. 89, 108, 338, 341, 342
Gatos, H.C. 211
Gauckler, L.J., see Hallstedt, B. 248–250
Gauckler, L.J., see Risold, D. 256, 260, 261, 267, 268
Gauckler, L.J., see Staub, U. 505
Gauckler, L.J., see Suzuki, R.O. 254, 257, 258
Gauillome, M., see Allenspach, P. 409
Gauthier, M. 433, 435
Gauthier, M., see Barbiellini, B. 440, 442, 443
Gauthier, M., see Blandin, P. 441
Gauthier, M., see Hoffmann, L. 432, 440
Gauthier, M., see Manuel, A.A. 433, 440
Gavalda, J., see Cabre, R. 134, 144, 153, 155
Gavaler, J.R. 4
Gavrin, A., see Xiao, G. 350
Gawalek, W., see Hu, A.M. 200
Gayle, F.W., see Wong-Ng, W. 299, 354
Gazda, M., see Sadowski, W. 155, 156
Gebhard, U., see Claus, H. 189
Geelen, G.P.J., see De Leeuw, D.M. 288–292
Gehring, P.M., see Matsuda, M. 396, 526
Gehring, P.M., see Thurston, T.R. 24
Gehring, P.M., see Tranquada, J.M. 408
Gelati, N., see Lenglet, M. 248
Gemmi, M., see Migliori, A. 264
Gen, T., see Zhang, D.M. 436, 438, 443
Gencer, F. 147
Genossar, J. 378
Genossar, J., see Shaltiel, D. 378
Genoud, J.Y., see Erb, A. 433, 445
Genoud, J.-Y. 169, 262, 263
Genoud, J.-Y., see Erb, A. 145, 147, 171, 205
Genoud, J.-Y., see Renner, C.H. 22
Genoud, P., see Barbiellini, B. 419, 427, 433, 434, 437
Genoud, P., see Jarlborg, T. 419, 428, 434
Genoud, P., see Massidda, S. 426, 427
Geny, J. 281, 293, 294
Genzel, L., see Thomsen, C. 326
George, E. 265, 267–269
Gerdanian, P. 345
Geremia, S. 354
Germi, P., see Sanfilippo, S. 469
Gerritsma, G.J., see Blank, D.H.A. 378
Gersten, J., see Felner, I. 403
Gervais, M., see Dembinski, D. 89, 147
Gervais, M., see Gotor, F.J. 318
Geshkenbein, V.B., see Blatter, G. 12
Ghamaty, S., see Markert, J.T. 5
Ghosh, B., see Mandal, P. 433, 439
Ghosh, B., see Pujari, P.K. 443, 444
Ghosh, K., see Sundaresan, A. 537
Ghosh, V.J., see Ashoka-Kumar, P. 425
Giaconia, C., see Tétot, R. 343
Giapintzakis, J., see Ding, H. 20–22
Giapintzakis, J., see Kim, J.T. 194
Giapintzakis, J., see Kouznetsov, K.A. 15
Giapintzakis, J., see Wollman, D.A. 14
Gibbs, D., see v. Zimmermann, M. 24
Giess, E.A., see Mehran, F. 380
Gin, Y., see Mathai, A. 14
Gingerich, K.A., see Brauer, G. 238
Ginley, D.S., see Garzon, F.H. 310
Ginley, D.S., see Jorgensen, J.D. 33
Ginsberg, D.M., see Kim, J.T. 194
Ginsberg, D.M., see Kouznetsov, K.A. 15
Ginsberg, D.M., see Martindale, J.A. 13
Ginsberg, D.M., see Rice, J.P. 208
Ginsberg, D.M., see Wollman, D.A. 14
Ginzburg, V.L. 454
Giurgiu, L.V., see Filip, C. 405
Giurgiu, L.V., see Kessler, C. 405
Gladyshevskii, R.E., see Bertrand, C. 93
Glarum, S.H., see Cava, R.J. 517, 518
Glarum, S.H., see Rosseinsky, M.J. 9
Glarum, S.H., see Schneemeyer, L.F. 505
Gleiser, M., see Hultgren, R. 231, 235, 237–239
Gleixner, R.A. 247
Glinchuk, M.D., see Pechoniy, A.P. 378
Glowasky, B.A., see Arnott, M. 91, 199
Glückler, H. 347
Glückler, H., see Niedermayer, C. 347
Gobel, I.R., see Hesselbarth, H.W. 81
Gofron, K. 457
Goldacker, W., see Foukis, V. 388
Goldacker, W., see Wolf, Th. 133, 147, 149, 150, 198
Golden, M.S., see Merz, M. 486

Goldman, A.I. 515
Goldman, A.I., see Cox, D.E. 276
Golikov, Yu.B., see Yankin, A.M. 256
Golnik, A., see Bernard, C. 6
Golnik, A., see Niedermayer, C. 347
Gomez-Romero, P., see Fuertes, A. 286
Gong, S. 152
Goodenough, J.B. 277
Goodenough, J.B., see Hou, C.J. 300
Goodenough, J.B., see Lightfoot, P. 284–286, 291, 292
Goodenough, J.B., see Manthiram, A. 98, 112, 330
Goodenough, J.B., see Smith, M.G. 269, 293
Goodenough, J.B., see Steinfink, H. 297
Goodilin, E.A. 82, 93–96, 101, 102, 104–106, 108, 111, 114, 115, 117–119, 138, 153, 160–162, 166, 167, 172, 175, 187, 193, 194, 208, 302, 303, 326
Goodilin, E.A., see Kambara, M. 90, 93–95, 102, 104–106, 117, 119, 212
Goodilin, E.A., see Limonov, M. 108, 192
Goodilin, E.A., see Saba, F. 71, 159
Goodilin, E.A., see Tretyakov, Y.D. 69, 73, 94, 101, 140, 141, 153, 171, 201, 212
Gooding, R.J., see Frenkel, D.M. 382
Goodman, G.L. 501, 507, 510, 524
Goodman, G.L., see Carnall, W.T. 498, 501, 509
Goodman, G.L., see Guo, J. 121
Goodman, G.L., see Soderholm, L. 349, 508, 510, 524, 526, 535
Goodwin, T.J. 526
Goodwin, T.J., see Staub, U. 524
Gopalakrishnan, I.K., see Pujari, P.K. 439, 443, 444
Gopalakrishnan, J., see Cox, D.E. 276
Gopalakrishnan, J., see Subramanian, M.A. 5
Gopalan, P. 433, 434, 440
Gopalan, S., see Andersen, O.K. 457
Gopinathan, K.P., see Gopalan, P. 433, 434, 440
Gorbenko, O.Yu., see Samoylenkov, S.V. 204
Gordeev, S.N. 205
Goremychkin, E.A. 520, 521
Goremychkin, E.A., see Amoretti, G. 508, 510, 520
Goremychkin, E.A., see Muzichka, Y.U. 502
Goremychkin, E.A., see Osborn, R. 508, 520–522
Goren, S.D., see Harrington, I. 347
Gorius, M.F., see Bordet, P. 350
Gorman, G., see Beyers, R. 516, 518
Gornert, P. 72, 157, 161, 164
Gornert, P., see Aichele, T. 163
Gorny, K. 22
Goshima, S., see Sakai, N. 93
Goshorn, D.P., see Newsam, J.M. 327
Gotoh, S., see Miyatake, T. 330
Gotoh, S., see Yamaguchi, K. 182
Gotor, F.J. 250, 318, 319
Gotor, F.J., see Odier, P. 190
Gottschall, R. 263
Gou, Z.H. 433
Gougeon, P., see Deville, A. 378
Gough, C.E., see Yang, G. 169
Goulan, A., see Lesueur, J. 14
Gourieux, T., see Maurer, M. 38
Goutenoire, F. 54
Goutenoire, F., see Hervieu, M. 54
Goutenoire, F., see Martin, C. 56
Goyal, A. 25, 71, 73, 142, 159, 180
Grabovenko, L.Yu., see Mikirticheva, G.A. 324, 325
Grabox, I.E., see Sedov, V.L. 438
Graboy, I.E., see Sedov, V.L. 433, 438
Grace, J.D., see Beno, M.A. 35, 299
Grace, J.D., see Jorgensen, J.D. 37
Grader, G.S., see Gallagher, P.K. 337
Gradinger, H., see Brauer, G. 241
Graebner, J.E., see Jin, S. 142
Graebner, P.-H., see Müller-Buschbaum, H. 241
Graf, T. 203, 265, 297, 299, 308, 310
Granado, E., see Sanjurjo, J.A. 499
Grande, B. 276
Grasmeder, J.R. 292
Gray, K.E., see Cooper, S.L. 18
Grayevsky, A., see Genossar, J. 378
Grayevsky, A., see Porath, D. 346
Grayevsky, A., see Shaltiel, D. 378
Greaney, M., see Ramanujachary, K.V. 348
Greaves, C. 270, 272, 317, 354
Greaves, C., see Al-Mamouri, M. 348
Greaves, C., see Babu, T.G.N. 260
Greaves, C., see Hodges, J.P. 272
Greaves, C., see Kissick, J.L. 348
Greaves, C., see Krekels, T. 355
Greaves, C., see Lobo, R.C. 259
Greaves, C., see Milat, O. 255, 260
Greaves, C., see Slater, P.R. 272
Greaves, C., see Zelenay, I. 209
Greb, B., see Erb, A. 147, 201–203

Grebenschikov, R.G., see Mikirticheva, G.A. 324, 325
Grebenyuk, V.D. 245
Greco, O., see Matacotta, F.C. 267
Greedan, J.E., see Lin, Y.P. 300
Greedan, J.E., see Soderholm, L. 505, 507, 520
Greedan, J.E., see Wegerer, R. 535, 537
Greedan, J.E., see Xue, J.S. 505
Green, R.W., see Garbauskas, M.F. 299
Greenblatt, M., see Li, S. 101, 302
Greenblatt, M., see Ramanujachary, K.V. 348
Greene, L.H., see Lepage, Y. 35
Greene, L.H., see Miceli, P.F. 352
Greene, L.H., see Orlando, T.P. 10
Greene, L.H., see Tarascon, J.M. 39, 70, 350
Greene, R.L., see Anlage, S.M. 11, 13
Greene, R.L., see Wu, D.-H. 13
Gregory, D.H., see Currie, D.B. 334
Gregory, R.B. 424
Grenier, J.C. 33
Grepstad, J.K., see Fjellvåg, H. 316, 317
Grevin, B. 156
Greznev, Yu.S., see Kataev, V.E. 390, 391
Greznev, Yu.S., see Teitel'baum, G.B. 390
Grigorashev, D.I. 93
Grigorashev, D.I., see Sedov, V.L. 444
Grilli, M., see Castellani, C. 23
Grilli, M., see Di Castro, C. 476
Grimsditch, M., see Welp, U. 468
Grimsditch, M., see Yang, K.Y. 297, 318
Grisenti, R., see Brusa, R.S. 437, 439
Groenke, D.A., see Vaughey, J.T. 355
Groenke, D.A., see Zhang, J.P. 355
Groult, D., see Raveau, B. 32, 42, 43, 46, 47, 59
Gruen, D.M. 240
Grundvig, S., see Christensen, A.N. 147, 153, 191
Grundvig, S., see Zhokhov, A.A. 147, 156
Gschneidner Jr, K.A. 231, 235, 237, 243, 244
Gschneidner Jr, K.A., see Damento, M.A. 148
Gschuster, G., see Anwand, W. 438
Gu, B.L., see Zhao, Y.G. 433, 441
Gu, C., see Gofron, K. 457
Gu, C., see Howell, R.H. 429
Gu, C., see Sun, A.G. 14
Gu, G.D. 169
Gu, G.D., see Zhu, J.S. 444
Gubbens, P.C.M., see Moolenaar, A.A. 155, 478
Gubser, D., see Batlogg, B.J. 69, 71, 72, 203, 209, 210
Güdel, H.U., see Furrer, A. 530
Gudilin, E.A. 81, 171
Gudmundsson, B. 319
Guertin, R.P., see Maple, M.B. 5, 6, 10, 16, 17
Gugenberger, F., see Meingast, C. 486
Guha, J.P. 253
Guha, S., see Cieplak, M.Z. 400, 403
Guillatt, I.F. 245
Guillaume, M. 299, 504, 505, 507, 508, 510, 515, 530, 531
Guillaume, M., see Allenspach, P. 508, 510, 515, 517
Guillaume, M., see Fauth, F. 528, 530
Guillaume, M., see Hellebrand, B. 209
Guillaume, M., see Henggeler, W. 531
Guillaume, M., see Staub, U. 508, 510, 516–518, 528, 530, 532, 537, 538
Guimpel, J., see Welp, U. 468
Guiyi, Z., see Chunlin, J. 153
Gunasekaran, R.A. 334
Gunasekaran, R.A., see Pujari, P.K. 441
Gundermann, J. 248
Gunnarsson, O., see Andersen, O.K. 457
Günther, W. 346, 347
Günther, W., see Weiss, M. 346
Guo, G.Y. 524, 528
Guo, H.S., see Zhang, J.C. 433, 434
Guo, J. 121
Guo, J.D., see Schilling, A. 4, 467
Guo, Y.M., see Rodriguez, M.A. 317
Guofan, Z., see Chunlin, J. 153
Gupta, A., see Kirtley, J.R. 14
Gupta, A., see Tsuei, C.C. 14
Gupta, L.C., see Huang, M.X. 409
Gupta, L.C., see Sundaresan, A. 537
Gupta, S.K. 203
Gupta, S.K., see Aswal, D.K. 147, 149, 150
Gür, T.M., see Ahn, B.T. 313–315
Gür, T.M., see Beyers, R. 516, 518
Guru Row, T.N., see Rangavittal, N. 305
Guskos, N. 263
Gustov, V.V., see Aravin, L.G. 434
Gutau, W. 263
Gutmann, M., see Staub, U. 520, 522, 523
Gvozdikov, V.M. 469
Györffy, B.L. 422
Györffy, B.L., see Suvasini, M.B. 422
Gyorffy, B.L., see Temmerman, W.M. 460
Gyorgy, E.M., see Mattheis, L.F. 9

Gyorgy, E.M., see Sunshine, S.A. 355

Haas, H. 279
Hack, K., see Boudene, A. 90
Hack, K., see Boudéne, A. 320
Hack, K., see Mey, S. 235
Hack, K., see Zimmermann, E. 245
Hackl, R., see Deveraux, T.P. 13
Hackl, R., see Stadloper, B. 11, 13
Haddon, R.C., see Rosseinsky, M.J. 9
Hadfield, H.F., see Schleger, P. 300
Hadfield, R., see Poulsen, H.F. 300
Hadjiev, V.G., see Atanassova, Y.K. 353
Haffner, R.H., see Hammel, P.Ch. 381
Hafiz, M.A., see Sedov, V.L. 433, 438
Hagemann, H., see Shaltiel, D. 384, 386, 404
Hagenmuller, P., see Trari, M. 279
Haggerty, J.S., see Figueredo, A.M. 153
Haghighi, H. 430–432, 457
Haghighi, H., see Howell, R.H. 429, 434
Hahn, T. 231
Haije, W.G., see Fu, W.T. 349
Haines, M.J., see Kirby, P.B. 350
Hajra, J.P., see Mathews, T. 254, 255
Hake, R.R., see Maple, M.B. 5, 6, 10
Halet, J.-F., see Mokhtari, M. 348
Hallenbeck, S.L., see Wang, H.H. 348
Halloran, J.W., see Garzon, F.H. 310
Hallstedt, B. 248–250
Hallstedt, B., see Risold, D. 256, 260, 261, 267, 268
Hambourger, P.D., see Hepp, A.F. 350
Hamet, J.F., see Raveau, B. 62, 318
Hamet, J.-F., see Hervieu, M. 272, 318
Hamilton, W.C., see Chessin, H. 247
Hamman, J., see Bertinotti, A. 263
Hammel, P.C., see Gorny, K. 22
Hammel, P.C., see Takigawa, M.A. 20
Hammel, P.Ch. 381
Hammonds, J.P., see Soderholm, L. 505, 507, 520
Han, C., see Qian, M. 350
Han, P.D. 259
Han, P.D., see Wang, Y.Y. 259
Han, P.D., see Zhang, H. 259
Han, S.H., see Jiang, C.N. 19, 20
Han, S.H., see Kleiner, R. 14
Han, S.H., see Kouznetsov, K.A. 15
Han, S.H., see Maple, M.B. 5, 16, 17
Han, S.H., see Sun, A.G. 14, 15
Han, T.D. 441
Hanic, F., see Sausa, O. 433, 440
Hardy, V., see Pelloquin, D. 169
Hardy, W., see Poulsen, H.F. 300
Hardy, W.N. 13
Hardy, W.N., see Bonn, D.A. 13
Hardy, W.N., see Casalta, H. 299
Hardy, W.N., see Hoffmann, L. 432, 440
Hardy, W.N., see Homes, C.C. 20
Hardy, W.N., see Jean, Y.C. 433, 438, 439
Hardy, W.N., see Liang, R.X. 148, 171, 196
Hardy, W.N., see Moler, K.A. 13
Hardy, W.N., see Schabel, M.C. 457
Hardy, W.N., see Schleger, P. 300, 338, 340–343
Hariharan, Y., see Bharathi, A. 426, 427, 433, 434, 439
Hariharan, Y., see Sundar, C.S. 433, 435, 436, 438, 439, 441
Hariharan, Y., see Vasumathi, D. 433, 434, 439
Harja, J.P., see Jacob, K.T. 273, 283
Harju, A., see Barbiellini, B. 427, 434
Harlow, R.L. 355
Harlow, R.L., see McCarron, E.M. 258, 268
Harnischmacher, J., see Drössler, H. 540
Harnischmacher, J., see Jostarndt, H.-D. 524, 525
Harrington, I. 347
Harris, A.B., see Sachidanandam, R. 528
Harris, P., see Casalta, H. 190–192, 299
Harrison, M.R., see Kirby, P.B. 350
Harshman, D.R. 433, 436
Harshman, D.R., see Chan, L.P. 429, 443, 444
Harshman, D.R., see Wachs, A.L. 441
Hårsta, A., see Ottosson, M. 319
Hartge, J., see Mandrus, D. 13
Hartman, P., see Sun, B.N. 133
Hartweg, M., see Heinau, M. 268
Hasegawa, K. 159
Hasegawa, M., see Matsushita, Y. 169, 257
Hasegawa, M., see Mizuno, F. 304
Hasegawa, T., see Kishio, K. 338
Hasegawa, Y., see Suzumura, Y. 23
Haselwimmer, R.K.W., see Julian, S.R. 9
Hashimoto, H., see Maeno, Y. 9
Hashimoto, K., see Wen, J.G. 159
Haskel, D. 290
Hastings, J.M., see Banks, E. 253
Hasty, E.F., see Vaughey, J.T. 355
Hasumi, M., see Kanoda, K. 378
Hata, H., see Mori, N. 154
Hatada, K., see Shimizu, H. 392, 393, 409
Hatano, T., see Ishibashi, S. 433, 438

Hatfield, E., see Goyal, A. 25
Hattori, O. 197
Hauck, J. 201, 238, 241, 242, 320, 346
Hauff, R. 203
Haussonne, J.M., see Caignaert, V. 38
Hautala, J., see Durny, R. 388
Hautojärvi, P. 420, 425
Hawkins, D.T., see Hultgren, R. 231, 235, 237–239
Hawsey, R. 25, 26
Hayakawa, H., see Yazawa, I. 248
Hayakawa, K., see Mizusaki, J. 299
Hayakawa, Y., see Aswal, D.K. 94, 112, 134, 153, 177
Hayashi, A., see Otzschi, K. 291
Hayashi, K. 177
Hayashi, N., see Chikumoto, N. 189, 208
Hayashi, N., see Nagashima, K. 205
Hayashi, S. 148
Hayashi, S., see Komatsu, H. 131
Haycock, P., see Wanklyn, B.M. 147
Hayden, M.E., see Jean, Y.C. 433, 438, 439
Hayden, S.M., see Aeppli, G. 379
Hayden, S.M., see Cheong, S.-W. 24
Hayden, S.M., see Leask, M.J.M. 529
Hayri, A., see Li, S. 101
Hayri, E.A. 292
Hayri, E.A., see Li, S. 302
Hazen, R.M., see Morris, D.E. 308
He, A.S., see Zhao, Y.G. 433, 441
He, Q., see Goyal, A. 25
Heald, S.M., see Yang, C.Y. 346
Heaney, P.J., see Morris, D.E. 308
Hebard, A.F., see Rosseinsky, M.J. 9
Hechel, D., see Felner, I. 352
Heffner, R.H., see Takigawa, M.A. 20
Hegedűs, Z., see Andersson, M. 349
Heger, G., see Roth, G. 37
Hehenkamp, T., see Hentrich, D. 433–436
Heinau, M. 268
Heinemann, K., see Ullmann, B. 350
Heinmaa, I., see Lütgemeier, H. 520
Heinrich, J., see Lenglet, M. 248
Heintz, J.M. 319
Hejtmanek, J., see Nevriva, M. 114, 147, 153, 194
Held, J.Th., see Weishaupt, K. 153
Helfand, E., see Werthamer, N.R. 10
Hellebrand, B. 209
Hellebrand, B., see Gunasekaran, R.A. 334
Hellenbrand, B., see Wang, X.Z. 159, 209
Henggeler, W. 520, 528, 531–534
Henggeler, W., see Allenspach, P. 409
Henggeler, W., see Furrer, A. 520, 521
Henggeler, W., see Guillaume, M. 505, 508, 510
Henggeler, W., see Staub, U. 508, 510, 537, 538
Henn, R. 473
Henry, J.Y., see Barbiellini, B. 433, 437
Henry, J.Y., see Moser, P. 433, 435
Henry, J.Y., see Rossat-Mignod, J. 20
Henry, J.Y., see Vettier, C. 300, 301
Henry, J.Y., see Yakhou, F. 263
Hensch, F., see Kremer, R.K. 381
Hentrich, D. 433–436
Hentsch, F., see Kremer, R.K. 518
Hepp, A.F. 350
Hergt, R., see Fischer, K. 89, 148
Herlasz, I., see Kajcsos, Z. 436, 438
Herman, H., see Gudmundsson, B. 319
Hermann, A.M. 148
Hermes, H. 433, 434, 438
Herrmann, D., see Hauff, R. 203
Herrmann, H.J. 142
Herrmann, J. 6
Hervieu, M. 39, 41, 46, 47, 54, 62, 272, 292, 318
Hervieu, M., see Bourgault, B. 52
Hervieu, M., see Caignaert, V. 38, 292
Hervieu, M., see Chen, B.-H. 260, 281
Hervieu, M., see Domengès, B. 37, 47, 48, 62, 190, 318
Hervieu, M., see Ferey, G. 350
Hervieu, M., see Goutenoire, F. 54
Hervieu, M., see Huvé, M. 54, 56
Hervieu, M., see Maignan, A. 318
Hervieu, M., see Martin, C. 53, 56
Hervieu, M., see Michel, C. 35, 305, 306
Hervieu, M., see Raveau, B. 32, 38, 42, 43, 46, 47, 53, 59, 318
Hervieu, M., see Retoux, R. 50
Hervieu, M., see Roth, G. 37
Hervieu, M., see Rouillon, T. 51, 52
Hervieu, M., see Wang, J. 319
Hesselbarth, H.W. 81
Hessen, B., see Cava, R.J. 275
Hettich, B., see Schulze, K. 267, 268
Hewat, A.W. 299
Hewat, A.W., see Capponi, J.J. 35
Hewat, A.W., see Cava, R.J. 191, 192, 299, 301, 517, 518

Hewat, A.W., see François, M. 299, 354
Hewat, A.W., see Kaldis, E. 307
Hewat, A.W., see Rey, M.-J. 354
Hewat, A.W., see Roessli, B. 515
Hewat, E.A., see Cava, R.J. 191, 192, 299, 301, 517, 518
Hewat, E.A., see Hewat, A.W. 299
Hewat, E.A., see Kaldis, E. 307
Hewat, E.A., see Marezio, M. 505, 537
Heyen, E.T. 535, 536
Hidaka, Y. 146
Hidaka, Y., see Matsuda, M. 396, 526
Hidaka, Y., see Shirane, G. 379
Hidaka, Y., see Yamada, K. 390
Higuchi, T. 205
Higuchi, T., see Koblischka, M.R. 72
Higuchi, T., see Murakami, M. 72, 93, 104, 204–206
Higuchi, T., see Osabe, G. 104
Higuchi, T., see Yoo, S.I. 205
Higuchi, T., see Zamboni, M. 194
Hikita, M., see Iwata, T. 93, 104, 114, 199
Hikita, M., see Tsurumi, S. 204
Hilczer, W., see Stankowski, J. 378
Hildenbrand, D.L., see Lamoreaux, R.H. 243
Hill, A.J. 433, 439
Hill, M.D., see Wong-Ng, W. 274, 303, 304
Hillebrecht, U., see Lengeler, M. 38
Hilscher, G. 72, 510, 524
Hilscher, G., see Nekvasil, V. 524
Hinks, D., see Basov, D.N. 11, 12
Hinks, D., see Beno, M.A. 35
Hinks, D.G., see Alp, E.E. 504, 510, 528
Hinks, D.G., see Beno, M.A. 299
Hinks, D.G., see Dąbrowski, B. 277
Hinks, D.G., see Haskel, D. 290
Hinks, D.G., see Jorgensen, J.D. 33, 37, 177, 299, 303, 381, 471
Hinks, D.G., see Segre, C.U. 101, 327
Hinks, D.G., see Shaked, H. 299, 344
Hinks, D.G., see Shimakawa, Y. 259
Hinks, D.G., see Sinha, S.K. 6
Hinks, D.G., see Soderholm, L. 523
Hinks, D.G., see Vaughey, J.T. 355
Hinks, D.G., see Zhang, K. 101, 302, 326, 327
Hioki, K., see Tanaka, I. 152
Hioki, T., see Oota, A. 326
Hirabayashi, I., see Hyun, O.B. 205
Hirabayashi, I., see Kitamura, T. 163, 164
Hirabayashi, I., see Mizuno, F. 304
Hirabayashi, I., see Nagaya, S. 212
Hirabayashi, I., see Yamada, Y. 116, 147, 163, 164, 199
Hirabayashi, M., see Oyanagi, H. 38
Hirabyashi, M., see Kajitani, T. 352
Hiraga, K., see Kajitani, T. 285
Hiraga, K., see Miyazaki, Y. 62, 260, 316, 318
Hiraga, K., see Tokiwa, A. 51
Hirai, T., see Akimitsu, J. 62
Hirai, T., see Ammamoto, Y. 293
Hirai, T., see Miyazaki, Y. 62, 260, 316, 318
Hirano, K., see Mizusaki, J. 299
Hiratani, M. 285, 287, 350
Hirayama, F., see Shimizu, T. 160
Hirayama, T. 189
Hirayama, T., see Nakamura, M. 187, 189, 206, 207
Hiroi, Z. 189, 259, 260, 293, 352
Hiroi, Z., see Azuma, M. 269
Hiroi, Z., see Ikeda, N. 293
Hiroi, Z., see Khasanova, N.R. 281
Hiroi, Z., see Kobayashi, N. 256, 260, 270
Hiroi, Z., see Shimakawa, Y. 259
Hiroi, Z., see Yamaura, K. 261
Hirst, L.L. 396
Hitterman, R.L., see Jorgensen, J.D. 37
Hitterman, R.L., see Shaked, H. 177, 191, 192
Hitterman, R.L., see Shimakawa, Y. 259
Hitterman, R.L., see Tallon, J.L. 466
Hizhnyakov, V. 518
Hizhnyakov, V., see Kremer, R.K. 381, 518
Hjorth, M. 254
Hjorth, M., see Norrestam, R. 296
Ho, J.C. 403
Ho, J.C., see Lai, C.C. 526
Ho, J.C., see Lin, J.G. 156, 204
Ho, J.C., see Shieh, J.H. 526
Ho, J.C., see Wahlbeck, P.G. 315
Hochheimer, H.D., see Weishaupt, K. 153
Hodby, J., see Rockenbauer, A. 406
Hodeau, J.L., see Bordet, P. 44, 47, 48, 307, 308, 352
Hodeau, J.L., see Chaillout, C. 48
Hodeau, J.L., see Karpinski, J. 307
Hodeau, J.L., see Renevier, H. 350, 352
Hodges, J.A. 515
Hodges, J.P. 272
Hodges, J.P., see Slater, P.R. 272
Hodorowicz, A., see Chodorowiczbak, A. 92
Hodorowicz, E. 295–298, 317
Hodorowicz, E., see Chodorowiczbak, A. 92
Hodorowicz, S.A. 92, 253, 276, 301–305, 328

Hodorowicz, S.A., see Hodorowicz, E. 295–298, 317
Hoen, S., see Crommie, M.F. 469
Hoffmann, J., see Freyhardt, H.C. 159
Hoffmann, L. 430, 432, 440
Hoffmann, L., see Adam, G. 432
Hoffmann, L., see Barbiellini, B. 433, 437, 440, 442, 443
Hoffmann, L., see Barnes, S.E. 433
Hoffmann, L., see Blandin, P. 441
Hoffmann, L., see Manuel, A.A. 433, 440, 457
Hoffmann, L., see Massidda, S. 426, 427
Hoffmann, L., see Peter, M. 429, 430, 432–436
Hoffmann, L., see Shukla, A. 424, 432, 433, 435, 442
Hoffmann, S.K. 379
Hofmeister, W.H., see Olive, J.R. 196, 212
Hohenberg, P.C., see Werthamer, N.R. 10
Hohlwein, D., see Sonntag, R. 300
Hohlwein, D., see Straube, E. 300
Hojaji, H., see Hu, S. 91
Holba, P., see Šesták, J. 324
Holczer, K. 9
Holland-Moritz, E., see Drössler, H. 540
Holland-Moritz, E., see Hilscher, G. 510, 524
Holland-Moritz, E., see Nekvasil, V. 524
Holland-Moritz, E., see Jostarndt, H.-D. 524, 525
Hollin, C.A., see Darlington, C.N.W. 148
Holtermann, C. 245
Holtzberg, F. 148
Holtzberg, F., see Kaiser, D.L. 148
Holtzberg, F., see Mehran, F. 378, 384, 386
Holubar, T., see Hilscher, G. 72, 510, 524
Homes, C.C. 20
Homes, C.C., see Basov, D.N. 11, 12
Homma, H., see Yang, K.Y. 297, 318
Honda, A., see Atake, T. 324
Hong, C.-W., see Kim, C.-J. 147
Hong, D.J.L., see Chang, E.K. 338
Hong, G.W., see Kim, C.-J. 140
Hongyiang, W., see Mingmei, W. 264
Hor, H.P., see Jean, Y.C. 433, 438, 439
Hor, P.H. 277, 298, 523
Hor, P.H., see Bharathi, A. 426
Hor, P.H., see Chu, C.W. 433
Hor, P.H., see Ho, J.C. 403
Hor, P.H., see Jean, Y.C. 443
Hor, P.H., see Lu, X. 433
Hor, P.H., see Sundar, C.S. 441, 443
Hor, P.H., see Wu, M.K. 5, 35, 454, 458
Hor, P.H., see Xiong, X. 277
Horiuchi, S., see Ono, A. 319
Horiuchi, S., see Sawa, H. 329
Horowitz, J.S., see Blackstead, H.A. 441
Horsch, P., see Martinez, G. 380
Horton, T.J., see Lesueur, J. 14
Hosaka, M., see Iijima, Y. 159
Hoshino, K., see Maeno, Y. 350
Hoshizaki, H., see Kawabata, S. 89, 324
Hosoya, S., see Kajitani, T. 285
Hou, C.J. 300
Howell, R.H. 429, 434, 441, 442
Howell, R.H., see Haghighi, H. 430–432, 457
Howell, R.H., see Harshman, D.R. 433, 436
Howell, R.H., see Jean, Y.C. 433, 438–440, 443
Howell, R.H., see Mosley, W.D. 444
Howell, R.H., see Sterne, P.A. 441
Howell, R.H., see Turchi, P.E.A. 426, 429, 441
Howell, R.H., see Wachs, A.L. 441
Hsu, H.M., see Steinfink, H. 297
Hu, A.M. 200
Hu, H., see Zhao, Y.G. 433, 441
Hu, S. 91
Hu, Y.L., see Chen, C.K. 112, 156
Huang, C., see Lin, J.G. 156, 204
Huang, C.Y., see Ho, J.C. 403
Huang, D.J., see Wang, N.L. 467
Huang Hanchen, see Li Anli 433, 439
Huang, J. 330
Huang, J.Z., see Jean, Y.C. 433, 438, 439
Huang, M.X. 409
Huang, Q. 352, 353, 355
Huang, Q., see Chmaissem, O. 264
Huang, Q., see Karen, P. 318, 319, 353
Huang, Q., see Khasanova, N.R. 281
Huang, Q., see Natali Sora, I. 353
Huang, S.-M., see Holczer, K. 9
Huang, T.C. 290
Huang, T.C., see Tokura, Y. 291
Huang, W., see Boudéne, A. 320
Huang, W.F. 439, 440
Huang, Y., see Chan, W.C. 194
Huang, Z.J., see Chu, C.W. 4, 433
Huang, Z.J., see Hor, P.H. 298, 523
Huang, Z.J., see Jean, Y.C. 443
Huang, Z.J., see Lu, X. 433
Huang, Z.J., see Sundar, C.S. 441, 443
Huang, Z.J., see Wu, M.K. 5, 35, 454, 458
Huant, S., see Stepanov, A.A. 393–395

Hubbard, C.R., see Lindemer, T.B. 316, 319, 338, 341, 342
Hubbard, M.A., see Movshovich, R. 15
Huber, D.L. 377
Hücker, M., see Kataev, V.E. 390–393
Huggins, R., see Ahn, B.T. 313
Huggins, R.A., see Ahn, B.T. 313–315
Huggins, R.A., see Beyers, R. 516, 518
Hull, G.N., see Lepage, Y. 35
Hull, G.W., see Orlando, T.P. 10
Hull, G.W., see Tarascon, J.M. 39, 350
Hull, R., see Cava, R.J. 517, 518
Hull, R., see Schneemeyer, L.F. 505
Hulliger, F., see Allenspach, P. 505, 508, 510, 515
Hultgren, C.T., see Morris, D.E. 308
Hultgren, R. 231, 235, 237–239
Hults, W.L., see Fowler, C.M. 458
Hults, W.L., see Gorny, K. 22
Hults, W.L., see Mueller, F.M. 458
Hundley, M.F. 277, 285
Hundley, M.F., see Crommie, M.F. 469
Hundley, M.F., see Fisk, Z. 285
Hundley, M.F., see Oseroff, S.B. 393, 526
Hung, K.C., see Lam, C.C. 433
Hung, K.C., see Li, J.Q. 440
Hunley, J.F., see Lindemer, T.B. 89, 108, 338, 341, 342
Hunt, J.D., see Jackson, K.A. 79
Hunt, R.D. 114, 121
Huntelaar, M.E., see Cordfunke, E.H.P. 253
Hunter, B., see Sun, B.N. 131
Hunter, B.A. 148, 191
Hunter, B.A., see Shimakawa, Y. 259
Hurle, D.T.J. 145, 211
Huse, D.A. 12
Hutchings, M.T. 497–499
Hutter, L., see Qian, M. 350
Hutton, D., see Shaltiel, D. 405, 523
Hutton, S.L., see Rubins, R.S. 388
Huvé, M. 54, 56
Hwang, D.M., see Lepage, Y. 35
Hwang, H.Y. 20
Hwang, H.Y., see Batlogg, B. 20
Hwang, J.G., see Yu, J.-T. 378
Hwang, N.M., see Roth, R.S. 254, 255
Hwu, S.-J., see Wang, G. 297, 318
Hybertson, B.M., see Montzka, S.A. 335
Hyde, B.G., see Sawyer, J.O. 238
Hyde, B.G., see Thompson, J.G. 335
Hyldtoft, J., see Hjorth, M. 254
Hylén, H., see Zakharov, A.A. 458
Hyun, O.B. 205

Ichihashi, T. 300
Ichikawa, N., see Boebinger, G.S. 18, 291
Ichikawa, N., see v. Zimmermann, M. 24
Ichinose, A. 329
Ichinose, A., see Wada, T. 295, 329, 330
Idemoto, Y. 91, 199, 282, 283, 294, 315
Idemoto, Y., see Fueki, K. 209
Idzerda, Y.U., see Merz, M. 486
Igarashi, H., see Manako, T. 355
Ignatiev, A. 159
Iguchi, Y., see Yamaguchi, S. 338
Ihara, H., see Oyanagi, H. 38
Ihara, H., see Yazawa, I. 248
Iijima, S., see Ichihashi, T. 300
Iijima, Y. 159
Ikeda, N. 293
Ikeda, S., see Ikuta, H. 149
Ikeda, S., see Julian, S.R. 9
Ikeda, T., see Maeda, M. 89, 95
Ikegawa, S., see Wada, T. 329
Ikuhara, Y., see Hirayama, T. 189
Ikuhara, Y., see Kitamura, T. 164
Ikuhara, Y., see Nakamura, M. 187, 189, 206, 207
Ikuma, Y. 346
Ikuta, H. 149
Ilyasov, A.Z. 438, 439
Ilynych, N. 320, 321
Imagawa, Y. 134, 135, 153
Imai, T. 20
Imanaka, Y., see Takenaka, K. 480
Impert, P., see Hodges, J.A. 515
Imura, T., see Kawabata, S. 324
Inameti, E.E., see Raven, M.S. 319
Inari, K., see Zenitani, Y. 348
Indenbom, M.V. 194
Indenbom, M.V., see D'Anna, G. 205
Ingalls, R., see Qian, M. 350
Ino, A., see Fujimori, A. 458
Inoue, T., see Hayashi, S. 148
Inoue, T., see Komatsu, H. 131
Ipposhi, T., see Takita, K. 101
Iqbal, Z. 318
Iqbal, Z., see Owens, F.J. 378, 385
Iqbal, Z., see Ramakrishna, B.L. 388
Irkhin, V.Yu., see Romanyukha, A.A. 410
Isawa, K. 279
Isawa, K., see Karppinen, M. 281

Ishibashi, S. 427, 433–436, 438–440
Ishibashi, S., see Doyama, M. 439
Ishibashi, S., see Erb, A. 433, 445
Ishibashi, S., see Matsui, M. 439
Ishida, Y. 163, 181
Ishida, Y., see Kimura, T. 164
Ishigaki, T., see Izumi, F. 37
Ishigaki, T., see Takita, K. 327
Ishikawa, M. 6
Ishikawa, M., see Nakazawa, Y. 300
Ishikawa, M., see Takabatake, T. 350, 352
Ishimaru, Y., see Usagawa, T. 160, 161
Ishizawa, Y., see Ono, A. 147
Ishizuka, H., see Fueki, K. 209
Islam, M.S., see Cherry, M. 347
Isobe, M., see Ramírez-Castellanos, J. 355
Itagaki, K., see Mey, S. 235
Itie, J.P., see Baudelet, F. 38
Ito, M., see Oka, K. 89
Ito, T. 20
Ito, T., see Oka, K. 151, 154, 155, 169
Ito, T., see Takenaka, K. 480
Ito, T., see Zhou Zhigang 441
Ito, T., see Zou, Z. 486
Ito, Y., see Hiratani, M. 350
Itoh, M., see Nakada, I. 139
Itoi, K., see Kuroda, K. 94, 101, 155, 183
Itti, R., see Karppinen, M. 281
Itti, R., see Sakai, H. 160
Itti, R., see Ting, W. 161, 190
Ivanov, A., see Casalta, H. 528
Ivanov-Emin, B.N. 240
Iver, R.M., see Pujari, P.K. 439
Iwahara, H. 346
Iwasaki, H., see Dalichaouch, Y. 17
Iwasaki, H., see Nakajima, S. 53
Iwasaki, H., see Oyanagi, H. 38
Iwata, T. 93, 104, 114, 152, 199
Iwata, T., see Tsurumi, S. 204
Iye, Y. 16
Iye, Y., see Asaoka, H. 147–150
Iye, Y., see Takei, H. 149
Iyer, R.M., see Pujari, P.K. 439, 443, 444
Iyer, R.M., see Tyagi, A.K. 348
Iyi, N., see Takekawa, S. 148
Izakovich, E.N. 296
Izumi, F. 37, 70, 71, 101, 102, 108, 190, 295
Izumi, F., see Goodilin, E.A. 93, 111
Izumi, F., see Khasanova, N.R. 281
Izumi, F., see Kikuchi, M. 272
Izumi, F., see Kinoshita, K. 287
Izumi, F., see Sawa, K. 285
Izumi, F., see Takayama-Muromachi, E. 285
Izumi, I., see Sawa, H. 59
Izumi, T. 154
Izumi, T., see Furuya, K. 149
Izumi, T., see Kakimoto, K. 163
Izumi, T., see Kambara, M. 136, 152
Izumi, T., see Nakamura, Y. 134, 153
Izumi, T., see Oka, A. 192, 205, 208

Jackson, K.A. 79
Jackson, K.A., see Perdew, J.P. 473
Jacob, K.T. 245, 267, 268, 273, 283, 288, 289
Jacob, K.T., see Azad, A.M. 282, 283
Jacob, K.T., see Kale, G.M. 251, 252, 273–275, 278, 282, 283
Jacob, K.T., see Mathews, T. 254, 255, 338, 340–343, 345
Jacobson, A., see Parks, M.E. 345
Jacobson, A.J. 253
Jacobson, A.J., see Hor, P.H. 277
Jacobson, A.J., see Newsam, J.M. 327
Jacobson, A.J., see Xiong, X. 277
Jager-Waldau, R., see Ramirez, A.P. 279
Jahn, W., see Gordeev, S.N. 205
Jahn, W., see Kupfer, H. 205
Jaime, M., see Movshovich, R. 15
James, A.C., see Cava, R.J. 34
James, A.C.W.P. 276
James, A.C.W.P., see Cava, R.J. 287, 288
James, A.C.W.P., see Schneemeyer, L.F. 505
JANAF 231, 238, 239
Janawadkar, M.P., see Bharathi, A. 433, 434, 439
Jandl, S. 499, 502–504, 533
Jandl, S., see Dufour, P. 502, 503
Jandl, S., see Martin, A.A. 499
Jandl, S., see Strach, T. 499, 503, 504
Janes, R. 379
Jang, W.J. 190
Jang, W.J., see Kutami, H. 190
Jang, W.J., see Rykov, A. 208, 209
Janning, E., see Hauck, J. 346
Janos, S., see Kristiakova, K. 439
Janossy, A. 404, 406–408
Janossy, A., see Rockenbauer, A. 406
Janossy, A., see Williams, G.V.M. 407
Jansen, M., see Köhler, B.U. 279
Japha, Y. 479
Jardim, R.F., see Castilho, J.H. 378

Jardim, R.F., see Maple, M.B. 5, 16, 17
Jarlborg, T. 419, 428, 434
Jarlborg, T., see Barbiellini, B. 419, 426, 427, 433, 434, 437, 440, 442, 443
Jarlborg, T., see Blandin, P. 441
Jarlborg, T., see Manuel, A.A. 433, 440, 457
Jarlborg, T., see Peter, M. 429, 433, 434
Jayamala, B., see Nagarajan, T. 441
Jayavel, R. 148
Jayavel, R., see Paul, D.P. 212
Jayavel, R., see Rao, C.R.V. 152
Jean, Y.C. 433, 438–440, 443
Jean, Y.C., see Bharathi, A. 426
Jean, Y.C., see Chu, C.W. 433
Jean, Y.C., see Haghighi, H. 430
Jean, Y.C., see Harshman, D.R. 433, 436
Jean, Y.C., see Lu, X. 433
Jean, Y.C., see Sundar, C.S. 441, 443
Jean, Y.C., see Turchi, P.E.A. 426, 429, 441
Jean, Y.C., see Wachs, A.L. 441
Jee, Chan-See, see Goldman, A.I. 515
Jefferson, J.H., see Feiner, L.F. 468
Jegondaz, J., see Shaltiel, D. 384, 404
Jegoudez, J., see Monod, Ph. 39
Jegoudez, J., see Revcolevschi, A. 72, 153
Jéhanno, G., see Hodges, J.A. 515
Jena, P., see McMullen, T. 426, 434, 441
Jenen, M., see Veal, B.W. 39
Jennings, G., see Campuzano, J.C. 430
Jennings, G., see Gofron, K. 457
Jensen, J., see Leask, M.J.M. 529
Jensen, K.O. 426–428, 434, 436
Jensen, K.O., see McMullen, T. 426, 434, 441
Jeong, D.Y., see Rubins, R.S. 388
Jeong, D.Y., see Wang, S.J. 433, 435, 438, 439
Jepsen, O., see Andersen, O.K. 457, 460, 462, 464–466, 475, 482
Jepsen, O., see Mazin, I.I. 457, 458
Jepsen, O., see Rodriguez, C.O. 457, 473
Jepsen, O., see Temmerman, W.M. 460
Jian, S.F., see Wang, S.J. 443
Jiang, C.N. 19, 20
Jiang, H., see Zhou, X.Y. 433, 434, 436
Jiang, S.F., see Gao, X.H. 443
Jiao, Z., see Cao, G. 152
Jilek, E., see Conder, K. 338, 340–343
Jilek, E., see Karpinski, J. 168, 307–309
Jilek, E., see Mangelschots, I. 331
Jilek, E., see Meingast, C. 468
Jin, S. 11, 142, 307
Jin, X., see Lam, C.C. 433
Jin, X., see Li, J.Q. 440
Jo, M., see Yazawa, I. 248
Jobst, B., see Lengeler, M. 38
John, A.M., see Jose, R. 158
Johnson Jr, D.W., see Mattheis, L.F. 9
Johnson, J.R. 346
Johnston, D.C., see Chou, F.C. 277
Johnston, D.C., see Fertig, W.A. 6
Johnston, D.C., see Moncton, D.E. 6
Jones, E.C., see Norton, D.P. 527
Jones, I.P., see Yang, G. 169
Jones, P.L., see Hill, A.J. 433, 439
Jorda, J.L. 273–275, 278, 284, 285
Jorda, J.L., see Bertrand, C. 93
Jorda, J.L., see Graf, T. 297
Jørgensen, C.K. 241
Jorgensen, J.D. 6, 33, 37, 177, 191, 192, 299, 300, 303, 381, 471
Jorgensen, J.D., see Basov, D.N. 20
Jorgensen, J.D., see Beno, M.A. 35, 299
Jorgensen, J.D., see Dąbrovski, B. 355
Jorgensen, J.D., see Dąbrowski, B. 277
Jorgensen, J.D., see Haskel, D. 290
Jorgensen, J.D., see LaGraff, J.R. 348
Jorgensen, J.D., see Lightfoot, P. 284–286, 291, 292
Jorgensen, J.D., see Miceli, P.F. 352
Jorgensen, J.D., see Pei, S. 296
Jorgensen, J.D., see Rodriguez, M.A. 317
Jorgensen, J.D., see Segre, C.U. 101, 327
Jorgensen, J.D., see Shaked, H. 299, 344
Jorgensen, J.D., see Shimakawa, Y. 259
Jorgensen, J.D., see Tallon, J.L. 466
Jorgensen, J.D., see Zhang, K. 302, 326, 327
Jorgenson, J.D., see Soderholm, L. 523
Jose, R. 158
Jostarndt, H.D., see Drössler, H. 540
Jostarndt, H.-D. 524, 525
Jostarndt, H.-D., see Hilscher, G. 510, 524
Jostarndt, H.-D., see Nekvasil, V. 524
Joubert, J., see Rey, M.-J. 354
Judd, B.R. 494, 495
Julian, S.R. 9
Jung, K. 433, 438, 439, 441
Junk, St., see Schwitzgebel, G. 343
Junod, A., see Erb, A. 433, 445
Junod, A., see François, M. 299, 354
Junod, A., see Genoud, J.-Y. 169, 262, 263
Junod, A., see Graf, T. 265, 308, 310
Jurgens, M.J., see Vettier, C. 300, 301
Jwo, D.S., see Chan, W.C. 194

Kabanov, V.V., see Aksenov, V.L. 520
Kabe, S., see Ikuma, Y. 346
Kabius, B., see Günther, W. 347
Kadoi, M., see Maeda, M. 89, 95
Kadowaki, H., see Matsuda, M. 396, 526
Kadowaki, K., see Ding, H. 20–22
Kadowaki, K., see Mijnarends, P.E. 443
Kadowaki, K., see Renner, C.H. 22
Kadyrova, N.I., see Dlyachkova, T.V. 319
Kagoshima, S., see Kanoda, K. 378
Kagunya, W., see Staub, U. 515, 520, 522, 523, 537–540
Kaindl, G., see Neukirch, V. 326
Kaise, M. 409, 410
Kaiser, D.L. 148
Kaiser, D.L., see Mehran, F. 378, 384, 386
Kaiser, D.L., see Vargas, J.L. 181, 189
Kaiser, D.L., see Wong-Ng, W. 299, 354
Kaiser, J.H., see Haghighi, H. 430–432, 457
Kaiser, J.H., see Howell, R.H. 429, 434, 441, 442
Kaiser, J.H., see Sterne, P.A. 441
Kaiser, J.H., see Turchi, P.E.A. 426, 429, 441
Kajcsos, Z. 436, 438
Kajitani, T. 285, 352
Kajitani, T., see Miyazaki, Y. 62, 260, 316
Kajitani, Y., see Miyazaki, Y. 318
Kakihana, M., see Petrykin, V. 93, 108, 111
Kakihana, M., see Petrykin, V.V. 93, 102, 111
Kakimoto, K. 93, 119, 124, 163
Kakimoto, K., see Imagawa, Y. 153
Kakimoto, K., see Ishida, Y. 163, 181
Kakurai, K., see Matsuda, M. 396, 526
Kakurai, K., see Yamada, K. 390
Kaldis, E. 299, 307
Kaldis, E., see Bordet, P. 47, 48, 307, 308
Kaldis, E., see Böttger, G. 330
Kaldis, E., see Bucher, B. 20
Kaldis, E., see Conder, K. 338, 340–343
Kaldis, E., see Karpinski, J. 89, 91, 92, 168, 307–309, 338
Kaldis, E., see Kruger, Ch. 192, 201
Kaldis, E., see Maciejewski, M. 319
Kaldis, E., see Mangelschots, I. 331
Kaldis, E., see Meingast, C. 468
Kale, G.M. 251, 252, 273–276, 278–280, 282, 283, 311–313
Kalenborn, J., see Drössler, H. 540
Kalenborn, J., see Jostarndt, H.-D. 524, 525
Kalitsounakis, N., see Psycharis, V. 334
Kallin, C., see Bonn, D.A. 13
Kalman, Z.H., see Shaltiel, D. 378
Kalnajs, J., see Abrahams, S.C. 245
Kamarád, J., see Šesták, J. 324
Kambara, M. 90, 93–95, 98, 101, 102, 104–106, 117, 119–121, 136, 152, 166, 212
Kambara, M., see Chauhan, H.S. 120, 121
Kambara, M., see Goodilin, E.A. 82, 93–96, 101, 102, 105, 106, 114, 115, 117, 118, 138, 160–162, 166, 167, 175, 187, 193, 194, 208, 302, 303, 326
Kambara, M., see Nakamura, M. 94, 105
Kambara, M., see Tagami, M. 326
Kambara, M., see Yoshizumi, M. 94, 104, 105, 112, 119, 212
Kambara, N., see Yao, X. 136, 151, 165, 167
Kamiyama, T., see Goodilin, E.A. 93, 111
Kamiyama, T., see Izumi, F. 295
Kamiyama, T., see Kuroda, K. 180
Kammlott, G.W., see Jin, S. 11, 142, 307
Kampmann, R., see Wagner, R. 74, 76
Kan, L. 391–393
Kan, L., see Kochelaev, B.I. 397–399, 403
Kanamaru, F., see Kikkawa, S. 269
Kanamori, Y. 131, 132, 183
Kanazawa, I., see Lynn, K.G. 437, 438
Kanbe, S., see Kishio, K. 5
Kandidov, A.V., see Rebane, Y.A. 203
Kaneko, H., see Kebukawa, T. 347
Kaneko, T., see Wada, T. 329
Kaner, R.B., see Holczer, K. 9
Kang, S.G., see Darracq, S. 293
Kang, Z.C. 238
Kanno, R., see Hiroi, Z. 352
Kanoda, K. 378
Kanthakumar, S.S., see Staub, U. 479
Kao, H.-C.I., see Wang, H.H. 348
Kao, H.L., see Hwang, H.Y. 20
Kapitulnik, A., see Loeser, A.G. 20
Kapitulnik, A., see Moler, K.A. 13
Kapitulnik, A., see Newsam, J.M. 327
Kapitulnik, A., see Puchkov, A.V. 20
Kapitulnik, A., see Shen, Z.-X. 13
Kaplan, N., see Porath, D. 346
Kaplan, N., see Shaltiel, D. 378
Kappler, J.P., see Baudelet, F. 38
Karen, P. 90, 93, 209, 250, 251, 253, 262, 271, 297–299, 302–307, 311–313, 316–319, 326–328, 330–333, 349, 352–354
Karen, P., see Andresen, P.H. 349, 350, 352
Karen, P., see Atanassova, Y.K. 353

Karen, P., see Fjellvåg, H. 275, 296–299, 316–319, 335–337
Karen, P., see Huang, Q. 352, 353
Karen, P., see Natali Sora, I. 353
Karen, V., see Karen, P. 318, 319
Karen, V.L., see Huang, Q. 352, 353
Karen, V.L., see Karen, P. 353
Karen, V.L., see Natali Sora, I. 353
Karion, A., see Kramer, M.J. 105, 199, 200
Karl, H., see Dortmann, G. 347
Karpinski, J. 72, 89, 91, 92, 168, 169, 260, 307–309, 338
Karpinski, J., see Bordet, P. 47, 48, 307, 308
Karpinski, J., see Bucher, B. 20
Karpinski, J., see Conder, K. 338, 340–343
Karpinski, J., see Kaldis, E. 307
Karpinski, J., see Maciejewski, M. 319
Karpinski, J., see Mangelschots, I. 331
Karpinski, J., see Meingast, C. 468
Karpinski, J., see Monayenkova, A.S. 321
Karpinski, J., see Schwer, H. 169
Karpov, A., see Petrykin, V. 93
Karppinen, M. 281
Karppinen, M., see Isawa, K. 279
Karppinen, M., see Peitola, K. 263
Karppinen, M., see Valo, J. 308
Kartouni, K., see Lenglet, M. 248
Kasarnowsky, J., see Bernal, J.D. 245
Kasper, J.S., see Garbauskas, M.F. 299
Kassman, A.J. 497
Kastner, M.A., see Aharony, A. 380
Kastner, M.A., see Matsuda, M. 396, 526
Kastner, M.A., see Shirane, G. 379
Kastner, M.A., see Thurston, T.R. 24
Kastner, M.A., see Yamada, K. 390
Kataev, V.E. 379, 390–393
Kataev, V.E., see Rameev, B. 390, 391
Kataev, V.E., see Teitel'baum, G.B. 390
Katano, S., see Nakata, H. 261
Katayama, S., see Yokota, K. 335
Katazawa, K., see Howell, R.H. 429
Kato, H., see Takita, K. 101
Kato, K., see Takayama-Muromachi, E. 285, 295
Kato, M., see Maeno, Y. 350
Kato, N., see Kikkawa, S. 269
Katoh, H., see Takita, K. 101, 111, 327
Katon, H., see Akinaga, H. 111
Katsnelson, M.I., see Romanyukha, A.A. 410
Katsui, A. 152
Katsuyama, S. 352
Kattner, U.R. 89
Katz, A.S., see Basov, D.N. 11, 12
Katz, A.S., see Kleiner, R. 14
Katz, A.S., see Kouznetsov, K.A. 15
Katz, A.S., see Sun, A.G. 14, 15
Katz, B., see Gudmundsson, B. 319
Katz, I.M., see Hill, A.J. 433, 439
Katz, J.J., see Gruen, D.M. 240
Katzan, C.M., see Davies, P.K. 305, 306
Kaufmann, H.J., see Ilyasov, A.Z. 438, 439
Kaul, A.R., see Rebane, J.A. 203
Kaul, A.R., see Samoylenkov, S.V. 204
Kaul, A.R., see Sedov, V.L. 433, 438
Kavich, I.V., see Grebenyuk, V.D. 245
Kawabata, K., see Tsukui, S. 202
Kawabata, S. 89, 324
Kawagoe, T., see Kanoda, K. 378
Kawaguchi, M., see Sakai, N. 93
Kawahara, N., see Kawabata, S. 89, 324
Kawai, T., see Koyama, S. 53
Kawai, T., see Nobumasa, H. 329
Kawaji, H., see Atake, T. 324
Kawano, M. 205
Kawasaki, K. 377
Kawashima, J., see Yamada, Y. 163, 164
Kawashima, T. 348
Kawashima, T., see Ramírez-Castellanos, J. 270
Kazakov, S.M. 260
Kazumata, Y., see Asaoka, H. 205, 208
Kebede, A., see Skanthakumar, S. 524
Kebukawa, T. 347
Kedrovskii, O.V. 245, 246
Keefer, K., see Aselage, T. 89, 102, 296, 326
Keimel, J., see Zhou, X.Y. 436
Keith, H.D., see Jin, S. 11
Keller, H., see Schneider, T. 466
Keller, J., see Becker, K.W. 520, 521
Keller-Berest, F. 331
Kelley, K.K., see Hultgren, R. 231, 235, 237–239
Kemmler-Sack, S. 396
Kemmler-Sack, S., see Kiemel, R. 350
Kemnitz, E. 201
Kendziora, C., see Mandrus, D. 13
Kerchner, H.R., see Norton, D.P. 526, 527
Kern, S. 524
Kern, S., see Soderholm, L. 510
Kershaw, R., see Collins, B.T. 248
Kess, P.H., see Maurer, M. 38
Kessler, C. 405
Kessler, C., see Filip, C. 405

Ketchen, M.B., see Kirtley, J.R. 14
Ketchen, M.B., see Tsuei, C.C. 14
Ketterson, J.B., see Wang, G. 297, 318
Khafiz, M.A., see Sedov, V.L. 438
Khalfi, A., see Cazy, E. 319
Khaliullin, G.G., see Alekseevskii, N.E. 378, 386
Khalliullin, G.G., see Kochelaev, B.I. 385, 386
Khanna, S.N., see McMullen, T. 426, 434, 441
Khasanova, N., see Goodilin, E.A. 93, 108, 111
Khasanova, N.R. 281
Khidekel, M.L., see Izakovich, E.N. 296
Khlybov, E.P., see Kochelaev, B.I. 385, 386
Khlybov, E.P., see Kuzmicheva, G.M. 293
Khomskii, D. 479
Khramova, N.V., see Mozhaev, A.P. 202
Khylbov, E.P., see Alekseevskii, N.E. 378, 386
Kief, R.F., see Jean, Y.C. 433, 438, 439
Kielwein, M., see Merz, M. 486
Kiemel, R. 350
Kikkawa, S. 269
Kikuchi, H. 397
Kikuchi, M. 272
Kikuchi, M., see Kajitani, T. 285, 352
Kikuchi, M., see Kikuchi, M. 272
Kikuchi, M., see Nakajima, S. 53
Kikuchi, M., see Tokiwa, A. 51
Kikuchi, R., see Sarikaya, M. 175
Kilcoyne, S.H., see Cywinski, R. 378
Kim, C., see Fujimori, A. 458
Kim, C.C. 156
Kim, C.-J. 140, 147
Kim, J.H., see Levin, K. 15
Kim, J.S., see Lee, J.Y. 291
Kim, J.-S. 89, 312, 313
Kim, J.T. 194
Kim, J.-T., see Kouznetsov, K.A. 15
Kim, K.-B., see Kim, C.-J. 147
Kim, S.F., see Garifullin, I.A. 385, 386
Kim, Y.C., see Thompson, J.R. 403, 404
Kimmel, G., see Harrington, I. 347
Kimura, S. 91
Kimura, T. 164
Kimura, T., see Ando, Y. 18
Kimura, T., see Boebinger, G.S. 18, 291
Kimura, T., see Fujihara, S. 166, 334
Kimura, T., see Fujimori, A. 458
Kimura, T., see Ishida, Y. 163, 181
Kimura, Y., see Oyanagi, H. 38
King, D.M., see Shen, Z.-X. 13
King, J.C., see Fowler, C.M. 458
King, J.C., see Mueller, F.M. 458
King, T., see Davies, P.K. 285–287
Kini, A.M., see Wang, H.H. 348
Kinoshita, K. 272, 287
Kinoshita, K., see Akimitsu, J. 62
Kinoshita, K., see Shibata, H. 272
Kinoshita, K., see Uehara, M. 9
Kinoshita, K., see Watanabe, T. 329
Kinoshita, M., see Asaoka, H. 147–150
Kipka, R. 263
Kippenhan, N., see Gschneidner Jr, K.A. 231, 243
Kirby, K.W., see Schwartz, R.N. 404
Kirby, P.B. 350
Kirkegaard, P. 424
Kirkland, A.I., see Ramírez-Castellanos, J. 270
Kirschner, J., see Kajcsos, Z. 436, 438
Kirschner, J.M., see Chang, E.K. 319
Kirtley, J.R. 14
Kirtley, J.R., see Tsuei, C.C. 14
Kiryakov, N.P., see Lee, S. 169
Kirzhnits, D.A., see Ginzburg, V.L. 454
Kiseleva, E.V., see Kedrovskii, O.V. 245, 246
Kishio, K. 5, 338
Kishio, K., see Ando, Y. 18
Kishio, K., see Boebinger, G.S. 18, 291
Kishio, K., see Fujimori, A. 458
Kissick, J.L. 348
Kitamura, T. 163, 164
Kitamura, T., see Hyun, O.B. 205
Kitamura, T., see Takagi, A. 163
Kitano, Y., see Nobumasa, H. 329
Kitazawa, K., see Howell, R.H. 434, 441, 442
Kitazawa, K., see Kishio, K. 5, 338
Kitazawa, K., see Sterne, P.A. 441
Kitazawa, K., see Takagi, H. 4
Kitsenko, S.V., see Skolis, Yu.Ya. 282, 283, 322, 323
Kittel, C., see Owen, J. 396
Kivelson, S.A., see Emery, V.J. 23, 381
Kiyoshima, Y., see Oota, A. 326
Kjekshus, A., see Andresen, P.H. 349, 350, 352
Kjekshus, A., see Atanassova, Y.K. 353
Kjekshus, A., see Fjellvåg, H. 275, 296–299, 316–319, 335–337
Kjekshus, A., see Huang, Q. 352, 353
Kjekshus, A., see Karen, P. 90, 93, 209, 250, 251, 253, 262, 271, 297–299, 302–307, 311–313, 316–319, 326–328, 330–333, 349, 352–354
Kjekshus, A., see Natali Sora, I. 353
Klabunde, C.E., see Goyal, A. 25

Klavins, P., see Folkerts, T.Y. 148
Kleb, R., see Jorgensen, J.D. 299, 471
Kleefisch, M.S., see Jorgensen, J.D. 37
Kleeman, P., see Filip, C. 405
Klein, L. 205
Klein, M.W. 469
Klein, O., see Alloul, H. 20
Klein, O., see Holczer, K. 9
Kleiner, R. 14
Klemenz, C. 94, 98, 133, 153, 163, 180
Klemenz, C., see Scheel, H.J. 156
Klester, K.L. 190
Klibanow, D. 92, 93, 305, 306
Klimczuk, T., see Luszczek, M. 156
Klimczuk, T., see Sadowski, W. 155, 156
Klinkova, L.A. 265
Kluin, J.E., see Hentrich, D. 433–436
Klunzinger, A.E., see Blackstead, H.A. 441
Knacke, O., see Barin, I. 336
Knauf, N., see Kataev, V.E. 390, 391
Knauf, N., see Teitel'baum, G.B. 390
Kniga, O.P., see Makarova, N.G. 90, 126
Knight, W.D., see Owen, J. 396
Knights, A.P., see Anwand, W. 438
Knot'ko, A.V., see Goodilin, E.A. 104, 119, 153, 166
Knupfer, M., see Merz, M. 486
Kobayashi, K. 346
Kobayashi, M., see Takayama-Muromachi, E. 295
Kobayashi, N. 256, 260, 270
Kobayashi, N., see Nakajima, S. 53
Kobayashi, N., see Tokiwa, A. 51
Kobets, M.I., see Stepanov, A.A. 393–395
Koblischka, M.R. 72
Kobyashi, N., see Noto, K. 326
Koch, R.H., see Chaudhari, P. 10
Kochelaev, B.I. 381–386, 397–399, 403
Kochelaev, B.I., see Alekseevskii, N.E. 378, 386
Kochelaev, B.I., see Sichelschmidt, J. 385–388
Koehler, W.C., see Gruen, D.M. 240
Koelling, D.D., see Yu, J. 432
Koenitzer, J.W., see Dąbrovski, B. 355
Kofstad, P., see Fjellvåg, H. 299, 335–337
Koga, K., see Nakada, I. 139
Koga, K., see Nakazawa, Y. 300
Koga, K., see Otzschi, K. 291, 293
Kogachi, M. 177
Kögel, G., see Zhou, X.Y. 433, 436
Kohara, K. 378
Kohayashi, S. 149
Köhler, B.U. 279
Köhne, S., see Wübbeler, G. 381
Kojima, H., see Howell, R.H. 429, 434, 441, 442
Kojima, H., see Tanaka, I. 152
Kojima, H., see Thurston, T.R. 24
Kojima, H.J., see Sterne, P.A. 441
Kojima, K., see Arai, J. 401
Kojo, H., see Chikumoto, N. 208
Kokusho, K., see Sawa, K. 285
Kolar, D., see Guha, J.P. 253
Kolbrecka, K., see Borowiec, K. 312, 313, 336
Kolesnikov, N.N., see Indenbom, M.V. 194
Kolesnikov, N.N., see Puchkov, A.V. 20
Kolyubakin, A.I., see Klinkova, L.A. 265
Komatsu, H. 131
Komatsu, M., see Isawa, K. 279
Komatsu, T. 335
Kometani, T., see Cava, R.J. 9
Konetzki, R. 235
Konetzki, R.A. 273, 278, 282
Konetzki, R.A., see Boudéne, A. 320
Kongkachuichay, P., see Gadalla, A.M. 274, 277
König, U., see Krüger, C. 254, 268
König, W., see Thomsen, C. 326
Konishi, M. 161
Konishi, M., see Hasegawa, K. 159
Kopnin, E., see Karpinski, J. 169
Kopnin, E.M., see Karpinski, J. 260
Kopnin, E.M., see Kazakov, S.M. 260
Kopnin, E.M., see Schwer, H. 169
Kopyto, M. 282, 283, 322, 323
Kordes, E., see Haas, H. 279
Kordis, J. 238
Kordis, J., see Bevan, D.J.M. 238
Kordis, J., see Burnham, D.A. 240
Korecz, L., see Janossy, A. 404
Korhonen, T., see Barbiellini, B. 427, 434
Koriyama, S., see Sakurai, T. 327
Korman, R., see Corbel, C. 433, 435, 436
Korn, C., see Harrington, I. 347
Korolev, Y.M., see Izakovich, E.N. 296
Korsakov, I.E., see Rebane, Y.A. 203
Kortan, A.R., see Rosseinsky, M.J. 9
Koscheeva, S.N. 297, 318
Kosenko, A.V., see Maljuk, A.N. 94, 285
Koshi, J., see Babu, T.G.N. 159
Koshizuka, K., see Egi, T. 153, 155, 205, 206
Koshizuka, N., see Chikumoto, N. 208

Koshizuka, N., see Egi, T. 153, 155, 173, 189
Koshizuka, N., see Gu, G.D. 169
Koshizuka, N., see Kuroda, K. 94, 101, 151, 155, 172, 183
Koshizuka, N., see Miyatake, T. 330
Koshizuka, N., see Pradhan, A.K. 72, 206
Koshizuka, N., see Sakurai, T. 327
Koshizuka, N., see Shibata, S. 155, 205
Koshizuka, N., see Ting, W. 161, 190
Koshizuka, N., see Watanabe, N. 104, 192
Koshta, A.A., see Romanyukha, A.A. 410
Koshuho, K., see Sawa, H. 59
Koshy, J., see Jose, R. 158
Kosinski, S.G., see Stavola, M. 355
Kosmynin, A.C. 324
Kosmyuin, A.S., see Fotiev, A.A. 274
Kossel, W. 80
Kosuge, K., see Imai, T. 20
Kosuge, K., see Katsuyama, S. 352
Kosuge, M., see Okai, B. 104
Kouba, R. 473
Koufodakis, A., see Guskos, N. 263
Koufoudakis, A., see Psycharis, V. 209, 334
Kouznetsov, K.A. 15
Kovacevic, Z. 520
Kovacik, V. 194
Kovalevskaya, Yu.A., see Amitin, E.B. 235
Kovba, L.M. 253
Kovba, L.M., see Antipov, E.V. 253
Kovba, M.L., see Maiorova, A.F. 264, 265
Kovba, M.L., see Skolis, Yu.Ya. 322, 323
Kovtunenko, I.V., see Kedrovskii, O.V. 245, 246
Kowal, D., see Yaron, U. 355
Kowalewski, J. 149
Kowalewski, J., see Frieling, T. 147
Koyama, S. 53
Koyama, S., see Kanamori, Y. 183
Koyama, S., see Kusao, T. 131, 179
Koyama, S., see Kutami, H. 208, 209
Koyama, S., see Namikawa, Y. 172, 177–180, 198
Koyama, S., see Oka, A. 176, 177, 192, 203, 205, 208
Koyama, S., see Usagawa, T. 160, 161
Koyama, S., see Zaina, H. 160
Koyama, T., see Hattori, O. 197
Koyanagi, Y., see Noto, K. 326
Kozhevnikov, V.L., see Patrakeev, M.V. 329, 338, 345
Kozin, M.G., see Andrianov, V.A. 153, 192
Krabbes, G. 89, 166
Krabbes, G., see Bieger, W. 102, 105, 166
Krabbes, G., see Ruck, K. 348
Krabbes, G., see Schatzle, P. 166
Krabbes, G., see Wiesner, U. 90, 149
Kraitchman, M., see Ceder, G. 300, 301, 344
Krajewski, J.J., see Cava, R.J. 9, 34, 49, 275, 287, 288, 299, 301, 307, 308, 329, 330, 517, 518, 526
Krajewski, J.J., see Huang, Q. 355
Krajewski, J.J., see Hwang, H.Y. 20
Krajewski, J.J., see Schneemeyer, L.F. 505
Krakauer, H. 458
Krakauer, H., see Allen, P.B. 458
Krakauer, H., see Cohen, R.E. 471, 473
Krakauer, H., see Pickett, W.E. 457, 471
Krakauer, H., see Singh, D.J. 426, 442, 443
Krakauer, H., see Von Stetten, E.C. 426, 427, 430, 433, 439
Krakauer, H., see Wei, S.-H. 470
Kramer, M. 92, 101, 102, 108, 111
Kramer, M.J. 105, 199, 200
Kramer, M.J., see Allenspach, P. 508, 510, 515, 517
Kramer, M.J., see Park, M. 112, 114, 305
Kramer, M.J., see Wu, H. 104, 105, 208, 302
Krantz, M. 460
Krasilnikov, V.N., see Bazuev, G.V. 265
Krauns, C. 148, 166, 200
Krauns, Ch. 91, 93–95, 98, 196
Krauns, Ch., see Nakamura, M. 94–96, 98, 133, 200
Krauns, Ch., see Sumida, M. 94, 112, 113
Krauns, Ch., see Tagami, M. 136, 161, 166, 177, 185, 186
Krauns, Ch., see Yamada, Y. 123, 180
Krausz, E.R., see Furrer, A. 530
Kraut, O. 468
Kraut, O., see Meingast, C. 468, 486
Krebs, H.U., see Ullmann, B. 350
Kreisler, A., see Alquie, G. 396
Krekels, T. 41, 318, 355
Krekels, T., see Reyes-Casga, J. 41
Krelaus, J., see Ullrich, M. 181
Kremer, R.K. 381, 518
Kremer, R.K., see Bernard, C. 6
Kresin, B.V.Z. 422
Krichene, S., see Wang, S.J. 433, 435, 438, 439
Kril, G., see Maurer, M. 38
Krill, G., see Baudelet, F. 38
Krischner, H., see Torkar, K. 263

Kristiak, J., see Bezakova, E. 438
Kristiak, J., see Kristiakova, K. 439
Kristiak, J., see Sausa, O. 433, 440
Kristiakova, K. 439
Kristiakova, K., see Sausa, O. 433, 440
Kristoffel, N., see Hizhnyakov, V. 518
Kroeger, D.M., see Goyal, A. 25, 71, 73, 142, 159, 180
Kroeger, D.M., see Williams, R.K. 310
Krol, D.M., see Stavola, M. 355
Krötzsch, M., see Herrmann, J. 6
Krucpzak, J., see Shi, D. 202
Krug, G., see Stadloper, B. 11, 13
Krüger, C. 254, 268
Krüger, C., see Böttger, G. 330
Krüger, C., see Maciejewski, M. 319
Kruger, Ch. 192, 201
Kruschel, G. 381, 399–403
Kruschel, G., see Kiemel, R. 350
Kruseman, A.C., see Ashoka-Kumar, P. 425
Ku, H.C., see Lai, C.C. 526
Ku, H.C., see Shieh, J.H. 526
Kubanek, F., see Straube, E. 300
Kubashevski, O., see Barin, I. 336
Kubat-Martin, K.A. 270, 271, 331
Kubo, Y. 441
Kubo, Y., see Ichihashi, T. 300
Kubo, Y., see Manako, T. 355
Kubota, N., see Zenitani, Y. 348
Kudo, T., see Hiratani, M. 350
Kuhns, P.L., see Gorny, K. 22
Kuk, I.-H., see Kim, C.-J. 147
Kukovitskii, E.F., see Kataev, V.E. 379, 391
Kukovitskii, E.F., see Rameev, B. 390, 391
Kulakov, A.B., see Maljuk, A.N. 94
Kulakov, M.P., see Indenbom, M.V. 194
Kumaki, Y., see Kebukawa, T. 347
Kumakura, H., see Doyama, M. 439
Kumakura, H., see Ishibashi, S. 439
Kumar, M.P.S., see Mukherjee, A. 520
Kumeda, M., see Morimoto, A. 378
Kumeda, M., see Moto, A. 410
Kund, M. 468
Kunnmann, W., see Banks, E. 253
Kupfer, H. 205
Kupfer, H., see Gordeev, S.N. 205
Kupfer, H., see Wolf, Th. 150, 152, 200, 203, 205
Kura, T., see Yokota, K. 335
Kuramoto, Y., see Watanabe, S. 527
Kurian, J., see Jose, R. 158
Kuribayashi, K., see Nagashio, K. 114, 136, 196, 212
Kuric, M.V., see Maple, M.B. 5, 6, 10
Kurkin, I.N. 409
Kurmayev, E.Z., see Kissick, J.L. 348
Kuroda, K. 94, 101, 151, 155, 172, 180, 183
Kuroda, K., see Egi, T. 153, 155, 173, 189, 205, 206
Kuroda, K., see Pradhan, A.K. 72, 205, 206
Kuroda, K., see Shibata, S. 155
Kuroda, K., see Ting, W. 161, 190
Kuroda, K., see Watanabe, N. 104, 192
Kurosky, R., see Qian, M. 350
Kusaba, K., see Kajitani, T. 352
Kusaka, T., see Takano, M. 260
Kusao, T. 131, 179
Kusz, B., see Sadowski, W. 155, 156
Kutami, H. 190, 208, 209
Kutami, H., see Nakamura, M. 187, 188, 190, 200, 206
Kůtek, F., see Petrů, F. 242
Kuwahara, K., see Egami, M. 128, 130
Kuzmenko, V.V., see Monayenkova, A.S. 321
Kuzmenko, V.V., see Rudnyi, E.B. 201, 320, 345
Kuzmicheva, G.M. 293
Kuznetsov, A.V., see Belyaev, V.N. 439
Kuznetsov, M.S., see Lee, S. 169
Kuznetsov, S.N., see Sedov, V.L. 422, 433, 444
Kvartalov, D.B., see Goodilin, E.A. 93, 114
Kwei, G.H., see Fisk, Z. 285
Kwei, G.H., see Harlow, R.L. 355
Kwei, G.H., see Kubat-Martin, K.A. 271
Kwestroo, W. 250, 253
Kwo, J., see Batlogg, B. 20
Kwo, J., see Hwang, H.Y. 20
Kwok, W.K., see Jorgensen, J.D. 299
Kwok, W.K., see Welp, U. 517
Kyle, J., see Jean, Y.C. 433, 438–440

La Placa, S.J. 280, 281
La Placa, S.J., see Banks, E. 253
La Placa, S.J., see Bringley, J.F. 260, 280, 281
Labbé, J. 37
Lacey, D.E., see Thomas, J.V. 149
Lachowski, E.E., see Sastry, P.V.P.S.S. 259, 260
Lachowski, E.E., see Skakle, J.M.S. 331
Lacorro, P., see Torrance, J.B. 468
Lada, T., see Morawski, A. 169
Laffez, P. 264–266
Laffez, P., see Wu, X.-J. 259

Laffitte, P., see Holtermann, C. 245
Lagouri, T. 433, 438, 439, 441
Lagouri, Th. 434
LaGraff, J.R. 202, 203, 348
Laguna, M.A., see Sanjuán, M.L. 503
Lahiri, K., see Shi, D. 134, 142
Lai, C.C. 526
Laibowitz, R.B., see Chaudhari, P. 10
Lakhtin, A.A., see Patrakeev, M.V. 329
Lalignant, Y., see Ferey, G. 350
Lam, C.C. 433
Lam, C.C., see Li, J.Q. 440
Lam, D.J., see Smedskjaer, L.C. 430
Lamberti, V.E. 90, 155, 323
Lamoreaux, R.H. 243
Lanckbeen, A. 343
Lander, G.H., see Kern, S. 524
Lang, H.P., see Scheel, H.J. 156
Langereis, C., see De Leeuw, D.M. 250, 253, 288–292, 297, 316, 318
Langereis, C., see Kwestroo, W. 250, 253
Lapertot, G., see Rossat-Mignod, J. 20
Lapertot, G., see Vettier, C. 300, 301
Lapinskas, S. 300
Lappas, A. 272
Larbalestier, D. 69
Larbalestier, D., see Batlogg, B.J. 69, 71, 72, 203, 209, 210
Larese, J.Z., see Hayri, E.A. 292
Larkin, A.I., see Blatter, G. 12
Lasocha, A., see Hodorowicz, S.A. 301
Lasocha, W., see Hodorowicz, S.A. 301
Lathrop, D.K., see Moeckly, B.H. 159
Laubschat, C., see Neukirch, V. 326
Laudise, R.A., see O'Bryan, H.M. 338
Laughlin, R.B. 15
Laurent, C., see Ausloos, M. 349
Lauriat, J.P., see Yakhou, F. 263
Lawanier, J.P. 316
Lawson, A.C., see Kubat-Martin, K.A. 271
Lay, K.W. 89
Lazuta, A.V. 378
Le Bail, A., see Ferey, G. 350
Le Floch, S., see Bordet, P. 350
Lea, K.R. 504, 538
Leach, D.H., see Deveraux, T.P. 13
Leandersson, M., see Zakharov, A.A. 458
Leask, M.J.M. 529
Leask, M.J.M., see Lea, K.R. 504, 538
Lebech, B., see Andersen, N.H. 299–301
Lebech, B., see Casalta, H. 190–192, 299
Lee, B., see Durny, R. 388
Lee, B.J. 90, 91, 95
Lee, B.W., see Dalichaouch, Y. 523
Lee, B.W., see Maple, M.B. 5, 6, 10, 16, 17, 156
Lee, B.W., see Markert, J.T. 5
Lee, B.W., see Vier, D.C. 378
Lee, B.W., see Yang, K.N. 515, 528
Lee, D.F., see Goyal, A. 25
Lee, D.F., see Salama, K. 142
Lee, D.N., see Lee, B.J. 90, 91, 95
Lee, J.Y. 291
Lee, P.A., see Nagaosa, N. 23
Lee, R., see Yang, K.Y. 297, 318
Lee, R.R., see Von Stetten, E.C. 426, 427, 433, 439
Lee, S. 169
Lee, S., see Petrykin, V. 93
Lee, S.-J., see Manthiram, A. 330
Lee, S.R., see Gudilin, E.A. 171
Lee, V.Y., see Ahn, B.T. 91, 112, 313–315
Lee, V.Y., see Beyers, R. 516, 518
Lee, W.C., see Martindale, J.A. 13
Lee, W.C., see Wollman, D.A. 14
Leenders, A., see Ullrich, M. 181
Leggett, A.J., see Wollman, D.A. 14
Legnini, D.G., see Smedskjaer, L.C. 430, 433, 434, 436–439
Legoudez, J., see Baudelet, F. 38
Legros, C., see Lanckbeen, A. 343
Lehmann, M.S., see Chaillout, C. 277, 381
Lehnig, M., see Foukis, V. 388
Lei, M. 469, 472
Leitus, G.M., see Shamrai, V.F. 297
Lejay, P., see Beille, J. 32
Lejay, P., see Capponi, J.J. 35
Lejay, P., see Michel, C. 35
Lemor, W., see Kochelaev, B.I. 381–384, 403
Lengeler, M. 38
Lenglet, M. 248
Lennikov, V.V., see Goodilin, E.A. 104, 119, 153, 166
Leonidov, I.A., see Patrakeev, M.V. 329, 338, 345
Leonyuk, L. 149, 190
Leonyuk, L., see Shvanskaya, L. 153
Lepage, Y. 35
Lera, F., see Fruchart, D. 347
Lerch, P., see Barbiellini, B. 419, 427, 434
Lerch, P., see Blandin, P. 441
Lerch, P., see Peter, M. 429, 433, 434

Leskelä, M., see Valo, J. 308
Lesueur, J. 14
Lesueur, J., see Burger, J.P. 346
LeTourneau, V., see Webb, A.W. 280
Leung, H.-T., see Lo, W. 142
Levet, J.C., see Deville, A. 378
Levi, A., see Tu, K.N. 201
Levi, B.G. 13, 15, 20, 24
Levi, Y., see Felner, I. 6
Levin, G.A., see Jiang, C.N. 19, 20
Levin, K. 15
Levine, M.M., see Cabrera, N. 84
Lewandowski, J.T., see Newsam, J.M. 327
Li, and G.Y., see Zhang, D.M. 443
Li, B., see Alcock, C.B. 257–259
Li, B.R., see Chen, A. 440
Li, B.R., see Tang, C.Q. 433, 434
Li, B.R., see Wang, S.J. 433, 438, 439
Li, B.R., see Zhi, Y. 433
Li Donghong, see Li Anli 433, 439
Li, G.Y., see Zhang, D.M. 436, 438, 443
Li, H.C., see Zhou, X.Y. 436
Li, J., see Gao, X.H. 443
Li, J., see Wang, S.J. 443
Li, J.Q. 318, 440
Li, S. 101, 302
Li, S., see Chen, T.G. 149
Li, S.Q., see Wang, S.J. 433, 438, 439
Li, W.-H. 526
Li, W.-H., see Skanthakumar, S. 524
Li, W.-H., see Yang, K.N. 515, 528
Li, X.H., see Wang, S.J. 433, 438, 439
Li, X.H., see Zhi, Y. 433
Li, X.S., see Von Stetten, E.C. 426, 427, 430, 433, 439
Li, Y. 210, 441
Li, Y., see McMullen, T. 426, 434, 441
Li, Y.H., see Crossley, A.L. 189
Li, Z.G., see Hor, P.H. 277
Li, Z.G., see Xiong, X. 277
Li Anli 433, 439
Liang, J., see Zhong, Q. 286, 288
Liang, R. 147, 148, 150, 338
Liang, R., see Bonn, D.A. 13
Liang, R., see Casalta, H. 299
Liang, R., see Hardy, W.N. 13
Liang, R., see Homes, C.C. 20
Liang, R., see Moler, K.A. 13
Liang, R., see Poulsen, H.F. 300
Liang, R., see Schleger, P. 300
Liang, R.X. 148, 171, 196
Liang, R.X., see Hoffmann, L. 432, 440
Liang, R.X., see Schabel, M.C. 457
Liang, W.Y., see Janossy, A. 406
Liang, W.Y., see Lin, C.T. 148–150, 174, 175
Liang, W.Y., see Liu, R.S. 330
Liang, W.Y., see Loram, J.W. 20
Liarokapis, E., see Kaldis, E. 299
Liarokapis, E., see Psycharis, V. 334
Libutzki, H., see Hauck, J. 346
Licci, F. 89, 324, 325
Licci, F., see Rodriguez, M.A. 350
Licci, F., see Scheel, H.J. 291
Lichtenberg, P., see Maeno, Y. 9
Lichtenstein, A.I., see Anisimov, V.I. 481
Liechtenstein, A.I. 481, 482, 484–486, 524, 528
Liechtenstein, A.I., see Andersen, O.K. 457, 460, 462, 464–466, 475, 482
Liechtenstein, A.I., see Mazin, I.I. 457, 458, 465, 486
Liechtenstein, A.I., see Rodriguez, C.O. 457, 473
Lightfoot, P. 284–286, 291, 292
Lightfoot, P., see Jorgensen, J.D. 299, 300
Lightfoot, S.P., see Jorgensen, J.D. 471
Lii, K.H., see Yu, J.-T. 378
Likodimos, V., see Guskos, N. 263
Lim, H.J. 439
Limonov, M. 108, 192
Limonov, M., see Goodilin, E.A. 108, 111
Lin, B.N., see Luo, H.M. 93
Lin, C.T. 104, 114, 147–151, 168, 169, 174, 175
Lin, C.T., see Strach, T. 499, 503, 504
Lin, G., see Chu, C.W. 433
Lin, J.G. 156, 204
Lin, J.J., see Subramanian, M.A. 5
Lin, S.-H. 271, 272
Lin, S.-Y., see Chaudhari, P. 14
Lin, Y.F., see Chan, W.C. 194
Lin, Y.H., see Luo, H.M. 93
Lin, Y.P. 300
Lindau, I., see Zakharov, A.A. 458
Lindemer, T.B. 89, 92, 93, 98, 104, 105, 108, 199, 204, 261–266, 302, 313, 315, 316, 319, 338, 341, 342
Lindén, J., see Valo, J. 308
Lines, D.R., see Weller, M.T. 254, 263
Liniger, E.G., see Frase, K.G. 297, 318
Linker, G., see Claus, H. 189
Linzen, D., see Fischer, K. 89, 148

Liolios, A., see Lagouri, T. 433, 438, 439, 441
Liolios, A., see Lagouri, Th. 434
Liolios, A.K. 433, 436, 438–440
Lippold, B., see Herrmann, J. 6
Lisitskii, V.N., see Aleshina, N.N. 90
List, F.A., see Goyal, A. 25
Lister, S.J.S. 192
Liszkay, L., see Balogh, A.G. 433, 438, 439
Little, M.R., see Janes, R. 379
Littlewood, P.B., see Varma, C.M. 15
Liu, A.Y., see Crommie, M.F. 469
Liu, F.Q., see Zhang, J.C. 433, 434, 440
Liu, H.B., see Lamberti, V.E. 323
Liu, J., see Doyama, M. 444
Liu, J.-H., see Doverspike, K. 286, 292
Liu, J.Z., see Haghighi, H. 431, 432, 457
Liu, J.Z., see Howell, R.H. 429, 434
Liu, J.Z., see Smedskjaer, L.C. 430
Liu, J.Z., see Welp, U. 517
Liu, J.Z., see Zhang, J.C. 433, 434, 440
Liu, R., see Thomsen, C. 326
Liu, R.L., see Gofron, K. 457
Liu, R.S. 330
Liu, S., see Brusa, R.S. 437, 439
Liu, S.H. 404
Liu, S.H., see Huang, W.F. 439
Liu, X.Y. 80
Liu, Z.X., see Zhang, J.C. 433
Lo, R.K., see Zhou, J. 161
Lo, W. 140, 142
Lo, W., see Liu, R.S. 330
Lo, W., see Tang, T.B. 201
Lobo, R.C. 259
Lobo, R.P.S.M., see Odier, P. 190
Löchner, V., see Paulus, E.F. 263
Lock, D.G. 419
Locquet, J.P., see Yang, K.Y. 297, 318
Loeffen, P.W., see Kaldis, E. 299
Loeser, A.G. 20
Loeser, T., see Shen, Z.-X. 13
Loewenhaupt, M. 528
Loewenhaupt, M., see Fulde, P. 523
Loh, R. 199
Loidl, A., see Elschner, B. 377, 379, 396, 399
Loidl, A., see Kochelaev, B.I. 381–384, 403
Loidl, A., see Sichelschmidt, J. 385–388
Lombardi, L.W., see Shen, Z.-X. 13
Lomer, J.N., see Cywinski, R. 378
Londos, C.A., see Guskos, N. 263
Long, Q., see Zhou, X.Y. 433, 434
Long, Q.W., see Zhu, J.S. 444
Longo, J.M. 276
Longo, V. 252
Lonzarich, G.G., see Julian, S.R. 9
Loong, C.K. 502, 504
Loong, C.K., see Kern, S. 524
Loong, C.-K. 502
Loong, C.-K., see Goodman, G.L. 501, 507, 510, 524
Loong, C.-K., see Soderholm, L. 505, 507, 508, 510, 520, 524, 535
Lopato, L.M. 250, 251, 253, 301
Loram, J.W. 20, 203
Loram, J.W., see Liu, R.S. 330
Loram, J.W., see Tallon, J.L. 20
Lovesey, S.W. 520, 523, 539
Lovesey, S.W., see Marshall, W. 500
Lovy, D., see Shaltiel, D. 384, 404
Lowe-Ma, C.K. 155, 156
Lowndes, D.H., see Norton, D.P. 526, 527
Lozanne, A. 183
Lu, J.P., see Levin, K. 15
Lu, X. 433
Lu, Xuekun, see Zhou, X.Y. 436
Lucas, J., see Perrin, C. 348
Lucco Bolera, M., see Abbattista, F. 297, 301
Lucco-Bolera, M., see Abbattista, F. 303, 305, 306
Lucco-Borlera, M., see Abbattista, F. 264
Luce, J.L. 168
Ludge, A., see Bohm, J. 130, 144
Ludwig, H.A. 299
Lugin, L.I., see Lopato, L.M. 250, 251
Lukas, H.L., see Boudéne, A. 320
Lukas, H.L., see Konetzki, R. 235
Lung, C.W., see Yang, Z. 438, 439
Lung, C.W., see Zhu, J. 439
Luo, C.Y., see Zhao, Y.G. 433, 441
Luo, H.M. 93
Luparev, V.V., see Kuzmicheva, G.M. 293
Luszczek, M. 156
Lutgemeier, H. 204
Lütgemeier, H. 520
Luzet, D., see Bertinotti, A. 263
Lykova, L.I., see Antipov, E.V. 253
Lykova, L.I., see Kovba, L.M. 253
Lynn, J.W. 6
Lynn, J.W., see Goodwin, T.J. 526
Lynn, J.W., see Huang, Q. 352, 353
Lynn, J.W., see Karen, P. 353
Lynn, J.W., see Li, W.-H. 526
Lynn, J.W., see Natali Sora, I. 353

Lynn, J.W., see Skanthakumar, S. 524, 528
Lynn, J.W., see Sumarlin, I.W. 526, 528, 532, 533
Lynn, J.W., see Yang, K.N. 515, 528
Lynn, K.G. 437, 438
Lynn, K.G., see Ashoka-Kumar, P. 425
Lynn, K.G., see Chan, L.P. 429, 443, 444
Lynn, K.G., see Usmar, S.G. 433, 434, 437–439

Ma, Q., see Li, Y. 441
Ma, Y., see Qian, M. 350
MacDougal, C.S., see Lindemer, T.B. 92, 93, 108
MacDougall, C.S., see Lindemer, T.B. 302, 313, 315
MacFarlane, A., see Bonn, D.A. 13
Machefert, J., see Lenglet, M. 248
Machi, T., see Chikumoto, N. 208
Machida, M. 264
Machin, D.J., see Arjomand, M. 264
Maciejewski, M. 319
MacKay, H.B., see Moncton, D.E. 6
Mackenzie, A.P., see Julian, S.R. 9
MacMannus-Driscoll, J.L., see Crossley, A.L. 189
MacManus, J.L. 348
Macmanus-Driscoll, J., see Auguste, F. 152
MacManus-Driscoll, J.L. 71–73, 90, 91, 112, 114, 149, 159, 313, 319
MacManus-Driscoll, J.L., see Qi, X. 94, 158, 159
Madsen, J., see Poulsen, H.F. 300
Madsen, J., see v. Zimmermann, M. 24
Maeda, A., see Wada, T. 93, 199, 204
Maeda, M. 89, 95
Maeda, T., see Morimoto, A. 378
Maekawa, S. 9
Maekawa, S., see Ohta, Y. 467
Maeno, Y. 9, 350
Maeno, Y., see Fujiita, T. 32
Maeno, Y., see Julian, S.R. 9
Magerkurth, C., see Wiesner, U. 149
Magnone, E. 152
Mahajan, A., see Alloul, H. 20
Maier, J. 338–340
Maier, J., see Murugaraj, P. 147
Maignan, A. 318
Maignan, A., see Goutenoire, F. 54
Maignan, A., see Hervieu, M. 54
Maignan, A., see Huvé, M. 54, 56
Maignan, A., see Martin, C. 56
Maignan, A., see Pelloquin, D. 169
Maignan, A., see Raveau, B. 53, 59
Maiorova, A.F. 264, 265
Maisnerowski, J., see Györffy, B.L. 422
Maister, I.M., see Lopato, L.M. 251
Majewska, K., see Skrzypek, D. 410
Majewski, P., see Schulze, K. 267, 268
Majumdar, C.K. 419
Majumdar, C.K., see Mandal, P. 433, 439
Majumdar, C.K., see Sen, P. 433, 439, 444
Makarova, N.G. 90, 126
Makhija, A.V., see Rosseinsky, M.J. 9
Maksimov, E.G., see Antonov, V.N. 428
Maletta, H. 515
Maletta, H., see Allenspach, P. 508, 510, 515, 517
Maletta, H., see Chattopadhyay, T. 515
Maletta, H., see Roessli, B. 515
Mali, M., see Erb, A. 433, 445
Mali, M., see Mangelschots, I. 331
Malik, S.K. 302
Maljuk, A.N. 94, 285
Manako, T. 355
Mandal, K., see Sanyal, D. 443
Mandal, P. 433, 439
Mandrus, D. 13
Mangelschots, I. 331
Mangelschots, I., see Böttger, G. 330
Mann, M.E., see Ceder, G. 300, 301, 344
Manohar, S.B., see Pujari, P.K. 439, 443, 444
Manthiram, A. 98, 112, 330
Manthiram, A., see Hou, C.J. 300
Manthiram, A., see Lightfoot, P. 284–286, 291, 292
Manthiram, A., see Smith, M.G. 269, 293
Manthiram, A., see Zhu, Y.T. 297
Manuel, A.A. 429, 430, 432, 433, 440, 457
Manuel, A.A., see Adam, G. 432
Manuel, A.A., see Barbiellini, B. 433, 437, 440, 442, 443
Manuel, A.A., see Barnes, S.E. 433
Manuel, A.A., see Blandin, P. 441
Manuel, A.A., see Erb, A. 433, 445
Manuel, A.A., see Hoffmann, L. 430, 432, 440
Manuel, A.A., see Jarlborg, T. 428
Manuel, A.A., see Massidda, S. 426, 427
Manuel, A.A., see Peter, M. 429, 430, 432–436
Manuel, A.A., see Shukla, A. 424, 432, 433, 435, 442
Mao, J., see Anlage, S.M. 11, 13
Mao, J., see Wu, D.-H. 13

Mao, S.N., see Anlage, S.M. 11, 13
Mao, S.N., see Wu, D.-H. 13
Mao, Z.Q., see Wang, N.L. 467
Maple, M.B. 5–8, 10, 16, 17, 156
Maple, M.B., see Ayoub, N.Y. 285
Maple, M.B., see Cox, D.L. 13, 14
Maple, M.B., see Dalichaouch, Y. 17, 523
Maple, M.B., see Early, E.A. 5
Maple, M.B., see Fertig, W.A. 6
Maple, M.B., see Jiang, C.N. 19, 20
Maple, M.B., see Jung, K. 433, 438, 439, 441
Maple, M.B., see Kleiner, R. 14
Maple, M.B., see Kouznetsov, K.A. 15
Maple, M.B., see Markert, J.T. 4–7, 10, 11
Maple, M.B., see Moncton, D.E. 6
Maple, M.B., see Neumeier, J.J. 16, 17, 527
Maple, M.B., see Sun, A.G. 14, 15
Maple, M.B., see Vier, D.C. 378
Maple, M.B., see Yang, K.N. 515, 528
Marathe, V.R., see Sundaresan, A. 537
Marchetta, M., see Dimesso, L. 166, 189
Marella, M. 142
Marezio, M. 11, 505, 537
Marezio, M., see Alario-Franco, M.A. 300
Marezio, M., see Bordet, P. 44, 307, 308, 352
Marezio, M., see Capponi, J.J. 35
Marezio, M., see Cava, R.J. 299, 301, 517, 518
Marezio, M., see Chaillout, C. 48, 277, 381
Marezio, M., see Chmaissem, O. 264
Marezio, M., see Fisk, Z. 285
Marezio, M., see François, M. 299, 354
Marezio, M., see Hewat, A.W. 299
Marezio, M., see Karpinski, J. 307
Marezio, M., see Kazakov, S.M. 260
Marezio, M., see Nuñez-Regueiro, M. 4
Marezio, M., see Putilin, S.N. 4
Marezio, M., see Radaelli, P.G. 59
Marezio, M., see Renevier, H. 350, 352
Marezio, M., see Strobel, P. 338
Marezio M, ., see Bordet, P. 47, 48
Maric, M., see Soderholm, L. 505, 507, 520
Maric, M., see Xue, J.S. 505
Marimuthu, K.N. 318
Marinel, S. 134
Markelz, A.G., see Morris, D.E. 308
Markert, J.T. 4–7, 10, 11
Markert, J.T., see Ayoub, N.Y. 285
Markert, J.T., see Early, E.A. 5
Markert, J.T., see Smith, M.G. 269, 293
Markert, J.T., see Stadloper, B. 11, 13
Marks, L.D., see Wang, G. 297, 318
Marks, L.D., see Wang, Y.Y. 259
Marks, L.D., see Zhang, H. 259
Marks, L.D., see Zhang, J.P. 355
Marquez, L., see Sandford, D. 147, 168
Marsh, P., see Cava, R.J. 34, 49, 287, 288, 330, 526
Marsh, P., see Schneemeyer, L.F. 505
Marshall, D., see Shen, Z.-X. 13
Marshall, D.S., see Loeser, A.G. 20
Marshall, J.H., see Cava, R.J. 517, 518
Marshall, J.H., see Schneemeyer, L.F. 505
Marshall, W. 500
Marti, W. 162, 177
Martin, A.A. 192, 499
Martin, C. 53, 56
Martin, C., see Bourgault, B. 52
Martin, C., see Huvé, M. 54, 56
Martin, F., see Erb, A. 433, 445
Martin, J., see Loewenhaupt, M. 528
Martin, K.A.K. 276
Martin, P.M., see Goyal, A. 25
Martin, P.M., see Lindemer, T.B. 92, 93, 104, 105, 108, 199, 302
Martin, P.M., see Williams, R.K. 310
Martin, R.L., see Bevan, D.J.M. 241, 242
Martin, S., see Fiory, A.T. 203
Martindale, J.A. 13
Martindale, J.A., see Gorny, K. 22
Martínez, B., see Fuertes, A. 286
Martinez, B., see Obradors, X. 153
Martinez, B., see Puig, T. 208
Martinez, B., see Sandiumenge, F. 153, 155, 200
Martinez, G. 380
Martinez, J.C., see Bordet, P. 307
Martinez, J.C., see Renevier, H. 352
Martinez, J.L., see Cheong, S.-W. 24
Martins, G.B., see Sanjurjo, J.A. 499
Marucco, J.F., see Corbel, C. 433, 435, 436
Marucco, J.F., see Gerdanian, P. 345
Marucco, J.F., see Lanckbeen, A. 343
Marucco, J.-F. 338
Maruyama, H., see Ishibashi, S. 436, 438
Mase, A., see Ikuta, H. 149
Masegi, T., see Yamada, Y. 163
Mason, T.E. 24
Mason, T.E., see Cheong, S.-W. 24
Mason, T.O., see Klibanow, D. 92, 93, 305, 306
Mason, T.O., see Pieczulewski, C.N. 301, 302
Mason, T.O., see Shen, L. 291
Mason, T.O., see Wang, G. 297, 318

Massalski, T.B. 231
Massidda, S. 426, 427, 433, 457
Massidda, S., see Adam, G. 432
Massidda, S., see Barbiellini, B. 433, 437, 440, 442, 443
Massidda, S., see Blandin, P. 441
Massidda, S., see Chan, L.P. 443, 444
Massidda, S., see Hoffmann, L. 432, 440
Massidda, S., see Manuel, A.A. 433, 440, 457
Massidda, S., see Yu, J. 432
Massons, J., see Cabre, R. 134, 144, 153, 155
Mastromonaco, M.D. 252
Masuda, H., see Mizuno, F. 304
Masuda, K., see Takita, K. 101
Matacotta, F.C. 267
Matacotta, F.C., see Amoretti, G. 378
Matacotta, F.C., see Blazey, K.W. 388
Matacotta, F.C., see Calestani, G. 317
Matacotta, F.C., see Migliori, A. 264
Matero, R., see Valo, J. 308
Mathai, A. 14
Mathews, T. 254, 255, 338, 340–343, 345
Mathews, T., see Jacob, K.T. 273, 283
Mathieu, J.C., see Boudéne, A. 320
Mathis, J., see Goyal, A. 25
Matskevich, N.I. 323
Matskevich, N.I., see Minenkov, Yu.F. 267
Matsubara, H., see Sawa, H. 59
Matsubara, H., see Sawa, K. 285
Matsubara, T., see Oyanagi, H. 38
Matsuda, A., see Watanabe, T. 329
Matsuda, M. 396, 526
Matsuda, M., see Shimizu, T. 160
Matsuda, M., see Thurston, T.R. 24
Matsui, M. 439
Matsui, M., see Doyama, M. 444
Matsui, Y., see Akimitsu, J. 62
Matsui, Y., see Izumi, F. 101, 102, 108
Matsui, Y., see Kawashima, T. 348
Matsui, Y., see Matveev, A.T. 256
Matsui, Y., see Ramírez-Castellanos, J. 270, 355
Matsui, Y., see Sawa, H. 329
Matsuishi, K., see Chu, C.W. 433
Matsukawa, M. 194
Matsumoto, T., see Ishibashi, S. 427, 433–436, 439, 440
Matsumura, M., see Kohara, K. 378
Matsunaga, Y., see Konishi, M. 161
Matsunaga, Y., see Yasuda, H. 76
Matsuoka, H., see Doyama, M. 444
Matsuoka, H., see Matsui, M. 439
Matsuoka, S., see Sumida, M. 153, 155
Matsushita, T., see Oyanagi, H. 38
Matsushita, Y. 169, 257
Matsuura, A., see Schabel, M.C. 457
Mattheis, L.F. 9
Mattheiss, L.F. 37, 442
Matthews, D.N., see Hunter, B.A. 148, 191
Matthews, D.N., see Sun, B.N. 131
Matthias, B.T., see Fertig, W.A. 6
Mattocks, P.G., see LaGraff, J.R. 348
Matusita, K., see Komatsu, T. 335
Matveev, A.T. 256
Maurer, M. 38
Maurer, M., see Baudelet, F. 38
Maximov, E.G., see Antonov, V.N. 428
Mayotte, J.R., see Williams, R.K. 310
Mazin, I.I. 457, 458, 465, 482, 486
Mazin, I.I., see Andersen, O.K. 457, 460, 462, 465, 466, 475, 482
Mazin, I.I., see Liechtenstein, A.I. 481, 482, 484–486, 524, 528
Mazin, I.I., see Rodriguez, C.O. 457, 473
Mazo, G.N., see Mozhaev, A.P. 202
Mazza, D. 262, 272
Mazza, D., see Abbattista, F. 93, 297, 298, 303–307, 327, 328
Mazza, D., see Vallino, M. 295–297, 301, 303–306
McAdams, J.E., see Pieczulewski, C.N. 301, 302
McCallum, R.W. 89
McCallum, R.W., see Allenspach, P. 508, 510, 515, 517
McCallum, R.W., see Damento, M.A. 148
McCallum, R.W., see Fertig, W.A. 6
McCallum, R.W., see Kramer, M. 92, 101, 102, 108, 111
McCallum, R.W., see Matskevich, N.I. 323
McCallum, R.W., see Park, M. 112, 114, 305
McCallum, R.W., see Ullman, J.E. 89, 112
McCallum, R.W., see Wu, H. 104, 105, 208, 302
McCallum, R.W., see Yoo, S.I. 92, 105, 106, 303, 304
McCarron, E.M. 258, 268
McCarron III, E.M. 330
McCarron III, E.M., see Gai, P.L. 290
McCarron III, E.M., see Parise, J.B. 330
McCarron III, E.M., see Zolliker, P. 277
McCarty, K.F. 277

McDaniel, D., see Shi, F. 293
McDevitt, J.T., see Zhou, J. 161
McElfresh, M.W., see Bringley, J.F. 260, 280, 281
McFadden, G.B., see Coriell, S.R. 88
McGinn, P.J. 153
McGuire, T.R., see Chaudhari, P. 10
McGuire, T.R., see Mehran, F. 378, 380, 384, 386
McGullough, J.D. 242
McKinnon, M.W., see Hervieu, M. 39, 41
McKinnon, W.R. 344, 378
McKinnon, W.R., see Lepage, Y. 35
McKinnon, W.R., see Orlando, T.P. 10
McKinnon, W.R., see Tarascon, J.M. 39, 70, 350
McMasters, O.D., see Gschneidner Jr, K.A. 231, 243
McMullen, T. 422, 426, 434, 441
McNiff Jr, E.J., see Orlando, T.P. 10
McNiff Jr, E.J., see Tarascon, J.M. 350
McWhan, D.B., see Moncton, D.E. 6
Medvedev, J.N., see Ivanov-Emin, B.N. 240
Meen, J.K., see Geny, J. 281, 293, 294
Meen, J.K., see George, E. 265, 267–269
Meen, J.K., see Lawanier, J.P. 316
Meen, J.K., see Tsang, C. 254–256
Meen, T.H., see Shih, C.R. 537
Mehran, F. 377, 378, 380, 384, 386
Mehring, M., see Filip, C. 405
Mehring, M., see Kessler, C. 405
Mehring, M., see Kremer, R.K. 381, 518
Mehrotra, P.N., see Sastry, R.L.N. 240
Mehta, A., see Chang, E.K. 338
Mehta, A., see Rapp, R.P. 281
Meier-Hirmer, R., see Wolf, Th. 150, 152, 200, 203, 205
Meijer, G.I., see Karpinski, J. 72, 168, 169, 260
Meijer, G.I., see Schwer, H. 169
Meingast, C. 468, 486
Meingast, C., see Kraut, O. 468
Meinhold, R., see Williams, G.V.M. 407
Meisel, K., see Wrigge, F.W. 248
Melamud, A., see Wong-Ng, W. 299
Melis, A.F.J., see Mijnarends, P.E. 443
Mellander, B.-E., see Tallon, J.L. 202
Melo, M.T., see Yadava, Y.P. 159
Mendels, P., see Alloul, H. 407
Mendels, P., see Grevin, B. 156
Meng, R.L., see Chu, C.W. 4, 433
Meng, R.L., see Ho, J.C. 403
Meng, R.L., see Hor, P.H. 298, 523
Meng, R.L., see Jean, Y.C. 433, 438, 439, 443
Meng, R.L., see Sundar, C.S. 441, 443
Meng, R.L., see Wu, M.K. 5, 35, 454, 458
Menken, M.J.V., see Moolenaar, A.A. 478
Menovsky, A.A., see Albino, J. 378
Menovsky, A.A., see Mijnarends, P.E. 443
Menovsky, A.A., see Moolenaar, A.A. 478
Mercey, B., see Chen, B.-H. 260, 281
Mercey, B., see Hervieu, M. 272, 318
Mercey, B., see Raveau, B. 62, 318
Mereiter, K., see Effenberger, H. 247
Merkle, K.L., see Gao, Y. 335
Merkle, K.L., see Selvduray, G. 337
Mersmann, A. 75
Merz, M. 153, 192, 486
Merzlyakov, M., see Felner, I. 403
Mesot, J. 72, 497, 508, 510, 515–521
Mesot, J., see Allenspach, P. 409, 508, 510, 515, 517
Mesot, J., see Fauth, F. 528, 530
Mesot, J., see Furrer, A. 517, 520, 521
Mesot, J., see Guillaume, M. 299, 504, 505, 507, 508, 510, 515, 530, 531
Mesot, J., see Henggeler, W. 531
Mesot, J., see Roessli, B. 515
Mesot, J., see Staub, U. 505, 510, 516–518, 528, 530, 532
Metgert, S., see Keller-Berest, F. 331
Methfessel, M., see Mazin, I.I. 457
Methfessel, M., see Rodriguez, C.O. 473
Metz, A., see Loewenhaupt, M. 528
Metz, H., see Guskos, N. 263
Metzger, R., see Torrance, J.B. 468
Meuffels, P. 299, 338, 340–344
Meuffels, P., see Lutgemeier, H. 204
Meuffels, P., see Lütgemeier, H. 520
Meuffels, P., see Pörschke, E. 338, 343, 344
Mey, S. 235
Miceli, P.F. 352
Michel, C. 31, 35, 292, 296, 304–306
Michel, C., see Beille, J. 32
Michel, C., see Bourgault, B. 52
Michel, C., see Caignaert, V. 292
Michel, C., see Domenges, B. 304, 305
Michel, C., see Domengès, B. 47, 48, 190
Michel, C., see Er-Rakho, L. 289–291
Michel, C., see Goutenoire, F. 54
Michel, C., see Hervieu, M. 46, 47, 54, 62, 292
Michel, C., see Huvé, M. 54, 56
Michel, C., see Maignan, A. 318

Michel, C., see Martin, C. 53, 56
Michel, C., see Nguyen, N. 34, 286, 289–291
Michel, C., see Raveau, B. 32, 38, 42, 43, 46, 47, 53, 59, 62, 318
Michel, C., see Retoux, R. 50
Michel, C., see Rouillon, T. 51, 52
Michiyama, M., see Tachibana, M. 170
Miehe, G., see Paulus, E.F. 263
Mighell, A.D., see Huang, Q. 352, 353
Mighell, A.D., see Karen, P. 318, 319, 353
Mighell, A.D., see Natali Sora, I. 353
Migliori, A. 264
Migliori, A., see Calestani, G. 317
Migliori, A., see Dimesso, L. 166, 189
Migliori, A., see Lei, M. 469, 472
Migliori, A., see Matacotta, F.C. 267
Mihalisin, T., see Skanthakumar, S. 524
Mihaly, L., see Mandrus, D. 13
Miheev, V.A., see Pechoniy, A.P. 378
Mijnarends, P.E. 419, 426, 443
Mijnarends, P.E., see Bansil, A. 427–430, 432
Mijnarends, P.E., see Pankaluoto, R. 432
Mijnarends, P.E., see Smedskjaer, L.C. 429
Mika, K., see Hauck, J. 201, 238, 241, 242, 320, 346
Mikhailin, A.V., see Ilyasov, A.Z. 438, 439
Mikhalenkov, V.S. 438
Mikheev, A.N., see Belyaev, V.N. 438, 439
Mikheeva, M.N., see Zakharov, A.A. 458
Mikirticheva, G.A. 324, 325
Mikirticheva, G.A., see Shitova, V.I. 89
Mikolaichuk, A.G., see Grebenyuk, V.D. 245
Mila, F., see Cieplak, M.Z. 400, 403
Milani, E., see Balestrino, G. 169
Milat, O. 255, 260
Milat, O., see Krekels, T. 318, 355
Miller, J.H. 14
Millet, P. 326
Millo, O., see Felner, I. 6
Mimura, T. 207
Minakov, A., see Felner, I. 403
Minami, A., see Maeno, Y. 350
Minami, T., see Nakata, H. 261
Minamigawa, S., see Kogachi, M. 177
Minenkov, Yu.F. 267
Mingmei, W. 264
Minguzzi, M., see Daturi, M. 285
Minichelli, D., see Longo, V. 252
Miraglia, S., see Santoro, A. 37
Miravitlles, C., see Fuertes, A. 286
Mirmelstein, A., see Genoud, J.-Y. 262, 263
Mironov, A.V., see Fomichev, D.V. 101
Mirza, K.A., see Loram, J.W. 20, 203
Mishra, S.K., see Pathak, L.C. 153
Misra, D.S., see Boothroyd, A.T. 502
Mitchell, A.W., see Haskel, D. 290
Mitchell, A.W., see Vaughey, J.T. 355
Mitchell, J.F., see Shimakawa, Y. 259
Mitin, A.V., see Alekseevskii, N.E. 378, 386
Mitin, A.V., see Kochelaev, B.I. 385, 386
Mitros, C., see Guskos, N. 263
Mitros, C., see Psycharis, V. 209, 334
Mitzi, D.B., see Chan, L.P. 443, 444
Mitzi, D.B., see Chen, B.-H. 260, 281
Mitzi, D.B., see Newsam, J.M. 327
Miura, S., see Wen, J.G. 159
Miyairi, H., see Kohayashi, S. 149
Miyajima, M., see Nagaya, S. 212
Miyake, K., see Kambara, M. 136, 152, 166
Miyake, K., see Watanabe, Y. 166
Miyamoto, M., see Takano, M. 260
Miyashita, S., see Nishimura, Y. 94, 112, 199
Miyatake, T. 330
Miyatake, T., see Sakurai, T. 327
Miyatake, T., see Yamaguchi, K. 169
Miyauchi, K., see Hiratani, M. 285, 350
Miyazaki, Y. 62, 260, 316, 318
Miyazaki, Y., see Akimitsu, J. 62
Mizoguchi, T., see Kanoda, K. 378
Mizokawa, T., see Fujimori, A. 458
Mizukoshi, T., see Matsukawa, M. 194
Mizukoshi, T., see Yao, X. 136, 151, 165, 172, 199
Mizuno, F. 304
Mizuno, M., see Kaise, M. 409, 410
Mizusaki, J. 299
Mizutani, U., see Mizuno, F. 304
Mizutani, U., see Takagi, A. 163
Mocala, K., see Parks, M.E. 345
Mochiku, T., see Ding, H. 20–22
Moeckly, B.H. 159
Mohammad, A., see Boudene, A. 90
Mohammad, A., see Boudéne, A. 320
Mohan Ram, R.A., see Raychandhuri, A.K. 326
Moiseev, G., see Ilynych, N. 320, 321
Moiseev, G.K. 320, 335
Moiseev, G.K., see Sestak, J. 90
Mokhtari, M. 348
Moler, K.A. 13
Molinas, B., see Marella, M. 142
Molinski, R., see Karpinski, J. 169
Molinski, R., see Schwer, H. 169

Molnar, B., see Balogh, A.G. 433, 438, 439
Monaenkova, A.S., see Maiorova, A.F. 264, 265
Monayenkova, A.S. 321
Moncton, D.E. 6
Moncton, D.E., see Lynn, J.W. 6
Monnereau, O., see Deville, A. 405
Monod, P., see Keller-Berest, F. 331
Monod, P., see Shaltiel, D. 384, 404
Monod, P., see Strobel, P. 338
Monod, Ph. 39
Monod, Ph., see Baudelet, F. 38
Monod, Ph., see Gotor, F.J. 318
Monot, I., see Desgardin, G. 140, 212
Monot, I., see Wang, J. 319
Monthoux, P. 476
Montzka, S.A. 335
Moodenbaugh, A.R., see Lynn, K.G. 437, 438
Moodenbaugh, A.R., see Usmar, S.G. 433, 434, 436–440
Moodenbaugh, A.R., see Xu, Y. 350, 352
Moodenbaugh, A.R., see Yang, C.Y. 346
Mook, H., see Cheong, S.-W. 24
Mook, H.A., see Aeppli, G. 379
Mook, H.A., see Mason, T.E. 24
Mook, H.A., see Sinha, S.K. 6
Moolenaar, A.A. 155, 478
Morán, E., see Garrote, I. 347
Morán, E., see Rial, C. 303
Morán, E., see Señaris-Rodriguez, M.A. 307
Morawitz, H., see Kresin, B.V.Z. 422
Morawski, A. 169
Moreau, J.M. 241
Moreo, A., see Randeria, M. 23
Moret, R. 290
Morgan, D.C., see Bonn, D.A. 13
Morgan, D.C., see Hardy, W.N. 13
Morgan, P.E.D. 248
Mori, H., see Egi, T. 153, 155, 173, 189
Mori, H., see Jang, W.J. 190
Mori, H., see Kutami, H. 190
Mori, N. 154
Mori, N., see Arai, J. 401
Môri, N., see Laffez, P. 264–266
Môri, N., see Uehara, M. 9
Môri, N., see Wu, X.-J. 259
Mori, T., see Aswal, D.K. 94, 153, 177
Morii, Y., see Kikuchi, M. 272
Morii, Y., see Miyazaki, Y. 62, 260, 316, 318
Morimoto, A. 378
Morimoto, A., see Moto, A. 410
Morishita, T., see Tanaka, N. 160
Morishita, T., see Wang, F. 161
Morishita, T., see Zama, H. 160
Morita, H., see Noto, K. 326
Moriwaki, Y., see Tatsuki, T. 348
Morosin, B. 348
Morosin, B., see Chaillout, C. 277, 381
Morosin, B., see Jorgensen, J.D. 33
Morris, D.E. 308, 327, 330
Morris, D.E., see Chandrachood, M.R. 90, 91, 280, 308, 319
Morris, D.E., see Singh, K.K. 204
Morris, G.D., see Bonn, D.A. 13
Morrison, J.C. 495
Morss, L., see Veal, B.W. 39
Morton, J.R., see McKinnon, W.R. 378
Mosca, R., see Geremia, S. 354
Moschalkov, V.V., see Kovacik, V. 194
Moser, P. 433, 435
Moshkin, S., see Yakhou, F. 263
Mosley, W.D. 444
Moss, S.C., see Xiong, X. 277
Moto, A. 410
Moto, A., see Morimoto, A. 378
Moudden, A.H., see Matsuda, M. 396, 526
Moudden, H., see Revcolevschi, A. 169
Mouhtari, E., see Liolios, A.K. 433, 440
Moulton, W.G., see Gorny, K. 22
Movshovich, R. 15
Mozhaev, A.P. 202
Mudretsova, S.N., see Maiorova, A.F. 264, 265
Mueller, F.M. 458
Mueller, F.M., see Fowler, C.M. 458
Mueller, F.M., see Zhu, Y.T. 297
Mukai, H., see Hasegawa, K. 159
Mukherjee, A. 409, 520
Mukherjee, A., see Boothroyd, A.T. 520, 521
Muller, D. 134
Muller, G. 139
Müller, H.-K., see Ruck, K. 348
Muller, J., see Bordet, P. 307
Muller, J., see Genoud, J.-Y. 262, 263
Muller, J., see Graf, T. 203, 265, 297, 299, 308, 310
Müller, K.A., see Bednorz, G. 454
Müller, K.A., see Bednorz, J.G. 2, 4, 31, 69, 303, 410
Müller, K.A., see Blazey, K.W. 388
Müller, K.A., see Kremer, R.K. 381, 518
Müller, K.A., see Sigmund, E. 380
Müller, R., see Staub, U. 505

Müller-Buschbaum, H. 235, 241, 250, 251, 276
Müller-Buschbaum, H., see Grande, B. 276
Müller-Buschbaum, H., see Gutau, W. 263
Müller-Buschbaum, H., see Kipka, R. 263
Müller-Buschbaum, H., see Paletta, E. 252
Müller-Buschbaum, H., see Teske, C.L. 254, 255, 257, 259, 263
Müller-Buschbaum, H.K. 33
Muller-Vogt, G., see Erb, A. 147, 201–203
Müller-Vogt, G., see Erb, A. 89
Müller-Vogt, G., see Kraut, O. 468
Müller-Vogt, G., see Meingast, C. 468
Müller-Vogt, G., see Nücker, N. 517
Müller-Buschbaum, H., see Freund, H.-R. 275
Müller-Buschbaum, H., see Schulze, A.-R. 250
Murakami, M. 72, 93, 104, 142, 204–206
Murakami, M., see Chikumoto, N. 189, 200, 208
Murakami, M., see Higuchi, T. 205
Murakami, M., see Koblischka, M.R. 72
Murakami, M., see Sakai, N. 93
Murakami, M., see Yamaguchi, K. 182
Murakami, M., see Yoo, S.I. 205
Murakami, T., see Noto, K. 326
Murakami, T., see Shirane, G. 379
Murakami, T., see Yamada, K. 390
Murani, A.P. 539
Murani, A.P., see Boothroyd, A.T. 520, 521
Murata, K., see Kambara, M. 136, 152, 166
Murata, K., see Watanabe, Y. 166
Murato, K., see Oyanagi, H. 38
Muroi, M. 156, 519, 520
Murphy, D.N., see Cava, R.J. 35
Murphy, D.W. 331
Murphy, D.W., see James, A.C.W.P. 276
Murphy, D.W., see Rosseinsky, M.J. 9
Murphy, D.W., see Santoro, A. 37
Murphy, D.W., see Siegrist, T. 268, 350
Murphy, D.W., see Sunshine, S.A. 355
Murray, B.G., see Raven, M.S. 319
Murray, B.T., see Coriell, S.R. 88
Murugakoothan, P., see Jayavel, R. 148
Murugakoothan, P., see Rao, C.R.V. 152
Murugaraj, P. 147
Murugaraj, P., see Maier, J. 340
Mussalitin, A.M., see Sedov, V.L. 433
Mutka, H., see Allenspach, P. 508, 510, 515, 517
Mutka, H., see Loewenhaupt, M. 528
Mutka, H., see Mesot, J. 497, 508, 510, 515–521
Mutka, H., see Staub, U. 505, 510, 516–518, 528
Muto, Y., see Kajitani, T. 285
Muto, Y., see Nakajima, S. 53
Muto, Y., see Noto, K. 326
Mutsaers, C.A.H.A., see De Leeuw, D.M. 250, 253, 288–292, 297, 316, 318, 331
Muzichka, Y.U. 502
Myasnikova, E.A., see Shamrai, V.F. 297
Mydosh, J.A., see Albino, J. 378, 410
Myers, D.L., see Wahlbeck, P.G. 315

Naeven, R., see Meuffels, P. 299, 338, 340–344
Nafidi, A., see Zelenay, I. 209
Nagano, M., see Isawa, K. 279
Nagano, M., see Karppinen, M. 281
Nagaosa, N. 23
Nagarajan, R. 318
Nagarajan, R., see Ganguli, A.K. 53
Nagarajan, T. 441
Nagashima, K. 205
Nagashio, K. 114, 136, 196, 212
Nagata, T., see Uehara, M. 9
Nagaya, S. 212
Nagoshi, M., see Tokiwa, A. 51
Naidu, S.V., see Wang, S.J. 433, 435, 438, 439
Nakada, I. 139
Nakada, I., see Kohara, K. 378
Nakada, I., see Sato, S. 296
Nakagawa, Z., see Kutami, H. 208, 209
Nakahara, S., see Jin, S. 142
Nakahigashi, K., see Kogachi, M. 177
Nakajima, S. 53
Nakamura, F. 405
Nakamura, M. 94–96, 98, 105, 133, 177, 187–190, 198, 200, 206, 207
Nakamura, M., see Hirayama, T. 189
Nakamura, M., see Kambara, M. 98, 101, 166
Nakamura, M., see Krauns, Ch. 196
Nakamura, M., see Kutami, H. 190
Nakamura, M., see Tagami, M. 161, 182, 185
Nakamura, M., see Yamada, Y. 123, 132, 133, 180
Nakamura, T., see Liang, R. 338
Nakamura, Y. 134, 149, 153
Nakamura, Y., see Endo, A. 134, 135
Nakamura, Y., see Furuya, K. 149
Nakamura, Y., see Izumi, T. 154
Nakamura, Y., see Kimura, S. 91
Nakamura, Y., see Shimpo, R. 282, 283

Nakamura, Y., see Sumida, M. 153, 155
Nakamura, Y., see Tranquada, J.M. 24, 403, 411
Nakamura, Y., see Yao, X. 155
Nakane, K., see Oka, K. 89
Nakanishi, H., see Jean, Y.C. 433, 438–440, 443
Nakanishi, S., see Kogachi, M. 177
Nakao, K., see Pradhan, A.K. 206
Nakata, H. 261
Nakata, H., see Akimitsu, J. 62
Nakata, H., see Uehara, M. 261
Nakazawa, Y. 300
Nambissan, P.M.G., see De, U.Y. 439, 444
Nambissan, P.M.G., see Mandal, P. 433, 439
Namikawa, Y. 123, 127–129, 133, 135–137, 151, 172, 177–180, 198
Namikawa, Y., see Yao, X. 136, 151, 165, 172, 199
Nandhini, K., see Nagarajan, T. 441
Nandor, V.A., see Gorny, K. 22
Nanjun, K.S., see Ganguli, A.K. 53
Narahara, Y., see Nakamura, F. 405
Nardin, G., see Geremia, S. 354
Narlikar, A.V., see Agarwal, S.K. 69, 70
Narozhnyi, V.N. 155, 486
Narwankar, P.K., see Morris, D.E. 327, 330
Natali Sora, I. 353
Natali Sora, I., see Karen, P. 353
Naumenko, I.G., see Emelchenko, G.A. 108, 150, 165, 174
Naumenko, I.G., see Indenbom, M.V. 194
Naumov, S., see Fischer, K. 91, 114, 150, 199
Navarro, J.M., see Fuertes, A. 286
Navrotskiy, A., see Lamberti, V.E. 155
Navrotsky, A. 320
Navrotsky, A., see Lamberti, V.E. 90, 323
Navrotsky, A., see Parks, M.E. 345
Navrotsky, A., see Rapp, R.P. 281
Navrotsky, A., see Rodriguez, M.A. 350
Navrotsky, A., see Takayama-Muromachi, E. 274
Navrotsky, A., see Zhou, Z. 89, 307, 308, 321, 323
Nazzal, A.I., see Huang, T.C. 290
Nazzal, A.I., see Tokura, Y. 291
Neiser, R.A., see Gudmundsson, B. 319
Nekvasil, V. 504, 524
Nekvasil, V., see Hilscher, G. 510, 524
Nekvasil, V., see Jandl, S. 499, 502–504, 533
Nekvasil, V., see Martin, A.A. 499
Nekvasil, V., see Muzichka, Y.U. 502
Nekvasil, V., see Strach, T. 499, 503, 504
Nelson, D.R., see Crabtree, G.W. 12
Nemetschek, R., see Stadloper, B. 11, 13
Nemoshkalenko, V.V., see Antonov, V.N. 428
Nenkov, K.A., see Narozhnyi, V.N. 155
Nessler, W., see Welp, U. 468
Nestler, B., see Seeßelberg, M. 76
Nestler, B., see Steinbach, I. 76
Neukirch, V. 326
Neumann, M., see Kissick, J.L. 348
Neumeier, J.J. 16, 17, 527
Neumeier, J.J., see Deveraux, T.P. 13
Neumeier, J.J., see Maple, M.B. 5, 6, 10, 156
Neumeier, J.J., see Markert, J.T. 5
Neuschütz, D., see Boudéne, A. 320
Neuschutz, D., see Mey, S. 235
Neuschütz, D., see Zimmermann, E. 245
Nevriva, M. 114, 147, 153, 194
Nevriva, M., see Muzichka, Y.U. 502
Nevřiva, M., see Šesták, J. 324
Newcomer, P.P., see Morosin, B. 348
Newman, D.J. 494, 498, 499
Newman, D.J., see Bradbury, M.I. 498
Newsam, J.M. 327
Ng, B., see Newman, D.J. 498, 499
Nguyen, N. 34, 286, 289–292
Nguyen, N., see Caignaert, V. 286, 292
Nguyen, N., see Capponi, J.J. 35
Nguyen, N., see Domenges, B. 304, 305
Niarchos, D., see Liolios, A.K. 433, 436, 438, 439
Niarchos, D., see Psycharis, V. 334
Nichols, D.H. 510
Nick, B., see Heinau, M. 268
Nickel, J.H., see Morris, D.E. 308, 327, 330
Nicolas, M., see Burger, J.P. 346
Niedarmeyer, C., see Lütgemeier, H. 520
Niedermayer, C. 347
Niedermayer, C., see Glückler, H. 347
Niedermayer, Ch., see Bernard, C. 6
Nielsen, B., see Ashoka-Kumar, P. 425
Nielsen, B., see Lynn, K.G. 437, 438
Nieminen, R.M. 422
Nieminen, R.M., see Barbiellini, B. 419, 427, 434
Nieminen, R.M., see Boronski, E. 419
Nieminen, R.M., see Jensen, K.O. 426–428, 434, 436
Nieminen, R.M., see Puska, M.J. 418, 434
Niemoeller, T., see v. Zimmermann, M. 24

Nieuwenhuys, G.J., see Albino, J. 378, 410
Nieva, G., see Maple, M.B. 156
Niggli, P. 248
Niinistö, L., see Peitola, K. 263
Niinistö, L., see Valo, J. 308
Niiori, Y., see Yamada, Y. 116, 147, 163, 164, 199
Nikiforov, V.N., see Kovacik, V. 194
Nikl, D., see Kowalewski, J. 149
Nikolaevskij, A.N., see Makarova, N.G. 90, 126
Nikolopoulos, C., see Liolios, A.K. 433, 440
Niraimathi, A.M., see Lin, C.T. 104, 114, 147, 151, 168, 175
Nishihara, C., see Kaise, M. 409, 410
Nishihara, Y., see Zhou Zhigang 441
Nishihara, Y., see Zou, Z. 5, 156, 486
Nishikawa, T., see Izumi, F. 37
Nishimura, Y. 94, 112, 199
Nishinaga, T., see Cheronov, A.A. 77, 79, 88
Nishinaga, T., see Danilewsky, A.N. 88
Nishino, M., see Takita, K. 327
Nishizaki, S., see Julian, S.R. 9
Nishizaki, S., see Maeno, Y. 9
Nissen, H.U., see Saito, K. 205
Nitta, T., see Arai, J. 401
Nizhankovskii, V.I., see Alekseevskii, N.E. 378, 386
Nizhanovskii, V.I., see Kochelaev, B.I. 385, 386
Noakes, D.R., see Bernard, C. 6
Noble, C., see Shaltiel, D. 405, 523
Nobumasa, H. 329
Noda, K., see Asaoka, H. 205, 208
Noel, H., see Deville, A. 378, 405
Noël, H., see Sanfilippo, S. 469
Nojima, T., see Maeno, Y. 350
Nölting, J., see Bormann, R. 312, 313
Nonaka, H., see Shimizu, T. 160
Norby, T. 346
Norby, T., see Fjellvåg, H. 299, 335–337
Norby, T., see Sutija, D.P. 346
Norman, M.R., see Ding, H. 20–22
Norrby, L.-J., see Åsbrink, S. 248
Norrestam, R. 275, 296
Norton, D.P. 526, 527
Norton, D.P., see Goyal, A. 25, 71, 73, 159
Noto, K. 326
Noto, K., see Matsukawa, M. 194
Noudem, J.G., see Reddy, E.S. 159
Nowicki, L.J., see Jorgensen, J.D. 191, 192, 299
Nowicki, L.J., see Smedskjaer, L.C. 433, 434, 436–439
Nowik, I., see Felner, I. 352
Nowotny, J. 312, 343
Nozaki, H., see Okai, B. 104
Nozaki, H., see Ono, A. 147
Nozar, P., see Calestani, G. 317
Nozar, P., see Matacotta, F.C. 267
Nozar, P., see Migliori, A. 264
Nozoye, H., see Kaise, M. 409, 410
Nücker, N. 517
Nucker, N., see Merz, M. 153, 192
Nücker, N., see Merz, M. 486
Numata, H., see Doyama, M. 444
Numata, H., see Matsui, M. 439
Nuñez-Regueiro, M. 4
Nygren, M., see Andersson, M. 349
Nygren, M., see Norrestam, R. 275

Obara, K., see Sawa, H. 329
Obhi, H.S., see Armstrong, A.R. 267, 272
Obradors, X. 153
Obradors, X., see Fuertes, A. 286
Obradors, X., see Puig, T. 208
Obradors, X., see Sandiumenge, F. 153, 156, 181
O'Brien, J., see Howell, R.H. 429
O'Bryan, H.M. 157, 338
O'Bryan, H.M., see Gallagher, P.K. 337
O'Bryan, H.M., see Jin, S. 307
Obst, B., see Wolf, Th. 133, 147, 149, 150, 198
Ochi, M., see Yokota, K. 335
Ochiai, S., see Osamura, K. 89
Ochiai, S., see Zhang, W. 101, 102, 261, 262
Ochiai, Y., see Nakamura, F. 405
O'Connor, B.H. 235
Oda, M., see Shirane, G. 379
Oda, Y., see Kohara, K. 378
Odier, P. 190
Odier, P., see Dembinski, D. 89, 147
Odier, P., see Gotor, F.J. 250, 318, 319
Ogawa, K., see Ishibashi, S. 433, 438
Ogawa, M., see Akimitsu, J. 62
Ogi, K., see Mori, N. 154
Ogita, N., see Nakata, H. 261
Ogura, I., see Nakada, I. 139
Oh-ishi, K., see Kajitani, T. 285
O'Hara, K.E., see Martindale, J.A. 13
Ohkubo, M., see Oota, A. 326
Ohnaka, I., see Yasuda, H. 76
Ohnishi, N., see Miyazaki, Y. 62, 318

Ohno, T., see Alloul, H. 407
Ohno, T., see Hayashi, S. 148
Ohshima, E., see Kikuchi, M. 272
Ohta, M., see Okai, B. 104
Ohta, Y. 467
Ohtsu, K., see Kanamori, Y. 183
Ohtsu, K., see Yao, X. 168
Ohtsuka, H., see Wang, F. 161
Oikawa, K., see Kuroda, K. 180
Oishi, T., see Suzuki, R.O. 273
Oka, A. 176, 177, 192, 203, 205, 208
Oka, A., see Goodilin, E.A. 82, 93, 102, 105, 108, 111, 117, 138, 160–162, 175, 187, 193
Oka, K. 89, 101, 105, 106, 114, 151, 152, 154, 155, 169, 285
Oka, K., see Shimizu, T. 160
Oka, K., see Yazawa, I. 248
Oka, K., see Zhou Zhigang 441
Oka, K., see Zou, Z. 5, 156, 486
Okada, H. 281
Okada, H., see Takano, M. 260
Okada, S., see Suzuki, R.O. 273
Okai, B. 104, 292, 293
Okamoto, H. 245
Okamoto, H., see Villars, P. 231
Okamoto, Y., see Danilewsky, A.N. 88
Okano, J., see Kuroda, K. 94, 101, 155, 183
O'Keeffe, M. 248
O'Keeffe, M., see Brese, N.E. 264
O'Keeffe, M., see Morgan, P.E.D. 248
Oku, T., see Tokiwa, A. 51
Oku, Y., see Miyazaki, Y. 260, 316
Okuya, M., see Boebinger, G.S. 18, 291
Olafsen, A. 243
Olcese, G.L., see Costa, G.A. 251
Olcese, G.L., see Magnone, E. 152
Olchowik, J., see Luszczek, M. 156
Olejniczak, J., see Shengelaya, A.D. 401, 403
Olesch, T., see Kemnitz, E. 201
Oleynikov, N.N., see Goodilin, E.A. 93, 101, 102, 104, 105, 114, 153, 172
Oleynikov, N.N., see Grigorashev, D.I. 93
Oleynikov, N.N., see Gudilin, E.A. 81, 171
Oleynikov, N.N., see Sedov, V.L. 444
Olive, J.R. 196, 212
Olsen, C.G., see Howell, R.H. 429
Onderka, B., see Przybylo, W. 92
Onderka, B., see Przybyło, W. 322, 323
Ong, E.W., see Iqbal, Z. 318
Ong, E.W., see Ramakrishna, B.L. 388
Ong, N.P., see Chien, T.R. 16
Oniyama, E. 114, 297
Ono, A. 147, 260, 292, 319
Ono, K., see Suzuki, R.O. 273
Onoda, M. 397
Oota, A. 326
Opila, E.J. 278, 290, 294
Opila, R.L., see Schneemeyer, L.F. 505
Opila, R.L., see Siegrist, T. 350
Oppermann, H., see Krüger, C. 254, 268
Orbach, R., see Chakravarty, S. 377, 378
O'Reilly, A.H., see Lin, Y.P. 300
Orera, V., see Fruchart, D. 347
Orlando, T.P. 10
Orlando, T.P., see Tarascon, J.M. 350
Orlova, T.S., see Ilyasov, A.Z. 438, 439
Ortiz, C., see Tokura, Y. 291
Osabe, G. 104
Osamura, K. 89, 90, 92, 93, 98, 101, 102, 104–106, 112–114
Osamura, K., see Zhang, W. 101, 102, 251–254, 261, 262, 306, 307
Osborn, R. 508, 520–522
Osborn, R., see Allenspach, P. 508, 510, 515, 517
Osborn, R., see Amoretti, G. 508, 510, 520
Osborn, R., see Boothroyd, A.T. 502–504, 508, 510, 511, 513, 524
Osborn, R., see Goremychkin, E.A. 520, 521
Osborn, R., see Guillaume, M. 504, 505, 508, 510, 515
Osborn, R., see Mesot, J. 497, 508, 510, 515–518
Osborn, R., see Staub, U. 479, 500, 501, 504, 508, 510, 515, 524, 526, 527
Oseroff, S., see Sanjurjo, J.A. 499
Oseroff, S.B. 393, 526
Oseroff, S.B., see Rao, D. 393
Oseroff, S.B., see Rettori, C. 388, 389
Oseroff, S.B., see Simon, P. 378
Oseroff, S.B., see Vier, D.C. 378
Oseroff, S.B., see Zysler, R.D. 393, 394
Oshima, T., see Takita, K. 101, 204
Osiko, V.V., see Badalyan, A.G. 406
Os'kina, T.E. 147
Osofsky, M.S., see Kim, C.C. 156
Osofsky, M.S., see Qadri, S.B. 189
Osofsky, M.S., see Webb, A.W. 280
Osrogorsky, A., see Muller, G. 139
Oss, S., see Brusa, R.S. 437, 439
Ostapchenko, E.P. 245
O'Sullivan, E.J.M. 201

Oszlany, G., see Janossy, A. 406–408
Oszlanyi, G., see Janossy, A. 404
Otsuka, M., see Chikumoto, N. 189
Ott, H.R., see Brauner, D.A. 14
Ott, H.R., see Schilling, A. 4, 467
Ott, H.R., see Staub, U. 502
Ott, K.C., see Takigawa, M.A. 20
Ottosson, M. 319
Otzschi, K. 291, 293
Ourmasd, A. 190
Ourmazd, A. 300
Ouseph, P.J., see Huang, W.F. 440
Ousset, J.C., see Maurer, M. 38
Owen, J. 396
Owens, F.J. 378, 385
Owens, J.M., see Wang, S.J. 433, 435, 438, 439
Oyagi, I., see Idemoto, Y. 282, 283
Oyama, Y., see Matsushita, Y. 257
Oyanagi, H. 38

Paatsch, T., see Dortmann, G. 347
Pachot, S., see Kazakov, S.M. 260
Pagano, R.P., see Hill, A.J. 433, 439
Pagliuso, P.G., see Sanjurjo, J.A. 499
Paletta, E. 252
Palles, D., see Psycharis, V. 334
Palstra, T.T.M., see Rosseinsky, M.J. 9
Pamplin, B. 79
Pan, G., see Zhou, X.Y. 433, 434
Panfilov, A., see Goodilin, E.A. 108, 111
Panfilov, A.G. 192
Pankajavalli, R. 282, 283
Pankajavalli, R., see Subasri, R. 282
Pankaluoto, R. 432
Pankaluoto, R., see Bansil, A. 427, 428, 430, 432
Pankaluoto, R., see Smedskjaer, L.C. 429
Pankratz, L.B. 231, 243, 244, 246, 247, 250
Pannetier, J., see Michel, C. 305, 306
Paoletti, A., see Balestrino, G. 169
Papaconstantopoulos, D.A., see DeWeert, M.J. 460
Papadimitriou, L., see Liolios, A.K. 433, 440
Pappalardo, R., see Jørgensen, C.K. 241
Paranthaman, M., see Goyal, A. 25
Paretzkin, B., see Wong-Ng, W. 92, 93, 101, 251, 274, 275, 297, 301–304
Parilla, P., see Crommie, M.F. 469
Parise, J.B. 330
Parise, J.B., see McCarron III, E.M. 330
Parise, J.B., see Zolliker, P. 277
Park, C., see Goyal, A. 25
Park, C.H., see Loeser, A.G. 20
Park, C.H., see Shen, Z.-X. 13
Park, C.-H., see Schabel, M.C. 457
Park, Key Taeck, see Massidda, S. 457
Park, M. 112, 114, 305
Park, S.I., see Tu, K.N. 201
Park, Y.S., see Zhu, Y.T. 297
Parker, M., see Janes, R. 379
Parker, V.B. 246, 247
Parkin, S.S.P., see Beyers, R. 516, 518
Parks, M.E. 345
Parks, T.C., see Bevan, D.J.M. 241, 242
Partin, D.E., see Morgan, P.E.D. 248
Pascard, H., see Corbel, C. 433, 435, 436
Pashchenko, V.A., see Stepanov, A.A. 393–395
Pashin, F.S., see Skolis, Yu.Ya. 322, 323
Passner, A., see Ando, Y. 18
Passner, A., see Boebinger, G.S. 18, 291
Pastor, A.C., see Schwartz, R.N. 404
Pastor, R.C., see Schwartz, R.N. 404
Pasturel, A., see Boudéne, A. 320
Paszewin, A., see Morawski, A. 169
Paterson, M.S., see Thompson, J.G. 335
Pathak, L.C. 153
Patil, K.C., see Ramdas, S. 240
Patrakeev, M.V. 329, 338, 345
Pattison, P., see Staub, U. 505
Patwe, S.J., see Tyagi, A.K. 348
Paukov, I.E., see Amitin, E.B. 235
Paul, D.M., see Boothroyd, A.T. 502–504, 511, 513
Paul, D.M., see Loewenhaupt, M. 528
Paul, D.M., see Mukherjee, A. 520
Paul, D.P. 212
Paulikas, A.P., see Jorgensen, J.D. 191, 192, 299, 300, 471
Paulikas, A.P., see Pei, S. 296
Paulikas, A.P., see Smedskjaer, L.C. 430, 433, 434, 436–439
Paulikas, A.P., see Veal, B.W. 39
Paulius, L.M., see Maple, M.B. 5, 16, 17
Paulsen, F., see Andersen, O.K. 460, 462, 464–466, 475
Paulus, E.F. 263
Paulus, W., see Niedermayer, C. 347
Payne, D.A., see Han, P.D. 259
Payne, D.A., see LaGraff, J.R. 202, 203
Payne, D.A., see Wang, Y.Y. 259
Payne, D.A., see Zhang, H. 259
Pechoniy, A.P. 378

Peck, W.F., see Cava, R.J. 9, 34, 275, 329, 526
Peck, W.F., see Huang, Q. 355
Peck Jr, W.F., see Cava, R.J. 287, 288, 299, 301, 307, 308, 330, 517, 518
Peck Jr, W.F., see Hwang, H.Y. 20
Peck Jr, W.P., see Schneemeyer, L.F. 505
Pederson, M.R., see Perdew, J.P. 473
Pederzolli, D.R. 279
Pei, S. 296
Pei, S., see Dąbrowski, B. 277
Pei, S., see Jorgensen, J.D. 33, 299, 300, 381
Pei, S., see Lightfoot, P. 284–286, 291, 292
Peitola, K. 263
Pekker, S., see Janossy, A. 404
Pellegrin, E., see Merz, M. 153, 192, 486
Pellegrin, E., see Nücker, N. 517
Pellerin, N., see Gotor, F.J. 250, 318, 319
Pellerin, N., see Odier, P. 190
Pelloquin, D. 169
Peña, O., see Perrin, C. 348
Peng, J.L., see Anlage, S.M. 11, 13
Peng, J.L., see Sumarlin, I.W. 526, 528, 532, 533
Peng, J.L., see Wu, D.-H. 13
Pennington, C.H., see Gorny, K. 22
Perdew, J.P. 473
Pérez, F., see Fuertes, A. 286
Perkins, A. 421
Perkins, G.K., see Thomas, J.V. 149
Perlov, A.Ya., see Antonov, V.N. 428
Pernet, M., see Sanfilippo, S. 469
Perrin, C. 348
Perrin, C., see Mokhtari, M. 348
Perroux, M., see Bordet, P. 350
Perroux, M., see Radaelli, P.G. 59
Peter, M. 429, 430, 432–436
Peter, M., see Adam, G. 432
Peter, M., see Barbiellini, B. 419, 427, 433, 434, 437, 440, 442, 443
Peter, M., see Barnes, S.E. 421, 433, 439
Peter, M., see Blandin, P. 441
Peter, M., see Friedel, J. 419
Peter, M., see Hoffmann, L. 430, 432, 440
Peter, M., see Jarlborg, T. 419, 428, 434
Peter, M., see Manuel, A.A. 433, 440, 457
Peter, M., see Shaltiel, D. 384, 386, 404
Peter, M., see Shukla, A. 424, 432, 433, 435, 442
Peters, K., see Lin, C.T. 104, 114, 147, 151, 168, 169, 175
Peterson, D., see Hawsey, R. 25, 26
Peterson, D.E., see Kubat-Martin, K.A. 270, 271, 331
Peterson, D.E., see Oniyama, E. 114, 297
Peterson, D.E., see Wu, X.D. 25
Peterson, D.E., see Zhu, Y.T. 297
Peterson, E.J., see Oniyama, E. 114, 297
Peterson, E.J., see Zhu, Y.T. 297
Peterson, S.C., see Cima, M.J. 335
Petitgrand, D., see Casalta, H. 528
Petriček, S. 264, 265
Petrů, F. 242
Petrykin, V. 93, 108, 111
Petrykin, V.V. 93, 102, 111
Petzow, G., see Schulze, K. 267, 268
Pezzolla, F., see Steinbach, I. 76
Pfeiffer, B., see Brauer, G. 240
Pfundtner, G., see Maier, J. 340
Phatak, G.M., see Pujari, P.K. 439, 443, 444
Picard, C., see Gerdanian, P. 345
Pickett, W.E. 443, 456, 457, 470, 471, 473, 481
Pickett, W.E., see Allen, P.B. 458
Pickett, W.E., see Cohen, R.E. 471, 473
Pickett, W.E., see DeWeert, M.J. 460
Pickett, W.E., see Krakauer, H. 458
Pickett, W.E., see Singh, D.J. 426, 432, 442, 443
Pickett, W.E., see Von Stetten, E.C. 426, 427, 430, 433, 439
Piechota, P., see Szymczak, R. 381
Pieczulewski, C.N. 301, 302
Piel, H., see Os'kina, T.E. 147
Pilbrow, J., see Shaltiel, D. 405, 523
Pines, D. 11
Pines, D., see Monthoux, P. 476
Pique, C., see Fruchart, D. 347
Pisch, A., see Boudéne, A. 320
Plackowski, T. 302
Plakhty, V., see Yakhou, F. 263
Plakida, N.M., see Kovacevic, Z. 520
Platt, F., see Wanklyn, B.M. 147
Plefka, T. 405
Pleizier, G., see McKinnon, W.R. 344
Plesch, G., see Sausa, O. 433, 440
Plewa, J., see Hauck, J. 346
Plewa, J., see Wiesner, U. 149
Podd, A., see Mandal, P. 433, 439
Poeppel, R.B., see Gao, Y. 335
Poeppel, R.B., see Selvduray, G. 337
Poeppelmeier, K.R., see Dąbrovski, B. 355
Poeppelmeier, K.R., see Wang, G. 297, 318
Poeppelmeier, K.R., see Zhang, J.P. 355

Polak, M., see Bezakova, E. 438
Pollert, E., see Nevriva, M. 114, 147, 153, 194
Pollert, E., see Šesták, J. 324
Poltavec, V., see Petrykin, V. 93
Pooke, D.M., see Tallon, J.L. 308, 349
Poon, S.J., see Subramanian, M.A. 5
Popov, G.Y., see Gudilin, E.A. 81
Popov, G.Yu., see Goodilin, E.A. 93, 101, 102, 104, 105, 153, 172
Popova, A.A., see Maiorova, A.F. 264, 265
Popova, A.A., see Monayenkova, A.S. 321
Poppe, U., see Günther, W. 347
Porat, O. 312, 313, 338
Porath, D. 346
Porcar, L. 194
Porjesz, T., see Kajcsos, Z. 436, 438
Pörschke, E. 338, 343, 344
Pörschke, E., see Maletta, H. 515
Post, J.E., see Morris, D.E. 308
Post, M., see Hervieu, M. 39, 41
Post, M.L., see Lin, Y.P. 300
Post, M.L., see McKinnon, W.R. 344
Postnikov, A.M., see Shamrai, V.F. 297
Potel, M., see Deville, A. 378, 405
Pouch, J.J., see Hepp, A.F. 350
Pouchard, M., see Grenier, J.C. 33
Pouchard, M., see Trari, M. 279
Pouget, J.P., see Moret, R. 290
Poulakis, N., see Kaldis, E. 299
Poulakis, N., see Psycharis, V. 334
Poulsen, H.F. 192, 300
Poulsen, H.F., see Andersen, N.H. 299–301
Poulsen, H.F., see Schleger, P. 300
Pourtier, F., see Sanfilippo, S. 469
Pozzi, R., see Erb, A. 433, 445
Prabha, V., see Nagarajan, T. 441
Pradhan, A.K. 72, 205, 206
Pradhan, A.K., see Shibata, S. 155, 205
Prado, F. 345
Prado, F., see Serquis, A. 285
Prakash, S. 347
Prakash, S., see Pujari, P.K. 439, 443, 444
Prandtl, W. 240
Prasad, R. 428
Prasad, R., see Bansil, A. 427, 428, 430, 432
Prasad, R., see Dash, S. 147
Prasad, R., see Malik, S.K. 302
Prassides, K., see Lappas, A. 272
Predel, B., see Osamura, K. 89
Prejean, J.J., see Bordet, P. 307
Prejean, J.J., see Renevier, H. 352
Prellier, W., see Hervieu, M. 272, 318
Premila, M., see Gopalan, P. 433, 434, 440
Presland, M.R., see Tallon, J.L. 308, 349
Preston, K.F., see McKinnon, W.R. 378
Price, R.D., see Markert, J.T. 5
Prim, R.C., see Burton, J.A. 123
Prince, A., see Villars, P. 231
Provost, J., see Beille, J. 32
Provost, J., see Bourgault, B. 52
Provost, J., see Marinel, S. 134
Provost, J., see Michel, C. 35
Provost, J., see Raveau, B. 38
Provost, J., see Rouillon, T. 51, 52
Provost, J., see Wang, J. 319
Przybylo, W. 92
Przybyło, W. 273, 282, 283, 322, 323
Przybylski, K., see Morawski, A. 169
Przyluski, J., see Borowiec, K. 336
Psycharis, V. 209, 334
Psycharis, V., see Guskos, N. 263
Puchkov, A.V. 20
Puff, W., see Balogh, A.G. 433, 438, 439
Puig, T. 208
Pujari, P.K. 439, 441, 443, 444
Pulling, D.B., see Blackstead, H.A. 441
Punnoose, A. 379
Puska, M.J. 418, 434
Puska, M.J., see Barbiellini, B. 419, 427, 434
Puska, M.J., see Jensen, K.O. 426–428, 434, 436
Putilin, S.N. 4
Putilin, S.N., see Chmaissem, O. 264
Putilin, S.N., see Kazakov, S.M. 260
Pye, S.L., see Lindemer, T.B. 302
Pyka, N.M., see Loewenhaupt, M. 528
Pyttlik, T. 528

Qadri, S.B. 189
Qadri, S.B., see Webb, A.W. 280
Qadri, S.B., see Weishaupt, K. 153
Qi, S.R., see Lam, C.C. 433
Qi, S.R., see Li, J.Q. 440
Qi, X. 94, 158, 159
Qian, M. 350
Qian, Y.T., see Chen, L. 149
Qiang, S., see Mingmei, W. 264
Qiao, Z., see Xing, X. 323
Qu, D., see Shi, D. 134, 142
Quadri, S.B., see Webb, A.W. 280
Qvarford, M., see Zakharov, A.A. 458

Rabe, K.M., see Cava, R.J. 299, 301, 517, 518
Rabenau, A., see Murugaraj, P. 147
Rabenberg, L., see Hou, C.J. 300
Rabier, J., see Sandiumenge, F. 156, 181
Raccah, P.M., see Longo, J.M. 276
Radaelli, P.G. 59
Radaelli, P.G., see Kazakov, S.M. 260
Radousky, H. 458, 477, 478
Radousky, H.B. 70, 72, 156, 523, 524
Radousky, H.B., see Goodwin, T.J. 526
Radousky, H.B., see Howell, R.H. 429
Radousky, H.B., see Staub, U. 524
Raghavan, S. 282, 283
Raimondi, R., see Feiner, L.F. 468
Rais, A., see Boudéne, A. 320
Rais, T., see Ait-Hou, A. 248
Raistrick, I.D., see Brosha, E.L. 89, 90, 264, 265, 275, 306, 307, 310, 311
Raistrick, I.D., see Garzon, F.H. 310
Raj, P.M., see Jacob, K.T. 245, 267, 268
Rajarajan, A.K., see Huang, M.X. 409
Rajasekharan, T., see Reddy, E.S. 112
Rajeev, K.P., see Raychandhuri, A.K. 326
Rajnak, K., see Carnall, W.T. 498, 501, 509
Rajnak, K., see Morrison, J.C. 495
Rajyashree-Prya, E., see Gopalan, P. 433, 434, 440
Rakoto, H., see Millet, P. 326
Ramachandra Rao, M.S., see Marimuthu, K.N. 318
Ramakrishna, B.L. 388
Ramakrishna, B.L., see Iqbal, Z. 318
Ramakrishna, B.L., see Owens, F.J. 378, 385
Ramakrishnan, S., see Sundaresan, A. 537
Ramanujachary, K.V. 348
Ramanujachary, K.V., see Li, S. 101, 302
Ramdas, S. 240
Rameev, B. 390, 391
Rameev, B., see Kataev, V.E. 390–393
Ramirez, A.P. 279
Ramirez, A.P., see Rosseinsky, M.J. 9
Ramirez, M.L., see Beyers, R. 516, 518
Ramírez-Castellanos, J. 270, 355
Rana, R.S., see Carnall, W.T. 498, 501, 509
Randaccio, L., see Geremia, S. 354
Randeria, M. 23, 457
Randeria, M., see Ding, H. 20–22
Rangavittal, N. 305
Range, K.-J., see Steiner, C. 281
Rao, C.N.R., see Ganguli, A.K. 53
Rao, C.N.R., see Nagarajan, R. 318
Rao, C.N.R., see Ramdas, S. 240
Rao, C.N.R., see Rangavittal, N. 305
Rao, C.N.R., see Raychandhuri, A.K. 326
Rao, C.N.R., see Sastry, R.L.N. 240
Rao, C.N.R., see Umarji, A.M. 318
Rao, C.R.V. 152
Rao, C.R.V., see Jayavel, R. 148
Rao, D. 393
Rao, D., see Oseroff, S.B. 393, 526
Rao, D., see Rettori, C. 388, 389
Rao, D., see Zysler, R.D. 393, 394
Rao, G., see Zhong, Q. 286, 288
Rao, H.L., see Batlogg, B. 20
Rao, K.V., see Tyagi, S. 378
Rao, R.S., see Bansil, A. 427, 428, 430, 432
Rao, U.R.K., see Tyagi, A.K. 348
Rapp, Ö., see Andersson, M. 349
Rapp, R.P. 281
Rashkeev, S.N., see Mazin, I.I. 457, 465
Rastelli, E. 528
Ratuszna, A., see Skrzypek, D. 410
Rauer, M., see Niedermayer, C. 347
Raveau, B. 32, 38, 42, 43, 46, 47, 53, 59, 62, 318
Raveau, B., see Bourgault, B. 52
Raveau, B., see Caignaert, V. 38, 286, 292
Raveau, B., see Capponi, J.J. 35
Raveau, B., see Chen, B.-H. 260, 281
Raveau, B., see Desgardin, G. 140, 212
Raveau, B., see Domenges, B. 304, 305
Raveau, B., see Domengès, B. 37, 47, 48, 62, 318
Raveau, B., see Er-Rakho, L. 289–291
Raveau, B., see Ferey, G. 350
Raveau, B., see Goutenoire, F. 54
Raveau, B., see Hervieu, M. 39, 41, 46, 47, 54, 62, 272, 292, 318
Raveau, B., see Huvé, M. 54, 56
Raveau, B., see Maignan, A. 318
Raveau, B., see Martin, C. 53, 56
Raveau, B., see Michel, C. 31, 35, 292, 296, 304–306
Raveau, B., see Nguyen, N. 34, 286, 289–292
Raveau, B., see Retoux, R. 50
Raveau, B., see Roth, G. 37
Raveau, B., see Rouillon, T. 51, 52
Raven, M.S. 319
Ravet, M.F., see Maurer, M. 38
Ravi Sekhar, Y., see Shaltiel, D. 386

Rawn, C.J., see Roth, R.S. 254, 255, 257, 258, 267, 268, 272, 273, 289, 290, 297, 316, 324, 333
Rawn, C.J., see Siegrist, T. 255, 260
Raychandhuri, A.K. 326
Rayner, S., see Haghighi, H. 430–432, 457
Rayner, S.L., see Howell, R.H. 429, 434
Rebane, J.A. 203
Rebane, Y.A. 203
Recknagel, E., see Glückler, H. 347
Recknagel, E., see Niedermayer, C. 347
Reddy, E.S. 112, 159
Reedyk, M., see Wegerer, R. 535, 537
Regnault, L.P., see Rossat-Mignod, J. 20
Regnault, L.P., see Vettier, C. 300, 301
Reiche, P., see Uecker, R. 177
Reichelt, W., see Krüger, C. 254, 268
Reichstein, S., see Bernal, J.D. 245
Reidinger, F., see Iqbal, Z. 318
Reilly, J.J., see Johnson, J.R. 346
Reilly, J.J., see Yang, C.Y. 346
Reimers, J.N., see Lin, Y.P. 300
Reinhart, F.-K., see Scheel, H.J. 156
Reiter, G., see Emery, V.J. 382
Rekas, M., see Nowotny, J. 312, 343
Remeika, J.P., see Aeppli, G. 379
Remeika, J.P., see Cava, R.J. 35
Remeika, J.P., see Wachs, A.L. 441
Ren, Y.Y., see Chang, H. 265
Ren, Z.F., see Tsuei, C.C. 14
Renevier, H. 350, 352
Renker, B., see Roth, G. 37
Renlund, G.M., see Lay, K.W. 89
Renner, C.H. 22
Rentschlev, J.A., see Ourmasd, A. 190
Ressouche, E., see Mokhtari, M. 348
Retoux, R. 50
Retoux, R., see Caignaert, V. 292
Retoux, R., see Hervieu, M. 292
Rettori, C. 378, 388, 389
Rettori, C., see Castilho, J.H. 378
Rettori, C., see Sanjurjo, J.A. 499
Rettori, C., see Zysler, R.D. 393, 394
Revaz, B., see Erb, A. 433, 445
Revaz, B., see Genoud, J.-Y. 169
Revaz, B., see Renner, C.H. 22
Revcolevschi, A. 72, 153, 169
Revcolevschi, A., see Shaltiel, D. 384, 404
Revcolevscki, A., see Monod, Ph. 39
Revcolevski, A., see Baudelet, F. 38
Rey, M.-J. 354
Reyes, A.P., see Gorny, K. 22
Reyes, A.P., see Hammel, P.Ch. 381
Reyes, P., see Takigawa, M.A. 20
Reyes-Casga, J. 41
Reyes-Casga, J., see Krekels, T. 41
Reynolds, J.R., see Wang, S.J. 433, 435, 438, 439
Rhyne, J.J., see Cieplak, M.Z. 350
Rial, C. 303
Rian, G. 262, 323
Ribaud, M., see Monod, Ph. 39
Ribault, M., see Aubin, H. 13
Ribault, M., see Keller-Berest, F. 331
Ricci, P., see Matacotta, F.C. 267
Ricciardiello, F., see Longo, V. 252
Rice, J.P. 208
Rice, T.M. 9
Rice, T.M., see Fahrenbacher, R. 5
Rice, T.M., see Fehrenbacher, R. 440, 479, 480, 483, 484, 486, 524, 528
Richards, D.R., see Dąbrowski, B. 277
Riches, J.D., see Alarco, J.A. 326
Rieder, G., see Prandtl, W. 240
Riedinger, R., see Dreysse, H. 81
Riess, I., see Porat, O. 312, 313, 338
Rietman, E.A., see Cava, R.J. 5, 6, 35, 299, 300, 516
Righi, L., see Calestani, G. 317
Rillo, C., see Fruchart, D. 347
Riseman, T.M., see Bonn, D.A. 13
Risold, D. 256, 260, 261, 267, 268
Risold, D., see Hallstedt, B. 248–250
Ritter, C., see Roessli, B. 515
Ritter, C., see Staub, U. 508, 515, 520, 523, 526, 529, 537–540
Ritter, J.J., see Roth, R.S. 254, 255, 267, 268
Ritter, J.J., see Siegrist, T. 255, 260
Rittershaus, E., see Jørgensen, C.K. 241
Rivera, J.P., see Schmid, H. 208
Roberts, H.S. 248
Robertson, A.D. 269, 270
Robertson, A.D., see Sastry, P.V.P.S.S. 259, 260
Roche, K.P., see Beyers, R. 516, 518
Rockenbauer, A. 406
Rockenbauer, A., see Janossy, A. 404
Rodrigues, M.A., see Lamberti, V.E. 155
Rodriguez, C.O. 457, 473
Rodriguez, C.O., see Andersen, O.K. 457
Rodriguez, C.O., see Mazin, I.I. 457
Rodriguez, M.A. 317, 350
Rodriguez, M.A., see Lamberti, V.E. 90, 323

Rodríguez-Carvajal, J., see Fuertes, A. 286
Rodríguez-Carvajal, J., see García-Muñoz, J.L. 275
Roessli, B. 515, 529, 539
Roessli, B., see Guillaume, M. 299, 507
Roessli, B., see Henggeler, W. 528, 532–534
Rogacki, K., see Dąbrovski, B. 355
Rogacki, K., see Plackowski, T. 302
Rogez, J., see Boudéne, A. 320
Rohberg, K., see Claus, H. 189
Röhler, J., see Kaldis, E. 299
Rojo, J.M., see Garrote, I. 347
Romanchuk, I.T., see Grebenyuk, V.D. 245
Romanov, D.I., see Mikirticheva, G.A. 324, 325
Romanyukha, A.A. 410
Romek, M., see Dryzek, J. 437
Rommers, P.J., see De Leeuw, D.M. 250, 253, 297, 316, 318
Roos, J., see Mangelschots, I. 331
Rosengren, A., see Lapinskas, S. 300
Rosenkranz, S., see Allenspach, P. 409
Rosenkranz, S., see Staub, U. 515, 520, 523, 537–540
Rosov, N., see Goodwin, T.J. 526
Rosov, N., see Huang, Q. 352, 353
Rosov, N., see Karen, P. 353
Rosov, N., see Natali Sora, I. 353
Rossat-Mignod, J. 20
Rossat-Mignod, J., see Uimin, G. 386
Rossat-Mignod, J., see Vettier, C. 300, 301
Rosseel, K., see Trappeniers, L. 205
Rosseinsky, M.J. 9
Rossel, C., see Karpinski, J. 260
Rotella, F.J., see LaGraff, J.R. 348
Rotella, F.J., see Miceli, P.F. 352
Rotella, F.J., see Rodriguez, M.A. 317
Roth, G. 37
Roth, G., see Brugger, T. 532, 534
Roth, R., see Os'kina, T.E. 147
Roth, R.S. 89, 147, 235, 254, 255, 257, 258, 267, 268, 272, 273, 289, 290, 297, 316, 318, 324, 333
Roth, R.S., see Cava, R.J. 329
Roth, R.S., see Schneider, S.J. 241
Roth, R.S., see Siegrist, T. 255, 260, 268
Roth, R.S., see Whitler, D.J. 231
Roth, R.S., see Wong-Ng, W. 245
Roth, R.S., see Wong-Ng, W.K. 261, 262
Rothman, S.J. 201, 202
Rouillon, T. 51, 52
Routbort, J.L. 202
Routbort, J.L., see Rothman, S.J. 201, 202
Rowell, J.M. 25
Rowles, S., see Currie, D.B. 334
Roy, B.N. 74, 75, 94, 145, 146
Ruan, Y.Z., see Zhu, J.S. 444
Rubenacker, G.V., see Rubins, R.S. 388
Rubins, R.S. 388
Ruck, K. 348
Ruckenstein, A.E., see Varma, C.M. 15
Rudenko, V.S. 240
Rudnyi, E.B. 201, 235, 320, 345
Rudolph, K., see Anwand, W. 438
Ruf, T. 535
Ruf, T., see Jandl, S. 499, 502–504, 533
Ruf, T., see Martin, A.A. 192, 499
Ruf, T., see Strach, T. 499, 503, 504
Ruf, T., see Wegerer, R. 535, 537
Ruiz, X., see Cabre, R. 134, 144, 153, 155
Rullier-Albenque, F., see Corbel, C. 433, 435, 436
Rulmont, A., see Ausloos, M. 349
Rundölf, H., see Peitola, K. 263
Rupp, L.W., see Cava, R.J. 34, 49, 517, 518, 526
Rupp, L.W., see Siegrist, T. 350
Rupp Jr, L.W., see Cava, R.J. 9, 287, 288, 299, 301, 307, 308
Rupp, M., see Kirtley, J.R. 14
Rupp, M., see Tsuei, C.C. 14
Rusiecki, S., see Bordet, P. 307
Rusiecki, S., see Conder, K. 338, 340–343
Rusiecki, S., see Kaldis, E. 307
Rusiecki, S., see Karpinski, J. 89, 91, 92, 168, 307–309, 338
Rusiecki, S., see Mangelschots, I. 331
Russek, S.E., see Moeckly, B.H. 159
Rutter, J.W. 77
Ryan, R.R., see Martin, K.A.K. 276
Rykov, A. 208, 209
Rykov, A.I., see Panfilov, A.G. 192
Rykzhkov, A.I., see Aravin, L.G. 434
Rytz, D., see Aeppli, G. 379
Rytz, D., see Schwartz, R.N. 404

Saba, F. 71, 159
Saba, F., see Goodilin, E.A. 108
Sabatini, R.L., see Usmar, S.G. 433, 434, 437, 439
Sabatini, R.L., see Xu, Y. 350, 352
Sachidanandam, R. 528
Sadakata, N., see Iijima, Y. 159

Sadowski, W. 148, 155, 156
Sadowski, W., see Barbiellini, B. 433, 437, 440
Sadowski, W., see Blandin, P. 441
Sadowski, W., see Hoffmann, L. 430, 432
Sadowski, W., see Luszczek, M. 156
Sadowski, W., see Manuel, A.A. 433, 440, 457
Sadowski, W., see Peter, M. 429, 432–434
Sadowski, W., see Shaltiel, D. 384, 386, 404
Sadowski, W., see Shukla, A. 442
Saffian, B., see Goyal, A. 25
Sagar, S., see Shi, D. 134, 142
Sahni, V.C., see Gupta, S.K. 203
Sahoda, S., see Zenitani, Y. 348
Saillard, J.-Y., see Mokhtari, M. 348
Saito, A., see Yamaguchi, S. 338
Saito, K. 205
Saito, M., see Oka, K. 89
Saito, S., see Hiratani, M. 287
Saito, Y., see Zhang, Q.-Z. 338
Saitoh, S., see Hiratani, M. 285
Sajith, P.K., see Jose, R. 158
Sakagami, E., see Kohara, K. 378
Sakai, F., see Matsushita, Y. 169
Sakai, H. 160
Sakai, K., see Sata, T. 315
Sakai, N. 93
Sakai, N., see Murakami, M. 72, 93, 104, 204–206
Sakai, N., see Osabe, G. 104
Sakai, N., see Yoo, S.I. 205
Sakuma, H., see Tachibana, M. 170
Sakurai, J., see Fujiita, T. 32
Sakurai, T. 327
Salama, K. 142, 153
Salamon, M.B., see Movshovich, R. 15
Sales, B.C., see Norton, D.P. 526, 527
Sales, B.C., see Thompson, J.R. 403, 404
Salikhov, I.Kh., see Kurkin, I.N. 409
Salje, E.K.H., see Lin, C.T. 175
Salling, C.T., see Vier, D.C. 378
Saltykova, I.A. 297, 318
Salvador, P.A., see Shen, L. 291
Samoilov, P.P., see Minenkov, Yu.F. 267
Samoylenkov, S.V. 204
Samuel, I., see Kirby, P.B. 350
Sandford, D. 147, 168
Sandiumenge, F. 153, 155, 156, 181, 200
Sandiumenge, F., see Dubs, C. 161, 190
Sandiumenge, R.Y.F., see Obradors, X. 153
Sandstrom, R.L., see Mehran, F. 378
Sanfilippo, S. 469
Sanjuán, M.L. 503
Sanjurjo, J.A. 499
Sankara Sastry, V., see Bharathi, A. 433, 434, 439
Santini, P., see Amoretti, G. 508, 510, 520
Santoro, A. 37
Santoro, A., see Bordet, P. 352
Santoro, A., see Cava, R.J. 330
Santoro, A., see Chmaissem, O. 264
Santoro, A., see Huang, Q. 352, 353, 355
Santoro, A., see Karen, P. 318, 319, 353
Santoro, A., see Khasanova, N.R. 281
Santoro, A., see Marezio, M. 505, 537
Santoro, A., see Natali Sora, I. 353
Sanyal, D. 443
Sanyal, D., see De, U.Y. 439, 444
Sanz, J., see Garrote, I. 347
Sarikaya, M. 175, 189, 205
Sarikaya, M., see Qian, M. 350
Sarma, D.D., see Neukirch, V. 326
Sarrao, J.L., see Lei, M. 469, 472
Sarrao, J.L., see Movshovich, R. 15
Sasagawa, T., see Fujimori, A. 458
Sasaki, Y., see Oota, A. 326
Sashin, I.V., see Muzichka, Y.U. 502
Sastry, P.V.P.S.S. 259, 260
Sastry, P.V.P.S.S., see Pujari, P.K. 439, 443, 444
Sastry, P.V.P.S.S., see Robertson, A.D. 269, 270
Sastry, R.L.N. 240
Sata, T. 315
Šatava, J., see Petrů, F. 242
Sathyamurthy, S., see Salama, K. 153
Sato, H., see Zhang, H. 467
Sato, I., see Noto, K. 326
Sato, M., see Onoda, M. 397
Sato, M., see Tranquada, J.M. 408
Sato, M., see Wang, F. 161
Sato, S. 296
Satoh, T., see Manako, T. 355
Satterfield, C.N. 245
Sauert, F., see Barin, I. 231, 247, 248
Saul, A. 429
Sausa, O. 433, 440
Sausa, O., see Bezakova, E. 438
Sausa, O., see Kristiakova, K. 439
Saveleva, M.E., see Shamrai, V.F. 297
Savrasov, S.Yu., see Antonov, V.N. 428
Sawa, H. 59, 329
Sawa, H., see Akimitsu, J. 59, 295
Sawa, H., see Izumi, F. 295
Sawa, K. 285

Sawyer, J.O. 238, 242, 243
Sayer, M., see Shaviv, R. 324
Saykov, R.A., see Ilyasov, A.Z. 438, 439
Scalapino, D.J. 11
Scalapino, D.J., see Jorgensen, J.D. 303
Scalettar, R.T., see Randeria, M. 23
Scardi, P., see Matacotta, F.C. 267
Schabel, M.C. 457
Schaefer, H.E., see Hermes, H. 433, 434, 438
Schaeffer, H. 396
Schäfer, W., see Kiemel, R. 350
Schatzle, P. 166
Schatzle, P., see Bieger, W. 102, 105, 166
Schatzle, P., see Krabbes, G. 89, 166
Schaudy, G., see Hilscher, G. 72, 510, 524
Scheel, H.J. 69, 71, 72, 80, 90, 114, 145, 156, 157, 161, 291
Scheel, H.J., see Barbiellini, B. 433, 437
Scheel, H.J., see Elwell, D. 75, 86, 89, 121, 139, 143, 171
Scheel, H.J., see Klemenz, C. 94, 98, 133, 153, 163, 180
Scheel, H.J., see Licci, F. 89, 324, 325
Scheel, H.J., see Marti, W. 162, 177
Scheel, H.J., see Shaltiel, D. 386
Scheikowski, M., see Müller-Buschbaum, H. 251
Scheler, H., see Krüger, C. 254, 268
Scherrer, S., see Claus, J. 201, 202
Scheurell, S., see Kemnitz, E. 201
Scheven, U.M., see Morris, D.E. 308
Schilling, A. 4, 467
Schirber, J.E., see Chaillout, C. 277, 381
Schirber, J.E., see Fisk, Z. 285
Schirber, J.E., see Hammel, P.Ch. 381
Schirber, J.E., see Hundley, M.F. 277, 285
Schirber, J.E., see Jorgensen, J.D. 33
Schirber, J.E., see McCarty, K.F. 277
Schirber, J.E., see Morosin, B. 348
Schirber, J.E., see Rettori, C. 388, 389
Schirmer, O.F. 381
Schirmer, O.F., see Wübbeler, G. 381
Schitova, V.I., see Mikirticheva, G.A. 324, 325
Schlabitz, W., see Drössler, H. 540
Schleger, P. 300, 338, 340–343
Schleger, P., see Casalta, H. 190–192, 299
Schleger, P., see Lapinskas, S. 300
Schleger, P., see Poulsen, H.F. 300
Schlenkrich, F., see Herrmann, J. 6
Schlichter, C.P., see Martindale, J.A. 13
Schlueter, J.A., see Wang, H.H. 348
Schmelz, M., see Dubs, C. 161, 190
Schmenn, S., see Lutgemeier, H. 204
Schmenn, S., see Lütgemeier, H. 520
Schmid, B., see Fischer, P. 515
Schmid, H. 208
Schmid, H., see Sun, B.N. 133, 147
Schmid, R. 248
Schmid-Fetzer, R., see Boudéne, A. 320
Schmid-Fetzer, R., see Konetzki, R. 235
Schmid-Fetzer, R., see Konetzki, R.A. 273, 278, 282
Schmidbauer, W., see Assmus, W. 72, 90, 146–148, 170
Schmidt, J.C., see Schmitz, G.J. 159, 164
Schmidt, P.H., see Moncton, D.E. 6
Schmidt, W., see Loewenhaupt, M. 528
Schmitt-Rink, S., see Varma, C.M. 15
Schmitz, G.J. 159, 164
Schmitz, G.J., see Seeßelberg, M. 76, 127
Schmitz, G.J., see Steinbach, I. 76
Schmitz, G.J., see Terborg, R. 76
Schmitz, G.J., see Todt, V.R. 196, 212
Schneemayer, L.F., see Santoro, A. 37
Schneemeyer, F., see Fiory, A.T. 203
Schneemeyer, L.F. 148, 150, 505
Schneemeyer, L.F., see Cava, R.J. 34, 49, 275, 287, 288, 526
Schneemeyer, L.F., see Harshman, D.R. 433, 436
Schneemeyer, L.F., see Murphy, D.W. 331
Schneemeyer, L.F., see Siegrist, T. 350
Schneemeyer, L.F., see Stavola, M. 355
Schneemeyer, L.F., see Sunshine, S.A. 147, 168, 355
Schneemeyer, L.F., see Von Stetten, E.C. 430
Schneider, J.R., see Poulsen, H.F. 192, 300
Schneider, J.R., see Schleger, P. 300
Schneider, J.R., see v. Zimmermann, M. 24
Schneider, J.S., see Cima, M.J. 335
Schneider, S.J. 241
Schneider, S.J., see Roth, R.S. 235
Schneider, T. 466
Schöllhorn, R., see Gottschall, R. 263
Schöllhorn, R., see Günther, W. 346, 347
Schöllhorn, R., see Lütgemeier, H. 520
Schöllhorn, R., see Niedermayer, C. 347
Schöllhorn, R., see Weiss, M. 346
Schonherr, E., see Henn, R. 473
Schönherr, E., see Heyen, E.T. 535, 536
Schonherr, E., see Lin, C.T. 169
Schönherr, E., see Wegerer, R. 535, 537

Schreiner, T., see Brugger, T. 532, 534
Schrieffer, J.R., see Bardeen, J. 466
Schroder, W., see Bohm, J. 130, 144
Schrott, A.G., see Shaw, T.M. 316, 319, 336
Schubert, J., see Günther, W. 347
Schuldt, H.S., see Baenziger, N.C. 240
Schuler, T., see Dubs, C. 161, 190
Schuller, I.K., see Beno, M.A. 35, 299
Schuller, I.K., see Jorgensen, J.D. 37
Schuller, I.K., see Neumeier, J.J. 17, 527
Schuller, I.K., see Segre, C.U. 327
Schuller, I.K., see Soderholm, L. 523
Schuller, I.K., see Yang, K.Y. 297, 318
Schuller, I.K., see Zhang, K. 302, 326, 327
Schultz, S., see Oseroff, S.B. 393, 526
Schultz, S., see Rao, D. 393
Schultz, S., see Rettori, C. 388, 389
Schultz, S., see Simon, P. 378
Schultz, S., see Vier, D.C. 378
Schultz, S., see Zysler, R.D. 393, 394
Schultze-Rhonhof, E., see Barin, I. 231, 247, 248
Schulze, A.-R. 250
Schulze, K. 267, 268
Schumacher, E.E. 243
Schuppler, S., see Merz, M. 486
Schüttler, H.B., see Benedek, R. 422
Schüttler, H.-B., see Jorgensen, J.D. 303
Schwab, H., see Wolf, L. 242
Schwaen, W., see Lengeler, M. 38
Schwartz, R.N. 404
Schwarz, R.B., see Brown, S.E. 523, 526
Schwarz, R.B., see Clarke, A.P. 315
Schwarz, R.B., see Fisk, Z. 285
Schwarz, R.B., see Hundley, M.F. 285
Schwarzmann, E., see Ullmann, B. 350
Schweiss, P., see Merz, M. 486
Schweiss, P., see Nücker, N. 517
Schweizer, M., see Grande, B. 276
Schweizer, T., see Staub, U. 505
Schwer, H. 169
Schwer, H., see Böttger, G. 330
Schwer, H., see Karpinski, J. 72, 168, 169, 260
Schwer, H., see Kruger, Ch. 192, 201
Schwitzgebel, G. 343
Scott, B.A., see Bringley, J.F. 260, 280, 281, 284
Scott, B.A., see Chen, B. 281
Scott, B.A., see Chen, B.-H. 260, 281
Scott, B.A., see La Placa, S.J. 280, 281
Scott, B.A., see Wang, Y. 256, 261
Scott, J.S., see Morris, D.E. 308, 327, 330
Seaman, C.L., see Ayoub, N.Y. 285
Seaman, C.L., see Dalichaouch, Y. 17, 523
Seaman, C.L., see Maple, M.B. 5, 16, 17
Seaman, C.L., see Markert, J.T. 5
Searl, J.W. 391
Sechnoi, A.I., see Shitova, V.I. 89
Sedov, V.L. 422, 433, 438, 444
Seebacher, B., see Lengeler, M. 38
Seebelberg, M., see Steinbach, I. 76
Seehra, M.S., see Castner, T.G. 379
Seeßelberg, M. 76, 127
Segawa, S., see Kuroda, K. 94, 101, 155, 172, 183
Segre, C.U. 101, 327
Segre, C.U., see Beno, M.A. 35, 299
Segre, C.U., see Jorgensen, J.D. 37
Segre, C.U., see Soderholm, L. 523
Segre, C.U., see Zhang, K. 101, 302, 326, 327
Seibt, E.W., see Voronkova, V.I. 149
Seiji, N. 308
Sekula, S.T., see Thompson, J.R. 403, 404
Selvduray, G. 337
Selwyn, L.S., see McKinnon, W.R. 344, 378
Sen, P. 433, 439, 444
Sen, P., see Mandal, P. 433, 439
Señaris-Rodriguez, M.A. 307
Separovic, F., see Bowden, G.J. 378
Sequis, A., see Prado, F. 345
Sergent, M., see Mokhtari, M. 348
Sergent, M., see Perrin, C. 348
Series, R.W., see Hurle, D.T.J. 211
Serquis, A. 285
Sestak, J. 89, 90
Šesták, J. 324
Šesták, J., see Ilynych, N. 320, 321
Šesták, J., see Moiseev, G.K. 320, 335
Severing, A., see Drössler, H. 540
Severing, A., see Jostarndt, H.-D. 524, 525
Sferlazzo, P., see Lynn, K.G. 437, 438
Sferlazzo, P., see Usmar, S.G. 433, 438, 439
Shabatin, V.P., see Sedov, V.L. 433, 438
Shafer, M.W., see Mehran, F. 378
Shah, S.S., see Sundaresan, A. 537
Shaked, H. 177, 191, 192, 299, 344
Shaked, H., see Harrington, I. 347
Shaked, H., see Jorgensen, J.D. 177
Shaked, H., see Shimakawa, Y. 259
Shaked, H., see Tallon, J.L. 466
Shaltiel, D. 378, 384, 386, 404, 405, 523
Shaltiel, D., see Genossar, J. 378

Shaltiel, D., see Porath, D. 346
Shamoto, S. 149
Shamoto, S., see Tranquada, J.M. 408
Shamrai, V.F. 297
Shang, J.X., see Zhang, J.C. 433
Shang, P., see Yang, G. 169
Shantarovich, V.P., see Aravin, L.G. 434
Shao, L.W., see Lam, C.C. 433
Shao, L.W., see Li, J.Q. 440
Sharma, S.C., see Wang, S.J. 433, 435, 438, 439
Sharon, M., see Sundaresan, A. 537
Shaviv, R. 324
Shavkin, S.V., see Belyaev, V.N. 439
Shaw, T., see Tsuei, C.C. 14
Shaw, T.M. 175, 316, 319, 336
Shaw, T.M., see Bringley, J.F. 260, 280, 281
Shechtman, V.Sh., see Bredikhin, S.I. 201, 202
Shelton, P., see Howell, R.H. 434
Shelton, R., see Haghighi, H. 431, 432, 457
Shelton, R., see Howell, R.H. 429
Shelton, R.N., see Folkerts, T.Y. 148
Shelton, R.N., see Goodwin, T.J. 526
Shelton, R.N., see Lynn, J.W. 6
Shelton, R.N., see Mosley, W.D. 444
Shelton, R.N., see Staub, U. 524
Shen, D.X., see Teng, M.K. 433, 438, 439
Shen, L. 291
Shen, Z.X., see Angadi, M.A. 205
Shen, Z.-X. 13, 457
Shen, Z.-X., see Fujimori, A. 458
Shen, Z.-X., see Loeser, A.G. 20
Sheng, Z.Z., see Hermann, A.M. 148
Shengelaya, A.D. 401, 403
Shenoy, G.K., see Alp, E.E. 504, 510, 528
Sherwin, M.S., see Crommie, M.F. 469
Sherwood, R.C., see Jin, S. 11
Sherwood, R.C., see O'Bryan, H.M. 338
Shevchenko, A.V., see Lopato, L.M. 250, 251
Shevchenko, S.A., see Klinkova, L.A. 265
Shi, D. 134, 142, 202
Shi, D., see Gong, S. 152
Shi, F. 293
Shi, H., see Jorgensen, J.D. 300
Shi, H., see Selvduray, G. 337
Shi, H., see Veal, B.W. 39
Shi, T.S., see Krekels, T. 41
Shibata, H. 272
Shibata, H., see Watanabe, T. 329
Shibata, S. 155, 205
Shieh, J.H. 526
Shieh, J.H., see Lai, C.C. 526
Shih, C.R. 537
Shimakawa, Y. 259
Shimakawa, Y., see Manako, T. 355
Shimizu, H. 392, 393, 396, 409
Shimizu, H., see Nakamura, F. 405
Shimizu, K., see Nobumasa, H. 329
Shimizu, T. 160
Shimizu, T., see Doyama, M. 444
Shimizu, T., see Imai, T. 20
Shimizu, T., see Matsui, M. 439
Shimizu, T., see Morimoto, A. 378
Shimizu, T., see Moto, A. 410
Shimojo, Y., see Kikuchi, M. 272
Shimoyama, J., see Boebinger, G.S. 18, 291
Shimoyama, J., see Kishio, K. 338
Shimpo, R. 282, 283
Shimpo, R., see Kimura, S. 91
Shinde, S.L., see Shaw, T.M. 175
Shindo, D., see Nakajima, S. 53
Shindo, H., see Kaise, M. 409, 410
Shinmura, M., see Aswal, D.K. 94, 112, 134
Shinohara, T., see Kawabata, S. 324
Shiohara, Y. 69–72, 77, 95, 133, 139, 142, 146, 154, 159, 164, 166, 194, 195, 205, 206, 212
Shiohara, Y., see Chauhan, H.S. 120, 121
Shiohara, Y., see Egami, M. 128, 130, 138, 172
Shiohara, Y., see Endo, A. 134, 135
Shiohara, Y., see Furuya, K. 149
Shiohara, Y., see Goodilin, E.A. 82, 93–96, 101, 102, 105, 106, 108, 111, 114, 115, 117, 118, 138, 160–162, 166, 167, 175, 187, 193, 194, 208, 302, 303, 326
Shiohara, Y., see Hattori, O. 197
Shiohara, Y., see Hirayama, T. 189
Shiohara, Y., see Imagawa, Y. 134, 135, 153
Shiohara, Y., see Izumi, T. 154
Shiohara, Y., see Kakinoto, K. 93, 119, 124, 163
Shiohara, Y., see Kambara, M. 90, 93–95, 98, 101, 102, 104–106, 117, 119–121, 136, 166, 212
Shiohara, Y., see Kanamori, Y. 131, 132, 183
Shiohara, Y., see Kimura, T. 164
Shiohara, Y., see Kitamura, T. 163
Shiohara, Y., see Krauns, Ch. 91, 93–95, 98, 196
Shiohara, Y., see Kusao, T. 131, 179
Shiohara, Y., see Kutami, H. 208, 209
Shiohara, Y., see Limonov, M. 108, 192
Shiohara, Y., see Matsukawa, M. 194

Shiohara, Y., see Nagashio, K. 114, 136, 196, 212
Shiohara, Y., see Nagaya, S. 212
Shiohara, Y., see Nakamura, M. 94–96, 98, 105, 133, 177, 187–190, 198, 200, 206, 207
Shiohara, Y., see Nakamura, Y. 134, 153
Shiohara, Y., see Namikawa, Y. 123, 127–129, 133, 135–137, 151, 172, 177–180, 198
Shiohara, Y., see Oka, A. 176, 177, 192, 203, 205, 208
Shiohara, Y., see Saba, F. 71, 159
Shiohara, Y., see Sakai, H. 160
Shiohara, Y., see Sumida, M. 94, 112, 113, 153, 155
Shiohara, Y., see Tagami, M. 94, 123–125, 155, 161, 166, 183, 185, 186, 191, 194, 326
Shiohara, Y., see Watanabe, Y. 166
Shiohara, Y., see Yamada, Y. 123, 132, 133, 136, 145, 151, 164, 177, 180, 202, 410
Shiohara, Y., see Yao, X. 72, 94, 96, 136, 151, 155, 162, 164–168, 172, 183, 198, 199
Shiohara, Y., see Yasuda, H. 76
Shiohara, Y., see Yoshizumi, M. 94, 104, 105, 112, 119, 212
Shiohara, Y., see Zama, H. 160
Shirane, G. 379
Shirane, G., see Lynn, J.W. 6
Shirane, G., see Matsuda, M. 396, 526
Shirane, G., see Moncton, D.E. 6
Shirane, G., see Thurston, T.R. 24
Shirane, G., see Tranquada, J.M. 408
Shirane, G., see Yamada, K. 390
Shiryaev, S.V., see Strach, T. 499, 503, 504
Shishido, T., see Ukei, K. 258
Shitova, V.I. 89
Shono, Y., see Tsukui, S. 202
Shore, H., see Zysler, R.D. 393, 394
Short, K., see Cava, R.J. 9
Shpanchenko, V.A., see Goodilin, E.A. 93, 101, 102, 104, 105, 153, 172
Shraiman, B.I., see Frenkel, D.M. 382
Shrivastava, K.N. 378
Shter, G.E., see Fotiev, A.A. 274
Shter, G.E., see Kosmynin, A.C. 324
Shtotsky, Yu.V., see Belyaev, V.N. 438, 439
Shu Sheng, W., see Barin, I. 231, 247, 248
Shukla, A. 156, 424, 432, 433, 435, 442
Shukla, A., see Barbiellini, B. 433, 437, 440
Shukla, A., see Barnes, S.E. 433
Shukla, A., see Erb, A. 433, 445
Shukla, A., see Hoffmann, L. 430, 432, 440
Shukla, A., see Manuel, A.A. 433, 440, 457
Shukla, A., see Peter, M. 429, 432–436
Shum, V., see Morris, D.E. 327
Shvachko, Yu.N., see Romanyukha, A.A. 410
Shvanskaya, L. 153
Si, Q., see Levin, K. 15
Sichelschmidt, J. 385–388
Sichelschmidt, J., see Kochelaev, B.I. 381–384, 403
Sid, R.L., see Morris, D.E. 308, 327, 330
Sieglaff, C.L. 238
Siegle, H., see Günther, W. 347
Siegrest, T., see Cava, R.J. 526
Siegrist, T. 255, 260, 268, 350
Siegrist, T., see Cava, R.J. 35, 49, 275, 329
Siegrist, T., see Ramirez, A.P. 279
Siegrist, T., see Schneemeyer, L.F. 505
Siegrist, T., see Sunshine, S.A. 147, 168, 355
Sienkiewicz, A. 400–403
Sienkiewicz, A., see Cieplak, M.Z. 400, 403
Sievers, R.E., see Montzka, S.A. 335
Siggia, E.D., see Frenkel, D.M. 382
Sigmund, E. 380
Sigmund, E., see Hizhnyakov, V. 518
Sigmund, E., see Kremer, R.K. 381, 518
Sigrist, M., see Rice, T.M. 9
Sigrist, T., see Schneemeyer, L.F. 148, 150
Simanovsky, S.B., see Klein, M.W. 469
Simmins, J.J., see Rodriguez, M.A. 317
Simmons, C.T., see Neukirch, V. 326
Simon, A. 300
Simon, A., see Kremer, R.K. 381, 518
Simon, P. 378
Simon, R., see Niedermayer, C. 347
Singh, A.K., see Barbiellini, B. 433, 437
Singh, A.K., see Jarlborg, T. 419, 428
Singh, D., see Von Stetten, E.C. 426, 427, 430, 433, 439
Singh, D.J. 426, 432, 440, 442, 443, 470
Singh, D.J., see Berko, S. 429
Singh, D.J., see Perdew, J.P. 473
Singh, D.J., see Pickett, W.E. 443, 457
Singh, K.K. 204
Singh, K.K., see Chandrachood, M.R. 90, 91
Singh, K.K., see Janes, R. 379
Singh, N.P., see Siegrist, T. 350
Singh, R.J., see Punnoose, A. 379
Singley, E.J., see Basov, D.N. 11, 12
Sinha, A.P.B., see Chandrachood, M.R. 280, 308, 319
Sinha, A.P.B., see Morris, D.E. 327, 330

Sinha, A.P.B., see Singh, K.K. 204
Sinha, S.K. 6
Siomi, K., see Tamaru, S. 247
Skakle, J.M.S. 70, 72, 101, 102, 274–276, 286, 288, 298, 302, 304, 328, 331–334
Skanthakumar, S. 505, 524, 525, 528
Skanthakumar, S., see Li, W.-H. 526
Skanthakumar, S., see Soderholm, L. 505, 507, 520, 526, 537
Skanthakumar, S., see Staub, U. 505, 508, 510, 514, 515, 520, 523, 526, 527, 537–540
Skelton, E.F., see Kim, C.C. 156
Skelton, E.F., see Qadri, S.B. 189
Skelton, E.F., see Webb, A.W. 280
Skolis, Yu.Ya. 282, 283, 322, 323
Skotheim, T., see Yang, C.Y. 346
Skrzypek, D. 410
Sladeczek, P., see Neukirch, V. 326
Slaski, M., see Al-Mamouri, M. 348
Slaski, M., see Hodges, J.P. 272
Slaski, M., see Slater, P.R. 272
Slaski, M., see Zhang, K. 302, 326, 327
Slater, P.R. 272
Slater, P.R., see Al-Mamouri, M. 348
Slater, P.R., see Greaves, C. 270, 272, 317, 354
Slater, P.R., see Hodges, J.P. 272
Sleight, A.W. 6
Sleight, A.W., see Cox, D.E. 276
Sleight, A.W., see Subramanian, M.A. 5
Sleight, W., see Huang, J. 330
Slichter, W.P., see Burton, J.A. 123
Sluiter, M., see Ceder, G. 300, 301, 344
Smedskjaer, L.C. 429–434, 436–439, 457
Smedskjaer, L.C., see Bansil, A. 427–430, 432
Smedskjaer, L.C., see Campuzano, J.C. 430
Smedskjaer, L.C., see Pankaluoto, R. 432
Smirnov, B.I., see Ilyasov, A.Z. 438, 439
Smirnov, V.I., see Ilyasov, A.Z. 438, 439
Smith, A.J. 252
Smith, D.S., see Cazy, E. 319
Smith, J.L., see Brown, S.E. 523, 526
Smith, J.L., see Fowler, C.M. 458
Smith, J.L., see Gorny, K. 22
Smith, J.L., see Mueller, F.M. 458
Smith, M.G. 269, 293
Smith, R.G., see Searl, J.W. 391
Smith, R.I., see Skakle, J.M.S. 331
Smoorenburg, H.C.A., see De Leeuw, D.M. 250, 253, 288–290, 297, 316, 318, 331
Smyth, D.M. 338
Smyth, D.M., see Chang, E.K. 338
Smyth, F.H., see Roberts, H.S. 248
Smyth, J.F., see Vier, D.C. 378
Snyder, R.L., see Rodriguez, M.A. 317
Soderholm, L. 349, 505, 507, 508, 510, 520, 523, 524, 526, 527, 535, 537
Soderholm, L., see Alp, E.E. 504, 510, 528
Soderholm, L., see Beno, M.A. 35, 299
Soderholm, L., see Goodman, G.L. 501, 507, 510, 524
Soderholm, L., see Jorgensen, J.D. 33, 37, 381
Soderholm, L., see Loong, C.-K. 502
Soderholm, L., see Loong, C.K. 502, 504
Soderholm, L., see Skanthakumar, S. 505, 525
Soderholm, L., see Staub, U. 479, 500, 501, 504, 505, 508, 510, 514, 515, 520, 523, 524, 526, 527, 537–540
Sokolovskaya, Z.D., see Izakovich, E.N. 296
Solal, F., see Haghighi, H. 431, 432
Solal, F., see Howell, R.H. 429, 434
Solal, F.R., see Haghighi, H. 457
Sole, R., see Cabre, R. 134, 144, 153, 155
Soloshenko, A.P., see Goodilin, E.A. 104, 119, 153, 166
Somasundaram, P., see Umarji, A.M. 318
Song, H., see Cao, G. 152
Song, J., see Yang, Z. 438, 439
Song, J., see Zhu, J. 439
Song, S.N., see Wang, G. 297, 318
Soni, N.C., see Malik, S.K. 302
Sonntag, R. 300
Sood, A.K., see Bharathi, A. 433, 434, 439
Sood, A.K., see Sundar, C.S. 433, 435, 436, 438, 439
Sood, A.K., see Vasumathi, D. 433, 434, 439
Sood, D.D., see Dash, S. 147
Sorbier, J.P., see Deville, A. 405
Sorrell, C.C., see Bowden, G.J. 378
Soubeyroux, J.L., see Aride, J. 275
Soubeyroux, J.L., see Capponi, J.J. 35
Soubeyroux, J.L., see Fruchart, D. 347
Soulen, R.J., see Webb, A.W. 280
Sowa, T., see Hiratani, M. 287
Soylu, B., see Arnott, M. 91, 199
Sparpaglione, M., see Amoretti, G. 508, 510, 520
Specht, E.D., see Goyal, A. 25, 73, 159
Specht, E.D., see Lindemer, T.B. 92, 93, 98, 104, 105, 108, 199, 204, 261–266, 302
Specht, E.D., see Williams, R.K. 310
Spector, V.N., see Izakovich, E.N. 296
Spence, J.C.H., see Ourmasd, A. 190

Spence, J.C.H., see Ourmazd, A. 300
Spencer, P.J., see Mey, S. 235
Spicer, W.E., see Shen, Z.-X. 13
Squires, G.L. 500
Sreedhar, K., see Raychandhuri, A.K. 326
Sreedharan, O.M., see Azad, A.M. 282, 283
Sreedharan, O.M., see Pankajavalli, R. 282, 283
Sreedharan, O.M., see Subasri, R. 251, 282
Sridharan, V., see Nagarajan, T. 441
Srinivas, S., see Prasad, R. 428
Srinivasan, S., see Nagarajan, T. 441
Stacy, A.M., see Luce, J.L. 168
Stacy, A.M., see Sandford, D. 147, 168
Stadlober, B., see Deveraux, T.P. 13
Stadloper, B. 11, 13
Stager, C.V., see Lin, Y.P. 300
Stahulak, M.D., see Smedskjaer, L.C. 430
Staines, M.P., see Tallon, J.L. 349
Stalick, J. 304
Stalick, J.K., see Cieplak, M.Z. 350
Stalick, J.K., see Wong-Ng, W. 274, 303, 304
Stankowski, J. 378
Stankowski, J., see Hoffmann, S.K. 379
Stanley, H.E., see Aharony, A. 380
Staub, U. 479, 500–502, 504, 505, 508, 510, 514–518, 520, 522–524, 526–530, 532, 537–540
Staub, U., see Allenspach, P. 508, 510, 515, 517
Staub, U., see Fauth, F. 528, 530
Staub, U., see Furrer, A. 517
Staub, U., see Guillaume, M. 299, 504, 505, 507, 508, 510, 515, 530, 531
Staub, U., see Lovesey, S.W. 520, 523
Staub, U., see Mesot, J. 497, 508, 510, 515–519
Staub, U., see Roessli, B. 515, 529, 539
Staub, U., see Soderholm, L. 505, 507, 520, 526, 537
Stavola, M. 355
Stedman, G.E., see Newman, D.J. 499
Steeman, R.A., see De Leeuw, D.M. 297
Steger, P.L., see Gunasekaran, R.A. 334
Steiger, J., see Dortmann, G. 347
Stein, T., see Jiang, C.N. 19, 20
Stein, T.W., see Satterfield, C.N. 245
Steinbach, I. 76
Steiner, C. 281
Steiner, P., see Bucher, B. 20
Steinfink, H. 297
Steinfink, H., see Lee, J.Y. 291
Steinmetz, P., see Lenglet, M. 248
Stenin, Yu.G., see Minenkov, Yu.F. 267
Stepanov, A.A. 393–395
Stepanov, V., see Uimin, G. 386
Stephen, A., see Nagarajan, T. 441
Stern, E.A., see Haskel, D. 290
Stern, E.A., see Qian, M. 350
Stern, E.A., see Sarikaya, M. 189, 205
Sterne, F.A., see Howell, R.H. 434
Sterne, P., see Howell, R.H. 429
Sterne, P.A. 441
Sterne, P.A., see Howell, R.H. 441, 442
Sterne, P.A., see Mosley, W.D. 444
Sternlieb, B.J., see Tranquada, J.M. 24, 403, 411
Stevens, K.W.H. 496, 501
Stevens, K.W.H., see Bleaney, B. 497
Stevens, K.W.H., see Mehran, F. 377
Stewart, A.M., see Thompson, J.G. 335
Stocks, G.M., see Györffy, B.L. 422
Stormer, J., see Zhou, X.Y. 436
Störmer, J., see Zhou, X.Y. 433, 436
Storz, O., see Lutgemeier, H. 204
Storz, O., see Lütgemeier, H. 520
Stotskii, Yu.V., see Belyaev, V.N. 439
Strach, T. 499, 503, 504
Strach, T., see Henn, R. 473
Strach, T., see Jandl, S. 499, 502–504, 533
Strach, T., see Martin, A.A. 192
Strasser, T., see Hu, A.M. 200
Stratilatov, A., see Yakhou, F. 263
Straube, E. 300
Strebel, O., see Neukirch, V. 326
Street, R., see Muroi, M. 156, 519, 520
Streitz, F.H., see Xiao, G. 350
Stritzker, B., see Dortmann, G. 347
Strobel, P. 338
Strobel, P., see Bordet, P. 352
Strobel, P., see François, M. 299, 354
Strobel, P., see Holtzberg, F. 148
Stronach, C.E., see Bernard, C. 6
Strong, S., see Chakravarty, S. 465, 469
Strongin, M., see Basov, D.N. 11, 12
Stroud, D., see Ebner, C. 388
Stucki, F., see Fischer, P. 515
Stucki, F., see Guillaume, M. 504, 505, 508, 510, 515
Studer, F., see Nguyen, N. 290
Suard, E., see Chen, B.-H. 260, 281
Suard, E.Y., see Chen, B. 281
Subasri, R. 251, 282

Subbana, G.N., see Rangavittal, N. 305
Subdo, A., see Chakravarty, S. 465, 469
Subramanian, C., see Paul, D.P. 212
Subramanian, M.A. 5
Subramanian, M.A., see Cox, D.E. 276
Subramanian, M.A., see Harlow, R.L. 355
Subramanian, M.A., see McCarron, E.M. 258, 268
Sudo, S., see Isawa, K. 279
Suematsu, H., see Karppinen, M. 281
Suematsu, H., see Kawano, M. 205
Suematsu, H., see Lee, S. 169
Suenaga, M., see Johnson, J.R. 346
Suenaga, M., see Usmar, S.G. 433, 434, 437–440
Suenaga, M., see Xu, Y. 350, 352
Suenaga, M., see Yang, C.Y. 346
Suenuga, K., see Ishibashi, S. 433, 435
Suga, M., see Hiratani, M. 287
Sugawara, H., see Noto, K. 326
Sugawara, K., see Yamada, Y. 410
Sugawara, Y., see Kakimoto, K. 163
Sugawara, Y., see Kitamura, T. 164
Sugawara, Y., see Tagami, M. 161, 182, 185
Sugii, N., see Kishio, K. 5
Sugise, R., see Yazawa, I. 248
Sui, Z.T., see Steinfink, H. 297
Sujata, K., see Klibanow, D. 92, 93, 305, 306
Sukharev, P.N., see Belyaev, V.N. 438, 439
Suleimanov, N.M., see Shengelaya, A.D. 403
Sułkovski, C., see Plackowski, T. 302
Sulpice, A., see Beille, J. 32
Sulpice, A., see Ferey, G. 350
Sumarlin, I.W. 526, 528, 532, 533
Sumida, M. 94, 112, 113, 153, 155
Sumida, M., see Krauns, Ch. 91, 93–95, 98
Sumida, M., see Tagami, M. 136, 161, 166, 177, 185, 186
Sumida, M., see Yao, X. 155
Summer, R., see Kleiner, R. 14
Sun, A.G. 14, 15
Sun, A.G., see Kleiner, R. 14
Sun, A.G., see Kouznetsov, K.A. 15
Sun, B.N. 131, 133, 147
Sun, B.N., see Schmid, H. 208
Sun, D.M., see Chen, L. 149
Sun Hancheng, see Li Anli 433, 439
Sun, J.Z., see Kirtley, J.R. 14
Sun, J.Z., see Tsuei, C.C. 14
Sunagawa, I. 86
Sundar, C.S. 433, 435, 436, 438, 439, 441, 443
Sundar, C.S., see Bharathi, A. 426, 427, 433, 434, 439
Sundar, C.S., see Gopalan, P. 433, 434, 440
Sundar, C.S., see Jean, Y.C. 433, 440
Sundar, C.S., see Vasumathi, D. 433, 434, 439
Sundaresan, A. 537
Sundman, B., see Boudéne, A. 320
Sunshine, S., see Cava, R.J. 35
Sunshine, S., see Murphy, D.W. 331
Sunshine, S.A. 147, 168, 355
Sunshine, S.A., see Huang, Q. 355
Sunshine, S.A., see Santoro, A. 37
Sunshine, S.A., see Stavola, M. 355
Suryanarayanan, R., see Harlow, R.L. 355
Suryanarayanan, R., see Zelenay, I. 209
Sutija, D.P. 346
Sutton Jr, A.L., see Lindemer, T.B. 338, 341, 342
Suvasini, M.B. 422
Suvasini, M.B., see Györffy, B.L. 422
Suvegh, K., see Kajcsos, Z. 436, 438
Suziki, N., see Sakurai, T. 327
Suzuki, K., see Kishio, K. 338
Suzuki, M., see Hidaka, Y. 146
Suzuki, M., see Shirane, G. 379
Suzuki, N., see Wada, T. 93, 199, 204, 330
Suzuki, N., see Yamaguchi, K. 169
Suzuki, R.O. 254, 257, 258, 273
Suzuki, S., see Akimitsu, J. 59, 295
Suzuki, S., see Sawa, H. 59
Suzuki, S., see Sawa, K. 285
Suzuki, Y., see Doyama, M. 439
Suzuki, Y., see Ishibashi, S. 433, 436, 438, 439
Suzuki, Y., see Matsui, M. 439
Suzumura, Y. 23
Swinnea, J.S., see Lee, J.Y. 291
Swinnea, J.S., see Steinfink, H. 297
Symko, O.G., see Durny, R. 388
Syono, H., see Tokiwa, A. 51
Syono, Y., see Kajitani, T. 285, 352
Syono, Y., see Kikuchi, M. 272
Syono, Y., see Nakajima, S. 53
Szczepanka, L., see Stankowski, J. 378
Szoteck, Z., see Györffy, B.L. 422
Szotek, Z., see Temmerman, W.M. 460
Szymczak, H., see Szymczak, R. 381
Szymczak, R. 381

Tabuchi, J., see Ichihashi, T. 300
Tachibana, K., see Nakamura, Y. 149
Tachibana, M. 170

Tada, M., see Kikkawa, S. 269
Tagami, M. 94, 123–125, 136, 155, 161, 166, 177, 182, 183, 185, 186, 191, 194, 326
Tagami, M., see Kambara, M. 90, 93–95, 102, 104–106, 117, 119, 212
Tagami, M., see Krauns, Ch. 91, 93–95, 98, 196
Tagami, M., see Saba, F. 71, 159
Tagami, M., see Sumida, M. 94, 112, 113
Tagami, M., see Yamada, Y. 123, 180
Tagawa, H., see Mizusaki, J. 299
Tagirov, L.R., see Alekseevskii, N.E. 378, 386
Tagirov, L.R., see Kochelaev, B.I. 385, 386
Taibi, M., see Aride, J. 275
Taillefer, L., see Aubin, H. 13
Taimatsu, H., see Kebukawa, T. 347
Tajima, S., see Goodilin, E.A. 93, 111
Tajima, S., see Jang, W.J. 190
Tajima, S., see Limonov, M. 108, 192
Tajima, S., see Mimura, T. 207
Tajima, S., see Panfilov, A.G. 192
Tajima, S., see Rykov, A. 208, 209
Tajima, S., see Yao, X. 168
Tajima, Y., see Tsurumi, S. 204
Takaba, M., see Fujimori, A. 458
Takabatake, T. 350, 352
Takabatake, T., see Nakazawa, Y. 300
Takagi, A. 163
Takagi, A., see Wen, J.G. 159
Takagi, H. 4, 526
Takagi, H., see Batlogg, B. 20
Takagi, H., see Cava, R.J. 275
Takagi, H., see Hwang, H.Y. 20
Takagi, H., see Kishio, K. 5
Takagi, H., see Tokura, T. 276, 285
Takagi, H., see Tokura, Y. 5, 7
Takagi, T., see Pradhan, A.K. 205
Takahashi, H., see Uehara, M. 9
Takahashi, K., see Okai, B. 104
Takahashi, M., see Kajitani, T. 285
Takahashi, T., see Ding, H. 20–22
Takahashi, T., see Kanoda, K. 378
Takamuku, K., see Gu, G.D. 169
Takamura, Y., see Nagashio, K. 114, 136, 196, 212
Takanashi, K., see Hayashi, K. 177
Takano, K., see Morris, D.E. 327
Takano, M. 9, 260
Takano, M., see Azuma, M. 269
Takano, M., see Hiroi, Z. 189, 259, 260, 352
Takano, M., see Ikeda, N. 293
Takano, M., see Khasanova, N.R. 281
Takano, M., see Kobayashi, N. 256, 260, 270
Takano, M., see Okada, H. 281
Takano, M., see Shimakawa, Y. 259
Takano, M., see Takita, K. 101, 204
Takano, M., see Yamaura, K. 261
Takata, M., see Komatsu, T. 335
Takata, T., see Yamaguchi, K. 169
Takayama, E., see Izumi, F. 37
Takayama-Muromachi, E. 274, 285, 295
Takayama-Muromachi, E., see Izumi, F. 70, 71, 190, 295
Takayama-Muromachi, E., see Kawashima, T. 348
Takayama-Muromachi, E., see Matveev, A.T. 256
Takayama-Muromachi, E., see Parks, M.E. 345
Takayama-Muromachi, E., see Ramírez-Castellanos, J. 270, 355
Takayama-Muromachi, E., see Sawa, H. 59
Takayama-Muromachi, E., see Sawa, K. 285
Takeda, Y., see Azuma, M. 269
Takeda, Y., see Hiratani, M. 285
Takeda, Y., see Hiroi, Z. 259, 352
Takeda, Y., see Okada, H. 281
Takeda, Y., see Takano, M. 260
Takeda, Y., see Takita, K. 101, 204
Takei, H. 149
Takei, H., see Asaoka, H. 147–150, 205, 208
Takei, H., see Matsushita, Y. 257
Takekawa, S. 148
Takekawa, S., see Izumi, F. 101, 102, 108
Takenaka, K. 480
Takenaka, K., see Ito, T. 20
Takeya, H., see Takei, H. 149
Takigawa, M., see Hammel, P.Ch. 381
Takigawa, M.A. 20
Takita, K. 101, 111, 204, 327
Takita, K., see Akinaga, H. 111
Talantsev, E.F. 153
Talashmanova, N.V., see Dlyachkova, T.V. 319
Tallon, J.L. 20, 202–204, 308, 349, 466
Tallon, J.L., see Bernard, C. 6
Tallon, J.L., see Williams, G.V.M. 407
Tamaru, S. 247
Tamasaku, K., see Boebinger, G.S. 18, 291
Tamasaku, K., see Fujimori, A. 458
Tamasaku, K., see Takenaka, K. 480
Tamura, M., see Asaoka, H. 147–150
Tamura, T., see Tatsuki, T. 348
Tan, Z. 295, 333

Tanabe, K., see Li, Y. 210
Tanabe, K., see Tatsuki, T. 348
Tanabe, N., see Iijima, Y. 159
Tanaka, I. 152
Tanaka, I., see Thurston, T.R. 24
Tanaka, M., see Nobumasa, H. 329
Tanaka, M., see Tsuda, K. 329
Tanaka, N. 160
Tanaka, O., see Komatsu, T. 335
Tanaka, S. 152, 468
Tanaka, S., see Gu, G.D. 169
Tanaka, S., see Ichinose, A. 329
Tanaka, S., see Kishio, K. 5
Tanaka, S., see Kitamura, T. 163
Tanaka, S., see Miyatake, T. 330
Tanaka, S., see Mizuno, F. 304
Tanaka, S., see Nagaya, S. 212
Tanaka, S., see Sakai, H. 160
Tanaka, S., see Sakurai, T. 327
Tanaka, S., see Takagi, H. 4
Tanaka, S., see Ting, W. 161, 190
Tanaka, S., see Wada, T. 295, 329, 330
Tanaka, S., see Yamada, Y. 116, 132, 133, 147, 199
Tanaka, S., see Yoo, S.I. 205
Tang, C., see Li, Y. 441
Tang, C.Q. 433, 434
Tang, C.Q., see Zhang, D.M. 436, 438, 443
Tang, M., see Shi, D. 202
Tang, T.B. 201
Tang, X.M., see Wan, R.X. 73, 139
Tang, X.X., see Manthiram, A. 98, 112
Tang, X.-X., see Lightfoot, P. 284–286, 291, 292
Tang, Z. 443
Tang, Z., see Wang, S.J. 443
Tanigawa, S. 430
Taniguchi, S., see Kitamura, T. 164
Tarascon, J.M. 39, 70, 350
Tarascon, J.M., see Hervieu, M. 39, 41
Tarascon, J.M., see Lepage, Y. 35
Tarascon, J.M., see Miceli, P.F. 352
Tarascon, J.M., see Orlando, T.P. 10
Tarka, M., see Reddy, E.S. 159
Tarka, M., see Schmitz, G.J. 159
Tarte, P., see Ausloos, M. 349
Tashiro, S., see Sata, T. 315
Tassi, A., see Rastelli, E. 528
Tatarchenko, V.A. 148
Tatsuki, T. 348
Tatsumi, Y., see Kebukawa, T. 347
Taya, N., see Kikkawa, S. 269
Taylor, A., see Mesot, J. 497, 508, 510, 515–518
Taylor, A.D., see Allenspach, P. 508, 510, 515, 517
Taylor, A.D., see Goremychkin, E.A. 520, 521
Taylor, A.D., see Guillaume, M. 504, 505, 508, 510, 515
Taylor, A.D., see Staub, U. 510, 516–518, 528
Taylor, G.M., see Lindemer, T.B. 92, 93, 108, 302
Taylor, J.A.T., see LaGraff, J.R. 348
Taylor, K.N.R. 496, 497
Taylor, K.N.R., see Sun, B.N. 131
Taylor, P.C., see Durny, R. 388
Taylor, R.H. 377, 396
Taylor, T.J., see Iqbal, Z. 318
Tebano, A., see Balestrino, G. 169
Teitel'baum, G.B. 390
Teitelbaum, G.B., see Kataev, V.E. 379, 390, 391
Teitelbaum, G.B., see Rameev, B. 390, 391
Telez, D.A.L., see Yadava, Y.P. 159
Tellez, D.A.L. 94
Tellgren, R., see Peitola, K. 263
Temkin, D.E. 80
Temmerman, W., see Györffy, B.L. 422
Temmerman, W.M. 460
Temmerman, W.M., see Guo, G.Y. 524, 528
Temmerman, W.M., see Györffy, B.L. 422
Temmerman, W.M., see Suvasini, M.B. 422
Tempelton, A., see Skakle, J.M.S. 331
Teng, M.K. 433, 438, 439
Tent, B., see Shi, D. 134
Teplov, M.A., see Kurkin, I.N. 409
Terabe, K., see Yamaguchi, S. 338
Terada, N., see Oyanagi, H. 38
Terada, N., see Yazawa, I. 248
Terakura, K., see Nakazawa, Y. 300
Terasaki, I., see Mimura, T. 207
Terborg, R. 76
Teske, C., see Müller-Buschbaum, H. 241
Teske, C.L. 254, 255, 257, 259, 263
Teske, K., see Anwand, W. 438
Tétot, R. 343
Thalmeier, P. 528, 536
Thalmeier, P., see Henggeler, W. 520, 528, 533
Thamizhavel, A., see Jayavel, R. 148
Thamizhavel, A., see Paul, D.P. 212
Thiel, B., see Qian, M. 350
Thiel, J.P., see Vaughey, J.T. 355

Thiele, E. 305
Tholence, J.L., see Beille, J. 32
Tholence, J.L., see Bordet, P. 350
Tholence, J.L., see Capponi, J.J. 35
Tholence, J.L., see Domengès, B. 37
Tholence, J.L., see Radaelli, P.G. 59
Tholence, J.-L., see Nuñez-Regueiro, M. 4
Thomas, J.V. 149
Thomas, K.A., see Calestani, G. 317
Thomas, K.A., see Matacotta, F.C. 267
Thombinson, W., see Lynn, J.W. 6
Thomlinson, W., see Moncton, D.E. 6
Thompson, A.R., see Wang, H.H. 348
Thompson, J.D., see Brown, S.E. 523, 526
Thompson, J.D., see Cheong, S.W. 273
Thompson, J.D., see Clarke, A.P. 315
Thompson, J.D., see Fisk, Z. 285
Thompson, J.D., see Hammel, P.Ch. 381
Thompson, J.D., see Hundley, M.F. 277, 285
Thompson, J.D., see Lei, M. 469, 472
Thompson, J.D., see Oseroff, S.B. 393, 526
Thompson, J.D., see Rao, D. 393
Thompson, J.D., see Takigawa, M.A. 20
Thompson, J.D., see Vier, D.C. 378
Thompson, J.G. 264, 266, 335
Thompson, J.R. 403, 404
Thompson, P., see Johnson, J.R. 346
Thomsen, C. 192, 326
Thomsen, C., see Dufour, P. 502, 503
Thomsen, C., see Günther, W. 347
Thomsen, C., see Wegerer, R. 535, 537
Thurston, T.R. 24
Thurston, T.R., see Matsuda, M. 396, 526
Thurston, T.R., see Yamada, K. 390
Tiefel, T.H., see Jin, S. 11, 142, 307
Tigges, A., see Schmitz, G.J. 159, 164
Tiller, W.A. 73, 81, 85, 86, 126, 138, 144, 181
Timusk, T., see Basov, D.N. 20
Timusk, T., see Homes, C.C. 20
Timusk, T., see Puchkov, A.V. 20
Ting, W. 161, 190
Ting, W., see Pradhan, A.K. 205
Tissot, P., see Licci, F. 89, 324, 325
Tiwari, P., see Wu, X.D. 25
Tobin, J., see Howell, R.H. 429
Todt, V.R. 196, 212
Toepfer, J., see Trari, M. 279
Tofield, B.C., see Jacobson, A.J. 253
Togano, K., see Doyama, M. 439
Togano, K., see Ishibashi, S. 439
Tohyama, T., see Ohta, Y. 467
Tokiwa, A. 51
Tokue, H., see Idemoto, Y. 294
Tokumoto, M., see Hayashi, K. 177
Tokumoto, M., see Oyanagi, H. 38
Tokura, T. 276, 285
Tokura, Y. 5, 7, 291
Tokura, Y., see Huang, T.C. 290
Tokura, Y., see Takagi, H. 526
Tolentino, H., see Baudelet, F. 38
Tolentino, H., see Maurer, M. 38
Tolentino, H., see Renevier, H. 352
Tomasi, A., see Matacotta, F.C. 267
Tomimoto, K., see Akimitsu, J. 62
Tomimoto, K., see Mimura, T. 207
Tomiyoshi, S., see Kajitani, T. 285
Torardi, C.C., see Subramanian, M.A. 5
Torikachvili, M.S., see Dalichaouch, Y. 523
Torikachvili, M.S., see Maple, M.B. 5, 6, 10
Torkar, K. 263
Tornau, E.E., see Lapinskas, S. 300
Torng, C.J., see Wu, M.K. 5, 35, 454, 458
Torrance, J.B. 468
Torrance, J.B., see Huang, T.C. 290
Torrance, J.B., see Tokura, Y. 291
Torriani, I., see Sanjurjo, J.A. 499
Torsti, T., see Barbiellini, B. 419, 427, 434
Toulemonde, P., see Bordet, P. 350
Toulins, G., see Veal, B.W. 39
Tourillon, G., see Baudelet, F. 38
Tourillon, G., see Maurer, M. 38
Tourillon, G., see Renevier, H. 352
Tournier, R., see Beille, J. 32
Tournier, R., see Capponi, J.J. 35
Tournier, R., see Domengès, B. 37
Tournier, R., see Ferey, G. 350
Tournier, R., see Michel, C. 35
Tovar, M., see Oseroff, S.B. 393, 526
Tovar, M., see Rao, D. 393
Tovar, M., see Rettori, C. 388, 389
Tovar, M., see Zysler, R.D. 393, 394
Town, S.L., see Hunter, B.A. 148, 191
Townsend, J., see Wu, X.D. 25
Trail, S.S., see Bringley, J.F. 260, 280, 281, 284
Tran Qui, D., see Fruchart, D. 347
Tranquada, J., see Goldman, A.I. 515
Tranquada, J.M. 24, 403, 408, 411
Tranquada, J.M., see v. Zimmermann, M. 24
Trappeniers, L. 205
Trari, M. 279
Trashchakov, V.Yu., see Arutyunov, N.Yu. 439
Traverse, J.-P., see Foëx, M. 235, 241, 242

Treror, P., see Cava, R.J. 517, 518
Tretyakov, Y., see Petrykin, V. 93, 108, 111
Tretyakov, Y.D. 69, 73, 94, 101, 140, 141, 153, 171, 201, 212
Tretyakov, Y.D., see Goodilin, E.A. 93, 114
Tretyakov, Y.D., see Gudilin, E.A. 81
Tretyakov, Yu.D., see Os'kina, T.E. 147
Tretyakov, Yu.D., see Rebane, J.A. 203
Trevor, P., see Cava, R.J. 49
Triftshaüser, W., see Zhou, X.Y. 436
Triftshäuser, W., see Zhou, X.Y. 433, 436
Tripathy, D.N. 422
Triscone, G., see Barbiellini, B. 442, 443
Triscone, G., see Genoud, J.-Y. 262, 263
Triscone, G., see Graf, T. 203, 265, 299, 308, 310
Triscone, G., see Sadowski, W. 148
Triscone, G., see Shaltiel, D. 386
Tříska, A., see Šesták, J. 324
Trivedi, N., see Randeria, M. 23
Trofimenko, E.A., see Grigorashev, D.I. 93
Trounov, V., see Guillaume, M. 505, 508, 510
Trounov, V., see Staub, U. 500, 501, 504, 508, 510
Trübenbach, K., see Simon, A. 300
Trunin, A.S., see Fotiev, A.A. 274
Trunin, A.S., see Kosmynin, A.C. 324
Truscott, A., see Sun, A.G. 14
Trybulski, J.D., see Lamberti, V.E. 90, 155, 323
Tsai, C.-C., see Yu, J.-T. 378
Tsai, P.K., see Dalichaouch, Y. 17
Tsang, C. 254–256
Tsapko, E.A., see Mikhalenkov, V.S. 438
Tseng, P.K., see Jean, Y.C. 433, 440
Tsetlin, M.B., see Zakharov, A.A. 458
Tsigelnik, O.A., see Sedov, V.L. 444
Tsuda, K. 329
Tsuei, C.C. 14
Tsuei, C.C., see Kirtley, J.R. 14
Tsuei, C.C., see Tu, K.N. 201
Tsukui, S. 202
Tsurumi, S. 204
Tsurumi, S., see Iwata, T. 93, 104, 114, 199
Tu, K.N. 201
Tuller, H.L., see Maier, J. 338–340
Tuller, H.L., see Opila, E.J. 278, 290, 294
Tuller, H.L., see Porat, O. 312, 313, 338
Turchi, P.E.A. 426, 429, 441
Turchi, P.E.A., see Haghighi, H. 430
Turchi, P.E.A., see Jean, Y.C. 433, 438–440, 443
Turchi, P.E.A., see Wachs, A.L. 441
Tyagi, A.K. 348
Tyagi, S. 378
Tycko, R., see Warren Jr, W.W. 20
Tyler, A.W., see Julian, S.R. 9
Tzagareishvili, D.S., see Sestak, J. 90

Uchida, S. 11
Uchida, S., see Boebinger, G.S. 18, 291
Uchida, S., see Fujimori, A. 458
Uchida, S., see Ito, T. 20
Uchida, S., see Kishio, K. 5
Uchida, S., see Sawa, H. 59
Uchida, S., see Sawa, K. 285
Uchida, S., see Takagi, H. 4, 526
Uchida, S., see Takenaka, K. 480
Uchida, S., see Tokura, T. 276, 285
Uchida, S., see Tokura, Y. 5, 7
Uchida, S., see Tranquada, J.M. 24, 403, 411
Uchida, S., see v. Zimmermann, M. 24
Uchida, Y., see Izumi, F. 37
Uchida, Y., see Takayama-Muromachi, E. 285, 295
Uchinokura, K., see Wada, T. 93, 199, 204
Udagawa, M., see Nakata, H. 261
Uecker, R. 177
Ueda, Y., see Imai, T. 20
Ueda, Y., see Katsuyama, S. 352
Ueda, Y., see Otzschi, K. 291, 293
Uehara, M. 9, 261
Uehara, M., see Akimitsu, J. 62
Uehara, M., see Zenitani, Y. 348
Ueltzen, M., see Wiesner, U. 149
Uemura, Y.J. 23
Uhlmann, D.R., see Jackson, K.A. 79
Uimin, G. 386
Ukei, K. 258
Ullman, J.E. 89, 112
Ullmann, B. 350
Ullrich, M. 181
Ullrich, M., see Krauns, C. 148, 166, 200
Umarji, A.M. 318
Umeda, T., see Chauhan, H.S. 120, 121
Umeda, T., see Goodilin, E.A. 82, 93–96, 101, 102, 105, 106, 114, 115, 117, 118, 138, 160–162, 166, 167, 175, 187, 193, 194, 208, 302, 303, 326
Umeda, T., see Kambara, M. 98, 101, 120, 121, 136, 166
Umeda, T., see Nakamura, M. 94, 105

Umeda, T., see Sumida, M. 94, 112, 113, 153, 155
Umeda, T., see Tagami, M. 94, 124, 125, 136, 166, 177, 326
Umeda, T., see Watanabe, Y. 166
Umeda, T., see Yao, X. 136, 151, 165, 167
Umeda, T., see Yoshizumi, M. 94, 104, 105, 112, 119, 212
Unoki, H., see Egi, T. 153, 155, 173, 189, 205, 206
Unoki, H., see Kuroda, K. 94, 101, 151, 155, 172, 183
Unoki, H., see Oka, K. 89, 101, 105, 106, 114, 152, 285
Unoki, H., see Rykov, A. 208, 209
Unoki, H., see Shibata, S. 155
Unternährer, P., see Allenspach, P. 520, 535, 536
Unternährer, P., see Fischer, P. 515
Unternährer, P., see Furrer, A. 504, 510, 514, 528
Unternährer, P., see Guillaume, M. 504, 505, 508, 510, 515
Urbach, J.S., see Moler, K.A. 13
Usagawa, T. 160, 161
Usha, R., see Nagarajan, T. 441
Usmar, S.G. 433, 434, 436–440
Usmar, S.G., see Lynn, K.G. 437, 438
Uspenskii, Yu.A., see Antonov, V.N. 428
Ustinov, V.V., see Romanyukha, A.A. 410
Utagawa, T., see Usagawa, T. 161

v. Zimmermann, M. 24
Vahlas, C. 319
Vajda, P., see Burger, J.P. 346
Valentine, T.M., see O'Connor, B.H. 235
Vallino, M. 295–297, 301, 303–306
Vallino, M., see Abbattista, F. 93, 264, 297, 298, 301, 303–307, 327, 328
Vallino, M., see Domenges, B. 304, 305
Vallino, M., see Mazza, D. 262, 272
Valo, J. 308
Van Bentum, P.J.M., see van de Leemput, L.E.C. 133
van Berkel, F.P.F., see Albino, J. 378, 410
van de Klundert, L.J.M., see Blank, D.H.A. 378
van de Leemput, L.E.C. 133
van den Berg, J., see Albino, J. 378, 410
Van Den Bogaert, N., see Dupret, F. 125
Van der Beek, C.J., see Fu, W.T. 331
van der Heijden, A.E.D.M. 75
Van der Kolk, G.J., see Lynn, K.G. 437, 438
Van der Woort, K., see Veal, B.W. 39
Van Dover, R.B., see Cava, R.J. 287, 288, 329
van Dover, R.B., see Cava, R.J. 5, 6
van Dover, R.B., see Jin, S. 11
Van Dover, R.B., see Murphy, D.W. 331
Van Hal, H.A.M., see De Leeuw, D.M. 331
Van Hal, H.A.M., see Kwestroo, W. 250, 253
Van Harlingen, D.J., see Wollman, D.A. 14
Van Landuyt, J., see Krekels, T. 41, 318
Van Landuyt, J., see Reyes-Casga, J. 41
van Loef, J.J., see Moolenaar, A.A. 155, 478
Van Rosmalen, G.M., see van der Heijden, A.E.D.M. 75
Van Ruitebeek, J.M., see Zandbergen, H.W. 50
Van Ruitenbeek, J.M., see Zandbergen, H.W. 349
Van Tendeloo, G. 190
Van Tendeloo, G., see Goutenoire, F. 54
Van Tendeloo, G., see Hervieu, M. 54
Van Tendeloo, G., see Hodges, J.P. 272
Van Tendeloo, G., see Huvé, M. 54, 56
Van Tendeloo, G., see Krekels, T. 41, 318, 355
Van Tendeloo, G., see Martin, C. 56
Van Tendeloo, G., see Milat, O. 255, 260
Van Tendeloo, G., see Reyes-Casga, J. 41
Van Tendeloo, G., see Zandbergen, H.W. 50
Van Vleck, J.H. 405
Vanacken, J., see Trappeniers, L. 205
Vanderah, T.A., see Lowe-Ma, C.K. 155, 156
Vanderschueren, H.W., see Ausloos, M. 349
Vandewalle, N. 142
Vandewalle, N., see Auguste, F. 152
Vandover, R.B., see Cava, R.J. 34, 35, 49
vanDover, R.B., see Cava, R.J. 526
Vanfleet, H.B., see Dąbrowski, B. 277
Vannerberg, N.-G., see Brosset, C. 245
Varadaraju, U.V., see Marimuthu, K.N. 318
Várez, A., see Señaris-Rodriguez, M.A. 307
Vargas, J.L. 181, 189
Varghese, V., see Jacob, K.T. 245
Varma, C.M. 15
Vasneva, G.A., see Atsarkin, V.A. 378, 407, 408
Vasumathi, D. 433, 434, 439
Vasumathi, D., see Erb, A. 433, 445
Vasumathi, D., see Sundar, C.S. 441
Vatolin, N., see Ilynych, N. 320, 321
Vatolin, N.A., see Moiseev, G.K. 320, 335
Vaughey, J.T. 355
Vazquez, J.E., see Beyers, R. 516, 518

Veal, B., see Welp, U. 468
Veal, B.W. 39
Veal, B.W., see Gofron, K. 457
Veal, B.W., see Jorgensen, J.D. 191, 192, 299, 300, 471
Veal, B.W., see Lei, M. 469, 472
Veal, B.W., see Pei, S. 296
Veal, B.W., see Shaked, H. 177, 191, 192
Veal, B.W., see Smedskjaer, L.C. 430, 433, 434, 436–439
Veal, B.W., see Sun, A.G. 14
Veblen, D.R., see Morris, D.E. 308
Vehanen, A., see Hautojärvi, P. 425
Velders, G.J.M., see Blank, D.H.A. 378
Venegas, P.A., see Castilho, J.H. 378
Venkatesan, T., see Anlage, S.M. 11, 13
Venturini, E.L., see Jorgensen, J.D. 33
Venturini, E.L., see Morosin, B. 348
Vera, A., see Amoretti, G. 378
Vera, A., see Blazey, K.W. 388
Verdaguer, M., see Baudelet, F. 38
Verheijen, A.A., see Fu, W.T. 291
Verhoeven, J.D., see Ullman, J.E. 89, 112
Vermeij, H., see Reyes-Casga, J. 41
Vertes, A., see Kajcsos, Z. 436, 438
Verweij, H. 300, 343
Verweij, H., see De Leeuw, D.M. 331
Vetkin, A., see Leonyuk, L. 190
Vettier, C. 300, 301
Vettier, C., see Rossat-Mignod, J. 20
Vier, D., see Rettori, C. 388, 389
Vier, D.C. 378
Vier, D.C., see Oseroff, S.B. 393, 526
Vier, D.C., see Rao, D. 393
Vier, D.C., see Zysler, R.D. 393, 394
Vietkine, A., see Revcolevschi, A. 169
Vigeland, B.E. 323
Vigliante, A., see v. Zimmermann, M. 24
Vijayaraghavan, R., see Huang, M.X. 409
Vikhreva, O.A., see Yankin, A.M. 256
Vilalta, N., see Sandiumenge, F. 153, 155, 156, 181, 200
Villars, P. 231
Villigier, J.C., see Sanfilippo, S. 469
Vincent, E., see Bertinotti, A. 263
Vinokur, V.M., see Blatter, G. 12
Visscher, W.M., see Lei, M. 469, 472
Vitebsky, I.M., see Stepanov, A.A. 393–395
Vlasov, M., see Yakhou, F. 263
Volkin, K.J., see Jorgensen, J.D. 37
Volmer, M. 83
Von Dreele, R.B., see Brese, N.E. 264
Von Ruitenbeek, H.W., see Fu, W.T. 291
von Schnering, H.G., see Müller-Buschbaum, H. 235
Von Stetten, E.C. 426, 427, 430, 433, 439
Von Stetten, E.C., see Berko, S. 429
Von Stetten, E.C., see Singh, D.J. 432
von Zimmermann, M., see Poulsen, H.F. 192, 300
Vorderwisch, P., see Fauth, F. 528, 530
Vorderwisch, P., see Henggeler, W. 520, 528, 532–534
Vorderwisch, P., see Staub, U. 528, 530
Voronin, G.F. 89, 91, 261–264, 266, 267, 308, 320–323, 345
Voronin, G.F., see Degterov, S.A. 89, 92
Voronin, G.F., see Hunt, R.D. 114, 121
Voronin, G.F., see Rudnyi, E.B. 201, 235, 320, 345
Voronkova, V.I. 149, 208, 209
Vosko, S.H., see Perdew, J.P. 473
Vostner, A., see Brandstatter, G. 191
Vyas, J.C., see Gupta, S.K. 203
Vyaselev, O.M., see Gorny, K. 22
Vydrin, S.N., see Aravin, L.G. 434

Wachs, A.L. 441
Wachs, A.L., see Haghighi, H. 430
Wachs, A.L., see Harshman, D.R. 433, 436
Wachs, A.L., see Jean, Y.C. 433, 438–440, 443
Wachs, A.L., see Turchi, P.E.A. 426, 429, 441
Wachter, P., see Bucher, B. 20
Wada, T. 93, 199, 204, 295, 329, 330
Wada, T., see Ichinose, A. 329
Wada, T., see Sakurai, T. 327
Wada, T., see Yamaguchi, K. 169
Wagman, D.D., see Hultgren, R. 231, 235, 237–239
Wagner, C., see Gundermann, J. 248
Wagner, R. 74, 76
Wahlbeck, P., see Oniyama, E. 114
Wahlbeck, P.G. 315
Wahlbeck, P.G., see Oniyama, E. 297
Waki, K., see Zamboni, M. 194
Walbrink, Th., see Schirmer, O.F. 381
Walker, D., see Chen, B. 281
Walker, D., see Chen, B.-H. 260, 281
Walker, D., see Wang, Y. 256, 261
Walker, E., see Barbiellini, B. 433, 437, 440
Walker, E., see Blandin, P. 441

Walker, E., see Erb, A. 145, 147, 148, 150, 171, 205
Walker, E., see Hoffmann, L. 430, 432, 440
Walker, E., see Manuel, A.A. 457
Walker, E., see Peter, M. 429, 433, 434
Walker, E., see Porath, D. 346
Walker, E., see Sadowski, W. 148
Walker, E., see Shaltiel, D. 384, 386, 404, 405, 523
Walker, E., see Shukla, A. 432, 433, 435, 442
Walker, E.J., see Manuel, A.A. 433, 440
Walstedt, R.E., see Warren Jr, W.W. 20
Walter, U., see Drössler, H. 540
Walter, U., see Hilscher, G. 510, 524
Walter, U., see Jostarndt, H.-D. 524, 525
Walter, U., see Nekvasil, V. 524
Walz, L., see Heinau, M. 268
Wan, K.T., see Bowden, G.J. 378
Wan, R.X. 73, 139
Wan, Y.M., see Raven, M.S. 319
Wang, C.A., see Tsuei, C.C. 14
Wang, C.Y., see Wang, N.L. 467
Wang, F. 161
Wang, F., see Yao, X. 168
Wang, F., see Zama, H. 160
Wang, G. 297, 318
Wang, G., see Zhang, H. 153
Wang, G.H., see Teng, M.K. 433, 438, 439
Wang, H., see Gudmundsson, B. 319
Wang, H.H. 348
Wang, J. 319
Wang, J., see Caignaert, V. 38
Wang, J., see Zhu, J. 439
Wang, J.H., see Tsuei, C.C. 14
Wang, L.Q., see LaGraff, J.R. 348
Wang, N.L. 467
Wang, R.L., see Zhou, X.Y. 436
Wang, S., see Zhao, Y.G. 433, 441
Wang, S.J. 433, 435, 438, 439, 443
Wang, S.J., see Chen, A. 440
Wang, S.J., see Jean, Y.C. 433, 438, 439
Wang, S.J., see Lu, X. 433
Wang, S.J., see Tang, Z. 443
Wang, S.J., see Zhi, Y. 433
Wang, S.S., see Wu, H. 208
Wang, W., see Li, Y. 441
Wang, X.G., see Gao, X.H. 443
Wang, X.-G., see Zhang, H. 433, 434, 438
Wang, X.Z. 159, 209
Wang, X.Z., see Hellebrand, B. 209
Wang, Y. 256, 261
Wang, Y., see Li, Y. 441
Wang, Y.J., see Zhao, Y.G. 433, 441
Wang, Y.Q., see Chang, H. 265
Wang, Y.Q., see Hor, P.H. 298, 523
Wang, Y.Q., see Wu, M.K. 5, 454, 458
Wang, Y.Y. 259
Wang, Y.Y., see Zhang, H. 259
Wang, Y.Z., see Wu, M.K. 35
Wang, Z., see Wang, S.J. 433, 438, 439
Wang, Z.Z., see Chien, T.R. 16
Wang, Z.Z., see Haghighi, H. 430
Wang, Z.Z., see Jean, Y.C. 433, 440, 443
Wanklyn, B.M. 147
Wanklyn, B.M., see Dufour, P. 502, 503
Wanklyn, B.M., see Jandl, S. 499, 502–504, 533
Ward, A.G., see Bernal, J.D. 245
Ward, R.C.C., see Leask, M.J.M. 529
Warren Jr, W.W. 20
Waseda, Y., see Jacob, K.T. 245, 267, 268, 288, 289
Washburn, F.A., see Lindemer, T.B. 313, 315
Waszczak, J.V., see Cava, R.J. 275, 287, 288, 330, 517, 518
Waszczak, J.V., see Harshman, D.R. 433, 436
Waszczak, J.V., see Schneemeyer, L.F. 148, 150, 505
Waszczak, J.V., see Siegrist, T. 350
Waszczak, J.V., see Stavola, M. 355
Waszczak, J.V., see Sunshine, S.A. 355
Waszczak, J.W., see Cava, R.J. 34
Waszczak, J.Y., see Santoro, A. 37
Watabe, H., see Sawa, H. 59
Watabe, H., see Sawa, K. 285
Watahiki, M., see Jang, W.J. 190
Watanabe, K., see Noto, K. 326
Watanabe, M., see Akimitsu, J. 59, 295
Watanabe, M., see Sawa, H. 59
Watanabe, M., see Sawa, K. 285
Watanabe, N. 104, 192
Watanabe, N., see Izumi, F. 37
Watanabe, S. 527
Watanabe, T. 329
Watanabe, Y. 166
Watanabe, Y., see Kambara, M. 166
Watkins, S.F., see Wong-Ng, W. 299, 354
Watson, A., see Boudéne, A. 320
Watson, R.E., see Freeman, A.J. 496, 506
Watson, R.E., see Wong-Ng, W. 299
Wattiaux, A., see Grenier, J.C. 33
Wattiaux, A., see Simon, P. 378

Watts, B.E., see Wanklyn, B.M. 147
Weast, R.C. 72
Webb, A.W. 280
Weber, H.W., see Brandstatter, G. 191
Weber, S., see Claus, J. 201, 202
Weckhuysen, L., see Trappeniers, L. 205
Weeber, A.W., see Mijnarends, P.E. 443
Wegerer, R. 535, 537
Wegerer, R., see Heyen, E.T. 535, 536
Wehler, D., see Os'kina, T.E. 147
Wei, J.Y.T., see Morris, D.E. 308, 327, 330
Wei, L., see Li, Y. 441
Wei, S., see Xing, X. 323
Wei, S.-H. 470
Weidinger, A., see Dortmann, G. 347
Weidinger, A., see Glückler, H. 347
Weidinger, A., see Niedermayer, C. 347
Weir, R.D., see Shaviv, R. 324
Weishaupt, K. 153
Weiss, F., see Boudéne, A. 320
Weiss, M. 346
Weiss, P.R., see Anderson, P.W. 405
Weissmann, M., see Saul, A. 429
Welch, A.J.E., see Smith, A.J. 252
Weller, M.T. 254, 263
Weller, M.T., see Currie, D.B. 334
Weller, M.T., see Dann, S.E. 292
Weller, M.T., see Grasmeder, J.R. 292
Wells, B.O., see Shen, Z.-X. 13
Wells, M.R., see Leask, M.J.M. 529
Wellstood, F.C., see Mathai, A. 14
Welp, U. 468, 517
Welp, U., see Nichols, D.H. 510
Welp, U., see Rothman, S.J. 201, 202
Welp, U., see Smedskjaer, L.C. 430–432
Welp, U., see Soderholm, L. 349, 524, 526
Welp, U.W., see Lei, M. 469, 472
Wen, J., see Usagawa, T. 160, 161
Wen, J., see Yao, X. 155
Wen, J.G. 159
Wen, J.G., see Egi, T. 153, 155, 173, 189, 205, 206
Wen, J.G., see Goodilin, E.A. 82, 93, 102, 105, 117, 138, 160–162, 175, 187, 193
Wen, J.G., see Konishi, M. 161
Wen, J.G., see Kuroda, K. 155, 172, 183
Wenzl, H., see Meuffels, P. 299, 338, 340–344
Wenzl, H., see Pörschke, E. 338, 343, 344
Weppner, W., see Nowotny, J. 312
Werder, D., see Cava, R.J. 299, 300, 516
Werthamer, N.R. 10
West, A.R., see Robertson, A.D. 269, 270
West, A.R., see Sastry, P.V.P.S.S. 259, 260
West, A.R., see Skakle, J.M.S. 274–276, 286, 288, 298, 302, 304, 328, 331–334
West, D.R.F. 105
West, R.N. 419, 423, 429, 432, 433, 457
West, R.N., see Haghighi, H. 430–432, 457
West, R.N., see Howell, R.H. 429, 434
West, R.N., see Lock, D.G. 419
West, R.N., see Turchi, P.E.A. 426, 429, 441
Westrum Jr, E.F., see Shaviv, R. 324
Wetzler, K.H., see Turchi, P.E.A. 426, 429, 441
Wetzler, K.H., see Wachs, A.L. 441
Whetten, R.L., see Holczer, K. 9
White, A.E., see Cava, R.J. 9
White, A.E., see Fiory, A.T. 203
White, J., see Gadalla, A.M.M. 254
White, T.J., see Thompson, J.G. 264
Whitler, D.J. 231
Whitler, J.D., see Roth, R.S. 272, 273, 289, 290, 297, 316, 324, 333
Widder, W., see Bauernfeind, L. 6
Wiesmann, J., see Freyhardt, H.C. 159
Wiesner, U. 90, 149
Wiesner, U., see Krabbes, G. 89, 166
Wild, R.K., see Flewitt, D.E.J. 171
Wilhelm, H. 281
Wilhelm, M., see Lengeler, M. 38
Wilke, K.-Th. 171
Wilke, T., see Seeßelberg, M. 127
Will, A., see Kupfer, H. 205
Will, E., see Torkar, K. 263
Williams, C.W., see Soderholm, L. 349, 524, 526, 537
Williams, G.V.M. 407
Williams, G.V.M., see Janossy, A. 406–408
Williams, G.V.M., see Tallon, J.L. 20
Williams, J.M., see Wang, H.H. 348
Williams, R.K. 89, 92, 310
Williams, R.K., see Lindemer, T.B. 92, 93, 108, 199, 204
Willis, J.O., see Brown, S.E. 523, 526
Wilson, A.F., see Barker, W.W. 241
Windsch, W., see Guskos, N. 263
Wirges, W., see Chattopadhyay, T. 515
Withers, R.L., see Thompson, J.G. 264, 266, 335
Wittlin, A., see Thomsen, C. 326
Włosewicz, D., see Plackowski, T. 302
Wltschek, G., see Paulus, E.F. 263
Wochner, P., see v. Zimmermann, M. 24

Woensdregt, C.F., see Sun, B.N. 133
Wold, A., see Collins, B.T. 248
Wold, A., see Doverspike, K. 286, 292
Wolf, L. 242
Wolf, M., see Ruck, K. 348
Wolf, T., see Foukis, V. 388
Wolf, T., see Gordeev, S.N. 205
Wolf, T., see Martin, A.A. 192, 499
Wolf, T., see Meingast, C. 468
Wolf, T., see Saito, K. 205
Wolf, Th. 72, 133–135, 147, 149, 150, 152, 198, 200, 203, 205
Wolf, Th., see Voronkova, V.I. 149, 208, 209
Wolf, W.P., see Hutchings, M.T. 498
Wolf, W.P., see Lea, K.R. 504, 538
Wolfe, J.C., see Miller, J.H. 14
Woll Jr, E.J., see Perkins, A. 421
Wollman, D.A. 14
Wollschläger, W., see Müller-Buschbaum, H. 276
Wollschlager, W., see Müller-Buschbaum, H.K. 33
Wong-Ng, W. 90, 92, 93, 101, 245, 251, 262, 274, 275, 289, 297, 299, 301–304, 326, 354
Wong-Ng, W., see Stalick, J. 304
Wong-Ng, W.K. 261, 262
Wong-Ng, W.K., see Roth, R.S. 272, 273, 289, 290, 333
Woods, S.I., see Basov, D.N. 11, 12
Woods, S.I., see Kleiner, R. 14
Woolf, L.D., see Moncton, D.E. 6
Worthington, T.K., see Holtzberg, F. 148
Worthington, T.K., see Kaiser, D.L. 148
Wrigge, F.W. 248
Wright, A.J., see Krekels, T. 355
Wright, F., see Oseroff, S.B. 526
Wrigth, F., see Oseroff, S.B. 393
Wu, D.-H. 13
Wu, D.-H., see Anlage, S.M. 11, 13
Wu, F., see Zhao, J. 268
Wu, H. 104, 105, 208, 302
Wu, H., see Zhang, H. 153
Wu, M., see Hu, A.M. 200
Wu, M.K. 5, 35, 454, 458
Wu, M.K., see Huang, W.F. 439
Wu, N.-L., see Lin, S.-H. 271, 272
Wu, X., see Laffez, P. 264–266
Wu, X.D. 25
Wu, X.J., see Goodilin, E.A. 93, 111
Wu, X.-J. 259
Wu, X.-J., see Tatsuki, T. 348
Wu, Y., see Shi, F. 293
Wu, Z.L., see Xie, X.M. 201, 202
Wübbeler, G. 381
Wübbeler, G., see Schirmer, O.F. 381
Wühl, H., see Kraut, O. 468
Wühl, H., see Ludwig, H.A. 299
Wühl, H., see Meingast, C. 468, 486
Wyard, S.J., see Searl, J.W. 391
Wybourne, B.G. 494, 497, 504, 510
Wyder, P., see Stepanov, A.A. 393–395

Xi, X.X., see Anlage, S.M. 11, 13
Xi, X.X., see Wu, D.-H. 13
Xianyu, Z., see Chen, T.G. 149
Xiao, G. 350
Xiao, G., see Cieplak, M.Z. 350, 400, 403
Xiao, G., see Sienkiewicz, A. 400–403
Xiao, J.Q., see Cieplak, M.Z. 400, 403
Xie, D., see Newsam, J.M. 327
Xie, H., see Kramer, M. 92, 101, 102, 108, 111
Xie, X.M. 201, 202
Xing, X. 323
Xiong, H.Q., see Lam, C.C. 433
Xiong, H.Q., see Li, J.Q. 440
Xiong, X. 277
Xu, J.A., see Durny, R. 388
Xu, J.H., see Miller, J.H. 14
Xu, M., see Basov, D.N. 11, 12
Xu, Q., see Fu, W.T. 291
Xu, Y. 350, 352
Xu, Y., see Usmar, S.G. 433, 436–440
Xu, Z.A., see Han, T.D. 441
Xu, Z.J., see Huang, W.F. 439, 440
Xue, J.S. 505
Xue, J.S., see Soderholm, L. 505, 507, 520
Xue, J.S., see Wegerer, R. 535, 537
Xue, Y.Y., see Bharathi, A. 426
Xue, Y.Y., see Chang, H. 265
Xue, Y.Y., see Chu, C.W. 4, 433
Xue, Y.Y., see Lin, J.G. 156, 204
Xue, Y.Y., see Lu, X. 433

Yabe, T., see Wada, T. 93, 199, 204
Yacoby, E.R., see Klein, L. 205
Yadava, Y.P. 159
Yadava, Y.P., see Tellez, D.A.L. 94
Yaegashi, Y., see Ichinose, A. 329
Yaegashi, Y., see Isawa, K. 279
Yaegashi, Y., see Wada, T. 329, 330
Yahagi, S., see Yamaguchi, S. 338

Yakhmi, J.V., see Pujari, P.K. 439, 441, 443, 444
Yakhou, F. 263
Yakovlev, N.V., see Rebane, J.A. 203
Yamada, K. 390
Yamada, K., see Matsuda, M. 396, 526
Yamada, K., see Thurston, T.R. 24
Yamada, T., see Kinoshita, K. 272, 287
Yamada, T., see Shibata, H. 272
Yamada, T., see Watanabe, T. 329
Yamada, Y. 116, 123, 132, 133, 136, 145, 147, 151, 163, 164, 177, 180, 199, 202, 410
Yamada, Y., see Hirayama, T. 189
Yamada, Y., see Ishida, Y. 163, 181
Yamada, Y., see Kanamori, Y. 183
Yamada, Y., see Kitamura, T. 163
Yamada, Y., see Kohara, K. 378
Yamada, Y., see Krauns, Ch. 91, 93–95, 98, 196
Yamada, Y., see Kuroda, K. 180
Yamada, Y., see Kutami, H. 190, 208, 209
Yamada, Y., see Nakamura, M. 177, 187, 189, 198, 206, 207
Yamada, Y., see Namikawa, Y. 127, 137
Yamada, Y., see Sakai, H. 160
Yamada, Y., see Tagami, M. 136, 161, 166, 177, 185, 186
Yamagata, H., see Kohara, K. 378
Yamaguchi, A., see Doyama, M. 439
Yamaguchi, A., see Ishibashi, S. 439
Yamaguchi, K. 169, 182
Yamaguchi, S. 338
Yamamoto, R., see Doyama, M. 439
Yamamoto, R., see Ishibashi, S. 427, 433–436, 438–440
Yamamoto, T., see Kishio, K. 338
Yamamoto, T., see Tsukui, S. 202
Yamanaka, A., see Panfilov, A.G. 192
Yamane, H., see Akimitsu, J. 62
Yamane, H., see Ammamoto, Y. 293
Yamane, H., see Miyazaki, Y. 62, 260, 316, 318
Yamaoka, S., see Matveev, A.T. 256
Yamashita, T., see Komatsu, T. 335
Yamashita, T., see Osamura, K. 89
Yamauchi, H., see Ichinose, A. 329
Yamauchi, H., see Isawa, K. 279
Yamauchi, H., see Karppinen, M. 281
Yamauchi, H., see Laffez, P. 264–266
Yamauchi, H., see Lee, S. 169
Yamauchi, H., see Peitola, K. 263
Yamauchi, H., see Sakurai, T. 327
Yamauchi, H., see Seiji, N. 308
Yamauchi, H., see Wada, T. 295, 329, 330
Yamauchi, H., see Wu, X.-J. 259
Yamaura, K. 261
Yan, Y., see Lin, C.T. 104, 114, 147, 151, 168, 175
Yang, B.X., see Goldman, A.I. 515
Yang, B.X., see Schleger, P. 338, 340–343
Yang, C.Y. 346
Yang, G. 169
Yang, H.D., see Shih, C.R. 537
Yang, J.H., see Zhao, Y.G. 433, 441
Yang, K.N. 515, 528
Yang, K.N., see Dalichaouch, Y. 523
Yang, K.N., see Maple, M.B. 5, 6, 10
Yang, K.Y. 297, 318
Yang, X.-Q., see Yang, C.Y. 346
Yang, Z. 438, 439
Yang, Z., see Zhu, J. 439
Yankin, A.M. 256
Yanovskii, V.K., see Voronkova, V.I. 149
Yao, T., see Oyanagi, H. 38
Yao, X. 72, 94, 96, 136, 151, 155, 162, 164–168, 172, 183, 198, 199
Yao, X., see Kambara, M. 90, 93–95, 102, 104–106, 117, 119, 166, 212
Yao, X., see Li, Y. 210
Yao, X., see Limonov, M. 108, 192
Yao, Y.D., see Chen, J.W. 349
Yaron, U. 355
Yaron, U., see Porath, D. 346
Yasnoka, K., see Machida, M. 264
Yasuda, H. 76
Yasuda, T., see Kishio, K. 5
Yasuoka, H., see Imai, T. 20
Yazawa, I. 248
Ye, J., see Zou, Z. 5, 156
Yehia, I., see Paulus, E.F. 263
Yelon, W.B., see Kramer, M. 92, 101, 102, 108, 111
Yelon, W.B., see Malik, S.K. 302
Yelon, W.B., see Newsam, J.M. 327
Yeshurun, Y., see Klein, L. 205
Yi, C.Y., see Teng, M.K. 433, 438, 439
Yildirim, T., see Sachidanandam, R. 528
Ying, Q.Y., see Miller, J.H. 14
Yokota, K. 335
Yokoya, T., see Ding, H. 20–22
Yongle, H., see Changkang, Ch. 149, 150
Yoo, S., see Zamboni, M. 194

Yoo, S.I. 92, 105, 106, 205, 303, 304
Yoo, S.I., see Higuchi, T. 205
Yoo, S.I., see Koblischka, M.R. 72
Yoo, S.I., see Kramer, M. 92, 101, 102, 108, 111
Yoo, S.I., see Murakami, M. 72, 93, 104, 204–206
Yoo, S.I., see Nagashima, K. 205
Yoo, S.I., see Osabe, G. 104
Yoo, S.I., see Sakai, N. 93
Yoo, S.-I., see Allenspach, P. 508, 510, 515, 517
Yoshi, I., see Noto, K. 326
Yoshiara, K., see Maple, M.B. 5, 16, 17
Yoshida, K., see Maeno, Y. 9
Yoshida, M., see Hyun, O.B. 205
Yoshida, N., see Fujihara, S. 166, 334
Yoshikawa, M., see Ikuta, H. 149
Yoshimura, M., see Ikuma, Y. 346
Yoshioka, J., see Chikumoto, N. 189, 200
Yoshizaki, R., see Movshovich, R. 15
Yoshizawa, S., see Kohayashi, S. 149
Yoshizumi, M. 94, 104, 105, 112, 119, 212
Young, D.A. 231
Young Jr, V.G., see Brese, N.E. 264
Yu, J. 432
Yu, J.J., see Blandin, P. 441
Yu, J.J., see Massidda, S. 426, 427
Yu, J.-T. 378
Yu, Jaejun, see Massidda, S. 457
Yu, R., see Sandiumenge, F. 153, 155, 200
Yu, W.Z., see Zhao, Y.G. 433, 441
Yu, X., see Shaviv, R. 324
Yu-Jahnes, L.S., see Kirtley, J.R. 14
Yufang, R., see Mingmei, W. 264
Yu-Jahnes, L.-S., see Tsuei, C.C. 14
Yvon, K., see François, M. 299, 354
Yvon, K., see Shaltiel, D. 386

Zaanen, J., see Liechtenstein, A.I. 481
Zaanen, J., see Mazin, I.I. 457
Zahurak, S., see Cava, R.J. 35
Zahurak, S.M., see Cava, R.J. 299, 300, 516
Zahurak, S.M., see James, A.C.W.P. 276
Zahurak, S.M., see Murphy, D.W. 331
Zahurak, S.M., see Rosseinsky, M.J. 9
Zahurak, S.M., see Siegrist, T. 268
Zainulin, Yu.G., see Dlyachkova, T.V. 319
Zainullin, A.R., see Aravin, L.G. 434
Zainullin, R.N., see Aravin, L.G. 434
Zaitseva, S.I., see Moiseev, G.K. 335
Zaitzeva, S., see Ilynych, N. 320, 321
Zakharchenko, V.N., see Belyaev, V.N. 439
Zakharov, A.A. 458
Zakharov, P.G., see Yankin, A.M. 256
Zama, H. 160
Zama, H., see Tanaka, N. 160
Zama, H., see Wang, F. 161
Zama, H., see Yao, X. 168
Zamboni, M. 194
Zandbergen, H.W. 50, 331, 349
Zandbergen, H.W., see Albino, J. 378, 410
Zandbergen, H.W., see Cava, R.J. 275, 329
Zandbergen, H.W., see De Leeuw, D.M. 297
Zandbergen, H.W., see Fu, W.T. 291, 331, 349
Zander, W., see Günther, W. 347
Zangrando, E., see Geremia, S. 354
Zecca, A., see Brusa, R.S. 437, 439
Zelenay, I. 209
Zemann, J., see Effenberger, H. 247
Zeng, Y., see Cao, G. 152
Zenitani, Y. 348
Zettl, A., see Crommie, M.F. 469
Zevin, V., see Genossar, J. 378
Zevin, V., see Japha, Y. 479
Zhang, C., see Gao, Y. 335
Zhang, C., see Selvduray, G. 337
Zhang, D.M. 436, 438, 443
Zhang, H. 153, 259, 345, 433, 434, 438, 440, 467
Zhang, H., see Gong, S. 152
Zhang, H., see Wang, Y.Y. 259
Zhang, H.K., see Jorgensen, J.D. 303
Zhang, H.-Z. 345
Zhang, J.C. 433, 434, 440
Zhang, J.P. 355
Zhang, K. 101, 302, 326, 327
Zhang, K., see Alp, E.E. 504, 510, 528
Zhang, K., see Beno, M.A. 35, 299
Zhang, K., see Bonn, D.A. 13
Zhang, K., see Hardy, W.N. 13
Zhang, K., see Jorgensen, J.D. 37
Zhang, K., see Segre, C.U. 101, 327
Zhang, K., see Soderholm, L. 523
Zhang, M., see Shi, F. 293
Zhang, N., see Vargas, J.L. 181, 189
Zhang, P., see Zhang, H. 345
Zhang, P.-M., see Zhang, H.-Z. 345
Zhang, Q., see Cao, G. 152
Zhang, Q., see Zhou, X.Y. 433, 434
Zhang, Q.R., see Han, T.D. 441

Zhang, Q.-Z. 338
Zhang, S.-C. 23
Zhang, T., see Li, Y. 441
Zhang, W. 101, 102, 251–254, 261, 262, 306, 307
Zhang, W., see Osamura, K. 89, 90, 92, 93, 98, 101, 102, 104–106, 112–114
Zhang, X., see Cao, G. 152
Zhang, X., see Ignatiev, A. 159
Zhang, X.L., see Zhi, Y. 433
Zhang, Y., see Zhong, Q. 286, 288
Zhang, Y., see Zhu, J. 439
Zhang, Y.H., see Zhu, J.S. 444
Zhanguo, F. 282, 283
Zhanguo, F., see Chunlin, J. 153
Zhao, G.M., see Wan, R.X. 73, 139
Zhao, J. 268
Zhao, Y.G. 433, 441
Zhao, Z.X., see Gou, Z.H. 433
Zhao, Z.X., see Hu, A.M. 200
Zhao, Z.X., see Li, J.Q. 318
Zhao, Z.X., see Tang, Z. 443
Zhao, Z.X., see Zhao, J. 268
Zhdanov, R.Sh., see Kurkin, I.N. 409
Zheltova, N.A., see Izakovich, E.N. 296
Zheng, D.J., see Durny, R. 388
Zheng, G.D., see Gao, X.H. 443
Zheng, S.G., see Gou, Z.H. 433
Zheng Shengnan, see Li Anli 433, 439
Zhi, Y. 433
Zhi, Y., see Chen, A. 440
Zhigunov, D.I., see Henggeler, W. 528, 533
Zhigunov, D.I., see Stepanov, A.A. 393–395
Zhigunov, D.I., see Strach, T. 499, 503, 504
Zhigunov, D.I., see Sumarlin, I.W. 526, 528, 532, 533
Zhokhlov, A.A. 165
Zhokhlov, A.A., see Bredikhin, S.I. 201, 202
Zhokhov, A.A. 147, 156
Zhokhov, A.A., see Christensen, A.N. 147, 153, 191
Zhokhov, A.A., see Emelchenko, G.A. 108, 150, 165, 174
Zhong, Q. 286, 288
Zhong, Q., see Ignatiev, A. 159
Zhongxian, Z., see Zhanguo, F. 282, 283
Zhou, G., see Gong, S. 152
Zhou, H., see Dalichaouch, Y. 523
Zhou, H., see Fauth, F. 528, 530
Zhou, H., see Maple, M.B. 5, 6, 10
Zhou, H., see Markert, J.T. 5
Zhou, H., see Staub, U. 528, 530, 532
Zhou, J. 161
Zhou, J., see Smith, M.G. 269, 293
Zhou, J.-S., see Goodenough, J.B. 277
Zhou, W., see Lin, C.T. 148–150
Zhou, W., see Liu, R.S. 330
Zhou, X.Y. 433, 434, 436
Zhou, X.Y., see Han, T.D. 441
Zhou, X.Y., see Zhu, J.S. 444
Zhou, Z. 89, 307, 308, 321, 323
Zhou Zhigang 441
Zhu, J. 439
Zhu, J., see Yang, Z. 438, 439
Zhu, J.S. 444
Zhu, N., see McGinn, P.J. 153
Zhu, Q., see Xiong, X. 277
Zhu, S.G., see Gou, Z.H. 433
Zhu Sheng Yu N., see Li Anli 433, 439
Zhu, Y. 192
Zhu, Y., see Gregory, R.B. 424
Zhu, Y.T. 297
Zhukhovitskii, A.A., see Bokshtein, B.S. 201
Zhukov, A.A., see Gordeev, S.N. 205
Zhukov, A.A., see Kupfer, H. 205
Zibrov, J.P., see Bykov, A.B. 89
Zimmermann, E. 245
Zimmermann, E., see Boudéne, A. 320
Zimmermann, H., see Mangelschots, I. 331
Zimmermann, M., see Schleger, P. 300
Zinn, W., see Kajcsos, Z. 436, 438
Zirngiebl, E., see Brown, S.E. 523, 526
Zolliker, M., see Roessli, B. 515, 529, 539
Zolliker, P. 277
Zou, Z. 5, 156, 486
Zou, Z., see Oka, K. 154, 155
Zou, Z.G., see Miller, J.H. 14
Zubkov, V.G., see Koscheeva, S.N. 297, 318
Zysler, R.D. 393, 394
Zysler, R.D., see Rettori, C. 388, 389

SUBJECT INDEX

ACAR (angular correlation of positron annihilation radiation) 423
AFM, *see* antiferromagnetic/ism (ch. 187) or atomic force microscopy (ch. 189)
A_{1g} phonons 470, 472
ARPES, *see* angle-resolved photoemission spectroscopy
Abrikosov–Gor'kov suppression 478
alkaline earth
– carbonates, thermodynamics 247
– oxides, thermodynamics 246
Andreev reflection 13
angle-resolved photoemission spectroscopy (ARPES) 13, 20, 457, 458
antibonding state 483
antiferromagnetic
– insulator 459
– – La_2CuO_4 6
– pairing mechanism 11
– spin fluctuations 11
antiferromagnetic insulating parent compounds 6, 14
antiferromagnetism 11
apical oxygens 460, 465, 468
applications
– current leads 25
– current limiters 25
– digital instruments 25
– magnetic energy storage 25
– magnetic resonance imaging (MRI) coils 25
– magnetic separation 25
– motors and generators 25
– NMR coils 25
– NMR microscopes 25
– power transmission lines 25
– research magnet systems 25
– SQUIDs 25
– single crystals 210
– superconducting electronics 24
– superconducting wires and tapes 11, 24, 25
– transformers 25
– wireless communications subsystems 25
atomic force microscopy (AFM) 182, 183

BSCCO 20, 23
BSCCO-2223 wire 25
$(Ba_{1-y}R_y)_2CuO_{4-w}$, R = Nd 303
$BaCuO_2$ 378
$BaCuO_{2+w}$ 262
$BaCuO_{3-w}$ 266
$BaCu_2O_2$ 263
$Ba_2Cu_3O_{6-w}$ 264
$Ba_8[Cu_{4+z}Y_{1+x}(CO_3)_{3-x-z}]O_{10+w}$ 316
Ba_2CuO_{4-w} 261
Ba_3CuO_4 264
$Ba_2CuO_2(CO_3)$ 267
$Ba_{1-x}K_xBiO_3$ 9, 444, 458
$BaLa_4Cu_5O_{13+w}$ 305
BaO–BaO_2 system 246
Ba(O)–Cu(O) 261, 265, 266
BaO–Cu_2O–O 262
Ba(O)–R(O) 251
$(Ba_{1-y}R_y)CuO_2$, R = Nd, Pr, La 303
band structure 453–486
barium cuprates 261–267
$Bi_2Sr_2Ca_{n-1}Cu_nO_x$ 9
$Bi_2Sr_2Ca_{n-1}Cu_nO_{2n+4}$ (n = 2,3) 11
$Bi_2Sr_2Ca(Cu_{1-x}Ni_x)_2O_8$ 15
$Bi_2Sr_2CaCu_2O_8$ 15
$Bi_2Sr_2CaCu_2O_{8+\delta}$ (BSCCO-2212) 20, 21, 443, 458
$Bi_2Sr_{2-x}La_xCuO_{4+\delta}$ 467
$Bi_2Sr_2R_{1-x}Ca_xCu_3O_8$ 501
$Bi_2Sr_2(R/Ca)Cu_2O_8$ 505
bismuth 61
bismuth bilayers 61
bismuth cuprates 53
– $Bi_{2-x}Pb_xSr_2Ca_{1-x}Y_xCu_2O_8$ 53
blocking layer 455–457, 459, 471, 473, 474, 476, 486
Bose–Einstein condensation 23
bulk Nd123 single crystals 206

Ca–Ba cuprates 270–272
Ca–Sr cuprates 267–270
$CaBa_4Cu_2CO_3O_6$ 272
$CaBa_4Cu_3O_w$ 271
$Ca_3Cu_2CO_3O_4$ 256
$CaCu_2O_3$ 255
CaCu(O)–BaCu(O)–LaCu(O) 331
$Ca_{1-y}CuO_2$ 255
Ca_2CuO_3 254
Ca doping 526, 527
Ca(O)–Ba(O)–Cu(O) 270, 271
Ca(O)–Cu(O) 254, 255
Ca(O)–R(O) 250
Ca(O)–Sr(O)–Cu(O) 267
$Ca_{1-y}Sr_yCuO_2$ 268
calcium cuprates 254–256
cation ordering 36, 55
c-axis Josephson tunneling 14, 15
CeO_w 241
Ce(O)–Nd(O)–Cu(O) 284, 285
cell symmetry 32, 35, 54, 59, 61
charge carriers 6
charge reservoirs 6
$CmBa_2Cu_3O_7$ 525
coherence lengths 12
coherent nonsuperconducting inclusions 205
contamination-free Nd_2O_3 crucibles 206
copper disproportionation 38, 39, 62
copper oxycarbonates 62
– $(Y_{1-x}Ca_x)_{0.95}Sr_{2.05}Cu_{2.4}(CO_3)_{0.6}O_y$ 62
– $YCaBa_4Cu_5(NO_3)_{0.3}(CO_3)_{0.7}O_{11}$ 62
– $Y_4Sr_8Cu_{11}CO_3O_{25}$ 62
Coulomb repulsion 476
coupling parameters 531, 532
critical current densities 9, 10, 25
critical fields 9, 10
critical temperature 32, 34, 35, 37, 47–49, 51, 54, 56, 59, 61, 62
– of substituted mercury cuprates 55
– variation of 38
crucibles
– afterheater effect 126
– Al_2O_3 147, 150, 165, 169, 197
– Au 147, 197
– $BaZrO_3$ 145, 147, 150, 169, 196, 197
– BeO 169
– binding substances 196
– choice of crucible 196
– comparison 196, 197
– contamination-free 95, 188, 196
– contamination of melt 197
– – control 196
– CuO 147
– deterioration of superconducting properties 147
– $LaAlO_3$ 196
– MgO 147, 162, 169, 196, 197
– Nd_2O_3 95, 151, 162, 165, 197
– prospective crucible materials 196
– protective layer 147
– Pt 147, 197
– reactive layer 196, 197
– reactivity of melt 147
– self-crucible 147, 197
– smooth inner wall 149
– SnO_2 147, 151, 168, 197
– solvent creep 197
– $SrTiO_3$ 196
– ThO_2 147
– TiO_2 197
– wetting 196
– Y_2O_3 147, 197
– YSZ 147, 150, 196, 197
– ZrO_2 147, 169
crystal chemistry 31–62
crystal field 500–502
– CEF energies 503, 508
– CEF parameters 497–500, 504, 506–510, 516, 517
– CEF potential 495, 504
– CEF splitting 516
– CEF wavefunctions 539
– line width 521–523
– point-charge approximation 498
– splittings 491–541
– Stevens operator 496, 497
– superposition modeling 498, 499
– tensor operators 495, 497
– transition probabilities 513
– wavefunctions 511, 512
crystal growth 67–214
– *see also* crystal pulling process, directional solidification, flux growth, hydrodynamics and computer simulation of crystal growth, mechanism of R123 crystal growth, self-flux method, single-crystal growth, whiskers
– assemblage of constituents 73
– crystallization as a first-order phase transformation 73
– diffusion control 78

– driving force 73, 78
– faceted growth 78
– growth modes 80, 136
– – continuous growth law 85
– – twin-plane-reentrant-edge growth 138, 162, 175
– interfacial kinetics 78
– mixed control 78
– rate limiting factors 77
– screw dislocation mechanism 162
– solute distribution 78
crystal pulling process 164
– advantage 145
– anisotropy of growth rate 133, 135, 136
– anisotropy of physical properties 193
– automatic pulling system 138
– – in high p_{O_2} atmosphere 164
– charge material 145
– cold finger 168
– comparison of $Nd_1Ba_2Cu_3O_z$ and "$Nd_2Ba_1Cu_3O_z$" single crystals 162
– computer simulations 128
– continuous growth of Y123 single crystals 145
– control of solid phase composition 166
– cooling process 197
– cracks in single crystal substrate 161
– crystal shapes 136, 137
– – concave 137, 172
– – pyramid-like overall 171, 172
– – round 138, 172
– – straight-body 171, 172
– crystal size enlargement 198
– crystallinity of single crystals 196
– Czochralski growth 145, 177
– detwinning 208
– diffusivity and interdiffusivity of cations 124
– floating particles 196
– growth spirals 132
– high-oxygen-pressure treatment 204
– increasing growth rate 198
– interface between Y123 and Pr123 single crystals 182, 185
– levitation force Y123 single crystal 194
– liquid composition control 165, 200
– low-p_{O_2} crystal growth 199
– macroscopic growth rates 136
– macroscopic steps 138, 179
– mass-balance equations for each element 125
– mixed Y–R123 (R = Nd, Sm) crystals 199
– morphology of crystals 171
– $Nd_{1+x}Ba_{2-x}Cu_{3-y}Ga_yO_z$ single crystals 168, 175
– $Nd_xBa_{2y}Cu_3O_z$ 160, 167, 176, 187
– $Nd_{1+x}Ba_{2-x}Cu_3O_z$ 194
– $Nd_{1.07}Ba_{1.95}Cu_3O_z$ single crystal 200
– $Nd_{1.10}Ba_{1.90}Cu_3O_z$ single crystal 200
– $Nd_{1.85}Ba_{1.15}Cu_3O_z$ single crystals 175, 192
– Nd123 single crystal 200, 206
– – largest, bulk 150, 165, 167
– Nd123 single-crystalline target 211
– necking 179, 180, 197
– Nikolov's empirical correlation 137
– novel technologies 211
– optimal oxygen content 203
– orthorhombic insulating Nd213 phase 161, 166
– "overdoped" crystals 203
– oxygenation procedure 200
– peak effect 188, 205–207
– permittivity of $Nd_{1.85}Ba_{1.15}Cu_3O_z$ crystal 194
– pinning properties 204
– $Pr_{1.14}Ba_{1.86}Cu_{2.95}Mg_{0.05}O_y$ crystals 191
– $Pr_{1+x}Ba_{2-x}Cu_3O_z$ crystals 191, 194
– Pr123 crystal 166
– practical ways of improvement 196
– pulling apparatus 145
– pyramid-like overall shape 136
– quasibinary assumption 122
– quasiternary phase diagram 106, 122, 124
– R123-based single-crystal materials as substrates 159, 160
– resistivity measurements 194, 195
– rotation rate 196
– seed crystal 197
– selected tie-line 125
– Sm123 single crystal 166, 200
– solute diffusion in Y123 crystal pulling 121
– solute-rich liquid crystal pulling (SRL–CP) method 145
– spiral pattern study 131
– superconducting characteristics improvement 199
– surface roughness of R123 substrate 160
– surface stability 161
– tie-line selection 122, 124
– top-seeded solution-growth technique 146
– transport of the solute 146
– twin-plane-reentrant-edge growth 162, 173
– "underdoped" crystals 203

crystal pulling process (*cont'd*)
– $YBa_2(Cu_{1-x}Zn_x)_3O_z$ crystals 168
– Y123 single crystals 151, 164, 191
crystal structure 31–62
– $HgBa_2La_2Cu_2O_{8+\delta}$ 54
– $Hg_{1.5}(Cu,Pr)_{0.5}Ba_2PrCu_2O_{8-\delta}$ 58
– $La_{2-x}A_xCuO_4$ 32
– $La_2CaCu_2O_6$ 34
– layered perovskite-like 6
– $(Ln_{1-x}Ce_x)_2(Ba_{1-y}Ln_y)_2Cu_3O_{10-\delta}$ 61
– $Nd_{2.64}Sr_{0.82}Ce_{0.54}Cu_2O_{8-y}$ 60
– $Pb_2A_2LnCeCu_3O_{10+\delta}$ 61
– $Pb_2Sr_{2-x}La_xCu_2O_{6+\delta}$ 50
– $Pb_2Sr_2Y_{1-x}Ca_xCu_3O_8$ 50
– $Tl_{1+x}A_{2-y}Ln_2Cu_2O_9$ 60
– $Tl_2Ba_2Ln_{2-x}Ce_xCu_2O_{10}$ 60
– $Tl_{1-x}Pr_xSr_{2-y}Pr_yCuO_5$ 53
– $YBa_2Cu_3O_{7-\delta}$ 36, 455
– $YBa_2Cu_3O_{8-x}$ 47
– $YBa_2Cu_4O_8$ 49
– $Y_2Ba_4Cu_7O_{15}$ 49
– $YBa_2Cu_3O_{6.3}$ (T1 phase) 36
crystalline electric field 491–541
$CsPrF_5$ 478
Cu–O 249
CuO
– chains 455, 457, 460, 473, 474
– layers 467
$[CuO]_\infty$
– chains 36
– rows 37, 39
CuO_2
– bilayer 464
– layers 455, 459, 460, 477
– – dimpling 465
– planes 6, 455, 460, 467, 468, 473
– sticks 37, 40, 51, 62
$[CuO_2]_\infty$
– chains 36
– layers 34, 36
– rows 39
$[CuO_{2.5}]_\infty$ layers 36, 37
CuO_4 square planar groups 33, 36, 40, 41, 43, 45, 46, 48
CuO_4 tetrahedra 44
CuO_5 pyramids 35–37, 40, 44, 47, 48
CuO_6 octahedra 44, 47
Cu s orbital 462
Cu substitution: $YBa_2(Cu_{3-x}M_x)O_{7-\delta}$ 440
cubic high-T_c superconductors 9
cuprates involving
– $Bi_2Sr_2Ln_{2-x}Ce_xCu_2O_{10}$ 61
– $(Ln_{1-x}Ce_x)_2(Ba_{1-y}Ln_y)_2Cu_3O_{10-\delta}$ 62
– $Nd_{2.64}Sr_{0.82}Ce_{0.54}Cu_2O_{8-y}$ 59
– $Pb_2Sr_2LnCeCu_3O_{10+\delta}$ 61
– $Tl_{1+x}A_{2-y}Ln_2Cu_2O_9$ 59
– $Tl_2Ba_2Ln_{2-x}Ce_xCu_2O_{10}$ 61
curve of T_c vs. carrier concentration 11

$d_{x^2-y^2}$ symmetry 11, 13, 15, 20
d-wave 478
de Haas–van Alphen 458
defects in cuprate superconductors
– *a–b* anisotropy of physical properties 175
– Burgers vector 181
– chemical macro-uniformity 183
– classification of 170
– cooling cracks 173
– copper deficiency 190
– crystallinity of single crystals 178
– detected by
– – acoustic microscopy 173
– – atomic force microscopy 184
– – EPMA (electron probe microanalysis) 183, 185, 187
– – four-circle diffractometer 190, 191
– – HREM 190
– – high-temperature (hot-stage) in situ optical microscopy 176, 177
– – ICP AES 183
– – Laue back-scattering X-ray diffraction (LBXRD) 177
– – – doubling reflections 175, 178
– – micro-EDX 187, 188
– – neutron diffraction 180, 191
– – optical microscopy 173, 175
– – pole figure measurement 180, 181
– – Raman spectroscopy 190, 192
– – SEM 183
– – scanning tunnel microscopy (STM) 190
– – TEM 182, 187
– – thermal expansion coefficient 162, 197
– – XRD line-broadening analysis 181
– – X-ray rocking curves 179
– – X-ray topography 179, 180
– detwinning 176, 190
– diagnostics of crystals 170
– differential interference contrast 180
– dislocation 181
– dispersed spots 189

– "equilibrium" defects 170
– etch figure analysis 172
– extra-planes 190
– hierarchy 171
– hillocks 173, 174, 179
– hollow core 173
– Hopper-like morphology 174
– inclusions (flux/foreign particle) 183, 185
– intergrowth 190
– macrocracks 179
– macrodefects 172
– macrospiral 173
– memory effect 209
– microcracks 174, 181
– microtopography 170
– mirror-like surfaces 180
– misfit dislocations 182
– misorientation angle within crystal body 180
– misoriented grains 177
– modulated structure 187, 207
– nanoscale composition fluctuations 187
– pinning centers 171, 207
– position occupancies 190
– screw dislocations 174
– stacking faults 190
– stress field in a crystal 181
– subgrains 179
– superstructure 162, 192, 193
– thermal shock 173, 197
– tweed structure 175, 177, 188
– twins 173
– – as-grown 176
– – behavior visualization 177
– – boundaries 194
– – onset of formation 176
– – twin-free crystals 152, 209
– – twins in a substrate 159
– wavy patterns 179
diffusion in single crystals
– cation diffusion 203
– chemical diffusion coefficients 201, 203
– crystallographic anisotropy 201
– fitting parameters 201
– intrinsic mechanism of oxygen diffusion 201
– oxygen diffusion 201
– oxygenation front movement 203
– self-diffusion coefficient 202
directional solidification
– anisotropy of growth 135, 136
– Bridgman methods 154
– growth rates 134
– interface morphology 134
– morphological changes 153, 155
– morphology of crystals 171
– Nd123 crystals 155
– planar front 154
– R123 crystals 154
– review 153
– rods, directionally solidified 171
– stability of planar interface 154
– textured in a microwave cavity 134
– traveling solvent floating zone (TSFZ) method 144
– – advantages 144
– – chain cuprates $SrCuO_2$, Sr_2CuO_3 169
– – important parameters 144
– – La123 crystals 151
– – $(Nd_{1.18}Ba_{1.53}Sr_{0.29}Cu_3O_z)$ crystals 152
– – Nd123 crystals 151, 172
– – peak effect 155
– – Sm123 crystals 151
– – spin-ladder $Sr_{14}Cu_{24}O_{41}$ 169
dislocations 181
double fluorite-type layers 34, 59–62
double mercury layers 55
double oxygen-deficient perovskite layers 34, 49
double perovskite layers 49
double rock-salt-type layers 52, 59
d-wave pairing 11
d-wave states 13
d-wave superconductivity 11
dynamical spin and charge stripe correlations 24

EDX analysis 188
Ehrenfest relation 468
elastic constants 472
electrical resistivities
– in-plane and perpendicular 18
– $\rho_{ab}(T)$ 16, 17, 20
– $\rho_c(T)$ 17
electron diffraction 42, 55
electron diffraction patterns 57
electron-doped cuprate superconductors 5
electron momentum
– density 426
– distribution 418
electron paramagnetic resonance 375–411
electron pattern 43

electron–hole symmetry 11
electronic phase separation 380, 381, 383
– $La_2CuO_{4+\delta}$ 381
electronic specific heat 13
electronic theory 453–486
$ErBa_2Cu_3O_{6+\delta}$ 409
$Er_2Ba_4Cu_7O_{15+\delta}$ 520, 521
$ErRh_4B_4$ 6
etching method 174
$EuBa_2Cu_3O_{6+\delta}$ 405
Eu_2CuO_4 393, 394
– crystal-field parameters 393
Eu(O)–Ba(O)–Cu(O) 301
$Eu_{1.10}Sr_{1.90}Cu_2O_{5.55}$ 35
$Eu_{1.30}Sr_{1.70}Cu_2O_{5.65}$ 35
$Eu_{1.40}Sr_{1.60}Cu_2O_{5.70}$ 35
exchange coupling parameters 529, 530, 532, 533
extended s-wave 13

4f state splittings 491–541
f–phonon interactions 534
Fehrenbacher–Rice model 479, 480, 483–485
Fermi energy 475
Fermi level 470
Fermi surface 426, 441, 444, 457, 473, 482
– $YBa_2Cu_3O_{7-\delta}$ 430
"fishtail" anomaly 433
floating particles 196
flux growth 143
– 124 and 247 homologues 168
– advantage 143
– crystals grown from flux 147
– disadvantage 143
– high-temperature solvents 147
– – molten hydroxide melt 168
– – solvent, ideal requirements 143
– problems 146
– Y123 single crystals 150
flux quantization 13
free-ion interactions 494
fullerene 458

$GdBa_2(Cu_{1-x}Ni_x)_3O_7$ 405
$GdBa_2Cu_3O_{6+\delta}$ 404–408
$GdBa_2Cu_3O_{6.05}$ 404
$GdBa_2Cu_3O_{7-\delta}$ 48
$GdBa_2Cu_3O_7$ 404
Gd_2BaCuO_5 380
Gd_2CuO_4 275, 393–395
– antiferromagnetic-resonance 393
Gd(O)–Cu(O) 280
Gd_2O_3–Cu_2O–O 279
$GdRuSr_2Cu_2O_8$ 6
$Gd_{1.10}Sr_{1.90}Cu_2O_{5.55}$ 35
$Gd_{1.30}Sr_{1.70}Cu_2O_{5.65}$ 35
$Gd_xY_{1-x}Ba_2Cu_3O_{6+\delta}$ 405, 406
Generalized Gradient Approximation (GGA) 473
generic phase diagram 23
g-factors 383, 385
grain boundary tunneling 14
growth mechanisms
– modes 82
– – screw dislocation 82
– – twin-plane re-entrant-edge growth 82
– – two-dimensional nucleation 82
g-shift 376, 377, 383, 385, 407
– in $Gd:YBa_2Cu_3O_{6.76}$ 406

$H[Cu_2]_\infty$ 39
HREM (high-resolution electron microscopy) 39, 45–47, 55, 57
Hall coefficient R_H 16
$HgBa_2Ca_2Cu_3O_8$ 4
$HgBa_2Ca_2Cu_3O_{8+\delta}$ 467
$HgBa_2La_2Cu_2O_{8+\delta}$ 55
$HgBa_2Nd_{1-x}Ca_xCu_2O_{6+\delta}$ 55
$Hg_{0.5}Bi_{0.5}Sr_2Ca_{1-x}Nd_xCu_2O_{6+\delta}$ 55
$Hg_{0.5}Bi_{0.5}Sr_2Ca_{0.65}Pr_{0.35}Cu_2O_{6+\delta}$ 55
$Hg_{0.5}Bi_{0.5}Sr_2Ca_{0.65}Y_{0.35}Cu_2O_{6+\delta}$ 55
$Hg_{0.5}Bi_{0.5}Sr_{2-x}La_xCuO_{4+\delta}$ 55
$Hg_{0.4}Ce_{0.5}Cu_{0.1}Sr_{2-x}La_xCuO_{4+\delta}$ 55
$Hg_{0.4}Ce_{0.5}Sr_{2.5}Ca_{0.5}Cu_{2.1}O_7$ 55
$Hg_{1.5}(Cu,Pr)_{0.5}Ba_2PrCu_2O_{8-\delta}$ 55
$Hg_{2-x}M_xBa_2Pr_2Cu_2O_{10-\delta}$ 58
$Hg_{1-x}M_xBa_2Y_{0.6}Ca_{0.4}Cu_2O_{6+\delta}$ 55
$Hg_{0.3}Pb_{0.7}Sr_2Ca_{0.7}Nd_{0.3}Cu_2O_7$ 55
$Hg_{0.3}Pb_{0.7}Sr_{2-x}La_xCuO_{4+\delta}$ 55
$Hg_{0.4}Pr_{0.6}Sr_2Ca_{1-x}Pr_xCu_2O_{6+\delta}$ 55
$Hg_{0.4}Pr_{0.6}Sr_2CuO_{4+\delta}$ 56
$Hg_{0.4}Pr_{0.6}Sr_{2.7}Pr_{0.3}Cu_2O_{6+\delta}$ 57
$Hg_{0.4}Pr_{0.6}Sr_{2-x}Pr_xCuO_{4+\delta}$ 55
$Hg_{0.4}Pr_{0.6}Sr_2Sr_{1-x}Pr_xCu_2O_{6+\delta}$ 55
high-frequency EPR 406
high p_{O_2} or oxidizing conditions 292, 293
high-resolution electron microscopy, *see* HREM
high-temperature superconductors
– normal-state properties 15–22
– overview 1–26

$(Ho_{0.33}Ce_{0.67})_3Sr_2Cu_3O_{11}$ 295
$HoMo_6S_8$ 6
hole concentration 516, 517
hole-doped cuprates 13, 459
holons 23
Hubbard model 456
hybridization 464, 465, 480, 482
– between Pr localized 4f states and valence-band states 5
hydrodynamics and computer simulation of crystal growth 125
– accelerated crucible rotation technique (ACRT) 126
– concave crystal–melt interface 126
– convection 123, 125
– – forced convection 126, 137
– – Marangoni convection 130
– – natural convection 126
– densities of Ba–Cu–O melts 126
– dimensionless analysis 128, 129
– fluid flow near a rotating disk 123
– governing equations 127
– heat transfers 126
– melt flow pattern 127
– meniscus 125, 138
– numerical simulation 127, 128
– solute pressure distribution 128
– surface tension 127
– three-phase boundary 126
– tie-line selection 124
– viscosity of the melts 126
hydrostatic pressure 468, 471

IBAD, *see* ion-beam assisted deposition
ideal single crystal 72, 170
idealized models 40, 44, 45
impurity phases 378
in-plane aligned YBCO coated conductors 25
incoherent *c*-axis conductivity 12
inelastic neutron scattering (INS) 499, 500
infinite layer cuprate 459
infrared absorption 20
(in)homogeneities 518–520
insulating behavior of $\rho_c(T)$ 18
interface between Y123 and Pr123 single crystals 185
interface kinetics 79
– cellular automata technique 80
– Jackson's parameter 98, 131
– Kossel's growth mechanism 81
– Periodic Bond Chain (PBC) concept 80
– – attachment energy 80
– – flat (F) faces 80
– – free bonds 80
– – lateral growth 80
– – morphologically more important faces 86
– – preferred sites for growth 80
– – stepped (S) faces 80
– thermodynamic roughening 79
intergrowth 32, 49, 59, 61, 62
– 1201–0201 54, 55
interlayer conductivity 12
interlayer hopping 464
internal strains 470, 471
ion-beam assisted deposition (IBAD) 25
isotope effect on T_c 11
isotope substitution 473

J_c 11
Josephson critical current I_c 15
Josephson effect 13, 14
Josephson tunneling measurements 20

k_z dispersion 464
k-dependence of the energy gap 20
Korringa relaxation 377, 390, 401
Korringa slope 390
Kossel's growth mechanism 80

LDA (local density approximation) 457, 460, 463–465, 475, 481
LDA + U 481, 482, 484
LPE, *see* liquid-phase epitaxy
LSCO 20, 23
$(La_{1-x}Ba_x)_2CuO_4$ 397
$(La_{1-x}Ba_x)_2SrCu_2O_{6+w}$ 334
$(La_{1-x}R'_x)_2CuO_4$, R′ = Dy, Tb and Gd 284
$(La_{1-x}R_x)_2CuO_{4+w}$ R = Sm, Eu, Gd, Tb, Dy, and Y 295
$(La_{1-x}Sr_x)_2Cu_{1-y}Mn_yO_4$ 398
$(La_{1-x}Sr_x)_8Cu_8O_{20-w}$ 291
$(La_{1-x}Sr_x)_2Cu_2O_5$; high pressure 293
$(La_{1-x}Sr_x)_2CuO_4$ 289, 291
$(La_{2-x}Sr_x)_2CuO_4$ 397
$(La_{1-x}Sr_x)_2SrCu_2O_{6+w}$ 291
$La_{2-x}A_{1+x}Cu_2O_{6-\delta}$ 34
$La_{2-x}A_xCuO_4$ 32
$La(Ba_{1-y-y'}Sr_yLa_{y'})_2Cu_3O_{6+w}$ 334
$LaBa_2Cu_3O_7$ 48
$La_{1-x}Ba_xCuO_4$ 403

$La_{2-x}Ba_xCuO_4$ 4
$La_2CaCu_2O_6$ 34
$La_2CaCu_2O_{6.04}$ 286
$LaCuO_{2.5}$ 9
$LaCuO_{3-w}$ 280
$La_2Cu_2O_{5+w''}$, $0.00 < w'' < 0.14$ 281
$La_5Cu_5O_{15-w'}$, $1.00 < w' < 1.90$ 281
$La_2Cu_{1-x}Zn_xO_4$ 379
La_2CuO_4 7, 32, 33, 276, 378, 393
La_2CuO_{4+w} 277
– low-temperature w–T diagram 277
$La_{2-x-y}Er_ySr_xCuO_4$ 392
$La_{2-x-y}Er_ySr_xCuO_{4+\delta}$ 391, 392
$La_{1.65}Eu_{0.24}Gd_{0.01}Sr_{0.1}Cu_4$ 391
$La_{2-x-y}Eu_ySr_xCuO_4$ 392
$La_2LuBa_3Cu_6O_{14+w}$ 329
$La_{2-x}M_xCuO_4$ 4, 5, 7, 9
$La_{1.48}Nd_{0.4}Sr_{0.12}CuO_4$ 24
$La_{1.6-x}Nd_{0.4}Sr_xCuO_4$ 24
$La_2Ni_{1-x}Cu_xO_4$ 380
La(O)–Ba(O)–Cu(O) 305, 306
La(O)–Ca(O)–Cu(O) 286, 288
La(O)–Cu(O) 274, 276
La(O)–Sr(O)–Cu(O) 289, 290, 293, 294
– high pressure 293
$La_6R'BaCu_8O_{20}$ 329
$La(Sr_{1-y}La_y)_2Cu_2O_{5+w}$ 292
$La_2Sr_{1-x}Ca_xCu_2O_6$ 35
$La_{2-x}Sr_xCaCu_2O_6$ 34
$La_{1-x}Sr_xCu_{1-y}Fe_yO_4$ 399
$La_{1.85}Sr_{0.15}Cu_{1-y}Fe_yO_4$ 400
$La_{1.85}Sr_{0.15}Cu_{0.973}Fe_{0.027}O_4$ 401
$La_{1.85}Sr_{0.15}Cu_{0.976}Fe_{0.024}O_4$ 402
$La_{2-x}Sr_xCu_{1-y}Fe_yO_4$ 400–402
$La_{1.7}Sr_{0.3}Cu_{1-y}Mn_yO_4$ 398, 399
$La_{1.8}Sr_{0.2}Cu_{0.98}Mn_{0.02}O_4$ 398
$La_{1+x}Sr_{2-x}Cu_2O_{5.5+\delta}$ 35
$La_{1.82}Sr_{0.18}(Cu_{1-x}Zn_x)O_4$ 379
$La_{1-x}Sr_xCuO_3$ 293
$La_{1.8}Sr_{0.2}CuO_4$ 397
$La_{1.85}Sr_{0.15}CuO_4$ 24
$La_{1.89}Sr_{0.11}CuO_4$ 403
$La_{2-x}Sr_xCuO_4$ 7, 11, 18, 24, 392, 396, 397, 441, 458
$La_{2-x}Sr_xCuO_{4+\delta}$ 381, 384, 388
– $La_{2-x}Sr_xCuO_4$ 390
– spin dynamics 390
– tetragonal phase 390
$La_{1.925}Sr_{0.075}CuO_4$ 382
$La_{2-x}Sr_xCuO_4$:Gd 389
lattice constants 35, 37, 470
– $Ln_{2-x}Sr_{1+x}Cu_2O_{6-x/2+\delta}$ 35
– oxides $La_{2-x}Ba_xCuO_{4-\delta}$ 33
– substituted mercury cuprates 55
lead cuprates 49
– copper disproportionation 50
linear expansivity 468
linear T-dependence of $\rho_{ab}(T)$ 18
linewidth 522
liquid-phase epitaxy (LPE) 133, 144
– basic principle 144
– critical current densities in LPE films 164
– crystal layers 161
– crystal orientation of films 163
– demands and restrictions for substrate materials 157, 158
– dipping techniques 161, 164
– homoepitaxy 144
– initial stages of growth 163
– investigation by atomic force microscopy 161
– island crystallite formation 163, 181, 184
– known substrate materials 157
– lattice misfit 158, 162
– layer-by-layer growth 157, 158, 163
– macrosteps 163
– monosteps 161
– $NdGaO_3$ perovskite material 177
– Nd123 layers 163
– oxide coated fibers 163
– practical importance 156
– preparation of high-quality seeds 156
– reviews 161
– surface roughness 163
– thermal expansion coefficient 158
$LnBa_2Cu_3O_{7-\delta}$ 8, 10, 11
$LnBa_2Cu_3O_7$ cuprates 47
$LnBa_{2-x}Ln_xCu_3O_{7+\delta}$ 48
Ln_2CuO_4 33
$Ln_{2-x}M_xCuO_{4-y}$ 7
$Ln_{2-x}M_xCuO_{4-y}$ (Ln = Pr, Nd, Sm, Eu; M = Ce, Th; $x \approx 0.1$–0.18; $y \approx 0.02$) 5
local density approximation, *see* LDA
local pairing of electrons (or holes) 23
local superstructures 39, 41, 42
low-temperature orthorhombic (LTO) phase 24
low-temperature tetragonal (LTT) phase 24
Löwdin perturbation theory 461
Lu(O)–Ba(O)–Cu(O) 295, 296

m-$CaCuO_2$ 256
MCu(O)–BaCu(O)–LaCu(O) 332
m-$R_2Cu_2O_5$, R = Nd and La 275
magnetic moment 515, 526, 539
magnetic ordering 533, 537
magnetic polaron 380, 383
magnetic susceptibility 20, 58, 433
maximum value of T_c 4
mean-field approximation 497, 498, 538, 539
mechanism of R123 crystal growth 89
– Ba partition ratio 117
– influence of additives 116
– – Ag 116, 149, 164
– – BaF_2 116, 149, 164
– interfacial phenomena 139
– liquid-phase epitaxy (LPE) 144
– liquidus curvature 119
– mass transport phenomena 121
– morphology of crystals 171
– Nd partition ratio 117
– primary crystallization field 114
– quantitative compositional relationships 116
– quasiternary phase diagram 124
– re-crystallization 139
– SRL–CP method 124, 145
– semisolid melt solidification 139
– spiral growth pattern 131
– steady state growth 123
– three-phase equilibrium point 117, 118
– tie-line selection 124
– traveling solvent floating zone (TSFZ) method 144
– Verneuil method 139
melt textured growth process 11
mercury bilayers 56
mercury cuprates 53
– $HgBa_2La_2CuO_{8+\delta}$ 54
– $Hg_{0.5}Bi_{0.5}Sr_2Ca_{1-x}Ln_xCu_2O_{6+\delta}$ 59
– $Hg_{0.5}Bi_{0.5}Sr_{2-x}La_xCuO_{4+\delta}$ 59
– $Hg_{1.5}(Cu,Pr)_{0.5}Ba_2PrCu_1O_{8-\delta}$ 56
– $Hg_{2-x}M_xBa_2Pr_2Cu_2O_{10-\delta}$ 56
– $Hg_{0.3}Pb_{0.7}Sr_{2-x}La_xCuO_{4+\delta}$ 59
– $Hg_{0.4}Pr_{0.6}Sr_2A_{1-x}Pr_xCu_2O_{6+\delta}$ 54
– $Hg_{0.4}Pr_{0.6}Sr_{2-x}Pr_xCuO_{4+\delta}$ 54
– $(Hg_{0.4}Pr_{0.6})Sr_2Sr_{1-x}Pr_xCu_2O_{6+\delta}$ 55
– $Nd_{1-x}Ca_xBa_2Hg_{1-x'}Cu_{2+x'}O_{6+\delta}$ 53
– $Y_{0.6}Ca_{0.4}Ba_2Cu_2(Hg_{1-x}M_x)O_{6+\delta}$ 53
MgO
– affecting T_c 183
– contamination 191
– dummy crystals 127
– impurities 94, 183
– precipitates 183, 185
– saturation concentration 196
– seeds 178
– single crystals 94
microwave penetration depth 11, 13
microwave surface conductivity 13
mixed valence of copper 36, 38

NMR (nuclear magnetic resonance)
– Knight shift 13, 20
– relaxation $1/T_1(T)$ 13
– spin–lattice relaxation rate 13, 20
Nb 10
Nb_3Ge 4
Nb_3Sn 10, 25
NbTi 10, 25
$(Nd_{1-x}Ca_x)_{1-y}CuO_2$ 285
$NdBa_2Cu_3O_{7-\delta}$ 48
$NdBa_2Cu_3O_7$ 482
$Nd_2Ba_4Cu_2O_9$ 305
$Nd_2Ca_2Cu_5O_{10}$ 285
$Nd_2CaCu_4O_8$ 285
$Nd_{2-x}Ce_xCuO_{4-y}$ 7, 11
$Nd_{2-x}Ce_xCuO_4$ 34, 441
$Nd_{2-x-y}Ce_xGd_yCuO_{4+\delta}$ 396
$NdCu_2O_4$ 281
$Nd_2Cu_2O_5$ 275
$Nd_{12}Cu_6O_{25}$ 281
$Nd_2Cu_{1-x}Zn_xO_4$ 379
Nd_2CuO_4 6, 7, 33, 276, 283, 396
Nd(O)–Ba(O)–Cu(O) 303, 304
Nd(O)–Ca(O)–Cu(O) 285, 287
Nd(O)–Cu(O) 274, 275
Nd213 phase 192
– insulating crystals 210
$NdSr_2Cu_2O_{5.66}$ 35
$NdSr_2Cu_2O_{5.76}$ 35
$Nd_{2-x}Th_xCuO_4$ 34
Nd123ss stability field 166
nearest-neighbor coupling 462
Néel temperature 515, 525, 526, 533, 537, 539
non-Fermi-liquid 459
non-stoichiometric oxides 37
nuclear magnetic resonance, *see* NMR
nucleation 73
– critical radius of nucleus 76
– 2D nucleation 83, 163
– driving force 74

nucleation (*cont'd*)
– Gibbs thermodynamic approach 74
– incubation or induction period 75
– metastable and labile zone 75
– metastable zone width 75, 165
– modeling of peritectic growth 76
– nucleation theories 75
– – cluster theory 76
– – Gibbs thermodynamic approach 75
– – phase-field model 76
– – spinodal decomposition 76
– two-dimensional nucleation 83

O–O hopping 462
o-$(R_{1-x}R'_x)_2BaCuO_5$ 327
o-R_2BaCuO_5, R = Lu, Yb, Tm, Er, Ho, Dy, Gd, Eu, Sm and Y 296
o-$R_2Cu_2O_5$, R = Dy–Lu, Y and Sc 275
o-R_2CuO_4, R = La 276
O s orbital 462
o-$SrCuO_{2+w}$ 257
"123" phases 35, 47, 48, 59
optical conductivity 480
optimal dopant concentration 11
– in $YBa_2Cu_3O_{7-\delta}$ 22
order parameter phase shift 15
over-doped 11
oxide carbonates 256
– Ba, Cu 267
– Ca, Ba, Cu 271
– Ca, Cu 256
– R 242
– Sr, Ba, Cu 272
– Sr, Cu 260
– Y, Ba 253
oxygen
– content 32
– ordering 40, 42
– stoichiometry 516
– vacancies 35, 39, 41, 43
oxygen-deficient
– perovskites 35, 44
– YBCO 20

PLD (pulsed laser deposition) 25
pairing 476
– mechanism 13
$PbBaSrY_{1-x}Ca_xCu_3O_{8-\delta}$ 51
$PbBaYSrCu_3O_{8-\delta}$ 51
$Pb_{2-x}Bi_xY_{1-y}Ca_yCu_3O_8$ 50
$Pb_2Sr_2Ca_{0.5}Y_{0.5}Cu_3O_8$ 50
$Pb_2Sr_{2-x}La_xCu_2O_{6+\delta}$ 50
$Pb_2Sr_2Ln_{1-x}Ca_xCu_3O_8$ 49
$Pb_2Sr_2R_{0.5}Ca_{0.5}Cu_3O_8$ 520
$Pb_2Sr_2R_{1-x}Ca_xCu_3O_8$ 500, 508
– Er 520
– Gd 526
– Ho 505, 507
– Nd 535, 537
– Pr 525–527
– Tb 514, 523, 537, 538
$Pb_{0.5}Sr_{2.5}Y_{1-x}Ca_xCu_2O_{7-\delta}$ 52
penetration depths 12
peritectic–eutectic reaction 107
phase diagrams
– for light rare-earth elements
– – melting reactions 109
– Y–Ba–Cu–O
– – monotectic reaction 149
phase diagrams of superconducting cuprates 229–355
– "anomalous" R123 113
– for light rare-earth elements 92
– – $BaCuO_2$–(Nd_2CuO_4 + CuO) section 101
– – construction of quasi-ternary phase diagrams 94
– – correct interpretation of phase relations 93
– – 3D model of phase relations 104–106
– – difficulties in phase formation 104
– – equilibrium solid-phase exchange 102
– – equilibrium tie-lines 93
– – high-temperature stable phase 93
– – incongruent melting points of R123 93, 99
– – liquidus curvature 119
– – liquidus curve of Nd 117
– – maximum melting/decomposition temperature 104
– – melting reactions 102
– – $Nd_4Ba_2Cu_2O_{10}$–($3BaCuO_2 + 2CuO$) section 101
– – peritectic–eutectic reaction 106
– – quasibinary sections 100
– – range of liquid compositions 106
– – two-phase coexistence region 101
– generic 23
– geometrical stability 98, 99
– Gibbs phase rule 91
– Pr 112
– – peritectic temperature of Pr123 113

- – $PrBaO_4$ phase 112, 122
- schematic diagrams 91
- second-periodicity phenomenon 112
- solid state 92
- substitution range 93
- tetragonal-to-orthorhombic second-order phase transition 177
- tetragonal–orthorhombic transition 174
- useful tools for optimizing 89
- visual representations 89
- Y–Ba–Cu–O
- – binary eutectics 90
- – calculated phase diagram 90, 91
- – characteristic features 92
- – decomposition temperature 91
- – expansion of the copper-rich liquid 90
- – green phase 93
- – liquid composition 90
- – melt-involved interactions 90
- – peritectic reaction 92
- – quasibinary Y_2BaCuO_5–("$Ba_3Cu_5O_8$") section 91
- – second liquid 90
- – ternary eutectics 90
- – univariant reactions 90
- – vertical section 90
- – $Y_2Cu_2O_5$ phases 101
- – Y132 phase 92
- – Y143 phase formation 90
- Yb 112
- – low-temperature stability boundary 114
- – peritectic temperature of Yb123 114

phonon interaction 522, 523
plane-chain hopping 465
Poisson's ratio 468
positron
- annihilation 417–445
- lifetime 424, 433

powder-in-tube technique 11
Pr 523–525
- f states 478

$PrBa_2Cu_3O_x$ 5
$PrBa_2Cu_3O_{7-\delta}$ 5
$PrBa_2Cu_3O_7$ 48, 323, 477–482, 485
$Pr_{2-x}Ce_xCuO_4$ 525
$(Pr_{1.5}Ce_{0.5})Sr_2Cu_2NbO_{10-\delta}$ 525, 526
PrF_3 478
$Pr_xNd_{1-x}Ba_2Cu_3O_7$ 485
PrO_w 242
PrO_2 478
Pr_2O_3 243, 244, 478
Pr_6O_{11} 478
Pr(O)–Ba(O)–Cu(O) 305
$Pr_{1-x}R_xBa_2Cu_3O_{7-\delta}$ 458
$Pr_xY_{1-x}Ba_2Cu_3O_7$ 485
pressure dependence of T_c 5, 473
progress in crystal size and perfection 211
pseudogap 20, 22
pulsed laser deposition, *see* PLD
p-wave superconductivity 9

quantum spin ladder materials 9
quasi-two-dimensional conductivity 459
quasiparticles (QP)
- bands 457, 458
- density of states (DOS) 21
- tunneling 13

R, R′(O)–Sr(O)–Cu(O) 295
R,R′(O)–Ba(O)–Cu(O) 326
$(R_{1-x}Ba_x)_2CuO_4$ 303
$(R_{1-x}Ca_x)_{1-y}CuO_2$, R = Y 285
$(R_{1-x}Ce_x)_2(Ba_{1-y}R_y)_2Cu_3O_{8-w}(O)_2$ 329
$(R_{1-x}Sr_x)_8Cu_8O_{20-w}$, R = Nd, Pr 293
R–Cu exchange interaction 532–534, 540
RABiTS (rolling assisted biaxially-textured substrates) 25
$R(Ba_{1-y}R_y)_2Cu_3O_{6+w+y}$, R = Gd, Eu, Sm, Nd, Pr, La 302
$RBa_2Cu_3O_x$ 500, 504, 505, 510, 520, 530
- Cm 525, 526
- Er 517–519
- Gd 523, 526
- Ho 504, 514, 517, 521, 528–530, 539
- Nd 535–537, 540
- Pr 525, 526
- Tb 522, 537
- Tm 521, 522
- $Y_{1-x}Ho_x$ 530–532
- Yb 505, 515

$RBa_2Cu_3O_{6+\delta}$
- crystal-field excitations 409
- crystal-field parameters 404

$RBa_2Cu_3O_{7-\delta}$ 5, 6
$RBa_2Cu_3O_7$ 477, 511, 515
- CEF parameters 506, 508
- chemical behaviour 334
- Cm 527
- defect chemistry approach 338
- energy-level schemes 509

$RBa_2Cu_3O_7$ (*cont'd*)
– geometrical factor 507
– ground-state wavefunction 512
– lattice-gas approach 343
– transition probabilities 513
$RBa_2Cu_4O_8$ 307, 501, 520
$R_2Ba_4Cu_7O_{14+w}$ 308
$R_2Ba_4Cu_7O_{14+x}$ 501
$RBa_4Cu_3O_{8.5+w}$, R = Lu, Yb, Tm, Er, Ho, Dy, Gd, Eu and Sm 297
$RBa_6Cu_3O_{10+w}$, R = Lu, Yb, Tm, Er, Ho, Dy, Gd, Eu and Sm 297
$RBa_2Cu_3O_{6+w}$; R = La–Yb 298
$R_{1-x}Ca_x(Ba_{1-y}La_y)_2Cu_3O_{6+w}$ 331
$(R_{1-x}Ca_x)Ba_2Cu_3O_7$ 330
$(R_{1-x}Ca_x)Ba_2Cu_4O_8$ 330
$RCa_2Cu_5O_{8+w}$, R = La 288
$R_{1-x}Ca_xCuO_4$
– Nd 502
$R_2CaCu_2O_6$ 286
$R_{1-x}Ce_xCuO_4$
– Pr 524
$R_{2-x}Ce_xCuO_4$ 500, 502–504, 511, 513, 532–534
– Cm 525, 526
– Gd 526
– Nd 502, 517, 533, 534
– Pr 520, 526, 532
$R_{1.4}Ce_{0.6}RuSr_2Cu_2O_{10-\delta}$ 6
r1113 crystals 152
$R_{4-4n}Cu_{8+2n}O_{14+8n}$ 275
$RCuO_2$, R = La, Pr, Nd, Eu, Y and Sc 279
RCu_2O_4, R = La–Lu 281
R(O)–Ba(O)–Cu(O) 324
– high oxidizing conditions 308
– moderate oxidizing conditions 295
– R = Gd, Eu 301
– reducing conditions 311
R(O)–Ba(O)–M,M′(O) 354
R(O)–Ba(O)–M(O) 352
R(O)–Ca,Ba(O)–Cu(O) 330
R(O)–Ca,Sr(O)–Cu(O) 329
R(O)–Ca(O)–Cu(O) 285
R(O)–Cu(O) systems 273
R(O)–Sr,Ba(O)–Cu(O) 333
R(O)–Sr(O)–Cu(O) 288
R(O)–Sr(O)–M,M′(O) 355
$R_{1-x}Pr_xBa_2Cu_3O_{7-\delta}$ 5
$(R_{1-x}R'_x)(Ba_{1-y}R'_y)_2Cu_3O_7$ 326
$(R_{1-x}R'_x)(Ba_{1-y}R'_y)_2Cu_4O_8$ 327
R123 single-crystal substrates 210
$RSr_2Cu_2O_6$ 292
$R_2Sr_6Cu_8O_{16}$ 291
$R_6Sr_2Cu_8O_{20}$ 291
$RSr_2Cu_3O_7(CeO_2)_2$ 295
$R_2SrCu_2O_6$ 291
RVB (resonating valence bond) model 16, 23
Raman scattering 13
Raman spectroscopy 11, 499, 533, 535
range of liquid compositions 108
rare-earth- and actinide-based cuprates 4
Rb_3C_{60} 9
reflectance $\mathcal{R}(\omega)$ measurements 11
resonating valence bond model, *see* RVB model
review of p_{O_2}–T–x pseudobinary phase diagrams 201
rolling assisted biaxially-textured substrates, *see* RABiTS
roughening temperature 138
Ruderman–Kittel–Kasuya–Yosida (RKKY) interaction 528

SQUIDs 10, 25
– SQUID interferometry 14
saddle points 476
– bifurcated 466
– extended 466
scanning tunneling spectroscopy 21
self-flux method 131, 148
– anisotropy in the step advancing velocity 174
– aspect ratio 133, 135, 148
– commonly used solvent 148
– density of the dislocation etch pits 174
– growth velocities of faces 134
– Hg-12(n – 1)n (n < 4) crystals 169
– high-gas-pressure technique 169
– isometric crystals 149
– isothermal growth 199
– leading-edge mechanism 134
– morphology 146, 171
– Nd123ss crystals 151, 152, 171, 172
– oscillatory thermal regime 149
– peak effect in Y123 crystals 205
– plate-like crystals 133
– $PrBa_2Cu_3O_{7-\delta}$ 152
– $PrBa_{2-x}Sr_xCu_3O_z$ crystals 152
– $R_{2-x}M_xCuO_4$ single crystals 169
– reviews 146
– self-flux growth 143

- separation of the grown crystals 148
- spiral steps 131
- thick crystals 149
- Tl-2223 crystals 169
- Tm123 crystals 149
- Y123 bicrystals 189
- Y123 crystals 149
- Y124 single crystals 169
semisolid melt solidification 139
- abbreviations 141
- anisotropy of growth 142
- cell-like inhomogeneities 142
- isothermal growth 140
- methods for creating supersaturation 140
- microstructural organization of precursors 140
- morphologies of melt textured Y123 phases 142
- - hillocks 142
- - macrospirals 142
- - pyramid-like growth patterns 142
- sample or furnace transport 140
- slow cooling 140
- top-seeded melt-texturing with constant undercooling 134, 135
single-crystal growth
- boundary layer 121, 123, 124, 130
- chemical and structural complexity 69
- classification of common techniques 139, 140
- common problems 69
- fundamental principles 72
- growth morphology 77
- - diffusion of solute 77
- - growth units attachment 77
- - latent heat of crystallization 77
- interfaces between phases 140
- motivations of single-crystal production 71, 209
- optimistic goal 71
- progress 146, 150, 211
- regions available for single-crystal growth 109
- shapes 171, 172
single fluorite-type layers 35, 59
single junction modulation 14
single perovskite layers 32, 49, 52
- oxygen-deficient 50
single rock-salt-type layers 32, 35, 49–51, 54, 62
sinusoidally modulated magnetic state 6
$Sm_{1.83}Ce_{0.17}CuO_{4-y}$ 17
Sm(O)–Ba(O) 251
$Sm_{1.10}Sr_{1.90}Cu_2O_{5.55}$ 35
$Sm_{1.30}Sr_{1.70}Cu_2O_{5.65}$ 35
solid solution 93
- empirical rule 112
- high-temperature modification of the Nd213 phase 111
- high-temperature XRD 102, 103
- "in-plane" ordering of Ba and Nd atoms 111
- maximal substitution 117
- $Nd_{1+x}Ba_{2-x}Cu_3O_z$ solid solution field 101, 106
- negative substitution 104
- oxygen nonstoichiometry 108
- - charge transfer 108
- - compositional ranges 111
- - copper valence 108, 112
- - p_{O_2}–T–x–z diagram 112
- - Raman spectra 111
- - relationship between the cation and oxygen nonstoichiometry 108
- - XANES spectra 111
- solidus of $Nd_{1+x}Ba_{2-x}Cu_3O_z$ in Arrhenius coordinates 104
- structural transformations 101, 111
- superconducting $Nd_{1.5}Ba_{1.5}Cu_3O_z$ 204
- supersaturated solid solution 208
- superstructure 102
- twin-plane-reentrant-edge growth 138
- "vertical" ordering of Nd and Ba 111
solubility of rare-earth elements in oxide fluxes 94
- Ba : Cu ratios 95
- bends in slopes 95
- copper valence 121
- direct solubility measurements 101
- equilibrium data collection 95
- heating and cooling DTA curves 115
- important factors for crystal growth 95, 96
- interrelations 98
- liquidus curvature 119, 136
- liquidus curve of Nd 117
- liquidus of R 95–97
- liquidus steepness 95
- methods of determination 94
- - dipping into the melt 94
- - high-temperature optical microscopy 94
- - liquid-phase epitaxy experiments 94

solubility of rare-earth elements in oxide fluxes – methods of determination (*cont'd*)
– – thermal analysis 94
– – visual-polythermal method 94
– Nd partition ratio 119
– Nd solubility data 95, 117
– peritectic temperature 95, 98
– polynomial regression analysis of the Nd concentration in the melt 117
– quasibinary assumption 98
– quasiternary phase diagram 124
– regular solution 98
– reproducibility 94
– thermodynamic parameters 98
– – congruent melting temperatures 98
– – dissolution enthalpy 98, 99
– – free energy of the peritectic reaction 98
– – thermal stability 98
– – thermodynamic stability 98
– XANES examination of molten state 119
– XANES of Ba–Cu–O fluxes 120
– yttrium liquidus lines 91, 95
specific heat 13, 20
spin and charge stripe phases 24
spin dynamics 377
spin fluctuations 377, 384, 386, 407
spin gap 386, 406
spin polaron 382, 383
spin pseudogap 23
spin susceptibility 407
spin–charge separation 23
spinodal decomposition
– Ba/Nd ratio fluctuation 188, 189
– demixing behavior 189
– – Bi–Pr–Sr–Ca–Cu–O 2212 superconductor 189
– – Nd123 crystal 188
– diagram of spinodally decomposing system 208
– macroscopically separated parts of 166
– modulated structure 207
– nanoscale composition fluctuations 188
– nanoscale EDX analysis 189
– oscillatory-increased copper concentration 189
– oxygen content microfluctuations 189
– peak effect 207, 208
– phase separation 189, 206
– theoretical model 76
spinons 23
spiral growth 83, 182, 183
– Archimedean shape 86
– Berg effect 87
– bunched steps 87, 88, 183
– Burton–Cabrera–Frank (BCF) theory 83
– composite spiral 86, 184
– dislocations with a screw component 83
– double-spiral growth steps 169
– eccentrical spirals 87
– elementary spiral steps 88
– fault line 87
– generators of elementary steps 83
– hollow core 87, 173
– independent spirals 86
– interacting spiral pattern 182
– macrospiral 173, 183, 184
– neighboring screw dislocations 86
– non-Archimedean spiral pattern 86
– polygonal spiral 86, 184
– re-entrant corners 87
– real crystal morphology 85
– rhythmic bunching pattern 87
– rounded spiral 183, 184
– screw dislocation mechanism 84
– spiral formations 182
– spiral steps coalesce 87
– square-shaped spirals 183
– step separation 86, 87, 132
$(Sr_{1-y}La_y)_{14}Cu_{24}O_{41}$ 289
Sr–Ba cuprates 272
$Sr_{0.4}Ca_{13.6}Cu_{24}O_{41.84}$ 9
$Sr_3Cu_2(CO_3)O_4$ 261
$SrCu_2O_2$ 259
$SrCu_2O_3$ 9
$Sr_2Cu_2O_5$ 9, 260
$Sr_{14}Cu_{24}O_{41}$ 258
$Sr_{n-1}Cu_{n+1}O_{2n}$ 260
$Sr_{1-y}CuO_2$ 260
Sr_2CuO_3 257
Sr_2CuO_{4-w} 259
$Sr_2CuO_2(CO_3)$ 260
$Sr_6Nd_3Cu_6O_{17}$ 35
$(Sr_{1-y}Nd_y)CuO_2$; high pressure 293
Sr(O)–Ba(O)–Cu(O) 273
Sr(O)–Ca(O)–Cu(O) 268–270
Sr(O)–Cu(O) 257–259
Sr(O)–R(O) 250
Sr_2RuO_4 9
steepness of the solidus 108
strain field 189

striations 88
– impurity distribution 88
– solute partition coefficient 89
– striation stripes 152
– types of concentration variations 88
strontium cuprates 257–261
structural defect 419
structural models
– $PbBaYSrCu_3O_7$ 51
– $(Y,Ca)_n(Ba,Sr)_{2n}Cu_{3n-1}O_{7n-3}CO_3$ 63
structure and charge carrier doping 6
structures
– 0201-type 54
– 1201-type 52, 54, 55
– 1212-type 52–55, 59
– 2212-type 56
– 2222-type 56
– 1201-type compound 53
substrate 166
substructure 455
superconducting energy gap 12
superconducting order parameter 11
superconducting pairing mechanism 11
superconducting penetration depth $\lambda(T)$ 13
superconducting phase transition 438
superconducting Pr123 phase
– explanations 156
– lattice constants 156
– preparation by TSFZ method 155
– reproduced 156
– superconductivity 155
superconducting wires and tapes 11, 24, 25
supercooling
– constitutional supercooling 76, 154
– interface stability 74, 77
– kinetic undercooling 81, 123, 136
– morphological perturbation 76
– pattern formation 77
superfluid density 12
supersaturation 136
– definition 74
– maximum 75
– nonideal solutions 75
– nonuniform 86
– relative 74
– supersaturation capability 98, 99
susceptibility 514, 515, 521, 539
s-wave 13
symmetry of the superconducting order parameter 12
TBCCO 15
t-$CaCuO_2$ 256
TLK (terrace–ledge–kink) model 85
– disappearance of the macrostep 88
– driving force 86
– growth terrace 85, 88
– kinetics of crystallization 86
– kinetics of the step bunching 88
– kink sites 81, 86
– lateral microscopic growth 85
– ledges 86
– local growth rates 88
– macrostep formation 88
– macrostep riser 88
– perpendicular macroscopic growth 85
– riser 85, 88
– terraces 163
– – decay 85
– tread 85
T1 phase 37
T2 phase 37
T3 phase 37
t-$(R_{1-x}Ba_x)_2BaCuO_5$, R = Nd, Pr, La 303
t-$(R_{1-x-x'}Ba_xR'_{x'})_2BaCuO_5$ 327
t-R_2CuO_4, R = Gd, Eu, Sm, Nd and Pr 275
t-$SrCuO_2$ 260
2D-ACAR (two-dimensional angular correlation of annihilation radiation) 457
thallium 61
thallium cuprates 52
– $TlBa_2Ca_{1-x}Y_xCu_2O_7$ 53
– $TlBa_2LnCu_2O_7$ 53
– $TlSr_2Ca_{1-x}Ln_xCu_2O_7$ 53
thallium monolayers 61
thermal conductivity 13, 15
thermodynamic data
– $BaCuO_{2.00}$ 267
– $BaCuO_2$ 321
– $BaCuO_{2+w}$ 267
– $BaCuO_{2.09}$ 267
– $BaCu_2O_2$ 267, 321
– Ba_2CuO_3 321
– Ba cuprates 266
– $CaCu_2O_3$ 256
– $Ca_{0.833}CuO_{1.93}$ 256
– Ca_2CuO_3 256
– Ca cuprates 256
– CeO_2 243, 244
– Ce_2O_3 243, 244
– Cu oxides 248

thermodynamic data (*cont'd*)
– $DyBa_2Cu_3O_7$ 323
– $DyBa_2Cu_4O_8$ 323
– Dy_2BaCuO_5 322
– $Dy_2Cu_2O_5$ 283
– Dy_2O_3 243, 244
– Er_2BaCuO_5 322
– $Er_2Cu_2O_5$ 283
– Er_2O_3 243, 244
– $EuBa_2Cu_3O_7$ 323
– $EuBa_2Cu_4O_8$ 323
– Eu_2BaCuO_5 322
– Eu_2CuO_4 283
– EuO 243, 244
– Eu_2O_3 243, 244
– Eu_3O_4 243, 244
– $GdBa_2Cu_3O_7$ 323
– $GdBa_2Cu_4O_8$ 323
– Gd_2BaCuO_5 322
– Gd_2CuO_4 283
– Gd_2O_3 243, 244
– $HoBa_2Cu_3O_7$ 323
– $HoBa_2Cu_4O_8$ 323
– Ho_2BaCuO_5 322
– $Ho_2Cu_2O_5$ 283
– Ho_2O_3 243, 244
– $(La_{1-x}Sr_x)_2CuO_{4-w}$ 293
– $(La_{1-x}Sr_x)_2CuO_4$ 294
– La_2CuO_4 283
– La_2O_3 243, 244
– $Lu_2Cu_2O_5$ 283
– Lu_2O_3 243, 244
– $NdBa_2Cu_3O_7$ 323
– Nd_2CuO_4 283
– Nd_2O_3 243, 244
– o-$Ba_2CuO_{3.3}$ 267
– $PrBa_2Cu_3O_7$ 323
– Pr_2O_3 243, 244
– R,Ba cuprates 319
– R_2BaCuO_5 322
– R cuprates 281
– $SmBa_2Cu_4O_8$ 323
– $SmCuO_2$ 282
– Sm_2CuO_4 283
– Sm_2O_3 243, 244
– $SrCuO_2$ 261
– $SrCu_2O_2$ 261
– $Sr_{14}Cu_{24}O_{41}$ 261
– Sr_2CuO_3 261
– Sr cuprates 260
– Tb_2O_3 243, 244
– t-$Ba_2CuO_{3.1}$ 267
– $TmBa_2Cu_3O_7$ 323
– Tm_2BaCuO_5 322
– Tm_2O_3 243, 244
– $YBa_2Cu_3O_6$ 321
– $YBa_2Cu_3O_{6+w}$ 341, 342
– $YBa_2Cu_3O_7$ 321, 323
– $YBa_2Cu_{3.5}O_{7.5}$ 321
– $YBa_2Cu_4O_8$ 321
– $YBa_2Cu_5O_9$ 321
– $YBa_4Cu_3O_{8.5}$ 321
– $Y_4Ba_3O_9$ 321
– Y_2BaCuO_5 321–323
– Y_2BaO_4 321
– $YCuO_2$ 282, 321
– $Y_2Cu_2O_5$ 283, 321
– Y_2O_3 243, 244
– Yb_2BaCuO_5 322
– $Yb_2Cu_2O_5$ 283
– Yb_2O_3 243, 244
thermodynamic properties 229–355
thermoelectric power $S(T)$ 20
thin films of $YBa_2Cu_3O_{7-\delta}$ 10
three-dimensional Fermi liquid behavior 17
tight-binding bands 463
tight-binding models 460, 461, 483
– minimal basis 459
$Tl_2Ba_2CaCu_2O_8$ 442
$[TlO]_\infty$ monolayers 52
$Tl_{1-x}Pr_xSr_{2-y}Pr_yCuO_{5-\delta}$ 52
tricrystal ring magnetometry 14
triple oxygen-deficient copper layers 51
triple perovskite layers 62
triple rock-salt-type layers 61
twin boundaries 44, 45
twin-plane-reentrant-edge growth (TPRE) 139
twinning domains 42–45, 174
two-dimensional character 36

ultrasonic attenuation coefficient $\alpha_s(T)$ 13
under-doping 11
uniaxial strain 459, 466, 468–470, 473–476
uniaxial stress 468–470
upper critical field $H_{c2}(T)$ 10

valence bond sums 468
van Hove singularities (vHs) 470, 475
vortex phases 12

whiskers 153
– Bi–Sr–Ca–Cu–O system 153
– Nd–Ba–Cu–O system 153
– needle-like crystals 171, 172
– production technique 153
– $SmBa_2Cu_3O_{7-\delta}$ (needle) crystals 153

Y123 91
$(Y,Ca)_n(Ba,Sr)_{2n}Cu_{3n-1}O_{7n-3}CO_3$ 62
Y–Cu–O 278
YBCO-123 15, 20, 23
YBCO-124 20, 23
YBCO coated samples 25
YBCO crystals 165
YBCO tapes 25
$Y(Ba_{1-y}Sr_y)_2Cu_3O_{6.95}$ 333
$Y(Ba_{1-y}Sr_y)_2Cu_4O_8$ 333
$YBa_2(Cu_{1-z}M_z)_3O_{6+w}$
– equilibrium phase compositions 350
$YBa_2(Cu_{1-z}M_z)_3O_{6+w}$ (M = Fe, Co, Mg/Ni/Zn) 351
$YBa_2Cu_{3-u}(CO_3)_uO_{6+w-3u/2}$ 318
$YBa_2Cu_3O_6$ 37
$YBa_2Cu_3O_{6+\delta}$ 384, 386, 387, 404, 409
– lower critical field 388
– orthohombic phases 386
$YBa_2Cu_3O_{6+w}$
– carbonatization 336
– isotherms 340, 343
– low-temperature w–T diagram 300
– reduction by high temperatures 315
– reduction by low p_{O_2} 312
$YBa_2Cu_3O_{6+x}$ 433, 480
$YBa_2Cu_3O_{6.3}$ 37
$YBa_2Cu_3O_{6.50}$
– redox 337
$YBa_2Cu_3O_{6.76}$ 406
$YBa_2Cu_3O_{6.8}$ 385
$YBa_2Cu_3O_{7-\delta}$ 5, 11, 37, 48, 426
$YBa_2Cu_3O_7$ 35, 455, 457–460, 462, 465, 466, 469, 472, 474, 475, 477, 480, 482
– copper disproportionation 38
– electron microscopy 39
– extended defects 46
– Fermi surface 460, 462
– isostructural triple perovskites 352
– microtwinning 42
– oxygen nonstoichiometry 37
– oxygen ordering 39
– structural and chemical variants 345
– substitution
– – by halogen 348
– – by hydrogen, proton and hydroxyl 345
– – by metal except A and R 348
– superconducting domains 39
$YBa_2Cu_4O_8$ 47, 48, 407, 408
– reduction by low p_{O_2} 311
$YBa_4Cu_3O_{9.2}$ 297
$YBa_6Cu_3O_{10.2}$ 297
$Y_2Ba_4Cu_7O_{15}$ 48
$YBa_2Cu_4O_8$, p–t diagram 309
$YBa_2Fe_3O_{8+w}$ 352
$Y_2(Ba_{1-y}Sr_y)CuO_5$ 333
Y_2BaCuO_5 378, 380
$(Y_{1-x}Ca_x)Ba_4Cu_3O_9$ 331
$Y_{1-x-y}Ca_yPr_xBa_2Cu_3O_{7-\delta}$ 17
$Y_2Cu_2O_5$ 275
YCu(O)–BaCu(O)–YFe(O)–BaFe(O) 354
$Y_{0.97}Er_{0.03}Ba_2Cu_3O_{6+\delta}$ 409
^{89}Y Knight shift 406, 407
Y(O)–Ba(O) 252
Y(O)–Ba(O)–Cu(O) 298, 307, 310, 311, 314, 324
– high pressure 316
$YO_{1.5}$–BaO–CuO–$CuO_{0.5}$ 312
Y(O)–Ca(O)–Cu(O) 285, 286
Y(O)–Cu(O) 274, 278
Y(O)–La(O)–Ba(O)–Cu(O) 327
Y(O)–Nd(O)–Ba(O)–Cu(O) 327, 328
Y(O)–Sr(O)–Ba(O)–Cu(O) 333
Y(O)–Sr(O)–Cu(O) 288, 289, 292
$Y(O/CO_3)$–$Ba(O/CO_3)$ 254
$Y(O/CO_3)$–$Ba(O/CO_3)$–$Cu(O/CO_3)$ 316, 317
$Y_{1-x}Pr_xBa_2Cu_3O_{7-\delta}$ 5, 17, 19, 20
$Y_{1-x}Pr_xBa_2Cu_3O_7$ 477, 478
$Y_{1-x}Pr_xBa_2Cu_4O_8$ 6
$YSr_2Cu_3O_w$ 292
Y substitution: $(Y_{1-x}R_x)Ba_2Cu_3O_{7-\delta}$ 440